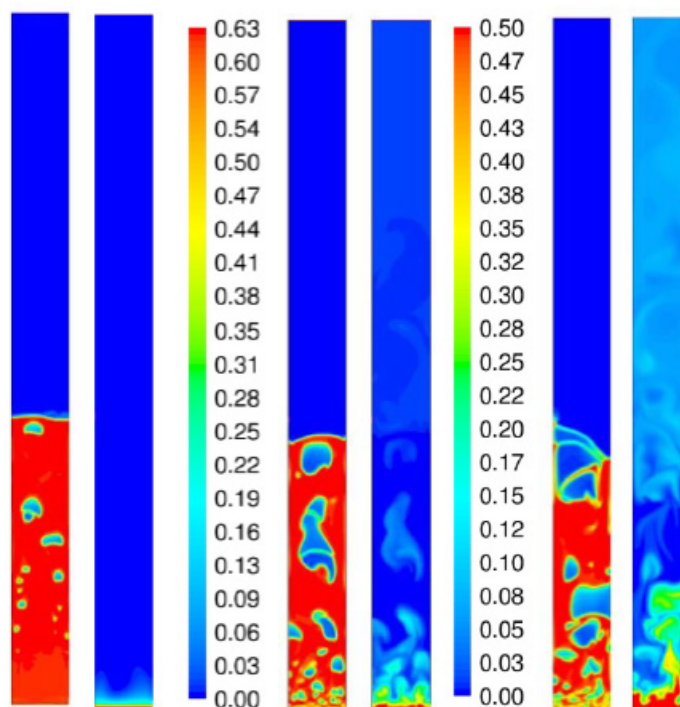# Report

Proceedings of the 8th International Conference on CFD in Oil & Gas, Metallurgical and Process Industries

Editors
Jan Erik Olsen
Stein Tore Johansen

SINTEF Materials and Chemistry
Process Technology
2012-03-23

Report

Proceedings of the 8th International Conference on CFD in Oil & Gas, Metallurgical and Process Industries

ABSTRACT

This report is the proceedings of 8th International Conference on CFD in Oil & Gas, Metallurgical and Process Industries hosted by SINTEF and NTNU (Norwegian University of Science & Technology) in Trondheim, June 2011.

SINTEF

Document history

VERSION	DATE	VERSION DESCRIPTION
1.0.	2012-03-23	Official proceedings from CFD2011

Table of contents

PROJECT NO.
801665

REPORT NO.
Report No.

VERSION
1.0

1 PREFACE

This document defines the proceedings of the 8th International Conference on Computational Fluid Dynamics in the Oil & Gas, Metallurgical and Process Industries. The conference was hosted by SINTEF and the Norwegian University of Science and Technology (NTNU) in Trondheim, Norway 21-23 June 2011. It was truly an international conference with 130 participants representing 22 nations. There were 96 technical presentations and 6 keynote lectures at the conference. They were organized in sessions such as multiphase pipe flows, fluidized beds, population balance, oil & gas applications, furnace modeling and more. A special topic at this conference were biomechanics focusing on fluid flow and modeling on phenomena such as blood flow, hearth mechanics and larynx dynamics often involving fluid structure interactions. Some presentations where not accompanied by a scientific paper and the keynote presentations where not processed through a referee assessment. These are not reproduced here, since the proceedings only include the papers approved by 2 referees.

The editors would like to thank our staff for organizing the conference and all presenters and reviewers for ensuring a high quality conference.

Stein Tore Johansen
Jan Erik Olsen

LIST OF PAPERS

Paper 060:
INSOLUBLE SURFACTANT EFFECTS ON EMULSION COARSENING IN A GRAVITATIONAL FIELD VIA PHASE-FIELD TERNARY MIXTURE MODEL, A.Lamorgese & S.Banerjee

Paper 064:
INCLUSION ELIMINATION IN STEELMAKING LADLE, P.Gardin, M.Simonnet & S.Gauthier

Paper 083:
NUMERICAL SIMULATION OF AN HORIZONTAL COUNTER-CURRENT TWOPHASE FLOW EXPERIMENT USING AN INTERFACIAL AREA DENSITY MODEL, T.Höhne, Deendarlianto, D.Lucas

Paper 084:
A CFD STUDY OF THE EFFECT OF THE CYCLONE BARREL HEIGHT ON ITS PERFORMANCE PARAMETERS, K.Elsayed & C.Lacor

Paper 085:
CFD MODELLING OF MAGNETIC STIRRING AT PV-SILICON CRYSTALLISATION, N.Dropka, U.Rehse & P.Rudolph

Paper 086:
MODELLING DISPERSION OF A HIGHLY LADEN POWDER JET, S.Puttinger, S.Pirker, H.Stocker & Arno Habermann

Paper 087:
MODELLING FLOW INDUCED AOD-CONVERTER SLOSHING BY ANALYTICAL CONSIDERATIONS, NUMERICAL SIMULATION AND COLD WATER EXPERIMENTS, S.Pirker, A.Aigner & G.Wimmer

Paper 088:
INFLUENCE OF POST COMBUSTION ON CHARACTERISTICS OF OXYGEN JET IN BOF, A.Kaizawa, N.Sasaki, T.Inomoto & Y.Ogawa

Paper 091:
A MODEL OF PARTICLE DEPOSITION ON A VERTICAL WALL FOR THE PARTICLE-WALL STICKING PROBABILITY LOWER THAN ONE, D.Eskin, J.Ratulowski & K.Akbarzadeh

Paper 092:
LARGE EDDY SIMULATION OF PARTICLE-LADEN SWIRLING FLOW WITH A PRESUMED FUNCTION METHOD OF MOMENTS, P.Dems, J.N.E.Carneiro & W.Polifke

Paper 093:
MODELING OF A GAS-LIQUID SLUG FLOW ACCOMPANIED WITH MASS TRANSFER THROUGH A LONG MICROCHANNEL, D.Eskin & F.Mostowfi

PROJECT NO.
801665

REPORT NO.
Report No.

VERSION
1.0

Î Á Ḣ

Paper 094:

LATTICE BOLTZMANN MICROCHANNEL SIMULATIONS VIA BINARY LIQUID MODEL, A.Kuzmin, D.Eskin & J.Derksen

Paper 095:

INTEGRATED CFD AND PROCESS MODELLING FOR IMPROVED PROCESS DESIGN, A.Runstedtler, P.Boisvert, A.J.Majeski, H.Gao & D.Tisdale

Paper 096:

HIGH ORDER NUMERICAL SIMULATION OF FLUID-STRUCTURE INTERACTION IN THE HUMAN LARYNX, M.Larsson & B.Müller

Paper 097:

A FLOWMETER BASED ON THE MEASUREMENT OF THE LOCAL HEAT TRANSFER COEFFICIENT AT THE FORWARD STAGNATION POINT OF A HEATED SPHERE PLACED IN A TURBULENT PIPE FLOW USING A MICRO-FOIL HEAT FLOW SENSOR, H.Koizumi & N.Imamura

Paper 099:

CFD MODELING STUDY OF A REFINERY HEATER AND COMPARISON TO FIELD DATA, A.Runstedtler, X.Landry & D.Brunet

Paper 100:

THE CHARACTERISTICS OF FLOW AND HEAT TRANSFER IN A CIRCULATING FLUIDIZED BED REACTOR, H.S.Choi & Y.S.Choi

Paper 101:

MECHANISTIC MODELLING OF PARTICLE-INTERFACE INTERACTION IN THREE-PHASE FLOWS, G.Wierink, C.Goniva, B.Niceno & K.Heiskanen

Paper 102:

NUMERICAL SIMULATION OF MULTIPHASE FLOWS OF CO2 STORAGE IN SALINE AQUIFERS IN DAQINGZIJING OILFIELD, CHINA. D.X. Yang, R.S. Zeng, Y. Zhang & C. Jin

Paper 103:

NUMERICAL STUDY OF THE WALL EFFECT ON THE LIQUID DISTRIBUTION IN A TRICKLE-BED REACTOR, M. Martinez, J. Pallares, A. Lopez, M.A. Garzia & F.X. Grau

Paper 104:

COMPARISON BETWEEN DIFFERENT METHODS FOR TURBULENT GAS-LIQUID SYSTEMS BY USING MULTIVARIATE POPULATION BALANCES, A. Buffo, M Vanni, D.L. Marchisio & R.O. Fox

Paper 106:

MODELING OF MASS- AND MOLE BASED MULTICOMPONENT DIFFUSION MODELS IN POROUS PELLETS FOR STEAM METHANE REFORMING PROCESS, K.R. Rout & H.A. Jakobsen

Paper 107:
CFD SIMULATIONS AND MEASUREMENTS OF THE INLINE PHASESPLITTER:
A COMPACT GAS / LIQUID SEPARATOR, R.W. Westra, E. De Haas, O.F. Salazar & B. Ibouhouten

Paper 108:
INVESTIGATION OF A FRICTIONAL PARTICLE-PARTICLE DRAG COEFFICIENT IN
A DENSE BINARY FLUIDIZED BED, Z. Chao, Y. Wang, J.P. Jakobsen, M. Fernandino & H.A. Jakobsen

Paper 109:
SOLUTION OF THE POPULATION BALANCE EQUATION USING THE
NORMALIZED QMOM (NQMOM), M. Attarakih, J. Kuhnert, T. Wächtler, M. Abu-Khader & HJ Bart

Paper 111:
HISTORY FORCE AND DRAG CORRELATION IN A LAGRANGIAN METHOD APPLIED
TO OIL-WATER SEPARATION, D.F Van Eijkeren & H. W.M Hoeijmakers

Paper 113:
CFD SIMULATION OF BUBBLY FLOW BASED ON THE DUAL-BUBBLE-SIZE
MODEL, Z. Wu, N. Yang, J. Chen & J. Li

Paper 115:
TESTING OF OPENFOAM CFD CODE FOR PLANE TURBULENT BLUFF BODY FLOWS WITHIN
CONVENTIONAL URANS APPROACH, D.A. Lysenko, I.S. Ertesvåg & K.E. Rian

Paper 116:
MODELLING AND CFD SIMULATION OF A FLUIDIZED BED REACTOR TO CAPTURE
CO_2 BY SOLID SORBENTS, M. Molaei, K.A. Pericleous & M.K. Patel

Paper 117:
CONSTRAINED REINITIALISATION OF THE CONSERVATIVE LEVEL SET METHOD, C. Walker &
B. Müller

Paper 118:
A STRONG FSI COUPLING SCHEME FOR SIMULATING BMHV DYNAMICS:
STUDY OF WALL SHEAR STRESS ON THE VALVE LEAFLETS, S. Annerek, J. Degroote, T.
Claessens, S.K. Dahl, B. Skallerud, L.R. Hellevik, P. van Ransbeeck, P. Segers, P. Verdonck & J.
Vierendeels

Paper 119:
NUMERICAL SIMULATION OF LARGE BUBBLES IN CHANNELS USING A FRONTTRACKING
METHOD, N. Hor, J. Hua, C.J. Lawrence & D.M. Spelt

Paper 120:
TECHNICAL APPLICATION OF A MULTIPHASE SOLVER IN THE COMPRESSIBLE FLOW OF A
GASEOUS AND A LIQUID PHASE, J. Nagy, C. Jordan & M. Harasek

Paper 121:
IN-LINE OIL-WATER SEPARATION IN SWIRLING FLOW, J.J. Slot, L.J.A.M. van Campen, H.W.M.
Hoeijmakers & R.F. Mudde

PROJECT NO.
801665

REPORT NO.
Report No.

VERSION
1.0

Ì Á -Á H́ Á

Paper 122:

CFD SIMULATION OF A HIGH TEMPERATURE FURNACE, J. Nagy, A. Horvath, C. Jordan & M. Harasek

Paper 124:

PARCEL-BASED APPROACH FOR THE SIMULATION OF GAS-PARTICLE FLOWS, S. Radl, C. Radeke, J.G. Khinast & S. Sundaresan

Paper 125:

A CFD STUDY OF ENTRAINED-FLOW GASIFIERS USING TWO FEED TYPES, V. Speedharan, B.H. Hjertager & T. Solberg

Paper 126:

IMPLEMENTATION OF THE QUADRATURE METHOD OF MOMENTS IN A 3D
CFD PIPE GEOMETRY FOR GIBBSITE PRECIPITATION, K. Hutton, D.W. Stephens & I. Livk

Paper 127:

EFFICIENT SOLUTION METHOD FOR THE STOKES EQUATIONS WITH VARIABLE VISCOSITY AND PERIODIC BOUNDARY CONDITIONS, J.S.B. van Zweiten, M.B. van Gijzen, C. Vuik, J. van Male & J.G.E.M. Fraaije.

Paper 128:

NUMERICAL SIMULATION OF SINGLE ELONGATED BUBBLE PROPAGATION IN INCLINED PIPES, J. Hua, M. Langsholt & C. Lawrence

Paper 129:

AN IMPROVED ROE SOLVER FOR THE DRIFT-FLUX TWO-PHASE FLOW MODEL, G.A. Reigstad & T. Flåtten

Paper 131:

APPLICATION OF THE LEAST-SQUARES METHOD TO THE MULTISCALE TRANSPORT EQUATION IN POROUS MEDIA, F. Sporleder & P.M. Dupuy

Paper 132:

STUDY OF THE STEEL/SLAG INTERFACE INSTABILITY AND THE INFLUENCE OF INJECTED GAS IN THE CONTINUOUS CASTING OF STEEL, Z. Kountour, K. Pericleous, G. Djambazov, J.F. Domgin & P. Gardin

Paper 133:

POPULATION BALANCE MODELLING OF ISOTHERMAL BUBBLY-CAP FLOWS USING TWO-GROUP AVERAGED BUBBLE NUMBER DENSITY APPORACH, S.C.P. Cheung, G.H. Yeoh, J.Y. Tu, E. Krepper & D. Lucas

Paper 135:

ON THE MODELLING OF ANODIC BUBBLES IN HALL-HÉROULT CELLS, K.E. Einarsrud & S.T. Johansen

PROJECT NO.
801665

REPORT NO.
Report No.

VERSION
1.0

JÁ -Ã HÍ Á

Paper 136:

UNSTRUCTURED MESH OF A DISC USING MULTIPLE TRANSFINITE MAPPINGS, F. Sporleder, C.A. Dorao & H.A. Jakobsen

Paper 137:

CFD MODELING OF SILICA FUME FORMATIONDURING REFINING OF SILICON METAL, J.E. Olsen, M. Næss & G. Tranell

Paper 140:

DIRECT NUMERICAL SIMULATION OF TWO-FLUID FLOWS WITH A LEVEL-SET METHOD, K. Voronetska, G. Vinay, A. Wachs & J.P. Caltagirone

Paper 141:

A MULTI-PURPOSE OPEN SOURCE CFD-DEM APPROACH, C. Goniva, C. Kloss, A. Hager, G. Wierink & S. Pirker

Paper 142:

APPLICATION OF A COMBINED CFD/EXPERIMENTAL APPROACH TO QUANTIFYING EROSION RATE, C.B. Solnordal & C.Y. Wong

Paper 143:

EFFECT OF NATURAL CONVECTION ON THE HEAT TRANSFER FOR A COLD SPOT IN A SUBSEA PIPELINE DURING SHUT-IN, B.H. Sannæs

Paper 144:

LIGGGHTS Open Source DEM: Models, Features, Parallelism and Quality Assurance, C. Kloss, C. Goniva, S. Amberger & S. Pirker

Paper 145:

INVESTIGATIONS OF TRANSITIONAL FLOWS USING IMAGE BASED HEMODYNAMICS, K. Valen-Sendstad, M. Mortensen, KA. Mardal, B.A: Pettersson Reif & H.P. Langtangen

Paper 146:

NUMERICAL MODELLING OF OIL SPILL RESPONSE ACTIONS, FLOATING BOOM, K. Aghajanloo & M.D. Pirooz

Paper 147:

INVESTIGATION OF TWO-PHASE SLUG FLOW IN A RISER USING PHYSICAL AND NUMERICAL SIMULATIONS, M. Abdulkadir, V. Hernandez-Perez, I. Lowndes & B.J. Azzopardi

Paper 148:

GPU-ACCELERATED LARGE-SCALE CFD-DEM COUPLING SIMULATION OF THREE-DIMENSIONAL GAS-SOLID FLUIDIZED BED, F. Chen, W. Ge & J. Li

Paper 149:

COMPARISON OF CFD TOOLS FOR MULTIPHASE FLOW APPLICATIONS, A. Singh, R. Menon & R. Henkes

Paper 150:

CFD MODELING OF TAPPING PROCESS IN FERROMANGANESE FURNACES, M. Kadkhodabeigi, H. Tveit & S.T. Johansen

PROJECT NO.
801665

REPORT NO.
Report No.

VERSION
1.0

F€Á -ÃĤÁ

PROJECT NO.
801665

REPORT NO.
Report No.

VERSION
1.0

FFÁ -Ã HÍ Á

Paper 164:
ANALYSIS OF NON-ROUND PARTICULATE MIXING IN A PLOUGH SHARE MIXER USING DEM, P.W. Cleary

Paper 165:
THREE DIMENSIONAL COUPLED DISCRETE ELEMENT-CFD MODELLING OF HIGH SPEED GAS-PARTICLE RACEWAY DYNAMICS, J.E: Hilton & P.W. Cleary

Paper 166:
DUST DISPERSAL MODELLING ON A CONVEYOR CHUTE USING A COUPLED DISCRETE ELEMENT AND CFD METHOD, J.E. Hilton & P.W. Cleary

Paper 167:
ADVANCES IN THE SIMULATION OF MULTIPHASE FLOWS IN PIPELINES, D. Lakehal, M. Labois & C. Narayanan

Paper 168:
UNDERSTANDING VISCOUS FLUID TRANSPORT AND MIXING IN A TWIN SCREW EXTRUDER, P.W. Cleary & M. Robinson

Paper 169:
EULER–LAGRANGE MODELING OF MELTING AND SOLIDIFICATION WITH MOVING SOLID PARTICLES, F. Dierich & P.A. Nikrityuk

Paper 170:
A NUMERICAL AND EXPERIMENTAL STUDY OF HYDRODYNAMIC BEHAVIOR OF BISOLID CIRCULATING FLUIDIZED BEDS, N. Nouyrigat, E. Bouquet, O. Simonin & V. Lalam

Paper 171:
INTERPENETRATING CONTINUA AND MULITIPHASE TURBULENCE, C.A. Petty & S. Muthu

Paper 172:
CFD SIMULATION OF HYDROCYCLONE PERFORMANCE UNDER DILUTE OPERATING CONDITIONS, A. Davailles, E. Climent & F. Bourgeois

Paper 173:
DESIGN OF A CHEMICAL LOOPING COMBUSTION SYSTEM USING PROCESS SIMULATION AND COMPUTATIONAL FLUID DYNAMICS, S. Cloete & S. Amini

Paper 174:
3D NUMERICAL STUDY OF THE INFLUENCE OF PARTICLE POROSITY ON THE HEAT AND FLUID FLOW, K. Wittig, A. Golia & P.A. Nikrityuk

Paper 176:
CFD SIMULATION OF BATH DYNAMICS IN THE HISMELT SMELT REDUCTION VESSEL FOR IRON PRODUCTION, D. Stephens, M. Tabib, M. Davis & P. Schwarz

Paper 177:
EFFECT OF SIO COMBUSTION ON NOX EMISSION: THEORY AND VALIDATION, B. Panjwani, S. Andersson & H. Midtdal

PROJECT NO.
801665

REPORT NO.
Report No.

VERSION
1.0

FG Ĺ -Ä Hĺ Á

Paper 178:
FLUID MOTION FOR MICRO-GRAVITY SIMULATION IN A RANDOM POSITIONING MACHINE, C.A.D. Leguy, R. Delfos, M.J.B.M. Pourquie, C. Poelma, J. Krooneman, J. Westerweel & J.J.W.A. van Loon

Paper 184:
THREE DIMENSIONAL NUMERICAL SIMULATION OF BUBBLE AND DROPLET DYNAMICS WITH A PARALLEL PARTICLE LEVEL SET SOLVER, H. Bihs

Paper 195:
ANALYSIS OF SUB-SEA GAS RELEASE BY AN EULERIAN-LAGRANGIAN MODELLING CONCEPT, P. Skjetne & J.E. Olsen

Day 1 (Tuesday, June 21)

Morning sessions: 8:55 – 13:15

Time	AUDITORIUM R5	AUDITORIUM R7	AUDITORIUM R8	AUDITORIUM R9
8:00 – 8:30	Registration			
8:30 – 8:55	Opening			
8:55 – 9:40		**Keynote:** Jos Derksen, Univ.of.Alberta DENSE SUSPENSIONS – THE RICHNESS OF SOLID-LIQUID INTERACTIONS AT THE PARTICLE SCALE		
9:45-11:15	**Session R5-01: Furnace Modelling** Chairman: Alireza Ashrafian	**Session R7-01: Oil-water Separation** Chairman: Jos Derksen	**Session R8-01: Gas-Particle Flows** Chairman: Gerald Pereira	**Session R9-01:Population Balance** Chairman: John Morud
9:45-10:15	Lead paper: 122: CFD SIMULATION OF A HIGH TEMPERATURE FURNACE, Harasek, Nagy, Horvath & Jordan	Lead Paper: 060: INSOLUBLE SURFACTANT EFFECTS ON EMULSION COARSENING IN A GRAVIT-ATIONAL FIELD VIA PHASE-FIELD TERNARY MIXTURE MODEL, Lamorgese & Banerjee	Lead paper: 086: MODELLING DISPERSION OF A HIGHLY LADEN POWDER JET, Pirker, Puttinger & Habermann	Lead paper: 109: SOLUTION OF THE POPULATION BALANCE EQUATION USING NQMOM, Attarakih, Kuhnert, Wächtler, Abu-Khader & Bart
10:15-10:35	095: INTEGRATED CFD AND PROCESS MODELLING FOR IMPROVED PROCESS DESIGN Runstedtler, Boisvert, Majeski, Gao & Tisdale	111: HISTORY FORCE AND DRAG CORRELATION IN A LAGRANGIAN METHOD APPLIED TO OIL-WATER SEPARATION, van Eijkeren & Hoeijmakers	91: A MODEL OF PARTICLE DEPOSITION ON A VERTICAL WALL FOR THE PARTICLE-WALL STICKING PROBABILITY LOWER THAN ONE, Eskin, Ratulowski, & Akbarzadeh	902: EULERIAN EQUILIBRIUM LES MODEL FOR POLYDISPERSED PARTICLE LADEN CHANNEL FLOW, Icardi, Marchisio & Narayanan
10:35-10:55	151 : THE APPLICATION OF CFD AND OVEN DESIGN OPTIMISATION IN THE BRITISH BREAD-BAKING INDUSTRY, Khatir, Thompson,Kapur,Toropov,Paton & Lawes	906: HYDRODYNAMIC STUDY OF A CONTINUOUS HORIZONTAL LIQUID-LIQUID SETTLER, Salim,Masbernat, Roig & Bech	142: APPLICATION OF A COMBINED CFD/EXPERIMENTAL APPROACH TO QUANTIFYING EROSION RATE, Solnordal & Wong	090: IMPLEMENTATION OF THE QUADRATURE METHOD OF MOMENTS IN A 3D CFD PIPE GEOMETRY, Hutton, Stephens & Livk
10:55-11:15	088: INFLUENCE OF POST COMBUSTION ON CHARACTERISTICS OF OXYGEN JET IN BOF, Kaizawa, Sasaki, Inomoto & Ogawa	121: IN-LINE OIL-WATER SEPARATION IN SWIRLING FLOW, Slot & Hoeijmakers	166: DUST DISPERSAL MODELLING ON A CONVEYOR CHUTE USING A COUPLED DEM AND CFD METHOD, Hilton & Cleary	
11:15-11:45	Coffee Break			
11:45-13:15	**Session R5-02: Numerical Methods** Chairman: Bernhard Müller	**Session R7-02: Biomechanics** Chairman: Leif Rune Hellevik	**Session R8-02: Pipe & Channel Flow** Chairman: Dmitry Eskin	**Session R9-02: Modelling Concepts** Chairman: Akio Tomiyama
11:45-12:15	Lead paper: 127: EFFICIENT SOLUTION METHOD FOR THE STOKES EQUATIONS WITH VARIABLE VISCOSITY AND PERIODIC BC. van Zwieten, van Gijzen, Vuik, van Male, & Fraaije	Lead paper: 145: INVESTIGATIONS OF TRANSITIONAL FLOWS USING IMAGE BASED HEMODYNAMICS, Valen-Sendstad et.al.	Lead paper: 920: LedaFlow-Q3D: A TRANSIENT MULTIDIMENSIONAL CFD TOOL FOR SIMULATION OF MULTIPHASE FLOW IN STRAIGHT AND CURVED PIPES, Ashrafian & Johansen et al.	Lead paper: 135: ON THE MODELLING OF ANODIC BUBBLES IN HALL-HÉROULT CELLS, Einarsrud & Johansen
12:15-12:35	094: LATTICE BOLTZMANN MICROCHANNEL SIMULATIONS VIA BINARY LIQUID MODEL, Kuzmin, Derksen & Eskin	153: POROUS AND VISCOUS FLOW MODELING ON THE STUDY OF CYST DEVELOPMENT IN THE HUMAN SPINAL CORD, Drøsdal et.al.	083: NUMERICAL SIMULATION OF AN HORIZONTAL COUNTER-CURRENT TWO-PHASE FLOW EXPERIMENT USING AN INTERFACIAL AREA DENSITY MODEL, Höhne & Lucas	101: MECHANISTIC MODELLING OF PARTICLE-INTERFACE INTERACTION IN THREE-PHASE FLOWS, Wierink, Goniva, Niceno & Heiskanen
12:35-12:55	129: AN IMPROVED ROE SOLVER FOR THE DRIFT-FLUX TWO-PHASE FLOW MODEL, Flåtten & Reigstad	905: IMPACT OF COMPETETIVE FLOW ON WALL SHEAR STRESS IN CORONARY SURGERY, Nordgaard et.al.	119: NUMERICAL SIMULATION OF LARGE BUBBLES IN CHANNELS USING A FRONT TRACKING METHOD, Hor, Hua, Spelt & Lawrence	103: NUMERICAL STUDY OF THE WALL EFFECT ON THE LIQUID DISTRIBUTION IN A TRICKLE-BED REACTOR, Martinez, Pallares, Lopez, Garcia & Grau
12:55-13:15	136: UNSTRUCTURED MESH OF A DISC USING MULTIPLE TRANSFINITE MAPPINGS, Sporleder, Dorao & Jakobsen	907: SIMULATING THE BLOOD FLOW IN CORONARY LIMA-TO-LAD BYPASSES USING AN ENHANCED BOUNDARY CONDITION MODEL, de Witte et.al.	097: A FLOWMETER BASED ON THE MEASUREMENT OF THE LOCAL HEAT TRANSFER COEFFICIENT AT THE FORWARD STAGNATION POINT OF A HEATED SPHERE PLACED IN A TURBULENT PIPE FLOW, Koizumi	087: MODELLING FLOW INDUCED AOD-CONVERTER SLOSHING BY ANALYTICAL CONSIDERATIONS, NUMERICAL SIMULATION AND COLD WATER EXPERIMENTS, Pirker & Wimmer
13:15-14:15	Lunch[1]			

Day 1 (Tuesday, June 21)

Afternoon sessions: 14:15 – 17:15

Time	AUDITORIUM R5	AUDITORIUM R7	AUDITORIUM R8
14:15-15:10		**Keynote:** Frans van de Vosse, Eindhoven Univ. Of Tech. CARDIOVASCULAR FLUID STRUCTURE INTERACTION	
15:15-16:45	**Session R5-03: Population Balance Method** Chairman: Daniele Marchisio	**Session R7-03: Biomechanics** Chairman: Frans van de Vosse	**Session R8-03: Oil & Gas Applications** Chairman: Knut Bech
15:15-15:45	Lead paper: 092: LARGE EDDY SIMULATION OF PARTICLE-LADEN SWIRLING FLOW WITH A PRESUMED FUNCTION METHOD OF MOMENTS, Dems, Carneiro & Polifke	Lead paper: 096: HIGH ORDER NUMERICAL SIMULATION OF FLUID-STRUCTURE INTERACTION IN THE HUMAN LARYNX, Larsson & Müller	Lead paper: 195: ANALYSIS OF SUB-SEA GAS RELEASE BY AN EULERIAN-LAGRANGIAN MODELLING CONCEPT, Skjetne & Olsen
15:45-16:05	104: COMPARISON BETWEEN DIFFERENT METHODS FOR TURBULENT GAS-LIQUID SYSTEMS BY USING MULTIVARIATE POPULATION BALANCES, Buffo, Vanni, Marchisio, Fox	118: A STRONG FSI COUPLING SCHEME FOR SIMULATING BMHV DYNAMICS: STUDY OF WALL SHEAR STRESS ON THE VALVE LEAFLETS, Annerel et.al.	161: AUTONOMOUS INFLOW CONTROL DEVICE: CFD SIMULATIONS OF FLUID-STRUCTURE INTERACTION, Gyllensten & Mathiesen
16:05-16:25	133: POPULATION BALANCE MODELLING OF ISOTHERMAL BUBBLY-CAP FLOWS USING TWO-GROUP AVERAGE BUBBLE NUMBER DENSITY APPORACH, Cheung, Yeoh, Krepper & Lucas	904: A BIOMECHANICAL MODEL FOR HUMAN UMBILICAL VEINS AND WHARTON'S JELLY, Leinan et.al.	143: HEAT TRANSFER IN A COLD SPOT ON A SUBSEA PIPELINE DURING SHUT-IN EFFECT OF NATURAL CONVECTION AND GRID RESOLUTION, Sannæs
16:25-16:45	154: IMPLEMENTATION OF THE SECTIONAL QUADRATURE METHOD OF MOMENTS IN FLUENT, Morud	178: FLUID MOTION FOR MICRO-GRAVITY SIMULATION IN A RANDOM POSITIONING MACHINE, Leguy et.al.	146: NUMERICAL MODELLINGS OF OIL SPILL RESPONSE ACTIONS, FLOATING BOOM Aghajanloo & Pirooz
16:45-17:15	**Afternoon Coffee**		

Day 2 (Wednesday, June 22)

Time	AUDITORIUM R5	AUDITORIUM R7	AUDITORIUM R8
8:30-9:25		**Keynote:** David Le Touzé, Ecole Centrale Nantes MESH-FREE LAGRANGIAN MODELLING OF FLUID DYNAMICS	
9:30-11:00	**Session R5-04: Separation & Mixing** Chairman: Leonard Kleiser	**Session R7-04: Particle-Based Methods** Chairman: David Le Touzé	**Session R8-04: Bubble & Droplet Dynamics** Chairman: Akio Tomiyama
9:30-10:00	Lead paper: 107: CFD SIMULATIONS AND MEASUREMENTS OF THE INLINE PHASESPLITTER: A COMPACT GAS/LIQUID SEPARATOR, Westra, de Haas, Salazar & Ibouhouten	Lead paper: 144: LIGGGHTS OPEN SOURCE DEM: MODELS, FEATURES, PARALLELISM AND QUALITY ASSURANCE, Kloss, Goniva, Amberger & Pirker	Lead paper: 158: TOWARDS A COMPUTATIONAL ANALYSIS OF BINARY COLLISIONS OF SHEAR-THINNING DROPLETS, Bothe & Focke
10:00-10:20	084: A CFD STUDY OF THE EFFECT OF CYCLONE BARREL HEIGHT ON ITS PERFORMANCE PARAMETERS, Elsayed & Lacor	162: A MASSIVELY PARALLEL INCOMPRESSIBLE SMOOTHED PARTICLE HYDRODYNAMICS SIMULATOR MOTIVATED BY OILFIELD APPLICATIONS, Dickenson & Dawes	930: EXPERIMENTAL AND NUMERICAL INVESTIGATION OF DROPLET-WIRE INTERACTIONS IN GAS-LIQUID FLOWS Marchetti, Svendsen & Skjetne
10:20-10:40	172: CFD SIMULATION OF HYDROCYCLONE PERFORMANCE UNDER DILUTE OPERATING CONDITIONS, Davailles, Climent & Bourgeois	168: UNDERSTANDING VISCOUS FLUID TRANSPORT AND MIXING IN A TWIN SCREW EXTRUDER, Cleary & Robinson	093: MODELING OF A GAS-LIQUID SLUG FLOW ACCOMPANIED WITH MASS TRANSFER THROUGH A LONG MICROCHANNEL, Eskin & Mostowfi
10:40-11:00	901: NUMERICAL MODELLING OF AN AUTOCLAVE, Appa, Deglon & Meyer	141: A MULTI-PURPOSE OPEN SOURCE CFD-DEM APPROACH, Goniva, Kloss, Hager, Wierink & Pirker	163: MODELING AND 3D SIMULATION OF PHYSICAL MASS TRANSFER AT SINGLE RISING GAS BUBBLES FOR MODERATE SCHMIDT NUMBERS, Bothe & Fleckenstein
11:00-11:30	Coffee Break		
11:30-13:00	**Session R5-05: Reactive Flows** Chairman: Charles Petty	**Session R7-05: Multiphase Pipe Flow** Chairman: Stein Tore Johansen	**Session R8-05: Fluidized Beds & CLC** Chairman: Koulis Pericleous
11:30-12:00	Lead paper: 125: A CFD STUDY OF ENTRAINED-FLOW GASIFIERS USING TWO FEED TYPES, Sreedharan, Hjertaker & Solberg	Lead paper: 167: ADVANCES IN THE SIMULATION OF MULTIPHASE FLOWS IN PIPELINES, Lakehal	Lead paper: 148: GPU-ACCELERATED LARGE-SCALE CFD-DEM COUPLING SIMULATION OF THREE-DIMENSIONAL GAS-SOLID FLUIDIZED BED, Chen, Ge & Li
12:00-12:20	137: CFD MODELING OF SILICA FUME FORMATION DURING REFINING OF SILICON METAL, Olsen, Næss & Tranell	128: NUMERICAL SIMULATION OF SINGLE ELONGATED BUBBLE PROPAGATION IN INCLINED PIPES, Hua, Langsholt & Lawrence	100: THE CHARACTERISTICS OF FLOW AND HEAT TRANSFER IN A CIRCULATING FLUIDIZED BED REACTOR, Choi
12:20-12:40	177: EFFECT OF SIO COMBUSTION ON NOX EMISSION: THEORY AND VALIDATION, Panjwani, Andersson & Midtdal	147: INVESTIGATION OF TWO-PHASE SLUG FLOW IN A RISER USING PHYSICAL AND NUMERICAL SIMULATIONS, Abdulkadir, Hernandez-Perez, Lowndes and Azzopardi	173: DESIGN OF A CHEMICAL LOOPING COMBUSTION SYSTEM USING PROCESS SIMULATION AND COMPUTATIONAL FLUID DYNAMICS, Cloete & Amini
12:40-13:00	099: CFD MODELING STUDY OF A REFINERY HEATER AND COMPARISON TO FIELD DATA, Runstedtler, Landry & Brunet	921: Quasi-3D MODELING OF SLUG FLOW IN HORIZONTAL AND VERTICAL PIPES, Ashrafian, Mo, Dijkhuizen & Johansen	170: A NUMERICAL AND EXPERIMENTAL STUDY OF HYDRODYNAMIC BEHAVIOR OF BISOLID CIRCULATING FLUIDIZED BED, Nouyrigat, .Lalam, .Bouquet & Simonin
13:00-14:00	Lunch[1]		

Day 2 (Wednesday, June 22)

Afternoon sessions: 14:00 – 16:40

Time	AUDITORIUM R5	AUDITORIUM R7	AUDITORIUM R8
14:00-14:55	**Keynote**: Leonhard Kleiser, ETH Zürich LARGE-EDDY SIMULATION OF SEPARATED VORTICAL FLOWS		
15:00-16:30	Session R5-06: Casting & Solidification Chairman: Ernst Meese	Session R7-06: OpenFoam Experiences Chairman: Jozsef Nagy	Session R8-06: Level Set Method Chairman: Dieter Bothe
15:00-15:30	Lead paper: 169: EULER-LAGRANGE MODELING OF MELTING AND SOLIDIFICATION WITH MOVING SOLID PARTICLES, Dierich & Nikrityuk	Lead paper: 115: TESTING OF OPENFOAM CFD CODE FOR PLANE TURBULENT BLUFF BODYFLOWS, Lysenko, Ertesvåg & Rian	Lead Paper: 117: CONSTRAINED REINITIALISATION OF THE CONSERVATIVE LEVEL SET METHOD, Walker & Müller
15:30-15:50	132: STUDY OF THE STEEL/SLAG INTERFACE INSTABILITY AND THE INFLUENCE OF INJECTED GAS IN THE CONTINUOUS CASTING OF STEEL, Pericleous et.al.	149: COMPARISON OF CFD TOOLS FOR MULTIPHASE FLOW APPLICATIONS, Henkes, Singh & Menon	140: DIRECT NUMERICAL SIMULATION OF TWO-FLUID FLOWS WITH A LEVEL-SET METHOD, Voronetska, Vinay, Wachs & Caltagirone
15:50-16:10	085: CFD MODELLING OF TRANSPORT PHENOMENA OCCURING DURING DIRECTIONAL SOLIDIFICATION OF mc-SILICON FOR PHOTOVOLTAIC APPLICATIONS, Dropka & Rehse	909: NUMERICAL SIMULATION OF SPECIES TRANSFER AT GAS-LIQUID INTERFACES USING OpenFoam, Marschall, Schuler, Hinterberger & Hinrichsen	184: THREE DIMENSIONAL NUMERICAL SIMULATION OF BUBBLE AND DROPLET DYNAMICS WITH A PARALLEL PARTICLE LEVEL SET SOLVER, Bihs
16:10-16:40	Afternoon Coffee		
19:00-23:00	Conference Dinner[2]		

Day 3 (Thursday, June 23)

Morning sessions: 8:30 – 13:00

Time	AUDITORIUM R5	AUDITORIUM R7	AUDITORIUM R8
8:30-9:25		Keynote: Tor Ytrehus, NTNU MOLECULAR-FLOW EFFECTS IN EVAPORATION AND CONDENSATION PHENOMENA	
9:30-11:00	Session R5-07: Discrete Element Method Chairman: Alexandre Lavrov	Session R7-07: Metallurgical Applications Chairman: Alireza Ashrafian	Session R8-07: Fluidized Beds & CCS Chairman: Shahriar Amini
9:30-10:00	Lead paper: 124: PARCEL-BASED APPROACH FOR THE SIMULATION OF GAS-PARTICLE FLOWS, Radl, Radeke, Khinast & Sundaresan	Lead paper: 064: INCLUSION ELIMINATION IN STEELMAKING LADLE, Gardin, Simonnet & Gauthier	Lead paper: 116: MODELLING AND CFD SIMULATION OF A FLUIDIZED BED REACTOR TO CAPTURE CO2 BY SOLID SORBENTS, Pericleous, Molaei & Patel
10:00-10:20	155:DE-MIXING OF BINARY PARTICLE MIXTURES DURING UNLOADING OF A V-BLENDER, Pereira & Cleary	150: CFD MODELING OF TAPPING PROCESS IN FERROMANGANESE FURNACES, Kadkhodabeigi, Tveit & Johansen	108: INVESTIGATION OF A FRICTIONAL PARTICLE-PARTICLE DRAG COEFFICIENT IN A DENSE BINARY FLUIDIZED BED, Chao et.al.
10:20-10:40	164: ANALYSIS OF NON-ROUND PARTICULATE MIXING IN A PLOUGH SHARE MIXER USING DEM, Cleary	152: CFD SIMULATION OF SLAG DROPLET FORMATION BY A SPINNING DISC IN DRY SLAG GRANULATION PROCESSES, Pan, Witt, Kuan & Xie	159: MAPPING OF THE OPERATING WINDOW OF A LAB SCALE BUBBLING FLUIDIZED BED REACTOR BY CFD AND DESIGNED EXPERIMENTS, Cloete & Amini
10:40-11:00	165: THREE DIMENSIONAL COUPLED DISCRETE ELEMENT-CFD MODELLING OF HIGH SPEED GAS-PARTICLE RACEWAY DYNAMICS, Hilton & Cleary	176: CFD SIMULATION OF BATH DYNAMICS IN THE HISMELT SMELT REDUCTION VESSEL FOR IRON PRODUCTION, Tabib, Stephens, Schwarz & Davis	102: NUMERICAL SIMULATION OF MULTIPHASE FLOWS OF CO2 STORAGE IN SALINE AQUIFERS IN DAQINGZIJING OILFIELD, CHINA, Yang, Zeng, Zhang, Wang & Jin
11:00-11:30	Coffee Break		
11:30-13:00	Session R5-08: Chairman:	Session R7-08: Multiphase Flows Chairman: Sanjoy Banerjee	Session R8-08: Porous Media Chairman: Dmitry Eskin
11:30-12:00		Lead paper: 171 : INTERPENETRATING CONTINUA AND MULTIPHASE TURBULENCE, Petty, Muthu, Koppula &Benard	Lead paper: 156: PREDICTION OF PERMEABILITY FOR DEM GENERATED PACKINGS OF SPHERICAL AND NON-SPHERICAL PARTICLES USING SPH AND LB, Pereira, Dupuy, Cleary & Delaney
12:00-12:20		120: TECHNICAL APPLICATION OF A MULTIPHASE SOLVER IN THE COMPRESSIBLE FLOW OF A GASEOUS AND A LIQUID PHASE, Nagy, Harasek & Jordan	174: 3D NUMERICAL STUDY OF THE INFLUENCE OF PARTICLE POROSITY ON THE HEAT AND FLUID FLOW, Wittig & Nikrityuk
12:20-12:40		160: INFLUENCE OF SUBCOOLING ON DENSITY WAVE OSCILLATIONS IN A HEATED PIPE, Strømsvåg, Ruspini, Fernandino & Dorao	106: A COMPARATIVE STUDY OF MASS- AND MOLE BASED MULTICOMPONENT DIFFUSION MODELS IN POROUS PELLETS FOR STEAM METHANE REFORMING PROCESS, Rout & Jakobsen
12:40-13:00		113: CFD SIMULATION OF GAS-LIQUID FLOW IN BUBBLE COLUMNS BASED ON THE DBS DRAG MODEL, Yang, Wu & Li	131: APPLICATION OF THE LEAST SQUARE METHOD TO THE MULTISCALE TRANSPORT EQUATION IN POROUS MEDIA, Dupuy & Sporleder
13:00-14:00	Lunch[1]		

Afternoon sessions: 14:00 – 15:30

Time	AUDITORIUM R5	AUDITORIUM R7	AUDITORIUM R8
14:00-14:45	Keynote: Akio Tomiyama INTERFACE TRACKING AND MULTI-FLUID SIMULATION OF BUBBLY FLOWS IN BUBBLE COLUMNS		
14:45-15:00	Awards / Closing		
15:00-15:30	Afternoon Coffee		

8th International Conference on CFD in Oil & Gas, Metallurgical and Process Industries
SINTEF/NTNU, Trondheim NORWAY
21-23 June 2011

CFD11-60

INSOLUBLE SURFACTANT EFFECTS ON EMULSION COARSENING IN A GRAVITATIONAL FIELD VIA PHASE-FIELD TERNARY MIXTURE MODEL

Andrea G. LAMORGESE[1*], **Sanjoy BANERJEE**[1†]

[1]Dept. Chem. Engr. & Energy Institute, City College New York, New York, USA

[*] E-mail: lga@che.ccny.cuny.edu
[†] E-mail: banerjee@che.ccny.cuny.edu

ABSTRACT

We investigate gravity-driven coarsening of binary immiscible fluids in the presence of surfactants via diffuse-interface modeling and simulation of amphiphilic fluids as ternary mixtures. The interface between immiscible fluids in the phase-field model is treated as a mixing layer whose evolution and properties are modeled based on a Flory-Huggins and Cahn-Hilliard representation of the excess and nonlocal components of the Gibbs free energy of mixing. As a result, artificial stresses arise in the mixing region coupling convection and diffusion via a nonequilibrium Korteweg force, expressing the tendency of the ternary system to minimize its free energy. Diffuse-interface simulations are conducted to investigate droplet interactions under gravitational forcing in an initially monodisperse array of heavy fluid droplets embedded in a continuous phase of light fluid, revealing the scaling laws of the characteristic coarsening length scales and the effect of an insoluble surfactant. As expected, flow-induced changes in surfactant concentration lead to surface tension gradients giving rise to Marangoni stresses effectively slowing down coarsening in the longitudinal and transverse directions with a similar (monotonic) Bond number dependence of the sedimentation rate. However, the diffuse-interface model only allows a mesoscale representation of surfactant effects and the determination of apparent coalescence and sedimentation rates due to coarse-graining of the actual film drainage and rupture processes in the phase-field model. We investigate basic statistics of sedimentation and their dependences on the relevant nondimensional groups.

Keywords: Bubble and droplet dynamics; Break-up and coalescence; Separation.

NOMENCLATURE

Greek Symbols

β	Free energy scale [kg/ms^2]
δ_{ij}	Kronecker symbol
η	Viscosity [kg/ms]
κ	Wavenumber [m^{-1}]
μ	Chemical potential
ν	Kinematic viscosity [m^2/s]
$\hat{\xi}$	Interfacial thickness (clean interface) [m]
ξ	Interfacial thickness [m]
ρ	Mass density [kg/m^3]
σ	Surface tension [kg/s^2]
τ	Stress tensor [kg/ms^2]
Φ	Phase field
ϕ	Molar fraction
Ψ	Surfactant concentration
ψ	Molar fraction
ψ_i	Chemical potential difference
Ψ_{ij}	Flory parameter
ω'	*rms* vorticity (dimensionless)

Latin Symbols

a, b	Double well parameters
C_1	Numerical parameter
c	Molar density [mol/m^3]
d	Drop diameter [m]
D_{ij}	Binary diffusivity [m^2/s]
$\mathbf{F}$	Korteweg force [kg/m^2s^2]
$\mathbf{F}_g$	Buoyancy force [kg/m^2s^2]
g	Molar Gibbs free energy [J/mol], acceleration [m/s^2]
$\hat{\mathbf{g}}$	Unit vector in direction of gravity
$\mathbf{J}$	Diffusive volume flux [m/s]
k	Square gradient coefficient [kgm/s^2]
L_c	Periodicity length [m]
$\mathscr{L}$	Coarsening length scale [m]
M_W	Molecular weight [g/mol]
$\mathbf{N}$	Nonlinear term (dimensionless)
N	Number of components
N_C	Courant number
n	Power-law exponent for charactertistic length scale
n_R	Power-law exponent for Reynolds number
p	Pressure [Pa]
$\mathbb{P}$	Helmholtz projection operator
R	Universal gas constant [$J/molK$]
$\mathbf{r}$	Position vector [m]
r	Exponent
T	Temperature [K]
t	Time [s]
Δt	Time-step [s]
u'	*rms* velocity (dimensionless)

u_a	Reference speed of sound $[m/s]$
u_s	Settling velocity $[m/s]$
U_c	Characteristic velocity $[m/s]$
V	Bulk velocity (dimensionless)
$\mathbf{v}$	Mass-average velocity $[m/s]$
x	Molar fraction, coordinate $[m]$
Δx	Grid spacing (dimensionless)
z	Vertical coordinate $[m]$
Bo	Bond number
Ca	Capillary number
Cn	Cahn number
Fr	Froude number
$\mathscr{G}$	Galileo number
Ma	Marangoni number
Pe	Peclet number
Re	Reynolds number
$\mathfrak{R}$	Reynolds number based on *rms* velocity and characteristic length $\mathscr{L}$
$\mathbb{R}$	Reynolds number based on *rms* velocity and vorticity
R_ϕ	Order-parameter Reynolds number
$\mathscr{R}$	Fluidity parameter
We	Weber number

Sub/superscripts

ex	Excess
id	Ideal
nl	Nonlocal
th	Thermodynamic
T	Transpose

INTRODUCTION

In this work, we study numerically surfactant effects on the buoyancy-driven segregation of binary immiscible fluid mixtures, with the main objective of elucidating dependences of statistics of the segregation process on the relevant nondimensional parameters for a surfactant-stabilized emulsion under gravitational forcing. In fact, although the ability of amphiphilic compounds to influence breakup and coalescence phenomena in emulsions is well known and has considerable practical importance, the detailed mechanisms of this influence remain poorly understood and have long been a topic of active research. Early reviews on multiphase flows with surfactants can be found in Edwards *et al.* (1991) as well as in Maldarelli and Huang (1996) and Kralchevsky *et al.* (1996), while more recent accounts have been provided by Binks (1998) and Dukhin *et al.* (2006). Experimentally, a number of works on gravitational phase separation have first been conducted in the absence of surfactants. Early studies on critical phase-separating mixtures have characterized the sequence of stages of the segregation process during the prevailing of gravity (Chan and Goldburg, 1987) as well as the growth law of single-phase microdomains during the so-called 'residual' sedimentation stage (Cau and Lacelle, 1993). Other experiments on gravitational phase separation have been limited to the effects of individual parameters (e.g. volumetric fraction or viscosity ratio) on the separation rate (To and Chan, 1992, 1994) or the regimes of phase separation (Sato and Sumita, 2007). Experimental investigations in the presence of surfactants have also been carried out dealing with emulsion stability as it affects

the rate of coalescence between drops or bubbles. In particular, some previous studies have been focused on the correlation between interfacial adsorption of surfactant and the time required for coalescence as a measure of emulsion stability (Giribabu and Ghosh, 2007). Other studies have characterized the successive stages of phase separation of concentrated surfactant-stabilized emulsions as coarsening by Ostwald ripening followed by coalescence and measured a characteristic coalescence frequency after this general type of behavior (Schmitt and Leal-Calderon, 2004).

On the numerical side, previous studies on gravitational phase separation without surfactant have been limited to the analysis of Bond number effects on growth laws during spinodal decomposition of critical mixtures (Badalassi *et al.*, 2004; Badalassi and Banerjee, 2005). For surfactant-stabilized emulsions, however, studies of buoyancy-driven interactions between multiple drops have been lacking to a large extent and only recently the case of two surfactant-covered drops has been considered in some detail (Rother and Davis, 2004; Rother *et al.*, 2006). (This is due to the fact that the vast majority of previous numerical works have been focused on a single surfactant-covered spherical drop moving under gravity.) In fact, the case of near-contact motion of two surfactant-laden spherical drops was considered by Cristini *et al.* (1998) while Ramirez *et al.* (2000) looked at surfactant effects on the flotation rate between a neutrally buoyant particle and a bubble with a nearly uniform coverage. Other works have looked into the rheology of a dilute emulsion of surfactant-covered spherical drops in linear flows allowing for redistribution of surfactant (Błlawzdziewicz *et al.*, 2000), with the analysis subsequently extended to time-dependent flows (Vlahovska *et al.*, 2002).

Although experiments and simulations on gravitational phase separation of emulsions have been carried out in the past, none of these previous studies has looked at phase separation statistics for a surfactant-stabilized emulsion in gravity systematically. In this work, we investigate binary liquid+surfactant systems via diffuse-interface modeling of amphiphilic fluids as ternary mixtures. The interface between immiscible fluids in the phase-field model is treated as a mixing layer whose evolution and properties are modeled based on a regular solution assumption and a Flory-Huggins and Cahn-Hilliard representation of the excess and nonlocal components of the Gibbs free energy of mixing. As a result, artificial stresses arise in the mixing region coupling convection and diffusion via a nonequilibrium Korteweg force, expressing the tendency of the ternary system to minimize its free energy. A model surfactant is introduced as an additional species and its interaction with the primary immiscible components described via pairwise interaction parameters arising in the Flory-Huggins component of the Gibbs free energy of mixing. It should be noted that many early phase-field models of binary liquid+surfactant systems which were mainly concerned with the influence of surfactants on the dynamics of phase separation (Laradji *et al.*, 1992; Komura and Kodama, 1997; Melenkevitz and Javadpour, 1997; Lamura *et al.*, 1999; Theissen and Gompper, 1999) were essentially unable to precisely account for the competing attractive/repulsive interactions between the component species since they were heuristically derived by introducing an additional order

parameter for surfactant concentration together with *ad hoc* coupling terms to the original free energy functional for the binary mixture. To our knowledge, modeling surfactant effects on binary immiscible fluid mixtures via Flory pairwise interaction parameters is reported here for the first time.

Although the focus of this investigation is on insoluble surfactants, it should be noted that phase-field modeling works on soluble surfactants have been reported recently. In particular, a diffuse interface model has been presented where the incompressible Navier-Stokes equations are solved together with transport equations for the bulk and interfacial concentrations of surfactant (Teigen *et al.*, 2011). On the other hand, the inclusion of realistic adsorption isotherms in the phase-field formulation has been addressed by van der Sman and van der Graaf (2006) and Liu and Zhang (2010). However, since the focus of this work is on insoluble surfactants, we leave considerations of interfacial adsorption and soluble surfactants for future work.

The rest of this paper is organized as follows. In the next section the governing equations are presented after which numerical methods are briefly outlined. Subsequently, we show the results of diffuse-interface simulations of droplet interactions during sedimentation of binary immiscible fluid mixtures, showing that the addition of surfactant slows down coarsening in the longitudinal and transverse directions while reducing the strength of fluid motion during emulsion resolution in the longitudinal and transverse directions as compared to surfactant-free simulations. These dependences are addressed as a function of the relevant nondimensional parameters At the end, a few conclusions are drawn.

THE GOVERNING EQUATIONS

Free energy of ternary mixtures

Although the diffuse-interface model was originally developed to describe near-critical behavior of single-component fluids and partially miscible binary mixtures (van der Waals, 1894; Cahn and Hilliard, 1959), recently a number of phase-field formulations have been applied to interfacial flows far from criticality. In particular, the phase-field method has been brought to bear on mixtures of binary immiscible components undergoing phase separation under shear (Badalassi *et al.*, 2003; Badalassi and Banerjee, 2005), as well as on the morphology and rheology of immiscible polymer blends (Keestra *et al.*, 2003; Prusty *et al.*, 2007), or the flow of microstructured fluids consisting of viscoelastic Oldroyd-B and Newtonian phases (Yue *et al.*, 2004). Of late, phase-field ternary mixture models have also been of interest for modeling many different physical phenomena, from solidification and microstructure evolution in ternary alloy systems (Kobayashi *et al.*, 2003) to mutual diffusion effects in partially miscible polymer blends (Tufano *et al.*, 2010).

In this work, using a phase-field ternary mixture model we intend to study insoluble surfactant effects on the coarsening of an emulsion under gravitational forcing. The starting point to this diffuse-interface model is a statement of the thermodynamic Gibbs free energy of mixing when the mixture has a uniform composition:

$$\Delta g^{th} = g^{th} - \sum_{k=1}^{N} g_k x_k, \qquad (1)$$

where g^{th} is the molar free energy of the mixture at equilibrium, while g_k is the molar free energy of pure species A_k at temperature T and pressure P. ($N \equiv 3$ in Eq. (1) and below although very similar expressions still hold for a general N-component mixture model of van der Waals fluids.) At a given T and P, the thermodynamic Gibbs free energy of mixing can be used to calculate the ternary phase diagram for the mixture. For example, under the so-called *regular* solution model assumption, the Gibbs free energy of mixing can be written as the sum of an ideal (or entropic) part,

$$g^{id} = RT \sum_{k=1}^{N} x_k \log x_k, \qquad (2)$$

which is proportional to the entropy of mixing for an ideal solution (R being the gas constant), and an enthalpic (so-called excess) part, g^{ex}, which can be expressed as

$$g^{ex} = \frac{1}{2} RT \sum_{i,k=1}^{N} \Psi_{ik} x_i x_k, \qquad (3)$$

where Ψ_{ik} denote pairwise interaction (Flory) parameters which are functions of T and P, with $\Psi_{ik} = \Psi_{ki}$ and $\Psi_{ii} = 0$. For a partially miscible three-component system, modeling the thermodynamic Gibbs free energy of mixing based on the Flory-Huggins expression (Eq. 3) allows representation of complex phase diagrams with phase separation into one, two or three phases. However, for phase-field modeling of binary immiscible fluids in the presence of surfactant, it is only required that an expression be available for the free energy of mixing with the ability to represent phase-separated equilibrium states for a ternary mixture in a two-phase region. In fact, such an expression can be obtained from a Taylor series expansion of the thermodynamic specific (i.e. per unit volume) free energy of mixing (obtained from Eqs. 2 and 3) at a fixed surfactant (x_2) concentration around the critical point of a two-phase region:

$$\Delta g^{th} = \beta \left\{ \frac{16}{3(1-x_2)^3} \frac{x_1^{*4}}{4} - 2 \left(\Psi_{13} - \frac{2}{1-x_2} \right) \frac{x_1^{*2}}{2} \right.$$
$$\left. + \frac{\Psi_{13}}{4}(1-x_2)^2 + (1-x_2) \log \frac{(1-x_2)}{2} + x_2 \log x_2 \right\}, \quad (4)$$

where $\beta \equiv \rho RT / M_W$ and $x_1^* \equiv x_1 - \frac{1-x_2}{2}$ while $\Psi_{13} > 2$ denotes a pairwise interaction parameter expressing the repulsive interaction between unlike molecules vs. that between like molecules. Note that, due to the artificial nature of the interface region, different specifications of Flory parameters in (4) would only influence the detailed variation of the phase field across the interface region at equilibrium so that, numerical considerations aside, they should be regarded as effectively equivalent. Equation (4) can be recast in the form:

$$\Delta g^{th} = \frac{a}{4} \left(x_1^* - \sqrt{\frac{b}{a}} \right)^2 \left(x_1^* + \sqrt{\frac{b}{a}} \right)^2 + fn(x_2), \quad (5)$$

with a, b denoting functions of x_2, which represents a symmetric double well potential (see Fig. 1). This then allows introduction of a scaled concentration (or phase field),
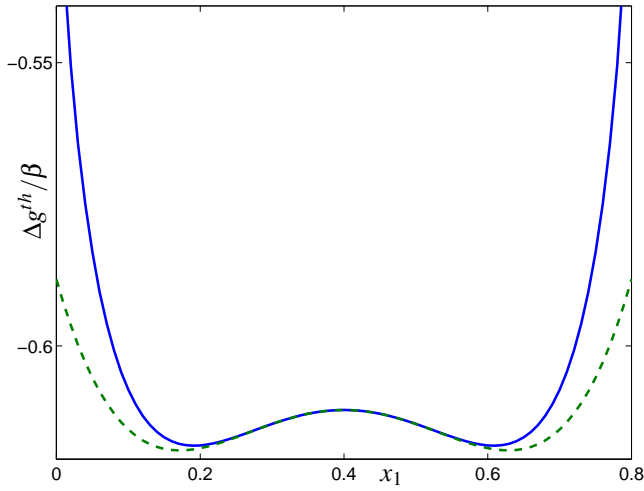
Figure 1: Gibbs free energy of mixing for homogeneous ternary mixture with prescribed surfactant concentration, $\langle x_2 \rangle = 0.2$, based on the Flory-Huggins model (Eqs. 2 and 3, solid) and its approximation based on a Taylor series expansion around the critical point (Eq. 4, dashed).

$\Phi \equiv x_1^* / \sqrt{b/a}$, which interpolates uniform values $\Phi = \pm 1$ in the two bulk fluids at any (prescribed) surfactant concentration. For this free energy model to be able to describe inhomogeneous mixtures, the effects of spatial inhomogeneities in the composition have to be accounted for by representing the generalized Gibbs free energy of mixing, $\tilde{g}$, as the sum of a thermodynamic part and a nonlocal part,

$$\tilde{g} = \Delta g^{th} + g^{nl}, \qquad (6)$$

where, following Cahn and Hilliard (1959), the latter is assumed to be given by the expression

$$g^{nl} = \frac{k}{2} \left[(\nabla x_1)^2 + (\nabla x_2)^2 + \nabla x_1 \nabla x_2 \right], \qquad (7)$$

where k incorporates the typical length scale of spatial inhomogeneities in the composition as $\hat{\xi} = \sqrt{k/\beta}$, which, as shown by van der Waals (1894), is proportional to the surface tension between two phases at equilibrium.
From the expression for the chemical potential of species i for homogeneous solution,

$$\mu_i^{th} = \left(\frac{\partial (cg^{th})}{\partial c_i} \right)_{T,P,c_j \neq i}, \qquad (8)$$

with $c_i = cx_i$ denoting the mole density of the ith species and $c = \sum c_i$ the total mole density, we see that for a ternary system the two quantities $\phi \equiv x_1$ and $\mu_1^{th} - \mu_3^{th}$ (and similarly $\psi \equiv x_2$ and $\mu_2^{th} - \mu_3^{th}$) are thermodynamically conjugated, i.e.,

$$\mu_i^{th} - \mu_3^{th} = \frac{\partial g^{th}}{\partial x_i} \quad (i = 1, 2). \qquad (9)$$

Cahn and Hilliard (1959) extended (9) to inhomogeneous mixtures in terms of the generalized (i.e. thermodynamic plus nonlocal) chemical potential difference:

$$\tilde{\mu}_{i3} = \frac{\delta \tilde{g}}{\delta x_i} = \frac{\partial g^{th}}{\partial x_i} - \nabla \cdot \left(\frac{\partial g^{nl}}{\partial \nabla x_i} \right) \quad (i = 1, 2). \qquad (10)$$

For clarity, expressions for these quantities are noted below based on the Taylor series expansion (above) for the thermodynamic Gibbs free energy of mixing:

$$\tilde{\mu}_{13} = \beta \left[\frac{16}{3(1-x_2)^3} x_1^{*3} - 2 \left(\Psi_{13} - \frac{2}{1-x_2} \right) x_1^* - \nabla^2 x_1^* \right], \qquad (11)$$

$$\tilde{\mu}_{23} = \beta \left[\log \frac{2x_2}{1-x_2} - \frac{\Psi_{13}}{2}(1-x_2) - \left(\Psi_{13} - \frac{2}{1-x_2} \right) x_1^* \right.$$
$$\left. + \frac{2}{(1-x_2)^2} x_1^{*2} + \frac{8}{3(1-x_2)^3} x_1^{*3} + \frac{4}{(1-x_2)^4} x_1^{*4} - \nabla^2 \left(\frac{x_1}{2} + x_2 \right) \right]. \qquad (12)$$

The equations of motion

In the absence of chemical reactions, the mass balance equation for each component can be written as

$$\partial_t \rho_k + \nabla \cdot (\rho_k \mathbf{v}_k) = 0, \qquad (13)$$

where the k-th species has density ρ_k and velocity $\mathbf{v}_k$. Now, define the mixture density and the mixture velocity as the following mass-average quantities,

$$\rho = \sum_{k=1}^{N} \rho_k, \qquad (14)$$

and

$$\mathbf{v} = \frac{1}{\rho} \sum_{k=1}^{N} \rho_k \mathbf{v}_k = \sum_{k=1}^{N} y_k \mathbf{v}_k, \qquad (15)$$

where $y_k = \rho_k / \rho$ is the mass fraction of the k-th component. Summing Eq. (13) for all k, we trivially obtain the continuity equation,

$$\partial_t \rho + \nabla \cdot (\rho \mathbf{v}) = 0. \qquad (16)$$

In the following, we assume that all components have the same density and molecular weight, so that $y_k = x_k$ represent the mass, volume and molar fractions of the k-th component. Consequently, since the mixture is assumed to be regular, Eq. (16) reduces to

$$\nabla \cdot \mathbf{v} = 0, \qquad (17)$$

while the species conservation equations become:

$$\dot{x}_k = \partial_t x_k + \mathbf{v} \cdot \nabla x_k = -\nabla \cdot \mathbf{J}_k, \qquad (18)$$

where the dot indicates the advective derivative with respect to the mixture velocity $\mathbf{v}$ and

$$\mathbf{J}_k = \sum_{k \neq j=1}^{N} x_j x_k (\mathbf{v}_k - \mathbf{v}_j) \qquad (19)$$

is the volumetric diffusive flux, depending on the the velocity of the k-th component with respect to the mean, with $\sum \mathbf{J}_k = \mathbf{0}$. Obviously, since $\sum x_k = 1$, only $N - 1$ of these equations are independent.
Equations (17) and (18) must be coupled with the Navier-Stokes equation

$$\rho \dot{\mathbf{v}} = -\nabla p + \nabla \cdot \tau + \mathbf{F}, \qquad (20)$$

where τ is the viscous stress tensor, while $\mathbf{F}$ is the Korteweg reversible body force. Using Hamilton's principle, $\mathbf{F}$ can be shown to be equal to

$$\mathbf{F} = \frac{\delta \widetilde{g}}{\delta \mathbf{r}} = \sum_{i=1}^{N} \widetilde{\mu}_i \nabla x_i, \tag{21}$$

which can be interpreted in terms of the generalized gradient (i.e. involving functional derivatives) of the specific (i.e. per unit volume) free energy. Note that, since $\widetilde{\mu}_i = \mu_i^{th} + \mu_i^{nl}$ and considering that

$$\sum \mu_i^{th} \nabla x_i = \nabla g^{th}, \tag{22}$$

after redefining the pressure as $p - g^{th}$, the above equation can be rewritten replacing $\widetilde{\mu}_i$ with μ_i^{nl}. Now, considering that $\sum x_i = 1$, we finally obtain:

$$\mathbf{F} = \sum_{i=1}^{N-1} \mu_{iN}^{nl} \nabla x_i. \tag{23}$$

The constitutive equations for the diffusive fluxes

We assume that the viscosities of all components are the same, so that the viscous stress in Eq. (20) can be written:

$$\tau = \eta \left[\nabla \mathbf{v} + (\nabla \mathbf{v})^T \right], \tag{24}$$

where η is the uniform viscosity of the mixture.

As for the material diffusive fluxes, generalizing the two component case, we use the following constitutive relations,

$$\mathbf{J}_i = -\sum_{i \neq j=1}^{N} D_{ij} x_i x_j \nabla \widetilde{\mu}_{ij}, \tag{25}$$

here $D_{ij} = D_{ji}$ and $\widetilde{\mu}_{ij} = \widetilde{\mu}_i - \widetilde{\mu}_j$, so that $\sum \mathbf{J}_i = \mathbf{0}$ identically, as it should.

Note that, had we assumed a constitutive relation of the form

$$\mathbf{J}_i = -D x_i \nabla \mu_i, \tag{26}$$

the sum of the diffusive fluxes $\mathbf{J}_i$ would not be zero, as the Gibbs-Duhem relation is not satisfied by the nonlocal part of the chemical potential. In particular, for ternary mixtures we obtain:

$$\mathbf{J}_1 = -D_{12} x_1 x_2 \nabla \widetilde{\mu}_{12} - D_{13} x_1 (1 - x_1 - x_2) \nabla \widetilde{\mu}_{13}, \tag{27}$$

$$\mathbf{J}_2 = -D_{21} x_1 x_2 \nabla \widetilde{\mu}_{21} - D_{23} x_2 (1 - x_1 - x_2) \nabla \widetilde{\mu}_{23}. \tag{28}$$

Note that this makes the species conservation equations non-linear fourth-order advection-diffusion equations, which is a generalization of the classical Cahn-Hilliard equation used to describe phase separation in binary mixtures.

Summarizing, we obtain the following system of equations for a binary immiscible fluid mixture in the presence of surfactant, which can be interpreted as a ternary version of model H, in the taxonomy of Hohenberg and Halperin

(1977):

$$\partial_t x_1 + \nabla \cdot x_1 \mathbf{v} = \nabla \cdot [D_{12} x_1 x_2 \nabla \widetilde{\mu}_{12} + D_{13} x_1 (1 - x_1 - x_2) \nabla \widetilde{\mu}_{13}], \tag{29}$$

$$\partial_t x_2 + \nabla \cdot x_2 \mathbf{v} = \nabla \cdot [D_{21} x_1 x_2 \nabla \widetilde{\mu}_{21} + D_{23} x_2 (1 - x_1 - x_2) \nabla \widetilde{\mu}_{23}], \tag{30}$$

$$\rho \left[\partial_t \mathbf{v} + \nabla \cdot \mathbf{vv} \right] = -\nabla p + \eta \nabla^2 \mathbf{v} - \left[x_1 \nabla \mu_{13}^{nl} + x_2 \nabla \mu_{23}^{nl} \right], \tag{31}$$

$$\nabla \cdot \mathbf{v} = 0. \tag{32}$$

Note that for modeling a non-ionic, bulk-insoluble surfactant to which we restrict attention in this work, the surfactant mass balance equation reduces effectively to that of a passive tracer, $\dot{x}_2 = 0$, since the ratios of the binary diffusivities of species 2 to the principal component diffusivity ($D \equiv D_{13}$) are assumed to be zero. Finally, we note that gravity effects can be included in the momentum balance, which is easily done within the frame of the Boussinesq approximation. In that case, a general expression for the buoyancy force is given by

$$\mathbf{F}_g = -x_1 \nabla (gz \frac{\partial \rho}{\partial x_1}) - x_2 \nabla (gz \frac{\partial \rho}{\partial x_2}), \tag{33}$$

where g is gravity and z is the vertical coordinate. Accordingly, the effects of gravity can be accounted for by simply adding the potentials $V_i = gz \frac{\partial \rho}{\partial x_i}$ ($i = 1, 2$) to the chemical potential difference terms in (31).

NUMERICAL METHODS

To investigate coalescence and separation in the presence of surfactant for a binary immiscible fluid mixture, the equations can be made dimensionless based on a convective scaling, defined by:

$$\widetilde{\mathbf{x}} = \frac{\mathbf{x}}{L_c}, \quad \widetilde{t} = \frac{U_c t}{L_c}, \quad \widetilde{\mathbf{v}} = \frac{\mathbf{v}}{U_c}, \tag{34}$$

$$Re = \frac{U_c L_c}{v_c}, \quad Ma = \frac{\Delta \sigma}{\eta_c U_c}, \quad Ca = \frac{\eta_c U_c}{\sigma_0}, \tag{35}$$

$$Bo = \frac{gd^2 \Delta \rho}{\sigma_0}, \quad Pe = \frac{U_c L_c}{D}. \tag{36}$$

Here, U_c is a characteristic velocity, L_c is a macro-length scale which in our case coincides with the periodicity length of the computational domain, while σ_0 is the surface tension corresponding to a clean interface (i.e., in the absence of surfactant). Using Eq. (7), it is easily seen that the free energy scale (β) and the interfacial thickness for a flat interface with adsorbed surfactant (ξ) control the scaling of surface tension as $\sigma \approx \beta (\Delta \phi_{eq})^2 \xi$ (with $\Delta \phi_{eq}$ denoting a function of $\langle x_2 \rangle$) which can then be used for scaling the Korteweg force in the Navier-Stokes equation in terms of a reciprocal Weber number ($We = ReCa$) and a Marangoni number combined as $(1 - MaCa)/We$. Finally, the governing equations (with all tildes dropped) based on the convective scaling can be rewritten as follows:

$$\partial_t \begin{Bmatrix} \Phi \\ \Psi \end{Bmatrix} + \nabla \cdot \begin{Bmatrix} \Phi \\ \Psi \end{Bmatrix} \mathbf{v} = \begin{Bmatrix} \frac{1}{Pe} \nabla \cdot \left[\frac{b}{a} \left(\frac{\Psi^2}{4} - \Phi^2 \right) \nabla \hat{\mu}_{13} \right] \\ 0 \end{Bmatrix}, \tag{37}$$

$$(\partial_t - Re^{-1} \nabla^2) \mathbf{v} = -\mathbb{P}(\nabla) \mathbf{N}, \tag{38}$$

where

$$\mathbf{N} = \nabla \cdot \mathbf{v}\mathbf{v} + \frac{1-MaCa}{WeCn}\left[\Phi\nabla\hat{\mu}_{13}^{nl} + \Psi\nabla\hat{\mu}_{23}^{nl}\right] - \frac{L_c^2}{d^2}\frac{Bo}{We}\hat{\mathbf{g}} \quad (39)$$

is the sum of inertial, Korteweg and gravitational forces, with Cn denoting the Cahn number, $Cn \equiv \xi/L_c$, and d drop diameter of an initially monodisperse array of surfactant-covered heavy fluid drops embedded in a continuous phase. In (37), Φ is the phase field and $\Psi \equiv x_2/\sqrt{b/a}$ is the nondimensional surfactant concentration, while $\hat{\mu}_{13}^{nl}$ and $\hat{\mu}_{23}^{nl}$ in (39) denote (dimensionless) nonlocal parts of the chemical potential differences.

Note that the pressure has no physical meaning in (31) since it only plays the role a multiplier for enforcing the incompressible constraint, Eq. (32). In fact, the Poisson equation for the pressure (which results after taking the divergence of the Navier-Stokes equation) can be formally solved in terms of the nonlocal operator ∇^{-2} (a formal inversion of the Laplacian) so that after eliminating the pressure gradient the buoyancy force together with the nonlinear terms in the Navier-Stokes equation are acted upon by the Helmholtz projection operator $\mathbb{P}(\nabla) := \delta_{ij} - \nabla^{-2}\partial_{ij}^2$, which guarantees a solenoidal velocity at all times.

We assume periodic boundary conditions which enables a pseudospectral discretization of the governing equations. In pseudospectral methods, however, aliasing errors are incurred unless special care is taken in the computation of nonlinear terms. Quadratic nonlinearities are usually made alias-free using the so-called padding method (Canuto *et al.*, 1988), consisting of collocating in physical space on a refined grid with $(3/2)^3$ as many grid points as the number of active modes in the calculation. Using the padding method, a refined grid of $(2N)^3$ points is required for dealiasing the cubic nonlinearities. In our production runs, the '3/2 rule' has been employed for both quadratic and cubic nonlinearities since the remaining aliasing errors were found to be negligible. Dealiasing by the '3/2 rule' was implemented in our code using the parallel strategy of Iovieno *et al.* (2001). The grid spacing is such that interface profiles are resolved with three collocation points, i.e., $\Delta x = \xi/2$. Finally, it is noted that the divergence form of the nonlinear term in the Navier-Stokes equation would normally require nine FFTs for its pseudospectral evaluation. However, using a technical improvement previously introduced by Basdevant (1983) (which is still applicable within the Boussinesq approximation) in our numerical algorithm, its computation requires only *eight* FFTs.

The system (37)-(38) is time-integrated using a third-order Runge-Kutta scheme, with a variable time step determined by the Courant-Friedrichs-Lewy (CFL) condition,

$$\Delta t = N_C \frac{\Delta x}{V}, \quad (40)$$

where Δx is the dimensionless grid spacing, N_C is the Courant number, and V is a characteristic dimensionless bulk velocity. However, when the convective Cahn-Hilliard equation is coupled to the Navier-Stokes equation, in addition to this natural CFL condtion other time step restrictions become relevant and, specifically, due to the presence of surface tension and gravitational forces the following constraints must

be considered (Badalassi and Banerjee, 2005):

$$\Delta t \leq C_1 We^{1/2} \min\{\Delta x^{3/2}, \Delta y^{3/2}, \Delta z^{3/2}\}, \quad \Delta t \leq Fr\Delta z, \quad (41)$$

where $Fr = We/Bo$ and $C_1 \leq 10$. For the sedimentation simulations, the Courant number was chosen such that the time-advancement scheme is numerically stable and the smallest dynamical motions are accurately computed. Unfortunately, the nonlinearity of the equations prevents a rigorous determination of the maximum acceptable Courant number. In our simulations, we chose $N_C = N_C^*$ (with $N_C^* = 10^{-4} \div 10^{-2}$ depending on the values for the pair $(Bo, \mathscr{R})$ as we found values $N_C > N_C^*$ such that the scheme is numerically unstable. An integrating factor was used for the purely diffusive terms in the phase-field and Navier-Stokes equations so that there is no concern for the viscous stability of the scheme for any values of the Courant number.

As previously mentioned, the initial condition consists of a monodisperse array of surfactant-covered spherical heavy fluid drops (at random locations in the computational domain) embedded in a continuous phase of light fluid and a zero velocity field. Different simulations are initialized with different values of Re, Bo, We and Ma.

RESULTS AND DISCUSSION

Numerical results from simulations in a periodic box are now described. The simulations were carried out in a box of size $\frac{N}{2}\xi$ at different resolutions, 48^3, 64^3, and 128^3. Initially, surfactant-free simulations were conducted with the governing equations made dimensionless within a diffusive scaling, where the independent nondimensional groups are the Bond number and the fluidity parameter:

$$\mathscr{R} = \frac{RT}{M_W}\frac{\hat{\xi}^2}{v_c^2}. \quad (42)$$

In diffuse-interface models of single-component and partially miscible binary mixtures, this quantity is typically introduced as an inverse capillary number (Vladimirova *et al.*, 1999), but in fact it can also be shown to play the role of an interfacial Reynolds number (Lamorgese and Mauri, 2005,
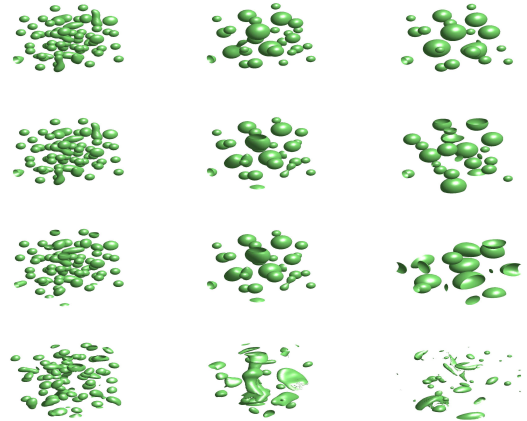

Figure 2: Snapshots of phase-field isosurfaces with $\mathscr{R} = 1000$ at different non-dimensional times $t = 0.1$, 0.5 and 1, with $\mathscr{G} = 0.01, 0.1, 1, 10$ from top to bottom.
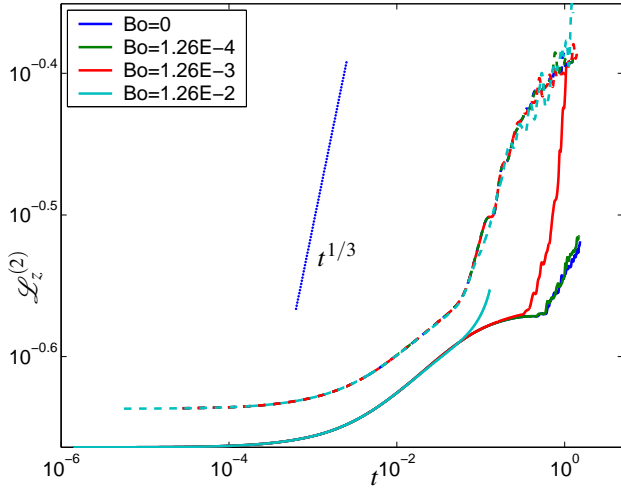
Figure 3: Square root of reciprocal second moment of structure factor in the longitudinal direction vs. time (made dimensionless within diffusive scaling) for surfactant simulations with a Marangoni number of $Ma \approx 1.68$ (solid) against surfactant-free simulations (dashed) with $\mathscr{R} = 1$ and different values of the Bond number.
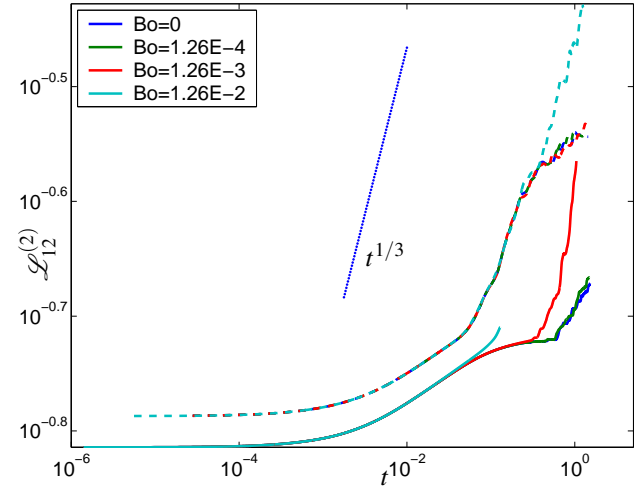

Figure 4: Square root of reciprocal second moment of structure factor in the transverse direction vs. time (made dimensionless within diffusive scaling) for surfactant simulations with a Marangoni number of $Ma \approx 1.68$ (solid) against surfactant-free simulations (dashed) with $\mathscr{R} = 1$ and different values of the Bond number.

2009). For reference, we show the Reynolds and Weber numbers within the convective scaling (Eq. 34) based on the settling velocity from the Hadamard-Rybczynski formula:

$$Re = \mathscr{R}\frac{d}{\hat{\xi}}Bo, \qquad We = \mathscr{R}\frac{d}{\hat{\xi}}Bo^2. \qquad (43)$$

As previously noted, we introduce this reference velocity in the convective scaling for studying sedimentation at small and moderately large Reynolds numbers, although it strictly applies to creeping flow conditions which can be made to occur at very small Bond numbers (with near unit nondimensional velocities). Within the diffusive scaling, the Bond number for a heavy fluid drop of diameter d embedded in a continuous phase of light fluid is given by

$$Bo = \left(\frac{d}{L_c}\right)^2 \frac{\mathscr{G}}{\mathscr{R}} Cn \frac{\Delta\rho/\rho}{(\Delta\phi)_{eq}^2 \sqrt{\Psi_{13} - 2}}, \qquad (44)$$

which can be varied independently by specifying different values of the nondimensional parameter $\mathscr{G} = \frac{gL_c^3}{v_c^2}$ (a Galileo number). In all simulations, drop diameter was fixed at $6\hat{\xi}$ with a fluidity of $\mathscr{R} = 1$, while the Bond number was varied changing the capillary length by prescribing $\mathscr{G} = 10^{-2}, 10^{-1}, 1, 10$. Values of dimensionless parameters achieved in simulation are summarized in Table 1. Note that the Peclet number does not play any role as a physical quantity due to its influence as a numerical parameter controlling the width of the interfacial region between immiscible fluids. In particular, the Peclet number was chosen such that at large times the contribution of residual diffusion to coarsening is negligibly small, so as to ensure independence of numerical results on the choice of Pe. It should be noted from the nondimensional governing equations that the rate of coarsening at a late stage is expected to be a function of a reduced

$\mathscr{G}$	Re	We	We^*	Ma	Bo
0.01	$7.57\,10^{-5}$	$9.55\,10^{-10}$	$2.6\,10^{-11}$	4170	$1.26\,10^{-5}$
0.1	$7.57\,10^{-4}$	$9.55\,10^{-8}$	$2.6\,10^{-9}$	417	$1.26\,10^{-4}$
1	$7.57\,10^{-3}$	$9.55\,10^{-6}$	$2.6\,10^{-7}$	41.7	$1.26\,10^{-3}$
10	$7.57\,10^{-2}$	$9.55\,10^{-4}$	$2.6\,10^{-5}$	4.17	$1.26\,10^{-2}$

Table 1: Values of dimensionless parameters in simulation based on convective scaling.

set of nondimensional parameters, which for the surfactant-free case corresponds to the 3-vector $(Re, \frac{1}{WeCn}, \frac{Bo}{We})$. Ideally, based on this reduced set it should be possible to build a map of coarsening regimes or phase diagram for emulsion separation in gravity with or without surfactant.

The addition of surfactant introduces the Marangoni number as an additional nondimensional parameter in the reduced set controlling late-stage growth, in the form $(Re, \frac{1-MaCa}{WeCn}, \frac{Bo}{We})$. To calculate the Marangoni number the average surfactant concentration was used in conjunction with a numerically determined equation of state, expressing the relation for a flat interface between the equilibrium surface tension and equilibrium surfactant concentration. This relation was determined from pseudospectral calculations of equilibrium flat interface profiles in a ternary system which phase separates into two stable phases after a deep quench from a one-phase region. In simulations based on the diffusive scaling, it follows from Eqs. (43) that the Marangoni number at a prescribed surfactant concentration is approximately determined as a reciprocal Bond number.

Next, we looked at surfactant effects on sedimentation for an initially monodisperse array of heavy fluid droplets in a continuous phase of light fluid. Again, simulations were con-
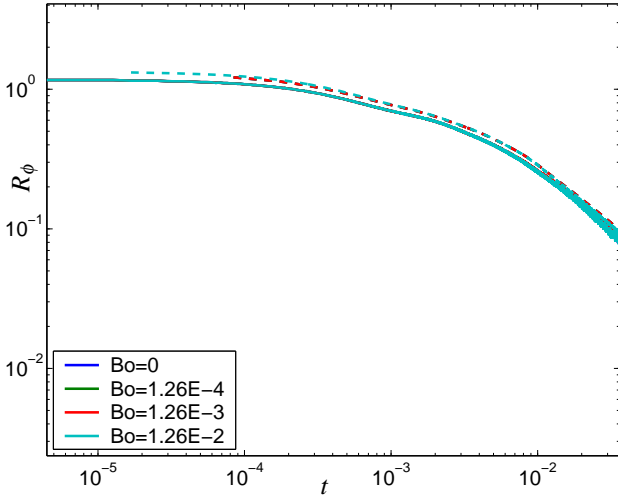
Figure 5: Order-parameter Reynolds number (Eq. 46) vs. time (dimensionless within diffusive scaling) from surfactant simulations with a Marangoni number of $Ma \approx 1.68$ (solid) against surfactant-free simulations (dashed) with $\mathscr{R} = 1$ and different values of the Bond number.
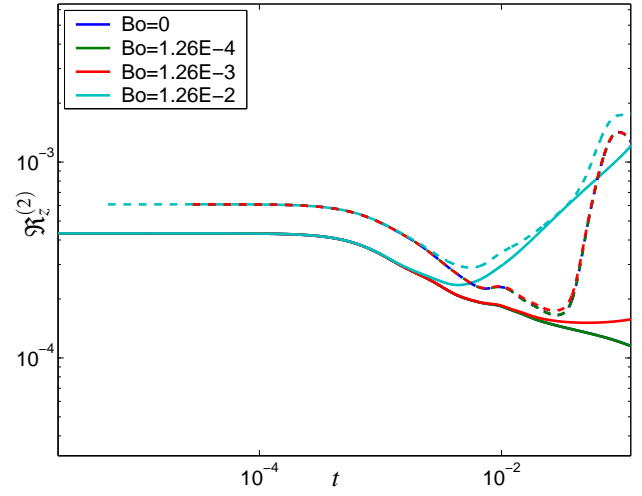

Figure 6: Reynolds number based on characteristic longitudinal length scale (from Eq. 45) vs. time (diffusive time units) for surfactant simulations with a Marangoni number of $Ma \approx 1.68$ (solid) against surfactant-free simulations (dashed) with $\mathscr{R} = 1$ and different values of the Bond number.

ducted with an initial drop diameter of $6\hat{\xi}$ and $\mathscr{R} = 1$, while the Bond number was varied through independent specification of $\mathscr{G} = 10^{-2}, 10^{-1}, 1, 10$. Snapshots of phase-field isosurfaces from surfactant-free simulations at different nondimensional times (in diffusive time units) during sedimentation with the same value of the fluidity and different values of the Bond number are shown in Figs. 2. The number of grid points for resolving a droplet in the initial configuration was investigated by looking at values of the settling velocity for an isolated droplet with prescribed fluidity ($\mathscr{R} = 10^3$) and and Bond number ($Bo = 1$). The values obtained support the conclusion that for the chosen fluidity and Bond number 64^3 is adequate for resolving the settling velocity. However, further analysis of resolution requirements for the concentration and velocity fields is required in future work. Note that, particularly for the case of an emulsion coarsening through multi-drop interactions, the Weber number should be more appropriately defined as $We^* = \left(\frac{u_s}{u_a}\right)^2 \frac{\xi}{d}$, with u_a, u_s denoting, respectively, a reference speed of sound ($u_a = \sqrt{RT/M_W}$) and the Hadamard-Rybczynski settling velocity, leading to somewhat smaller values achieved in simulation (see Table 1).

To study the longitudinal and transverse rates of coarsening during sedimentation, we defined the longitudinal and transverse length scales based on the reciprocal first and second moments of the spherically averaged structure factor, i.e.,

$$\mathscr{L}_{12}^{(r)} = \left[\frac{\sum_{\boldsymbol{\kappa}} \langle |\hat{\Phi}_{\boldsymbol{\kappa}}|^2 \rangle}{\sum_{\boldsymbol{\kappa}} \langle |\kappa_{12}|^r |\hat{\Phi}_{\boldsymbol{\kappa}}|^2 \rangle}\right]^{1/r}, \quad \mathscr{L}_z^{(r)} = \left[\frac{\sum_{\boldsymbol{\kappa}} \langle |\hat{\Phi}_{\boldsymbol{\kappa}}|^2 \rangle}{\sum_{\boldsymbol{\kappa}} \langle |\kappa_z|^r |\hat{\Phi}_{\boldsymbol{\kappa}}|^2 \rangle}\right]^{1/r},$$
(45)

($r = 1, 2$) where $\kappa_{12}^2 = |\boldsymbol{\kappa}|^2 - \kappa_z^2$, κ_z being the longitudinal wavenumber (i.e. in the direction of gravity). The time-dependent structure factor is defined as the Fourier transform of the pair correlation function, having the meaning of a spectral density of phase-field variance in wavenum-

ber space. The length scales defined in (45) can be introduced after a generalized dynamical scaling assumption (Puri *et al.*, 1992), which is appropriate when different characteristic length scales exist in different directions. However, generalized dynamical scaling *per se* does not imply a late stage power-law behavior of the characteristic length scales. In fact, due to the relatively low resolution of our simulations, we do not address scaling questions here and limit ourselves to surfactant effects on the rate of coarsening as reflected in the growth laws for the characteristic length scales.

Figures 3 and 4 show reciprocal second moments of the spherically averaged structure factor in the longitudinal and transverse directions from simulations (based on the diffusive scaling) on a 64^3 grid. As can be seen, in all cases without surfactant (and for some surfactant simulations) there are hints of a $t^{1/3}$ power-law behavior in the growth law at small times, which is reminiscent of a coagulation mechanism where droplets of different sizes undergoing Brownian motion collide and coalesce to give a larger droplet. Also note the slowing down of coarsening in the presence of surfactant and the qualitatively different effect of Bond number in the surfactant simulations. Specifically, while in the absence of surfactant there appears to be a Bond-number-independent incubation time before the relative magnitude of gravity/surface tension has a controlling influence on the growth law, the surfactant simulations reveal a first-order dependence of the incubation time on the Bond number. We also looked at a dimensionless rate of coarsening defined as

$$R_\phi = Re \mathscr{L}_z \dot{\mathscr{L}}_z, \quad (46)$$

which has been characterized previously as an order-parameter Reynolds number (Kendon *et al.*, 1999; Kendon, 2000; Kendon *et al.*, 2001). This quantity has been used in conjunction with a capillary number to characterize the binary fluid coarsening problem (in the absence of gravity),
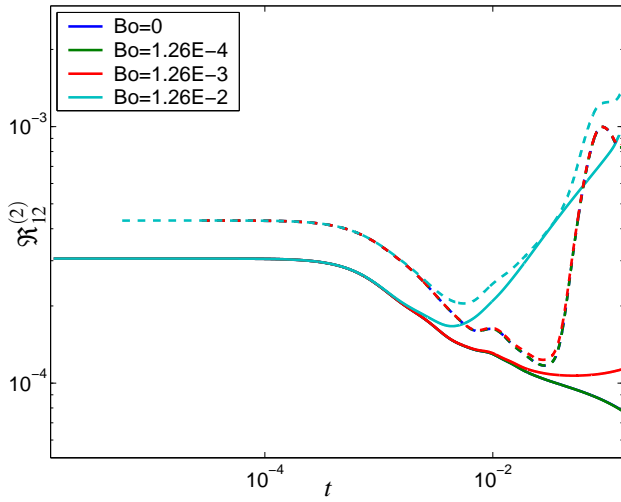
Figure 7: Reynolds number based on characteristic transverse length scale (Eq. 45) vs. time (diffusive time units) for surfactant simulations with a Marangoni number of $Ma \approx 1.68$ (solid) against surfactant-free simulations (dashed) with $\mathscr{R} = 1$ and different values of the Bond number.
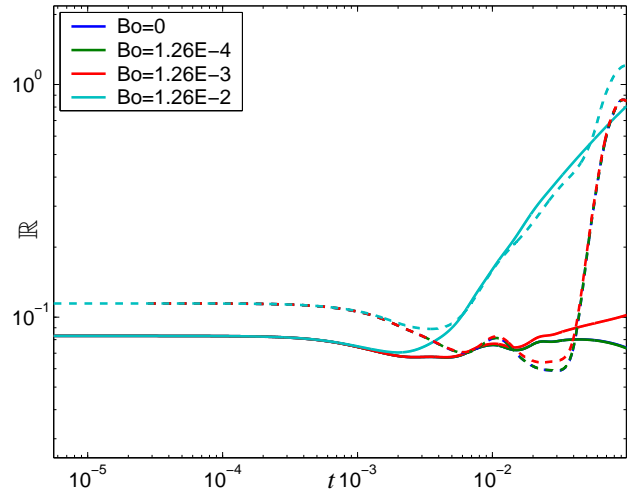

Figure 8: Reynolds number based on *rms* velocity and vorticity (Eq. 48) vs. time (dimensionless within diffusive scaling) from surfactant simulations with a Marangoni number of $Ma \approx 1.68$ (solid) against surfactant-free simulations (dashed) with $\mathscr{R} = 1$ and different values of the Bond number.

where $R_\phi \ll 1$ and $Ca \sim 1$ at early times, while at late times $R_\phi Ca \sim 1$ and $Ca \ll 1$. Obviously, any power-law behavior detected in the temporal evolution of this Reynolds number translates into power-law information for the characteristic length scale, with a growth exponent $n = \frac{n_R + 1}{2}$ (n_R being the power-law exponent for the Reynolds number). Again, numerical results (Fig. 5) show the dimensionless coarsening rate from surfactant simulations to be consistently smaller than its surfactant-free counterpart, with hints of a $t^{1/3}$ power-law behavior at small times. However, due to the relatively low resolution of our simulations, questions of scaling cannot be reliably addressed using the present dataset due to finite box size effects which spoil (any) scaling behavior at large times.

Finally, as a measure of the strength of the fluid motion induced by the phase segregation, we introduce a Reynolds number based on the *rms* fluctuation over the mean settling velocity, u', and the characteristic size of single-phase microdomains in the longitudinal and transverse directions, i.e.,

$$\mathfrak{R}_i^{(r)} = \mathscr{R} u' \mathscr{L}_i^{(r)} \quad (i = l, t). \tag{47}$$

These quantities are compared to their surfactant-free counterparts in Figs. 6 and 7. As can be seen, the Reynolds numbers corresponding to the surfactant simulations are always smaller than their surfactant-free counterparts, suggesting a reduction in the strength of fluid motion in the longitudinal and transverse directions due to the presence of surfactant. Similar behavior (although not always strictly monotonic with respect to absence/presence of surfactant) is shown by another Reynolds number solely based on the mixture velocity, given by:

$$\mathbb{R} = \mathscr{R} \frac{u'^2}{\omega'}, \tag{48}$$

(all quantities here and in (47) being dimensionless within the diffusive scaling) where ω' denotes the *rms* vorticity fluc-

tuation (see Fig. 8).

CONCLUSIONS

In conclusion, preliminary results on insoluble surfactant effects on emulsion coarsening in a gravitational field show a characteristic surfactant-induced retardation of the rate of coarsening as well as a reduction in the strength of fluid motion during emulsion resolution in the longitudinal and transverse directions as compared to surfactant-free simulations.

REFERENCES

BADALASSI, V.E. and BANERJEE, S. (2005). "Nanostructure computation with coupled momentum phase ordering kinetics models". *Nucl. Eng. Des.*, **235**, 1107–15.

BADALASSI, V.E. *et al.* (2003). "Computation of multiphase systems with phase field models". *J. Comput. Phys.*, **190(2)**, 371–97.

BADALASSI, V.E. *et al.* (2004). "Gravitational effects on structure development in quenched complex fluids". *Ann. N. Y. Acad. Sci.*, **1027**, 371–82.

BASDEVANT, C. (1983). "Technical improvements for direct numerical simulation of homogeneous three-dimensional turbulence". *J. Comput. Phys.*, **50**, 209–14.

BINKS, B.P. (1998). "Emulsions–recent advances in understanding". B.P. Binks (ed.), *Modern Aspects of Emulsion Science*, 1–55. Royal Society of Chemistry.

BŁAWZDZIEWICZ, J. *et al.* (2000). "Rheology of a dilute emulsion of surfactant-covered spherical drops". *Physica A*, **276**, 50–85.

CAHN, J.W. and HILLIARD, J. (1959). "Free energy of a nonuniform system: III. Nucleation in a two-component incompressible fluid". *J. Chem. Phys.*, **31**, 688–99.

CANUTO, C. *et al.* (1988). *Spectral Methods in Fluid Dynamics*. Springer, New York.

CAU, F. and LACELLE, S. (1993). "Late-stage phase separation and sedimentation in a binary liquid mixture". *Phys. Rev. E*, **47(2)**, 1429–32.

CHAN, C.K. and GOLDBURG, W.I. (1987). "Late-stage phase separation and hydrodynamic flow in a binary liquid mixture". *Phys. Rev. Lett.*, **58(7)**, 674–7.

CRISTINI, V. *et al.* (1998). "Near-contact motion of surfactant-covered spherical drops". *J. Fluid Mech.*, **366**, 259–87.

DUKHIN, S.S. *et al.* (2006). "An experimental and theoretical approach to the dynamic behavior of emulsions". J. Sjöblom (ed.), *Emulsions and Emulsion Stability*, 2nd ed., 1–106. CRC Press.

EDWARDS, D. *et al.* (1991). *Interfacial Transport Processes and Rheology*. Butterworth-Heinemann, New York.

GIRIBABU, K. and GHOSH, P. (2007). "Adosrption of nonionic surfactants at fluid-fluid interfaces: Importance in the coalescence of bubbles and drops". *Chem. Eng. Sci.*, **62**, 3057–67.

HOHENBERG, P.C. and HALPERIN, B.I. (1977). "Theory of dynamic critical phenomena". *Rev. Mod. Phys.*, **49**, 435–79.

IOVIENO, M. *et al.* (2001). "A new technique for a parallel dealiased pseudo-spectral Navier-Stokes code". *Comp. Phys. Comm.*, **141(3)**, 365–74.

KEESTRA, B. *et al.* (2003). "Diffuse interface modeling of the morphology and rheology of immiscible polymer blends". *Phys. Fluids*, **15(9)**, 2567–75.

KENDON, V.M. (2000). "Scaling theory of three-dimensional spinodal turbulence". *Phys. Rev. E*, **61**, R6071–4.

KENDON, V.M. *et al.* (1999). "3D spinodal decomposition in the inertial regime". *Phys. Rev. Lett.*, **83(3)**, 576–9.

KENDON, V.M. *et al.* (2001). "Inertial effects in three-dimensional spinodal decomposition of a symmetric binary fluid mixture". *J. Fluid Mech.*, **440**, 147–203.

KOBAYASHI, H. *et al.* (2003). "Phase-field model for solidification of ternary alloys coupled with thermodynamic database". *Scr. Mater.*, **48**, 689–94.

KOMURA, S. and KODAMA, H. (1997). "Two-order-parameter model for an oil-water-surfactant system". *Phys. Rev. E*, **55(2)**, 1722–7.

KRALCHEVSKY, P. *et al.* (1996). "Thin liquid film physics". R. Proud'homme and S. Khan (eds.), *Foams. Surfactant Science Series vol. 57*, 1–98. Dekker.

LAMORGESE, A.G. and MAURI, R. (2005). "Nucleation and spinodal decomposition of liquid mixtures". *Phys. Fluids*, **17**, 034107.

LAMORGESE, A.G. and MAURI, R. (2009). "Diffuse-interface modeling of liquid-vapor phase separation in a van der Waals fluid". *Phys. Fluids*, **21**, 044107.

LAMURA, A. *et al.* (1999). "A lattice Boltzmann model of ternary fluid mixtures". *Europhys. Lett.*, **45(3)**, 314–20.

LARADJI, M. *et al.* (1992). "The effects of surfactants on the dynamics of phase separation". *J. Phys.: Cond. Mat.*, **16**, 6715–28.

LIU, H. and ZHANG, Y. (2010). "Phase-field modeling droplet dynamics with soluble surfactants". *J. Comput. Phys.*, **229**, 9166–87.

MALDARELLI, C. and HUANG, W. (1996). "The effects of surfactants on the motion of bubbles and drops".

U. Schaflinger (ed.), *Flow of Particles and Suspensions*, 125–60. CISM vol. 370.

MELENKEVITZ, J. and JAVADPOUR, S.H. (1997). "Phase separation dynamics in mixtures containing surfactants". *J. Chem. Phys.*, **107**, 623–9.

PRUSTY, M. *et al.* (2007). "Experimental and computational study on structure development of PMMA/SAN blends". *Chem. Eng. Sci.*, **62(6)**, 1825–37.

PURI, S. *et al.* (1992). "Dynamical scaling in anisotropic phase-separating systems in a gravitational field". *Phys. Rev. B*, **46(1)**, 98–105.

RAMIREZ, J. *et al.* (2000). "Microflotation of fine particles in the presence of bulk-insoluble surfactant". *Int. J. Multiphase Flow*, **26**, 891–920.

ROTHER, M.A. and DAVIS, R.H. (2004). "Buoyancy-driven coalescence of spherical drops covered with incompressible surfactant at arbitrary Peclet number". *J. Colloid Interface Sci.*, **270**, 205–20.

ROTHER, M.A. *et al.* (2006). "Surfactant effects on buoyancy-driven viscous interactions of deformable drops". *Coll. Surf. A: Physicochem. Eng. Aspects*, **282-3**, 50–60.

SATO, M. and SUMITA, I. (2007). "Experiments on gravitational phase separation of binary immiscible fluids". *J. Fluid Mech.*, **591**, 289–319.

SCHMITT, V. and LEAL-CALDERON, F. (2004). "Measurement of the coalescence frequency in surfactant-stabilized concentrated emulsions". *Europhys. Lett.*, **67(4)**, 662–8.

TEIGEN, K.E. *et al.* (2011). "A diffuse-interface method for two-phase flows with soluble surfactants". *J. Comput. Phys.*, **230**, 375–93.

THEISSEN, O. and GOMPPER, G. (1999). "Lattice-Boltzmann study of spontaneous emulsification". *Eur. Phys. J. B*, **11**, 91–100.

TO, K.W. and CHAN, C.K. (1992). "Scaling behavior in the demixing of a binary liquid mixture under gravity". *Europhys. Lett.*, **19(4)**, 311–6.

TO, K.W. and CHAN, C.K. (1994). "Morphology and dynamics of a separating immiscible binary liquid mixture under gravity". *Physica A*, **205**, 320–9.

TUFANO, C. *et al.* (2010). "Effects of partial miscibility on drop-wall and drop-drop interactions". *J. Rheol.*, **54(1)**, 159–83.

VAN DER SMAN, R.G.M. and VAN DER GRAAF, S. (2006). "Diffuse interface model of surfactant adsorption onto flat and droplet interfaces". *Rheol. Acta*, **46**, 3–11.

VAN DER WAALS, J.D. (1894). "The thermodynamic theory of capillarity under the hypothesis of a continuous variation of density". *Z. Phys. Chem. Stöchiom. Verwandtschaftsl.*, **13**, 657. Translated and reprinted in J. Stat. Phys. **20**, 200–44 (1979).

VLADIMIROVA, N. *et al.* (1999). "Diffusiophoresis of two-dimensional liquid droplets in a phase-separating system". *Phys. Rev. E*, **60**, 2037–44.

VLAHOVSKA, P. *et al.* (2002). "Nonlinear rheology of a dilute emulsion of surfactant-covered spherical drops in time-dependent flows". *J. Fluid Mech.*, **463**, 1–24.

YUE, P. *et al.* (2004). "A diffuse-interface method for simulating two-phase flows of complex fluids". *J. Fluid Mech.*, **515**, 293–317.

8th International Conference on CFD in Oil & Gas, Metallurgical and Process Industries
SINTEF/NTNU, Trondheim Norway
21-23 June 2011

CFD11-64

INCLUSION ELIMINATION IN STEELMAKING LADLE

Pascal GARDIN[1]* , Marie SIMONNET[1], Ségolène GAUTHIER[1]

[1] ARCELORMITTAL Maizières, 57283 Maizières-lès-Metz Cedex, FRANCE

* E-mail: pascal.gardin@arcelormittal.com

ABSTRACT

The paper describes the inclusion behaviour inside a ladle submitted to pneumatic stirring. Different phases are simultaneously considered: liquid steel, slag layer, top gas, argon bubbles and inclusions. A modelling of inclusion dewetting is presented, and allows us to adjust and justify the criteria for the efficient capture of inclusions at interfaces. It is based on the calculation of the liquid film drainage when the inclusion comes in contact with the interface.

To get the best agreement with measurements already published on the kinetics of inclusion elimination, we have to consider that only the interface between liquid steel and slag is active to eliminate the inclusions. It means that inclusions captured by the gas bubbles injected for the stirring have globally no effect: inclusions are probably captured but they should be released in the liquid steel when gas bubbles cross the upper interface.

Keywords: CFD, steelmaking, ladle, interface, multiphase flow, dewetting.

NOMENCLATURE

Greek Symbols

ρ Density, [kg/m^3].

ε Dissipation rate of turbulent kinetic energy, [m^2/s^3].

μ Dynamic viscosity of liquid steel, [kg/m.s].

ν_t Turbulent diffusivity, [m^2/s].

τ Time scale for inclusion elimination, [s].

θ Contact angle between liquid steel and inclusion, [rad].

σ_i Surface tension of inclusions, [N/m].

σ_m Surface tension of liquid metal, [N/m].

$\sigma_{i/m}$ Interface tension between inclusions and liquid metal, [N/m].

Latin Symbols

$C(t)$ Total number of inclusions at time t, [-].

C_{init} Total number of inclusions at initial time, [-].

D Inclusion diameter, [m].

d_B Bubble diameter, [m].

Eo Eötvös number= $\dfrac{g(\rho_{steel} - \rho_{gas})d_B^2}{\sigma_m}$.

e Dewetting distance, [m].

G Free energy, [J/m^2].

h Thickness of the liquid film, [m].

p Pressure, [Pa].

Q_N Standard flow rate of argon, [l/min].

v_r Radial velocity, [m/s].

INTRODUCTION

In the steel industry, a lot of metallurgical treatments are realised before the continuous casting during the secondary metallurgy processes, generally in a reactor called ladle. One important treatment is the steel de-oxidizing: aluminium pellets are injected in the ladle and, after the pellet melting, aluminium reacts with dissolved oxygen to create solid alumina particles. These particles, called inclusions, are lighter than steel. They should be eliminated as quickly as possible, otherwise, if they are captured by the solidifying shell at the continuous casting machine, they will create quality problems in the final product. An efficient stirring of the ladle is then necessary to transport the inclusions towards the surface which is covered by a slag layer absorbing them. This stirring is usually realised by injecting an inert gas through one or several porous plugs located in the bottom part of the ladle, see Domgin et al., (1999).

A lot of work was already achieved for modelling the flows inside steelmaking ladle. Initial works started more than twenty years ago, Grevet et al. (1981), Schwarz and Turner (1988), Ilegbusi and Szekely (1990). Progressively, two-phase flow models (Euler-Euler, Euler-Lagrange) were used and inclusion elimination at interface was considered, Johansen and Boysan (1988), Schwarz (1996), Zhang (2000), Cournil et al. (2001), Hallberg et al. (2005). Recently, the free surface deformation inside a ladle was simulated, Sheng (2007), Olsen and Cloete (2009), Llanos et al. (2010), allowing for the prediction of complex interface, such as open-eye occurrence: the top slag layer is locally pulled

aside and the liquid steel is in direct contact with the atmosphere.

But the prediction of the kinetics of inclusion elimination was never totally convincing, since too many assumptions were made: flat top interface, no prediction of the slag behaviour and interaction with the liquid steel flow, no criteria for inclusion entrapment efficiency including thermodynamic conditions... It is the reason why we decided to simulate more precisely the interface between liquid steel and slag, using the Volume Of Fluid technique included in the Fluent CFD package, with some adaptation of the turbulence model to represent the turbulence redistribution at the interface. It is then possible to predict the inclusion entrapment at the interface, which is continuously deforming. In addition, a theoretical study based on existing literature allows us to adjust and justify the criteria for the efficient capture of inclusions at interfaces. It is based on the calculation of the liquid film drainage when the inclusion comes in contact with the interface.

MODEL DESCRIPTION

The commercial CFD software Fluent[TM] (6.3 release) was selected for the study. The simulation domain consists of five phases: liquid steel, slag layer, inclusions, argon and top gas. Fluid phases (liquid or gas) are considered non-miscible, and the interface is calculated by the Volume Of Fluid method, associated with the Piecewise-Linear Interface Construction (PLIC). The classical continuum surface force model is also included to take account of the surface tension effect. The inclusions are considered as solid spherical particles. Discrete Phase Model method (DPM) is used to calculate the trajectory of particles, with a stochastic model to deal with the turbulent fluctuations induced by the flow.

The rising bubbles create a source term in the momentum equation of liquid steel, and supply its motion. In 2D, bubbles are tracked by VOF method but, in 3D, DPM is selected, since it reduces drastically the computer time compare to VOF. Of course, the price to be paid is that the size of bubbles has to be imposed. Realisable k-ε turbulence model is used with standard logarithmic wall functions. More details can be found in Jiroveanu et al. (2007). The geometry of the domain corresponds to a cylindrical vessel, see Figure 1. The 3D mesh consists of 146000 cells, supplemented with an adaptive refinement to better describe interfaces (approximately 5 cells in thickness to describe the slag interface). Typical time step for the calculations is around 10^{-3} s, corresponding to a CFL condition of 0.2. All calculations are realised on a 2.8 GHz desktop PC. It takes approximately 3 CPU hours for predicting 1 second of inclusion elimination.
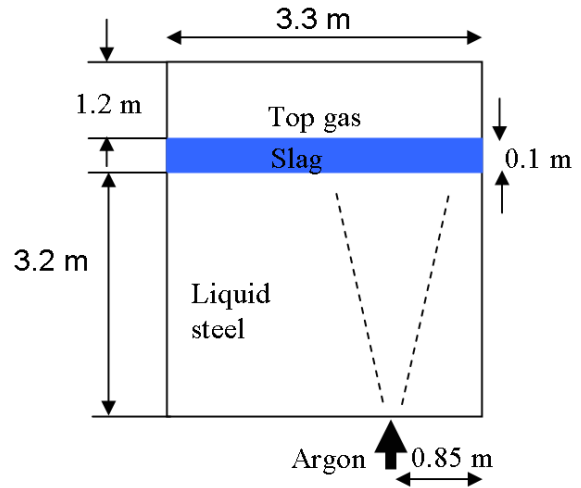

Figure 1: Geometry of the ladle.

The liquid steel phase is initially uniformly seeded with 200000 inclusions; then, at t = 0 s, argon is injected and inclusions are tracked by DPM. We checked that, provided the inclusions are smaller than 50 μm diameter, the normalised elimination rate of inclusion is almost independent of their size. Then, it is possible to compare the predictions to measurements, where the size distribution is never mentioned.

To account for the elimination of inclusions, a routine has been developed, considering the volume fraction C1, C2 and C3 for argon, slag and top gas respectively: when an inclusion is located in an area where Ci > 0.5, the inclusion is captured by the phase number i and a counting file dedicated to phase i is incremented by 1.

This technique allows quantifying the changes over time in the number of remaining inclusions in the computational domain, and identifying whether the inclusions are trapped by the bubbles, by the slag or by the top gas. Example of such elimination is illustrated in Figure 2. In 3D, the bubbles are tracked by lagrangian method and the condition for inclusion entrapment depends on the void fraction deduced from the DPM concentration.
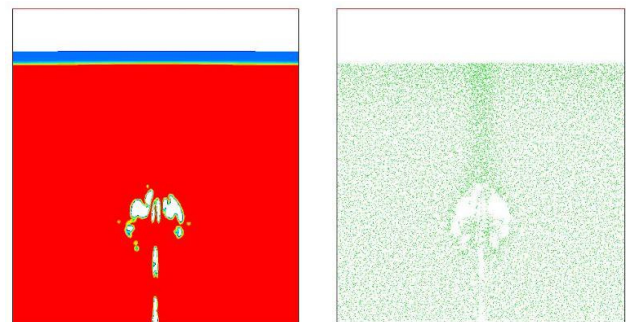

Figure 2: Typical 2D distribution of phases (left) and corresponding inclusion field (right) – in 3D, bubbles are tracked by lagrangian approach.

The validation for open-eye prediction was already realised in a 3D configuration by successful comparison with visualisations performed on cold water model, with

an oil layer to simulate the slag and different positions of the gas injection, see Gardin et al. (2011).

Inclusion elimination at interface

We will now define the conditions for the entrapment of inclusions at interfaces. Former work of Kozakevitch and Lucas (1968) was analysed. These authors considered an inclusion arriving at the interface between the liquid metal and a gaseous atmosphere; the size of this inclusion, which has a lamella shape, is small so that only the surface phenomena are predominant for determining the free energies.

There is a thermodynamically spontaneous emergence to go from state 1 to state 2 (Figure 3) if the emergence is accompanied by a decrease of free energy from G_1 to G_2.
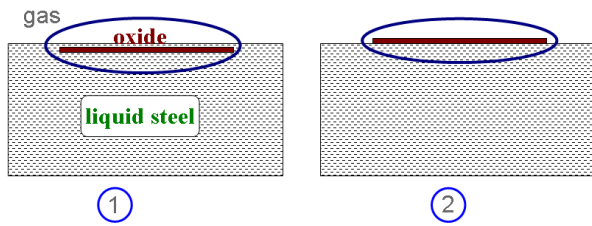
Figure 3: Spontaneous emersion of inclusion.

By neglecting the thickness of the lamella, the free energies for unit surfaces are expressed as follows:

$$G_1 = \sigma_{i/m} + \sigma_{i/m} + \sigma_m \qquad (1)$$

$$G_2 = \sigma_{i/m} + \sigma_i \qquad (2)$$

$$\text{Or } \Delta G = G_2 - G_1 = \sigma_i - \sigma_{i/m} - \sigma_m \qquad (3)$$

Using the equilibrium of the triple line (Figure 4):

$$\sigma_i - \sigma_m \cos\theta - \sigma_{i/m} = 0 \qquad (4)$$

and for ΔG :

$$\Delta G = \sigma_m (\cos\theta - 1) \qquad (5)$$
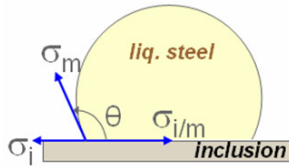
Figure 4: Young's relation

Table 1 gives some values for ΔG; the values are negative which demonstrates the spontaneous thermodynamic emersion of inclusions.

Table 1: Evolution of free energy between states 1 and 2, Kozakevitch and Olette (1971).

Inclusion: alumina	θ	σ_m (N/m)	ΔG (J/m^2)
Pure iron	140°	1.80	-3.179
Fe, 4% carbon	133°	1.73	-2.910
Fe, 0.07% oxygen	80°	1.10	-0.909
Fe, 0.02% sulfur	140°	1.39	-2.455

Another point we have studied is the kinetics of the liquid film withdrawal. To do this, we consider a configuration where two menisci are face to face, as shown in Figure 5, which is the section of a unique meniscus cut by a vertical plane crossing the axis of symmetry. The condition for the meniscus to be removed is that the pressure gradient is favourable: the pressure at the meniscus (liquid steel side), must be greater than the pressure far from it, which means that $p_1 > p_2$ (Figure 6). The relationship between r, the radius of the meniscus, and h, the height of the film, is given in Figure 5.
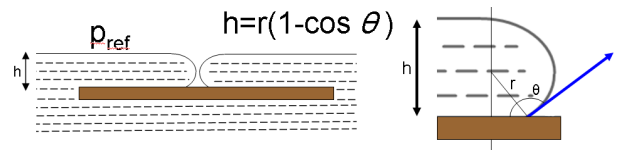

Figure 5: Withdrawal of liquid film, Riboud and Olette (1976)

The meniscus is characterized by two curvatures: one is concave and the other is convex (Figure 6), leading to respectively a positive and a negative effect on the film withdrawal.
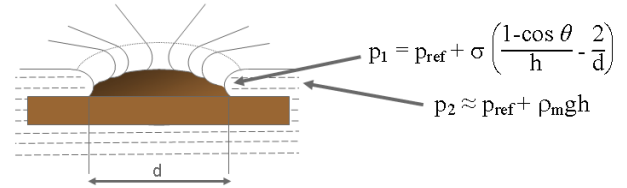

Figure 6: Dewetting of the inclusion surface

We can then write the condition for the immobility of the film, corresponding to $p_1 = p_2$:

$$h^2 + \frac{2\sigma}{\rho g d} h - \frac{\sigma}{\rho g}(1 - \cos\theta) = 0 \qquad (6)$$

When d is small:

$$h \approx d(1 - \cos\theta)/2 \qquad (7)$$

Or

$$d_{crit} \approx \frac{2h}{1 - \cos\theta} \qquad (8)$$

Numerical application: for $\theta = 110°$, h=5 µm, σ=1.4 N/m: d_{crit}=7.45 µm

It is therefore important to keep in mind that the withdrawal of the meniscus can be initiated only when the thickness of the gas hole is larger than d_{crit}. This can be promoted by means of an inclusion roughness. For

instance, an asperity with a plane shape will very easily increase locally the liquid steel pressure and facilitate the film repulsion, see Figure 7.

$$p_1 = p_{ref} + \sigma \left(\frac{1-\cos\theta}{h} \right) > p_{ref} + \sigma \left(\frac{1-\cos\theta}{h} - \frac{2}{d} \right)$$
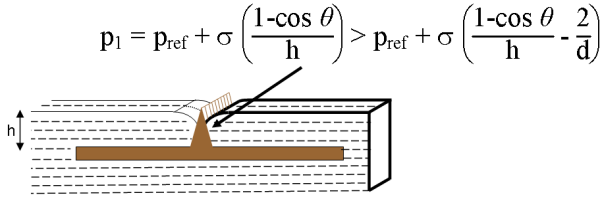
Figure 7: Initiation of dewetting by a plane asperity

Now suppose $d > d_{crit}$ and let us try to estimate how long it takes for the meniscus to withdraw completely across the diameter D of the inclusion. The main notations are shown in Figure 8.
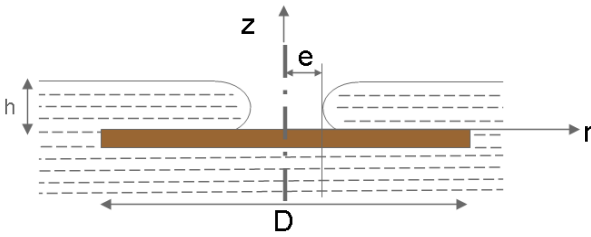
Figure 8: Meniscus position

2D Navier-Stokes equation can be solved using axisymmetrical coordinates:

$$\rho \left(\frac{\partial v_r}{\partial t} + v_r \frac{\partial v_r}{\partial r} \right) =$$
$$-\frac{\partial p}{\partial r} + \mu \left[\frac{\partial}{\partial r} \left(\frac{1}{r} \frac{\partial}{\partial r} (rv_r) \right) + \frac{\partial^2 v_r}{\partial z^2} \right] \tag{9}$$

With the following hypothesis:

$$\frac{1}{h} \int_0^h v_r dz \approx \frac{de}{dt} \quad \text{when } r \to e \tag{10}$$

$$\left(\frac{\partial v_r}{\partial z} \right)_{z=h} = 0 \tag{11}$$

and, using the continuity equation:

$$r \left(\frac{1}{h} \int_0^h v_r dz \right) \approx e \frac{de}{dt} \tag{12}$$

With the laminar flow assumption, the velocity profile obeys a parabolic law in the z direction and can be expressed as:

$$v_r = \frac{3}{2} \frac{de}{dt} \frac{1}{h^2} z(2h-z) \frac{e}{r} \tag{13}$$

Or:

$$v_r = \frac{3}{4r} \frac{de^2}{dt} \frac{1}{h^2} z(2h-z) \tag{14}$$

Finally, we have to solve:

$$\frac{d^2 E}{dt^2} = \frac{9}{15E} \left(\frac{dE}{dt} \right)^2 - \frac{2\sqrt{E}}{\rho} \frac{\partial p}{\partial r} - 3\nu \frac{dE}{dt} \frac{1}{h^2} \tag{15}$$

With the following approximation for the pressure gradient:

$$\frac{\partial p}{\partial r} \propto \frac{\rho g h - \sigma \left(\frac{1-\cos\theta}{h} - \frac{1}{\sqrt{E}} \right)}{\frac{D}{2} - \sqrt{E}} \tag{16}$$

where $E = e^2$, with the following initialisation: $2e_{t=0} = d_{crit}$ and $(de/dt)_{t=0} = 0$.

We used the Scilab™ software to solve this equation with the parameters shown in Figure 9. There is a gradual withdrawal of the meniscus, with an acceleration in the periphery of inclusion, as a result of high values of the pressure gradient. To remove a film of 100 μm radius, it takes approximately 50 microseconds.
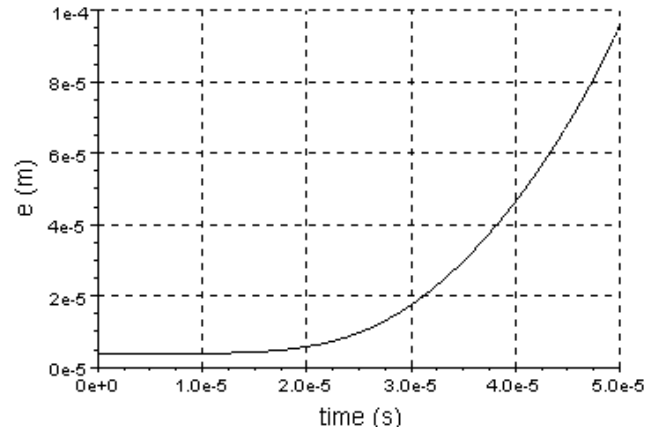
Figure 9: Time evolution of the dewetting with constant thickness, h=5 μm, θ=110°, σ_m=1.4 N/m, D=200 μm.

We also realised another calculation with the very pessimistic assumption, in terms of withdrawal time, that the rim of the dewetting film has an annulus shape, which partly collects the liquid steel after the dewetting, see Figure 10, and limits the positive pressure in the concave part of the meniscus. This was already observed and studied by Buguin et al. (1999), for the dewetting of water on an hydrophobic plate.
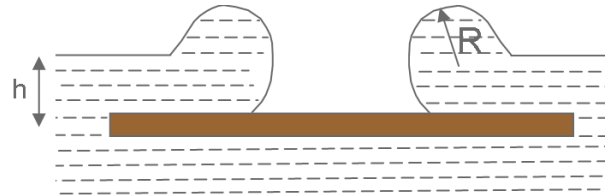
Figure 10: Withdrawal of the liquid film, rim with a toric shape.
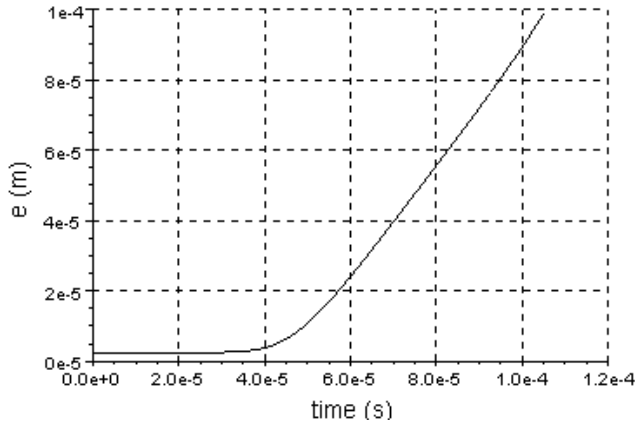
Then R can be expressed as:

$$R \propto \sqrt{\frac{eh}{2\pi}} \frac{1}{\sqrt{\pi - \frac{\theta_0 - \sin\theta_0}{2}}} \tag{17}$$

with $\theta_0 = 2(\pi - \theta)$.

The result is drawn in Figure 11. Since the pressure in the concave part of the meniscus is now decreased compared to the previous situation, the dewetting is slower, with a constant velocity of the rim from t=5.0 10^{-5} s. The total duration for the removal of the film is now 105 microseconds.

Figure 11: Rim with a toric shape, h=5 µm, θ=110°, σ_m=1.4 N/m, D=200 µm.

The calculations were repeated for different initial film thicknesses between 2 µm and 12 µm (Figure 12). The dewetting was always found to be lower than 200 microseconds.

The curve displays a minimum, which is the results of complex interactions. The dewetting force acting on the meniscus depends on the pressure gradient and the shear stress exerted by the liquid film on the inclusion surface; for h ≈ 5µm, the ratio between the pressure gradient force and the viscous force is maximum, resulting in a minimum dewetting duration.
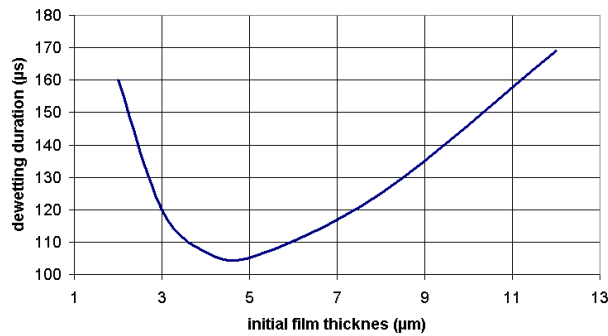
Figure 12: Dewetting times, for different initial thicknesses of the film, θ=110°, σ_m=1.4 N/m, D=200 µm.

We have now to determine the time scale of the most active turbulent eddies, which should be smaller than the dewetting time to be able to disturb significantly the film withdrawal and to remove the inclusions from the interface. Bubble induced turbulence, due to vortex shedding from the rising bubbles, Michiyoshi et al. (1986), Deen et al. (2001), is the key mechanism for the creation of turbulent eddies in this situation, and the time scale was already proposed by Lopez de Bertodano (1992):

$$\tau_{turb} = \frac{2C_{VM} d_B}{3C_D \left\| \vec{U}_R \right\|} \qquad (18)$$

where C_{VM} is the virtual mass coefficient (considered to be equal to 0.5 here), C_D the bubble drag coefficient:

$$C_D = \frac{8}{3} \frac{Eo}{Eo + 4} \qquad (19)$$

Eo: Eötvös number
and U_R is the relative velocity between gas and liquid, approximated to the bubble terminal velocity.

Figure 13 shows that the turbulent time scale is always larger than the dewetting time; it means that the dewetting should not be disturbed by the turbulence and should occur with an optimum efficiency.
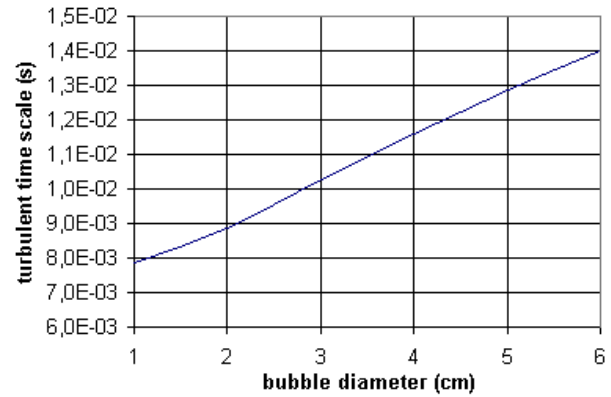
Figure 13: Time scale for bubble induced turbulence.

We can therefore draw the following conclusions:

1°/ For an axisymmetrical configuration, there is a critical size of the gas hole below which the liquid film cannot withdraw without the supply of external energy. But, if the inclusion has some roughness, the spontaneous dewetting can occur very easily.

2°/ If the film is removed, the order of magnitude of the withdrawal characteristic time is, at maxium, a hundred microseconds (for the parameters listed in Figure 9); this time is much lower than the characteristic time of turbulence: the withdrawal should be quite independent of the flows which, then, do not disrupt the process of inclusion entrapment; the entrapment efficiency is maximum and close to 1.

3°/ The adhesion of the inclusions inside the bubbles should be robust, since this position corresponds to a minimization of free energy and the external system must provide some energy (e.g. to break the bubbles) to re-introduce the inclusions inside the liquid steel.

Turbulence damping at interface

Turbulence is a key mechanism for inclusion tracking at interface vicinity, since it will partly determine the inclusion mass flux transferred to the interface which will be eliminated. As it was already mentioned by Hunt and Graham (1978), close to the interface, turbulent tangential shear stresses increase at the expense of the

normal ones. This will deeply influence the inclusion trajectory since, as inclusions are characterized by very low Stokes number, their motion is totally dependent on the instantaneous fluid velocity. There is very few information on this point in the literature and commercial CFD packages do not include any turbulence redistribution near the interface for RANS models. As far as we know, only CFX developers made specific adaptations on this topic. In case of k-ω turbulence model of Wilcox, Egorov and Menter (2004) proposed to add a source term for ω transport equation only at the free surface, which was tracked by VOF method. Franck (2005), Höhne (2009) and Bartosiewicz (2010) also used this adaptation for two-phase flow in horizontal pipes. We made exactly the same and, for want of anything better, the tuning parameter in the source term for ε equation was adjusted so that there was no turbulent diffusivity in the thin slag layer: since the characteristic Reynolds number is much smaller in the slag layer than inside the ladle, this should lead to a sudden decrease of the effective diffusivity from the liquid steel to the slag layer. It can be observed on Figure 14 that the turbulent diffusivity ν_t is very low in the thin film corresponding to the slag layer. Without the turbulence damping, there is continuity of ν_t across the different phases.
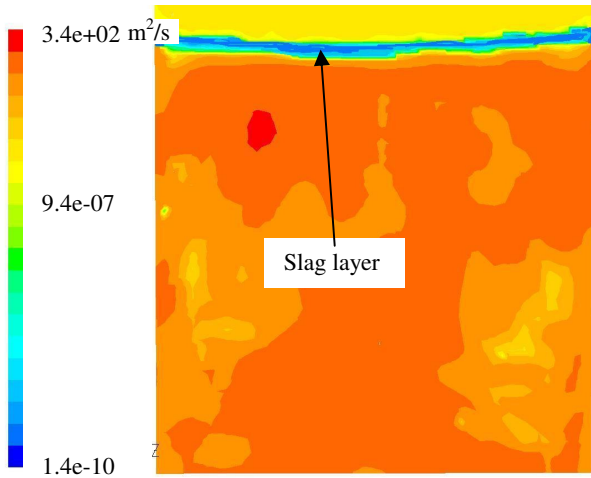
Figure 14: Turbulent diffusivity in a vertical plane out side the bubble plume – instantaneous field –logarithmic scale.

RESULTS

For standard condition (530 Nl/min of argon), a pronounced dome is observed, with the occurrence of a relatively large open-eye region, see Figure 15. The stability of this dome was predicted to be significantly decreased when argon was injected along the vessel axis. This is the reason why industrial practice retains off-center gas injection.
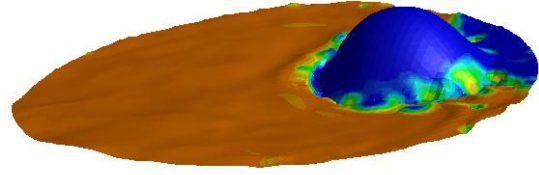
Figure 15: Position of liquid steel interface - brown: contact with slag, blue: open-eye – instantaneous field.

If we zoom in on the flow near the dome, Figure 16, we see that the flow is deviated by the dome and does not follow the top interface, as it should be the case with the flat interface assumption. As this is the key region for inclusion entrapment by the slag, the requirement to consider the free surface deformation for the prediction of inclusion behaviour is clearly emphasized.
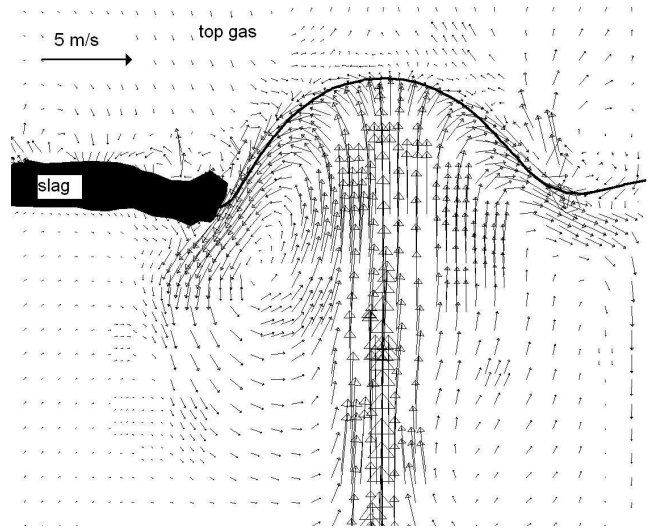
Figure 16: Velocities in the vicinity of the open-eye – the black line represents the liquid steel / top gas interface – instantaneous field.

Further calculations were realised to test the reliability of our model. Data gathered by Zhang and Thomas (2002) for different steelmaking processes totally or partially devoted to inclusion elimination were used. They put on the same diagram the characteristic elimination times of inclusions. The evolution was supposed to obey the following relationship:

$$C(t) = C_0 \exp(-t/\tau) \qquad (20)$$

Our calculations confirm that this kind of relation can be used, provided that the flow has a steady state behaviour. For example, in the case of Q_N=530 Nl/min (Figure 17), the correlation:

$$C(t)/C_{init} = \exp(-t/770) \qquad (21)$$

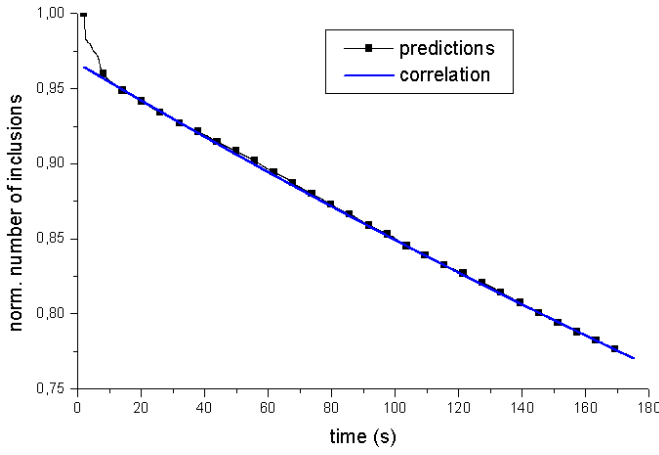fits quite well the predictions and the characteristic time is then τ = 770 s.

Figure 17: Q_N=530 Nl/min.

Figure 18 displays the comparison between calculations and measurements, where $K_0 = 1/\tau$ and τ is expressed in minutes. Abscissa represents the stirring energy of the ladle and is expressed as the mean dissipation rate of kinetic energy. The different conditions that have been investigated for the inclusion eliminations are summarised on Table 2.

**Table 2:** Summary of the conditions for the simulations.

caption on Figure 18 and Figure 19 ↓		Argon bubbles	Slag layer	Top gas
Initial results	Damping of turbulence	no	no	no
	Active for incl. elimination	yes	yes	yes
Damping of turb. at VOF interfaces	Damping of turbulence	no	yes	yes
	Active for incl. elimination	yes	yes	yes
Damping of turb. and only slag eliminates incl.	Damping of turbulence	no	yes	yes
	Active for incl. elimination	no	yes	no

The standard modelling (caption: initial results with 3D model), with the assumption that all the interfaces contribute to the inclusion elimination, provides a very rapid decrease of the concentration, Figure 18. This is in agreement with the results already published by Aoki, Zhang and Thomas (2005), who observed the same discrepancy. An important improvement is obtained when the turbulence damping is considered. Nevertheless, the decrease is still too rapid.
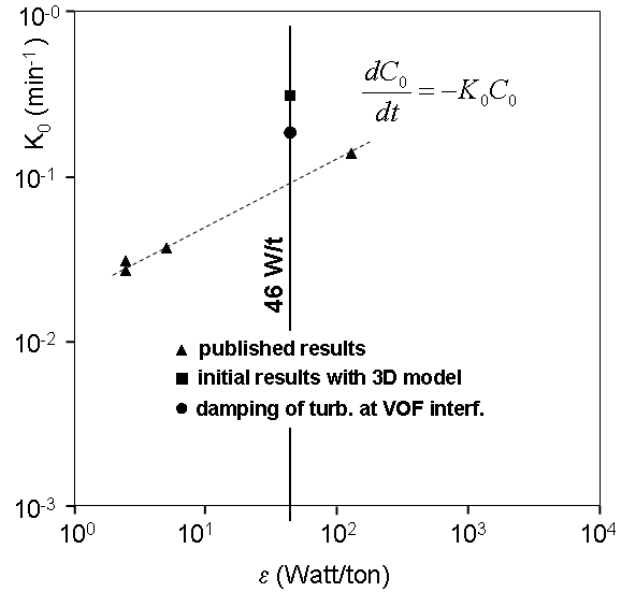
Figure 18: Q_N=530 Nl/min, first comparisons with industrial data.

For the third simulation, we considered that the inclusions could be captured by the bubbles and that they were all released inside the liquid steel when the bubbles escaped from the interface. To facilitate the calculations, we assumed that this was analogous to a situation with no entrapment by bubbles and top gas.

Figure 19 displays the comparison. The kinetics of inclusion elimination is then, as expected, much slower than previously and agrees quite well with the measurement.
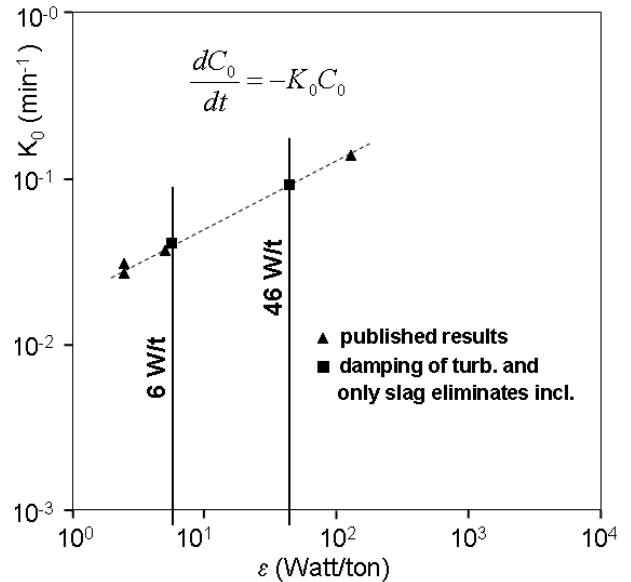
Figure 19: Q_N=530 Nl/min and Q_N=53 Nl/min, second comparison with industrial data.

To make sure that the modelling can also be applied in a situation without open-eye formation, a much smaller stirring intensity was simulated (Q_N=53 Nl/min). The concentration decrease is drawn on Figure 20, and the correlation is expressed as:

$$C(t)/C_{init} = \exp(-t/1400) \qquad (22)$$

The comparison with measurement is given on Figure 19 and turns out to be also quite good.

However, it is important to mention that we do not have any information on the accuracy of the measurements and that the comparisons should be considered with some caution. Nevertheless, the predictions provide some insight into the physical mechanisms affecting the inclusion elimination and help to select the important options for the modelling.
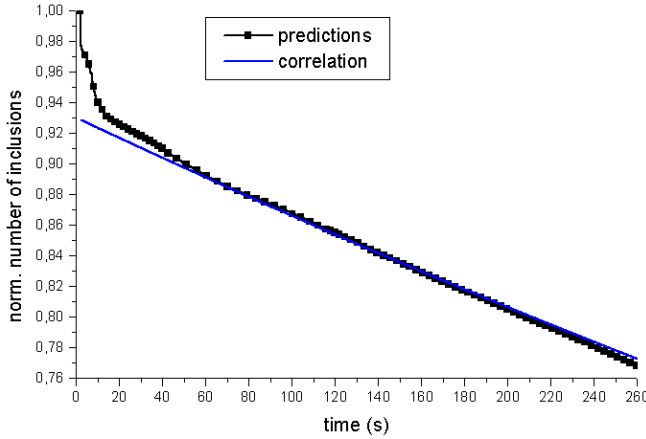

Figure 20: Q_N=53 Nl/min.

The scenario we can propose for the inclusion elimination by bubbles is then the following:

1-Inclusions are captured by bubbles, and they slip towards the bottom of each bubble, as this was already observed by Huang et al. (2011); there, they can grow by agglomeration since the contact time is large enough.

2-When the bubbles cross the metal/top gas interface, inclusions remain at the open-eye interface; they are entrained by the mean flow and submitted to centrifugal, buoyancy and drag forces; the radial velocity was expressed by Brouwers (2002) as:

$$u_r = \frac{(\rho_{steel} - \rho_{incl})D^2 \Omega^2 r}{18\mu} \qquad (23)$$

D is the inclusion diameter, which is supposed to be spherical, Ω is the angular velocity which can be approximated by V_T/R, where V_T is the tangential velocity and R the radius of the dome (see Figure 16), Then, for $r = R$ which is the critical region for inclusion entrapment by interface, we have:

$$u_R = \frac{(\rho_{steel} - \rho_{incl})D^2 V_T^2 / R}{18\mu} \qquad (24)$$

using Figure 16: $R \approx 0.22$ m and $V_T \approx 1$m/s.

Figure 21 shows the typical radial velocities: when an inclusion is transported in the dome region, it will not flow along the interface but will be deviated towards the centre of the dome, as the more easily as the inclusion diameter is large. Then, the inclusion will escape from the entrapment region.
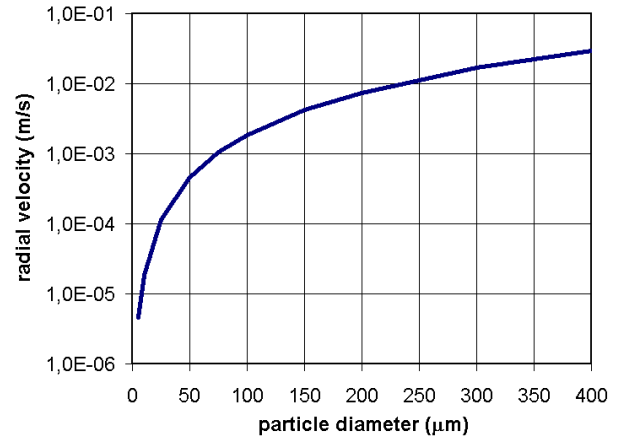

Figure 21: Radial velocity of inclusions.

3-Once the inclusion has left the interface, it is transported inside the liquid steel; globally, there is no contribution to the elimination balance.

Specific experiments should be designed to strengthen this scenario, especially to understand the effect of intense local mixing produced by the interface disturbed by the bubbles.

CONCLUSION

We realised a preliminary study on the dewetting of the liquid film when an inclusion comes in contact with an argon bubble. We concluded that, as soon as the dewetting occurred, it was a very rapid mechanism compared to the typical time scale of turbulence. This study strengthens the assumption that collision efficiency of inclusion on bubble should be almost 1; furthermore, the adhesion is robust, on a thermodynamic point of view. This simplifies the condition for inclusion entrapment at interface: as soon as an inclusion touches another phase than steel, it is entrapped.

Unsteady calculations for the multiphase description of the ladle were realised. Interface deformation was considered and we showed that the dome formation in the open-eye region deeply affected the flow compared to the classical flat surface assumption.

Standard modelling of inclusion elimination leads to a too rapid elimination of inclusions. Damping of interfacial turbulence provides an improvement but cannot totally compensate the discrepancy with measurements.

To get the best agreement with the measurements already published, we have to consider that only the interface between liquid steel and slag is active to eliminate the inclusions. It means that inclusions captured by the gas bubbles injected for the stirring have globally no effect on the elimination rate: inclusions are certainly captured but they should be released in the liquid steel when gas bubbles cross the upper interface.

REFERENCES

AOKI, J., ZHANG, L., THOMAS, B.G., (2005), "Modeling of Inclusion Removal in Ladle Refining"; *3rd Internat. Congress on Science & Technology of Steelmaking*, Charlotte, NC, May 9.

BARTOSIEWICZ, Y., SEYNHAEVE, J.M., VALLÉE, C., HÖHNE, T., LAVIÉVILLE J.M., (2010), "Modeling free surface flows relevant to a PTS scenario: Comparison between experimental data and three RANS based CFD-codes. Comments on the CFD-experiment integration and best practice guideline", *Nuclear Engineering and Design*, **240**, 2375-2381.

BROUWERS, J.J.H, (2002), "Phase separation in centrifugal fields with emphasis on the rotational particle separator", *Experimental Thermal and Fluid Science*, **26**, 325-334.

BUGUIN, A., VOVELLE, L., BROCHARD-WYART, F., (1999), "Shocks in Inertial Dewetting", *Physical Review Letters*, **83(6),** 1183-1186.

COURNIL, M., GRUY, F., GARDIN, P., SAINT-RAYMOND, H. (2001), "Modelling of inclusion aggregation and elimination in ladle and RH reactors", *ICS 2001, 2nd International Congress on the Science & Technology of Steelmaking*, Swansea (UK), 10-11 April.

DEEN, N.G., SOLBERG, T., (2001), "Large eddy simulation of the gas-liquid flow in a square cross-sectioned bubble column", *Chemical Engineering Science*, 56, 6341-6349.

DOMGIN, J.F., GARDIN, P., BRUNET, M., (1999), "Experimental and numerical investigation of gas stirred ladles", *Proc. 2nd Int. Conf. on CFD in the Minerals and Process Industries*, Melbourne, Australia, 6-8 December.

FRANK, T, (2005), "Numerical simulation of slug flow regime in horizontal pipes", *The 11th International Topical Meeting on Nuclear Reactor Thermal-Hydraulics (NURETH-11)*, Avignon, France, October 2-6.

GARDIN, P., GAUTHIER, S., SIMONNET M., LEHMANN, J., (2011), "Multiphase model for predicting the elimination of inclusions inside a liquid steel ladle", to be published in *Advanced Engineering Materials*.

GREVET, J. H., J. SZEKELY, J., EL-KADDAH, N., (1981), "An experimental and theoretical study of gas bubble driven circulation system". *International J. Heat Mass Transfer*, **25(4)**, 487–497.

HALLBERG, M., JÖNSSON, P.G., JONSSON, T.L.I., ERIKSON, R., (2005), "Process model of inclusion separation in a stirred steel ladle", *Scandinavian Journal of Metallurgy*, **34**, 41-56.

HÖHNE, T., (2009), "Experiments and numerical simulations of horizontal two phase flow regimes", *Proc. 2nd Int. Conf. on CFD in the Minerals and Process Industries*, Melbourne, Australia, 6-8 December.

HUANG, Z., LEGENDRE, D., GUIRAUD, P., (2011), "A new experimental method for determining particle capture efficiency in flotation", *Chemical Engineering Science*, **66**, 982-997.

HUNT, J. C. R., GRAHAM, J. M. R., (1978), "Free stream turbulence near plane boundaries", *J. Fluid Mech.*, **84**, 209-235.

ILEGBUSI, O.J., SZEKELEY, J., (1990), "The modeling of gas-bubble driven circulation systems", *ISIJ International*, **30(9)**, 731-739.

JIROVEANU, D., GARDIN, P., DOMGIN, J.F., (2007), "Modelling and numerical simulation of 3D bubble flow by the Eulerian-Lagrangian approach", *Progress In Computational Fluid Dynamics*, **7**, 163-169.

JOHANSEN, S.T., BOYSAN, F., (1988), "Fluid dynamics in bubble stirred ladles: Part II – Mathematical modelling", *Metallurgical and Materials Transactions*, **19B**, 755-764.

KOZAKEVITCH, P., LUCAS, M., (1968) "Rôle des phénomènes de surface dans l'élimination d'inclusion solides d'un bain métallique", *Revue de Métallurgie,* 589-598.

KOZAKEVITCH, P., OLETTE, M., (1971) "Rôle des phénomènes superficiels dans le mécanisme d'élimination des inclusions solides", *Revue de Métallurgie,* 635-646.

LLANOS, C., GARCIA-HERNANDEZ, S., RAMOS-BANDERAS, J.A., de J. BARRETO, J., SOLORIO-DIAZ, G., (2010), "Multiphase Modeling of the Fluid Dynamics of Bottom Argon Bubbling during Ladle Operations", *ISIJ International*, **50(3)**, 396-402.

LOPEZ DE BERTODANO, M.A., (1992), "Turbulent bubbly two-phase flow in a triangular duct", PhD Dissertation, Rensselaer Polytechnic Institute.

MICHIYOSHI, I., SERIZAWA, A., (1986), "Turbulence in two-phase bubbly flow", *Nuclear Engineering and Design*, **95**, 253-267.

OLSEN, J.E., CLOETE, S., (2009), "Coupled DPM and VOF for analyses of gas stirred ladles at higher gas rates", *Proc. 7th Int. Conf. on CFD in the Minerals and Process Industries*, Melbourne, Australia, 9-11 December.

RIBOUD, P., OLETTE, M., (1976), "Cours théorique de base pour l'élaboration de la fonte et de l'acier", *Lecture Institut de la Recherche en Sidérurgie*.

SHENG, D.Y., (2007), "Study on steel-slag interaction in a gas stirring ladle by numerical simulation and physical modelling experiment", *International Conference on Clean Steel 7*, Balatonfüred, Hungary, 4-6 June.

SCHWARZ, M.P., TURNER, W.J., (1988), "Applicability of the standard k-ε turbulence model to gas-stirred baths", *Applied Mathematical Modelling*, **12**, 273-279.

SCHWARZ, M.P., (1996), "Simulation of gas injection into liquid melts", *Applied Mathematical Modelling*, 20(1), 41-51.

YEGOROV, Y., MENTER, F., (2004), "Contact condensation in stratified steam-water flow", EVOLECORA-D 07.

ZHANG, L., (2000), "Mathematical simulation of fluid flow in gas-stirred liquid systems", *Modelling Simul. Mater. Sci. Eng.*, **8**, 463–476.

ZHANG, L., Thomas, B.G., (2002), "Alumina Inclusion Behavior during Steel Deoxidation", *7th European Steelmaking Conference*, Venice, Italy.

NUMERICAL SIMULATION OF AN HORIZONTAL COUNTER-CURRENT TWO-PHASE FLOW EXPERIMENT USING AN INTERFACIAL AREA DENSITY MODEL

Thomas Höhne, Deendarlianto, Dirk Lucas

Helmholtz-Zentrum Dresden-Rossendorf e.V., Institute of Safety Research,

P.O. Box 510 119, D-01314 Dresden, Germany

Corresponding author's e-mail: t.hoehne@hzdr.de

ABSTRACT

In order to improve the understanding of counter-current two-phase flows, a CFD simulation of 1/3rd scale model of the hot leg of a German Konvoi pressurized water reactor (PWR) with rectangular cross section was performed. A selected air-water counter-current flow limitation (CCFL) experiment at the Helmholtz-Zentrum Dresden-Rossendorf (HZDR) at 0.306 MPa and room temperature (experimental running of 30-05) was calculated with three-dimensional two-fluid models of computer code ANSYS CFX 13. It was simulated using the multi-fluid Euler-Euler modeling approach. The transient calculation was carried out using a gas/liquid inhomogeneous multiphase flow model coupled with a SST turbulence model for each phase. In the simulation, the surface drag was approached by a new correlation inside the Algebraic Interfacial Area Density (AIAD) model. The AIAD model allows the detection of the morphological form of the two phase flow and the corresponding switching via a blending function of each correlation from one object pair to another. As a result this model can distinguish between bubbles, droplets and the free surface using the local liquid phase volume fraction value. A comparison with the high-speed video observations shows also a good qualitative agreement. The results indicated also that quantitative agreement of the CCFL characteristics between calculation and experimental data was obtained. The goal is to provide an easy usable AIAD framework for all users, with the possibility of the implementation of their own correlations.

Keywords: CFD, multiphase flow, horizontal flow, CCFL, AIAD model

NOMENCLATURE

A	Interfacial area density (m^{-1})
C_D	Drag coefficient (-)
d	Diameter (m)
F_D	Interfacial friction force (N)
f	Blending function (-)
g	Gravitational constant (ms^{-1})
H	Channel height (m)
J_k^*	Non dimensional superficial velocity by Wallis (-)
r	Void fraction (-)
p	Pressure (Nm^{-2})
U	Velocity (ms^{-1})

Greek letters

ρ	Density (kg/m^3)
μ	Dynamic viscosity (Pa.s)
η	Viscosity (Pas)
τ	Shear stress (N/m^2)

Subscripts

|	
B	Bubble
D	Droplet
FS	Free surface
G	Gas phase
k	Gas or Liquid phase
L	Liquid phase

INTRODUCTION

The counter-current gas-liquid two-phase flow in the hot leg of a pressurized water reactor (PWR) has received special attention in nuclear reactor safety research.

In the event of a loss-of-coolant-accident (LOCA) in a pressurized water reactor (PWR), emergency strategies have to be mapped out in order to guarantee a safe removal of the decay heat from the reactor core - also in case of a component breakdown. During a hypothetical small break LOCA with failure of the high pressure emergency core cooling system (ECC) and of the main feed pumps, a natural circulation starts in the primary circuit. This allows the heat removal, also if steam is generated in the reactor core due to the depressurization of the primary circuit. But if during the further run, the water level in the reactor pressure vessel (RPV) falls below the hot-leg inlet, only steam will flow to the steam generator. Therefore, the natural circulation breaks down and switches to the reflux condenser mode.

In the reflux condenser mode, the steam coming from the RPV condenses in the vertical U-tubes of

the steam generator. In each half of the steam generator, the condensate flows down the tube in which it has been formed. Therefore, about one half of the condensate flows as usual over the pump to the downcomer, whereas the other half flows over the hot-leg back to the upper plenum. In the hot-leg, the condensate has to flow in counter-current to the steam.
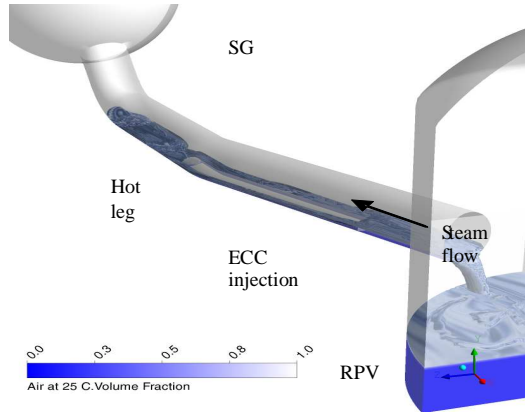
Fig. 1   Counter-current gas-liquid two-phase flow in PWR Hot leg

The horizontal stratified counter-current flow of condensate and steam is only stable for a certain range of flow rates. If the steam flow increases too much, the condensate is clogged in the hot-leg. This is the beginning of the counter-current flow limitation (CCFL): the liquid is deflected by the steam and partially entrained in opposite direction to the steam generator. As a consequence, the hot-leg and steam generator are flood, which decreases the water level in the RPV and reduces the core cooling. In case of an additional increase of the steam flow, the condensate is completely blocked and the cooling of the reactor core from the hot-leg is impossible. The detailed examples of such LOCA scenarios leading to the reflux condenser mode can be found in Jeong (2002).

The flow conditions governing the reflux condenser mode or the counter-current flow limitation cannot be predicted with the required accuracy and spatial resolution by the state of the art one-dimensional system codes. In order to improve the modeling of these flow regimes, computational fluid dynamics (CFD) codes are currently under development. In CFD, closure models are required that must be validated, especially if they are to be applied to reactor safety issues. The aim of our experimental investigations of stratified two-phase flows is mainly to deliver high resolution data that is needed for the validation of CFD codes. In order to improve the transient analysis of counter-current two-phase flows, a 1/3rd scale model of the hot leg PWR of a German Konvoi Pressurized Water

Reactor with rectangular cross section was used at Helmholtz-Zentrum Dresden-Rossendorf (HZDR) to perform experiments related to CCFL flow regimes (Vallée et al. 2009).

The widely used analysis to model the counter-current flow limitation is the used of the one dimensional two-fluid models as reported by Ardron & Banerjee (1986), Bertadano (1994) and Wongwises (1996).

Wang & Mayinger (1995) simulated two-dimensional analysis of counter-current model of UPTF Test A2 & Test 11 using a two-fluid model. They implemented the interfacial friction factor proposed by Lee & Bankoff (1983) and Ohnuki (1986) into the code FLOW3D. They reported that satisfactory results were obtained, whereas, under the reflux condensation conditions, numerical computation reveals that different flow structures appeared in the region away from CCFL line and in the region near the CCFL line. Next, Minami et al. (2009) and Murase et al. (2009) conducted a three dimensional CFD simulation on the counter-current gas-liquid flow in a PWR hot-leg air-water flow in a 1/15th scale model. They used the VOF and Euler-Euler model of the commercial CFD code FLUENT. In their simulations, the interfacial friction factors were adopted from the empirical correlations obtained from literatures for the cases of annular and slug flow. Those correlations were obtained on the basis of one dimensional analysis.

This paper provides a post-test CFD calculation of the air-water CCFL experiment 30-05 at the TOPFLOW Hot Leg model. The aim of this simulation is the validation of prediction of CCFL in a model hot leg PWR with newly developed and implemented multiphase flow models in the code ANSYS CFX. The Algebraic Interfacial Area Density (AIAD) model (Höhne, 2010) was used, which allows the detection of the morphological form of the two phase flow and the corresponding switching via a blending function of each correlation from one object pair to another. The new drag correlation obtained from this model considered the 3D effects of the simulated phenomenon.

THE HOT LEG MODEL OF TOPFLOW

The details of the experimental apparatus and procedure used in the present study were described in the previous papers (Deendarlianto et al., 2008 & Vallée et al. 2009) and only the main features are presented here. Fig. 2 shows a photo of the experimental facility. Fig. 3 shows a schematic diagram of the CCFL counter current flow experiments. Two vessels simulate the reactor pressure vessel (RPV) simulator and steam generator (SG) separator are connected by a test

Numerical simulation of an horizontal counter-current two-phase flow experiment using an interfacial area density model

CFD11-083

section that simulates the 1/3rd scale model of the hot leg PWR of a German Konvoi Pressurized Water Reactor. Both the RPV simulator and SG separator are identical vessels with 0.8 m × 0.5 m × 1.55 m (D × W × H) cubic shape. The water levels in both vessels were determined by the measurement of the differential pressure between the top and the bottom of the vessels with differential pressure transducers. A vortex meter was used to measure the injected water mass flow rate. The injected air mass flow rate was measured and controlled using a thermal mass flow meter.

Fig. 2: TOPFLOW Hot leg model in front of the pressure chamber
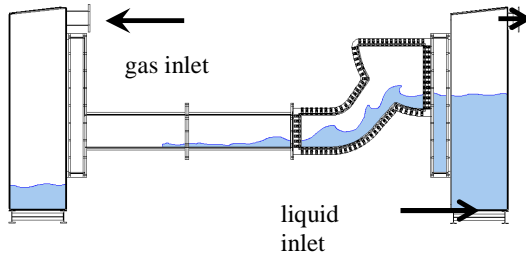
Fig. 3: Schematic diagram of the CCFL counter current flow experiments

The test section is composed of a horizontal rectangular channel, a bend that connects it to an upward inclined and expended channel, and a quarter of a circle representing the steam generator inlet chamber. The horizontal part of test section is 2.12 m long and has a rectangular cross-section of 0.05 m × 0.25 m. The riser is 0.23 m long, has an inclination of 50° to the horizontal plane and an expansion angle of 7.5°. The inner and outer bend radii of curvature were 0.25 and 0.5 m, respectively. The test section was made of stainless steel and was equipped with glass windows to allow visual observation. The flow behavior was recorded by a high-speed video camera at frequencies of 60–100 Hz and a shutter speed of 1/1000 s.

In the experiment, a constant water flow rate was injected at the bottom of the SG simulator from where it can flow through the test section to the RPV simulator. The gas was injected into the RPV simulator from the top and flowed through the test section in counter-current to the water flow to the SG separator (Fig. 3). The increase of the water level in the RPV simulator was used to determine the water flow rate streaming over the test section (discharge flow). The onset of flooding was defined as the limiting point of stability of the counter-current flow, indicated by the maximum air mass flow rate at which the down-flowing water mass flow rate is equal to the inlet water mass flow rate.

This experimental apparatus is put in a pressure chamber, where it was operated in pressure equilibrium with the inner atmosphere of the tank. A compressor system allows an increase of the air pressure in the chamber to a maximum of 5 MPa, which is also the maximum operation pressure of the hot leg model. The detailed principle of the pressure equilibrium technique was described by Prasser et al. (2006).

COMPUTATIONAL MODELLING

Free Surface Modeling

The CFD simulation of free surface flows can be performed using the multi-fluid Euler-Euler modeling approach available in ANSYS CFX. Detailed derivation of the two-fluid model can be found in the book of Ishii and Hibiki (2006). However, it requires careful treatment of several aspects of the model:

The interfacial area density should satisfy the integral volume balance condition. In the case when surface waves are present, their contribution to the interfacial area density should be taken into account.

In the present simulation, the conservation and momentum equations of the two-fluid model are solved, which have the following form
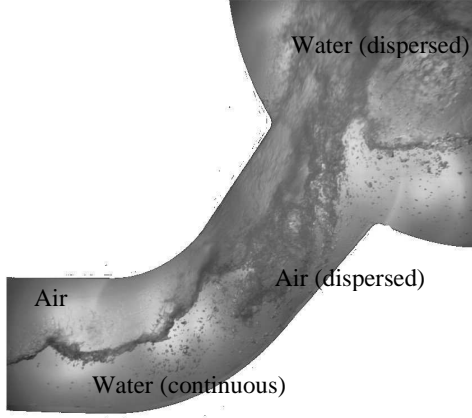
$$\frac{\partial(\alpha_k \rho_k)}{\partial t} + \nabla(\alpha_k \rho_k U_k) = 0 \qquad (1)$$

$$\frac{\partial(\alpha_k \rho_k)}{\partial t} + \nabla(\alpha_k \rho_k U_k U_k) =$$
$$-\alpha_k \nabla p_k + \alpha_k \rho_k g + \nabla \alpha_k (\tau^v + \tau_k^t) + \tau_{D,k} \qquad (2)$$

where the subscript k denotes phase gas or liquid, ρ is the density, u is the velocity vector, t is the time, p is the pressure, g is the gravitational acceleration, r is the volume fraction, τ is the shear stress (τ^v is

the average viscous shear stress, τ^t is the turbulent shear stress) and τ_D is the interfacial shear stress.

Fig.4: Different morphologies under slug flow conditions

In slug flow simulations, the air bubble in the water can be resulted by the drag force. The total drag force is derived from the interfacial shear stress ($F_D = \tau_D . A$), is most conveniently expressed in terms of the dimensionless drag coefficient C_D

$$F_D = C_D \, A \, \rho_{LG} \left| (U_L - U_G) \right|^2 \qquad (3)$$

where ρ_{LG} is the average density, $\left| (U_L - U_G) \right|$ is the relative velocity and A is the projected area of the body in flow direction (interfacial area density).

The Algebraic Interfacial Area Density (AIAD) Model

Fig. 4 shows different morphologies at slug flow conditions. Separate models are necessary for dispersed particles and separated continuous phases (interfacial drag etc.). Two approaches are possible within the Euler-Euler methodology:

- Four phases: Bubble/Droplet generation and degassing have to be implemented as sources and sinks
- Two phases: Momentum exchange coefficients depend on local morphology

For the second approach Egorov (2004) proposed an Algebraic Interfacial Area Density (AIAD) Model. The basic idea of the model is:

The interfacial area density allows the detection of the morphological form and the corresponding switching of each correlation from one object pair to another.

- It provides a law for the interfacial area density and the drag coefficient for full range 0≤r≤1.
- The model improves the physical modeling in the asymptotic limits of bubbly and droplet flows.
- The interfacial area density in the intermediate range is set to the interfacial area density for free surface

The AIAD model applies three different drag coefficients, $C_{D,B}$ for bubbles, $C_{D,D}$ for the droplets and $C_{D,FS}$ for free surface. Non-drag forces (e.g. lift force and turbulent dispersion force) are neglected at the moment. The interfacial area density A also depends on the morphology of the phases. For bubbles it is

$$A_B = \frac{6r_G}{d_B} \qquad (4)$$

where the interface area density is equal to the surface area of the spheres of diameter d_B, which occupy the gas volume fraction r_G.

For a free surface an important requirement for the model is the normalizing condition: the volume integral of the area density must be equal to the real surface area. It means that integration of the area density along a normal to the surface must yield unity:

$$\int_{-\infty}^{+\infty} A \, dn = 1 \qquad (5)$$

A model, which satisfies this condition, calculates the interface area density as the absolute value of the volume fraction gradient:

$$A_{FS} = \left| \nabla r_L \right| = \frac{\partial r_L}{\partial n} \qquad (6)$$

if n is directed to the bulk liquid phase. For ρ the average density is applied, i.e.

$$\rho = r_G \rho_G + r_L \rho_L \qquad (7)$$

where r_L and r_G are the liquid and the gas phase density respectively. In the bubbly regime, where ρ_G is low, the average density ρ is close to the liquid phase density ρ_L. According to the flow regime (bubbly flow, droplet flow or stratified flow with a free surface) the corresponding drag coefficients and interfacial area densities have to be applied.

The simplest switching procedure for the interfacial area density, uses the blending function F_d. Introducing void fraction limits, the weights for

Numerical simulation of an horizontal counter-current two-phase flow experiment using an interfacial area density model

CFD11-083

flow regimes and length scales for bubbly and droplet flow (d_B, d_D) are the following:

$$f_D = \left[1 + e^{a_D(r_L - r_{D,Limit})}\right] \tag{8}$$

$$f_B = \left[1 + e^{a_B(r_G - r_{B,Limit})}\right] \tag{9}$$

$$f_{FS} = 1 - f_B - f_D \tag{10}$$

$$A = f_{FS}A_{FS} + f_B A_B + f_D A_D \tag{11}$$

$$C_D = f_{FS}C_{D\,FS} + f_B C_{D\,B} + f_D C_{D\,D} \tag{12}$$

After a validation study for the simulation of slug flow the void fraction limits of $r_{B,limit}$=0.3 resp. $r_{D,limit}$=0.3 and blending coefficients of a_B=a_D=70 were used.

Modeling the free surface drag

In simulations of free surface flows eq. (3) does not represent a realistic physical model. It is reasonable to expect that the velocities of both fluids in the vicinity of the interface are rather similar. To achieve this result, a shear stress like a wall shear stress is assumed near the surface from both sides to reduce the velocity differences of both phases.

A viscous fluid moving along a "solid" like boundary will incur a shear stress, the no-slip condition, the morphology region "free surface" is the boundary layer, the shear stress is imparted onto the boundary as a result of this loss of velocity

$$\tau_W = \mu \frac{\partial u}{\partial y} \Big|_{y=0} \tag{13}$$

The components of the Normal vector at the free surface are taken from the gradients of the void fraction in x,y,z directions. To use these directions of the normal vectors the gradients of gas/liquid velocities which are used to calculate the wall shear stress onto the free surface are weighted with the absolute value of components of the normal vector:

$$\tau_{L,G} = \mu_{L,G} \sqrt{\left(\frac{\partial u_{x,L,G}}{\partial x} \cdot \frac{\left(\frac{\partial r_{L,G}}{\partial x}\right)}{A_{FS}}\right)^2 + \left(\frac{\partial u_{y,L,G}}{\partial y} \cdot \frac{\left(\frac{\partial r_{L,G}}{\partial y}\right)}{A_{FS}}\right)^2 + \left(\frac{\partial u_{z,L,G}}{\partial z} \cdot \frac{\left(\frac{\partial r_{L,G}}{\partial z}\right)}{A_{FS}}\right)^2} \tag{14}$$

As a result the modified drag coefficient is dependent on the viscosities of both phases, the local gradients of gas/liquid velocities normal to the free surface, the liquid density and the slip velocity between the phases:

$$C_{D,FS} = \frac{2\left[r_L \tau_{W,L} + r_G \tau_{W,G}\right]}{\rho_L \cdot U^2} \tag{15}$$

**Numerical Setup & Boundary Conditions**

The gas/liquid CCFL phenomenon in the hot-leg model was calculated with Euler-Euler inhomogeneous mixture model using ANSYS CFX 12.1. ANSYS CFX-12 is an element-based finite-volume method with second-order discretization schemes in space and time. It uses a coupled algebraic multigrid algorithm to solve the linear systems arising from discretization. The discretization schemes and the multigrid solver are scalably parallelized. CFX-12 works with unstructured hybrid grids consisting of tetrahedral, hexahedral, prism and pyramid elements. The calculation model is shown in Fig. 5.

Table. 1: Calculation run

Exp. Run	m_L [kg/s]	m_G [kg/s]	System pressure [MPa]
30-05 (Air-water)	0.3	0.183-0.274	0.15

In CFD analysis, demonstration of grid independence is a basic requirement as indicated in The ERCOFTAC Best Practice Guidelines (2001), which were specified for nuclear reactor safety calculations within the ECORA project (Menter, 2002). In the present simulations, very carefully developed structured mesh for most of the flow field was adequate, at which the local refinement on them were carried out. Here, the effect of numerical diffusion can be minimized by using meshes with a finer resolution, higher order discretization methods and suitable time step sizes. As a result, a structured mesh consisted of 248,610 hexahedral elements and 281,076 nodes.

The calculation has been performed of HZDR experimental run (30-05), which is summarized in Table 1. The injected gas mass flow rates used in the present calculation were a function of time as shown in Fig. 7.
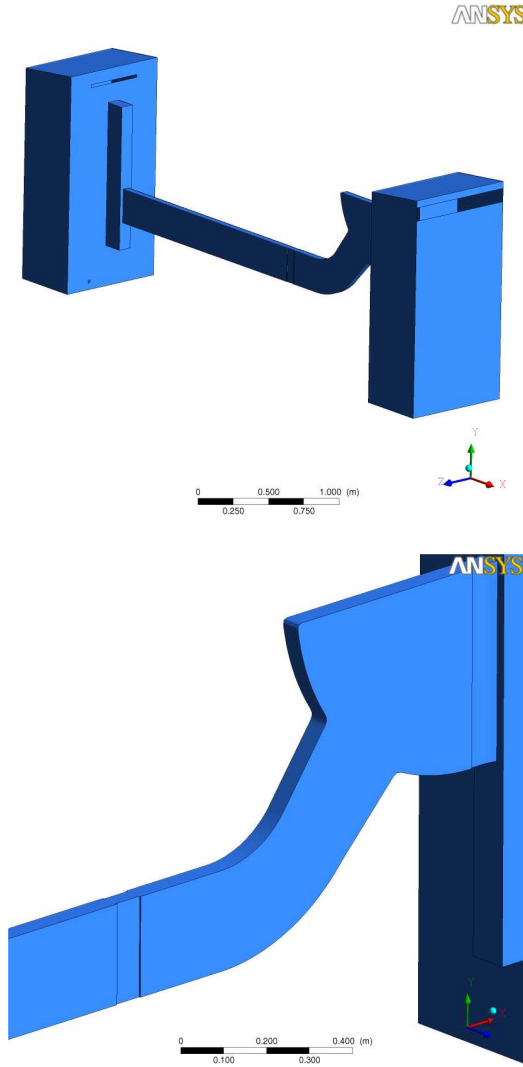
Fig. 5: Calculation domain

The SST turbulence model was used. The SST model works by solving a turbulence/frequency-based model (k–ω) at the wall and standard k–ω in the bulk flow. A blending function ensures a smooth transition between those two models (Menter, 1993).

Both phases have been treated as isothermal and incompressible. Buoyancy effects between the two phases were taken into account by the direction of gravity term. The turbulence properties at the inlet of air and water were set using the "turbulence intensity of 5% in both phases". The air outlet was modeled with an opening boundary condition. The inner surface of the channel walls has been defined as hydraulically smooth with a non-slip boundary condition applied to both gas and liquid phases. The

Drag coefficient, C_D, was determined by the AIAD model (Eq. (15), and its implementation into CFX was done via the command language CCL (CFX expression language). The calculations were performed in parallel of 4 processors of HZDR Linux cluster. Typical computation time for each case was about 4 months.

RESULTS & DISCUSSIONS

The simulation for the experiment 30-05 (see Table 1) has focused primarily on the comparison of typical flow processes and code validation. CFD studies without using the AIAD model and using a uniform C_D have showed, that CCFL phenomena could not be predicted.

Air-Water-CCFL Experiment 30-05

The initial conditions of the calculation are shown in Fig. 6. Here the water is modeled at the SG simulator bottom and flows in the direction of RPV simulator. There, the water level is lower than in the channel. Moreover, the figure shows the hydrostatic pressure in the water phase.
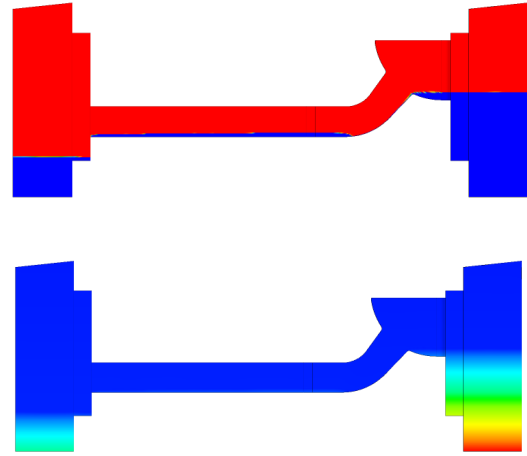

Fig. 6: Water level initial condition: Overflow elbow (left), hydrostatic pressure in the water phase (right)

The measurement data of the air mass flow of the experiment in Fig. 7 were used as boundary conditions for the CFD calculation.

Fig. 8 shows snapshots of the time course of development of the flow. First, the water can still flow freely to the RPV simulator (Fig. 8a). As in this experiment, a hydraulic jump is observed below the elbow (see also Fig. 9). After increasing the air mass flow a partial counter-current flow limitation is observed (Fig. 8b). Finally, no more

Numerical simulation of an horizontal counter-current two-phase flow experiment using an interfacial area density model

CFD11-083

water can flow against the air stream (Fig. 8c) and the water is gradually pushed back towards the bend (Fig. 8d). This results in the formation of swirls in the manifold. These phenomena were also observed in the experiment. Figures 9 to 12 give further qualitative flow phenomena of the CFD calculation in comparison with the experiment. Thus, in Fig. 9, a hydraulic jump at the SG bottom is observed.
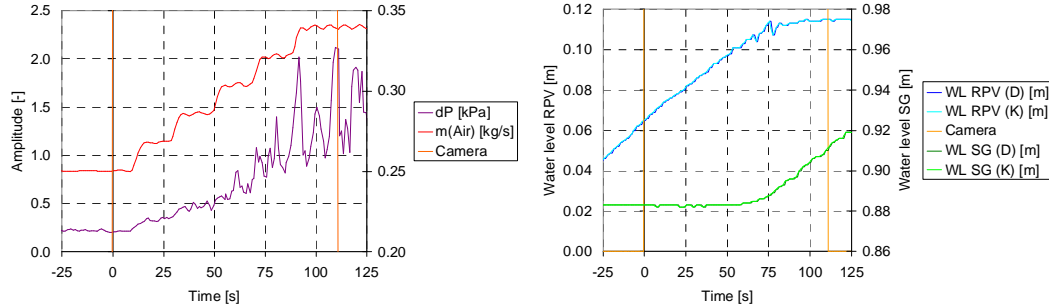
Fig. 7: Experiment 30-05 - used as a boundary condition data, left: air mass flow and pressure difference between the two separators, right: water levels
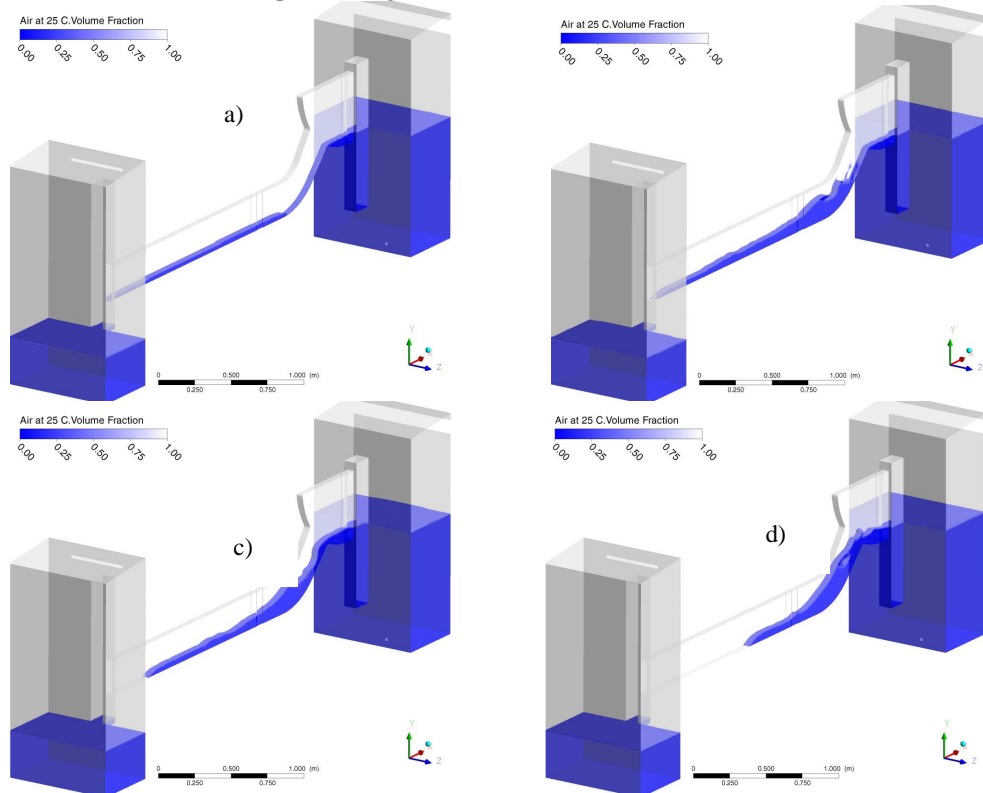
Fig. 8: Snapshots from the CFD simulation: a) counter-current flow without limitation, b) flow with partial counter-current limitation, c) full counter-current limitation, d) pushing back the water
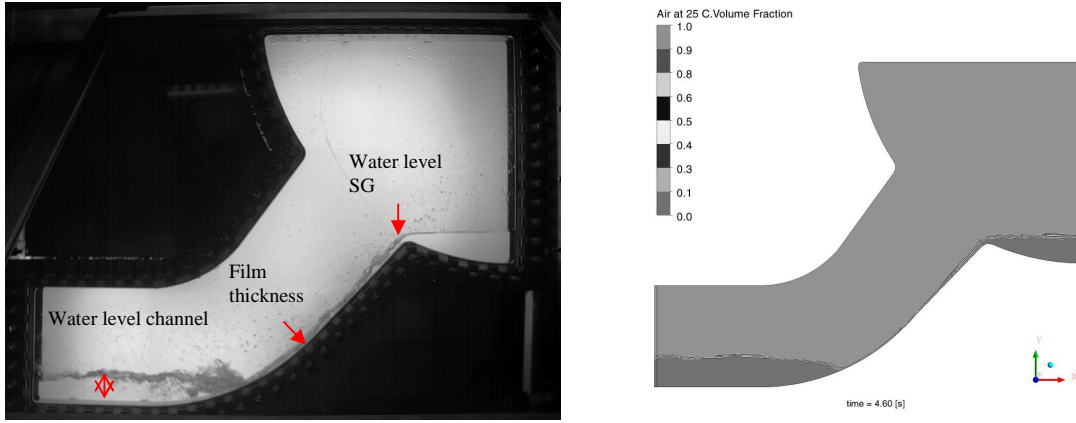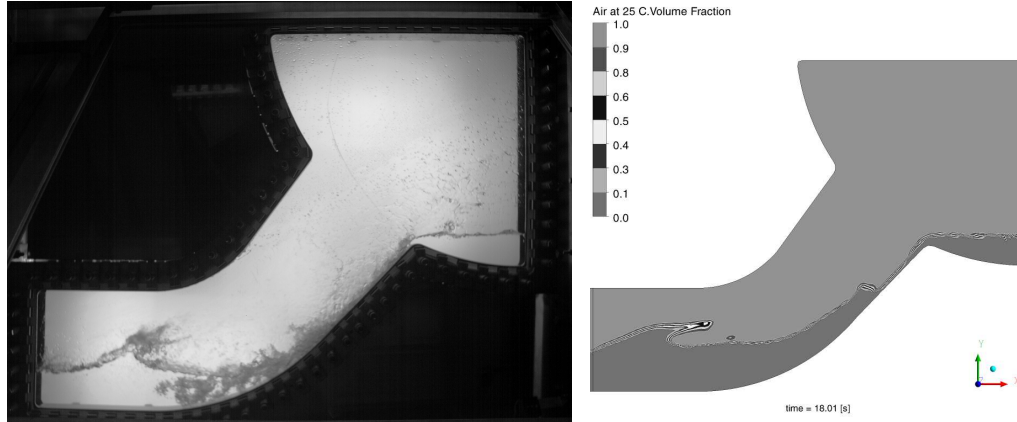
Fig. 9: Comparison of experiment and simulation for the flow before the onset of the counter-current flow limitation
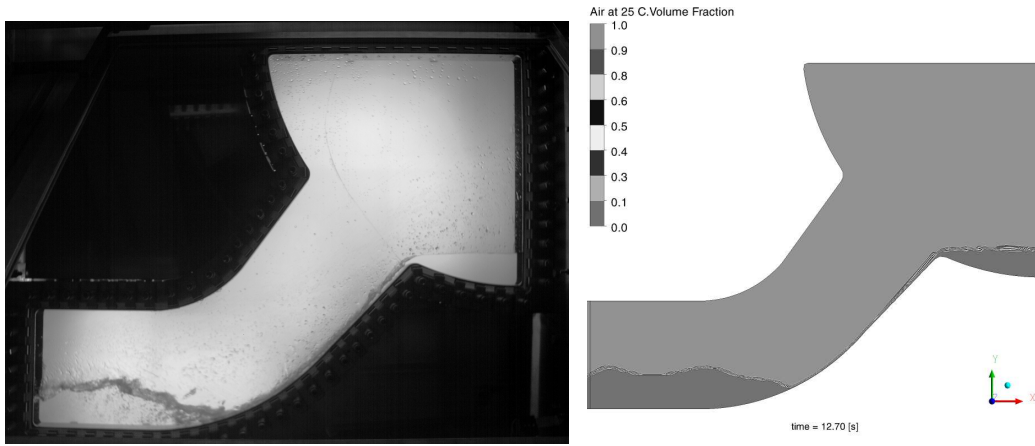
Fig. 10: Comparison of experiment and simulation for the flow at the start of wave formation
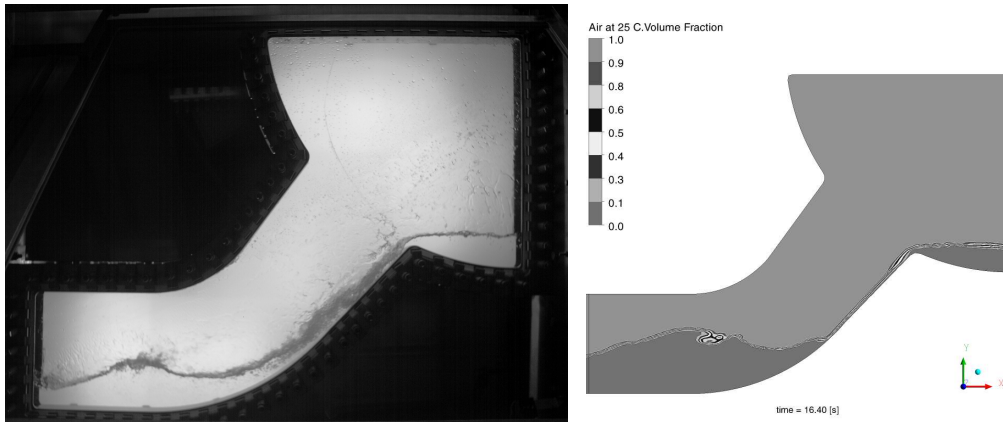
Fig. 11: Comparison of experiment and simulation for the flow with droplets

Numerical simulation of an horizontal counter-current two-phase flow experiment using an interfacial area density model

CFD11-083

Fig. 12: Comparison of experiment and simulation for wavy flow, starting in the elbow region

Fig. 10 similar wave formations can be seen. A drop can be seen in Fig. 11. Fig. 12 shows in both cases, a high migration of the crests of the waves towards the SG bottom, so that the down-running film disturbed.

A quantification of the flow patterns is very expensive. The Table 2 is an attempt of a quantitative comparison of the water level in the channel, the film thickness in the elbow and the water level in the SG bottom (see Fig. 12). The quantitative agreement of calculations and measurements is quite good, especially with regard to water levels. Comparing the film thickness must be remembered that the video camera recorded the entire width including side walls, while the calculation data extraction includes only a central section plane. Thus, the film thickness in the calculation is smaller.

Table. 2: Quantitative comparison of calculation and experiment

Quantitative comparison	Experiment	CFX
Water Level Channel:	26 mm	30 mm
Film thickness:	6,7 mm	3,4 mm
Water Level SG:	7 mm	7,5 mm

SUMMARY AND OUTLOOK

A three-dimensional CFD simulation of the CCFL phenomenon of gas-liquid two-phase flow in a model of hot leg a German Konvoi Pressurized Water Reactor with rectangular cross section has been performed using the Euler–Euler inhomogeneous mixture model. A selected air-water HZDR TOPFLOW Hot Leg experiment was chosen for a transient CFD simulation. An Algebraic Interfacial Area Density (AIAD) model on the basis of the Euler-Euler two fluid model was implemented. A picture sequence recorded during the CCFL experiment was compared with CFD simulation of the commercial code of ANSYS CFX 12.0. The calculated water volume fraction indicate that the basic flow characteristics of the experiment such as the hydraulic jump near the bended region of the hot leg PWR and the occurrence of roll wave were reproduced in simulation, while a minor deviation require a continuation of the work. The usage of the morphology detection algorithm AIAD should also be possible in vertical flow regimes. Therefore it is necessary to include the modelling of non-drag forces (lift force, wall lubrification force, virtual mass force etc.) as well as the MUlti bubbe SIze Group (MUSIG) model for polydispersed flows. The goal is to provide an easy usable AIAD framework for all users, with the possibility of the implementation of their own correlations.

ACKNOWLEDGEMENTS

REFERENCES

ARDRON, K.H., et al., 1986, International Journal of Multiphase Flow, Vol. 12-4, pp. 543-558.

BERTADANO, M.L., 1994, Nuclear Science and Engineering, Vol. 117, pp. 126-133.

DEENDARLIANTO, et al., 2008, Nuclear Engineering and Design, Vol. 238-12, pp.3389-3402.

GEWEKE, M., et al., 1992, In: Proceeding of European Two-Phase Flow Group Meeting, Stockholm, June, Paper No. J1.

HÖHNE, T.; VALLÉE, C. 2010 The Journal of Computational Multiphase Flows 2(2010)3, 131-143

HÖHNE, T., AND VALLÉE, C., 2009, In: Proceeding of the 13th International Topical Meeting on Nuclear Reactor Thermal Hydraulics (NURETH-13), Kanazawa, Japan.

JEONG, H.Y., 2002, Annals of Nuclear Energy, Vol. 29-5, pp. 571-583.

KUKITA, ET AL., et al., 1987, In: Proceeding the Winter Annual meeting of the ASME, Boston, USA, 111-116.

LEE, S.C., AND BANKOFF, S.G., 1983, Journal of Heat Transfer, Vol. 105, pp. 713-718.

MENTER, F.R., 1993, AIAA, Vol. 93,p. 2906.

MENTER, F.R., 2002, ECORA FIKS-CT-2001-00154.

OHNUKI, A., 1986, Journal of Nuclear Science and Technology, vol. 23, pp. 219-232.

PRASSER, H.M., et al., 2006, Kerntechnik, Vol. 71, pp. 163–173.

VALLÉE, C., et al., 2009, In: Proceeding of the 13th International Topical Meeting on Nuclear Reactor Thermal Hydraulics (NURETH-13), Kanazawa, Japan (2009)

WANG, M.J., AND MAYINGER, F., 1995, Nuclear Engineering and Design, Vol 155, pp. 643-652.

WONGWISES, S., 1996, Nuclear Engineering and Design, Vol. 166-2, pp. 121-133.

YEGOROV, Y., 2004, EVOL-ECORA- D07 (2004).

8th International Conference on CFD in Oil & Gas, Metallurgical and Process Industries
SINTEF/NTNU, Trondheim NORWAY
21-23 June 2011

CFD11-84

A CFD STUDY OF THE EFFECT OF THE CYCLONE BARREL HEIGHT ON ITS PERFORMANCE PARAMETERS

Khairy ELSAYED[1][*], **Chris LACOR**[2][†]

[1]Vrije Universiteit Brussel, Pleinlaan 2, 1050 Brussels, Belgium

[2]Vrije Universiteit Brussel, Pleinlaan 2, 1050 Brussels, Belgium

[*] E-mail: kelsayed@vub.ac.be
[†] E-mail: chris.lacor@vub.ac.be

ABSTRACT

The effect of the cyclone barrel height on the performance and flow field pattern has been investigated computationally using the Reynolds stress turbulence model for four cyclone separators. The results show that the maximum tangential velocity in the cyclone decreases with increasing the cyclone barrel height. The maximum tangential velocity is nearly constant throughout the same cyclone. Increasing the barrel height, makes a small change in the axial velocity. Increasing the cyclone barrel height decreases both the pressure drop & the cut-off diameter. The changes in the performance beyond $h/D = 1.8$ are small, where h is the barrel height and D is the barrel diameter.

Keywords: Cyclone separator, Barrel height, Reynolds stress turbulence model (RSM), Discrete phase modelling (DPM) .

INTRODUCTION

Cyclones are one of the most widely used separators, which rely on centrifugal forces to separate particles from a gas stream. The main advantages are economy, simplicity in construction, and adaptable to a wide range of operating conditions. The flow phenomena in cyclone separators are complex; the flow is highly swirling and fully three dimensional (Elsayed and Lacor, 2011). This leads to many investigations in order to understand the effect of different geometrical & operating parameters on the performance & hydrodynamics of cyclone separators (Hoekstra *et al.*, 1999; Solero and Coghe, 2002; Hu *et al.*, 2005; Yazdabadi *et al.*, 1994; O'Doherty *et al.*, 1999; Zhang and Hui, 2007; Griffiths and Boysan, 1996; Gimbun *et al.*, 2005a,b; Zhao *et al.*, 2006; Elsayed and Lacor, 2010a).

Numerous studies have been performed for the effect of geometrical parameters on the flow pattern and performance (Boysan *et al.*, 1983; Xiang *et al.*, 2001; Gimbun *et al.*, 2005a; Lim *et al.*, 2004; Raoufi *et al.*, 2008; Elsayed and Lacor, 2011) whereas only a limited number of studies have been devoted to the effect of the cyclone height. Zhu and Lee (1999) have conducted detailed experiments on cyclones of different height and found that the cyclone height can influence considerably the separation efficiency of the cyclones. However they did not provide any information about the flow pattern nor an explanation for the efficiency results. Hoffmann *et al.* (2001) investigated the effect of the cyclone height on the separation efficiency and the pressure drop ex-

perimentally and theoretically. They studied different cyclones of total height varying from 3.35 to 6.85 cyclone diameters at constant cone height of 2.05 cyclone diameters. They found improvement in cyclone performance with increasing the total height H_t up to 5.5 times cyclone diameters beyond this length the separation efficiency was dramatically reduced. But they did not present any contour plot for the velocity components or velocity profile to support the explanation for the effect of the cyclone height on the performance. Recently Xiang and Lee (2005) have repeated the study of Zhu and Lee (1999) for the effect of cyclone height via steady three-dimensional simulations using the Reynolds stress turbulence model (RSM). They found that the tangential velocity decreases with increasing the cyclone height, which is responsible for the lower separation efficiency observed in long cyclones. The reason for this behavior however was not analyzed in detail. Moreover, no particle tracking study was presented.

The present study is intended to computationally investigate the effect of increasing the cyclone barrel height on pressure drop and cut-off diameter and to obtain more details about the flow field pattern and velocity profiles. A Reynolds-Averaged Navier-Stokes (RANS) approach with the Reynolds stress turbulence model (RSM) is used.

NUMERICAL SETTINGS

Selection of the turbulence model

The Fluent 6.3.26 solver has many turbulence models available for simulating turbulent flow. Only the Reynolds stress model (RSM) and large eddy simulation (LES) can capture the main features of the highly complicated swirling flow in cyclone separators (Slack *et al.*, 2000; Hoekstra, 2000; Kaya and Karagoz, 2008; Elsayed and Lacor, 2010b, 2011; Bernardo *et al.*, 2006; Chuah *et al.*, 2006; Zhao *et al.*, 2006; Xiang and Lee, 2005; Gimbun *et al.*, 2005c,a,b). The Reynolds stress turbulence model has been used in this study to reveal the effect of changing the barrel height on the turbulent flow in the cyclone separator. For the detailed governing equation for both the Reynolds averaged Navier-Stokes equation (RANS) & the discrete phase modelling (DPM) we refer to Elsayed and Lacor (2011). In Fluent solver, all default settings for RSM model and its constants have been used. The enhanced wall treatment has been used as a wall function. For the discrete phase modelling only the drag force has been taken into consideration. No particle-particle or particle gas interaction has been considered in the current study.
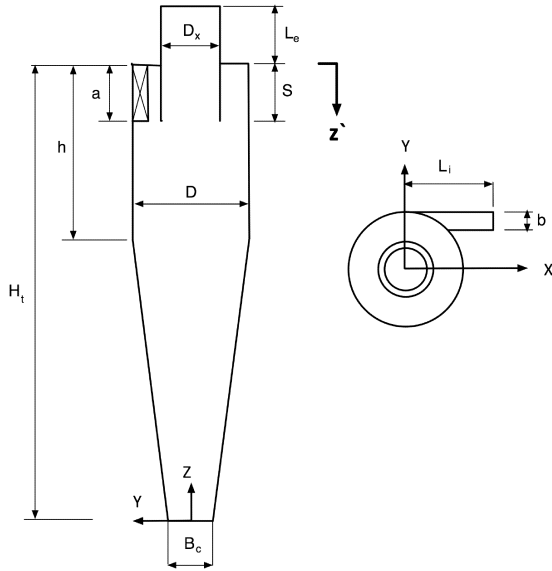
(a) The cyclone geometry
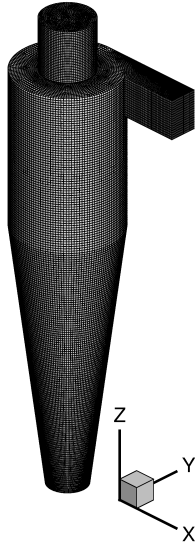
(b) The surface mesh for cyclone II

Figure 1: Schematic diagram for the cyclone separator

Configuration of the tested cyclones

The numerical simulations were performed on four cyclones with different barrel heights (at constant cone height). Figure 1 and Table 1 give the cyclones dimensions.

Boundary conditions

Table 2 shows the details of the boundary conditions. The air volume flow rate Q_{in}=50 l/min for all cyclones, air density 1.0 kg/m^3 and dynamic viscosity of 2.11E-5 Pa s. The turbulent intensity equals 5% and characteristic length equals 0.07 times the inlet width (Hoekstra, 2000; Elsayed and Lacor, 2011).

Selection of the numerical schemes

The following numerical schemes have been used in the current simulations. The QUICK scheme for momentum discretization, the Presto scheme for pressure interpolation. The SIMPLEC algorithm for pressure velocity coupling, the second order upwind scheme for turbulent kinetic energy and the first order upwind for the Reynolds stress.

Table 1: The dimensions of the tested cyclones*

Dimension	Cyclone	dimension/D	h_c/h	H_t
Inlet height, a		0.375		
Inlet width, b		0.2625		
Gas outlet diameter, D_x		0.5		
Vortex finder insertion length, S		0.5		
Cone tip-diameter, B_c		0.375		
Cone height, h_c †		2.5		
	I	1.0	2.5	3.5
Barrel height, h	II	1.5	1.666	4.0
	III	2.0	1.25	4.5
	IV	2.5	1.0	5.0

* Body diameter, $D = 31$ mm. The outlet section is above the cylindrical barrel surface by $L_e = 0.5D$. The inlet section located at a distance $L_i = D$ from the cyclone center.

† The cone height is $h_c = H_t - h$. Cyclone II has the same h/D as in case of Stairmand high efficiency cyclones.

Table 2: The boundary conditions

Boundary	Inlet	Outlet	Dust outlet	Other surfaces
Condition	Velocity inlet	Outflow	Wall (no-slip)	Wall (no-slip)

The simulations have been performed on 8 nodes CPU Opteron 64 Linux cluster using FLUENT 6.3.26 finite volume commercial solver. All simulations have been converged with the selected time step of 1E-4 s and the mentioned numerical settings.

Grid independency study

A grid independency study has been performed for the tested cyclones. Three different grids have been tested for each cyclone, to be sure that the obtained results are mesh independent. For example, meshes with respectively 490164, 714029 and 1174029 cells have been used for cyclone II. The computational results on the three grids are presented in Table 3. As can be seen the maximum difference between the results is less than 5%, so the results on the 490164 cells grid can already considered as sufficiently accurate. However, for excluding any uncertainty, computations have been performed using the 714029 cells grid, where the total number of grid points was not that critical with respect to the computation overhead (Benim *et al.*, 2007; Elsayed and Lacor, 2011).

Figure 1(b) shows the surface grid of cyclone II used in this study. Table 4 gives the total number of computational cells used for each cyclone after the grid independency study. The hexahedral computational grids were generated using the GAMBIT grid generator.

Table 3: The grid independence study for cyclone II

Number of cells	$\mathbf{Eu_S}$ [a]	$\mathbf{Eu_T}$	$\mathbf{Stk_{50}}$x10^{3} [b]
490164	3.475	4.231	1.188
714029	3.654	4.409	1.2
1174029	3.573	4.328	1.224
% difference [c]	2.74	2.29	2.94

[a] Euler number is the dimensionless pressure drop (= pressure drop/average kinetic energy at inlet) $\mathbf{Eu} = \Delta P/(\frac{1}{2}\rho V_{in}^2)$ where ΔP is the pressure drop, ρ is the gas density, V_{in} is the gas inlet velocity. The subscript S denotes the static pressure drop and the subscript T denotes the total pressure drop.

[b] The Stokes number based on the cut-off diameter; $\mathbf{Stk_{50}} = \rho_p x_{50}^2 V_{in}/(18\mu D)$ (Derksen *et al.*, 2006). It is the ratio between the particle relaxation time; $\rho_p x_{50}^2/(18\mu)$ and the gas flow integral time scale; D/V_{in} where ρ_p is the particle density =860 kg/m^3, μ is the gas viscosity. The values of the cut-off diameters x_{50} are obtained from the discrete phase modelling.

[c] The percentage difference between the coarsest and finest grid

Table 4: The number of cells of the tested cyclones

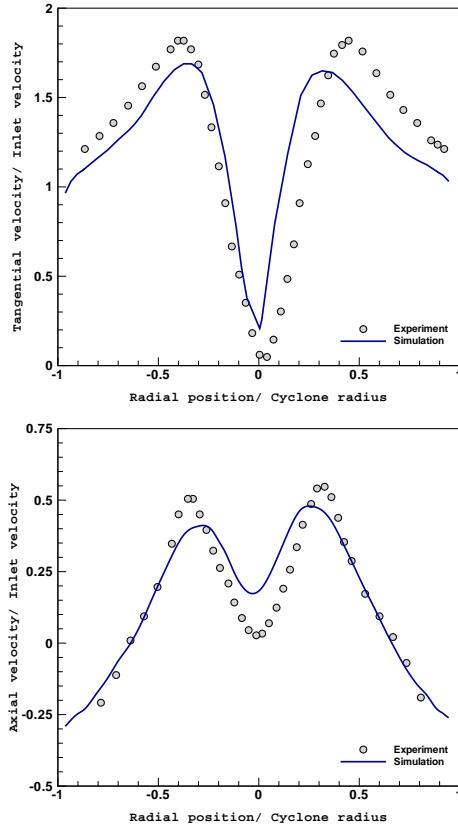| Cyclone	I	II	III	IV
Number of cells	688170	714029	712183	786865

Figure 2: Comparison of the time averaged tangential and axial velocity between the LDA measurements, (Hoekstra, 2000) and the current Reynolds stress turbulence model (RSM) results at 87 cm from the cyclone bottom. From left to right tangential and axial velocity, D_x/D=0.5, The inlet velocity=10 m/s.

VALIDATION OF THE NUMERICAL MODEL

To validate the obtained results, the present simulations are compared with the measurements obtained from (Hoekstra, 2000). Figure 2 shows that the RSM simulation matches the experimental velocity profile with underestimation of the maximum tangential velocity, and overestimation of the axial velocity at the central region. Considering the complexity of the turbulent swirling flow in the cyclones, the agreement between the simulations and measurements is considered to be quite acceptable.

A comparison of calculated Euler number (the dimensionless pressure drop based on both, the static ($\mathbf{Eu}_S$) and total pressure ($\mathbf{Eu}_T$)), Stokes number (the dimensionless cut-off diameter (at particle density of 2740 kg/m^3)) with the experimental data (Hoekstra, 2000), is shown in Table 5. Table 5 indicates a very small deviation from the experimental values. Consequently, the numerical model employed in this study can be used to analyze the gas flow field and performance of the cyclone separator.

RESULTS

The axial variation of the flow properties

The flow velocity can be decomposed into three components. The tangential & the axial velocity components are the major

Table 5: Validation of the computational pressure drop and cut-off diameter

Approach	$\mathbf{Eu}_S$	$\mathbf{Eu}_T$	$\mathbf{Stk}_{50}$x10^3
Experimental (Hoekstra, 2000)	6.0	6.259	0.349
CFD	6.18	6.439	0.325
% error	3	2.8	6.87

Table 6: The position of different plotting sections

Section	S1	S2	S3	S4	S5	S6	S7	S8	S9
z`/D^a	2.75	2.5	2.25	2	1.75	1.5	1.25	1.0	0.75

^{a} z`measured from the inlet section top (cf. Fig. 1(a)).

velocity components in comparison with the radial velocity component. Xiang and Lee (2005) stated that the tangential velocity is the dominant gas velocity in gas cyclones, which results in the centrifugal force for particle separation. The axial component is responsible for the two flow streams (downward & upward).

Figure 3 presents the radial profiles of the time-averaged tangential & axial velocity at nine axial stations (cf., Table 6). As expected, the tangential velocity profiles exhibit the so-called Rankine vortex, which consists of two parts, an outer free vortex and an inner solid rotation in the center (Fig. 3). The tangential velocity distribution in the inner region is rather similar at different sections for the same cyclone. In the outer region, due to the sharp drop in velocity magnitude in the near wall region, the distribution is different but the maximum tangential velocity is similar for all sections. The axial velocity profiles at nine different stations are shown in Fig. 3. All cyclones show the inverted W profile but the central dip decreases with increasing the barrel height.

The effect of barrel height on the pressure profile

Figure 4 compares the static pressure profiles for the four cyclones at section S3, S6 & S9 (as a representative for the other sections, because the axial variations in the flow variables are small). From the comparison between the radial profiles of the four cyclones, the minimum pressure at the cyclone center is almost the same for all cyclones. The slope of the static pressure radial profile becomes more flat with increasing the barrel height.

The effect of barrel height on the velocity profiles

The tangential and axial velocity profiles at sections S3, S6 & S9 for the four cyclones are compared in Fig. 4. As is clear from Fig. 4 the variation of axial velocity with changing barrel height is limited close to the wall especially in the cylindrical part. In the central region the change in axial velocity profile is more pronounced with the dip in axial velocity decreasing with increasing the barrel height. This is the result of the flatting of the pressure distribution results in a smaller pressure force. This may explain also the change of the axial velocity from cyclones I to IV. Increasing the cyclone barrel height slightly decreases the maximum tangential velocity. Cyclone I has the maximum tangential velocity in comparison with the other cyclones. The effect of increasing the barrel height on the maximum tangential velocity is limited.

The effect of barrel height on the flow pattern

Figure 5 shows the contour plots of the time-averaged static pressure, tangential and axial velocity. The time-averaged static pressure decreases radially from wall to center. A negative pressure zone appears in the forced vortex region (central

region) due to high swirling velocity. The pressure gradient is largest along the radial direction, whereas the gradient in axial direction is very limited. The cyclonic flow is not symmetrical as is clear from the shape of the low pressure zone at the cyclone center (twisted cylinder). Two vortical motions are exist one moving down (outer vortex) and the other moving up (inner vortex). It is observed that, the highest value of the static pressure decreases with increasing the barrel height. The tangential velocity pattern is very similar for all cyclones (Rankine profile). The highest value decreases with increasing the barrel height but the differences between the four cyclones are small. The axial velocity patterns for the four cyclones have the shape of an inverted W profile.

The effect of barrel height on the performance

In order to estimate the effect of cyclone barrel height on the performance parameters, the Stokes number (dimensionless cut-off diameter) and the Euler number (dimensionless static pressure drop) have been calculated and presented in Fig. 6 & Table 7. A discrete phase modeling (DPM) study has been performed by injecting 10^4 particles from the inlet surface with a particle density of 860 kg/m^3 and with a particle size ranging from 0.025 till 5 micron. The collection efficiency of each individual particle size is calculated (η = the mass of collected particles / mass of injected particles). The cut-off diameter x_{50} is the particle diameter that represent 50% collection efficiency. Figure 6 & Table 7 show a sharp decrease of the Euler number with increasing the barrel height until $h/D = 1.8$ ($H_t/D = 4.3$) and a gradual decrease beyond. This behavior can be explained as follows. The pressure drop in the cyclone is composed of three main contributions (Elsayed and Lacor, 2011): (1) the pressure drop at the inlet section. (2) the pressure drop in the cyclone body due to swirling motion and due to wall friction, this contribution may increase with increasing the cyclone height as the wall friction will increase due to friction with a larger wall surface, or decreases as the vortex strength will decrease because the maximum tangential velocity decreases. (3) the main contribution to the cyclone pressure drop is the energy loss in the exit tube, which mainly depends on the maximum tangential velocity in the cyclone. As is clear from Fig. 4 the maximum tangential velocity decreases with increasing cyclone barrel height. As the inlet section is the same in all cyclones, the pressure drop in the inlet section does not vary with increasing barrel height. The sharp decrease of the Euler number between cyclones I & II is due to the decrease in the pressure drop as a result of the decrease in the maximum tangential velocity. There are two competing contributions: increase of the pressure drop due to friction and decrease of the pressure drop due to reduction in the vortex strength. At the beginning the wall friction effect is small in comparison with the effect of vortex strength, and for longer cyclones this effect become larger (but still less than that of vortex strength decay). That also explains the small variation of the Euler number with the barrel height for $h/D > 1.8$, that is also clear from Fig. 4 where the maximum tangential velocity of cyclones III & IV are very close.

The behavior of the Stokes number curve as a function of barrel height is quite reasonable with increasing barrel height (i.e., separation becomes more effective with increasing the separation space), the possibility of particles to be captured increases due to the increased cyclone space. However, the vortex strength decreased slightly with the maximum tangential velocity, the main contribution here is the collecting surface. The Stokes number curve becomes nearly flat between

cyclones III & IV due to the small changes in both the axial & the tangential velocity profile between the two cyclones. Both Ramachandran (Ramachandran *et al.*, 1991) and Iozia (Iozia and Leith, 1989) models agree with the CFD results in the trend of decreasing both the Euler number and Stokes number with increasing barrel height, but differ in slope and values.

Table 7: The Euler numbers and Stokes numbers at the cut-off diameter for the tested cyclones

Cyclone	I	II	III	IV
h/D	1.0	1.5	2.0	2.5
h_c/h	2.5	1.666	1.25	1.0
H_t/D	3.5	4	4.5	5.0
Eu	4.39	3.654	3.33	3.09
Eu (Ramachandran *et al.*, 1991)	5.71	4.77	4.17	3.73
Stk$_{50}$ x 10^3	1.32	1.2	1.01	0.95
Stk$_{50}$ x 10^3 (Iozia and Leith, 1989)	1.94	1.82	1.72	1.64

CONCLUSIONS

Four cyclones of different barrel height have been simulated using the Reynolds stress model (RSM), to study the effect of cyclone barrel height on the cyclone separator performance and flow pattern. The following conclusions have been obtained.

- The maximum tangential velocity in the cyclone decreases with increasing the cyclone barrel height.

- No acceleration occurs in the cyclone space (the maximum tangential velocity is nearly constant throughout the same cyclone).

- Increasing the barrel height, makes a small change in the axial velocity.

- Increasing the cyclone barrel height decreases the pressure drop & the cut-off diameter. But the changes in the performance beyond $h/D = 1.8$ are small.

In the current study, the particle-particle and the particle gas interaction were not taken into consideration. Consequently, the obtained results are valid only for very small mass loading.

As a recommendation of future work, the same study is to be performed but at different flow rates and different particle densities. Also the effect of increasing the cyclone barrel height on natural vortex length and precessing vortex core needs more investigation.

REFERENCES

BENIM, A., OZKAN, K., CAGAN, M., GUNES, D. (2007). "Computational investigation of turbulent jet impinging onto rotating disk". *International Journal of Numerical Methods for Heat & Fluid Flow*, **17(3)**, 284 – 301.

BERNARDO, S., MORI, M., PERES, A., DIONISIO, R. (2006). "3-D computational fluid dynamics for gas and gas-particle flows in a cyclone with different inlet section angles". *Powder Technology*, **162(3)**, 190 – 200.

BOYSAN, F., EWAN, B. C. R., SWITHENBANK, J., AYERS, W. H. (1983). "Experimental and theoretical studies of cyclone separator aerodynamics". *IChemE Symp Series*, **69**, 305 – 320.

CHUAH, T., GIMBUN, J., CHOONG, T. S. (2006). "A CFD study of the effect of cone dimensions on sampling aerocyclones performance and hydrodynamics". *Powder Technology*, **162**, 126 – 132.

DERKSEN, J. J., SUNDARESAN, S., VAN DEN AKKER, H. E. A. (2006). "Simulation of mass-loading effects in gas–solid cyclone separators". *Powder Technology*, **163**, 59–68.

ELSAYED, K., LACOR, C. (2010a). "The effect of cyclone height on the flow pattern and performance using LES". *Tenth International Congress of Fluid Dynamics (ICFD10), ASME, Egypt, ICFD10-EG-3003*. Ain Soukhna, Red Sea, Egypt.

ELSAYED, K., LACOR, C. (2010b). "Optimization of the cyclone separator geometry for minimum pressure drop using mathematical models and CFD simulations". *Chemical Engineering Science*, **65(22)**, 6048–6058.

ELSAYED, K., LACOR, C. (2011). "The effect of cyclone inlet dimensions on the flow pattern and performance". *Applied Mathematical Modelling*, **35(4)**, 1952–1968.

GIMBUN, J., CHUAH, T., CHOONG, T., FAKHRU'L-RAZI, Y. (2005a). "A CFD study on the prediction of cyclone collection efficiency". *International Journal for Computational Methods in Engineering Science and Mechanics*, **6(3)**, 161 – 168.

GIMBUN, J., CHUAH, T., FAKHRU'L-RAZI, A., CHOONG, T. S. Y. (2005b). "The influence of temperature and inlet velocity on cyclone pressure drop: a CFD study". *Chemical Engineering & Processing*, **44(1)**, 7–12.

GIMBUN, J., CHUAH, T. G., CHOONG, T. S. Y., FAKHRU'L-RAZI, A. (2005c). "Prediction of the effects of cone tip diameter on the cyclone performance". *Aerosol Science and Technology*, **36**, 1056–1065.

GRIFFITHS, W.D., BOYSAN, F. (1996). "Computational fluid dynamics (CFD) and empirical modelling of the performance of a number of cyclone samplers". *Journal of Aerosol Science*, **27(2)**, 281–304.

HOEKSTRA, A.J. (2000). *Gas flow field and collection efficiency of cyclone separators*. Ph.D. thesis, Technical University Delft.

HOEKSTRA, A. J., DERKSEN, J. J., VAN DEN AKKER, H. E. A. (1999). "An experimental and numerical study of turbulent swirling flow in gas cyclones". *Chemical Engineering Science*, **54**, 2055–2065.

HOFFMANN, A. C., DE GROOT, M., PENG, W., DRIES, H. W. A., KATER, J. (2001). "Advantages and risks in increasing cyclone separator length". *AIChE Journal*, **47(11)**, 2452–2460.

HU, L. Y., ZHOU, L. X., ZHANG, J., SHI, M. X. (2005). "Studies on strongly swirling flows in the full space of a volute cyclone separator". *AIChE Journal*, **51(3)**, 740–749.

IOZIA, D.L., LEITH, D. (1989). "Effect of cyclone dimensions on gas flow pattern and collection efficiency". *Aerosol Science and Technology*, **10(3)**, 491–500.

KAYA, F., KARAGOZ, I. (2008). "Performance analysis of numerical schemes in highly swirling turbulent flows in cyclones". *Current Science*, **94(10)**, 1273 – 1278.

LIM, K. S., KIM, H. S., LEE, K. W. (2004). "Characteristics of the collection efficiency for a cyclone with different vortex finder shapes". *Journal of Aerosol Science*, **35(6)**, 743–754.

O'DOHERTY, T., GRIFFITHS, A. J., SYRED, N., BOWEN, P. J., FICK, W. (1999). "Experimental analysis of rotating instabilities in swirling and cyclonic flows". *Developments in Chemical Engineering and Mineral Processing*, **7**, 245–267.

RAMACHANDRAN, G., LEITH, D., DIRGO, J., FELDMAN, H. (1991). "Cyclone optimization based on a new empirical model for pressure drop". *Aerosol Science and Technology*, **15**, 135–148.

RAOUFI, A., SHAMS, M., FARZANEH, M., EBRAHIMI, R. (2008). "Numerical simulation and optimization of fluid flow in cyclone vortex finder". *Chemical Engineering and Processing*, **47**, 128–137.

SLACK, M. D., PRASAD, R. O., BAKKER, A., BOYSAN, F. (2000). "Advances in cyclone modeling using unstructured grids". *Trans IChemE.*, **78 Part A, (2000)**.

SOLERO, G., COGHE, A. (2002). "Experimental fluid dynamic characterization of a cyclone chamber". *Experimental Thermal and Fluid Science*, **27**, 87–96.

XIANG, R., PARK, S. H., LEE, K. W. (2001). "Effects of cone dimension on cyclone performance." *Journal of Aerosol Science*, **32(4)**, 549–561.

XIANG, R.B., LEE, K.W. (2005). "Numerical study of flow field in cyclones of different height". *Chemical Engineering and Processing*, **44**, 877–883.

YAZDABADI, P. A., GRIFFLTHS, A. J., SYRED, N. (1994). "Characterization of the PVC phenomena in the exhaust of a cyclone dust separator". *Experiments in Fluids*, **17**, 84–95.

ZHANG, B., HUI, S. (2007). "Numerical simulation and PIV study of the turbulent flow in a cyclonic separator". *International Conference on Power Engineering*. Hangzhou, China.

ZHAO, B., SU, Y., ZHANG, J. (2006). "Simulation of gas flow pattern and separation efficiency in cyclone with conventional single and spiral double inlet configuration". *Chemical Engineering Research and Design*, **84**, 1158–1165.

ZHU, Y., LEE, K. W. (1999). "Experimental study on small cyclones operating at high flow rates." *Journal of Aerosol Science*, **30**, 1303–1315.
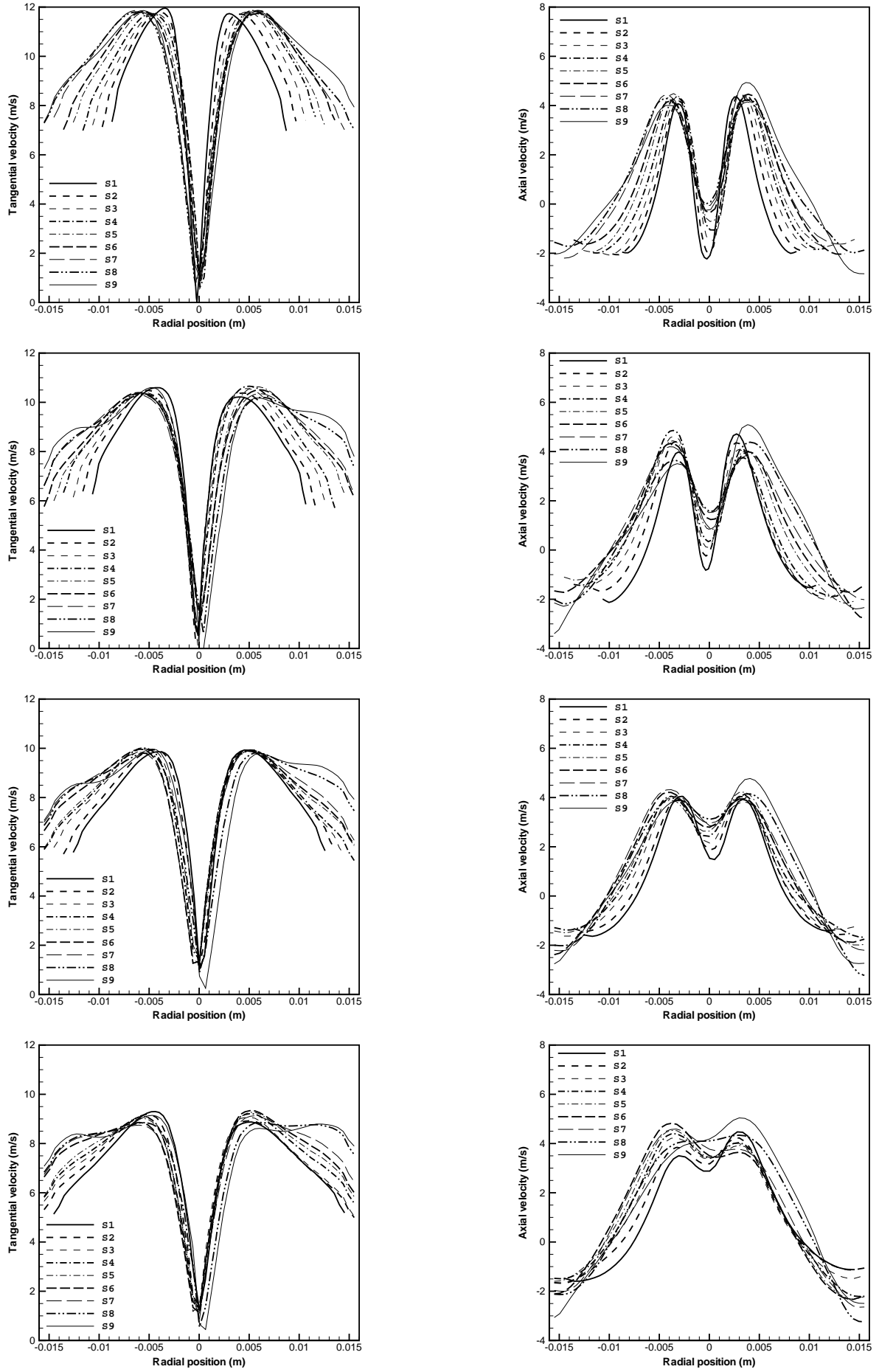
Figure 3: The radial profile for the time averaged tangential and axial velocity at different sections for the four cyclones. From left to right: tangential and axial velocity. From top to left: cyclone I - IV.
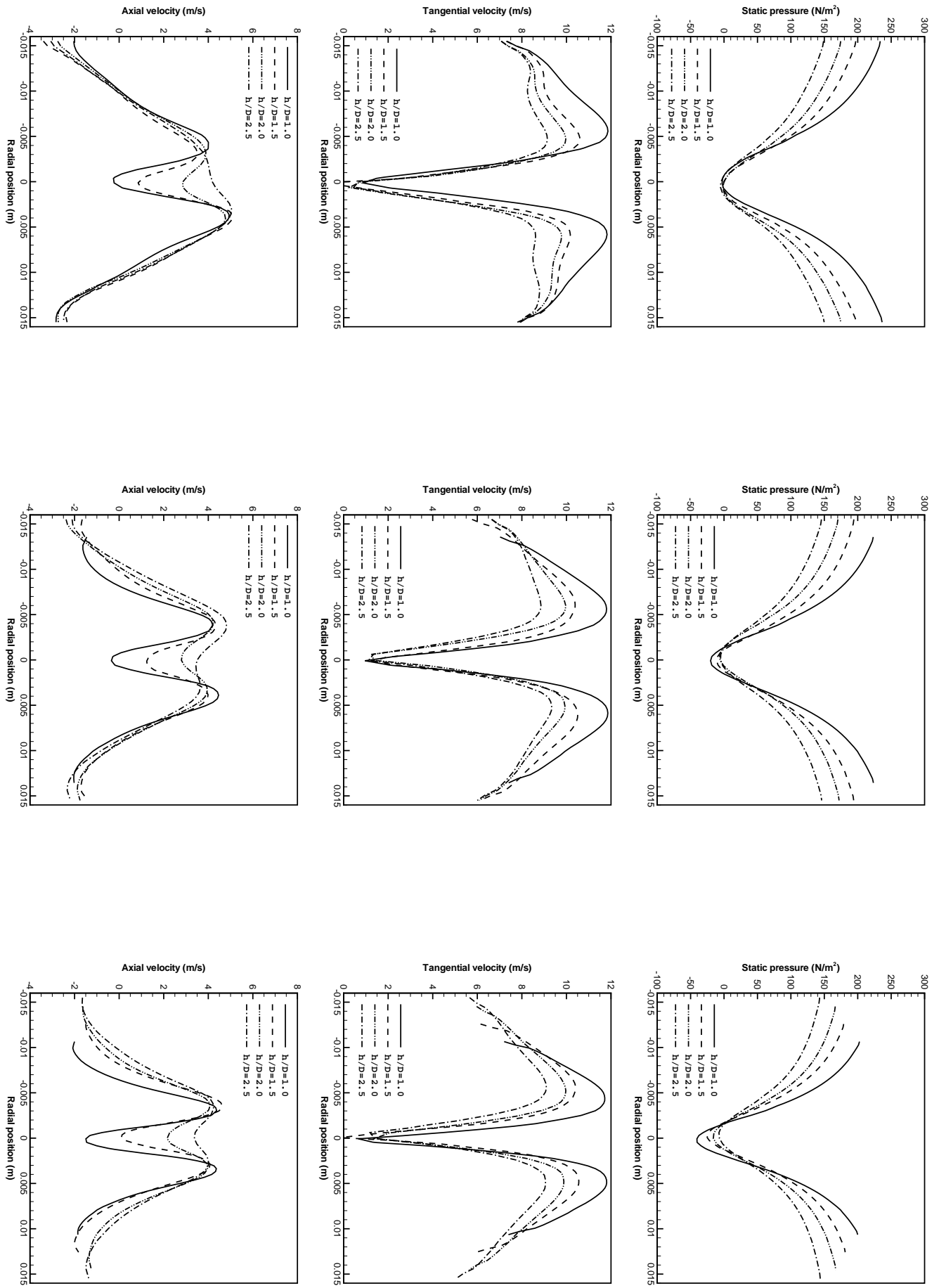
Figure 4: Comparison between the radial profiles for the time averaged static pressure, tangential and axial velocity at sections S9, S6 & S3. From left to right S9 - S3.
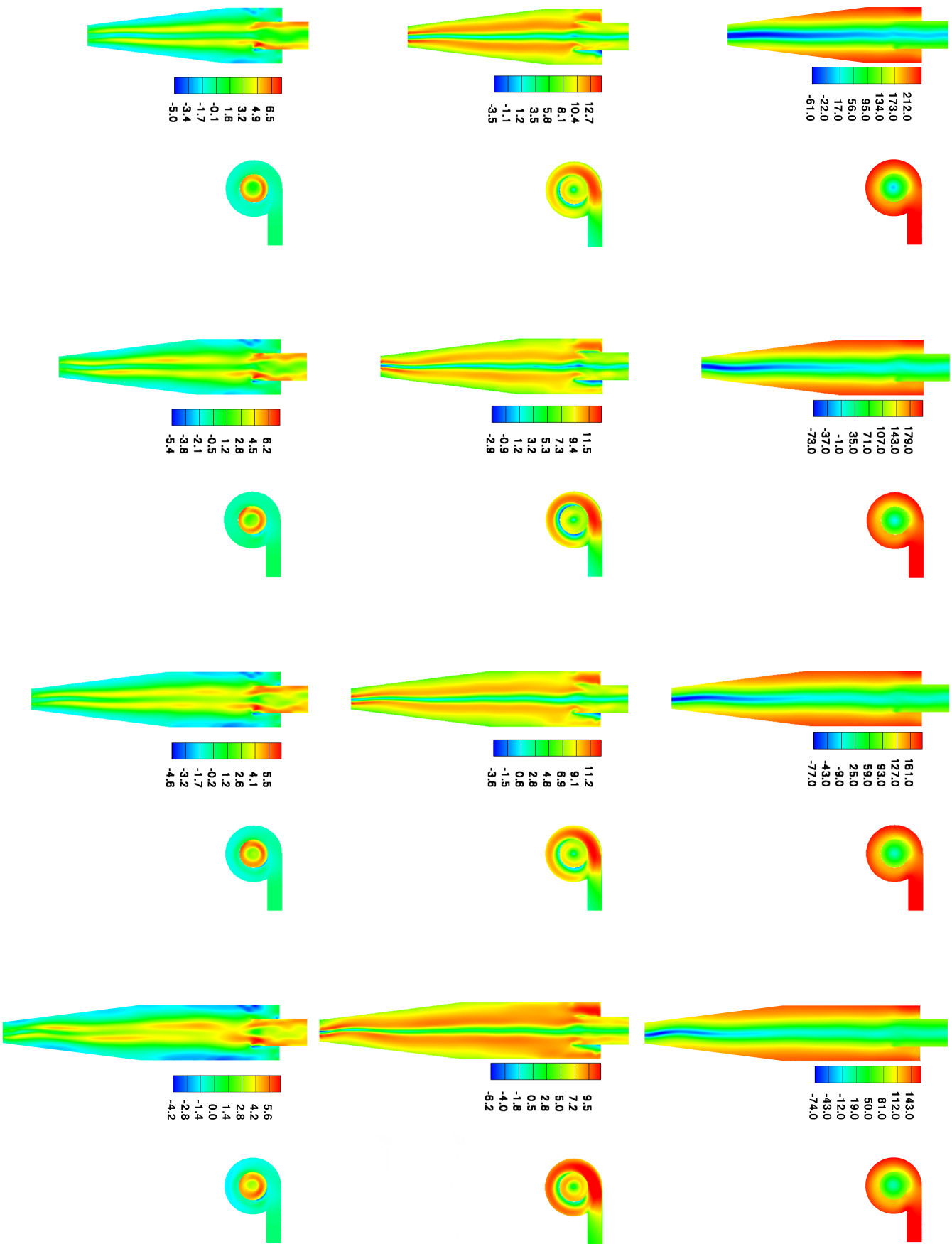
Figure 5: The contour plots for the time averaged flow variables at sections Y=0 and throughout the inlet section. From top to bottom: the static pressure (N/m²), the tangential velocity (m/s) and the axial velocity (m/s). From left to right cyclone I - IV.
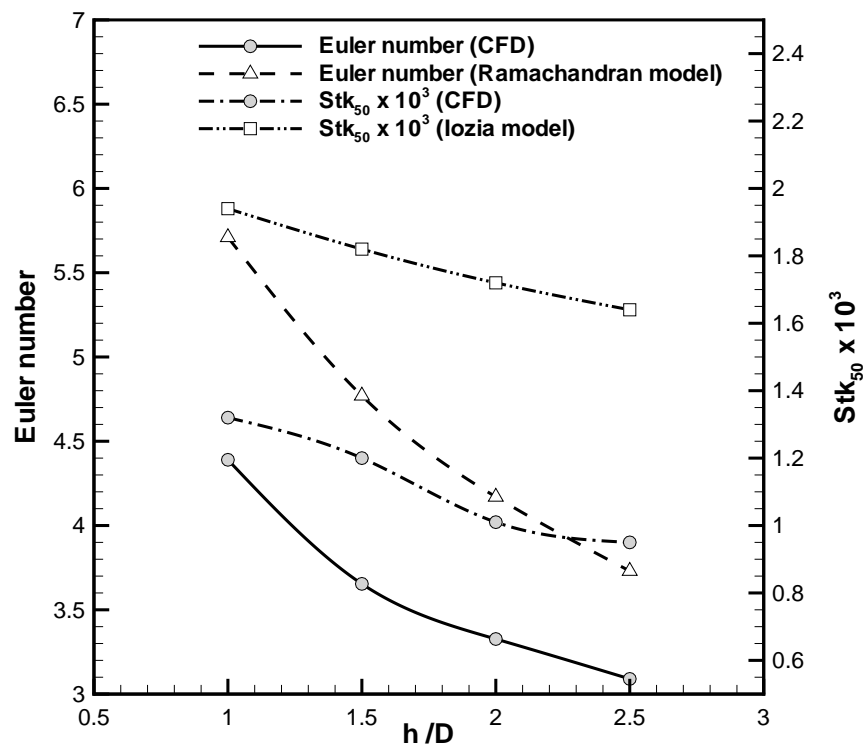
Figure 6: The effect of barrel height on the Euler number and the Stokes number.

CFD MODELLING OF MAGNETIC STIRRING AT PV-SILICON CRYSTALLISATION

Natasha Dropka*, Uwe Rehse, Peter Rudolph

Leibniz Institute for Crystal Growth in Berlin, GERMANY
E-mail*: dropka@ikz-berlin.de

ABSTRACT

The further development of directional solidification as a key technology for production of mc-silicon ingots for photovoltaics (PV) requires CFD simulations due to its multi-disciplinary nature, its complex multi-parameter space, the lack of axial symmetry of the equipment and the running scaling problem. We studied the time evolution of a melt flow exposed to different non-steady magnetic fields generated by the KRIST*MAG*® bottom and side heater-magnetic coils. Particularly, single- and double-frequency traveling, alternating and carrousel magnetic fields were compared. The stirring potentials of the studied magnetic fields were appraised using fully developed buoyancy flow as a benchmark. The key factors for the duration of the transition to the hydro-dynamically developed flow were identified.

Our numerical results confirmed the necessity of CFD simulations for deeper understanding of directional solidification process and optimization of magnetic fields for its further improvement.

Keywords: A1. Computer simulation A1. Fluid flows A1. Magnetic fields A1.Solidification B2. Semi conducting silicon
PACS: 81.10.Fq, 47.11.Df, 47.20.Bp, 81.05.Cy

NOMENCLATURE

B magnetic induction [T]
Cp specific heat [J/kg·K]
g gravity acceleration [m/s^2]
h melt height [m]
F_L Lorentz force density [N/m^3]
f frequency of AC current [Hz]
H magnetic field [A/m]
j current density [A/m^2]
L melt characteristic size [m]
P pressure [Pa]
Pr Prandtl number [-]
T temperature [K]
t time [s]
Re Reynolds number [-]
Ra Rayleigh number [-]
Ta Taylor number [-]
$\vec{u}(u,v,w)$ velocity [m/s]

x,y,z Cartesian coordinates [m]
ϕ phase shift [°]
λ thermal conductivity [W/m·K]
σ electric conductivity [A/V·m]
ν kinematic viscosity [m^2/s]
μ relative magnetic permeability of material [-]
μ_0 magnetic permeability of free space [H/m]
ρ density [kg/m^3]

Subscripts

av   average volume
buoy buoyancy
MF   magnetic field
visc   viscous

INTRODUCTION

Directional solidification (DS) proves to be one of the key technologies for the production of mc-silicon ingots for the current commercial photovoltaic market. Nowadays, about a half of the solar wafer production is based on crystallization of rectangular ingots. During this process, liquid silicon in Si_3N_4-coated rectangular fused silica crucibles is unidirectionally solidified from below to the top in a relative low vertical temperature gradient. Mostly, solidification is achieved by the principle of vertical gradient freezing (VGF) (Monberg, 1994), i.e. by the electronically controlled lowering of the system temperature with a specific cooling rate. In such a thermal stable regime the buoyancy driven convection is too week for reduction of the diffusion boundary layer at the propagating interface which is formed due to the segregation effect. As a result, high-concentration impurities like carbon and nitrogen exceed here the solubility limit generating SiC and Si_3N_4 precipitations which are then incorporated into the crystallizing silicon. The presence of such second phase inclusions evokes short circuit within the solar cells and must be, therefore, prevented.

Among conventional mechanical or electrical mixing (Ottino, 1990; Dimotakis, 2005), forced convection induced by variable magnetic fields turns out to be the

most efficient method for the removal of the diffusion boundary layer and, hence, for obtaining precipitate-free and low-impurity ingots. There are different magnetic stirring technologies based on rotating (RMF), traveling (TMF), alternating magnetic field (AMF) or some combinations of them (Rudolph, 2008; Eckert et al., 2009; Dropka et al., 2010; Nikrityuk et al., 2005, 2006, 2010; Willers et al., 2008; Kojima et al., 1983, Mitric and Duffar, 2008). However, the flow intensification must be controlled very carefully since too strong turbulent flows lead to erosion of the crucible wall cover and in turn to the pollution of the melt. Powerful numeric modeling is required to find out the optimal flow pattern.

Until now most simulations of stirring regimes by unsteady magnetic fields were performed in axi-symmetrical geometry (2D), for laminar flowing me-tallic melts and for low magnetic Taylor (Ta) numbers $\leq 10^3$ comparable with microgravity conditions. Recent results showed the superiority of TMF versus RMF for VGF arrangements (Nikrityuk et al., 2010). However, also in case of TMF increasing ingot sizes decrease the central stirring efficiency of the Lorentz forces (F_L) generated outside the melt periphery. Therefore, further efforts are required to match the magnetic field configuration for the present and future industrial demands as best as possible.

In this study, 3D magnetic and CFD transient calculations with the commercial software ANSYS 12.1 were applied. For the crystallization model the KRIST*MAG*® concept (www.kristmag.com) is used where-upon a heater magnetic module (HMM) is placed around the crucible producing heat by DC and unsteady magnetic field by AC simultaneously (Rudolph, 2008). First, the melt flows in rectangular silicon melts in up- and downwards single-frequency TMFs are analyzed (Dropka et al., 2010). Then, double-frequency TMF is applied combining two opposite directed traveling fields of different strength, frequency and phase shift (Dropka et al., 2011; Büllesfeld et al., 2008). Due to the skin effect the high frequency part of the total F_L acts mainly in the melt periphery whereas the low-frequency component produces the more extensive force reaching the central bulk region. After that, the stirring potential of AMFs was studied. For that, HMMs supplied by in-phase AC were placed at the crucible side and bottom, respectively. Such arrangement differs from a single AMF coil reported by Mitric and Duffar (Mitric and Duffar, 2008). Finally, we studied the flow patterns in the carousel magnetic field (CMF) generated within four bottom HMMs placed around the vertical ingot axis and supplied by out-of-phase AC (Dropka et al., 2010). A likewise idea was proposed by Ciscato et al. (Ciscato et al., 2009) using four bottom high-frequency (15 kHz) induction heaters without phase shift which, however, cannot act as effective melt stirrers for large melt volumes due to their very low skin depth.

MODEL AND METHODOLOGY

Fully 3D numerical calculations were carried out for a solidification furnace with one top standard resistance heater, four KRIST*MAG*® coil-shaped side heaters

(Rudolph, 2008) as well as four spiral bottom heaters positioned around the crucible axis (Dropka et al., 2010). The thermal boundary conditions (BCs) for the local simulation of the melt flow were provided by global thermal analyses with neglected gas flow (Figure 1). Radiative heat transfer in the furnace was described by discrete transfer radiation method. The calculations were performed for completely molten silicon bulks of different size. The computational domain for local melt simulations consisted typically of 3.4 x 10^6 tetra and prismatic mesh elements. BCs for the flow were no slip at solid walls but free slip at the free melt surface. Effect of turbulent fluctuations was accounted by using kω-SST model. In the transient calculations, the time step was adjusted to Courant number ≤ 1. 3D magnetic calculations provided time average Lorentz force density field that was used, in the second step, as a momentum source in the momentum equation.

To study the interplay between the flow and the magnetic fields during crystallization we used a finite-volume commercial code ANSYS CFX 12.1. 3D magnetic simulations were obtained by finite elements commercial code ANSYS Emag. The magnetic heaters were supplied by AC current differing in magnetic parameters, as shown in Table 1. Case 1 represents flows exposed to downwards directed TMF. Case 2 considers the double-frequency upwards directed TMF. In cases 3 and 4 we studied the melt flow exposed to AMFs generated by side and bottom heaters, respectively. Case 5 represents CMF driven flow. The stirring potential of different magnetic fields was app-raised using corresponding fully developed buoyancy flow field as an initial state and as a benchmark.

The transport phenomena occurring during directional solidification of silicon in the presence of magnetic fields are governed by the equations of continuity (1), Navier Stokes (2), energy balance (3) and Maxwell (4) together with the Ohms law (5). The influence of the silicon melt flow on induced current j, i.e. the term u x B in Equation (5) can be neglected (Spitzer, 1999). The resulting volume F_L is given by Equation (6).

$$\frac{\partial \rho}{\partial t} + \nabla(\rho \vec{u}) = 0 \tag{1}$$

$$\rho \frac{\partial \vec{u}}{\partial t} + \vec{u} \nabla \vec{u} = \rho \vec{g} - \nabla P + \nu \nabla^2 \vec{u} + \vec{F}_L \tag{2}$$

$$\rho C_P(\frac{\partial T}{\partial t} + \vec{u} \nabla T) = \lambda \nabla^2 T \tag{3}$$

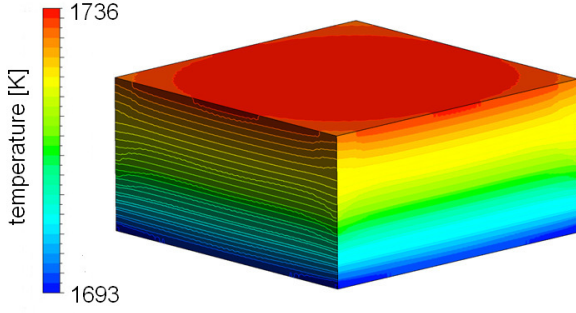$$\nabla \times \vec{H} = \vec{j}$$

$$\nabla \times \vec{E} = -\frac{\partial \vec{B}}{\partial t} \tag{4}$$

$$\nabla \vec{B} = 0$$

$$\nabla \vec{E} = 0$$

$$\vec{j} = \sigma(\vec{E} + (\vec{u} \times \vec{B})) \approx \sigma \vec{E} \tag{5}$$

$$\vec{B} = \mu \mu_0 \vec{H}$$

$$\vec{F}_L = \vec{j} \times \vec{B} \tag{6}$$

In case of double-frequency TMF, when the AC currents with different frequencies are combined, the resulting F_L is obtained by simply adding the corresponding single-frequency F_L as given in (7) (Dropka et al., 2010; Spitzer et al., 1996).

$$\vec{F}_L = \vec{F}_L(f_1) + \vec{F}_L(f_2) \tag{7}$$

Figure 1: Thermal BC for the local simulation of the melt flow resulted from the global 3D simulation (case 2, 4 and 5).

case	1	2	3	4	5
MF type	1f TMF	2f TMF	AMF	AMF	CMF
F_L direction	down	up	horiz	up	up
HMM position	side	side	side	down	down
ϕ [a.u.]	-1	±1	0	0	1
f [a.u.]	1	1; 25	1	2	2
L [a.u.]	0.27	1	0.27	1	1

Table 1: Studied cases and their important features.

We calculated pure buoyancy driven melt flows until the pseudo steady state was achieved, defined as a moment when the temporal change of velocity in monitoring points is less than 1%. Particularly, the time evolution of velocity and temperature was traced both in different monitoring points in the melt as well as the volume averaged values (8).
Volume average velocity u_{av} is defined as follows:

$$u_{av} = \frac{1}{L^2 h} \iiint_V u \, dx \, dy \, dz \tag{8}$$

The development of the velocity profile is given on the time scale normalized by viscous time t_{visc}:

$$t_{visc} = \frac{L^2}{\nu} \tag{9}$$

The time normalization was introduced to enable the comparison of the flows occurring in the melts of different sizes. Similarly, the normalization of the velocity using the pure buoyancy as a benchmark facilitates decoupling of the magnetic from the buoyancy driven flow.
Additionally, the influence of F_L on the form of velocity streamlines was analyzed for different magnetic fields and visualized at different cross sections in the melt.

RESULTS AND DISCUSSION

The calculation of the fully developed flow field required an overall CPU time of about $1 \cdot 10^7$ s on 8x2 dual core 1.6 GHz processors, 32GB RAM server, for each examined condition.

Lorentz Force Density Distributions

Some typical results for F_L distribution generated by HMMs are given in Figures 2-5.
If side magnetic heaters are used for generation of TMF (case 1 and 2, Table 1), the maximal F_L is obtained at the side walls (Figure 2). The direction of the F_L depends on the selected frequency and the phase shift. The superposition of two opposite directed longitudinally TMFs increases the horizontal component of F_L in the vicinity of the side walls simultaneously shifting the zone of steep meridional F_L towards melt core (Figure 2). This kind of force distribution is beneficial for introduction of impulse into the melt flow, i.e. for the enhanced stirring without generation of high velocities in the vicinity of the crucible protection layer. No phase shift among side coils generates AMF with horizontal directed F_L (case 3, Table 1). Correspondingly, in-phase AC current supply to bottom coils generates AMF with vertical directed F_L (case 4, Table 1), as shown in Figure 3.
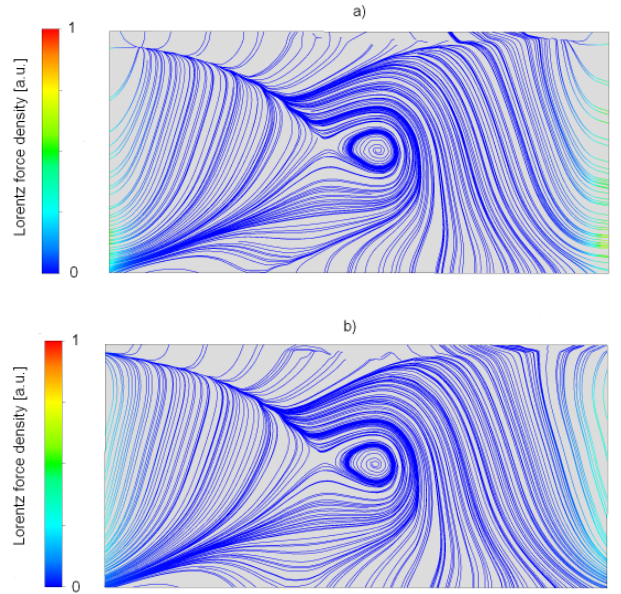
Figure 2: F_L streamlines in the middle vertical cross section of the melt generated by: a) double-frequency upwards TMF and b) partial single-frequency upwards TMF (case 2, Table 1).

If bottom magnetic heaters are supplied with out-of-phase AC current (case 5, Table 1), the CMF will be generated having F_L revolving around the vertical melt axis, with the maximum in meridional direction at the crucible bottom, decreasing upwards (Figure 4, 5). In longitudinal direction, the F_L maximum is observed at the melt core and it is decreasing towards the crucible side walls. The selected frequency determines the penetration, i.e. skin depth of F_L and can serve as a tuning parameter. Without phase shift, F_L is upwards

directed and pulses in the pace of AC frequency. If we compare CMF with the AMF generated by bottom heaters without phase shift among coils (Figure 3, 4), it can be noticed that the phase shift is responsible for banding of the force trajectories in the vicinity of the crucible bottom and decrease of the F_L intensity. For example, the maximal value of F_L vector for the case 5 dropped to 57% of its value for the case 4. On the other hand, the vertical component of F_L vector decreased only to 76% of the value for the case 4. The reason for different retarding effects of the phase shift on F_L with respect to its vertical component lays in the increase of the horizontal F_L components, i.e. inclination of the F_L vector that brings swirling effect into the melt flow, enhancing stirring of the melt.
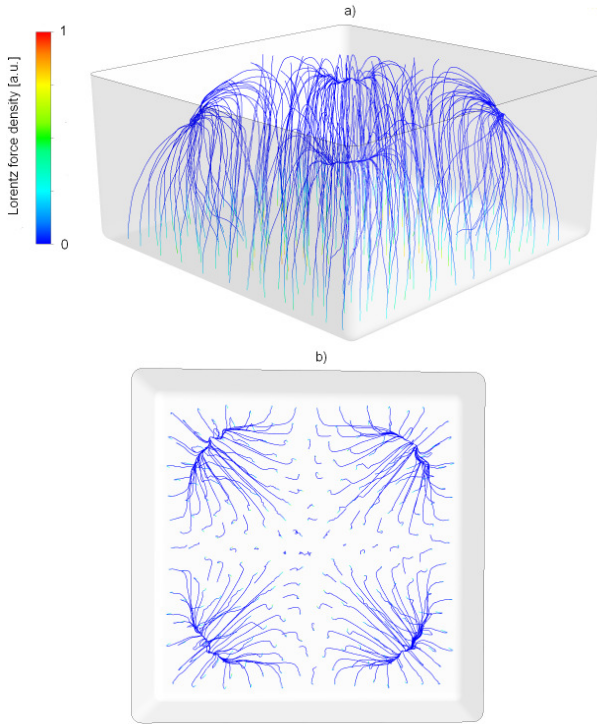
Figure 3: F_L streamlines in the melt generated by vertical AMF originated from bottom heaters (case 4, Table 1) viewing from: a) side and b) top.

Flow Fields in the Melt

Figures 6-8 shows snapshots of the velocity flow fields presented either in 3D or as 2D cross sections of the melt for the cases described in Table 1. In case of the pure buoyancy flow, if the temperature distribution at the melt side boundaries is quasi-symmetrical, a sliced flow with one dominating central vortex will be obtained (Figure 6). Asymmetry in thermal BCs brought by e.g. asymmetry in the design of the side heaters, position of the crucible towards coils etc, can generate more instability in the flow, i.e. more vortexes as shown in Figure 7c.
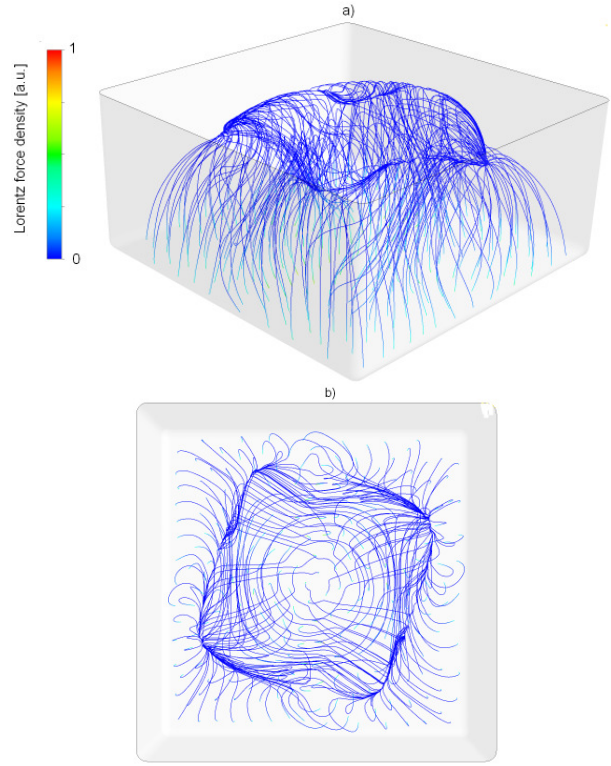
Figure 4: F_L streamlines in the melt generated by CMF with phase shift among heater coils (case 5, Table 1) viewing from: a) side and b) top.

Introduction of different magnetic fields into the system tailors the melt flow in different ways. Downwards directed F_L trigger the flow in both meridional and longitudinal directions, as shown in Figure 7a. The obtained 3D flow pattern can be beneficial for stirring and removal of the diffusion boundary layer. AMFs with horizontal F_L intensify the flow in horizontal direction (Figure 7b) with respect to the pure buoyancy (Figure 7c).
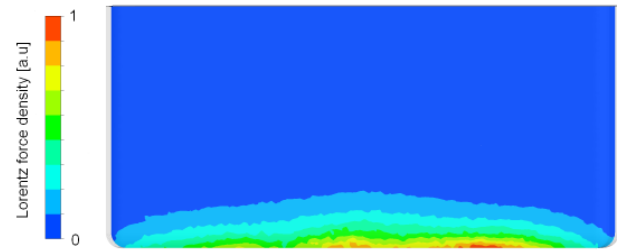
Figure 5: Contour of time averaged F_L in the middle vertical cross section of the melt for CMF generated by the bottom heaters (case 5, Table 1).

The superposition of TMFs of different frequencies (Figure 2) shifts the flow maximum from the peripheral region towards the melt bulk increasing the melt mixing within the central region and improves, therewith, the process purity, as reported by Dropka et al. (Dropka et al., 2011).
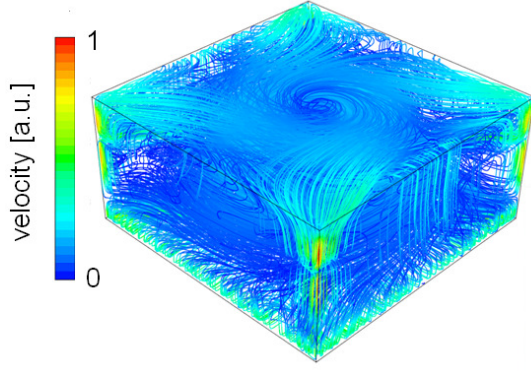
Figure 6: Velocity streamlines in the silicon melt driven by pure buoyancy (benchmark for cases 1, 4, and 5, Table 1).

CMFs with revolving predominantly upwards directed F_L (Figure 4, 5) provoke strong circulation in the lower part of the melt in a form of vortex (Figure 8) that slows down towards melt free surface. Intensified horizontal mixing is enriched with acceleration of the upwards flow observed through the increase of vertical velocity component u after introduction of CMF to the buoyancy flow (Figure 10). These observations underline the feasibility of application of CMF, particularly for large melts. However, for the successful application of CMFs, the proper design of bottom coils is crucial, since they

In all studied cases, the system requires a characteristic time to become hydro-dynamically developed. Independent of the type of imposed magnetic field, i.e. the intensity and direction of generated F_L in the melt, after initial speed-up time, little evolution in established velocity profile is noticeable thereafter. If we compare the results of cases 1 and 3, velocity profile development proceeds more rapidly for the magnetic driven flows with horizontal directed F_L of AMF in comparison to flows exposed to forces generated by downward 1f TMF (Figure 9). The same is valid for the comparison between the predominantly vertically directed Lorentz forces from CMF and upwards directed F_L from 1f (shown elsewhere) and 2f TMFs. The stronger the F_L, the longer the initial adjustment time.

model	1	2	3	4	5
Re_{MF}/Re_{buoy}	1.09	2.24	1.06	1.21	1.76
Ra_{MF}/Ra_{buoy}	1.0005	1	0.999	0.999	1
Pr	0.17	0.17	0.17	0.17	0.17

Table 2: Characteristic non-dimensional numbers used in this study.

Finally, it can be summarized that the use of tailor-made volume force distribution can be beneficial for removal of diffusion boundary layer, for mass transport of
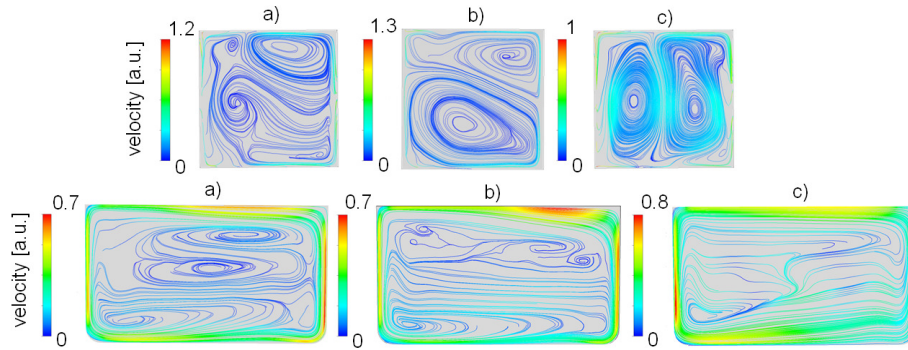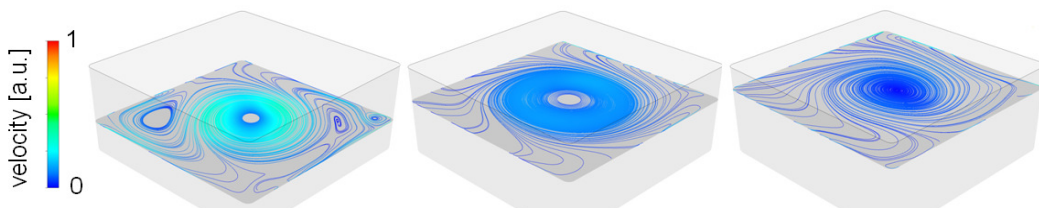

Figure 7: Snapshots of the velocity streamlines in middle horizontal (upper row) and middle vertical (lower row) cross sections of the melt driven by a) 1f TMF down (case 1, Table 1), b) AMF generated by side heaters (case 3, Table 1), and c) pure buoyancy.

should be used only for generation of F_L. Their thermal effects must be negligible or otherwise neutralized.

The acceleration of the liquid phase measured via the increase of Re number for several cases of magnetic driven flows (Table 2) was studied by depicting the temporal profiles of volume average velocity of the melt exposed to magnetic fields scaled with volume average velocity at fully developed buoyancy.

impurities from the crucible walls directly towards melt free interface or on contrary for better complete mixing of the melt. The choice of the most appropriate magnetic field proves to be different in each specific case depending on the system and pure buoyancy configurations.

Figure 8: Snapshots of the velocity streamlines along (x,y)-plane at different heights of the melt stirred by CMF (case 5, Table 1).
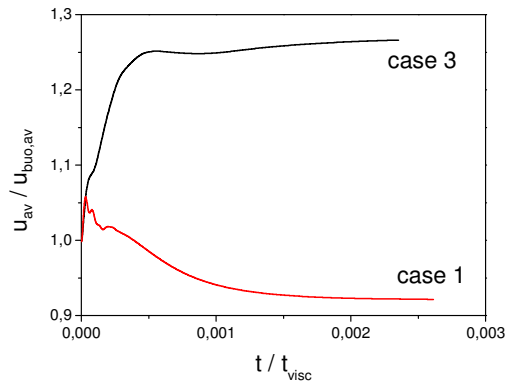
Figure 9: Time history of volume averaged velocities in a melt driven by downwards TMF (case 1, Table 1) and horizontal AMF (case 3, Table 1).
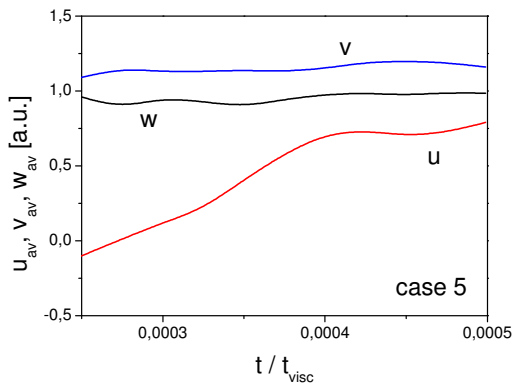
Figure 10: Time history of volume averaged velocity components (u, v, w) in a melt driven by CMF (case 5, Table 1).

CONCLUSIONS

Our simulations confirmed the inevitable role of 3D CFD simulations for understanding and further optimization of directional solidification processes of mc-Si. It has been shown that different sophisticated volume force distributions in addition to well established single-frequency TMFs can be achieved, such as double-frequency TMFs, AMFs or CMFs. Favorable flow distributions for enhanced process purity can be selected by using one of such or combined magnetic fields. The optimal F_L distribution represents an intrinsic property of each set-up, i.e. its size, design and selected process parameters.

ACKNOWLEDGEMENTS

REFERENCES

MONBERG, E. M.,"Bridgman and related growth techniques", in: *Handbook of Crystal Growth*, Vol. 2a, Basic Techniques, Ed. D.T.J. Hurle (North Holland, Amsterdam, 1994), 52-99.

RUDOLPH, P., (2008), *J. Crystal Growth*, **310,** 1298-1306.

ECKERT, S. et al., (2009), *Int. J. Cast Metals Res.*, **22**, 78-81.

DROPKA, N., MILLER, W., MENZEL, R., REHSE, U., (2010), *J. Crystal Growth,* **312**, 1407-1410.

NIKRITYUK, P.A., ECKERT, K., GRUNDMANN, R., (2010), *Met. Mat. Trans.* B, 41, **1**, 94-111.

NIKRITYUK, P.A., ECKERT, K., GRUNDMANN, R., (2006), *Acta Mechanica*, **186**, 17–35.

NIKRITYUK, P.A., UNGARISH, M., ECKERT, K., GRUNDMANN, R., (2005), *Physics of Fluids*, **17**, 067101.

WILLERS, B. et al., (2008), *Metall. Mater. Trans*. B, **39**, 304.

KOJIMA, S. et al., (1983), *Proc. 66th Int. Conf. Steelmaking, ISS-AIME*, Atlanta, USA, 127-131.

DROPKA, N. et al*., J. Crystal Growth,* doi: 10.1016/ j.jcrysgro.2010.10.094, in Press.

OTTINO, J. M., (1990), "Mixing, chaotic advection, and turbulence", *Annual Review of Fluid Mechanics,* **22**, 207-253.

DIMOTAKIS, P. E., (2005), "Turbulent mixing", *Annual Review of Fluid Mechanics,* **37**, 329-356.

DROPKA, N., FRANK-ROTSCH, Ch., REHSE, U., LANGE, P., RUDOLPH, P.,(2010), patent description DE 10 2010 041 061.

CISCATO, D., DUGHIERO, F., FORZAN, M., (2009), "A Comparison between resistance and induction DSS furnace for SoGSi production", *Proc.EPM 2009*, Dresden, Germany, October 19-23.

SPITZER, K.-H., REITER, G., SCHWERDTFEGER, K., (1996), *ISIJ International*, **36,** 487.

SPITZER, K.-H., (1999), *Prog. Crystal Growth and Charact*. , **38,** 39-58.

MITRIC, A., DUFFAR, Th., (2008), *J. Crystal Growth,* **310,** 1511–1517.

BÜLLESFELD, F., SAHR, U., MILLER, W., RUDOLPH, P., REHSE, U., DROPKA, N., patent description DE 10 2008 059 521.

8th International Conference on CFD in Oil & Gas, Metallurgical and Process Industries
SINTEF/NTNU, Trondheim Norway
21-23 June 2011

CFD11-86

MODELLING DISPERSION OF A HIGHLY LADEN POWDER JET

Stefan PUTTINGER[1] , Stefan PIRKER[1,2]*, Hugo Stocker[3] and Arno HABERMANN[3]

[1]Christian Doppler Laboratory on Particulate Flow Modelling, Linz, Austria

[2]Institute of Fluid Mechanics and Heat Transfer, Linz, Austria

[3]voestalpine Donawitz, Donawitz, Austria

* E-mail: stefan.pirker@jku.at

ABSTRACT

Latin Symbols

B

d

v

Sub/superscripts

p

INTRODUCTION

Keywords:

NOMENCLATURE

Greek Symbols

ρ

μ

μ

σ

Λ

τ

ρ_p $\qquad d_p$

μ_g

$$\tau_p = \rho_p d_p \big/ \mu_g$$

EXPERIMENTAL APPROACH

The pneumatic test facility
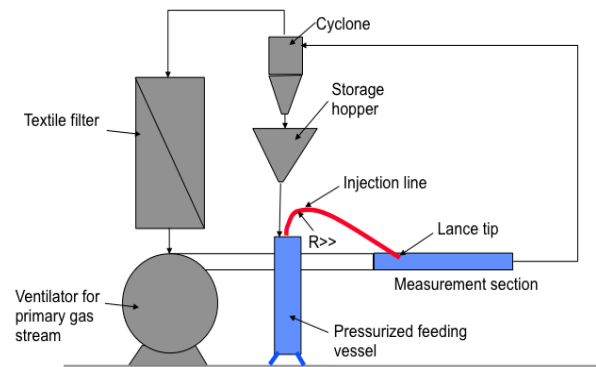
Figure 1:

Setup of the PCI experiments

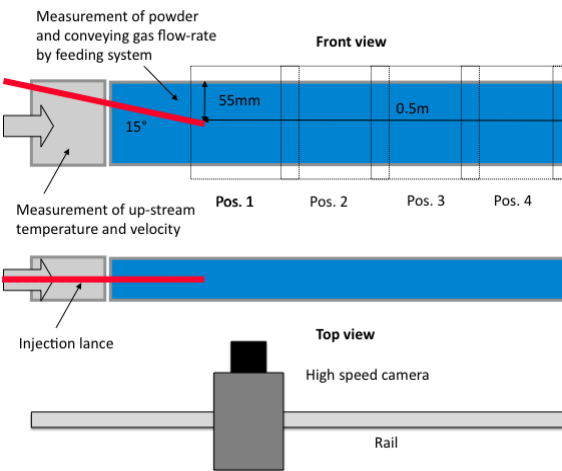$$d_p = \quad \mu m \qquad\qquad \rho_p = \qquad /$$

Figure 2:
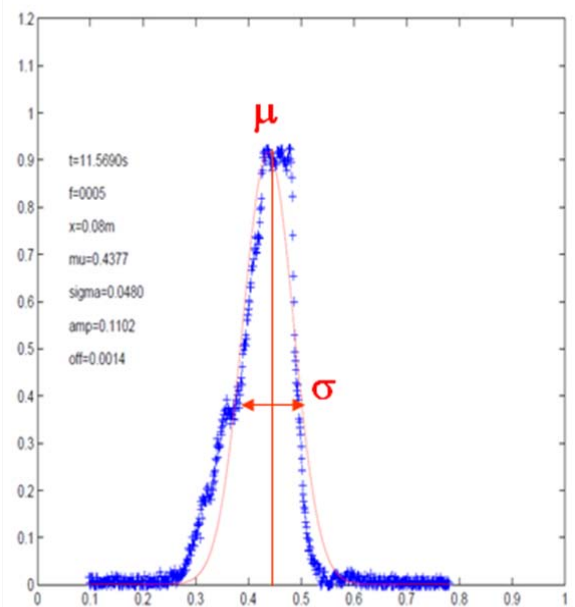
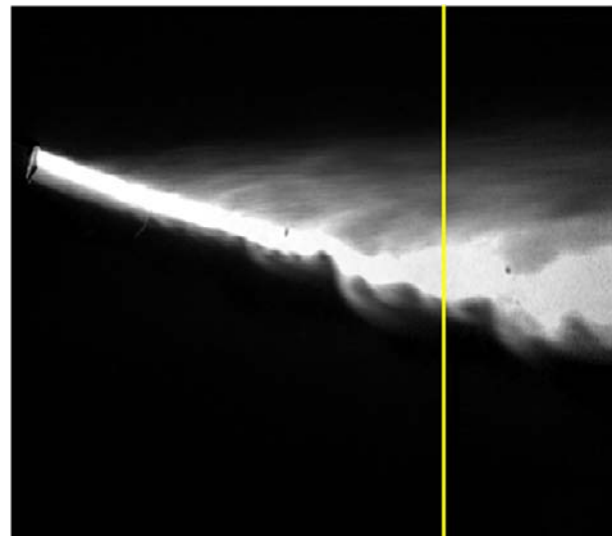**Data analysis and experimental results**
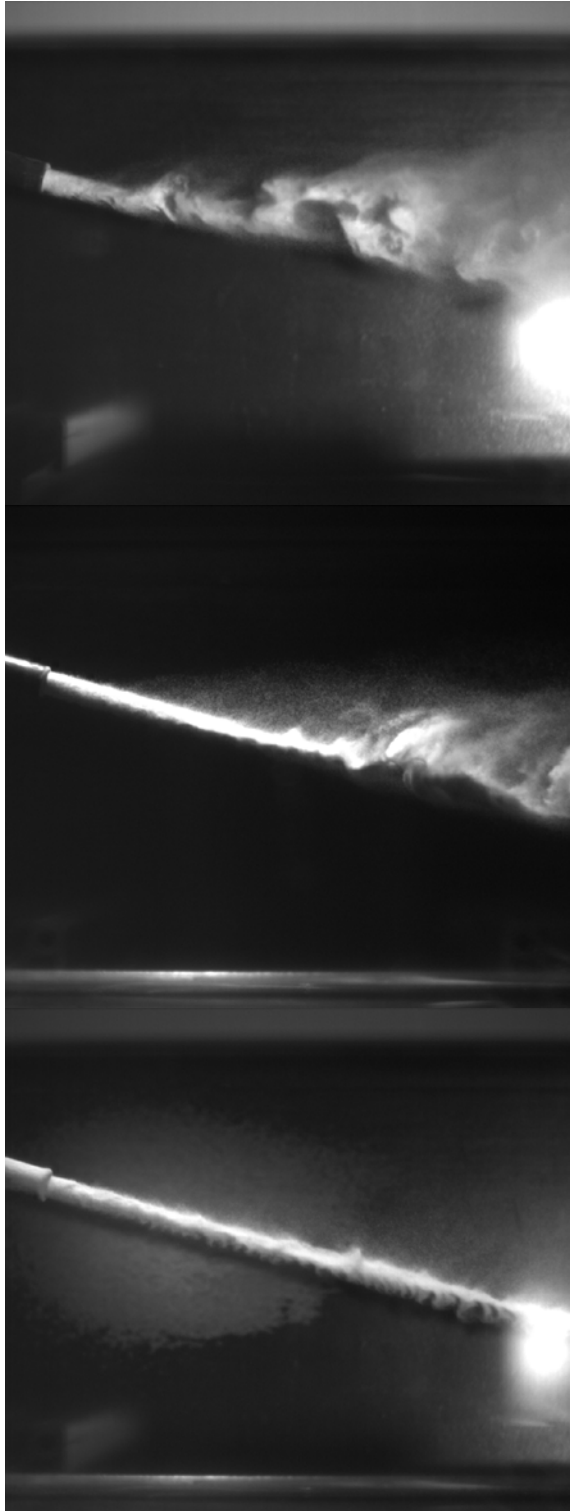
Figure 3

Figure 4:

A
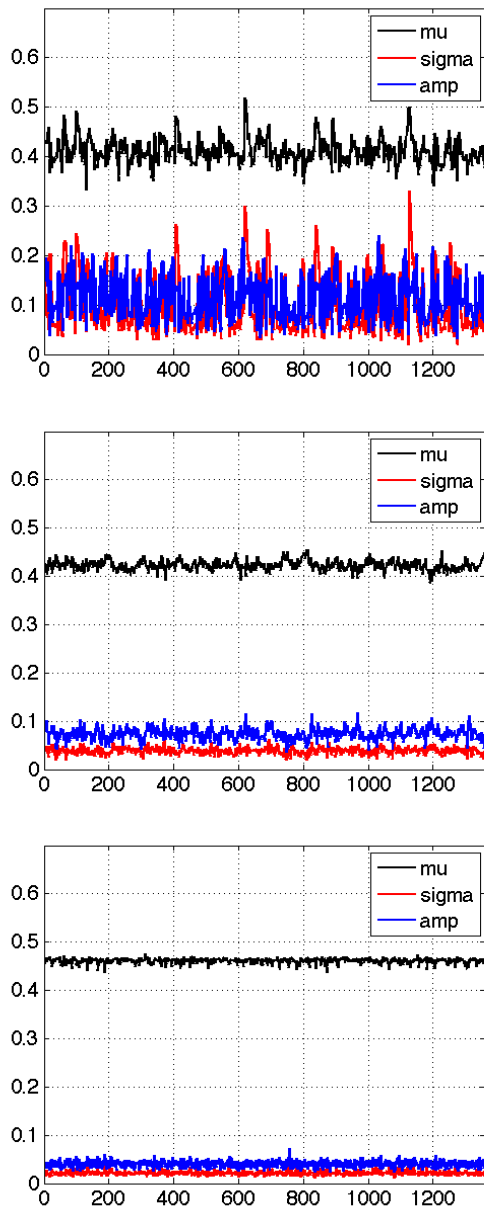
Figure 5
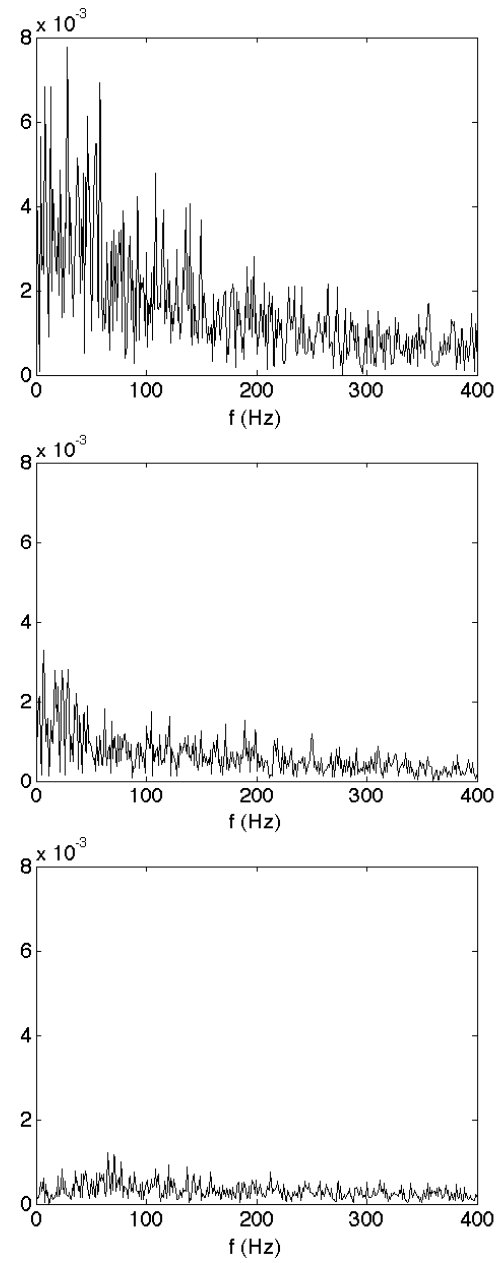
Figure 6:
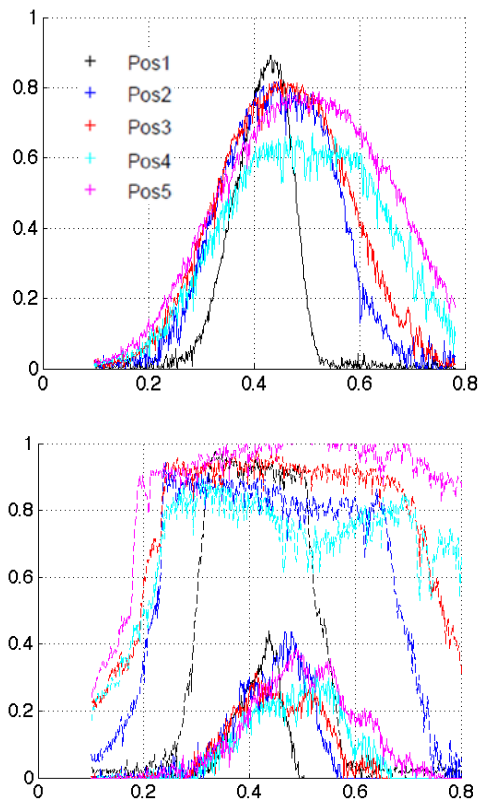
Numerical results

Figure 7:

NUMERICAL APPROACH
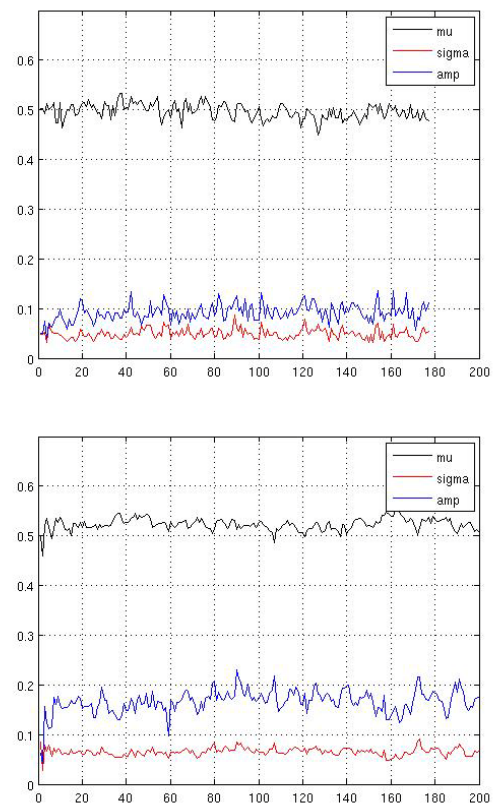
Figure 8:
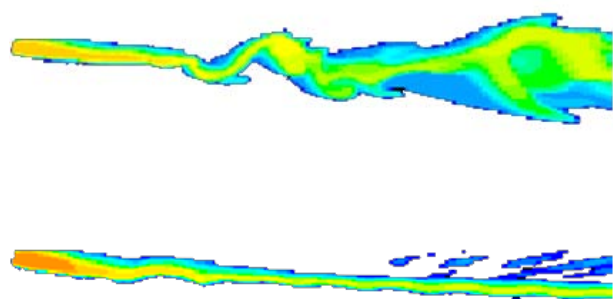
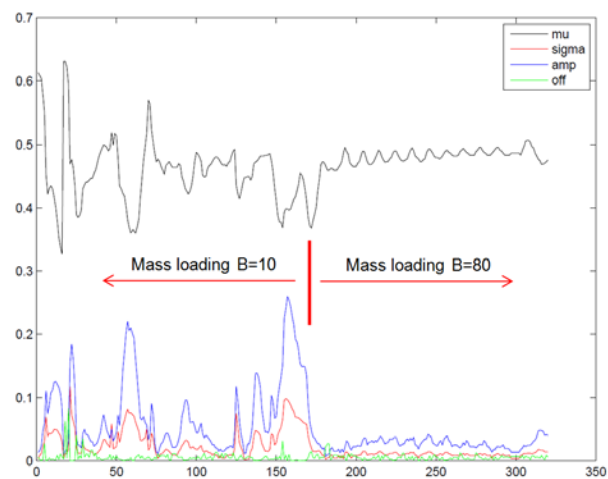**DISCUSSION OF NUMERICAL MODELLING**

Figure 9:

Figure 10:

•

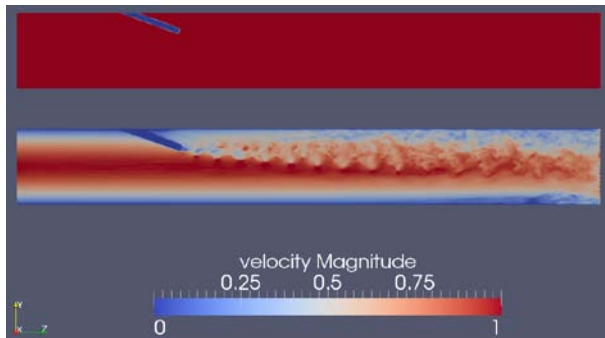**Figure 11:**

REFERENCES

Phys. Fluids A **3**

Int. J. Multiphase Flow **36**

ICMF conf. proc.

Powder Techn **204**

J. Fluid Eng. **100**

Month. Weather Rev. **164**

Flow Turb. Combust **82**

Powder Techn **125**

CONCLUSION

•

APPENDIX A

•

MODELLING FLOW INDUCED AOD-CONVERTER SLOSHING BY ANALYTICAL CONSIDERATIONS, NUMERICAL SIMULATION AND COLD WATER EXPERIMENTS

Stefan PIRKER[1,2,*] , Andreas AIGNER[2] and Gerald WIMMER[3]

[1] Christian-Doppler Laboratory on Particulate Flow Modelling, Johannes Kepler University, Linz, Austria

[2] Inst. of Fluid Dynamics and Heat Transfer, Johannes Kepler University, Linz, Austria

[3] Siemens VAI Metals Technologies GmbH, Linz, Austria

* E-mail: stefan.pirker@jku.at

ABSTRACT

Keywords:

NOMENCLATURE

Greek Symbols
α
β
Δ
$\dot{\gamma}$
μ
ω

φ
ρ
$\bullet$

Latin Symbols
$a\ b$
A
C_D
C_S
d
g
h
I
k
L
$m\ n$
M
N
$\mathbf{u}$
V

Sub/superscripts
b
d .
sg
sp .

INTRODUCTION
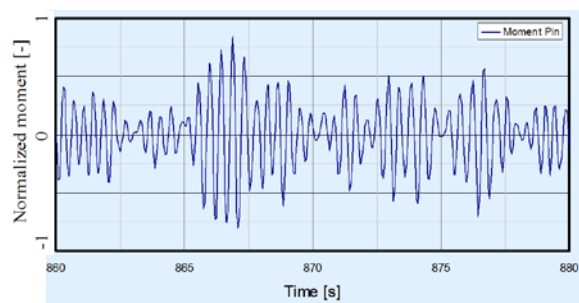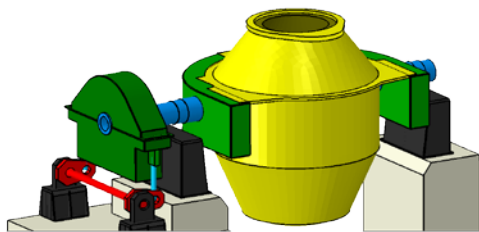
Figure 1:

EXPERIMENTAL FACILITY

Figure 2:

k L_{Sp}

$$d_n =$$

$$\dot{V}_g = \qquad - \qquad /s$$
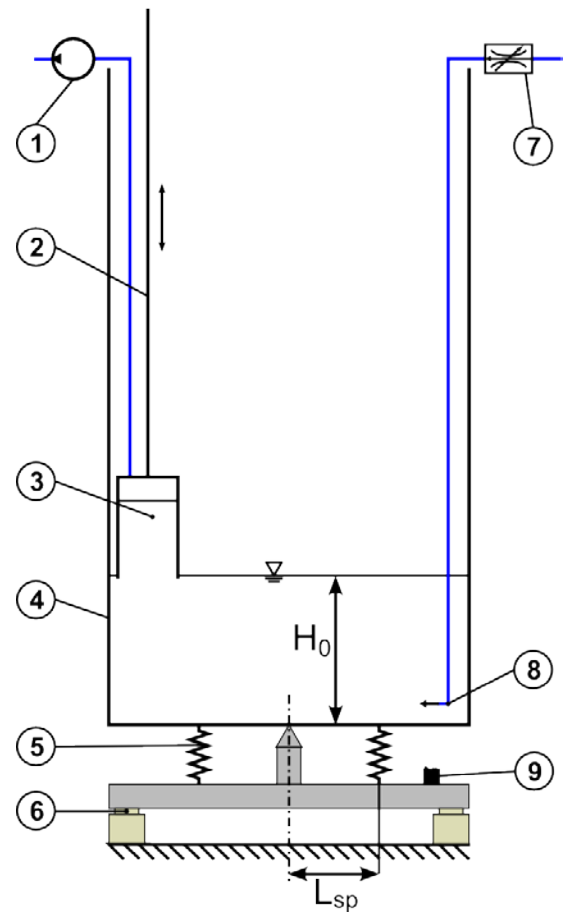
ANALYTIC CONSIDERATIONS AND NUMERICAL MODELLING

Analytical considerations

$$M_x = I_{xx}\,\frac{\varphi}{}$$

φ

M_x

$$M_x = F_{sp} L_{sp} = -\,k_{sp} L_{sp}\quad(\varphi)$$

φ

$$\phi = A \quad (\omega t) \quad (k(z+h))$$

ω

h

k

A

$\mathbf{u}$

$\mathbf{u}\text{-}\mathbf{u}_{gr}$ $\mathbf{u}_{gr}$

$k \qquad \omega$

$$\omega = gk \quad (kh)$$

g

$-z$

$$k = \pi \left(\frac{m}{a} + \frac{n}{b} \right)$$

$a \qquad b$

$m \qquad n$

$$\bullet = \mu \left(\nabla \mathbf{u} + \nabla \mathbf{u}^T \right)$$

μ

$$\mu = \sum_q \alpha_q \mu_q$$

Numerical modelling

μ

μ_{sg}

$$\mu_{sg} = \left(C_s \Delta_{gr} \right) \dot{\gamma}$$

Δ_{gr}

C_s

$$\frac{\partial \alpha_q \rho_q}{\partial t} + \nabla \cdot \left(\alpha_q \rho_q \mathbf{u} \right) =$$

$$C_s = \qquad \dot{\gamma}$$

α_q

ρ_q

$\mathbf{u}$

$$\frac{\partial (\rho \mathbf{u})}{\partial t} + \nabla \cdot (\rho \mathbf{uu}) = -\nabla p + \nabla \cdot \quad + \rho \mathbf{g}$$

$$\rho = \sum_q \alpha_q \rho_q$$

p $\mathbf{g}$

$\bullet$

$$L_g = -\alpha_l \bar{d}_b \frac{\rho}{\rho_l} \quad L_l = -\alpha_b \bar{d}_d \frac{\rho}{\rho_g} \quad L = \beta L_g + (-\beta) L_l$$

$\bar{d}_b \qquad \bar{d}_d$

β

$$\beta = \left(\quad \left(\left(\frac{\quad}{\quad} - \alpha_b \right) \right) \right)$$

$$\alpha_b \qquad\qquad \alpha_g$$

$$\alpha_b$$

$$C_D$$

$$C_D = \beta C_D \quad + \left(\quad - \beta \right) C_D$$

$$F_{drag} = C_D \rho \frac{\alpha_l \alpha_b}{L} \left| \mathbf{u\text{-}u}_b \right| \left(\mathbf{u\text{-}u}_b \right)$$

Dam break induced sloshing in fixed tank

$$F_{drag} V_c = \sum_i \frac{m_{b\,i}}{N_{b\,i}} f_{drag\,i}$$

$$V_c \qquad\qquad\qquad N_{b\,i}$$

$$m_{b\,i}$$

RESULTS

Gas injection induced sloshing in fixed tank
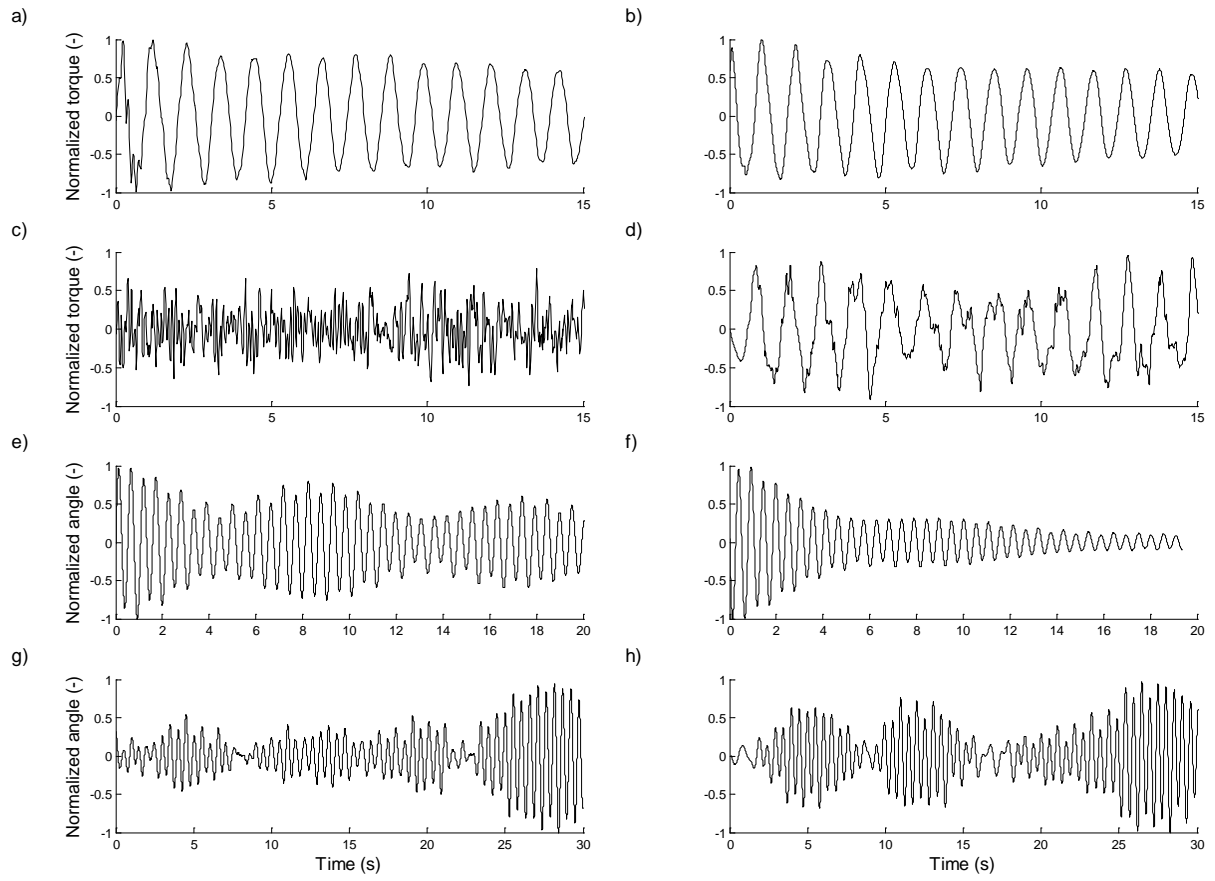
Figure 3:

Initial tilting induced sloshing in a spring mounted tank
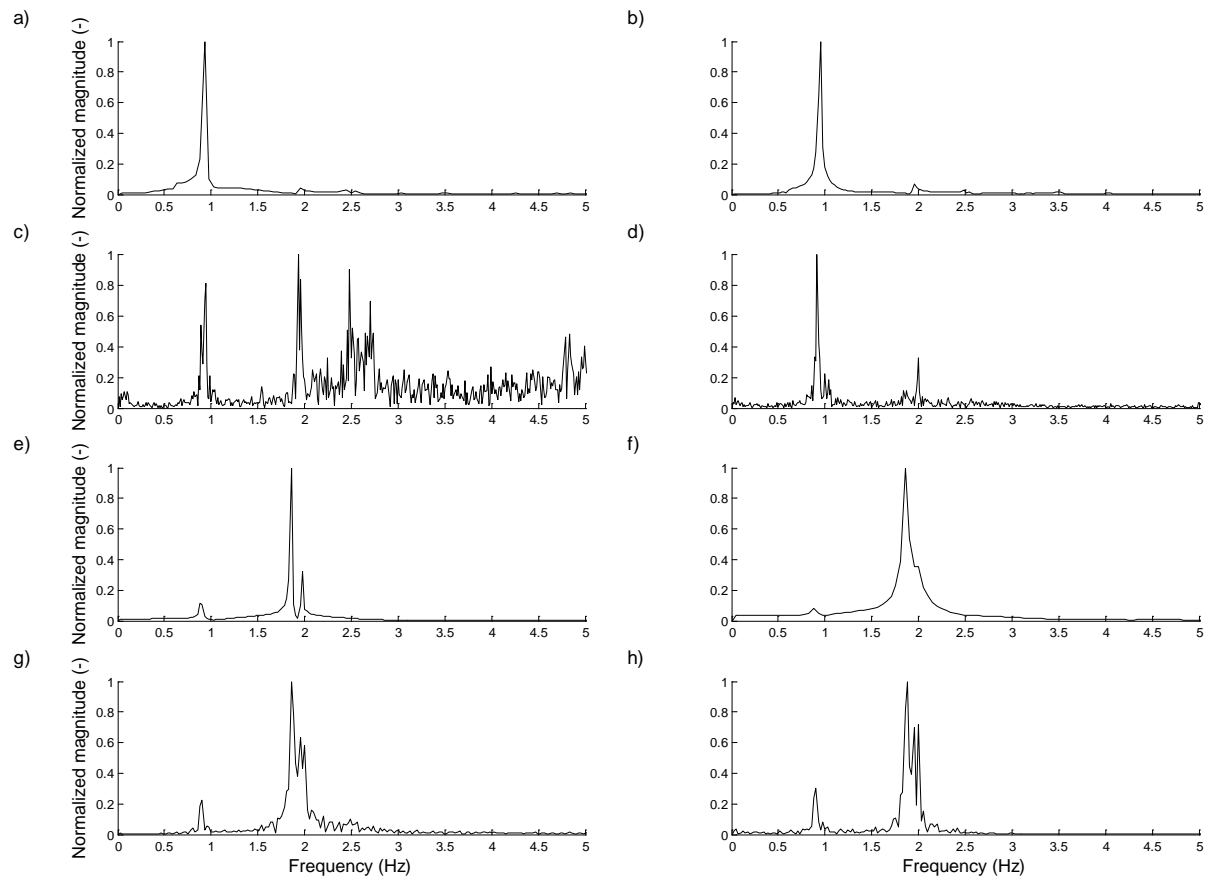
Figure 4:

Gas injection induced sloshing in a spring mounted tank

CONCLUSION
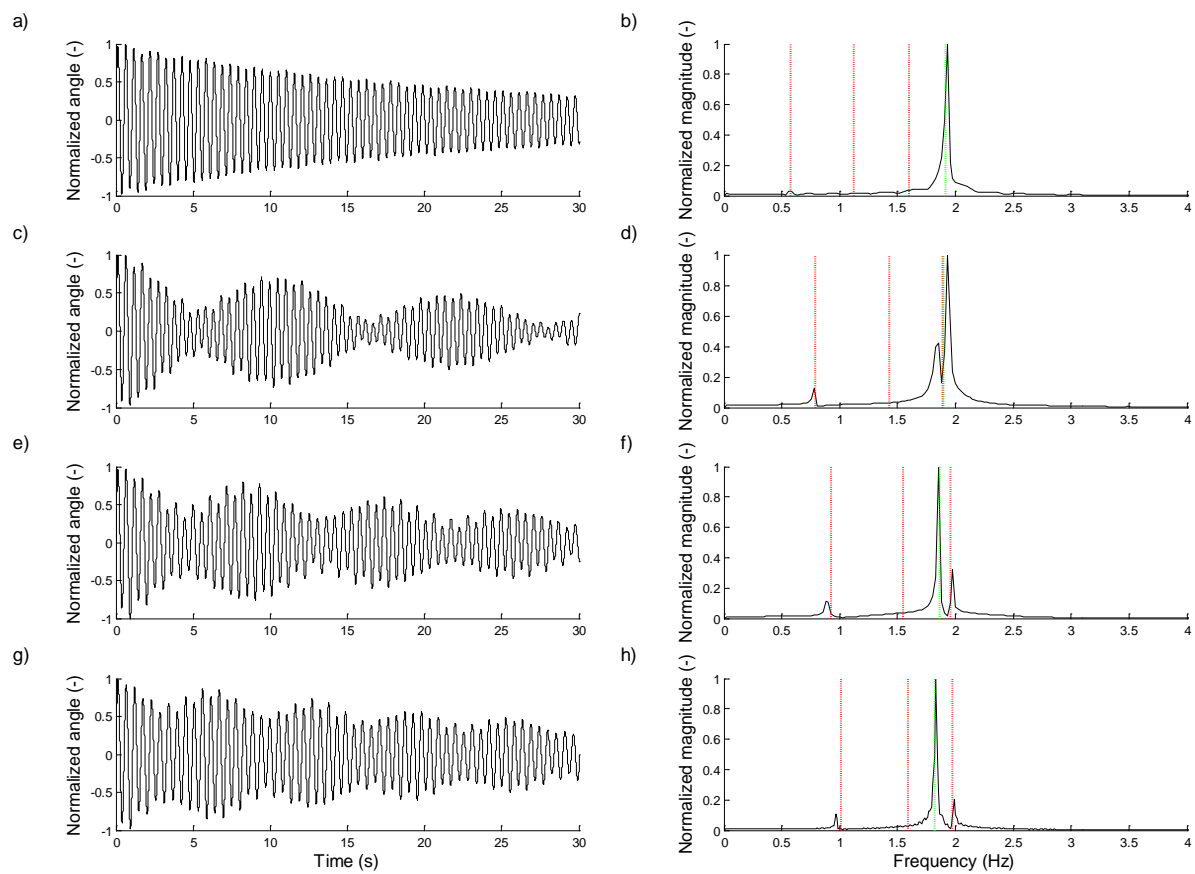
Figure 5:

REFERENCES

INFLUENCE OF POST COMBUSTION
ON CHARACTERISTICS OF OXYGEN JET IN BOF

Akihide KAIZAWA*, Naoto SASAKI, Takeo INOMOTO, Yuji OGAWA

Nippon Steel Corporation Environment & Process Technology Center, 20-1 Shintomi, Futtsu, Chiba, JAPAN

* E-mail: kaizawa.akihide@nsc.co.jp

ABSTRACT

j j
R
P

INTRODUCTION

Keywords:

NOMENCLATURE

Greek Symbols
ε
v
ρ

Latin Symbols
d
k
L_c
L_{cn}
M
P_d
P_S
R
r
T
v
x
Y

Sub/superscripts
i i

COMBUSTION EXPERIMENT
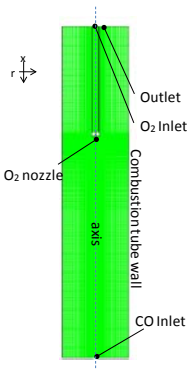
Figure 2:

Table 1:

	Turbulence	Combustion	Radiation	Gas density / Compressibility
	ε			
	ε			
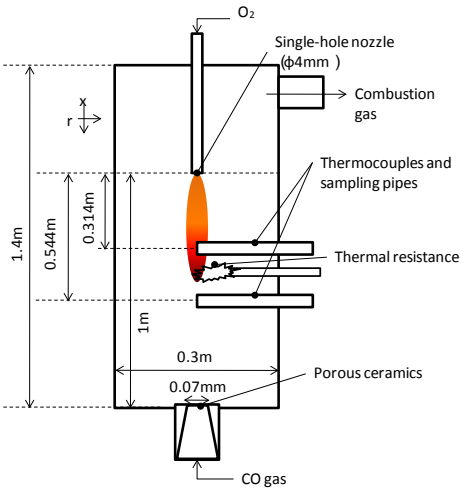
Figure 1:

CFD SIMULATION

i r $R_{i,r}$

$$R_{i\,r}^{\ R} \;=\; \nu_{i\,r}^{\ R} M_i \rho \frac{\varepsilon}{k} \min_{R}\left(\frac{Y_R}{\nu_{R\,r} M_R} \right)$$

$$R_{i\,r}^{\ P} \;=\; \nu_{i\,r}^{\ P} M_i \rho \frac{\varepsilon}{k}\left(\frac{\sum_P Y_P}{\sum_j^N \nu_{j\,r} M_j} \right)$$

Y_P P

Y_R R

k ε

k ε

RESULTS AND DISCUSSION

Comparison of calculations and experiments

Table 2

Parameter	Value
	^{o}C

Table 3

Properties	Value
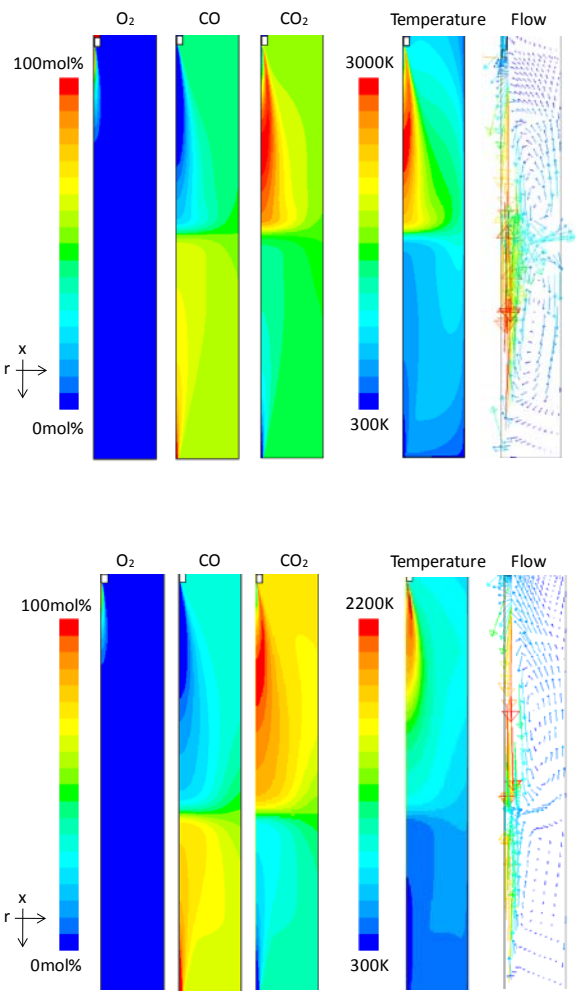
Figure 3:

Figure 4:

$k/\varepsilon,$

Figure 5:

$$CO + -O \rightarrow CO$$
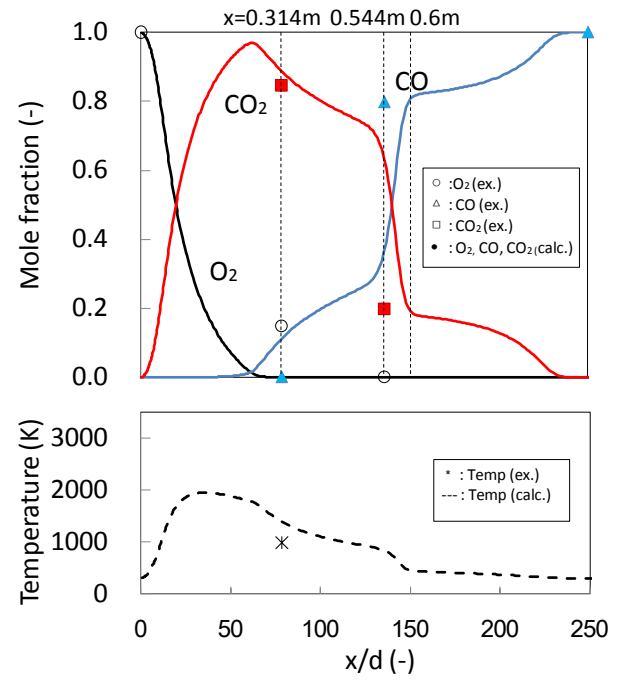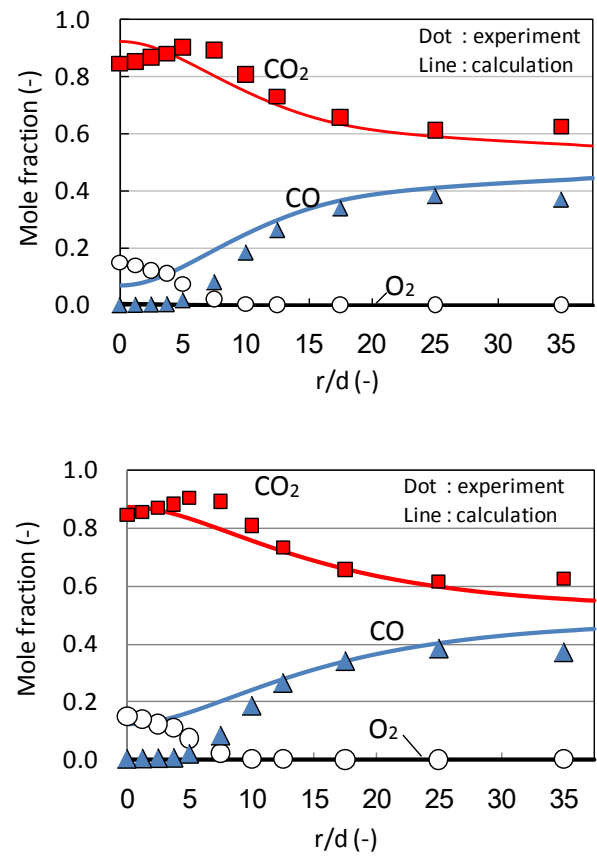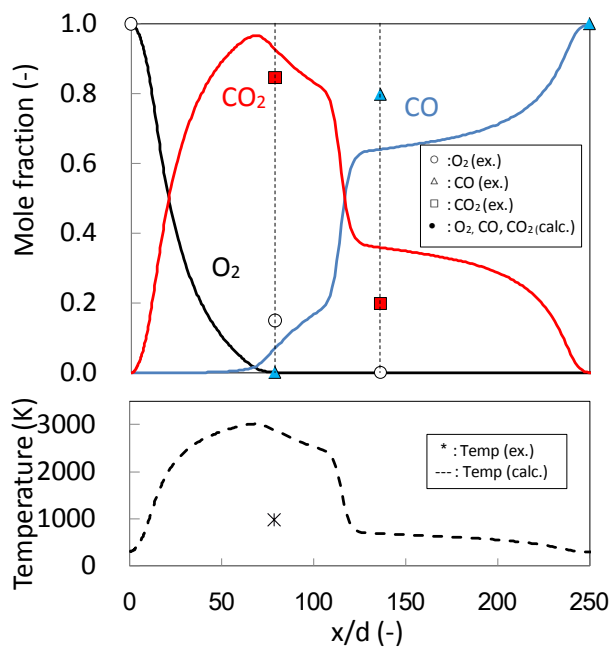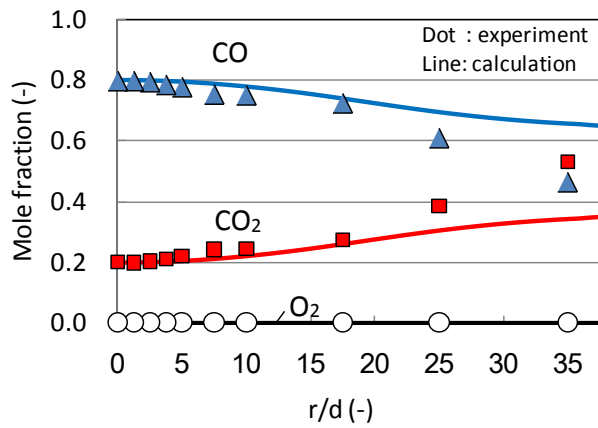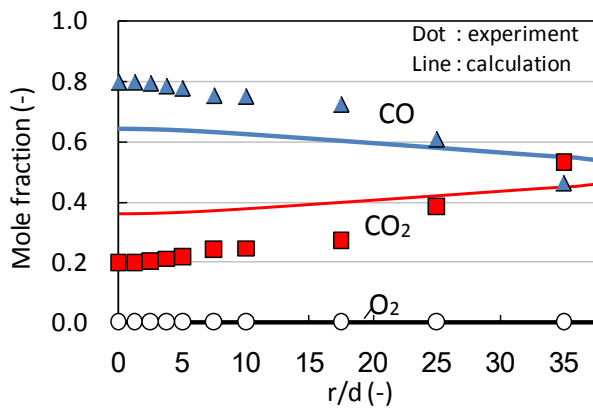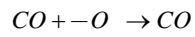
Figure 7

Figure 6:

The characteristics of the top blown jet in the combustion field

Figure 8:

Figure 9:

Figure 10:

ρ
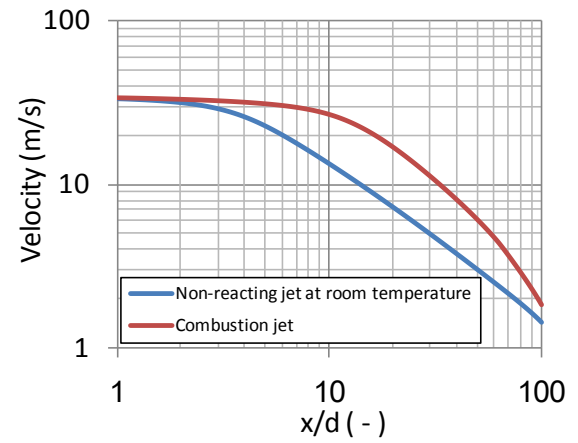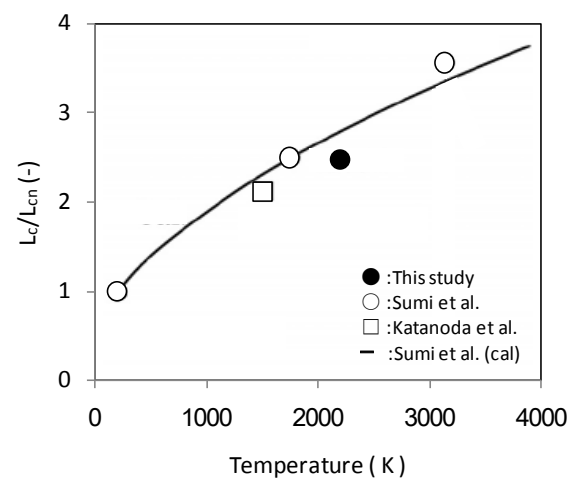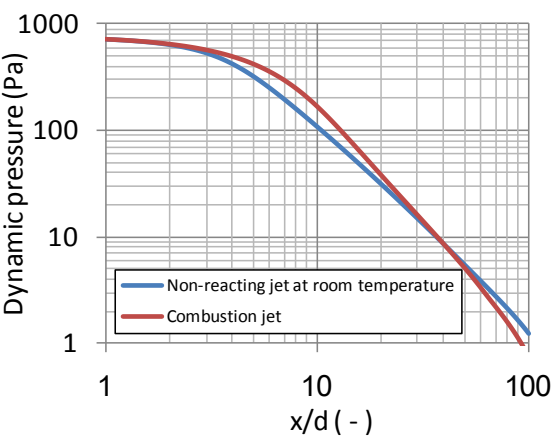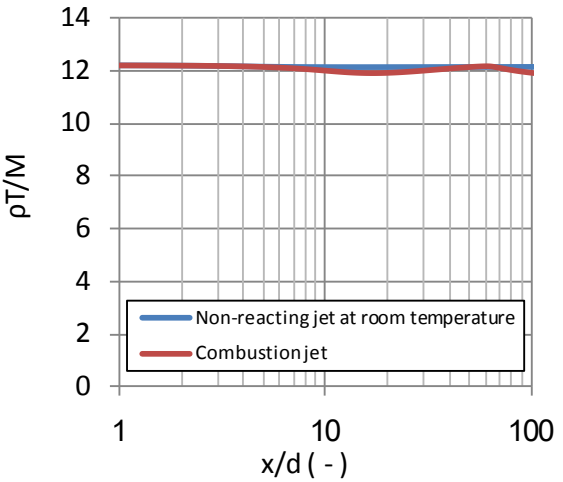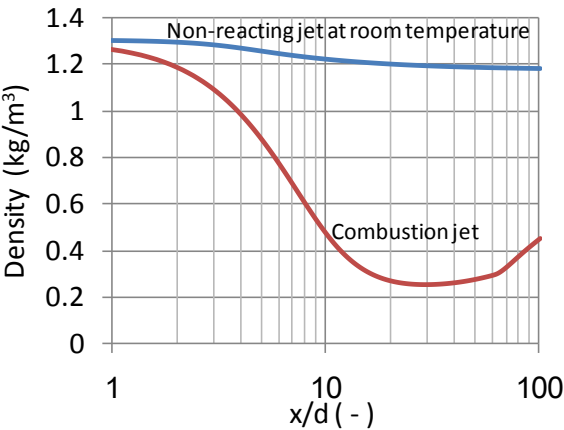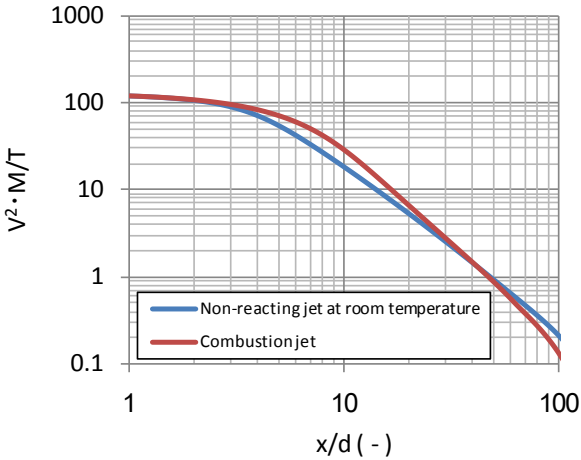
Figure 11: ρ

Figure 12:

$$P_S = \frac{\rho R T}{M} = const$$

$$P_d = -\rho v = -\rho \cdot \frac{T}{M} \cdot v \cdot \frac{M}{T}$$

ρ $v^2 M/T$

ρ

$v^2 M/T$

Table 4

	Velocity, v			

CONCLUSION

23

Scottish Academic Press

REFERENCES

Proc. of the Seetharaman-Seminar

Tetsu-to-Hagané **58**

Chem. Eng. Sci. **21**

Tetsu-to-Hagané **76**

Tetsu-to-Hagané **74**

46

A MODEL OF PARTICLE DEPOSITION ON A VERTICAL WALL FOR THE PARTICLE-WALL STICKING PROBABILITY LOWER THAN ONE

Dmitry ESKIN*, John RATULOWSKI and Kamran AKBARZADEH

SCHLUMBERGER DBR Technology Center, 9450-17 Ave., Edmonton, AB T6N 1M9, CANADA

* E-mail: deskin@slb.com

ABSTRACT

Keywords:

NOMENCLATURE

Greek Symbols

$\bullet$
ε
ε_0
κ
μ_f
ν_f
ρ
τ_I
τ
τ_w
υ
υ'
ξ

Latin Symbols

c
c_D
c_0
B
c_w
D
d_p
F_{af}
F_B
F_d
F_E
F_L
F_{pG}
F_{tb}
F_{vm}
G
g
J
k_B
m_p
$p^\bullet$
q
q_{max}
R
r_p
Re
s
Sc
t
T
T_L
T_p
V
V_{dep}
V_E
u_*
x
y
W_p

Sub/superscripts

B
f
p
T
$+$

INTRODUCTION

τ

$$V_{dep} = -\left(D_{pt} + D_B\right)\frac{dc}{dy} + cV_p^y$$

c

$D_B = k_B T / 3\pi\mu_f d_p$

$k_B = 1.3806504 \ 10^{23} \ J/K$

T

D_{pt}

y

V_p^y

$$\tau = \frac{\rho_p d_p^2}{18\mu_f}$$

d_p

μ_f

ρ_p

τ

MODEL DESCRIPTION

$$V_p$$

$$m_p \frac{dV_p^x}{dt} = m_p \left(\frac{\partial V_p^x}{\partial x} V_p^x + \frac{\partial V_p^x}{\partial y} V_p^y \right) =$$

$$= m_p V_p^y \frac{dV_p^x}{dy} = F_{af}^x + F_d^x + F_{vm}^x + F_B^x + F_{pG}^x + G^x + B^x$$

$$F_{af}$$

$$F_B$$

$$F_d \qquad F_{pG}$$

$$F_{vm} \qquad\qquad G \qquad\qquad m_p$$

$$V_{dep} = \frac{1}{2} \upsilon' p c_w$$

$$m_p \frac{dV_p^y}{dt} = m_p \left(\frac{\partial V_p^y}{\partial x} V_p^x + \frac{\partial V_p^y}{\partial y} V_p^y \right) =$$

$$c_w$$

$$p \qquad\qquad\qquad \upsilon'$$

$$= m_p V_p^y \frac{dV_p^y}{dy} = F_d^y + F_{tb}^y + F_L^y + F_{vm}^y + F_B^y + F_E^y$$

$$F_{tb} \qquad\qquad\qquad F_L$$

$$F_E$$

$$F_{pG}$$

$$F_B$$

$$F_{af}$$

$$\kappa V_p^y \frac{dV_p^x}{dy} = -V_p^y \frac{dV_f^x}{dy} + \frac{\left(V_f^x - V_p^x\right)}{\tau_I} + \left(\ -\frac{}{s}\right)g^x$$

$$\kappa V_p^y \frac{dV_p^y}{dy} = -\frac{V_p^y}{\tau_I} - \frac{d\overline{V'^{y2}_p}}{dy} +$$

$$\frac{0.171 d_p}{\tau}\left(\frac{1}{\nu_f}\left|\frac{dV_f^x}{dy}\right|\right)^{\frac{1}{2}}\left(V_f^x - V_p^x\right) - \frac{V_E}{\tau}$$

$$g^x$$
$$s = \rho_p/\rho_f$$

$$\rho_f,\ \rho_p$$
$$V'^y_p$$

$$V_E$$
$$\kappa = 1 + 1/2s$$
$$\tau_I = \tau\ 24/(Re\ c_D)$$
$$Re = |V_f - V_p| d_p/\nu_f$$
$$c_D$$

$$V_{dep}^+ = -\left(D_{pt}^+ + D_B^+\right)\frac{dc^+}{dy^+} + c^+ V_p^{y+}$$

$$V_{dep}^+ = V_{dep}/(u_* c_0)$$
$$V_p^{y+} = V_p^y/u_*$$

$$u_* = (\tau_w/\rho_f)^{1/2}$$
$$\tau_w$$

$$c^+ = c/c_0$$
$$c_0$$
$$y^+ = y/\delta$$
$$\delta = \nu_f/u_*$$

$$\kappa V_p^{y+} \frac{dV_p^{x+}}{dy^+} = \frac{1}{s}V_p^{y+}\frac{dV_f^{x+}}{dy} + \frac{\left(V_f^{x+} - V_p^{x+}\right)}{\tau_I} + \left(1 - \frac{1}{s}\right)g^{x+}$$

$$\kappa V_p^{y+}\frac{dV_p^{y+}}{dy^+} =$$

$$-\frac{V_p^{y+}}{\tau_I^+} - \frac{d\overline{V'^{y+2}_p}}{dy^+} + \frac{0.171 d_p^+}{\tau^+}\left|\frac{dV_f^{x+}}{dy^+}\right|^{\frac{1}{2}}\left(V_f^{x+} - V_p^{x+}\right) - \frac{V_E^+}{\tau^+}$$

$$g^{x+} = g^x \nu_f/u_*^3$$

$$\tau_I^+ = \tau_I\ u_*^2/\nu_f$$
$$,\ d_p^+ = d_p/\delta$$

$$V_f^{x+}(y^+),$$
$$D_{pt}^+(y^+)$$

$$\overline{V'^{y+2}_p}(y^+)$$

$$\varepsilon_t^+(y^+)$$
$$\sqrt{\overline{V'^{y+}_f}(y^+)}$$

$$dV_f^{x+}/dy^+$$

$$\frac{V_E}{\tau} = \frac{1}{\tau}\frac{q^2}{48\pi^2 \varepsilon_0 \mu_f d_p y^2}$$

$$q$$
$$\varepsilon_0 \approx 8.85\ 10^{-12}$$

$$\xi$$

$$q = \xi \cdot q_{max}$$

$$q_{max} = 500 \times \left(1 \times 10^{-19}\right)\left(10^6 \times d_p\right)$$

$$\frac{dV_f^{x+}}{dy^+} = \frac{}{+\varepsilon_t^+}$$

$$D_{pt}^+ = \varepsilon_t^+/Sc_{pt}$$
$$Sc_{pt}$$

$$Sc_t\ \varepsilon_t^+/D_t^+\quad D_t^+$$

$$Sc_t$$

$$Sc_t = 0.8$$

$$Sc_t = 0.87$$

$$Sc_{pt} \quad Sc_{t}.$$

$$Sc_{pt}$$

$$\overline{V'_{p}^{y+}} = \overline{V'_{f}^{y+}} \frac{}{+ \quad . \quad \left(\tau_{I}^{+}/T_{L}^{+}\right)}$$

$$T_{L}^{+} = \varepsilon_{t}^{+}/\overline{V'_{f}}^{y+2}$$

Figure1:

$$\varepsilon_{pt}^{+} = T_{p}^{+}\overline{V'_{p}}^{y+2}$$

$$T_{p}^{+}$$

$$T_{p}^{+}$$

$$T_{p}^{+} = T_{L}^{+} + \tau_{I}^{+} = T_{L}^{+}\left(+ \tau_{I}^{+}/T_{L}^{+}\right)$$

Boundary Conditions

$$\frac{\varepsilon_{pt}^{+}}{\varepsilon_{t}^{+}} = \frac{+ \tau_{I}^{+}/T_{L}^{+}}{+ \quad . \quad \tau_{I}^{+}/T_{L}^{+}}$$

$$J^{+} = \int_{}^{R^{+}} c^{+}\left(r^{+}\right)V_{p}^{x+}\left(r^{+}\right) \pi r^{+} dr^{+} = const$$

$$r^{+}$$

$$R^{+}$$

$$Sc_{pt} = Sc_{t}\frac{\varepsilon_{t}^{+}}{\varepsilon_{pt}^{+}} = Sc_{t}\frac{1 + 0.7\,\tau_{I}^{+}/T_{L}^{+}}{1 + \tau_{I}^{+}/T_{L}^{+}}$$

$$r_{p}$$

$$V_{p}^{y+}\left(R^{+}\right) =$$
$$V_{p}^{x+}\left(R^{+}\right) = V_{f}^{x+}\left(R^{+}\right) + \tau_{I}^{+}\left(R^{+}\right)g^{x+}$$

$$p.$$

$$V_{p}^{+}$$

$$V_f^{x+} - V_p^{x+} = \left(-\left(-\frac{}{s} \right) g^{x+} + \left(-\frac{}{s} \right) V_p^{y+} \frac{dV_f^{x+}}{dy^+} \right) \tau^+$$

$$V_p^{y+} = \cfrac{\left(-\overline{\cfrac{dV'_p^{y+}}{dy^+}} - \quad . \quad d_p^+ \overline{\left| \cfrac{dV_f^{x+}}{dy^+} \right|} \left(-\frac{}{s} \right) g^{x+} \right) \tau^+ - V_E^+}{- \quad . \quad \left(-\frac{}{s} \right) d_p^+ \overline{\left| \cfrac{dV_f^{x+}}{dy^+} \right|} \cfrac{dV_f^{x+}}{dy^+} \tau^+}$$

$$V_p^{y+}(r_p^{+})$$

$$V_{dep}^+(r_p^+) = p \frac{c^+(r_p^+) V_p^{y+}(r_p^+)}{} \left[\begin{array}{c} + erf\left(\cfrac{V_p^{y+}(r_p^+)}{\upsilon_m^+(r_p^+)} \right) + \\ \cfrac{}{\pi \cdot} \cfrac{\upsilon_m^+(r_p^+)}{V_p^{y+}(r_p^+)} exp\left(-\cfrac{V_p^{y+}(r_p^+)}{\upsilon_m^+(r_p^+)} \right) \end{array} \right]$$

$$\upsilon_m^+ = \upsilon_B^+ + \upsilon_{pt}^+(r_p^+)$$
$$\upsilon_B^+$$

$$\upsilon_{pt}^+(r_p^+)$$

$$V_{dep}^+ = -\left(D_{pt}^+ + D_b^+ \right) \frac{dc^+}{dy^+} + c^+ V_p^{y+} \Big|_{r_p^+}$$

$$V_{dep}^+$$

$$\upsilon_B^+ \qquad \upsilon_{pt}^+(r_p^+)$$

$$V_{dep}^{+} = \frac{1}{2} \, pc(r_p^{+})\left(\upsilon_B^{+} + \upsilon_{pt}^{+}(r_p^{+})\right)$$

$y^{+}{=}30$

Figure 2

$c^{+}(30){=}1$

$V_p^{\,y+}{=}0$

ε_t^{+}

$$V_{dep}^{+} = - \, pc^{+}(r_p^{+})\left[\upsilon_B^{+} + \upsilon_{pt}^{+}(r_p^{+})\right]$$

$$c^{+}(r_p^{+}) = \frac{}{+ - p \, Sc_t\left[\upsilon_B(r_p^{+}) + \upsilon_{pt}(r_p^{+})\right] \times \left[\quad . \quad + \quad . \quad (\psi(\ ) - \psi(r_p^{+}))\right]}$$

$$\psi(\chi) = \frac{1}{6b^{2}} \ln\left(\frac{\chi + b}{\chi^{2} - b\chi + b^{2}}\right) + \frac{1}{b^{2}\sqrt{3}} \, arctg\left(\frac{2\chi - b}{b\sqrt{3}}\right)$$

$$\chi = y^{+}/14.5 \quad b = \left(D_B^{+} \, Sc_t\right)^{1/3}$$

$$Sc_t{=}1$$

$D{=}12.7 \; mm$

$\bullet_f{=}1.26 \; kg/m^{3}$

$\mu_f{=}1.1983 \; 10^{-5} \; Pa \; s.$

$p{=}1$

$d_p{=}1.4{-}21 \; \mu m$

$s{=}770$

COMPUTATIONAL EXAMPLES AND DISCUSSION

$p{<}1$

$Re{=}10^{4} \qquad 5{\times}10^{4}$

$Sc_t{=}0.85$

$p{=}1$

$p{<}1$

$Re{=}10^{4}$

$Re{=}5{\times}10^{4}.$

τ_I^{+}

$c_D{=}(24/Re)(1{+}0.15Re^{0.687})$

$d_p \leq 9.5 \mu m$

$log_{10}\tau^+ \leq 0.97$

V_p^{y+}

$\xi=0.05$

$log_{10}\tau^+ = [-3; 3]$.

Figure 3

Figure 4

$c^+(r_p^+)$

p
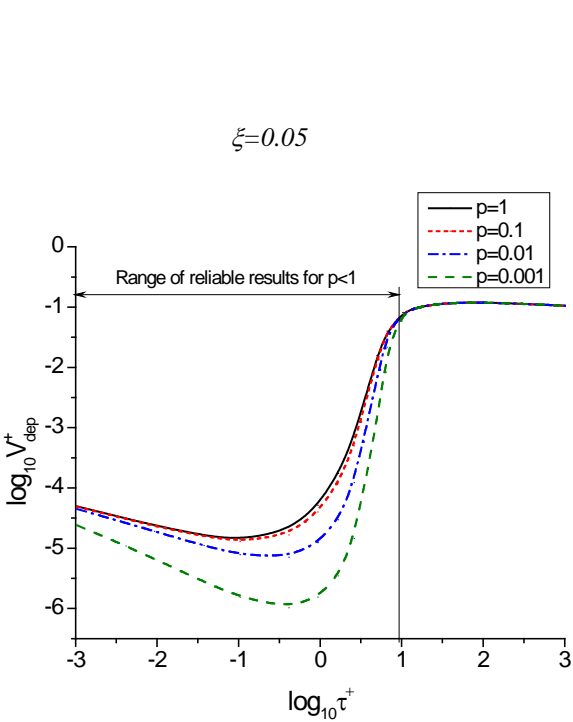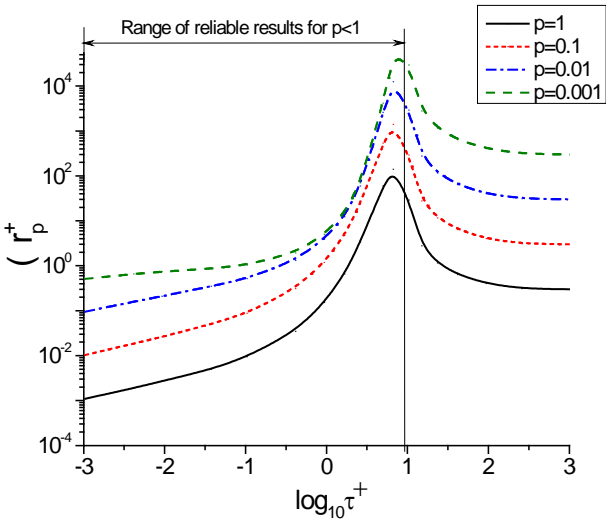
V_{dep}^+

r_p^+

$c^+(r_p^+)=0)$

V_p^{y+}.

$(p=1)$.

$p=1$

$p=0.1, 0.01, 0.001$.

p

$(dc(r_p^+)/dr^+)$

CONCLUSION

ACKNOWLEDGEMENT

$(log_{10}\tau^+=0.477, 0.699 \text{ and } 1.0)$

REFERENCES

Nucl. Sci. Eng., **40**

$(log_{10}\tau^+=0.97),$

Int. J. Multiph. Flow **17**

Phys. Fluids **6**

The Canadian Journal of Chemical Engineering

$log_{10}\tau^+\approx 0.75$

Ind. Eng. Chem **49**

Annual Review of Fluid Mechanics **40**

International Journal of Multiphase Flow **17**

Chem. Eng. Sci. **17**

Proceedings of the 7th Int. Conference on CFD in the Minerals and Process Industries

Int. J. Multiphase Flow **15**

J. Chem. Eng. Jpn. **5**

J . Fluid Mech **181**

Industrial and Eng. Chemistry **45**

. Aerosol Sci. **5**

J. Fluid Mech **468**

Int. J. Multiph. Flow **24**

Int. J. Multiphase Flow **12**

J. Colloid Interface Sci. **113**

J. Fluid Mech. **340**

Appendix A

Inertial term caused by the fluid acceleration

$$F_{af} = \rho_f W_p \frac{dV_f}{dt}$$

W_p V_f

F_{af}

$$F_{af} = \rho_f W_p \frac{dV_f^x}{dt} = \rho_f W_p V_p^y \frac{dV_f^x}{dy}$$

Appendix B

B.1 Brownian Mechanism

$$\upsilon_B = \left(\frac{2}{3}\langle \upsilon_B^2 \rangle\right)^{\frac{1}{2}} = \left(\frac{2k_B T}{m_p}\right)^{\frac{1}{2}}$$

k_B
T $\langle \upsilon_B^2 \rangle = 3k_B T / m_p$

$$\upsilon_B^+ = \upsilon_B / u_*.$$

B.2. Turbulence mechanism

$$\frac{\upsilon_{pt}}{\upsilon_{ft}} = \frac{1}{\sqrt{1 + 0.7\left(\tau_I^+ / T_L^+\right)}}$$

$$\upsilon_{ft} = \sqrt{2 \overline{V_f'^2} / 3}$$

$$\overline{V'^2_f} = 3\overline{V'^{y2}_f}$$

$$\overline{V'^{y2}_f}$$

$$\sqrt{\overline{V'^{y+2}_f}} = \sqrt{\overline{V'^{y2}_f}} \Big/ u_*$$

$$\upsilon^+_{pt} = \frac{\sqrt{2} \cdot \sqrt{\overline{V'^{y+2}_f}}}{\sqrt{1 + 0.7\left(\tau^+_I / T^+_L\right)}}$$

8th International Conference on CFD in Oil & Gas, Metallurgical and Process Industries
SINTEF/NTNU, Trondheim NORWAY
21-23 June 2011

CFD11-92

LARGE EDDY SIMULATION OF PARTICLE-LADEN SWIRLING FLOW WITH A PRESUMED FUNCTION METHOD OF MOMENTS

Patrick DEMS[1][*], **João N.E. CARNEIRO**[2], **Wolfgang POLIFKE**[3]

[1]Lehrstuhl für Thermodynamik, TU-München, Boltzmannstr. 15, 85748 Garching, Germany

[2]Instituto SINTEF do Brasil, Rua Lauro Müller 116/2201, 22290-160, Rio de Janeiro, Brazil

[3]Lehrstuhl für Thermodynamik, TU-München, Boltzmannstr. 15, 85748 Garching, Germany

[*] E-mail: dems@td.mw.tum.de

ABSTRACT

In the present paper a Large Eddy Simulation approach is presented for Eulerian-Eulerian polydisperse two-phase flows. It is based on a moments model, considering the size dependency of particle motion and phase interaction forces by transporting the moments of the particle size distribution with their individual moment transport velocities. The filtered gas phase equations were closed using standard subgrid-scale models. Filtering of the dispersed phase equations was carried out using a rather phenomenological approach resulting in a closed set of dispersed phase equations as well as moments model equations. The overall computational cost for the polydisperse LES is only about twice those of the single-phase one, which is very favorable. Comparison of the numerical results with the experimental data of Sommerfeld and Qiu (1991) shows that complex two-phase flows can be predicted accurately.

Keywords: Polydisperse flows, LES, Euler/Euler, Moments Model .

NOMENCLATURE

Greek Symbols

ρ	Density,	$[kg/m^3]$
μ	Dynamic viscosity,	$[kg/ms]$
ν	Kinematic viscosity,	$[m^2/s]$
τ	Stress tensor,	$[N/m^2]$
τ^t	Turbulent stress tensor,	$[N/m^2]$

Latin Symbols

g	Gravitational acceleration,	$[m/s^2]$
p	Pressure,	$[Pa]$
u	Velocity,	$[m/s]$
D	Particle diameter,	$[m]$

Sub/superscripts

c	Continuous phase
d	Dispersed phase

INTRODUCTION

Simulation of complex multi-phase flows as they occur e.g. in liquid fueled burners, fluidized beds or oil and metallurgy industry requires advanced methods and models describing phase dynamics and phase interaction. The computational effort of an Euler/Lagrange simulation increases strongly with the large number of particles necessary for representing industrial-scale systems. In addition, difficulties concerning stability and parallelisation have recently motivated the development of Euler/Euler methods. Eulerian-Eulerian simulation of polydisperse flows in the LES context is a very complex topic and not many successful applications have been reported until now in the literature. In the last few years, however, an increasing research activity can be observed. Pandya and Mashayek (2002) derived a set of dispersed phase equations in LES context. In Riber *et al.* (2006) a LES model is formally derived for the dispersed phase from the Williams spray equation using the concept of "random uncorrelated motion", in order to take into account the deviation of the individual particle velocities from the mean velocity of the particle cloud, even though this approach is not strictly polydisperse in terms of diameter space. Chan *et al.* (2010) combined DQMOM and LES for the simulation of exhaust particle formation in the wake of ground vehicles.

Carneiro *et al.* (2008, 2009) proposed a moments model to describe polydisperse multi-phase flows based on the transport of moments of the particle size distribution function (in the following denoted as "Moments Model"). The size dependency of the particle velocities is captured by transporting the moments with individual moment transport velocities (Carneiro *et al.*, 2010). The phase interaction forces, formally obtained by integration over the diameter spectrum, can be expressed using the moments. Unknown moments, needed for the closure of the exchange terms, can be calculated assuming a functional form of the particle size distribution function. 2D simulations using RANS have shown that polydisperse effects in bubbly flows and spray configurations can be captured well. The present paper focuses on the combination of this model with LES to be able to simulate complex flows more accurately, especially in terms of the gas phase fluid dynamics. A proper derivation of LES equations for the Moments Model equations is neither from a physical point of view nor from a mathematical point of view straight forward, since two averaging procedures applies, the size-weighting of the Moments Model and the filtering of the LES, respectively. Therefore, the present paper proposes a rather simple idea for obtaining filtered two-phase LES equations. Results show, however, that most of the features of the considered experimental configuration can be successfully reproduced. A detailed description of the Moments Model used in this work to capture polydispersity in particle-laden flows can be found elsewhere (Carneiro *et al.*, 2009, 2010). Therefore only a brief overview of the basic

model equations is given in the next section, followed by the LES-filtering procedure and related assumptions made. Some comments on the implementation in the open source CFD library OpenFOAM are given afterwards. The model is then validated against the experimental data of Sommerfeld and Qiu (1991).

MODEL DESCRIPTION

Moments Model

The Moments Model describes the dispersed phase dynamics through integral properties of the population of particles, providing closure for the phase interaction forces such as drag, lift, etc. It uses a presumed functional form to represent the particle size distribution. By transporting the moments of number density distribution function $f(D)$ with their individual moment transport velocities, it is possible to capture the effect of particle size on particle phase dynamics. The moment of k-th order is defined as

$$M^{(k)} \equiv \int_0^\infty D^k f(D) dD \,, \tag{1}$$

where the following physical interpretation can be associated to the lower order moments:

$M^{(0)}$:	total number of particles (per unit volume)
$M^{(1)}$:	sum of particle diameters (per unit volume)
$\pi M^{(2)}$:	total surface area of particles (per unit volume)
$\frac{\pi}{6} M^{(3)}$:	total volume of particles (per unit volume) or the local volume fraction of the particles

The volume fraction α is related to the number density distribution function through $\alpha = \int_0^\infty f(D) \frac{\pi D^3}{6} dD$. Transport equations for the moments and their transport velocities can be derived by integrating the Eulerian particle equations (Multi-Fluid model) over the diameter spectrum. The moment transport equations read (without mass transfer between phases and assuming the dispersed phase density to be constant)

$$\frac{\partial M^{(k)}}{\partial t} + \nabla \cdot \left(M^{(k)} \mathbf{u}^{(k)} \right) = 0 \,. \tag{2}$$

The moment transport velocities $\mathbf{u}^{(k)}$ are defined as

$$\mathbf{u}^{(k)} \equiv \frac{1}{M^{(k)}} \int_0^\infty \mathbf{u}(D) D^k f(D) dD \,, \tag{3}$$

where it is assumed that particles with the same diameter D_i have the same velocity $\mathbf{u}(D_i)$. In principle equations for the moment flux of the k-th moment (in case of $M^{(3)}$ the momentum) can be solved for the determination of the $\mathbf{u}^{(k)}$ (e.g. in Beck and Watkins, 2003). However, this would be opposed to the idea of creating a computationally cost-efficient model for polydisperse flows, especially in the LES context. Therefore only the transport equation for the flux of the third moment $M^{(3)} \mathbf{u}^{(k)}$ is solved for. To calculate the unknown moment transport velocities, e.g. $\mathbf{u}^{(1)}$ or $\mathbf{u}^{(2)}$, Carneiro *et al.* (2010) derived an integrated version of the relaxation approach of Bollweg *et al.* (2007), which determines minor particle size velocities from a linear interpolation between a reference particle velocity - here the mass averaged particle phase velocity $\mathbf{u}^{(3)}$ - and the gas phase velocity. This approach used the idea of the "Equilibrium Eulerian Method" originally introduced by Ferry and Balachandar (2001, 2002). With help of the integral relaxation times

$\tau^{(k)}$ the integral form can be written as

$$\mathbf{u}^{(k)} \approx \mathbf{u}_c + \frac{\tau^{(k)}}{\tau^{(3)}} \left(\mathbf{u}^{(3)} - \mathbf{u}_c \right) \,. \tag{4}$$

Thus, $\mathbf{u}^{(k)}$ is approximately determined with knowledge of the gas phase velocity $\mathbf{u}_c$, $\mathbf{u}^{(3)}$ and the relaxation times. The $\tau^{(k)}$ are related to the moments by

$$\tau^{(k)} \propto \frac{M^{(k+2)}}{M^{(k)}} \,. \tag{5}$$

With the introduction of the relaxation approach, a closure problem arises determining the moment $M^{(k+2)}$. This can be solved, if the functional form of the distribution is assumed, for example, the Gamma or Beta distribution as it is shown later on in detail.

Integration of the momentum equation over the diameter spectrum gives

$$\frac{\partial \left(M^{(k)} \mathbf{u}^{(k)} \right)}{\partial t} + \nabla \cdot \left(M^{(k)} \mathbf{u}^{(k)} \mathbf{u}^{(k)} \right)$$
$$= \frac{1}{\rho_d} \left[-M^{(k)} \nabla p + \nabla \cdot \left(M^{(k)} \boldsymbol{\tau}_d \right) \right.$$
$$\left. - \int_0^\infty D^{k-3} \mathbf{M}_{\text{PIF}} dD \right] + M^{(k)} \mathbf{g} \tag{6}$$

including the assumption[1] that $\int_0^\infty \mathbf{u}(D)\mathbf{u}(D)D^k f(D)dD = M^{(k)}\mathbf{u}^{(k)}\mathbf{u}^{(k)}$ and where $\int_0^\infty D^{k-3}\mathbf{M}_{\text{PIF}} dD$ is the integral phase interaction force, in general including drag, lift, etc. $\mathbf{M}_{\text{PIF}}$ represents the common (volumetric) formulation of the different phase interaction forces. The factor D^{k-3} transforms this volumetric formulation of the forces into differently averaged expressions e.g. in terms of the particle surface, diameter, etc. In the present paper only drag was considered, i.e.: $\mathbf{M}_{\text{PIF}} = \mathbf{M}_{\text{Drag}}$. It is shown that the term for Stokes drag can be closed analytically (see Carneiro *et al.*, 2009), which reads for k=3 (momentum conservation) $\int_0^\infty \mathbf{M}_{\text{Drag}} dD$ and contains $M^{(1)}$ and $\mathbf{u}^{(1)}$. The exact integral formulation of the Schiller-Naumann correction term, as proposed by Schiller and Naumann, reads[2]

$$\int_0^\infty \mathbf{M}_{\text{Drag, S\&N-ext.}} dD$$
$$= 18 \frac{\mu_c}{\nu_c^{0.687}} 0.15 \int_0^\infty (\mathbf{u}(D) - \mathbf{u}_c)$$
$$\cdot |\mathbf{u}(D) - \mathbf{u}_c|^{0.687} D^{1.687} f(D) dD \,. \tag{7}$$

The analytical closure of this extension in terms of moments and their transport velocities is not obvious. Therefore an approximation was used to obtain the present results, which can be derived by setting $\mathbf{u}(D) = \mathbf{u}^{(1)}$ in the term

---

[1] If $\mathbf{u}(D)$ is decomposed into a mean particle velocity and a component $\mathbf{u}'(D)$, which represents the deviation of the individual particle velocity to the mean velocity of the particle cloud, the term $\int_0^\infty \mathbf{u}'(D)\mathbf{u}'(D)D^k f(D)dD$, generated by the integration, is unknown and is neglected here.

[2] In the simulations of the Sommerfeld and Qiu configuration performed in this study, particle Reynolds numbers up to the order of 10 are expected

$|\mathbf{u}(D) - \mathbf{u}_c|^{0.687}$:

$$\int_0^\infty \mathbf{M}_{\text{Drag}} dD = 18\mu_c \left[\underbrace{M^{(1)} \left(\mathbf{u}^{(1)} - \mathbf{u}_c \right)}_{\text{analytically (Stokes)}} \right.$$

$$\left. + \underbrace{0.15 \left(\frac{|\mathbf{u}^{(1)} - \mathbf{u}_c|}{\nu_c} \right)^{0.687} M^{(1.687)} \left(\mathbf{u}^{(1.687)} - \mathbf{u}_c \right)}_{\text{approximated (Schiller and Naumann)}} \right]. \quad (8)$$

The use of $\mathbf{u}(D) = \mathbf{u}^{(1)}$ approximating $\mathbf{u}(D)$, is in line with the analytical expression for Stokes drag. The influence of replacing it by $\mathbf{u}(D) = \mathbf{u}^{(2)}$ or $\mathbf{u}(D) = \mathbf{u}^{(3)}$ has not been investigated so far. Finally $\mathbf{u}^{(1.687)}$ is given by:

$$\mathbf{u}^{(1.687)} = \mathbf{u}_c + \frac{M^{(3.687)} M^{(3)}}{M^{(1.687)} M^{(5)}} \left(\mathbf{u}^{(3)} - \mathbf{u}_c \right). \quad (9)$$

Extension to LES

Filtering of the gas phase equations can be carried out as usual. The smallest structures of the gas flow are expected to be smaller than the cell width. Compared to single phase equations the gas phase equations of the two-phase system contain the volume fraction as an additional multiplicator e.g. in the time and convective term. It is defined as such that it represents a cell-averaged property. Therefore it does not correlate with the density or the velocity, which means that a filtered product of the volume fraction and another variable is equal to the product of the filtered variables: $\overline{\alpha_c \phi} = \overline{\alpha_c}\,\overline{\phi}$. It is implicitly assumed that the LES filter width is approximately equal to the cell width.

Considering the particle phase equations we have two averaging operations, the integration over the diameter spectrum and the LES filtering. Here the sequence of their application is an important issue. First, the integration over the diameter spectrum has been applied as shown in the section before, since we want to derive equations for new variables, independent of the numerical CFD method applied afterwards to solve these equations. Second the LES filtering will be applied as preparation for the numerical tool as shown below. The strict mathematical filtering of the disperse phase equations would yield to terms containing high order correlations whose appropriate closure is still an open question. Therefore a rather phenomenological approach is used here. The integration over the diameter spectrum, as done for the derivation of the moments model equations, can be already seen as a kind of cell average, since we integrate automatically over all particles present in the cell. Therefore the moments are cell-averaged properties as well, which leads to the assumption that a decomposition into a mean and a deviation part is dispensable, again using a LES filter width equal to the cell width. It follows that $\overline{M^{(k)} \phi} = \overline{M^{(k)}}\,\overline{\phi}$.

Making similar considerations for the moment transport velocities $\mathbf{u}^{(k)}$, it can be stated that they represent cell-averaged property as well, however, implying to additional aspects. First, arguing for constant values of $\mathbf{u}^{(k)}$ over the cell, it has to be considered, that $\mathbf{u}(D)$ in the Moments Model does not allow multiple velocities for particles with the same diameter. This characteristic of the Moments Model reduces the problem by one "dimension". Second, the decomposition of the particle velocities into a mean part, representing the particle cloud velocity, and deviation part, representing the deviation of the individual particle velocity from the cloud velocity, has been already carried out in the derivation of the Moments Model equations. The term $\int_0^\infty \mathbf{u}'(D) \mathbf{u}'(D) D^k f(D) dD$, which was neglected in the integration procedure (see footnote 1), is sometimes denoted as pseudo turbulence (Prosperetti and Tryggvason, 2007). In this light, the moment transport equations can be seen as cell-averaged properties already including the "particle turbulence". Therefore the "turbulence" term, usually occurring after filtering[3], has already been dealt with. Summarising, it follows that

$$\overline{M^{(k)} \mathbf{u}^{(k)} \phi} = \overline{M^{(k)}}\,\overline{\mathbf{u}^{(k)}}\,\overline{\phi}. \quad (10)$$

Considering the above conclusions, the application of the LES filtering to the moment flux transport equation, gives[4]:

$$\frac{\partial \left(M^{(k)} \mathbf{u}^{(k)} \right)}{\partial t} + \nabla \cdot \left(M^{(k)} \mathbf{u}^{(k)} \mathbf{u}^{(k)} \right)$$

$$= -M^{(k)} \frac{\nabla \overline{p}}{\overline{\rho}_d} + \frac{1}{\overline{\rho}_d} \nabla \cdot \left(M^{(k)} \overline{\boldsymbol{\tau}_d} \right)$$

$$- \frac{1}{\overline{\rho}_d} \overline{\int_0^\infty D^{k-3} \mathbf{M}_{\text{Drag}} dD} + M^{(k)} \mathbf{g}. \quad (11)$$

The filtering of the gas phase equations can be carried out in the common manner, using standard eddy viscosity models for the sgs-stresses. The only term which needs additional attention is the phase interaction term. Considering first only Stokes drag, it can be filtered straight forward, since it depends linearly on the moment transport velocity $\mathbf{u}^{(1)}$ and $\mathbf{u}_c$. Filtering gives the corresponding counterpart of the filtered variables. The filtered momentum equation of the gas phase reads

$$\frac{\partial \left(\alpha_c \mathbf{u}_c \right)}{\partial t} + \nabla \cdot \left(\alpha_c \mathbf{u}_c \mathbf{u}_c \right)$$

$$= -\alpha_c \frac{\nabla \overline{p}}{\overline{\rho}_c} + \frac{1}{\overline{\rho}_c} \nabla \cdot \left(\alpha_c \left(\overline{\boldsymbol{\tau}_c} + \overline{\boldsymbol{\tau}_c^t} \right) \right)$$

$$+ \frac{1}{\overline{\rho}_c} \overline{\int_0^\infty \mathbf{M}_{\text{Drag}} dD} + \alpha_c \mathbf{g}. \quad (12)$$

The conclusion that no additional terms arise due to the filtering, however, does not necessarily mean, that the dispersed phase flow field is fully resolved, since assumptions made earlier in the derivation of the Moments Model. The question arises, however, where the interaction between sgs-structures of the gas phase and the droplets is considered. This part of the drag that is generated by the interaction of the turbulent gas phase fluctuations and the particles is called "turbulent dispersion". Subfilter-scale structures of the dispersed phase arising due to the gas phase sgs-vortices are of the same order as the gas phase fluctuations in case of Stokes particles. Since gas phase fluctuations are modelled with the eddy viscosity model, dispersed phase fluctuations should be captured by introducing a turbulent dispersion term into the dispersed phase moment flux equations. However, as shown before, neither the integration nor the filtering of the drag term does produce

---

[3]Filtering of standard Two-Fluid model equations, considering the decomposition of the particle velocity, yields to an unknown term, namely the dispersed phase velocity fluctuation correlation term. Its closure is mostly done in literature by using a combined Smagorinsky-Yoshizawa eddy viscosity model for the shear stresses.

[4]The filtering bars for the integral values α_c, α_d, $M^{(k)}$ and $\mathbf{u}^{(k)}$ are omitted in the following for simplicity.

new terms. The question is if turbulent dispersion for Stokes particles is fully described by considering only the mean relative velocity between gas and particles. To give a final answer is not aim of the present explanation. For high-Reynolds particles the present filtering procedure does not yield further term as well. Unfiltered variables can be replaced by filtered variables. In this case, however, assumptions have been made in the integration of the high-Reynolds drag term. This analytical unclosed term can be seen as predestinated candidate containing the effect of turbulent dispersion.

Validity of Moment Sets

In general, the reconstruction of a distribution function from a finite set of moments is only possible, if the moment set satisfies the conditions given by the Hankel-Hadamard determinants (see Shohat and Tamarkin, 1963). For each moment set, the corresponding determinants, given by the following condition, must be satisfied.

$$\Delta_{k,l} = \begin{vmatrix} M^{(k)} & M^{(k+1)} & \cdots & M^{(k+l)} \\ M^{(k+1)} & M^{(k+2)} & \cdots & M^{(k+l+1)} \\ \vdots & \vdots & \ddots & \vdots \\ M^{(k+l)} & M^{(k+l+1)} & \cdots & M^{(k+2l)} \end{vmatrix} \geq 0 \quad (13)$$

with $k = 0, 1, 2, ..., 2l + 1$. To be able to reconstruct the Beta distribution (with $D_{min} = 0$), four consecutive moments must be known, which were chosen to be $M^{(0)} - M^{(3)}$. The set should include the third moment to ensure mass conservation. With this choice we have $k = k_{\min} = 0, l = 1$ resulting in the following two conditions:

$$M^{(2)}M^{(0)} - (M^{(1)})^2 \geq 0, \quad (14)$$

$$M^{(3)}M^{(1)} - (M^{(2)})^2 \geq 0, \quad (15)$$

which are the Hankel-Hadamard determinant Δ_{01} and Δ_{11}, respectively. These conditions are independent on the choice of the functional form of the distribution. They constitute a sufficient condition that a function exists for the given moment combination. However, with a specific choice of the functional form of the distribution function, further conditions arise due to the characteristics of the underlying mathematical function and the reconstruction algorithm. In the case of the Beta distribution

$$f(D) = \frac{C_0}{B(p,q)} \frac{D^{p-1}(D_{\max} - D)^{q-1}}{D_{\max}^{p+q-1}}, \quad (16)$$

with $B(p,q)$ being the Beta function, the moments can be calculated using

$$M^{(k)} = C_0 D_{\max}^k \frac{B(p+k,q)}{B(p,q)}. \quad (17)$$

The parameters C_0, $D_{\max}$, p and q can be determined using the first four moments by

$$D_{max} = \frac{2(M^{(1)})^2 M^{(3)} - M^{(1)}M^{(2)^2} - M^{(0)}M^{(2)}M^{(3)}}{M^{(1)^2}M^{(2)} - 2M^{(0)}M^{(2)^2} + M^{(0)}M^{(1)}M^{(3)}}, \quad (18)$$

$$p = \frac{M^{(1)}(D_{max}M^{(1)} - M^{(2)})}{D_{max}(M^{(0)}M^{(2)} - M^{(1)^2})}, \quad (19)$$

$$q = \frac{(D_{max}M^{(0)} - M^{(1)})(D_{max}M^{(1)} - M^{(2)})}{D_{max}(M^{(0)}M^{(2)} - M^{(1)^2})}, \quad (20)$$

$$C_0 = M^{(0)}. \quad (21)$$

In practical simulations, it is extremely difficult to guarantee the validity of moment sets throughout the whole computational domain and time, even if the initial and boundary moment sets fulfil these conditions (see e.g. Watkins, 2005; Petitti *et al.*, 2010). For unsteady, turbulent LES simulations a bounding procedure ensuring valid moment sets for every cell at every time is a crucial requirement for a stable simulation. For the practical implementation, conditions must be derived to be able to limit the moments in such a way that the conditions are surely fulfilled with a minimal change in the moment values. It is shown in the following how a reasonable procedure can be achieved.

First of all, the moments have to be positive due to their special physical meaning in the context of a particle size distribution function. Starting with the parameters p and q, it is of practical advantage to restrict both parameters to be positive due to the characteristics of the Gamma function. This leads in combination with the positive Hankel-Hadamard determinant Δ_{01}, which occurs in the denominator of both parameters, and the obvious condition that $D_{\max} > 0$ to the following restriction due to the enumerator of p:

$$D_{max}M^{(0)} - M^{(1)} \geq 0 \Leftrightarrow D_{max} \geq D_{10}, \quad (22)$$

which directly leads to the second condition resulting from the enumerator of the parameter q:

$$D_{max}M^{(1)} - M^{(2)} \geq 0 \Leftrightarrow D_{max} \geq D_{21}. \quad (23)$$

The second condition is a non-functional relation between the moments $M^{(1)}$ and $M^{(2)}$, which would give problems in terms of finding a bounding rule for one moment dependent on the other. Fortunately, it can be shown that these two conditions are automatically fulfilled by the convexity condition (also frequently called "Schwarz's Inequalities"), $M^{(k)}M^{(k-2)} - M^{(k-1)^2} \geq 0$, which implies: $D_{max} \geq \ldots \geq D_{21} \geq D_{10}$. Furthermore, the convexity condition is already included in the Hankel-Hadamard determinants. Therefore the further discussion of these two conditions is reduced to their visual representation as shown in Fig. 1. Forcing both enumerator and denominator of the $D_{\max}$ term, as formulated in the Eqn.18, to be positive yields the following restrictions:

$$M^{(1)}\Delta_{11} \geq M^{(3)}\Delta_{01} \quad (24)$$

$$M^{(2)} \geq -\frac{M^{(0)}M^{(3)}}{2M^{(1)}} + \sqrt{\frac{M^{(0)^2}M^{(3)^2}}{4M^{(1)^2}} + 2M^{(1)}M^{(3)}}. \quad (25)$$

and

$$M^{(0)}\Delta_{11} \geq M^{(2)}\Delta_{01} \quad (26)$$

$$M^{(2)} \geq \frac{M^{(1)^2}}{4M^{(0)}} + \sqrt{\frac{M^{(1)^4}}{16M^{(0)^2}} + \frac{M^{(1)}M^{(3)}}{2}} \quad (27)$$

Both equations can be recast to have $M^{(2)}$ as a function of the other moments, which is part of the chosen bounding procedure, where $M^{(1)}$ and $M^{(2)}$ are modified - if necessary - and holding $M^{(0)}$ and $M^{(3)}$ constant since they represent total particle number and volume. Both properties are conservative in non-evaporating sprays without coalescence and break-up. To be able to determine the final range of valid $M^{(1)} - M^{(2)}$ combinations for given $M^{(0)}$ and $M^{(3)}$, it is helpful to plot all constraints in a $M^{(1)}$ over $M^{(2)}$ graph. The map shown in Fig. 1 is normalised with the coordinates of the critical point

$(M^{(1)}_{\max}, M^{(2)}_{\max})$. It marks the maximum valid values of $M^{(1)}$ and $M^{(1)}$ for given $M^{(0)}$ and $M^{(3)}$. It is characterised as intersection of several conditions, from which it can be derived that.

$$M^{(1)}_{\max} = \sqrt[3]{M^{(0)^2} M^{(3)}} \qquad M^{(2)}_{\max} = \sqrt[3]{M^{(0)} M^{(3)^2}} \,. \quad (28)$$

In Fig. 1 it is obvious that the conditions 22 and 23 are im-
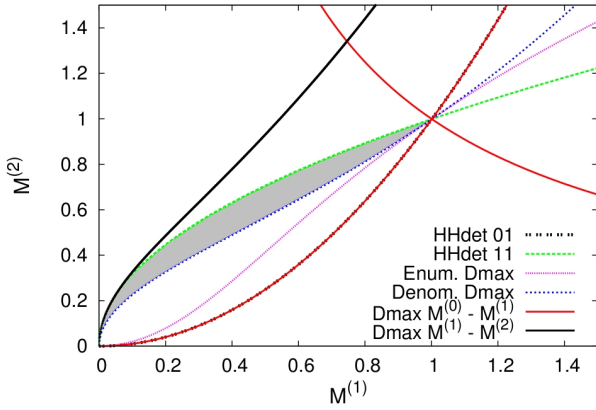

Figure 1: Resulting zone for valid $M^{(1)}$-$M^{(2)}$ combinations (grey zone) for given $M^{(0)}$ and $M^{(3)}$. The lines show each condition's individual border between valid and invalid moment combination.

plicitely fullfilled in stricter constraints, as mentioned before. As resulting bounding algorithm the following procedure has been proven to be a practical solution (concerning code stability and validity of moment sets). First $M^{(1)}$ is bounded due to the maximal valid value and afterwards $M^{(2)}$ due to either the condition for $D_{\max}$ (Eqn. 27) or Δ_{11}. However, the parameters p and q as well as $D_{\max}$ can still become very large, which results in abnormal distribution shapes. This can be avoided with additional constraints, which are e.g. demonstrated by Watkins (2005).

IMPLEMENTATION IN OPENFOAM

In line with the work of Rusche (2002), phase-intensive versions of the moment, moment flux and gas phase momentum transport equations were derived. This was done by factoring out the time and convective term on the left hand side and including the moment conservation equation:

$$\frac{\partial \mathbf{u}^{(k)}}{\partial t} + \mathbf{u}^{(k)} \nabla \cdot \mathbf{u}^{(k)}$$

$$= -\frac{\nabla \overline{p}}{\overline{\rho_d}} + \frac{\nabla \cdot \left(M^{(k)} \overline{\boldsymbol{\tau}_d} \right)}{\overline{\rho_d} M^{(k)}}$$

$$- \frac{1}{\overline{\rho_d} M^{(k)}} \overline{\int_0^\infty D^{k-3} \mathbf{M}_{\mathrm{Drag}} \, dD} + \mathbf{g} \quad (29)$$

as well as for the gas phase momentum equation (including the gas phase continuity equation):

$$\frac{\partial \mathbf{u}_c}{\partial t} + \mathbf{u}_c \nabla \cdot \mathbf{u}_c$$

$$= -\frac{\nabla \overline{p}}{\overline{\rho_c}} + \frac{\nabla \cdot \left(\alpha_c \left(\overline{\boldsymbol{\tau}_c} + \overline{\boldsymbol{\tau}_c^t} \right) \right)}{\overline{\rho_c} \alpha_c}$$

$$+ \frac{1}{\overline{\rho_c} \alpha_c} \overline{\int_0^\infty \mathbf{M}_{\mathrm{Drag}} \, dD} + \mathbf{g} \,. \quad (30)$$

The OpenFOAM solver `twoPhaseEulerFoam` can be used as basis since it provides the framework for an Eulerian-Eulerian two-phase solver. OpenFOAM is a modular built open-source code for various CFD applications and it is a convenient tool for the implementation and testing of new submodels or solvers. Carneiro *et al.* (2008) presented the implementation of the Moments Model in the context of the `twoPhaseEulerFoam`. In the current work the turbulence modelling has been extended from the standard k-ε model to LES closure (indeed any available eddy viscosity model can be used similar to the way as in the incompressible single phase solver `pisoFoam`).

The structure of the `twoPhaseEulerFoam` requires pressure terms for both phases (since it solves for a pressure equation due to the pressure-velocity coupling). Therefore the pressure gradient in the dispersed phase equation remains and the pressure is set equal to the gas phase pressure. It is difficult, however, to justify the continuum assumption for a droplet-phase representing a dilute dispersion without particle-particle interaction. Dispersed phase pressure and shear-stresses become from the physical point of view meaningless. Therefore, the dispersed phase "molecular viscosity" is set to a value orders of magnitude lower than the corresponding gas phase value, $\nu_p << \nu_g$. The shear stress term can be consequently neglected entirely (Crowe *et al.*, 1998) with the same effect, which is done in the current approach. Only the pressure term remains due to stability reasons (avoiding shock-like velocity gradients and very high droplet number gradients) and due to the structure of the pressure-based solver `twoPhaseEulerFoam` as mentioned before.

The implementation of the moment transport equations can be found elsewhere (Carneiro *et al.*, 2008). For the reconstruction algorithm as well as for the calculation of the unknown moments of higher order, algebraic equation have to be solved. The bounding of the moments is done as outlined before.

RESULTS

Test Case Description

Sommerfeld and Qiu (1991) investigated a swirling, particle-laden flow configuration to provide experimental data as basis for validating two-phase solvers and models. The setup consists of two coaxial inlet pipes and a cylindrical main chamber. The central inlet pipe contains the particle-air mixture, the surrounding coaxial annulus provides a swirled, pure air stream, which is, in combination with the area expansion between inlet pipes and the main chamber, responsible for the vortex breakdown and the formation of a central recirculation zone. The air of the central jet will flow radially outwards when approaching the stagnation point, which forms due to the opposite flow direction between central jet and the recirculating air. The particles (mainly the bigger ones),

however, are not able to follow the swirling air and penetrate the recirculation zone as deep as their inertia allows. This phenomenon is clearly dependent on the particles diameter. Since particle Reynolds numbers numerically determined by Oefelein (2006) for the same configuration and similar flow conditions are clearly different comparing the mean diameter of $45\mu m$ and larger diameters (particles with $60\mu m$ are shown), differences between monodisperse and polydisperse simulation results are expected, especially affecting the particle mass flux. The geometrical dimensions including the locations of the measurement planes are shown in Fig. 2 as well as the experimental particle size distribution and its mathematical approximation using a Beta distribution in Fig. 3. The inlet values for mass fluxes, mean particle sizes and moments of the size distribution are given in Table 1. Glass beads were used as particles.

Table 1: Inlet conditions of the particle phase

D10	$45.5\,\mu$m	$M^{(0)}$	$=2.18266\cdot10^{8}\,\mathrm{m}^{-3}$
ρ_p	$2500\,\mathrm{kgm}^{-3}$	$M^{(1)}$	$=1.00612\cdot10^{4}\,\mathrm{m}^{-2}$
$\dot{m}_p$	$0.34\,\mathrm{gs}^{-1}$	$M^{(2)}$	$=5.25831\cdot10^{-1}\,\mathrm{m}^{-1}$
Loading	0.034	$M^{(3)}$	$=3.05577\cdot10^{-5}$
$\mathrm{D}_{\mathrm{min}}$-$\mathrm{D}_{\mathrm{max}}$	20-$80\,\mu$m	α	$=1.60000\cdot10^{-5}$

Numerical Setup

The computational mesh contains only 933,000 hexahedral cells, which is rather low number for such a configuration concerning resolution requirements for LES. Most of the cells, however, by applying a complex mesh structure, are placed in the region of the vortex break-up and the recirculation zone and only rather few cells cover the domain towards the outlet. The boundary layers at the walls are not resolved. With this approach, the computational costs could be kept low as shown below. The CFL number has to be below 1 to ensure stable simulation. The WALE model is used to model the sgs-viscosity. This model has been chosen due to its superior performance for wall bounded flows without explicitly solving for the boundary layer. The axial and azimuthal velocity profiles at the coflow inlets are considered, but without imposing turbulent fluctuations to the mean flow. This is not expected to influence results significantly, since the flow field is mainly determined by the shear layers between the inlet jets and the area expansion, respectively. The discretisation is limited due to the available schemes in OpenFOAM to low order in time (`backward`, second order implicit) and space (second order). Moments equations are discretised using the second order `limitedLinear` scheme.
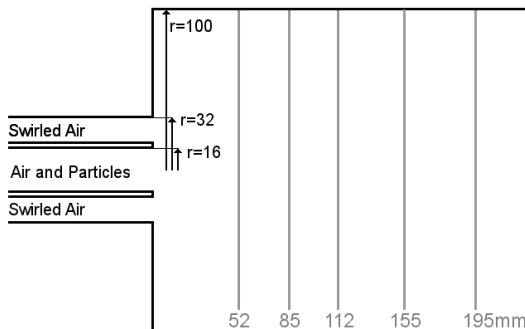

Figure 2: Geometrical dimensions of the experiment of Sommerfeld and Qiu and measurement planes
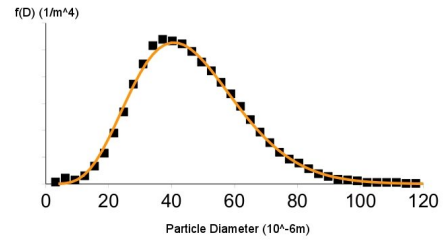

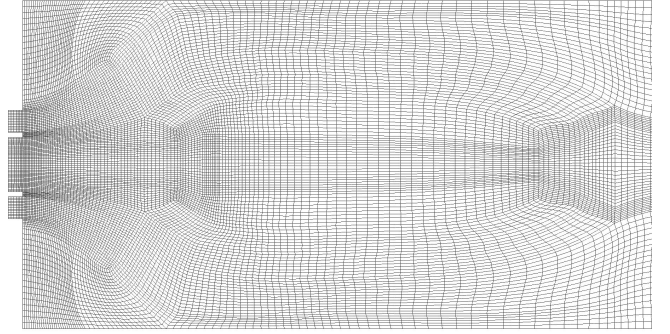Figure 3: Inlet size distribution of particles (experimental and approximation with Beta distribution)

Figure 4: Numerical mesh created with ANSYS ICEM CFD

Computational Costs

A comparison of the computational costs for single-phase, monodisperse and polydisperse two-phase simulations is shown in Table 2. The presented data are taken from sim-

Table 2: Comparison of computational costs

	sec/iter on 24 proc.
single-phase LES	1.37
monodisperse two-phase LES	2.07 (+50%)
polydisperse two-phase LES	3.24 (+136% / +56%)

ulations computed on 3 dual socket quad core Nehalem units with Infiniband connection. The additional computing time compared to the single-phase LES is 50% for the monodisperse and 136% for the polydisperse two-phase case. Comparing both two-phase solvers, the amount of computing time for the Moments Model including moment transport, reconstruction and bounding is about 56% in addition to the monodisperse solver. The additional computing time associated with the polydisperse solver is expected to be worth especially in configurations with higher level of polydispersity or evaporating flows as discussed briefly later on in the results section.

Results

Both, monodisperse and polydisperse simulations have been carried out. The monodisperse results are obtained using the experimentally given mean number diameter of 45μm, the polydisperse results imposing the moment values on the inlet as listed in Table 1. All other settings were the same. The mean and RMS values shown are time averaged over 1s physical time for both cases. Fig. 5 shows a snapshot of the gas velocity, where the vortex breakdown and the inner recirculation zone are clearly visible. Comparison of the mean velocity profiles and RMS values for the three velocity com-

Figure 5: Instantaneous (top) and mean (bottom) contours of gas phase velocity magnitude (m/s)

ponents shows a very good overall agreement with the experimental data (Figures 6 and 7 as well as Figures 10 and 11 shown in the appendix). The upper part of each figure shows the gas phase velocity, the lower part the volume-weighted particle velocities. The difference between monodisperse
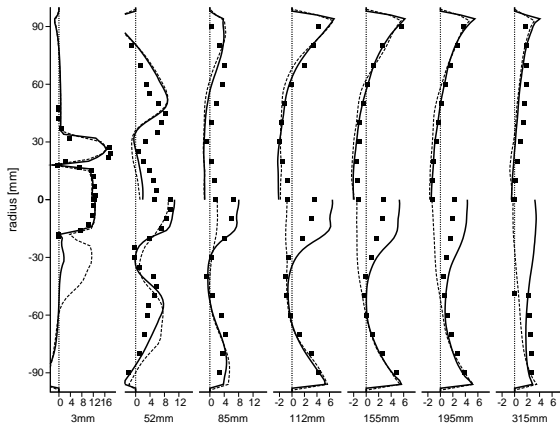

Figure 6: Axial mean velocity (m/s) of gas (top) and particles (bottom). Exp. (symbols) - monodispersed (dashed) - polydispersed (solid)
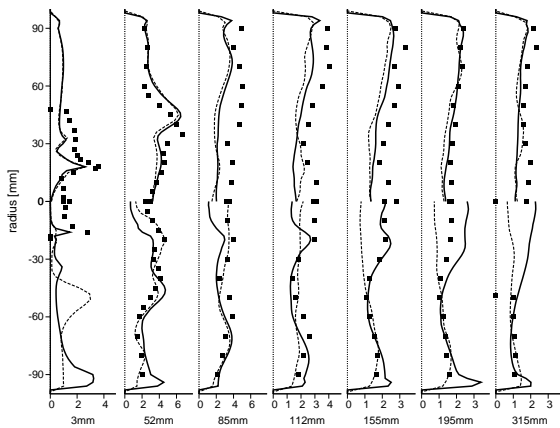

Figure 7: Axial RMS velocity (m/s) of gas (top) and particles (bottom). Exp. (symbols) - monodispersed (dashed) - polydispersed (solid)

and polydisperse results is, however, in most of the domain marginal. This can be expected, since the rather small particles lying mostly in the Stokes regime. A closer look on
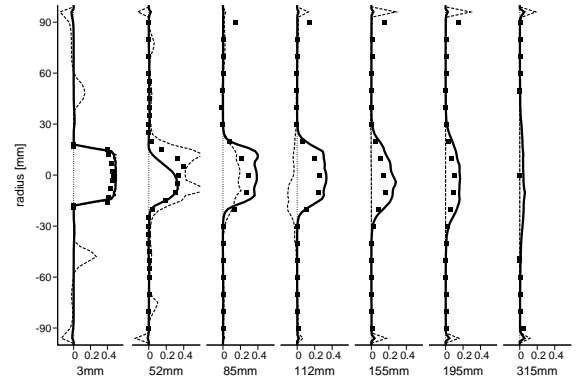

Figure 8: Particle mass flow rate ($kg/m^2 s$). Exp. (symbols) - monodispersed (dashed) - polydispersed (solid)

the region where particles enter the recirculation zone, offers a different behaviour of monodisperse compared to polydisperse results (see Fig. 6). This is due to the inertia of the particles which plays a significant role in this area, since bigger particles tend to penetrate further in the recirculation zone. In the monodisperse results, the stagnation point is far more upstream than in the results predicted by the Moments Model. This effect can be seen also in the particle mass flux, which is shown in Fig. 8, indicating that the monodisperse simulation can not predict the correct behaviour. In case of a configuration with droplet evaporation and combustion, this could have significant impact on the combustion due to corresponding differences in fuel vapor concentrations in this area, where a flame would stabilise. In the polydisperse results, however, it can be seen that the particle velocity and the mass flow are slightly overpredicted. A reason can be seen in the assumptions made for the drag term closure - further models will be tested in the future.

The mean diameters, given by ratios of the moments, obey the formula $D_{ab} = \left(M^{(a)}/M^{(b)} \right)^{1/a-b}$. The snapshot of the number mean diameter D_{10} (Fig. 9) shows a correct qualitative behaviour in some aspects. Small droplets, for example, escaping the central jet in radial direction, are characterised by a low D_{10} since the ratio of diameter sum to particle number decreases with smaller droplets. The strong decrease downwards within the central jet, however, is opposite to the expectations and the experimental results. Analysing the local
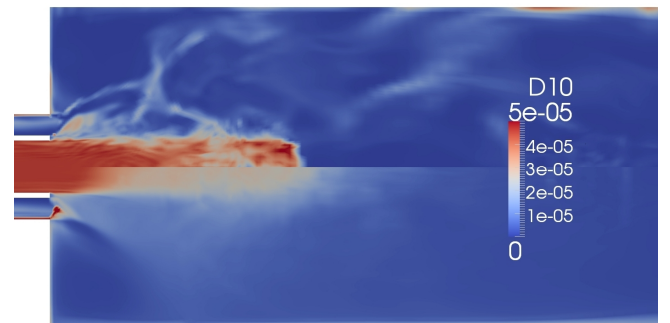

Figure 9: Instantaneous (top) and mean (bottom) contours of D_{10} (m)

particle size distributions shows, that the parameters of the Beta distribution often reach values, which give unphysical

distribution shapes, e.g. distributions with particle numbers approaching infinity when diameters come close to zero or D_{max}. This is clearly unphysical. A detailed study of the relation between the bounding algorithm in combination with appropriate parameter ranges have to be done to solve this shortcoming of the current state of the Moments Model LES solver. Nevertheless, results for velocity and mass-flux profiles indicate that moments and overall exchange terms with the gas phase are correctly predicted.

CONCLUSION

A polydisperse two-phase LES model has been proposed and was applied to a particle-laden, swirling flow configuration. A model, based on the transport of moments of the particle size distribution to consider the size dependency (polydispersity) of particle motion and forces, has been transfered to LES context. The integral moment and moment flux transport equations, describing the dispersed phase, remain closed after the applied LES filtering due to the characteristics of the transported variables. Filtering has been applied to the gas phase equations in the established way using a common sgs model for closure. The drag force term is closed after filtering. The extension of the OpenFOAM solver `twoPhaseEulerFoam` to LES turbulence modelling has been shown to work in combination with the moments model used.

Numerical results for the test case of Sommerfeld and Qiu (1991) demonstrate the capability of the presented approach to predict complex, particle-laden turbulent flows accurately. The flow field is captured very well in general by both the monodisperse and polydisperse model, since the particles used in the experiment behave mostly like Stokes particles. Significant differences between the monodisperse and polydisperse results, however, can be observed at the particle mass flow rate into the recirculating gas phase. There, the polydisperse results are much closer to the experimental findings than the monodisperse counterpart. The increase in computational costs for the polydisperse simulation compared to a single-phase LES is only about a factor of two, which is quite attractive for computational expensive industrial configurations.

Further work has to be done on the correct prediction of the mean diameters and particle size distributions. Future improvements could include a more accurate closures for the Moments Model, especially for the drag closure and the dispersed phase velocity correlation term, as well as a more strict filtering procedure of the dispersed phase equations.

REFERENCES

BECK, J.C. and WATKINS, A.P. (2003). "On the Development of a Spray Model Based on Drop-Size Moments". *Proc. R. Soc. Lond. A.*, **459**, 1365–1394.

BOLLWEG, P. *et al.* (2007). "Derivation and Application of a Poly-celerid Method for Polydispersed Two-phase Flows". *6th International Conference on Multiphase Flow, Leipzig, Germany.*

CARNEIRO, J.N.E. *et al.* (2008). "Implementation of a Moments Model in OpenFOAM for Polydispersed Multiphase Flows". *Open Source CFD International Conference, Berlin, Germany.*

CARNEIRO, J.N.E. *et al.* (2009). "Numerical Simulation of Droplet Dispersion and Evaporation with a Moments-based CFD Model". *Proceedings of COBEM.*

CARNEIRO, J.N.E. *et al.* (2010). "Eulerian Simulations of Polydisperse Flows Using a Moments Model with a Relaxation Approach for the Moment Transport Velocities". *7th ICMF 2010, Tampa, FL.*

CHAN, T.L. *et al.* (2010). "Direct Quadrature Method of Moments for the Exhaust Particle Formation and Evolution in the Wake of the Studied Ground Vehicle". *Journal of Aerosol Science*, **41**, 553–568.

CROWE, C. *et al.* (1998). *Multiphase Flows with Droplet and Particles.* CRC Press.

FERRY, J. and BALACHANDAR, S. (2001). "A First Eulerian Method for Disperse Two-phase Flow". *Int. J. of Multiphase Flow*, **27**, 1199–1226.

FERRY, J. and BALACHANDAR, S. (2002). "Equilibrium Expansion for the Eulerian Velocity of Small Particles". *Powder Technology*, **125**, 131–139.

OEFELEIN, J.C. (2006). "Large Eddy Simulation of Turbulent Combustion Processes in Propulsion and Power Systems". *Progress in Aerospace Sciences*, **42**, 2–37.

PANDYA, R.V.R. and MASHAYEK, F. (2002). "Two-Fluid Large-Eddy Simulation Approach for Particle-Laden Turbulent Flows". *Int. J. of Heat and Mass Transfer*, **45**, 4753–4759.

PETITTI, M. *et al.* (2010). "Bubble Size Distribution Modeling in Stirred Gas-liquid Reactors with QMOM Augmented by a new Correction Algorithm". *AIChe Journal*, **56**, 36–53.

PROSPERETTI, A. and TRYGGVASON, G. (2007). *Computational Methods for Multiphase Flows.* Cambridge University Press.

RIBER, E. *et al.* (2006). "Development of Euler-Euler LES Approach for Gas-Particle Turbulent Jet Flow". *Proceedings of FEDSM2006, ASME Joint U.S. - European Fluids Engineering Summer Meeting.*

RUSCHE, H. (2002). *Computational Fluid Dynamics of Dispersed Two-phase Flows at High Phase Fractions.* Ph.D. thesis, Imperial College of Science, Technology and Medicine, UK.

SHOHAT, J.A. and TAMARKIN, J.D. (1963). "The Problem of Moments". *Providence, RI: American Mathematical Society.*

SOMMERFELD, M. and QIU, H.H. (1991). "Detailed Measurements in a Swirling Particulate Two-Phase Flow by a Phase-Doppler Anemometer". *Int. J. Heat and Fluid Flow*, **12(1)**.

WATKINS, A.P. (2005). "The application of Gamma and Beta number size distributions to the modelling of sprays". *Proceedings of the 20th ILASS-Europe, Orléans, France, September.*

APPENDIX A

For completeness, the radial and azimuthal mean velocity component and RMS values of the gas phase and the particles are shown in the following figures. Symbols represent the experimental data, dashed lines indicate the monodisperse results using a number mean diameter of $45, 5\mu m$, polydisperse results are shown by the solid lines. The upper part of each figure shows the gas phase velocity, the lower part the volume-weighted particle velocities. Noticeable is the good agreement of the RMS values, especially when considering the fact that neither terms for particle turbulence nor for turbulent dispersion have been considered in the simulations.
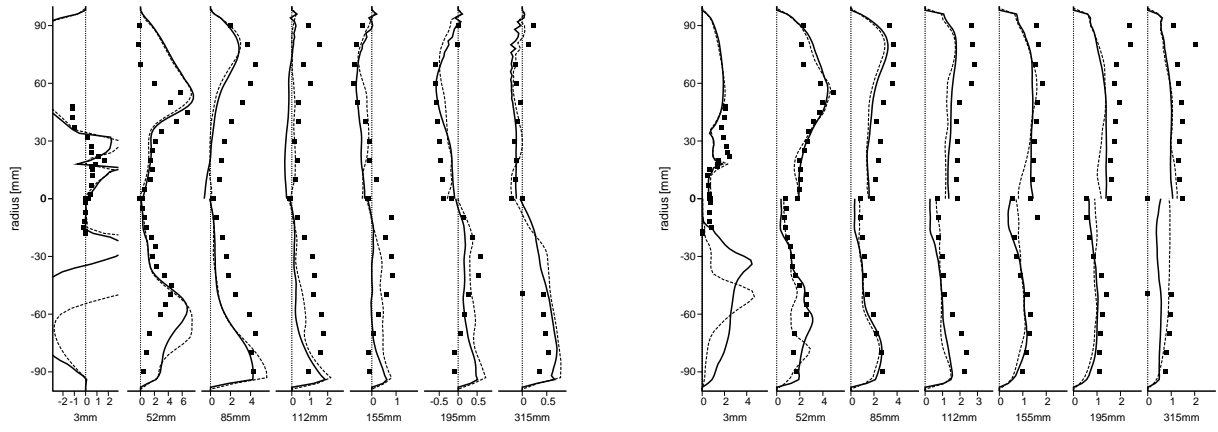
Figure 10: Radial mean(left) and RMS(right) velocity (*m/s*) of gas (top) and particles (bottom). Experiment (symbols) - monodispersed (dashed) - polydispersed (solid)
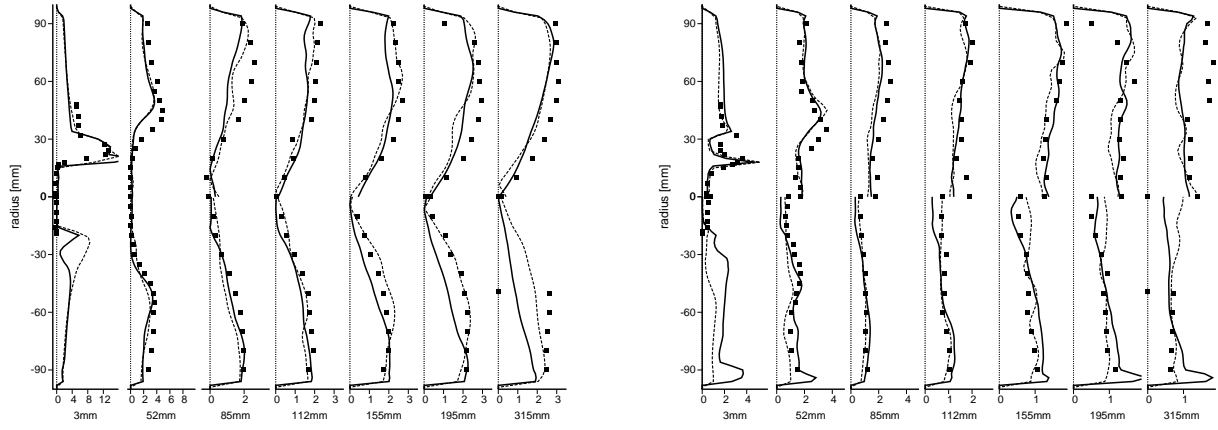
Figure 11: Azimuthal mean(left) and RMS(right) velocity (*m/s*) of gas (top) and particles (bottom). Experiment (symbols) - monodispersed (dashed) - polydispersed (solid)

MODELING OF A GAS-LIQUID SLUG FLOW ACCOMPANIED WITH MASS TRANSFER THROUGH A LONG MICROCHANNEL

Dmitry ESKIN[*] and Farshid MOSTOWFI

SCHLUMBERGER DBR Technology Center, 9450-17 Ave., Edmonton, AB T6N 1M9, CANADA

* E-mail: deskin@slb.com

ABSTRACT

Keywords:

NOMENCLATURE

Greek Symbols
Δ
$\Delta p/L$.
δ
ε
ε_L
γ
μ_f
ρ

Latin Symbols
Ca
c
c_m

c_0

c_s
D
D_B
D_c
f
H
$k_L a$
$k_{L,cap}$
L_B
L_{lB}
L_{sl}
M
p
Q_G
Q_L
q
q_s

R
Re
R_B
R_c
T
U_B
U_{GS}
U_{LS}
U_m
W_B
W_s

W_{se}

Sub/superscripts
bf
cf
G
B
i   .
L

sl
Σ

INTRODUCTION

et al.

et al
et al.

μ

(D$_c$=1.5   2.2 mm).

D$_c$ 1.5, 2,   3 mm

et al.

sl
Σ

MODEL DESCRIPTION
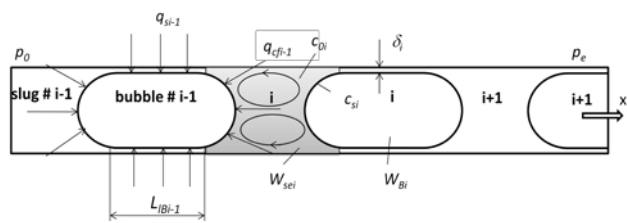
Figure 1:

Bubble Size Evolution

1,…. i-1, i, i+1…..

CH $C_{10}H_{22})$

$\approx$

p_i R

T

et al.

p_i

x

L

et al.

W_{Bi}

Bubble-Liquid Mass Transfer

$$U_{Bi} = \frac{U_{sli}}{\left(1 - \dfrac{\delta_i}{R_c}\right)^2}$$

U_{sli}

δ_i

U_{mi}

i.e.

c_{0i}

c_{0i}

c_{si}

$$U_{sli} = \frac{U_{LS}}{1 - \varepsilon_i}$$

$U_{LS} = Q_L/F$

F

Q_L

Figure 2:

ε_i
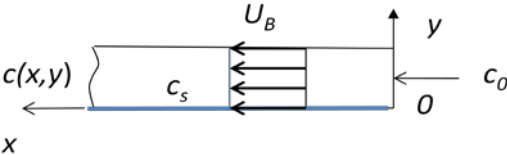
Mass transfer from a liquid film to a cylindrical bubble part

et al

U_B

U_{Bi}

U_{mi}

c

$0<Ca<2$

D

$(U_{Bi}\text{-}U_{mi})/U_{Bi}$

δ_i/R_c

e.g.,

c_0

—— ——

c_s

—

H

——

$$\frac{c(x,y)-c_s}{c_0-c_s}=\frac{2}{\pi}\sum_{n=1}^{\infty}\frac{1-(-1)^n}{n}\exp\left[-\left(\frac{\pi n}{2}\right)^2\frac{Dx}{U_B\delta^2}\right]\sin\left[\frac{\pi n}{2}\frac{y}{\delta}\right]$$

—

—   **Liquid Slug Mass Balance**

$$c_m\left(L_{lB}\right)=c_s+\left(c_0-c_s\right)\times$$

$$\frac{4}{\pi^2}\sum_{n=1}^{\infty}\frac{1-(-1)^n}{n^2}\exp\left[-\left(\frac{\pi n}{2}\right)^2\frac{DL_{lB}}{U_B\delta^2}\right]\times\left[1-\cos\left(\frac{\pi n}{2}\right)\right]$$

D_c=1.5 - 3 mm

et   al.

—

Mass transfer through the semi-spherical caps

$$dx = U_{Bi}dt,$$

$$x$$

CALCULATION EXAMPLES AND DISCUSSION

$$k_L a = \frac{q_\Sigma}{(c_0 - c_s)(W_s + W_b)}$$

$$\Delta = \frac{c_0 - c_s}{c_0}$$

Δ

Δ

e.g.,

Δ

C_1 C_{10} $(CH_4 - C_{10}H_{22})$.

f

et al

p_0 T L_{s0}

p_b f $L_{s0}=U_{sl0}/f$ U_{sl0}

p_e

C_{10}

)

$c_0=14.19$ kg/m^3

webbook.nist.gov/chemistry

$H=2.43\cdot10^5$ m^2/s^2

R 518 $J/(kg\ K)$.

Figure 5

Figure 3:

Ca

D_c 25,

50, 100, *and* 200 μm

Figure 4:

k_La

k_La

L

$k_L a$

Dc=50 micrometers

L=0.25 m
L=0.50 m
L=1.00 m

Figure 6:

Δ

Δ

μ

Δ

Δ

Δ

c_0-c_s

c_0

Δ

c_0-c_s

Δ

Δ

Δ

D_c=50 μm
L=0.25, 0.5   1 m

f

50 μm

1 m

f=100, 300, 600, 1000 Hz

f=100Hz –

L_{s0}=3.2 mm, f=1000 Hz – L_{s0}=0.34 mm

L= 1 m
Dc=50 micrometers

f=100   Hz
f=300   Hz
f=600   Hz
f=1000 Hz
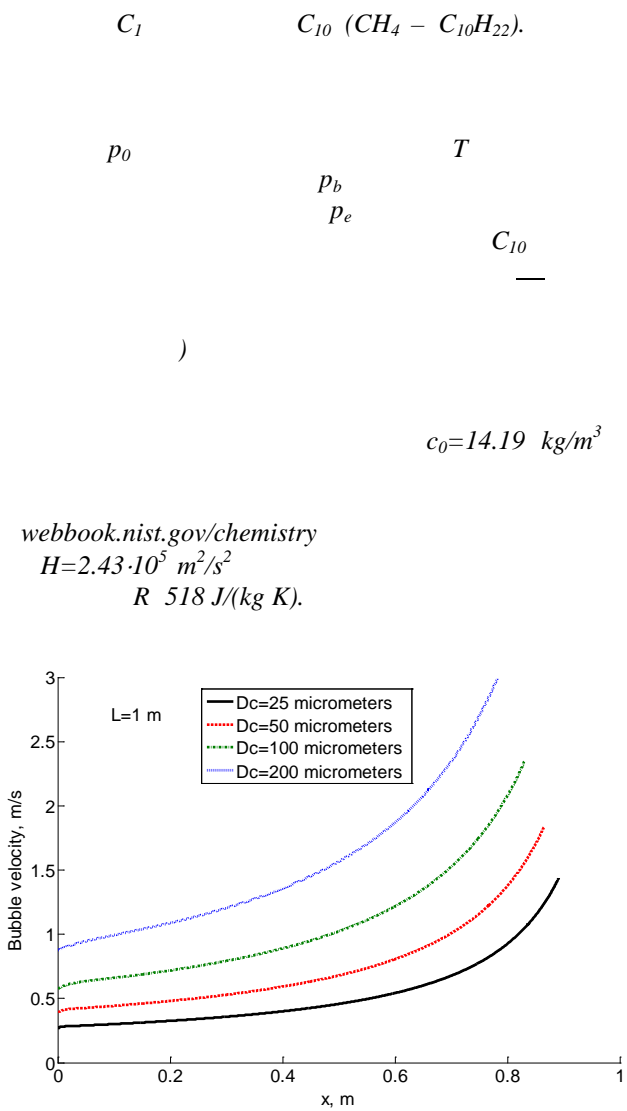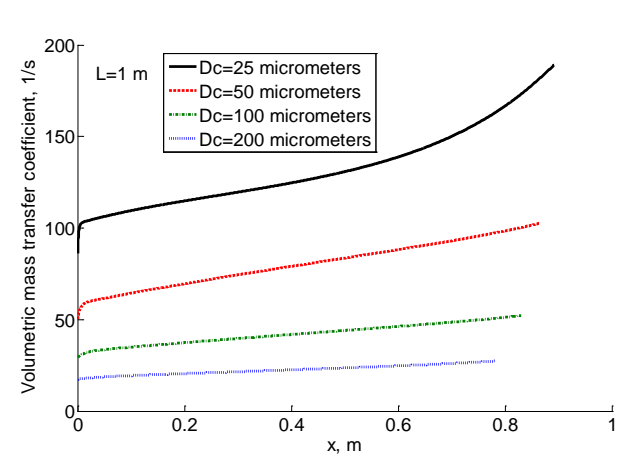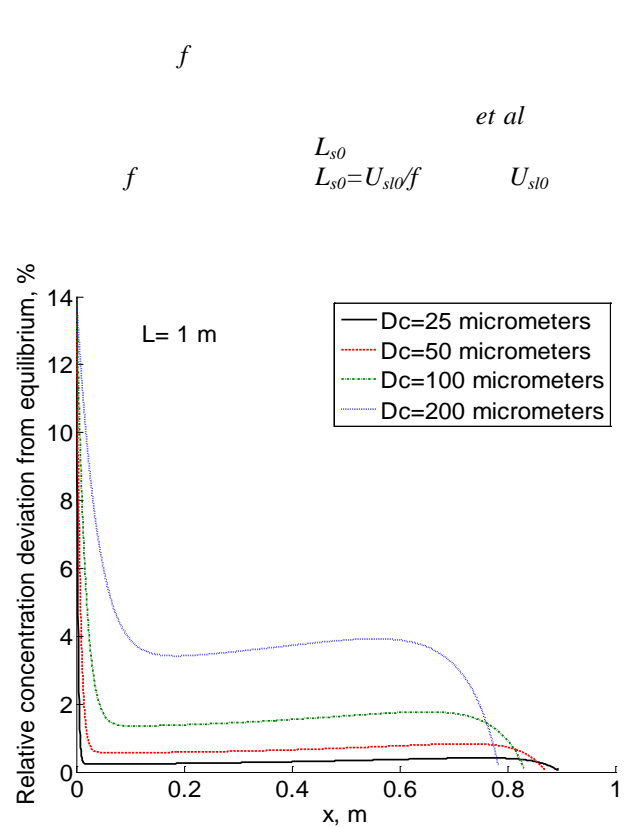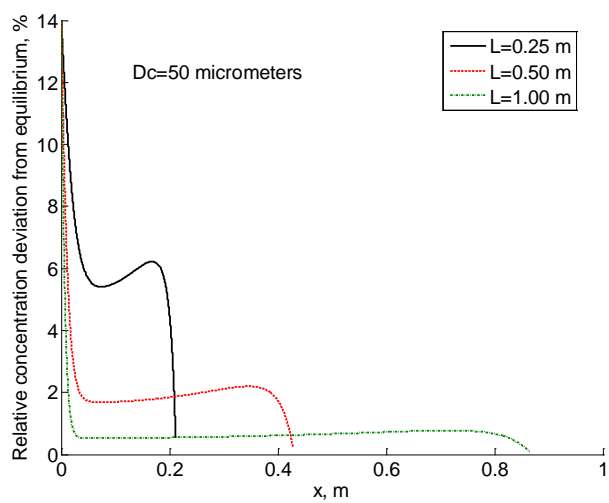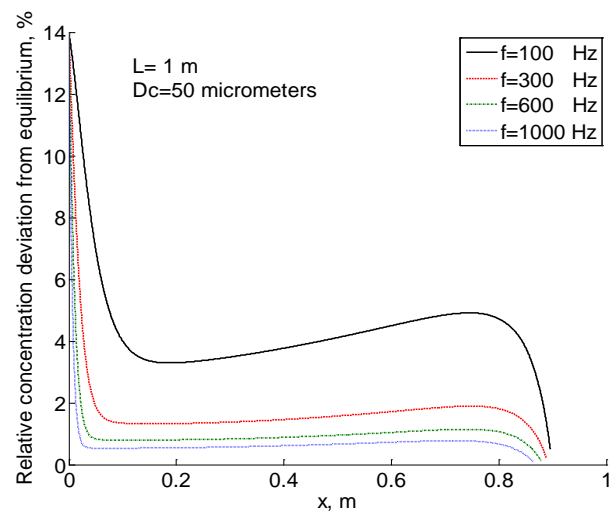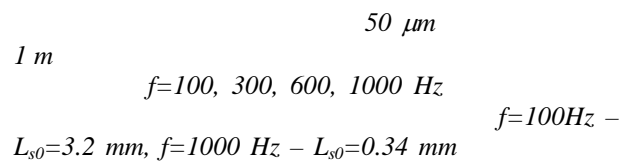
Figure 7:

CONCLUSIONS

APPENDIX A

ACKNOWLEDGEMENT

$Ca<0.04$

$$\frac{\Delta p}{L} = \frac{2\rho_L f U_m^{\,2}}{D}\left(1-\varepsilon\right) = \frac{32}{D^2}\mu_L U_m \varepsilon_L\left(1+0.17\frac{D}{L_{sl}}\left(\frac{Re}{Ca}\right)^{\frac{1}{3}}\right)$$

REFERENCES

L_{sl} $\qquad\qquad U_m=U_{GS}+U_{LS}$

$$U_{GS} = \frac{Q_G}{F}$$

Proc. IMechE 222. Part C: J. Mechanical Engineering Science

$$U_{LS} = \frac{Q_L}{F}$$

F

Physics of Fluids, **12**

Q_G $\qquad Q_L$

$\varepsilon_L=1\text{-}\varepsilon$

Chem. Eng. Sci., **52**

$$U_m\varepsilon_L = \left(U_{GS}+U_{LS}\right)\varepsilon_L = \frac{Q_G+Q_L}{F}\left(1-\varepsilon\right) = \frac{Q_L}{F} = U_{LS}$$

Transport Phenomena

J. Fluid Mech., **10**

Canadian Journal of Chemical Engineering **70**

Computers and Chem. Eng., **13,**

$$L_{sl} = \frac{W_{se}}{\pi R_c^2} = \frac{W_s}{\pi R_c^2} - \frac{2\pi\left(R_c - \frac{\delta}{2}\right)\delta L_{lB}}{\pi R_c^2} \approx \frac{W_s}{\pi R_c^2} - 2\frac{\delta}{R_c}L_{lB}$$

AIChE J., **51**

R_c $\qquad\qquad W_s$

W_{se} $\qquad\qquad\qquad W_s$

Chem. Eng. Sci **54**

δ

Langmuir, **19**

Lab on a Chip

et al.

J. Fluid Mech. **10**

8th International Conference on CFD in Oil & Gas, Metallurgical and Process Industries
SINTEF/NTNU, Trondheim NORWAY
21-23 June 2011

CFD11-94

LATTICE BOLTZMANN MICROCHANNEL SIMULATIONS VIA BINARY LIQUID MODEL

Alexandr KUZMIN[1][*], **Dmitry ESKIN**[2][†], **Jos DERKSEN**[3][‡]

[1]Chemical and Materials Engineering, University of Alberta, 9107-116 Street, T6G 2V4 Edmonton,

CANADA

[2]DBR Schlumberger Technology Center, 9450 17 Ave NW, T6N 1M9 Edmonton, CANADA

[3]Chemical and Materials Engineering, University of Alberta, 9107-116 Street, T6G 2V4 Edmonton,

CANADA

[*] E-mail: kuzmin@ualberta.ca
[†] E-mail: deskin@slb.com
[‡] E-mail: jos@ualberta.ca

ABSTRACT

In this work a free-energy binary liquid lattice Boltzmann scheme is used to simulate Taylor/Bretherton flow in a micro-channel where elongated gas bubbles move through a liquid with thin liquid films between the bubbles and the channel walls. The main focus of our work is a feasibility study of the binary-liquid model lattice Boltzmann model to simulate the Bretherton/Taylor phenomena. The numerical scheme has a diffuse interface, and we thoroughly assess resolution requirements for correctly resolving the liquid film and bubble motion. The simulations are two-dimensional and three-dimensional and span a capillary number range of 0.03 to 0.8 (for 2D) and range of 0.1 to 1.0 where the capillary number is based on the liquid's viscosity, the velocity of the bubble's interface, and the interfacial tension. The flow is driven by a body force, and periodic boundary conditions are applied in the streamwise direction. We obtain grid independent results as long as the liquid film thickness is at least two times the width of the diffuse interface. The results show that the lattice Boltzmann free energy binary liquid model can be used to simulate the Bretherton problem with good accuracy.

Keywords: CFD, Multiphase Flows, Lattice Boltzmann Method, Microchannel flow, Bretherton problem, Binary liquid, Free energy method.

NOMENCLATURE

Greek Symbols
ρ Uniform density, $[kg/m^3]$
μ LBM chemical potential, $[lbu]$
ν LBM dynamic viscosity, $[lbu]$
τ LBM relaxation parameter, $[lbu]$
γ LBM intefacial tension, $[lbu]$
ξ LBM characteristic length for the interface thickness, $[nodes]$.

Latin Symbols
$\frac{dP}{dx}$ LBM pressure gradient, $[lbu]$
k LBM intefacial tension coefficient, $[lbu]$
A LBM free energy model parameter, $[lbu]$
U_{bubble} Bubble interface velocity magnitude, $[m/s]$.

Sub/superscripts
liq   Liquid
gas   Gas
i   Index related to the lattice direction
α, β Index related to the coordinate *x*, *y* or *z* direction

INTRODUCTION

The Taylor/Bretherton (Bretherton, 1960) flow deals with long gas bubbles moving through liquid in narrow channels. Depending on the geometry it was found that the deposited film thickness is a complicated function of the capillary number *Ca*, Eq. (1). For example, the deposited film thickness is proportional to $Ca^{2/3}$ in the range of small capillary numbers for circular channels (Bretherton, 1960; Heil, 2001).

The problem of predicting flow patterns and associated mass transfers for the Bretheron-type flows is of significant interests for chemical industry as it is widely used in chemical monolith microreactors (Kreutzer *et al.*, 2005). While it is possible to calculate the flow analytically for small capillary numbers (Bretherton, 1960), it's not possible to extrapolate it to the wider range of capillary numbers used in the chemical industry. Thus, the desire of consistent numerical simulations arises.

For what follows we distinguish two- and three-dimensional cases and give a detailed acount of the literature.

2D case Bretherton made analytical assymptotic analysis and predicted the $Ca^{2/3}$ dependency of the film thickness for the circular shaped microchannels in the range of the small capillary numbers (typically Ca < 0.003), where capillary number is defined as:

$$\mathrm{Ca} = \frac{\mu_{\mathrm{liq}} U_{\mathrm{bubble}}}{\gamma}, \qquad (1)$$

where μ_{liq} is the liquid's kinematic viscosity, U_{bubble} is the bubble velocity, and γ is the interfacial tension between gas and liquid. For the case of the continuous interface models, U_{bubble} is the interface velocity.

Later on, it was realized (Wong *et al.*, 1995a,b) that the film thickness is proportional to $Ca^{2/3}$ only in the certain region behind the front meniscus. Overall, the film thickness varies over the bubble length for bubbles of finite or infinite length (Hazel and Heil, 2002). Numerical simulations (Giavedoni and Saita, 1997) and experimental studies (Kreutzer *et al.*, 2005) showed a deviation from the $Ca^{2/3}$ rule and Reynolds number effects on the film thickness for capillary numbers larger than 0.003.

To consistently predict a flow pattern for capillaries in different ranges of the capillary number, simulations have been conducted. The simulations are typically validated with analytical solutions in the range of the small

capillary numbers and then extended to more practical regimes.

There are a number of numerical methods which were used for the simulation of the Taylor/Bretherton flow. van Baten and Krishna (2004) studied the mass transfer and film thickness for rising bubbles in a circular capillary using the finite volume method. Kreutzer *et al.* (2005) also used the finite volume method to perform simulations of a circular capillary for a number of different Reynolds and capillary numbers. Heil (2001) and Ingham and Ritchie (1992) studied gas finger propagation in a two-dimensional channel for a range of Reynolds and capillary numbers using the finite element method. Giavedoni and Saita (1997) performed cross validation of the finite element solution with previously published results. The solutions were obtained for circular and planar cases. Smooth particle hydrodynamics (SPH) is presented by Liu *et al.* (2007). However except showing that the SPH is able to reproduce the gas-liquid interface, there is no thorough study of the deposited film thickness.

3D case In comparison with the two-dimensional Bretherton flow there is a vast number of experimental results available for the three-dimensional case. For instance, Han and Shikazono (2009) obtained experimental results for the deposition length dependency on the capillary number for ethanol/air and water/air mixtures and for square, circular and triangular shaped microchannels. Thulasidas *et al.* (1995) performed a lot of experiments for a buble-train flow in capillaries of circular and square cross section for horizontal, upward and downward flows. The interested reader is referred to these works for comprehensive experimental correlations.

The experimental works supported by numerical simulations reveal interesting phenomena occuring in three-dimensional geometry cases. It was found (Hazel and Heil, 2002; Wong *et al.*, 1995a) that for rectangular or square shaped capillaries there is a transition for a certain capillary number, where the bubble crosssection changes from the non-axisymmetric to axisymmetric case, Fig. 5. From hereon, we limit ourselves to the case of microchannels with square crosssections. Non-axisymmetric case is attributed to the situation where the axial radius is different from the diagonal radius and the bubble has the non-circular shape in the channel crossection. In this case the bubble shape mimics the shape of the square and looks like a rounded square. The dependence of the diagonal and axial radii on the capillary number is shown in Fig. 1. The transition capillary number $(\widehat{Ca})$ between non-axisymmetric case and symmetric is indicated in a number of works as $\widehat{Ca} = 0.04$ (Thulasidas *et al.*, 1995), $\widehat{Ca} = 0.1$ (Kolb and Cerro, 1993), $\widehat{Ca} = 0.033$ (Hazel and Heil, 2002). If the capillary number is larger than the critical capillary number, i.e. $Ca > \widehat{Ca}$, then the bubble becomes axisymmetric with the radius of the droplet dependant on the capillary number. One example for the bubble radii dependence on the capillary number is in Fig. 1.

Hazel and Heil (2002) also indicated another interesting phenomenon. They indicated the transition capillary number where the streamlines pattern changes from having a vortex in front of the bubble and not having it
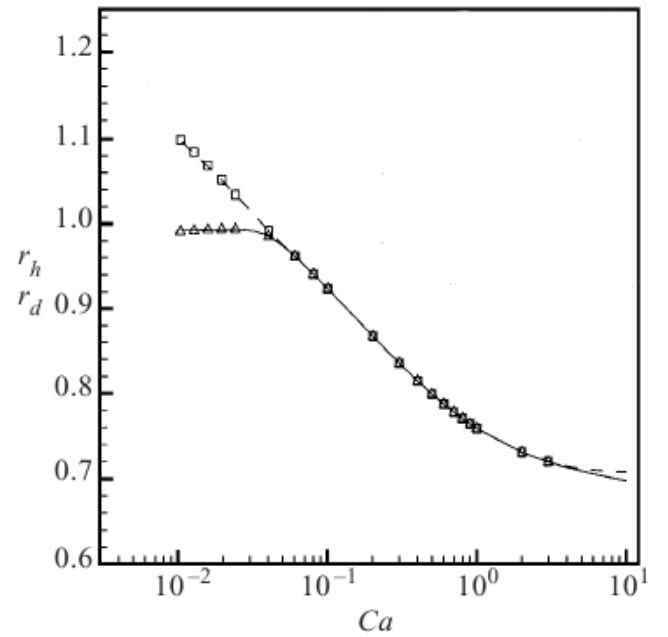

Figure 1: Hazel and Heil (2002) results for the variation of the deposited liquid for the range of capillary number. One can see the asymmetry between diagonal (r_d) and axial r_h radii for the capillary number $Ca \leq \widehat{Ca} = 0.04$. Courtesy of Hazel and Heil (2002).

for larger capilllary numbers, Fig. 7. For the square channel the critical number is $Ca = 0.691$.

There are also a number of numerical works for the three-dimensional case. For instance, Wong *et al.* (1995a,b) studied three-dimensional bubbles in polygonal capillaries and calculated bubble shapes for different slug and bubble cross sections and menisci appearance. Hazel and Heil (2002) performed three-dimensional simulations for circular shaped, square and rectangular shaped capillaries. Also, they investigated gravitational effects for circular shaped capillaries. They also found an empirical correlation which allows one to place different aspect ratio rectangular channels simulation results on one curve. Liu and Wang (2008) performed numerical simulations by the VOF technique for the non-circular shaped capillaries as square and triangular shaped capillaries. The VOF technique is the continuous interface method based on a non-uniform grid. It is of particular interest for us to compare it with the continuous interface method by the LBM implementation. They also performed numerical simulations for the determination of the critical capillary number $\widehat{Ca}$.

Almost all the simulations indicated above for the two-dimensional and three-dimensional cases are performed with the help of the finite element method (Ingham and Ritchie, 1992; Heil, 2001; Hazel and Heil, 2002). However, this method is of limited applicability for problems involving complex geometries, free interface motion, or for problems involving coalescence and/or droplet breakup. The continuous interface models are more flexible for this kind of simulations. However, if the interface is smeared out over several grid nodes, the question of proper film resolution in comparison with the interface resolution arises. Therefore, the *goal* of this work is to reproduce the numerical results and

phenomena presented above with the help of the continuous interface binary liquid free energy lattice Boltzmann model. We focus on exploring the parameter range of the binary liquid lattice Boltzmann method for correctly resolving the flow in a range of capillary numbers.

The lattice Boltzmann method (LBM) has emerged as a successful method to simulate a wide variety of phenomena including hydrodynamics (Yu *et al.*, 2003), thermal flows (Ansumali *et al.*, 2003), microflows (Ansumali *et al.*, 2006), ferrofluids (Falcucci *et al.*, 2009), and multiphase flows (Swift *et al.*, 1995; Shan and Chen, 1994). Thanks to its kinetic nature, LBM as a particle method easily tackles complex geometries and allows incorporation of physical phenomena on the microscopic level, as in the case of multiphase models. Most multiphase lattice Boltzmann models (Swift *et al.*, 1995; Shan and Chen, 1994) resolve the interface using continuous interface methods where the interface spans over several grid nodes. Such a representation brings issues of the film thickness resolution versus interface resolution – the diffuse interface should be dealt with in such a way as to have a negligible effect on the physics of the film.

The binary liquid free-energy LB model due to Swift *et al.* (1995) we used simulates two liquids with the assumption of uniform overall density. While the classical Bretherton problem is stated for gas and liquid, which are of significantly different densities and viscosities, it was indicated (Bretherton, 1960) that inertia effects can be neglected. Moreover, the results of Giavedoni and Saita (1997) and Heil (2001) show negligible Reynolds number effects on the film thickness for a relatively wide range of Reynolds numbers. Therefore, a major governing factor for microchannel flows is not the density ratio, but the viscosity ratio. The goal of this work is to do a feasibility study of the LBM binary-liquid model to simulate and correctly predict flow patterns for the Bretherton/Taylor problem. The work results are in good agreement with other simulations (Giavedoni and Saita, 1997; Heil, 2001; Hazel and Heil, 2002).

One should also acknowledge the works of Ledesma-Aguilar *et al.* (2007) on menisci in thin films for fingering phenomena. Yang *et al.* (2002) performed lattice Boltzmann simulations of two-dimensional channel flows for a relatively large capillary numbers, and found discrepancies with the classical Bretherton theory, which is limited to the low capillary number regime (Giavedoni and Saita, 1997).

The paper is organized as follows. First, we briefly explain the binary liquid lattice Boltzmann model. Then, the preliminary results for the two-dimensional and for the three-dimensional case are presented in the results section. The paper is concluded with a summary of the main findings.

LATTICE BOLTZMANN BINARY LIQUID MODEL

The lattice Boltzmann equation (LBE) operates on a rectangular grid representing the physical domain. It utilizes probability distribution functions (also known as particle populations) containing information about macroscopic variables, such as fluid density and momentum. LBE consists of two parts: a local collision step, and a propagation step which transports information from one node to another in certain directions specified by the discrete velocity set. The LBE is

typically implemented as follows:

$$f_i^*(\boldsymbol{x},t) = \omega f_i^{eq}(\boldsymbol{x},t) - (1-\omega)f_i(\boldsymbol{x},t) + F_i, \quad \text{collision step}$$
$$f_i(\boldsymbol{x}+\boldsymbol{c_i},t+1) = f_i^*(\boldsymbol{x},t), \qquad\qquad \text{propagation step,} \tag{2}$$

where f_i is the probability distribution function in the direction $\boldsymbol{c_i}$, ω is the relaxation parameter, and F_i is the external force population.

The binary fluid LB model is based on a free-energy functional (Swift *et al.*, 1995; Landau and Lifshitz, 1987), and operates with two sets of populations: one to track the pressure and the velocity fields, and another to represent the phase field ϕ indicating gas or liquid. The equilibrium populations (Pooley *et al.*, 2008) are defined as:

$$
\begin{aligned}
f_i^{eq} &= w_i\left(3p_0 - k\phi\Delta\phi + \frac{u_\alpha c_{i\alpha}}{c_s^2} + \frac{Q_{i\alpha\beta}u_\alpha u_\beta}{2c_s^4}\right)\\
&\quad + kw_i^{\alpha\beta}\partial_\alpha\phi\partial_\beta\phi, i = 1 \div Q-1\\
f_0^{eq} &= \rho - \sum_{i\neq 0} f_i^{eq}\\
g_i^{eq} &= w_i\left(\Gamma\mu + \frac{\phi c_{i\alpha}u_{i\alpha}}{c_s^2} + \phi\frac{Q_{i\alpha\beta}u_\alpha u_\beta}{2c_s^4}\right), i = 1\div Q-1\\
g_0^{eq} &= \phi - \sum_{i\neq 0} g_i^{eq},
\end{aligned}
\tag{3}
$$

where Γ is the mobility parameter; the chemical potential $\mu = -A\phi + A\phi^3 - k\Delta\phi$; k is the parameter related to the surface tension; A is the parameter of the free-energy model; Q is the number of the directions (9 and 19 for the *D2Q9* and *D3Q19* models, correspondingly); the tensor $Q_{i\alpha\beta} = c_{i\alpha}c_{i\beta} - c_s^2\delta_{\alpha\beta}$ with the sound speed parameter $c_s^2 = 1/3$. The bulk pressure is expressed as $p_0 = c_s^2\rho + A(-0.5\phi^2 + 0.75\phi^4)$. The particular weights and velocity sets for the *D2Q9* and *D3Q15* models are indicated in Appendix A.

The set of equations (3) restores the macroscopic fluid equations as:

$$
\begin{aligned}
&\partial_t\rho + \partial_\alpha\rho u_\alpha = 0\\
&\rho\left(\partial_t + u_\beta\partial_\beta\right)u_\alpha = -\partial_\beta P_{\alpha\beta} + \nu\partial_\beta\left(\rho\partial_\alpha u_\beta + \rho\partial_\beta u_\alpha\right) \quad (4)\\
&\partial_t\phi + \partial_\alpha\phi u_\alpha = M\partial_{\beta\beta}^2\mu,
\end{aligned}
$$

where $\nu = c_s^2(\tau - 1/2)$ is the dynamic viscosity, $M = \Gamma(\tau_\phi - 1/2)$ is the mobility parameter, and $\tau = \frac{1}{\omega}$ and τ_ϕ are the relaxation parameters of density and phase fields.

The system allows the separation of the liquid phase with $\phi = 1$ and a so-called gas phase with $\phi = -1$. The relaxation time is taken as linearly dependent on the relaxation times τ_{gas} and τ_{liq}: $\tau = \tau_{\text{gas}} + \frac{\phi+1}{2}(\tau_{\text{liq}} - \tau_{\text{gas}})$. This allows to change viscosity from the gas viscosity $\nu_{\text{gas}} = \frac{1}{3}\left(\tau_{\text{gas}} - \frac{1}{2}\right)$ to the liquid viscosity $\nu_{\text{liq}} = \frac{1}{3}\left(\tau_{\text{liq}} - \frac{1}{2}\right)$ while phase changes accordingly. The surface tension in the framework of the binary liquid model is $\sqrt{\frac{8kA}{9}}$.

NUMERICAL BENCHMARK

To be able to properly simulate and compare simulation results with data published in the literature, one needs to design a numerical benchmark addressing all the challenges for the lattice Boltzmann method. That includes the diffuse nature of the interface which needs to have a negligible effect on the results. Also, as far as the density is uniform, the binary liquid model can address only different viscosities of

gas and liquid. Another challenge is boundary conditions because one needs to couple inlet and outlet boundary conditions (Hazel and Heil, 2002) for the film thickness to establish. The geometry of the problem is also of concern. In the literature, most numerical simulations are done for a channel with circular cross section, which is quite difficult to address in terms of lattice Boltzmann framework. We thoroughly discuss all the challenges associated with the lattice Boltzmann microchannel simulations in our recent work (Kuzmin *et al.*, 2010).

Given all the concerns and challenges, the suggested lattice Boltzmann framework is a two-dimensional flow between plates and three-dimensional square shaped microchannels, both driven by a body force. We limit ourselves to the study of body force driven flows, because of their simplicity and better numerical stability. This implies that we can use the periodic boundary conditions in the streamwise direction. As soon as the periodic boundary conditions are applied, not a single bubble but a bubble train is simulated. In this case one needs to ensure that the channel length is large enough to exclude mutual bubble influence. The channel length is taken to be 15 channel heights with the bubble length to be 5 channel heights. The chosen numbers are shown to be sufficient to give results consistent with the theory, i.e. for the the film thickness to stabilize and to exclude mutual bubble influence. The geometry dimensions are represented in Fig. 2.
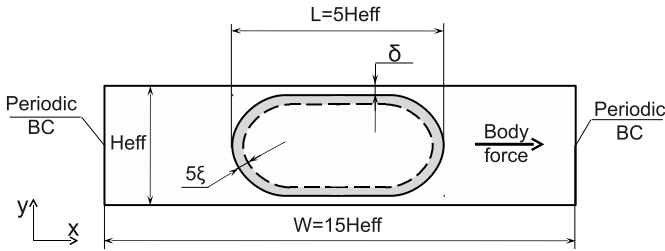

Figure 2: The $x - y$ benchmark crosssection. δ corresponds to the film thickness. 5ξ corresponds to the interface thickness. We take the microchannel length to be 15 times larger than its height. The threedimensional benchmark has the same geometry extending it in the z dimension to have a square shaped crosssection.

RESULTS

2D results

Two-dimensional binary-liquid simulations are presented in our recent work (Kuzmin *et al.*, 2010). Here we outline the two most important results. The first one addresses the question of how the interface should be resolved to obtain grid independent result. Though the simulations are performed for the lattice Boltzmann model, the results can be applied for any uniform grid continuous interface method. The second part of results are comparisons with the literature for the film thickness dependency on the capillary number.

Grid refinement

To properly estimate the interface resolution one needs to study the convergence as a function of the grid resolution. To do that the grid resolution is varied while all remaining parameters, including the bubble velocity and the capillary number, are fixed. Our goal is to determine the ratio of the interface thickness to the film thickness at which results are no longer dependent on the grid resolution.

N_x	N_y	δ	U_{bubble}	$\frac{5\xi}{H_{\text{film}}}$	N_{iter}
1500	102	0.0694	0.0041	0.824	200000
1875	127	0.0688	0.0041	0.646	250000
2250	152	0.0676	0.0040	0.539	300000
2625	177	0.0679	0.0040	0.453	350000
3000	202	0.0668	0.0041	0.400	400000
3375	227	0.0663	0.0039	0.355	450000

Table 1: The parameters and results for grid resolution. The simulated domain is of size $N_x \times N_y$. U_{bubble} is the interface velocity of the bubble center measured at the front meniscus. N_{iter} is the number of simulation time iterations. 5ξ is the interface thickness. $H_{\text{film}} = \delta(N_y - 2)$ is the size of the film in lattice Boltzmann units.

We performed a number of simulations for grids indicated in Table 1. Other parameters are defined as $k = 0.04$, $A = 0.04$ and $\Gamma = 1.0$. Note that in the case of the half-way bounce-back walls (Yu *et al.*, 2003) which are used in the simulations one needs to calculate the film thickness as:

$$\delta = (\phi_0 - 0.5)/(N_y - 2) = (\phi_0 - 0.5)/H_{\text{eff}}, \qquad (5)$$

where ϕ_0 is the grid coordinate where phase field is 0, $H_{\text{eff}} = N_y - 2$ is the effective channel height. If the grid size in the y direction is N_y, then one has $N_y - 1$ regions representing the physical domain with top and bottom nodes being bounce-back nodes. Then the effective wall location is in the middle between bounce-back and fluid nodes. Overall there are $N_y - 2$ nodes representing the fluid. Note that it is a simplification to impose the boundary in the middle between the bounce-back node and the fluid node. The location of the wall for bounce-back nodes is viscosity dependent (Ginzburg and d'Humières, 2003). However, the effective location of the wall for the multiphase models to the best authors' knowledge is not yet derived. The bubble is initialized as a rectangular box with coordinates $y = 7 \times \frac{H_{\text{eff}}}{100} \ldots N_y - 7 \times \frac{H_{\text{eff}}}{100} - 1$, $x = \frac{N_x}{3} \ldots \frac{2N_x}{3}$ and phase $\phi_{\text{bubble}} = -1$. All other nodes are initialized with the phase field $\phi = 1$. The initialization procedure is done to keep the self-similarity. The initial width and body force were chosen to aim for the capillary number Ca $= 0.05$ (Kuzmin *et al.*, 2010). After choosing the reference parameters, the grid refinement procedure needs to keep the macroscopic parameters constant. It is easy to check that it yields the following quantity to be independent of grid size $H_{\text{eff}}^2 \frac{dP}{dx} = (N_y - 2)^2 \frac{dP}{dx} = \text{const}$. For the grid $H_{\text{eff}} = 100$ we chose the body force as $\frac{dP}{dx} = 1.508 \times 10^{-6}$ lattice units. The simulation results in terms of the film thickness δ, interface bubble velocity U_{bubble} and associated capillary numbers are summarized in Table 1. The unified scaled profiles are shown in Fig. 3. One can see that results converge for $H_{\text{eff}} \geq 175$. To calculate how well the interface is resolved, the ratio of the interface thickness to the film thickness is calculated. The interface itself occupies approximately 5ξ, where $\xi = \sqrt{k/A} = 1$. The ratio of the interface thickness to the film thickness $5\xi/H_{\text{film}}$ is shown in Table 1.

Based on these results one can conclude that the interface needs to be resolved as $40 - 50$ percent of the expected film thickness for simulations to be grid independent. We further examine the velocities in the center of the bubble to calculate the capillary number. One can see from Table 1 that the bubble velocities are consistent and the calculated capillary number corresponding to these velocities is 0.07.
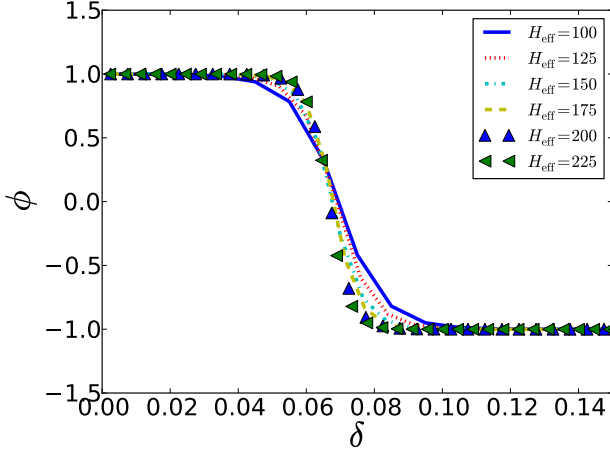
Figure 3: Grid-refined profiles for the effective channel widths $H_{\text{eff}} = 100, 125, 150, 175, 200, 225$. δ is scaled on H_{eff} and $\delta = 0$ corresponds to the wall location. The profiles were taken at $x = 14$ (nondimensional coordinates). Capillary number we aim for is Ca $= 0.05$. The capillary number obtained from simulations Ca $= 0.07$.

Capillary number region

The purpose of this section is to validate the correlations of Giavedoni and Saita (1997) and Heil (2001) for a film thickness dependancy on the range of capillary numbers. Because of limited computational resources, we skip the small capillary numbers and make calculations for the range of capillary numbers $0.03 - 0.8$, which is a computationally reasonable task. To be consistent with the grid independant results, we choose the grid to be 202×3001. Then 5 lattice Boltzmann units do not occupy more than 60 percent of the effective film thickness. Because the simulation gets unstable with smaller grids and larger gradients, all the capillary number simulations were performed on the same grid. To properly initialize the body force, the proportionality law was utilized. The forcing $6 \cdot 10^{-6}/16$ was chosen to obtain the predicted capillary number 0.05. The forcing for other grids can be obtained using simple proportionality relationships:

$$\begin{aligned}
\text{Ca}_{\text{lit}} &\propto U_{\text{bubble}} \\
U_{\text{bubble}} &\propto \frac{\mathrm{d}P}{\mathrm{d}x} N_y^2 \\
\text{Ca}_{\text{lit}} &\propto \frac{\mathrm{d}P}{\mathrm{d}x} N_y^2 \text{ or} \\
\frac{\mathrm{d}P}{\mathrm{d}x} &\propto \frac{\text{Ca}_{\text{lit}}}{N_y^2},
\end{aligned} \tag{6}$$

where the subscript „lit" stands for the predicted capillary number (Giavedoni and Saita, 1997; Heil, 2001). The grid number N_y is not involved because all simulations are conducted on the same grid. The pressure gradient can be obtained through the capillary number ratio:

$$\frac{\mathrm{d}P}{\mathrm{d}x} = 6 \cdot 10^{-6}/16 \frac{\text{Ca}_{\text{lit}}}{0.05} \tag{7}$$

The film thickness is initialized through the ratio of capillary numbers as well:

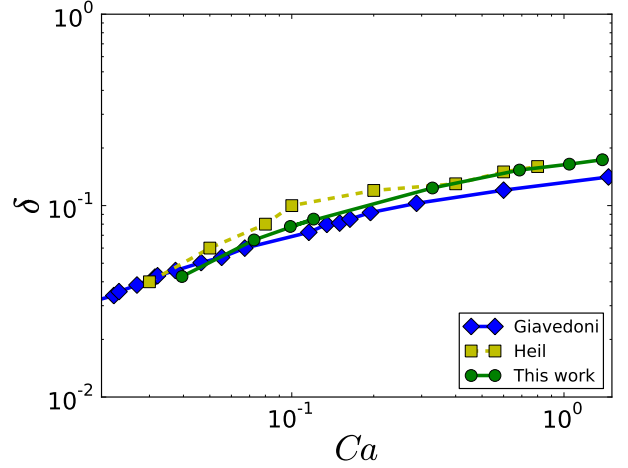$$w = 12 \frac{\text{Ca}_{\text{lit}}}{0.05}$$

Figure 4: A comparison between simulation results and results of Giavedoni and Saita (1997) and Heil (2001). One can see a reasonable agreement. The plots depict the film thickness as a function of the the capillary number.

Ca_{lit}	δ_{lit}	δ	U_{bubble}	Ca
0.03	0.04	0.042	0.0022	0.039
0.05	0.06	0.066	0.0041	0.072
0.08	0.08	0.085	0.0068	0.120
0.1	0.1	0.077	0.0055	0.098
0.2	0.12	0.123	0.0185	0.328
0.4	0.13	0.153	0.0388	0.686
0.6	0.15	0.164	0.0592	1.046
0.8	0.16	0.173	0.0782	1.383

Table 2: The parameters and results for capillary number region simulations. δ_{lit} is the film thickness with corresponding Ca_{lit} taken from literature. δ_{sim} is the simulation film thickness with corresponding Ca. U_{bubble} is the bubble interface velocity. Ca is based on the interface bubble velocity U_{bubble}.

The results obtained after $2 \cdot 10^5$ steps are presented in Table 2. One can see that the calculated capillary numbers are over-predicted (the actual capillary number is larger than the capillar number we aim for, Ca $>$ Ca$_{\text{lit}}$). We extracted the data of Giavedoni and Saita (1997) and Heil (2001) with the help of software "Engauge Digitizer" and compared them with our results (see Fig. 4).

3D results

One can see from Fig. 1 that the difference between the axial and diagonal radii happens at the capillary numbers less than 0.1. However the axial radius has a value around $0.99H_{\text{eff}}$. Therefore, the film occupies $0.01H_{\text{eff}}$ which needs to be resolved with at minimum 10 lattice units (see results for grid independency). This condition implies grids to be at least size $1000 \times 1000 \times 15000$, which is not a computationally feasible task. Even the symmetric and non-symmetric profiles are obtained by current simulations, Fig. 5, the grid independence is only guaranteed for symmetric cases. Therefore our target simulations are for Ca ≥ 0.1, where the axial radius equals to the diagonal radius. In what follows we will show two particular simulations. One is for the dependance of the bubble radius on the capillary number. Another one is for the velocity patterns. In comparison with simulations

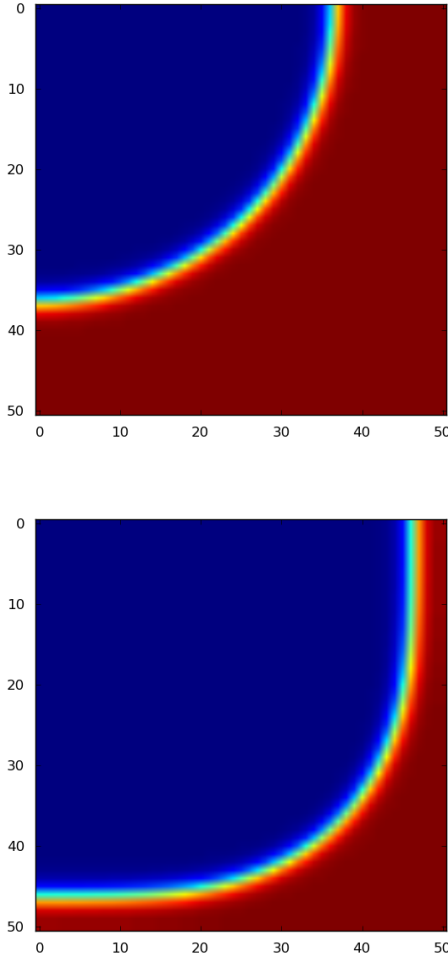of Hazel and Heil (2002) the transition capillary number is located in the range $0.47 < Ca < 0.63$.

Figure 5: Symmetric ($Ca = 0.63$) and non-symmetric ($Ca = 0.026$) crosssections in the middle of the bubble. One can see that for the symmetric profile $R_h = R_d$ and for the antisymmetric $R_h \neq R_d$.

We also simulate only the quarter of the channel by imposing the mirror boundary conditions. This gives an improvement in memory requirements and simulation time by factor of four.

Capillary region

We performed a number of simulations of grid size $52 \times 52 \times 1500$ for the quarter of geometry and of refined grid size $82 \times 82 \times 1500$. Other parameters were chosen as $k = 0.04, A = 0.04$, and $\Gamma = 1.0$.

The results are presented in Fig. 6 along with reference data obtained by Hazel and Heil (2002). One can see that refined grids produce the same results. Thus, the grid of size $52 \times 52 \times 1500$ for the quarter of geometry is enough to obtain grid independent results for $Ca \geq 0.1$. The capillary number is calculated based on the interface velocity along the center axis. The simulations results as radii values are underestimated in comparison with the reference data by Hazel and Heil (2002). This can be explained by the influence of inertia. For example, one can refer to experimental data obtained by Han and Shikazono (2009) with differ-
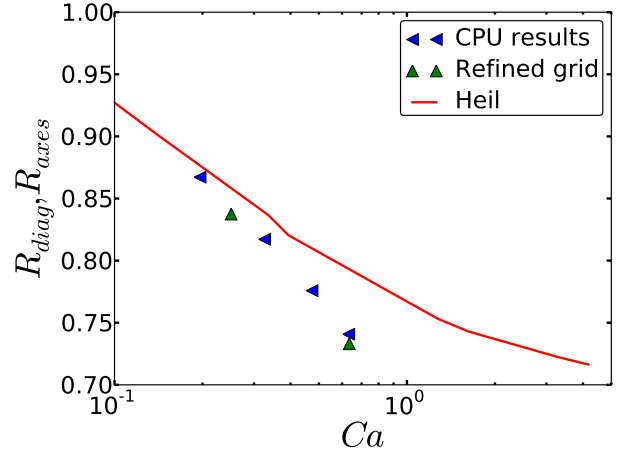

Figure 6: The comparison between reference data by Hazel and Heil (2002) and simulation for the axial and the diagonal radiuses versus capillary numbers.

ent liquids where real liquid results can be located below or above the reference curve.

Velocity pattern

We examined velocity patterns to identify the moment of the streamlines pattern change. We chose two representative capillary numbers as $Ca = 0.47$ and $Ca = 0.61$. Scaled velocity profiles in the center plane are shown in Fig. 7. For demonstration purposes, we restricted the size of shown velocity vector maps to apply certain scaling and to be able to show the vortex in the slug. Velocity vector maps are generated in the reference frame of the moving bubble. One can see a clear transition between associated patterns. The transition capillary number (Hazel and Heil, 2002) is slightly higher than the simulation results. We outline that this fact can be attributed to the binary-liquid simulations instead of the free-surface classical Bretherton problem.

CONCLUSION

This work presents numerical studies of the Bretherton/Taylor problem using the binary liquid lattice Boltzmann method. The bubble was chosen sufficiently long for the film thickness to stabilize, and periodic boundary conditions were used to keep the simulations robust. The distance between bubbles was taken large enough to minimize the mutual influence of neighboring bubbles. The computational results in terms of capillary number dependence and shape of the bubbles show consistency with the previously published data in two and three dimensions. The simulations show that in the range of low capillary numbers the binary liquid model can be used to simulate gas finger/bubbles propagation in the microchannel. The model is able to catch not only the film thicknesses but also the change in velocity patterns. An examination of the influence of grid resolution on the results allowed us to determine that the phase interface should be resolved as at least 50 percent of the film thickness in order for the simulations to be grid independent. Though our results are specific to the binary liquid lattice Boltzmann method, the numerical hints and procedures can be used for any continuous interface method.
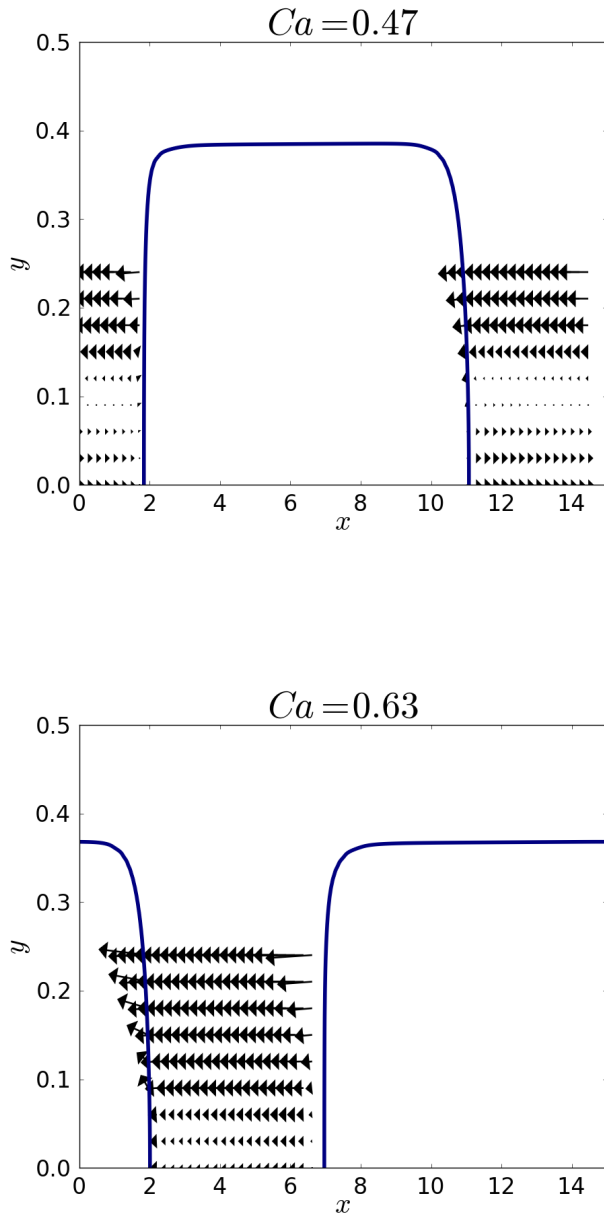
Figure 7: Velocity vector maps for Ca = 0.47 and Ca = 0.63. One can see that there are no vortexes created before the bubble for Ca = 0.63. The transition happens between Ca = 0.47 and Ca = 0.63, which is a different value than Ca = 0.69 (Hazel and Heil, 2002).

REFERENCES

ANSUMALI, S. *et al.* (2003). "Minimal entropic kinetic models for hydrodynamics". *Europhys. Lett.*, **63lu(6)**, 798–804.

ANSUMALI, S. *et al.* (2006). "Entropic lattice Boltzmann method for microflows". *Physica A*, **359**, 289–305.

BRETHERTON, F. (1960). "The motion of long bubbles in tubes". *J Fluid Mech.*, **10(2)**, 166–188.

FALCUCCI, G. *et al.* (2009). "Rupture of a ferrofluid droplet in external magnetic fields using a single-component lattice Boltzmann model for nonideal fluids". *Phys. Rev. E*, **79(056706)**, 1–5.

GIAVEDONI, M. and SAITA, F. (1997). "The axisymmetric and plane cases of a gas phase steadily displacing a Newtonian liquid - A simultaneous solution of the governing equations". *Phys. Fluids*, **9(8)**, 2420–2428.

GINZBURG, I. and D'HUMIÈRES, D. (2003). "Multireflection boundary conditions for lattice Boltzmann models". *Phys. Rev. E*, **68(066614)**, 1–30.

HAN, Y. and SHIKAZONO, N. (2009). "Measurement of liquid film thickness in micro square channel". *Int. J. Multiph. Flow*, **35**, 896–903.

HAZEL, A. and HEIL, M. (2002). "The steady propagation of a semi-infinite bubble into a tube of elliptical or rectangular cross-section". *J. Fluid Mech.*, **470**, 91–114.

HEIL, M. (2001). "Finite Reynolds number effects in the Bretherton problem". *Phys. Fluids*, **13(9)**, 2517–2521.

INGHAM, D. and RITCHIE, J. (1992). "The motion of a semi-infinite bubble between parallel plates". *Z. Math. Phys.*, **43**, 191–206.

KOLB, W. and CERRO, R. (1993). "Film Flow in the Space between a Circular Bubble and a Square tube". *J. Coll. Int. Sci.*, **159**, 302–311.

KREUTZER, M. *et al.* (2005). "The pressure drop experiment to determine slug lengths in mulitphase monoliths". *Catalysis Today*, **105**, 667–672.

KUZMIN, A. *et al.* (2010). "Simulations of gravity-driven flow of binary liquids in microchannels". *Chem. Eng. J.*, **submitted**, 1–20.

LANDAU, L. and LIFSHITZ, E. (1987). *Fluid Mechanics*. Pergamon, Oxford.

LEDESMA-AGUILAR, R. *et al.* (2007). "Three-dimensional aspects of fluid flows in channels. II. Effects of meniscus and thin film regimes on viscous fingers". *Phys. Fluids*, **19(102113)**, 1–8.

LIU, D. and WANG, S. (2008). "Hydrodynamics of Taylor flow in noncircular capillaries". *Chem. Eng. and Processing*, **47**, 2098–2106.

LIU, M. *et al.* (2007). "Dissipative particle dynamics simulation of multiphase ïñĆuid ïñĆow in microchannels and microchannel networks". *Phys. Fluids*, **19(033302)**, 1–11.

POOLEY, C. *et al.* (2008). "Contact line dynamics in binary lattice Boltzmann simulations". *Phys. Rev. E*, **78(056709)**, 1–9.

SHAN, X. and CHEN, H. (1994). "Simulation of nonideal gases and gas-liquid phase transitions by the lattice Boltzmann Equation". *Phys. Rev. E*, **49(4)**, 2941–2948.

SWIFT, M. *et al.* (1995). "Lattice Boltzmann Simulation of Nonideal Fluids". *Phys. Rev. Lett.*, **75(5)**, 831–834.

THULASIDAS, T. *et al.* (1995). "Bubble-train flow in

capillaries of circular and square cross section". *Chem. Eng. Sci.*, **50(2)**, 183–199.

VAN BATEN, J. and KRISHNA, R. (2004). "CFD simulations of mass transfer from Taylor bubbles rising in circular capillaries". *Chem. Eng. Sc.*, **59**, 2535–2545.

WONG, H. *et al.* (1995a). "The motion of long bubble in polygonal capillaries. Part 1. Thin films". *J. Fluid Mech.*, **292**, 71–94.

WONG, H. *et al.* (1995b). "The motion of long bubbles in polygonal capillaries. Part 2. Drag, fluid pressure and fluid flow". *J. Fluid Mech.*, **292**, 95–110.

YANG, Z. *et al.* (2002). "Numerical simulation of bubbly two-phase flow in a narrow channel". *Int. J. Heat and Mass Transfer*, **45**, 631–639.

YU, D. *et al.* (2003). "Viscous flow computations with the method of lattice Boltzmann equation". *Progress in Aerospace Sciences*, **39**, 329–367.

APPENDIX A

Specific realization of *D2Q9* and *D3Q15* models.

D2Q9 **model**

Velocity set is defined as $c_{ix} = \{0, 1, 0, -1, 0, 1, -1, -1, 1\}$ and $c_{iy} = \{0, 0, 1, 0, -1, 1, 1, -1, -1\}$. Parameters specific to the D2Q9 grid are the weights $w_i = \{\frac{4}{9}, \frac{1}{9}, \frac{1}{9}, \frac{1}{9}, \frac{1}{9}, \frac{1}{36}, \frac{1}{36}, \frac{1}{36}, \frac{1}{36}\}$. The weights related to the inclusion of the surface tension coefficient into the equations are as follows: $w_{1-2}^{xx} = w_{3-4}^{yy} = 1/3$, $w_{3-4}^{xx} = w_{1-2}^{yy} = -1/6$, $w_{5-8}^{xx} = w_{5-8}^{yy} = -1/24$, $w_{1-4}^{xy} = 0$, $w_{5-6}^{xy} = 1/4$ and $w_{7-8}^{xy} = -1/4$.

D3Q15 **model**

Velocity set is defined as:

$$c_{ix} = \{0, 1, -1, 0, 0, 0, 0, 1, -1, 1, -1, 0, 0, 0, 0, 1, -1, 1, -1\}$$
$$c_{iy} = \{0, 0, 0, 1, -1, 0, 0, 1, 1, -1, -1, 1, -1, 1, -1, 0, 0, 0, 0\}$$
$$c_{iz} = \{0, 0, 0, 0, 0, 1, -1, 0, 0, 0, 0, 1, 1, -1, -1, 1, 1, -1, -1\}.$$
(8)

The weights are $w_0 = 0$, $w_{1-6} = \frac{1}{6}$ and $w_{7-18} = \frac{1}{12}$. The weights related to the inclusion of the surface tension are:

$$w_{1-2}^{xx} = w_{3-4}^{yy} = w_{5-6}^{zz} = \frac{5}{12}$$

$$w_{3-6}^{xx} = w_{1-2,5-6}^{yy} = w_{1-4}^{zz} = -\frac{1}{3}$$

$$w_{7-10,15-18}^{xx} = w_{7-14}^{yy} = w_{11-18}^{zz} = -\frac{1}{24}$$

$$w_{11-15,}^{xx} = w_{15-18}^{yy} = w_{7-10}^{zz} = \frac{1}{12}$$

$$w_{7,10}^{xy} = -w_{8,9}^{xy} = w_{11,14}^{yz} = -w_{12,13}^{yz} = w_{15,18}^{zx} = -w_{16,17}^{zx} = \frac{1}{4}.$$
(9)

8th International Conference on CFD in Oil & Gas, Metallurgical and Process Industries
SINTEF/NTNU, Trondheim Norway
21-23 June 2011

CFD11-095

INTEGRATED CFD AND PROCESS MODELLING FOR IMPROVED PROCESS DESIGN

Allan RUNSTEDTLER[1]*, **Patrick G. BOISVERT**[1], **Adrian J. MAJESKI**[1], **Haining GAO**[1], **David TISDALE**[2]

[1] Natural Resources Canada, CanmetENERGY, 1 Haanel Dr., Ottawa, Ontario, K1A 1M1, CANADA

[2] Xstrata Nickel, Sudbury Smelter, Falconbridge, Ontario, P0M 1S0, CANADA

* E-mail: allan.runstedtler@nrcan.gc.ca

ABSTRACT

Keywords:

2

1.0 INTRODUCTION

2.0 INVESTIGATION OF CFD/PROCESS MODEL

2.1.0 Electric Furnace
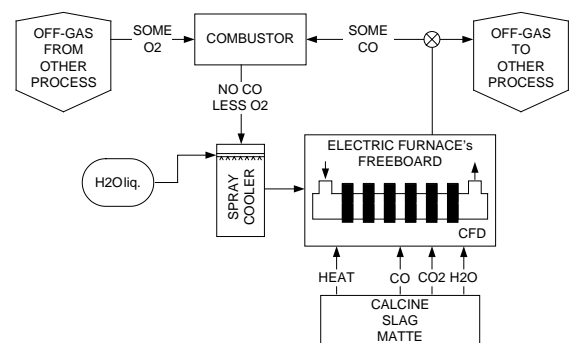
Figure 2:

2.1.1 Electric Furnace Model Implementation
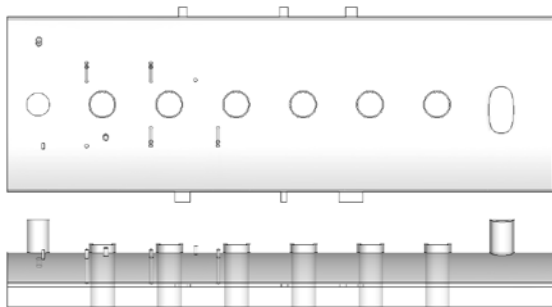
Figure 1:
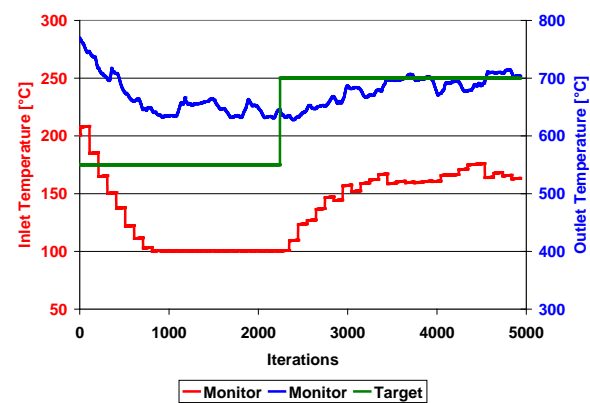
Figure 3: Inlet and outlet temperatures during simulation.

2.1.2 Electric Furnace Results Discussion
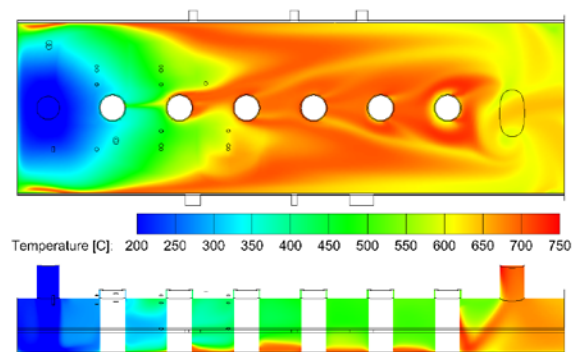
Figure 4:

Table 1:
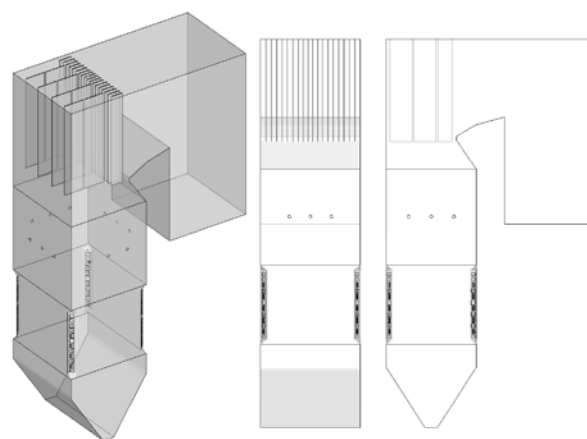
Figure 5:

2.2.0 Coal-Fired Boiler
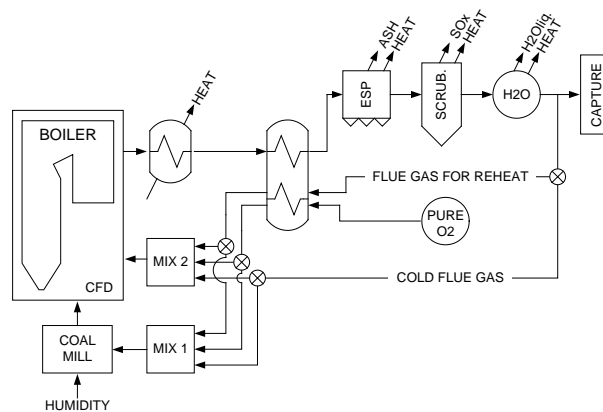
Figure 6:

2.2.1 Coal-Fired Boiler Model Implementation

2.2.2 Coal-Fired Boiler Results Discussion
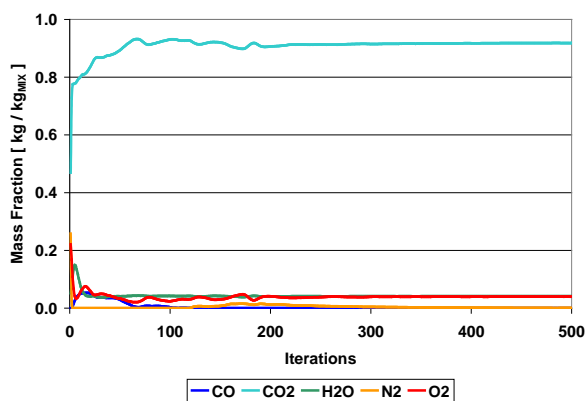
Figure 7:

Table 2:

3.0 CONCLUSION

Figure 8:

2   2
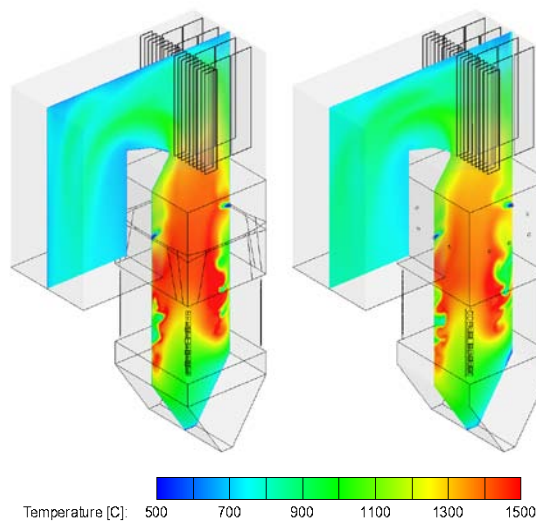
ACKNOWLEDGEMENT

REFERENCES

"

Fuel **82**

CIM Bulletin **77 866**

IEA GHG 1ˢᵗ Oxyfuel Combustion Conference

Applied Thermal Engineering **27**

Energy for Sustainble Development **14 3**

Fuel **89 10**

Symposium (International) on Combustion **14 1**

Seventh International Conference on CFD in the Minerals and Process Industries

Chemical Engineering and Processing **44**

European Symposium on Computer Aided Process Engineering—12

Journal of Heat Transfer **120**

8th International Conference on CFD in Oil & Gas, Metallurgical and Process Industries
SINTEF/NTNU, Trondheim NORWAY
21-23 June 2011

CFD11-096

HIGH ORDER NUMERICAL SIMULATION OF FLUID-STRUCTURE INTERACTION IN THE HUMAN LARYNX

Martin LARSSON[1*], **Bernhard MÜLLER**[2†]

[1]NTNU Department of Energy and Process Engineering, 7491 Trondheim, NORWAY

[2]NTNU Department of Energy and Process Engineering, 7491 Trondheim, NORWAY

[*] E-mail: martin.larssom@ntnu.no
[†] E-mail: bernhard.muller@ntnu.no

ABSTRACT

We have developed a 2D model to capture the effect of self-sustained oscillations of vocal fold tissue in the human larynx due to the interaction with the airflow from the lungs. We describe the flow by the compressible Navier-Stokes equations in the arbitrary Lagrangian–Eulerian (ALE) formulation and the structure by the linear elastic wave equation. The solver utilizes globally fourth order accurate summation by parts (SBP) finite difference operators in space and the classical fourth order explicit Runge-Kutta method in time. Simultaneous approximation term (SAT) expressions are derived to weakly impose the velocity and traction boundary conditions for the structure.

We have performed simulations for the explicitly coupled fluid-structure system with realistic parameters for human phonation. We have been able to model the self-sustained oscillations at the expected frequency.

Keywords: fluid-structure interaction, high order finite difference method, phonation .

NOMENCLATURE

Greek Symbols
Λ Eigenvalue matrix for linear elastic equations.
λ, μ Lamé parameters; λ also refers to an eigenvalue.
σ Cauchy stress tensor.
ξ, η Computational coordinates.

Latin Symbols
A, B Coefficient matrices for the linear elastic wave equation.
c_p, c_s Primary and secondary wave speeds in the structure.
F, G Flux vectors in x- and y-directions.
f, g, h Components of the Cauchy stress tensor σ in the structure.
$F^{c,v}, G^{c,v}$ Inviscid (c) and viscous (v) flux vectors.
$g^{I,II}$ Functions representing the boundary conditions for characteristic variables $u^{I,II}$.
H Diagonal norm matrix associated with Q.
J^{-1} Jacobian determinant of coordinate transformation.
$k = \xi, \eta$ Computational coordinate.
p Pressure in the fluid.
Q Finite difference operator.
$q, \hat{q}$ Vector of unknowns in the structure in physical and computational coordinates.
$\hat{\mathbf{q}}$ Grid function of unknowns in the structure in computational coordinates.
R, L Matrices for right and left going characteristic variables at right and left boundaries.
$\mathrm{SAT}_i^{(k)}$ Vector value of SAT expression in characteristic variables at grid point i in direction $k = \xi, \eta$.
$\overline{\mathrm{SAT}}_i^{(k)}$ Vector value of SAT expression in standard variables at grid point i in direction $k = \xi, \eta$.
$\widehat{\mathrm{SAT}}_{i,j}$ Vector value of total SAT expression in standard variables at grid point i, j.
T Matrix of eigenvectors.
$\bar{\mathbf{t}}$ Traction from the fluid at fluid-structure interface.
t Time.
$U, \hat{U}$ Vector of conservative variables in the fluid in physical and computational coordinates.
u, v Velocity components in the structure.
$u^{I,II}, \mathbf{u}^{I,II}$ Characteristic variables corresponding to positive and negative eigenvalues and their corresponding grid functions.
$\bar{u}(k = k_0, t), \bar{v}(k = k_0, t)$ Specified boundary conditions on variables u, v at $k = k_0$.
$\hat{\mathbf{U}}'$ Grid function of conservative perturbation variables in the fluid in computational coordinates.
$\mathbf{u}$ Discrete solution.
x, y Cartesian coordinates.

Sub/superscripts
$'$ Perturbation variables.
i, j Indices i, j.
n Time level n.

INTRODUCTION

Our voice is generated in our larynx by the vibrating vocal folds interacting with the airstream from the lungs. The vocal folds, or vocal cords, are two symmetric membranes that protrude from the walls of the larynx at the top of the trachea of humans and most mammals forming a slit-like opening known as the glottis in the airway. In a simplified three-layer model, the vocal folds are composed of the thyroarytenoid muscle, also known as the vocal fold muscle, and the vocal ligament covered by a mucous layer, cf. Figure 1. During normal breathing, the vocal tract is open and air can pass unobstructedly. During phonation, the vocal fold muscle is tensed in the longitudinal direction so that the glottal opening becomes narrower. As the high-pressure air expelled from the lungs is forced through this narrow opening, it pushes the vocal folds apart. The air column gains momen-
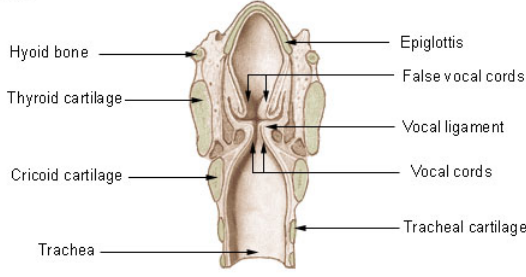
Figure 1: Schematic view of the human larynx

tum, and the velocity in the glottis increases. The increase in velocity causes a pressure drop in the glottis according to the Bernoulli principle. The decrease in pressure leads to an aerodynamic force which together with the elastic force in the vocal folds strives to close the glottis. A build-up in pressure upstream of the glottis resulting from the closure leads to a pressure force which opens the vocal folds and allows the passage of air. Under favorable circumstances, this process is repeated in a self-sustained manner and driven only by the pressure from the lungs. It is important to point out that no periodic contraction of muscles occurs during phonation. The opening and closing of the glottis is in this respect a passive process (Titze, 2000).

During normal speech, the vocal folds collide with each other, closing the glottis completely. However, in certain types of phonation such as a very breathy voice or while whispering, the vocal folds do not necessarily make contact. The outermost mucous layer of the vocal folds have been shown to play an important role in the self-sustained oscillation, facilitating the vibrations of the much stiffer ligament (Titze, 2000).

As the vocal folds oscillate rapidly, they generate a fundamental frequency. When we speak normally only the lowest mode of vibration is excited, in which all the layers of the vocal folds vibrate symmetrically and as a whole. Higher modes of oscillation can, however, be excited to produce higher pitched tones for example when singing. By stretching the vocal fold muscle, the vocal fold length changes as well as the stiffness, and higher modes can thus be created. These higher modes correspond to an oscillation concentrated mainly to the ligament or the mucous layer and have a higher frequency. The different modes of oscillation are commonly referred to as registers (modal, falsetto etc) and singers are often particularly good at smoothing out the transition between these registers (Titze, 2008).

The acoustic signal resulting from the glottal flow interacting with the vibrating vocal folds is further modified by the vocal tract which functions as an acoustic filter. By changing the shape of the vocal tract, different frequencies are amplified and suppressed so that a multitude of different vowels can be formed from the same source signal.

The computational models for self-sustained vibrations of vocal folds have advanced from simple models based on the Bernoulli equation for the airflow and mass-spring models for the vocal folds used in the 1970ies to full-fledged 2D and 3D unsteady fluid-structure interactions (FSI) coupling the Navier-Stokes equations and Navier's equation (Titze, 2000; Luo *et al.*, 2008; Link *et al.*, 2009). In general, lower order finite difference, volume and element methods have been used.

In this paper, we employ a high order finite difference approach based on summation by parts (SBP) operators (Strand, 1994; Gustafsson *et al.*, 1995; Gustafsson, 2008) to solve the compressible Navier–Stokes equations and the linear elastic wave equation, i.e., Navier's equation. Fluid and structure interact in a two-way coupling, meaning that fluid stresses deform the flexible structure which in turn causes the fluid to conform to the new structural boundary via no-slip boundary conditions. The traction boundary conditions and the location and velocity of the vocal fold boundaries are communicated between structure and fluid at the beginning of each time step of the explicit Runge-Kutta time stepping of fluid and structure. While the velocity and traction boundary conditions for the structure are weakly imposed using the simultaneous approximation term (SAT) approach (Larsson and Müller, 2011), the no-slip boundary conditions for the fluid are enforced by injecting the data supplied by the structure. The approach has been tested for a 2D model of the larynx and the vocal folds.

The present work is based on Martin Larsson's PhD thesis (Larsson, 2010) and the six papers by Larsson and Müller (Larsson and Müller, 2009a,b, 2011, 2010b,a,c) contained therein.

GOVERNING EQUATIONS

Compressible Navier–Stokes equations

The perturbation formulation is used to minimize cancellation errors when discretizing the Navier–Stokes equations for compressible low Mach number flow (Sesterhenn *et al.*, 1999; Müller, 1996). The 2D compressible Navier–Stokes equations in conservative form can be expressed in perturbation form as (Müller, 2008; Larsson and Müller, 2009a)

$$U'_t + F^{c\prime}_x + G^{c\prime}_y = F^{v\prime}_x + G^{v\prime}_y, \qquad (1)$$

where the vector U' denotes the perturbation of the conservative variables with respect to the stagnation values. U' and the inviscid (superscript c) and viscous (superscript v) flux vectors can be found in, e.g., (Larsson and Müller, 2009a).

General moving geometries are treated by a time dependent coordinate transformation $\tau = t$, $\xi = \xi(t,x,y)$, $\eta = \eta(t,x,y)$. The transformed 2D conservative compressible Navier–Stokes equations in perturbation form read (Larsson and Müller, 2009a)

$$\hat{U}'_\tau + \hat{F}'_\xi + \hat{G}'_\eta = 0, \qquad (2)$$

where $\hat{U}' = J^{-1}U'$, $\hat{F}' = J^{-1}(\xi_t U' + \xi_x(F^{c\prime} - F^{v\prime}) + \xi_y(G^{c\prime} - G^{v\prime}))$ and $\hat{G}' = J^{-1}(\eta_t U' + \eta_x(F^{c\prime} - F^{v\prime}) + \eta_y(G^{c\prime} - G^{v\prime}))$. Equation (2) constitutes the arbitrary Lagrangean–Eulerian (ALE) formulation of the 2D compressible Navier–Stokes equations in perturbation form.

No-slip adiabatic wall boundary conditions are used at the upper and lower walls of the vocal tract including the moving boundaries of the upper and lower vocal folds, cf. Figure 2. The Navier–Stokes Characteristic Boundary Conditions (NSCBC) technique by (Poinsot and Lele, 1992) is employed at the outflow, i.e., the right boundary in Figure 2 (Larsson and Müller, 2009b). At the inflow, i.e., the left boundary in Figure 2, the pressure, temperature and y-component of velocity are imposed as $p = p_{\mathrm{atm}} + \Delta p$, $T = T_0 = 310\,\mathrm{K}$, and $v = 0$, respectively. The x-component of velocity u at the inflow and the pressure p at the walls are computed from the 2D compressible Navier–Stokes equations (2) discretized at the boundaries.
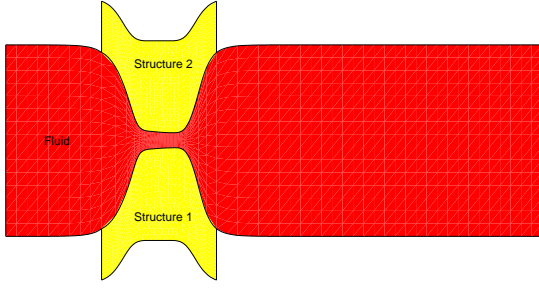
Figure 2: Computational fluid and structure domains of airflow and vocal folds, respectively

Linear elastic wave equation

The 2D linear elastic wave equation written as a first order hyperbolic system reads in Cartesian coordinates

$$q_t = Aq_x + Bq_y, \tag{3}$$

where the unknown vector $q = (u, v, f, g, h)^{\mathrm{T}}$ contains the velocity components u, v and the stress components f, g, h. The coefficient matrices A, B depend on the the Lamé parameters λ, μ and the density ρ which are here all taken to be constant in space and time, e.g., (Fornberg, 1998; LeVeque, 2002; Larsson and Müller, 2010c).

The linear combination $P(k_x, k_y) = k_x A + k_y B$ can be diagonalized with real eigenvalues and linearly independent eigenvectors. The eigenvalue matrix is defined as the diagonal matrix with the eigenvalues of $P(k_x, k_y)$ in decreasing order,

$$
\begin{aligned}
\tilde{\Lambda}(k_x, k_y) &= (k_x^2 + k_y^2)^{1/2} \mathrm{diag}(c_p, c_s, 0, -c_s, -c_p) \\
&= \mathrm{diag}\left\{ \tilde{\lambda}_i(k_x, k_y) \right\}_{i=1}^5, \tag{4}
\end{aligned}
$$

where the wave speeds are $c_p = \sqrt{(\lambda + 2\mu)/\rho}$ and $c_s = \sqrt{\mu/\rho}$, referred to as primary (or pressure) and secondary (or shear) wave speeds, respectively.

To treat curvilinear grids we introduce the mapping $x = x(\xi, \eta)$, $y = y(\xi, \eta)$. The Jacobian determinant J^{-1} of the transformation is given by $J^{-1} = x_\xi y_\eta - x_\eta y_\xi$ and the linear elastic wave equation can then be written as

$$\hat{q}_t = (\hat{A}\hat{q})_\xi + (\hat{B}\hat{q})_\eta \tag{5}$$

where the hats signify that the quantities are in transformed coordinates, i.e., $\hat{q} = J^{-1}q$, $\hat{A} = \xi_x A + \xi_y B$ and $\hat{B} = \eta_x A + \eta_y B$.

Characteristic variables

In order to describe the simultaneous approximation term (SAT) expressions in transformed coordinates we need to find the characteristic variables for the transformed equation in which the coefficient matrices are linear combinations of the coefficient matrices in the x- and y-directions.

$$\hat{q}_t = ((k_x A + k_y B)\hat{q})_k \tag{6}$$

where $k = \xi, \eta$. We form the linear combination $P(k_x, k_y) = k_x A + k_y B$. The coefficient matrices A and B have the same set of eigenvalues $\Lambda = \mathrm{diag}(c_p, c_s, 0, -c_s, -c_p)$, whereas for the linear combination $P(k_x, k_y)$ we get $\tilde{\Lambda}(k_x, k_y) = (k_x^2 + k_y^2)^{1/2}\Lambda$. To find the linearly independent eigenvectors of $P(k_x, k_y)$, we solve the underdetermined system $(P(k_x, k_y) -$

$\tilde{\lambda}_i I)v_i = 0$ for $i = 1, ..., 5$. These five eigenvectors v_i become the columns in the eigenvector matrix $T(k_x, k_y)$, cf. Appendix A. We have some degrees of freedom in choosing T, because each column can be scaled by any nonzero constant. The inverse of this matrix is obtained with a symbolic computer program, cf. Appendix A. In Appendix A, we have introduced the following abbreviations $\bar{k} = (k_x^2 - k_y^2)/(k_x^2 + k_y^2)$, $r = (k_x^2 + k_y^2)^{1/2}$, $\tilde{c}_p = rc_p$, $\tilde{c}_s = rc_s$, $\alpha = (\lambda + 2\mu)/\lambda$ and $\beta = \alpha\lambda/\mu$. For all directions (k_x, k_y) we have that $T^{-1}(k_x, k_y)P(k_x, k_y)T(k_x, k_y) = \tilde{\Lambda}(k_x, k_y)$. The transformation to characteristic variables u is given by $u^{(k)} = T^{-1}(k_x, k_y)\hat{q}$ for each of the two coordinate directions $k = \xi, \eta$. The transformation back to flow variables is given by $\hat{q} = T(k_x, k_y)u^{(k)}$.

TIME STABLE HIGH ORDER DIFFERENCE METHOD

Energy method

The energy method is a general technique to prove sufficient conditions for well-posedness of partial differential equations (PDE) and stability of difference methods with general boundary conditions.

Consider the solution of the model problem in 1D with

$$u_t = \lambda u_x, \, \lambda > 0, \, 0 \le x \le 1, \, t \ge 0, \, u(x, 0) = f(x), \, u(1, t) = g(t). \tag{7}$$

Here, the symbol λ represents a general eigenvalue for the hyperbolic system and should not be confused with the Lamé parameter. Define the L_2 scalar product for real functions v and w on the interval $0 \le x \le 1$ as

$$(v, w) = \int_0^1 v(x)w(x)dx \tag{8}$$

which defines a norm of the continuous solution at some time t and an energy $E(t) = ||u(\cdot, t)||^2 = (u, u)$. Using integration by parts $(v, w_x) = v(1, t)w(1, t) - v(0, t)w(0, t) - (v_x, w)$, we get $\frac{dE}{dt} = \frac{d||u||^2}{dt} = (u_t, u) + (u, u_t) = \lambda[(u_x, u) + (u, u_x)] = \lambda[(u_x, u) + [u^2]_0^1 - (u_x, u)] = \lambda[u^2(1, t) - u^2(0, t)]$. If $\lambda > 0$, the boundary condition $u(1, t) = 0$ yields a non-growing solution (note that periodic boundary conditions would also yield a non-growing solution), i.e., $E(t) \le E(0) = ||f(x)||^2$. Thus, the energy of the solution is bounded by the energy of the initial data. As a unique solution of the initial-boundary value problem (IBVP) (7) exists, the problem is well-posed.

Summation by parts operators

The idea behind the summation by parts technique for first order IBVP is to devise difference approximations Q of the first spatial derivative satisfying the discrete analogue of integration by parts called the summation by parts (SBP) property (Gustafsson, 2008). To outline the idea for the numerical solution of (7), we introduce the equidistant grid $x_j = jh$, $j = 0, ..., N$, $h = 1/N$, and a solution vector containing the solution at the discrete grid points, $\mathbf{u} = (u_0(t), u_1(t), ..., u_N(t))^{\mathrm{T}}$. The semi-discrete problem can be stated using a difference operator Q approximating the first derivative in space,

$$\frac{d\mathbf{u}}{dt} = \lambda Q\mathbf{u}, \, u_j(0) = f(x_j). \tag{9}$$

We also define a discrete scalar product and corresponding norm and energy by

$$(\mathbf{u}, \mathbf{v})_h = h\sum_{i,j} h_{ij}u_i v_j = h\mathbf{u}^{\mathrm{T}}H\mathbf{v}, \quad E_h(t) = ||\mathbf{u}||_h^2 = (\mathbf{u}, \mathbf{u})_h, \tag{10}$$

where the symmetric and positive definite norm matrix $H = \text{diag}(H_L, I, H_R)$ has components h_{ij}. In order for (10) to define a scalar product, H_L and H_R must be symmetric and positive definite. We say that the difference operator Q satisfies the summation by parts property (SBP), if

$$(\mathbf{u}, Q\mathbf{v})_h = u_N v_N - u_0 v_0 - (Q\mathbf{u}, \mathbf{v})_h. \tag{11}$$

It can be seen that this property is satisfied, if the matrix $G = HQ$ satisfies the condition that $G + G^T = \text{diag}(-1, 0, ..., 0, 1)$. If Q satisfies the SBP property (11), then the energy method for the discrete problem yields:

$$
\begin{aligned}
\frac{dE_h}{dt} &= \frac{d\|\mathbf{u}\|_h^2}{dt} = (\mathbf{u}_t, \mathbf{u})_h + (\mathbf{u}, \mathbf{u}_t)_h \\
&= \lambda[(Q\mathbf{u}, \mathbf{u})_h + (\mathbf{u}, Q\mathbf{u})_h] \\
&= \lambda[(Q\mathbf{u}, \mathbf{u})_h + u_N^2 - u_0^2 - (Q\mathbf{u}, \mathbf{u})_h] \\
&= \lambda[u_N^2 - u_0^2].
\end{aligned} \tag{12}
$$

How to obtain time stability $dE_h/dt \leq 0$, i.e., no energy growth in time, is the topic of the next section.

For diagonal H_L and H_R, there exist difference operators Q accurate to order $\mathscr{O}(h^{2s})$ in the interior and $\mathscr{O}(h^s)$ near the boundaries for $s = 1, 2, 3$ and 4. These operators have an effective order of accuracy $\mathscr{O}(h^{s+1})$ in the entire domain. Explicit forms of such operators Q and norm matrices H were derived by (Strand, 1994).

For this study, we use an SBP operator based on the central sixth order explicit finite difference operator ($s = 3$) which has been modified near the boundaries in order to satisfy the SBP property giving an effective $\mathscr{O}(h^4)$ order of accuracy in the whole domain (Strand, 1994).

Simultaneous approximation term

Since the term λu_N^2 in (12) is non-negative, time stability does not follow when using the injection method for the summation by parts operator, i.e., by using $u_N(t) = g(t)$. For injection affects the operator Q and the SBP property (11) (Strand, 1994; Gustafsson, 2008). In contrast, the simultaneous approximation term (SAT) method by (Carpenter *et al.*, 1994) is an approach where a linear combination of the boundary condition and the differential equation is solved at the boundary. This leads to a weak imposition of the physical boundary condition. The imposition of SAT boundary conditions is accomplished by adding a source term to the difference operator, proportional to the difference between the value of the discrete solution u_N and the boundary condition to be fulfilled. The SAT method for the semidiscrete advection equation (9) can be expressed as

$$\frac{d\mathbf{u}}{dt} = \lambda Q\mathbf{u} - \lambda \tau \mathbf{S}(u_N - g(t))$$

where $\mathbf{S} = h^{-1}H^{-1}(0, 0, ..., 0, 1)^T$ and τ is a free parameter. The added term does not alter the accuracy of the scheme, since it vanishes when the analytical solution is substituted. Thus, we can imagine the SAT expression as a modification to the difference operator so that we are effectively solving an equation $\mathbf{u}_t = \lambda \tilde{Q}\mathbf{u}$ with $\tilde{Q} = Q + Q^{\text{sat}}$ where the boundary conditions are accounted for by the operator itself. When H is diagonal, the scheme is only modified at one point, namely at the point where the boundary condition is imposed. We can now show that this scheme is time stable for $g(t) = 0$. The energy rate for the solution of the semi-discrete equation is $\frac{dE_h}{dt} = \frac{d\|\mathbf{u}\|_h^2}{dt} = (\mathbf{u}_t, \mathbf{u})_h + (\mathbf{u}, \mathbf{u}_t)_h$

$= \lambda[(Q\mathbf{u} - \tau \mathbf{S}u_N, \mathbf{u})_h + (\mathbf{u}, Q\mathbf{u} - \tau \mathbf{S}u_N)_h] = \lambda[(Q\mathbf{u}, \mathbf{u})_h - \tau(\mathbf{S}, \mathbf{u})_h u_N + (\mathbf{u}, Q\mathbf{u})_h - \tau(\mathbf{u}, \mathbf{S})_h u_N] = \lambda[(1 - 2\tau)u_N^2 - u_0^2]$ since $(\mathbf{S}, \mathbf{u})_h = (\mathbf{u}, \mathbf{S})_h = h\mathbf{u}^T H h^{-1} H^{-1}(0, 0, ..., 0, 1)^T = u_N$. The discretization is time stable if $\tau \geq 1/2$.

The extension of the time stable SAT method to 1D hyperbolic systems

$$u_t = \Lambda u_x \tag{13}$$

with a diagonal $r \times r$ coefficient matrix Λ is performed in the following way (Carpenter *et al.*, 1994). The coefficient matrix Λ is chosen such that the diagonal entries appear in descending order, i.e., $\lambda_1 > \lambda_2 > ... > \lambda_k > 0 > \lambda_{k+1} > ... > \lambda_r$. The solution vector u is split into two parts corresponding to positive and negative diagonal elements $u^I = (u^{(1)}, ..., u^{(k)})^T$ and $u^{II} = (u^{(k+1)}, ..., u^{(r)})^T$, where $u^{(i)}$ is the ith component of u. Since the ith component of (13) reads $u_t^{(i)} = \lambda_i u_x^{(i)}$, the vectors u^I and u^{II} are transported to the left and right, respectively. Therefore, boundary conditions have to be prescribed on u^I at the right boundary $x = 1$ and on u^{II} at the left boundary $x = 0$. To allow for coupling of the in- and outgoing variables at the boundaries, we introduce a $k \times (r - k)$ matrix R and a $(r - k) \times k$ matrix L. We define boundary functions $g^I(t) = (g^{(1)}(t), ..., g^{(k)}(t))$ and $g^{II}(t) = (g^{(k+1)}(t), ..., g^{(r)}(t))$. Then, the boundary conditions are given by

$$u^I(1, t) = Ru^{II}(1, t) + g^I(t), \quad u^{II}(0, t) = Lu^I(0, t) + g^{II}(t). \tag{14}$$

Under the constraint $|R||L| \leq 1$, the IBVP (13) with (14) is well-posed (Carpenter *et al.*, 1994), where the matrix 2-norm is defined by $|R| = \sqrt{\rho(R^T R)}$ and $\rho(A)$ is the spectral radius of A.

We define the grid functions of the components of u as $\mathbf{u}^{(i)} = (u_0^{(i)}, ..., u_N^{(i)})^T$, where $u_j^{(i)} = u^{(i)}(x_j)$. Then, we define the grid functions of u^I and u^{II} as $\mathbf{u}^I = (\mathbf{u}^{(1)}, ..., \mathbf{u}^{(k)})$ and $\mathbf{u}^{II} = (\mathbf{u}^{(k+1)}, ..., \mathbf{u}^{(r)})$. The boundary conditions (14) for the semi-discretization of (13) are imposed by the SAT method as (Carpenter *et al.*, 1994)

$$
\begin{aligned}
\frac{d\mathbf{u}^{(i)}}{dt} &= \lambda_i Q\mathbf{u}^{(i)} - \lambda_i \tau \mathbf{S}^{(i)}(u_N^{(i)} - (R\mathbf{u}_N^{II})^{(i)} - g^{(i)}(t)), \\
&\quad 1 \leq i \leq k \\
\frac{d\mathbf{u}^{(i)}}{dt} &= \lambda_i Q\mathbf{u}^{(i)} + \lambda_i \tau \mathbf{S}^{(i)}(u_0^{(i)} - (L\mathbf{u}_0^I)^{(i-k)} - g^{(i)}(t)), \\
&\quad k + 1 \leq i \leq r
\end{aligned}
$$
$$\tag{15}$$

where $\mathbf{S}^{(i)} = h^{-1}H^{-1}(0, 0, ..., 1)^T$ for $1 \leq i \leq k$ and $\mathbf{S}^{(i)} = h^{-1}H^{-1}(1, 0, ..., 0)^T$ for $k + 1 \leq i \leq r$. Regarding the notation, $(R\mathbf{u}_N^{II})^{(i)}$ should be interpreted as follows: $\mathbf{u}_N^{II} = (u_N^{(r-k)}, ..., u_N^{(r)})^T$ is the last row of u^{II} transposed. Multiplying R by $\mathbf{u}_N^{II}$ yields a new vector of which the (i)th component is taken. The interpretation of $\mathbf{u}_0^I$ is similar with $\mathbf{u}_0^I = (u_0^{(1)}, ..., u_0^{(k)})^T$. As shown by (Carpenter *et al.*, 1994), the SAT method is both stable in the classical sense and time stable provided that

$$\frac{1 - \sqrt{1 - |R||L|}}{|R||L|} \leq \tau \leq \frac{1 + \sqrt{1 - |R||L|}}{|R||L|}. \tag{16}$$

SAT EXPRESSIONS FOR THE LINEAR ELASTIC WAVE EQUATION

Notation for boundary conditions

We adopt the notation $u(k_0, t) = \bar{u}(k = k_0, t)$ to represent a 1D boundary condition on the solution variable u in any direction k where $k = \xi$ or $k = \eta$ and $\bar{u}(k, t)$ is the given functions of time on the boundaries $k_0 = 0$ and $k_0 = 1$ which the

solution variable u should match on those boundaries. For example, $\bar{u}(\xi = 1, t)$ is the given u-velocity at the boundary $\xi = 1$ and $u(1, t)$ is the corresponding solution to the equations. In 2D, the boundary condition also depends on the second coordinate direction, which we indicate by $\bar{u}(\xi = 1, \eta, t)$ and $\bar{u}(\xi, \eta = 1, t)$ for boundary conditions in the ξ- and η-directions, respectively. Finally, for the discretized 2D boundary conditions, we write instead $\bar{u}_j(\xi = 1, t) = \bar{u}(\xi = 1, \eta_j, t)$ and $\bar{u}_i(\eta = 1, t) = \bar{u}(\xi_i, \eta = 1, t)$.

Presentation of SAT expressions

The SAT expressions for the linear elastic wave equation derived in (Larsson and Müller, 2010c) are summarized here.

To apply the theory for 1D linear diagonalized hyperbolic systems (13), we have to express (6) in characteristic form, i.e., $u_t = \tilde{\Lambda} u_k$. $u = u^{(k)} = T^{-1}(k_x, k_y)\hat{q}$ is the vector of the characteristic variables in the k-direction where $\hat{q} = J^{-1}(u, v, f, g, h)^{\mathrm{T}}$. $\tilde{\Lambda} = \tilde{\Lambda}(k_x, k_y)$ is the diagonal matrix with the eigenvalues of $P(k_x, k_y)$ where $k = \xi$ or $k = \eta$, and $u_k = \frac{\partial u}{\partial k}$.

We form the two sub-vectors corresponding to positive and negative eigenvalues as

$$u^{\mathrm{I}}(k_x, k_y) = (u_1, u_2)^{\mathrm{T}}, \, u^{\mathrm{II}}(k_x, k_y) = (u_4, u_5)^{\mathrm{T}} \qquad (17)$$

with the aim to form boundary conditions with the matrices R and L. Since the components of u^{I} and u^{II} contain velocity and stress components in positive or negative pairs, it is easy to find 2×2 matrices L and R in Equation (14) in order to prescribe velocity or traction components as boundary conditions g^{I} and g^{II}. Let us illustrate this approach for prescribing the velocity components u and v at the boundaries. Looking at the characteristic variables, we find the following identities to prescribe the velocity components $u_n = (k_x u + k_y v)/r$ and $u_t = (-k_y u + k_x v)/r$ normal and tangential, respectively, to a grid line $k = const$:

$$u^{\mathrm{I}}(k_x, k_y) - \begin{bmatrix} 0 & 1 \\ -1 & 0 \end{bmatrix} u^{\mathrm{II}}(k_x, k_y) = \frac{J^{-1}}{r} \begin{bmatrix} \frac{\lambda}{\tilde{c}_p} u_n \\ u_t \end{bmatrix} \quad (18)$$

$$u^{\mathrm{II}}(k_x, k_y) - \begin{bmatrix} 0 & -1 \\ 1 & 0 \end{bmatrix} u^{\mathrm{I}}(k_x, k_y) = \frac{J^{-1}}{r} \begin{bmatrix} u_t \\ -\frac{\lambda}{\tilde{c}_p} u_n \end{bmatrix} (19)$$

Thus, using the matrices $L = \begin{bmatrix} 0 & -1 \\ 1 & 0 \end{bmatrix}$ and $R = \begin{bmatrix} 0 & 1 \\ -1 & 0 \end{bmatrix}$ in Equation (14), we can prescribe boundary conditions for $g^{\mathrm{I}}(k_x, k_y, t) = \frac{J^{-1}}{r^2} \begin{bmatrix} \frac{\lambda}{\tilde{c}_p}(k_x u + k_y v) \\ -k_y u + k_x v \end{bmatrix}$ and

$g^{\mathrm{II}}(k_x, k_y, t) = \frac{J^{-1}}{r^2} \begin{bmatrix} -k_y u + k_x v \\ -\frac{\lambda}{\tilde{c}_p}(k_x u + k_y v) \end{bmatrix}$, cf. (20) and (21) below. Note that L and R are independent of the direction, but depend on the particular type of boundary condition to be imposed (velocity or traction). For boundary conditions on the velocities u and v, we get using the identities (18)–(19) the following expressions

$$g^{\mathrm{I}}(k_x, k_y, t) = \frac{J^{-1}}{r^2} \begin{bmatrix} \frac{\lambda}{\tilde{c}_p}(k_x \bar{u}(k = 1, t) + k_y \bar{v}(k = 1, t)) \\ -k_y \bar{u}(k = 1, t) + k_x \bar{v}(k = 1, t) \end{bmatrix},$$

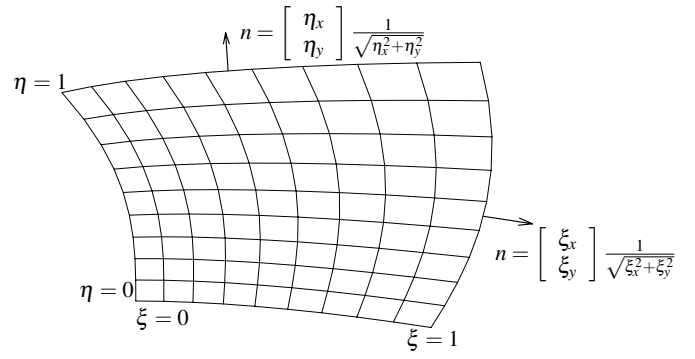$$R = \begin{bmatrix} 0 & 1 \\ -1 & 0 \end{bmatrix} \qquad (20)$$

Figure 3: Coordinate transformation

$$g^{\mathrm{II}}(k_x, k_y, t) = \frac{J^{-1}}{r^2} \begin{bmatrix} -k_y \bar{u}(k = 0, t) + k_x \bar{v}(k = 0, t) \\ -\frac{\lambda}{\tilde{c}_p}(k_x \bar{u}(k = 0, t) + k_y \bar{v}(k = 0, t)) \end{bmatrix},$$

$$L = \begin{bmatrix} 0 & -1 \\ 1 & 0 \end{bmatrix} \qquad (21)$$

where $\bar{u}(k, t), \bar{v}(k, t)$ are the given boundary conditions on u, v at the boundaries.

The boundary conditions on the stresses come from a traction boundary condition of the form $\sigma \mathbf{n} = \bar{\mathbf{t}}$ where $\bar{\mathbf{t}} = (\bar{t}_x, \bar{t}_y)^{\mathrm{T}}$ is the given traction vector from the fluid and $\sigma = \begin{bmatrix} f & g \\ g & h \end{bmatrix}$ is the Cauchy stress tensor in the structure. The unit normal $\mathbf{n}$ can be expressed in terms of the coordinate transformation as $\mathbf{n} = (1/r)(k_x, k_y)^{\mathrm{T}}$, cf. Figure 3, and the components of g^{I} and g^{II} for traction boundary conditions can be written as

$$g^{\mathrm{I}}(k_x, k_y, t) = \frac{J^{-1}}{r^2} \begin{bmatrix} \frac{1}{\alpha r}(k_x \bar{t}_x(k = 1, t) + k_y \bar{t}_y(k = 1, t)) \\ \frac{r}{\rho \tilde{c}_s}(-k_y \bar{t}_x(k = 1, t) + k_x \bar{t}_y(k = 1, t)) \end{bmatrix},$$

$$R = \begin{bmatrix} 0 & -1 \\ 1 & 0 \end{bmatrix}, \qquad (22)$$

$$g^{\mathrm{II}}(k_x, k_y, t) = \frac{J^{-1}}{r^2} \begin{bmatrix} \frac{r}{\rho \tilde{c}_s}(k_y \bar{t}_x(k = 0, t) - k_x \bar{t}_y(k = 0, t)) \\ \frac{1}{\alpha r}(k_x \bar{t}_x(k = 0, t) + k_y \bar{t}_y(k = 0, t)) \end{bmatrix},$$

$$L = \begin{bmatrix} 0 & 1 \\ -1 & 0 \end{bmatrix}. \qquad (23)$$

Therefore it is sufficient to specify the two parameters $\bar{t}_x$ and $\bar{t}_y$ on each boundary instead of all of the three $\bar{f}, \bar{g}, \bar{h}$, which might otherwise violate well-posedness.

Inserting the definitions of $g^{\mathrm{I,II}}$ and R, L gives with Equation (15) a SAT expression (which we simply call SAT) for each of the five equations in characteristic variables. At a general index $i \in \{0, 1, ..., N\}$ in the k-direction, the SAT vector for prescribed velocity components will be $SAT_i^{(k)}(k_x, k_y, t) = -\frac{\tau J^{-1}}{h_k r^2}$

$$\begin{bmatrix} \lambda h_{NN}^{-1} \delta_{iN}[k_x(u_N - \bar{u}(k = 1, t)) + k_y(v_N - \bar{v}(k = 1, t))] \\ \tilde{c}_s \bar{k} h_{NN}^{-1} \delta_{iN}[-k_y(u_N - \bar{u}(k = 1, t)) + k_x(v_N - \bar{v}(k = 1, t))] \\ 0 \\ \tilde{c}_s \bar{k} h_{00}^{-1} \delta_{i0}[-k_y(u_0 - \bar{u}(k = 0, t)) + k_x(v_0 - \bar{v}(k = 0, t))] \\ -\lambda h_{00}^{-1} \delta_{i0}[k_x(u_0 - \bar{u}(k = 0, t)) + k_y(v_0 - \bar{v}(k = 0, t))] \end{bmatrix},$$

where h_{00} and h_{NN} are the first and last entries, respectively, of the diagonal norm matrix H. Note that the SAT term for the characteristic variable u_3 with characteristic speed zero
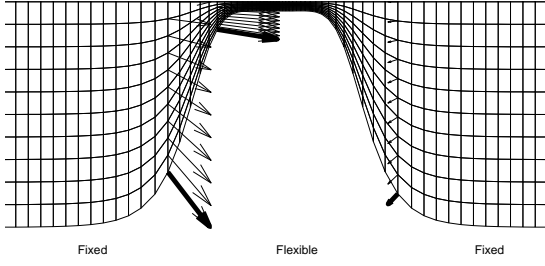
Figure 4: The boundary of the fluid domain consists of fixed and flexible parts. The velocity at the boundary of the flexible part determines the internal grid point velocity. Only the lower half of the domain is shown.

is zero, because for u_3 no boundary condition must be given. For $k = \xi$, we use the index i, while for $k = \eta$ we employ index j for i and M for N. Equation (16) implies $\tau = 1$.

For each of the two spatial directions, the transformation matrix $T(k_x, k_y)$ is applied to get the corresponding SAT expressions in flow variables.

$$\overline{\text{SAT}}_i^{(k)} = T(k_x, k_y)\text{SAT}_i^{(k)}(k_x, k_y) \tag{24}$$

for $k = \xi$ and η. Finally, the total SAT expression is then the sum of the two contributions from the two coordinate directions.

$$\widehat{\text{SAT}}_{i,j} = \overline{\text{SAT}}_{i,j}^{(\xi)}(\xi_x, \xi_y) + \overline{\text{SAT}}_{i,j}^{(\eta)}(\eta_x, \eta_y) \tag{25}$$

FLUID-STRUCTURE INTERACTION

Arbitrary Lagrangean–Eulerian (ALE) formulation

The displacement of the fluid-structure interface determines the shape of the fluid domain, and the structure velocity at the interface determines the internal grid point velocities in the fluid domain. The left and right boundaries of the fluid domain are the in- and outflow, respectively. The top and bottom parts of the fluid domain are bounded by the flexible vocal folds and the inner wall of the vocal tract which is here assumed to be rigid. As we do not assume symmetry with respect to the streamwise centerline of the vocal tract, the motions of the two vocal folds are solved individually. In our arbitrary Lagrangean–Eulerian (ALE) formulation, the positions and velocities of the grid points in the fluid domain are linearly interpolated along the grid lines connecting the upper and lower vocal folds where the positions and velocities are given by the structure solution. Figure 4 shows the given structure velocities with bold arrows and the interpolated grid point velocities $\dot{x}, \dot{y}$ (thin arrows) for three grid lines.

To obtain the time derivative of J^{-1} as needed in (2), a geometric invariant (Visbal and Gaitonde, 2002) is used. This geometric conservation law states that

$$(J^{-1})_\tau + (J^{-1}\xi_t)_\xi + (J^{-1}\eta_t)_\eta = 0. \tag{26}$$

The time derivatives of the computational coordinates ξ, η can here be obtained from the grid point velocities $\dot{x}, \dot{y}$ as $\xi_t = -(\dot{x}\xi_x + \dot{y}\xi_y)$, $\eta_t = -(\dot{x}\eta_x + \dot{y}\eta_y)$ which can be seen by differentiating the transformation with respect to τ. With the ξ- and η-derivatives in (26) discretized by the globally fourth order SBP operator, we get the time derivative $(J^{-1})_\tau$ at each time level. The Jacobian determinant J^{-1} of the coordinate transformation is determined by $J^{-1} = x_\xi y_\eta - x_\eta y_\xi$ and the metric terms by $J^{-1}\xi_x = y_\eta$, $J^{-1}\xi_y = -x_\eta$, $J^{-1}\eta_x = -y_\xi$, $J^{-1}\eta_y = x_\xi$.

Description of fluid-structure interaction algorithm

At the start of a simulation, we construct the fixed reference configuration for the structure and set the initial variables to zero (zero velocity and no internal stresses). The initial conditions for the perturbation variables U' in the fluid domain are taken equal to zero as well (stagnation conditions). In the first time step, the fluid domain is uniquely determined by the reference boundary of the structure. To go from time level n to $n+1$, we first take one time step for the fluid with imposed pressure boundary conditions at the inflow and adiabatic no-slip conditions on the walls, i.e., $\mathbf{u} = \mathbf{u}_w$ and $\partial T / \partial n = 0$. After the fluid time step, the fluid stress on the wall is calculated based on the new fluid velocities and pressures. These fluid stresses σ^f are passed on to the structure solver via the traction boundary condition. The force per unit area exerted on a surface element with unit normal $\mathbf{n}$ is $\bar{\mathbf{t}} = \sigma^f \mathbf{n}$, where $\mathbf{n}$ is here the outer unit normal of the structure, calculated from the displacement vector field.

The traction computed at time level n for the fluid is then used to advance the structure solution to time level $n+1$. Note that the traction $\bar{\mathbf{t}}^n$ is used, although $\bar{\mathbf{t}}^{n+1}$ is available. For we employ explicit time integration where we start from time level n for both structure and fluid. The solution for the structure at the new time level gives the velocities and displacements on the boundary, which in turn are used to generate the new fluid grid and internal grid point velocities. This procedure is repeated for each time step.

The fluid-structure interaction algorithm is summarized as follows:

1. Generate the initial fluid grid based on the reference configuration for the structure. $\Rightarrow x^0, \dot{x}^0$.

2. Give initial values for the fluid and the structure. $\Rightarrow F^0, S^0$.

3. For time step $n = 1, 2, ...$, do:

   (a) Calculate the fluid stress on the boundary and calculate the force per unit area, i.e., traction, on the structure via the unit normal. Store the traction vector $\bar{\mathbf{t}}^n$.

   (b) Take one time step for the fluid: $F^{n+1} = F(x^n, \dot{x}^n)$.

   (c) Calculate the traction force from the fluid on the structure on the boundary, cf. Figure 5(a). $\Rightarrow \bar{\mathbf{t}}^{n+1}$.

   (d) Take one time step for the structure using the boundary conditions $\bar{\mathbf{t}}^n$: $S^{n+1} = S(\bar{\mathbf{t}}^n)$.

   (e) Recalculate the fluid grid and the grid point velocities based on the new structure solution, cf. Figure 5(b). $\Rightarrow x^{n+1}, \dot{x}^{n+1}$.

4. Repeat from 3 with time step $n+1$ until the final time is reached.
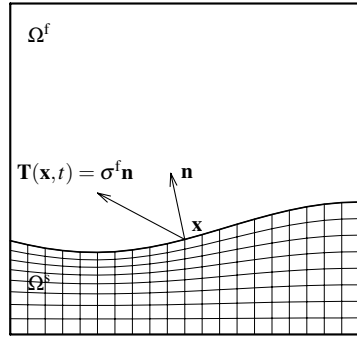
DISCRETIZATION

Notation

The Kronecker product of an $n \times m$ matrix C and a $k \times l$ matrix D is the $n \times m$ block matrix
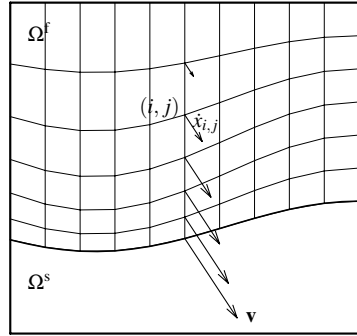
$$C \otimes D = \begin{bmatrix} c_{11}D & \cdots & c_{1m}D \\ \vdots & \ddots & \vdots \\ c_{n1}D & \cdots & c_{nm}D \end{bmatrix}. \tag{27}$$

This notation will be useful for writing the discretization in a compact form.

(a) The traction vector $\mathbf{T}(\mathbf{x},t) = \bar{\mathbf{t}}(\mathbf{x},t)$ exerted on the structure by the fluid is calculated on the fluid-structure interface as the fluid stress tensor times the outward unit normal.

(b) The grid point velocity $\dot{x}_{i,j}$ at grid point (i,j) is interpolated from the given velocity $\mathbf{v}$ of the structure on the interface.

Figure 5: Illustration of fluid-structure interaction algorithm.

Linear elastic wave equation

Introduce a vector $\hat{\mathbf{q}} = (\hat{q}_{ijk})^{\mathrm{T}} = (\hat{q}_{001},...,\hat{q}_{005},\hat{q}_{101},...,\hat{q}_{105},...,\hat{q}_{NM5})^{\mathrm{T}}$ where the three indices i, j and k represent the ξ-coordinate, η-coordinate and the solution variable, respectively. We define difference operators in terms of Kronecker products that operate on one index at a time.

Let $\mathbf{Q}_\xi = Q_\xi \otimes I_M \otimes I_5$ and $\mathbf{Q}_\eta = I_N \otimes Q_\eta \otimes I_5$ where Q_ξ and Q_η are 1D difference operators in the ξ- and η-directions, respectively, satisfying the SBP property (11). The identity operators I_N and I_M are unit matrices of size $(N+1) \times (N+1)$ and $(M+1) \times (M+1)$, respectively. The computation of the spatial differences of $\hat{\mathbf{q}}$ can then be seen as operating on $\hat{\mathbf{q}}$ with one of the Kronecker products, i.e., $\mathbf{Q}_\eta \hat{\mathbf{q}}$ operates on the second index and yields a vector of the same size as $\hat{\mathbf{q}}$ representing the first derivative approximation in the η-direction. To express the semi-discrete linear elastic wave equation, we also need to define $\hat{\mathbf{A}} = I_N \otimes I_M \otimes \hat{A}$ and $\hat{\mathbf{B}} = I_N \otimes I_M \otimes \hat{B}$. Note that these products are never actually explicitly formed as they are merely theoretical constructs to make the notation more compact. The products correspond well to the actual finite difference implementation, i.e., the approximations of the first derivatives are calculated by operating on successive lines of values in the computational domain. Using the Kronecker products defined above, the semi-discrete linear elastic wave equation with constant coefficients including the SAT expression can be written as

$$\frac{d\hat{\mathbf{q}}}{dt} = \mathbf{Q}_\xi(\hat{\mathbf{A}}\hat{\mathbf{q}}) + \mathbf{Q}_\eta(\hat{\mathbf{B}}\hat{\mathbf{q}}) + \widehat{\mathbf{SAT}} \tag{28}$$

where $\widehat{\mathbf{SAT}}$ is the SAT expression in transformed coordinates defined in Equation (25).

Navier–Stokes equations

For the fluid equations, we employ a similar procedure, i.e., we define vectors for the solution variables $\hat{\mathbf{U}}' = (\hat{U}'_{ijk})^{\mathrm{T}} = (\hat{U}'_{001},...,\hat{U}'_{004},\hat{U}'_{101},...,\hat{U}'_{104},...,\hat{U}'_{NM4})^{\mathrm{T}}$, and similarly for the two flux vectors $\hat{\mathbf{F}}'$ and $\hat{\mathbf{G}}'$, where again the three indices i, j and k represent the ξ-coordinate, η-coordinate and the solution variable, respectively. The same difference operators are used as for the linear elastic wave equation. The discretized fluid equation can thus be written as

$$\frac{d\hat{\mathbf{U}}'}{d\tau} = -\mathbf{Q}_\xi\hat{\mathbf{F}}' - \mathbf{Q}_\eta\hat{\mathbf{G}}' \tag{29}$$

Time integration

The systems (28) and (29) of ordinary differential equations can readily be solved by the classical 4th order explicit Runge–Kutta method. For the linear elastic wave equation, calling the right-hand side of (28) $\mathbf{f}(t_n,\hat{\mathbf{q}}^n)$ at the time level n, we advance the solution to level $n+1$ by performing the steps

$$
\begin{aligned}
\mathbf{k}_1 &= \mathbf{f}(t_n,\hat{\mathbf{q}}^n) \\
\mathbf{k}_2 &= \mathbf{f}\left(t_n + \frac{\Delta t}{2}, \hat{\mathbf{q}}^n + \frac{\Delta t}{2}\mathbf{k}_1\right) \\
\mathbf{k}_3 &= \mathbf{f}\left(t_n + \frac{\Delta t}{2}, \hat{\mathbf{q}}^n + \frac{\Delta t}{2}\mathbf{k}_2\right) \\
\mathbf{k}_4 &= \mathbf{f}(t_n + \Delta t, \hat{\mathbf{q}}^n + \Delta t\mathbf{k}_3) \\
\hat{\mathbf{q}}^{n+1} &= \hat{\mathbf{q}}^n + \frac{\Delta t}{6}(\mathbf{k}_1 + 2\mathbf{k}_2 + 2\mathbf{k}_3 + \mathbf{k}_4)
\end{aligned}
$$

and similar expressions for the fluid equations (29). The boundary conditions are updated only after all four stages for the respective field have been completed. That is to say, the structure solution at level $n+1$ is obtained using only the fluid stress at time level n. Likewise, the fluid solution at time level $n+1$ is based only on the position and velocity of the structure at time level n.

RESULTS

Verification

Our fluid solver has previously been verified and tested for numerical simulation of Aeolian tones (Müller, 2008) and qualitatively tested for simulation of human phonation on fixed grids (Larsson and Müller, 2009a) as well as moving grids in ALE formulation (Larsson, 2007).

The solver for the linear elastic equations with the SAT expression has been tested with a manufactured solution (Larsson and Müller, 2011, 2010c) and an academic 2D test case (Larsson and Müller, 2010c) where we obtained a rate of convergence of 3.5 to 4 in the 2-norm.

Problem parameters

The initial geometry for the vocal folds is here based on the geometry used in (Zhao *et al.*, 2002) for an oscillating glottis with a given time dependence. The initial shape of the vocal tract including the vocal fold is given as

$$r_w(x) = \frac{D_0 - D_{\min}}{4} \tanh s + \frac{D_0 + D_{\min}}{4}, \tag{30}$$

where r_w is the half height of the vocal tract, $D_0 = 5D_g$ is the height of the channel, $D_g = 4$ mm is the average glottis height, $D_{min} = 1.6$ mm is the minimum glottis height, $s = b|x|/D_g - bD_g/|x|$, $c = 0.42$ and $b = 1.4$. For $-2D_g \leq x \leq 2D_g$, the function (30) describes the curved parts of the reference configuration for the top and bottom (with a minus sign) vocal folds. The x-coordinates for the in- and outflow boundaries are $-4D_g$ and $10D_g$, respectively.

Vocal fold material parameters

The density in the reference configuration is $\rho_0 = 1043\,\text{kg/m}^3$, corresponding to the measured density of vocal fold tissue as reported by (Hunter *et al.*, 2004). The Poisson ratio is chosen as $\nu = 0.47$ for the tissue, corresponding to a nearly incompressible material with $\nu = 0.5$ being the theoretical incompressible limit. The Lamé parameters are chosen as $\mu = 3.5\,\text{kPa}$ and λ given by $\lambda = 2\mu\nu/(1-2\nu)$.

Fluid model

We use a Reynolds number of 3000 based on the average glottis height $D_g = 0.004\,\text{m}$ and an assumed average velocity in the glottis of $U_m = 40\,\text{m/s}$. We employ these particular values in order to be able to compare with previously published results by (Zhao *et al.*, 2002; Zhang *et al.*, 2002) and by (Larsson, 2007; Larsson and Müller, 2009a). The Prandtl number is set to 1.0, and the Mach number is 0.2 based on the assumed average velocity and the speed of sound. We deliberately use a lower value for the speed of sound $c_0 = 200\,\text{m/s}$ in order to speed up the computations. We implemented the higher Mach number by using the stagnation density ρ_0, the lowered stagnation speed of sound c_0 and $\rho_0 c_0^2$ as reference values of the nondimensional density, velocity and pressure, respectively. The air density is $1.3\,\text{kg/m}^3$, and the atmospheric pressure is $p_{atm} = 101325\,\text{Pa}$. The equation of state is the perfect gas law, and we assume a Newtonian fluid. At the inlet, we impose a typical lung pressure during phonation with a small asymmetric perturbation by setting the acoustic pressure to $p_{acoustic} = p - p_{atm} = (1 + 0.025\sin 2\pi\eta)2736\,\text{Pa}$, where $\eta = 0$ at the lower vertex and $\eta = 1$ at the upper vertex of the inflow boundary. The outlet pressure is set to atmospheric pressure, i.e., $p - p_{atm} = 0\,\text{Pa}$.

Numerical simulation

Both fluid and structure use the same set of variables for nondimensionalization, and the same time step is used for both fields so that the two solutions can exchange information at the same time levels. The structure grid consists of 81×61 points for each vocal fold, i.e., for the upper and the lower vocal folds, and the fluid grid has 241×61 points. The time step is determined by the stability condition for the fluid, which is satisfied here by requiring $CFL \leq 1$. Since the fluid domain changes with time, the CFL condition puts a stricter constraint on the time step when the glottis is nearly closed. The solution is marched in time with given initial and boundary conditions to dimensional time $t = 12\,\text{ms}$ (total number of time steps 277310).

The solution is first integrated to time $t = 6\,\text{ms}$ so that the effect of initial conditions will be negligible. After that, the solution is recorded at consecutive $2\,\text{ms}$ intervals as shown in Figure 6 where the vorticity and pressure contours are depicted in the left and right columns, respectively.

Initially, a starting jet is formed in the glottis which becomes unstable near the exit and creates the beginnings of vortical structures at time $t = 6\,\text{ms}$. Since the boundary conditions are not symmetric with respect to the centerline, also the solution is not symmetric. In the following, vortices are shed near the glottis and propagate downstream driven by the pressure gradient. The pressure plots indicate a sharp pressure drop just before the orifice. Downstream, the pressure minima occur in the vortex centers as expected.

The observed frequency of the vortex shedding is about $80\,\text{Hz}$, which is close to the typical phonation frequencies of $100\,\text{Hz}$ for men and $200\,\text{Hz}$ for women.

CONCLUSIONS

Our 2D model for the vocal folds based on the linear elastic wave equation in first order form and the airflow based on the compressible Navier–Stokes equations in the vocal tract proves to be able to capture the self-sustained pressure-driven oscillations and vortex generation in the glottis. The high order method for the linear elastic wave equation with a SAT formulation for the boundary conditions ensures a time-stable solution. The fluid and structure fields are simultaneously integrated explicitly in time and boundary data is exchanged only at the end of a time step. With this formulation, there is no need for iterations in order to find the equilibrium displacement for the structure depending on the fluid stresses. For the problem we consider here, the limiting factor on the time step is the CFL condition from the compressible Navier–Stokes equations. Since the fluid grid of the vocal tract has more grid points than the structure grids of the vocal folds and the nonlinear flow equations are more involved than the linear structure equations, the effort of integrating the linear elastic wave equation to get the structure displacement is small compared to the flow solution.

ACKNOWLEDGEMENTS

REFERENCES

CARPENTER, M.H. *et al.* (1994). "Time-stable boundary conditions for finite-difference schemes solving hyperbolic systems: Methodology and application to high-order compact schemes". *J. Comput. Phys.*, **111**, 220 – 236.

FORNBERG, B. (1998). *A practical guide to pseudospectral methods*. Cambridge University Press.

GUSTAFSSON, B. (2008). *High order difference methods for time-dependent PDE*. Springer-Verlag, Berlin Heidelberg.

GUSTAFSSON, B. *et al.* (1995). *Time dependent problems and difference methods*. John Wiley & Sons, New York.

HUNTER, E. *et al.* (2004). "A three-dimensional model of vocal fold abduction/adduction". *J. Acoust. Soc. Am.*, **115(4)**, 1747 – 1759.

LARSSON, M. (2007). "Numerical simulation of human phonation, Master thesis, Uppsala University, Department of Information Technology".

LARSSON, M. (2010). *Numerical modeling of fluid-structure interaction in the human larynx*. Ph.D. thesis, Norwegian University of Science and Technology.

LARSSON, M. and MÜLLER, B. (2009a). "Numerical simulation of confined pulsating jets in human phonation". *Computers & Fluids*, **38**, 1375 – 1383.

LARSSON, M. and MÜLLER, B. (2009b). "Numerical simulation of fluid-structure interaction in human phonation". B. Skallerud and H. Andersson (eds.), *MekIT 09 Fifth national conference on Computational Mechanics*, 261 – 280. Tapir Academic Press, Trondheim, Norway.
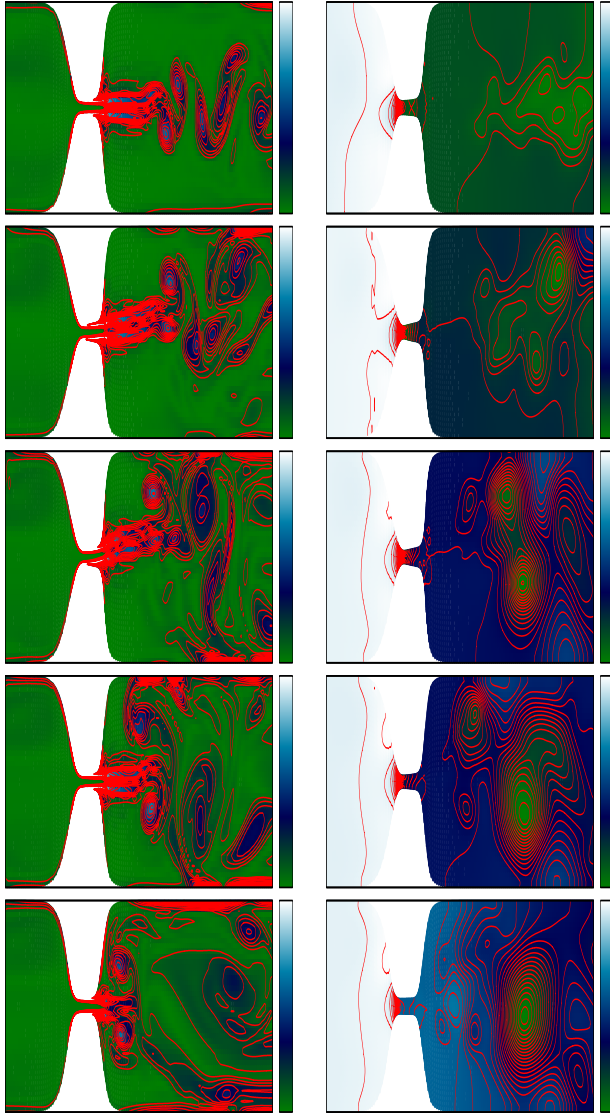
Figure 6: Vorticity and pressure contours at 2 ms intervals. The left column shows vorticity contours, the right column shows pressure contours. The top row shows the solution evaluated at $t = 6$ ms, the second row is at $t = 8$ ms and so on up to $t = 14$ ms (last row). The colorbar in the vorticity column stretches from 0 to $50\,000\,\text{s}^{-1}$ and the contour levels are spaced $3750\,\text{s}^{-1}$ apart. For the pressure column, the inflow is at $p = p_\infty + \Delta p$, the outflow is at (approximately) $p = p_\infty$ and the contour levels are spaced 71 Pa apart.

LARSSON, M. and MÜLLER, B. (2010a). "High order numerical simulation of fluid-structure interaction in human phonation". Proceedings of ECCOMAS CFD 2010 conference, Lisbon, Portugal, 14–17 June 2010.

LARSSON, M. and MÜLLER, B. (2010b). "Numerical simulation of fluid-structure interaction in human phonation: Application". G. Kreiss, P. Lötstedt, A. Målqvist and M. Neytcheva (eds.), *Numerical Mathematics and Advanced Applications 2009 (Proceedings of ENUMATH 2009 Eighth European Conference on Numerical Mathematics and Advanced Applications, 29 June - 3 July 2009), Uppsala, Sweden), Part 2*, 571 – 578. Springer-Verlag, Berlin.

LARSSON, M. and MÜLLER, B. (2010c). "Strictly stable high order difference method for the linear elastic wave equation". Submitted.

LARSSON, M. and MÜLLER, B. (2011). "Numerical simulation of fluid-structure interaction in human phonation: Verification of structure part". J. Hesthaven and E. Rønquist (eds.), *Spectral and High Order Methods for Partial Differential Equations (Selected papers from the ICOSAHOM '09 conference, 22-26 June 2009, Trondheim, Norway)*, 229 – 236. Springer-Verlag, Berlin.

LEVEQUE, R. (2002). *Finite volume methods for hyperbolic problems*. Cambridge University Press.

LINK, G. *et al.* (2009). "A 2D finite-element scheme for fluid-solid-acoustic interactions and its application to human phonation". *Methods in Applied Mechanics and Engineering*, **198**, 3321 – 3334.

LUO, H. *et al.* (2008). "An immersed-boundary method for flow - structure interaction in biological systems with application to phonation". *J. Comput. Phys.*, **227**, 9303 – 9332.

MÜLLER, B. (1996). "Computation of compressible low Mach number flow, Habilitation thesis, ETH Zurich".

MÜLLER, B. (2008). "High order numerical simulation of aeolian tones". *Computers & Fluids*, **37(4)**, 450 – 462.

POINSOT, T. and LELE, S. (1992). "Boundary conditions for direct simulations of compressible viscous flows". *J. Comput. Phys.*, **101**, 104 – 129.

SESTERHENN, J. *et al.* (1999). "On the cancellation problem in calculating compressible low Mach number flows". *J. Comput. Phys.*, **151**, 597 – 615.

STRAND, B. (1994). "Summation by parts for finite difference approximations for d/dx". *J. Comput. Phys.*, **110**, 47 – 67.

TITZE, I. (2000). *Principles of voice production*. National Center for Voice and Speech, Iowa City.

TITZE, I. (2008). "The human instrument". *Scientific American*, **298**, 94 – 101.

VISBAL, M. and GAITONDE, D. (2002). "On the use of higher-order finite-difference schemes on curvilinear and deforming meshes". *J. Comput. Phys.*, **181**, 155 – 185.

ZHANG, C. *et al.* (2002). "Computational aeroacoustics of phonation, Part II". *J. Acoust. Soc. Am.*, **112(5)**, 2147 – 2154.

ZHAO, W. *et al.* (2002). "Computational aeroacoustics of phonation, Part I: Computational methods and sound generation mechanisms". *J. Acoust. Soc. Am.*, **112(5)**, 2134 – 2146.

APPENDIX A

The eigenvector matrix $T(k_x, k_y)$ of $P(k_x, k_y)$ reads
$$T(k_x, k_y) =$$

$$
\begin{bmatrix}
k_x \tilde{c}_p / \lambda & -k_y & 0 & -k_y & -k_x \tilde{c}_p / \lambda \\
k_y \tilde{c}_p / \lambda & k_x & 0 & k_x & -k_y \tilde{c}_p / \lambda \\
k_x^2 \alpha + k_y^2 & -\frac{2 k_x k_y \tilde{c}_s \rho}{r^2} & k_y^2 & \frac{2 k_x k_y \tilde{c}_s \rho}{r^2} & k_x^2 \alpha + k_y^2 \\
2 k_x k_y \mu / \lambda & \rho \tilde{c}_s \bar{k} & -k_x k_y & -\rho \tilde{c}_s \bar{k} & 2 \mu k_x k_y / \lambda \\
k_y^2 \alpha + k_x^2 & \frac{2 k_x k_y \tilde{c}_s \rho}{r^2} & k_x^2 & -\frac{2 k_x k_y \tilde{c}_s \rho}{r^2} & k_y^2 \alpha + k_x^2
\end{bmatrix}
$$
$$(31)$$

The inverse of this matrix reads
$$T(k_x, k_y)^{-1} =$$

$$
\frac{1}{2 r^2}
\begin{bmatrix}
\dfrac{k_x \lambda}{\tilde{c}_p} & \dfrac{k_y \lambda}{\tilde{c}_p} & \dfrac{k_x^2}{\alpha r^2} & 2 \dfrac{k_y k_x}{\alpha r^2} & \dfrac{k_y^2}{\alpha r^2} \\[2ex]
-k_y & k_x & -\dfrac{k_x k_y}{\rho \tilde{c}_s} & \dfrac{\bar{k} r^2}{\rho \tilde{c}_s} & \dfrac{k_x k_y}{\rho \tilde{c}_s} \\[2ex]
0 & 0 & -\dfrac{2\bar{k}}{\alpha} + \dfrac{4 k_y^2}{\beta r^2} & -8 \dfrac{k_x k_y (\lambda + \mu)}{r^2 (\lambda + 2\mu)} & \dfrac{2\bar{k}}{\alpha} + 4 \dfrac{k_x^2}{\beta r^2} \\[2ex]
-k_y & k_x & \dfrac{k_x k_y}{\rho \tilde{c}_s} & -\dfrac{\bar{k} r^2}{\rho \tilde{c}_s} & -\dfrac{k_x k_y}{\rho \tilde{c}_s} \\[2ex]
-\dfrac{\lambda k_x}{\tilde{c}_p} & -\dfrac{\lambda k_y}{\tilde{c}_p} & \dfrac{k_x^2}{\alpha r^2} & 2 \dfrac{k_y k_x}{\alpha r^2} & \dfrac{k_y^2}{\alpha r^2}
\end{bmatrix}
$$
$$(32)$$

where the parameters are defined by $\bar{k} = (k_x^2 - k_y^2)/(k_x^2 + k_y^2)$,
$r = (k_x^2 + k_y^2)^{1/2}$, $\tilde{c}_p = r c_p$, $\tilde{c}_s = r c_s$, $\alpha = (\lambda + 2\mu)/\lambda$ and
$\beta = \alpha \lambda / \mu$.

8th International Conference on CFD in Oil & Gas, Metallurgical and Process Industries
SINTEF/NTNU, Trondheim Norway
21-23 June 2011

CFD11-97

A FLOWMETER BASED ON THE MEASUREMENT OF THE LOCAL HEAT TRANSFER COEFFICIENT AT THE FORWARD STAGNATION POINT OF A HEATED SPHERE PLACED IN A TURBULENT PIPE FLOW USING A MICRO-FOIL HEAT FLOW SENSOR

Hiroyoshi KOIZUMI[1*] , Naoki IMAMURA[2]

[1,2] Department of Mechanical Engineering and Intelligent Systems
The University of Electro-Communications, Tokyo 182-8585, JAPAN

[*]E-mail: koizumi@mce.uec.ac.jp

ABSTRACT

A simple method for measuring large volumetric flow rates with high precision and low cost is proposed for industrial use. A micro-foil heat flow sensor (*HFS*) was attached to the forward stagnation point of a heated sphere which was placed in a fully developed turbulent pipe flow. The time-averaged local Nusselt number at the forward stagnation point, $\overline{Nu_s}$, was calculated by $\overline{Nu_s} = \frac{\overline{h_s}d}{\lambda} = \frac{\overline{q_s}d}{(T_w - T_f)\lambda}$. Numerical simulation was performed using unsteady axisymmetric Reynolds equations and the low-Reynolds number k-ε model. In order to clarify the effects on the $\overline{Nu_s}$ due to the anisotropic turbulence intensity ($g = \overline{v_r^2} - \overline{v_\theta^2}$) during which the streamwise main velocity was being reduced toward the forward stagnation point, we proposed a simplified algebraic equation for *g*. It was found experimentally and numerically that $\overline{Nu_s}$ is directly proportional to the volumetric flow rate Q_v for the flow rate below 273 Nm³/hr (Reynolds number, $\text{Re}_D = V_m D / \nu \leqq 60,000$). Q_v can be obtained by using this linear relationship.

Keywords: Flow meter, Volumetric flow rate, Forced convection, Heated sphere, Pipe flow, Micro-foil heat flow sensor (*HFS*), low-Reynolds number $k - \varepsilon$ model, CFD .

NOMENCLATURE

Latin Symbols
$C_1, C_2, C_{\varepsilon 1}, C_{\varepsilon 2}, C_\mu$ Turbulent constant, [-].
c_P Specific heat at constant pressure, [J/(kg·K)].
d   Outer diameter of heated sphere, [20 mm].
D   Inner diameter of pipe, [107 mm].
g   Anisotropic turbulent intensity, $\overline{v_r^2}$ - $\overline{v_\theta^2}$ [m²/s²].
h_s Heat transfer coefficient at forward stagnation point, [W/m²·K].
k   Turbulent kinetic energy, [m²/s²].
Nu_s Nusselt number at forward stagnation point, $\frac{h_s d}{\lambda} = \frac{q_s d}{(T_w - T_f)\lambda}$ [-].
P   Pressure, [Pa].
Pr   Prandtl number, ν/α [-].

q_s Heat flux at forward stagnation point, [W/m²].
Q_v Volumetric flow rate, [Nm³/hr].
Q_m Mass flow rate, [kg/hr].
Re_d Reynolds number based on sphere or cylinder diameter d, $V_m d/\nu$ [-].
Re_D Reynolds number based on inner pipe diameter D, $V_m D/\nu$ [-].
t   Time, [s].
T   Temperature, [K].
T_w Uniform temperature of sphere surface, [K].
T'   Fluctuation temperature, [K].
v   Fluctuation velocity component, [m/s].
V   Time-averaged velocity component, [m/s].
V_m Mean velocity in pipe, [m/s].
$v_{r\,FI}$ Fluctuation intensity of instantaneous local velocity, $\sqrt{v_r^2}/V_m \times 100$ [%].

Greek Symbols
α   Thermal diffusivity, $\kappa/(\rho c_p)$ [m²/s].
ε   Turbulent energy dissipation rate, [m²/s³].
κ   Thermal conductivity, [W/(m·K)].
ν   Kinematic viscosity, [m²/s].
ν_t Turbulent kinematic viscosity, [m²/s].
ρ   Fluid density, [kg/m³].
$\sigma_\kappa, \sigma_\varepsilon, \sigma_T$ Turbulent Prandtl number, [-].

Subscripts
θ   Angular displacement from the reference direction around the sphere, (Fig. 3).
r   Distance from the origin in the radial coordinate around the sphere, (Fig. 3).

Overline
$\overline{\bullet}$ Time-averaged value of physical amount of •.

INTRODUCTION

Flow measurement is a classical field of measuring technology. A large number of researchers have already developed large flow rate measuring methods based on a wide variety of principles [1, 2]. There are two classifications for flow measurements:

non-thermal and thermal. The most popular non-thermal flowmeters are based on a mechanical working principle. Orifice and nozzle flowmeters are commonly used for deriving flow rate by measuring the pressure drop through an orifice plate and nozzle across which a pressure difference is generated by the flow [3]. For the vortex flowmeter, a Karman vortex street is a term used in fluid dynamics for a repeating pattern of swirling vortices caused by the unsteady separation of a fluid flow over bluff bodies. Using this measuring principle, a bluff body in the flow can be used to measure flow rate indirectly by the shedding frequency of swirling vortices. A volumetric flow rate is obtained by using the linear relationship between the shedding frequency and the flow velocity (relationship between the Strauhal number and the Reynolds number). This kind of flowmeter has been widely used in industrial gas, liquid and steam flow measurements because of its simple installation, high reliability and high accuracy. It is usually employed to measure the volumetric flow rate, but several methods using a vortex flowmeter to detect mass flow rate have been recently introduced [4]. One particular true mass flowmeter, which is now sold widely and is commercially available, is a Coriolis flowmeter based on a Coriolis force which acts on an oscillating tube with fluid flowing inside [5].

On the contrary, in situations where a high volumetric flow rate is required to be metered, only a few of them are by thermal flow measurements because the heating capacity of the sensor becomes great as the flow rate enlarges. In this paper, a new thermal measurement method of a large flow rate with high precision and low cost is proposed for industrial use [6]. The method is based on the local heat transfer coefficient of a heated sphere at the forward stagnation point which is inserted inline with the pipe flow. It was found that the time-averaged local Nusselt number at the forward stagnation point $\overline{Nu_s}$ is directly proportional to the volumetric flow rate Q_v in a pipe. Thus, Q_v can be obtained by using this linear relationship. The validity of measuring the flow rates below 273 Nm^3/hr for air was confirmed both experimentally and numerically.
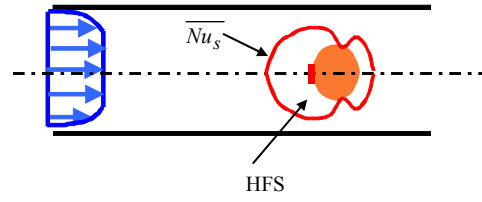
MEASUREMENT PRINCIPLE

Figure 1 shows the measurement principle of the new flowmeter. Figure 1(a) is the schematic drawing of a heated sphere placed in the center part of a fully developed turbulent pipe flow. When the local Nusselt number of a heated sphere at the forward stagnation point, $\overline{Nu_s}$, is directly proportional to the volumetric flow rate Q_v for a wide range of a turbulent flow as shown in Fig. 1(b), Q_v can be obtained by using the linear relationship between $\overline{Nu_s}$ and Q_v. This measuring method is usable for all gases and liquids.

The density of liquid ρ is mostly unaffected by the change of ambient temperature and pressure under normal operations, therefore, conventional mass flow rate Q_m is simply derived from the volumetric flow rate Q_v multiplied by liquid density ρ. On the other hand, the fluid volume of gases is a function of ambient fluid temperature T and pressure P. Thus, the mass flow rate can be calculated as $Q_m =\rho(P,\ T)\cdot Q_v$, and its density ρ

of gas can be obtained by measuring both P and T of a flowing gas.

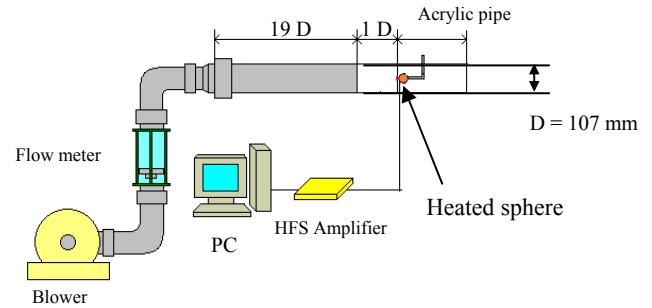(a) Schematic drawing of flow meter.
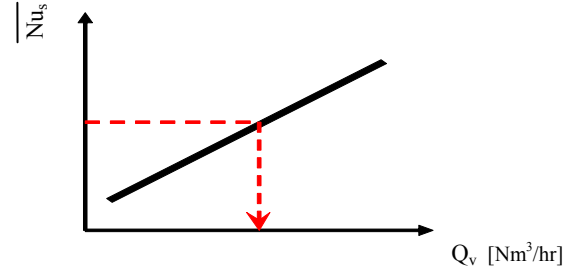
(b) Relationship between $\overline{Nu_s}$ and Q_v.
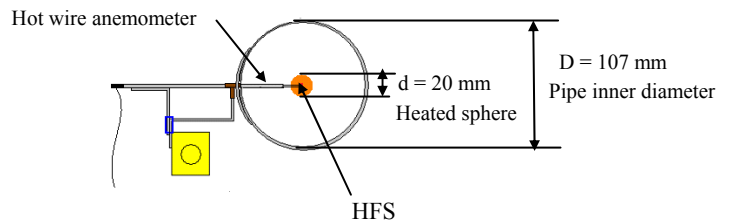
Figure 1: Measurement principle.

EXPERIMENT
Experimental Setup

Figure 2 shows the schematic view of the experimental apparatus. Figure 2(a) shows the schematic drawing of setup and Fig. 2(b) shows the cross section of the pipe.

(a) Schematic drawing of setup.

(b) Cross section of pipe.

Figure 2: Experimental apparatus.

The working medium was air (Prandtl number Pr=0.71) which was compressed by a blower and sent into a horizontal straight pipe downstream of a turbulence promoter. The pipe was 2 m long and made of transparent acrylic 3 mm thick with an inner diameter (D) of 107 mm. The sphere was made of 1 mm thick copper with an outer diameter (d) of 20 mm, and was set in the center part of the pipe. The dimensionless hydrodynamic entrance length is independent on the Reynolds number for the turbulent flow: 20×D, where D is the pipe inner diameter [7]. Therefore, in order to obtain a fully developed turbulent flow within a shorter entrance length, it was better to promote the turbulence by setting a turbulence promoter. The sphere was horizontally attached to one end of a stainless-steel pipe, which served as a support. The pipe had a 2 mm outer diameter and was 50 mm in length and was fixed to the traversing system. The blockage ratio of the sphere in the pipe, d/D, was 0.187. The flow velocity of the air was measured by the hot wire anemometer (HWA). A wire diameter of 5 μm and a 1.2 mm prong length were used.

Nusselt Number
Figure 3 shows the schematic drawing of the measuring position of the heated sphere and the coordinate system.

Axisymmetric condition: $\frac{\partial}{\partial \phi} \equiv 0$

d = 20 mm, D = 107 mm
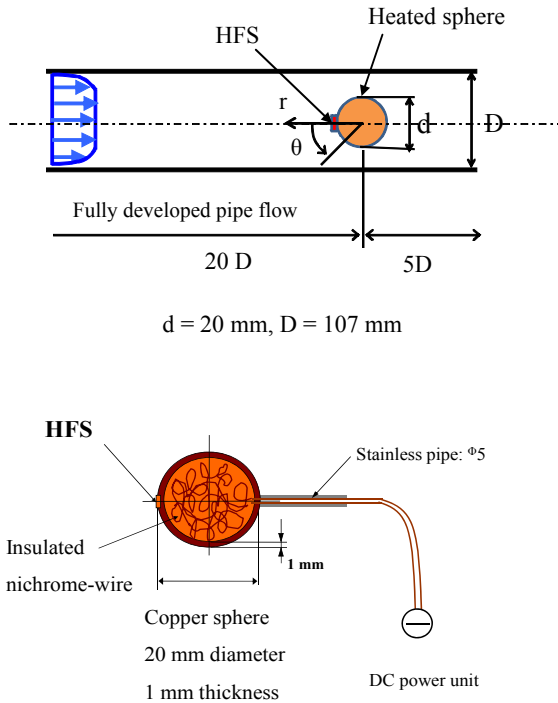
Figure 3: Schematic layout of heated sphere and sensor.

A nichrome-wire, which was inserted into a flexible tube with an outer diameter of 1 mm and electrically insulated, was inserted into the sphere through the opening of an inner diameter of 2 mm as shown in the lower part of Fig. 3, and it was electrically heated by a constant direct current. The isothermal boundary condition of the sphere surface was checked by thermocouples, and the surface temperature was kept uniform and constant to within 1 K at Re_D=10,000. The temperature difference between the uniform forced flow and the sphere was set to about 20 K. The experiments were carried out at several Reynolds numbers up to 60,000.

The main structure of the thermal flowmeter consisted of a micro-foil heat flow sensor (*HFS*) and a heater, and an electric circuit. The heat transfer coefficient at the forward stagnation point of a heated sphere placed in a fully developed turbulent pipe flow was measured using a *HFS* with a thickness of 75 μm, a sensing area of 1.5×4 mm² and a response time of about 0.02 s. The spatial resolution of the *HFS* was about 8.6° around the sphere. The *HFS* was pasted on the heated sphere surface at the forward stagnation point as shown in Fig. 3, and its output was amplified 100,000 times. The amplified output was then passed through a low-pass filter with a cut-off frequency of 20 Hz. The time-averaged heat flux, $\overline{q_s}$, from the amplified time series of the *HFS* was obtained using a personal computer. The time-averaged Nusselt number at the forward stagnation point of a heated sphere $\overline{Nu_s}$, was calculated by

$\overline{Nu_s} = \frac{\overline{h_s}d}{\lambda} = \frac{\overline{q_s}d}{(T_w - T_f)\lambda}$. Six thousand data points were

sampled from a time series of the *HFS* output using an *AD* converter with a 16 bit resolution, and the sampling time was set to 0.01 s.

NUMERICAL SIMULATION
Numerical simulation provides a powerful tool for analyzing flowmeter behavior. Therefore, it can be used to determine the design of the measurement device and the validity of the flow measurement principle. The following flow characteristics exist in this flow system:
(i) A strong anisotropic turbulence is produced due to a large reduction rate of the streamwise main velocity in line of the forward stagnation point of a bluff body such as a sphere and a cylinder which is placed against the main flow [10]-[12]. In order to predict the anisotropic turbulent structure, which strongly affects the heat transfer performance at the forward stagnation point of a sphere, the simplified algebraic stress model for the anisotropy is proposed.
(ii) A thin stagnant layer is produced along the forward stagnation point of the bluff body [13]. Therefore, it is necessary to set the zero velocity such as the mean velocity components and turbulent quantities around a sphere surface.
(iii) The heated sphere is placed in the center part of the turbulent pipe flow, and then the body-fitted coordinate system, which is provided in the commercial software package CFD2000 [9], is employed.

The standard k - ε model is known to yield less accurate predictions of flows with strong anisotropic turbulence such as a rectangular duct turbulent flow which produces the secondary flow in a cross section [14]. Furthermore, it is necessary to set zero turbulence quantities such as k , ε and other turbulence stresses

to the sphere surface. Therefore, in order to more simply predict the turbulent structure near the forward stagnation point of a bluff body for industrial use, a simplified algebraic anisotropic stress model was proposed. Then, we customized the proposed turbulence model into a low-Reynolds number k - ε model, which is provided in the commercial software package CFD2000 [9].

Basic Equations

In order to promote the realization of the flow fields, such as flow pattern and turbulent structure near the forward stagnation point of the heated sphere which is placed in the center part of the turbulent pipe flow, the basic equations and turbulent model are described using a spherical coordinate system. The following assumptions were made for this flow system.

(i) Flow in the pipe is assumed to be fully developed, and the flow field around the sphere also has a symmetric nature for time-averaged values in the azimuthal direction ($\frac{\partial}{\partial \phi} \equiv 0$).

(ii) The mixed convection parameter of Gr/Re_D^2 is between 10^{-3} and 10^{-5}, therefore this flow is considered as a pure forced convection [10]. Also, the radiation heat transfer effect is neglected.

(iii) The physical properties of the fluid are assumed to be constant.

Continuity equation

$$\frac{1}{r}\frac{\partial(r^2 V_r)}{\partial r} + \frac{1}{\sin\theta}\frac{\partial(V_\theta \sin\theta)}{\partial\theta} = 0 \qquad (1)$$

Momentum equations for V_r and V_θ

$$V_r\frac{\partial V_r}{\partial r} + \frac{V_\theta}{r}\frac{\partial V_r}{\partial\theta} - \frac{V_\theta^2}{r} = -\frac{1}{\rho}\frac{\partial P}{\partial r}$$
$$+ \nu\left(\nabla^2 V_r - \frac{2}{r^2}\frac{\partial V_r}{\partial\theta} - \frac{1}{r^2}V_\theta\cos\theta\right)$$
$$- \frac{1}{r^2}\frac{\partial\left(r\overline{v_r^2}\right)}{\partial r} - \frac{1}{r}\frac{\partial\left(\overline{v_r v_\theta}\right)}{\partial\theta} + \frac{\overline{v_\theta^2}}{r} \qquad (2)$$

$$V_r\frac{\partial V_\theta}{\partial r} + \frac{V_\theta}{r}\frac{\partial V_\theta}{\partial\theta} - \frac{V_r V_\theta}{r} = -\frac{1}{\rho r}\frac{\partial P}{\partial\theta}$$
$$+ \nu\left(\nabla^2 V_\theta + \frac{2}{r^2}\frac{\partial V_r}{\partial\theta} - \frac{V_\theta}{r^2 sin^2\theta}\right) - \frac{1}{r^2}\frac{\partial\left(r^2\overline{v_r v_\theta}\right)}{\partial r} - \frac{1}{r}\frac{\partial\left(\overline{v_\theta^2}\right)}{\partial\theta} \qquad (3)$$

with Laplacian operator

$$\nabla^2 = \frac{1}{r^2}\frac{\partial}{\partial r}\left(r^2\frac{\partial}{\partial r}\right) + \frac{1}{r^2\sin\theta}\frac{\partial}{\partial\theta}\left(\sin\theta\frac{\partial}{\partial\theta}\right)$$

Energy equation

$$V_r\frac{\partial T}{\partial r} + \frac{V_\theta}{r}\frac{\partial T}{\partial\theta} = \frac{1}{r^2}\frac{\partial}{\partial r}\left[r^2(\alpha\frac{\partial T}{\partial r} - \overline{v_r T'})\right]$$
$$+ \frac{1}{r^2\sin\theta}\frac{\partial}{\partial\theta}\left[\sin\theta(\alpha\frac{\partial T}{\partial\theta} - \overline{v_\theta T'})\right] \qquad (4)$$

Turbulence Model

The Reynolds stresses of $\overline{v_r^2}$ and $\overline{v_\theta^2}$ which appear in the above Reynolds equations of (2) and (3) are modeled using the low-Reynolds number k - ε turbulence model. The transport equations for turbulence energy k and its dissipation rate ε adopted are equivalent to those used for the standard model [14].

Transport equation for k

$$V_r\frac{\partial k}{\partial r} + \frac{V_\theta}{r}\frac{\partial k}{\partial\theta} = -(\overline{v_r^2} - \frac{2}{3}k)\frac{\partial V_r}{\partial r} + \frac{(\overline{v_\theta^2} - 2k/3)}{r}\frac{\partial V_\theta}{\partial\theta} + \frac{1}{r^2}\frac{\partial}{\partial r}\left(r^2\left(\nu + \frac{\nu_t}{\sigma_k}\right)\frac{\partial k}{\partial r}\right)$$
$$+ \frac{1}{r^2\sin\theta}\frac{\partial}{\partial\theta}\left(\sin\theta\left(\nu + \frac{\nu_t}{\sigma_k}\right)\frac{\partial k}{\partial\theta}\right) + \varepsilon \qquad (5)$$

Transport equation for ε

$$V_r\frac{\partial\varepsilon}{\partial r} + \frac{V_\theta}{r}\frac{\partial\varepsilon}{\partial\theta} = -C_{\varepsilon 1}\frac{\varepsilon}{k}((\overline{v_r^2} - \frac{2}{3}k)\frac{\partial V_r}{\partial r} + \frac{(\overline{v_\theta^2} - 2k/3)}{r}\frac{\partial V_\theta}{\partial\theta})$$
$$+ \frac{1}{r^2}\frac{\partial}{\partial r}\left(r^2\left(\nu + \frac{\nu_t}{\sigma_\varepsilon}\right)\frac{\partial\varepsilon}{\partial r}\right) + \frac{1}{r^2\sin\theta}\frac{\partial}{\partial\theta}\left(\sin\theta\left(\nu + \frac{\nu_t}{\sigma_\varepsilon}\right)\frac{\partial\varepsilon}{\partial\theta}\right) + C_{\varepsilon 2}f_\varepsilon\left(\varepsilon - 2\nu\left(\frac{\partial\sqrt{k}}{\partial r}\right)^2\right) \qquad (6)$$

The accelerated velocities along the sphere in the angular direction of $\frac{1}{r}\frac{\partial V_\theta}{\partial\theta}$ which appear in the production terms in equations (5) and (6) are replaced by the streamwise main velocity reduction rate of $\frac{\partial V_r}{\partial r}$ using equation (7). From the potential theory [11], the reduction rate of the main streamwise velocity toward the forward stagnation point becomes twice that of the acceleration rate towards the downward direction along the sphere surface from the stagnation point as given by the following relation:

$$-\frac{\partial V_r}{\partial r} = 2\frac{1}{r}\frac{\partial V_\theta}{\partial\theta} \qquad (7)$$

A strong non-homogeneous turbulent structure due to the large reduction rate of the streamwise main flow is produced in this flow situation, which is important for determining how to model the turbulent production terms in the transport equations of k and ε in the first terms on the right hand sides of equations (5) and (6). Therefore, instead of using the full transport equations of $\overline{v_r^2}$ and $\overline{v_\theta^2}$, we propose a simplified algebraic stress model for industrial use. At first, the advection and diffusion terms are neglected in the $\overline{v_r^2}$ and $\overline{v_\theta^2}$ equations, because it is assumed that both terms have negligible effects on the turbulent production which are controlled by the reduction rate of the main streamwise velocity near the forward stagnation point. The quantity $-(\overline{v_r^2} - \frac{1}{2}\overline{v_\theta^2} + \frac{1}{3}k)$ appearing in the production terms $P_{k,\varepsilon} = -(\overline{v_r^2} - \frac{1}{2}\overline{v_\theta^2} + \frac{1}{3}k)\frac{\partial V_r}{\partial r}$ of both equations (5) and (6) is approximated using the following relation, $\frac{1}{2}(\overline{v_r^2} + \overline{v_\theta^2}) = \overline{v_z^2} = \frac{2}{3}k$. When the normal Reynolds stress difference of $g = \overline{v_r^2}$ - $\overline{v_\theta^2}$ is introduced, the normal

Reynolds stresses $\overline{v_r^2}$ and $\overline{v_\theta^2}$ are rewritten as k and *g*: $\overline{v_r^2} = \frac{2}{3}k + \frac{g}{2}$ and $\overline{v_\theta^2} = \frac{2}{3}k - \frac{g}{2}$. As the production terms are rewritten by $P_{k,\varepsilon} = -(\frac{3}{4}g + \frac{2}{3}k)\frac{\partial V_r}{\partial r}$ in terms of *g* and *k* instead of $\overline{v_r^2}$ and $\overline{v_\theta^2}$, the simplified algebraic stress equation of *g* is made. Next, the redistribution terms are modelled using Launder's proposal [15]. The modelled Reynolds stress equations for normal stresses $\overline{v_r^2}$ and $\overline{v_\theta^2}$ are as follows:

$$0 = 2\frac{\overline{v_\theta^2}}{r}\frac{\partial \overline{V_\theta}}{\partial \theta} - \frac{2}{3}\varepsilon - [C_1\frac{\varepsilon}{k}(\overline{v_\theta^2} - \frac{2}{3}k) + C_2(2\frac{\overline{v_\theta^2}}{r}\frac{\partial V_\theta}{\partial \theta} - \frac{2}{3}P_{kk})]$$

(8)

$$0 = -2\overline{v_r^2}\frac{\partial V_r}{\partial r} - \frac{2}{3}\varepsilon - [C_1\frac{\varepsilon}{k}(\overline{v_r^2} - \frac{2}{3}k) + C_2(-2\overline{v_r^2}\frac{\partial V_r}{\partial r} - \frac{2}{3}P_{kk})]$$

----------- ----- ---

Production Dissipation   Redistribution term

(9)

Subtract equation (9) from equation (8), and then relation (7) is inserted into the resulting equation. Then the stress equation of $g = \overline{v_r^2} - \overline{v_\theta^2}$ is given in the following:

$$0 = C_1 \frac{\varepsilon}{k} g + (1 - C_2)(\overline{v_\theta^2} + 2\overline{v_r^2})\frac{\partial V_r}{\partial r}$$

(10)

Finally, by inserting the relations $\overline{v_r^2} = \frac{2}{3}k + \frac{g}{2}$ and $\overline{v_\theta^2} = \frac{2}{3}k - \frac{g}{2}$ into the above equation (10), the algebraic stress equation of *g* is given by equation (11).

Algebraic stress equation for g

$$g = \overline{v_r^2} - \overline{v_\theta^2} = 2(1 - C_2)k\frac{\partial V_r}{\partial r} / \left\{\frac{1}{2}(1 - C_2)k\frac{\partial V_r}{\partial r} + C_1\frac{\varepsilon}{k}\right\}$$

(11)

In addition, we use the Boussinesq's concept of eddy viscosity for shear stress $\overline{v_r v_\theta}$, and heat fluxes $\overline{v_r T'}$ and $\overline{v_\theta T'}$:

$$\overline{v_r v_\theta} = -\nu_t \frac{\partial V_r}{\partial r} \qquad \overline{v_r T'} = -\frac{\nu_t}{\sigma_T}\frac{\partial T}{\partial r}$$

$$\overline{v_\theta T'} = -\frac{\nu_t}{\sigma_T}\frac{1}{r}\frac{\partial T}{\partial \theta}$$

(12)

The turbulent eddy viscosity is given by the following relation: $\nu_t = C_\mu f_\mu \frac{k^2}{\varepsilon}$

where $f_\mu = exp[-2.5/(1 + R_t/50)]$, $R_t = k^2/(\nu\varepsilon)$.

The above algebraic stress equation of *g* was transformed into the body-fitted coordinate and was combined with the CFD2000 [9]. The empirical constants which appear in the above equations are given by the following standard values:
$C_1 = 1.5$, $C_2 = 0.6$, $C_{\varepsilon1} = 1.44$, $C_{\varepsilon2} = 1.92$, $C_\mu = 0.09$, $\sigma_k = 1.0$, $\sigma_\varepsilon = 1.3$, $\sigma_T = 0.9$.

Calculation Procedure

The body-fitted coordinate was used in this calculation. The boundary conditions were no slip at the pipe inner wall and at the sphere surface. The inlet flow conditions were set to the fully developed turbulent flow, and the outlet flow condition was set to free stream, that is, the gradients of all variables along the streamwise direction were set to zero. The convective terms were discretized using a second order accurate upwind difference scheme. The *ADI* (Alternating Direction Implicit) method was used to solve a set of basic equations [9]. A *LU* incomplete factorization method was used to solve the pressure field. All calculations were carried out with double precision using a personal computer.

The computational domain extends from 10 times the pipe inner diameter of D in the upstream regime around the heated sphere and to 5D in the downstream regime. A non-uniform 400 (in the streamwise direction)×30 (in the radial direction) grid with a finer mesh near the sphere was used. Prior to the final computations, grid independence tests were performed for all the Reynolds number flows. Calculation was carried out for air flow (*Pr*=0.71).

RESULTS

Time-averaged Velocity

Figure 4 shows the characteristics of the streamwise mean velocity in line of the forward stagnation point of a heated sphere which was placed in the center part of the turbulent pipe flow at Re_D=10,000. Figure 4(a) shows the main streamwise velocity V_r, and Fig. 4(b) shows the reduction rate of the streamwise main velocity dV_r/dr which was obtained from the velocity distribution of Fig. 4(a), respectively. The solid line represents the experimental result and the dashed line represents the calculated result. The dash-dotted lines show the analysed result of a sphere placed in a uniform velocity flow by the potential theory [11].

The reduction rate of the experimental result is in good agreement with that of the potential theory, but a small discrepancy is produced between the experimental result shown by the solid line and the calculated result indicated by the dotted line for 2r/d<0.1 specified by mark ↓. In total, the proposed turbulence model mostly predicts the main stream reduction phenomena toward the forward stagnation point of a sphere which was placed in the center part of the turbulent pipe flow. The reduction rate of the main velocity by the potential theory near the forward stagnation point is linearly decreased. On the contrary, V_r is rapidly decreased from 2r/d ≈ 0.5 to the stagnation point. That is, a large discrepancy is produced between the result of the potential theory shown by the dotted and dashed line, and the experimental and simulated results in a pipe flow, because the flow near the forward stagnation point of a sphere placed in the center part of a pipe is strongly influenced by the main streamwise reduction effect not only due to the existence of the sphere but also due to the restriction of no slip condition by the peripheral pipe wall.
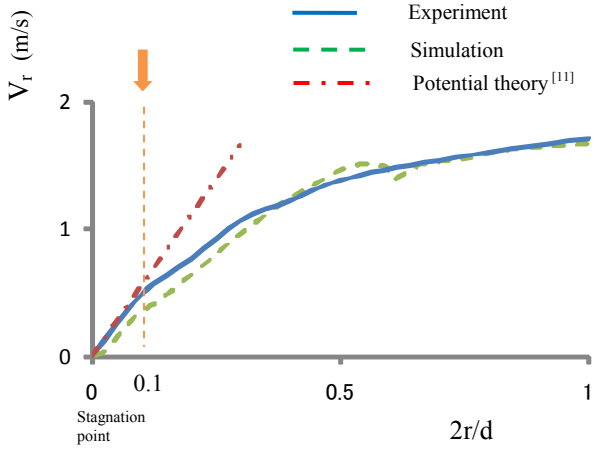
(a) Streamwise main velocity.
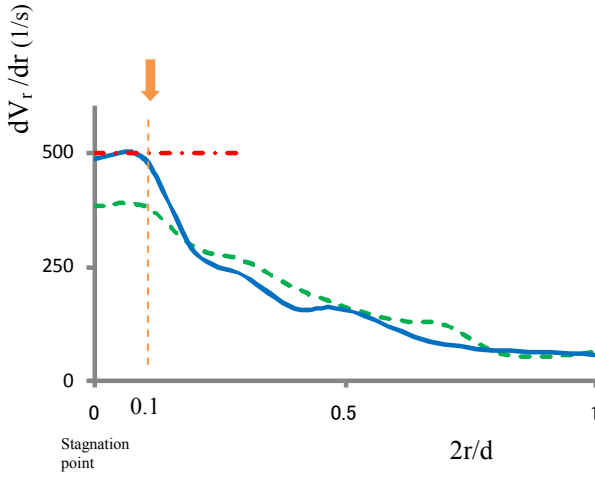
(b) Reduction rate of the streamwise main velocity.

Figure 4: Streamwise velocity in line of the forward stagnation point of a sphere.

Turbulent Structure

Figure 5 shows the turbulent structure in line of the forward stagnation point of a heated sphere at $Re_D=10,000$. Figure 5(a) shows the anisotropic turbulence of $g = \overline{v_r^2} - \overline{v_\theta^2}$ and Fig. 5(b) indicates the turbulence intensity of $v_{r\ FI}$, respectively. The solid line represents the experimental result and the dashed line is the simulated result.

As expected, the anisotropy of g is seen to increase rapidly from $2r/d \approx 0.25$ toward the forward stagnation point. The experimental turbulence intensity, v_{FI}, shown by the dotted line is also in good agreement with that of the calculated result for $2r/d > 0.1$. The maximum values of g and v_{FI} taken at around $2r/d \approx 0.1$, originate exactly in the same place where the highest reduction rate of the streamwise main velocity is located as shown by mark ↓ in Fig 4(b). This rapid increase of $V_{r\ FI}$ near

the forward stagnation point was mainly caused by the amplification of anisotropic turbulence of g due to the large reduction rate of dV_r/dr as shown in equation (11). That is, it is found that the simplified algebraic stress model predicts well the reduction rate of the streamwise main flow which affects the turbulence near the forward stagnation point.
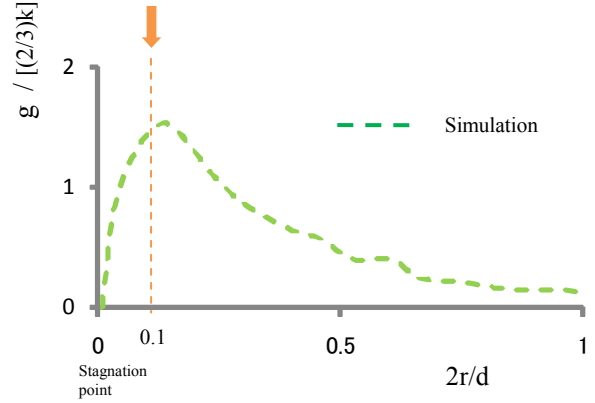
(a) Anisotropic turbulence of $g = \overline{v_\theta^2} - \overline{v_r^2}$.
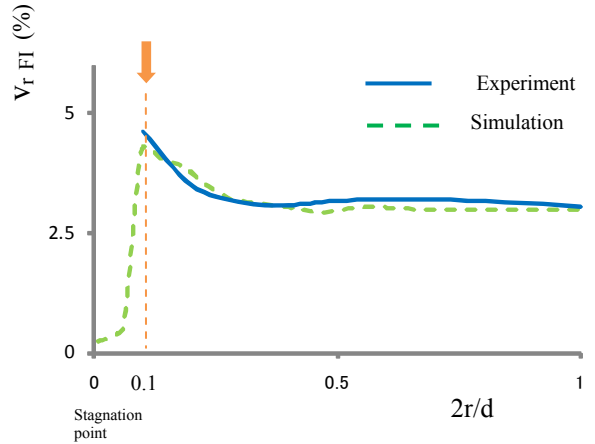
(b) Turbulence intensity of $v_{r\ FI}$.

Figure 5: Turbulent structure in line of the forward stagnation point of a sphere.

Nusselt Number

Figure 6 shows the relationship between the time-averaged local Nusselt number at the forward stagnation point, $\overline{Nu_s}$, and the volumetric flow rate, Q_v for $5,000 \leqq Re_D \leqq 60,000$. The corresponding Reynolds number based on the sphere diameter, $Re_d=V_m d/\nu$, ranges from 930 ($Re_D=5,000$) to 11,200 ($Re_D=60,000$). The solid line represents the asymptotic linearized line which interporates the simulated results shown by marks ◆. The experimental results shown by marks ■ are in good agreement with those of the simulated results for Reynolds number, Re_D, ranging from 10,000 to 40,000.

Also, it is found that this flowmeter reflects well both the wide linear range and high sensitivity, both of which are critical parameters for designing the flowmeters. That is, it is found that heat transfer enhancement at the forward stagnation point was mainly caused by the amplification of turbulence intensity of $v_{r\,FI}$ as is shown in Fig. 5(b) due to the large reduction rate of the main streamwise velocity near the forward stagnation point.
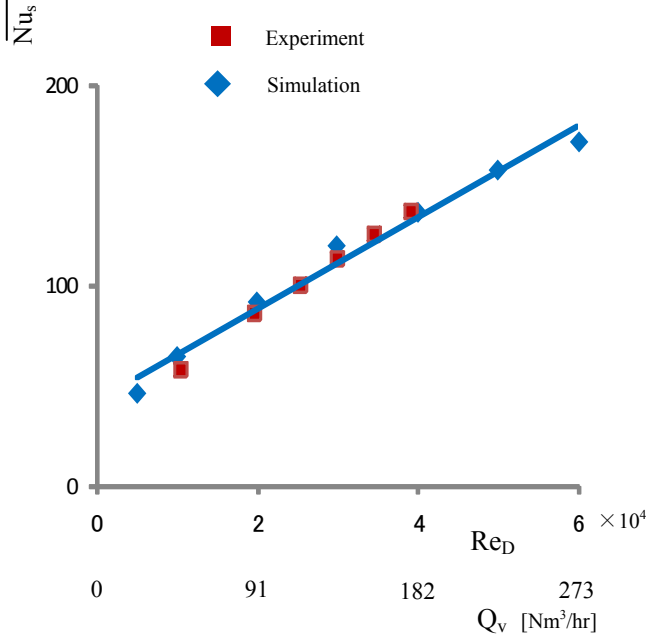

Figure 6: Relationship between $\overline{Nu_s}$ and Re_D.

Conversion Factor

In the case of the measurement of different kinds of gases and liquids, it is necessary to obtain the Nusselt number at the forward stagnation point for each fluid flow. Therefore, it is essential to calculate the conversion factor using CFD2000 in advance, which indicates the multiplication number based on the output of *HFS* for air flow for Q_v= 45 Nm^3/hr (Re_D=10,000). Table 1 shows the conversion factors, thermal diffusivity α , density ρ and Prandtl number Pr for representative gases. Thus, it is not necessary to conduct an experiment in advance for various fluid flows by using the conversion factor.

Table 1: Conversion factor.

	Conversion factor	α [mm^2/s]	ρ [kg/m^3]	Pr
H$_2$	**0.331**	155	0.0818	0.710
He	**0.312**	181	0.163	0.678
Air	**1.0**	22	1.18	0.717
CO$_2$	**1.348**	11	1.80	0.767

CONCLUSION

A new measurement technique for determining large volumetric flow rates with high precision and low cost has been proposed for industrial use. A micro-foil heat flow sensor (*HFS*) was attached to the forward stagnation point of a heated sphere which was placed in a fully developed turbulent pipe flow. It was found that the local Nusselt number at the forward stagnation point, $\overline{Nu_s}$, is directly proportional to the volumetric flow rate Q_v. Thus, Q_v in a pipe can be obtained by using the linear relationship.

In order to clarify the effect on the local Nusselt number of the forward stagnation point due to the anisotropy of the turbulence intensity ($g = \overline{v_0^2} - \overline{v_r^2}$) during which the streamwise main velocity was reduced toward the forward stagnation point, we proposed the simplified algebraic equation of g which appears in the production terms of k and ε transport equations. The algebraic stress equation of g was combined with the CFD2000 software [9], and the calculation was performed by using a low-Reynolds number k - ε turbulence model.

The new measurement technique has been demonstrated experimentally and numerically by using air flow over a range of volume flow rates from 23 to 273 Nm^3/hr (Reynolds number, $5{,}000 \leqq Re_D = V_m D / \nu \leqq 60{,}000$).

REFERENCES

[1] For example, MATSUSHIRO, M. (1968), "Flow Measurement" [Revised Edition] (in Japanese), Corona publishing Co., LTD.

[2] UPP, E. L. and LANASA, P. J. (2002), "Fluid Flow Measurement (A practical guide to accurate flow measurement)", Elsevier.

[3] DOBLHOFF-DIER, K., KUDLATY, K., WIESINGER, M. and GROSCHL, M. (2011), "Time resolved measurement of pulsating flow using orifices", *Flow Measurement and Instrumentation,* **22**, 97-103.

[4] ZHANG, H., HUANG, Y. and SUN, Z. (2006), "A study of mass flow rate measurement based on the vortex shedding principle", *Flow Measurement and Instrumentation,* **17**, 29-38.

[5] ANKLIN, M., DRAHM, W. and RIEDER, A. (2006), "Coriolis mass flowmeters: Overview of the current state of the art and latest research", *Flow Measurement and Instrumentation,* **17**, 317-323.

[6] KOIZUMI, H. (2010), "The flow meter and its measurement method", Patent Application No. 2010-106761 [JP] (Date 06-05-2010).

[7] Handbook of Fluid Dynamics (in Japanese), Maruzen publishing Co. (1987): published by Japan Society of Fluid Mechanics, 201.

[8] NAGANO, Y., HISHIDA, M. and ASANO, T. (1984), "Modified k - ε turbulence model considering the performance of a near wall turbulence", (in Japanese) *Trans. of JSME*, **50**, 2022-2031.

[9] Storm/CFD2000 Version 5.0, Adaptive Research.

[10] KOIZUMI, H., UMEMURA, Y., HANDO, S. and SUZUKI, K. (2010), "Heat transfer performance and the transition to chaos of mixed convection around an isothermally heated sphere placed in a uniform, downwardly directed flow", *Int. J. Heat Mass Transfer,* **53**, 2602-2614.

[11] YOSHIDA, H. (2004), "Sphere and cylinder which are thoroughly similar from some angles, but are falsely similar from other angles" (in Japanese), *J. Heat Transfer Society of Japan,* **43**, 15-25.

[12] HIJIKATA, K. YOSHIDA, H. and MORI, Y. (1982), "Theoretical and experimental study of turbulence effects on heat transfer around the stagnation point of a cylinder", *Proceedings of 7th International Heat Transfer Conference,* Munchen, **3**, 165-170.

[13] SCHLICHTING, H. (1966), Boundary-Layer Theory (6th Edition), McGRAW-HILL, Inc.

[14] LAUNDER, B. E. and YING, W. M. (1973), Prediction of flow and heat transfer in ducts of square cross-section, *Heat and Fluid Flow*, **3**, 115-121.

[15] LAUNDER, B. E., REECE, G. J., RODI, E. (1975), "Progress in the development of a Reynolds-stress turbulence closure", *J. Fluid Mech.*, **68**, 537-566.

(i) Mean velocity of V_z.

(ii) Turbulence intencity of $v_{z\,FI}$.
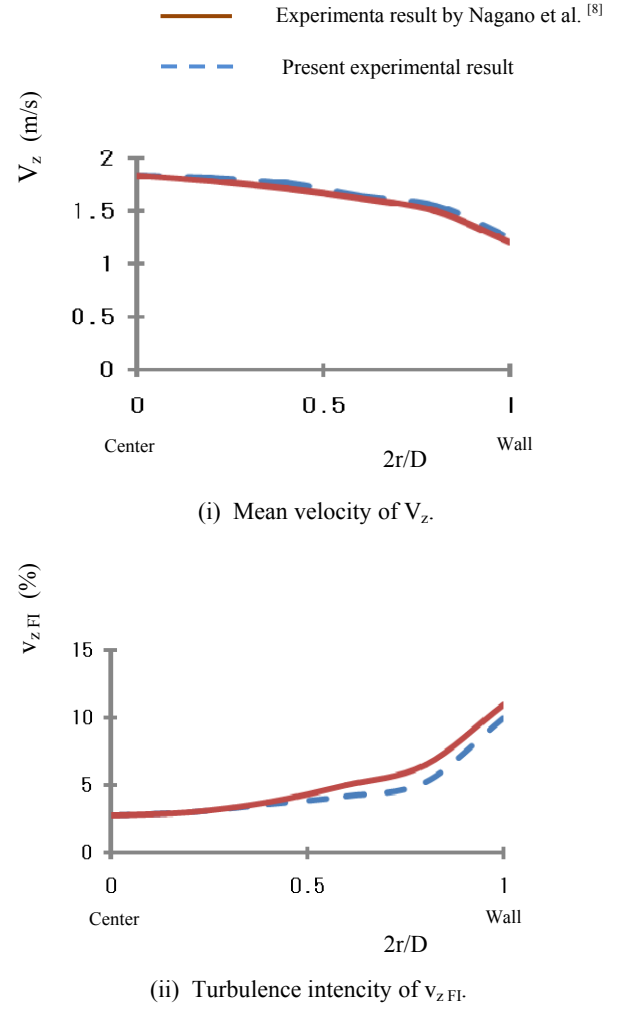
Figure A: Mean velocity and turbulence intensity distributions in a fully developed pipe flow.

APPENDIX A

Turbulent Structure in a Fully Developed Pipe Flow

Prior to the experiment of inserting the sphere into a pipe, it was confirmed that the flow without a sphere was in a fully developed turbulent region at Re_D=10,000. The measuring position of the velocity field was 20 D downstream from the tube inlet as shown in Fig. 3. Figure A shows the turbulent structure in a fully developed pipe flow. Figure A(i) shows the streamwise mean velocity distribution across the pipe cross-section, V_z, Fig. A(ii) shows the turbulence intensity, $v_{z\ FI}$, respectively. The solid lines are the experimental present results of Nagano et al. [8], and the dashed lines are the present experimental results using a HWA. The mean velocity profile, V_z, fits well to the one-seventh law. The present experimental results were in good agreement with those of the experimental results of Nagano et al. [8]. As we confirmed the experimental accuracy, the experiment which was inserted a sphere into the center part of a tube was performed.

APPENDIX B

Flow Characteristics Around the Forward Stagnation Point of a Cylinder Placed in a Uniform Flow

In order to clarify the predictability of the proposed algebraic stress model shown in equation (11), we compared the present results with those of the calculated results of Hijikata et al. [12] whose model is the full transport equation for $g = \overline{v_\theta^2} - \overline{v_r^2}$ in the case of the flow around a cylinder. The turbulence model also uses the low-Reynolds number k - ε turbulence model. The Reynolds number based on the sphere diameter is Red=50,000 and the turbulence intensity in the uniform flow is 10%. A non-uniform 200 (in the streamwise direction)×60 (in the radial direction) grids with a finer mesh near the cylinder was used. Calculation was carried out for air flow (*Pr*=0.71).

Figure B shows the turbulent structures in line of the forward stagnation point of a cylinder. Figure B(i) shows the turbulence intensity, $v_{r\ FI}$ (%), and Fig. B(ii) shows the anisotropy, g/(2k/3). The dashed lines show the present results using the algebraic stress model

which is based on equation (11), and the solid lines show the results of Hijikata et al. [12] using the full anisotropic stress equations of $g = \overline{v_\theta^2} - \overline{v_r^2}$. The present simulated results shown by the dashed lines which are used by the simplified algebraic stress model are mostly in agreement with those of the simulated results shown by the solid lines which used the full transport equation of $g = \overline{v_\theta^2} - \overline{v_r^2}$. That is, it is found that the proposed simplified algebraic stress model, of which both advection and diffusion terms of g are neglected, could predict the turbulent structures of which strongly affects the heat transfer characteristics in line of the forward stagnation point.

The paper [12] described in the conclusion that heat transfer enhancement at the forward stagnation point was found mainly caused by the amplification of turbulence energy due to the large reduction rate of the main streamwise velocity in line of the forward stagnation point. The numerical results calculated by the turbulence model suggested in this paper were found to agree well with the experimental results reported so far.

(i) Turbulence intensity of $v_{r\,FI}$.

(ii) Anisotropy of g.
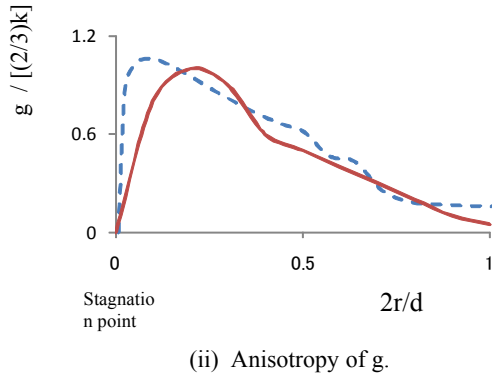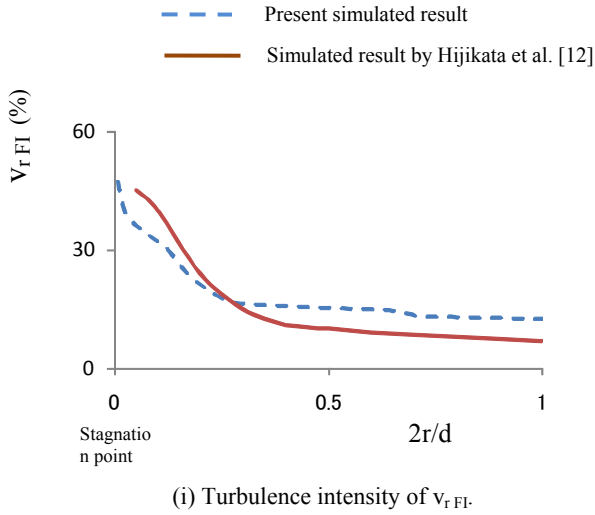
Figure B: Turbulent structure in line of the forward stagnation point of a cylinder.

CFD MODELING STUDY OF A REFINERY HEATER AND COMPARISON TO FIELD DATA

Allan RUNSTEDTLER[1]*, Xavier LANDRY[1], Dennis BRUNET[2]

[1] Natural Resources Canada, Ottawa, Canada

[2] Shell Projects and Technology, Calgary, Canada

* E-mail: arunsted@nrcan.gc.ca

ABSTRACT
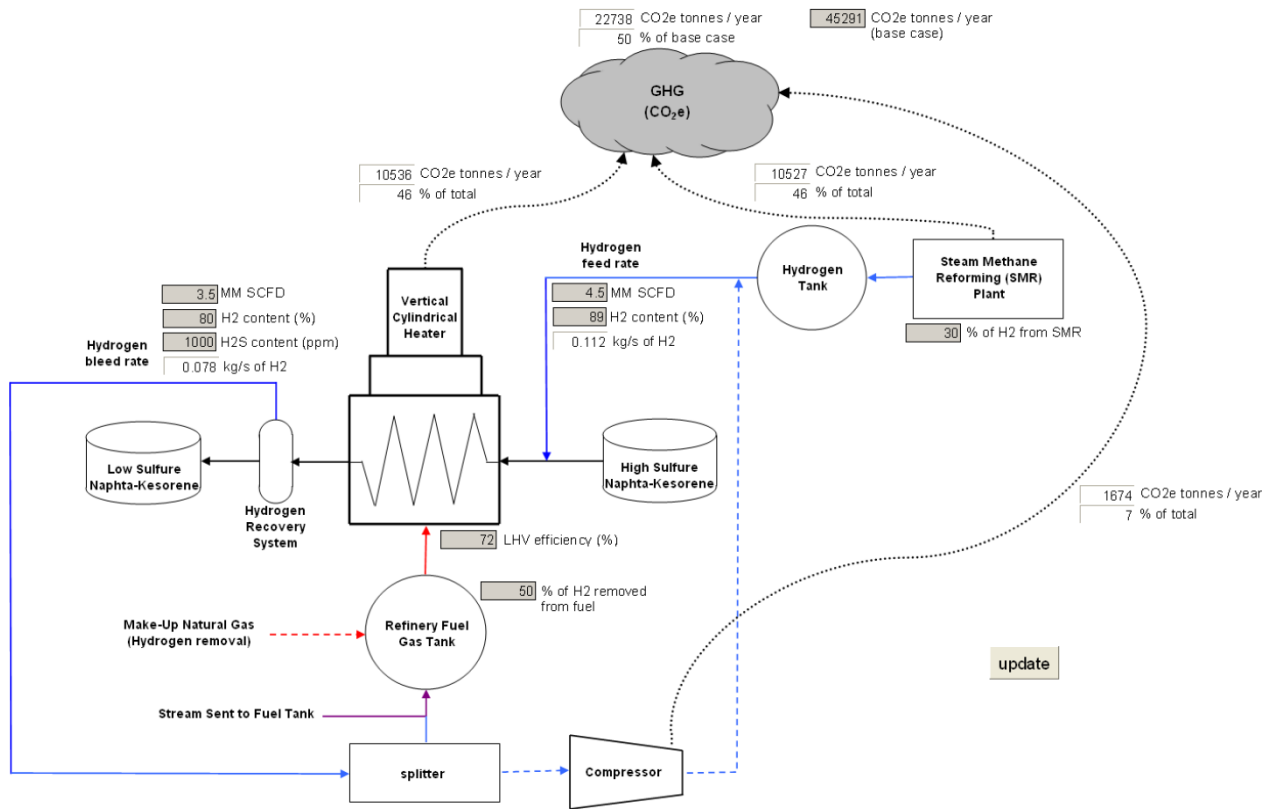
Keywords:

1. INTRODUCTION

22738	CO2e tonnes / year
50	% of base case

45291	CO2e tonnes / year (base case)

GHG (CO₂e)

10536	CO2e tonnes / year
46	% of total

10527	CO2e tonnes / year
46	% of total

Hydrogen feed rate

Vertical Cylindrical Heater

Hydrogen Tank

Steam Methane Reforming (SMR) Plant

3.5	MM SCFD
80	H2 content (%)
1000	H2S content (ppm)
0.078	kg/s of H2

Hydrogen bleed rate

4.5	MM SCFD
89	H2 content (%)
0.112	kg/s of H2

30	% of H2 from SMR

Low Sulfure Naphta-Kesorene

Hydrogen Recovery System

High Sulfure Naphta-Kesorene

72	LHV efficiency (%)

50	% of H2 removed from fuel

Make-Up Natural Gas (Hydrogen removal)

Refinery Fuel Gas Tank

1674	CO2e tonnes / year
7	% of total

update

Stream Sent to Fuel Tank

splitter

Compressor

Figure 1:

2. THE REPRESENTATIVE HEATER

3.1 Models

3.2 The Computational Mesh

3.3 Boundary Conditions
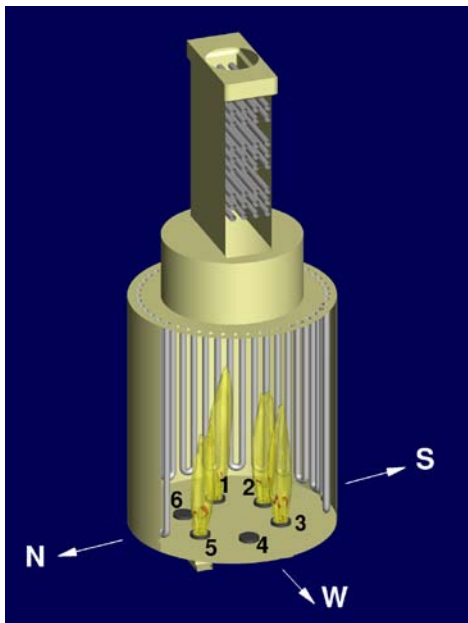
Figure 2:

3. THE FURNACE CFD MODEL

Table 1:

Table 2:
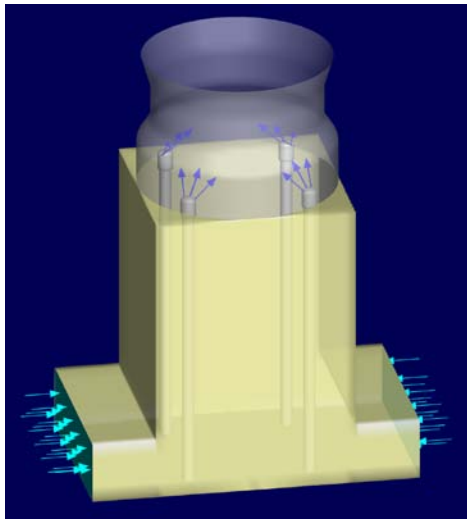
Figure 3:

Table 3:

3.4 Results and Comparison to Operation Data

Table 4:
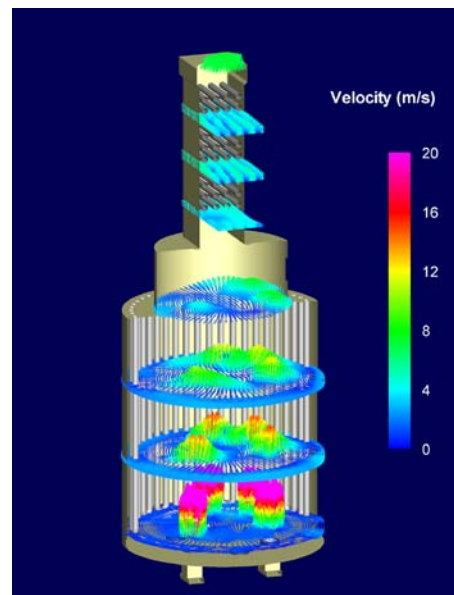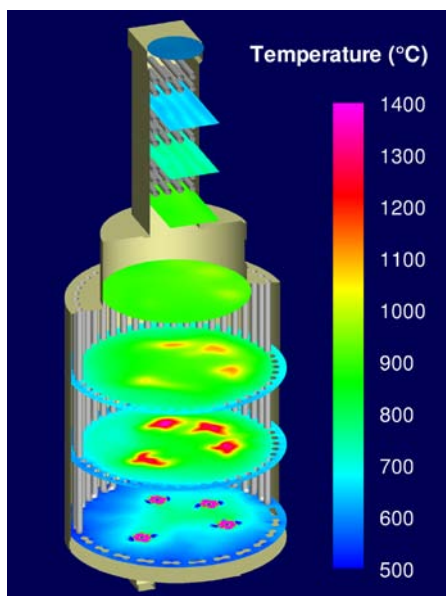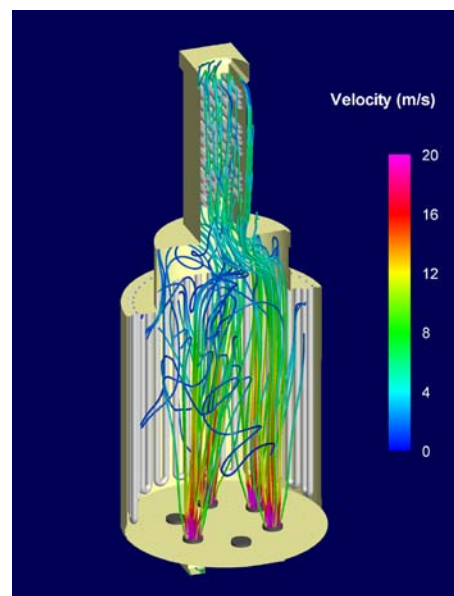
Figure 6:

Figure 4:

Figure 7:
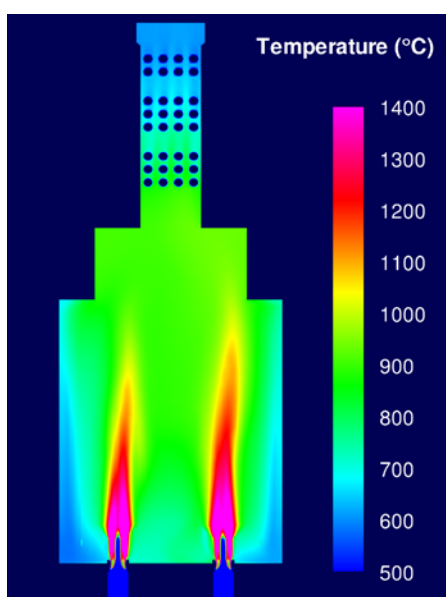
Figure 5:
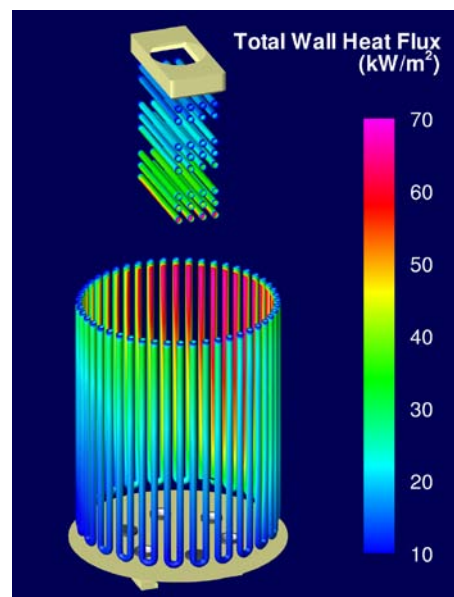
Figure 8:
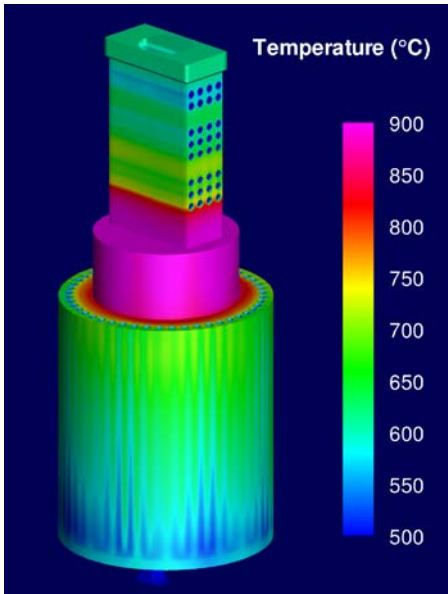
Figure 9:

4. THE CONVECTION SECTION CFD MODEL

4.1 Models

Table 5:

4.2 The Computational Mesh
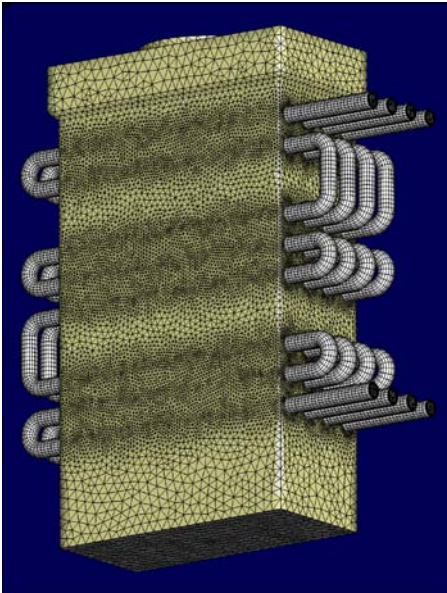
Figure 10:
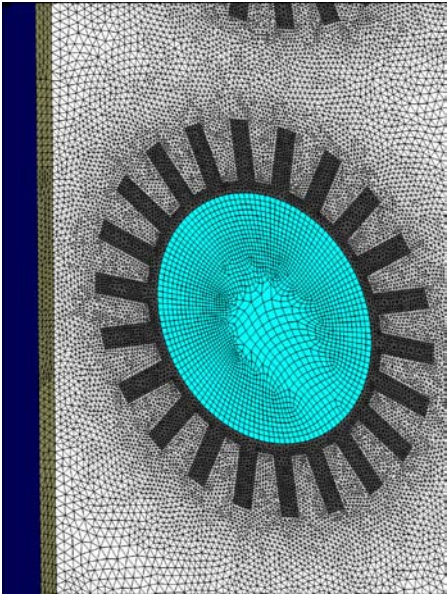
Figure 11:

4.3 Boundary Conditions

Table 6:

5. CONCLUSIONS

4.4 Results and Comparison to Operation Data
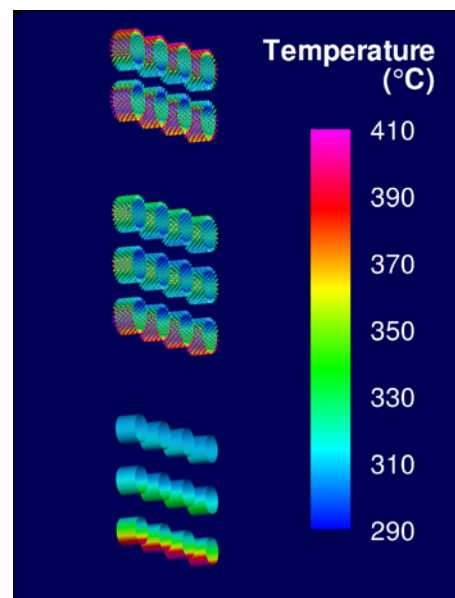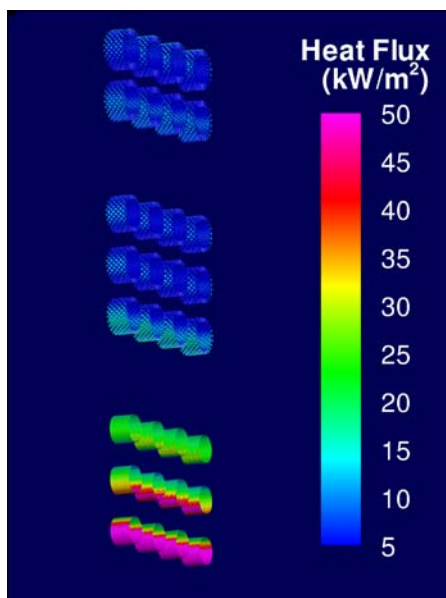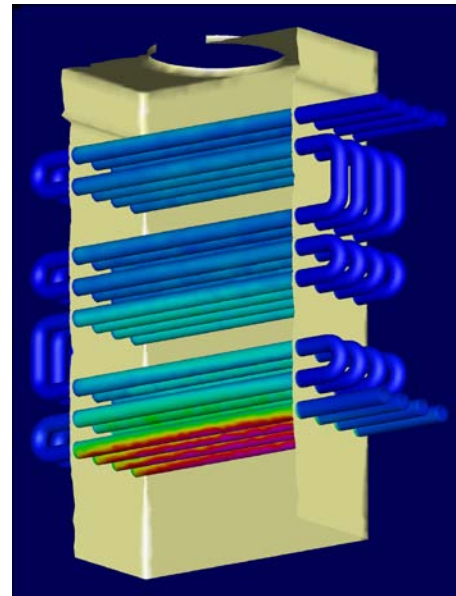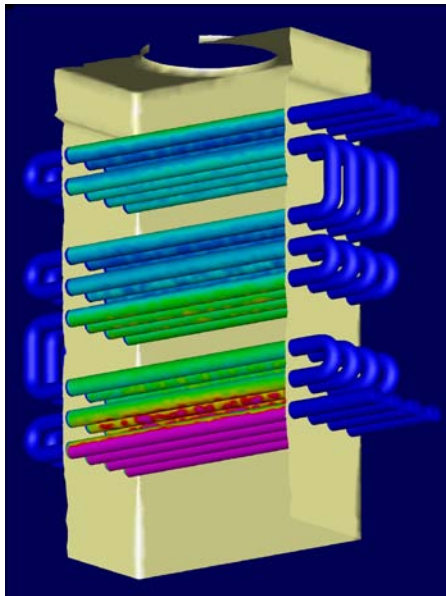
Figure 12:

Figure 13:

ACKNOWLEDGEMENT

REFERENCES

8th International Conference on CFD in Oil & Gas, Metallurgical and Process Industries
SINTEF/NTNU, Trondheim Norway
21-23 June 2011

CFD11-100

THE CHARACTERISTICS OF FLOW AND HEAT TRANSFER IN A CIRCULATING FLUIDIZED BED REACTOR

Hang Seok CHOI[1*] , Yeon Seok CHOI[1]

[1] Environment and Energy Systems Research Division, Korea Institute of Machinery and Materials, 104 Sinseongno, Yuseong-gu, Daejeon, 305-343, SOUTH KOREA

* E-mail: hschoi@kimm.re.kr

ABSTRACT

In the present study, to investigate the heat transfer characteristics of gas-solid flow in a circulating fluidized bed reactor, numerical approach is applied by using CFD (computational fluid dynamics). For the multiphase thermal flow fields between gas and solid, an Eulerian-Eulerian approach is applied. To investigate the characteristics of wall heat transfer, walls are heated with constant temperature and cold gas and sand are inserted at the bottom and side inlets, respectively. Hence, heat transfer occurs from the wall to the bed material. The flow and heat transfer characteristics of the circulating fluidized bed reactor are fully investigated with varying superficial gas velocity. In particular, the rising and falling solid motions and their roles for the wall heat transfer are studied. From the predicted results, it is fully scrutinized that the heat transfer between bed material and wall is mainly governed by particular solid motions and these are changed by varying superficial gas velocity.

Keywords: CFD, Circulating fluidized bed, Gas-solid flow, Heat transfer.

NOMENCLATURE

Greek Symbols
ε volume fraction.
ρ density, [kg/m^3].
τ_g deviatoric stress tensor for gas phase, [Pa].
γ gas-solid heat transfer coefficient, [J/m^3•K•s].

Latin Symbols
C_p specific heat capacity at constant pressure, [J/kg•K].
F coefficient for interphase force, [kg/m^3•s].
$\boldsymbol{g}$ gravitational acceleration, [m/s^2].
k gas or solid thermal conductivity [J/m•K•s]
p pressure, [Pa].
T temperature, [K].
t time, [s].
q conductive heat flux, [J/m^2•s].
$\boldsymbol{S}_{sj}$ solid phase stress tensor, [Pa].
$\boldsymbol{v}$ velocity, [m/s].

Sub/superscripts
g gas phase.
sj jth solid phase.

INTRODUCTION

The circulating fluidized bed (CFB) reactors have been widely used in industry such as power and heat generation because of their higher combustion efficiency, their applicability for the wide range of lower grade solid fuels and lower pollutant, etc. If the reaction temperature should be carefully controlled in the operation of the reactor, the characteristics of the gas-solid flow and consequent heat transfer become very important. Hence, to optimally design the circulating fluidized bed reactor, the design factors such as heat transfer coefficient should be obtained with high fidelity. However, computational fluid dynamics (CFD) studies are rare, which find out the heat transfer characteristics of circulating fluidized bed reactor for the application of its optimal scale-up design (Almuttahar and Taghipour, 2008, Zhang et al., 2010). In this regard, a numerical study with computational fluid dynamics has been carried out to investigate the gas-solid flow and heat transfer characteristics of a circulating fluidized bed reactor. For the simulation of the multiphase thermal flow fields between gas and solid, an Eulerian-Eulerian approach is applied for the circulating fluidized bed reactor considering computational cost and accuracy. Especially, the gas and solid phase conductivities are calculated by the method of Kuipers et al. (1992). To look into the wall heat transfer characteristics, the reactor walls are heated with higher temperature and cold gas and sand are inserted into the bottom and side inlets. Hence, the heat is transferred from the walls to the cold solid particles and gas flow in the reactor and this transferred heat is convected over the entire reactor by the gas and solid emulsion flows. In the present study, the flow and thermal characteristics of the reactor are fully investigated with varying superficial gas velocity. In particular, the contributions of the gas and solid emulsion phase flows on the wall heat transfer are scrutinized. Following the normal direction of the reactor, the solid volume fraction and solid flow behaviour are calculated and analysed, especially at very close to the wall. Because the typical solid flow moving from the wall to the bed center has a great effect on the

wall heat transfer. From the predicted results, it is fully elucidated that the heat transfer mechanism are mainly governed by the particular gas flow motions and related solid emulsion flow. In particular, the heat transfer coefficients are calculated and obtained and this may be very helpful to the optimal design of the circulating fluidized bed reactor.

MODEL DESCRIPTION

Governing Equations

The governing equations for gas-solid multiphase flow are chosen according to Wachem et al. (2001) and are given as follows.

For continuity equations

$$\frac{\partial}{\partial t}\left(\varepsilon_g \rho_g\right)+\nabla\cdot\left(\varepsilon_g \rho_g \mathbf{v}_g\right)=0, \tag{1}$$

$$\frac{\partial}{\partial t}\left(\varepsilon_{sj} \rho_{sj}\right)+\nabla\cdot\left(\varepsilon_{sj} \rho_{sj} \mathbf{v}_{sj}\right)=0, \tag{2}$$

here subscript 'g' and 'sj' mean gas and j^{th} solid phase, respectively and ε is the volume fraction of gas or solid phase.

For momentum equations

$$\frac{\partial}{\partial t}\left(\varepsilon_g \rho_g \mathbf{v}_g\right)+\nabla\cdot\left(\varepsilon_g \rho_g \mathbf{v}_g \mathbf{v}_g\right)=-\varepsilon_g \nabla P_g +\nabla\cdot\boldsymbol{\tau}_g, \\ +\sum_{j=1}^{n} F_{gsj}\left(\mathbf{v}_{sj}-\mathbf{v}_g\right)+\varepsilon_g \rho_g \mathbf{g} \tag{3}$$

$$\frac{\partial}{\partial t}\left(\varepsilon_{sj} \rho_{sj} \mathbf{v}_{sj}\right)+\nabla\cdot\left(\varepsilon_{sj} \rho_{sj} \mathbf{v}_{sj} \mathbf{v}_{sj}\right)=-\varepsilon_{sj} \nabla P_g +\nabla\cdot\mathbf{S}_{sj}, \\ -F_{gsj}\left(\mathbf{v}_{sj}-\mathbf{v}_g\right)+\sum_{k=1}^{n} F_{sksj}\left(\mathbf{v}_{sk}-\mathbf{v}_{sj}\right)+\varepsilon_{sj} \rho_{sj} \mathbf{g} \tag{4}$$

here, $\mathbf{v}$ is velocity vector and $\boldsymbol{\tau}_g$ and $\mathbf{S}_{sj}$ are the gas phase deviatoric stress tensor and j^{th} solid phase stress tensor, respectively. The F_{gsj} and F_{sksj} are coefficients for interphase force between gas and solid phases and between solid phases, respectively.

For energy equations

$$\varepsilon_g \rho_g C_{pg}\left(\frac{\partial T_g}{\partial t}+\mathbf{v}_g\cdot\nabla T_g\right)=-\nabla\cdot\mathbf{q}_g+\sum_{j=1}^{n}\gamma_{gsj}\left(T_{sj}-T_g\right), \tag{5}$$

$$\varepsilon_{sj} \rho_{sj} C_{psj}\left(\frac{\partial T_{sj}}{\partial t}+\mathbf{v}_{sj}\cdot\nabla T_{sj}\right)=-\nabla\cdot\mathbf{q}_{sj}-\gamma_{gsj}\left(T_{sj}-T_g\right), \tag{6}$$

here T is temperature and $\mathbf{q}$ is the conductive heat flux for gas or solid phase. The γ_{gsj} is the gas-solid heat transfer coefficient.

For fluid-solid drag formula of the momentum equations, the following equation is adopted, which was derived by Syamlal and O'Brien (1988).

$$F_{gsj}=\frac{3\varepsilon_{sj}\varepsilon_g \rho_g}{4 v_{tsj}^2 d_{sj}} C_{Ds}\left(\frac{\text{Re}_{sj}}{v_{tsj}}\right)\left|\boldsymbol{v}_{sj}-\boldsymbol{v}_g\right|, \tag{7}$$

where v_{tsj} is the terminal velocity of jth solid particle (Garside and Dibouni, 1977), C_{Ds} is the single particle drag function and Reynolds number for j^{th} solid particle is defined as $\text{Re}_{sj}=\dfrac{\rho_g\left|\boldsymbol{v}_{sj}-\boldsymbol{v}_g\right|d_{sj}}{\mu_g}$.

For solids-solids momentum transfer, the drag coefficient developed by Syamlal (1987a) is applied as follows.

$$F_{sjsk}=\frac{3\left(1+e_{sjsk}\right)\left(\dfrac{\pi}{2}+\dfrac{C_{fsjsk}\pi^2}{8}\right)\varepsilon_{sj}\rho_{sj}\varepsilon_{sk}\rho_{sk}\left(d_{sj}+d_{sk}\right)^2 g_{gsjsk}\left|\boldsymbol{v}_{sj}-\boldsymbol{v}_g\right|}{2\pi\left(\rho_{sj}d_{sj}^3+\rho_{sk}d_{sk}^3\right)}, \tag{8}$$

here e_{sjsk} is the coefficient of restitution, C_{fsjsk} is the coefficient of friction between j^{th} and k^{th} solid phase particles and the radial distribution function at contact is defined as follows (Lebowitz, 1964).

$$g_{gsjsk}=\frac{1}{\varepsilon_g}+\frac{3d_{sj}d_{sk}}{\varepsilon_g^2\left(d_{sj}+d_{sk}\right)}\sum_{\lambda=1}^{m}\frac{\varepsilon_{s\lambda}}{d_\lambda}. \tag{9}$$

In the present calculation, the solid phase stress tensor, $\mathbf{S}_{sj}$, in equation (4) is treated differently for two distinct flow regimes, which are plastic flow and viscous flow regimes. For the viscous flow regime, granular temperature, Θ_{sj}, is adopted to solve the solid phase stress tensor. In the present study, a simplified algebraic expression for the granular temperature is adopted as follows (Syamlal, 1987b).

$$\Theta_{sj}=\left[\frac{-K_{1sj}\varepsilon_{sj}tr\left(\boldsymbol{D}_{sj}\right)+\sqrt{K_{1sj}^2 tr^2\left(\boldsymbol{D}_{sj}\right)\varepsilon_{sj}^2+4K_{4sj}\varepsilon_{sj}\left(K_{2sj}tr^2\left(\boldsymbol{D}_{sj}\right)+2K_{3sj}tr\left(\boldsymbol{D}_{sj}^2\right)\right)}}{2\varepsilon_{sj}K_{4sj}}\right]^2, \tag{10}$$

here, $\boldsymbol{D}_{sj}$ is solid phase rate of strain tensor and K_{isj} is granular stress constant.

To calculate interphase heat transfer between gas and solid phases (see Eqs. (5) and (6)), the interphase heat transfer coefficient, γ_{gsj}, is assumed that there is no mass transfer between gas and solid phases in the present study. Then, the interphase heat transfer coefficient is defined as followings.

$$\gamma_{gsj}=\frac{6\kappa_g\left(1-\varepsilon_g\right)Nu_{sj}}{d_{sj}^2}, \tag{11}$$

$$Nu_{sj}=\left(7.0-10\varepsilon_g+5\varepsilon_g^2\right)\left(1.0+0.7\,\text{Re}_{sj}^{0.2}\,\text{Pr}^{1/3}\right) \\ +\left(1.33-2.4\varepsilon_g+1.2\varepsilon_g^2\right)\text{Re}_{sj}^{0.7}\,\text{Pr}^{1/3}, \tag{12}$$

here the Prandtl number is defined as $\text{Pr}=C_{Pg}\mu_g/k_g$

For conductive heat flux for gas and solid phases (see Eqs. (5) and (6)), Fourier's law is applied as follows.

$$\mathbf{q}_g=-\varepsilon_g k_g \nabla T_g, \tag{13}$$

$$\mathbf{q}_{sj}=-\varepsilon_{sj} k_{sj} \nabla T_{sj}. \tag{14}$$

Here, microscopic gas and solid conductivities, k_g and k_{sj}, are obtained following Kuipers et al. (1992). The

details of the computational theory and techniques used above governing equations can be found in MFIX documentation theory guide (Syamlal et al., 1993).

Computational Procedures

Figure1 shows the computational domain used in the present study. Cold gas (air) flow is issued uniformly into the bottom of the reactor to circulate a sand bed. Cold sand is inserted into the solid inlet and the sand particles and gas go out together from the outlet. The reactor side walls are heated at 373K and the sand particles and gas are heated by the hot walls. The geometry of circulating fluidized bed reactor and calculation conditions used in the present study are shown in Table 1. For the solid particles, the diameters are set as 400μm for sand and in this case particles are classified into Geldart B particle (Kunii and Levenspiel 1991).

For the temporal discretization of the governing equations, the first-order implicit Euler scheme is used. For the spatial ones, the first-order UPWIND scheme is adopted. The time step is changed and adjusted during the calculation for reducing total computational time.

For grid allocation, total grid number is 20 x 200, which is carefully selected through grid dependency test. In the present calculation, several cases are solved with increasing superficial gas velocity or inlet gas velocity from 2.0 m/s to 6.0 m/s to look into the effect of circulating flow field on the passive scalar evolution.

RESULTS AND DISCUSSION

Figure2 shows the instantaneous gas-solid flow and thermal fields for case 1. Figures 2(a) and 2(b) represent the contour of gas volume fraction and solid phase velocity vector map, respectively. The solid particles mainly go downward near the wall and go upward at the middle of the circulating fluidized bed reactor. This is typical solid flow characteristics in a circulating fluidized bed reactor. Hence, the solid particles circulate through the fluidized bed reactor according to the upward and downward flow motions.

Table1: Calculation conditions

Computational domain (2- dimensional)	
Length (x)	0.1 m
Height (y)	4.5 m
Grid allocation (x,y)	20 x 200
Boundary conditions	
Gas inlet	Case 1: $V_{g\ inlet}$ = 2.0m/s, $T_{g\ inlet}$=298 K)
	Case 2: $V_{g\ inlet}$ = 4.0m/s, $T_{g\ inlet}$=298 K)
	Case 3: $V_{g\ inlet}$ = 6.0m/s, $T_{g\ inlet}$=298 K)
Solid inlet	Dirichlet $V_{s\ inlet}$, $T_{s\ inlet}$=298 K
Outlet	Neumann
wall	No-slip for gas, Johnson & Jackson for solid, T_{wall}=373 K
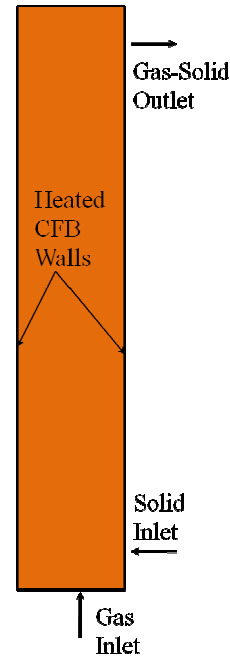
Figure 1: Computational domain.

(a) ε_g (b) V_s (c) T_s
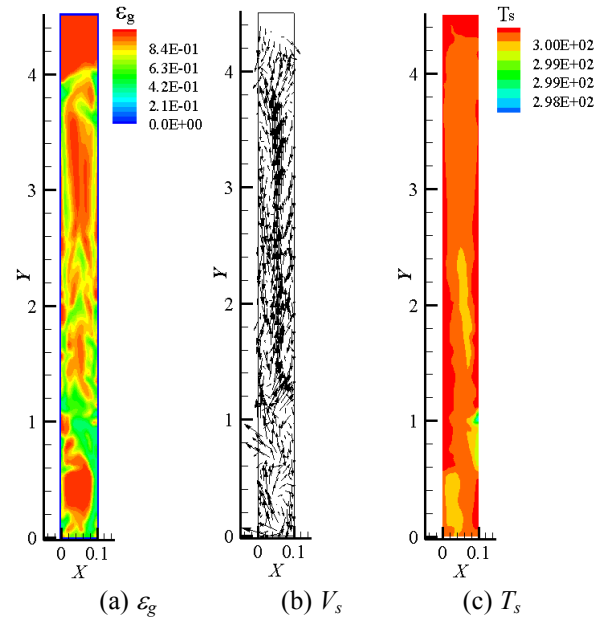
Figure 2: Instantaneous flow and thermal fields for case 1.

During the circulation, solid particles and gas are heated by the hot walls. Figure 2 (c) shows the contour of solid phase temperature and at this moment the cold solid lumps are going upward, which are inserted in the solid inlet. However, the solid phase temperature is higher near the walls where the downward solid flow appears as in Figure 2 (b). It is noted that the magnitude of near-wall solid phase velocity is lower compared with the solid phase velocity near the middle of the reactor. And the heated solid particles near wall are convected into the middle of the reactor resulting in heat transfer from the wall to the circulating fluidized bed. This greatly helps the wall heat transfer and this will be discussed in detail in the following figures.
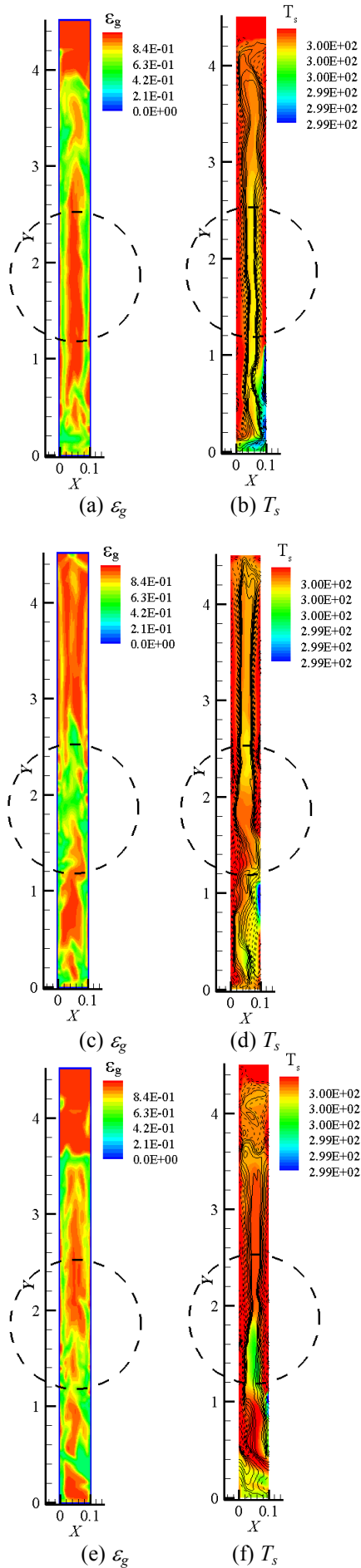
Figure 3: Instantaneous contours of gas volume fraction and solid phase temperature for the three different instantaneous times for case 1.

Figure 3 shows the instantaneous contours of gas volume fraction and solid phase temperature for the three different instantaneous times for case 1. For reference, the black lines on the contours of solid phase temperature represent solid phase streamwise velocity. In the line, solid line indicates positive value and dotted line means negative one. In the dashed circle of Figures (a) and (b), the gas flow is passing through the middle of the reactor with higher velocity and the solid flow is going down following the walls. During downward solid flow, the solid lumps are heated by the hot walls. After short period, upward solid flow is generated in Figures 3 (c) and (d). As in Figure 3 (c), the hot solid particles are moved from the wall to the entire circulating fluidized bed region of the dashed circle. These hot solid lumps are mixed with the cold solid particles from the solid inlet as well as cold gas. Hence, firstly, the heat is transferred to the near-wall solid flow and then the heat is transported into the reactor inside by the convection of the heated solid particles. After another short period, the gas flow is passing through the middle of the reactor with higher velocity and the solid flow is going down following the walls again in Figures 3(e) and 3 (f).

To look into the effects of gas-solid flow fields on the wall heat transfer, calculation is made with increasing superficial gas velocity or gas inlet velocity. Figure 4 shows the instantaneous contours of gas volume fractions for the three different cases with varying superficial gas velocity. With increasing superficial gas velocity, the gas volume fraction is increased. In other word, with increasing superficial gas velocity, solid circulation rate is increased for the same mass flow rate of the solid then the depth of the near-wall solid flow is decreased. In this case, the heat is mainly transferred to the gas flow, where no solid lumps exist. Especially, solid lumps only can be seen near the solid inlet in case3. This may decrease the wall heat transfer rate.

(a) case 1   (b) case 2   (c) case 3
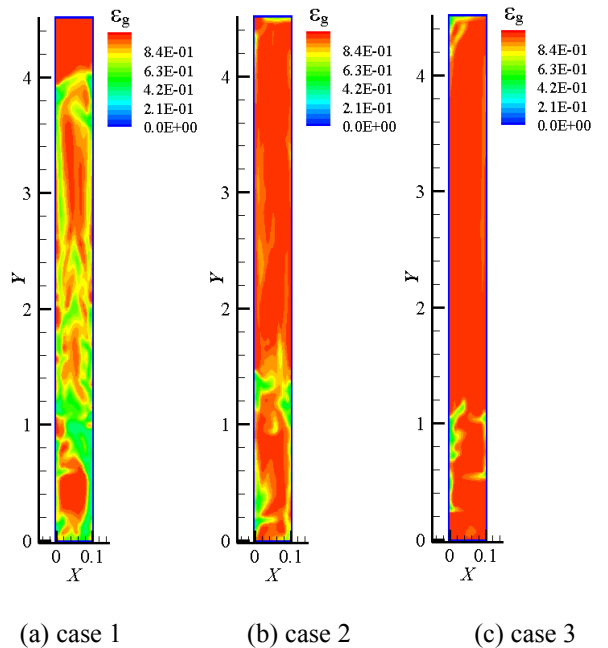
Figure 4: Instantaneous contours of gas volume fraction with increasing superficial gas velocity.

Figure 5 shows the distribution of time-averaged gas volume fraction over an appropriate time span at y=2m for the three different cases. The gas volume fraction is increased from the case 1 to case 3 as the superficial gas velocity is increased. It is noted that the gas volume fraction is rapidly decreased near the wall region and this region indicates the near-wall solid flow. As expected from Figure4, the gas volume fraction of this rapid decrease region is lower as the superficial gas velocity is decreased, which represents the increase of the depth of near-wall solid flow. The downward near-wall solid flow can be found in Figure 6. Figure 6 shows the distribution of time-averaged streamwise solid phase velocity over an appropriate time span at y=2m for the three different cases. The rapid decrease region of gas volume fraction coincides with that of higher negative streamwise velocity regions. This means that solid downward volume flow rate is increased near the wall with decreasing superficial gas velocity. This may affect the wall heat transfer and will be discussed in the following figure.

Figure 7 shows the distribution of instantaneous heat transfer coefficient for the three different cases. Here, the wall heat transfer coefficient is defined as $h_{ins\tan t} = \dfrac{q_{wall}}{A_{wall}\left(T_{wall} - T_{bulk}\right)}$ and q_{wall} is heat flux from the wall to the circulating bed and defined as $q_{wall} = -A[\varepsilon_g k_g \dfrac{\partial T_g}{\partial n} + (1-\varepsilon_g)k_{sj}\dfrac{\partial T_{sj}}{\partial n}]$. Where, A is the heat transfer area, n is the normal direction to the wall, $h^*_{instant}$ is non-dimensional heat transfer coefficient normalized by the maximum value and t^* is non-dimensional time normalized by time interval in Figure7. For reference, the experimental data for instantaneous local heat transfer coefficient obtained by Wu et al. (1991) are compared with the present CFD results. The heat transfer coefficient is increased as decreasing superficial gas velocity due to the mechanism of wall heat transfer in a circulating fluidized bed as discussed before. Hence, the behaviour of the near-wall solid flow plays an important role on the wall heat transfer.

Figure 5: Distribution of time-averaged gas volume fraction at y=2m for the three different cases.

Figure 7: Distribution of instantaneous heat transfer coefficients for the three different cases.

CONCLUSION

In the present study, to investigate the heat transfer characteristics of gas-solid flow in a circulating fluidized bed reactor, numerical approach is applied by using CFD. For the multiphase thermal flow fields between solid and gas, an Eulerian-Eulerian approach is applied. To investigate the characteristics of the wall heat transfer, walls are heated by constant temperature and cold gas and sand particles are inserted at the bottom and side inlets, respectively. Hence, heat transfer from the wall to the bed material occurs. From the results, at a instant, gas flow is passing through the middle of the reactor with higher velocity an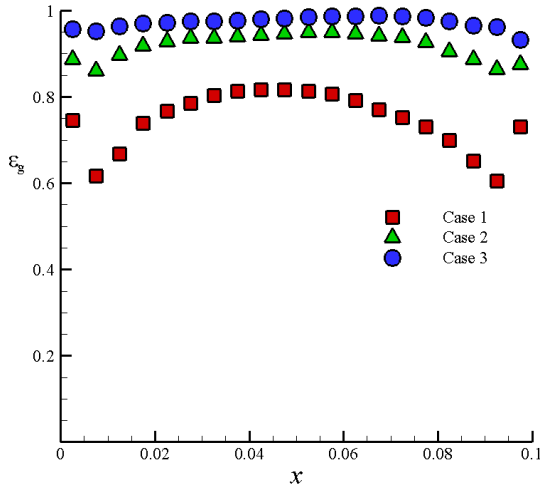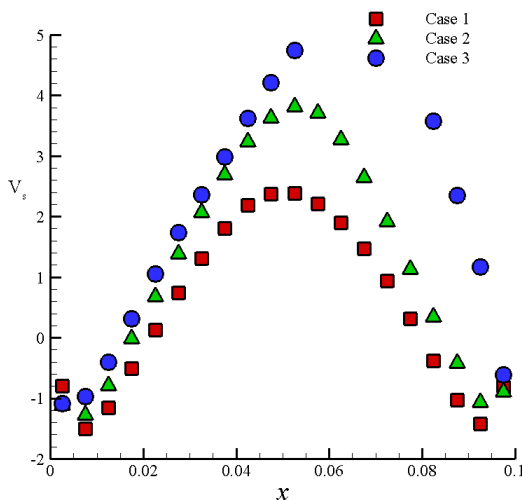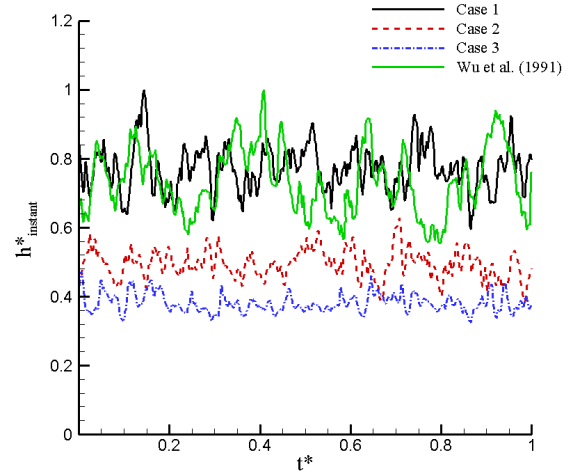d the solid flow is going down following the walls. During downward solid flow, the solid lumps are heated by the hot walls. However, after short period, upward solid flow is generated and the hot solid particles are moved from the wall to the entire circulating fluidized bed region. These hot solid

Figure 6: Distribution of time-averaged streamwise solid phase velocity at y=2m for the three different cases.

lumps are mixed with the cold solid particles from the solid inlet as well as gas. Hence, firstly, the heat is transferred to the near-wall solid flow and then the heat is transported into the reactor inside by the convection of the heated solid particles. With increasing superficial gas velocity, the gas volume fraction of the rapid decrease region near the wall is decreased as the superficial gas velocity is decreased, which represents the increase of the depth of near-wall solid flow. This means that near the wall solid downward volume flow rate is increased with decreasing superficial gas velocity. This greatly affects the mechanism of wall heat transfer. Hence, the behaviour of the near-wall solid flow plays an important role on the wall heat transfer.

REFERENCES

Almuttahar, A. and Taghipour, F., (2008), "Computational fluid dynamics of a circulating fluidized bed under various fluidization conditions," *Chemical Engineering Science*, **63**, 1696-1709.

Zhang, N., Lu, B., Wang, W. and Li, J., (2010), "3D CFD simulation of hydrodynamics of 150 MWe circulating fluidized bed boiler," *Chemical Engineering Journal*, **162**, 821-828.

Kuipers, J.A.M., Prins, W. and van Swaaij, W.P.M., (1992), "Numerical calculation of wall-to-bed heat transfer coefficients in gas-fluidized beds," *AIChE Journal*, **38**, 1079-1091.

Wachem, B.G. M., Schouten, J.C., Bleek, C.M., Krishna, R. and Sinclair, J. L., (2001), "Comparative analysis of CFD models of dense gas-solid systems," *AIChE Journal*, **47**, 1035-1051.

Syamlal, M. and O'Brien, T.J., (1988), "Simulation of granular layer inversion in liquid fluidized beds," *Int. J. Multiphase Flow*, **14**, 473-481.

Garside, J. and Al-Dibouni, M. R., (1977), "Velocity-voidage relationship for fluidization and sedimentation," *I&EC Proc. Des. Dev.*, **16**, 206-214.

Syamlal, M., (1987a), "The particle-particle drag term in a multiparticle model of fluidization," DOE/MC/21353-2373, NTIS/DE87006500, National Technical Information Service, Springfield, VA.

Lebowitz, J. L., (1964) "Exact solution of generalized Percus-Yevick equation for a mixture of hard spheres," *Phys. Rev.*, **A133**, 895-899.

Syamlal, M., (1987b), "A review of granular stress constitutive relations," DOE/MC/21353-2372, NTIS/DE87006499, National Technical Information Service, Springfield, VA.

Syamlal, M., Rogers, W. and O'Brien, T.J., (1993), "MFIX Documentation Theory Guide; Technical Note," DOE/METC-94/1004, NTIS/DE94000087, U.S. Department of Energy, Office of Fossil Energy, Morgantown Energy Technology Center Morgantown, WV, National Technical Information Service, Springfield, VA .

Kunii, D. and Levenspiel, O., (1991), "Fluidization Engineering," second edition, Butterworth-Heinemann.

Wu, R., L., Lim, C. J., Grace, R. and Brereton, C. M. H., (1991), "Instantaneous local heat transfer and hydrodynamics in a circulating fluidized bed," *Int. J. Heat Mass Transfer*, **34**, 2019-2027.

8th International Conference on CFD in Oil & Gas, Metallurgical and Process Industries
SINTEF/NTNU, Trondheim NORWAY
21-23 June 2011

CFD11-101

MECHANISTIC MODELLING OF PARTICLE-INTERFACE INTERACTION IN THREE-PHASE FLOWS

Gijsbert WIERINK[1]*, **Christoph GONIVA**[2], **Bojan NIČENO**[3],

Kari HEISKANEN[1]

[1]Aalto University - School of Science and Technology, Research Group of Mechanical Process

Technology and Recycling, Espoo, FINLAND

[2]Christian Doppler Laboratory on Particulate Flow Modelling, Linz, AUSTRIA

[3]Laboratory for Thermal Hydraulics, Paul Scherrer Institute, Villigen, SWITZERLAND

* E-mail: gijsbert.wierink@aalto.fi

ABSTRACT

The understanding of meso-scale phenomena in multiphase flows plays a critical role in accurate multiphase modelling. For many process applications control and manipulation of multiphase flow dynamics is a key issue that requires deeper understanding of interfacial phenomena. In mineral froth flotation, in particular, an accurate model of the behavior of fine solids at the gas-liquid interface is of major importance in macro-scale modelling. In this paper we discuss a method where momenta of liquid, gas, and solid particles are coupled. In order to describe systems characterized by high volume fraction of solids, particles are modelled using the Discrete Element Method (DEM) while fluids are modelled separately in the CFD code. Particle and fluid momenta are then transferred between the codes and coupled as source terms in the momentum equations. The modelling method presented in this work can give valuable insight in the behavior of three-phase systems and can contribute to better statistical models for industrial applications.

Keywords: CFD-DEM, multiphase flow, mineral froth flotation, bubble-particle interaction .

NOMENCLATURE

Greek Symbols
α Phase void fraction, $[-]$.
β Coefficient in Eqs.(9) and (10), $[-]$.
γ Surface tension, $[N/m]$.
δ Particle overlap distance, $[m]$
θ Contact angle, $[rad]$.
ε Turbulent kinetic energy dissipation rate, $[m^2/s^3]$.
κ Curvature, $[m^{-1}]$.
ρ Density, $[kg/m^3]$.
$\overleftrightarrow{\sigma}$ Total stress tensor, $[kg/ms^s]$.
τ Particle time step in Eqs.(9) and (10), $[-]$.
ϕ Physical property in Eq.(5) and angle in Eq.(15).
ω Angle in Fig. 3, $[rad]$.

Latin Symbols
c Compression factor in Eq.(7), $[-]$.

C Damping coefficient, $[kg/s]$.
d Diameter, $[m]$.
$\mathbf{F}$ Force, $[N]$.
g Gravitational constant, $[m/s^2]$.
k Stiffness coefficient in Eqs.(9-10) and turbulent kinetic energy in Fig. 1, $[kg/s^2, m^2/s^2]$.
$\hat{\mathbf{n}}$ Interface normal vector, $[m^{-1}]$.
p Pressure, $[Pa]$.
r Radius, $[m]$.
$\mathbf{U}$ Velocity, $[m/s]$.
z Deflection depth, $[m]$.

Sub/superscripts
12   Interaction between particle 1 and 2.
a Attachment.
c Compression in Eq.(7).
cap Capillary.
g Gas.
hyd Hydrostatic.
i Index i.
j Index j.
l Liquid.
n Normal in Eq.(9).
p Particle.
t Tangential in Eq.(10).

INTRODUCTION

The understanding of meso-scale phenomena in multiphase flows plays a critical role in accurate multiphase modelling. In many process applications control and manipulation of multiphase flow dynamics is a key issue that requires deeper understanding of interfacial phenomena. For this discussion it is helpful to define three spatial (and temporal) scales for modelling of multiphase processes; the macro-, meso-, and micro-scale, respectively. The macro-scale is the level of industrial applications, such as the length and time scales of interest in modelling of an entire tank cell or column. Typical length scales are in the order of 10^{-1}-10^1 m. In industrially meaningful simulations, the number of

particles is so high that commonly a statistical approach is necessary to model the process. Processes that take place on the meso-scale are those that directly interact with both the macro- and micro-scale. Length and time scales at this level of observation are typically of the scale of a few bubbles and particles. Length scales are in the order of $\sim 10^{-5}$-10^{-1} m. The micro-scale, then, is the scale at which close range forces occur. At the micro-scale the characteristic length scales are in the order of 10^{-10}-10^{-5} m. Many experimental and theoretical findings at the micro-scale could serve as valuable input in statistical or Lagrangian approaches at the macro-scale. However, this scale-up requires scalability of the findings and modelling at the micro-scale. It is the meso-scale that is key in scale-up to and formulation of input for macro-scale modelling.

The central aim of this paper is to introduce a computational framework for modelling of meso-scale phenomena in multiphase flows. Accurate meso-scale models can improve the quality and predictive power of global statistical modelling at the macro-scale.

The modelling framework has been set up using the open source CFD package OpenFOAM (OpenCFD Ltd., 2009). The modular and open structure of the code has allowed to develop a transparent computational framework for evaluate and improve micro- and meso-scale physicochemical phenomena. A central issue is to capture local kinetic phenomena in meso-scale models and use these in modelling of macro-scale processes. The relative motion and kinetic interaction between disperse media, i.e. momentum coupling, is an area of particular interest. In many industrial processes the distances between bubbles or particles are in the range of bubble or particle diameter (Wierink and Heiskanen, 2008). Under these dense conditions, the coupling between dispersed phases is in the regime of four-way coupling (Elghobashi, 1991), as shown in Fig. 1. For particles in the size range found in typical flotation process, say 10-150 μm, and an average bubble diameter of 1 mm, the momentum coupling regime for the system lies in the upper right corner of Fig. 1. The need for a modelling approach with four-way momentum coupling is therefore evident.

Four-way momentum coupling entails coupling between particles and carrier phase, between bubbles and carrier phase, between bubbles and bubbles, and between particles and particles. In the current approach, particles are tracked in a Lagrangian frame of reference and momenta are completely coupled. This approach allows for simulation of flows with higher void fraction. For systems with very high solid void fraction, a Discrete Element Method (DEM) is coupled with the CFD simulations.

MODEL DESCRIPTION

The modelling methods in this work fall into two categories. The first is the development of a Lagrangian particle class that includes interaction forces between particles and a gas-liquid interface. This class is developed within the framework of the open source CFD toolbox Open-FOAM (OpenCFD Ltd., 2009). The second development is the implementation of the kinetics described below, in the CFD-DEM coupled code CFDEM (CFDEM, 2011). These modelling methods are discussed in the following sections.

Gas-liquid model

Motion of the gas-liquid system is computed using the Volume of Fluid (VOF) method (Hirt and Nichols, 1981). The authors are aware that the VOF method is not particularly suitable for two-phase flows where surface tension plays an important role (Weller, 2008). An interface tracking method, rather than a interface capturing method, would be more suitable for surface tension dominated flows. However, dynamic re-meshing and topological changes in the mesh make bubble break-up and coalescence mathematically challenging and computationally heavy. The authors aim to include an interface sharpening method in the current VOF model to counter this issue, although the compromise is clear.

In the VOF method for incompressible, isothermal two-phase flow, the transport of a phase fraction parameter α is computed on the computational domain. The set of equations describing the system are the continuity equation, the phase transport equation, and the momentum equation, respectively (Weller, 2008):

$$\nabla \cdot \mathbf{U} = 0, \tag{1}$$

$$\frac{\partial \alpha}{\partial t} + \nabla \cdot (\alpha \mathbf{U}) = 0, \tag{2}$$

$$\frac{\partial (\rho \mathbf{U})}{\partial t} + \nabla \cdot (\rho \mathbf{U}\mathbf{U}) = -\nabla \cdot \overleftrightarrow{\sigma}, \tag{3}$$
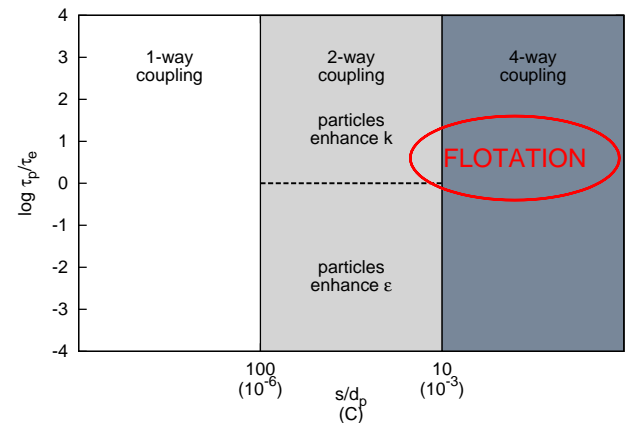

Figure 1: Momentum coupling regimes for the log of the ratio of particle response time τ_p and fluid response time τ_f (log Stokes number)versus particle-particle distance s, normalized by particle diameter d_p (after Elghobashi (1991)). Approximate volumetric concentration C of the dispersed phase is indicated in brackets.

where $\overleftrightarrow{\sigma}$ is the total stress tensor composed of the normal stress tensor, i.e. pressure, the shear stress tensor, and the surface stress tensor as:

$$\overleftrightarrow{\sigma} = \overleftrightarrow{\sigma}_n + \overleftrightarrow{\sigma}_\tau + \overleftrightarrow{\sigma}_\sigma. \qquad (4)$$

Physical properties, such as density and viscosity in Eq.(4), are locally averaged according to:

$$\phi = \alpha\phi_1 + (1 - \alpha)\phi_2, \qquad (5)$$

where ϕ_1 and ϕ_2 are the physical properties of phase 1 and phase 2, respectively. In the standard VOF approach the interface disperses due to numerical diffusion (Weller, 2008), but the diffuse interface is also a characteristic of the VOF method itself. To counter this effect in a numerically stable manner, Weller (2008) implemented a counter-gradient transport equation (Weller, 1993). This equation takes the form of:

$$\frac{\partial \alpha}{\partial t} + \nabla \cdot (\alpha \mathbf{U}) + \nabla \cdot [\mathbf{U}_c \alpha (1 - \alpha)] = 0, \qquad (6)$$

where the interface compression velocity $\mathbf{U}_c$ is defined as:

$$\mathbf{U}_c = min\left(c_\alpha |\mathbf{U}|, max(|\mathbf{U}|)\right) \frac{\nabla \alpha}{|\nabla \alpha|} \qquad (7)$$

In Eq.(7), c_α is an interface compression factor, here set to 1. Hence, $\mathbf{U}_c$ is a contribution to flux normal to the gas-liquid interface, resulting in interface compression. Note that the interface compression only contributes at the gas-liquid interface due to the term $\alpha(1 - \alpha)$ in Eq.(6).

Particle-particle model

The motion of particles is modelled in a Lagrangian frame of reference. The governing equation is:

$$m_p \frac{d\mathbf{U}_p}{dt} = \sum \mathbf{F}, \qquad (8)$$

where $\mathbf{F}$ contains the relevant forces acting on the particle. Commonly these are the drag force, the buoyancy force, and a driving force due to pressure gradient. Interfacial, electrostatic, and other forces can be added in Eq.(8) to accommodate the physics specific to the system at hand. The particle forces described in the current and next section are models found in literature and are surely incomplete. However, the structure of the current modelling framework allows to continuously update the particle model according to experimental and theoretical findings.

To account for particle-particle collisions in more dense dispersed flows a soft-sphere collision model (Bertrand *et al.*, 2005; Cundall and Strack, 1979) was implemented. Particles are represented by spheres with a center point and a radius. During particle-particle collision the particles are allowed a small overlap δ_p, as shown in Fig. 2. The normal force $\mathbf{F}_{cn,i,j}$ between particles i and j are the calculated as (Bertrand *et al.*, 2005):

$$\mathbf{F}_{cn,i,j} = k_n \delta_{n,i,j}^{\beta_1} + C_n \frac{\partial \delta_{n,i,j}}{\partial \tau} \qquad (9)$$

and the tangential force as:

$$\mathbf{F}_{tn,i,j} = k_t \delta_{t,i,j}^{\beta_2} + C_t \frac{\partial \delta_{t,i,j}}{\partial \tau}, \qquad (10)$$

where k_n, k_t are the stiffness coefficients and C_n, C_t are the damping coefficients, in the normal direction n and tangential direction t, respectively. In this work a linear collision model is used so that the coefficients β_1 and β_2 are both set to 1. The forces in Eqs.(9) and (10) are then added to the right hand side of Eq.(8). In the results presented here, k is $0.9 \ kg/s^2$ and C is $800 \ kg/s$. The values for k and C are not based on physical particle properties, but rather to ensure that particles do not overlap and collide with reasonable restitution and to provide a proof of concept. At a later stage physical parameters are to be tested, such as those reported by Malone and Xu (2008).
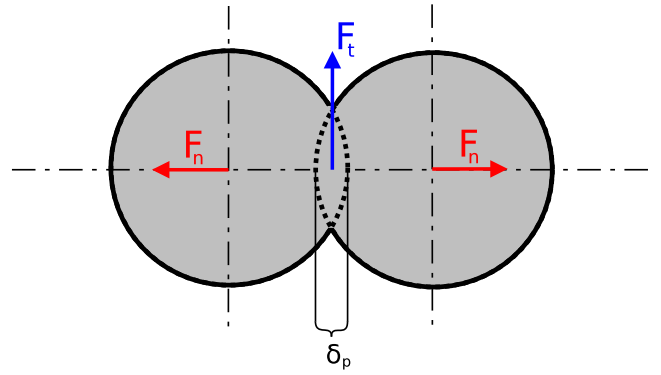

Figure 2: Particles colliding using the soft-sphere collision model. The particles overlap by distance δ_p, $\mathbf{F}_n$ is the normal force and $\mathbf{F}_n$ the tangential force.

Particle-interface interaction

As a particle approaches the gas-liquid interface a net attachment force occurs. This net attachment force is the result of a balance of many forces, e.g. forces related to the film rupture and lubrication (Ivanov *et al.*, 1978; Schulze, 1983; Barnocky and Davis, 1989), as well as DLVO forces (Israelachvili, 1992). The characteristic length scale for calculation of DLVO forces in particular, is in the order of 10^0 to 10^3 nm, the latter for very clean systems. In the current work, the particle-interface attachment force is modelled as a function of particle position relative to the interface and physical parameters, such as surface tension and three-phase contact angle. The attachment force $\mathbf{F}_a$ is modelled as:

$$\mathbf{F}_a \propto -\hat{\mathbf{n}} f(\alpha) F_a, \qquad (11)$$

where $f(\alpha)$ is a function centering the force at the interface. In the VOF method the gas-liquid interface is diffuse, but we can use a chosen center value $\tilde{\alpha}$ to represent the surface. In this work the interfacial center is chosen to be at a gas void fraction of 0.5, i.e. $\tilde{\alpha} = 0.5$. The smooth function $tanh(\alpha - \tilde{\alpha})$ is used to represent $f(\alpha)$ in and on both sides of the gas-liquid interface. In Eq.(11) $\hat{\mathbf{n}}$ is the interfacial normal vector and defined as:

$$\hat{\mathbf{n}} = \frac{\nabla \alpha}{|\nabla \alpha|} \tag{12}$$

The attachment force $\mathbf{F}_a$ in Eq.(11) is also proportional to a physical force F_a. Force F_a is related to surface tension and the three-phase contact angle. Schulze (1983) identified the attachment force between the gas-liquid interface and the solid particle as the sum of the capillary force and the hydrostatic pressure force. The capillary force $\mathbf{F}_{cap}$ can be written as (Schulze, 1983):

$$\mathbf{F}_{cap} = -\pi r_p^2 sin^2(\omega) \rho_l gz_0, \tag{13}$$

where the angle ω and the deflection depth z_0 are indicated in Fig. 3. When the density of the air is neglected we can write for the hydrostatic force (Schulze, 1983):

$$\mathbf{F}_{hyd} = -2\pi r_p \gamma sin(\omega) sin(\omega + \theta) \hat{\mathbf{n}}, \tag{14}$$

where θ is the contact angle. To quantify the capillary force the deflection depth z_0 must be determined. From Fig. 3 we can estimate the that

$$z_0 \approx \frac{r_0}{2} tan(\phi_0), \tag{15}$$

where r_0 is the particle radius at the three-phase contact line, as shown in Fig. 3. For the angle ϕ_0 Shang *et al.* (2009) write:

$$sin(\phi_0) = cos\left(\tfrac{3}{4}\pi - \omega - \theta\right) \tag{16}$$

Combining Eqs.(15) and (16) and using $r_0 = r_p sin(\omega)$, we can write for the deflection depth:

$$z_0 \approx \frac{r_p}{2} sin(\omega) tan\left\{ sin^{-1}\left[cos\left(\tfrac{3}{4}\pi - \omega - \theta\right)\right]\right\} \tag{17}$$

Now, using the estimate that $\omega \approx \pi - \theta/2$ (see Schulze (1993)), we can write for the attachment force F_a in Eq.(11) as:

$$\begin{aligned} F_a &= |\mathbf{F}_{cap} + \mathbf{F}_{hyd}| \\ &= \pi r_p sin(\omega)\left[r_p sin(\omega)\rho_l gz_0 + 2\gamma sin(\omega + \theta)\right] \\ &\approx \pi r_p sin(\pi - \theta/2) \\ &\quad \left[r_p sin(\pi - \theta/2)\rho_l gz_0 + 2\gamma sin(\pi + \theta/2)\right] \end{aligned} \tag{18}$$

At this point it must be pointed out that in the particle-interface force model above, in particular in Eqs.(13) and (14), it is assumed that the particle is already attached to the gas-liquid interface. The model would improve considerably when dynamic forces are included. This is, however, beyond the scope of this paper.

CFD-DEM coupling

In the modelling of particulate flows two main strategies can be followed; the continuum and the discrete approach (Goniva *et al.*, 2010). In a continuum approach the multitude of particles is considered as an artificial continuum and is based on the solution of the underlying conservation equations (Gidaspow *et al.*, 1992). In the discrete approach,

however, the motion of each individual particle is described, with a special treatment of eventual particle-particle and particle-wall collisions. This allows the application of DEM especially for dense particulate flows. Additional forces acting on the particles can be considered, such as electromagnetic forces, or as described in the present paper, particle-interface forces.

The most important discrete model is the Discrete Element Method (Cundall and Strack, 1979). The nature of the DEM allows accurate capture of all granular physical phenomena and thus accurately model granular flow. CFDEM (CFDEM, 2011) is an open source code dedicated to the coupling of the CFD package OpenFOAM (OpenCFD Ltd., 2009) and the DEM solver LIGGGHTS (LIGGGHTS, 2011). LIGGGHTS allows accurate particle-particle interaction calculation within its own computational domain. In this work a linear Hooke law is used to model particle-particle collisions. The advantage of LIGGGHTS over a classical Discrete Phase Model (DPM) is that LIGGGHTS can handle higher void fraction and is a flexible open-source model, where case-specific sub-models can be readily implemented (Kloss *et al.*, 2009).

The CFDEM coupling routine between can be described as follows (Goniva *et al.*, 2010):

1. The DEM solver calculates the particles positions and velocities;

2. The particles positions and velocities are passed to the CFD solver and for each particle, the corresponding cell in the CFD mesh is determined;

3. For each cell, the particle volume fraction as well as a mean particle velocity is determined;

4. Based on the particle volume fraction, the momentum exchange between particles and carrier phases is calculated;

5. The forces acting on each particle are sent to the DEM solver and used within the next time step. They are assumed to be constant over the coupling interval and treated as explicit term in the integration of the particles trajectory;
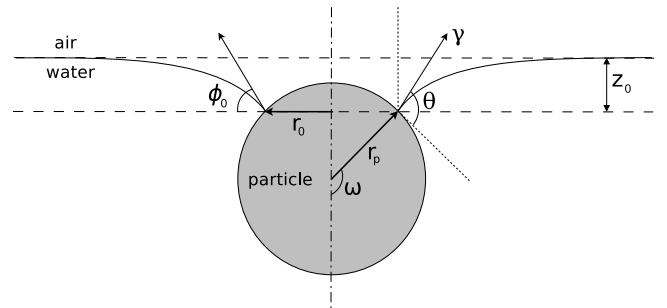

Figure 3: Spherical particle adhering to a gas-liquid interface (after Schulze (1983)).

6. The CFD solver calculates the fluid velocity taking into account local volume fraction and momentum exchange. Hereby particles volume fraction is treated explicitly in the volume averaged Navier Stokes equations, whereas the momentum exchange term is treated semi-implicitly for sake of stability (Goniva *et al.*, 2010);

7. The routine is repeated from (1).

Currently, the particle-interface force model, detailed in this paper, has been implemented as an additional sub-module within CFDEM framework. This allows for implementing new models which directly resolve particle-bubble interaction. The parallel nature of the underlying codes enables to use arbitrary geometries and large numbers of particles. Preliminary results are presented in Results Section.

Computational domain and solution procedure

The computational domain consists of an orthogonal structured mesh and is $13d_b$ wide in all three orthogonal directions to minimize wall effects. In order to maintain this domain width, the central part of the mesh was refined. The total amount of computational cells was 152,000 hexahedral cells. The bottom and walls have a no-slip boundary condition for velocity and zero flux condition for pressure. At the top of the domain an outlet boundary condition is set for the void fraction α and the velocity field. For the pressure field a total pressure condition is set at the outlet. The solution procedure is based on the Pressure Implicit Splitting of Operators (PISO) (Issa, 1986). The computational model is fully parallelized using the MPI library specification. The 152,000 cell case is computed in about 5 hours per ms, scaled to a single CPU. At the present stage of development excessive code efficiency studies have not yet been carried out, however first tests of the parallel performance of the coupling show promising results.

RESULTS AND DISCUSSION

Comparison with the Young-Laplace equation

A measure of the accuracy of a numerical method for modelling of gas-liquid systems is assessment of the pressure jump condition across the interface. (Brackbill *et al.*, 1992) assessed the accuracy of the normal boundary condition of an interface of an incompressible and inviscid fluids by calculating the surface pressure p_s for constant surface tension coefficient. Under the aforementioned conditions, the surface stress boundary condition reduces to the Young-Laplace equation (Landau and Lifshitz, 1987):

$$p_s \equiv p_2 - p_1 = \gamma\kappa, \tag{19}$$

where κ is the interface curvature and p_1 and p_2 are the pressure outside and inside the drop, respectively. The comparison of the numerical calculation of surface pressure to the analytical value of Eq.(19), is therefore proportional to the accuracy of the interfacial curvature calculation (Brackbill *et al.*, 1992). Brackbill *et al.* (1992) used a two-dimensional drop of 4 cm in diameter, centered in a square numerical domain of 6 by 6 cm. In this test, the mesh resolution is 60 by 60 cells, drop density is 1000 kg/m³,

background density is 500 kg/m³, surface tension is constant at 0.02361 N/m. Under these conditions the pressure jump condition can be estimated by:

$$p_s = \gamma\kappa = \frac{\gamma}{R}, \tag{20}$$

where R is the drop radius. From Eq.(20), p_s is 1.1805 Pa. (Brackbill *et al.*, 1992) computed the mean drop pressure by:

$$\langle p \rangle = \frac{1}{N_d} \sum_{i,j=1}^{N_d} p_{i,j}, \tag{21}$$

for computational cells (i, j). The number of "drop cells" N_d is defined as the number of cells for which $\rho \geq 990$ kg/m³. The comparison between p_s of Eq.(20) and $\langle p \rangle$ of Eq.(21) is shown in Fig 4. The results of this test for the VOF solver used in this work, shows a downward deviation from the analytical solution in the order of 15 to 20%. This suggests a similar deviation for the curvature calculation of around 1.5 to 2 times the analytical value for curvature, as reported by Brackbill *et al.* (1992) and Ubbink (1997). For the current purpose this level of accuracy is sufficient.
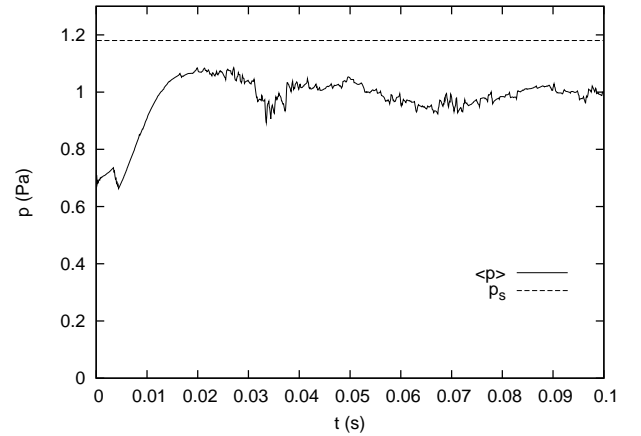

Figure 4: Result of the droplet surface pressure test (Brackbill *et al.*, 1992) for computed mean drop pressure $\langle p \rangle$ in Eq.(21) and analytical surface pressure p_s according to the Young-Laplace equation, Eq.(19).

Simulation of particle capture

The method described above allows for simulation of three-phase flow systems. With regard to mineral froth flotation the capture of solid particles by air bubbles is of particular interest. A numerical simulation is performed, where a 1 mm air bubble rises in stagnant liquid and collides with three mineral particles of 100 μm in diameter. The density of the particles is 3000 kg/m³. The gas-liquid surface tension coefficient is kept constant at 70 mN/m and the three-phase contact angle is 1.15 rad, or 66°. Fig. 5 shows a sequence of snapshots of the air bubble encountering solid particles. Since the actual position of the gas-liquid interface is not exactly known when using the VOF method, the $\alpha = 0.5$ contour is chosen to represent

the bubble surface. The result shown in Fig. 5 have been computed using a set of special particle classes developed in the OpenFOAM package, as detailed in the above sections.

Three particles are released at different positions above the bubble, as shown on the left in Fig. 5. In the second and third snapshots in Fig. 5 the particles slide along the surface of the bubble and are exposed to the addition force described by Eq.(18). After colliding with each other the first and second particle detach from the bubble surface and continue their way through the liquid. The third particle stays attached to the bubble and rises with it to the surface.
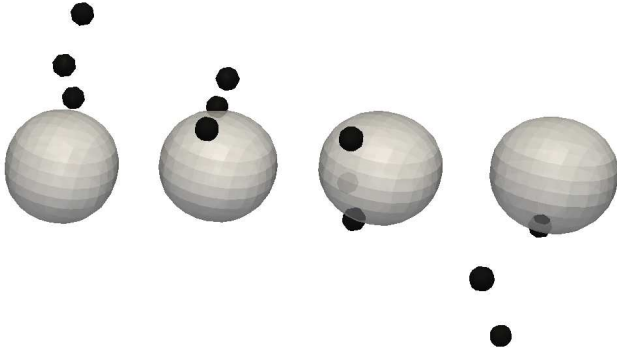

Figure 5: A 1 mm air bubble rising and colliding with three particles at 5 ms intervals. The particles are 100 μm in diameter and have a density of 3000 kg/m^3.

In order to accommodate heavy mass loading by dispersed media and allow for complex particle mechanics, the flotation particle classes and solver have been ported to the coupled CFD-DEM code CFDEM (CFDEM, 2011). Preliminary results of bubble-particle interaction calculations are shown in Fig. 6. Particle and fluid motion are computed by different solvers using different meshes and different time stepping. As such, both routines can be optimized more efficiently. In both the CFD and the CFDEM approach, particle positions and momenta are computed for every particle and therefore particle forces can be calculated. These force calculations can be used for validation against experimental findings of interface kinetics and it must be noted that the current computational framework is operational, yet needs more input of force models.

CONCLUSION

The interaction between small drops or solid particles and a gas-liquid interface is a physico-chemical phenomenon of major importance in many process applications. The scale of most industrial (macro-scale) processes makes detailed modelling commonly infeasible and semi-statistical or empirical models are needed. The micro-scale models that constitute the physico-chemical basis of the macro-scale are typically geared towards semi-static systems of a single particle and a single bubble. This approach has proven useful in the design and optimization of many industrial

applications. However, the predicitve power independent of specific process characteristics, such as particle properties, is commonly poor. In this work we present a computational framework for modelling of bubble-particle interaction on the meso-scale, i.e. for swarms of bubbles and particles. A deeper understanding of the kinetics at this scale can lead to better statistical models for simulation of processes at a scale meaningful for industrial application. The physico-chemical submodels still lack many parts; the particle-particle collision parameters need a physical basis, the particle-interface force model needs improvement, and the effect of turbulence must be introduced. The development of the modelling framework presented is, however, a major step forward in unifying physical and (physico-)chemicial micro-scale phenomena to larger scales. This is the aim of this paper.

The computational platforms for the investigation reported here are the CFD package OpenFOAM (OpenCFD Ltd., 2009) and CFDEM (CFDEM, 2011) code, coupling Open-FOAM and the DEM code LIGGGHTS (LIGGGHTS, 2011).
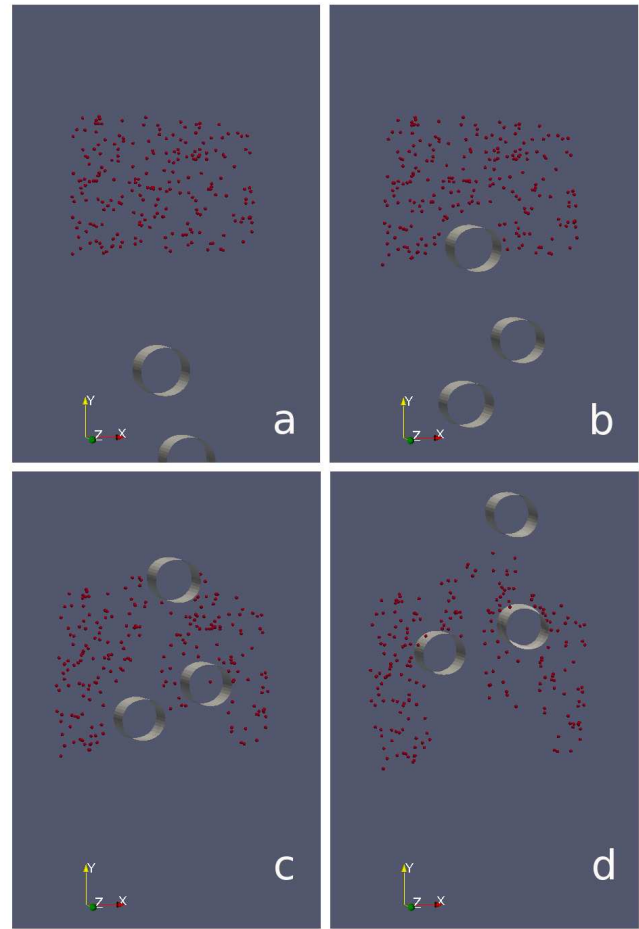

Figure 6: Three 1 mm air bubbles rising through a cloud of 100 μm mineral particles in snapshots after 0.1 s (a), 0.3 s (b), 0.5 s (c), and 0.6 s (d), respectively, as computed using CFDEM (CFDEM, 2011) in 2D.

All of the aforementioned packages are open source software. The Volume of Fluid (VOF) method (Hirt and Nichols, 1981) is used to compute the motion of gas an liquid. In principle, the VOF method is not particularly suitable for surface tension dominated flows. However, since the prospect is to also investigate bubble breakup and coalescence during interaction between bubble and particle swarms, the VOF method was chosen to eliminate the need for complex topological changes in the computational mesh. A soft-sphere model has been implemented to account for particle-particle collisions when particle void fraction is higher. Particles close to the gas-liquid interface experience an attractive force as a function of contact angle, surface tension, particle size, and density.

The model presented in this paper is work in progress and can form a good basis for further development because of its modular and open structure. The current modelling framework shows promising first results. Bubble-particle interaction has been simulated on the scale of several bubbles and particles, here referred to as the meso-scale. Meso-scale phenomena such as particle capture and detachment have been observed. The findings of the current and future generations of the model describe in this paper can provide valuable input for larger scale models through a unified approach.

ACKNOWLEDGEMENTS

REFERENCES

BARNOCKY, G. and DAVIS, R.H. (1989). "The lubrication force between spherical drops, bubbles and rigid particles in a viscous fluid". *Int J Multiphase Flow*, **15(4)**, 627–638.

BERTRAND, F. *et al.* (2005). "DEM-based models for the mixing of granular materials". *Chem Eng Sci*, **60(8-9)**, 2517–2531.

BRACKBILL, J.U. *et al.* (1992). "A continuum method fo modeling surface tension". *J Comp Phys*, **100(2)**, 335–354.

CFDEM (2011). "CFDEM - Open Source CFD, DEM and CFD". URL http://www.cfdem.com.

CUNDALL, P.A. and STRACK, O.D.L. (1979). "A discrete numerical model for granular assemblies". *Géotechnique*, **29(1)**, 47–65.

ELGHOBASHI, S. (1991). "Particle-laden turbulent flows: Direct simulation and closure models". *Appl Sci Res*, **48(3-4)**, 301–314.

GIDASPOW, D. *et al.* (1992). "Hydrodynamics of Circulating Fluidized Beds, Kinetic Theory Approach". *Proc. Fluidization VII, Proceedings of the 7th Engineering Foundation Conference on Fluidization*, 75–82.

GONIVA, C. *et al.* (2010). "An Open Source CFD-DEM Perspective". *Proc. 5th OpenFOAM workshop*. Chalmers University, Gothenburg, Sweden.

HIRT, C.W. and NICHOLS, B.D. (1981). "Volume of fluid (VOF) method for the dynamics of free boundaries". *J Comp Phys*, **39(1)**, 201–225.

ISRAELACHVILI, J.N. (1992). *Intermolecular and surface forces*. 2nd ed. Academic Press, London.

ISSA, R.I. (1986). "Solution of the implicitly discretised fluid flow equations by operator-splitting". *J Comp Phys*, **62(1)**, 40–65.

IVANOV, I.B. *et al.* (1978). "Hydrodynamics of thin films. rate of expansion of the perimeter of the three-phase contact". *J Colloid Interf Sci*, **63(1)**, 166–168.

KLOSS, C. *et al.* (2009). "Comprehensive DEM-DPM-CFD simulations - Model synthesis, experimental validation and scalability". *Proc. 7th Int. Conf. CFD in the Minerals and Process Industries (CFD 2009)*. CSIRO, Melbourne, Australia.

LANDAU, L. and LIFSHITZ, E. (1987). *Fluid Mechanics*, vol. 6 of *Course of Theoretical Physics*. 2nd ed. Pergamon Press, New York.

LIGGGHTS (2011). "LAMMPS Improved for General Granular and Granular Heat Transfer simulations". URL http://www.liggghts.com.

MALONE, K.F. and XU, B.H. (2008). "Determination of contact parameters for discrete element method". *Particuology*, **6(6)**, 521–528.

OpenCFD Ltd. (2009). "OpenFOAM - The open source CFD toolbox". URL http://www.openfoam.com.

SCHULZE, H.J. (1983). *Physico-chemical elementary processes in flotation*, vol. 4 of *Developments in Mineral Processing*. Elsevier, Amsterdam, The Netherlands.

SCHULZE, H.J. (1993). *Flotation as a heterocoagulation process: Possibilities of calculating the probability of flotation*. No. 47 in Surfactant Science Series, Ch. 7, p. 321–353. Dekker, New York.

SHANG, J. *et al.* (2009). "Force measurements between particles and the air-water interface: Implications for particle mobilization in unsaturated porous media". *Water Resour Res*, **45(6)**, W06420.

UBBINK, O. (1997). *Numerical prediction of two fluid systems with sharp interfaces*. Ph.D. thesis, Imperial College London.

WELLER, H. (2008). "A New Approach to VOF-based Interface Capturing Methods for Incompressible and Compressible Flow". Tech. Rep. TR/HGW/04, OpenCFD Ltd. URL http://www.opencfd.co.uk.

WELLER, H.G. (1993). "The development of a new flame area combustion model using conditional averaging". Tech. Rep. TF 9307, Imperial College of Science, Technology and Medicine.

WIERINK, G.A. and HEISKANEN, K. (2008). "Momentum coupling in flotation modelling". *Proc. Computational Modelling '08*. Cape Town, South Africa.

NUMERICAL SIMULATION OF MULTIPHASE FLOWS OF CO2 STORAGE IN SALINE AQUIFERS IN DAQINGZIJING OILFIELD, CHINA

Duo X. YANG[1,2]*, Rong S.ZENG[2], Y.ZHANG[1],S. WANG[2], C.JIN[2]

[1] Research Institute of Innovative Technology for the Earth, Kyoto 619-0292, JAPAN

[2] Institute of Geology and Geophysics, Chinese Academy of Sciences, Beijing, 100029, CHINA

* E-mail:

ABSTRACT

Keywords:

NOMENCLATURE

Greek Symbols

ρ

μ

φ

ϕ

K

Latin Symbols

p

$\mathbf{u}$

ξ

INTRODUCTION

Interface treatment method

(<
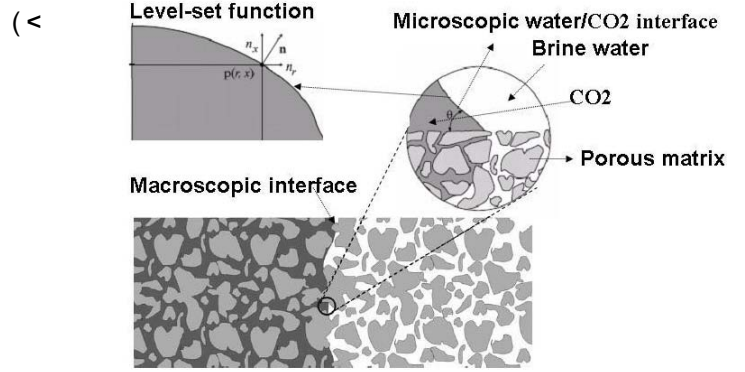
Figure 1:

MODEL DESCRIPTION

Governing equations

Continuity equation
$$\nabla \cdot \mathbf{u} =$$

Momentum equation
$$\frac{\partial \rho \mathbf{u}}{\partial t} + \nabla \cdot \left(\frac{1}{\varphi} \rho \mathbf{u}\mathbf{u} \right) = -\varphi \nabla p + \nabla \mu \nabla \mathbf{u} + \varphi \mathbf{F}_{L}$$

$$\mathbf{F}_{L} = -\frac{\mu \mathbf{u}}{K} - \left(\frac{f_b}{\sqrt{K}} \mathbf{u}\|\mathbf{u}\| \right) - \mathbf{F}_{SV}$$

Level-set function
$$\frac{\partial \varphi \phi}{\partial t} + \nabla \cdot (\phi \mathbf{u}) =$$

Surface tension equation
$$\mathbf{F}_{SV} = \xi \ \phi \ \delta \ \phi \ \nabla \phi$$

ϕ

δ ξ
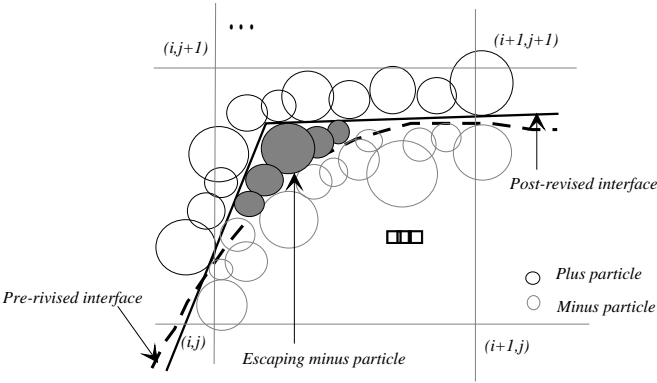
Table 1:

Figure 2:

CE/SE scheme
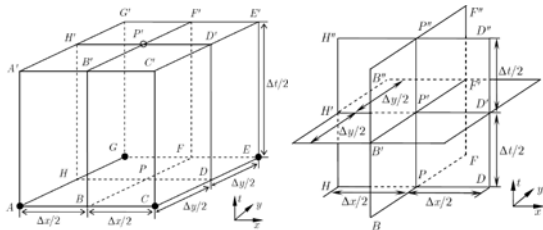
Figure 3:

NUMERICAL VALIDATION
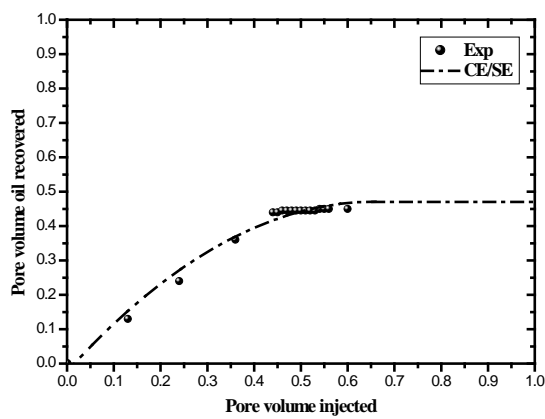
Figure 4:

RESULTS

Figure 5:

Figure 6:

Figure 7:

℃
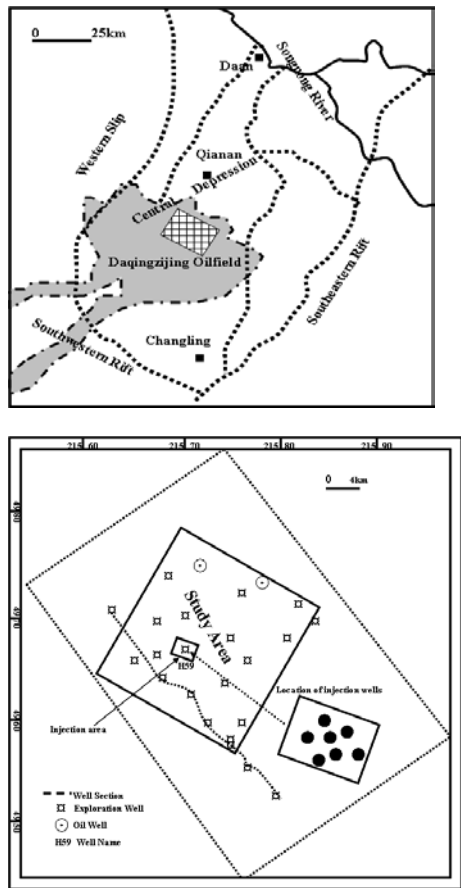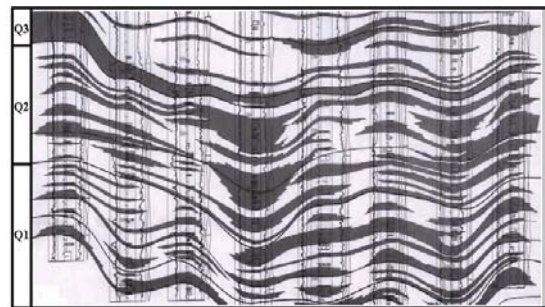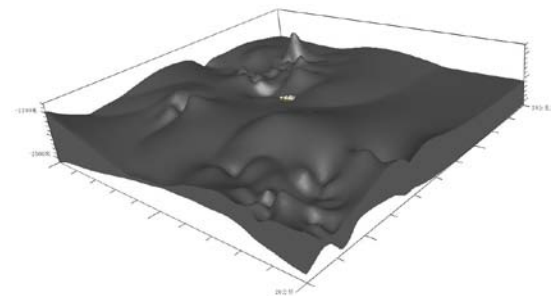
/100m
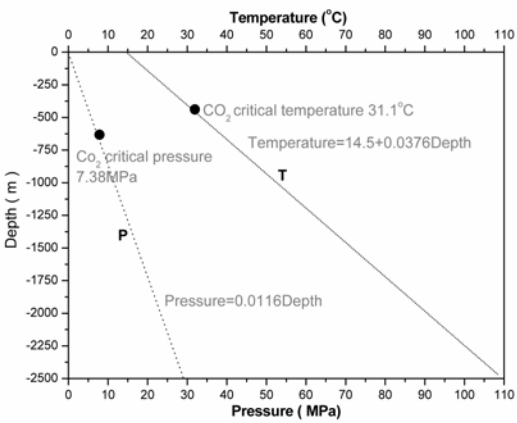
※   5×10⁻⁵

※

Figure 8:

Table 2:

μ
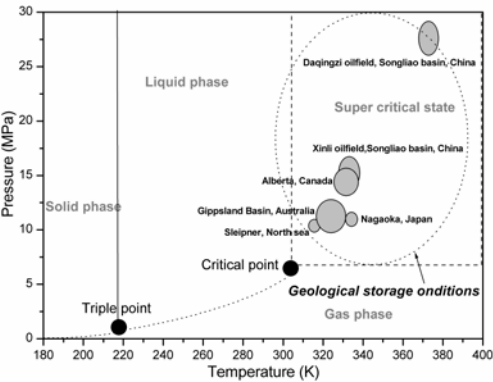
Table 3:

5×10⁻⁴
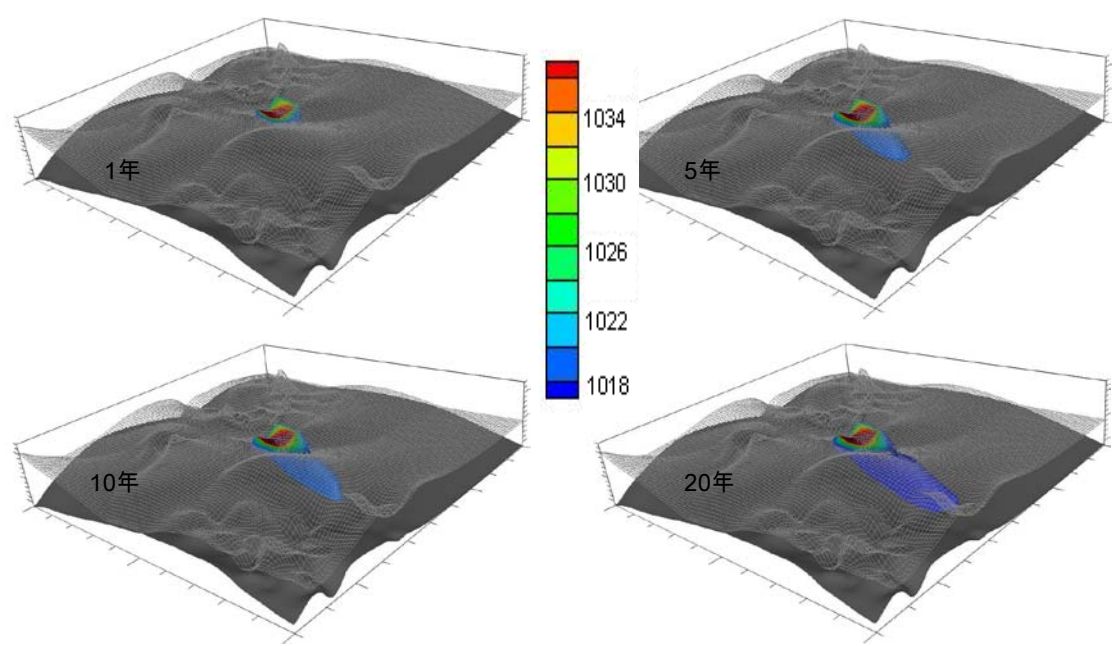
Figure 9:
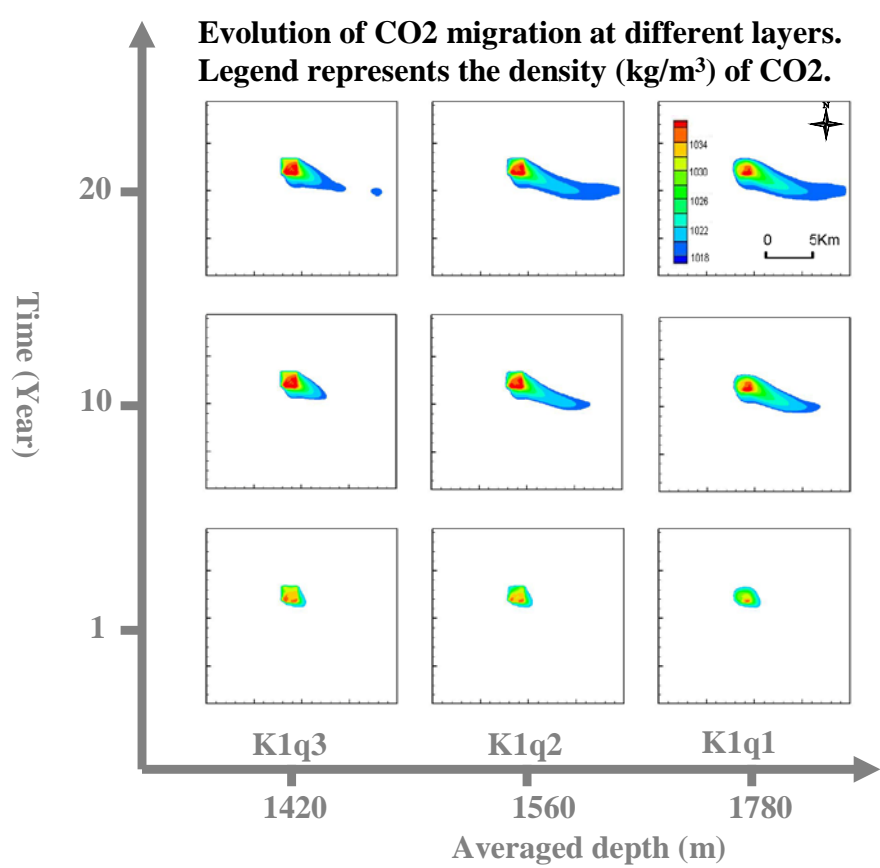
Figure 10:

ACKNOLODGEMENTS

REFERENCES

Energy Convers. Manage **35**

Energy Convers Manage
41

J. Comput. Phys **100**

Adv. Water Resour **32(1)**

J. Comput. Phys **176**

CONCLUSION

SIAM Journal on Scientific Computing **21** ~

Soc. Pet. Eng. J.

Energy Convers. Manage, **49**

EFS-FWF-LFUI Conference on CO2 Geological Storage: Latest Progress

Energy Conversion and Management **45**

J. Comput. Phys. **114**

Transport in Porous Media **25**

Comput Fluid **38(3)**

Commun. Comput.Phys **6(1)**

Acta Geologica Sinica (in Chinese) **83(6)**

Chinese J. Geophys. (in Chinese) **53(1)**

Aerosol Air Qual. Res **9(2)** ~

Book of Abstracts of the 5th Conference international Marangoni association (IMA5): Interfacial Fluid Dynamics and Process

Int. J. Greenhouse Gas Contro

Int. J. Greenhouse Gas Contro **3(2)**

8th International Conference on CFD in Oil & Gas, Metallurgical and Process Industries
SINTEF/NTNU, Trondheim NORWAY
21-23 June 2011

CFD11-103

NUMERICAL STUDY OF THE WALL EFFECT ON THE LIQUID DISTRIBUTION IN A TRICKLE-BED REACTOR

Manuel MARTINEZ[1][*], **Jordi PALLARES**[1], **Antonio LOPEZ**[2], **Miguel A. GARCIA**[2],

Francesc X. GRAU[1]

[1]Mechanical Engineering Department, University Rovira i Virgili, 43007 Tarragona, SPAIN

[2]Repsol Technological Center, 28931 Mostoles, SPAIN

[*] E-mail: manuel.martinezd@urv.cat

ABSTRACT

Numerical simulations of the two-phase flow distribution in the packed bed of a reactor used for fuel hydrodesulfuration are reported. The reactor considered has, above the bed, a distribution tray equipped with chimneys. The boundary conditions at the inlet of the reactor bed were obtained from simulations of the flow at the exit of a chimney. An Eulerian three-phase model that considers the particles of catalyst as a granular static phase has been used following the Holub single slit model for particle fluid interaction to compute the liquid-solid and gas-solid drag coefficients. Physical properties of the fluids are assumed to be constant and no chemical reactions, mass and heat transfer processes between the phases are taken into account. A previous study hinted at the possibility of a liquid tendency to attach the wall of the reactor as the depth of the bed is increased. In the present study, this phenomenon is further studied in a deeper bed. In the first 11 m of the reactor, there is no suction effect on the flow caused by the wall. As the two-phase flow moves downward by the bed, a slow radial liquid spreading takes place. However, flow distribution is not completely uniform, at least at a distance of 11 m from the inlet, although it improves as the flow descends.

Keywords: Hydrodesulfuration reactor, CFD, trickle-bed, liquid distribution, wall effect .

NOMENCLATURE

Greek Symbols
θ Volume fraction, [*Dimensionless*]
μ Viscosity, [*Pa s*]
ρ Density, [*kg/m³*]

Latin Symbols
$\mathbf{g}$ Gravity vector, [*m/s²*]
K Drag coefficient, [*kg/m³s*]
P Pressure, [*Pa*]
t Time, [*s*]
$\mathbf{u}$ Velocity vector, [*m/s*]

Sub/superscripts
f Fluid
k Phase Index
s Solid

INTRODUCTION

In the trickle bed reactors used in the petrochemical industry for fuel hydrodesulfuration processes, gas and liquid flow co-currently downward through a packed bed of catalytic solid particles. The uniformity of the two-phase flow in the bed is an important parameter for the correct operation of the catalyst. For example, a poor distribution of the liquid-gas mixture reduces the effective volume of the reactor in which the hydrodesulfuration takes place, and thus can produce hot spots that may decrease the life of the catalyst.

One of the causes of flow maldistribution is the phenomenon known as wall effect, where the liquid flowing downwards tends to attach the wall of the column. An increased wall flow causes the large-scale liquid maldistribution, as reported by Wang et al. (1996). Several authors have studied this effect, which is one to be avoided in order to have a good liquid distribution, as noted by Hoftyzer (1964). Other interesting studies on liquid maldistribution on packed columns include those by Gunn (1987), Cairns (1948), Cihla and Schmidt (1957), Marchot et al. (1999) and Baker et al. (1935).

MODEL DESCRIPTION

Figure 1 shows a sketch of the reactor considered in this study. There is a distribution tray above the catalytic beds, which contains chimneys to distribute the liquid flow entering the reactor before it descends towards the beds. There is a void space between this distribution tray and the first of the beds, where the flow freely moves downwards. Below this space there are the four particle beds. The first three beds are 150 mm high while the fourth one is 15560 mm. The main characteristics of the different particles for each bed are shown in Table 1, while Table 2 shows the ratio of the physical properties of the fluids, which are assumed to be constant. Chemical reactions and heat and mass transfer processes between the phases are not taken into account.

Numerical simulations for the two-phase flow through the reactor beds have been performed using the commercial CFD code Fluent (2006). An Eulerian three-phase model has been used in a three-dimensional domain, where continuity (Eq. 1) and momentum (Eq. 2) equations are solved individually for each phase. Drag terms are modelled using the Holub model (1992).

$$\frac{\partial \theta_k}{\partial t} + \nabla \cdot \theta_k \mathbf{u_k} = 0 \qquad (1)$$

$$\theta_k \frac{\partial \mathbf{u_k}}{\partial t} + \theta_k (\mathbf{u_k} \cdot \nabla) \mathbf{u_k} = -\frac{1}{\rho_k} \nabla P + \frac{\mu_k}{\rho_k} \nabla (\theta_k \nabla (\mathbf{u_k})) + \\ + \theta_k \mathbf{g} + \frac{1}{\rho_k} \theta_k \theta_f K_f (\mathbf{u_f} - \mathbf{u_k}) + \frac{1}{\rho_k} \theta_k \theta_s K_s (-\mathbf{u_k}) \qquad (2)$$

Due to the nature of this case, calculations are carried out in sections, since simulating the whole reactor would result in a very large number of cells and an extremely high computational cost. The first 11 m of the reactor have been simulated, since it is considered that this is enough to appreciate any possible wall effect on the flow behaviour.
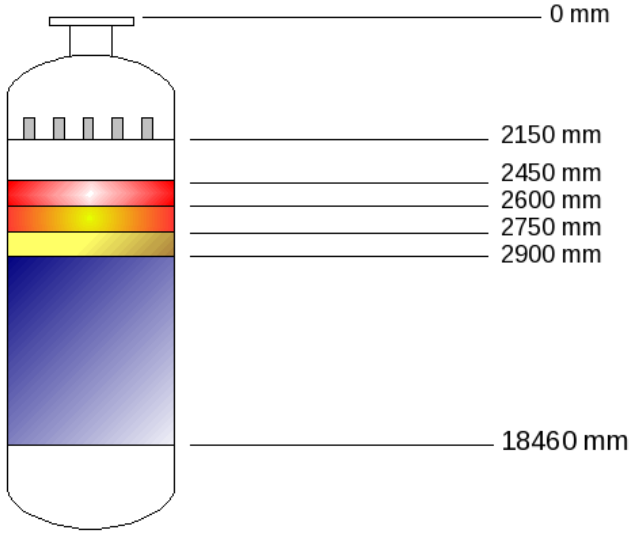

Figure 1: Sketch of the reactor.

Table 1: Beds characteristics

Bed	Porosity	Depth (*mm*)
1	0.33	150
2	0.53	150
3	0.45	150
4	0.40	15560

Table 2: Physical properties ratios

Density ratio (Liquid / Gas)	29.3
Viscosity ratio (Liquid / Gas)	6.7

Numerical procedure

As shown in Figure 2, the reactor has been divided in sections which are 15 cm deep, where the volume fractions and velocities distribution results at the outlet in each of these sections are taken as the inlet conditions of the following section. This contributes to speed up calculations, although, due to the large number of simulations needed to obtain meaningful results of the flow distribution through the reactor, time for calculations is also large. To avoid a possible distortion in the results caused by the outlet boundary condition, which seems to have an influence at the exit zone in each simulation, it has been decided to simulate sections 20 cm deep but taking only the first 15 cm as valid.

Time calculation optimization

Simulations varying the section depths were carried out to optimize the calculation time. Table 3 shows the comparison of the studied cases. The improvement factor in the simulation efficiency by using 20-cm sections is 1.56.

In order to speed up calculations even more, two processors are working in parallel. Table 4 shows the comparison between the serial and parallel computations. It can be seen that Fluent parallelizes in a very efficient manner the simulation with two processors, with a speed up factor of 2.

The overall improvement factor in the computation efficiency, using two processors working in parallel and simulating 15-cm sections (real depth) is 3.12.

Table 3: Simulation time comparison

Simulated section depth (*cm*)	10	20
Real section depth (*cm*)	5	15
Number of cells	1244720	2489440
Time per iteration (*min/iteration*)	2.97	5.72

Table 4: Parallel computation

Number of processors	1	2
Real section depth (*cm*)	15	15
Number of cells	2489440	2489440
Time per iteration (*min/iteration*)	5.72	2.86

RESULTS AND DISCUSSION

Liquid volume fraction isosurfaces

Figure 3 shows the inlet boundary condition used in the simulations. As it can be seen in the liquid volume fraction contours shown, the liquid focuses distribution is in agreement with the chimneys distribution on the distribution tray. Figure 4 shows the zone in which liquid isosurfaces will be shown later enclosed in a rectangle.

In order to show in an easier understandable manner the information contained in the liquid isosurfaces as the liquid flows downwards through the reactor beds, it is better to present this information on three different figures. Figures 5.a to 5.c show liquid volume fraction isosurfaces of 0.10. Figure 5.a shows the liquid distribution in the first 4.5 m of the reactor, Figure 5.b from 4.5 m to 9.5 m and Figure 5.c from 9.5 m to 11 m.

It can be observed in those figures that the liquid spreads slowly in the radial direction, reaching a more uniform distribution in the central zone than in the near-wall zone. It should be noted that the isosurfaces shown provide only a partial information of what is really happening in the reactor. In order to obtain a more detailed view of reality, it
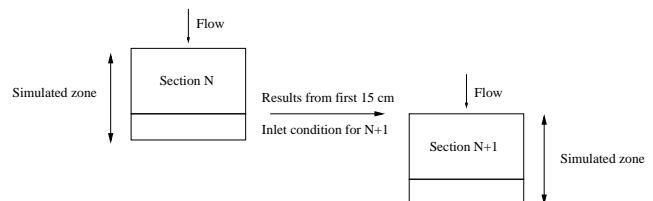
Figure 2: Sketch of the simulation procedure in sections.

is required to resort to liquid volume fraction contours and profiles at different reactor depths.
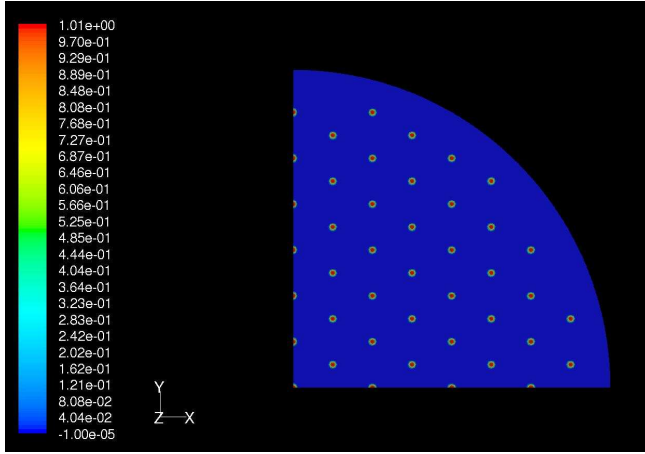
Figure 3: Inlet boundary condition. Liquid volume fraction contours.
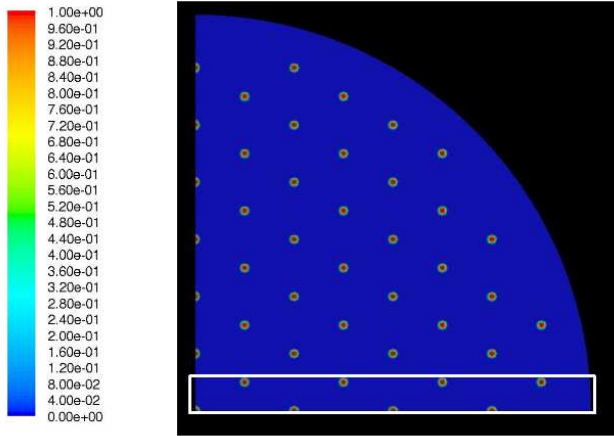
Figure 4: Inlet boundary condition. Liquid volume fraction contours.

Liquid volume fraction contours

Figures 6 to 8 show liquid volume fraction contours at different depths. The red colour represents liquid and the blue colour gas, with the colour gradation representing different values of liquid volume fraction according to the colour scale shown at the left side of the contours. It can be seen that, as the flow descends through the reactor beds the liquid spreads radially improving phase distribution. While not perfectly uniformly distributed, from a depth of 8 m on the liquid is under a reasonably good distribution. This is seen in a more detailed manner in the volume fraction profiles shown later.

Liquid volume fraction profiles

Two different planes have been chosen to show the liquid volume fraction profiles. The first of these planes is marked with a line in Figure 9.

Figures 10 to 12 show the liquid volume fraction profiles at different reactor depths in the aforementioned plane. The reactor radius is shown on the horizontal axis while the liquid volume fraction is shown in the vertical axis. It can be seen in these figures, in the region close to the inlet, around
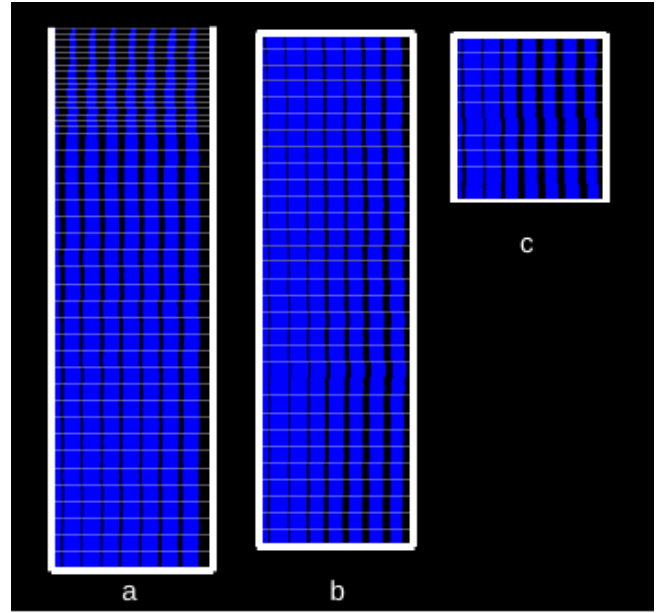
Figure 5: Liquid volume fraction isosurfaces of 0.10. (a) Zone comprised between 0 m and 4.5 m. (b) Zone comprised between 4.5 m and 9.5 m. (c) Zone comprised between 9.5 m and 11 m.
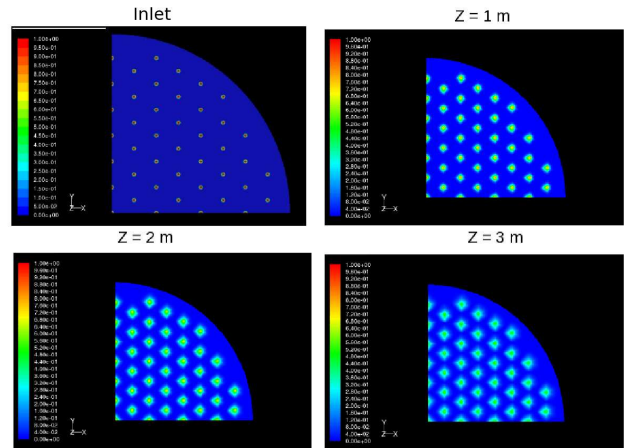
Figure 6: Liquid volume fraction contours. Slices at 0 m, 1 m, 2 m and 3 m.
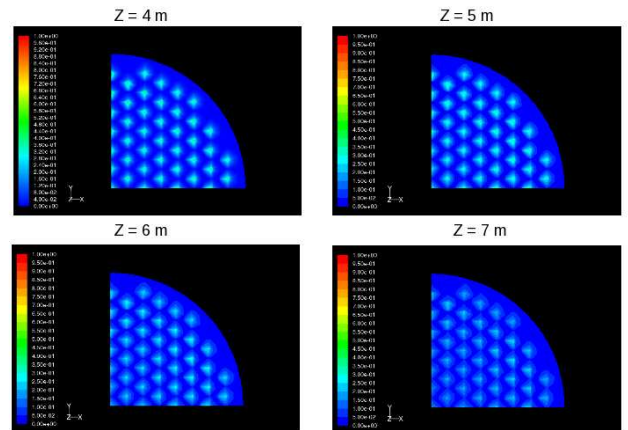
Figure 7: Liquid volume fraction contours. Slices at 4 m, 5 m, 6 m and 7 m.

the first 3 m, that the liquid volume fraction decreases faster in the chimneys placed near the wall than in the central ones. In other words, chimneys which are close to the wall spread the liquid radially faster than those in the central region of the reactor. This phenomenon balances between 3 m and 5 m of the reactor. From that depth on, the central chimneys start spreading faster than those near the wall. It can be seen, for a depth of 11 m, that in the first 0.3 m in radial direction the liquid distribution is uniform. Figure 13 shows simultaneously liquid volume fraction profiles at different depths.

The second plane chosen to show these profiles is the one shown in Figure 14. Figures 15 to 17 show liquid volume fraction profiles at different reactor depths. As it can be seen, the results obtained are similar to those seen in the other plane. Figure 18 shows simultaneously liquid volume fraction profiles at different depths.

A characteristic of the liquid distribution worth mentioning is the lack of symmetry in the plumes as the flow descends through the reactor beds. As it can be seen in Figures 10 to 13 and Figures 15 to 18, the plume region close to the wall is narrower than the plume region close to the center of the reactor, or in other words, there is a suction effect on the flow from the central zone of the reactor, which is explained later.
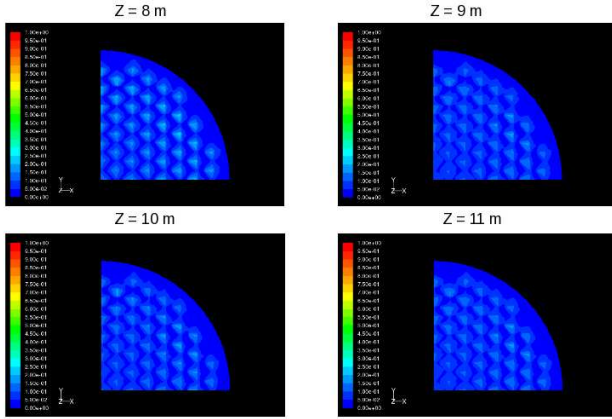
Figure 8: Liquid volume fraction contours. Slices at 8 m, 9 m, 10 m and 11 m.
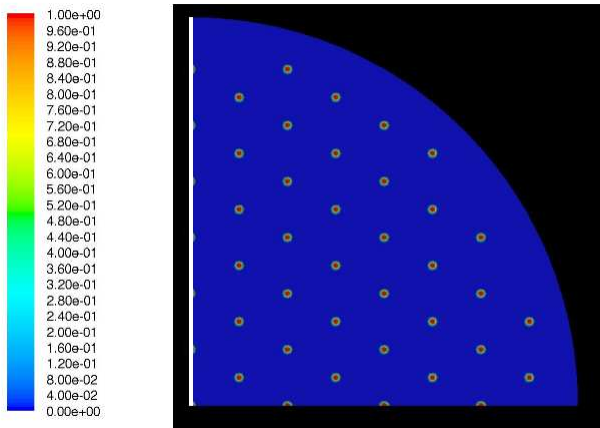
Figure 9: Plane on the symmetry axis chosen to show the liquid volume fraction profiles.

Liquid velocity profiles

Figures 19 and 20 show the liquid axial velocity profiles, at different depths, for the planes shown in Figures 9 and 14, respectively. As it can be seen in these figures, liquid descends with higher velocity through the central zone of the reactor than in the near-wall region. This would explain the effect of liquid displacement towards the central region of the reactor, previously commented, resulting in a better liquid distribu-

Figure 10: Liquid volume fraction profiles in the plane shown Figure 9. Slices at 0 m, 1 m, 2 m and 3 m.

Figure 11: Liquid volume fraction profiles in the plane shown Figure 9. Slices at 4 m, 5 m, 6 m and 7 m.

Figure 12: Liquid volume fraction profiles in the plane shown Figure 9. Slices at 8 m, 9 m, 10 m and 11 m.

tion in the central region of the reactor.

Evolution of the center of the plumes

Figures 21 and 22 show the evolution of the center of the plumes for the central and near-wall chimneys in the planes shown in Figures 9 and 14, respectively. The point of maximum liquid volume fraction is considered the center of the plume. The horizontal axis shows the point of maximum liq-

uid volume fraction for the plume, in other words the center, while the depth of the bed is shown in the vertical axis. As it can be seen, in the first 3 m the plume of the near-wall chimney is displaced faster than the one of the central region, with a change in tendency happening at 5 m. The same phenomenon takes place in both planes, so it is assumed that it happens in the whole reactor.
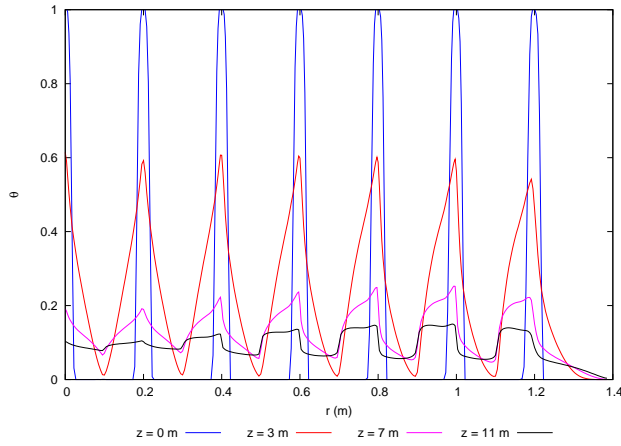
Figure 13: Liquid volume fraction profiles in the plane shown Figure 9. Slices at 0 m, 3 m, 7 m and 11 m.

Figure 16: Liquid volume fraction profiles in the plane shown Figure 14. Slices at 4 m, 5 m, 6 m and 7 m.

Figure 14: Plane chosen to show the liquid volume fraction profiles.
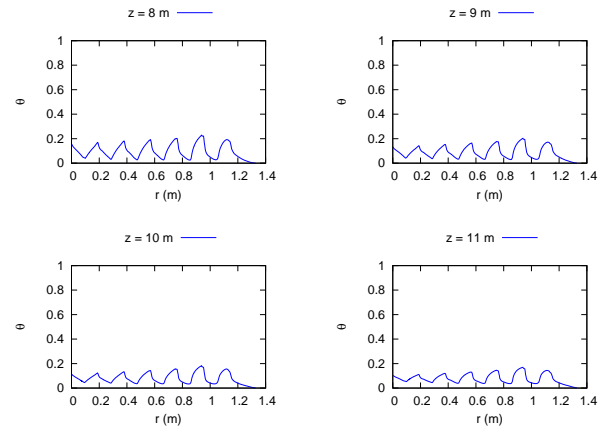
Figure 17: Liquid volume fraction profiles in the plane shown Figure 14. Slices at 8 m, 9 m, 10 m and 11 m.
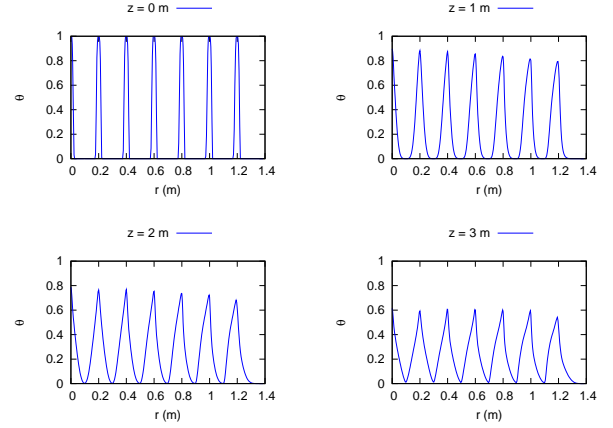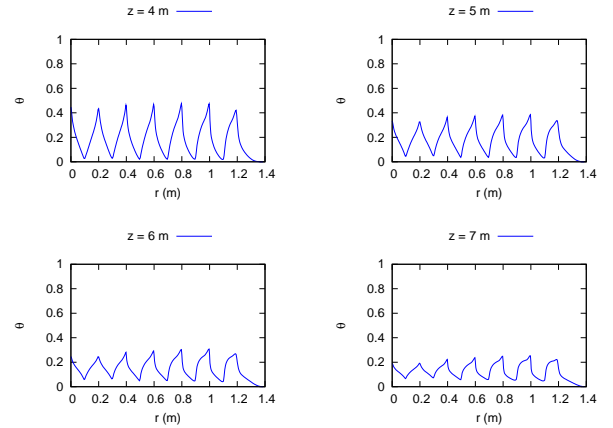

Figure 15: Liquid volume fraction profiles in the plane shown Figure 14. Slices at 0 m, 1 m, 2 m and 3 m.

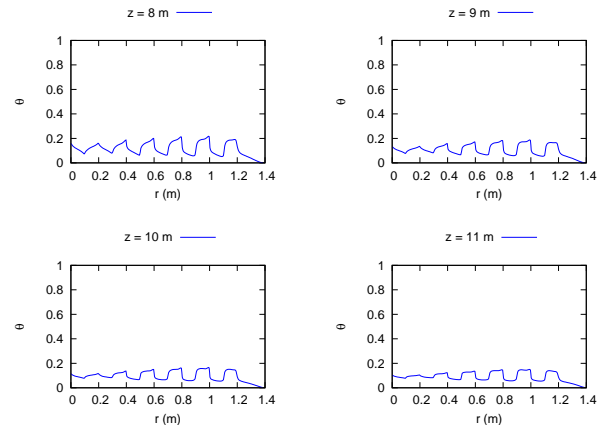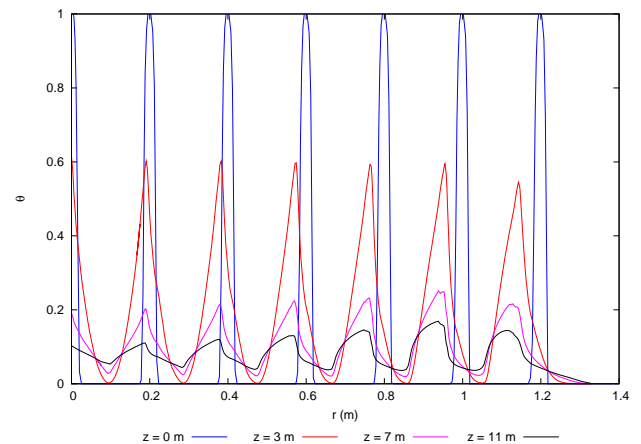Figure 18: Liquid volume fraction profiles in the plane shown Figure 14. Slices at 0 m, 3 m, 7 m and 11 m.

Half-width

An efficient manner to measure dispersion in porous media is the half-width. In a gaussian distribution, the half-width is defined as the distance that links the two points of value half of the maximum of the distribution at both sides of this maximum. Figures 23 and 24 show the evolution of the half-width along the reactor in the planes shown in Figures 9 and 14, respectively. As it can be seen, until a depth of 5 m the plume of the near-wall chimney is wider than the central region one. However, from a depth of 6 m on the central plume is clearly wider than the one in the near-wall region. From a depth of 8 m on, it is considered that in the central region the liquid is well enough distributed so there is no need to represent the half-width.

Distance to the wall

Figure 25 shows the distance between the center of the plume which is nearest the wall and the wall in the planes shown in Figures 9 and 14. As it can be seen, from a depth between 5 m and 6 m, the plume starts to move away from the wall. Thus, any suction effect by the wall is discarded. On the contrary, and as previously discussed, the liquid tends to move towards the center of the reactor.

CONCLUSIONS

According to the simulations, in the first 11 m of the reactor no suction effect by the wall is observed, since the center of the outer plumes not only does not approach the wall, but from a depth of 5 m on it starts to move away from it. As the two-phase flow descends through the beds of the reactor, a slow spreading of the liquid is observed in the radial direction. Liquid distribution is not completely uniform, at least at a depth of 11 m from the inlet, although it improves as the flow descends. A uniform liquid distribution can be considered for the central region of the reactor, in a radius of 0.3 m.

AKNOWLEDGEMENTS

Figure 19: Liquid axial velocity profiles in the plane shown in Figure 9. Slices at 3 m, 7 m and 11 m.
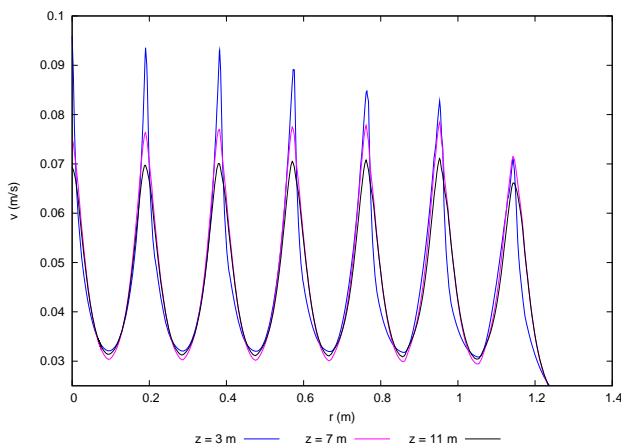
Figure 20: Liquid axial velocity profiles in the plane shown in Figure 14. Slices at 3 m, 7 m and 11 m.
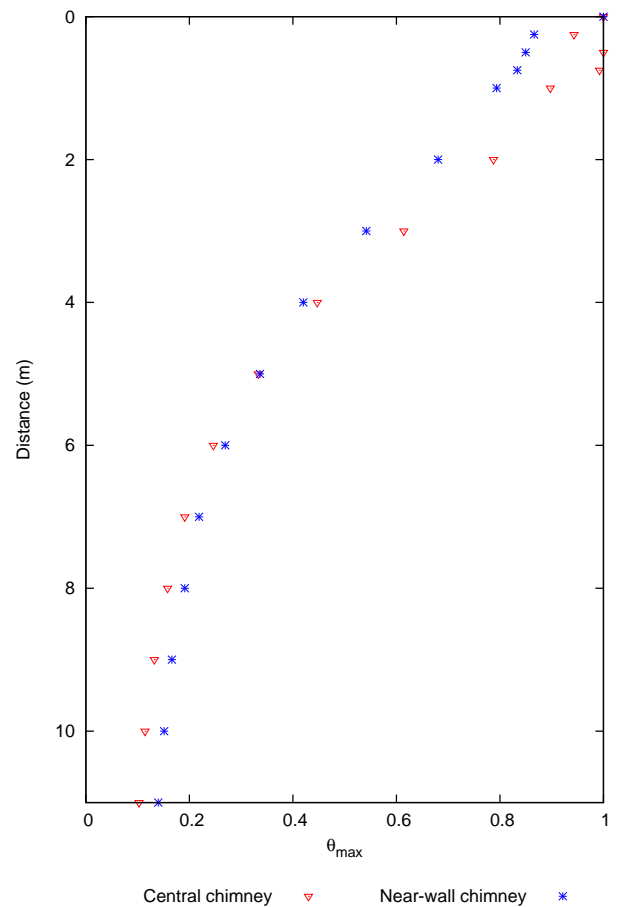
Figure 21: Evolution of the center of the plumes for the near-wall and central chimneys in the plane shown in Figure 9.
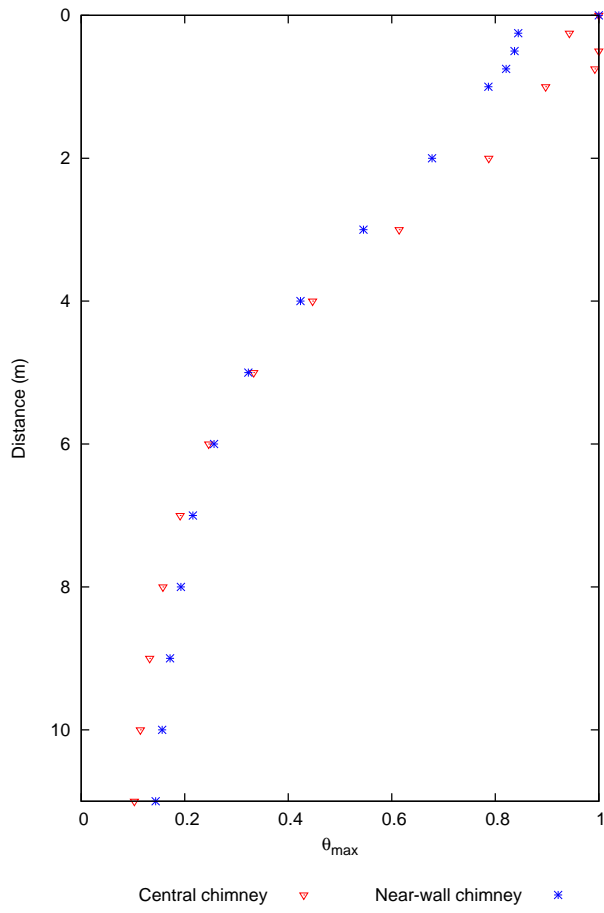
Figure 22: Evolution of the center of the plumes for the near-wall and central chimneys in the plane shown in Figure 14.
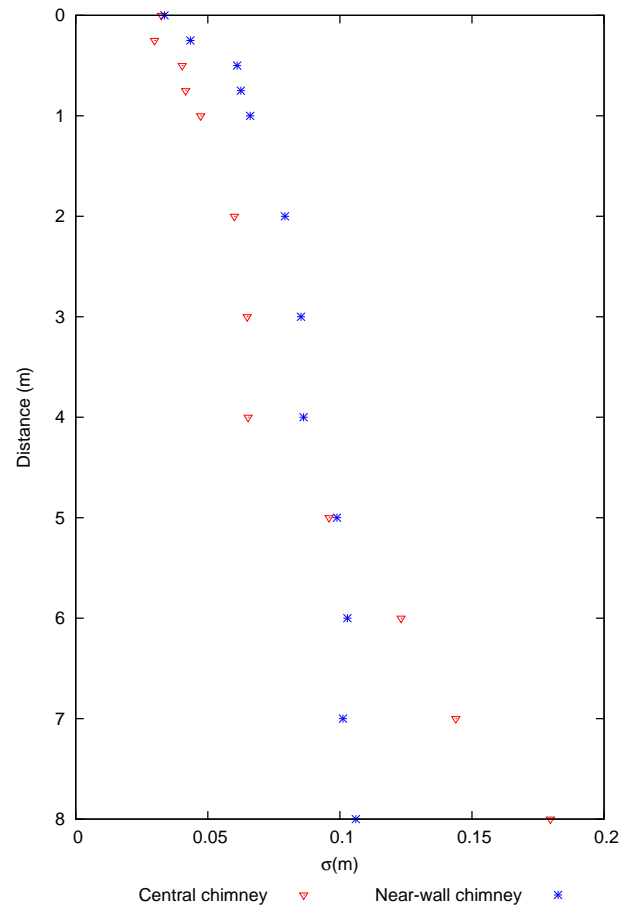
Figure 23: Evolution of the half-width for the near-wall and central chimneys in the plane shown in Figure 9.
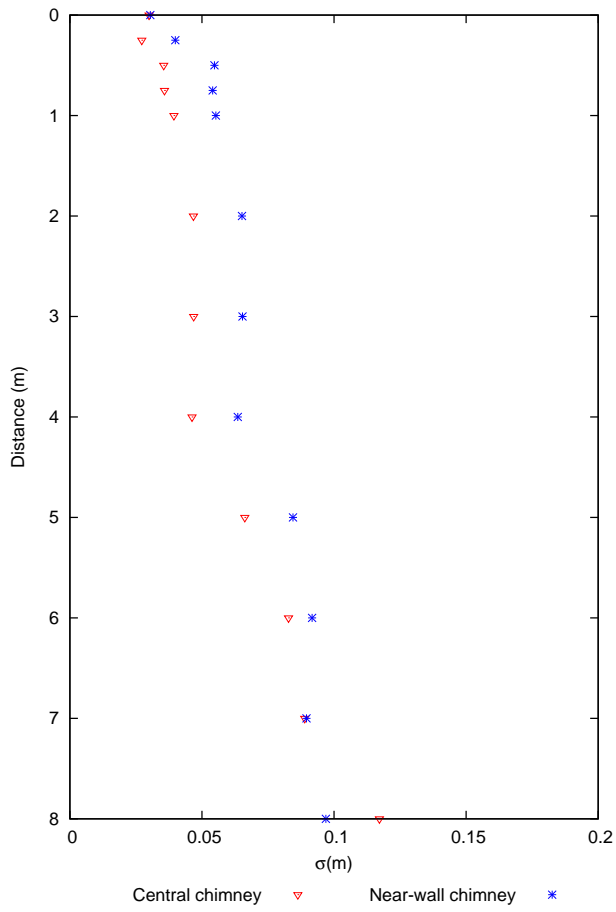
Figure 24: Evolution of the half-width for the near-wall and central chimneys in the plane shown in Figure 14.
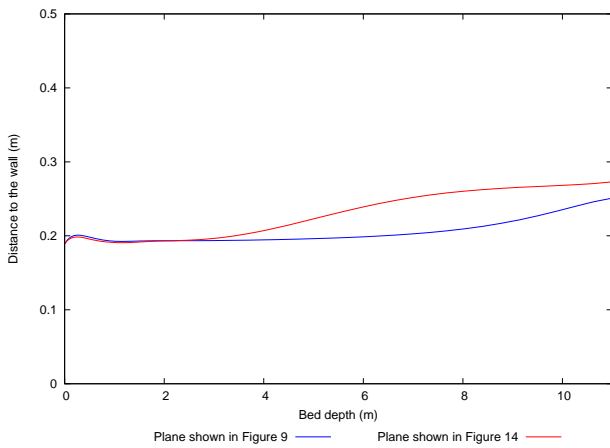
Figure 25: Evolution of the distance between the center of the plume of the nearest-wall chimney and the wall.

REFERENCES

BAKER, T. *et al.* (1935). "The course of liquor flow in packed towers". *Wilmington, Delaware, Meeting*.

CAIRNS, W. (1948). "Liquid distribution characteristics of tower packing materials". *Canadian Chemistry and Process Industries*, 314.

CIHLA, Z. and SCHMIDT, O. (1957). "A study of the flow of liquid when freely trickling over the packing in a cylindrical tower". *Collection Czechoslov. Chem. Commun.*, **22**, 896.

FLUENT (2006). "Fluent 6.3 documentation".

GUNN, D. (1987). "Axial and radial dispersion in fixed beds". *Chemical Engineering Science*, **42**, 363.

HOFTYZER, P. (1964). "Liquid distribution in a column with dumped packing". *Trans. Instn Chem. Engrs*, **42**, T109.

HOLUB, R. *et al.* (1992). "A phenomenological model for pressure drop, liquid holdup, and flow regime transition in gas-liquid trickle flow". *Chemical Engineering Science*, **47**, 2343.

MARCHOT, P. *et al.* (1999). "Investigation of liquid maldistribution in packed columns by x-ray tomography". *Trans IChemE*, **77**, 511.

WANG, Y. *et al.* (1996). "Scale and variance of radial liquid maldistribution in trickle beds". *Chemical Engineering Science*, **53**, 1153.

8th International Conference on CFD in Oil & Gas, Metallurgical and Process Industries
SINTEF/NTNU, Trondheim NORWAY
21-23 June 2011

CFD11-104

COMPARISON BETWEEN DIFFERENT METHODS FOR TURBULENT GAS-LIQUID SYSTEMS BY USING MULTIVARIATE POPULATION BALANCES

Antonio BUFFO[1]*, **Marco VANNI, Daniele L. MARCHISIO, Rodney O. FOX**[2]

[1]DISMIC Politecnico di Torino, Corso Duca degli Abruzzi 24, 10129 Torino, ITALY

[2]Department of Chemical and Biological Engineering, 2114 Sweeney Hall, Iowa State University, Ames, IA 50011-2230, USA

* E-mail: antonio.buffo@polito.it

ABSTRACT

Multidimensional population balance models, formulated in the case of turbulent gas-liquid flow, are very useful tools to describe the interactions between the continuous liquid phase and the gas bubbles, as well as the interactions among different gas bubbles (e.g., coalescence and break-up), both in terms of momentum and mass coupling. Moreover, these models are able to quantify the effects of the interactions on the population of dispersed bubbles and to estimate the distributions of different properties of the bubbles (i.e., velocity, size, temperature, composition), as well as the state of the continuous phase. In this work, two different methods based on moments quadrature (i.e., Direct Quadrature Method of Moments and Conditional Quadrature Method of Moments) for solving the multidimensional Population Balance Equation (PBE) are summarized, compared on several simplified cases. Moreover these models can be easily coupled to a CFD simulation in order to locally consider the poly-dispersity of the dispersed phase. In this paper, only preliminary results for a realistic gas-liquid stirred tank reactor are reported and eventually compared with experimental data from the literature.

Keywords: Multiphase flow, Population balance, Bubble size distribution, Direct Quadrature Method of Moments (DQMOM), Conditional Quadrature Method of Moments (CQMOM), Gas-liquid stirred tank, CFD .

NOMENCLATURE

Greek Symbols

α	Volume fraction.
β	Breakage kernel, $[1/s]$.
γ	Order of generic moment.
ϵ	Dissipation of turbulent kinetic energy, $[m^2/s^3]$.
η	Coalescence efficiency.
μ	Molecular viscosity, $[Pa\,s]$.
μ_{in}	Mean of initial BSD, $[m]$.
ν	Kinematic viscosity, $[m^2/s]$.
ϱ	Mass density, $[kg/m^3]$.
σ	Surface tension, $[N/m]$.
σ_{in}	Standard deviation of initial BSD.
ϕ	Number of moles, $[mol]$.
$\dot\phi$	Rate of mass transfer, $[mol/s]$.
ψ	Chemical concentration, $[mol/m^3]$.
Ω	Phase space.

Latin Symbols

a_i	Source term of DQMOM, $[1/m^3 s]$.
$\mathbf{a}$	Acceleration, $[m/s^2]$.
b_i	Source term of DQMOM, $[m/m^3 s]$.
B	Rate of bubble birth, $[1/m^3 s]$.
c_i	Source term of DQMOM, $[mol/m^3 s]$.
C_D	Drag coefficient.
C_l	Conditional moment of NDF, $[mol^l]$.
$C_{k,l}$	Corrective term of DQMOM, $[m^k mol^l/m^3]$.
d	Diameter, $[m]$.
D	Dispersion coefficient, $[1/s]$.
D	Rate of bubble death, $[1/m^3 s]$.
$\mathcal{D}$	Molecular diffusion, $[m^2/s]$.
g	Gravity, $[m/s^2]$.
G	Rate of Bubble growth, $[m/s]$.
h	Coalescence kernel, $[m^3/s]$.
H	Collisional term of GPBE, $[1/m^3 s]$.
$\mathcal{H}$	Henry constant, $[mol/m^3 atm]$.
k_A	Surface shape factor.
k_L	Mass transfer coefficient, $[m/s]$.
k_V	Volumetric shape factor.
L	Bubble size, $[m]$.
$M_{k,l}$	Generic moment of the NDF, $[m^k mol^l/m^3]$.
$n(L,\phi_b)$	Number Density Function, $[1/m^4 mol]$.
N	Number of quadrature nodes.
p	Pressure, $[Pa]$.
P	Daughter distribution function, $[1/m^3]$.
$\mathbf{u}$	Velocity, $[m/s]$.
u_{gs}	Superficial velocity based on sparger area, $[m/s]$.
t	Time, $[s]$.
w	Number density, $[1/m^3]$.
$\mathbf{x}$	Spatial coordinates.

Sub/superscripts

b	Bubble.
c	Continuous phase.
d	Dispersed phase.
i,j,k,l	Genericic indices.
in	Inlet.
p	Pores.
s	Sparger.
T	Super: Transpose. Sub: Terminal.
$*$	Collisional term.
$^-$	Moment transform.

A. Buffo, M. Vanni, D. L. Marchisio, R. O. Fox

INTRODUCTION

Turbulent gas-liquid systems, such as bubble columns and stirred tank reactors are very common in the process industry. For the design and scale-up of these equipments, many correlations based on experiments have been developed and are currently being used, with the important limitation that their validity is guaranteed only in specific vessel geometries and operating conditions close to those experimented. Moreover this approach considers only volume-averaged properties, neglecting the significant spatial inhomogeneities that characterize the behavior of the industrial scale reactors. Computational Fluid Dynamics (CFD) offers the possibility to overcome these issues and correctly simulate the behavior of large scale reactors. Nevertheless, some limitations need to be properly addressed.

The description of reacting turbulent gas-liquid systems has been historically carried out with the implicit assumption that the evolution of the disperse phase (i.e., gas bubbles) is completely separated from the fluid dynamics and phase-coupling issues, considering a non-physical population of bubbles with a monodisperse and constant distribution of size, velocity and composition (as in the mixture and multi-fluid model). However, in realistic systems, the gas phase is polydispersed, namely it is constituted by bubbles characterized by a distribution of properties; the phase coupling and the mass transfer rates can be successfully described only if the existence of these distributions is accounted for, by considering a Multidimensional Population Balance Equation that correctly treats the interactions between continuous liquid phase and the disperse gas bubbles, as well as all the other possible interactions (such as bubble coalescence and breakage).

A very promising approach for solving this equation is represented by quadrature-based moments methods due to their low computational demands. In these methods the evolution of the relevant properties are recovered by considering some lower-order moments of the distribution. In this work, two different approaches are considered: the Conditional Quadrature Method of Moments (CQMOM) calculates the evolution of some moments and recovers weights and nodes of quadrature approximation by using specific inversion procedure (Cheng et al., 2010; Cheng and Fox, 2010); the Direct Quadrature Method of Moments (DQMOM) directly calculates the evolution of weights and nodes of the quadrature approximation by tracking some specific moments of the distribution (Marchisio and Fox, 2005).

The remainder of the paper is the following. First the governing equations are presented, showing the differences between DQMOM and CQMOM. Then the test cases and the numerical details are introduced and eventually simulation results and comparison with experimental data are discussed.

MODEL DESCRIPTION

A population constituted by a number of dispersed bubbles in a turbulent liquid, each one characterized by a different property such as size L and chemical composition $\boldsymbol{\phi}_b$ (internal coordinates) can be modeled by using a smooth and differentiable Number Density Function (NDF)(Fox, 2007). The NDF is defined so that the following quantity

$$n(L, \boldsymbol{\phi}_b; \mathbf{x}, t) \, dL \, d\boldsymbol{\phi}_b \, d\mathbf{x} \qquad (1)$$

represents the expected number of bubbles in the infinitesimal volume $d\mathbf{x} = dx_1 \, dx_2 \, dx_3$ around the physical point $\mathbf{x} = (x_1, x_2, x_3)$, with bubble size in the infinitesimal range between L and $L + dL$ and composition between $\boldsymbol{\phi}_b$ and $\boldsymbol{\phi}_b + d\boldsymbol{\phi}_b$ at the instant t. Although there is no limitation on the number of internal coordinates (other properties of the population, for example the velocity components of bubbles or the temperature, could be easily taken into account), in this work, only size and composition are considered. We assumed that the system was isothermal, with low gas hold-up, where the effects of bubble collision, coalescence and breakage on momentum exchange could be neglected.

The continuity statement of the NDF is the well-known Generalized Population Balance Equation (GPBE)(for an exhaustive dissertation, see Ramkrishna, 2000; Marchisio, 2007):

$$\frac{\partial n}{\partial t} + \frac{\partial}{\partial \mathbf{x}} \cdot (n \mathbf{u}_b) + \frac{\partial}{\partial L} \cdot (n G) + \frac{\partial}{\partial \boldsymbol{\phi}_b} \cdot \left(n \dot{\boldsymbol{\phi}}_b \right) = H(L, \boldsymbol{\phi}_b; \mathbf{x}, t),$$
$$(2)$$

where $\mathbf{u}_b$ is the bubble velocity, G is the rate of continuous change of bubble size usually related to molecular processes, due to the addition (or depletion) of single molecules (e.g., evaporation, condensation or expansion due to pressure changes), $\dot{\boldsymbol{\phi}}_b$ is the continuous rate of change of bubble composition (with respect to the different chemical components) as a result of chemical reactions and/or mass transfer between phases. The term on the right-hand side of the Eq. (2) is the discontinuous event term, accounting in this case for instantaneous changes of size and composition due to bubble collisions, coalescence and breakage. For this specific problem, the collisional term can be written in the following form (Marchisio et al., 2003b):

$$H(L, \boldsymbol{\phi}_b) = B(L, \boldsymbol{\phi}_b) - D(L, \boldsymbol{\phi}_b), \qquad (3)$$

where $B(L, \boldsymbol{\phi}_b)$ and $D(L, \boldsymbol{\phi}_b)$ are respectively the rates of birth and death of bubbles due to collisions, coalescence and breakage. Obviously, the dimension of the vector $\boldsymbol{\phi}_b$ depends on the number of chemical components considered; in this work only two components are considered (i.e., oxygen and nitrogen) with only one active chemical component (i.e., oxygen) transferring between phases. The composition is therefore represented by a scalar ϕ_b, namely the number of moles of oxygen within one single bubble.

The problem is here solved in terms of the moments of the NDF, that can be written as follows:

$$M_{k,l} = \int_{\Omega_L} \int_{\Omega_{\phi_b}} n(L, \phi_b) L^k \phi_b^l \, dL \, d\phi_b,$$

where Ω_L and Ω_{ϕ_b} are the phase spaces of all the possible values of the internal coordinates. It is interesting to remind that some lower-order moments have important physical meaning: in fact, $M_{0,0}$ is the total number of bubbles per unit volume, $M_{1,0}$ the total bubble length per unit volume, $M_{0,1}$ the total oxygen moles in the bubbles per unit volume, $M_{2,0}$ is related to the total surface area per unit volume through the shape factor, k_A, whereas $M_{3,0}$ is proportional to the total bubble volume fraction through the volumetric shape factor, k_V (for spherical bubbles $k_A = \pi$ and $k_V = \pi/6$). By applying the moment transform to Eq. (2), the transport equation for a generic moment of the NDF can be obtained (for a detailed derivation see Marchisio et al., 2003a). All the methods that solve the GPBE through the moments are called Methods of Moments (MOM). The so-called "closure problem" arising from this approach can be overcome by assuming a functional form of the NDF. As it will become clearer below,

from this choice the two different methods adopted in this work follow.

A simple form for the NDF can be a summation of delta functions centered on the nodes of a quadrature approximation:

$$n(L, \phi_b) = \sum_{i=1}^{N} w_i \delta(L - L_i) \delta(\phi_b - \phi_{b;i}), \qquad (4)$$

where w_i represent the quadrature weight, namely the number density (i.e., number of bubbles per unit of total volume) of the bubbles with size equal to L_i and with composition equal to $\phi_{b;i}$. Each delta function is characterized by a different index i and it can be thought of as a group of bubbles having the same size and composition, each group representing one of N nodes of the quadrature approximation.
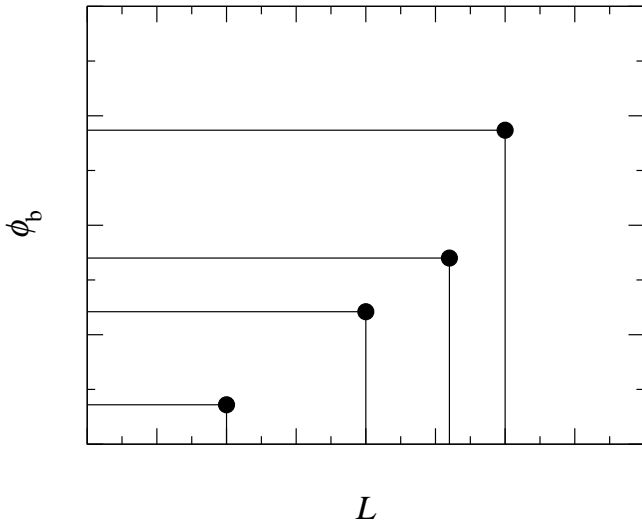

Figure 1: Representation of the "summation of delta" functional form of NDF in DQMOM, in the plane of the two internal coordinates, with $N = 4$.

Starting from this form of the NDF, numerous methods for the solution of the multivariate GPBE have been derived, such as the Direct Quadrature Method of Moments (Marchisio and Fox, 2005), Brute-Force method (Wright *et al.*, 2001) and Tensor-Product method (Yoon and McGraw, 2004a,b; Fox, 2009a), and the Conditional Quadrature Method of Moments (CQMOM) (Cheng *et al.*, 2010; Cheng and Fox, 2010). In this work, only DQMOM and CQMOM, are considered and treated in the following sections.

Direct Quadrature Method of Moments

By using DQMOM, weights and nodes of the quadrature approximation are calculated directly in every point of the computational domain, without recurring to any inversion algorithm. In fact, the set of governing equations can be recovered by substituting Eq. (4) into Eq. (2) and then applying the moment transform, resulting in:

$$\frac{\partial}{\partial t}(w_i) + \frac{\partial}{\partial \mathbf{x}} \cdot (w_i \mathbf{u}_{b,i}) = a_i, \qquad (5)$$

$$\frac{\partial}{\partial t}(w_i L_i) + \frac{\partial}{\partial \mathbf{x}} \cdot (w_i \mathbf{u}_{b,i} L_i) = b_i = b_i^* + w_i G(L_i, \phi_{b;i}), \qquad (6)$$

$$\frac{\partial}{\partial t}(w_i \phi_{b,i}) + \frac{\partial}{\partial \mathbf{x}} \cdot (w_i \mathbf{u}_{b,i} \phi_{b;i}) = c_i = c_i^* + w_i \dot{\phi}_b(L_i, \phi_{b;i}), \qquad (7)$$

with $i = 1, ..., N$. The total number of nodes of the quadrature determines the error of the approximation: by increasing the number of nodes, the accuracy of the approximation, used to overcome the closure problem, improves, resulting in more detailed reconstructions of the NDF, but with higher computational costs. The right-hand side of the Eqs. (5-7) (i.e., a_i, b_i^* and c_i^*) are calculated by tracking some specific moments of the NDF, and solving the linear system generated by the following equation:

$$\sum_{i=1}^{N} \left[(1 - k - l) L_i^k \phi_{b;i}^l a_i + k L_i^{(k-1)} \phi_{b;i}^l b_i^* + l L_i^k \phi_{b;i}^{(l-1)} c_i^* \right] = \bar{H}_{k,l}^{(N)}. \qquad (8)$$

where different $k = k_j$ and $l = l_j$ values (with $j = 1, \ldots, 3N$) are considered and where $\bar{H}_{k,l}^{(N)}$ represents the source term of the transport equation for the generic moment of the NDF (i.e., moment transform of right hand side of the Eq. (2). In a contract form, it is possible to write:

$$\mathbf{As} = \mathbf{d}, \qquad (9)$$

where

$$\mathbf{s} = [a_1, \ldots, a_N, b_1^*, \ldots, b_N^*, c_1^*, \ldots, c_N^*]^{\mathrm{T}}$$

and

$$\mathbf{d} = [\bar{H}_{k_1,l_1}, \bar{H}_{k_2,l_2}, \ldots, \bar{H}_{k_{3N},l_{3N}}]^{\mathrm{T}}.$$

The $3N$ pairs of indices (k_j, l_j) represent the $3N$ moments whose evolution is tracked with the quadrature. For example for $N = 2$, six moments have to be tracked and $(k, l) = (0, 0; 1, 0; 0, 1; 1, 1; 2, 0; 0, 2)$ is the easiest choice. The expression of the matrix $\mathbf{A}$ in Eq. (9) depends on the set of moments that one chooses to track. The choice of these moments is completely arbitrary, and an optimal selection is not trivial. As discussed in Fox (2009b), it is important to use six moments that results in a full rank matrix $\mathbf{A}$, for all possible N distinct and non-degenerate nodes (i.e., L_i and $\phi_{b;i}$) and the nodes should include all linear independent moments of a particular order $\gamma = k + l$, before including moments of higher order.

These criteria always permit the solution of Eq. (9), but this is not the only possible strategy. Another possibility can be tracking only pure moments of the multidimensional NDF with respect of size and composition (Buffo *et al.*, 2010), decoupling the evolution of the multi-variate distribution by using lower-order moments of the equivalent mono-variate distributions. In this work, in order to allow the comparison of DQMOM and CQMOM, the strategy behind the choice of moments is left to CQMOM, which, as explained in the following section, automatically defines the moment set.

Conditional Quadrature Method of Moments

This method is an extension of the Quadrature Method of Moments (QMOM), specifically designed for univariate problems (McGraw, 1997), to multivariate problems. As in QMOM, transport equations for a set of moments of the NDF are solved in the computational domain. As in DQMOM the closure problem is overcome by using a quadrature approximation and a proper inversion algorithm is needed. In univariate cases, weight and nodes of the quadrature approximation can be calculated by using the Product-Difference (PD) or Wheeler algorithms (Gordon, 1968; Wheeler, 1974); for multivariate cases, CQMOM uses a particular procedure

to calculate the weight and nodes of the quadrature approximation. This inversion procedure can be easily understood by rewriting the functional assumption for the NDF based on the quadrature approximation as follows:

$$n(L, \phi_b) = \sum_{i=1}^{N_1} w_i \delta(L - L_i) \sum_{j=1}^{N_2} w_{i,j} \delta(\phi_b - \phi_{b;i,j}), \qquad (10)$$

where w_i is the number density on the direction of the sizes, while the numerical fraction $w_{i,j}$ and the compositions $\phi_{b;i,j}$ are "conditioned" on the value of the first internal coordinate L_i with number density w_i. It should be noticed that Eqs. (4) and (10) can be written in a consistent way with a proper change of indices. The total number of nodes N, is now written as $N_1 \cdot N_2$, where N_1 represents the nodes used for bubble size and N_2 represents the nodes used for bubble composition. In other words, each one of the N_1 groups of bubbles characterized by a size L_i is subdivided into N_2 groups of bubbles characterized by different compositions $\phi_{b,ij}$. It is interesting to notice that, in this case, a preliminary choice related to the order of the internal coordinates has to be made; this decision is not trivial and depends on the particular problem under study. This aspect is currently under investigation and will be addressed in further work. The graphical representations of the two functional assumptions in DQMOM and CQMOM are reported in Fig. 1 and 2, respectively. The differences between the two functional forms are evident, and it is also equally clear that the two expressions can be perfectly equivalent in the case of $N_2 = 1$ and $N_1 = N$.
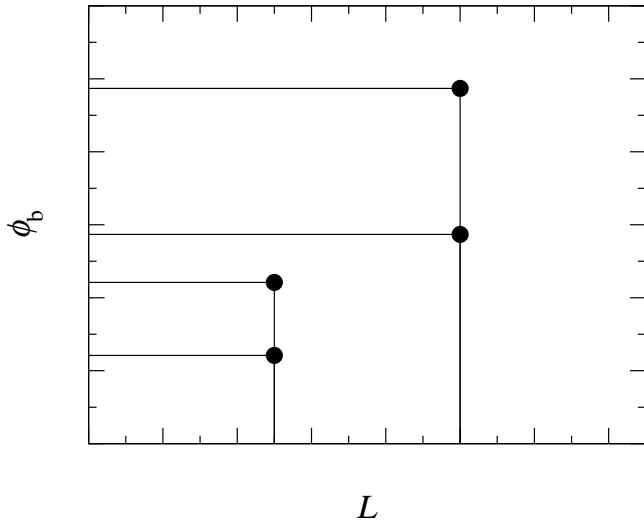
Figure 2: Representation of the "conditional" functional form of NDF in CQMOM, in the plane of the two internal coordinates, with $N_1 = 2$ and $N_2 = 2$

The inversion algorithm used in CQMOM is explained. The construction of the multidimensional distribution starts with the calculation of the univariate quadrature of order N_1 for the first internal coordinate by using the PD or Wheeler algorithms for the first $2N_1$ moments of the distribution. In this case, this statement means that $2N_1$ pure moments with respect to the size are transported and used to recover the

quadrature approximation in the following way:

$$
\begin{matrix}
M_{0,0} \\
M_{1,0} \\
\vdots \\
M_{2N_1-2,0} \\
M_{2N_1-1,0}
\end{matrix}
\rightarrow \text{PD/Wheeler} \rightarrow
\begin{matrix}
w_1 & L_1 \\
w_2 & L_2 \\
\vdots & \vdots \\
w_{N_1-1} & L_{N_1-1} \\
w_{N_1} & L_{N_1}
\end{matrix}. \qquad (11)
$$

Then, by recurring to the definition of the conditional density function, it is possible to write:

$$n(L, \phi_b) = n(L) n(\phi_b | L), \qquad (12)$$

where $n(L|\phi_b)$ is the probability of having ϕ_b in an infinitesimal limit when L is fixed and equal to a certain value. Recurring to the definition of the generic moment of order k and l and by using the Eq. (12), it follows that:

$$M_{k,l} = \int_{\Omega_L} n(L) L^k \int_{\Omega_{\phi_b}} n(\phi_b|L) \phi_b^l \, dL \, d\phi_b. \qquad (13)$$

By applying the quadrature approximation for the first part of this double integral, Eq. (13) becomes:

$$M_{k,l} = \sum_{i=1}^{N_1} w_i L_i^k C_l(L_i), \qquad (14)$$

where

$$C_l(L_i) = \int_{\Omega_{\phi_b}} n(\phi_b|L_i) \phi_b^l \, d\phi_b, \qquad (15)$$

represents the conditional moment of order l with respect to bubble composition, "conditioned" on the value of the first internal coordinate L_i. The conditional moments can be used to calculate the conditional weights $w_{i,j}$ and conditional abscissas $\phi_{b;i,j}$ of Eq. (10), by using the PD or Wheeler algorithms:

$$
\begin{matrix}
1 \\
C_1(L_i) \\
\vdots \\
C_{2N_2-2}(L_i) \\
C_{2N_2-1}(L_i)
\end{matrix}
\rightarrow \text{PD/Wheeler} \rightarrow
\begin{matrix}
w_{i,1} & \phi_{b;i,1} \\
w_{i,2} & \phi_{b;i,2} \\
\vdots & \vdots \\
w_{i,N_2-1} & \phi_{b;i,N_2-1} \\
w_{i,N_2} & \phi_{b;i,N_2}
\end{matrix}, \qquad (16)
$$

with $i = 1, 2, ..., N_1$. It is clear that the first $2N_2$ conditional moments are necessary to calculate N_1 quadratures, for each of the N_1 nodes previously calculated. These conditional moments can be obtained by using the Eq. (14), resulting in the following linear system of rank N_1:

$$
\mathbf{KG}
\begin{pmatrix}
C_l(L_1) \\
C_l(L_2) \\
\vdots \\
C_l(L_{N_1-1}) \\
C_l(L_{N_1})
\end{pmatrix}
=
\begin{pmatrix}
M_{0,l} \\
M_{1,l} \\
\vdots \\
M_{N_1-1,l} \\
M_{N_1,l}
\end{pmatrix}, \qquad (17)
$$

where the coefficient matrices are defined as follows:

$$
\mathbf{K} =
\begin{pmatrix}
1 & \cdots & 1 \\
L_1 & \cdots & L_{N_1} \\
\vdots & \ddots & \vdots \\
L_1^{N_1-1} & \cdots & L_{N_1}^{N_1-1}
\end{pmatrix}, \qquad (18)
$$

and

$$
\mathbf{G} =
\begin{pmatrix}
w_1 & & \\
& \ddots & \\
& & w_{N_1}
\end{pmatrix}, \qquad (19)
$$

with $l = 1, 2, ..., 2N_2 - 1$. Equation (17) constitutes a Vandermonde linear system, and it can be efficiently solved by using the algorithm proposed by Rybicki (Press *et al.*, 1992). It is trivial to show that Eq. (17) cannot lead to a singular system if the L_i nodes are distinct.

The total number of moments to transport depends on the number of nodes N_1 for the first internal coordinate (in this case, bubble size) and on the number of conditional nodes N_2 of the second internal coordinate (in this case, bubble composition). Firstly, the first $2N_1$ pure moments with increasing order with respect to size are necessary to calculate the quadrature in the first internal coordinate, then $2N_1(2N_2 - 1)$ moments in the order indicated in Eq. (17) must be used to evaluate all the conditional moment useful to calculate the N_1N_2 conditional weights and abscissas in the second internal coordinate. For this reason, the choice of the set of transported moments is fixed a priori and determined by the desired accuracy for the quadrature approximation.

Population Balance Modeling and CFD coupling

It is now necessary to define the different terms of the model in order to solve Eq. (2) by using DQMOM and CQMOM. The expression of the collisional term appearing in Eq. (3) derives from the theory of coalescence and breakage problems (Marchisio *et al.*, 2003b) and for the sake of brevity will not be discussed in details here. The final form of the source term of the generic moment, required by both methods used, is reported here for DQMOM:

$$\bar{H}_{k,l}^{(N)} = \frac{1}{2} \sum_{i=1}^{N} \sum_{j=1}^{N} w_i w_j h_{i,j} \left[(L_i^3 + L_j^3)^{k/3} (\phi_{b;i} + \phi_{b;j})^l \right.$$

$$\left. - L_i^k \phi_{b;i}^l - L_j^k \phi_{b;j}^l \right] + \sum_{i=1}^{N} w_i \beta_i [\bar{P}_{k,l}^{(i)} - L_i^k \phi_{b;i}^l], \qquad (20)$$

and for CQMOM:

$$\bar{H}_{k,l}^{(N)} = \frac{1}{2} \sum_{i=1}^{N_1} \sum_{p=1}^{N_2} \sum_{j=1}^{N_1} \sum_{q=1}^{N_2} w_i w_j w_{ip} w_{jq} h_{i,j} \left[(L_i^3 + L_j^3)^{k/3} \right.$$

$$\left. (\phi_{b;i,p} + \phi_{b;j,q})^l - L_i^k \phi_{b;i,p}^l - L_j^k \phi_{b;j,q}^l \right]$$

$$+ \sum_{i=1}^{N_1} \sum_{p=1}^{N_2} w_i w_{ip} \beta_i [\bar{P}_{k,l}^{(i)} - L_i^k \phi_{b;i,p}^l], \qquad (21)$$

where $h_{i,j} = h(L_i, L_j)$ is the coalescence kernel, $\beta_i = \beta(L_i)$ is the breakage kernel and $\bar{P}_{k,l}^{(i)}$ is the generic moment of the daughter distribution function.

Many models are available in literature to relate kernels and daughter distributions to local physical and fluid dynamic properties, as extensively reviewed by Laakkonen *et al.* (2007). Our work is based on the conclusions of Petitti *et al.* (2010). The range of validity of the kernels employed here corresponds to the experimentally investigated operating conditions (Laakkonen *et al.*, 2006). As a first approximation, coalescence and breakage kernels are assumed to depend only on bubble size; however, bubble composition dependencies can be accounted for in a second time. Different kernels are studied: for model verification a constant breakage kernel is employed, whereas for simulations under realistic conditions the following kernel expression is used:

$$\beta(L) = 6.0 \, \epsilon^{1/3} \text{erfc} \left(\sqrt{0.04 \frac{\sigma}{\varrho_c \epsilon^{2/3} L^{5/3}} + 0.01 \frac{\mu_c}{\sqrt{\varrho_c \varrho_b} \epsilon^{1/3} L^{4/3}}} \right). \qquad (22)$$

The fragmentation of bubbles is modeled by means of a daughter distribution function. Different functional forms can be used in this context for representing symmetric breakage, erosion and other mechanism. The daughter distribution function used here is a $\beta-$Probability Density Function, that assuming binary breakage reads as follows:

$$P(L, \phi_b | \lambda, \phi_{b,\lambda}) = 180 \frac{L^2}{\lambda^3} \left(\frac{L^3}{\lambda^3} \right)^2 \left(1 - \frac{L^3}{\lambda^3} \right)^2 \delta \left(\phi_b - \frac{L^3}{\lambda^3} \phi_{b,\lambda} \right), \qquad (23)$$

where λ and $\phi_{b,\lambda}$ represents the properties of the parent bubble, while L and ϕ_b the properties of the daughter bubble. By applying the moment transform, it is possible to write:

$$\bar{P}_{k,l}^{(i)} = 3240 \frac{L_i^k \phi_{b;i}^l}{(3l + k + 9)(3l + k + 12)(3l + k + 15)}. \qquad (24)$$

As far as coalescence of bubbles is concerned, both a constant kernel and the following kernel, are used here:

$$h(\lambda, L) = 0.88 \, \epsilon^{1/3} (\lambda + L)^2 (\lambda^{2/3} + L^{2/3})^{1/2} \eta(\lambda, L), \qquad (25)$$

where the coalescence efficiency $\eta(\lambda, L)$ is written as follows:

$$\eta(\lambda, L) = \exp \left(-6 \cdot 10^9 \frac{\mu_c \varrho_c \epsilon}{\sigma^2} \left(\frac{\lambda L}{\lambda + L} \right)^4 \right). \qquad (26)$$

A proper functional form for G_i and $\dot{\phi}_{b;i}$, taking into account the mass transfer must be introduced. Since only mass transfer of a single component is considered, the continuous rate of change of bubble composition can be written as:

$$\dot{\phi}_{bi} = \frac{6k_L}{L_i} \left(\psi_c - \mathcal{H} \frac{\phi_{b;i}}{k_V L_i^3} \right), \qquad (27)$$

where k_L is the mass transfer coefficient, $\phi_{b,i}$ is the number of moles of oxygen within the ith gas bubble node, ψ_c is the concentration of oxygen in the continuous liquid phase.

Mass transfer affects also the size of the bubbles through the bubble growth rate and with a simple mass balance on a single bubble the following expression is obtained:

$$G_i = \frac{2k_L M_w}{\varrho_b} \left(\psi_c - \mathcal{H} \frac{\phi_{b;i}}{k_V L_i^3} \right). \qquad (28)$$

Many correlations are available in the literature in order to estimate the mass transfer coefficient k_L. A complete review about this topic can be found in Gimbun *et al.* (2009) and it is out of the scope of this discussion. In this work, the approach of Lamont and Scott (1970), based on the local value of the turbulent dissipation rate was used:

$$k_L = 0.4 \mathcal{D}^{0,5} \left(\frac{\epsilon}{\nu_c} \right)^{0,25}. \qquad (29)$$

The forces acting on a single bubble must be accounted for calculating the bubble velocity, $\mathbf{u}_b$. This is done in this work by coupling DQMOM and CQMOM with the multi-fluid model. The force per unit volume acting on the bubbles is calculated in this work as follows:

$$\varrho_b \mathbf{a}_{b,i} = -\frac{\partial p}{\partial \mathbf{x}} + \varrho_b \mathbf{g} + \frac{3}{4} \frac{\alpha_c C_{D,i} \varrho_c}{L_i} \|\mathbf{u}_c - \mathbf{u}_{b,i}\| (\mathbf{u}_c - \mathbf{u}_{b,i}), \quad (30)$$

where $\mathbf{a}_b, i$ is the acceleration acting on the bubbles, α_c is the liquid volume fraction and $(\mathbf{u}_c - \mathbf{u}_{b,i})$ is the slip velocity,

namely the velocity difference between the continuous phase and the bubbles and $C_{D,i} = C_D(L_i)$ is the drag coefficient, calculated by using the formulation of Haberman and Morton (1956) for a rising bubble with terminal velocity $\mathbf{u}_T$ in stagnant liquid. The approach used in this work to evaluate the terminal velocity, considering the effect of the other bubbles and the effect of the turbulence, is described in the work of Petitti *et al.* (2010).

All the transport equations constituting both methods are closed and through their solution it is possible to predict the evolution of this poly-disperse gas-liquid system. As far as coupling with the multi-fluid model is concerned (within CFD codes), additional comments are required. Regarding DQMOM, it is necessary to rewrite governing equations in terms of volume fractions by using the following relationship:

$$\alpha_i = w_i k_V L_i^3, \tag{31}$$

as in the work of Fan *et al.* (2004). From this point of view, DQMOM can be seen as an extension of the multi-fluid model that it takes into account the poly-dispersity of some properties of the population of bubbles, by introducing some additional scalars, with their source terms, in the CFD solver. For CQMOM, instead, it is possible to follow the approach of Petitti *et al.* (2010) in the univariate case, where the calculated moments of the distribution are considered like scalars moving with the same velocity of the dispersed bubbly phase.

TEST CASES AND NUMERICAL DETAILS

In this work various simulations for different purposes were carried out. For the sake of model verification, some preliminary simulations were performed under the hypothesis of perfect mixing for the liquid phase and of perfect mixing for the gas phase, in a homogeneous system composed by water (continuous phase) and air (disperse phase). The physical properties used in all the simulations are reported in Tab. 1. The two methods (i.e., DQMOM and CQMOM) are verified by implementing and solving the governing equations for a quadrature approximation with two, three and four nodes ($N = 2, 3, 4$). In this work, in order to make comparable DQMOM and CQMOM, only the case of $N_2 = 1$ is considered. The interesting case of $N_2 > 1$ is currently under verification and will be treated in future works. Equations were solved in Octave. When perfect mixing for both phases occurs, all spatial derivatives are neglected and the governing equations can be reduced to a system of ordinary differential equations (ODEs), integrated using the standard solver `lsode` (Hindmarsh, 1983). Different tests were conducted, using both constant and realistic kernels for coalescence and breakage. Finally mass transfer is also considered and monitored by tracking the concentration of oxygen in the continuous liquid phase.

Then a flowing gas phase in a stagnant liquid phase under the hypothesis of perfect mixing was considered. This type of simulation represents the case of a CSTR, where the gas phase enters and exits from the domain, subject to coalescence, breakage and mass transfer, while the oxygen in the liquid phase reaches the equilibrium. Even in this case, the spatial derivatives disappear and a system of ODEs is solved, but some issues may arise due to the intrinsic inhomogeneity of the problem.

As it has been said before, preliminary CFD simulations of the realistic gas-liquid system were also carried. The configuration studied in this work was investigated from the experimental and modeling point of view by Laakkonen *et al.*

Table 1: Summary of gas and liquid properties used.

ϱ_c	998.2	kg/m^3
ϱ_d	1.255	kg/m^3
ϵ	$4.824 \cdot 10^{-2}$	m^2/s^3
μ_c	$1.0 \cdot 10^{-3}$	$Pa\,s$
μ_d	$1.78 \cdot 10^{-5}$	$Pa\,s$
σ	0.07	N/m
$\mathcal{D}$	$1.970 \cdot 10^{-9}$	m^2/s
$\mathcal{H}$	$1.303 \cdot 10^{-3}$	$kmol/m^3\,atm$

(2006), where detailed local measurements of Bubble Size Distribution (BSD) in different points of the reactor and mass transfer rates for air-water system were collected. This reactor is a 194 liter tank with four baffles (with a particular configuration with upper extensions), agitated by a standard six-blade Rushton turbine with a circular metal porous sparger with external diameter of 3.3 cm and pores with an average diameter of 15 μm, situated about at 10.5 cm under the impeller. The vessel dimensions and the position of the measurement points are reported in Fig. 3.
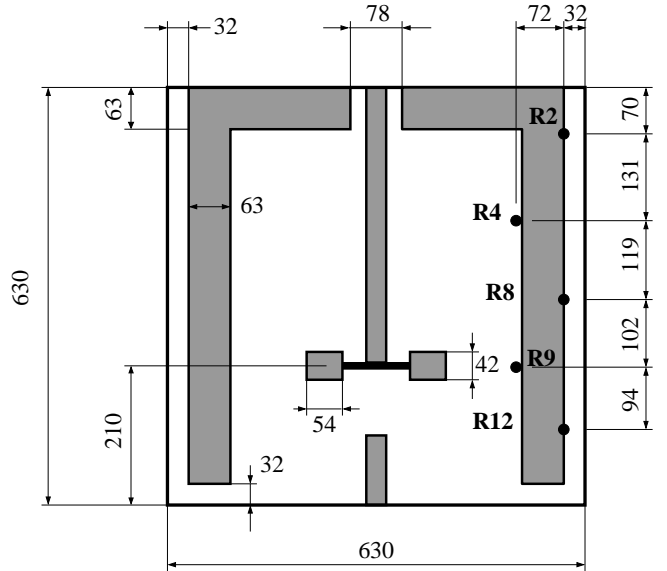
Figure 3: Representation of the simulated stirred tank and location of the sample points in which BSD data were measured (Units in mm).

Steady state CFD simulations were carried out recurring to the commercial code FLUENT 12. In this first part of the work, DQMOM equations and the drag force formulation based on bubble terminal velocity are implemented through User-Defined Functions and Subroutines and by solving additional equations for User-Defined Scalars. The motion of the Rushton turbine was modeled by using the Multiple Reference Frame (MFR) approach, in order to reduce the computational time requested for each simulation. Thanks to geometrical symmetry and periodicity only half of the stirred tank was considered. The predicted BSDs were compared with the experimental data for the different measurement points and for a wide range of operating conditions. The air flow rate ranged from 0.018 to 0.093 volumes of gas per volume of reactor per minute (vvm) and the stirring rate ranged between 155 and 250 rpm, with global hold-up values up to 1.5 %.

Let us discuss with more details the case of DQMOM with two nodes. The entire multiphase system is subdivided into one continuous liquid phase (water) and two dispersed gaseous phases (air) whose volume fractions, characteristic composition and sizes are calculated by solving the appropriate transport equations. At the wall of the domain, non-slip boundary conditions are assumed for all phases. The gas enters into the system through the porous sparger, modeled as a velocity inlet ($u_{in} = 9.94$ *m/s*) for the two gas phases; the overall gas volume fraction was calculated recurring to the relative gassing rate. The liquid velocity components on the gas sparger were assumed equal to zero. The upper surface of the vessel was modeled as a pressure outlet; by resorting to this particular condition all the gas bubbles could exit from the system and, in the case of a backflow, the flow that enters into the surface and it is composed only by the liquid phase.

As far as the initial and boundary conditions for the Population Balance Model (PBM) are concerned, experimental studies of bubble formation at metal porous spargers conducted on water-air systems show that the BSD above the sparger can be assumed as a log-normal distribution with a standard deviation σ_{in} equal to 0.15, with a mean Sauter bubble size ($d_{32,in}$, namely the ratio between the moment of order three and the moment order two with respect to the bubble size), calculated by the following expression (Kazakis *et al.*, 2008):

$$d_{32,in} = 7.35 \left[\text{We}^{-1.7} \text{Re}^{0.1} \text{Fr}^{1.8} \left(\frac{d_p}{d_s} \right)^{1.7} \right]^{1/5}, \qquad (32)$$

where the numbers of Froude (Fr), Weber (We), Reynolds (Re) are written in the following way:

$$\text{Fr} = \frac{u_{gs}}{d_s \, g}, \qquad (33)$$

$$\text{We} = \frac{\varrho_c u_{gs}^2 d_s}{\sigma}, \qquad (34)$$

$$\text{Re} = \frac{\varrho_c u_{gs} d_s}{\mu_c}, \qquad (35)$$

and where u_{gs} is the superficial velocity based on sparger area. By assuming a log-normal shape for the initial/inlet BSD, with the knowledge of the Sauter diameter, it is possible to calculate the mean and the generic moments of the univariate distribution with respect to the bubble size. Moreover, at the beginning of the simulation, it is reasonable to assume that all the bubble have the same concentration of oxygen, equal to $\psi_{b,in} = 8.56$ *mol/m³* (corresponding to the oxygen concentration in air at 25 °C and 1 atm), obtaining in this way the expression for a generic moment of the NDF:

$$M_{k,l} = (k_v \psi_{b,in})^l M_{0,0} \exp\left((k+3l)\mu_{in} + 0.5(k+3l)^2 \sigma_{in}^2\right). \quad (36)$$

The inlet values of weights and nodes of the quadrature approximation for DQMOM simulations can be calculated with the CQMOM inversion algorithm, imposing in this case with $N_1 = 2$ and $N_2 = 1$. Thanks to this procedure the inlet volume fractions for the two different bubble classes (α_1, α_2), their characteristic sizes (L_1, L_2) and their compositions ($\phi_{b,1}$, $\phi_{b,2}$) are used in the predictions of the simplified system or prescribed at the inlet surface of the sparger in the CFD simulations.

RESULTS AND DISCUSSION

Simplified test cases

The numerous tests conducted in this part of the work aim at verifying the two approaches (i.e., DQMOM and CQMOM) and at establishing the equivalence between them. In Fig. 4
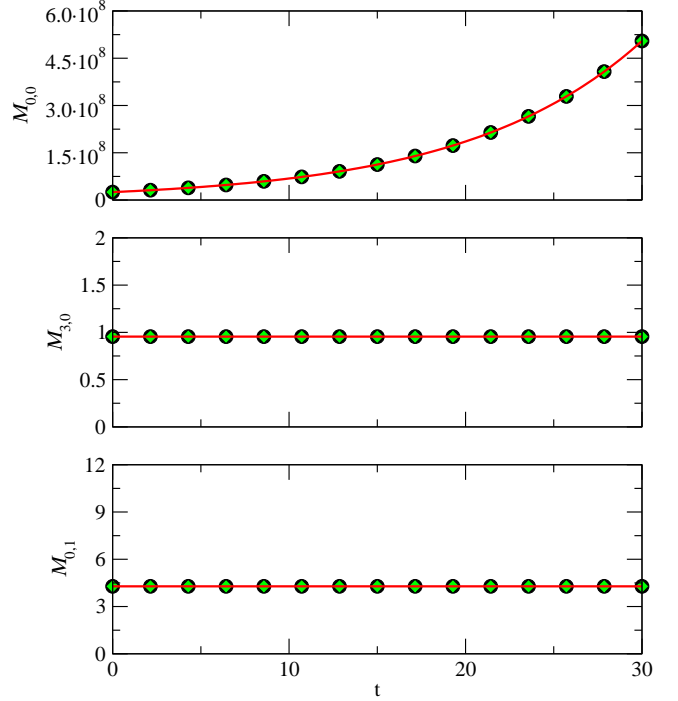

Figure 4: Evolution in time (s) of some moments of the NDF in the case of pure breakage. Red line: analytical solution. Black circles: DQMOM solution. Green diamonds: CQMOM solution.
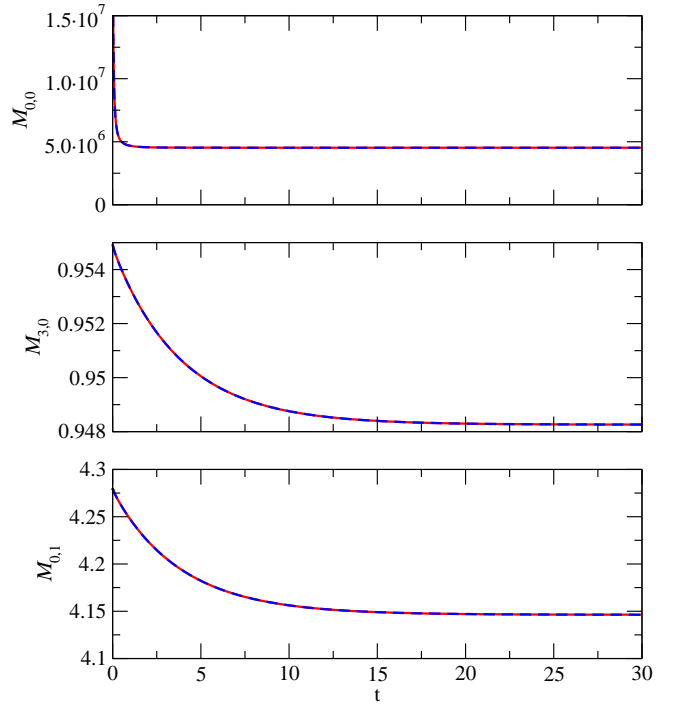

Figure 5: Evolution in time (s) of some moments of the NDF in the case of realistic coalescence, breakage and mass transfer. Red line: DQMOM. Dotted blue line: CQMOM. Two lines are perfectly overlapping.

the evolution in time of some specific moments of the NDF, in the case of pure breakage with constant kernel and no mass transfer for the simple zero-dimensional closed system are reported and compared with the available analytical solutions.

The number of nodes considered in this case for the quadrature approximation is $N = 2$ for DQMOM and $N_1 = 2$, $N_2 = 1$ for CQMOM. As it is possible to see, both methods show perfect agreement with the analytical solutions and all the moments tracked behave as expected: $M_{0,0}$ increase in time due to breakage of bubbles, whereas $M_{3,0}$ and $M_{0,1}$ remain constant because pure breakage does not modify the total volume fraction of gas and the total number of oxygen moles in the gas phase. Several tests were also conducted with increasing number of nodes, obtaining the same results seen in Fig. 4. Some simulations with realistic kernels with mass transfer were also performed in the zero-dimensional closed system.
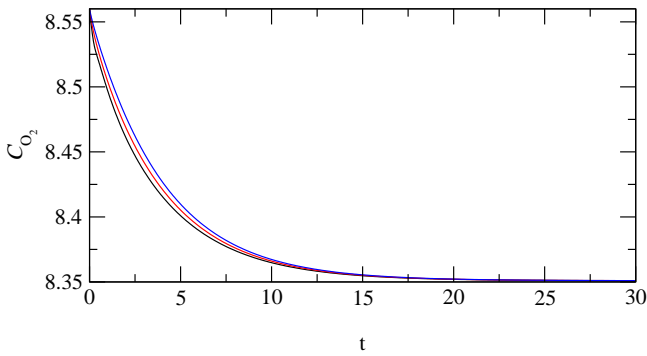

Figure 6: Evolution in time (s) of concentration of oxygen in the different group of bubbles for DQMOM ($N = 3$). From black to blue line: smaller to larger bubble size groups.
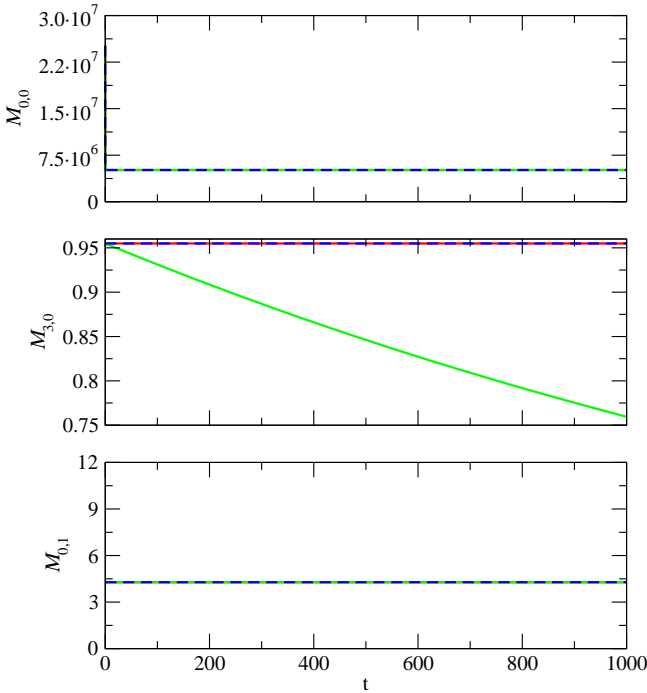

Figure 7: Evolution in time (s) of some moments of the NDF in the case of realistic coalescence and breakage, in the case of flowing gas phase in a stagnant liquid phase. Red line: CQMOM solution ($N_1 = 4$, $N_2 = 1$). Green line: DQMOM without correction ($N = 4$). Dotted blue line: DQMOM with proper correction ($N = 4$).

The physical values used to calculate the kernels and mass transfer coefficient are reported in Tab. 1. In this case, analytical solutions are not available and the comparison can be made only between the results obtained with the two methods. As it is possible to see in Fig. 5, also in this case the results obtained with the two models, for $N = 3$ and $N_1 = 3$ and $N_2 = 1$, are perfectly equivalent: $M_{0,0}$ decreasing in time indicates the prevail of coalescence over the breakage, while, correctly, $M_{3,0}$ and $M_{0,1}$ are not preserved since mass transfer occurs. In fact, part of oxygen in the gas bubbles transfers from gas to liquid, respecting, however, the total oxygen mass balance (gas and liquid). In Fig. 6 the concentration of oxygen in the different groups of bubbles, corresponding to each node of the quadrature, are plotted. The presented behavior can be easily explained as follows: all the bubble have the same concentration at the beginning of the simulation, then the concentrations in different nodes start to decrease with different dynamics, due to different mass transfer rates for each group of bubbles. Eventually the same value, corresponding to the equilibrium with the liquid phase, is reached. In fact, bubbles with small size have a faster dynamics than large ones, and PBM is the only way to capture and properly describe this phenomenon.

Another comparison between CQMOM and DQMOM is reported in Fig. 7, in the case of gas bubbles flowing in a stagnant liquid phase under the hypothesis of perfect mixing, with realistic coalescence and breakage kernels and no mass transfer. As it is possible to see, CQMOM and DQMOM result in different predictions if the correction in DQMOM is neglected. This system is intrinsically characterized by a dispersion coefficient that goes to infinity, while all gradients of properties tend to zero. With CQMOM, the diffusion does not lead to spurious terms in the formulation resulting in the correct conservation of $M_{3,0}$ and $M_{0,1}$. With DQMOM, instead, a proper correction must be formulated and properly accounted for (**Marchisio and Fox, 2005**), in order to correct the evolution of all the moments with order $\gamma \geq 2$. The following correction must appear as an additional source term in Eq. (8) and for the simple homogeneous system under investigation reads as follows:

$$
\begin{aligned}
C_{k,l} = D \sum_{i=1}^{N} & w_i k(k-1) L_i^{k-2} \phi_{b;i}^{l} (L_{i,\text{in}} - L_i)^2 \\
& + 2 w_i k l L_i^{k-1} \phi_{b;i}^{l-1} (L_{i;\text{in}} - L_i)(\phi_{b;i,\text{in}} - \phi_{b;i}) \\
& + w_i l(l-1) L_i^{k} \phi_{b;i}^{l-2} (\phi_{b;i,\text{in}} - \phi_{b;i})^2,
\end{aligned}
\tag{37}
$$

where $L_{i;\text{in}}$ and $\phi_{b;i,\text{in}}$ represent the inlet values of bubble size and composition, while D is the dispersion coefficient. This coefficient must be found by means of a simple "trial and error" procedure, because no specific analytical formulation is available for this zero-dimensional system. In this case, the difference between the two approaches is not negligible. This highlights that although DQMOM was successfully used in many cases it can be problematic for spatially distributed systems, especially for CFD applications where even if in the equations no explicit diffusion term appears, some diffusion is eventually introduced from the finite-volume discretization. For this reason, the CQMOM turns out to be more interesting than DQMOM, however its implementation in CFD codes is still under investigation, therefore in the next section only CFD results with DQMOM will be presented.

CFD analysis of the realistic test case

As mentioned earlier, the CFD implementation of DQMOM with two nodes ($N = 2$) is used to simulate the experimental data from the work of Laakkonen *et al.* (2006). The predictions of hold-up and velocities profiles for this configuration were validated in our previous work (Petitti *et al.*, 2010) and will not be discussed here.

The results of a typical CFD simulation are shown in Fig. 8. As it has been already said before, the different nodes of the quadrature approximation can be thought of as two different groups of bubbles with characteristic volume fractions (α_1, α_2), sizes (L_1, L_2) and compositions ($\phi_{b;1}$, $\phi_{b;2}$), which exchange mass and momentum with the continuous liquid phase and interact with each other by means of coalescence and breakage. It is clear that, through this approach, the evo-
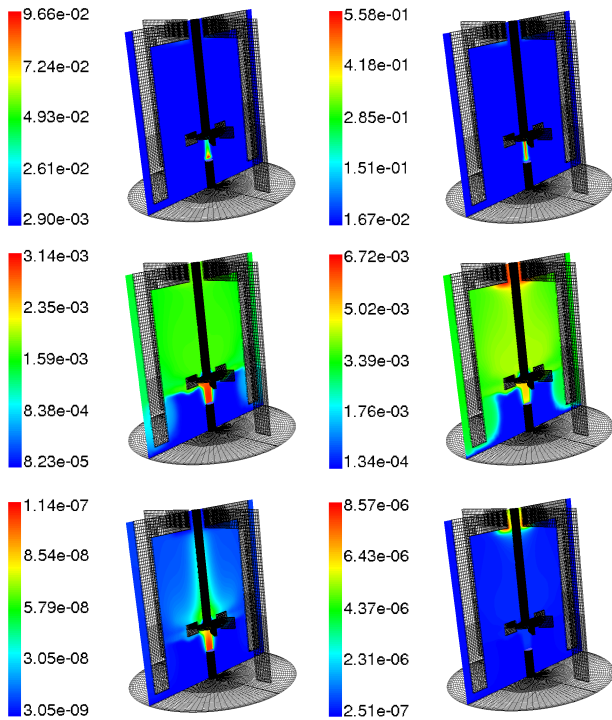

Figure 8: Contour plots of gas volume fraction (first row), bubble size (m) (second row) and bubble composition (mol) (third row) for the two nodes of quadrature approximation, in the case of stirring rate of 155 rpm and gassing rate of 0.018 vvm.
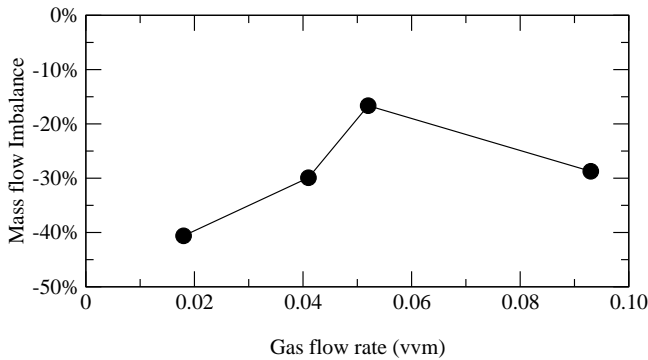

Figure 9: Error between inlet and outlet gas flow rate, in function of the inlet flow rate. Negative values: outlet gas flow rate is greater than inlet flow rate.

Table 2: Experimental and simulated mean Sauter diameter d_{32} (mm) in five different points of the stirred tank. Mean percentage error considering these points is also reported.

Stirring rate (rpm)	Gassing rate (vvm)		R2	R4	R8	R9	R12
155	0.018	Exp.	2.37	2.48	2.29	1.65	3.31
		Sim.	3.10	2.56	2.57	2.63	3.09
Mean percentage error					22.5%		
220	0.041	Exp.	2.56	3.34	2.57	1.76	3.81
		Sim.	2.66	3.04	2.47	2.50	3.20
Mean percentage error					15.0%		
220	0.052	Exp.	2.74	2.93	2.17	2.01	3.18
		Sim.	2.45	3.31	2.55	2.65	3.57
Mean percentage error					17.0%		
250	0.093	Exp.	2.96	3.24	2.44	2.25	3.33
		Sim.	2.82	3.27	2.60	2.71	3.35
Mean percentage error					6.7%		

lution of the multidimensional NDF is tracked in every cell of the computational domain.

The comparison between experimental data and modeling predictions for the operating conditions investigated is reported in Tab. 2, where the physical quantity compared, the mean Sauter diameter d_{32}, has been calculated from the CFD as the ratio between the pure moments of order three and two with respect to bubble size. As it is seen, weights and nodes calculated directly by resorting to DQMOM properly predict the local value of mean Sauter Diameter experimentally observed. In general, this model shows a good approximation of the experimental trends under all the operating conditions investigated. It is important to point out here that all the parameters of the CFD model (especially in the coalescence and breakage kernels) are mainly derived from theory and are not adjusted in this work to fit the experimental data. Moreover, no correction was added to take into account the added diffusional term given by the numerical discretization.

Regarding mass transfer, different tests were performed to determine the feasibility of the simulation, with the current geometry where the gas-liquid interface is not considered. In Fig. 9 the relative mass flow imbalance is plotted as a function of the gas flow rate entering in the system. In all the cases considered, the error is significant and the effects may affect the prediction of mass transfer. The reason for this error lies on the condition imposed on the top surface, because the condition of pressure outlet combined with the backflow of liquid allows more gas flow to escape than to enter. This problem is currently under investigation and promising results are obtained by using a different boundary condition. These results, obtained with the CFD implementation of DQMOM, will be further analyzed in our future work and will be compared with results obtained with the CFD implementation of CQMOM.

CONCLUSION

In this work, two different methods (i.e., DQMOM and CQMOM) for the solution of a multidimensional population balance have been formulated and used for the description of poly-disperse turbulent gas-liquid system. The two approaches have been tested for several simplified cases, prior

to the implementation in the CFD code. Tests conducted on a zero-dimensional homogeneous system with constant kernels showed perfect agreement with the analytical solutions for both methods. CQMOM and DQMOM are perfectly equivalent when $N_2 = 1$; even in the case of realistic coalescence and breakage kernels with mass transfer and the evolution of the moments are consistent with the theory. Moreover, in this case, it has been seen how the multidimensional population balance are able to capture the different dynamics through which different bubbles evolve in time.

Simulations for a zero-dimensional semi-batch system, with well-mixed stagnant liquid and flowing bubbles indicated instead different behaviors between the two methods. In this case, while CQMOM showed consistent results, DQMOM needed a proper corrective term to conserve the moments of the distribution. This issue is well-known (Marchisio and Fox, 2005), and must be accounted when dispersion/diffusion is present.

Eventually DQMOM has been coupled to a commercial CFD code to predict the evolution of the gas-liquid system for a real stirred reactor, for which experimental data concerning local BSD and mass transfer rate are available (Laakkonen *et al.*, 2006). Results with two nodes of quadrature and no mass transfer showed qualitative and quantitative agreement with experiments, even in the case of a boundary condition that gives mass flow imbalance. First promising results are obtained with a new boundary condition and will be explained in future works. Further steps of this work are directed to the implementation of CQMOM in order to compare the results obtained with the two methods.

REFERENCES

BUFFO, A. *et al.* (2010). "Multidimensional population balance model for the simulation of turbulent gas-liquid system in stirred tank reactors". *Chemical Engineering Science*. Submitted.

CHENG, J.C. and FOX, R.O. (2010). "Kinetic Modeling of Nanoprecipitation using CFD Coupled with a Population Balance". *Industrial & Engineering Chemistry Research*, **49(21)**, 10651–10662.

CHENG, J.C. *et al.* (2010). "A competitive aggregation model for Flash NanoPrecipitation". *Journal of Colloid and Interface Science*, **351(2)**, 330–342.

FAN, R. *et al.* (2004). "Application of the direct quadrature method of moments to polydisperse gas-solid fluidized beds". *Powder Technology*, **139(1)**, 7–20.

FOX, R.O. (2007). "Introduction and fundamentals of modeling approaches for polydisperse multiphase flows". D.L. Marchisio and R.O. Fox (eds.), *Multiphase Reacting Flows: Modelling and Simulation*, vol. 492 of *CISM International Centre for Mechanical Sciences*, 1–40. Springer Vienna.

FOX, R.O. (2009a). "Higher-order quadrature-based moment methods for kinetic equations". *Journal of Computational Physics*, **228(20)**, 7771–7791.

FOX, R.O. (2009b). "Optimal Moment Sets for Multivariate Direct Quadrature Method of Moments". *Industrial & Engineering Chemistry Research*, **48(21)**, 9686–9696.

GIMBUN, J. *et al.* (2009). "Modelling of mass transfer in gas-liquid stirred tanks agitated by Rushton turbine and CD-6 impeller: A scale-up study". *Chemical Engineering Research & Design*, **87(4A, Sp. Iss. SI)**, 437–451.

GORDON, R.G. (1968). "Error bounds in equilibrium statistical mechanics". *Journal of Mathematical Physics*, **9**, 655–667.

HABERMAN, W.L. and MORTON, R.K. (1956). "An experimental study of bubble moving in liquids". *Transactions of the American Society of Civil Engineers*, **121**, 227–252.

HINDMARSH, A.C. (1983). "ODEPACK, A Systematized Collection of ODE Solvers". R.S. Stepleman (ed.), *IMACS Transactions on Scientific Computation*, vol. 1, 55–64. Scientific Computing, North-Holland Amsterdam.

KAZAKIS, N.A. *et al.* (2008). "Experimental study of bubble formation at metal porous spargers: Effect of liquid properties and sparger characteristics on the initial bubble size distribution". *Chemical Engineering Journal*, **137(2)**, 265–281.

LAAKKONEN, M. *et al.* (2006). "Validation of bubble breakage, coalescence and mass transfer models for gas-liquid dispersion in agitated vessel". *Chemical Engineering Science*, **61(1)**, 218–228.

LAAKKONEN, M. *et al.* (2007). "Modelling local bubble size distributions in agitated vessels". *Chemical Engineering Science*, **62(3)**, 721–740.

LAMONT, J.C. and SCOTT, D.S. (1970). "An eddy cell model of mass transfer into the surface of a turbulent liquid". *AICHE Journal*, **16**, 513–519.

MARCHISIO, D.L. (2007). "Quadrature method of moments for poly-disperse flows". D.L. Marchisio and R.O. Fox (eds.), *Multiphase Reacting Flows: Modelling and Simulation*, vol. 492 of *CISM International Centre for Mechanical Sciences*, 41–77. Springer Vienna.

MARCHISIO, D.L. and FOX, R.O. (2005). "Solution of population balance equations using the direct quadrature method of moments". *Journal of Aerosol Science*, **36(1)**, 43–73.

MARCHISIO, D.L. *et al.* (2003a). "Implementation of the quadrature method of moments in CFD codes for aggregation-breakage problems". *Chemical Engineering Science*, **58(15)**, 3337–3351.

MARCHISIO, D.L. *et al.* (2003b). "Quadrature method of moments for aggregation-breakage processes". *Journal of Colloid and Interface Science*, **258(2)**, 322–334.

MCGRAW, R. (1997). "Description of aerosol dynamics by the quadrature method of moments". *Aerosol Science and Technology*, **27(2)**, 255–265.

PETITTI, M. *et al.* (2010). "Bubble Size Distribution Modeling in Stirred Gas-Liquid Reactors with QMOM Augmented by a New Correction Algorithm". *AICHE Journal*, **56(1)**, 36–53.

PRESS, W.H. *et al.* (1992). *Numerical recipes in C (2nd ed.): the art of scientific computing*. Cambridge University Press, New York, NY, USA.

RAMKRISHNA, D. (2000). *Population Balances*. Academic Press, New York, USA.

WHEELER, J.C. (1974). "Modified moments and gaussian quadratures". *Rocky Mountain Journal of Mathematics*, **4(2)**, 287–296.

WRIGHT, D.L. *et al.* (2001). "Bivariate extension of the quadrature method of moments for modeling simultaneous coagulation and sintering of particle populations". *Journal of Colloid and Interface Science*, **236(2)**, 242–251.

YOON, C. and MCGRAW, R. (2004a). "Representation of generally mixed multivariate aerosols by the quadrature method of moments: I. Statistical foundation". *Journal of Aerosol Science*, **35(5)**, 561–576.

YOON, C. and MCGRAW, R. (2004b). "Representation of generally mixed multivariate aerosols by the quadrature method of moments: II. Aerosol dynamics". *Journal of Aerosol Science*, **35(5)**, 577–598.

8th International Conference on CFD in Oil & Gas, Metallurgical and Process Industries
SINTEF/NTNU, Trondheim NORWAY
21-23 June 2011

CFD11-106

MODELING OF MASS- AND MOLE BASED MULTICOMPONENT DIFFUSION MODELS IN POROUS PELLETS FOR STEAM METHANE REFORMING PROCESS

K. R. ROUT[*], **H. A. JAKOBSEN**[1]

[1]Chemical Engineering Department, 7491 Trondheim, NORWAY

[*] E-mail: rout@nt.ntnu.no

ABSTRACT

The objective of this work has been to compare steady state mass- and mole based diffusion flux models, convection and fluid velocity for steam methane reforming (SMR) process. Mass diffusion fluxes are described according to the rigorous Maxwell Stefan model, dusty gas model and the more simple Wilke- and Wilke-Bosanquet models. The accuracy of choosing the Wilke- and Wilke-Bosanquet model to describe multicomponent mass diffusion instead of using the more rigorous Maxwell-Stefan- and Dusty gas models have been investigated. The simulations performed confirm the limiting Wilke model assumptions which imply that the Wilke model does not generally fulfill the restrictions that the sum of species composition should be unity, and that the diffusion fluxes should sum to zero. The Maxwell-Stefan and dusty gas multicomponent diffusion model results are consistent and slightly different from those obtained with the Wilke approximate model. These fluxes are defined with molar- and mass averaged velocities. In the case of mass based pellet models, a consistent set of equations are obtained considering only mass averaged velocity. But in the case of molar based pellet models, we need to consider both mass- and mole averaged velocities. The results of mass- and mole based models were not identical; however, the deviations are small. It is anticipated that these discrepancies are due to some unspecified numerical inaccuracies. However, efficiency factors have been computed for both processes and the values obtained are well agreement with the found literature data. The model evaluations revealed that: As the Wilke model does not necessarily conserve mass, we propose optimal diffusion flux model is Maxwell Stefan model. As mass- and mole based model deviates with some percents, it is not elucidated whether these deviations are numerical problems arising from large gradients of this process, or related to the choice of diffusion model.

Keywords: Multicomponent diffusion, Porous media, Mass- and mole based pellet model .

NOMENCLATURE

D = diffusivity, m^2/s
ΔH = heat of reaction, J/kmol
h = heat transfer coefficient, W/m²K
J = mole based diffusion flux, kmol/m² sec
j = mass based diffusion flux, kg/m² sec
k = mass transfer coefficient, m/s
M = molecular mass, $kg/kmol$
P = total pressure, pas
Q = heat flux, w/m²
R = gas constant, J/kmoleK

$\mathbf{r}$ = reaction rate, (kmol/kg(cat)h)
$\mathbf{r_1}$ = reaction rate for (I) , (kmol/kg(cat)h)
$\mathbf{r_2}$ = reaction rate for (II), (kmol/kg(cat)h)
$\mathbf{r_3}$ = reaction rate for (III), (kmol/kg(cat)h)
r = radial position at the bed, m
T = Temperature, k
u = mass averaged velocity, m/sec
u^* = mole averaged velocity, m/sec
w = mass fraction
x = mole fraction
Greek letters
ε = particle porosity
η = internal effectiveness factor
λ_p = conductivity, W/mK
ρ = density, kg/m^3
τ = tortuosity
Subscripts
cat = catalyst
e = effectiv
g = gas
j = different components
r = radious
Superscripts
b = bulk

INTRODUCTION

Hydrogen has long been an important raw material for the manufacture of commodity chemicals such as ammonia and methanol. With the growing global population, the number of vehicles and the energy demand for transportation are both projected to grow (1). Steam methane reforming (SMR) is a heterogeneous catalyzed process where methane and steam react over a nickel-based catalyst at high temperatures to produce synthesis gas which is a gas mixture of H_2, CO and CO_2. The primary reactions involved in H_2 production from natural gas are steam methane reforming (I) and (II) and water gas shift (III).The three main reactions in a SMR are represented by following equations (2).

$$CH_4(g) + H_2O(g) = CO(g) + 3H_2(g) \qquad \text{(I)}$$

$$CH_4(g) + 2H_2O(g) = CO_2(g) + 4H_2(g) \qquad \text{(II)}$$

$$CO(g) + H_2O(g) = CO_2(g) + H_2(g) \qquad \text{(III)}$$
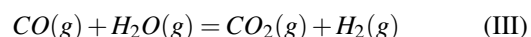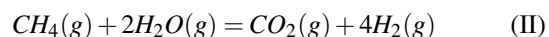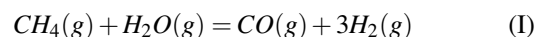
There are several models for the multicomponent diffusion fluxes. In the Wilke model (3; 4), the binary diffusion coefficient is replaced by an effective multicomponent diffusion coefficient. This model represents a simplified version of the more rigorous Maxwell-Stefan model (3; 4). The Dusty gas model denotes an extension of the Maxwell-Stefan model in which Knudsen diffusion is considered. As an approach to calculate the combined bulk and Knudsen flux using the Fickian formulation, the Bosanquet formula is suggested in literature (8; 4).

The conventional modelling considers the mass averaged mixture velocity as a primitive variable instead of the number or molar averaged mixture velocity. The mass averaged velocity is natural and most convenient basis for the laws of conservation of mixture mass, momentum and energy. It is true that total number of moles of the molecules in a mixture is not necessarily conserved, where as the mixture mass must be conserved. Separate equations of motion and energy for each species can be derived by continuum arguments. However, for mixtures containing a large number of different species the resulting sets of separate species mole, momentum and energy equations are neither feasible nor needed for solving transport problems. Besides, the species momentum and energy fluxes are not measurable quantities. Therefore, for the calculation of multicomponent problems containing convective transport phenomena the mass averaged velocity based description of the diffusion has en great advantage. If this description has been chosen, then all the conservation equations contain only mass average velocities, while in the molar description of the diffusion the equations of motion and energy contain mass average velocities. So in the molar based model we have converted the molar averaged velocity to mass averaged velocity to use in the equations of motion and energy(5). Hence, in the molar description of the diffusion model we will have two velocities, one is mass averaged velocity and the other one is mole averaged velocity. The two velocities are equal only when all the components of the system have same molar mass.

The fixed bed reactor models are usually grouped in to two broad categories i.e., the pseudo-homogeneous and the heterogeneous models. The pseudo-homogeneous models do not account explicitly for the presence of catalyst, in contrast to the heterogeneous models, which led to separate equations for the fluid phase species mass balance, the fluid inside the catalyst pores, and for the heat transport phenomena in the solid material and the fluid in the pores. However, the pseudo-homogeneous models require an effectiveness factor to account for the diffusion resistance across the external film and inside the pores of the pellet. These diffusion resistances decrease the effective reaction rate, hence the efficiency factors normally have values $0 \leq \eta \leq 1$.

The internal effectiveness factor η, with respect to the external surface conditions of the pellet, is defined by (6):

$$\eta = \frac{\text{actual overall rate of reaction}}{\text{rate of reaction with surface conditions}} \qquad \text{(IV)}$$

A large number of assumption are generally adopted for the mathematical description of intra-particle process. The governing equation for pellet model can be simplified by assuming the uniform temperature across the pellet, anticipating diffusion flux dominates over convective flux and neglect convective part. According to Burghardt and Aerts (1988), the pressure changes in the catalyst particle are probably so small, that they can be neglected in the process calculation(7). We have checked whether the temperature-

and pressure varies throughout catalyst particle or not.

MODEL DESCRIPTION

In this study we used a more general model for the macro-particle or pellet in which the reactions take place on the active sites on the macro-particles or channels. A mean pore diameter is assumed and the ratio between the porosity and tortuosity is used to characterize a fixed structure of the pellet. Variable pressure and temperature changes are modelled. Steady state models, containing several closure models for the multicomponent diffusion fluxes and including convection times, have been investigated.

Mass Base Model Equations

The general steady state mass-balance equation for a chemical species j in a reacting fluid flow having varying density, pressure, velocity, temperature and composition is written as:

$$\nabla .(\rho_j u) + \nabla .(j_j) = R_j \qquad \text{(V)}$$

where j_j is the mass based diffusion flux defined later in equations (XVIII), (XX), (XXI), (XXIII) and R_j denotes reaction rate. For a symmetric sphere, eq (V) reduces to a one dimension model, hence the transport equation for porous sphere may be given as:

$$\frac{1}{r^2}\frac{\partial}{\partial r}(r^2 u_r \rho_g w_j) = -\frac{1}{r^2}\frac{\partial}{\partial r}(r^2 j_{j,r}) + S_{w_j} \qquad \text{(VI)}$$

in which the mass fraction of species j is defined by:

$$w_j = \frac{\rho_j}{\rho_g} \qquad \text{(VII)}$$

and S_{w_j} is a generic reaction rate representing different pellet designs. The continuity can be obtained by adding up the species balances (VI) for all the species, hence:

$$\sum_j \frac{1}{r^2}\frac{\partial}{\partial r}(r^2 u_r \rho_g w_j) = -\sum_j \frac{1}{r^2}\frac{\partial}{\partial r}(r^2 j_{j,r}) + \sum_j S_{w_j} \qquad \text{(VIII)}$$

Equation (VIII) can be simplified subject to the rigorous constraints: $\sum_j w_j = 1$ and $\sum_j j_{j,r} = 0$, which results in:

$$\frac{1}{r^2}\frac{\partial}{\partial r}(r^2 u_r \rho_g) = 0 \qquad \text{(IX)}$$

It is noted that the Wilke equation does not generally satisfy the constraints (4). Nevertheless, by substituting equation (IX) into (VI), yields:

$$u_r \rho_g \frac{\partial w_j}{\partial r} = -\frac{1}{r^2}\frac{\partial}{\partial r}(r^2 j_{j,r}) + S_{w_j} \qquad \text{(X)}$$

The source term S_{w_j} is:

$$S_{wj} = (1 - \varepsilon_{cat})\rho_{cat}\mathbf{r_j} \qquad \text{(XI)}$$

A consistent one-dimensional heat equation in terms of temperature yields:

$$\rho_g C p_g u_r \frac{\partial T}{\partial r} = -\frac{1}{r^2}\frac{\partial}{\partial r}(r^2 Q_r) + S_T \qquad \text{(XII)}$$

The source term S_T is:eq (XIII):

$$S_T = (1 - \varepsilon_{cat})\rho_{cat}\sum(-\Delta H_{r_j})\mathbf{r_j} \qquad \text{(XIII)}$$

In equations (XI) $\mathbf{r_j}$ is the reaction rate for the methanol synthesis reactions $j =$ I, II, III.

The heat flux is defined by Fourier's law:

$$Q_r = -\lambda_p \frac{\partial T}{\partial r} \qquad \text{(XIV)}$$

where the λ_p values for the solid- and gas conductivity has been estimated from (9):

The viscous gas velocity in the catalyst pores is driven by a pressure gradient that is caused by temperature evolution created by chemical reactions and the potential non-uniform spatial species composition.

The Darcy's law represents a relation between the viscous gas velocity and the pressure gradient (3; 4):

$$\mathbf{u} = -\frac{\beta_0}{\mu}\nabla P \qquad \text{(XV)}$$

In the parallel-pore model pores are assumed to be cylindrical, hence the permeability can be computed from the Poiseuille flow relationship (3):

$$\beta_0 = \frac{\varepsilon}{\tau}\frac{d_0^2}{32} \qquad \text{(XVI)}$$

the porosity-tortuosity factor ε/τ is introduced to characterize the pellet structure. The ideal gas law has been used to calculate mixture density:

$$\rho_g = \frac{PM_w}{RT} \qquad \text{(XVII)}$$

Several diffusion flux models have been used to close the species mole balance. In our model, we have used 4 diffusion flux closures:

(1) The Mass based Wilke model for bulk diffusion (4):

$$\mathbf{j}_j = -\rho_g D_{jm}^e \nabla w_j \qquad \text{(XVIII)}$$

where the mass based Wilke effective diffusion coefficient is represented by:

$$D_{jm}^e = \left(M_w \sum_{\substack{i=1 \\ i \neq j}}^{n} \frac{w_i}{M_{w_i}D_{ji}^e}\right)^{-1} \qquad \text{(XIX)}$$

For the present model the Wilke diffusivity (XIX) is used for catalyst pellet analysis, even though its general validity is restricted to cases wherein the species j diffuses into a mixture of stagnant species (3).

(2) The Explicit Mass based Maxwell-Stefan model (4):

$$\mathbf{j}_j = \frac{\frac{M_w}{\rho_g}\sum_{\substack{i=1 \\ i \neq j}}^{n}\frac{w_j j_i}{M_{w_i}D_{ji}^e} - w_j\nabla ln(M_w) - \nabla w_j}{\frac{M_w}{\rho_g}\sum_{\substack{i=1 \\ i \neq j}}^{n}\frac{w_i}{M_{w_i}D_{ji}^e}} \qquad \text{(XX)}$$

The multicomponent Maxwell-Stefan model can give more accurate results for multicomponent mixtures in comparison to the approximated results obtained by use of the extended Fick diffusion flux model originally designed for binary mixtures (3).

(3) The Explicit Mass based Dusty gas model (4):

$$\mathbf{j}_j = \frac{M_w^2\sum_{\substack{i=1 \\ i \neq j}}^{n}\frac{w_j j_i}{M_{w_i}D_{ji}^e} - w_j\nabla ln(M_w) - \nabla w_j}{M_w^2\sum_{\substack{i=1 \\ i \neq j}}^{n}\frac{w_i}{M_{w_i}D_{ji}^e} + \frac{M_w}{D_{jk}^e}} \qquad \text{(XXI)}$$

where D_{jK}^e can be expressed as (12):

$$\frac{1}{D_{jk}^e} = 97.0\, r(T/M_j)^{0.5} \qquad \text{(XXII)}$$

The Dusty gas approach attempts to provide a more realistic description of the diffusion mechanism in the combined bulk and Knudsen regime based on the Maxwell-Stefan approach.

(4) If the Knudsen diffusion is important, the mass based Wilke model is modified by applying the Bosanquet approach (8; 4):

$$\mathbf{j}_j = -\rho_g D_{j,eff}^e \nabla w_j \qquad \text{(XXIII)}$$

where (8; 4):

$$\frac{1}{D_{j,eff}^e} = \frac{1}{D_{jm}^e} + \frac{1}{D_{jk}^e} \qquad \text{(XXIV)}$$

Mole Base Model Equations

The general steady state mole-balance equation for a chemical species j in a reacting fluid flow having varying concentration, pressure, velocity, temperature and composition is written as:

$$\nabla\cdot(c_j u^*) + \nabla\cdot(J_j) = r_j \qquad \text{(XXV)}$$

where J_j is the mole based diffusion flux defined later in equations (XL), (XLII) and (XLIII), (XLV), and r_j denotes reaction rate. For a symmetric sphere, eq (XXV) reduces to a one dimension model, hence the transport equation for porous sphere may be given as:

$$\frac{1}{r^2}\frac{\partial}{\partial r}(r^2 u_r^* c_g x_j) = -\frac{1}{r^2}\frac{\partial}{\partial r}(r^2 J_{j,r}) + s_{x_j} \qquad \text{(XXVI)}$$

in which the mole fraction of species j is defined by:

$$x_j = \frac{c_j}{c_g} \qquad \text{(XXVII)}$$

and s_{w_j} is a generic reaction rate representing different pellet designs. The continuity can be obtained by adding up the species balances (XXVI) for all the species, hence:

$$\sum_j \frac{1}{r^2}\frac{\partial}{\partial r}(r^2 u_r^* c_g x_j) = -\sum_j\frac{1}{r^2}\frac{\partial}{\partial r}(r^2 J_{j,r}) + \sum_j s_{x_j} \qquad \text{(XXVIII)}$$

Equation (XXVIII) can be simplified subject to the rigorous constraints: $\sum_j x_j = 1$ and $\sum_j J_{j,r} = 0$, which results in:

$$\frac{1}{r^2}\frac{\partial}{\partial r}(r^2 u_r^* c_g) = \sum_j s_{x_j} \qquad \text{(XXIX)}$$

It is noted that the Wilke equation does not generally satisfy the constraints (4). Nevertheless, by substituting equation (IX) into (XXVI), yields:

$$u_r^* c_g \frac{\partial x_j}{\partial r} = -\frac{1}{r^2}\frac{\partial}{\partial r}(r^2 J_{j,r}) + s_{x_j} - x_j\sum_j s_{x_j} \qquad \text{(XXX)}$$

The source term s_{x_j} is:

$$s_{xj} = (1-\varepsilon_{cat})\rho_{cat}\mathbf{r_j} \qquad \text{(XXXI)}$$

A consistent one-dimensional heat equation in terms of temperature yields:

$$\rho_g Cp_g u_r \frac{\partial T}{\partial r} = -\frac{1}{r^2}\frac{\partial}{\partial r}(r^2 Q_r) + s_T \qquad \text{(XXXII)}$$

The source term s_T is:eq (XXXII):

$$s_T = (1 - \varepsilon_{cat})\rho_{cat}\sum(-\Delta H_{r_j})\mathbf{r_j} \qquad \text{(XXXIII)}$$

In equations (XXXI) $\mathbf{r_j}$ is the reaction rate for the methanol synthesis reactions $j = $ I, II, III.

The heat flux is defined by Fourier's law:

$$Q_r = -\lambda_p \frac{\partial T}{\partial r} \qquad \text{(XXXIV)}$$

where the λ_p values for the solid- and gas conductivity has been estimated from (9):

The viscous gas velocity in the catalyst pores is driven by a pressure gradient that is caused by temperature evolution created by chemical reactions and the potential non-uniform spatial species composition.

The Darcy's law represents a relation between the viscous gas velocity and the pressure gradient (3; 4):

$$u = -\frac{\beta_0}{\mu}\nabla P \qquad \text{(XXXV)}$$

In the parallel-pore model pores are assumed to be cylindrical, hence the permeability can be computed from the Poiseuille flow relationship (3):

$$\beta_0 = \frac{\varepsilon}{\tau}\frac{d_0^2}{32} \qquad \text{(XXXVI)}$$

the porosity-tortuosity factor ε/τ is introduced to characterize the pellet structure.

The velocity in equation (XXXII)and (XXXV) is the mass averaged velocity, so we have calculated mass averaged velocity from mole averaged velocity with the equation(5):

$$u = u^* + \sum_j w_j(u_j - u^*) \qquad \text{(XXXVII)}$$

where u_j is the velocity of species j with respect to fixed coordinates. u_j can be calculated from the equation:

$$\mathbf{J}_j = c_j(u_j - u^*) \qquad \text{(XXXVIII)}$$

where c_j is the concentration of species j.

The ideal gas law has been used to calculate mixture concentration:

$$c_g = \frac{P}{RT} \qquad \text{(XXXIX)}$$

Several diffusion flux models have been used to close the species mass balance. In our model, we have used 4 diffusion flux closures:

(1) The Mole based Wilke model for bulk diffusion (4):

$$\mathbf{J}_j = -c_g D_{jm}^e\nabla x_j \qquad \text{(XL)}$$

where the mole based Wilke effective diffusion coefficient is represented by:

$$D_{jm}^e = \frac{1 - x_j}{\sum\limits_{\substack{i=1 \\ i\neq j}}^{n}\frac{x_i}{D_{ji}^e}} \qquad \text{(XLI)}$$

(2) The Explicit Mole based Maxwell-Stefan model (4):

$$\mathbf{J}_j = \frac{\sum\limits_{\substack{i=1 \\ i\neq j}}^{n}\frac{x_j J_i}{D_{ji}^e} - c_g\nabla w_j}{\sum\limits_{\substack{i=1 \\ i\neq j}}^{n}\frac{x_i}{D_{ji}^e}} \qquad \text{(XLII)}$$

(3) The Explicit Mole based Dusty gas model (4):

$$\mathbf{J}_j = \frac{\sum\limits_{\substack{i=1 \\ i\neq j}}^{n}\frac{x_j J_i}{D_{ji}^e} - \frac{c_i u^*}{D_{jk}^e} - c_g\nabla x_j}{\sum\limits_{\substack{i=1 \\ i\neq j}}^{n}\frac{x_i}{D_{ji}^e} + \frac{1}{D_{jk}^e}} \qquad \text{(XLIII)}$$

where D_{jK}^e can be expressed as (12):

$$\frac{1}{D_{jk}^e} = 97.0\,r(T/M_j)^{0.5} \qquad \text{(XLIV)}$$

(4) If the Knudsen diffusion is important, the mole based Wilke model is modified by applying the Bosanquet approach (8; 4):

$$\mathbf{J}_j = -c_g D_{j,eff}^e\nabla x_j \qquad \text{(XLV)}$$

where (8; 4):

$$\frac{1}{D_{j,eff}^e} = \frac{1}{D_{jm}^e} + \frac{1}{D_{jk}^e} \qquad \text{(XLVI)}$$

Chemical Model

Steam methane reforming on nickel-based catalysts is the main process for industrial production of hydrogen or synthesis gas. Xu and Froment (2) investigated a large number of detailed mechanisms and derived a set of intrinsic rate equations for the steam reforming of methane on nickel-alumina catalysts which have been widely used. Their rate equations were also used in our simulations:

$$\mathbf{r}_1 = \frac{k_1}{p_{H_2}^{2.5}}\left[\frac{p_{CH_4}p_{H_2O} - p_{H_2}^3 p_{CO}/K_1}{DEN^2}\right] \qquad \text{(XLVII)}$$

$$\mathbf{r}_2 = \frac{k_2}{p_{H_2}}\left[\frac{p_{CO}p_{H_2O} - p_{H_2}p_{CO_2}/K_2}{DEN^2}\right] \qquad \text{(XLVIII)}$$

$$\mathbf{r}_3 = \frac{k_3}{p_{H_2}^{3.5}}\left[\frac{p_{CH_4}p_{H_2O}^2 - p_{H_2}^4 p_{CO_2}/K_3}{DEN^2}\right] \qquad \text{(XLIX)}$$

where

$$DEN = 1 + K_{CO}p_{CO} + K_{H_2}p_{H_2} + K_{CH_4}p_{CH_4} + K_{H_2O}p_{H_2O}/p_{H_2} \qquad \text{(L)}$$

R_1, R_2, R_3 correspond to the reactions (I), (III) and (II), respectively.

Initial and Boundary conditions for Mass Based Model

The initial conditions are as follows:

$$\left.\begin{array}{l} w_j = w_j^b \\ T = T^b \\ \rho = \rho^b \end{array}\right\} \qquad \text{for} \qquad t = 0, \forall r \qquad \text{(LI)}$$

The initial conditions for the species differential variable $j_{j,r}$ in equation (X) are given by:

$$j_{j,r} = 0 \qquad \text{for} \qquad r = 0; \qquad \text{due to symmetry} \qquad \text{(LII)}$$

and for the differentiated variable w_j in the equation (XVIII), (XX) or (XXI):

$$j_{j,r} + u_r\rho_g w_j = -\rho_g k_j(w_j^b - w_j) \qquad \text{for} \qquad r = r_p \qquad \text{(LIII)}$$

where k_j signifies the mass transfer coefficient for species j computed from dimensionless numbers (10), w_j^b denotes the species j mass fraction in bulk, and r_p is the pellet radius. Equation (XII) holds the following initial conditions for the differentiated variable Q_r:

$$Q_r = 0 \qquad \text{for} \qquad r = 0; \qquad \text{due to symmetry} \qquad \text{(LIV)}$$

and for the Fouriers law (XIV), the following initial conditions are used for the differentiated variable T:

$$\rho_g \, Cp_g \, u_r \, T + Q_r = -h(T^b - T) \qquad \text{for} \qquad r = r_p \qquad \text{(LV)}$$

where h represents the heat transfer coefficient between the bulk gas and the pellet surface, computed from expression (11). The boundary condition for the velocity derivative in the continuity equation (IX), yields:

$$u_r = 0 \qquad \text{for} \qquad r = 0 \qquad \text{(LVI)}$$

The initial condition for the pressure derivative in the Darcy law (XV):

$$P = P^b \qquad \text{for} \qquad r = r_p \qquad \text{(LVII)}$$

Initial and Boundary conditions for Mole Based Model

The initial conditions are as follows:

$$\left.\begin{array}{l} x_j = x_j^b \\ T = T^b \\ c = c^b \end{array}\right\} \qquad \text{for} \qquad t = 0, \forall r \qquad \text{(LVIII)}$$

The initial conditions for the species differential variable $J_{j,r}$ in equation (XXX) are given by:

$$J_{j,r} = 0 \qquad \text{for} \qquad r = 0; \qquad \text{due to symmetry} \qquad \text{(LIX)}$$

and for the differentiated variable x_j in the equation (XL), (XLII) or (XLIII):

$$J_{j,r} + u_r c_g x_j = -c_g k_j \left(w x_j^b - x_j \right) \qquad \text{for} \qquad r = r_p \qquad \text{(LX)}$$

where k_j signifies the mass transfer coefficient for species j computed from dimensionless numbers (10), x_j^b denotes the species j mole fraction in bulk, and r_p is the pellet radius. Equation (XXXIII) holds the following initial conditions for the differentiated variable Q_r:

$$Q_r = 0 \qquad \text{for} \qquad r = 0; \qquad \text{due to symmetry} \qquad \text{(LXI)}$$

and for the Fouriers law (XXXIV), the following initial conditions are used for the differentiated variable T:

$$c_g \, Cp_g \, u_r \, T + Q_r = -h(T^b - T) \qquad \text{for} \qquad r = r_p \qquad \text{(LXII)}$$

where h represents the heat transfer coefficient between the bulk gas and the pellet surface, computed from expression (11). The boundary condition for the velocity derivative in the continuity equation (XXIX), yields:

$$u_r = 0 \qquad \text{for} \qquad r = 0 \qquad \text{(LXIII)}$$

The initial condition for the pressure derivative in the Darcy law (XXXV):

$$P = P^b \qquad \text{for} \qquad r = r_p \qquad \text{(LXIV)}$$

MODEL SOLUTION

The steady state governing equations are solved using the least square spectral spectral element method. The least square spectral method (LSQ) is a well-established numerical method for solving a wide range of mathematical problems (13; 14; 15; 16; 17). The basic idea in the LSQ is to minimize the integral of the square of the residual over the computational domain.

Symmetry is assumed in the sphere which results in one independent spatial variable in the radial dimension which is discretized by the method of weighted residuals concepts. The Gauss-Legendre-Lobatto collocation points are used.

The governing equation in the solution process, a system of nondimensionalized model equations has been used.

For the cases of the SMR process the LSQ-Spectral element method has been used. In this processes the computational domain has been divided into 4 elements with 15 collocation points has been used for the whole domain.

The Least Square Method

The Least Square method formulation is based on the minimization of a norm-equivalent functional. This consists of finding the minimizer of the residual in a certain norm. The norm-equivalent functional for an integro-differential problem in which the unknown is f:

$$\mathscr{J}(f) = \frac{1}{2} \left(\|\mathscr{L}f - g\|_{Y(\Omega)}^2 + \|\mathscr{B}f - f_0\|_{Y(Y_0)}^2 \right) \qquad \text{(LXV)}$$

with $\mathscr{L}$ the integro-differential operator containing all the conservation equations, $\mathscr{B}$ the boundary condition operator acting on f, and g the source term. As the momentum conservation equations are non-linear in nature, we adopt the Picard successive substitution technique for the linearization. Moreover, in this work, the minimization is based on a L_2 norm, i.e. $\|.\|_{Y(\Omega)}^2 = \|.\|_{X(\Omega)}^2$. Based on variational analysis, the minimization statement is equivalent to Find $f \in X(\Omega)$ such that:

$$\lim_{x \to 0} \frac{d}{d\varepsilon} \mathscr{J}(f + \varepsilon v) = 0 \qquad \forall v \in X(\Omega) \qquad \text{(LXVI)}$$

where $X(\Omega)$ is the space of the admissible functions and v is any test function. Consequently, the necessary condition can be written as Find $f \in X(\Omega)$ such that:

$$A(f, v) = F(v) \qquad \forall v \in X(\Omega) \qquad \text{(LXVII)}$$

with

$$A(f, v) = \langle \mathscr{L}f, \mathscr{L}v \rangle_{X(\Omega)} + \langle \mathscr{B}_0 f, \mathscr{B}_0 v \rangle_{X(Y_0)} \qquad \text{(LXVIII)}$$

$$F(v) = \langle g, \mathscr{L}v \rangle_{X(\Omega)} \langle f_0, \mathscr{B}_l v \rangle_{X(Y_0)} \qquad \text{(LXIX)}$$

where $A : X \times X \longrightarrow R$ is a symmetric, continuous bilinear form, and $F : X \longrightarrow R$ a continuous linear form.

Model Convergence

In order to assess the convergence of the model, we define two convergence criteria like:

$$Residual = \sqrt{\langle \mathscr{L}f_N - g, \mathscr{L}f_N - g \rangle} \leq e^-5 \qquad \text{(LXX)}$$

$$\varepsilon_{iteration} = \sqrt{f_N^{it} - f_N^{it-1}, f_N^{it} - f_N^{it-1}} \leq e^-10 \qquad \text{(LXXI)}$$

The Residual denotes a measure for the overall error obtained for the system of equations discretized by the least squares method. The iteration overall error denotes a measure of the difference in variable values between the second last- and the last preceding iterations, for a preliminary $\mathscr{L}$ representing a linearized integro-differential operator using the Picard iteration technique.
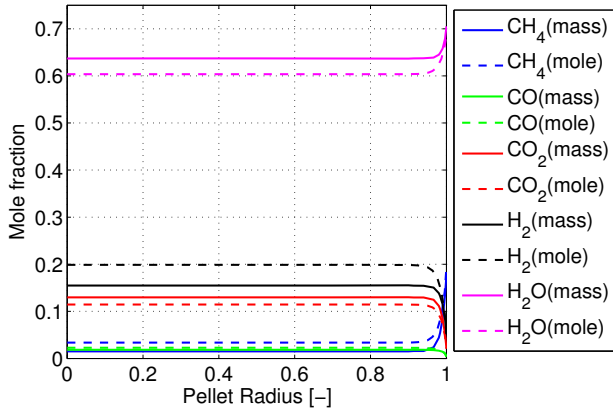
Figure 1: Comparasion of mass-and mole base model in a catalyst particle for Wilke model.

Figure 2: Comparasion of mass-and mole base model in a catalyst particle for Maxwell-Stefan model.

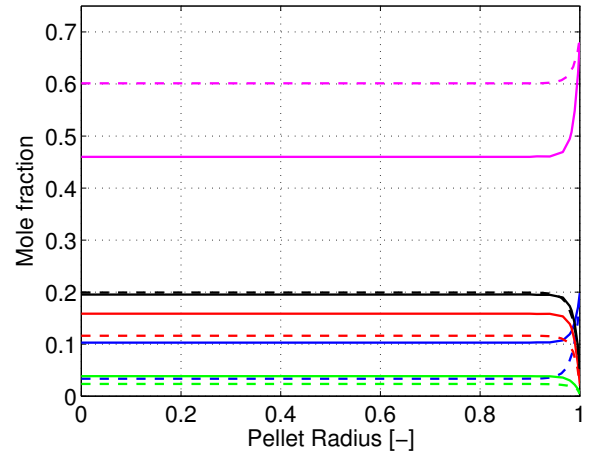Figure 3: Comparasion of mass-and mole base model in a catalyst particle for Dusty gas model.

Figure 4: Comparasion of mass-and mole base model in a catalyst particle for Wilke-Bosanquet model.
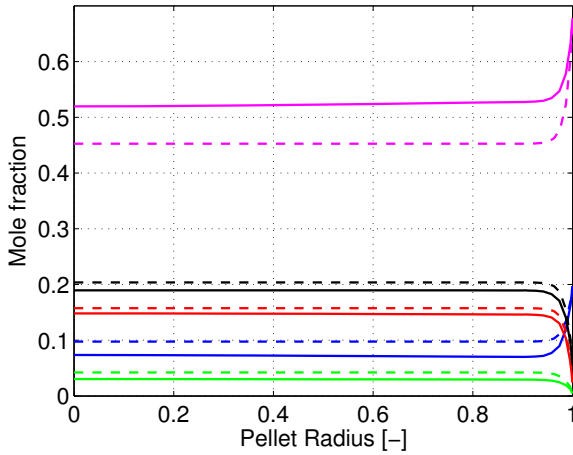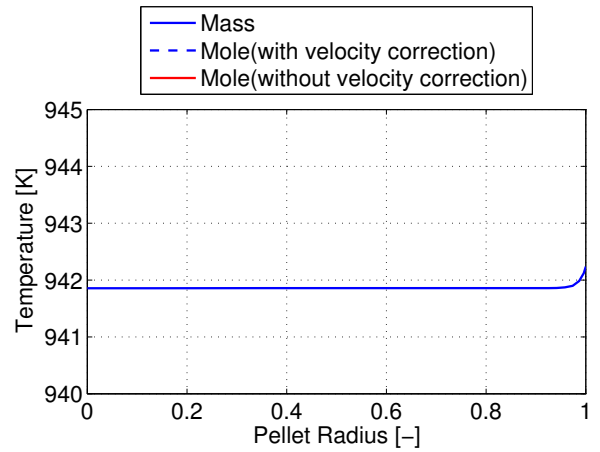

Figure 5: Comparison of temperature profile across the pellet for mass-and mole base model of Dusty gas model.
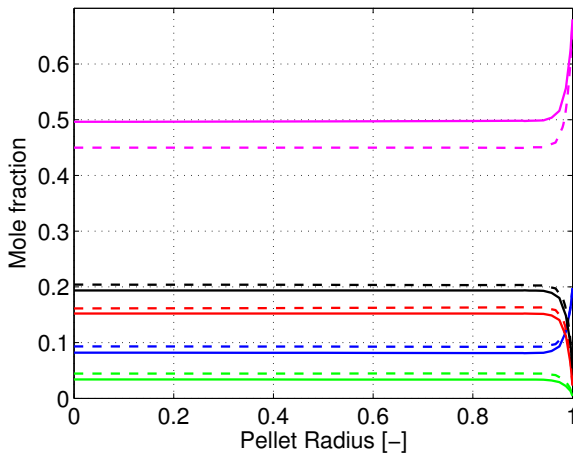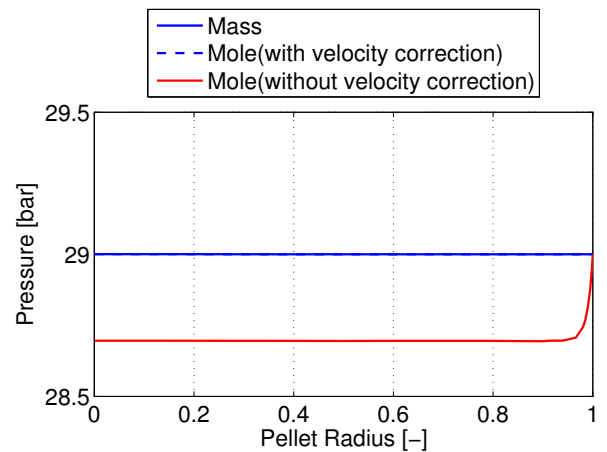

Figure 6: Comparison of pressure profile across the pellet for mass-and mole base model of the Dusty gas model.

RESULTS AND DISCUSSION

The mass- and mole based steady state model describes the evolution of species mass composition, pressure, concentration, temperature, gas velocity, mass- and mole diffusion flux, heat flux and convection for SMR process have been simulated by the Least square spectral element method (LSM-SPE). The pellet model consistency, temperature- and pressure profile across the pellet have calculated after converting the mole averaged velocity to mass averaged velocity for the mole based model, which has been used in the temperature and Darcy law equation. Table 1 shows the parameter used for solving pellet equations.
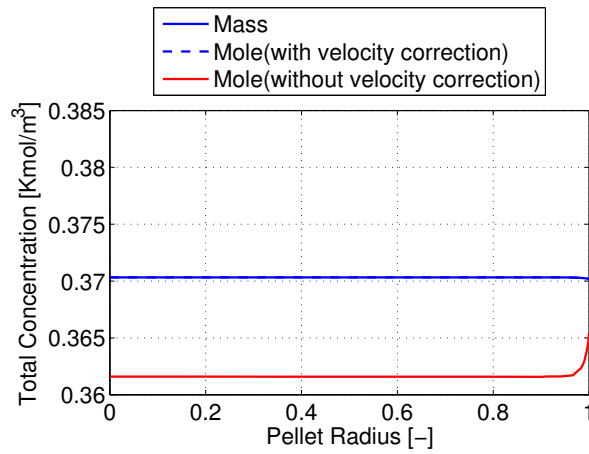

Figure 7: Comparison of total concentration profile across the pellet for mass-and mole base model of the Dusty gas model.

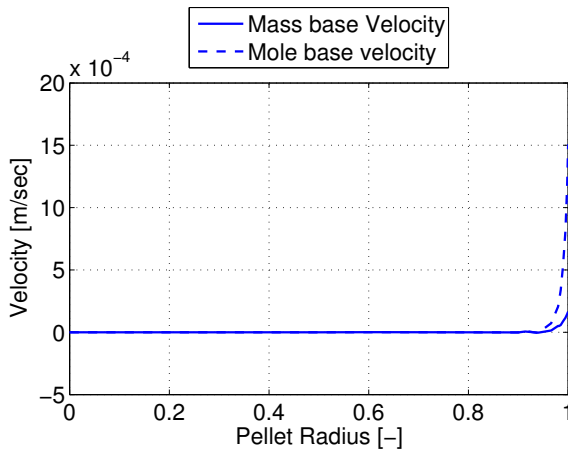
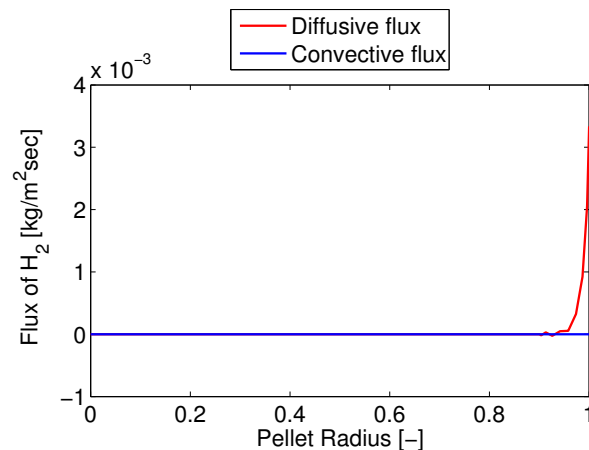Figure 8: Comparison of velocity profile across the pellet for mass-and mole base model of the Dusty gas model.

Figure 9: Comparison of convective- and diffusive flux across the pellet for mass-and mole base model of Dusty gas model.

Model Validation

The internal effectiveness factors (IV) of the mass- and mole based model for the SMR reactions have the values in the range of 10^{-2}-10^{-3}, see table 2, which are in agreement with those reported by Elnashaie et al.(1992)(18).

Consistency of the mass- and mole based diffusion models

The numerical results of the mole- and mass base multicomponent models did not give completely identical results.

Figure 1, figure 2, figure 3 and figure 4 compares the species mole fraction results of different diffusion models obtained from mole- and mass based pellet model. A maximum deviation of 10 % is observed for the mass- and mole based diffusion models of SMR process. The modified Wilke model for combined bulk and Knudsen diffusion obtains nearly identical results to the more rigorous dusty gas model, while the Maxwell-Stefan and the ordinary Wilke model give slightly different results. However, it should be noted that the sum of the species composition must be unity and that the sum of the diffusion fluxes must equal zero.

The SMR process is characterized by high diffusional limitations, that is the reactions are completed in a thin shell near the surface of the catalyst pellet. Hence, much larger gradients occur in this process. These large gradients might have caused some numerical problems in the SMR process influencing the results.

Jannike et al. (2011) used the SMR- and methanol synthesis processes to check the consistency of the mass- and mole based model equations(20). They used the orthogonal collocation method to solve the model equations. However they have not converted the mole averaged velocity to mass averaged velocity for solving molar based model equations which should be used in the Darcy and temperature equations. Therefore, they do not have consistent pressure- and temperature profiles across the pellet for both mass- and mole based models. In their calculation, they get hardly no difference of the mass- and mole based models for the methanol process, as the mole fraction profiles of the methanol process across the pellet is smooth. But in the case of SMR process, there is a steep gradient near the surface of the pellet. However, increasing the the number of grid points- and the elements close the surface does not improve the solutions.

Figure 5 shows the temperature profile across the pellet for Dusty gas model, which are in agreement with the literature (19). From this figure it has been confirmed that there is very little temperature variation (less then 0.5 K) between the surface and center of the pellet. There is hardly any difference between the temperature profiles resulting from the mass- and mole based models. However, in the mole based formulation, the velocity in the temperature equation is a mass averaged velocity. In our calculation we have converted the mole averaged velocity to mass averaged velocity and used it in temperature equation. Here we have found also

temperature is not varying much in the case of mole based pellet model for without- and with velocity correction.

Figure 6 shows there is almost no variation of pressure from surface to the center of the catalyst pellet and they are consistent for both mass- and mole base Dusty gas model. The pressure has been calculated from the Darcy law in both the mass- and mole base models. However, in the mole based formulation, the velocity in the Darcy law is a mass averaged velocity. In our calculation we have converted the mole averaged velocity to mass averaged velocity and used it in the Darcy law. According to Burghardt and Aerts (1988) the pressure changes in a catalyst pellet under conditions normally encountered in industry are probably so small that can be neglected in the process calculation. Hence, our results agree with those reported by Burghardt and Aerts(1988)(7). However, we have calculated the pressure profile without velocity correction for mole base model also. We have found that the pressure is not identical for with- and without velocity correction. The pressure is varying less then 2% across the pellet for without velocity correction which is shown in the figure 6.

FIgure 7 shows the total concentration profile for the Dusty gas model, the total concentration is increasing from the surface to the center of the pellet. However, we have calculated the total concentration using mole averaged velocity in the mole based model, which is commonly used the pellet model. We have found that total concentration is varying less then 3% across the pellet which is also shown in the figure figure 7.

For the case of mole base model, we have two type of velocity, one is mass averaged velocity and the other one is mole averaged velocity. Figure 8 shows the mass- and mole averaged velocity for the mole base dusty gas model.

Figure 9 shows that close to external surface, the diffusion fluxes clearly dominate over the convective fluxes, hence neglecting the convective flux terms in the governing equations for pellet model is a reasonable model approximation.

Table 2 shows the comparison of internal effectiveness factor for both mass- and mole based Dusty gas models. It seems that the internal effectiveness factors are not so different for both the models.

It can be concluded that in the pellet model, we can neglect convective part, we can assume the pellet model as a uniform temperature across the pellet and isobaric condition. These assumptions will help us to get faster convergence for heterogeneous reactor models.

Table 1: Simulation parameters for SMR process

Mass fractions		
CH_4	0.1911	-
CO	0.0001	-
CO_2	0.0200	-
H_2	0.0029	-
H_2O	0.7218	-
N_2	0.0641	-
Pressure	$29 \cdot 10^5$	Pa
Temperature	1000	K
Physical Parameters:		
Density of catalyst	2300	kg cat/m^3
void fraction	0.528	-
Pellet diameter	0.0173	m
Tortuosity	3.5	-
Mean pore diameter	150	nm
Heat capacity of solids	850	J/kgK

Table 2: Internal effectiveness factors for the SMR process.

	Reaction	η
	I	0.01
Mass base Model	II	0.005
	III	0.09
	I	0.0098
Mole base Model	II	0.005
	III	0.088

CONCLUSION

In this work, a mathematical model has been formulated for the SMR process to verify pellet model consistency with respect to mass- and mole averaged velocity for different multicomponent diffusion models and validated with the found literature data. The model evaluations revealed that:

1. The mass- and mole based pellet model did not give identical result, where the large gradients are assumed to cause numerical problems.

2. The simulated results for pellet models show that there are small differences between the different mass diffusion models. The simulated results reveal the limitations of the Wilke model formulation, the species composition approximations are not accurate. Hence, the more rigorous Maxwell-Stefan model seems to be better choice.

3. The pellet model results generally support the conventional model approximations like uniform temperature across the pellet as the temperature variation between the surface and the center of the pellet is less then 0.5K, and for $Kn < 10$ constant pressure within the pellets. Moreover, the magnitude of the diffusion fluxes generally dominate over the convective fluxes.

ACKNOWLEDGMENT

REFERENCES

[1] Ogden JM (2001) Review of small stationary reformers for hydrogen production. The international Energy Agency, Golden IEA/H2/TR-02/002.

[2] Xu J, Froment GF (1989) Methane steam reforming, methanation and water-gas shift:I. Intrinsic kinetics. A.I.Ch.E. Journal 30:88-96

[3] Krishna R, Wesselingh JA (1996) The Maxwell-Stefan Approach to Mass transfer. Chemical Engineering Science 52 (6):861-911

[4] Jakobsen HA (2008) Chemical Reactor Modeling. Multiphase Reactive Flows, Springer, 1 edn

[5] Bird RB; Stewart WE; Lightfoot EN (1924) Transport Phenomena, John Wiley and Sons, Inc, 2 edn

[6] Foglert HS (2006) Elemets of Chemical Reaction Engineering. Prentice Hall

[7] Burghardt A, Aerts J (1988) Pressure changes during diffusion with chemical reaction in a porous pellet. Chem. Eng. Process 23:77-87

[8] Krishna R (1992) Problems and pitfalls in the use of the Fick formulation for intraparticle diffusion. Chemical Engineering Science 48 (5):845-861

[9] Chemical Properties Hand Book, Mc Graw Hill (1999)

[10] Wakao N, Funazkri T (1978) Effect of Fluid Dispersion Coeffcients on Particle-to-Fluid Mass Transfer Coeffcients in Packed Beds. Chemical Engineering Science 33:1375-1384

[11] Rusten HK, Fernndez EO, Chen D Jakobsen HA (2007) Numerical Investigation of sorption enhanced steam methane reforming using *LiZrO* as a CO-accepter. Ind. Eng. Chem. Res.46:4435-4443

[12] Geankoplis CJ (1993) Transport Processes and Unit Operations, Prentice-Hall International, 3rd edn

[13] Jiang K (1998a) The Least-square Finite Element Method: Theory and applications in Computational Fluid Dynamics and Electromagnetics. Springer, Berlin

[14] Bochev P (2001) Finite Element Methods based on least-squares and modified variational principles. Technical Report, POSTECH

[15] Proot MMJ, Gerritsma MI (2002) A least-squares spectral element formulation for stokes problem. Journal of Scientific Computing 17 (1-4):285-296

[16] De Maerschalck B (2003) Space-time least squares spectral element method for unsteady flows-application and evaluation for linear and non-linear hyperbolic scaler equations. Master Thesis Report, Delft University of Technology, Department of Aerospace Engineering, The Netherlands

[17] Pontaza JP, Reddy JN (2004) Spectral-time coupled spectral/hp least squares finite element formulation for the incompressible Navier-Stokes equation. Journal of Computational Physics 197 (2):418-459

[18] Elnashaie SSEH, Adris AM, Soliman MA, AL-Ubaid AS (1992) Digital Simulation of Industrial Steam Reformers for Natural Gas Using Heterogeneous Models. The Canadian Journal of Chemical Engineering 70 (4):786-793

[19] Oliveira ELG, Grande CA, Rodrigues AE (2009) Steam Methane Reforming in a Ni/$\alpha - Al_2O_3$ Catalyst: Kinetics and Diffusional Limitations in Extrudates . The Canadian Journal of Chemical Engineering 87:945-966

[20] Solsvik J, Jakobsen HA (2011) Modeling of Multi-component mass diffusion in porous spherical pellets: Application to steam methane reforming and methanol synthesis. Chemical Engineering science 66:1986-2000

8th International Conference on CFD in Oil & Gas, Metallurgical and Process Industries
SINTEF/NTNU, Trondheim Norway
21-23 June 2011

CFD11-107

CFD SIMULATIONS AND MEASUREMENTS OF THE INLINE PHASESPLITTER: A COMPACT GAS / LIQUID SEPARATOR

Remko W. WESTRA[*] , **Erica DE HAAS, Oscar F. SALAZAR, Boubker IBOUHOUTEN**

ØT ÔÁ^&@][[*a•ÁÁÔÖÙÁÛ^]æ‡æ‡}ÁÛ•c{•ĂÌGÍTÞÁŒ}@{ĂVÒÁÒVÒÙŠŒÖÙÁ

EÁÒ‡æ‡‡Á^{\[È‡^•¢æÓ-{&æèÈ{{Á

ABSTRACT

The InLine PhaseSplitter is a compact cyclonic separator used for bulk separation of gas and liquid. CFD is an appropriate tool that can be used for further understanding and improvement of the design. Simulations have been performed and compared with experimental results at similar conditions. The simulations are performed in Fluent using the Eulerian multiphase model. The bubble size is estimated using the Levich equation. A similar gas core is seen both the CFD and the experiments. The simulated pressure drop dependency on flow rate shows a similar trend as in the measurements. The simulations under predict the pressure drops by about 30%. The separation performance is somewhat over predicted by the simulations, especially regarding liquid quality. It is concluded that CFD can be used to predict trends in geometry changes and changing process conditions and that it can be improved further by including coalescence and break-up models.

Keywords: Separation, compact, gas/liquid, Eulerian, multiphase, swirling flow, subsea, Fluent.

NOMENCLATURE

Greek Symbols

α	volume fraction, [-].
ε	Turbulence dissipation rate, [m^2/s^3].
μ	dynamic viscosity, [kg/(m.s)]
ρ	density, [kg/m^3].
σ	surface tenstion, [N/m]
τ	stress-strain tensor, [$kg/(m.s^2)$]

Latin Symbols

d	bubble diameter, [m].
gvf	gas volume fraction, [-].
lvf	liquid volume fraction, [-].
p	pressure, [Pa].
t	time, [s].
u	velocity, [m/s].
C_D	drag coefficient, [-]
K	momentum exchange coefficient, [$kg/(m^2.s^2)$]
Re	Reynolds number, [-]
We	Weber number, [-]

Sub/superscripts

crit	critical
g	gas phase
l	liquid phase
max	maximum
32	Sauter-mean
,	fluctuation

INTRODUCTION

In recent years the interest in InLine cyclonic separation devices has grown rapidly, due to its compactness in terms of size and weight, making this type of equipment a very attractive option for offshore platforms and subsea separation applications. These compact separators are mostly based on the principle of generating a swirling flow, resulting in centrifugal forces that induce separation of the light and the heavy phase (gas and liquid). In these devices the force intensity is much larger than in conventional gravity separators, allowing the construction of much more compact equipment.

FMC Technologies / CDS Separation systems has developed such applications for gas/liquid, liquid/liquid, and solids separation (Fantoft et al., (2010) and Kremleva et al., (2010)). One such application is the InLine PhaseSplitter, which is a gas/liquid separator in a pipe segment. In the last two years a optimization program has been carried out for the PhaseSplitter in which many different configurations were investigated both by simulations using Computational Fluid Dynamics (CFD) and by experiments in the lab. All essential components of the PhaseSplitter have been investigated and optimized. The principle of operation of the PhaseSplitter is shown in Figure 1.
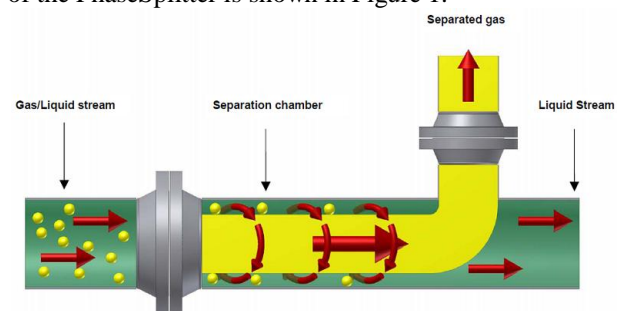

Figure 1: InLine PhaseSplitter operating principle.

The operating principle of the InLine PhaseSplitter is as follows: the incoming gas/liquid mixture is homogeneously mixed inside a mixing element (located upstream of Figure 1). Next, the mixture is put into rotation by a static swirl element. The swirling element consists of several (stationary) curved blades which induce the required rotation for separation. Due to the generated centrifugal force the gas moves towards the centre of the separation chamber, whereas the liquid moves towards the outside. The resulting gas core is extracted via the central gas outlet and the liquid via the liquid outlet.

In this paper we present a CFD simulation of such a unit, using Fluent. First an analysis is made of the generated bubble size inside the PhaseSplitter, which plays an important role in the separation performance. CFD models are presented and discussed next, including multiphase and turbulence model. Furthermore, the experimental setup is discussed followed by a discussion of CFD results including a qualitative and a quantitative comparison with experimental results. Finally, some conclusions are formulated.

BUBBLE SIZE

The bubble size inside the PhaseSplitter is important, since it determines how well the gas and liquid separate. Large bubbles tend to separate fast, whereas small bubble will separate slowly or not all. Bubbles are created in the mixing element where a homogenous mixture of gas and liquid is generated. The turbulence generated by the mixing element can be used to estimate the average bubble size.

According to dispersion theory developed independently by Kolmogoroff (1949) and Hinze (1955) a maximum stable bubble or droplet size, d_{max}, can be determined by the balance between turbulent fluctuations (enabling break-up), and the surface tension force (resisting break-up). The critical We number gives the ratio of these two forces for $d = d_{max}$

$$We_{crit} = \frac{\rho_l u'^2}{\sigma / d_{max}} \qquad (1)$$

Using dispersion theory Hinze derived a general equation to determine d_{max}

$$d_{max} = \left(\frac{We_{crit}}{2}\right)^{0.6} \left(\frac{\sigma}{\rho_l}\right)^{0.6} \varepsilon^{-0.4} \qquad (2)$$

We_{crit} depends on the system. The frequently used constant $(We_{crit}/2)^{0.6} = 0.725$ was derived by Hinze for liquid-liquid dispersions, and is not appropriate for bubbly flows. For a water-air bubbly flow system Hesketh et al. (1987) derived $We_{crit} = 10.6$.

Levich (1962) further refined this theory by accounting for the balance of the internal pressure of the bubble

with the capillary pressure of the deformed bubble. He defines a modified We^* number

$$We^*_{crit} = \frac{\rho_l u'^2}{\sigma / d_{max}} \left(\frac{\rho_g}{\rho_l}\right)^{1/3} \qquad (3)$$

For a water-air bubbly flow system Hesketh derived $We^*_{crit} = 1.1$. The following equation for d_{max} is derived, which differs mainly from the Hinze equation in the fact that the dispersed phase density (in this case the gas phase) is considered.

$$d_{max} = \left(\frac{We^*_{crit}}{2}\right)^{0.6} \left(\frac{\sigma^{0.6}}{\rho_l^{0.4} \rho_g^{0.2}}\right)^{0.6} \varepsilon^{-0.4} \qquad (4)$$

The Sauter-mean diameter d_{32} is a good representation of the average bubble size d_g. According to Kocamustafagullari et al. (1994) it is related to d_{max} by

$$d_{max} / d_{32} = 4.01 \qquad (5)$$

Note that other authors report lower values for the ratio given above. However we decided to use the equation above in order to be conservative, since smaller bubbles tend to separate slower.

The turbulence dissipation rate generated by the mixing element has been investigated as function of the flow rate on a range of 50-100 m^3/h for the current tests by means of CFD. The resulting turbulence dissipation rates are shown in Figure 2.

The data in Figure 2 has been utilized in combination with Eqns. (4) and (5) to estimate the generated bubble sizes in the mixing element. The results are shown in Figure 3. The estimated bubble size d_{32} according to Levich will be used in the CFD modelling, as will be discussed in the next section.
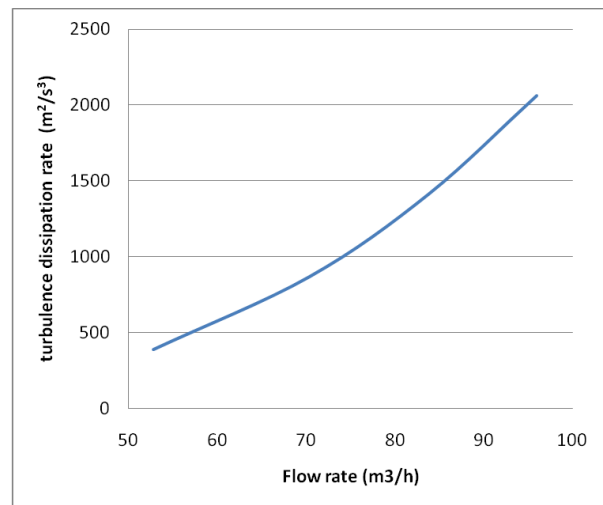
Figure 2: Turbulence dissipation rate downstream of the mixing element as function of the flow rate. Results are generated by CFD simulations (not presented here).
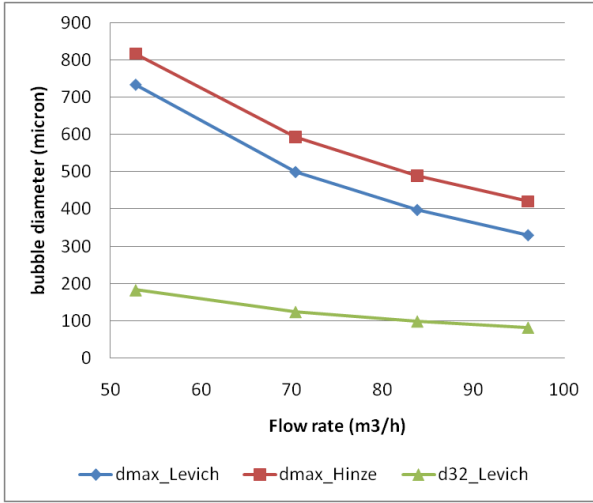
Figure 3: Predicted bubble size generated by the mixing element according to Hinze and Levich using estimated turbulence dissipation at mixing element.

CFD MODELING

A CFD study has been carried out in Ansys Fluent 12.1. The models that have been selected are presented in this section.

The Eulerian multiphase model has been utilized to describe the multiphase flow dynamics inside the PhaseSplitter. In this model the phases are described as interpenetrating continua based on the volume fraction α ($\alpha_g + \alpha_l = 1$). The conservation equations are solved for each phase. The continuity equation for the liquid phase l is given by,

$$\frac{\partial(\alpha_l \rho_l)}{\partial t} + \nabla \cdot (\alpha_l \rho_l \mathbf{u}_l) = 0 \qquad (6)$$

The conservation of momentum for the liquid phase is described by,

$$\frac{\partial(\alpha_l \rho_l \mathbf{u}_l)}{\partial t} + \nabla \cdot (\alpha_l \rho_l \mathbf{u}_l \mathbf{u}_l) = -\alpha_l \nabla p \\ + \nabla \cdot \tau_l + \alpha_l \rho_l g + K_{lg} \qquad (7)$$

The momentum exchange coefficient K_{lg} incorporates the drag force and it is given by the Schiller-Naumann model,

$$K_{lg} = \frac{3\alpha_g \alpha_l \rho_l C_D |\mathbf{u}_g - \mathbf{u}_l|(\mathbf{u}_g - \mathbf{u}_l)}{d_g} \qquad (8)$$

$$C_D = \begin{cases} 24(1 + 0.15\,\mathrm{Re}^{0.687})/\mathrm{Re} & \mathrm{Re} \le 1000 \\ 0.44 & \mathrm{Re} > 1000 \end{cases} \qquad (9)$$

where the Reynolds number is defined by

$$\mathrm{Re} = \frac{\rho_l |\mathbf{u}_g - \mathbf{u}_l| d_g}{\mu_l} \qquad (10)$$

The flow is simulated as incompressible. This is a reasonable assumption since the Mach numbers are

quite low (Ma << 1). However, the gas does expand due to reduction in pressure across the PhaseSplitter ($\Delta p/p \approx$ 0.1-0.2). This effect has not been considered in the current simulations.

The Reynolds Stress Model (RSM) turbulence model has been applied to simulate the turbulence inside the PhaseSplitter. This is a turbulence model accounts for the anisotropy of the swirling flow and has been applied by several others for these kind of applications, see for instance Slot et al. (2010).

At the inlet of the domain a uniform velocity profile is prescribed. The flow is assumed to be homogeneously mixed. The turbulence intensity at the inlet of the domains is set at 5%. At the outlets volumetric flow split boundary conditions are applied, that prescribe the flow split towards the gas and liquid outlet.

The geometry of the PhaseSplitter that is considered is shown in Figure 4. The mixture comes in at the left side and is put into rotation by the swirl element. The gas moves towards the centre of the unit and leaves through the central gas outlet. The liquid moves towards the outside and leaves through the liquid outlet. The mesh consists of 602,078 hexahedral elements.

Figure 4: PhaseSplitter geometry considered.

The CFD simulations are all run in steady state first. Subsequently, they are switched to unsteady mode and run for approximately 5-10 residence times.

Note that simulations are run with a constant bubble size. Coalescence and break-up inside the PhaseSplitter itself, are not considered.

EXPERIMENTAL SETUP

Experiments have been carried out with the PhaseSplitter. For most of these tests a non-transparent PhaseSplitter was used. However, for some lower flow rates a Plexiglas unit was also used, in order to view separation phenomena.
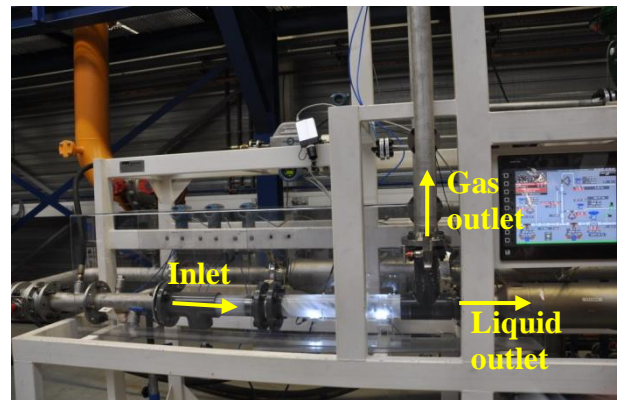
Figure 5: PhaseSplitter test loop near the test unit.

Tests were carried out using water and air at near atmospheric pressures. In Figure 5 a picture of the test setup is shown and in Figure 6 a flow diagram is presented. The incoming gas flow and liquid flow are measured by Coriolis flow meters. The liquid quality at the liquid outlet is measured by using a Gamma density meter. The amount of liquid in the gas outlet is measured by accumulation in a small scrubber. Pressure meters are located at the inlet and outlets of the PhaseSplitter.
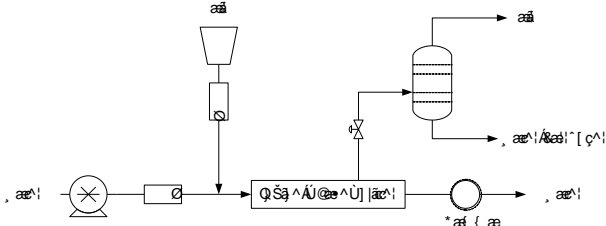
Figure 6: Flow diagram of the experimental test setup.

In the current work we compare the results for experiments and measurements of a small scale PhaseSplitter. The tests were carried out at gas volume fractions (gvf) of 20% and total flow rates of 52.8, 70.4 and 83.8 m^3/h. For these measurements the PhaseSplitter was fabricated in steel. Qualitative transparent measurements were also carried out, but at a lower flow rate of 44 m^3/h.

RESULTS

In this section the results are discussed. We start by making a qualitative comparison between transparent measurements and the CFD simulations. In Figure 7 the gas core inside the PhaseSplitter is shown downstream of the swirl eleme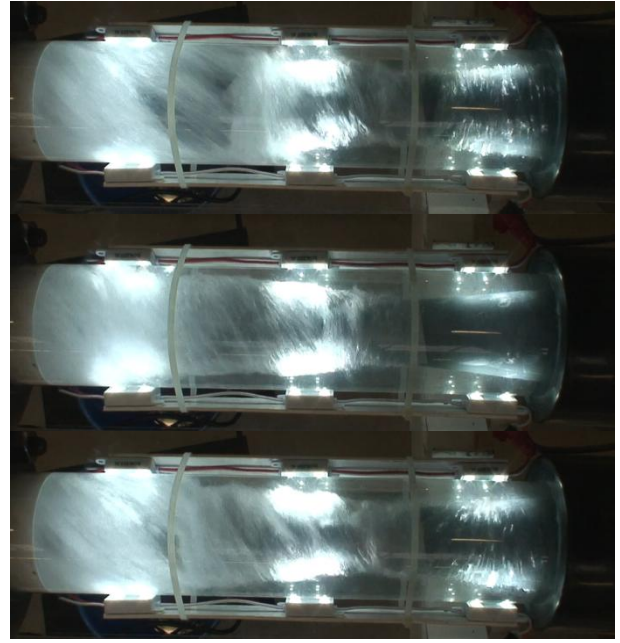nt at three different points in time. It can be seen that the gas core changes a bit in shape in time. This is mainly due to the some pressure fluctuations in the test loop. These pressure fluctuations have a periodic oscillatory nature. This effect is seen to a smaller extend in the CFD simulations.

Figure 7: Gas core, as seen in transparent measurements after 0, 3 and 6 seconds. Total flow rate 44 m^3/h.

The simulation results for the three cases are shown in Figure 8 after approximately 10 residence times. It is observed that the gas core extends a bit further towards the liquid outlet for the higher flow rates. This is most likely due to the reduced bubble size for the larger flow rates. Note that small fluctuations were also seen in the gas core for the numerical simulations, however they were much smaller than observed in the experiments.
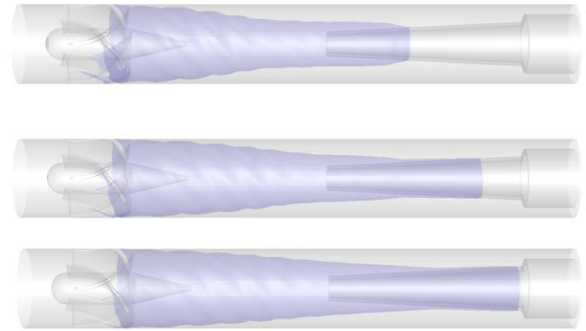
Figure 8: Gas core as simulated by CFD for total flow rates of 52.8 (top), 70.4 (middle) and 83.8 m^3/h (bottom). The gas core is represented by an iso-surface of gvf = 0.1.

There is clearly a good qualitative agreement between the measurements and the CFD simulations. Note that the transparent measurements were carried out at a slightly lower flow rate than the CFD simulations. The main difference between measurements and CFD are the fluctuations in the gas core which were larger in the measurements, than in the simulations. In Figure 9 the gas volume fraction is displayed for the largest flow rate.

4
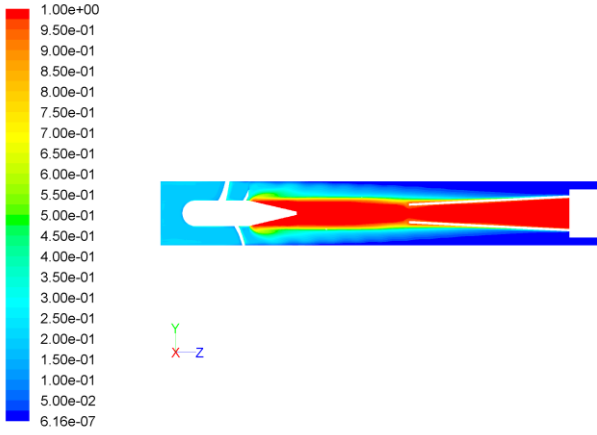
Figure 9: Simulated gas volume fraction distribution for a total flow rate of 83.8 m^3/h.

The axial velocity distribution is shown in Figure 10. It can be seen that downstream of the swirl element in the centre of the tube back flow regions occur (negative axial velocities). Furthermore, the axial velocity increases in radial direction, which is typical for swirling flow applications (see for example Kegge (2000), Kitoh (1991) and Slot et al. (2010)). At the start of the gas outlet a region of large axial velocity is also observed, which is a consequence of the relative small through flow area at that location.
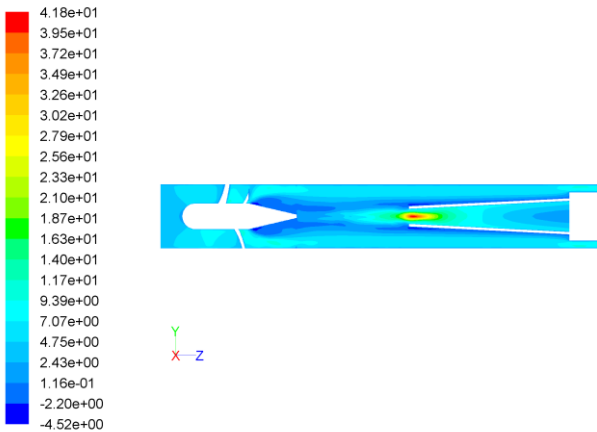
Figure 10: Simulated axial velocity distribution (m/s) for a total flow rate of 83.8 m^3/h.

The tangential (= swirl) velocity distribution is shown in Figure 11. It can be seen that downstream of the swirl element several regions of large tangential velocities are observed. Note that the two regions of large tangential velocity in the centre of the tube are generally not seen for swirling pipe flows, and are most likely a consequence of the location of the gas outlet. This large tangential velocity can have a positive influence on separation, since possible droplets entrained in the gas core could still be separated due to increased centrifugal force.

Figure 11: Simulated tangential velocity distribution for a total flow rate of 83.8 m^3/h.

The turbulence dissipation rate is shown in Figure 12. The turbulence dissipation rate is important, since it dictates the maximum stable droplet and bubble size. Firstly, a region of very large turbulence (> 1000 m^2/s^3) is seen near the gas outlet. This can be responsible for creating small droplets, and could reduce the gas quality at the gas outlet. The large turbulence at the gas outlet is caused by the large (axial) velocities in that region as shown i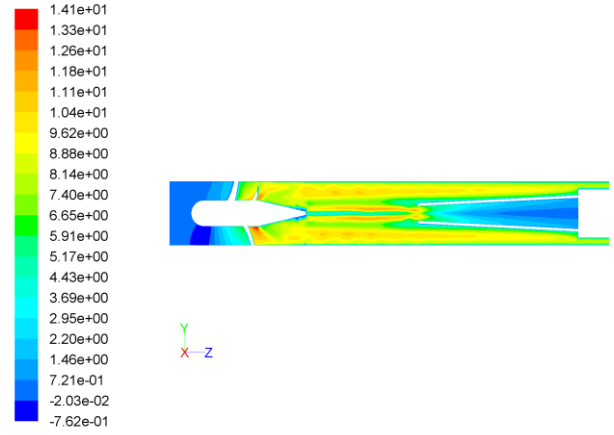n Figure 10. Downstream of the swirl element another region of high turbulence is seen. The turbulence dissipation rate (~800 m^2/s^3) is smaller than what was considered downstream of the mixing element for the same flow rate (~2000 m^2/s^3), see Figure 3), and therefore should not lead to a significant reduction in bubble size and consequently separation performance.
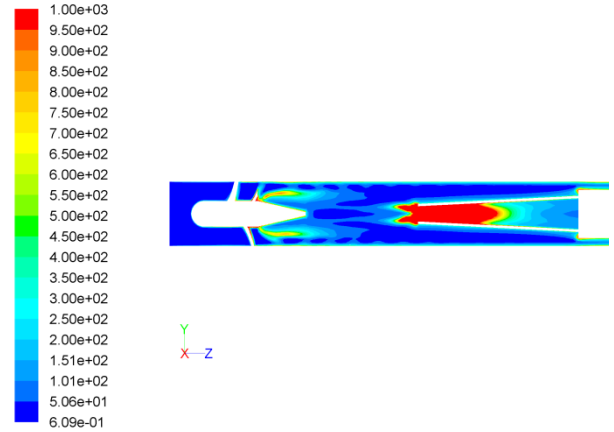
Figure 12: Simulated turbulence dissipation rate (m^2/s^3) for a total flow rate of 83.8 m^3/h. A maximum of 1000 m^2/s^3 is selected.

The pressure distribution inside the PhaseSplitter is shown for the largest flow rate in Figure 13. A characteristic pressure distribution for swirling flows is obtained, i.e. a low pressure region in the centre of the pipe downstream of the swirling element, which increases in radial direction.
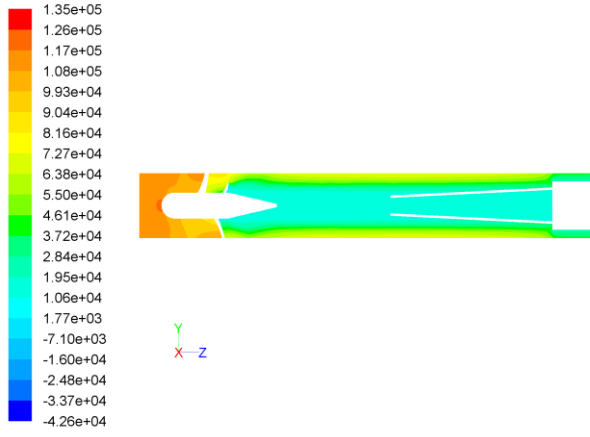
Figure 13: Pressure distribution as simulated by CFD (Pa) for a total flow rate of 83.8 m^3/h.

The pressure drop over the PhaseSplitter is taken from the CFD results and is compared with the measurements in Figure 14. For both measurements and simulations an increasing pressure drop is obtained for an increase in total flow rate. Furthermore, a slightly larger pressure drop over the gas outlet than over the liquid outlet is seen for both. However, the CFD simulations under predict the pressure drop by approximately 30%. The reason for this is discrepancy is unclear, but it could be caused by additional pressure losses downstream of the PhaseSplitter outlets.
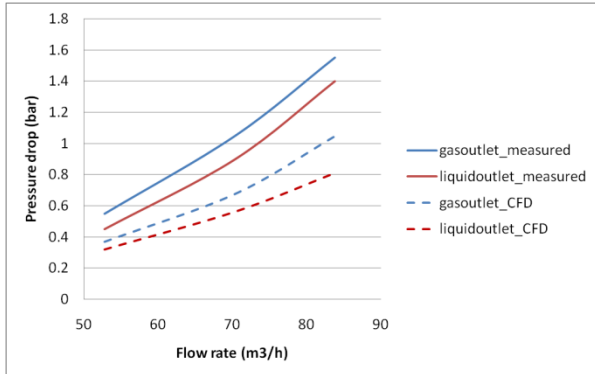
Figure 14: Pressure drop from inlet to gas outlet and from inlet to liquid outlet as simulated by CFD (dashed) and obtained from measurements (solid).

The gas quality and liquid quality are obtained as results of the simulations and they are compared to measurement curves in Figure 15. Note that the measurements have been done for different valve positions, corresponding to different flow splits. The CFD simulations have been performed for a single flow split only. It can be seen that the simulations give a similar gas quality as is seen in the measurements, i.e. between 0-2% liquid volume fraction (lvf). The liquid qualities predicted by the simulations on the other hand are over predicted, with GVF values lower than 0.3%, whereas measurements are in the range of 0.2 - 1.5%.
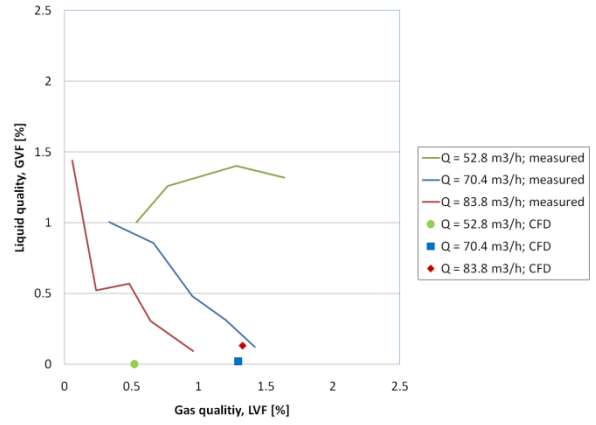

Figure 15: Gas quality at the gas outlet, and liquid quality at the liquid outlet measured for different flow splits, compared with CFD results for a single flow split.

In general it can be said that the CFD simulations over predict the separation efficiency of the PhaseSplitter. One of the explanations for this could be that the simulations are carried out for a uniform bubble size, whereas in reality a bubble size distribution will exist. Small bubbles that are not considered in the simulation are not likely to be separated and hence the CFD over predicts the separation performance. Another reason for the difference is that in the CFD simulations only small fluctuations in the gas core were seen, whereas in experiments larger fluctuations were observed, possibly due to the flow loop, which will reduce the separation performance. Finally, certain physical phenomena like bubble coalescence and break-up are not considered in the simulations. These phenomena are expected to have a significant influence in the separation performance.

CONCLUSION

CFD simulations have been carried out to simulate the multiphase flow inside the InLine PhaseSplitter. The results are compared with measurements. There is good qualitative similarity between the experimental observations and the CFD simulations with regards to the size and shape of the gas core. Furthermore, a similar trend in pressure drop with flow rate is observed for measurements and experiments, both for the gas outlet and the liquid outlet. The CFD under predicts the pressure drop by about 30%.

The separation performance is over predicted by the CFD simulations, especially regarding the liquid quality. Additional investigations are needed regarding the impact of the bubble size distribution and missing physical phenomena on the CFD model.

The pressure and velocity profiles simulated by the CFD are in agreement with general observations for swirling flows. In the centre of the tube a low pressure region is present. The pressure increases radially outward. At the gas outlet a region of large axial velocity and large turbulence is seen. Two regions of large tangential velocity in the centre of the tube are predicted by the CFD simulations. These could be a consequence of the location of the gas outlet, but this is something that still needs to be verified.

The study shows that CFD can be used to analyse the multiphase flow dynamics and separation inside the PhaseSplitter. It is however, difficult to predict the exact separation performance. In the opinion of the authors CFD can be used adequately to analyse differences in geometry and in process conditions. For that reason it is a good tool to use when optimizing geometry and to see the influence of operating pressure and fluid properties.

REFERENCES

ANSYS FLUENT 12, (2009), "Theory guide", Chapter 4 Turbulence, Chapter 16 Multiphase flows.

FANTOFT, R. and AKDIM, M.R and MIKKELSEN, R. and ABDALLAH, T. and WESTRA, R.W. and DE HAAS, E., (2010), "Revolutionizing the offshore production by InLine separation technology", *ATCE 2010*, Florence, SPE 135492.

HESKETH, R.P. and FRASER RUSSEL, T.W. and ETCHELLS, A.W., (1987), "Bubble size in horizontal pipelines", *A.I.Ch.E J.*, **33**(4)**,** 663-667.

HINZE, J.O., (1955), "Fundamentals of hydrodynamic mechanism of splitting in dispersion processes", *A.I.Ch.E J.*, **1,** 289-295.

KEGGE, S.J., (2000), "Numerical simulation of an axial flow hydrocyclone", Delft, The Netherlands.

KITOH, O., (1991), "Experimental study of turbulent swirling flow in a straight pipe", *Journal of Fluid Mechanics*, **225**, 445-479

KOCAMUSTAFAOGULLARI, G. and SMITS, S.R. and RAZI, J., (1994), "Maximum and mean droplet sizes in annular two-phase flow", *Int. J. Heat Mass Transfer*, **37**(6)**,** 955-965.

KOLMOGOROFF, A.N., (1949), *Doklade Akda. Nauk. SSSR*, **66,** 825-828.

KREMLEVA, E. and FANTOFT, R. and MIKKELSEN, R. and AKDIM, M.R., (2010), "InLine technology – New solutions for gas liquid separation", *SPE Russian oil & gas technical conference and exhibition*, Moscow, SPE 136390.

LEVICH, V.G., (1962), "Physicochemical Hydrodynamics", Prentice Hall, Englewood Cliffs, New Jersey.

SLOT, J.J. and VAN CAMPEN, L.J.A.M. and HOEIJMAKERS, H.W.M and MUDDE, R.F., (2010), "Separation of oil droplets in swirling water flow", *ICMF 2010*, Tampa, Florida.

8th International Conference on CFD in Oil & Gas, Metallurgical and Process Industries
SINTEF/NTNU, Trondheim Norway
21-23 June 2011

CFD11-108

INVESTIGATION OF A FRICTIONAL PARTICLE-PARTICLE DRAG COEFFICIENT IN A DENSE BINARY FLUIDIZED BED

Zhongxi Chao [1] , **Yuefa Wang** [1], **Jana P. Jakobsen** [2] **Maria Fernandino** [3], **Hugo A. Jakobsen** [1]

[1] Department of Chemical Engineering, 7491 Trondheim, NORWAY

[2] SINTEF Energy, 7491 Trondheim, NORWAY

[3] NTNU Department of Energy and Process Engineering, 7491 Trondheim, NORWAY

* E-mail: chao@chemeng.ntnu.no

ABSTRACT

Keywords:

NOMENCLATURE

$^{fri}_{ik}$

$_{ik}$

d
d_{ik}
e_{ik}

g_{ik}

m_0

h_{ini}

N^{fri}
n
p
k_g
s

Greek Symbols
α
ρ
Θ
μ

β_{ik}

β_i

ε_g

Subsripts
g
i
k
col
fri
kin
$large$
$small$
Supersripts
max

INTRODUCTION

$$\tau_i = -\left(\left(\nabla v_i \right)^T + \nabla v_i \right) - \nabla \cdot v_i$$

$$p_{col} = \sum_{k=}^{N} \frac{\pi \alpha_k \rho_i \rho_k}{m} \left(+ e_{ik} \right) d_{ik} g_{ik} \left(\Theta_i + \Theta_k \right)$$

$$\mu_{i\,col} = \frac{\sqrt{\pi}}{} \left(+ e_{ik} \right) g_{ik} d_{ik} \frac{\alpha_k \rho_i \rho_k}{m}$$

$$\left(\bar{\Theta}_k + \bar{\Theta}_i - \bar{\Theta}_i \bar{\Theta}_k \right)$$

$$\mu_{i\,B} = \frac{\sqrt{\pi}}{} \left(+ e_{ik} \right) g_{ik} d_{ik} \frac{\alpha_k \rho_i \rho_k}{m}$$

$$\left(\bar{\Theta}_k + \bar{\Theta}_i - \bar{\Theta}_i \bar{\Theta}_k \right)$$

$$q_{i\,kin} \quad \alpha_i k_{i\,kin} \nabla \Theta_i$$

$$k_{i\,kin} = \frac{k_{i\,dilute}}{\frac{}{N} \sum_{k=}^{N} \left(+ e_{ik} \right) g_{ik}} \left\{ + - \sum_{k=}^{N} \alpha_k \left(+ e_{ik} \right) g_{ik} \right\}$$

MODEL DESCRIPTION

$$k_{i\,dilute} = \frac{\rho_i \Theta_i}{\sum_{k=}^{N} \pi \sqrt{\pi} n_k d_{ik} \, \bar{\Theta}_i + \bar{\Theta}_k - \Theta_i \Theta_k}$$

$$q_{col} = -\alpha_i k_{i\,col} \nabla \Theta_i$$

$$\frac{\partial}{\partial t} \left(\alpha_i \rho_i \right) + \nabla \cdot \alpha_i \rho_i v_i =$$

$$k_{i\,col} = \sum_{k=}^{N} \frac{\pi}{m} \frac{\alpha_k \rho_i \rho_k}{m} + e_{ik} g_{ik} d_{ik} \sqrt{\Theta_i}$$

$$\frac{\partial}{\partial t} \left(\alpha_i \rho_i v_i \right) + \nabla \cdot \alpha_i \rho_i v_i v_i = -\alpha_i \nabla p_g -$$

$$\nabla \cdot \left(\tau_{kin} + \tau_{col} + \tau_{fri} \right) + \varphi_i + \beta_i \left(v_g - v_i \right) + \alpha_i \rho_i g$$

$$-\frac{\partial}{\partial t} \left(\alpha_i \rho_i \Theta_i \right) + -\nabla \cdot \alpha_i \rho_i v_i \Theta_i = -\left(\tau_{i\,col} + \right.$$

$$\left. \tau_{i\,kin} + \tau_{i\,fri} \right) : \nabla v_i - \nabla \cdot \left(q_{col} + q_{kin} \right) - \beta_i \Theta_i + \gamma_i$$

$$\gamma_i = \sum_{k=}^{N} \frac{\pi}{} d_{ik} g_{ik} \frac{m_i m_k n_i n_k}{m} \left(e_{ik} - \right) \left(\frac{\sqrt{}}{\sqrt{\pi}} \left(\bar{\Theta}_i + \bar{\Theta}_k \right) + \Theta_i \bar{\Theta}_k + \bar{\Theta}_i \Theta_k \right) -$$

$$\frac{\pi}{} d_{ik} g_{ik} \frac{m_i m_k n_i n_k}{m} \left(e_{ik} - \right) \left(\nabla \cdot v_k \left(\Theta_i + \Theta_k \right) + \nabla \cdot v_i \left(\Theta_k + \Theta_i \right) \right)$$

$$\tau_{kin} \quad \alpha_i \left(p_{i\,kin} \quad \mu_{i\,kin} v_i \right)$$

$$p_{i\,kin} = \rho_i \Theta_i$$

$$\tau_{fri} \quad \alpha_i \left(p_{i\,fri} \quad \mu_{i\,fri} v_i \right)$$

$$\mu_{i\,kin} = \frac{\mu_{i\,dilute}}{\frac{}{N} \sum_{k=}^{N} \left(+ e_{ik} \right) g_{ik}} \left\{ + - \sum_{k=}^{N} \alpha_k \left(+ e_{ik} \right) g_{ik} \right\}$$

$$p_{i\,fri} \begin{cases} F \dfrac{\left(\sum_{i=}^{N} \alpha_i - \alpha \right)^{r}}{\sum_{i=}^{N} \alpha_i \left(\alpha - \sum_{i=}^{N} \alpha_i \right)^{s}} & if \sum_{i=}^{N} \alpha_i > \alpha \\[20pt] & if \sum_{i=}^{N} \alpha_i \le \alpha \end{cases}$$

$$\mu_{i\,dilute} = \frac{\rho_i \Theta_i}{\sum_{k=}^{N} \pi \sqrt{\pi} n_k d_{ik} \, \bar{\Theta}_i + \bar{\Theta}_k - \Theta_i \Theta_k}$$

$$\tau_{i\,col} \quad \alpha_i p_{i\,col} - \sum_{k=}^{N} \alpha_i \left(\mu_{i\,col} S_i + \mu_{i\,B} \nabla \cdot v_i \quad \mu_{k\,col} S_k + \mu_{k\,B} \nabla \cdot v_k \right)$$

$$\mu_{i\,fri} \quad \frac{p_{i\,fri} \sqrt{\varphi}}{\alpha_i \sqrt{v_i : v_i + \Theta_i d_i}}$$

$$\beta_{ik}^{flu} = \frac{m_i m_k n_i n_k}{m} d_{ik} \quad + e_{ik} \ g_{ik}$$

$$\underline{\pi} v_{ik} - \quad v_{ik} \quad \Theta_i \quad + \Theta_k \quad - \quad \Theta_i \quad \Theta_k$$

$\varphi \qquad$ ₒ
F
r
s
α

$$\beta_{ik}^{sym} = \frac{+ e_{ik} \ \pi \ m_i m_k n_i n_k d_{ik} \ g_{ik} C_{fri} v_{ik}}{\left(\rho_i d_i \ + \rho_k d_k \right)}$$

$$\beta_i = \begin{cases} \dfrac{\mu_g \ - \alpha_g \ \alpha_i}{\alpha_g d_i} + \dfrac{\alpha_i \rho_g \left| v_g - v_i \right|}{d_i} & \alpha_g \leq \\[3mm] \dfrac{C_D \rho_g \alpha_i \left| v_g - v_i \right|}{d_i} \alpha_g^{\ -} & \alpha_g > \end{cases}$$

K_{fri}

$$C_D$$

$$C_D \quad \begin{cases} \dfrac{\quad}{\ _{pi}} \Big[\ + \ (\quad _{pi}) \ \Big] & if \quad _{pi} < \\[3mm] & if \quad _{pi} \geq \end{cases}$$

$$\beta_{ik}^{fri} = K_{fri} \ \frac{\pi m_i m_k n_i n_k}{m} d_{ik} \ g_{ik} C_{fri} v_{ik}$$

$$_{pi} = \frac{\alpha_g d_i \rho_g \left| v_g - v_i \right|}{\mu_g}$$

$$k - \varepsilon$$

$$g_k = \left(\ - \left(\frac{\alpha_k}{\alpha} \right)^{\ -} \ \right)^{\ -}$$

$$\frac{\partial}{\partial t} \ \alpha_g \rho_g \ + \nabla \cdot \left(\alpha_g \rho_g \ _g \right) =$$

$$\frac{\partial}{\partial t} \left(\alpha_g \rho_g \ _g \right) + \nabla \cdot \left(\alpha_g \rho_g \ _g \ _g \right) = -\alpha_g \nabla p_g +$$
$$\nabla \cdot \left(\alpha_g \tau_g + \alpha_g \tau \ \right) + \alpha_g \rho_g \ + \sum_k \beta_k \left(\ _k - \ _g \right)$$

$$g_{ik} = \frac{d_i g_i + d_k g_k}{d_i + d_k}$$

$$\frac{\partial}{\partial t} \left(\alpha_g \rho_g k_g \right) + \nabla \left(\alpha_g \rho_g k_g \ _g \right) =$$
$$\nabla \cdot \left(\alpha_g \frac{\mu_g^t}{\sigma_{kg}} \nabla k_g \right) + \alpha_g \tau \quad : \nabla \quad _g \quad \alpha_g S_{kg} - \alpha_g \rho_g \varepsilon_g$$

$$\varphi_i = \sum_{k=}^{N} \beta_{ik} \left(\ _k - \ _i \right)$$

$$\frac{\partial}{\partial t} \left(\alpha_g \rho_g \varepsilon_g \right) + \nabla \left(\alpha_g \rho_g \varepsilon_g \ _g \right) = \nabla \cdot \left(\alpha_g \frac{\mu_g^t}{\sigma_{\varepsilon g}} \nabla \varepsilon_g \right) +$$
$$\alpha_g C \frac{\varepsilon_g}{k_g} \tau \quad : \nabla \quad _g \quad \alpha_g C \frac{\varepsilon_g}{k_g} S_{kg} - \alpha_g \rho_g C \frac{\varepsilon_g}{k_g}$$

$$\beta_{ik} = \beta_{ik}^{pec} + \beta_{ik}^{flu} + \beta_{ik}^{fri}$$

$$\tau_g \quad \mu_g \left(-\left((\nabla \ _g)^T + \nabla \ _g \right) - - \nabla \cdot \ _g \right)$$

$$\overset{ik}{\beta_{ik}^{pec}} = \frac{m_i m_k n_i n_k}{m} d_{ik} \quad + e_{ik} \ g_{ik}$$

$$\left(\ \sqrt{\ \pi} \Theta_i^{\ -} + \sqrt{\ \pi} \Theta_k^{\ -} - \sqrt{\ } \Theta_i \quad \Theta_k \ \right)$$

$$\tau \quad - - \rho_g k_g \quad \mu_g^t \left(-\left((\nabla \ _g)^T + \nabla \ _g \right) - - \nabla \cdot \ _g \right)$$

$$\mu_g^t = \rho_g C_\mu \frac{k_g}{\varepsilon_g}$$

kg   m
mm
C_{fri}
e_{ik}

$$_{kg} = \sum_{k=}^{N} C_b \beta_k \left(v_k - v_g \right)$$

			$k - \varepsilon$		
C_μ	σ_{kg}	$\sigma_{\varepsilon g}$	C	C	C_b

FRICTIONAL DRAG MODEL VALIDATIONS

$$\langle h_i \rangle = \frac{\sum_{cell} \alpha_{i\ cell} h_{cell}}{\sum_{cell} \alpha_{i\ cell}}$$

$$\alpha_{i\ cell}$$

$$h_{cell}$$

$$s = \frac{S -}{S \ -}$$

$$S \qquad S$$

$$S \quad = \quad - x_{small} \qquad - x_{small}$$

$$S = \langle h_{small} \rangle \ \langle h_{l\quad e} \rangle$$

$$x_{small}$$

$$_{i\ z}\big|_{wall} = -\lambda_i \frac{\partial\ _{i\ z}}{\partial n}$$

$$\lambda_i = \frac{d_i}{\alpha_i^{\ /}} \quad _{i\ z}$$

$$s$$

Table 4 Four cases in calculations

Case number	Case 1	Case 2	Case 3	Case 4
Initial bed height H_{ini} ,cm	15	30	15	15
Gas fluidization velocity v_g , m/s	1.1	1.1	1.15	1.15
x_{small}	0.5	0.5	0.5	0.25
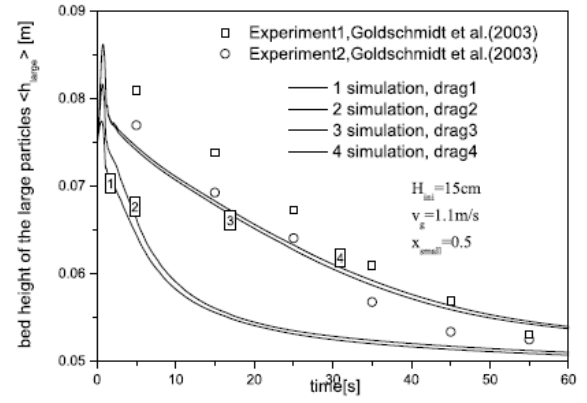
Figure 1c: Bed height of large particles in case 1.

Figure 1a: Segregation rates in case1.

Figure 2a: Segregation rates in case2.

Figure 1b: Bed height of small particles in case 1.

Figure 2b: Bed height of small particles in case 2.

Figure 2c: Bed height of large particles in case 2.

Figure 3a: Segregation rates in case 3.

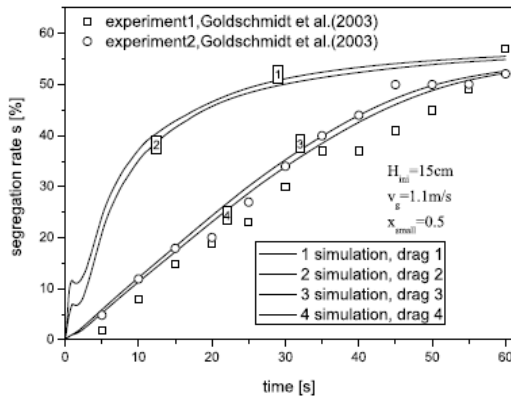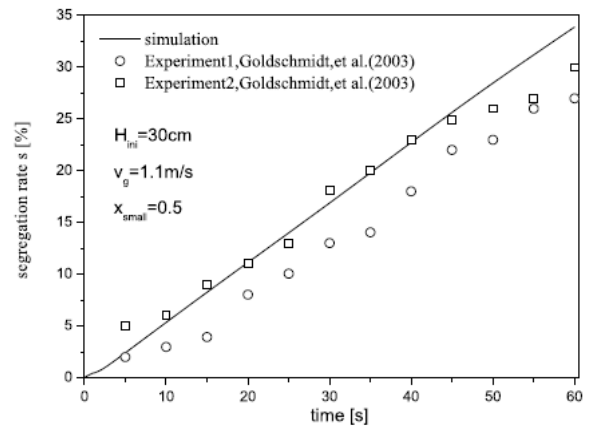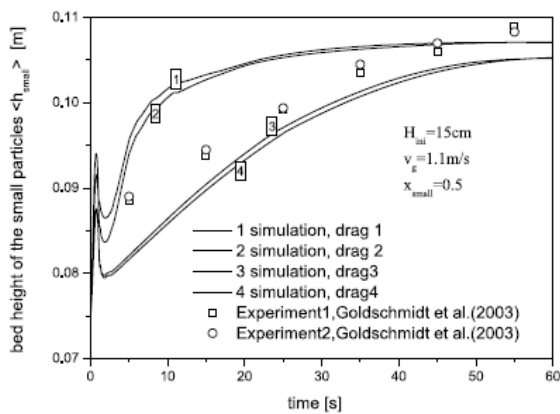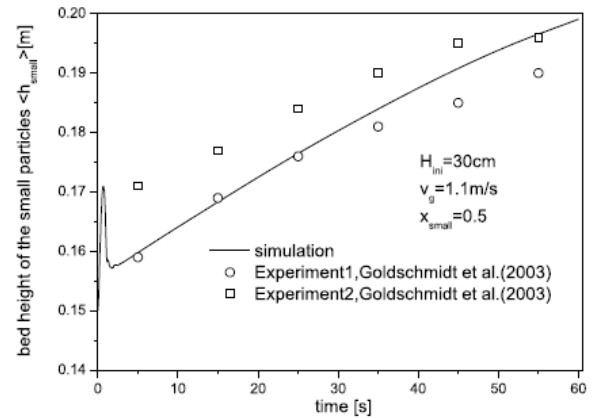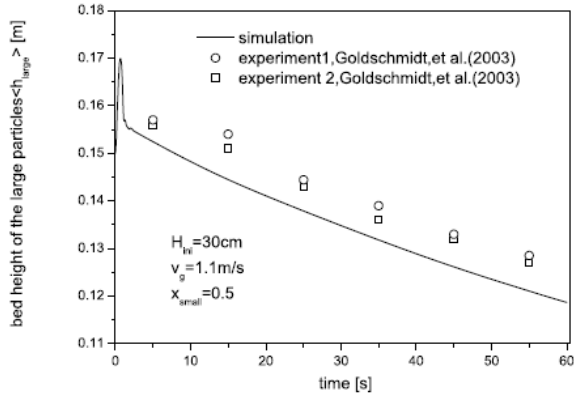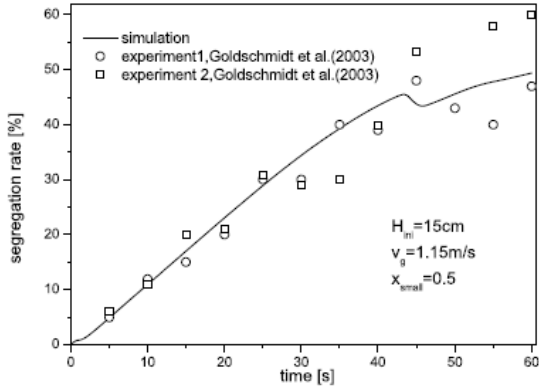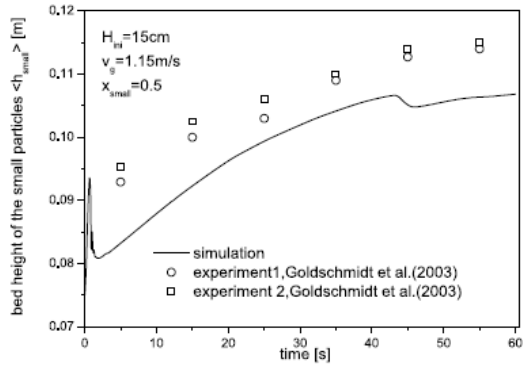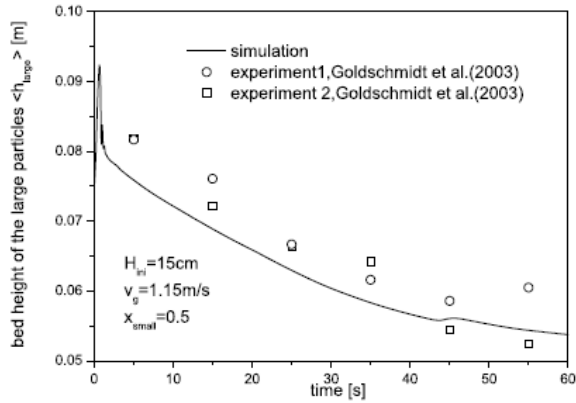Figure 3b: Bed height of small particles in case 3.

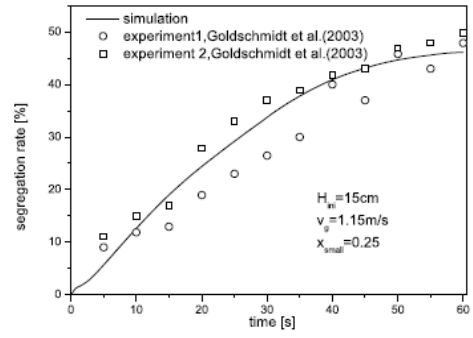Figure 3c: Bed height of large particles in case 3.
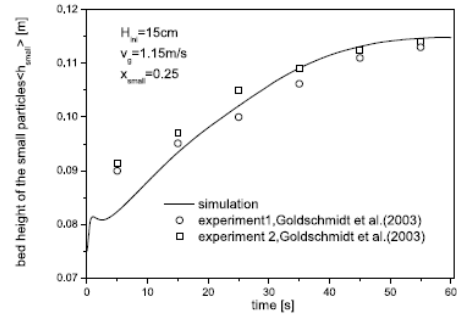

Figure 4a: Segregation rates in case 4.
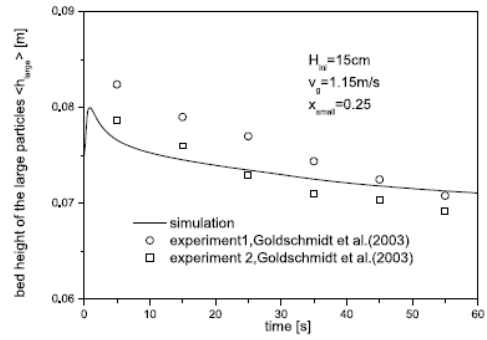

Figure 4b: Bed height of small particles in case 4.

Figure 4c: Bed height of large particles in case 4.

CONCLUSION

REFERENCES

Chemical Engineering Science

8th International Conference on CFD in Oil & Gas, Metallurgical and Process Industries
SINTEF/NTNU, Trondheim Norway
21-23 June 2011

CFD11-109

SOLUTION OF THE POPULATION BALANCE EQUATION USING THE NORMALIZED QMOM (NQMOM)

Menwer ATTARAKIH[1,4,6*] , Jörg KUHNERT [2],Timo Wächtler[3] Mazen Abu-KHADER[1], Hans-Jörg BART[4,5]

[1] AL-BALQA APPLIED UNIVERSITY, Faculty of Eng. Tech. Chem. Eng. Dept.,POB 15008, 11134 Amman, JORDAN
[2] FRAUNHOFER INSTITUT TECHNO- UND WIRTSCHAFTSMATHEMATIK, 67663 Kaiserslautern, GERMANY
[3] FACHBEREICH MATHEMATIK, TU KAISERSLAUTERN, 67653 Kaiserslautern, GERMANY
[4] LEHRSTUHL FÜR. THERMISCHE VERFAHRENSTECHNIK, TU Kaiserslautern, 67653 Kaiserslautern, GERMANY
[5] CENTER FOR MATHEMATICAL AND COMPUTATIONAL MODELING, Kaiserslautern, GERMANY
[6] THE UNIVERSITY OF JORDAN, Faculty of Eng. & Tech. Chem. Eng. Dept., 11942 Amman, JORDAN

* Corresponding author's e-mail: attarakih@yahoo.com

ABSTRACT

This contribution presents a newly transformed population balance equation (PBE), which consists of a set of moment and momentum balances to describe the evolution and motion of particulate systems. In a multidimensional space, the result is a system of partial differential equations, which can be cast into a system of conservation laws with integral source terms. The moment equations are normalized with respect to the total number concentration (zero moment) to avoid numerical instabilities due to the increase stiffness of the quadrature nodes and weights, which is the case in the QMOM and DQMOM. The unclosed integrals over the unknown population density are approximated by a Normalized Quadrature Method Of Moments (NQMOM). The NQMOM makes use of a uniform and adaptive two-weight quadrature, which is of second order accuracy in the regions of smooth distribution and is reduced automatically to a first order accuracy in the sharp regions. The reduced model is tested against known analytical solutions of the homogeneous PBE with respect to space. The NQMOM is integrated successfully into the Finite Point Method (FPM), which is essentially a mesh- free Lagrangian method for modelling and solving complex fluid flow problems.

Keywords: NQMOM, Population balance, CFD, hydrodynamics, mesh free methods.

NOMENCLATURE

Greek Symbols

α Volume fraction, [-].

β Daughter particle distribution, [1/m].

Γ Breakage frequency, [1/s].

ζ Spatial coordinate, [m].

ρ Mass density, [kg/m^3].

σ Surface tension, [N/m].

$\hat{\sigma}, \sigma'$ Population variances, [N/m].

λ Quadrature weight, [1/m^3].

μ Moment, [depends on moment order].

$\hat{\mu}$ Normalized moment, [depends on moment order].

ω Aggregation frequency, [m^3/s].

Latin Symbols

C_D Drag coefficient, [-].

d_{30} Mass-number mean particle diameter , [m].

f Number density per unit volume, [1/m^3].

$\mathbf{g}$ Acceleration of gravity, [m/s^2].

p Pressure, [Pa].

S Population balance source term, [depends on moment order].

t Time, [s].

$\mathbf{u}$ Velocity, [m/s].

v Particle size, [m^3].

Sub/superscripts

c continuous phase.

d dispersed phase.

r moment index.

j quadrature index.

INTRODUCTION

The population balance equation finds many scientific and engineering applications with mono and multivariate number density functions. Such applications include multiphase flows and turbulence modelling, aerosol science and kinetic theory and biological and biomedical engineering (McGraw, 1997, Ramkrishna, 2000, Piskunov and Golubev, 2002, Hjortso, 2004, Rosner et al., 2004, Marchisio and Fox, 2005, Raikar et al., 2006, Attarakih et al., 2009a, b, Strumendo and Arastoopour, 2009,Fox, 2008, 2009) Fluid phases which are discrete either at the molecular

or particle level can be described by a statistical Boltzmann-type equation, which is called the population balance equation (PBE) (Ramkrishna, 2000, Fox, 2008]. The PBE determines the temporal and spatial evolution of particle distribution due to the interactions within the population of particles on the one hand, and the interaction of particles and the continuous phase in which they are imbedded on the other hand (Ramkrishna, 2000). The PBE is a hyperbolic integro-partial differential equation characterized by a nonlinear integral source term. This source term accounts for various mechanisms with which particles of a specific state can either form or disappear from the system. These mechanisms are discrete and relatively instantaneous compared to the system scale such as particle breakage, aggregation, growth and nucleation (Rankrishna, 2000). These interactions can describe the system behavior up to any degree of detail. Thus, such population balance models are very suitable for understanding and investigating many single processing units, not to mention, crystallizers, turbulent flame reactors, polymerization reactors, bubble phase reactors, and extraction columns (Motz, 2002, Rosner, 2006, Abedini and Shahrokhi, 2008, Drumm et al., 2010).

Computational Fluid Dynamics (CFD) methods used with great success to explore the detailed flow fields in a very complex real geometry with an obvious need to detailed modeling of the dispersed phase. The excessive computational burden placed by including the population balance equation as a dispersed phase modeling tool limits such benefits even with super speed computers (Motz, 2002, Rosner, 2006, Fox, 2008, Tiwari et al., 2008, Drumm et al., 2010). Therefore, there is an engineering need to have a simple reduced model for discrete phases, without losing the detailed description of single phenomena inherently embedded in the population balance equation. One of the popular model formulations is the transformation of the population balance equation into a set of self-contained integral equations that describe the moments' evolution of the particle size distribution. In general, these methods belong to the moment transformation of the population balance equation at the expense of destroying the distribution itself (McGraw, 1997, Ramkrishna, 2000, Piskunov and Golubev, 2002, Marchisio and Fox, 2005, Drumm et al., 2010). In contrast to the classical method of moments, where closure problem is overcome by a priori assumed distribution or simplified kernel functions (Ramkrishna, 2000, Diemer and Olson, 2002), the Quadrature Method Of Moments (QMOM) provides not only an efficient closure to the moment problem, but also an extremely efficient Gauss-like integration quadrature. For critical evaluation and improvements in the QMOM literature, the reader can consult Grosch et al. (2007) and Attarakih et al. (2009a). The QMOM is based on the known low-order moments of the weight function (here in the population balances equation it is the unknown distribution) and requires only few nodes (two or three) to converge, even for sharply changing integrands. In general, the QMOM or the moment transformed population balance equations have the advantage of using small number of equations and at the same time

use less degree of details required by the physical model. This is because the calculation of most average physical properties of the particulate phase do not require a full knowledge of the size distribution. This is in particularly true for properties most relevant to engineering applications such as mean particle size, mean surface area, and average dispersed phase holdup (Piskunov and Golubev, 2002, Attarakih et al., 2006, Drumm et al., 2010).

However, the QMOM and its variants (e.g. DQMOM) suffer from numerical instabilities (Su et al., 2008, Attarakih et al., 2010) when large variation in the moments is encountered or the population tends to a monosize distribution. In both QMOM and the DQMOM an inevitable division by the zero moment is needed during the course of the moment inversion problem. As a result of this, coupling the PBE with CFD solvers results in a serious initialization problems where subregions in the physical space are not occupied by the dispersed particles. This usually causes either numerical instabilities or non physical solutions, which usually alleviated by an ad hoc problem dependent procedures (Marchisio, & Fox 2005). In this work, we introduce the normalized adaptive QMOM of first and second order accuracy in the sense of uniform Gauss-Christoffel quadrature. This avoids the division by the zero moment and adapts automatically to a first order quadrature when the population of particles tends to a monosize distribution. The reduced population balance model is written for the population balance itself and for the momentum balance to describe the motion of the particulate phase. Due to the normalized nature of the moment equations, and the nature of the normalized closure rule, the method is given the name: The Normalized QMOM or shortly: NQMOM. The NQMOM is first tested against known analytical solutions of the homogeneous population balance equation (w.r.t. space) and then integrated into the Finite Point Method (FPM) (Tiwari et al., 2008) as a mesh-free Lagrangian CFD modelling and simulation environment.

THE POPULATION BALANCE EQUATION

The superstructure of the population balance equation and its general derivation based on the Reynolds transport theorem is give in Ramkrishna (Ramkrishna, 2000). This transport equation can be written as

$$\frac{\partial f}{\partial t} + \nabla \cdot \left(\mathbf{u} f \right) = S \qquad (1)$$

In the most general way, the particles are assumed to have a spectrum of sizes, which can be represented by a number density function per unit volume of physical space with the particle size (volume) as an independent variable. So, let $f(v, \zeta, t) dv$ be the average number of particles per unit volume of a fixed subspace at time t, then the above population balance equation can be formally interpreted as follows: The first term on the left-hand side denotes the accumulation of particles having size v, the second term is the convection of particles along the physical coordinate ζ and the source

term on the right-hand side represents the net number of particles produced due to breakage and aggregation per unit time and volume of the physical space.

The source term for particle breakage and aggregation is given by Eq.(2) below. In this equation the first two terms represent particles, which are lost and formed by breakage with frequency (Γ) and the second two terms accounts for loss and formation of particles due to binary aggregation of two particles having sizes v and v' with collision frequency ω.

$$S = -\Gamma f + \int_v^\infty \Gamma(v',\zeta,t)\beta(v\,|\,v')f(v',\zeta,t)dv'$$

$$+\frac{1}{2}\int_0^v \omega(v.v',\zeta)f(v-v',\zeta,t)f(v',\zeta,t)dv' \qquad (2)$$

$$-\int_0^\infty \omega(v.v',\zeta)f(v,\zeta,t)f(v',\zeta,t)dv'$$

The particle size distribution due to breakage of mother particle of size v' is given by $\beta(v|v')$. This distribution should satisfy number and mass conservation constraints (Ramkrishna, 2000).

The Moment Equations

The moments (μ_r) per unit volume of subspace with respect to particle size v is defined as

$$\mu_r = \int_0^\infty v^r f dv \qquad (3)$$

Applying this moment transformation to Eqs.(1) and (2) one gets the following set of moment equations:

$$\frac{\partial \mu_r}{\partial t} + \nabla \cdot \left(\overline{\mathbf{u}}\mu_r\right) = S_r, \quad r = 0,1,.... \qquad (4)$$

Where $\overline{\mathbf{u}}$ is the average velocity of particles conditioned on mean particle size d_{30}. Here d_{30} is the mass-number average mean particle diameter, which is an adaptive one-node Gauss quadrature (see Eq.(9) below) (Attarakih et al., 2008, Drum et al., 2010). The transformed source term (Eq.(2)) is given by:

$$S_r = \int_0^\infty v^r \Gamma f (\pi_r - 1)dv$$

$$+\frac{1}{2}\int_0^\infty \int_0^\infty \omega f(v)f(v')f(v)\times \qquad (5)$$

$$\left[(v^r + v'^r) - v^r - v'^r\right]dvdv'$$

where $\pi_r = \int_0^{\min(v,v')}\left(\dfrac{v}{v'}\right)^r \beta(v\,|\,v')dv$.

This transformed source is consistent in conserving total number of particles ($r = 0$) and total volume (mass) when $r = 1$.

Note that the above source term can't be closed (written in terms of μ_r) due the open form of breakage and coalescence frequencies (ω and Γ). Actually, there is only a few cases when these frequencies result in a

closed source term with respect to the low order moments appearing in Eq.(4). The standard QMOM (McGraw, 1997) provides an effective closure to the source term without paying much attention to the form of the number density function f. The QMOM assumes f to be represented by a sum of Dirac delta functions with adaptive nodes and weights that are expressible in terms of the low-order moments (μ_r). The numerical solution for these weights and nodes is called the inversion of the moment problem and is accomplished using the Product Difference algorithm (PDA) as proposed by McGraw (1997). The PDA proceeds in constructing a symmetric positive definite matrix from the low-order moments, which unfortunately rather involved in terms of division by many low-order moments. The adaptive nodes and weights of the aforementioned Dirac delta functions are obtained numerically by solving a stable eigenvalue problem as long as the low-order moments satisfy certain determinant conditions and are not close to zero (Attarakih et al., 2010). To shed more light on this problem, we present here the analytical expressions for the weights of the two-point quadrature derived by Attarakih et al. (2009a):

$$\lambda_{1,2} = \mu_0 \left(\frac{\sigma'}{v_m - v_{1,2}}\right)^2 \frac{1}{1 + \sigma'/[v_m - v_{1,2}]^2} \qquad (6)$$

In the above equation v_m is the mean particle size, $v_{1,2}$ are the two nodes of the adaptive Gauss quadrature and σ'^2 is the population variance. Here, the PDA fails when the particle size distribution becomes very narrow ($v_{1,2} \to v_m$) and suffers heavily from numerical round-off errors due to loss of significance even when double precision arithmetic is used. The second issue is that the population variance σ'^2 becomes unbounded for small values of μ_0 and the algorithm fails completely in the subspaces where the population density tends to zero. The same difficulties are also found in the nodes' formulas. This calls for an ad hoc procedures to avoid division by zero and to keep a finite mean particle size to be used in predicting the mean particle velocity as predicted by the momentum balance (Marchisio & Fox, 2005). The source term for the momentum balance depends on the particle diameter due to the interfacial momentum transfer (drag force) as follows:

$$\rho_d \alpha_d \frac{D\mathbf{u}}{Dt} = -\alpha_d \nabla p + \alpha_d (\rho_d - \rho_c)\mathbf{g} - \mathbf{F}_d \qquad (7)$$

Where ρ_c and ρ_d are the densities of continuous and dispersed particles respectively, α_d is the volume fraction of the dispersed phase, p is the pressure shared by both phases, $\mathbf{g}$ is the gravitational vector and the mean drag force felt by the population of particles is given by:

$$\mathbf{F}_d = \frac{3}{4}\rho_c \int_0^\infty \frac{v(d)}{d} fC_D(d)|\mathbf{u} - \mathbf{u}_c|(\mathbf{u} - \mathbf{u}_c)\partial d$$

$$\approx \frac{3}{4}\rho_c \frac{\alpha_d}{d_{30}} fC_D(d_{30})|\overline{\mathbf{u}} - \mathbf{u}_c|(\overline{\mathbf{u}} - \mathbf{u}_c) \qquad (8)$$

Here $\mathbf{u}_c$ is the velocity of the continuous phase and C_D is the drag coefficient. So, in the subspaces of the flow domain where the local number density function is small, numerical instabilities are more likely to occur due to difficulties in computing the mass-number mean particle diameter (Drum et al., 2010):

$$d_{30} = \sqrt[3]{\frac{6}{\pi} \frac{\mu_1}{\mu_0}} \qquad (9)$$

By examining the above equation the difficulties in computing the mass-number mean diameter due to small values of μ_0 can be overcome if the normalized moment $\widehat{\mu}_1 = \mu_1 / \mu_0$ can be computed directly. This calls for tracking the low-order normalized moments rather than the low-order moments themselves to avoid numerical inaccuracies due to division by small values. So, the normalized QMOM (NQMOM) comes to fulfil this task.

THE NORMALIZED QMOM

To facilitate the derivation of the normalized moment equations, Lagrangian frame of reference is used, where Eq.(4) can be written as:

$$\frac{D\mu_r}{Dt} + \mu_r \nabla \cdot (\overline{\mathbf{u}}) = S_r, \quad r = 0,1,.... \qquad (10)$$

The normalized total derivative can be written as:

$$\frac{D\widehat{\mu}_r}{Dt} = \frac{D\mu_r}{Dt} - \frac{\widehat{\mu}_r}{\mu_0} \frac{D\mu_0}{Dt} \qquad (11)$$

Now, by combining Eqs.(9) and (10) on gets the following normalized moment equations:

$$\frac{D\widehat{\mu}_r}{Dt} + \widehat{S}_0 \widehat{\mu}_r = \widehat{S}_r, \quad r = 1,2,.... \qquad (12)$$

To reconstruct the non-normalized moments from the normalized ones ($\mu_r = \mu_0 \widehat{\mu}_r$), one needs a transport equation for the zero moment; which can be obtained from Eq.(10) by setting $r = 0$.
The source term given by Eq.(5) normalized with respect to the zero moment can be written using the standard idea of the QMOM ($f = \sum_{j=1}^{N_q} \lambda_j \delta(v - v_j)$) as follows:

$$\widehat{S}_r = \frac{1}{\mu_0} \sum_{j=1}^{N_q} \lambda_j \Gamma_j \left(\pi_{r,j} - 1\right)$$
$$+ \frac{1}{2\mu_0} \sum_{j=1}^{N_q} \sum_{m=1}^{N_q} \lambda_j \lambda_m \omega_{j,m} \left[(v_j + v_m)^r - v_j^r - v_m^r\right] \qquad (13)$$

Unfortunately, the last equation introduces a stiff source term to the normalized moment equations (Eqs.(12)). To overcome this problem, an equal-weight quadrature can be used for which $\lambda_1 = \lambda_2 = ... \lambda_{Nq} = \mu_0/N_q$.

Accordingly, Eq.(13) is reduced to:

$$\widehat{S}_r = \frac{1}{N_q} \sum_{j=1}^{N_q} \Gamma_j \left(\pi_{r,j} - 1\right)$$
$$+ \frac{\mu_0}{2N_q^2} \sum_{j=1}^{N_q} \sum_{m=1}^{N_q} \omega_{j,m} \left[(v_j + v_m)^r - v_j^r - v_m^r\right] \qquad (14)$$

Where N_q is the number of quadrature nodes. In this work, only the one and two-point equal weight quadratures are introduced. The weight of the one-point quadrature ($N_q = 1$) is μ_0 and its node is given by Eq.(9), while the weights of the two-weight quadrature are: $\lambda_1 = \lambda_2 = \mu_0/2$. The two nodes represent the fluctuation of the particle size around its mean:

$$v_{1,2} = \widehat{\mu}_1 \pm \widehat{\sigma},$$
$$\widehat{\sigma} = \widehat{\mu}_2 - \widehat{\mu}_1^2 \qquad (15)$$

It is interesting to note that Eqs.(15) are reduced to the one-point quadrature when $\widehat{\sigma}$ tends to zero (monosize distribution). This makes the quadrature given by Eqs.(15) an adaptive integration quadrature. This desirable property does not exist in the standard QMOM or DQMOM, where the PDA or the direct computation of the quadrature nodes fail for this particular case.
The mean mass of the population as calculated using Eq.(15) is nothing more than the arithmetic mean of v_1 and v_2 (the two quadrature nodes). Based on this, the mean population diameter is again given by Eq.(9). This justifies the use of d_{30} as the mean particle diameter when closing the mean drag force given by Eq.(8).
Note that despite the low-order approximation of the number density f, the one-point quadrature offers the two-equation reduced population balance model, which was able for the first time to simulate a fifty-compartment pilot plant extraction column using commercial CFD software FLUENT 6.6 (Drum et al., 2010).

NQMOM-FPM COUPLED SOLVER

In this section, we describe briefly the coupled NQMOM-FPM solver as a first attempt to test in a rigours way the applicability of the NQMOM when coupled to detailed CFD solvers. The Finite Point Method (FPM) is essentially a mesh-free Lagrangian numerical method for solving fluid Dynamic equations (Tiwari & Kuhnert, 2007). The basis of computation is a point cloud, which referred to as particles or numerical grid points. These numerical particle are allowed to move with fluid velocity, and they carry all relevant physical information. The point cloud represents the flow field and is initially distributed to cover the whole computational domain. The distribution of numerical points should fulfil certain adaptive criteria; that is, particles are not allowed to cluster (provide more

information than necessary) or to form holes (to find sufficient neighbours to exchange information). The point cloud is a geometrical basis, which allow FPM to be a general finite difference idea. FPM is a strong formulation technique for modelling partial differential equations by direct approximation of the differential operators. The method uses a moving least-square idea, which was especially developed for FPM. The continuous phase is modelled by the Navier-Stokes equations. The motion of the particulate phase is described by the equation of motion in which inertia, drag and buoyancy forces are taken into account (see Eq.(8)).

The coupling strategy of the NQMOM with the FPM is as follows: Separate point clouds are established for each phase. The continuous and particulate phases are solved using their respective point clouds. These point clouds are decoupled from each other; however, the necessary information like velocities, volume fractions etc. are exchanged between these clouds. Concerning the PBE, a two-way coupling is achieved in which the mean particle diameter (d_{30}) is calculated on the PBE solver side using the NQMOM and returned to the FPM side to evaluate the mean drag force and hence the particulate mean velocity (**u**) as given by Eq.(8). For more details about FPM the reader can consult Tiwari and Kuhnert (2007) and the references therein.

NUMERICLA RESULTS AND DISCUSSION

In this section, the normalized QMOM is tested first using the homogeneous population balance equation with respect to space. This is to compare the results with the available standard analytical solutions for the homogeneous PBE. Secondly, the normalized moment equations are coupled with the FPSM (Finite Point Set Method) CFD solver in a simple geometry to test the robustness of the NQMOM population balance solver.

The Homogeneous PBE

To test the NQMO against available analytical solutions, particle aggregation with constant aggregation frequency is simulated in a one homogeneous spatial cell. For this case, Eq.(12) is reduced to a set of ordinary differential equations in the absence of the spatial derivative (convection part). Fig.(1) presents sample of the numerical results using two-equal weight quadrature. The numerical results are indistinguishable from the analytical solution (Gelbard and Seinfeld , 1978). The ODEs describing the evolution of the normalized moments are found nonstiff and are solved easily using a general purpose ODE solver. Note that no divisions by μ_0 is required, which enhances the stability of the numerical solver.

In Fig.(2), particle aggregation with sum aggregation frequency ($\omega = v + v'$) is simulated using the NQMOM as a closure rule. This case is known to be difficult to simulate even using the analytical solution itself. This is due to the sharp increase of the moments as function of dimensionless time. The analytical solution (Seinfeld, 1978) involves Bessel function, which becomes unbounded for long simulation time. Despite this fact, the NQMOM simulates successfully this case without any notable problem concerning the ODE solver. The

direct computation of d_{30} using Eq.(9) is straight forward and does not need checking for small values of μ_0.
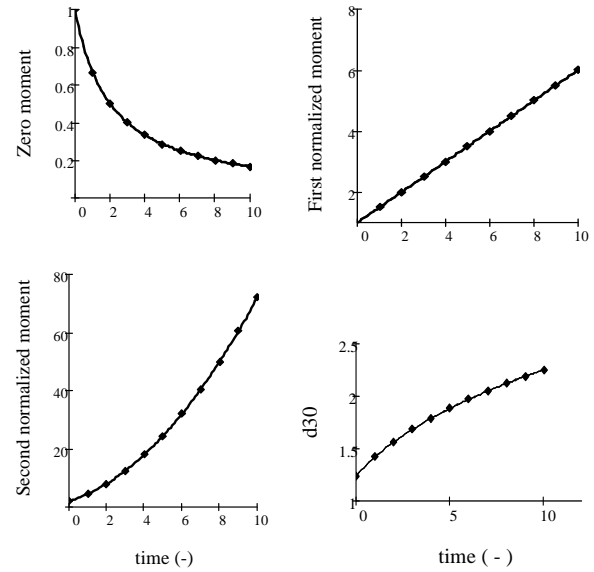
Figure 1: Evolution of zero, normalized first, second order moments and the mean particles diameter (d_{30}) for constant particle aggregation frequency in a one homogeneous spatial cell using a two-node quadrature as function of normalized time. Sold lines and dots are analytical and numerical solutions respectively.
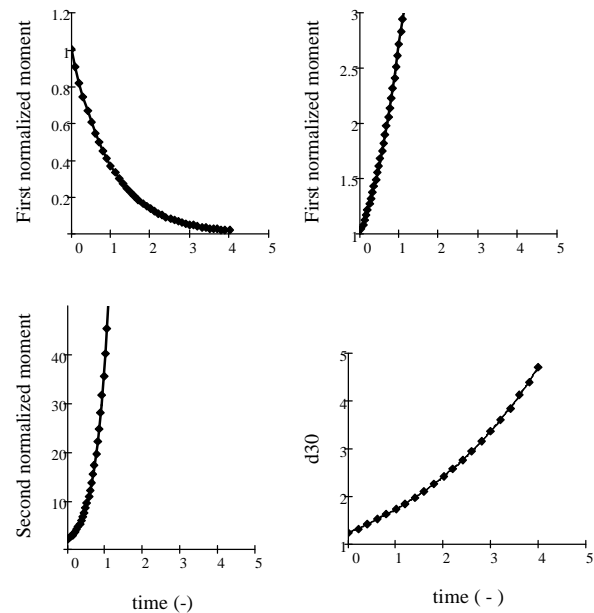
Figure 2: Evolution of zero, normalized first, second order moments and the mean particles diameter (d_{30}) for sum particle aggregation frequency in a one homogeneous spatial cell using a two-node quadrature as function of normalized time. Sold lines and dots are analytical and numerical solutions respectively.

Fig.(3) shows the simulated results for the case of particle breakage in a homogenous spatial cell. The evolution of the normalized moments and the mean

particle diameter is predicted accurately with small error in the second normalized moment. Since the second-order quadrature is exact for polynomial integrands up to degree two (one weight and two nodes are used), this error may be attributed to the accumulation of round off errors due to the very small values of the second normalized moments. Nevertheless, the accuracy of the mean particle diameter is not affected as can be seen from the last panel of Fig.(3).

Therefore , coupling of the NQMOM and FPM will not be affected since it depends only on the mean droplet diameter d_{30}. It is worthmentioning that when using only one point quadrature, the QMOM yields exact solution for many popular breakage and aggregation frequencies as shown by Attarakih et al. (2009a).

Figure 3: Evolution of zero, normalized first, second order moments and the mean particles diameter (d_{30}) for particle breakage (Γ = v and β = 2/v') in a one homogeneous spatial cell using a two-node quadrature as function of normalized time. Sold lines and dots are analytical and numerical solutions respectively.
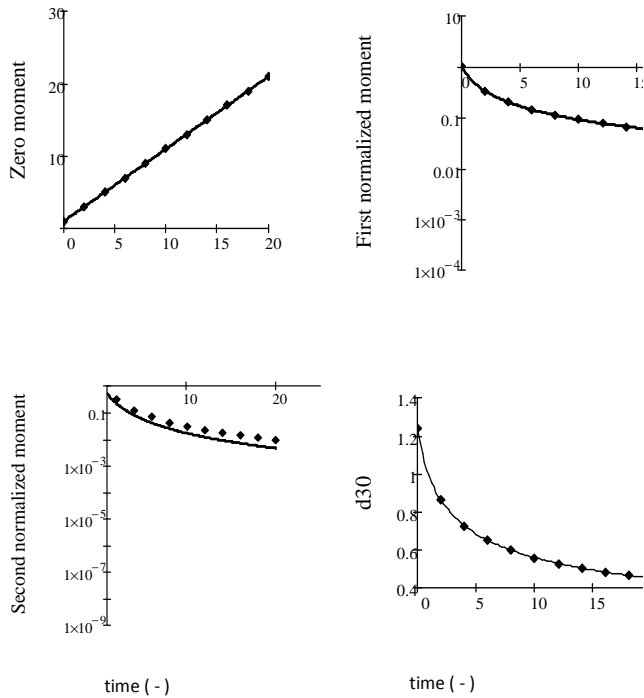
Coupling of the NQMOM to FPM CFD solver

As mentioned previously , coupling of the PBE based on the QMOM or the DQMOM needs careful computation of the mean particle size in order to compute the average velocity of the particulate phase.

In spite of the reliability of the two-unequal weight quadrature described above, it collapses when the population function tends to a monosize distribution and it sufferss from serious round-off errors when the distribution becomes very narrow. This problem is inherited from the PDA itself due to the use of many quantities suffering from loss of significance. Therefore,, the simplicity and accuracy (subjected to less round-off error) are behind the formulation of the NQMOM using an equal-weight quadrature. The

numerical algorithms for solving the transport equations (continuity, momentum & population balance equations) are similar to that described in our previous work (Tiwari et al., 2008) and implemented within the FPM software environment. FPM is an in-house software belonging to Fraunhofer Institute for Industrial Mathematics, where access to the source code is permitted.

In this section, the coupling of the NQMOM to the FPM software is tested using a two-dimensional representation of a liquid spray chamber. A simplified geometry of the chamber, shown in Fig.(4), has a length to diameter ratio L/D = 2. The cross-sectional area is 0.5 m^2. Water is the continuous phase flowing from top to bottom with a velocity of 0.1 m/s. The particulate phase (dispersed phase) is toluene and introduced from the bottom of the chamber at a flow rate of 200 litre/h using a distributer immersed in the continuous phase. The inlet velocity of droplets is estimated from the peak terminal velocity equation for droplets formed at the tip of the nozzles immersed in the continuous phase (Lo et al. , 1983):

$$u_{in} = c\left(\frac{\sigma(\rho_c - \rho_d)g}{\rho_c^2}\right)^{1/4} \qquad (16)$$

where c is an empirical constant of magnitude 1.59 and σ is the interfacial tension. The mean size of these liquid droplets is taken as 5 mm (same as the distributer holes).

Figure 4: Schematic diagram of spray chamber geometry.

The physical properties used in the simulation are those of the toluene -water system at 25 °C. To determine the boundary conditions of the system and by referring to Fig.(4), the following scheme is applied. On the left side of the spray chamber, the inflow boundary of the particulate phase is defined and the rest is no-slip boundary for the this phase. The outflow boundary is considered for the continuous phase. On the right side inlet, the inflow boundary for the continuous phase is defined and the rest is the no-slip boundary for the this phase. Two-point clouds are dedicated for the continuous and dispersed phase respectively with total number of particles around 13300. This number is not fixed and used only to satisfy the following required criteria :" no cluster and no holes are allowed in FPM". In this work, only one-point quadrature (equivalent to one population balance numerical particle) is used to estimate the unclosed integrals appearing in the source terms of the normalized moment equations and the mean drag force appearing in the momentum balances for both phases. This is equivalent to the two-equation model developed in our previous work and used

successfully to simulate a full pilot plant extraction column (Drum et al., 2010).

Fig.(5) shows the evolution of the mean particle diameter (d_{30}) as represented by a cloud of moving

$v_c = 0.1$ m/s, $t = 2$ s

$v_c = 0.0$, $t = 2$ s

$v_c = 0.1$ m/s, $t = 8$ s

$v_c = 0.0$, $t = 8$ s
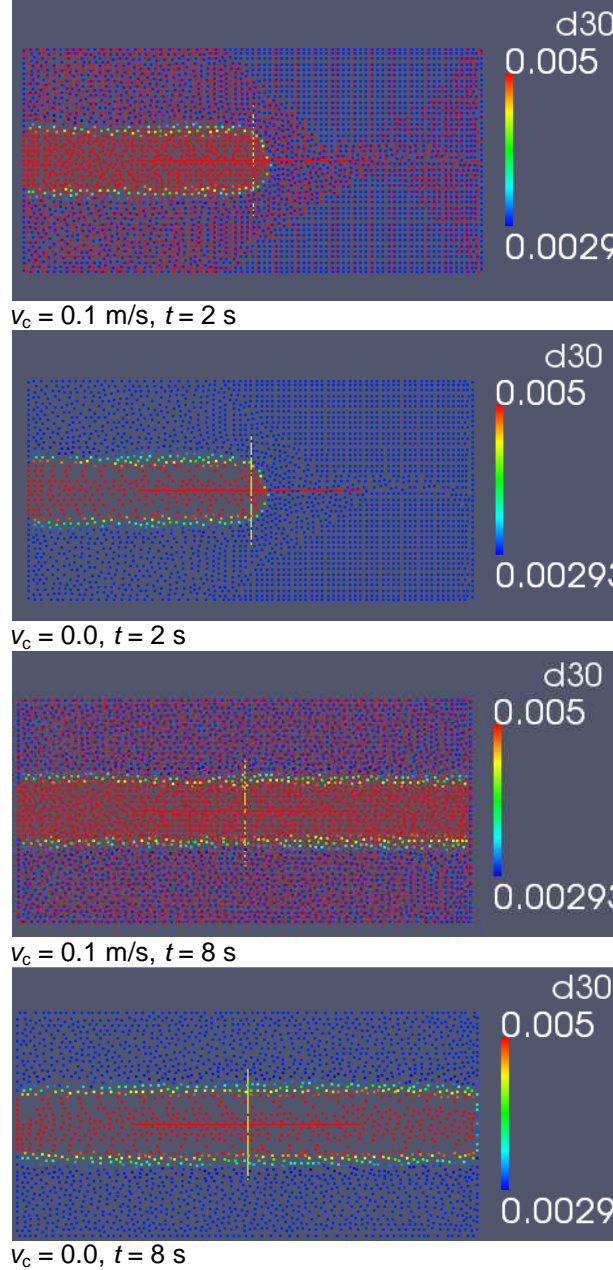
Figure 5: Evolution of the mean droplet diameter along the spray chamber as function of time. The points are the FPM cloud points of the dispersed phase where flow is from left to right. The Inlet and initial droplet diameters are 5 and 3 mm respectively where breakage and coalescence are neglected.

phase particles. As can be seen in from this figure, dispersed phase particles rising freely in a stagnant continuous phase moves relatively faster (less dense

$v_c = 0.1$ m/s, $t = 2$ s

$v_c = 0.0$, $t = 2$ s

$v_c = 0.1$ m/s, $t = 8$ s

$v_c = 0.0$, $t = 8$ s
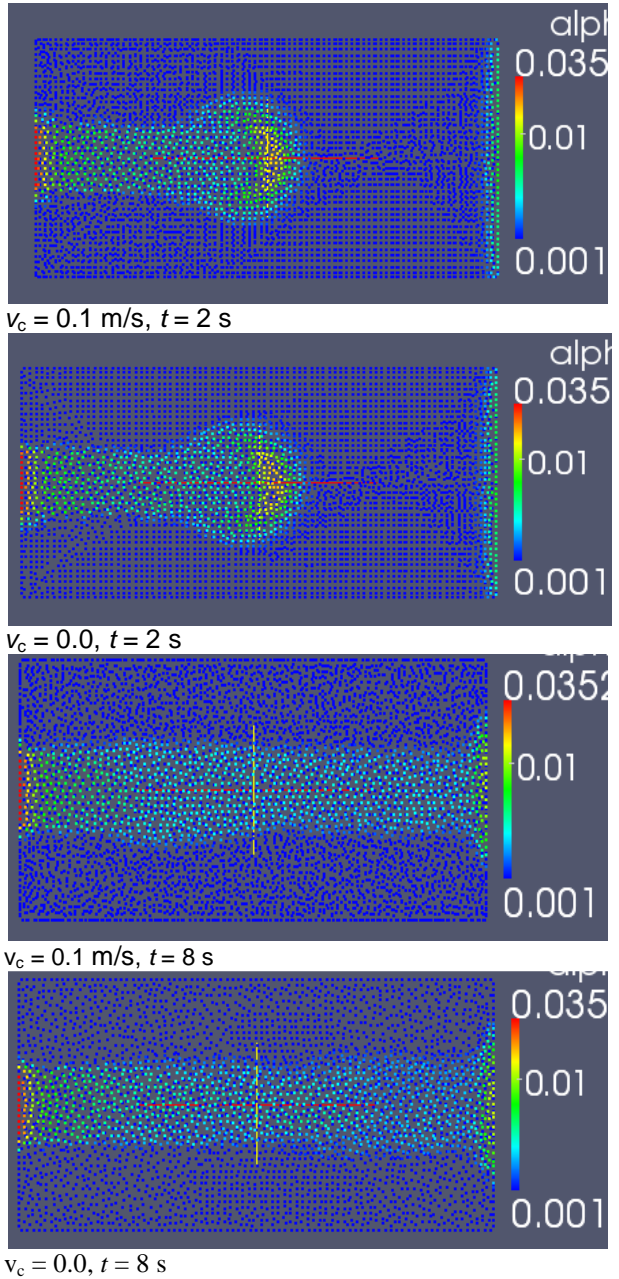
Figure 6: Evolution of the dispersed phase volume fraction along the spray chamber as function of time. The points are the FPM cloud points of the dispersed phase where flow is from left to right. The initial particulate phase fraction is 0.001 with negligible breakage and coalescence rates.

particles along the chamber height after 2s of the dispersed phase injection. It is clear that the dispersed phase particle (here the population of particles is represented by only one population balance numerical particle, and this particle is represented numerically by cloud of FPM particles) is transported with its inlet unchanged diameter due to the switch off of breakage and aggregation frequencies in the normalized population balance equations (source term is zero).

The two upper panels of Fig.(5) compare the effect of the continuous phase velocity on the flow of dispersed

cloud of particles) due to less flow resistance induced by the continuous phase. This is clear by comparing the volume fraction of these particles appearing in the two upper panels of Fig.(6). Again the head of the moving cloud is distorted by the resistance of the continuous phase, which is large in the case of counter current flow. The lower two panels of Fig.(5) shows the fully developed mean droplet diameter of the dispersed phase after 8 s for the case of 0.1 and 0.0 continuous phase velocity.

Again, the dense cloud of particles corresponding to the particulate phase are found in the case of counter current flow of the continuous phase. This is physically expected since the residence time of the flowing dispersed phase particles increases by increasing the flow of the continuous phase. This argument is supported by referring to the corresponding dispersed phase volume fraction shown in the two lower panels of Fig.(6). For this case, the phase fraction is compressed and distorted due to the flow of the continuous phase.

The CPU time required to perform a 10 second simulation for the above case is around 30 minutes using lap top Intel (R) Core (TM) i5 CPU 2.4 GHz with 6 GB installed memory.

SUMMARY AND CONCLUSIONS

In this work, a robust population balance solver is developed based on the concept of the Normalized QMOM, where round-off errors and loss of significant (major source of instability in the QMOM & DQMOM) are minimized. This is accomplished by introducing the idea of normalized moment equations, which transformed the population balance equation into a finite set of conservation equations with integral source terms. The NQMOM is used to approximate these unclosed integrals appearing in the convective and source terms of the population balance equation and the momentum balances for both the continuous and dispersed phases. The advantages of the NQMOM are shown in its stability through avoiding division by small numbers even zero and adaptive nature where it can be reduced automatically from second order accuracy for wide distributions to first order accuracy when the distribution becomes narrow and approaches the monosize distribution. This property can't be achieved without resource to the uniform weight Gauss like quadrture, which realized the normalization concept behind the NQMOM.

The NQMOM is tested intensively against known analytical solutions of the homogeneous PBE including particle breakage, aggregation and many other cases, which will be presented separately. For coupling purposes to CFD solvers, the NQMOM is integrated into the FPM software (in house property of Fraunhofer Institute for Industrial Mathematics). The simulated case in this work (liquid spray chamber) shows the robustness and stability of the NQMOM in dealing with real flow problems. Many other cases including breakage, aggregation and simultaneous breakage and aggregation are already simulated and will be presented separately.

To sum up, the coupled NQMOM-FPM solver is a rapid and effective modelling and simulation tool for particulate systems, where ignoring the discrete nature of such systems is no longer acceptable from practical and engineering point of view.

ACKNOWLEDGMENTS

REFERENCES

ABEDINI, H. , SHAHROKHI, M., (2008), " Inferential closed-loop control of particle size distribution for styrene emulsion polymerization*"*, *Chem. Eng. Sci.* 63, 2378 - 2390.

ATTARAKIH, M., JARADAT, M., HLAWITSCHKAH, M., BART, H.-J. and KUHNERT, J., (2010), **"**Solution of the population balance equation using the Cumulative Quadrature Method Of Moments (CQMOM)", 4*th International Conference on Population Balance Modelling* hosted by the Max Plank Institute for Dynamics of Complex Technical Systems, 15-17.09.2010, Berlin, Germany.

ATTARAKIH, M. M., DRUMM, C., and BART, H.-J., (2009a), "Solution of the population balance equation using the sectional quadrature method of moments (SQMOM)", *Chem. Eng. Sci.,* **64**, 742-752.

ATTARAKIH, M., JARADAT, M., DRUMM, C., BART, H.-J., TIWARI, S., SHARMA, V. K., KUHNERT, J. and KLAR, A. (2009b), "A multivariate population balance model for liquid extraction columns," *19th European Symposium on Computer Aided Process Engineering – ESCAPE19*, J. Jeżowski and J. Thullie (Editors), Elsevier, poland.

ATTARAKIH, M., BART, H.-J., and FAQIR, N., (2006), "Numerical Solution of the Bivariate Population Balance Equation for the Interacting Hydrodynamics and Mass Transfer in Liquid-Liquid Extraction Columns*", Chem. Eng. Sci.*, **61**: p. 113-123.

DIEMER, R.B., OLSON, J.H., (2002), "A moment methodology for the coagulation and breakage problems: Part 2-moment models and distribution reconstruction", *Chem. Eng. Sci.* **57**, 2211-2228.

DRUMM, C., ATTARAKIH, M., HLAWITSCHKA, M.W., BART, H.-J.., (2010), "One-Group Reduced Population Balance Model for CFD Simulation of a Pilot-Plant Extraction Column", *Ind. Eng. Chem. Res.* **49**, 3442–3451.

FOX, R., (2009), "Optimal Moment Sets for Multivariate Direct Quadrature Method of Moments", . *Ind. Eng. Chem. Res.* **48**, 9686–9696.

FOX, R.O., (2008), "A quadrature-based third-order moment method for dilute gas-particle flows", *J. Comp. Phys.,* **227**, 6313–6350.

GELBARD, F., SEINFELD, J.H. (1978), " Numerical solution of the dynamic equation for particulate systems", . *J. Comput. Phys.* **28**, 357-375.

GROSCH, R., BRIESEN, H., MARQUARDT, W., WULKOW, M., (2007), "Generalization and Numerical Investigation of QMOM", *AIChE J.*, **53**, 207-227.

HJORTSO, M. A., (2004), "*Population Balances in Biomedical Engineering*", McGraw-Hill Co..

LO, T.C., M.H.I. BAIRD, and C. HANSON, (1983), "*Handbook of solvent extraction"*, New York: John Wiley and Sons.

MARCHISIO, D.L., FOX, R.O., (2005), "Solution of population balance equations using the direct quadrature method of moments", *Aeros. Sci.*, **36**, 43-73.

McGRAW, R., (1997), "Description of aerosol dynamics by the Quadrature Method of Moments", *Aerosol Sci. and Tech.,* **27**, 255-265.

MOTZ, S. , MITROVIC, A. and GILLES, E.-D., (2002), "Comparison of numerical methods for the

simulation of dispersed phase systems", *Chem. Eng. Sci.* **57**, 4329 - 4344.

PISKUNOV, V. .N., & GOLUBEV, A.I., J. , (2002), *Aerosol Sci.,* **33**, 51-63.

RAIKAR, N.B., BHATIA, S.R., MALONE, M.F., HENSON, M.A., (2006), " Self-similar inverse population balance modeling for turbulently prepared batch emulsions Sensitivity to measurement errors", *Chem. Eng. Sci.*, **61** 7421 - 7435.

RAMKRISHNA, D., (2000), " *Population Balance: Theory and Applications to Particulate Systems in Engineering"*, Academic Press: San Diego.

ROSNER, D. E., (2006), " Improved Rate Laws and Population Balance Simulation Methods; CRE Applications, Including the Combustion Synthesis of Valuable Nano Particles", *Int. J. Chem. Reactor Eng.* **4**, 1 - 11.

ROSNER, D.E., McGRAW, R., TANDON, P., (2003), "Multivariate Population Balances via Moment and Monte Carlo Simulation Methods: An Important Sol Reaction Engineering Bivariate Example and "Mixed" Moments for the Estimation of Deposition, Scavenging, and Optical Properties for Populations of Nonspherical Suspended Particles", *Ind. Eng. Chem. Res.*, **42**, 2699-2711.

STRUMENDO, M., ARASTOOPOUR, H., (2009), "Solution of Bivariate Population Balance Equations Using the Finite Size Domain Complete Set of Trial Functions Method of Moments (FCMOM)", *Ind. Eng. Chem. Res.*, **48**, 262-273.

SU, J., GU, Z., Li, Y., FENG, S., XU, X.Y., (2008), " An Adaptive Direct Quadrature Method of Moment for Population Balance Equations",. *AIChE J.*, **54**, 2872-2887.

TIWARI, S., DRUMM, C., ATTARAKIH, M., KUHNERT, J. and BART, H.-J., (2008), " *Lecture Notes in Computational Science and Engineering: Meshfree Methods for Partial Differential Equations IV*", *M. Griebel; M.A. Schweitzer (Eds.)* **65**, *Springer Verlag.* 315-334.

TIWARI, S. and KUHNERT, J., (2007), "Modeling of two-phase flows with surface tension by Finite Pointset Method (FPM)", *J. Comp. Appl. Math.*, 203, 376-386.

HISTORY FORCE AND DRAG CORRELATION IN A LAGRANGIAN METHOD APPLIED TO OIL-WATER SEPARATION

Dirk F. VAN EIJKEREN[*], **Harry W.M. HOEIJMAKERS**[†]

University of Twente, Faculty of Engineering Technology, Enschede, THE NETHERLANDS

[*] E-mail: d.f.vaneijkeren@utwente.nl
[†] E-mail: h.w.m.hoeijmakers@utwente.nl

ABSTRACT

In the oil industry, both settling tanks and swirling flow separators are used to achieve separation of phases. In the present research, the motion of oil droplets is investigated numerically for the case of dilute suspensions in swirling flow fields as well as in quiescent fluids. The motion of the droplets is investigated using Lagrangian particle tracking. Resulting predictions show that the choice of drag correlation and inclusion of the history force are important for accurate prediction of the particle motion. A drag dependent kernel is used for the history force, and simulations for impulsively started motion using the Lattice Boltzmann Method show that not only the diffusive time scale is important, but also the wave propagation time scale.

Keywords: Dispersed droplet dynamics, separation, Lagrangian particle tracking, history force, drag coefficient .

NOMENCLATURE

Greek Symbols

α Dimensionless rotation of particle, $[-]$
β Dimensionless rotation of the flow field, $[-]$
Γ Dimensionless history time, $[-]$
ρ Mass density, $[\mathrm{kg\,m^{-3}}]$
$\boldsymbol{\sigma}$ Stress tensor, $[\mathrm{Pa}]$
ν Kinematic viscosity, $[\mathrm{m^2\,s^{-1}}]$
τ Characteristic, and integration time, $[\mathrm{s}]$
ψ Coefficient in drag factor relation, $[-]$
$\boldsymbol{\omega}$ Rate of rotation, $[\mathrm{s^{-1}}]$
ω Gauß-Hermite quadrature weight, $[-]$
Ω Lamb-Oseen vortex strength, $[\mathrm{m^2\,s^{-1}}]$

Latin Symbols

$\mathbf{c}$ Molecular velocity, $[\mathrm{m\,s^{-1}}]$.
$\mathbf{C}$ Peculiar velocity $\mathbf{C} \equiv \mathbf{c} - \mathbf{u}$, $[\mathrm{m\,s^{-1}}]$.
C Coefficient, $[-]$.
D Diameter, $[m]$.
f Drag factor, $[-]$.
f Probability density function, $[\mathrm{s^3\,m^{-6}}]$.
$\mathbf{f}$ Volumetric force per unit mass, $[\mathrm{m\,s^{-2}}]$.
$\mathbf{F}$ Force, $[\mathrm{N}]$.
g Gravitational acceleration ~ 9.81, $[\mathrm{m\,s^{-2}}]$.
$\mathbf{g}$ Gravitational force per unit mass, $[\mathrm{m\,s^{-2}}]$.
I Scalar moment of inertia, $[\mathrm{kg\,m^2}]$.
$\mathbf{I}$ Moment of inertia tensor, $[\mathrm{kg\,m^2}]$.

k Boltzmann constant, $[\mathrm{J\,K^{-1}}]$.
K Kernel of history force integral, $[-]$.
n Number density, $[\mathrm{m^{-3}}]$.
$\mathbf{n}$ Unit normal, $[-]$.
N Number, $[-]$.
m Particle, or molecule mass, $[\mathrm{kg}]$.
p Pressure, $[\mathrm{Pa}]$.
$\mathscr{P}$ Probability function, $[\mathrm{s^3\,m^{-3}}]$.
$\mathbf{Q}$ Unit quadrature vector, $[-]$.
r radius, $[\mathrm{m}]$.
Re   Diameter based particle Reynolds number, $[-]$.
S Surface, $[\mathrm{m^2}]$.
$\mathbf{T}$ Torque, $[\mathrm{N\,m}]$.
$\mathbf{u}$ Flow field velocity, $[\mathrm{m\,s^{-1}}]$.
$\mathbf{v}$ Particle velocity, $[\mathrm{m\,s^{-1}}]$.
$\mathbf{w}$ Relative velocity $\mathbf{v} - \mathbf{u}$, $[\mathrm{m\,s^{-1}}]$.
V Volume, $[\mathrm{m^3}]$.

Sub/superscripts

$\hat{}$ Dimensionless quantity
0 Reference state
$^{(0)}$ Equilibrium
AM Added mass
c Quantity of continuous phase
d Diffusive
D Drag
$\mathscr{D}$ Dimensions
H History
ι Lattice direction
L,M Magnus lift
L,S Saffman lift
$L\&M$ by (Lawrence and Mei, 1995)
p Quantity of particle
t Terminal

INTRODUCTION

In oil industry, water is used to maintain pressure in oil wells during the process of extraction of oil. Therefore, a mixture of oil and water is produced during the extraction process. Separation of this oil-water mixture is required to extract the desired oil as wall as to treat the produced water. Separation of phases takes place in several stages. The first stage is the bulk separation, in which the mixture is separated in two phases with a residual of the other phase remaining. Secondary separation is then required

for the removal of the undesired pollution of oil and water. One of the stages of secondary separation is the produced water treatment. Tiny oil droplets that remain in the water after bulk separation will need to be removed in order to obtain sufficiently clean water.

Separation of oil and water can be achieved making use of the density difference between oil and water. The conventional method used to achieve phase separation is gravity settling. The mixture enters the settling tank, and oil will gradually move upwards towards the surface of the mixture and is then extracted. Settling time of the mixture is smaller for mixtures with large oil droplets. For produced water treatment the diameter of the droplets can be in the order of microns, and settling times tend to infinity for these droplets. Therefore advanced methods of water treatment have been developed, such as swirling flow separators and flotation tanks.

A first indicator for the settling time of a droplet is the terminal velocity for a particle in Stokes' flow. The terminal velocity is the velocity at which forces are in balance. For a particle with a specific density ratio $\hat{\rho}$ with respect to the carrier fluid, and a diameter of D the terminal velocity can be expressed as

$$\mathbf{v}_{t,\text{Stokes}} = \frac{D^2 \mathbf{g}(\hat{\rho} - 1)}{18\nu_c} = \frac{\tau_d}{18}\mathbf{g}(\hat{\rho} - 1), \qquad (1)$$

with τ_d the diffusive time scale and $\hat{\rho}$ the density ratio defined as

$$\tau_d \equiv \frac{D^2}{\nu_c}, \quad \hat{\rho} \equiv \frac{\rho_p}{\rho_c}. \qquad (2)$$

Swirling flow separators make use of an increased effective force field due to the pressure gradient as a result of the swirl. Flotation tanks, in which oil droplets adhere to gas bubbles utilize the decreased effective relative density, caused by the lower density of the gas inside the bubbles.

To control the efficiency of separators, it is not only necessary to be able to accurately predict the flow field in the settling device, but also to be able to accurately predict the droplet trajectories. A small change in settling velocity of a particle could imply other design requirements for the separator device, such as length or shape. Therefore, in the present study the equations of motion for a particle have been investigated in order to enable the prediction of particle behaviour adequately. These studies involve both particle behaviour in settling tank conditions and particle behaviour in a generic swirling flow field.

In the present research the forces on the oil droplets in another liquid is approximated assuming spherical solid particles. For these particles the drag force and the history force, which arise in Lagrangian particle tracking, have been investigated. Particle trajectories have been estimated using different drag coefficient correlations, and with and without taking the history force into account. The parameters contained in the expression of the history force are investigated both using experimental data in literature, e.g. (Mordant and Pinton, 2000), as well as using Lattice Boltzmann simulations for the impulsively started uniform flow about a sphere.

MODEL DESCRIPTION

The motion of the fluid and particle is considered both at the scale of the particle as well as at the general fluid flow scale. Forces exerted by the fluid on the particle lead to the equation of motion for the particle, while at least on the particle scale the particle has a considerable influence on the fluid flow. On the larger scale, the fluid flow is barely influenced by the presence and motion of the particle and the large scale flow field can be used as input for the particle motion. First the equation of motion for the particle will be derived. Subsequently the equations governing the flow about the particle will be derived, and discretized leading to the Lattice Boltzmann equations.

Particle equation of motion

The motion of a particle is governed by the forces acting on the particle. Newton's second law applied to the motion of the particle states that

$$\frac{\mathrm{d}}{\mathrm{d}t}(m\mathbf{v}) = \mathbf{F}_p, \qquad (3)$$

with $\mathbf{v}$ the particle velocity, and m the mass of the particle.

Volumetric forces and the surface stresses contribute to the force on the particle, and $\mathbf{F}_p$ can therefore be expressed as

$$\mathbf{F}_p = \iint_{\partial V_p} \boldsymbol{\sigma} \cdot \mathbf{n}\, \mathrm{d}S + \iiint_{V_p} \rho_p \mathbf{f}\, \mathrm{d}V, \qquad (4)$$

The volumetric force per unit mass $\mathbf{f}$ is usually the gravitational acceleration $\mathbf{g}$ and the surface stress $\boldsymbol{\sigma}$ results from the motion of the fluid about the particle, consisting of the pressure and the viscous stress. The volumetric and surface part of the force, as well as the important variables of the flow field, are shown in figure 1. It can be observed that the motion of the particle also involves the rate of rotation of the particle due to torque, which is expressed, similar to equations (3) and (4), as

$$\frac{\mathrm{d}}{\mathrm{d}t}(\mathbf{I} \cdot \boldsymbol{\omega}_p) = \mathbf{T}_p, \qquad (5)$$

with $\mathbf{I}$ the moment of inertia tensor of the particle, evaluated at the centre of mass $\mathbf{x}_p$ of the particle. The centre of mass is defined as

$$\mathbf{x}_p \equiv \frac{1}{m} \iiint_{V_p} \rho_p \mathbf{x}\, \mathrm{d}V. \qquad (6)$$

Volumetric forces and the surface stresses contribute to the the torque $\mathbf{T}_p$, which becomes

$$\mathbf{T}_p = \iint_{\partial V_p} (\mathbf{x} - \mathbf{x}_p) \times (\boldsymbol{\sigma} \cdot \mathbf{n})\, \mathrm{d}S$$
$$+ \iiint_{V_p} \rho_p (\mathbf{x} - \mathbf{x}_p) \times \mathbf{f}\, \mathrm{d}V. \qquad (7)$$

The contribution of the volume integral is equal to zero in a constant volumetric force field, as the particle location $\mathbf{x}_p$ is taken to coincide with its centre of mass. For a spherical particle with constant density the moment of inertia tensor $\mathbf{I}$ can be replaced by the scalar moment of inertia I.

To obtain the surface stress, a fully resolved simulation of the flow about the particle is required. For most practical applications this is not feasible. Therefore, the

surface integral is approximated by a sum of forces that represents separate effects of the flow field and the particle motion. These forces depend on the large-scale flow field, using the variables and their derivatives of the flow at the the centre of mass of the particle. The effects taken into account in present research are the volumetric forces, drag, stress gradient, added mass, Saffmann and Magnus lift forces and the history force. Therefore the force on the particle is approximated by

$$\mathbf{F}_p \approx \mathbf{F}_{\text{volume}} + \mathbf{F}_{\nabla\boldsymbol{\sigma}} + \mathbf{F}_{AM} + \mathbf{F}_{L,S} + \mathbf{F}_{L,M} + \mathbf{F}_D + \mathbf{F}_H. \quad (8)$$

The volumetric force is the approximation of the volume integral in equation (4), while the sum of the other forces is the approximation of the surface integral in equation (4). The flow variables, taken at the centre of mass of the particle, can be corrected by the Faxen force correction. Taking into account the Laplacian of required flow field variables and derivatives provides is sufficient to capture both first and second order effects for a spherical particle.

Volumetric, stress gradient and added mass force

The volumetric force contribution is

$$\mathbf{F}_{\text{volume}} = m\mathbf{f} \quad (9)$$

The stress gradient force $\mathbf{F}_{\nabla\boldsymbol{\sigma}}$ represents the surface integral of the stress of the large scale flow field acting at the surface of the particle, i.e. the surface integral of $\boldsymbol{\sigma} \cdot \mathbf{n}$. The surface integral of a variable times the normal can be expressed as a volume integral of its integral. Therefore the surface integral of the stress acting at the surface can be expressed as the volume integral of the gradient of the stress. Using the Navier-Stokes equations the stress gradient is subsequently rewritten in terms of the material derivative of the flow field velocity $\frac{D\mathbf{u}}{Dt}$ and the volumetric force $\mathbf{f}$. This results in

$$\mathbf{F}_{\nabla\boldsymbol{\sigma}} = m\frac{\nabla \cdot \boldsymbol{\sigma}}{\rho_p} = \frac{m}{\hat{\rho}} \left\{ \frac{D\mathbf{u}}{Dt} - \mathbf{f} \right\}, \quad (10)$$

with the material derivative defined as

$$\frac{D}{Dt} \equiv \frac{\partial}{\partial t} + \mathbf{u} \cdot \nabla. \quad (11)$$

The volumetric force (9) and the stress gradient (10) are often combined, leading to what is often called the buoyancy force and to the non-hydrostatic stress gradient force

$$\mathbf{F}_{\text{buoyancy}} + \mathbf{F}_{\nabla\boldsymbol{\sigma}_{\text{non-HS}}} = \frac{m}{\hat{\rho}} \left\{ (\hat{\rho} - 1)\mathbf{f} + \frac{D\mathbf{u}}{Dt} \right\} \quad (12)$$
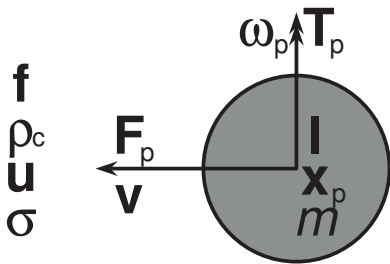

Figure 1: A particle in a flow field subjected to volumetric forces and the stress of the flow field exerted at the surface of the particle

When the particle is accelerating with respect to the acceleration of the large scale flow, not only the particle itself is accelerated, but also about an equal volume of the continuous phase is accelerated in the direction opposite to the direction of the particle acceleration. This causes the particle to appear heavier than its actual mass, and is called, the added, or virtual mass effect,

$$\mathbf{F}_{AM} = C_{AM}\frac{m}{\hat{\rho}} \left(\frac{D\mathbf{u}}{Dt} - \frac{d\mathbf{v}}{dt} \right). \quad (13)$$

The added mass coefficient for a spherical particle has been proposed as $C_{AM} = \frac{1}{2}$ for the inviscid flow limit, (Auton *et al.*, 1988). This added mass coefficient has been shown to be accurate for a fairly large range of Reynolds numbers, (Loth and Dorgan, 2009).

Lift forces and torque

The Saffman and Magnus lift forces represent phenomena related to rotation of particle and in flow field. The Saffman lift captures the effect of a higher fluid velocity on one side of the particle relative to that at the other side of the particle, i.e. the effect due to the existence of a flow field velocity gradient. This causes the pressure to be varying along the particle surface resulting in a lift force. The direction of this force is perpendicular to the direction of the rotation in the flow field as well as the direction of the relative velocity.

The Magnus lift force represents the effect of the flow field being deflected by the rotation of the particle. Rotation of the particle causes a change in angle between the flow ahead of the particle and the flow in the wake of the particle. This is caused by a force of the particle on the flow and vice versa. Some authors use the relative rotation for the Magnus lift, e.g. (Crowe *et al.*, 1998), while others use the absolute rotation of the particle, e.g. (Loth and Dorgan, 2009). For the cases studied here, both methods have been investigated, and differences between both approaches appear to be negligible. An approach using the absolute rotation will be used for the results presented.

The Saffman lift force per unit mass is, (Crowe *et al.*, 1998),

$$\mathbf{F}_{L,S} = m\frac{9.66C_{L,S}}{\pi\hat{\rho}\sqrt{\tau_d |\boldsymbol{\omega}_c|}} \boldsymbol{\omega}_c \times \mathbf{w}, \quad (14)$$

with the rotation of the large scale flow field expressed as the vorticity of the flow field

$$\boldsymbol{\omega}_c \equiv \nabla \times \mathbf{u}, \quad (15)$$

and the relative velocity

$$\mathbf{w} = \mathbf{v} - \mathbf{u}. \quad (16)$$

The Saffman lift coefficient $C_{L,S}$ used is, (Mei, 1992)

$$C_{L,S} = \begin{cases} 0.3314\sqrt{\frac{\beta}{2}}\left(1 - e^{-\frac{Re}{10}}\right) \\ \qquad\qquad\qquad + e^{-\frac{Re}{10}} & Re \leq 40, \\ 0.0524\sqrt{\frac{\beta Re}{2}} & Re > 40, \end{cases} \quad (17)$$

where the Reynolds number Re is based on the particle diameter

$$Re \equiv \frac{D|\mathbf{w}|}{\nu_c}, \quad (18)$$

and

$$\beta \equiv \frac{\tau_d \, |\boldsymbol{\omega}_c|}{\mathrm{Re}}, \tag{19}$$

relates the rotation of the flow field and the particle velocity. For low Reynolds numbers the contribution of the part with β becomes negligible as a Taylor series expansion of the exponential part results in

$$\sqrt{\beta}\left(1 - e^{-\frac{\mathrm{Re}}{10}}\right) = \tau_d \, |\boldsymbol{\omega}_c| \sum_{n=1}^{\infty} \frac{(-1)^{n-1} \sqrt{Re}^{2n-1}}{10^n n!}, \tag{20}$$

and the expression reduces to the originally proposed expression for the Saffman lift, (Saffman, 1965). For high Reynolds numbers the lift coefficient in equation (17) leads to a good approximation of numerical results, (Dandy and Dwyer, 1990).

The Magnus lift force is

$$\mathbf{F}_{L,M} = \frac{3}{4}\frac{m}{\hat{\rho}}C_{L,M}\boldsymbol{\omega}_p \times \mathbf{w}. \tag{21}$$

The Magnus lift coefficient $C_{L,M}$ corrects the Magnus lift force for inertial and spin effects. It was originally derived by Rubinow and Keller, (Rubinow and Keller, 1961). A relation for the lift coefficient that gives values in the same order of magnitude as measurements is, (Loth and Dorgan, 2009)

$$C_{L,M} = 1 - \left\{\frac{5}{8} + 0.15\left[1 - \tanh\left(0.28\left[\alpha - 2\right]\right)\right]\right\} \\ \times \tanh\left(0.18\sqrt{\mathrm{Re}}\right), \tag{22}$$

where α relates the rotation of the particle and the relative velocity

$$\alpha \equiv \frac{\tau_d \, |\boldsymbol{\omega}_p|}{\mathrm{Re}}. \tag{23}$$

The torque $\mathbf{T}_p$ on a particle tends to force the rate of rotation of the particle to the rotation of the flow. The relation for the torque accounting for rotation in fluid flow as well as rotation of the particle (Crowe *et al.*, 1998) is combined with the relation for torque in a quiescent fluid, including a correction for rotational inertia effects (Crowe *et al.*, 1998). It is here assumed that the Reynolds number correction will be approximately valid for the relation with fluid flow. This leads to the expression for the torque

$$\mathbf{T}_p = 2.01\rho_c D^3 v_c \left(1 + 0.1005\sqrt{\alpha\mathrm{Re}}\right) \\ \times \left(\frac{1}{2}\boldsymbol{\omega}_c - \boldsymbol{\omega}_p\right). \tag{24}$$

Drag force

The drag approximates the effect that the particle is forces to move with the large-scale flow field velocity. Both viscous drag due to boundary layer development and pressure drag due to flow separation at the surface of the sphere are included. The common expression for the drag involves a drag coefficient C_D and is expressed as

$$\mathbf{F}_D = -m\frac{3C_D\,(\mathrm{Re})}{4D\hat{\rho}}\,|\mathbf{w}|\,\mathbf{w}. \tag{25}$$

A first approximation for the drag coefficient was derived for Stokes' flow,

$$C_{D,\mathrm{Stokes}} = \frac{24}{\mathrm{Re}}. \tag{26}$$

This drag coefficient is often used to scale the actual drag coefficient, leading to the drag factor

$$f \equiv \frac{C_D}{C_{D,\mathrm{Stokes}}}. \tag{27}$$

Therefore, the drag can also be expressed using the drag factor

$$\mathbf{F}_D = -m18\frac{f\,(\mathrm{Re})}{\hat{\rho}\tau_d}\mathbf{w}. \tag{28}$$

In present research several relations for the drag factor have been employed and their impact on the predicted particle trajectories has been examined. The examined drag factor expressions, shown in figure 2, are

- (Clift and Gauvin, 1970) - semi-analytic

$$f = 1 + 0.15\mathrm{Re}^{0.687} + \frac{0.0175\mathrm{Re}}{1 + 4.25 \cdot 10^4\mathrm{Re}^{-1.16}} \tag{29}$$
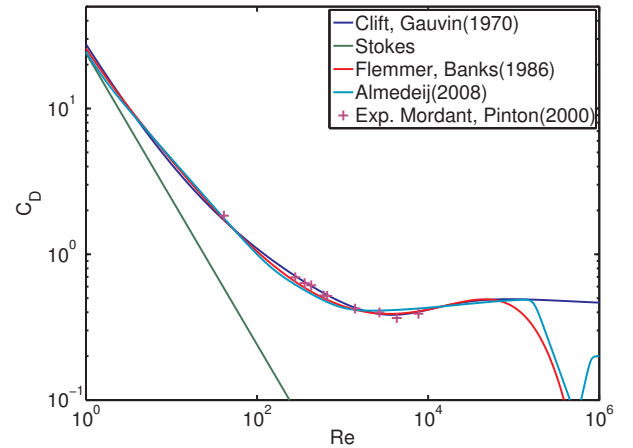

Figure 2: The examined drag coefficient relations and experimental data, (Mordant and Pinton, 2000), as a function of the Reynolds number
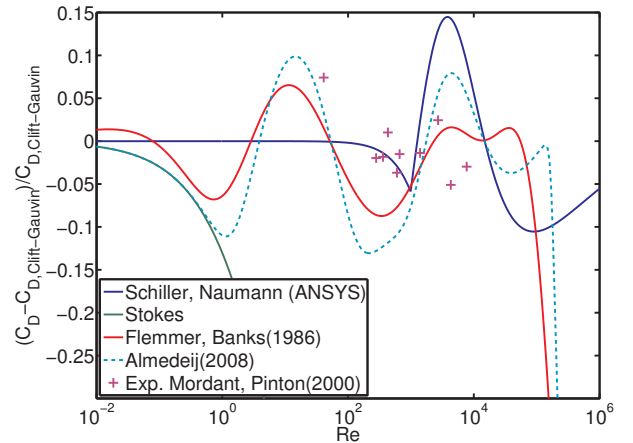

Figure 3: The scaled deviation of the examined drag coefficient relations and experimental data with respect to the relation by (Clift and Gauvin, 1970)

- (Almedeij, 2008) - empirical fit

$$\psi_1 = 1 + \left[\frac{7}{8}\mathrm{Re}^{0.33}\right]^{10} + \left[\frac{1}{6}\mathrm{Re}^{0.67}\right]^{10}$$
$$+ \left[\frac{1}{60}\mathrm{Re}\right]^{10}, \tag{30a}$$

$$\frac{1}{\psi_2} = \left[\frac{0.037}{6}\mathrm{Re}^{-0.89}\right]^{-10} + \left[\frac{\mathrm{Re}}{28}\right]^{-10}, \tag{30b}$$

$$\psi_3 = \left[\frac{1.75 \cdot 10^8}{24}\mathrm{Re}^{-0.625}\right]^{10}, \tag{30c}$$

$$\frac{1}{\psi_4} = \left[25 \cdot 10^{-19}\mathrm{Re}^{-1.63}\right]^{-10} + \left[\frac{\mathrm{Re}}{120}\right]^{-10}, \tag{30d}$$

$$f^{10} = \frac{\psi_3(\psi_1 + \psi_2)}{\psi_1 + \psi_2 + \psi_3} + \psi_4. \tag{30e}$$

- (Flemmer and Banks, 1986) - empirical fit

$$\log_{10} f = 0.261\mathrm{Re}^{0.369} - 0.105\mathrm{Re}^{0.431}$$
$$- \frac{0.124}{1 + (\log_{10}\mathrm{Re})^2}. \tag{31}$$

A further drag factor, (Schiller and Naumann, 1933), in a formulation bounded by $0.44\frac{\mathrm{Re}}{24}$ in the Newton regime is commonly used in commercial CFD software such as ANSYS-CFX . This drag factor is not employed, as it does not deviate that much from (29) in the low Reynolds regime, while it is a very crude approximation in the regime of the used experimental data. Figure 3 shows the scaled deviation of the examined drag coefficient correlations with respect to the relation by (Clift and Gauvin, 1970). It can be observed that the expression for Stokes' drag starts to deviate very rapidly from most other correlations for Reynolds numbers of order $\mathrm{Re} \sim 10^{-2} - 10^{-1}$. However, the correlation proposed by (Almedeij, 2008) only starts to deviate at Reynolds numbers in the order of $\mathrm{Re} \sim 1$. It can also be observed that none of the correlations manage to capture the general behaviour of the experimental data. Other relations, e.g. (Cheng, 2009) are still to be considered, combined with efforts to obtain drag coefficients from numerical simulations.

History force

The history force takes into account the time dependency of the flow about a sphere. All expressions for the drag force only depend on the present Reynolds number. This implies that boundary layer and wake react instantaneously to the relative velocity in time. The history force takes into account the remainder for unsteady behaviour of the flow about a sphere, i.e. the force accounts for the lagging transient boundary layer development, as well as that of the particle wake. To capture the transient effects, an integral over time is required from the start of particle movement to the present time. The integral has a kernel $K(t, \tau)$ that relates the acceleration of the particle at time τ to the resulting force at time t, and the force therefore becomes

$$\mathbf{F}_H = -\frac{18m}{\tau_d\hat{\rho}} \int_{-\infty}^{t} K(t, \tau) \left.\frac{d\mathbf{w}}{dt}\right|_{\tau} d\tau. \tag{32}$$

The assumption of Stokes' flow, leads to the Basset kernel, e.g. (Clift and Gauvin, 1970),

$$K_{\mathrm{Basset}}(t, \tau) = \frac{1}{\sqrt{4\pi}} \sqrt{\frac{\tau_d}{t - \tau}} \tag{33}$$

The history force, expressed using this kernel is often called the Basset force. The diffusive time scale τ_d is the only flow property that influences the rate of decay of the kernel in time. It has been observed that the long time behaviour of the kernel shows a faster decay than the Basset kernel predicts, e.g. (Mei *et al.*, 1991; Loth and Dorgan, 2009; Mordant and Pinton, 2000). Therefore, the kernel leads to a significant overprediction of the history force.

To obtain a more accurate prediction of the history force, the kernel should take inertia effects into account. Therefore a kernel was proposed, (Mei *et al.*, 1991; Mei and Adrian, 1992), that takes into account effects due to inertia. The kernel was subsequently refined using the drag factor, (Lawrence and Mei, 1995), leading to

$$K_{L\&M}(t, \tau) = \frac{3\tau_d^2 \left(f(t) + \mathrm{Re}(t)f'(t)\right)f'(\tau)}{\left[\int_{\tau}^{t}\mathrm{Re}(\tau')\,d\tau'\right]^2}, \tag{34}$$

where

$$f'(t) \equiv \left.\frac{df}{d\mathrm{Re}}\right|_{\mathrm{Re}(t)} \tag{35}$$

This kernel was adapted to obtain the Basset kernel in the inertialess limit, (van Eijkeren and Hoeijmakers, 2010)

$$K(t, \tau) = \frac{f_H(t, \tau)}{\left[\left[\frac{f^2(t)\Gamma(t,\tau)}{\mathrm{Re}(t)}\right]^{\frac{1}{4}} + \Gamma(t, \tau)\right]^2}, \tag{36}$$

with the history drag factor

$$f_H \equiv 3\left(f(t) + \mathrm{Re}(t)f'(t)\right)f'(\tau), \tag{37}$$

and the dimensionless history time

$$\Gamma(t, \tau) \equiv \int_{\tau}^{t} \frac{\mathrm{Re}(\tau')}{\tau_d f(\tau')}\,d\tau'. \tag{38}$$

Numerical simulation

Analytic calculation of the equation of motion of a particle is only possible for generic cases with simplified force models. For numerical simulation the equations of motion need to be discretized. A four-stage Runge-Kutta scheme is used to obtain a prediction of the particle trajectory, velocity and rate of rotation.

Lattice Boltzmann Equation

A fluid exists of a collection of molecules, interacting with each other. These molecules are subjected to forces like gravity. Some of the molecules will also interact with wall molecules. Each molecule has a specific velocity at a specific position and time. However, for a large number of molecules it becomes increasingly difficult to predict these specific velocities. Therefore, for practical flow problems equations for the average properties of these

molecules have been developed. On a very large scale with respect to the molecules, these average properties are described by the Navier-Stokes equations.

The probability that a molecule with a specific velocity **c** can be observed in a volume around point **x** at time t is $\mathscr{P}(\mathbf{c};\mathbf{x},t)$ and if the volume is large enough

$$\int \mathscr{P}(\mathbf{c};\boldsymbol{x},t)\,\mathrm{d}\mathbf{c} \equiv 1. \qquad (39)$$

A specific number of molecules is present in a volume around point **x**. Therefore, a number density $n(\mathbf{x},t)$ exists for any arbitrary volume located at **x** at time t. Scaling of the probability function with the number density leads to a probability density function $f(\mathbf{c};\mathbf{x},t)$, defined as

$$f(\mathbf{c};\mathbf{x},t) \equiv n(\mathbf{x},t)\,\mathscr{P}(\mathbf{c};\mathbf{x},t). \qquad (40)$$

Macroscopic variables are variables such as the number density n of molecules with mass m, the mass density ρ, the velocity **u** and the temperature T. These variables are the average properties of the molecules at $\mathbf{x},t$, and can be calculated by taking the moments of the distribution function in velocity space. The number density, mass density, velocity and temperature are obtained as

$$n(\mathbf{x},t) \equiv \int f(\mathbf{c};\mathbf{x},t)\,\mathrm{d}\mathbf{c}, \qquad (41a)$$

$$\rho(\mathbf{x},t) \equiv \int mf(\mathbf{c};\mathbf{x},t)\,\mathrm{d}\mathbf{c}, \qquad (41b)$$

$$n(\mathbf{x},t)\mathbf{u}(\mathbf{x},t) \equiv \int \mathbf{c}f(\mathbf{c};\mathbf{x},t)\,\mathrm{d}\mathbf{c}, \qquad (41c)$$

$$n(\mathbf{x},t)\frac{3kT(\mathbf{x},t)}{m} \equiv \int |\mathbf{c}-\mathbf{u}(\mathbf{x},t)|^2 f(\mathbf{c};\mathbf{x},t)\,\mathrm{d}\mathbf{c}, \qquad (41d)$$

where k is the Boltzmann constant, $k = 1.3806504 \cdot 10^{-23}\,\left[\mathrm{J\,K^{-1}}\right]$.

An integral equation for the probability density function was first given by Boltzmann. A thorough derivation of the Boltzmann equation in its various expressions and its implications is provided in (Chapman and Cowling, 1991). The equation describes the change of the probability density function in time, space and velocity space, due to the movement of molecules with velocity **c** subjected to a force field. A source term, taking into account the intermolecular interaction, couples the differential equation for velocity **c** with the equations for the other velocities

$$\frac{\partial f}{\partial t} + \mathbf{c}\cdot\boldsymbol{\nabla}_{\mathbf{x}}f + \mathbf{f}\cdot\boldsymbol{\nabla}_{\mathbf{c}}f = \frac{\partial_e f}{\partial t}. \qquad (42)$$

The collision term, $\frac{\partial_e f}{\partial t}$, describes the interaction between molecules due to intermolecular forces. Calculating this collision term involves integration over the entire velocity space, and for long range intermolecular interactions over the entire volume. To simplify the equation, it is assumed that collisions will force the distribution function to its local equilibrium distribution function $f^{(0)}$ in a specific relaxation time τ, (Bhatnagar *et al.*, 1954), leading to the BGK formulation

$$\frac{\partial_e f}{\partial t} = -\frac{f - f^{(0)}}{\tau}. \qquad (43)$$

The relaxation time τ on the micro scale is observed at the macro scale in the viscous behaviour of a fluid. The dependency of the viscosity on the relaxation time is

$$\nu = \frac{kT}{m}\tau. \qquad (44)$$

The local equilibrium distribution function, is taken as the Maxwellian distribution

$$f^{(0)} = n\left(\frac{m}{2\pi kT}\right)^{\frac{N_{\mathscr{D}}}{2}} e^{-\frac{m|\mathbf{C}|^2}{2kT}}, \qquad (45)$$

with **C** the peculiar velocity $\mathbf{C} \equiv \mathbf{c}-\mathbf{u}$, and $N_{\mathscr{D}}$ the number of spatial dimensions. The equilibrium distribution function is derived, such that moments of the function lead to the macroscopic variables. Therefore, the moments of the distribution function can be replaced by the moments of the equilibrium distribution function and vice versa. This property of the two distribution fuctions is used to evaluate the moments using a Gauß-Hermite quadrature. The discretization of the velocity space using quadrature weights ω_t for a finite number of velocities $\mathbf{c}_t$ leads to

$$\rho \approx \sum_t \omega_t m \left(\frac{2kT}{m}\right)^{\frac{N_{\mathscr{D}}}{2}} f_t, \qquad (46a)$$

$$\rho u \approx \sum_t \omega_t \mathbf{c}_t m \left(\frac{2kT}{m}\right)^{\frac{N_{\mathscr{D}}}{2}} f_t \qquad (46b)$$

$$\rho\frac{3kT(\mathbf{x},t)}{m} \approx \sum_t \omega_t |\mathbf{c}-\mathbf{u}|^2 m \left(\frac{2kT}{m}\right)^{\frac{N_{\mathscr{D}}}{2}} f_t. \qquad (46c)$$

Standard approach, e.g. (Chen and Doolen, 1998), for the Lattice Boltzmann Method is to take $\mathbf{c}_t$ for the case of an isothermal stationary fluid. For the 3-D lattice model with a 3 point quadrature (D3Q27), the lattice velocities become

$$\mathbf{c}_t = \mathbf{c}_{i,j,k} = \sqrt{\frac{3kT_0}{m}}\left(\mathbf{Q}_i,\mathbf{Q}_j,\mathbf{Q}_k\right)^T, \qquad (47)$$

where

$$\mathbf{Q} = (-1,0,1)^T. \qquad (48)$$

Two more generally applied quadratures D3Q15 and D3Q19, are obtained by a multi-scale expansion of a Gauß-Hermite quadrature. For the case for which an isothermal stationary fluid is used for the lattice velocities, the lattice function f_t becomes

$$f_t = f(\mathbf{c}_t)\, e^{\frac{m|\mathbf{c}_t|^2}{2kT_0}}. \qquad (49)$$

The lattice equilibrium distribution function for the isothermal case therefore becomes

$$f_t^{(0)} = n\left(\frac{m}{2\pi kT_0}\right)^{\frac{N_{\mathscr{D}}}{2}} e^{\frac{m}{kT_0}\left\{\mathbf{c}_t\cdot\mathbf{u}-\frac{1}{2}|\mathbf{u}|^2\right\}}, \qquad (50)$$

and the right hand side of equation (50) is usually expanded in a Taylor series up to second order accuracy for $\sqrt{\frac{m}{kT_0}}\mathbf{u} \approx \mathbf{0}$, where it is assumed that $|\mathbf{u}| \ll \sqrt{\frac{kT_0}{m}}$, i.e. a low Mach number for a calorically perfect gas. If the thermal case is considered, the lattice equilibrium function requires additional terms. If an isothermal stationary

fluid is used for the lattice velocities, the lattice equilibrium becomes

$$f_l^{(0)} = n \left(\frac{mT_0}{2\pi kT^2} \right)^{\frac{N_\mathscr{Q}}{2}} \tag{51}$$
$$\times e^{\frac{m}{kT} \left\{ \mathbf{c}_l \cdot \mathbf{u} - \frac{1}{2}|\mathbf{u}|^2 + \frac{1}{2}|\mathbf{c}_l|^2 \left(\frac{T}{T_0} - 1 \right) \right\}}.$$

Expansion of equation (51) in a Taylor series is not trivial, and involves careful consideration.

It is assumed that the term involving the derivative of the distribution function with respect to the molecular velocity can be approximated by the derivative of the equilibrium distribution function, i.e.

$$\mathbf{f} \cdot \nabla f \approx \mathbf{f} \cdot \nabla f^{(0)} = -\frac{m\mathbf{f} \cdot \mathbf{C}}{kT} f^{(0)}. \tag{52}$$

The BGK Boltzmann equation for each lattice velocity $\mathbf{c}_l$ becomes

$$\frac{\partial f(\mathbf{c}_l)}{\partial t} + \mathbf{c}_l \cdot \nabla_{\mathbf{x}} f(\mathbf{c}_l) = $$
$$-\frac{f(\mathbf{c}_l) - f^{(0)(\mathbf{c}_l)}}{\tau} + \frac{m\mathbf{f} \cdot (\mathbf{c}_l - \mathbf{u})}{kT} f^{(0)}(\mathbf{c}_l). \tag{53}$$

Wall boundary conditions for stationary walls in the Lattice Boltzmann equation are implemented using the so called bounce-back principle. The probability to observe a molecule with velocity $\mathbf{c} = \mathbf{c}_l$ at the wall is equal to the probability to observe a molecule with the opposite velocity $\mathbf{c} = -\mathbf{c}_l$, i.e.

$$f_{\text{wall}}(\mathbf{c}_l) = f_{\text{wall}}(-\mathbf{c}_l). \tag{54}$$

In present research, the BGK Boltzmann equation is discretized using a Crank-Nicolson scheme, see also (Crank and Nicolson, 1996), while the spatial derivative is discretized in the lattice velocity direction with a second order accurate finite difference scheme. This differs from the standard approach, in which the space discretization is along the characteristics $\frac{d\mathbf{x}_l}{dt} = \mathbf{c}_l$. Moreover, the standard approach is to assume that the equilibrium function does not change during the discrete time step such that the implicit second-order scheme can be calculated explicitly. This assumption limits the time step size, and therefore the spatial resolution, required for a stable solution. Also treatment of wall boundary conditions for a discretization along characteristics is not trivial for walls that are not located exactly halfway between lattice points.

The BGK approach results in a prediction for an ideal gas. In the present research liquid behaviour is achieved, using a volumetric force field that includes the non-ideal effects of the pressure in the equations. This force is defined as

$$\mathbf{f}_{\text{non-ideal}} \equiv \nabla p - \nabla p_{\text{ideal}}, \tag{55}$$

where the pressure is obtained from density and temperature using an equation of state, e.g. for water the equation of state provided in (Jeffery and Austin, 1999) is used, namely

$$\frac{p}{\rho kT} = m - mb^* \rho - \frac{a_{VW} \rho}{kT} + \frac{m\alpha\rho}{1 - \lambda b(T)\rho}, \tag{56}$$

with b^*, a_{VW}, α and $b(T)$ parameters that represent the effect of attractive and repulsive forces such as Van der Waals-forces and hydrogen bonds.

RESULTS AND DISCUSSION
Particle motion

Table 1: Variables for simulation settling sphere.

ρ_c [kg m^{-3}]	v_c [m^2 s^{-1}]	g [m s^{-2}]
997	$8.92 \cdot 10^{-7}$	9.807

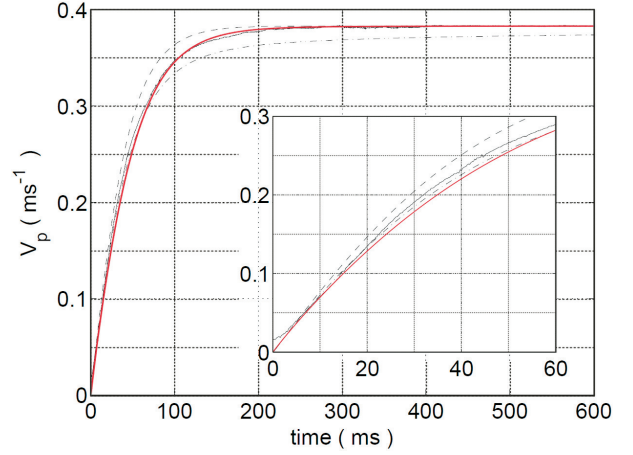| D [m]	ρ_p [kg m^{-3}]
$1 \cdot 10^{-3}$	7850

Figure 4: Prediction velocity for a settling sphere, drag correlation used: (Clift and Gauvin, 1970) (solid red). Experimental data (solid black) and numerical simulations with (dash-dotted) and without (dashed) Basset force by (Mordant and Pinton, 2000). Used parameters as in table 1. Particle density modified in simulation to match terminal velocity with experiment.
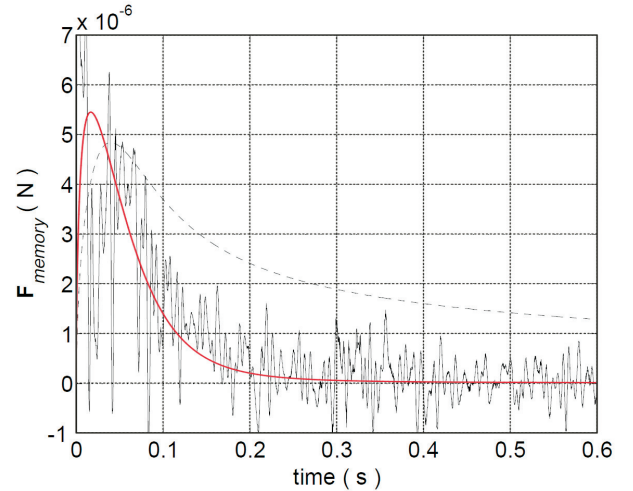

Figure 5: Prediction history force for a settling sphere (solid red). Experimentally determined history force (solid black oscillatory), and predicted Basset kernel (dashed) by (Mordant and Pinton, 2000).Variables as in figure 4

Settling sphere

Simulations have been performed to predict the velocity of an initially stationary settling sphere. Variables

have been taken to match the variables in the experiments, (Mordant and Pinton, 2000). Table 1 summarizes the variables for the simulations. Figure 4 shows the resulting prediction of the velocity of the sphere employing the drag correlation of (Clift and Gauvin, 1970). It can be observed that the Basset kernel significantly underpredicts the acceleration of the sphere and terminal velocity will only be reached after a much longer timespan, while not taking the history force into account results in an overprediction of the acceleration. The kernel used in the present research results in a good prediction for the observed particle velocity. Moreover, the kernel results in a history force that agrees well with experimentally determined history force, as shown in figure 5. However, results for other, especially very large, Reynolds numbers do not agree as well. This can be caused by an inaccurate expression for the drag coefficient as well as by an inaccurate history kernel.

The drag relations introduced in the model description have been used in simulations for the variables presented in table 1. Predicted velocities are shown in figure 6. Differences in terminal velocity up to 10% have been found, which is in the same order of magnitude as relative differences between the drag relations presented in figure 3. Moreover, the predicted time required for the particle to reach the terminal velocity is considerably longer using the relation of (Flemmer and Banks, 1986), compared to the result obtained using other relations. This implies that the prediction of the final drag as well as the prediction of the drag during the acceleration is important.

Table 2: Parameters used for swirling flow.

Ω [m^2 s^{-1}]	τ_v [s]	U [m s^{-1}]
2	500	2

Swirling flow

To examine the influence of the choice of the drag correlation and the inclusion of the history force for swirling flow fields, simulations have been performed for an oil droplet in a generic swirling flow field. The velocity field used is that of a Lamb-Oseen vortex, namely
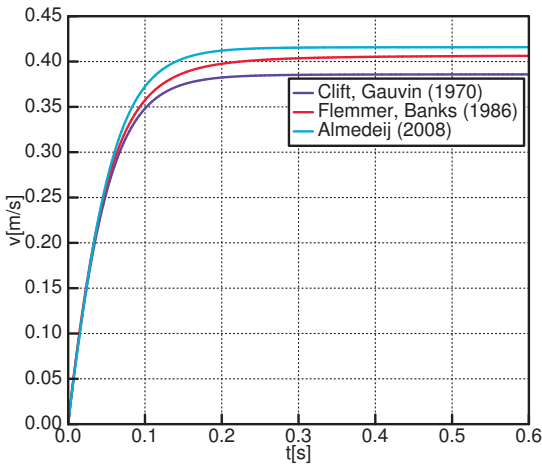
$$\mathbf{u} = \begin{pmatrix} -\frac{\Omega y}{2\pi r^2}\left(1 - e^{-\frac{r^2}{\tau_v[s]v_c}}\right) \\ \frac{\Omega x}{2\pi r^2}\left(1 - e^{-\frac{r^2}{\tau_v[s]v_c}}\right) \\ U \end{pmatrix}, \qquad (57)$$

with γ, τ_v and U flow parameters, provided in table 2.

The oil droplets in the swirling flow will gradually move to the axis of rotation due to the pressure gradient as a result of the swirl. Faxen force correction terms have been used in the simulations, using the analytical expression for the second order derivatives of the enforced flow field. Although the influence of the lift forces is barely noticeable, they have been used as described above.

Figure 7 shows the resulting particle trajectories. Differences between the results for the various drag correlations are in the same order of magnitude as the differences due to including or excluding the history force. The result shows, that in order for the particle to reach e.g. a fifth of the original radius, the particle needs to travel $\sim 10 - 20\%$ further along the pipe. The result implies that, for an accurate prediction of particle trajectories, it is not only important to correct for history effects, but more importantly to use a proper drag correlation. This is even more important for a drag dependent history kernel.

3-D flow about a sphere

The described lattice Boltzmann scheme, is used to simulate the impulsively started motion about a sphere at Re = 250 in water at $T = 298$ [K]. The fluid is considered to be an ideal gas in one case and is considered to be a liquid in the other case. In this way insight is obtained in the effect of the wave propagation speed during the unsteady start-up as well as in the compressibility effects in the final steady state.

The simulations have been performed on a coarse grid with $24 \times 24 \times 46$ elements to examine the effect of the wave propagation speed during unsteady start-up. Figure 8 shows a snapshot of the iso-surfaces of the velocity component in flow direction. A boundary layer is developing from its initial state presented in figure 9. It has to be noted that, contrary to the standard approach, the exact location of the surface of the sphere is used during the calculation. Therefore, the sphere will be better described with the current approach than using the standard approach on the coarse grid.

Figure 6: Prediction of velocity for a settling sphere, using the introduced drag correlations. Simulation flow variables are presented in table 1
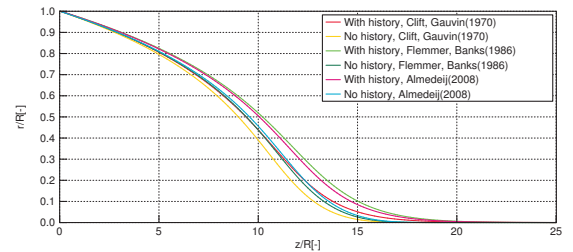

Figure 7: Prediction for distance of oil droplet to axis of rotation versus distance travelled along axis for an oil droplet, $D = 1 \cdot 10^{-4}$ [m], $\rho_p = 800$ [kg m^{-3}], in a swirling flow field, using different drag correlations and including or excluding the history force

The forces on the sphere have been calculated using the bounce-back condition at the surface of the sphere. The resulting drag is presented in figure 10. The use of a correction for the the case of a liquid results in a very rapid reaction, much more abrupt than for the case of the gas. This implies that the wave travelling speed is an important parameter for the expression of the history force. The effect of the wave travelling speed on the history force can explain the initial peak observed in the experimentally determined history force, figure 5.
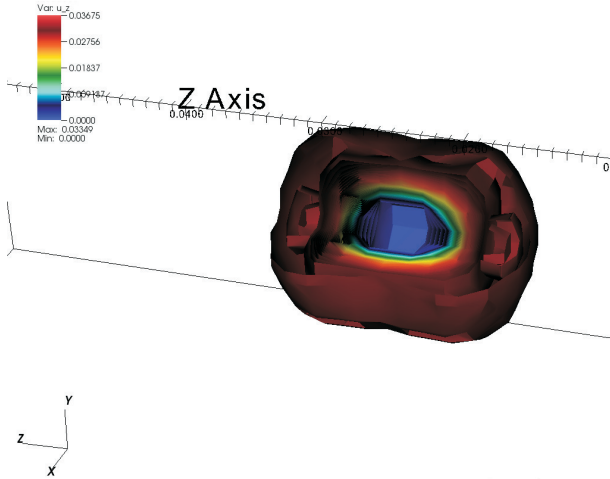
In the present study the isothermal case was considered for the flow about a sphere. For a liquid, the temperature can have a large influence on the density and pressure. Therefore, thermal effects should be examined. Implementation of thermal effects in a lattice Boltzmann method is not trivial, and is out of the scope of the present study.

CONCLUSIONS

The nature and approximation of the history force have been examined on the scale of the particle as well as on the large scale. A kernel has been implemented that includes inertia effects as well as the drag coefficient. This implementation increases the importance of an accurate prediction of the drag coefficient for high as well as low Reynolds numbers. Moreover, taking the history force into account significantly increases the time required for an oil droplet to reach the axis of rotation in a swirling flow field.

Several expressions for the drag coefficient, found in the literature, have been considered, and results show that differences up to 10% in C_D are not uncommon, for high as well as low Reynolds numbers. Results also show that still alternative expressions for the drag coefficients need to be considered that can fit the experimental data by (Mordant and Pinton, 2000).

An implicit lattice Boltzmann method has been implemented to examine the flow about a sphere on the scale of the particle. Both results for an isothermal gas as well as an isothermal liquid are presented. Initial results show that the wave travelling speed can have a major influence on the resulting transient boundary layer development. Therefore, the wave travelling speed should be considered in the expression for the history force. Thermal effects can be of major impact on initial results and should therefore be considered in further research.

ACKNOWLEDGEMENTS

Figure 8: Iso-surfaces of velocity component in flow direction, (z), for the flow about a sphere, $D = 7.0625 \cdot 10^{-3}$ [m], impulsively started to Re = 250 for isothermal water described as an at $T = 298$ [K] during the start-up process to steady state solution. An implicit D3Q27 lattice Boltzmann scheme using $24 \times 24 \times 46$ grid points, with $\Delta x = 5 \cdot 10^{-4}$ [m] and $\Delta t = 1.40735 \cdot 10^{-9}$ [s] is used.
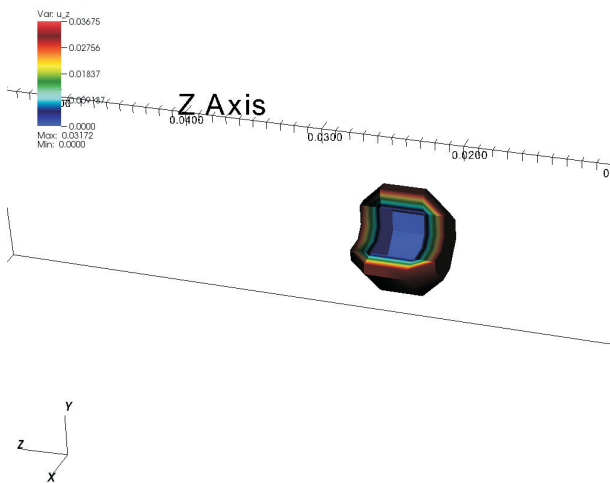

Figure 9: Initial iso-surfaces of velocity component in z-direction for the flow about the sphere presented in figure 8, indicating the level of detail of the solution in figure 8
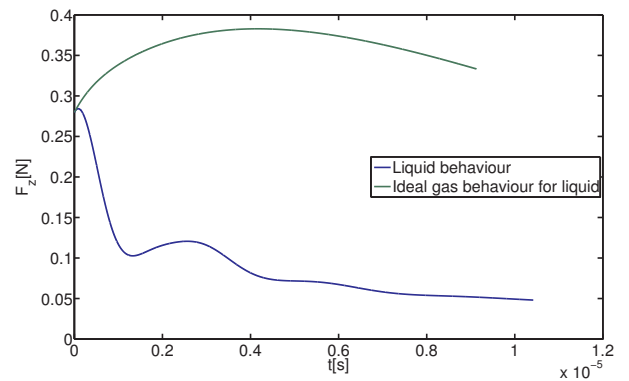

Figure 10: Predicted force in flow direction for the flow about a sphere at the conditions in figure 8 for isothermal liquid behaviour as well as isothermal ideal gas behaviour. Steady state has not yet been reached.

REFERENCES

ALMEDEIJ, J. (2008). "Drag coefficient of flow around a sphere: Matching asymptotically the wide trend". *Powder Technology*, **186(3)**, 218 – 223.

AUTON, T.R. *et al.* (1988). "The force exerted on a body in inviscid unsteady non-uniform rotational flow". *Journal of Fluid Mechanics*, **197**, 241–257.

BHATNAGAR, P.L. *et al.* (1954). "A model for collision processes in gases. i. small amplitude processes in charged and neutral one-component systems". *Physical Review*, **94(3)**, 511–525.

CHAPMAN, S. and COWLING, T. (1991). *The Mathematical Theory of Non-uniform Gases*. Cambridge Mathematical Library, 3rd ed. Cambridge University Press, The Pitt Building, Trumpington Street, Cambridge CB2 1RP.

CHEN, S. and DOOLEN, G.D. (1998). "Lattice Boltzmann method for fluid flows". *Annual Review of Fluid Mechanics*, **30**, 329–364.

CHENG, N.S. (2009). "Comparison of formulas for drag coefficient and settling velocity of spherical particles". *Powder Technology*, **189(3)**, 395 – 398.

CLIFT, R. and GAUVIN, W.H. (1970). "The motion of particles in turbulent gas streams". *Proceedings of Chemeca*, **1**, 14–28.

CRANK, J. and NICOLSON, P. (1996). "A practical method for numerical evaluation of solutions of partial differential equations of the heat-conduction type". *Advances in Computational Mathematics*, **6**, 207–226. 10.1007/BF02127704.

CROWE, C.T. *et al.* (1998). *Multiphase flows with droplets and particles*. CRC Press, 6000 Broken Sound Parkway, NW, (Suite 300) Boca Raton, Florida 33487, USA.

DANDY, D.S. and DWYER, H.A. (1990). "A sphere in shear flow at finite reynolds number: effect of shear on particle lift, drag, and heat transfer". *Journal of Fluid Mechanics*, **216**, 381–410.

FLEMMER, R. and BANKS, C. (1986). "On the drag coefficient of a sphere". *Powder Technology*, **48(3)**, 217 – 221.

JEFFERY, C.A. and AUSTIN, P.H. (1999). "A new analytic equation of state for liquid water". *Journal of Chemical Physics*, **110(1)**, 484–496.

LAWRENCE, C.J. and MEI, R. (1995). "Long-time behaviour of the drag on a body in impulsive motion". *Journal of Fluid Mechanics*, **283**, 307–327.

LOTH, E. and DORGAN, A.J. (2009). "An equation of motion for particles of finite Reynolds number and size". *Environmental Fluid Mechanics*, **9(2)**, 187–206.

MEI, R. (1992). "An approximate expression for the shear lift force on a spherical particle at finite Reynolds number". *International Journal of Multiphase Flow*, **18(1)**, 145–147.

MEI, R. and ADRIAN, R.J. (1992). "Flow past a sphere with an oscillation in the free-stream velocity and unsteady drag at finite Reynolds number". *Journal of Fluid Mechanics*, **237**, 323–341.

MEI, R. *et al.* (1991). "Unsteady drag on a sphere at finite Reynolds-number with small fluctuations in the free-stream velocity". *Journal of Fluid Mechanics*, **233**, 613–631.

MORDANT, N. and PINTON, J.F. (2000). "Velocity measurement of a settling sphere". *European Physical Journal B*, **18(2)**, 343–352.

RUBINOW, S.I. and KELLER, J.B. (1961). "The transverse force on a spinning sphere moving in a viscous fluid". *Journal of Fluid Mechanics*, **11(03)**, 447–459.

SAFFMAN, P.G. (1965). "The lift on a small sphere in a slow shear flow". *Journal of Fluid Mechanics*, **22(2)**, 385–400.

SCHILLER, L. and NAUMANN, A. (1933). "Über die grundlegenden berechungen bei der schwerkraftaufbereitung". *Vereines Deutscher Ingenieure*, **77**, 318–320.

VAN EIJKEREN, D.F. and HOEIJMAKERS, H.W.M. (2010). "Influence of the history term in a Lagrangian method for oil-water separation". *Proceedings of 7th International Conference on Multiphase Flow 2010*, 6.2.1.

CFD SIMULATION OF BUBBLY FLOW BASED ON THE DUAL-BUBBLE-SIZE MODEL

Zongying WU[1,2], Ning YANG[1*], Jianhua CHEN[1], Jinghai LI[1]

[1] State Key Laboratory of Multi-Phase Complex System, Institute of Process Engineering, Chinese Academy of Sciences, P. O. Box 353, Beijing, 100190, P.R.CHINA

[2] Department of Chemical Engineering, Xi'an Jiaotong University, Xi'an, 710049, PR CHINA

* E-mail: nyang@home.ipe.ac.cn

ABSTRACT

Sub/superscripts

INTRODUCTION

Keywords:

NOMENCLATURE

Latin Symbols

MODEL DESCRIPTION

SETTINGS OF CFD SIMULATION

$$U \quad + U \quad = U$$

$$f \rho g = \frac{f}{\pi / \cdot d} \cdot C \quad \frac{\pi}{} d \quad \cdot - \rho \left(\frac{U}{f} - \frac{U}{-f} \right)$$

$$i$$

EFFECT OF BUBBLE DIAMETER

$$\sum_i N \quad _i + N \quad = \quad i =$$

$$C \quad = \quad \frac{}{} + \quad \frac{}{} - \frac{Eo}{Eo+}$$

$$C \quad = C \quad - \varepsilon_g \quad ^p$$

C $=$ C C C

C $= \sqrt{}$ C $=$

EFFECT OF CORRECTION FACTOR

p
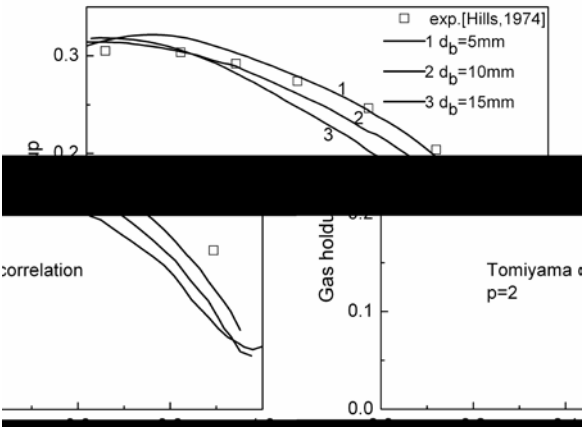
Simulation of radial profile of gas holdup with different bubble diameter (d_b).
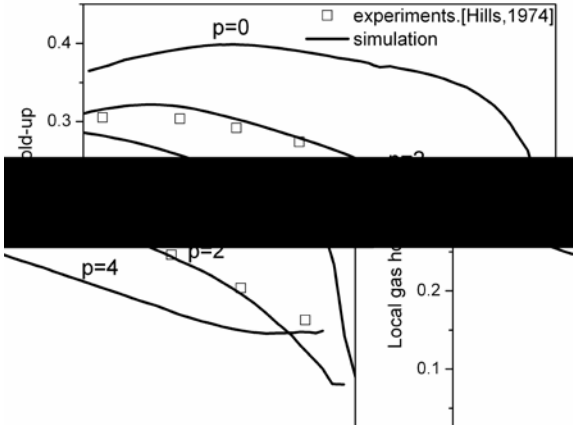
Simulation of radial gas holdup with different correction factor (p).

p

p

Simulation of radial profile of liquid velocity with different bubble diameter.

INTEGRATION OF THE DBS MODEL WITH CFD SIMULATION

$$C_D \, d_b = \begin{cases} - & U_g + & U_g & U_g \leq \\ - & U_g + & U_g & U_g > \end{cases}$$
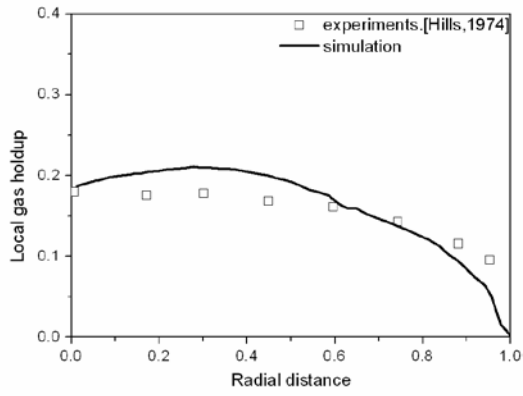
Simulation of local gas holdup with the DBS drag model for Ug=0.038m/s.

Simulation of the total gas holdup with the DBS drag model.
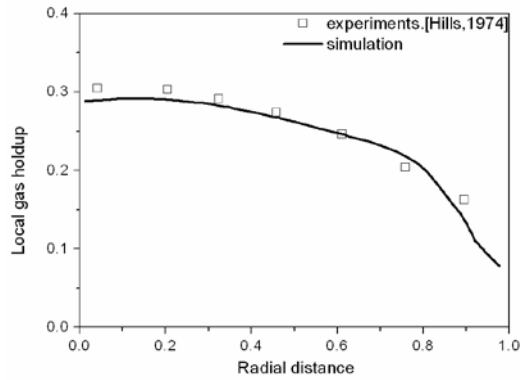
Simulation of local gas holdup with the DBS drag model for Ug=0.095m/s.
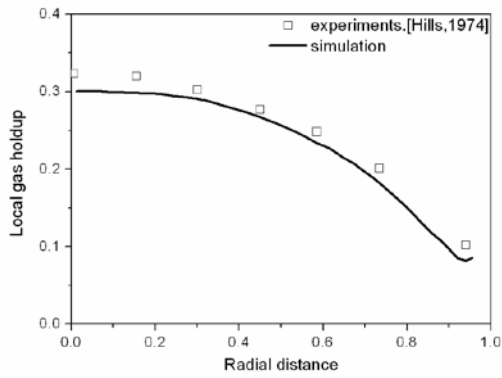
Simulation of local gas holdup with the DBS drag model for Ug=0.127m/s.
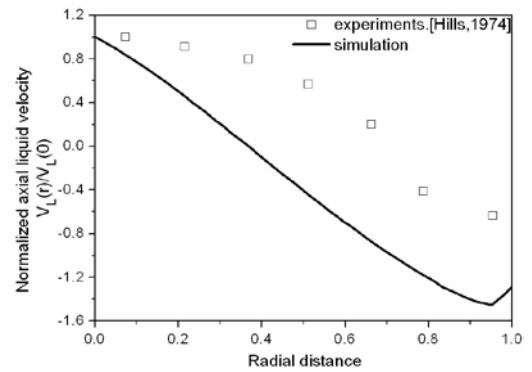
Simulation of the normalized axial liquid velocity for Ug=0.038m/s.
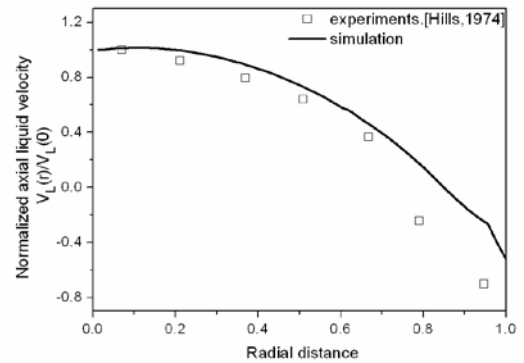
Simulation of the normalized axial liquid velocity for Ug=0.095m/s.

$U_g=0.038m/s$ $U_g=0.095m/s$ $U_g=0.127m/s$

Gas

Liquid
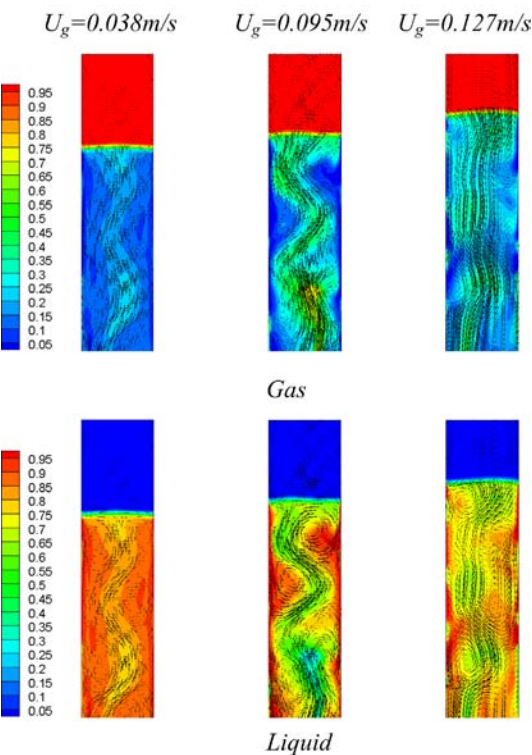
Flow fields and gas holdup distribution at a cross-section of the 3D bubble column at t=160s.

CONCLUSIONS

REFERENCES

Ind. Eng. Chem. Res. **48**

Ind. Eng. Chem. Res. **48**

Chem. Eng. Sci. **51**

Chem. Eng. Sci. **62**

Transactions of the Institution of Chemical Engineers **52**

Chem. Eng. Sci. **58**

Multiphase Science and Technology **10**

Chem. Eng. Sci. **65**

Chem. Eng. Sci.

8th International Conference on CFD in Oil & Gas, Metallurgical and Process Industries
SINTEF/NTNU, Trondheim NORWAY
21-23 June 2011

CFD11-115

TESTING OF OPENFOAM CFD CODE FOR PLANE TURBULENT BLUFF BODY FLOWS WITHIN CONVENTIONAL URANS APPROACH

Dmitry A. LYSENKO[1*], **Ivar S. ERTESVÅG**[1], **Kjell E. RIAN**[2]

[1]NTNU Department of Energy and Process Engineering, 7491 Trondheim, NORWAY

[2]Computational Industry Technologies AS, 7462 Trondheim, NORWAY

[*] E-mail: dmitry.lysenko@ntnu.no

ABSTRACT

Plane turbulent bluff-body flows were numerically analyzed using compressible formulation of the conventional URANS approach. The low-Reynolds-number $k - \varepsilon$ turbulence model of Launder and Sharma was applied for the closure problem. Numerical simulation was carried out using the state-of-the-art OpenFOAM technology for the three popular test problems in fluid dynamics: 1) plane laminar (Re = 140) and turbulent (Re = 3900) compressible (M = 0.2) flows over a circular cylinder; 2) turbulent bluff-body flow in the channel (Re = 17500, M = 0.03) replicating the Fujii lab-test conditions; 3) turbulent bluff-body flow in the channel (Re = 45000, M = 0.05) replicating the Volvo test rig. It was found out that compressible solutions provide more accurate ($\approx 20\%$) predictions of the recirculation zone length behind a bluff-body than incompressible. Satisfactory agreement between numerical and measured data for the main integral and local flow characteristics was achieved which indicates on the adequacy and accuracy of the established numerical method, implemented in the OpenFOAM toolbox, for prediction of plane turbulent, separated and weakly compressible bluff-body flows.

Keywords: Compressible URANS, low-Re-number $k - \varepsilon$ turbulence model, bluff-body aerodynamics, turbulent separated flows.

NOMENCLATURE

Greek Symbols

ΔP Static pressure drop, $\Delta P = 2\Delta P / \left(\rho u_{inf}^2 \right)$.

ε Dissipation rate of turbulence kinetic energy, $[\mathrm{m^2/s^3}]$.

γ NVD GAMMA differencing scheme parameter.

κ von Kármán constant.

μ, μ_τ Dynamic molecular and turbulence viscosity, $[\mathrm{kg/m/s}]$.

ω Specific rate of turbulence energy dissipation, [Hz].

Latin Symbols

$-C_{pb}$ Mean base suction coefficient.

B Channel blockage ratio, $B = D/H$.

C_μ Constant, $C_\mu = 0.09$.

C_d Drag coefficient.

C_l Lift coefficient.

C_p Mean (time-averaged) pressure coefficient, $Cp = 2(P - P_{inf}) / \left(\rho u_{inf}^2 \right)$.

$C_{\varepsilon 1}, C_{\varepsilon 3}$ Constants in production and sink terms of ε equa-

tion.

D Bluff-body diameter or base, [m].

F First row size in the boundary layer, [m].

G Growth factor of the cells in the boundary layer.

H Channel height, $[m]$.

J The number of rows in the BL.

K Normalized turbulence kinetic energy, $K = \sqrt{4/3k}/u_{inf}$.

L Channel length, [m].

L_r Recirculation zone length, normalized by D.

N The number of cells (intervals).

P Static pressure, [Pa].

R Bluff-body half-diameter or base $(R = D/2)$, [m].

T Temperature, [K].

U Velocity, normalized by u_{inf}.

f von Kármán vortex shedding frequency, [Hz].

f_2 Function in sink term of ε equation.

id Mesh identification number.

k Turbulence kinetic energy, $[\mathrm{m^2/s^2}]$.

t^* Dimensionless time, $t^* = tu_{inf}/D$.

u Velocity, [m/s].

x,y Axial and vertical direction, normalized by D.

y^* Dimensionless distance from the wall.

z Axial direction, normalized by recirculation zone length.

CFL   Courant number

M   Mach number

Re   Reynolds number, based on a bluff-body diameter or base

Re_τ Turbulent Reynolds number

St   Strouhal number

Sub/superscripts

$\overline{\phi}$ Mean (or time-averaged) value of ϕ.

ϕ' Fluctuation component of a value ϕ.

bb   Bluff-body walls.

ch   Channel walls.

inf   Value in an incoming flow.

min   Minimum value.

INTRODUCTION

The OpenFOAM toolbox was originally developed as hi-end C++ classes library (Field Operation and Manipulation) for a broad range of fluid dynamics applications and quickly became very popular in industrial engineering as well as in academic research. The basic numerical approach for Navier-

Stokes (NS hereafter) equations solution is based on the so-called projection procedure (Chorin, 1968) in the frame of the factorized finite-volume method. The wide list of the numerical schemes and mathematical models, implemented in OpenFOAM, provides robustness and accuracy of this technology for a wide spectrum of fluid dynamics problems.

Nevertheless, in spite of many attractive features, the OpenFOAM toolbox has some disadvantages, as well. The most crucial among them are: 1) the absolute lack of default settings; 2) the huge amount of different numerical schemes and models (or an advantage for the expert users); 3) the absence of the quality certification and as a consequence – the absence of high-quality documentation and references. Thus, the problem of validation and verification for OpenFOAM capabilities becomes more principal and fundamental compared to commercial CFD codes.

This paper presents some results dedicated to the validation of the mathematical method for turbulent separated flows modeling using the OpenFOAM technology within the conventional compressible URANS approach. First, the numerical method based on the state-of-the-art transient compressible URANS solver with the definite numerical schemes, boundary conditions and the two-equation turbulence model was established. Second, the method was tested for a laminar unsteady flow over a circular cylinder and then was extended for a turbulent flow (subcritical regime) over a circular cylinder. At the third step, the chosen generalized setup was applied for the numerical simulations of the fully-developed turbulent flows in a channel with a triangular cylinder. Detailed comparison of the numerically predicted and experimentally measured data shown reasonable agreement between them. Based on such optimistic results, the established numerical method may be extended for the simulations of the turbulent reacting flows.

OVERVIEW OF THE FLUID MECHANICS OF PLANE (2D) BLUFF-BODY FLOWS

The structure of the bluff-body flow field consists of three regions: the boundary layer along the bluff-body, the separated free shear layer, and the wake. One can find the precise description of the detailed fluid dynamics for such type of flows, for example in Shanbhogue *et al.* (2009). Here, we provide some limited description, closely following Shanbhogue *et al.* (2009). A boundary layer (hereafter BL) is formed on the bluff-body leading edge and finalized with flow separation at the bluff-body base. It is worth noting, that for the obstacles with circular shape there is no sharp edge that selects *a priory* the location of flow separation and this location is only fixed by the flow regime or the upstream conditions (Parnaudeau *et al.*, 2008). Shear layers are started in the points of flow separation at the base and organized recirculation bubble behind the bluff-body when top and bottom layers are merged with each other and begin to interact. This recirculation flow region starts to form the wake. For Reynolds numbers with a length scale equal to the obstacle base, Re < 200000, the boundary layer may be assumed as laminar (analogue to a circular cylinder and referred to as the 'sub-critical regime'), and the dynamics of the downstream flow field is largely driven by the shear layer and wake processes alone (Shanbhogue *et al.*, 2009). Both asymmetric vortex shedding (the Bénard/von Kármán instability) and convective instabilities (Helmholtz instability) of the separated shear layer may exist (Shanbhogue *et al.*, 2009). The main goal of this study is to provide methodical validation of the numerical method for accurate predictions of the plane turbulent bluff-body flows.

BRIEF DESCRIPTION OF NUMERICS

The OpenFOAM code (Weller *et al.*, 1998) v.1.7.1 was used for numerical simulations. The standard solver rhoPisoFOAM was utilized for unsteady compressible Reynolds-averaged Navier-Stokes equations (URANS) modeling based on the finite-volume (FVM) factorized method (Geurts, 2004) and the predictor-corrector PISO algorithm (Issa, 1986). Typically three and one (or two) iterations were set for a PISO loop and for non-orthogonal corrections.

The modified low-Reynolds-number $k - \varepsilon$ turbulence model of Launder and Sharma (hereafter LSKE) was chosen (Launder and Sharma, 1974) for NS equations closure. Such approach does not require the specification of the 'wall-functions' as used in high-Reynolds-number formulations to describe the near-wall-region treatment. So-called 'damping functions' were introduced and incorporated in $k - \varepsilon$ model by Jones and Launder (1972). It was later re-optimized by Launder and Sharma (1974), and demonstrated satisfactory results in many applications. The wide acceptance of such formulation gradually granted the status of the benchmark for low-Reynolds-number $k - \varepsilon$ turbulence model (Cotton and Kirwin, 1995). In this work the model was applied with the following differences in the sink term of the ε equation compare to the 'baseline' model of Launder and Sharma (1974):

1. Low-Reynolds-number function f_2 was slightly changed:

$$f_2 = 1 - 0.3 \exp\left(-\min\left(\text{Re}_\tau^2, 50\right)\right).$$

2. The model constant $C_{\varepsilon 3}$ was updated from the 'baseline' value $C_{\varepsilon 3} = 2$ to

$$C_{\varepsilon 3} = \left(-0.33 - \frac{2}{3}C_{\varepsilon 1}\right).$$

The generalized fully second-order setup (in space and time) was used for all simulations. The NVD type differencing scheme – GAMMA (Jasak *et al.*, 1999) with $\gamma = 0.1$ was applied for all convective terms approximation. A second-order implicit Euler method (BDF2 formula, (Geurts, 2004)) was used for time integration together with dynamic adjustable time stepping technique to guarantee the local Courant number less then CFL < 0.5. Preconditioned (bi-) conjugate gradient method (Hestens and Steifel, 1952)) with incomplete-Cholesky preconditioner (ICCG) by (Jacobs, 1980) was used for solving linear systems with the local accuracy of 10^{-7} for all depended variables at each time step. The under-relaxation factors (0.3 for pressure and 0.7 for all other terms) were set to prove stability of calculations. The following boundary conditions were applied. Inlet: fixed values for velocity, temperature, turbulence kinetic energy and dissipation rate; pressure – zero gradient. Outlet: non-reflecting (Poinsot and Lele, 1992) boundary conditions (NRBC) for pressure and zero gradients for velocity, temperature and turbulent properties. Bluff-body and channel walls were treated as isothermal no-slip conditions. The upper and down buffer domain boundaries were used as symmetry planes. The turbulence intensity at the inlet was set equal to 4% that is common for the typical wind tunnels. The characteristic scale of the turbulence was set equal to the bluff-body diameter (or base). The molecular viscosity and the thermal conductivity were taken to be constant. The Prandtl number was assumed to be 0.75, and the ratio of specific heats is 1.4 (the ideal gas).

RESULTS

Laminar unsteady flow over a circular cylinder ($Re = 140$, $M = 0.2$)

At the first step, methodical investigation of an unsteady laminar flow around a circular cylinder at a Reynolds number, $Re = 140$ and Mach number, $M = 0.2$ was carried out with the goal of validation, verification and understanding of the numerical methods and their capabilities implemented in OpenFOAM. The unsteady laminar flow was simulated in two different formulations: incompressible and compressible.
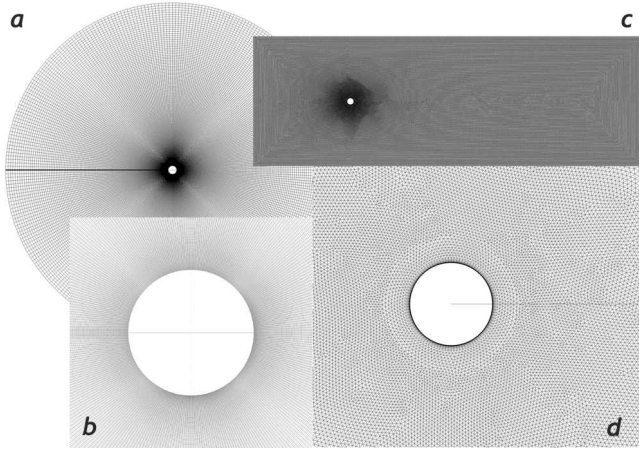

Figure 1: Descriptions of computational grids: curvilinear O-type orthogonal (*a,b*) and unstructured triangular (*c,d*).

Two types of the grids were used: unstructured, based on triangular elements and structured curvilinear (polar) O-type.

Table 1: The parameters of the designed computational grids.

id	Mesh type	Size	Domain
1	Unstructured triangular	0.327×10^6	$L \times H = 6.5\,\text{m} \times 2\,\text{m}$
2	O-type quad	325×325	$40 \times R$
3	O-type quad	600×600	$100 \times R$

O-type grid (Fig. 1,*a-b*): the configuration of the region surrounding the cylinder from the center had the form of a circle. A cylinder of diameter, $D = 0.1\,\text{m}$ is located in the center of the computational domain. The integration domain had a radial extension of $40 \times R$ (or $20 \times D$), which was chosen based on preliminary investigations (Isaev *et al.*, 2005) and it's assumed sufficient for incompressible flow simulation. The grid points were clustered in the vicinity of the cylinder. The obstacle as well as the outer boundary profiles were divided into 325 equal intervals. Radial states were divided into 325 intervals with an expansion factor of 1.020. However, for compressible simulations such grid with an radial extension of $40 \times R$ is not sufficient (Müller, 2008) and farfield boundary typically is chosen to $R = 80 - 100$ calibers (or sometimes, additional buffer domain is used with the domain extension up to $R = 500 - 750$). So for compressible laminar flow simulation updated O-type grid with radial extension $100 \times R$ (or $50 \times D$) was used with size of $[600 \times 600]$. The expansion factor for radial states was the same as in the first grid.

Unstructured triangular grid (Fig. 1,*c-d*): the computational region represented the rectangle of a size $L \times H = 6.5\,\text{m} \times 2\,\text{m}$. For consistency with previous results, the computational domain replicated solutions discussed by Isaev *et al.*

(2005), where generally satisfactory results were obtained for this problem. A cylinder of diameter, $D = 0.1\,\text{m}$ was located at a distance of 17.5 calibers (or cylinder diameters, D) from the inlet and symmetrically relative to the upper and bottom boundaries. The obstacle was surrounded by a structured ring grid (so called viscous BL) with a minimum near-wall step size of $F = 5 \times 10^{-6}\,\text{m}$. The cylinder profile was divided into $N = 100$ equal intervals. The cell size at the outer boundaries was fixed and equal to 0.015 m, leading to smooth grid refinement in the vicinity of the cylinder (Fig. 1,*c*).
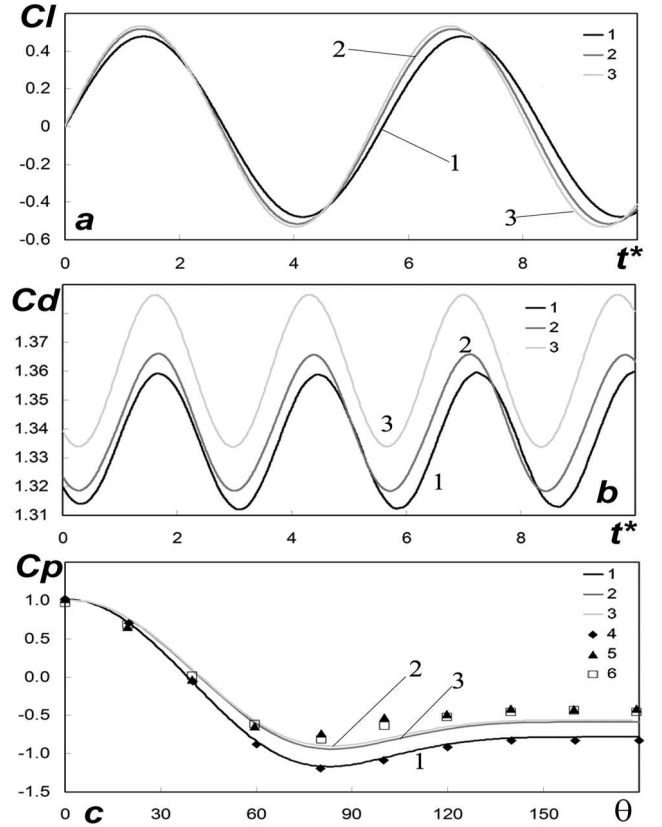
Figure 2: Time evolution of the lift (*a*) and drag (*b*) coefficients and comparison of time averaged pressure coefficient distribution over the cylinder's base (*c*): 1-3 – current numerical results (1 – compressible flow, O-type mesh, 2,3 – incompressible flow, O-type and unstructured meshes, respectively); 4 – Inoue and Hatakeyama (2002); 5,6 – Grove *et al.* (1964).

Some results are shown in Fig. 2. In general, a satisfactory agreement between numerical and experimental results (drag, lift coefficients and its fluctuations, mean base pressure coefficient, pressure coefficient distribution over cylinder and wake frequency) was obtained using different grids (structured and unstructured), solvers (incompressible, compressible) and codes (OpenFOAM, FLUENT).

The time history of the lift C_l and drag C_d coefficients are presented at Fig. 2,*a-b*. Results obtained both for structured and unstructured grids with incompressible/compressible formulations are in quite good agreement between each other. The discrepancies for the C_d distributions (Fig. 2,*b*) may be associated with distinct mesh topologies resulted in the slightly different pressure field prediction (Fig. 2,*c*). Signals obtained at the O-type grids are quite close to each other in opposite to one related with the unstructured triangular mesh. Isaev *et al.* (2005) discussed the same numerical re-

sults using FLUENT and the in-house VP2/3 code.

The mean drag coefficient was determined in the range $\overline{C_d} = 1.34 - 1.36$. These values agree with the data obtained by Müller, (2008). The amplitudes of the lift and drag coefficients are $C'_l = 0.48 - 0.53$ and $C'_d = 0.023 - 0.026$. These nondimensional force amplitudes are in good agreement with Inoue and Hatakeyama (2002), who reported $C'_l = 0.52$ and $C'_d = 0.026$, respectively, for inlet freestream Mach number M = 0.2. Müller, (2008) using a high-order finite difference method (HOFDM), got $C'_l = 0.5203$ and $C'_d = 0.02614$, respectively.

The Strouhal number, i.e. the nondimensional frequency of the vortex shedding, was computed to St $= 0.18 - 0.184$. Inoue and Hatakeyama (2002) found the value of St $= 0.183$ in their DNS, who used a compact HOFDM to solve the 2D compressible NS equations. Müller, (2008) predicted the value of St ≈ 0.1831 in the similar conditions. Williamson (1996) discussed in detail the Strouhal-Reynolds number relationship for the laminar shedding regime $(47 < \mathrm{Re} < 200)$. Over a period of 100 years (Williamson, 1996), beginning with the vortex frequency measurements of Strouhal (1878), there has existed of the order of 20% disparity among the many measurements of Strouhal number vs. Reynolds number, for this regime. The more recent results show the single St–Re function and have an agreement to the 1% level of St–Re relationship for laminar parallel shedding using different techniques, such as a wind tunnel facility and a water facility known as a towing tank. The generalized St–Re curve proposed by Williamson (1996) has the following equation:

$$\mathrm{St} = \frac{A}{\mathrm{Re}} + B + C \cdot \mathrm{Re}$$
$$A = -3.3265, \ B = 0.1816, \ C = 1.6 \times 10^{-4},$$

which leads to an experimental Strouhal number, St $= 0.18$. Williamson (1996) provides the plot of the base suction coefficient $(-C_{pb})$ over wide range of Reynolds numbers also. For Re=140, the experimental value of $-C_{pb} = 0.84$ can be determined and correlates well with the numerically predicted values of $-C_{pb} = 0.842 - 1.060$. The distribution of the time-averaged pressure coefficient over a circular cylinder is presented in Fig 2,c. The numerical results obtained for compressible flow matched well with the DNS (Inoue and Hatakeyama, 2002). Data from incompressible flow calculations obtained at different grids are very close to each other on the one hand, and on the other hand – close to experimental results by Grove *et al.* (1964). The gap between the distributions of mean pressure coefficient can be explained by the difference in the implementation of NS equations solution algorithms in compressible and incompressible flow formulations. The DNS as well as the current compressible simulation were carried out for the Mach number M = 0.2. Experimentally measured values by Grove *et al.* (1964) are close to the results obtained with incompressible flow assumption. Thus, we can suppose that the last one was obtained in ambient conditions with weak compressibility (M < 0.1).

It should be noticed, that there is some underprediction of integral parameters and fluctuations values in the force coefficients, predicted by FLUENT (see Table 2) and reported by Isaev *et al.* (2005). The main reason for such lower values may be treated as a result of excessive numerical scheme dissipation when the dynamic mesh adaptation algorithm is applied.

Finally, Fig. 3 represents an instantaneous field of the radi-

ated density gradient that depicts clearly the unsteady nature of the compressible laminar flow over a circular cylinder and the qualitative assessment of applied NRBC.
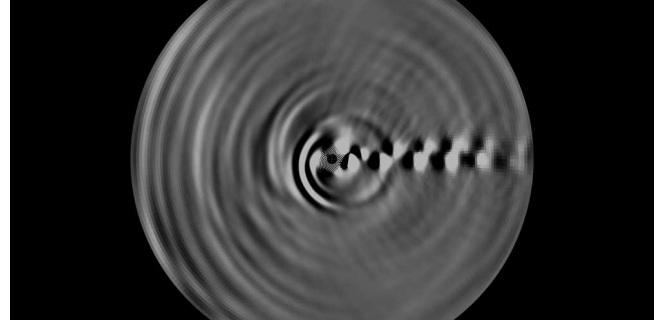

Figure 3: The contours of instantaneous radiated density gradient field (256 values from [0.0 0.025]).

Turbulent flow over a circular cylinder (Re $= 3900$, M $= 0.2$)

The turbulent flow over a circular cylinder at Re $= 3900$ is probably the more documented one in the literature and can be viewed as a generic benchmark for the subcritical regime (Parnaudeau *et al.*, 2008). Nevertheless, there are relatively few hot-wire anemometry (HWA) measurements available in the near wake of the circular cylinder due to some experimental difficulties (the presence of the recirculation zone and high instantaneous flow angles). The pioneer work was done by Ong and Wallace (1996), who managed to accurately measure velocity and vorticity vectors in the near wake outside the recirculation bubble $(3 < x/D < 10)$. To avoid the restrictions associated with the presence of back flow, the techniques of particle image (PIV) or laser Doppler (LDV) velocimetry are more appropriate (Parnaudeau *et al.*, 2008). Lourence and Shih (1993) performed very early in the PIV history, time resolved measurements at Re $= 3900$ in the recirculation region. Statistical quantities were assessed even this PIV experiment was not designed for this purpose. Recently, the flow over a circular cylinder was studied by Parnaudeau *et al.* (2008) in the near wake $(0 < x/D < 10)$ at Re $= 3900$ both numerically (LES) and experimentally with PIV and HWA. 2D2C PIV experiments (two in-plane velocity components in a plane field) were carried out with a NewWave lase Solo 3 based on Nd:YAG with an energy pulse of 50 J and two PCO cameras SensiCam. HWA was carried out with a X-wire probe. The sampling frequency was 6000 Hz and the analog low-pass filter cutoff frequency was 3000 Hz.

Several runs were conducted using both incompressible and compressible flow assumption for the grids with $id = 2$ and $id = 2, 3$ (Table 1, respectively). The free stream turbulence intensity was set to 0.12% in all runs.

The distribution of the mean pressure coefficient on the surface of the cylinder is plotted in Fig. 4,a. The computed drag coefficient $\overline{C_d} = 1.069 - 1.094$ and the back-pressure coefficient $-C_{p,b} = 1.15 - 1.16$ are not much too high ($\approx 10\%$) compared with experimental measurements of Norberg (1994), who measured $\overline{C_d} = 0.98$ and $-C_{p,b} = 0.9$ respectively. In general, the numerical and measured data are in a satisfactory agreement, however, one can observed small deviations between incompressible and compressible conditions, which can be explain by their different numerical algorithm implementation. The computed values of the Strouhal number of the vortex shedding frequency
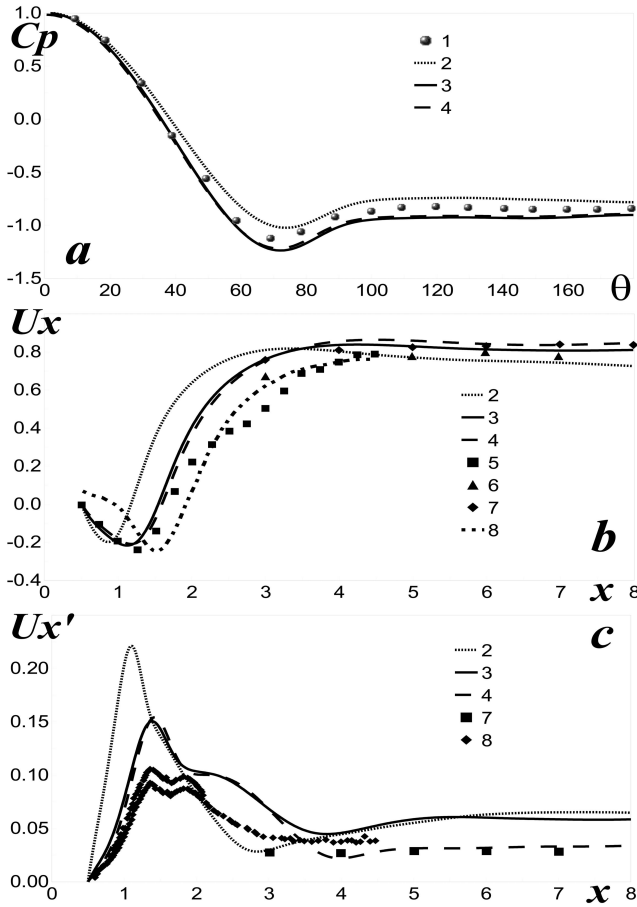
Figure 4: Mean pressure coefficient distribution over the cylinder's base (*a*); Normalized mean *x*-velocity in the wake centerline (*b* and its variance (*c*). Experiment: 1 – (Norberg, 2001), 5 – (Lourenco and Shih, 1993), 6 – (Ong and Wallace, 1996), 7,8 – PIV and HWA by Parnaudeau *et al.* (2008). Present calculations: incompressible (2) and compressible (3-4) runs with grid *ids* $= 2, 2, 3$ from Table 1.

$St = 0.215 - 0.216$ are found to be within the experimental range of $St = 0.203 - 0.215$ (see Table 2).

Fig. 4,*b* presents mean axial velocity in the wake centerline and its variance (Fig. 4,*c*). The mean streamwise velocity is zero at the base of the cylinder (no-slip condition). It reaches a negative minimum ($U_{x,min}$) in the recirculation zone and converges asymptotically and monotonously toward the external velocity. Current URANS results predicted $U_{x,min} = -0.21 - 0.22$, which are in reasonable agreement with the results reported by Parnaudeau *et al.* (2008): $U_{x,min} = -0.26$ and $U_{x,min} = -0.34$ for their LES and PIV, respectively. However, there are some deviations in the data related to the recirculation zone length (L_r), defined (hereafter) as the distance in streamwise direction between the bluff-body downstream edge and the location, where the mean axial velocity in the central-line turns from negative to positive values. Present numerical simulations predicted $L_r = 0.68$ for the incompressible setup and $L_r = 1.05 - 1.1$ for the compressible. The last values are close to the experiment ($L_r = 1.19$) of Lourence and Shih, (1993) and DNS ($L_r = 1.12$), performed by Ma *et al.* (2000). LES and PIV results, obtained by Parnaudeau *et al.* (2008) as well as DNS and PIV results by Dong *et al.* (2006) demonstrated more extended length of the recirculation bubble $L_r = 1.36 - 1.56$. It is known that the recirculation zone length L_r is slightly dependent on

the aspect ratio and (or) blocking effects. $U_{x,min}$ value may be more sensitive to these effects (Parnaudeau *et al.*, 2008). Kravchenko and Moin (2000) suggested that the smaller recirculation length is a consequence of an earlier transition in the shear layer due to inflow disturbances. A lack of statistical convergence could also be suggested (Parnaudeau *et al.*, 2008), since the PIV experiments have been conceived and optimized more for a dynamic study of the flow that for a statistical analysis. The variance of of the axial velocity is also zero at the base of the cylinder and reaches two peaks (according to PIV measurements) before its slow monotonous decay toward zero. However, there are no second peak, but only light step in the present compressible URANS results (Fig. 4,*c*).

Plane turbulent bluff-body flow – Fujii test case (Re = 17500, M = 0.03)

Experiments (Fujii *et al.*, 1978; Fujii and Eguchi, 1981) were carried out in an open circuit, forced flow type of wind tunnel at ambient conditions ($P_{inf} \approx 100$ kPa, $T_{inf} = 280$ K). A sketch is presented in Fig. 5,(*a*). An equilateral ($D = 0.025$ m) triangular rod was placed inside the channel passage of 0.05 m-square cross section. The channel blockage ratio in this test was, $B = 0.5$. The velocity in a front of the bluff-body was limited to $u_{inf} = 10$ m/s. The turbulence intensity level at the inlet of the test section was about $2 - 4\%$. Thus, the corresponding Reynolds number based on the bluff-body base was about Re ≈ 17500 and the Mach number, M ≈ 0.03.
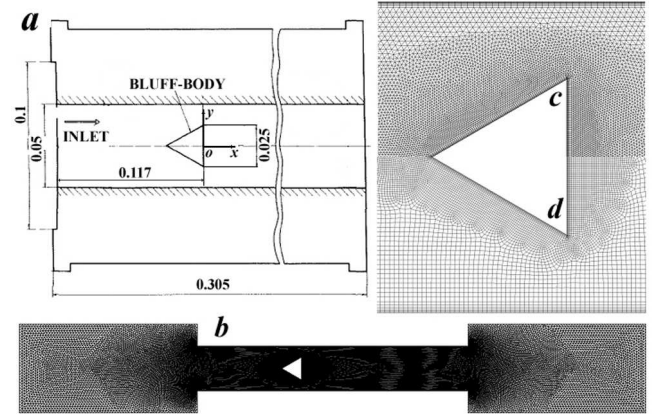
Figure 5: A general view of the experimental test rig (*a*) taken from Fujii *et al.* (1978), computational domain (*b*) and the fragments of the designed grids (*c-d*) at the vicinity of the bluff-body.

The two dimensional computational domain (Fig. 5,(*b*)) was chosen in such a way to replicate lab test conditions. The channel length and height were set to $L = 0.305$ m and $H = 0.05$ m, respectively. The bluff-body was located at $x = 0.117$ m from the channel inlet. Two additional buffer domains with length 0.05 m and height 0.1 m were attached to the channel. The inlet buffer domain was used to avoid setting of the turbulent velocity and temperature profiles at the channel inlet since it was not measured in lab tests and to avoid investigating the influence of the boundary layer width on the flow parameters.

Two finite-element baseline grids with different cell types were used in the simulations:

- Unstructured triangular mesh (Fig. 5,(*c*)). Viscous BLs were attached to the obstacle with the following parameters: $F = 5 \times 10^{-5}$ m, $G = 1.25$ and $J = 7$ in or-

Table 2: Integral characteristics for 2D unsteady laminar and turbulent flows over a circular cylinder.

Contributors	Method	Re	M	$\overline{C_d}$	C_d'	C_l'	St	$-C_{pb}$	L_r
(Williamson, 1996)	EXP	140					0.180	0.84	
(Müller, 2008)	HOFDM	150	0.2	1.340	0.026	0.520	0.183		
(Inoue and Hatakeyama, 2002)	DNS	150	0.2		0.026	0.520	0.183		
(Isaev *et al.*, 2005)	URANS	140	–	1.270	0.011	0.400	0.172		
Current results									
id = 1	URANS	140	–	1.360	0.026	0.533	0.184	0.842	
id = 2	URANS	140	–	1.342	0.024	0.518	0.184	0.860	
id = 3	URANS	140	0.2	1.340	0.023	0.480	0.180	1.060	
(Lourenco and Shih, 1993) data taken from (Beaudan and Moin, 1994)	PIV	3900		0.99			0.215		1.19
(Norberg, 1994)	EXP	3900		0.98				0.9	
(Ong and Wallace, 1996)	HWA	3900					0.21		
(Ma *et al.*, 2000)	DNS	3900		0.96			0.203	0.96	1.12
(Dong *et al.*, 2006)	PIV/DNS	3900					0.203		1.36 -1.47
(Parnaudeau *et al.*, 2008)	HWA/PIV	3900					0.208		1.51
Current results									
id = 2	URANS-LSKE	3900	–	1.197	0.044	0.82	0.22	0.92	0.68
id = 2	URANS-LSKE	3900	0.2	1.094	0.041	0.488	0.215	1.16	1.05
id = 3	URANS-LSKE	3900	0.2	1.069	0.028	0.464	0.216	1.15	1.1

Table 3: The description of the designed computational grids for the Fujii lab test simulations.

id	Mesh type	Mesh size N cells	Domain size (m)	Bluff-Body N intervals	BL channel (F,G,J)	BL obstacle (F,G,J)	$\overline{y_{ch}^*}$	$\overline{y_{bb}^*}$
1	triangular	84K	0.0010	3×80	$5 \times 10^{-5}, 1.3, 7$	$5 \times 10^{-5}, 1.25, 7$	0.5	0.6
2	quad	56K	0.0015	3×60	$1 \times 10^{-4}, 1.3, 7$	$5 \times 10^{-5}, 1.25, 7$	1.6	0.6
3	quad	110K	0.0010	3×80	$1 \times 10^{-4}, 1.3, 7$	$5 \times 10^{-5}, 1.25, 7$	1.6	0.6
4	quad	277K	0.0005	3×160	$1 \times 10^{-4}, 1.3, 7$	$5 \times 10^{-5}, 1.25, 6$	1.6	0.5

der to describe very accurately the development and detachment of the BL. The same (except G) viscous BL was applied for the channel walls. Each edge of the bluff-body was divided into $N = 80$ equal intervals. The computational domain was meshed with the size of 0.001 m, which guarantees smooth grid distribution from the inlet and outlet to the triangular rod. All these features provided good near-to-wall mesh resolution and allowed to apply the low-Reynolds-number $k - \varepsilon$ turbulence model;

- Baseline unstructured quadrilateral mesh (Fig. 5,(*d*)) was designed in the same manner;

- To check solution mesh independence, two additional grids were built, both with the quad cells. The type of the attached viscous BLs was the same as in the baseline quad mesh and domain was meshing with sizes of 0.0015 m and 0.0005 m, respectively. Parnaudeau *et al.* (2008) suggested that for the flows, where the BLs remains laminar, the use of nonrefined near-wall spatial resolution can be accepted, by assuming that the influence of the detailed structure of the BL on the wake statistics (integral flow parameters) is rather weak.

The details of the designed grids for this test case are summarized in Table 3.

Time-averaged measured and numerically predicted streamlines of the flow around the triangular bluff-body are presented in Fig. 6,(*a*). The results of the CFD analysis (lower part of the frame Fig. 6,(*a*)) provided a more extended length of the reversed zone, $L_r = 2.67$ compared to the measured

one (upper part of the frame Fig. 6,(*a*)), $L_r = 2.2$. Thus, the difference between them was $\approx 18\%$.

Time-averaged pressure coefficient distribution downstream the bluff-body inside the recirculation bubble is shown in Fig. 6,(*b*). Present numerical results obtained at the baseline grids (with $id = 1$ and $id = 3$ from Table 3) demonstrated quite similar behavior with experimental results. Minimum values were also in a good agreement between numerical ($C_{p,min} = -2.7$) and measured ($C_{p,min} = -2.73$) data. The normalized turbulence kinetic energy distribution along the central axis in the recirculation zone is provided in Fig. 6,(*c*). Hereafter the following assumption is used for measured and numerical turbulence kinetic energy definition:

$$k = \frac{3}{4} \left(\overline{u_x'^2} + \overline{u_y'^2} \right). \qquad (1)$$

The normalisation is defined as:

$$K = \frac{\sqrt{4/3k}}{u_{inf}}. \qquad (2)$$

One can observe the non-significant shift between numerically predicted data that is the influence of the grid topology. Overall, the good qualitative and quantitative agreement for K distribution between lab test and numerical modelling data was achieved.

The time history of the normalized instantaneous *y*-velocity numerically predicted are presented in Fig. 6,(*d*). The probe location was in the same position as in the lab test ($x = 1.2$ and $y = 0.6$). As expected, periodic sinusoidal type signals that were obtained clearly illustrate self-regular vortex shedding behavior of the wake. All curves according to Table 3)
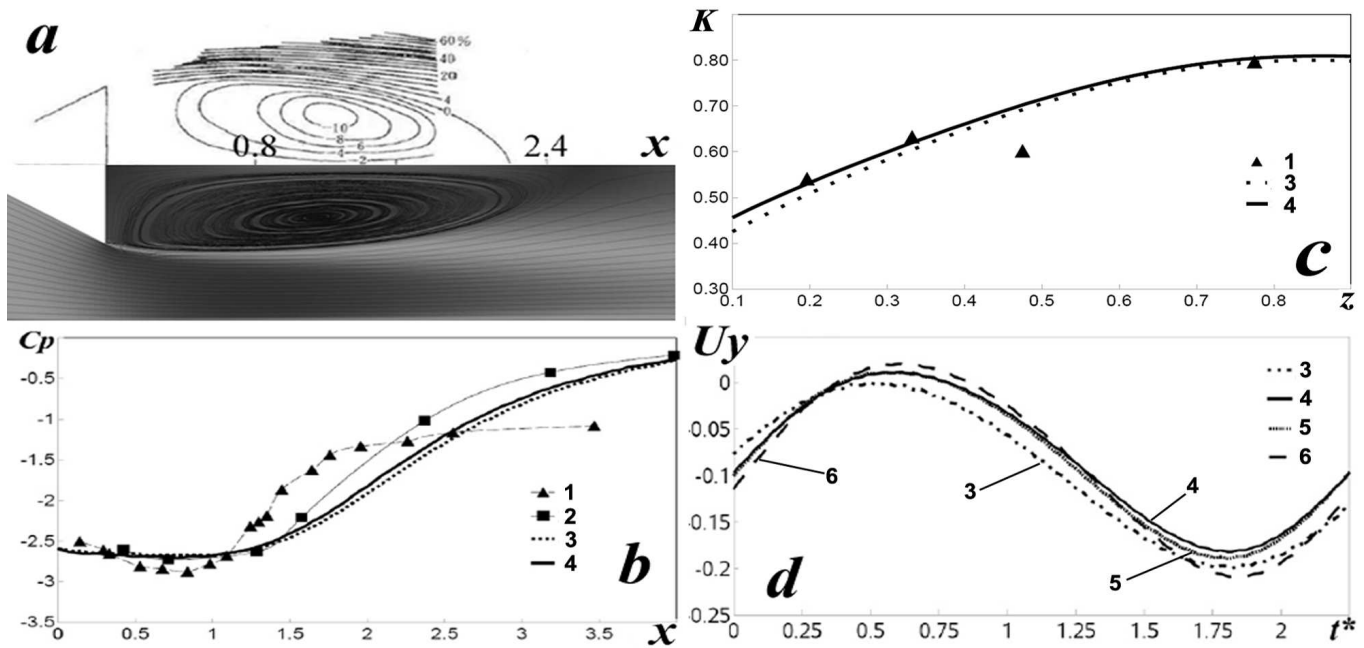
Figure 6: Time-averaged integral flow characteristics: a – the recirculation bubble (**Fujii and Eguchi** (1981) – the upper side and present results – the down side); mean pressure coefficient distribution (b) and normalized turbulent kinetic energy (c) in the wake centerline; d – time history of the instantaneous normalized y-velocity, obtained numerically. Experiments: 1 – (**Sullerey *et al.***, 1975); 2 – (**Fujii and Eguchi**, 1981). Present numerical runs: 3-6 with grid $ids = 1, 3, 2, 4$ according to Table 3.

Table 4: Integral parameters for the Fujii lab test.

Contributors	Method	B	Re	M	$C_{p,min}$	L_r	St
(Sullerey *et al.*, 1975)	EXP	0.25	11500	0.03	2.87	2.3	0.18
(Fujii *et al.*, 1978; Fujii and Eguchi, 1981)	LDV	0.5	17500	0.03	2.73	2.2	0.40
Current work	URANS-LSKE	0.5	17500	0.03	2.7	2.67	0.45
	URANS-LSKE	0.5	17500	–	2.65	2.87	0.45

are quite close to each other and can confirm mesh independence of the numerical solution. The averaged calculated Strouhal number was, St = 0.44, with the corresponding main frequency, $f = 177$ Hz. This is in a quite good agreement with experimental values of **Fujii and Eguchi** (1981), where a pronounced frequency, $f = 160$ Hz, and the corresponding Strouhal number St = 0.4, was detected.

Plane turbulent bluff body flow – Volvo test rig (Re = 45000, M = 0.05)

Fig. 7,(a) shows a schematic drawing of the test section. The test set-up consisted of a straight channel with a rectangular cross-section, divided into an inlet section (with length of 0.5 m) and a channel passage section with length of 1 m and 0.12 m × 0.24 m cross-section. The inlet section was used for flow straightening and turbulence control. The air entering the inlet section was distributed over the cross-section by a critical plate that, at the same time, isolated the channel acoustically from the air supply system. The channel passage section ended in a circular duct with a large diameter. The triangular bluff-body (with base diameter, $D = 0.04$ m) was mounted with its reference position 0.681 m upstream of the channel exit. The blockage ratio for this test case was $B = 1/3$.

The cold flow measurements were conducted in the ambient conditions ($T_{inf} = 288$ K and $P_{inf} = 100$ kPa, and corresponding Mach number, M = 0.05). Honeycombs and screens controlled the approximate inlet turbulence level of $3 - 4\%$. The test point that was chosen as baseline for the investigation in a numerical study, had the corresponding
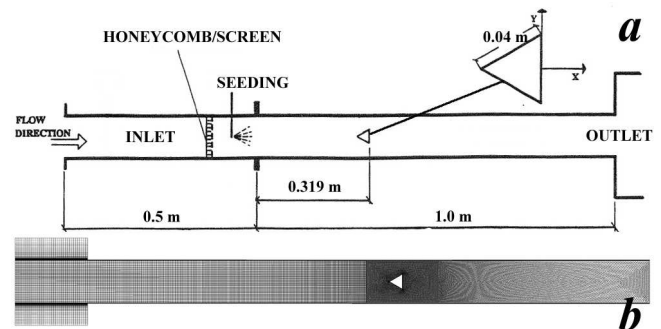

Figure 7: The sketch of the Volvo test rig (a) taken from **Sjunnesson *et al.*** (1991) and the general view of the computational domain (b).

Reynolds number, Re = 45000, based on the bluff-body diameter, which gave the inlet flow velocity in the front of the bluff-body, $u_{inf} = 16.6$ m/s. A two-component LDA system was used for the x and y velocity components and its fluctuations measurements, which consisted of 5 W Ar+ laser. To capture turbulence information small seeding particles (0.05 nm γ-alumina) were used. Further detailed description of the LDA system, experimental procedure and sampling technique can be found in **Sjunnesson *et al.*** (1991).

The two-dimensional computational domain is presented in Fig. 7,b and consisted of an inlet buffer domain (size of 0.2 m × 0.24 m) and a channel passage (size of 1.5 m × 0.12 m). It was decided to attach an inlet buffer domain to the main computational area allowing inlet velocity and tem-

Table 5: Parameters of the designed computational grids for the Volvo test rig.

id	Mesh type	Domain 1 Size (m)	Domain 2 Size (m)	Domain 3 Size (m)	Bluff-body N intervals	Mesh size	BL obstacle (F,G,J)	$\overline{y_{ch}^*}$	$\overline{y_{bb}^*}$
1	quad	0.0015	0.0007	0.00150	3×72	282K	$5 \times 10^{-5}, 1.4, 7$	1.5	1.2
2	quad\triangular	0.0030	0.0015	0.00300	3×46	88K	$5 \times 10^{-5}, 1.4, 7$	1.4	1.2
3	quad\triangular	0.0015	0.0007	0.00150	3×72	366K	$5 \times 10^{-5}, 1.4, 7$	1.5	1.2
4	quad\triangular	0.0015	0.0004	0.00070	3×144	754K	$5 \times 10^{-5}, 1.4, 5$	1.4	1.2

perature profiles to form implicitly in the computations. The integration domain was split into three blocks to generate a high-quality unstructured quad/triangular mesh:

1. the inlet buffer and a part of the channel without bluff-body;

2. the central part of the channel passage including the obstacle (size of 0.2 m × 0.12 m), with the domain's central location as described in the sketch at Fig. 7,(*a*);

3. the remaining downstream part of the channel. A total of four unstructured grids were designed and used in this work, with a detailed description presented in Table 5. It should be noticed that the first domain was meshed with quad cells in all cases. Two baseline grids (quadrilateral and triangular, with $id = 1$ and $id = 3$, from Table 5) were chosen to check the influence of the grid topology on the solution. Two additional triangular grids (with $id = 2$ and $id = 4$, from Table 5) were constructed to check the mesh independence. All grids were built in such a way to resolve explicitly BLs at the surface of the bluff-body and at the channel walls to guarantee $y* \approx 1.0$. The BLs attached to the channel walls was the same for all grids.

Table 5 gives an overview of these grids, meshing details, BLs parameters, corresponding numbers of the control volumes and averaged values of $y*$.

Several problem-related articles were found where URANS calculations had been carried out for the Volvo test rig. But it is important to notice that all of them were performed with the incompressible flow assumption. Among them were: 1) the study by Johansson *et al.* (1993) with the results for standard high-Reynolds-number $k - \varepsilon$ model, which was also recitated by Rodi (1993); 2) the paper by Strelets (2001) with some limited results available for URANS with the one-equation Spalart-Allmaras model; 3) the simulation done by Durbin (1995) with the $k - \varepsilon - v^2$ model; 4) the paper by Hasse *et al.* (2009) where brief results for URANS with $k - \omega$ SST model were discussed. Thus this work may be considered as the first one, where a compressible URANS approach has been applied to replicate the Volvo test rig.

Johansson *et al.* (1993) calculated the vortex shedding flow past a triangular flame holder. They employed the standard $k - \varepsilon$ model with wall functions (Launder and Spalding, 1972) and the hybrid central/upwind differencing scheme for the convective terms discretization. The agreement was fairly good, and profiles of the total fluctuations were also shown to be in good agreement with measured data (Sjunnesson *et al.*, 1991). Furthermore, the calculated Strouhal number, St = 0.26, was in good agreement with the experimental value of 0.25. The turbulent separated flow around a triangular cylinder in the same conditions was computed with the $k - \varepsilon - v^2$ model without any wall or damping functions by Durbin (1995), and good agreement between experiment and prediction was found. The flow around a triangular bluff-body was investigated in details by Hasse *et al.* (2009) by URANS and DES based on $k - \omega$ SST model. It was shown that this

type of a flow is essentially more dominated by the eddies created in the shear layers behind the obstacle than by incoming eddies from the transient turbulent inflow. Statistical turbulent flow quantities of URANS were compared to the experiments and it was found that URANS predictions were generally satisfactory.
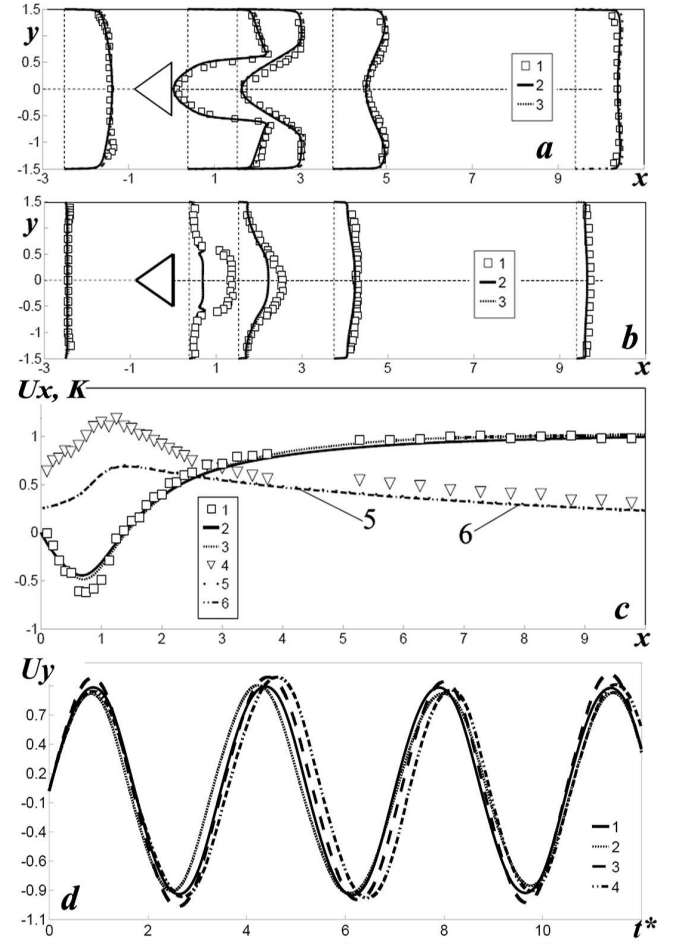

Figure 8: Mean normalized *x*-velocity (*a,c*) and turbulence kinetic energy (*b,c*) profiles in five cross sections (*a,b*) with axial coordinates of -2.5, 0.375, 1.525, 3.75 and 9.4 and in the wake centerline (*c*): 1,4 – Sjunnesson *et al.* (1991); 2-3,5-6 – present results for baseline quad (2,5) and triangular (3,6) grids, with $id = 1$ and $id = 3$, (Table 5), respectively. Time history of normalized instantaneous *y*-velocity numerically predicted at all designed grids, all curves correlate with grid *ids* according to Table 5. The monitor point was located at the same position as in the lab test of Sjunnesson *et al.* (1991) with the coordinates: $x = 1$, $y = 0$.

Fig. 8 represents some results. As was reported by Sjunnesson *et al.* (1991), the experimental profile of axial velocity component was slightly skewed due to small misalignment in the flange between the inlet section and the channel passage. However, fully symmetrical inlet veloc-

Table 6: Comparison of the integral flow characteristics for the Volvo test rig simulations.

Contributors	Method	Re	M	L_r	St
(Sjunnesson *et al.*, 1991)	EXP/LDA	45000	0.05	1.33	0.250
(Johansson *et al.*, 1993)	URANS–SKE	45000	–	1.30	0.270
(Durbin, 1995)	URANS–$k-\varepsilon-v^2$	45000	–	1.30	0.285
(Strelets, 2001)	URANS–SA	45000	–	0.90	–
(Hasse *et al.*, 2009)	URANS–SST	45000	–	0.94	0.296
Current work	URANS–LSKE	45000	0.05	1.36	0.28
	URANS–LSKE	45000	–	1.57	0.28

ity profile was implicitly formed during flow development in the numerical simulations. In both cases one could observe the outer regions of BLs at the channel walls, witch corresponded very well with the '1/7 power law profile' typical for fully developed turbulent channel flows. Fig. 8,*a-b* shows the normalized mean axial velocity (*a*) and normalized turbulence kinetic energy (*b*) at several vertical cross sections in the channel. One can see that there are low discrepancies between numerical data obtained at grids with different topology as well as between measured and numerically predicted data for mean axial velocity. At the same time, a strong underproduction of numerically predicted turbulence kinetic energy was observed inside the recirculation zone, meanwhile the same level of turbulence kinetic energy was contained both in the downstream of the bluff-body and in the upstream part of channel, after the separation bubble was vanished. In Fig. 8,*c* the comparison between measured and numerically predicted normalized turbulence kinetic energy along the central axis is shown. One can observe the same trend between experimentally measured and numerical data. However the numerical experiment significantly underpredicted fluctuation's level inside the recirculation zone. This indicates that the vortex shedding is much stronger in the physical experiment and, in spite of that, it can be considered as plane, has deep three-dimensional nature.

Fig. 8,*c* shows the measured and numerically simulated normalized mean axial velocity and turbulence kinetic energy along the central-line behind the obstacle. It should be noticed a 18% underprediction of the minimum axial velocity in the recirculation zone independently of the grid type. But, overall, there is good match between numerical and experimentally measured data. For example, the same level of under-prediction was observed by Hasse *et al.* (2009) for URANS (with $k-\omega$ SST) data. Current numerical results showed good prediction for the recirculation lengths: calculated $L_r = 1.36$ in comparison with the measured (Sjunnesson *et al.*, 1991) value of $L_r = 1.33$. For example, the recirculation zone lengths obtained for URANS and DES by Hasse *et al.* (2009) were only 0.94 and 1.18, respectively.

A numerically predicted frequency of von Kármán vortex shedding matched quite well to experimental data: $f = 117$ Hz vs. $f = 105$ Hz in experimental data, and St $= 0.28$ vs. St $= 0.25$, respectively, which are differences of about 10%. These results correspond well also with those obtained by Hasse *et al.* (2009): $f = 122$ Hz and $f = 117$ Hz peak frequencies for URANS and DES, respectively.

Although the accuracy of the pressure loss measurements was not too high, as it was mentioned by Sjunnesson *et al.* (1991), it is still of interest in many engineering applications. The experimental value for the normalized pressure drop was measured (between axial states $x = -5$ and $x = 10$) to $\Delta P = 0.6$ while the numerically predicted value was $\Delta P \approx 0.7$, which correspond quite well between each other.

It should be noticed that unstructured grids with triangular and quadrilateral cell types were used, but with the same viscous BLs. The comparison provided in Fig. 8 for the mean axial velocity and turbulence kinetic energy show very small (about $1-2\%$) errors between the numerical solutions. Fig. 8(*d*) displays time history of the normalized *y*-velocity measured at the same probe location and obtained for all the meshes in this work is presented. The distribution of the curves confirms the mesh independence of the solutions since the variations between them are quite small (about $\pm 5\%$ both for the frequencies and amplitudes).

CONCLUSION

1. The generalized numerical setup for solving compressible URANS equations (based on a factorized FVM with global second-order accuracy both in space and in time, modified low-Reynolds-number $k-\varepsilon$ turbulence model of Launder and Sharma, PISO pressure-velocity coupling algorithm, GAMMA differencing scheme for convective terms approximation, BDF2 formula with dynamic time stepping technique for time integration and NRBC) was established.

2. The proposed methodology was preliminary tested for the plane laminar compressible flow over a circular cylinder. Predicted main flow parameters were in a good compliance (the deviations less than 5%) with the experimental data and other numerical results. Then, the turbulent compressible flow over a circular cylinder at Re $= 3900$ was analyzed. On the one hand, the present results were in reasonable agreement with the experiments of Ong and Wallace (1996) and Lourenco and Shih, (1993). On the other hand, there were some deviations ($\approx 20\%$) between present results and recent experiment by Parnaudeau *et al.* (2008).

3. The numerical method was validated in detail for two selected plane turbulent bluff-body flows with excessive measured data of Fujii *et al.* (1978); Fujii and Eguchi (1981) and Sjunnesson *et al.* (1991). The latter is quite popular among researchers, and several articles were found in literature where this test was used for a verification of quite close numerical procedures. But it is important to notice that all the studies found were done in an incompressible formulation. No results were found for the Fujii lab test. We can consider that this paper is the first one where the conventional URANS approach has been utilized for numerical modelling and replication these lab tests in a compressible formulation (with weak compressibility, since the Mach numbers were limited as M ≤ 0.05 in the mentioned experiments). It is worth noting that for all test cases compressible simulations provide more accurate prediction ($\approx 20\%$) of the recirculation zone length in compare to the incompressible runs.

4. All numerical results presented and discussed in this paper showed a non-significant (less than 5%) sensitivity from the different grid topologies. The mesh independence study was carried out to demonstrate mesh independence solutions for all test cases.

5. Overall, satisfactory agreement (with deviations of $10 - 20\%$) between numerical and measured data for integral and local flow characteristics was achieved for the selected benchmarks which indicates on the adequacy and accuracy of the established generalized numerical setup. The described numerical methods can be used for calculating unsteady separation flows and the simplified quasi-two-dimensional approach can be used for numerical representation of a three-dimensional vortex flow in a wake.

ACKNOWLEDGMENT

REFERENCES

BEAUDAN, P. and MOIN, P. (1994). "Numerical experiments on the flow past a circular cylinder at sub-critical reynolds numbers". Tech. rep., Technical Report TF-62, Center Turb. Res., Stanford.

CHORIN, A. (1968). "Numerical solution of Navier-Stokes equations". *Math. Computation*, **22**, 745–762.

COTTON, M. and KIRWIN, P. (1995). "A variant of the low-reynolds-number two-equation turbulence model applied to variable property mixed convection flows". *Int. J. Heat Fluid Flow*, **16(6)**, 486–492.

DONG, S. *et al.* (2006). "A combined direct numerical simulation-particle image velocimetry study of the turbulent near wake". *J. Fluid Mech.*, **569**, 185–207.

DURBIN, P. (1995). "Separated flow computations with the $k - \varepsilon - v^2$ model". *AIAA J.*, **33**, 659–664.

FUJII, S. and EGUCHI, K. (1981). "A comparison of cold and reacting flows around a bluff body flame stabilizer". *ASME J.*, **103**, 328–334.

FUJII, S. *et al.* (1978). "Cold flow tests of a bluff body flame stabilizer". *ASME J.*, **100**, 323–332.

GEURTS, B. (2004). *Elements of direct and large-eddy simulation*. R.T.Edwards.

GROVE, A. *et al.* (1964). "An experimental investigation of the steady separated flow past a circular cylinder". *J. Fluid Mech*, **19**, 60–80.

HASSE, C. *et al.* (2009). "Hybrid URANS/LES turbulence simulation of vortex shedding behind a triangular flameholder". *Flow Turbulence Combust.*, **83**, 1–20.

HESTENS, M. and STEIFEL, E. (1952). "Methods of conjugate gradients for solving systems of algebraic equations". *J. Res. Nat. Bur. Stand*, **29**, 409–436.

INOUE, O. and HATAKEYAMA, N. (2002). "Sound generation by a two-dimensional circular cylinder in a uniform flow". *J. Fluid Mech.*, **471**, 285–314.

ISAEV, S. *et al.* (2005). "Comparative analysis of the calculation data on an unsteady flow around a circular cylinder obtained using the VP2/3 and FLUENT packages and the Spalart-Allmaras and Menter turbulence models". *J. Engin. Phys. Thermophys*, **78(6)**, 1199–1213.

ISSA, R. (1986). "Solution of the implicitly discretized fluid flow equations by operator splitting". *J. Comput. Phys*, **62**, 40–65.

JACOBS, D. (1980). "Preconditioned conjugate gradient methods for solving systems of algebraic equations". Tech. rep., Central Electricity Research Laboratories, Leatherhead, Surrey, England.

JASAK, H. *et al.* (1999). "High resolution NVD differencing scheme for arbitrarily unstructured meshes". *Int. J. Numer. Meth. Fluids*, **31**, 431–449.

JOHANSSON, S. *et al.* (1993). "Numerical simulation of vortex shedding past triangular cylinders at high reynolds number using a $k - \varepsilon$ turbulence model". *Int. J. Numer. Meth. Fluids*, **16**, 859–878.

JONES, W. and LAUNDER, B. (1972). "The prediction of laminarization with a two-equation model of turbulence". *Int. J. Heat Mass Transfer*, **15**, 301–314.

KRAVCHENKO, G. and MOIN, P. (2000). "Numerical studies of flow over a circular cylinder at Re=3900". *Phys. Fluids*, **12(2)**, 403–417.

LAUNDER, B. and SHARMA, B. (1974). "Application of the energy-dissipation model of turbulence to the calculation of flow near a spinning disc". *Letters Heat Mass Transfer*, **1**, 131–138.

LAUNDER, B. and SPALDING, D. (1972). *Lectures in mathematical models of turbulence*. Academic Press, London, England.

MA, X. *et al.* (2000). "Dynamics and low-dimensionality of a turbulent near wake". *J. Fluid Mech*, **410**, 29–65.

MÜLLER, B. (2008). "High order numerical simulation of aeolian tones". *Computers and Fluids*, **37**, 450–462.

NORBERG, C. (1994). "Experimental investigation of the flow around a circular cylinder: influence of aspect ratio". *J. Fluid Mech*, **258**, 287–316.

NORBERG, C. (2001). "Flow around a circular cylinder: aspects of fluctuating lift". *J. Fluids Struct.*, **15**, 459–469.

ONG, L. and WALLACE, J. (1996). "The velocity field of the turbulent very near wake of a circular cylinder". *Exp. in Fluids*, **20**, 441–453.

PARNAUDEAU, P. *et al.* (2008). "Experimental and numerical studies of the flow over a circular cylinder at reynolds number 3900". *Phys. Fluids*, **20**, 085101.

POINSOT, T. and LELE, S. (1992). "Boundary conditions for direct simulations of compressible viscous flows". *J. Comput. Phys.*, **101**, 104–129.

RODI, W. (1993). "On the simulation of turbulent flow past bluff bodies". *J. Wind Eng. Ind. Aerodyn.*, **46 and 47**, 3–19.

SHANBHOGUE, S. *et al.* (2009). "Lean blowoff of bluff body stabilized flames: scaling and dynamics". *Prog Energy Combust Sci*, **35**, 98–120.

SJUNNESSON, A. *et al.* (1991). "LDA measurements of velocities and turbulence in a bluff body stabilized flame". Tech. rep., Volvo Flygmotor AB, Trollhättan, Sweden.

STRELETS, M. (2001). "Detached eddy simulation of massively separated flows". *AIAA Aerospace Sciences Meeting and Exhibit,* January 8-11, 2001/Reno, NV.

SULLEREY, R. *et al.* (1975). "Similarity in the turbulent near wake of bluff bodies". *AIAA J.*, **13**, 1425–1429.

WELLER, H. *et al.* (1998). "A tensorial approach to computational continuum mechanics using object-oriented techniques". *Computer in Physics*, **12(6)**, 620–631.

WILLIAMSON, C. (1996). "Vortex dynamics in the cylinder wake". *Annual Rev. Fluid. Mech*, **28**, 477–539.

MODELLING AND CFD SIMULATION OF A FLUIDIZED BED REACTOR TO CAPTURE CO2 BY SOLID SORBENTS

M. Molaei, K.A. Pericleous, M.K. Patel
Centre for Numerical Modelling and Process Analysis
University of Greenwich, Lonson SE10 9LS, UK

Corresponding author Email: k.pericleous@gre.ac.uk

ABSTRACT

KEYWORDS

CFD simulation, fluidized bed reactor, CO2 capture, carbonation

INTRODUCTION

MODEL DEVELOPMENT

Hydrodynamics of the reactor

—

——   —

S

u $P.$

Particle equations

—

——   —— ——

m_p $u_{p,i}$ x y
                    i $u_{f,i}$

d_P

Re

d

p_e

V_p

Carbonation kinetic model

Gemma et al.

2009

i

k

ε

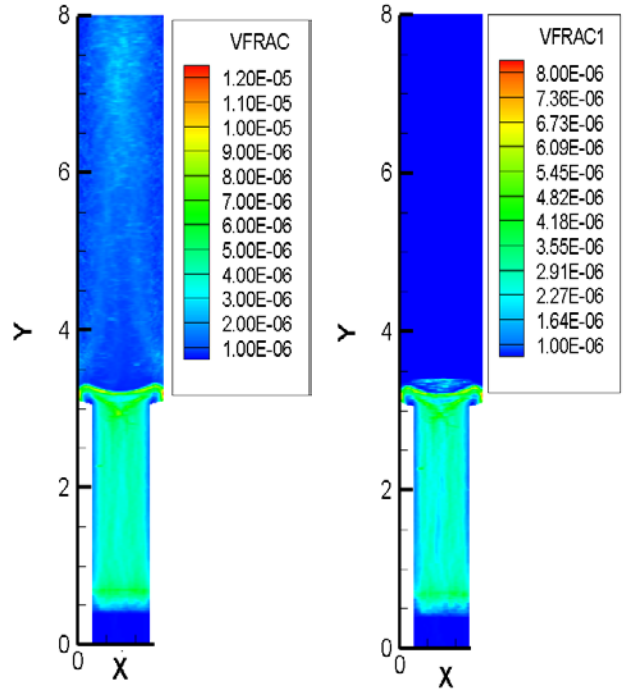X CaO D_P

D k_s

S_0
L_0

m_p
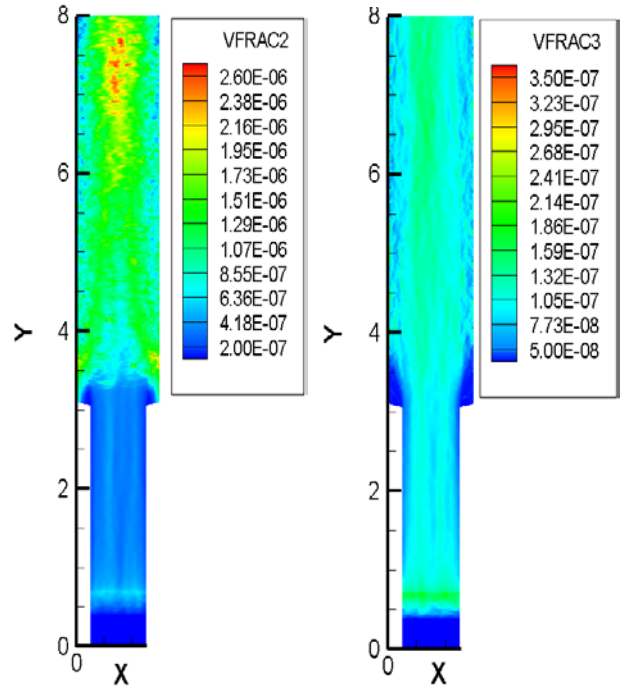
3

Boundary conditions

0.7m   1.0m

0.2m

3m

8m.

50nm

Gemma et., al 2008

| Description	Value
Particle density(kg/m^3)	
Particle diameter(m)	
Particles initial velocity(m/s)	
Gas inlet velocity(m/s)	
Gas initial temperature($^{\circ}$C)	
Bed width(m)	
Bed high(m)	
Particles sphericity	

Table1: boundary conditions

RESULTS AND DISCUSSION

    : Solid volume fraction inside the reactor for all particles together (vfrac) and for particles with 200μm diameter (vfrac1), 150μm (vfrac2) and 100 μm (vfrac3)

μ

4
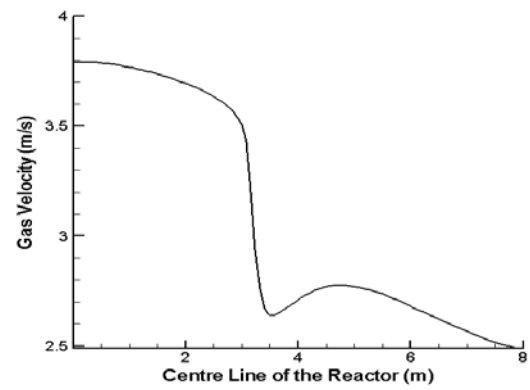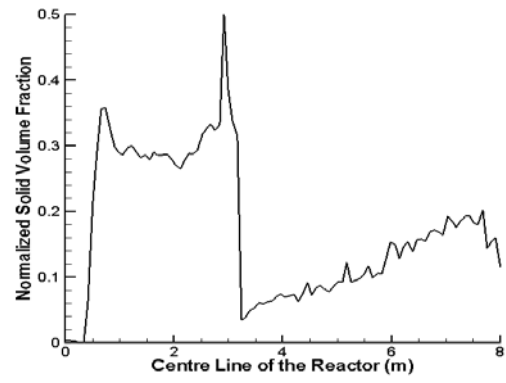
solid volume fraction profile along the centre of the reactor (top), gas velocity (bottom)
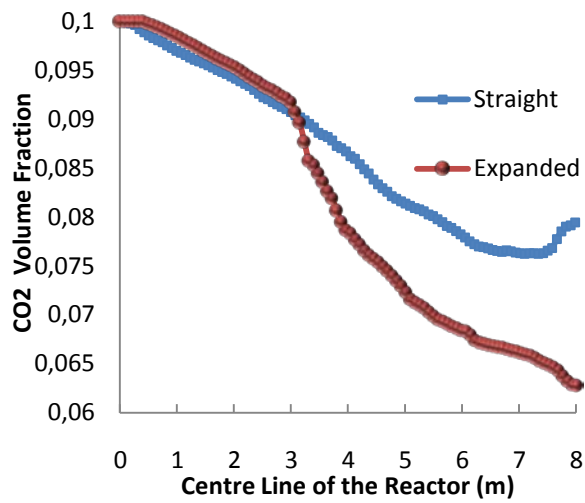

Figure 2. comparison of CO2 concentration profile along the centre of the reactor in two different geomteries.
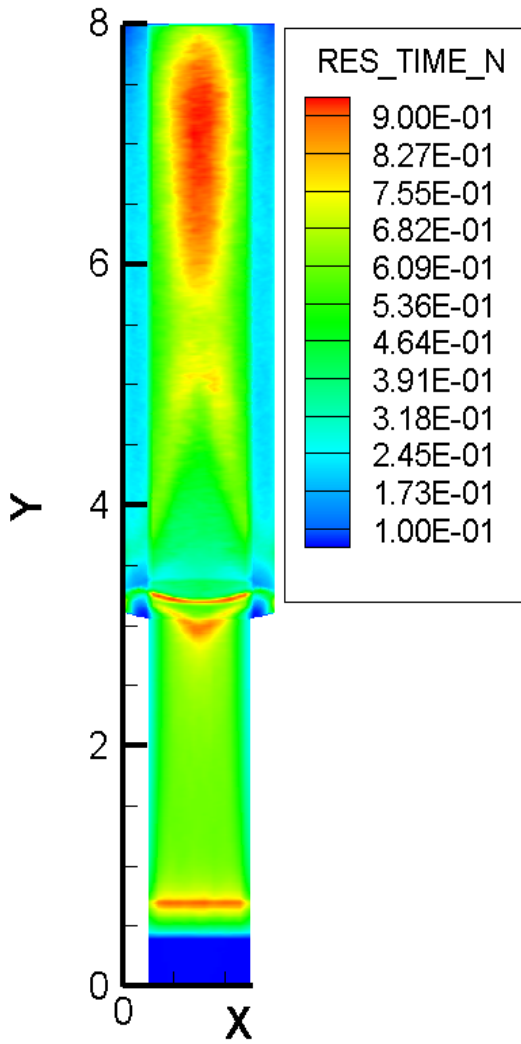
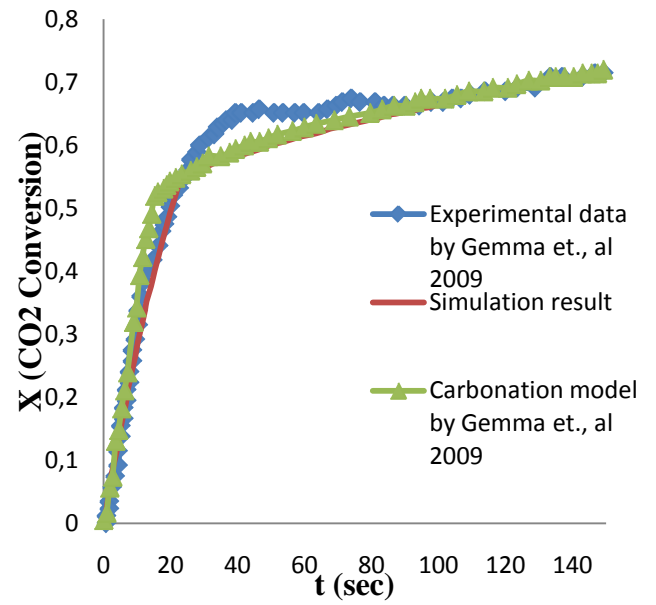*Figure 4. Normalized particles residence time inside the reactor*

Figure 5. comparison on conversion curves: a simulation result (Left) and those predicted by Grasa et al. (2009) in different Cycles via experimental work.

Grasa (2009)

i

CONCLUSIONS

NOMENCLATURE

REFERENCES

M. Fernández Bertos, S.J.R. Simons, C.D. Hills, P.J. Carey 'A review of accelerated carbonation technology in the treatment of cement-based materials and sequestration of CO2',

Bhurisa Thitakamol, Amornvadee Veawab, Adisorn Aroonwilas, 'Environmental impacts of absorption-based CO2 capture unit for post-combustion treatment of flue gas from coal-fired power plant', international journal l of greenhouse gas control 1 (2 0 0 7) 3 1 8 – 3 4 2.

Carbon8 Systems, http://www.c8s.co.uk/technology.php

Carlo Giavarini, Filippo Maccioni, Maria Laura Santarelli,' CO2 sequestration from coal fired power plants', Fuel 89 (2010) 623–628.

C. Salvador a, D. Lua, E.J. Anthony , J.C. Abanades, 'Enhancement of CaO for CO2 capture in an FBC environment', Chemical Engineering Journal 96 (2003) 187–195

D. Gidaspow, Multiphase Flow and Fluidization—Continuum and Kinetic Theory Descriptions, Academic Press, New York, 1994.

Ding and Gidaspow, 1990 J. Ding and D. Gidaspow, A bubbling fluidization model using kinetic theory of granular flow, A.I.Ch.E. Journal 36 (1990), pp. 523–538.

D.J. Patil, A.V. Annaland and J.A.M. Kuipers, Critical comparison of hydrodynamic models for gas–solid fluidized beds—part II: freely bubbling gas–solid fluidized beds, Chemical Engineering Science 60 (1) (2005), pp. 73–84.

Gemma Grasa, Ramon Murillo, Monica Alonso and J. Carlos Abanades, 'Application of the Random Pore Model to the Carbonation Cyclic Reaction', AIChE Journal, 2009 Vol. 55, No. 5.

Gemma S. Grasa, J. Carlos Abanades b, M´onica Alonso, Bel´en Gonz´alez Instituto 'Reactivity of highly cycled particles of CaOin a carbonation/calcination loop', Chemical Engineering Journal 137 (2008) 561–567.

H. Enwald, E. Peirano, A.E. Almstedt, Eulerian two-phase flow theory applied to fluidization, Int. J. Multiph. Flow 22 (1996) 21– 66.

Huilin and Gidaspow, 2003 L. Huilin and D. Gidaspow, Hydrodynamics of binary fluidization in a riser: CFD simulation using two granular temperatures, Chemical Engineering Science 58 (2003), pp. 3777–3792.

IPCC, 2005 - Bert Metz, Ogunlade Davidson, Heleen de Coninck, Manuela Loos and Leo Meyer (Eds.) Cambridge University Press, UK. pp 431.

Juan C. Abanades, Edward S. Rubin and Edward J. Anthony 'Sorbent Cost and Performance in CO₂ Capture Systems',   , 2004, 43 (13), pp 3462–3466.

Juan Carlos Abanades, 'The maximum capture efficiency of CO2 using arbonation/calcination cycle of CaO/CaCO3,' Chemical Engineering Journal 90 (2002) 303–306.

Luis M. Romeo, Yolanda Lara, Pilar Lisbona, Jesús M. Escosa, 'Optimizing make-up flow in a CO2 capture system using CaO', Chemical Engineering Journal 147 (2009) 252–258.

N. Rodríguez, M. Alonso, J.C. Abanades, 'Average activity of CaO particles in a calcium looping system', Chemical Engineering Journal 156 (2010) 388–394.

Neri and Gidaspow, 2000 A. Neri and D. Gidaspow, Riser hydrodynamics: simulation using kinetic theory, A.I.Ch.E. Journal 46 (2000), pp. 52–67.

Ping Sun, John R. Grace, C. Jim Lim, Edward J. Anthony, 'Determination of intrinsic rate constants of the CaO–CO2 reaction', Chemical Engineering Science 63 (2008) 47 – 56.

Rao, A. B. and E. S. Rubin, "A Technical, Economic and Environmental Assessment of Amine-Based CO2 Capture Technology for Power Plant Greenhouse Gas Control," Env. Sci. Technol., 36, 4467 (2002).

Robert T.Symondsa, DennisY.Lua,, ArturoMacchib, RobinW.Hughesa, EdwardJ.Anthony,' CO2 capture from syngas via cyclic carbonation/calcinations for an aturally occurring limestone: Modelling and bench-scaletesting', Chemical Engineering Science 64 (2009) 3536 – 3543.

S. Benyahia, H. Arastoopour, T.M. Knowlton and H. Massah, Simulation of particles and gas flow behaviour in the riser section of a circulating fluidized bed using the kinetic theory approach for the particulate phase, Powder Technology 112 (1–2) (2000), pp. 24–33.

8th International Conference on CFD in Oil & Gas, Metallurgical and Process Industries
SINTEF/NTNU, Trondheim NORWAY
21-23 June 2011

CFD11-117

CONSTRAINED REINITIALISATION OF THE CONSERVATIVE LEVEL SET METHOD

Claudio WALKER[1][*], **Bernhard MÜLLER**[2][†]

[1]NTNU Department of Energy and Process Engineering, 7491 Trondheim, NORWAY

[2]NTNU Department of Energy and Process Engineering, 7491 Trondheim, NORWAY

[*] E-mail: claudio.walker@ntnu.no
[†] E-mail: bernhard.muller@ntnu.no

ABSTRACT

In this paper it is shown that the reinitialisation of the conservative level function introduces spurious displacements of the interface. A method which prevents the interface in conventional level set methods from moving during the reinitialisation is adopted for the conservative level set method. It is shown that using the constrained reinitialisation with an adaptive distributed forcing retains the shape of the interface during reinitialisation. This eliminates the negative effects if too many reinitialisation steps are applied. However, our numerical experiments show that fixing of the interface during reinitialisation spoils the mass conservation of the conservative level set method.

Keywords: Multiphase flow, Level set method .

NOMENCLATURE

Greek Symbols
β Forcing distribution factor.
Γ Set of points addjacent to the interface.
δ Least squares weights.
ε Width parameter for the conservative level set function.
κ Interface curvature.
ρ Distance to domain center.
τ Pseudo time.
ϕ Conservative level set function.
Ψ Stream function.
ψ Signed distance function.

Latin Symbols
C Set of points with nonzero foring term.
e Error.
F Forcing term.
f Numerical flux.
h Grid spacing.
$\mathbf{n}$ Interface normal.
m Number of grid points.
t Time.
S Set of neighbouring points on opposit side of the interface.
$\mathbf{u}$ Velocity.
$\mathbf{x}$ Position.

Sub/superscripts
α Index α.
i Index i.
j Index j.
n Discrete time level.

INTRODUCTION

The level set method (LSM) is a popular method to describe the location of the interface in multiphase flow computations. It represents the interface with the help of a signed distance function which is advected by the fluid velocity. For a more thorough discussion of the LSM and its application to multiphase flow we refer the reader to the review by (Sethian and Smereka, 2003). This representation has the advantage of relatively simple calculations of interface normals and curvatures. Another often cited advantage of the LSM is that the parallelisation is straightforward. Due to the advection the level set function loses its signed distance property. Therefore it has to be reinitialised after a few advection steps. This is done by solving a reinitialisation equation. The deformation of the interface during this reinitialisation is a known problem and an explanation of the cause and a possible remedy was given by (Russo and Smereka, 2000). There exists a number of methods to reduce the displacement of the signed distance function during reinitialisation. Among these methods is the Constrained Reinitialisation (CR) (Hartmann *et al.*, 2008), which is minimising the displacement of the intersection points between the grid lines and the zero level set contour.

However, the LSM has an important disadvantage, it does not conserve the mass of the two fluids. Different approaches have been developed to satisfy the mass conservation of the level set method. Examples include the conservative level set method (CLSM) (Olsson and Kreiss, 2005) (Olsson *et al.*, 2007), the particle level set method (PLS) (Enright *et al.*, 2002) and the coupled level set/volume-of-fluid (CLSVOF) (Sussman and Puckett, 2000). The added complexity for both PLS and CLSVOF are significant. On the other hand the conservative level set method improves the mass conservation and keeps the simplicity of the original method.

We discovered that during the reinitialisation of the CLSM the interface is displaced considerably. In most applications of the CLSM this problem is not evident since typically only a few reinitialisation steps are conducted, and the deformation becomes only significant for high numbers of reinitialisation steps. There is no general rule on how frequent the CLSM has to be reinitialised and how many reinitialisation steps should be applied each time. It is therefore important

to make sure that too many reinitialisation steps do not compromise the accuracy of the CLSM. Recently Hartmann et al. published a technique called high-order constrained reinitialisation (HCR) (Hartmann *et al.*, 2010) for the conventional LSM. But its implementation through a source term allows the adoption of HCR to do a constrained reinitialisation of the CLSM.

In the present paper a short introduction to the conservative level set method and its discretisation is given. Then we present an overview of the HCR and show how it can be adopted for the CLSM. Finally we show some numerical experiments and explain why it is after all not advisable to fix the interface during the reinitialisation of the CLSM.

CONSERVATIVE LEVEL SET METHOD

In level set methods the interface is defined as the iso contour of a smooth function. For ordinary level set methods this function is the signed distance from the interface, and the interface location is where the distance function is zero. The conservative level set function replaces the distance function by a hyperbolic tangent function ϕ with values between zero and one (Olsson and Kreiss, 2005). The position of the interface is located at the $\phi = 0.5$ contour line. Since we have smooth functions which are defined in the entire computational domain in both cases, we can easily extract additional geometrical information about the interface. For example the interface normal **n** and the curvature κ are defined as

$$\mathbf{n} = \frac{\nabla \phi}{|\nabla \phi|} \tag{1}$$

and

$$\kappa = \nabla \cdot \mathbf{n}. \tag{2}$$

The interface is transported simply by advecting the level set function using the advection equation $\phi_t = -\mathbf{u} \cdot (\nabla \phi)$. If we have a divergence free velocity field, as it is the case for incompressible flow, the interface transport can be written as a conservation law.

$$\frac{\partial \phi}{\partial t} + \nabla \cdot (\mathbf{u}\phi) = 0 \tag{3}$$

Since all numerical methods will introduce an error as ϕ is advected, it will lose its hyperbolic tangent shape. The diffusion of the advection schemes will increase the distance in which ϕ rises from zero to one. (Olsson *et al.*, 2007) propose the following reinitialisation equation to force ϕ back to its hyperbolic tangent shape, which is solved to steady state with respect to the pseudo time τ:

$$\frac{\partial \phi}{\partial \tau} + \nabla \cdot (\phi(1-\phi)\hat{\mathbf{n}} - \varepsilon((\nabla \phi \cdot \hat{\mathbf{n}})\hat{\mathbf{n}})) = 0, \tag{4}$$

where $\hat{\mathbf{n}}$ is the normal at the beginning of the reinitialisation, and ε determines the width of the hyperbolic tangent. It is important to note that also the reinitialisation equation is a conservation law. The first flux term causes a compression of the profile, whereas the second term is a diffusive flux. By multiplications with the normal $\hat{\mathbf{n}}$ there are only fluxes in the direction of the normal. This forced flux direction for both the compression and the diffusion term are essential to improve the mass conservation of the method. Indeed it was shown that the CLSM conserves mass as ε approaches 0. To illustrate the nature of Equation (4), we use a one-dimensional example. Suppose that the interface is located at $x = 0$. Then the normal reduces to $n = -1$ or $n = 1$. In the

example we use the latter. In this case a steady state solution to Equation (4) is:

$$\phi = \frac{1}{2}\left(1 + \tanh\left(\frac{x}{2\varepsilon}\right)\right). \tag{5}$$

The solution is shown Figure 1, together with the compression and the diffusion terms. It is clearly visible that at steady state the compression and the diffusion are balanced. If ϕ would be too diffusive the compression term would outweigh the diffusive term and ϕ would be forced back to the steady state solution.
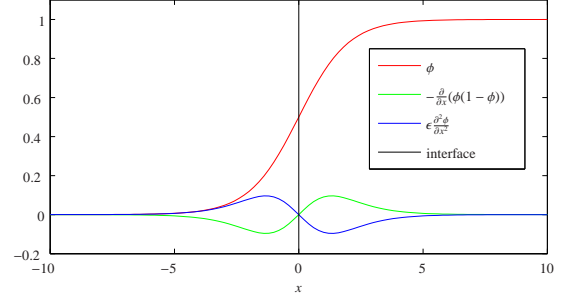

Figure 1: Illustration of the reinitialisation equation.

Discretisation

Advection

The divergence in the advection equation (3) is discretised by a 5th order finite difference weighted essentially non-oscillatory (WENO) scheme using a Lax-Friedrichs flux splitting (Shu, 1998). For time discretisation the 3rd order TVD Runge-Kutta method by (Shu and Osher, 1988) is applied.

Interface normal

In order to keep the stencils for the reinitialisation equation as small as possible (Desjardins *et al.*, 2008) proposed to compute the fluxes of the reinitialisation equation (4) at the cell faces. As a consequence the normal is required at the cell faces. It was also proposed by the authors to compute the normal from a signed distance function ψ which in turn is computed using a fast marching method (FMM). The reason for this is that the gradient of the conservative level set function ϕ becomes extremely small far away from the interface. In this region with small gradients small errors in ϕ can lead to a normal pointing in the wrong direction. Close to the interface, however, the gradient of ϕ is large enough such that a reliable normals can be computed directly form ϕ. Further away from the interface the accuracy of the normal is not so important anymore, but they should be continuous and not contain spurious oscillations. In the present work the normal are computed directly form the conservative level set function where $0.0001 \leq \phi \leq 0.9999$, otherwise they are computed from a signed distance function.

The gradient for the normal on the cell faces in x-direction at $x = x_{i-1/2,j}$ is approximated by the following stencil:

$$(\nabla \phi)_{x\,i-1/2,j} \approx \frac{\phi_{i,j} - \phi_{i-1,j}}{h} \tag{6}$$

$$(\nabla \phi)_{y\,i-1/2,j} \approx \frac{\phi_{i-1,j+1} + \phi_{i,j+1} - \phi_{i-1,j-1} - \phi_{i,j-1}}{4h}. \tag{7}$$

The gradient at the cell faces in y-direction $(\nabla \phi)_{i,j-1/2}$ is treated analogously. Finally the normal can be computed

from the gradient using equation (1). Note grid points where $|\nabla \phi| = 0$ have to be treated separately, here we chose to fill the normal at these points with a unit vector pointing in an arbitrary direction.

Reinitialisation

A central difference method on a staggered grid is used to discretise the reinitialisation equation (4). The fluxes in x-direction as well as those in y-direction are computed on the corresponding cell faces. First the convective fluxes are obtained at the cell centers from the level set function i.e. $f_{c\,i,j} = \phi_{i,j}(1 - \phi_{i,j})$ and then they are interpolated to the cell faces using linear interpolation e.g. $f_{c\,i+1/2,j} = \left(f_{c\,i,j} + f_{c\,i+1,j}\right)/2$. The diffusive fluxes are computed directly at the cell faces to keep the stencil as small as possible. Accordingly the diffusive fluxes at the cell faces in x-direction read:

$$f_{d\,i-1/2,j} = \varepsilon \left((\nabla \phi)_{x\,i-1/2,j} \cdot n_{x\,i-1/2,j}\right.$$
$$\left. + (\nabla \phi)_{y\,i-1/2,j} \cdot n_{y\,i-1/2,j}\right), \qquad (8)$$

where $n_{x\,i-1/2,j}$ and $n_{y\,i-1/2,j}$ are the x- and y-components of the interface normal. This leads to the total fluxes in x- and y-directions:

$$f_{i-1/2,j} = \left(f_{c\,i-1/2,j} - f_{d\,i-1/2,j}\right) \cdot n_{x\,i-1/2,j} \qquad (9)$$

$$g_{i,j-1/2} = \left(f_{c\,i,j-1/2} - f_{d\,i,j-1/2}\right) \cdot n_{y\,i,j-1/2} . \qquad (10)$$

Eventually the total residual of the reinitialisation equation is:

$$\frac{\partial \phi}{\partial \tau} \approx -\frac{f_{i+1/2,j} - f_{i-1/2,j}}{h} - \frac{g_{i,j+1/2} - g_{i,j-1/2}}{h}. \qquad (11)$$

The forward Euler scheme is used to advance the conservative level set function in the pseudo time τ. To ensure stability the time step must fulfill:

$$\Delta\tau\left(\frac{2}{h} + \frac{4}{h^2}\varepsilon\right) \leq 1. \qquad (12)$$

CONSTRAINED REINITIALISATION

We observed that the convergence of the reinitialisation with the described discretisation was poor for simple cases. In Figure 2 the result of the reinitialisation of a circle is shown. During the first few iterations the residual drops fast and then the convergence is slowed down. During this period of small convergence rate the interface develops towards a rhombus. This tendency to deform the interface is not reduced as the grid is refined. In most applications this defect is not evident since typically only a few reinitialisation steps are conducted and the residual is not reduced until the numerical steady state.

Constrained reinitialisation for conventional level set methods

A similar problem appears in conventional level set methods. Recently (Hartmann *et al.*, 2010) proposed a method to reduce the displacement of the signed distance function ψ during reinitialisation. The idea is to add a source term to the residual of the differential equation, which minimises the displacement of the intersection points between the zero contour of ψ and the grid lines in a least squares sense.

If two grid points $\mathbf{x}_{i-1,j}$ and $\mathbf{x}_{i,j}$ which are located on opposite sides of the interface, the condition that the linear interpolation of the intersection point between the zero contour line and the grid line between those two points does not move during reinitialisation, can be reduced to $\frac{\tilde{\psi}_{i,j}}{\tilde{\psi}_{i-1,j}} = \frac{\psi_{i,j}}{\psi_{i-1,j}}$, where $\tilde{\psi}$ and ψ are the signed distance functions before and after reinitialisation, respectively. In general a grid point can have several neighbours which are on the opposite side of an interface. The previous condition cannot be fulfilled for all involved neighbours, since the problem is overdetermined. Let $S_{i,j}$ be the set of all neighbouring grid points of $\mathbf{x}_{i,j}$ which are on the opposite side of the interface, and $M_{i,j}$ the number of grid points in $S_{i,j}$. Further we denote an arbitrary point in $S_{i,j}$ by $\mathbf{x}_{(i,j)\alpha}$ such that $\alpha = 1...M_{i,j}$. In the constrained reinitialisation CR-1 (Hartmann *et al.*, 2010) the following least squares function is minimised.

$$L_{i,j} = \sum_{\alpha=1}^{M_{i,j}} \delta_{i,j}^{\alpha} \left(\psi_{i,j} - \psi_{(i,j)\alpha} \cdot r_{(i,j)\alpha}^{i,j}\right)^2, \qquad (13)$$

$$r_{(i,j)\alpha}^{i,j} = \frac{\tilde{\psi}_{i,j}}{\tilde{\psi}_{i-1,j}} \qquad (14)$$

(Hartmann *et al.*, 2010) chose the weights $\delta_{i,j}^{\alpha} = 1$. If $L_{i,j}$ is derived with respect to $\psi_{i,j}$ and this is set equal to zero we get the target value for the distorted signed distance function, such that it minimises the displacement of the interface.

$$T_{i,j} = \frac{\sum_{\alpha=1}^{M_{i,j}} \delta_{i,j}^{\alpha} \left(\psi_{(i,j)\alpha} \cdot r_{(i,j)\alpha}^{i,j}\right)}{\sum_{\alpha=1}^{M_{i,j}} \delta_{i,j}^{\alpha}} \qquad (15)$$

Finally the CR-1 correction term at the nth reinitialisation time step is formulated as the difference between $T_{i,j}^n$ and $\psi_{i,j}^n$:

$$F_{i,j}^n = \frac{\beta_{i,j}}{h} \left(\psi_{i,j}^n - T_{i,j}^n\right). \qquad (16)$$

Here $\beta_{i,j}$ is a coefficient which distributes the correction between neighbouring grid points. For consistency the sum $\beta_{i,j} + \beta_{(i,j)\alpha}$ must always be equal to 1. Setting $\beta_{i,j} = 0.5$ corresponds to do half of the correction on either side of the interface. Since the forcing leads to an instability when one of points of the set $S_{i,j}$ changes its sign during reinitialisation,
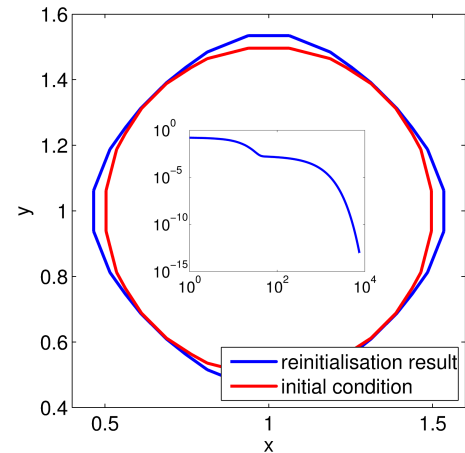

Figure 2: Reinitialisation result of a circle with 8 grid points per diameter, the small insert shows the evolution of the reinitialisation residual over the number of time levels.

the forcing is not applied at the grid points in this particular $S_{i,j}$.

Adaptation to the conservative level set method

The idea is to apply the CR-1 forcing to the reinitialisation of the CLSM to avert an undesirable movement of the interface during reinitialisation. In the CLSM the interface is given as the 0.5 contour line. Therefore ψ in equation (13) to (16) must be replaced by $\phi^- = \phi - 0.5$.

Stabilising CR-1

An essential difference between the signed distance function ϕ and the conservative level set function ψ is that the latter has larger gradients at the interface. As a consequence the forcing term for the CLSM tends to be stronger. For points where the distance to the interface approaches h the magnitude of the forcing term is increasing rapidly. It was observed in numerical experiments that if the distance between the intersection point and the grid point becomes smaller than $0.01h$ the constrained reinitialisation of ϕ becomes unstable. Imagine two bars which cross each other. Suppose one is only allowed to move one end of one bar to adjust the position of the crossing point. If now the crossing point is close to the fixed end of the moving bar, the free end has to be moved relatively far to obtain a given displacement of the crossing point. On the other hand if one could move the end which is closer to the crossing point a much smaller movement is required to obtain the same displacement of the crossing point. The correction can also be divided to both ends where the necessary corrections at each end are multiplied by factors which have to add to one. These factors are the distribution factors $\beta_{i,j}$.

In order to stabilise the constrained reinitialisation of the CLSM the forcing for pairs where the crossing point is close to one of the points should be distributed better, which means adjusting $\beta_{i,j}$ in equation (16). For pairs where both neighbours have $M_{i,j} = 1$, $\beta_{i,j}$ can be chosen such that the forcing term has the same magnitude on both sides. As an example if both $M_{i,j}$ and $M_{i-1,j}$ are equal to 1 and the crossing point is either close to $\mathbf{x}_{i,j}$ or $\mathbf{x}_{i-1,j}$ set

$$\beta_{i,j} = \left(\frac{\psi_{i,j} - T_{i,j}}{\psi_{i-1,j} - T_{i-1,j}} + 1 \right) \tag{17}$$

$$\beta_{i-1,j} = 1 - \beta_{i,j}. \tag{18}$$

This choice of distribution coefficients ensures that the forcing term is equal for both points.

In general $M_{i,j} > 1$ especially for points which are close to the interface. There $\beta_{i,j}$ cannot be adjusted to an arbitrary value since $\beta_{i,j} + \beta_{(i,j)\alpha} = 1$, and the set $S_{i,j}$ often overlaps with the sets from the neighbouring points. Therefore setting $\beta_{i,j}$ gives a condition to a number of β from neighbouring grid points. A solution to keep the effect of choosing $\beta_{i,j}$ local is to use the weights $\delta_{i,j}^{\alpha}$ in the least squares function (13). If a grid point $\mathbf{x}_{i,j}$ is too close to an intersection point $\beta_{i,j}$ is set to 1. This would require to set all $\beta_{(i,j)\alpha} = 0$. Instead we choose $\delta_{(i,j)\alpha}^{\hat{\alpha}} = 0$ in all the neighbouring cells where $\hat{\alpha}$ points to cell (i,j). That is equivalent to do the complete forcing on the grid point close to the intersection and ignoring the constraint at all the neighbouring points.

Summary of the constrained reinitialisation

Only at points adjacent to the interface the operations for the level set forcing have to be conducted, we define therefore

the set

$$\Gamma = \left\{ \mathbf{x}_{i,j} \colon \left(\phi_{i,j}^- \phi_{i',j}^- \leq 0 \right) \vee \left(\phi_{i,j}^- \phi_{i,j'}^- \leq 0 \right) \right\}, \tag{19}$$

where $i' \in \{i-1, i+1\}$ and $j' \in \{j-1, j+1\}$. For sets $S_{i,j}$ where ϕ at one of the points changes its sign during reinitialisation the forcing is not applied. To that effect the following set of grid points will have a forcing term $F_{i,j} \neq 0$:

$$C^n = \left\{ \mathbf{x}_{i,j} \in \Gamma \colon \phi_{i,j}^{-n} \phi_{(i,j)\alpha}^{-n} < 0 \,\forall \alpha \in \{1,...,M_{i,j}\} \right\}. \tag{20}$$

Using these definitions the steps for the constrained reinitialisation of the CLSM are:

1. Compute the interface normal. and (7))

2. Compute the shifted conservative level set function before reinitialisation $\tilde{\phi}^- = \tilde{\phi} - 0.5$.

3. Find all points in Γ.

4. Update the set $S_{i,j}$, and compute $r_{(i,j)\alpha}^{i,j}$ for all points in Γ.

5. Find points where $r_{(i,j)\alpha}^{i,j} < \text{TOL}$

   - If $M_{i,j} = M_{(i,j)\alpha} = 1$, flag points for equal forcing
   - Else, set $r_{(i,j)\alpha}^{i,j} = 0$, reduce $M_{i,j}$ by 1 and flag $\mathbf{x}_{i,j}$ as point with $\beta_{i,j} = 1$

6. For all points with $\beta_{i,j} = 1$, do for all (i',j') where $\mathbf{x}_{(i',j')\alpha} = \mathbf{x}_{i,j}$, $\delta_{i',j'}^{\hat{\alpha}} = 0$ and reduce $M_{i',j'}$ by 1 where $\mathbf{x}_{(i',j')\hat{\alpha}} = \mathbf{x}_{i,j}$.

7. Remove points $\mathbf{x}_{i,j}$ where $M_{i,j} = 0$ from Γ.

8. Solve the constrained reinitialisation problem by performing the following steps for each iteration:

   (a) Compute the shifted conservative level set function at pseudo time step n: $\phi^{-n} = \phi^n - \frac{1}{2}$.

   (b) Update the set C^n

   (c) For all grid points in C^n compute the forcing terms given by equation (16), use $\beta_{i,j} = 0.5$ unless the point is flagged for $\beta_{i,j} = 1$ or equal correction.

   (d) Compute residual from the PDE (4).

   (e) Advance ϕ one pseudo time step.

NUMERICAL EXPERIMENTS

Reinitialisation

To test the constrained reinitialisation method described in the previous section we consider a circle with radius $R = \frac{1}{2}$ which is placed in the center of a square domain with unit length. The initial condition is $\tilde{\phi} = \left(1 + \exp\left(\frac{3(\rho - R)}{2\varepsilon} \right) \right)^{-1}$, where $\rho = \sqrt{\left(x - \frac{1}{2} \right)^2 + \left(y - \frac{1}{2} \right)^2}$ is the distance from the center of the domain. For this case the exact steady state solution of equation (4) is:

$$\phi_{\text{exact}} = \left(1 + \exp\left(\frac{\rho - R}{\varepsilon} \right) \right)^{-1}. \tag{21}$$

The reinitialisation equation was iterated until the 2-norm of the residual was below 10^{-13}. The error norm is computed as follows:

$$e = \frac{1}{m} \left(\sum_{i,j=1}^{m} \left(\phi_{\text{exact } i,j} - \phi_{i,j} \right)^2 \right)^{\frac{1}{2}}, \qquad (22)$$

where m is the number of grid points in each direction. To assess the deformation of the interface the reinitialised ϕ was interpolated to a fine grid with 500 points in each direction using bi-cubic splines. On this fine grid the position of all intersection points between the grid lines and the 0.5 contour line were computed using a 1-dimensional cubic spline interpolation. The position error of the interface e_p is then given as the 2-norm of the distance between each interpolated intersection point and its correct position.

Analytic normal

The errors after the reinitialisation with analytic normal and a fixed $\varepsilon = 0.044$ are presented in Figure 3. The error norm e is reduced with second order which is consistent with the discretisation scheme. To find the position of the interface we need to interpolate it. This interpolation is the reason that the position error of the interface is one order higher than the order of the discretisation scheme. Special attention should be payed to the results with $m = 81$. At this grid resolution 16 grid points were marked since their distance to the interface was smaller than $0.01h$. These grid points where treated with the procedure explained previously. Without this improved distribution of the forcing term the reinitialisation is unstable for $m = 81$. As it can be seen in Figure 3, the convergence rate of the position error is slightly reduced due to the unequal distribution of the forcing term. For comparison the errors without the CR-1 are plotted in Figure 3 as well. Since the interface is developing a rhombus shape (see Figure 2) at all grid resolutions neither the error norm nor the position error are converging with grid refinement. In Table 1 we list the number of reinitialisation steps which were required to reduce the residual to the target value of 10^{-13}. The constrained reinitialisation accelerates the convergence of the residual significantly. For the unconstrained reinitialisation of the circle with $m = 64$ and $m = 81$ the target residual was not reached after 100000 reinitialisation steps. The residuals at $n = 100000$ were $1.55 \cdot 10^{-5}$ and $4.03 \cdot 10^{-5}$ for $m = 64$ and $m = 81$, respectively.

Table 1: Number of iterations required to reach a residual of 10^{-13} during the reinitialisation of a circle.

m	8	16	32	64	81
CR-1	165	318	943	3654	4760
without	372	7536	96637	> 100000	> 100000

Numeric normal

The same test as in the previous section is repeated, but the interface normal is computed numerically. For a constant $\varepsilon = 0.044$ the results are almost identical to the reinitialisation

with the analytic interface normal. Since the mass conservation of the CLSM is improved as ε is decreased, the reinitialisation of the circle was repeated once with $\varepsilon = 0.2\sqrt{h}$ and with $\varepsilon = 0.6h$. As ε is decreased the width of tangent hyperbolic is also decreased, which means that there are less grid points resolving the area where ϕ changes from 0 to 1. The result is that the convergence rate is reduced if ε is decreasing together with the grid width. The errors for simultaneous reduction of h and ε are shown in Figure 4.

Advection and Reinitialisation

Initially a circle of radius $R = 0.1$ is placed at $(0.5, 0.7)$ in a square domain with unit length. The circle is advected with an external velocity field with the stream function

$$\Psi = -\pi \left(x^2 + y^2 - x - y \right). \qquad (23)$$

This velocity field is advecting the circle anticlockwise around the center of the computational domain. To keep the error contribution from the temporal discretisation negligible a small CFL number of 0.05 was chosen for all examples. After 100 time steps a reinitialisation was performed. During the reinitialisation the residual was reduced to 10^{-8} or a maximum of 500 iterations were done. The convergence of the errors for the constrained CLSM is plotted in Figure 5 for
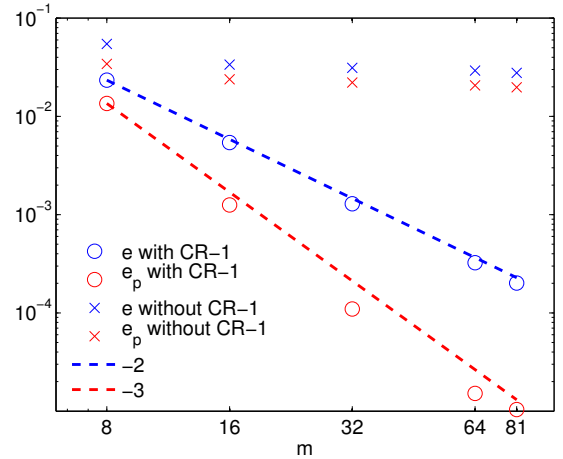

Figure 3: Error convergence for the reinitialisation of a circle with analytic interface normal and $\varepsilon = 0.044$.
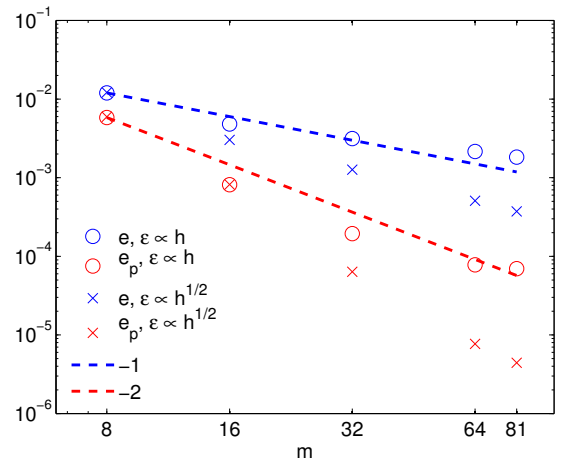

Figure 4: Error convergence for the reinitialisation of a circle with numeric interface normal and $\varepsilon \propto h$ or $\varepsilon \propto \sqrt{h}$.

$\varepsilon = 0.1 \cdot m^{-1/2}$. Figure 6 shows the interface position after one revolution for $m = 51$. For the case where the reinitialisation was done with CR-1 the interface retains a circular shape but the area is reduced significantly. On the other hand, if the unconstrained reinitialisation is used, the area is conserved but the interface loses its circular shape. Here we exaggerated this effect by the large number of reinitialisation steps. If e.g. every 100 advection steps only 10 reinitialisation steps are conducted, the interface position error is reduced by almost a factor of 16. If the interface is only advected and never reinitialised, the area loss is smaller than for the CR-1 reinitialisation and the circular shape is retained. The area loss for the three different reinitialisations is summarised in Table 2. The reduction of ε leads only for the CLSM without CR-1 to a reduction in the area change. For the constrained CLSM and if the circle is only advected, the area change decreases with increasing ε. This is due to the fact that the conservative level set function is less steep for larger ε, and therefore the diffusive error of the advection scheme is reduced.

The large mass loss for the constrained reinitialisation can be explained as follows. Initially the level set function can be compared with a cylinder with height 1 and the radius of the circle. If the circle has a radius of 1 then the volume of the cylinder is π. Since the numerical advection is diffusive, we assume the advected cylinder will transform to the shape of a cone with height of 1. The conservative advection will conserve the volume of the cylinder. For this reason the radius of the cone at a height of 0.5 will be only $\frac{\sqrt{3}}{2}$ instead of 1. During a constrained reinitialisation a new cylinder with this smaller cross section will be created and the cycle starts again.
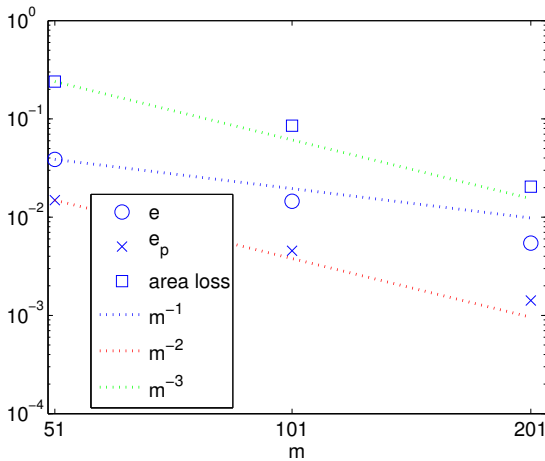

Figure 5: Errors for the advected circle after one revolution.

Table 2: Area change in % for the advected circle with $m = 51$.

ε	0.1	0.2	0.3
CLSM CR-1	-23.98	-11.14	-4.93
CLSM	0.10	0.60	0.65
Advection	14.49	5.60	1.43

CONCLUSION

We applied the constrained reinitialisation CR-1 by (Hartmann *et al.*, 2010) to the reinitialisation of the conservative level set function. The larger modulus of the gradient of the conservative level set function can cause instabilities during the constrained reinitialisation, if the interface is located close to a grid point. This instability can be avoided, if the forcing is not divided equally between two neighbouring points. Evidence was given that the constrained reinitialisation prevents spurious interface deformation during the reinitialisation independent of the number of reinitialisation steps, and that the convergence of the residual is accelerated. However, numerical experiments showed that preventing the interface from moving during reinitialisation spoils the mass conservation of the CLSM. It was also shown that care has to be taken that the number of reinitialisation steps of the unconstrained CLSM is not too large such that the reinitialisation introduces spurious interface deformations.

REFERENCES

DESJARDINS, O. *et al.* (2008). "An accurate conservative level set/ghost fluid method for simulating turbulent atomization". *Journal of Computational Physics*, **227(18)**, 8395–8416.

ENRIGHT, D. *et al.* (2002). "A hybrid particle level set method for improved interface capturing". *Journal of Computational Physics*, **183(1)**, 83–116.

HARTMANN, D. *et al.* (2008). "Differential equation based constrained reinitialization for level set methods". *Journal of Computational Physics*, **227(14)**, 6821 – 6845.

HARTMANN, D. *et al.* (2010). "The constrained reinitialization equation for level set methods". *Journal of Computational Physics*, **229(5)**, 1514 – 1535.

OLSSON, E. and KREISS, G. (2005). "A conservative level set method for two phase flow". *Journal of Computational Physics*, **210(1)**, 225–246.

OLSSON, E. *et al.* (2007). "A conservative level set method for two phase flow II". *Journal of Computational Physics*, **225(1)**, 785–807.

RUSSO, G. and SMEREKA, P. (2000). "A remark on computing distance functions". *Journal of Computational Physics*, **163(1)**, 51 – 67.
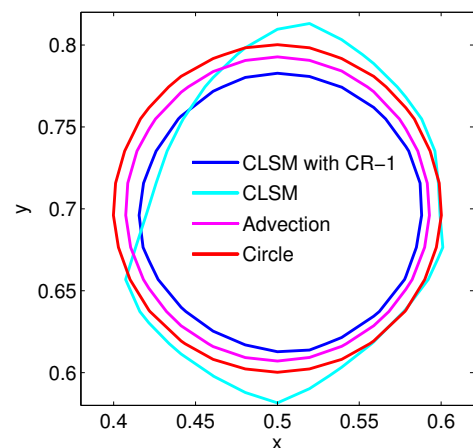
SETHIAN, J.A. and SMEREKA, P. (2003). "Level set

Figure 6: Advected circle, interface position after one revolution.

methods for fluid interfaces". *Annual Review of Fluid Mechanics*, **35(1)**, 341–372.

SHU, C.W. (1998). *Essentially Non-oscillatory and Weighted Essentially Non-oscillatory Schemes for Hyperbolic Conservation Laws*, in: A. Quarteroni (ed.), Advanced Numerical Approximation of Nonlinear Hyperbolic Equations, 325–432. Springer Berlin / Heidelberg.

SHU, C.W. and OSHER, S. (1988). "Efficient implementation of essentially non-oscillatory shock-capturing schemes". *Journal of Computational Physics*, **77(2)**, 439 – 471.

SUSSMAN, M. and PUCKETT, E.G. (2000). "A coupled level set and volume-of-fluid method for computing 3D and axisymmetric incompressible two-phase flows". *Journal of Computational Physics*, **162(2)**, 301–337.

8th International Conference on CFD in Oil & Gas, Metallurgical and Process Industries
SINTEF/NTNU, Trondheim Norway
21-23 June 2011

CFD11 - 118

A STRONG FSI COUPLING SCHEME FOR SIMULATING BMHV DYNAMICS: STUDY OF WALL SHEAR STRESS ON THE VALVE LEAFLETS

Sebastiaan Annerel[1]*, Joris Degroote[1], Tom Claessens[2], Sigrid K. Dahl[3,4], Bjørn Skallerud[3], Leif Rune Hellevik[3], Peter Van Ransbeeck[2], Patrick Segers[5], Pascal Verdonck[5] and Jan Vierendeels[1]

[1] Department of Flow, Heat and Combustion Mechanics, Ghent University, Ghent, BELGIUM

[2] Department of Mechanics, University College Ghent, Ghent, BELGIUM

[3] Department of Structural Engineering, NTNU, Trondheim, NORWAY

[4] Simula Research Laboratory, Oslo, NORWAY

[5] IBiTech-bioMMeda, Ghent University, Ghent, BELGIUM

* E-mail: Sebastiaan.Annerel@UGent.be

ABSTRACT

One of the major challenges in the design of Bileaflet Mechanical Heart Valves (BMHVs) is reduction of the blood damage generated by non-physiological blood flow. Numerical simulations provide relevant insights into the (fluid) dynamics of the BMHV and are used for design optimization. In this paper, a strong coupling algorithm for the partitioned fluid-structure interaction (FSI) simulation of a BMHV is presented. The convergence of the coupling iterations between the flow solver and the leaflet motion solver is accelerated by using a numerically calculated Jacobian with the derivatives of the pressure and viscous moments acting on the leaflets with respect to the leaflet accelerations. The developed algorithm is used to simulate the dynamics of a 3D BMHV in three different geometries, allowing an analysis of the solution process. Moreover, the leaflet kinematics and the general flow field are discussed, with special focus on the shear stresses on the valve leaflets.

Keywords: Fluid-Structure Interaction, Algorithm, BMHV, Biomedical applications.

NOMENCLATURE

Greek Symbols
δ Perturbation, [rad/s^2].
ε Threshold.
θ Angular position, [rad].
$\dot{\theta}$ Angular velocity, [rad/s].
$\ddot{\theta}$ Angular acceleration, [rad/s^2].
$\Delta\ddot{\theta}$ Acceleration perturbation vector, [rad/s^2].

Latin Symbols
I Moment of Inertia, [kg·m^2].
M Moment, [N·m].
ΔM Moment data vector, [N·m].
t Time, [s].
Δt Time step size, [s].

Subscripts
0   FSI convergence threshold.
1   First leaflet;
     Flow solver convergence threshold.
2   Second leaflet;
     Jacobian update threshold.
i,j   Leaflet.
max Maximal value.
min Minimal value.
ref Reference.

Superscripts
a   First acceleration perturbation vector.
b   Second acceleration perturbation vector.
k   Coupling iteration.
n   Time step.
r   Reaction moment.
ref Reference.

INTRODUCTION

Since the first clinical success with an artificial heart valve by Dr. Hufnagel in 1952, the implantation of valve prostheses has become a routine treatment for severe heart valve failure. However, despite sixty years of research, modern valve prostheses still have severe design deficiencies. The widely used and preferred Bileaflet Mechanical Heart Valves (BMHVs), for example, still have poor hemodynamic properties and patients need to undergo life-long anti-coagulation therapies (Dasi et al. 2009). Therefore, one of the major challenges in the design of BMHVs is the reduction of the accumulated blood damage which is, among others, caused by non-physiological flow patterns and elevated shear stress levels on the leaflets. Numerical simulations of the (blood) flow provide relevant insights into the valve dynamics (Dasi et al. 2009) and are used for design optimization. Unfortunately, such numerical simulation of a BMHV is a complex Fluid-Structure Interaction (FSI) problem because the movement of the

leaflets strongly interacts with the surrounding fluid motion and, therefore, the equilibrium at the fluid-structure interface needs to be taken into account.

In this paper, a strong coupling algorithm for the simulation of a BMHV by a partitioned solver is presented and used to study the wall shear stresses on the valve leaflet surfaces. The algorithm predicts the leaflet moments (and thus the leaflet angular accelerations) of the next coupling iteration through a linearization of Newton's Second Law with a finite difference approximation of the Jacobian. The components of this Jacobian are the derivatives of the moments (exerted by the flow on the leaflets) with respect to the leaflet angular accelerations. The Jacobian is numerically calculated from the flow solver by variations of the leaflet positions. This quasi-Newton method was first introduced in Vierendeels et al. (2005) for one stiff leaflet and subsequently used to simulate a BMHV (Dumont et al. 2005, 2007). However, the algorithm described in Vierendeels et al. (2005) had only one degree of freedom which implied a symmetrical motion of both leaflets when simulating a BMHV. Therefore, the algorithm was extended to two degrees of freedom in Annerel et al. (2010) and Dahl et al. (2010), thus allowing the two leaflets to move asynchronously. In this paper, the convergence process is accelerated by the use of a variable time step size, extrapolation techniques and reuse of data from previous time steps. Also, the calculation process of the Jacobian is made more efficient, thus resulting in faster convergence.

The paper is organized as follows. First, the algorithm is derived and its implementation in a commercially available black box flow solver is analysed. Secondly, the algorithm is used to simulate a 3D BMHV in three different geometries, allowing an analysis of the leaflets kinematics and the wall shear stresses on the valve leaflet surfaces.

METHODS

In this section, the developed algorithm is presented. The flow chart is visualized in Figure 2 and each component is explained hereafter. Subsequently, the setup of the 3D simulations of the BMHV is discussed.

FSI coupling algorithm

Governing equations

A BMHV can be modelled as a rigid casing in which two separate rigid leaflets rotate around their hinge axes (see Figure 1). Because the position of each rigid leaflet is solely determined by its opening angle, the bileaflet valve has two degrees of freedom.

The movement of a rigid leaflet i is governed by Newton's Second Law, which states that the moment about its hinge (M_i) must be in equilibrium with the product of its moment of inertia (I_i) and its angular acceleration ($\ddot{\theta}_i$). For two leaflets, this leads to the following two equations:

$$\begin{cases} M_1 = I_1 \cdot \ddot{\theta}_1 \\ M_2 = I_2 \cdot \ddot{\theta}_2 \end{cases} \quad (1)$$

When the hinges are modelled as frictionless, the moment acting on the leaflet is the pressure and viscous moment exerted by the flow.

Figure 1: View on the ATS Open Pivot[IM] Standard Heart Valve with leaflets (marked in black) in the open position. The casing is visible (in white) with the blocking mechanism at the hinges.
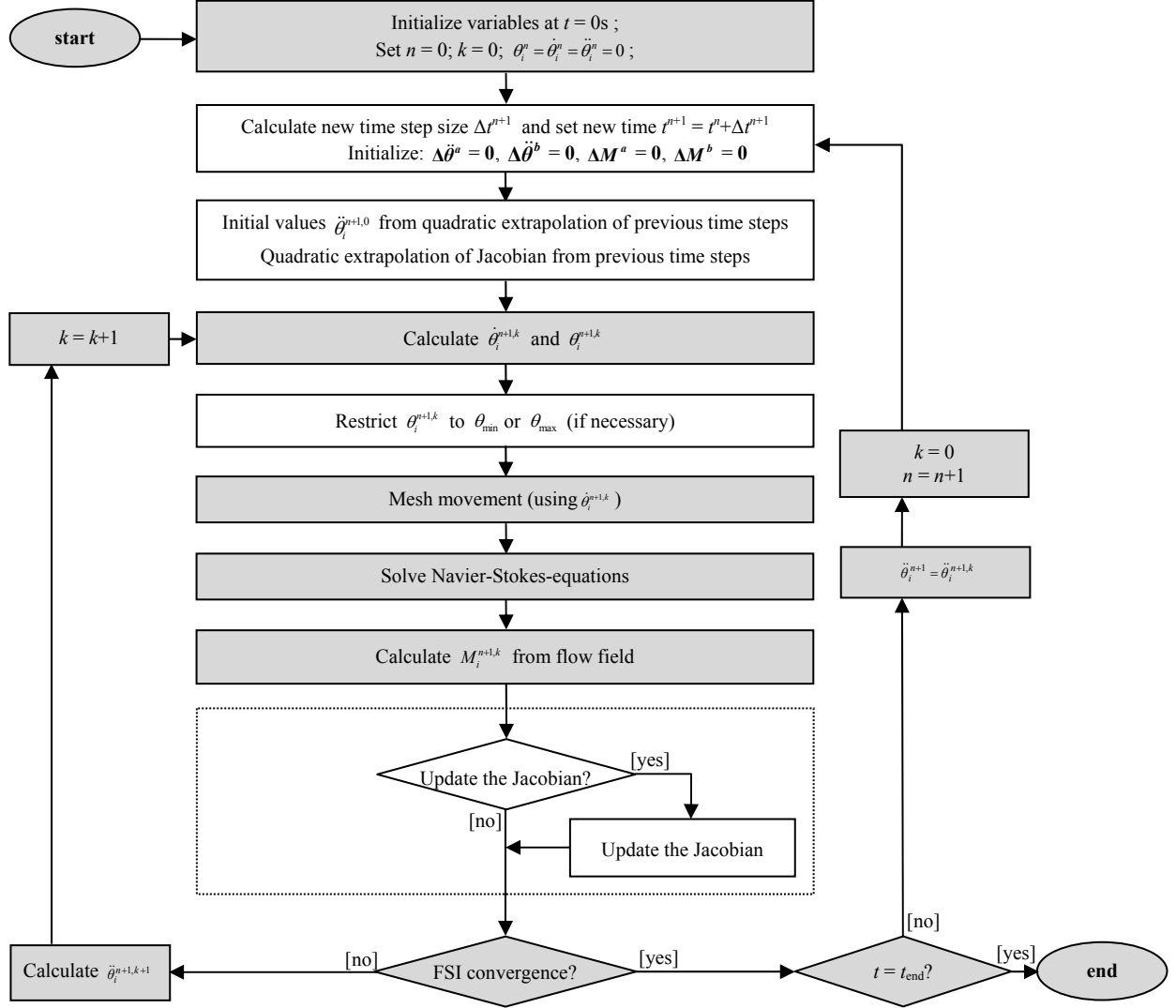
Linearization

Strong coupling schemes achieve this dynamic equilibrium at the fluid-structure interface by introducing a coupling iteration loop within each time step. Generally, each of the coupling iterations follows the same pattern, as is visualized in Figure 2 (shaded). At the beginning of each coupling iteration k of time step $n+1$, the motion of the leaflets is computed from the angular accelerations $\ddot{\theta}_i^{n+1,k}$. Subsequently, the mesh is moved and the Navier-Stokes equations are solved. From the flow field, the moments $M_i^{n+1,k}$ are calculated. Finally, the convergence of the dynamic equilibrium at the fluid-structure interface (i.e. the "FSI convergence", expressed by Equation (1)) is checked. When this FSI convergence is obtained, a new time step is initiated. However, when the FSI convergence is not achieved, a new coupling iteration $k+1$ is initiated and thus new angular accelerations $\ddot{\theta}_i^{n+1,k+1}$ need to be calculated. Therefore, the introduction of a coupling iteration loop requires, in each coupling iteration k of time step $n+1$, a stable and efficient approximation of the angular accelerations for the next coupling iteration $k+1$.

Such a stable prediction of $\ddot{\theta}_i^{n+1,k}$ can be achieved through a linearization of Newton's Second Law, as analysed by Vierendeels et al. (2005) for a monoleaflet heart valve. Thus, while taking into account the mutual interaction between the leaflets, Equation (1) is linearized for each coupling iteration $k+1$ of time step $n+1$:

$$\begin{cases} M_1^{n+1,k} + \left(\frac{\partial M_1}{\partial \ddot{\theta}_1}\right)^{n+1,k}\left(\ddot{\theta}_1^{n+1,k+1} - \ddot{\theta}_1^{n+1,k}\right) + \left(\frac{\partial M_1}{\partial \ddot{\theta}_2}\right)^{n+1,k}\left(\ddot{\theta}_2^{n+1,k+1} - \ddot{\theta}_2^{n+1,k}\right) = I_1 \cdot \ddot{\theta}_1^{n+1,k+1} \\ M_2^{n+1,k} + \left(\frac{\partial M_2}{\partial \ddot{\theta}_1}\right)^{n+1,k}\left(\ddot{\theta}_1^{n+1,k+1} - \ddot{\theta}_1^{n+1,k}\right) + \left(\frac{\partial M_2}{\partial \ddot{\theta}_2}\right)^{n+1,k}\left(\ddot{\theta}_2^{n+1,k+1} - \ddot{\theta}_2^{n+1,k}\right) = I_2 \cdot \ddot{\theta}_2^{n+1,k+1} \end{cases}$$

$$(2)$$

The derivatives $\partial M_i / \partial \ddot{\theta}_j$ are the components of the Jacobian of the moments with respect to the angular accelerations, further referred to as "the Jacobian". Equation (2) can be rearranged as follows:

$$\begin{cases} I_1 \cdot \ddot{\theta}_1^{n+1,k+1} - \left(\frac{\partial M_1}{\partial \ddot{\theta}_1}\right)^{n+1,k}\ddot{\theta}_1^{n+1,k+1} - \left(\frac{\partial M_1}{\partial \ddot{\theta}_2}\right)^{n+1,k}\ddot{\theta}_2^{n+1,k+1} = M_1^{n+1,k} - \left(\frac{\partial M_1}{\partial \ddot{\theta}_1}\right)^{n+1,k}\ddot{\theta}_1^{n+1,k} - \left(\frac{\partial M_1}{\partial \ddot{\theta}_2}\right)^{n+1,k}\ddot{\theta}_2^{n+1,k} \\ I_2 \cdot \ddot{\theta}_2^{n+1,k+1} - \left(\frac{\partial M_2}{\partial \ddot{\theta}_1}\right)^{n+1,k}\ddot{\theta}_1^{n+1,k+1} - \left(\frac{\partial M_2}{\partial \ddot{\theta}_2}\right)^{n+1,k}\ddot{\theta}_2^{n+1,k+1} = M_2^{n+1,k} - \left(\frac{\partial M_2}{\partial \ddot{\theta}_1}\right)^{n+1,k}\ddot{\theta}_1^{n+1,k} - \left(\frac{\partial M_2}{\partial \ddot{\theta}_2}\right)^{n+1,k}\ddot{\theta}_2^{n+1,k} \end{cases}$$

$$(3)$$

start

Initialize variables at $t = 0$s ;
Set $n = 0$; $k = 0$; $\theta_i^n = \dot{\theta}_i^n = \ddot{\theta}_i^n = 0$;

Calculate new time step size Δt^{n+1} and set new time $t^{n+1} = t^n + \Delta t^{n+1}$
Initialize: $\Delta\ddot{\theta}^a = \mathbf{0}$, $\Delta\ddot{\theta}^b = \mathbf{0}$, $\Delta M^a = \mathbf{0}$, $\Delta M^b = \mathbf{0}$

Initial values $\ddot{\theta}_i^{n+1,0}$ from quadratic extrapolation of previous time steps
Quadratic extrapolation of Jacobian from previous time steps

$k = k+1$

Calculate $\dot{\theta}_i^{n+1,k}$ and $\theta_i^{n+1,k}$

Restrict $\theta_i^{n+1,k}$ to $\theta_{\min}$ or $\theta_{\max}$ (if necessary)

Mesh movement (using $\dot{\theta}_i^{n+1,k}$)

Solve Navier-Stokes-equations

Calculate $M_i^{n+1,k}$ from flow field

Update the Jacobian? [yes]
[no]
Update the Jacobian

$k = 0$
$n = n+1$

$\ddot{\theta}_i^{n+1} = \ddot{\theta}_i^{n+1,k}$

Calculate $\ddot{\theta}_i^{n+1,k+1}$ ← [no] FSI convergence? [yes] → $t = t_{\text{end}}$? [no] / [yes] end

Figure 2: Flow chart of the presented quasi-Newton coupling algorithm with two degrees of freedom. n = time step, k = coupling iteration step, i = leaflet number. *Shaded*: standard strong coupling scheme, *unshaded*: extra components of the presented scheme.

This can be written in matrix notation:

$$\begin{bmatrix} I_1 - \left(\dfrac{\partial M_1}{\partial \ddot{\theta}_1}\right)^{n+1,k} & -\left(\dfrac{\partial M_1}{\partial \ddot{\theta}_2}\right)^{n+1,k} \\ -\left(\dfrac{\partial M_2}{\partial \ddot{\theta}_1}\right)^{n+1,k} & I_2 - \left(\dfrac{\partial M_2}{\partial \ddot{\theta}_2}\right)^{n+1,k} \end{bmatrix} \cdot \begin{bmatrix} \ddot{\theta}_1^{n+1,k+1} \\ \ddot{\theta}_2^{n+1,k+1} \end{bmatrix} = \begin{bmatrix} M_1^{n+1,k} - \left(\dfrac{\partial M_1}{\partial \ddot{\theta}_1}\right)^{n+1,k} \ddot{\theta}_1^{n+1,k} - \left(\dfrac{\partial M_1}{\partial \ddot{\theta}_2}\right)^{n+1,k} \ddot{\theta}_2^{n+1,k} \\ M_2^{n+1,k} - \left(\dfrac{\partial M_2}{\partial \ddot{\theta}_1}\right)^{n+1,k} \ddot{\theta}_1^{n+1,k} - \left(\dfrac{\partial M_2}{\partial \ddot{\theta}_2}\right)^{n+1,k} \ddot{\theta}_2^{n+1,k} \end{bmatrix}$$

(4)

For a well-posed problem, the first matrix has to be nonsingular. In that case, previous equation can be rewritten as

$$\begin{bmatrix} \ddot{\theta}_1^{n+1,k+1} \\ \ddot{\theta}_2^{n+1,k+1} \end{bmatrix} = \begin{bmatrix} I_1 - \left(\dfrac{\partial M_1}{\partial \ddot{\theta}_1}\right)^{n+1,k} & -\left(\dfrac{\partial M_1}{\partial \ddot{\theta}_2}\right)^{n+1,k} \\ -\left(\dfrac{\partial M_2}{\partial \ddot{\theta}_1}\right)^{n+1,k} & I_2 - \left(\dfrac{\partial M_2}{\partial \ddot{\theta}_2}\right)^{n+1,k} \end{bmatrix}^{-1} \cdot \begin{bmatrix} M_1^{n+1,k} - \left(\dfrac{\partial M_1}{\partial \ddot{\theta}_1}\right)^{n+1,k} \ddot{\theta}_1^{n+1,k} - \left(\dfrac{\partial M_1}{\partial \ddot{\theta}_2}\right)^{n+1,k} \ddot{\theta}_2^{n+1,k} \\ M_2^{n+1,k} - \left(\dfrac{\partial M_2}{\partial \ddot{\theta}_1}\right)^{n+1,k} \ddot{\theta}_1^{n+1,k} - \left(\dfrac{\partial M_2}{\partial \ddot{\theta}_2}\right)^{n+1,k} \ddot{\theta}_2^{n+1,k} \end{bmatrix}$$

(5)

In order to solve Equation (5) and thus to calculate the angular accelerations of the new coupling iteration $k+1$, the Jacobian has to be known. However, when a black box flow solver is used, these derivatives are not accessible. Fortunately, they can be approximated by finite differences ($i,j = 1,2$):

$$\frac{\partial M_i}{\partial \ddot{\theta}_j} \approx \frac{\Delta M_i}{\Delta \ddot{\theta}_j} \qquad (6)$$

which are calculated by solving the following system of equations:

$$\begin{cases} \left(\dfrac{\Delta M_1}{\Delta \ddot{\theta}_1}\right) \cdot \Delta\ddot{\theta}_1^a + \left(\dfrac{\Delta M_1}{\Delta \ddot{\theta}_2}\right) \cdot \Delta\ddot{\theta}_2^a = \Delta M_1^a \\[2ex] \left(\dfrac{\Delta M_2}{\Delta \ddot{\theta}_1}\right) \cdot \Delta\ddot{\theta}_1^a + \left(\dfrac{\Delta M_2}{\Delta \ddot{\theta}_2}\right) \cdot \Delta\ddot{\theta}_2^a = \Delta M_2^a \\[2ex] \left(\dfrac{\Delta M_1}{\Delta \ddot{\theta}_1}\right) \cdot \Delta\ddot{\theta}_1^b + \left(\dfrac{\Delta M_1}{\Delta \ddot{\theta}_2}\right) \cdot \Delta\ddot{\theta}_2^b = \Delta M_1^b \\[2ex] \left(\dfrac{\Delta M_2}{\Delta \ddot{\theta}_1}\right) \cdot \Delta\ddot{\theta}_1^b + \left(\dfrac{\Delta M_2}{\Delta \ddot{\theta}_2}\right) \cdot \Delta\ddot{\theta}_2^b = \Delta M_2^b \end{cases} \qquad (7)$$

resulting in

$$\begin{cases} \left(\dfrac{\Delta M_1}{\Delta \ddot{\theta}_1}\right) = \dfrac{\Delta M_1^a \cdot \Delta\ddot{\theta}_2^b - \Delta M_1^b \cdot \Delta\ddot{\theta}_2^a}{\Delta\ddot{\theta}_1^a \cdot \Delta\ddot{\theta}_2^b - \Delta\ddot{\theta}_1^b \cdot \Delta\ddot{\theta}_2^a} \\[2ex] \left(\dfrac{\Delta M_1}{\Delta \ddot{\theta}_2}\right) = \dfrac{\Delta M_1^b \cdot \Delta\ddot{\theta}_1^a - \Delta M_1^a \cdot \Delta\ddot{\theta}_1^b}{\Delta\ddot{\theta}_1^a \cdot \Delta\ddot{\theta}_2^b - \Delta\ddot{\theta}_1^b \cdot \Delta\ddot{\theta}_2^a} \\[2ex] \left(\dfrac{\Delta M_2}{\Delta \ddot{\theta}_1}\right) = \dfrac{\Delta M_2^a \cdot \Delta\ddot{\theta}_2^b - \Delta M_2^b \cdot \Delta\ddot{\theta}_2^a}{\Delta\ddot{\theta}_1^a \cdot \Delta\ddot{\theta}_2^b - \Delta\ddot{\theta}_1^b \cdot \Delta\ddot{\theta}_2^a} \\[2ex] \left(\dfrac{\Delta M_2}{\Delta \ddot{\theta}_2}\right) = \dfrac{\Delta M_2^b \cdot \Delta\ddot{\theta}_1^a - \Delta M_2^a \cdot \Delta\ddot{\theta}_1^b}{\Delta\ddot{\theta}_1^a \cdot \Delta\ddot{\theta}_2^b - \Delta\ddot{\theta}_1^b \cdot \Delta\ddot{\theta}_2^a} \end{cases} \qquad (8)$$

The superscripts a and b refer to data obtained from three coupling iterations between which the leaflet angular accelerations of two coupling iterations have differences (according to the vectors $\Delta\ddot{\theta}^a$ and $\Delta\ddot{\theta}^b$) with

respect to the angular accelerations of a reference coupling iteration:

$$\Delta\ddot{\theta}^a = \begin{bmatrix} \ddot{\theta}_1^a - \ddot{\theta}_1^{ref} \\ \ddot{\theta}_2^a - \ddot{\theta}_2^{ref} \end{bmatrix} = \begin{bmatrix} \Delta\ddot{\theta}_1^a \\ \Delta\ddot{\theta}_2^a \end{bmatrix}$$

$$\Delta\ddot{\theta}^b = \begin{bmatrix} \ddot{\theta}_1^b - \ddot{\theta}_1^{ref} \\ \ddot{\theta}_2^b - \ddot{\theta}_2^{ref} \end{bmatrix} = \begin{bmatrix} \Delta\ddot{\theta}_1^b \\ \Delta\ddot{\theta}_2^b \end{bmatrix} \tag{9}$$

These differences in accelerations ($\Delta\ddot{\theta}^a$ and $\Delta\ddot{\theta}^b$) induce differences in the calculated flow fields and thus also in the calculated moments, respectively denoted by ΔM^a and ΔM^b:

$$\Delta M^a = \begin{bmatrix} M_1^a - M_1^{ref} \\ M_2^a - M_2^{ref} \end{bmatrix} = \begin{bmatrix} \Delta M_1^a \\ \Delta M_2^a \end{bmatrix}$$

$$\Delta M^b = \begin{bmatrix} M_1^b - M_1^{ref} \\ M_2^b - M_2^{ref} \end{bmatrix} = \begin{bmatrix} \Delta M_1^b \\ \Delta M_2^b \end{bmatrix} \tag{10}$$

The data $\Delta\ddot{\theta}^a$, $\Delta\ddot{\theta}^b$, ΔM^a and ΔM^b can be obtained from three coupling iterations by several methods.

Update of the Jacobian

A method to obtain the necessary data ($\Delta\ddot{\theta}^a$, $\Delta\ddot{\theta}^b$, ΔM^a and ΔM^b) is described in Annerel et al. (2010) and Dahl et al. (2010). In this method, three consecutive coupling iterations are needed of which the leaflet acceleration perturbation vectors $\Delta\ddot{\theta}^a$ and $\Delta\ddot{\theta}^b$ are perpendicular to each other and significantly large.

This method can be improved in two ways. First, it is not necessary that the acceleration perturbation vectors $\Delta\ddot{\theta}^a$ and $\Delta\ddot{\theta}^b$ are completely perpendicular to each other. To calculate a good estimation of the Jacobian, it is already sufficient that their perpendicular components are significantly large. Secondly, the three coupling iterations do not have to be consecutive.

The calculation of the Jacobian can thus be made more efficient by the use of a criterion that selects two appropriate acceleration perturbation vectors (e.g. from previous coupling iterations), without the need for extra coupling iterations with perpendicularly perturbed accelerations. Therefore, the selection criterion needs to check the direction and the magnitude of the two acceleration perturbation vectors. Such a criterion can be derived from an error propagation study, which states that the error of the estimation of the angular acceleration of the next coupling iteration should be small enough. It can be shown that this results in the following criterion:

$$\frac{\max\limits_{i=1,2}\left(\sqrt{\left(\Delta\ddot{\theta}_i^a\right)^2 + \left(\Delta\ddot{\theta}_i^b\right)^2}\right)}{\left|\Delta\ddot{\theta}_2^b \cdot \Delta\ddot{\theta}_1^a - \Delta\ddot{\theta}_2^a \cdot \Delta\ddot{\theta}_1^b\right|} \cdot \frac{\varepsilon_1}{\min\limits_{i=1,2}(I_i)} \le \varepsilon_2 \tag{11}$$

with the Jacobian update threshold ε_2 and the flow solver convergence threshold ε_1, which is the accuracy of the moments calculated by the flow solver. The optimal values for ε_1 and ε_2 can be determined by a sensitivity analysis.

This criterion is used in an algorithm that makes it possible to update the Jacobian in every coupling iteration with data obtained from the coupling iterations in the current and previous time steps. This algorithm for the update of the Jacobian is constructed as follows:

At the beginning of the simulation, all the variables are equal to zero (in particular $\Delta\ddot{\theta}^a$, $\Delta\ddot{\theta}^b$, ΔM^a, ΔM^b and all the components of the Jacobian). Also, when going to each new time step, the data vectors ($\Delta\ddot{\theta}^a$, $\Delta\ddot{\theta}^b$, ΔM^a and ΔM^b) are set to zero (see further).

The data obtained in the first coupling iteration ($k = 0$) of each time step are used as the reference (i.e. $\ddot{\theta}_i^{ref}$ and M_i^{ref}) for the Jacobian update. Also, in this first coupling iteration a first estimation of the Jacobian is obtained from an extrapolation of previous time steps (see further).

In each of the following coupling iterations ($k > 0$), this Jacobian can be updated with useable data obtained in the coupling iterations. First, it is checked whether or not the data of the current coupling iteration k are useable as an acceleration perturbation vector. Subsequently, the Jacobian can be updated in three ways, depending on the acceleration perturbation vectors $\Delta\ddot{\theta}^a$ and $\Delta\ddot{\theta}^b$ available from the (current and previous) coupling iterations (a detailed description can be found in Appendix A):

- If no appropriate acceleration perturbation vectors are available, then the Jacobian cannot be updated and thus the extrapolated Jacobian is still used;
- If one acceleration perturbation vector is available, then the Jacobian can be updated. The data for the other acceleration perturbation vector are obtained from the acceleration perturbation vectors of previous time steps, or this data can be calculated by the extrapolated Jacobian;
- If both acceleration perturbation vectors are available, the Jacobian is calculated with both vectors and becomes independent of data from previous time steps.

In the following, the other components of the developed quasi-Newton algorithm are discussed. The flow chart of this algorithm is visualized in Figure 2.

Check FSI Convergence

The subsequent coupling iterations are performed until the dynamic equilibrium at the fluid-structure interface is achieved. This equilibrium is checked by the FSI convergence criterion. For each leaflet i, this FSI convergence criterion is given by:

$$\left| M_i^{n+1,k} - I_i \cdot \ddot{\theta}_i^{n+1,k} \right| < \varepsilon_0 \tag{12}$$

The FSI convergence threshold ε_0 is set relative to a reference moment M_{ref}. This reference moment M_{ref} sets the minimal accuracy of the dynamic equilibrium needed to capture the general leaflet dynamics.

When the FSI convergence criterion (Equation (12)) is fulfilled, a new time step is initiated. However, when the FSI convergence criterion is not fulfilled, then a new coupling iteration ($k+1$) is started.

Control quality of the Jacobian and calculate angular accelerations of the new coupling iteration

Before calculating the appropriate angular accelerations $\ddot{\theta}_i^{n+1,k+1}$ for the new coupling iteration $k+1$, the quality of the Jacobian is checked by evaluating the decrease in moment unbalance during the last two coupling iterations. For example, an arbitrary criterion of two orders of magnitude between these two consecutive coupling iterations is used:

$$\left| M_i^{n+1,k} - I_i \cdot \ddot{\theta}_i^{n+1,k} \right| < \frac{\left| M_i^{n+1,k-1} - I_i \cdot \ddot{\theta}_i^{n+1,k-1} \right|}{100} \tag{13}$$

When this expression is fulfilled, then the quality of the Jacobian of coupling iteration k-1 is good. Therefore, it

can be concluded that the Jacobian of the current coupling iteration k will probably also result in fast convergence, since this Jacobian can only become an improvement of the Jacobian of coupling iteration k-1. This is because when the Jacobian is updated in coupling iteration k, this update is done with more (or equally) relevant data (i.e. data of time step $n+1$ and not of time step n) than was available in coupling iteration k-1. Subsequently, the angular accelerations of the next coupling iteration $k+1$ are calculated by Equation (5) with the Jacobian of coupling iteration k and this next coupling iteration is initiated.

However, when Equation (13) is not fulfilled, then the quality of the Jacobian of coupling iteration k-1 is insufficient. Therefore, it is uncertain whether or not the Jacobian of coupling iteration k will result in fast convergence. The angular accelerations of the next coupling iteration $\ddot{\theta}_i^{n+1,k+1}$ are thus chosen in such a way that it will certainly become possible to calculate a good Jacobian in the next coupling iteration using the acceleration and moment data generated in this next coupling iteration.

The angular acceleration of this extra coupling iteration is thus chosen in one of three possible ways, depending on the acceleration perturbation vectors $\Delta\ddot{\theta}^a$ and $\Delta\ddot{\theta}^b$ already obtained in the coupling iterations (a detailed description can be found in Appendix B):

- If no acceleration perturbation vectors are available from the coupling iterations (i.e $\Delta\ddot{\theta}^a = 0$ and $\Delta\ddot{\theta}^b = 0$), then the angular acceleration of one leaflet is perturbed with a significant parameter δ in the next coupling iteration, as is described in (Annerel et al. 2010, Dahl et al. 2010);
- If one acceleration perturbation vector is already available (i.e. $\Delta\ddot{\theta}^a \neq 0$ and $\Delta\ddot{\theta}^b = 0$), then the leaflet accelerations of the next coupling iteration are perturbed in a direction that is perpendicular to $\Delta\ddot{\theta}^a$;
- If both acceleration perturbation vectors are available (i.e $\Delta\ddot{\theta}^a \neq 0$ and $\Delta\ddot{\theta}^b \neq 0$), then no extra coupling iteration is needed. Therefore, the Jacobian is kept since the slow residual drop rate is inherent to the problem and will mostly not be efficiently resolved by generating extra data. The angular acceleration of the next coupling iterations are thus calculated by Equation (5).

Increasing the efficiency

The efficiency of the algorithm is increased in several ways. In the following, the use of a variable time step size and the extrapolation of data from previous time steps are discussed.

Variable time step size. Since a heart valve is most of the time in the closed or open position, its leaflets are only moving in a very small fraction of the time cycle. However, when the leaflets are moving, very small time steps are needed for reasons of accuracy. Therefore, there is a clear advantage in the use of a variable time step size which allows a relatively large time step size when the valve is at rest, and a smaller time step size when the valve is moving, since it decreases the total number of time steps in a time cycle and thus lowers the computational cost. For these reasons, a variable time step size is commonly used when simulating heart valves (Bang et al. 2006; Choi et al. 2009; De Tullio et al. 2009).

When the leaflets are moving, the maximum allowable time step size is restricted by the maximum allowable mesh motion, and thus by grid characteristics. This is due to limitations of the mesh motion algorithm, since the remeshing occurs when going to a new time step, and in the coupling iterations within a time step only grid node relocation can be used. So, there is a maximum allowable mesh motion in order to retain an accurate and high-quality mesh (and, in worst case, to avoid highly skewed or even inverted cells).

A criterion for the time step size can be proposed based on this maximum leaflet movement ($\Delta\theta_{max}$):

$$\dot{\theta}_i^n \cdot \Delta t^{n+1} \leq \Delta\theta_{max} \quad \Rightarrow \quad \Delta t^{n+1} \leq \min_{i=1,2}\left(\frac{\Delta\theta_{max}}{\dot{\theta}_i^n}\right) \quad (14)$$

When the leaflet velocity is large, then the time step size will be small and vice versa. Furthermore, the time step size is limited by a maximal value Δt^{max}, otherwise the time step size would become infinite when none of the leaflets is moving (i.e. zero velocity).

Extrapolation from previous time steps. When advancing to a new time step, the angular accelerations for the first coupling iteration ($k = 0$) are estimated based on a quadratic extrapolation from previous time steps. This initial prediction of the values results in fewer coupling iterations per time step.

Also, the Jacobian's components are quadratically extrapolated from previous time steps. This is meaningful since the Jacobian is not changing much per time step.

Therefore, the extrapolation of data from previous time steps decreases the number of coupling iterations per time step and lowers the computational cost.

Initialization at the beginning of a new time step

When going to a new time step $n+1$, the variables are initialized. This is done by setting $t^{n+1} = t^n + \Delta t^{n+1}$, $\Delta\ddot{\theta}^a = \mathbf{0}$, $\Delta\ddot{\theta}^b = \mathbf{0}$, $\Delta M^a = \mathbf{0}$, $\Delta M^b = \mathbf{0}$ and $k = 0$.

Time integration scheme and leaflet behaviour at the limited position

Backward Euler time integration. The angular velocity and angular position of each leaflet on the time level $n+1$ are calculated from the angular accelerations using a time-integration scheme. Because the flow solver in which the algorithm is implemented uses a backward Euler scheme, this scheme is also preferred for the structural movement:

$$\begin{cases} \ddot{\theta}_i^{n+1,k+1} = \dfrac{\dot{\theta}_i^{n+1,k+1} - \dot{\theta}_i^n}{\Delta t} \\ \dot{\theta}_i^{n+1,k+1} = \dfrac{\theta_i^{n+1,k+1} - \theta_i^n}{\Delta t} \end{cases} \Rightarrow \begin{cases} \dot{\theta}_i^{n+1,k+1} = \dot{\theta}_i^n + \Delta t \cdot \ddot{\theta}_i^{n+1,k+1} \\ \theta_i^{n+1,k+1} = \theta_i^n + \Delta t \cdot \dot{\theta}_i^n + \Delta t^2 \cdot \ddot{\theta}_i^{n+1,k+1} \end{cases} \quad (15)$$

If the time discretization schemes of the flow and the structural solver do not match, then spurious oscillations can occur, as is shown in Vierendeels et al. (2005).

Leaflet behaviour in open and closed position. The angular position of each leaflet is restricted by a minimum and a maximum angle, indicating, respectively, the fully closed and fully open position. In reality, this is usually achieved by a physical blocking mechanism incorporated in the design of the leaflet hinges. These limitations can be numerically modelled by setting the angular position equal to the limited

position and the angular velocity and angular acceleration equal to zero, as briefly suggested by Guivier et al. (2007). However, they did not explain how to make the transition from a moving to a resting leaflet.

In the developed algorithm, this transition is modelled by setting the position equal to the limitation and recalculating the angular velocity and acceleration. This is implemented as follows. When the calculated position of a leaflet exceeds its limitations (i.e. $\theta_i^{n+1,k+1} < \theta_{\min}$ or $\theta_i^{n+1,k+1} > \theta_{\max}$), then the position is set equal to this limitation (i.e. $\theta_i^{n+1,k+1} = \theta_{\min}$ or $\theta_i^{n+1,k+1} = \theta_{\max}$). In order to move exactly to the limited position in the time step, the angular velocity $\dot{\theta}_i^{n+1,k+1}$ and acceleration $\ddot{\theta}_i^{n+1,k+1}$ are subsequently recalculated (using the backward Euler scheme):

$$\theta_i^{n+1,k+1} = \theta_{\min} \text{ or } \theta_{\max}$$
$$\dot{\theta}_i^{n+1,k+1} = \frac{\theta_i^{n+1,k+1} - \theta_i^n}{\Delta t} \qquad (16)$$
$$\ddot{\theta}_i^{n+1,k+1} = \frac{\dot{\theta}_i^{n+1,k+1} - \dot{\theta}_i^n}{\Delta t}$$

Furthermore, the previously described FSI convergence criterion must be changed when the position is limited since the FSI convergence criterion should no longer depend on the absolute value of $\left(M_i^{n+1,k} - I_i \cdot \ddot{\theta}_i^{n+1,k}\right)$, but merely on its mathematical sign. This can be understood by adding $M_i^{r,n+1,k}$ to the moment equation, with $M_i^{r,n+1,k}$ being the reaction moment of the blocking mechanism exerted on the leaflets in coupling iteration k of time step $n+1$:

$$M_i^{r,n+1,k} + M_i^{n+1,k} = I_i \cdot \ddot{\theta}_i^{n+1,k} \qquad (17)$$

or

$$M_i^{r,n+1,k} = -\left(M_i^{n+1,k} - I_i \cdot \ddot{\theta}_i^{n+1,k}\right) \qquad (18)$$

In order to maintain contact between the leaflet and the blocking mechanism, this reaction moment will be either negative or positive (depending on the leaflet and on the limiting position: $\theta_{\min}$ or $\theta_{\max}$). As FSI convergence criterion, it is checked whether or not the reaction moment has this appropriate mathematical sign. Therefore, when the motion of leaflet i is limited, the FSI convergence criterion (Equation (12)) of this leaflet i is replaced by

$$M_i^{r,n+1,k} \leq 0 \qquad (19)$$

or

$$M_i^{r,n+1,k} \geq 0 \qquad (20)$$

depending on the orientation of the leaflet and on whether the leaflet is fully open or fully closed.

Simulation setup

The new quasi-Newton algorithm is used to simulate the dynamics of a 3D BMHV. This BMHV is a model of the 25mm ATS Open Pivot[TM] Standard Heart Valve in aortic position with the orifice inner diameter measuring 20.8mm. The valve is simplified at the hinge regions by cutting away the blocking mechanism and hinges at the casing.

The valve is subsequently placed in three geometries. The first geometry consists of a rigid straight tube (visualized in Figure 3). The second geometry also consists of a rigid straight tube upstream of the valve, but rigid Valsalva sinuses are added downstream of the valve. Such Valsalva sinuses are anatomically present in the ascending aortic root and have an influence on the

valve closing. The Valsalva sinuses are based on the geometry described in Reul et al. (1990) and are positioned symmetrically with respect to the leaflets rotation axes (Figure 4). In the third geometry, the same Valsalva sinuses are used, but they are positioned asymmetrically (rotated over angle of 30 degrees) with respect to the leaflet rotation axes in such a way that one of the leaflets faces directly one sinus (Figure 5).

For the geometries, the upstream tube has a diameter of 22mm and measures 75mm in length. The downstream geometry has a length of 95mm. The diameter of the downstream tube is 27.36 mm for the Valsalva sinuses and 22mm for the straight tube.

It is noted that these geometries are based on clincial practice since, when implanting the BMHV, the surgeon can choose to preserve the Valsalva sinuses or to cut them away and replace the entire ascending aortic root (in the so-called Bentall procedure (Bentall et al. 1968)). Moreover, the surgeon can choose to position the valve symmetrical to the anatomical Valsalva sinuses, or to position it asymmetrical.
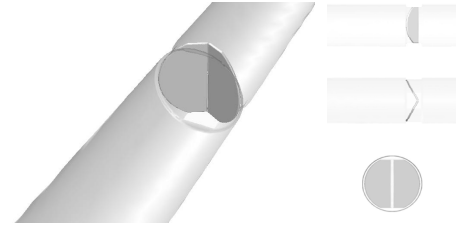
Figure 3: View on the first geometry with straight tube downstream of the valve: isometric (*left*), from front side (*up*), from top side (*middle*) and from inlet (*down*).
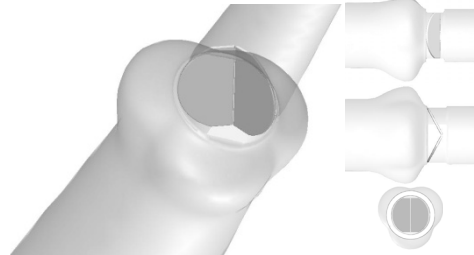
Figure 4: View on the second geometry with symmetrically placed Valsalva sinuses downstream of the valve: isometric (*left*), from front side (*up*), from top side (*middle*) and from inlet (*down*).
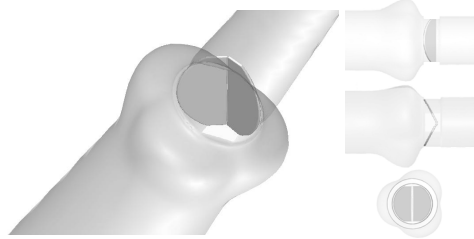
Figure 5: View on the third geometry with asymmetrically placed Valsalva sinuses downstream of the valve: isometric (*left*), from front side (*up*), from top side (*middle*) and from inlet (*down*).

An unstructured grid is generated in the geometries, consisting of approximately 800 000 tetrahedral cells. Two cell layers are generated in the gap (measuring 0.1mm) between the leaflets and the casing near the hinge region. The grids are constructed by defining the mesh size at the leaflet walls. Subsequently, a size function is applied at these leaflet walls, which means that in the direction perpendicular to the leaflet walls,

the grid size in the geometry increases at a specified rate. Therefore, a very fine grid size can be obtained at the leaflet walls, resulting in an accurate calculation of the wall shear stress magnitude and distribution.

The ALE-approach is followed, which means that the fluid grid follows the motion of the structure and subsequently needs an update. This update is done using a local remeshing method and spring-based smoothing. Due to the ALE approach, this remeshing can only be performed when going to a new time step. During the subsequent coupling iterations, the grid motion is performed with spring-based smoothing in order to maintain good mesh quality. The maximum time step size Δt^{max} is set to 0.001s.

An inlet aortic flow pulse with a period of 1s (displayed in Figure 6) is imposed upstream and was previously used in Dumont et al. (2005, 2007) and Annerel et al. (2010). The flow pulse profile is uniform. A physiological pressure profile is imposed at the downstream outlet boundary. Note, however, that in a rigid geometry the pressure level does not affect the flow field (only the pressure gradient appears in the equations).

Blood is modelled as an incompressible Newtonian fluid with density and viscosity respectively equal to 1050kg/m^3 and 4E-3Pa·s. No turbulence model is used, thus implying laminar flow. A no-slip boundary condition is applied at the walls. The valve is initially set in the closed position. The moment of inertia of one rigid valve leaflet about its rotation axis is equal to 9.94E-9 kg·m^2.

Each simulation is run in parallel on eight cores (2 x Quad-Core Intel Xeon 2.66GHz) with 8GB RAM.

The FSI convergence threshold ε_0 is chosen as (with reference moment equal to 1E-9Nm):

$$\varepsilon_0 = \frac{M_{ref}}{1E4} = \frac{1E-9}{1E4} = 1E-13\,\text{Nm} \qquad (21)$$

The optimal values for ε_1 and ε_2 are derived from a sensitivity analysis (not included in the paper) and are equal to:

$$\varepsilon_1 = \frac{\varepsilon_0}{100}$$
$$\varepsilon_2 = 0.001 \qquad (22)$$

RESULTS

In this section, the performance of the presented coupling algorithm is evaluated. Subsequently, the leaflet dynamics and the general flow field are discussed. Finally, the maximal wall shear stress that occurs during opening of the valve leaflets is studied in the three geometries.
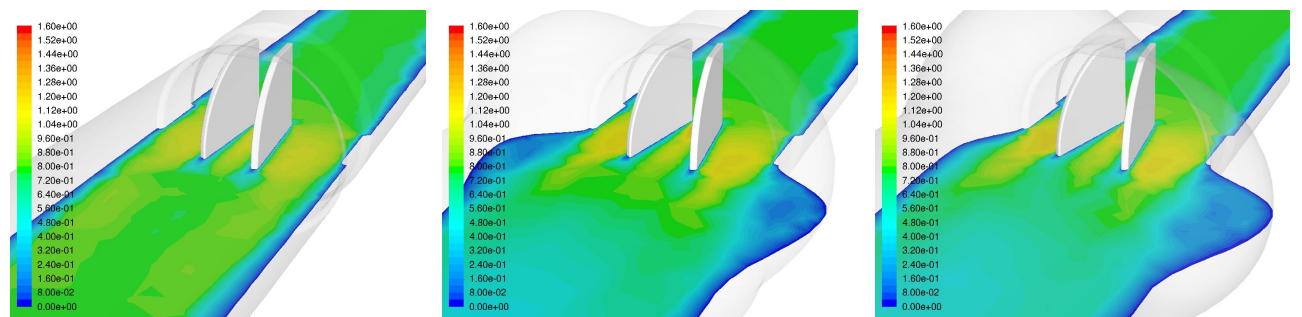
Solution process

The average number of coupling iterations per time step for the first geometry is given in Table 1. This solution process shows that during valve movement the developed algorithm reaches convergence in each time step within approximately four coupling iterations (see Table 1, "opening" and "closing", with ε_0=1E-13Nm).

Table 1: Averaged needed number of coupling iterations per time step for the presented coupling scheme, in the first geometry (straight tube) with $\varepsilon_0 = M_{ref}/10000$, $\varepsilon_1 = \varepsilon_0/100$ and $\varepsilon_2 = 0.001$.

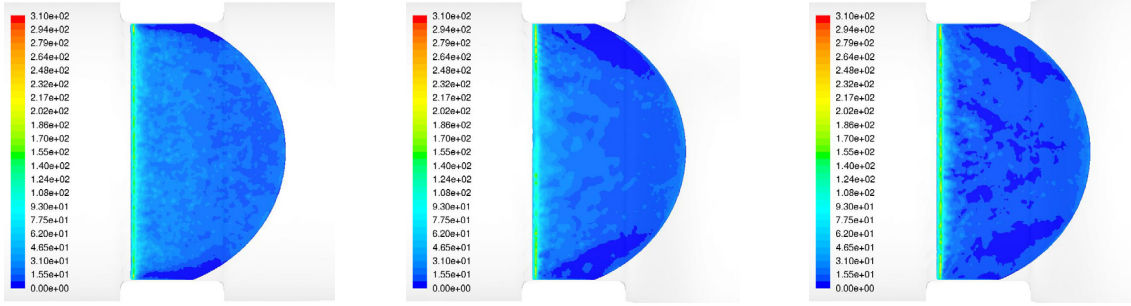| Opening (t=0s .. 0.0725s)	Open (t=0.0725s .. 0.325s)	Closing (t=0.325s .. 0.3925s)	Closed (t=0.3925s .. 1s)	Total (t=0s .. 1s)
4.064	1	3.984	1	2.279

Leaflet kinematics and flow field

The results of the simulations are depicted in Figure 6 and Figure 7.

The angular positions of the leaflets are presented in Figure 6, relative to the fully open position. Therefore, 0 and 1 refer, respectively, to the fully closed and fully open position. For the first geometry (straight tube), the leaflets of the valve reach the open position. Moreover, the resulting movement of the leaflets is symmetrical. Such symmetry in leaflet movement is also (approximately) found in the second geometry with symmetrical placed Valsalva sinuses. However, the leaflets do not reach the completely open position in this geometry. Finally, in the third geometry with asymmetrically placed Valsalva sinuses, both leaflets do not open completely and they do not behave symmetrically.
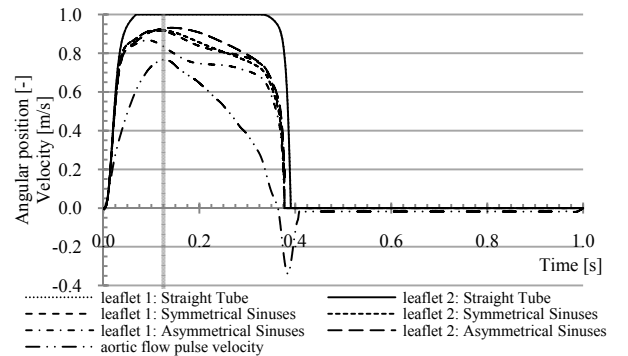
Figure 6: Angular position of the leaflets (relative to maximal opening angle) and the aortic flow pulse velocity. The leaflets of the straight tube geometry move symmetrically. The gray vertical line denotes "peak systole" ($t = 0.125$s), the time level at which Figure 7 is taken.

Figure 7: Velocity Magnitude in m/s at peak systole ($t = 0.125$s) visualized on a longitudinal section perpendicular to the leaflet rotation axes, for the geometry with the straight tube (*left*), the symmetrically placed Valsalva sinuses (*middle*) and the asymmetrical Valsalva sinuses (*right*).

Figure 8: Distribution of wall shear stress magnitude in Pa on one valve leaflet surface during peak systole ($t = 0.125$s), front view seen from the b-datum gap, for the geometry with the straight tube (*left*), the symmetrically placed Valsalva sinuses (*middle*) and the asymmetrical Valsalva sinuses (*right*).

Figure 7 shows the velocity field for the geometries at peak systole. Downstream of the valve, the flow pattern consists of three jets, which is typical for a BMHV. The recirculation zones of the blood flow in each sinus of Valsalva is clearly visible. Furthermore, downstream these Valsalva sinuses, the flow velocity is lower than in the geometry with the straight tube due to the difference in downstream tube diameter.

Maximal wall shear stress on the valve leaflets

The amount of blood damage can be related to the magnitude and the duration (exposure time) of the applied shear stresses (Dumont et al. 2007). In this section, the magnitudes of the wall shear stresses on the valve leaflets are discussed. Since the difference in leaflet opening movement between the three geometries is a main interest of this paper, only the forward flow is studied.

In all geometries, the maximal wall shear stress during forward flow is observed at $t = 0.125$s (peak systole). Furthermore, because this time level corresponds with the maximal blood inflow velocity, the maximal wall shear stress is located at the (b-datum) leading edge of the leaflets, as is visualized in Figure 8. For the first geometry (with straight tube), a maximal wall shear stress of 274Pa is calculated at both leaflets. In the second geometry (with symmetrically placed Valsalva sinuses), the magnitude of the maximal wall shear stress is approximately the same: 272Pa for both leaflets. Finally, the third geometry (with asymmetrically placed Valsalva sinuses), induces the same value of 276Pa at one leaflet, but a significantly larger maximal wall shear stress of 304Pa is observed at the other leaflet (i.e. at "leaflet 2", the leaflet that faces directly one sinus).

Subsequently, the wall shear stresses are spatially averaged on the leaflets during peak systole. This results in an average wall shear stress of 28.8Pa for both leaflets in the first and second geometry. For the third geometry, however, a slightly larger value of 29Pa is calculated for "leaflet 2" and a smaller average shear stress of 28.2Pa is observed on the other leaflet. The values of the average shear stress are in the same magnitude as calculated in previous studies (Dumont et al. 2005, 2007).

DISCUSSION

The results indicate that the presented algorithm has a stable and efficient solution process.
Furthermore, the resulting leaflet positions agree well with Feng et al. (1999, 2000) and De Tullio et al. (2009).

In particular, the results show that the maximum open position of the valve leaflets is not reached in the geometries with the Valsalva sinuses. Such incomplete opening for the ATS Open Pivot[TM] Standard Heart Valve in a divergent geometry is explained due to the greater sensitivity of the leaflet movement to the downstream flow field compared to other BMHV designs, since the leaflets extend farther in the flow downstream of the orifice than is the case in other designs. Therefore, the valve does not open completely in the divergent transvalvular flow caused by the Valsalva sinuses enlargement, since the leaflets tend to align with the streamlines (Feng et al. 1999, 2000). In the straight tube, however, a full opening of the valve leaflets is observed.

Moreover, it is observed that the two leaflets have differences in movement for the third geometry (with asymmetrically placed Valsalva sinuses). This asynchrony is triggered by the presence of the asymmetry in the geometry downstream of the valve. In the symmetrical geometries, no differences in movement between the two leaflets are observed. The asynchronous leaflet movement caused by the asymmetrically placed Valsalva sinuses is consistent with De Tullio et al. (2009).

Finally, for forward flow, the maximal wall shear stresses generated at a valve leaflet is significantly lower in the symmetrical geometries than is the case in the geometry with asymmetrically placed Valsalva sinuses. Because the maximal magnitude of wall shear stress is related to the acquired blood damage, it can be concluded that, in case of the ATS Open Pivot[TM] Standard Heart Valve, placing the downstream geometry symmetrically with respect to the valve leaflets reduces the accumulated amount of blood damage during forward flow.

CONCLUSION

In this paper, a strong coupling scheme for the partitioned simulation of a BMHV is presented and evaluated. The convergence of the coupling iterations between the flow solver and the leaflet motion solver is accelerated using the Jacobian with the derivatives of the pressure and viscous moments acting on the leaflets with respect to the leaflet accelerations. This Jacobian is numerically calculated from the data in the coupling iterations. A criterion is used for the selection of useable coupling iterations.

Subsequently, the algorithm is used to simulate an ATS Open Pivot[TM] Standard Heart Valve in three different geometries. The results show that the presented scheme

is stable and converges within a few coupling iterations. Moreover, it is observed that the leaflets tend to align with the streamlines. As a consequence, the leaflets perform an asynchronous movement in an asymmetric (downstream) geometry and they do not open completely in a divergent downstream geometry. Since symmetrical downstream geometries induce the smallest wall shear stress during systole, such geometries are preferred for valve replacement.

ACKNOWLEDGEMENTS

REFERENCES

ANNEREL, S., DEGROOTE, J., CLAESSENS, T., VIERENDEELS, J., (2010), Evaluation of a new Implicit Coupling Algorithm for the Partitioned Fluid-Structure Interaction Simulation of Bileaflet Mechanical Heart Valves, *IOP Conf Ser: Mater Sci Eng*, **10**, 012124.

BANG, J.S., YOO, S.M., KIM, C.N., (2006), Characteristics of Pulsatile Blood Flow Through the Curved Bileaflet Mechanical Heart Valve Installed in Two Different Types of Blood Vessels: Velocity and Pressure of Blood Flow, *ASAIO J*, **52**, 234-242.

BENTALL, H., DE BONO, A., (1968), A technique for complete replacement of the ascending aorta, *Thorax*, **23**, 338-339.

CHOI, C.R., KIM, C.N., (2009), Numerical Analysis on the Hemodynamics and Leaflet dynamics in a Bileaflet Mechanical Heart Valve Using a Fluid-structure Interaction Method, *ASAIO J.*, **55**(5), 428-437.

DAHL, S.K., VIERENDEELS, J., DEGROOTE, J., ANNEREL, S., HELLEVIK, L.R., SKALLERUD, B., (2010), FSI-simulation of asymmetric mitral valve dynamics during diastolic filling, *Comput Method Biomec*, DOI: 10.1080/10255842.2010.517200.

DASI, L.P., SIMON, H.A., SUCOSKY, P. & YOGANATHAN A.P., (2009), Fluid mechanics of artificial heart valves, *Clin Exp Pharmacol Physiol*, **36**, 225-237.

DE TULLIO, M.D., CRISTALLO, A., BALARAS, E., VERZICCO, R., (2009), Direct numerical simulation of the pulsatile flow through an aortic bileaflet mechanical heart valve, *J Fluid Mech*, **622**, 259-290.

DUMONT, K., VIERENDEELS, J., SEGERS, P., VAN NOOTEN, G., VERDONCK, P., (2005), Predicting ATS Open Pivot™ Heart Valve Performance with Computational Fluid Dynamics, *J Heart Valve Dis*, **14**, 393-399.

DUMONT, K., VIERENDEELS, J., KAMINSKY, R., VAN NOOTEN, G., VERDONCK, P., BLUESTEIN, D., (2007), Comparison of the Hemodynamic and Thrombogenic Performance of Two Bileaflet Mechanical Heart Valves Using a CFD/FSI Model, *J Biomech Eng*, **129**, 558-565.

FENG, Z., UMEZU, M., FUJIMOTO, T., TSUKAHARA, T., NURISHI, M., KAWAGUCHI, D., MASUDA, S., (1999), Analysis of ATS leaflet behaviour by in vitro experiment, *J Artif Organs*, **2**, 46-52.

FENG, Z., UMEZU, M., FUJIMOTO, T., TSUKAHARA, T., NURISHI, M., KAWAGUCHI, D. (2000). In Vitro Hydrodynamic Characteristics Among Three Bileaflet Valves in the Mitral Position, *J Artif Organs*, **24**(5), 346-352.

GUIVIER, C., DEPLANO, V., PIBAROT, P., (2007), New insights into the assessment of the prosthetic valve performance in the presence of subaortic stenosis through a fluid-structure interaction model, *J Biomech*, **40**, 2283-2290.

REUL, H., VAHLBRUCH, A., GIERSIEPEN, M., SCHMITZ-RODE, T.H., HIRTZ, V., EFFERT, S., (1990), The geometry of the aortic root in health, at valve disease and after valve replacement, *J Biomech*, **23,** 181-191.

VIERENDEELS, J., DUMONT, K., DICK, E., VERDONCK, P., (2005), Analysis and Stabilization of Fluid-Structure Interaction Algorithm for Rigid-Body Motion, *AIAA J*, **43**, 2549-2557.

APPENDIX A

The update of the Jacobian at coupling iteration k of time step $n+1$, can be categorized into three cases, depending on the acceleration perturbation vectors ($\Delta\ddot{\theta}^a$ and $\Delta\ddot{\theta}^b$) obtained in previous coupling iterations:

1. Vectors $\Delta\ddot{\theta}^a = \mathbf{0}$ and $\Delta\ddot{\theta}^b = \mathbf{0}$

This means that none of the previous coupling iterations of that time step resulted in useable data to update the Jacobian (i.e. the acceleration perturbation and moment data vectors are equal to zero).

The data generated in the current coupling iteration k will be evaluated on its usability by checking the Jacobian update criterion (Equation (11)). For doing so, the vector $\Delta\ddot{\theta}^a$ is set as the difference between the accelerations of coupling iteration k and the accelerations of the reference coupling iteration (i.e. $k = 0$):

$$\Delta\ddot{\theta}^a = \begin{bmatrix} \Delta\ddot{\theta}_1^{n+1,k} \\ \Delta\ddot{\theta}_2^{n+1,k} \end{bmatrix} = \begin{bmatrix} \ddot{\theta}_1^{n+1,k} - \ddot{\theta}_1^{n+1,0} \\ \ddot{\theta}_2^{n+1,k} - \ddot{\theta}_2^{n+1,0} \end{bmatrix} \tag{23}$$

For the second vector (i.e. $\Delta\ddot{\theta}^b$), three possibilities can be distinguished:

- $\Delta\ddot{\theta}^b = \Delta\ddot{\theta}^{a,n}$, with $\Delta\ddot{\theta}^{a,n}$ the vector $\Delta\ddot{\theta}^a$ used in previous time step n;
- $\Delta\ddot{\theta}^b = \Delta\ddot{\theta}^{b,n}$, with $\Delta\ddot{\theta}^{b,n}$ the vector $\Delta\ddot{\theta}^b$ used in previous time step n;
- $\Delta\ddot{\theta}^b = \Delta\ddot{\theta}^{a\perp}$, with $\Delta\ddot{\theta}^{a\perp}$ the vector perpendicular to $\Delta\ddot{\theta}^a$:

$$\begin{cases} \Delta\ddot{\theta}_1^{a\perp} = -\Delta\ddot{\theta}_2^a \\ \Delta\ddot{\theta}_2^{a\perp} = \Delta\ddot{\theta}_1^a \end{cases} \tag{24}$$

The moments corresponding with $\Delta\ddot{\theta}^{a\perp}$ are estimated by using the Jacobian of previous coupling iteration k-1:

$$\begin{cases} \Delta M_1^{a\perp} = \left(\dfrac{\Delta M_1}{\Delta\ddot{\theta}_1}\right)_{k-1} \cdot \Delta\ddot{\theta}_1^{a\perp} + \left(\dfrac{\Delta M_1}{\Delta\ddot{\theta}_2}\right)_{k-1} \cdot \Delta\ddot{\theta}_2^{a\perp} \\ \Delta M_2^{a\perp} = \left(\dfrac{\Delta M_2}{\Delta\ddot{\theta}_1}\right)_{k-1} \cdot \Delta\ddot{\theta}_1^{a\perp} + \left(\dfrac{\Delta M_2}{\Delta\ddot{\theta}_2}\right)_{k-1} \cdot \Delta\ddot{\theta}_2^{a\perp} \end{cases} \tag{25}$$

The possibility for $\Delta\ddot{\theta}^b$ that results in the smallest left-hand side of Equation (11) is chosen.

When this smallest value is smaller than or equal to ε_2 (i.e. Equation (11) is fulfilled), then the update of the Jacobian is done by Equation (8), with

$$\Delta M^a = \begin{bmatrix} \Delta M_1^{n+1,k} \\ \Delta M_2^{n+1,k} \end{bmatrix} = \begin{bmatrix} M_1^{n+1,k} - M_1^{n+1,0} \\ M_2^{n+1,k} - M_2^{n+1,0} \end{bmatrix} \qquad (26)$$

and ΔM^b set equal to the moment data corresponding with the chosen $\Delta\ddot{\theta}^b$. After this Jacobian update, the vector $\Delta\ddot{\theta}^b$ is discarded by setting $\Delta\ddot{\theta}^b = \mathbf{0}$ (and $\Delta M^b = \mathbf{0}$), since ΔM^b is not derived from coupling iterations in the current time step and hence does not need to be stored.

However, when the smallest value for the left-hand side is greater than ε_2 (i.e. Equation (11) is not fulfilled), the Jacobian will not be updated. Both vectors $\Delta\ddot{\theta}^a$ and $\Delta\ddot{\theta}^b$ (and their moment data ΔM^a and ΔM^b) are then discarded by setting them equal to $\mathbf{0}$.

2. Vector $\Delta\ddot{\theta}^a \neq \mathbf{0}$ and vector $\Delta\ddot{\theta}^b = \mathbf{0}$

An appropriate vector $\Delta\ddot{\theta}^a$ (with moment data ΔM^a) is already obtained in a previous coupling iteration.

The data generated in this coupling iteration k will first be evaluated on its usability by checking the Jacobian update criterion (Equation (11)). For doing so, the vector $\Delta\ddot{\theta}^b$ is set as the difference between the accelerations of coupling iteration k and the accelerations of the reference coupling iteration (i.e. $k = 0$):

$$\Delta\ddot{\theta}^b = \begin{bmatrix} \Delta\ddot{\theta}_1^{n+1,k} \\ \Delta\ddot{\theta}_2^{n+1,k} \end{bmatrix} = \begin{bmatrix} \ddot{\theta}_1^{n+1,k} - \ddot{\theta}_1^{n+1,0} \\ \ddot{\theta}_2^{n+1,k} - \ddot{\theta}_2^{n+1,0} \end{bmatrix} \qquad (27)$$

Also, the data concerning the moments is set:

$$\Delta M^b = \begin{bmatrix} \Delta M_1^{n+1,k} \\ \Delta M_2^{n+1,k} \end{bmatrix} = \begin{bmatrix} M_1^{n+1,k} - M_1^{n+1,0} \\ M_2^{n+1,k} - M_2^{n+1,0} \end{bmatrix} \qquad (28)$$

When the Jacobian update criterion (Equation (11)) is satisfied, the Jacobian components are updated by solving Equation (8) with $\Delta\ddot{\theta}^a$ and $\Delta\ddot{\theta}^b$ (and their corresponding moment data ΔM^a and ΔM^b).

If the Jacobian update criterion is not fulfilled, then the Jacobian is not updated and the vector $\Delta\ddot{\theta}^b$ (and its moment data ΔM^b) is not used. The vector $\Delta\ddot{\theta}^b$ is then discarded (i.e. $\Delta\ddot{\theta}^b = \mathbf{0}$ and $\Delta M^b = \mathbf{0}$).

3. Vector $\Delta\ddot{\theta}^a \neq \mathbf{0}$ and vector $\Delta\ddot{\theta}^b \neq \mathbf{0}$

Two vectors $\Delta\ddot{\theta}^a$ and $\Delta\ddot{\theta}^b$ (with corresponding ΔM^a and ΔM^b), appropriate for the update of the Jacobian, have already been generated in previous coupling iterations. So, in a previous coupling iteration, the Jacobian was already updated with that data. Therefore, the Jacobian is kept.

APPENDIX B

When the quality of the (last used) Jacobian is insufficient, the angular accelerations of the next coupling iteration $k+1$ are calculated in such a way that it will become possible to calculate a good Jacobian in the next coupling iteration by the acceleration and moment data generated in this next coupling iteration.

In order to calculate such appropriate angular accelerations, three cases can be distinguished, depending on $\Delta\ddot{\theta}^a$ and $\Delta\ddot{\theta}^b$ (and thus depending on the amount of data that are already acquired in previous coupling iterations):

1. Vectors $\Delta\ddot{\theta}^a = \mathbf{0}$ and $\Delta\ddot{\theta}^b = \mathbf{0}$

This means that the current and previous coupling iterations do not result in useable data for the update of the Jacobian. So, in the next coupling iteration $k+1$, one of the leaflets will be perturbed with a significant parameter δ, since this will result in an appropriate $\Delta\ddot{\theta}^a$ (and ΔM^a) in this next coupling iteration, as is described in (Annerel et al. 2010, Dahl et al. 2010). For example,

$$\begin{cases} \Delta\ddot{\theta}_1^{n+1,k+1} = \delta \\ \Delta\ddot{\theta}_2^{n+1,k+1} = 0 \end{cases} \Rightarrow \begin{cases} \ddot{\theta}_1^{n+1,k+1} = \ddot{\theta}_1^{n+1,k=0} + \delta \\ \ddot{\theta}_2^{n+1,k+1} = \ddot{\theta}_2^{n+1,k=0} \end{cases} \qquad (29)$$

The method is not sensitive to the exact value of this parameter δ (Vierendeels et al. 2005). It should be chosen so that it is large enough to result in a significant change of the moments (i.e. ΔM^a must become significantly large with respect to the flow solver convergence threshold). However, it should not be chosen too large, because this could result in a failing mesh motion. For the cases simulated in this paper, $|\delta|$ is equal to 10 rad/s^2. The mathematical sign of δ depends on the movement phase (opening or closing) and the specific leaflet.

2. Vector $\Delta\ddot{\theta}^a \neq \mathbf{0}$ and vector $\Delta\ddot{\theta}^b = \mathbf{0}$

The data of one of the current or previous coupling iterations (stored as $\Delta\ddot{\theta}^a$ with ΔM^a) can thus still be used to update the Jacobian in the next coupling iteration.

To ensure that the perturbation of the leaflet accelerations in the next coupling iteration will generate data that will result in a good update of the Jacobian (i.e. the data of the next coupling iteration $k+1$ are useable as $\Delta\ddot{\theta}^b$ with ΔM^b), the leaflets are perturbed in a direction that is perpendicular to vector $\Delta\ddot{\theta}^a$. For example,

$$\begin{cases} \Delta\ddot{\theta}_1^{n+1,k+1} = -\Delta\ddot{\theta}_2^a \\ \Delta\ddot{\theta}_2^{n+1,k+1} = \Delta\ddot{\theta}_1^a \end{cases} \Rightarrow \begin{cases} \ddot{\theta}_1^{n+1,k+1} = \ddot{\theta}_1^{n+1,0} - \Delta\ddot{\theta}_2^a \\ \ddot{\theta}_2^{n+1,k+1} = \ddot{\theta}_2^{n+1,0} + \Delta\ddot{\theta}_1^a \end{cases} \qquad (30)$$

or

$$\begin{cases} \Delta\ddot{\theta}_1^{n+1,k+1} = \Delta\ddot{\theta}_2^a \\ \Delta\ddot{\theta}_2^{n+1,k+1} = -\Delta\ddot{\theta}_1^a \end{cases} \Rightarrow \begin{cases} \ddot{\theta}_1^{n+1,k+1} = \ddot{\theta}_1^{n+1,0} + \Delta\ddot{\theta}_2^a \\ \ddot{\theta}_2^{n+1,k+1} = \ddot{\theta}_2^{n+1,0} - \Delta\ddot{\theta}_1^a \end{cases} \qquad (31)$$

However, it must be checked whether or not these perturbations exceed the limited position of the leaflets. So, when one of these perpendicular perturbations is blocked, then one of the two leaflets is perturbed with the small parameter δ:

$$\begin{cases} \Delta\ddot{\theta}_1^{n+1,k+1} = \delta \\ \Delta\ddot{\theta}_2^{n+1,k+1} = 0 \end{cases} \Rightarrow \begin{cases} \ddot{\theta}_1^{n+1,k+1} = \ddot{\theta}_1^{n+1,0} + \delta \\ \ddot{\theta}_2^{n+1,k+1} = \ddot{\theta}_2^{n+1,0} \end{cases} \qquad (32)$$

or

$$\begin{cases} \Delta\ddot{\theta}_1^{n+1,k+1} = 0 \\ \Delta\ddot{\theta}_2^{n+1,k+1} = \delta \end{cases} \Rightarrow \begin{cases} \ddot{\theta}_1^{n+1,k+1} = \ddot{\theta}_1^{n+1,0} \\ \ddot{\theta}_2^{n+1,k+1} = \ddot{\theta}_2^{n+1,0} + \delta \end{cases} \qquad (33)$$

depending on which of the two perturbations is resulting in the smallest left-hand side of the Jacobian update criterion (Equation (11)).

3. Vector $\Delta\ddot{\theta}^a \neq \mathbf{0}$ and vector $\Delta\ddot{\theta}^b \neq \mathbf{0}$

No extra data are needed, since all the data that are used to update the Jacobian, depend already on time step $n+1$. The slow residual drop rate is hence inherent to the problem and cannot be resolved efficiently by generating extra data. The Jacobian is thus kept. The angular accelerations of the next coupling iteration are thus calculated by Equation (5) with the Jacobian and this next coupling iteration is subsequently initiated.

NUMERICAL SIMULATION OF LARGE BUBBLES IN CHANNELS USING A FRONT-TRACKING METHOD

Nicholas HOR[1,2]*, Jinsong HUA[1], Christopher J. LAWRENCE[1], Peter D.M. SPELT [2,3]

[1] Institute for Energy Technology, Process and Fluid flow Technology, PO Box 40, NO-2027 Kjeller, NORWAY

[2] Department of Chemical Engineering, Imperial College London, South Kensington Campus, London SW7 2AZ

[3]LMFA, CNRS, Ecully, France, and Department of Mechanical Engineering, Université de Lyon 1 (Claude Bernard), France

* E-mail: nick.hor@ife.no

ABSTRACT

Re

Keywords:

NOMENCLATURE

Greek Symbols

κ

ρ

σ

θ

τ

μ

Latin Symbols

Ar

Bo

D

d

Fr

$\mathbf{g}$

h

$\mathbf{n}$

p

Re

t

$\mathbf{u}$

$\mathbf{x}$

Sub/superscripts

f

l

m

n　　　　n

p

σ

T

∞

INTRODUCTION

et al

et al　　*et al*

et al

Re

Re

Re

•

$$U_\infty/\sqrt{gD} \qquad\qquad \rho_l gD\;\big/\sigma\;,$$
$$g\mu\;\big/\rho_l\sigma$$

$$\rho_l\,gD\;\big/\mu\;>\;\times \qquad Bo> \qquad\qquad Fr<$$
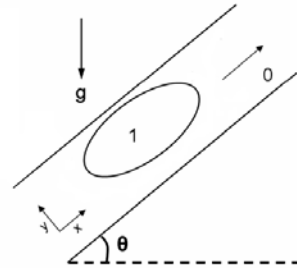
Figure 1

Front tracking method

Governing equations

Bo

et al *et al*

et al $$\nabla\cdot\mathbf{u}=$$

Re *Bo*

$$\frac{\partial\;\rho\mathbf{u}}{\partial t}+\nabla\cdot\rho\mathbf{u}\mathbf{u}=-\nabla p+\nabla\cdot\left[\mu\;\nabla\mathbf{u}+\nabla^T\mathbf{u}\;\right]$$
$$+\int_\Gamma\sigma_f\kappa_f\mathbf{n}_f\delta\;\mathbf{x}\text{-}\mathbf{x}_f\;ds+\;\rho-\rho_l\;\mathbf{g}$$

et al

$$\delta\quad=\delta\;x\;\delta\;y$$

Bo

$$\mathbf{x}^*=\mathbf{x}/D\quad\mathbf{u}^*=\mathbf{u}/\sqrt{gD}\quad\tau^*=t\sqrt{g/D}\quad\rho^*=\rho/\rho_l$$
$$p^*=p/\rho_l gD\quad\mu^*=\mu/\mu_l\quad\kappa^*=D\kappa\quad\;^*=\;/g$$
$$g=\|\mathbf{g}\|$$

et al

Bo

Bo *Re* *Re*

$$\frac{\partial\;\rho\mathbf{u}}{\partial t}+\nabla\cdot\rho\mathbf{u}\mathbf{u}=-\nabla p+\frac{}{Ar}\nabla\cdot\left[\mu\;\nabla\mathbf{u}+\nabla^T\mathbf{u}\;\right]$$
$$+\frac{}{Bo}\int_\Gamma\kappa_f\mathbf{n}_f\delta\;\mathbf{x}\text{-}\mathbf{x}_f\;ds+\;\rho-\;\mathbf{g}$$

MODEL DESCRIPTION

Bo

$$Ar$$
$$Ar=\rho_l g\;\;D\;\big/\mu_l$$

$$Bo=\rho_l gD\;\big/\sigma$$

$$x\;y \qquad\qquad y$$
$$x$$

n $\mathbf{x}_f^{n+}$ *(n+1)*

$= \rho_l D U_\infty / \mu_l$

$Fr = U_\infty / \sqrt{gD}$ *Re=Ar·Fr.*

$_f \quad _f \, t \; = \sum \quad t \; D \quad - \quad _f$

Discontinuities across the interface

$_f^{n+} \; = \; _f^n \; + \; _f^n \Delta t$

Flow solver

et al

Moving reference frame

$D \; \mathbf{x}$

$$D\,\mathbf{x} - \mathbf{x}_f \; = \left\{ \begin{array}{l} h^- \displaystyle\prod_{i=} \left(+ \; \left(\frac{\pi}{h} |\mathbf{x} - \mathbf{x}_f| \right) \right) \quad \textit{if} \quad |\mathbf{x} - \mathbf{x}_f| < h \\[2mm] \qquad\qquad\qquad\qquad \textit{otherwise} \end{array} \right.$$

Figure 2: *et al*

et al

et al

Tracking the moving interface

$_f \quad _f \, t$

XY

$X'Y'$

$\mathbf{x}_f^n$ XY $X'Y'$ $\mathbf{x}_p$ $\mathbf{x}_p$

$\mathbf{x}_m$

$\mathbf{u}\,\mathbf{x}\,t$ $\mathbf{u}\,\mathbf{x}_p\,t$

XY *X'Y'*

$\mathbf{u}_m\,t$

$$\mathbf{x}_p = \mathbf{x}_m + \mathbf{x}_p$$

$$\mathbf{u}\,\mathbf{x}\,t = \mathbf{u}_m\,t + \mathbf{u}\,\mathbf{x}_p\,t$$

$\mathbf{u}_f^n$

$\mathbf{u}^n$

$\mathbf{u}_f^n$

$$\frac{\partial\,\rho\mathbf{u}}{\partial t} + \nabla\cdot\rho\mathbf{u}\,\mathbf{u} + \rho\frac{d\mathbf{u}_m}{dt} = -\nabla\,p + \frac{1}{Ar}\nabla\cdot\left[\mu\,\nabla\mathbf{u} + \nabla^T\mathbf{u}\;\right]$$

$\mathbf{x}_f^{n+}$

$$+\frac{1}{Bo}\int_\Gamma \kappa_f\mathbf{n}_f\delta\,\mathbf{x}\,\cdot\,\mathbf{x}_f\,ds + \rho - \,\mathbf{g}$$

$$\nabla\cdot\mathbf{u} =$$

$\mathbf{u}^{n+}$

$\mathbf{X}_B$ p^{n+}

$$\mathbf{u}\,\mathbf{x}_B\,t = \mathbf{u}\,\mathbf{x}_B\,t - \mathbf{u}_m\,t$$

RESULTS

$d\mathbf{u}_m/dt$

$\mathbf{a}$

$\mathbf{a}$

et al.

NUMERICAL METHOD

$\mu/\mu_l =$ $\rho/\rho_l =$

Table 1:

p

$\partial p/\partial n$

$\partial u/\partial n =$

Re

et al

Validation

et al

Figure 4:
et al   *Re*

$\mu/\mu_l =$ $\rho/\rho_l =$ *Bo*

Re

•

et al.

Re

Bo

et al

Re

Figure 3

et al   *Re*

Re

Re

Re

Re
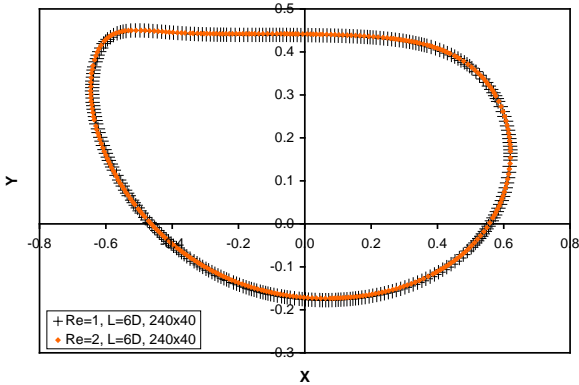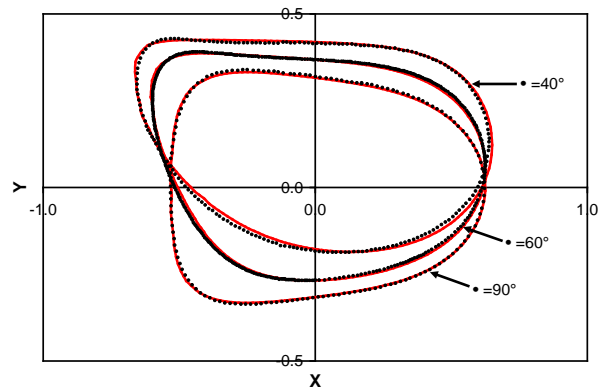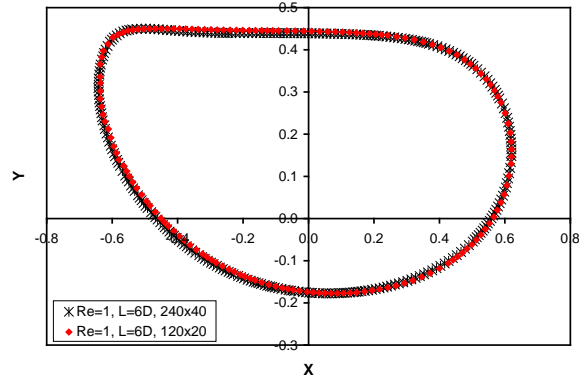
Figure 5:

Re   *Re*   •

•   *Re*

et al

•

•
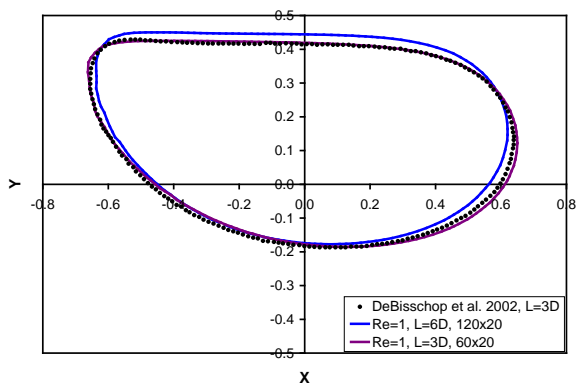
Figure 6:

et al

•

Effect of Bond number

Stagnant liquid

Bo

Fr   *Bo*   *Re*

Re   *Bo*   *Re*   *Bo*

Re   *Bo*

Bo

Re

Streamlines and bubble shape

Figure 7:

•   •

•   •   *Re*   *Bo*

•   •   •

Re   *Bo*

•   •

•

•

•
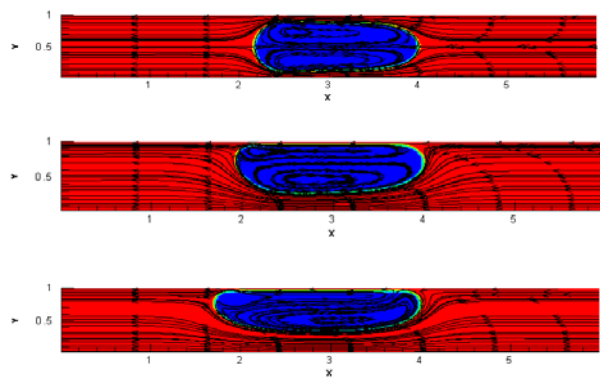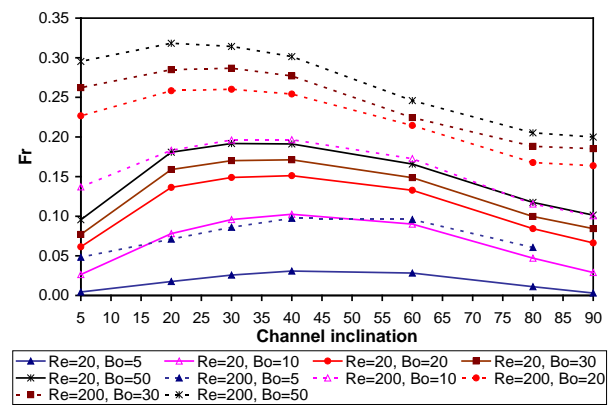
Figure 8:   *Fr*   *Bo*

Bo

Re

Re

Bo   *Re*

Bo

Bo

Re   *Bo*   •

Bo   *Bo*

                                                                                    •

                                        et al
et al   *Re*
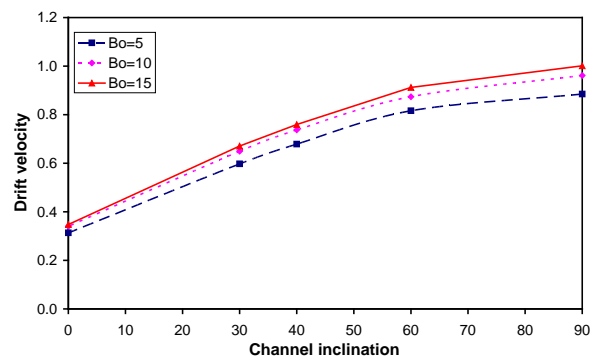
Figure 10:
  Bo

Bo

                          •

                                      •

Effect of Reynolds number

                          •

Moving liquid with periodic boundary condition
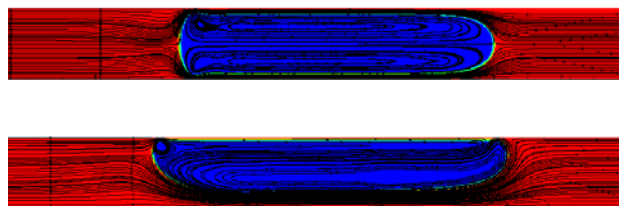
Figure 11:   •
                •   *Re*   *Bo*

                                              Re   *Fr*

                                                    Bo

                                      Fr   *Re*
              Re   *Bo*

Figure 9:
  Bo

                                                              Re

                    Re

                        Bo

                        Re

                                                              et al

Figure 12:   *Fr*   *Re*   *Bo*   *Bo*

Re

Re

Re

Re   *et al*

        Re   *Re*

    Re   *Re*

      et al

  Bo

Re   *Re*

  Bo

    Bo

    Bo

    Bo

           Re

Bo

  Bo   *Re<*

      Re>

        Re   *Bo*

Wall shear stress and normal stress

      x

    x

           $\mu_l \, du/dy$

      $\mu_l \sqrt{g/D}$

        y

    x

x/D

x/D

Figure 13:

        Re   *Bo*   •

Figure 14:

        Re   *Bo*   •

x
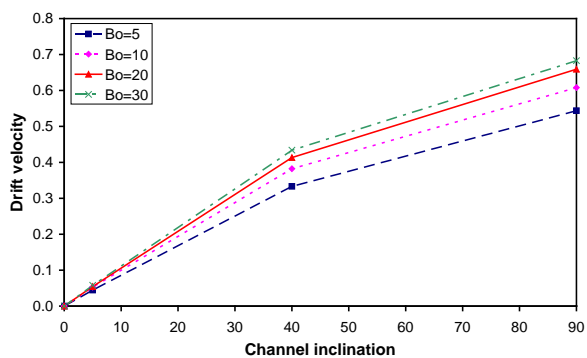
                      et al

CONCLUSIONS

$$- \ p - p_{ref} \ + \mu_l \ dv/dy$$

Re   Bo

Bo

Re

y

Bo

et   al

dp/dx

Bo
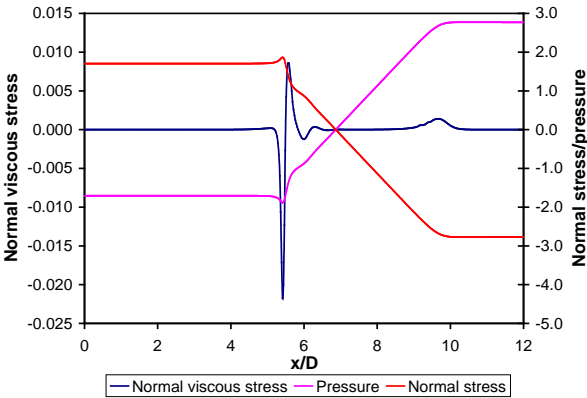
Figure 15:

Re   *Bo*   •
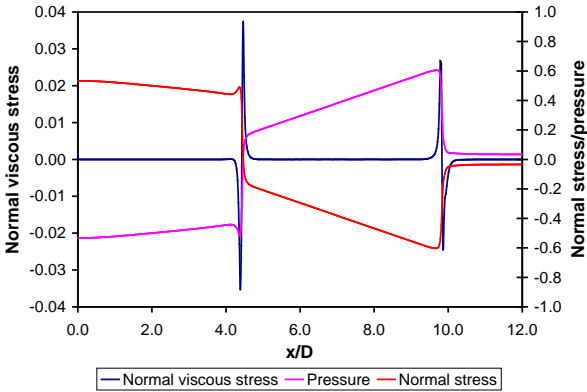
Figure 16:

Re   *Bo*   •

•

•

•

•

•

REFERENCES

Journal of Computational Physics **100**

Journal of Fluid Mechanics, **466**

Journal of Fluid Mechanics **387**   .

Journal of Fluid Mechanics, **89**

Journal of Fluid Mechanics **184**

Proceedings of the Royal Society of London. Series A, Mathematical and Physical Sciences **200**

Physics of Fluids **14**

Journal of Computational Physics **227**

Journal of Computational Physics **222**

IFE/KR/F-2002/064

International Journal of Multiphase Flow **1,**

Chemical Engineering Science **49**

Journal of Fluid Mechanics **108**

Journal of Computational Physics **25**

Ph.D

Chemical Engineering Science **56**

Journal of Computational Physics **169**

Journal of Computational Physics **100**

Journal of Fluid Mechanics **494**

AIChE Journal **12**

Chemical Engineering Science **17**

Journal of Fluid Mechanics **25**

8th International Conference on CFD in Oil & Gas, Metallurgical and Process Industries
SINTEF/NTNU, Trondheim NORWAY
21-23 June 2011

CFD11-120

TECHNICAL APPLICATION OF A MULTIPHASE SOLVER IN THE COMPRESSIBLE FLOW OF A GASEOUS AND A LIQUID PHASE

Jozsef NAGY[*], **Christian JORDAN, Michael HARASEK**[1]

[1]Institute of Chemical Engineering, Vienna University of Technology, Getreidemarkt 9/166, A-1060 Vienna, AUSTRIA

[*] E-mail: jnagy@mail.zserv.tuwien.ac.at

ABSTRACT

In this work the simulation of the compressible multiphase flow in a fire extinguishing system is investigated. Challenges with the simulation of these conditions include both algorithmic issues like the correct depiction of the momentum transfer between the gaseous and the liquid phase and practical issues like the compatibility with other software tools (e.g. CAD, meshing tools) in order to simulate such flows with an arbitrary mesh. Also the amount of cells needed for adequate resolution of the flow requires parallelization of the simulation in order to maintain reasonable calculation times. The information of the movement of the liquid extinguishing material calculated by the simulation is characteristic for the subsequent progress in the pipes. Simulation results of an actual fire extinguishing process are compared to the experimental data.

Keywords: CFD, multiphase, compressible, pipe flow, experimental validation.

NOMENCLATURE

Greek Symbols
ρ Mass density, $[kg/m^3]$.
ρ_0 Constant value of mass density at reference conditions for liquid equation of state, $[kg/m^3]$.
α Volume fraction of phase, $[-]$.
ν Kinematic viscosity, $[m^2/s]$.
ψ Proportionality factor between pressure and density, $[s^2/m^2]$.

Latin Symbols
a Fit constant for equation of state of gas, $[-]$.
b Fit constant for equation of state of liquid, $[-]$.
u   Velocity vector, $[m/s]$.
p Absolute pressure, $[Pa]$.
T Temperature, $[K]$.
R Universal gas constant = 8.314472, $[J/(mol\,K)]$.
m Mass, $[kg]$.
m_{mol} Molar mass, $[kg/mol]$.
S   Shear stress tensor, $[m^2/s^2]$.
g   Acceleration of gravity, $[m/s^2]$.
F   Volumetric force density, $[kg/(m^2 s^2)]$.
E Specific energy per unit mass, $[J/kg]$.
Ma Mach number, $[-]$.
c_V Specific heat at constant volume, $[J/(kg\,K)]$.
t_0 Initial time, $[s]$.

Sub/superscripts
g Gas phase.
l Liquid phase.
t Turbulent value.
1st First order discretization scheme.
2nd Second order discretization scheme.
sm Smagorinsky turbulence model.
sp Spalart Allmaras turbulence model.
$bottle$ Value of the high pressure gas bottle.
σ Index for surface tension.

INTRODUCTION

Computational fluid dynamics is a useful tool for the description of flows of both academic and industrial needs for prediction, visualization and optimization purposes. The simulation of compressible multifluid flow is a challenging task especially in arbitrary geometries given by industrial machines or other equipments. There is a limited number of programs, in which the gaseous phase can be calculated as a compressible fluid, but the possibility to depict pressure or even shock waves in both the gaseous and the liquid phase is still a marginally explored area of the flow simulation field. Also the creation of the calculation domain (i.e the mesh in the investigated volume) with both structured and unstructured cells is a requirement for solving industrial questions. An adequate grid resolution has to be assured to guarantee the desired refinement. For that reason the possibility of parallelization of the calculation on multiple computer processor cores is an important feature of a software, that enables the reduction of calculation time, the increase of the cell number and with it the resolution of the flow.

These features are all available in the software OpenFOAM (Weller *et al.*, 1996; OpenCFD Limited, 2011). The presented results in this work were simulated using this open source CFD software. The code is written in the object oriented programming language C++. This guarantees the possibility to change, rewrite and create new code segments. The existing classes were taken and used with newly implemented code segments to create a new solver (Nagy and Harasek, 2010) for the simulation of highly compressible multiphase flows like e.g. the velocity induced breakup of water droplets or the simulation of newly developed environmental friendly drilling heads in the geothermal industry (Voglsam and Winter, 2010). In these cases pressure differences of a

factor of 10^2-10^3 are not uncommon. Velocities exceed the supersonic threshold reaching to Mach numbers of 3-4. The depiction of shock waves in both phases is important, as these phenomena determine most parts of the flow regime.

Another application of this solver is in the lower pressure region up to approximately 10 MPa, where the gaseous phase is definitely compressible (e.g. like in fire extinguishing systems, see figure 1) and cannot be considered to be an ideal gas. On the other hand liquid phases are mostly incompressible. The simulation of field quantities like pressure and temperature as well as of the interaction and movement of a liquid phase due to high pressure gas is an important task in order to guarantee the correctness of the results calculated by the solver handling both phases in a compressible way.
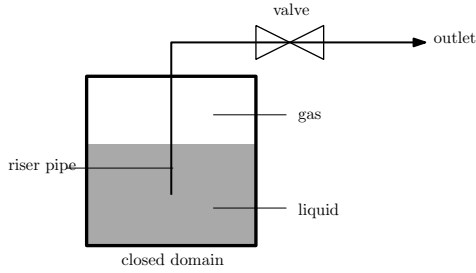
Figure 1: Schematic sketch of subject

A future goal of investigation is the inclusion of phase change into the code. At this stage it is important to test the solver for its capabilities concerning the solution of a compressible multiphase flow. The implementation of this additional phenomenon can occur after this step. This work is dealing with these tests of the solver regarding the multiphase flow without phase change. Both simulation and experimental data are presented and compared. An important question is, if the newly developed solver is able to simulate pressure and temperature with less errors than the measuring error of the sensors and at which point deviations, that are not within this range, appear due to neglecting phase change.

The actual investigated problem is the flow of a fire extinguishing procedure out of a bottle filled with the liquid agent (like carbon dioxide, various halogenated hydrocarbons etc., (Andersson and Blomqvist, 2011; Saito *et al.*, 1996)) into a system of conduit tubes through specially constructed nozzles into the room. Such extinguishing systems can be found for example in server rooms, storage rooms of museums or libraries.

Thus local phenomena can be analyzed via CFD, field values at a certain location of the flow. One can only put a finite number of sensors into the flow, but the simulation can reproduce field values for the whole domain of investigation. This solver can contribute to the development of analytic solutions for the flow through the system of pipes with several turns and the homogenous fluid distribution through several nozzles. Because of the fact, that the used CFD tool Open-FOAM can be parallelized, systems of multiple bottles (actual real life setup) and long systems of tubes can be investigated and compared to experimental data.

A simple numerical example is shown, where grid convergence and differences between two selected turbulence models as well as first and second order discretization are investigated. Also two experiments with such a fire extinguishing system are investigated comparing experimental and simulation data.

MODEL DESCRIPTION

Equation of state

Throughout the simulations the pressure values do not exceed 5 MPa and the temperature range is between 230 K and 310 K, thus these regions of pressure and temperature are considered to be relevant for the equations of state. The fire extinguishing fluid considered in the experiments is stored under pressure in liquefied state. After releasing the fluid into the piping system, part of the fluid evaporates. For the gaseous phase the density can be described by a polynomial of fourth order in pressure and it is indirectly proportional to the temperature (NIST Chemistry WebBook, 2011). In figure 2 one can see the comparison between values out of the literature and the polynomial.
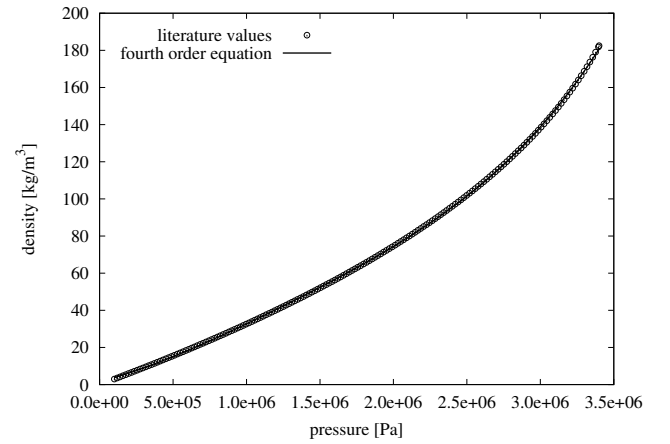
Figure 2: Function describing the equation of state of the gaseous phase at 285 K (NIST Chemistry WebBook, 2011)
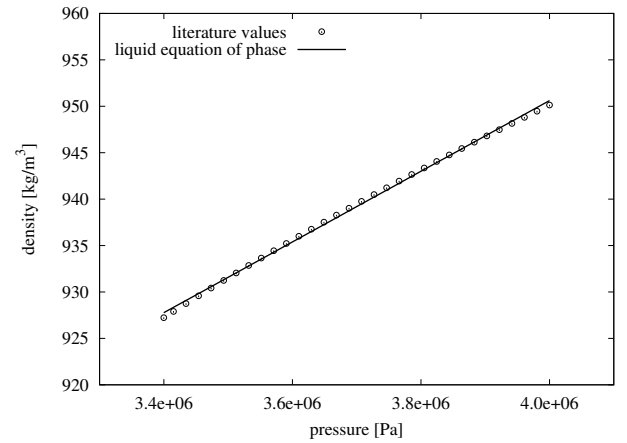
Figure 3: Function describing the equation of state of the liquid phase at 285 K (NIST Chemistry WebBook, 2011)

$$\rho_g = (a_1 p^4 + a_2 p^3 + a_3 p^2 + a_4 p + a_5)\, \psi_g \qquad (1)$$

Here,

$$\psi_g = 1/(\tilde{R}_g T) \qquad (2)$$

is indirectly proportional to the temperature, where $\tilde{R}_g = R/m_{mol,g}$. The liquid equation of state can be described by a linear function in pressure, as can be seen in figure 3.

$$\rho_l = \psi_l p + \rho_0 \qquad (3)$$

Here the coefficient ψ_l is also indirectly proportional to the temperature

$$\psi_l = b/(\tilde{R}_l T), \qquad (4)$$

where $\tilde{R}_l = R/m_{mol,l}$.

Governing equations

Simulation of flows driven by fluids at high pressures investigated in this work must consider the compressibility of the fluids (Mueller *et al.*, 2009; Chang and Liou, 2007; Nourgaliev *et al.*, 2006). For that reason the continuity, the momentum and the energy equations are solved consecutively without a velocity pressure coupling. The description of multiple phases is done by the standard ansatz of the *volume of fluid method* (OpenCFD Limited, 2011; Raessi *et al.*, 2010) using a scalar α for the phase volume fraction, that is transported with the velocity. A mean density is calculated with the phase fraction and used in the following calculations.

$$\rho = \alpha \rho_l + (1 - \alpha)\rho_g \qquad (5)$$

The continuity equation is solved with a non-constant density ρ.

$$\frac{\partial \rho}{\partial t} + \nabla \cdot (\rho \mathbf{u}) = 0 \qquad (6)$$

This modified density is used for the calculation of the momentum equation. The value of pressure p is calculated out of the density ρ with the equation of state (see equations 1 and 3)

$$\frac{\partial \rho \mathbf{u}}{\partial t} + \nabla \cdot (\rho \mathbf{u}\mathbf{u}) = -\nabla p +$$
$$\nabla \cdot [\rho (\nu + \nu_t)2\mathbf{S}] + \rho \mathbf{g} + \mathbf{F}_\sigma \qquad (7)$$

Here, ν and ν_t are the laminar and the turbulent viscosity, $\mathbf{S}$ is the shear rate tensor, $\mathbf{g}$ is the acceleration of gravity and the term $\mathbf{F}_\sigma$ is the volumetric force density resulting from surface tension (Dijkhuizen *et al.*, 2005; OpenCFD Limited, 2011). With the term of ν_t turbulence is introduced. Turbulence modeling is achieved in the form of the LES model (Bech, 2005; Weller *et al.*, 1996; OpenCFD Limited, 2011). For sub-grid scale turbulence two different models are investigated. On the one hand the Smagorinsky model is used with the code internal default values used for different constants in the model (OpenCFD Limited, 2011). On the other hand the Spalart Allmaras one equation model is investigated in order to consider a more sophisticated turbulence modeling. In the next step the equation of energy is solved

$$\frac{\partial E}{\partial t} + \nabla \cdot (E + p\mathbf{u}) = 0 \qquad (8)$$

One has to consider the fact, that $E = \rho c_v T + \frac{1}{2}\rho \mathbf{u}^2$ is the sum of the specific internal and specific kinetic energy per unit mass with c_v being the specific heat at constant volume and T being the absolute temperature of the fluid.

With the calculated value for T one can calculate the values for ψ_g and ψ_l in equations 2 and 4 and with it ρ_g and ρ_l in equations 1 and 3. With this a new time step is initiated and the procedure is continued.
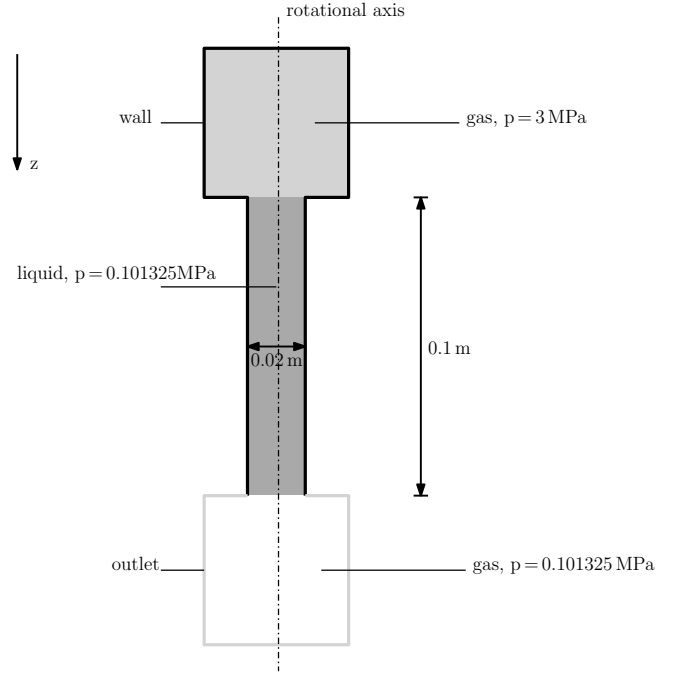
Figure 4: Schematic sketch of simplified test geometry

NUMERICAL INVESTIGATION

As the code has not been used before in the described area of relatively low pressure flow simulation a short numerical test with some parameter studies is presented. This test is supposed to show a rough estimation of parameter settings, the magnitude of different errors and which of these errors dominate. For this reason a simple idealized geometry was created (see figure 4). In this example a high pressure gas at 3 MPa is driving a liquid phase at ambient pressure out of a tube. Ideal equilibrium of temperature is assumed here and the value was set to 293 K. The gas is contained in a chamber, that is connected to the tube holding the liquid. At the bottom end of the tube the liquid phase is able to exit into the gas phase at ambient conditions. At time $t_0 = 0.0$ s an infinitesimal thin wall separating the liquid from the gas is removed, starting the expansion process of the gas, which drives the fluid.
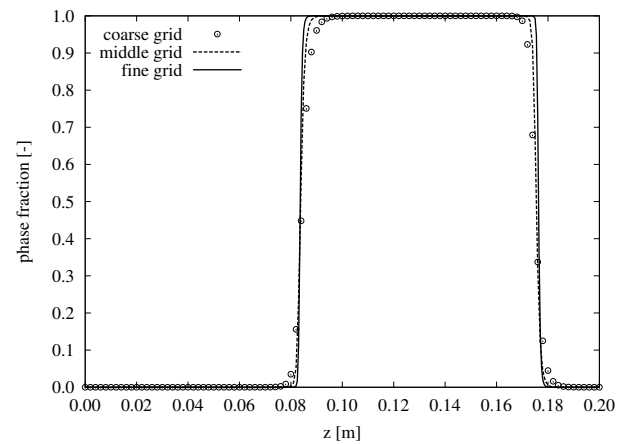
Figure 5: Test for grid convergence at t = 1.5 ms

The geometry is fully three-dimensional, with a rotational axis. The reason for not using this symmetry of the geometry was to assure the calculation of turbulence three-

dimensionally and to exclude possible artifacts of the symmetry boundary condition. Goal of this test was to depict the movement of the liquid phase due to the driving force from the high pressure gas. The diameter of the tube was set to 0.02 m to guarantee similarity between the dimensions in this example and the diameter of the tubes used in the following simulations.

Three different meshes are investigated with 26400, 215400 and 1796800 hexahedral cells (coarse, middle and fine grid). This gives a refinement factor of the cell edge length of about 2 with each mesh. Shown diagrams are plotted for values on the rotational axis of the geometry. As one can see in figure 5 the liquid phase has been moved by 0.033 m after 1.5 ms and partially has left the tube placed between 0.05 m and 0.15 m. However it has not reached the outlet, so at this point no effects from the outlet boundary condition have to be considered. The sharp steps in the phase fraction in figure 5 show the convergence of the results with the refinement of the grid.
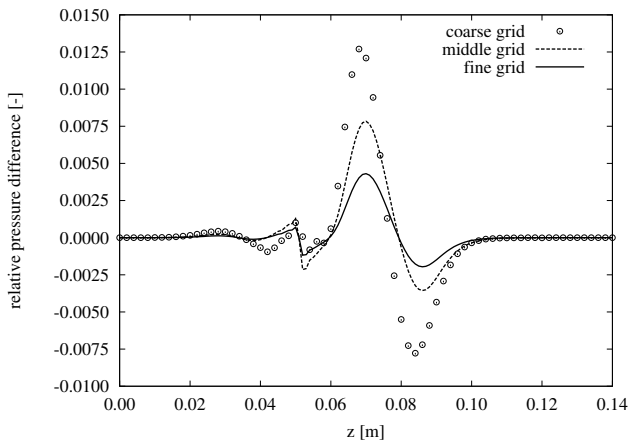
Figure 6: Relative difference of pressure between first and second order discretization at t = 0.1 ms
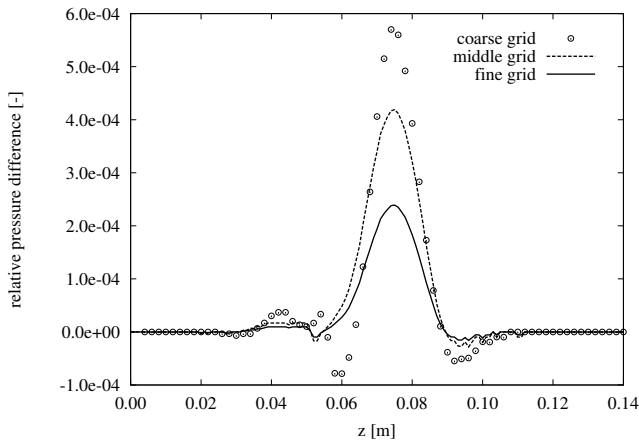
Figure 7: Relative difference of pressure between Smagorinsky and Spalart Allmaras turbulence model at t = 0.1 ms

For one the more stable *upwind* (OpenCFD Limited, 2011) first order discretization scheme is used for the calculation of the divergence terms in the transport equations and all other differential operations are discretized of first order accuracy, however it introduces numerical diffusion, that might lead to unacceptable errors. For avoiding the problems of artificial diffusion the second order central differences scheme *linear*

(OpenCFD Limited, 2011) is also investigated for the divergence terms and second order schemes are used for other operators as well.

In figure 6 one can see the relative difference in pressure between first and second order discretization after 0.1 ms. At this point of time the pressure wave is propagating through the liquid phase, but is not reflected or compromised in any way, so numerical effects can be visualized easily. Here the value $(p_{2nd} - p_{1st})/p_{2nd}$ is shown. The errors occurring with different discretization schemes are less than 1.5 % in this test case, which are within or of the magnitude of the measuring errors of pressure sensors at the considered pressure values.

An important issue is the error, which different turbulence models may introduce into the simulation. Both Smagorinsky and Spalart Allmaras calculate very similar results for the given case. In figure 7 the relative difference $(p_{sp} - p_{sm})/p_{sp}$ is presented. It can be seen, that differences are of at least one magnitude lower than that due to discretization. This shows, that under these circumstances the correct discretization reduces errors in a higher magnitude than a more sophisticated turbulence model.

The conclusions of the numerical example are, that the results are *converging with refinement of the grid* and that overall errors (in pressure) are less than 1.5 % and these can be mainly attributed to *discretization*.

'FIRE EXTINGUISHING' EXPERIMENT

The flow of a fire extinguishing fluid out of a high pressure bottle is mainly determined by the driving force of the pressure difference between the pressure inside the bottle and the pressure outside of it. If the fluid is present in both liquid and gaseous form in a geometry as shown in figure 8 the high pressure gas located in the upper part of the bottle pushes the liquid located in the lower part of the bottle through a riser pipe out of the bottle. Before the initial time, the fluid is contained by a valve within the bottle. After opening the valve, the liquid phase is able to escape the containment vessel. If the pressure of the liquid falls below the vapor pressure vaporization starts, which is the second main determining factor of the flow.

Experimental setup

A fire extinguishing system was investigated both experimentally and by simulation. For the first experiment the bottle was connected to a system of conduit tubes with a diameter of 0.0216 m and an overall length of 16.7 m. One bent and eight straight tubes with lengths between approximately 0.3 m and 4.5 m were connected by seven elbows. One single nozzle was put to the very end of the system of conduit tubes. The fluid leaves the bottle, flows through the pipes and exits through the nozzle. Of main interest in this investigation was the movement of the gaseous and the liquid phase out of the bottle itself. For that reason the gas pressure, that is equal to the liquid pressure (negligible hydrostatic pressure), and temperature in the upper part of the bottle outside the riser pipe were measured (see figure 8). The cross section of the pipe is not entirely circular, so the sensors can fit through the neck of the bottle. Also a temperature sensor was placed in the bottom part of the geometry for the measurement of the temperature of the liquid phase. The measurement of these values occurred with a temporal resolution of 0.1 s.

In the second experiment some changes to the this setup were made. Three nozzles were added to the conduit tubes throughout the whole length of the system in order to achieve
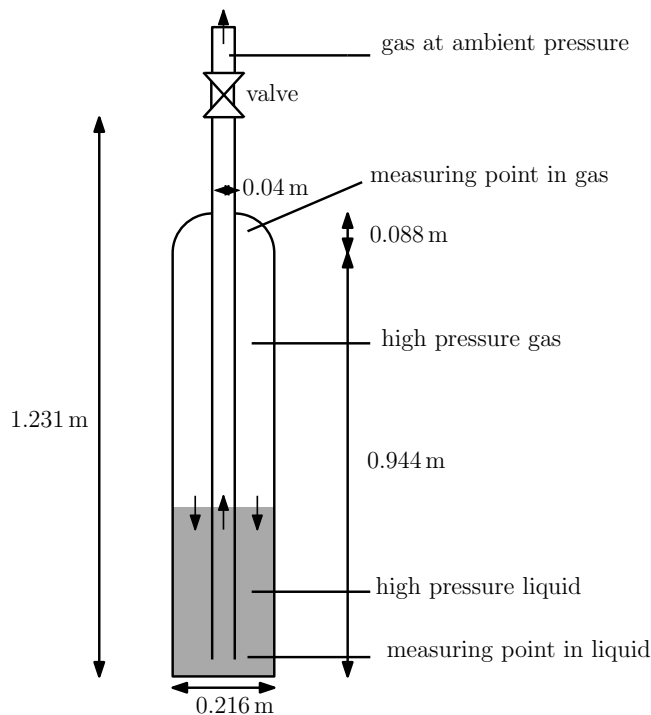
Figure 8: Schematic sketch of the gas cylinder geometry for experiment and CFD (initial conditions)
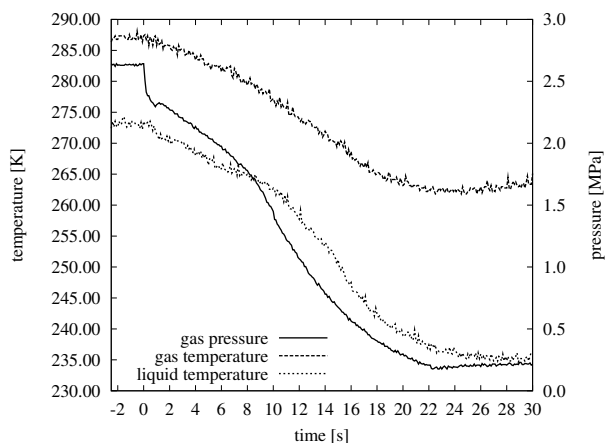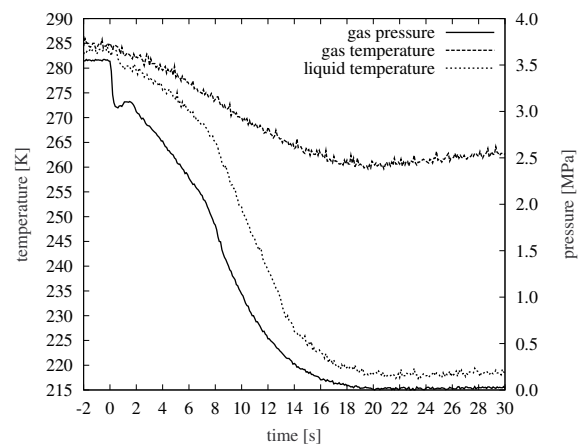

Figure 9: Experimental data of the gas pressure and temperature as well as the liquid temperature in the first run (detailed values of the first two seconds can be seen in figures 11 - 13)

the process of a real life fire extinguishing system in a small room. In the first run 15 kg and in the second run 25.2 kg of extinguishing fluid was filled into the bottle prior to the experiments.

Figure 9 shows the gas temperature and pressure as well as the liquid temperature in the first experiment. After pressure and temperature values stabilized at a constant value, the measurement was started (point of time $t = 0$ s in figure 9) by opening the valve. Three main regions can be seen. The first 0.9 s of the pressure curve shows the free expansion of the gaseous phase, whereas between 0.9 and 1.2 s the pressure rises quickly and after this point of time decreases throughout the whole extinguishing processes. Also the liquid temperature is more or less constant up until this point of time at 0.9-1.0 s, after this point the temperature values in both gaseous and liquid phase decrease. At this point the vapor pressure is reached and vaporization starts.

Figure 10: Experimental data of the gas pressure and temperature as well as the liquid temperature in the second run (detailed values of the first two seconds can be seen in figures 14 - 16)

In figure 10 the experimental values of the second run can be seen. A similar characteristic of the curves can be observed. The differences are due to different initial values of pressure, and temperature. In this case free expansion can be seen in the plot of pressure up until 0.6 s (higher discharge rate due to increased number of nozzles), thereafter an increase of pressure occurs due to phase change between 0.6 s and 1.5 s. Also the liquid temperature starts to drop at this point of time because of evaporation.

The simulation of the flow up until and after this point of vaporization is a significant indicator for the correctness of the simulation model, as results can be compared to both experimental data with and without phase change. For that reason the first two seconds of the measurement are important for consideration.

Simulation settings

The whole three dimensional geometry with bottle and conduit tubes is implemented in the simulation geometry, yet of main interest is the movement and interaction of gaseous and liquid phase inside the bottle.

The simulation of the first run is carried out with 1146827 cells and the simulation of the second experiment with 1203041 cells. The difference is due to the differing meshes at the additional nozzles. As explained in section *'Numerical investigation'* errors of highest magnitude are introduced into the simulation due to discretization. For that reason the calculations are carried out with second order discretization schemes, also investigated in section *'Numerical investigation'*. Thermodynamic data is taken from (NIST Chemistry WebBook, 2011). In the 'single nozzle' simulation two turbulence models Smagorinsky and Spalart Allmaras are used, whereas in the run with four nozzles Spalart Allmaras is used. For the stability of the solution a maximal Courant number of 0.3 is used. The simulations are parallelized 32 fold and the calculation times for the investigated 2 s are for both experiments about 8 days (on the phoenix2-cluster of the Central Informatics Department of the Vienna University of Technology (Vienna University of Technology, 2011)).

A simplification is made in the region of the conduit tubes by setting the initial fluid instead of air at ambient pressure to extinguishing gas at ambient pressure. This does not introduce considerable errors, as the density and other thermodynamic

properties are similar. For the determination of the height of the liquid phase the volume of the liquid is calculated out of the measured initial overall mass m with a certain density of the liquid and the gaseous phases at the measured initial temperature values. The mass m is given by

$$m = \rho_l V_l + \rho_g \left(V_{bottle} - V_l \right) \tag{9}$$

By rearranging the equation to V_l one is able to calculate the height of the liquid. Temperature of gas and liquid in the simulation is also patched with the mean experimental values of temperature prior to the start of the experiment (first run: $T_g = 286.4$ K, $T_l = 273.3$ K, second run: $T_g = 284.65$ K, $T_l = 283.65$ K). Temperature on the outside of the bottle was also measured during the process, however during the investigated first two seconds temperature values on the wall of the bottle did not change considerably. Thus fixed values can be used for the temperature on the walls of the implemented geometry in the simulations. The initial pressure is set to 2.642 MPa in the first case and to 3.54 MPa in the second case up to the height of the opening valve (see figure 19). Outlet faces are used at the location of the nozzle(s).

Experimental and simulation results

In figure 11 the values of pressure during the first two seconds of the first experiment are plotted. One can see the two different shapes of characteristics, on the one hand the free expansion, on the other hand the sudden additional increase in pressure due to phase change at 0.9 s. Simulation results with both turbulence models follow the curve of measurement values up to this point and do not show the increase in pressure after it. Measuring error of the pressure sensor is given by the manufacturer by approximately ± 0.05 MPa, thus simulation results lie within these values. After 0.9 s this is not the case and the solver results are considerably from this point of time on due to phase change. However pressure values show, that apart from phase change the movement and interaction of a compressible high pressure gas and liquid are depicted correctly within the measuring error intervals.
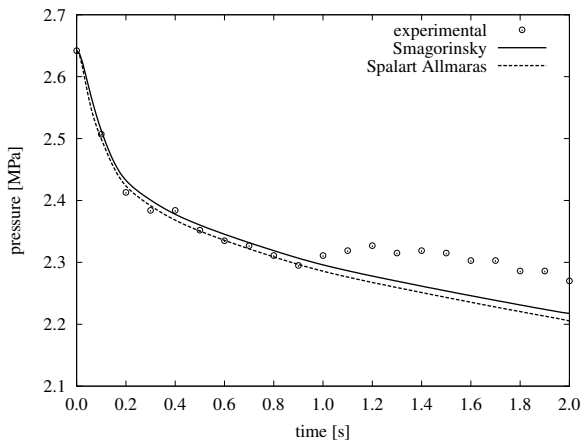
Figure 11: Experimental and simulation results of pressure during the first two seconds (first run)

In figure 12 one can see the temperature of the gaseous phase. Both turbulence models show similar characteristics, however lie about 1 K underneath the mean experimental values. The accuracy of thermocouples used is approximately ± 1 K. Figure 13 shows the temperature in the liquid phase. Simulation results suggest a more or less constant temperature in this region of the fluid. Experimental values oscillate around
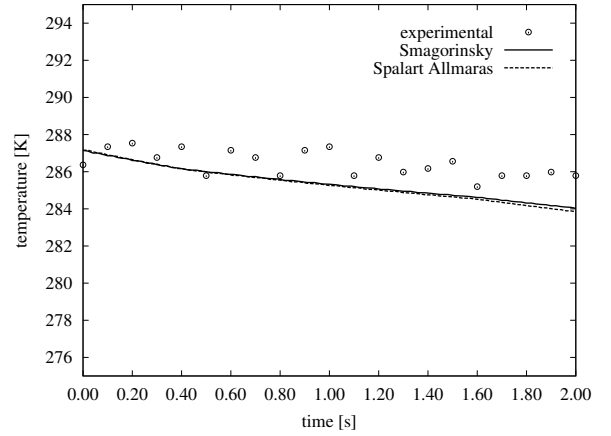
Figure 12: Experimental and simulation results of gas temperature during the first two seconds (first run)
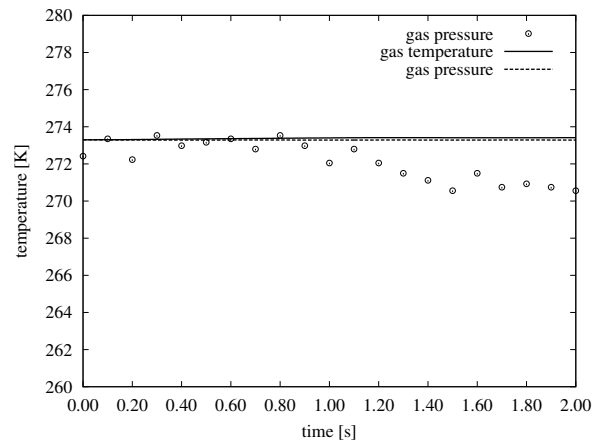
Figure 13: Experimental and simulation results of liquid temperature during the first two seconds (first run)
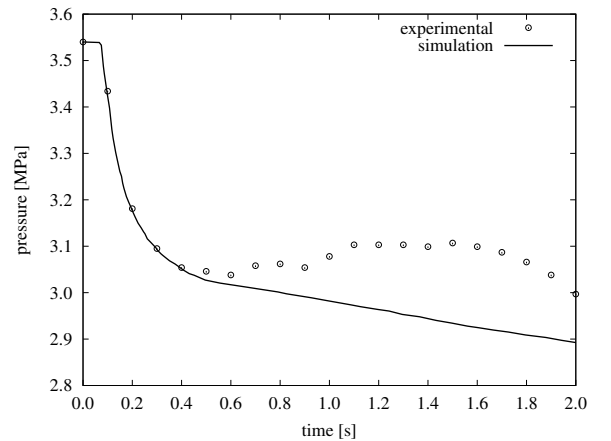
Figure 14: Experimental and simulation results of pressure during the first two seconds (second run)

273 K up until the point of time of about 0.9 s and start to decrease rapidly. From this point on vaporization heat is deducted from the liquid and the temperature drops throughout the whole measurement.

In the second experimental run the initial values were different. Firstly the pressure was higher because of the higher temperature of the fluid. But also a more even temperature distribution inside the bottle could be achieved, as the tem-
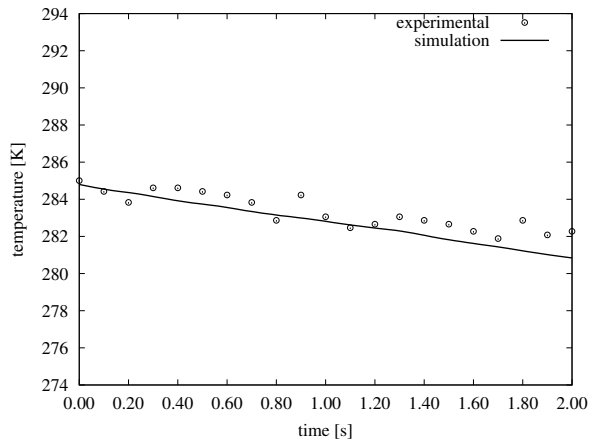
Figure 15: Experimental and simulation results of gas temperature during the first two seconds (second run)
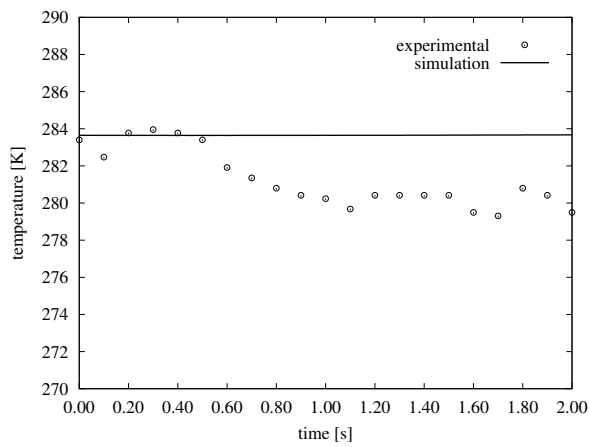
Figure 16: Experimental and simulation results of liquid temperature during the first two seconds (second run)

perature of the liquid was 1 K less than the temperature of the gas. One has to compare this to the difference of the over 13 K difference in the first run. This results in the fact, that the value of vapor pressure is increased and vaporization starts already between 0.5-0.6 s. The characteristics of the pressure during the first two seconds follow the experimental values of pressure up until the point of phase change. In this case the expected deviations due to the missing implementation of phase change also appear, which are not inside the measuring errors of the sensors. The actual point of time of opening the valve was not at t = 0.0 s, but 0.06-0.07 s later, but the temporal resolution cannot depict this difference, that is the reason, why the start of the simulation results had to be shifted in figures 14, 15 and 16.

Figure 15 shows the temperature of the gaseous phase. Also in this case temperature values lie about 1 K below the experimental values.

In figure 16 one can see the temperature in the liquid phase. The used turbulence model calculates constant values for temperature of liquid, where experimental values also in this case drop at the point of phase change.

At the initial stage, after the valve is opened a pressure wave at high velocity travels through the conduit pipes. The formation of this wave can be seen in figures 19-22. As the gaseous fluid is used for the gas initially located in the conduit tubes, the pressure wave can only be depicted qualitatively, but not quantitatively. Also a low pressure and a high pressure re-

gion can be seen in the 90° turn at the end of the riser pipe. As the pressure wave is traveling at the speed of sound high velocities can be found at the initial stage of the procedure.
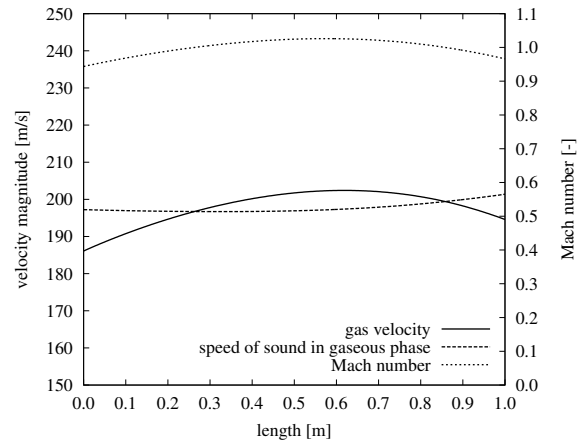
Figure 17: Velocity magnitude, speed of sound and Mach number after t = 0.05 s in the conduit pipe between the second and third elbow

Velocity magnitudes of the entire flow reach over a considerable region. In figure 17 one can see the velocity magnitude, speed of sound and the Mach number at an early stage of the process at t = 0.05 s in a straight section of the conduit pipe connected to the bottle between the first and the second elbow. At this initial point of time the high pressure gas initially contained above the liquid in the riser pipe escapes the bottle and at this stage the pressure difference between high pressure gas and ambient gas drives the flow of the process in the conduit tubes. Here one can see, that in the simulation the flow is in the transonic range and even a Mach number Ma = 1 is exceeded at certain points. With time these values of velocity magnitude decrease to Ma < 0.2-0.3.
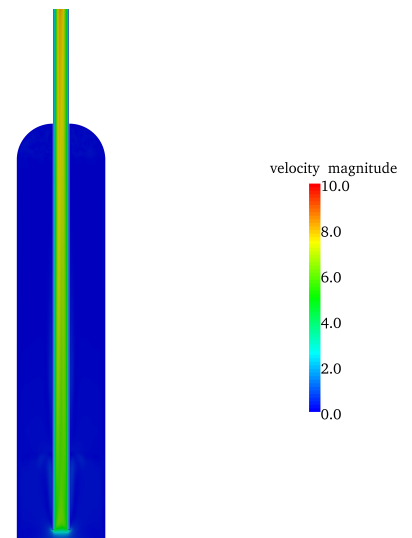
Figure 18: Velocity magnitude after 0.8 s inside the bottle along the middle plane of the bottle

On the other hand inside the bottle velocity magnitudes do not reach such values. In figure 18 the velocity magnitude inside the bottle at the later point of time t = 0.8 s can be seen. The flow inside the bottle is slower than 10 m/s at this later stage of the experiment. One can see that the velocity increases near the symmetry axis of the riser pipe. The reasons

are twofold. On the one hand density of the liquid decreases as a result of the decrease of pressure along the riser pipe and the increase of temperature due to increased turbulent energy dissipation in the upper part of the riser tube. On the other hand the velocity magnitude profile changes as velocity is decreased along the walls by turbulence as well as the no-slip boundary condition and thus is increased close to the symmetry axis of the riser pipe. Thus the velocity profile changes from a profile with a more even distribution in the bottom part of the pipe to a profile with increased velocity magnitude in the middle and upper part of the tube. However the integral mass flow over two cross sections is maintained throughout the riser pipe.

The conclusion of both the 'single nozzle' and the 'four nozzle' investigation is the fact, that both *pressure and temperature* values inside the bottle lie within the measuring error intervals and *follow the characteristics of the experiment* up to the point, where vaporization starts and phase change occurs. These differences will be simulated by the future implementation of phase change.

CONCLUSION

The aim of the investigation was the analysis of the results of the the simulation of a multiphase compressible flow in a technical application from the industry. For the correct simulation results a solver is needed, that is treating both phases in a compressible way in order to depict pressure waves in the flow. As sufficient resolution of the geometry by the calculation mesh has to be assured, parallelization of the code had to be used to reach reasonable simulation times. A solver, that was originally implemented for supersonic multifluid flows in OpenFOAM, was used for these lower pressure ranges. A small numerical test case was conducted in order to assess the errors made by the solver in the given pressure and temperature range. With these experiences gained the simulation of two fire extinguishing processes were conducted and differences between experimental data and simulation were analyzed.

Conclusions:

1. Errors of highest magnitude are attributed to discretization. For that reason second order discretization was assured throughout the simulations.

2. Results converge with the refinement of the grid.

3. The comparison between experimental data of the fire extinguishing processes and simulation results show, that errors made by the solver are within the measuring error of the sensors up to the point of phase change.

As results are within measuring errors up until the point of phase change, the next step will be the implementation of this phenomenon into the code. Also the breakup of liquid at the exit of an injector nozzle will be investigated.

REFERENCES

ANDERSSON, B. and BLOMQVIST, P. (2011). "Experimental study of thermal breakdown products from halogenated extinguishing agents". *Fire Safety Journal*, **46(3)**, 104–115.

BECH, K. (2005). "Les of a rectangular bubble column". *Fourth International Conference on CFD in the Oil and Gas, Metallurgical & Process Industries*. SINTEF/NTNU Trondheim, Norway.

CHANG, C. and LIOU, M. (2007). "A robust and accurate approach to computing compressible multiphase flow: Stratified flow model and ausm+ -up scheme". *Journal of Computational Physics*, **225**, 840–873.

DIJKHUIZEN, W. *et al.* (2005). "Numerical investigation of closures for interface forces in dispersed flows using a 3d front tracking model". *Fourth International Conference on CFD in the Oil and Gas, Metallurgical & Process Industries*. SINTEF/NTNU Trondheim, Norway.

NIST Chemistry WebBook (2011). U.S. Secretary of Commerce, URL http://webbook.nist.gov/.

OpenCFD Limited (2011). "OpenFOAM source code". URL http://www.openfoam.com/.

Vienna University of Technology (2011). "Vienna university of technology home page". URL http://www.zid.tuwien.ac.at/zserv/applikationsserver/phoenix_linux_cluster/about/.

MUELLER, S. *et al.* (2009). "Comparison and validation of compressible flow simulations of laser-induced cavitation bubbles". *Computers & Fluids*, **38**, 1850–1862.

NAGY, J. and HARASEK, M. (2010). "Simulation procedure of supersonic multiphase flows with arbitrary grid". In review process.

NOURGALIEV *et al.* (2006). "Adaptive characteristics-based matching for compressible multifluid dynamics". *Journal of Computational Physics*, **213**, 500–529.

RAESSI, M. *et al.* (2010). "A volume-of-fluid interfacial flow solver with advected normals". *Computers & Fluids*, **39**, 1401–1410.

SAITO, N. *et al.* (1996). "Flame-extinguishing concentrations and peak concentrations of nitrogen, argon, carbon dioxide and their mixtures for hydrocarbon fuels". *Fire Safety Journal*, **27(3)**, 185–200.

VOGLSAM, S. and WINTER, F. (2010). "Investigation on nitromethane combustion mechanisms for simulation of micro-detonations". *Junior Scientist Conference 2010, Vienna*, 73–74. ISBN: 978-3-200-01797-9.

WELLER, H. *et al.* (1996). "A tensorial approach to continuum mechanics using object-oriented techniques". *Computers in Physics*, **12(6)**, 620–631.
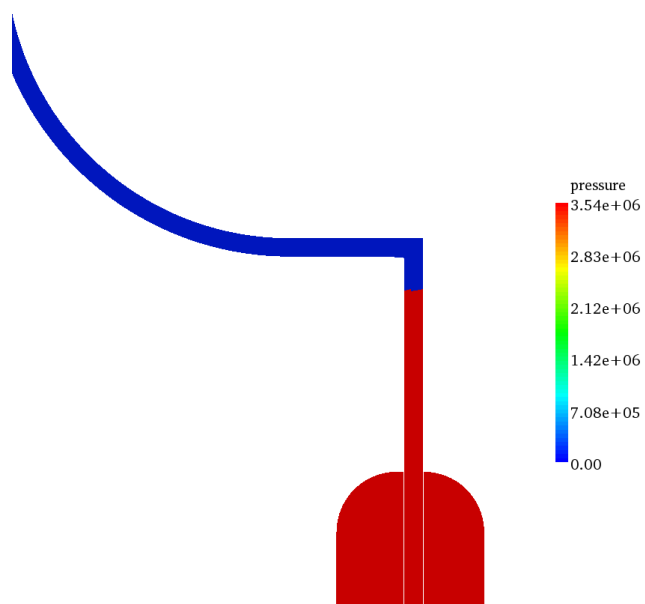
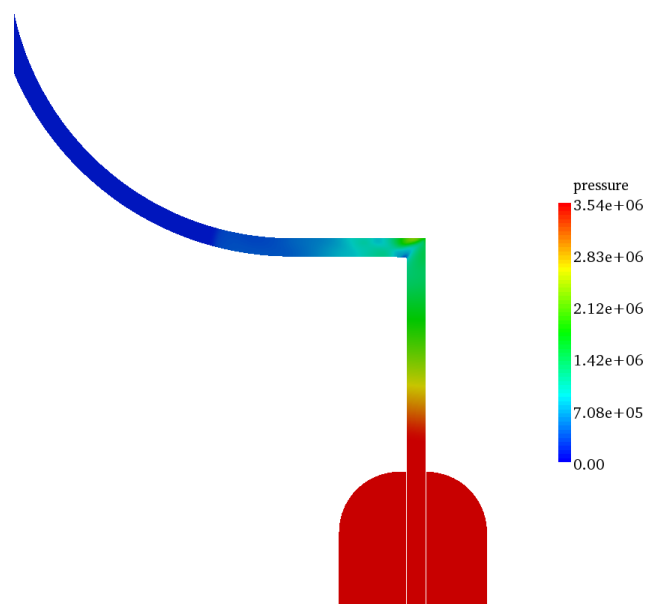Figure 19: Pressure wave at t = 0 s (valve opening)
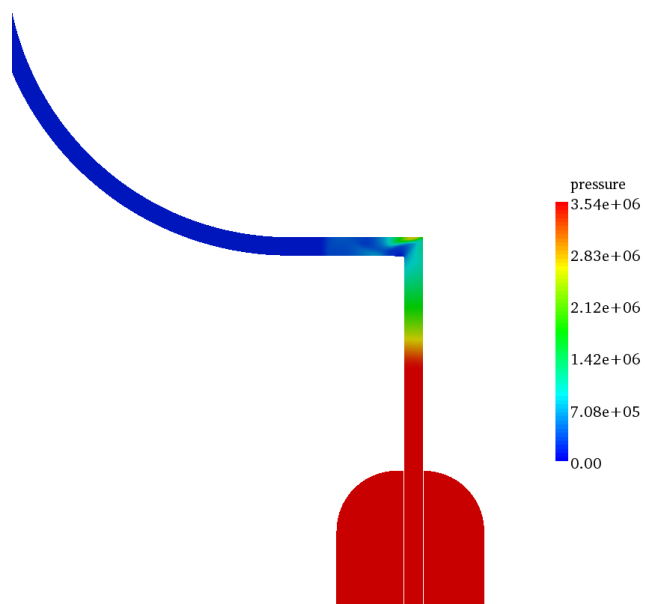

Figure 21: Pressure wave at t = 0.002 s
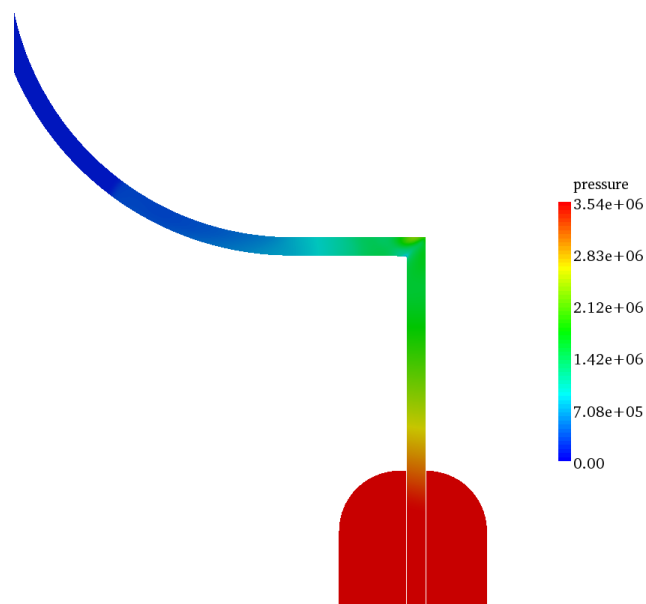

Figure 20: Pressure wave at t = 0.001 s

Figure 22: Pressure wave at t = 0.003 s

IN-LINE OIL-WATER SEPARATION IN SWIRLING FLOW

J.J. SLOT[1]*, **L.J.A.M. VAN CAMPEN**[2]†, **H.W.M. HOEIJMAKERS**[1], **R.F. MUDDE**[2]

[1]University of Twente, Faculty of Engineering Technology, Enschede, The Netherlands

[2]Department of Applied Sciences, Delft University of Technology, The Netherlands

* E-mail: j.j.slot@ctw.utwente.nl
† E-mail: l.j.a.m.vancampen@tudelft.nl

ABSTRACT

An in-line oil-water separator has been designed and is investigated for single- and two-phase flow. Numerical single-phase flow results show an annular reversed flow region. This flow pattern agrees qualitatively with results from measurements. In the two-phase flow simulations two different drag laws have been used to model the interaction between the phases. The velocity field of the single- and the two-phase flow is shown to be very similar. However, the oil volume fraction distribution is strongly affected by the choice of the drag law. Furthermore, compared to experimental results for both drag laws the separation efficiency is greatly overestimated.

Keywords: Oil-water separation, CFD, two-fluid model .

NOMENCLATURE

NOMENCLATURE

Greek Symbols

α Volume fraction, $[-]$
γ Volume porosity, $[-]$
θ Azimuthal coordinate, $[rad]$
μ Dynamic viscosity, $[kg/ms]$
ν Kinematic viscosity, $[m^2/s]$
ρ Mass density, $[kg/m^3]$
σ Viscous stress tensor, $[kg/ms^2]$

Latin Symbols

C_D Drag coefficient, $[-]$
D Droplet diameter, $[m]$
g Gravitational acceleration, $[m/s^2]$
$\mathbf{K}_{loss}$ Inertial loss coefficients, $[kg/m^2s^2]$
M Interfacial momentum transfer, $[kg/m^2s^2]$
p Static pressure, $[kg/ms^2]$
r Radial coordinate, $[m]$
Re_D Reynold number, $[-]$
S_M Momentum loss term, $[kg/m^2s^2]$
$\mathbf{U}$ Instantaneous velocity, $[m/s]$
$\mathbf{u}$ Mean velocity, $[m/s]$
$\mathbf{u}'$ Turbulent velocity fluctuations, $[m/s]$
z Axial coordinate, $[m]$

Sub/superscripts

θ Azimuthal
b Bulk
k Phase k
m Mixture
o Oil
w Water
z Axial

INTRODUCTION

The oil market faces an ever increasing worldwide demand for oil, while the number of easily accessible oil-fields is decreasing. Therefore, new technologies are required for fields with hydrocarbons that are difficult to produce, such as offshore or sub-sea. Furthermore, as an oil field matures, the crude oil is produced with increasing quantities of water. Therefore, the efficient separation of oil from water becomes an increasingly important processing step. This separation of the phases is required in order to reduce the demands on the transport facilities and to facilitate re-injecting the separated water into the reservoir to maintain the well pressure.

Traditionally, separation is mostly achieved in very large vessels using the action of gravity. However, the large weight and space requirements of these vessels lead to high investment costs for the necessary on-site processing facilities. The present research investigates a much smaller and cheaper alternative for the oil-water separation, namely utilizing in-line equipment that uses swirling flow to separate the phases. Moreover, the smaller equipment size leads to a reduced hydrocarbon inventory. This in turn leads to reduced safety risks. Also, lower costs for maintenance and inspection can be achieved using piping rather than vessels.

Swirling flow has been used successfully for the separation of solids from either gas (Hoekstra, 2000) or liquid (Bradley, 1965). Liquid-liquid separation presents more challenges due to the smaller density difference, high volume fractions of the dispersed phase, poor coalescence and the danger of emulsion formation. Dirkzwager (1996) designed an in-line liquid-liquid separator. Subsequently, single-phase experiments were carried out for this separator. Murphy *et al.* (2007) compared results from these measurements with numerical results from two different commercial CFD packages. It was found that the main features of the flow were qualitatively well represented in the numerical simulations. However, large quantitative differences were observed between the numerical results mutually and between numerical results and experimental data. An oil extraction outlet was added

to the in-line separator by Delfos *et al.* (2004), who further investigated this design numerically.

Much work has been done on single-phase simulations of strongly swirling flow in separators (Ko, 2005; Kharoua *et al.*, 2010). However, the two-phase flow calculations have received less attention. For lower concentrations of the dispersed phase, the behavior of the dispersed phase can be calculated by Lagrangian particle-tracking, see for instance Derken (2003). However, in separators high concentrations of the dispersed phase are often encountered. For these applications, mixture models (Manninen and Taivassalo, 1996) or two-fluid models (Drew, 1983; Prosperetti and Tryggvason, 2007) can be used to predict the flow. Contrary to mixture models, in the two-fluid model for each phase separate continuity and momentum equations are solved. This allows the velocity field of both phases to be different, so that more physics can be incorporated in the simulation. This two-fluid model has more recently been applied to hydrocyclones (Noroozi and Hashemabadi, 2009; Paladino *et al.*, 2007).

The current project aims at the design and investigation, both numerically and experimentally, of an oil-water bulk separator using swirling flow. The intended use is for separation of oil-in-water mixtures with relatively high oil volume fractions. These are mixtures that cannot be considered dilute. For this purpose an in-line separator has been designed and an experimental facility has been built. This paper will discuss the flow patterns observed in the newly designed separator for both single-phase water and two-phase oil-water flows. The single-phase water solution from the computation will be compared to LDA measurements to assess to accuracy of the numerical results. For the two-phase flow two widely used drag law formulations will be used and results will be compared to the experimentally determined separation efficiency.

IN-LINE SWIRL SEPARATOR DESIGN

The present prototype for in-line oil-water separation features a stationary internal swirl element (**ISE**) which is placed within a pipe with a 100 mm internal diameter. This ISE consists of a central body equipped with 9 vanes which are attached to the wall of the pipe and to the surface of the central body, as is shown in figure 1. The incoming flow is accelerated towards the narrow vaned section. The vanes deflect the fluid, generating the swirling flow. The higher axial velocity, and the relatively large radius at which the vanes are placed, both contribute to increases in angular momentum. Downstream of the ISE the strongly swirling flow, with centrifugal forces up to 300 g, will force the lighter oil phase to the center of the pipe where it is collected by a pick-up tube further downstream. Since both water and oil phase flow downstream this is a co-current separator, contrary to the counter-
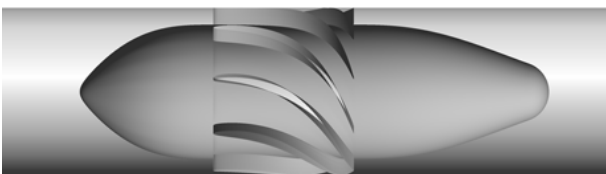
Figure 1: Cut-away of 100 mm diameter pipe showing internal swirl element (ISE). Non-swirling fluid enters from the left.
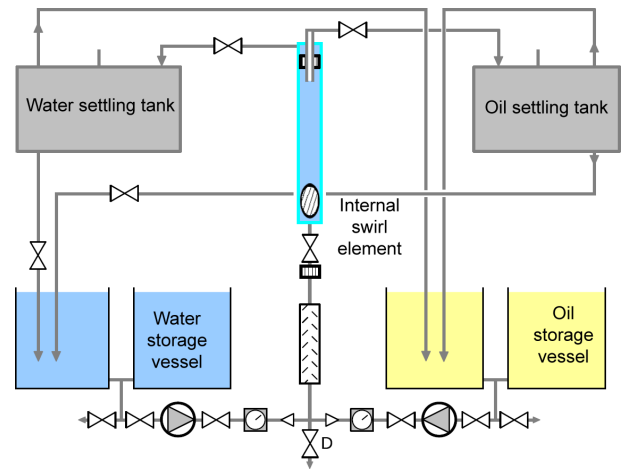
Figure 2: Flow scheme of experimental setup.

current design of Delfos *et al.* (2004). The pick-up tube is placed 1.7 m downstream of the ISE. It is a straight pipe with an outer diameter of 50mm and wall thickness of 1 mm which is concentrically placed within the 100mm diameter pipe.

Experimental setup

At Delft University of Technology an experimental setup of the separator has been built to perform both single and two-phase flow measurements on the separator. The main components can be seen in figure 2. Large storage vessels for water and oil, respectively, feed centrifugal pumps which can produce a mixture of widely varying oil volume fraction. The oil-water mixture passes a static mixer and a flow straightener before it enters the ISE. Downstream of the ISE the stainless steel pick-up tube is placed to collect the bulk of the oil. Subsequently this stream flows into the oil settling tank. In the annular pipe leading to the outlet of the heavier phase, a flow straightener is placed 215 mm downstream of the pick-up tube entrance. This flow straightener eliminates the swirl, which would otherwise lead to air being sucked into the separator from the water settling tank. In the the settling tanks complete separation is achieved and the oil and water flow to their respective storage vessels.

Downstream of the ISE, a Poly Methyl MethAcrylate (PMMA) measurement pipe segment is placed to provide optical access for the Laser Doppler Anemometry (LDA) measurements. The PMMA tube is surrounded by a square box filled with water to reduce refraction of laser light. An Argon laser is used, from which the 488.0 nm beams are used for the axial velocity component and the 514.5 nm beams for the azimuthal velocity component. The burst correlation is conducted in a Dantec F60 BSA signal processor. The average velocity is calculated using a software package developed by Belt (2007), correcting the LDA time-averaged results for white noise, multiple validation and a bias towards high velocities.

The flow through each pump is measured and can be adjusted, additionally a Coriolis flow meter is placed in the pipe leading to the water settling tank. The combination of this data completely determines the flow split and volume fractions of the two outlet flows. Separation efficiencies can be derived from that data.

COMPUTATIONAL FLUID DYNAMICS

The flow field in the new separator design is investigated by solving the Reynolds averaged Navier-Stokes equations for transient incompressible flow.

Single-phase flow

For single-phase flow the governing equations are given by:

$$\nabla.\mathbf{u} = 0 \tag{1}$$

$$\frac{\partial \mathbf{u}}{\partial t} + (\mathbf{u}.\nabla)\mathbf{u} = -\frac{\nabla p}{\rho} + \nu \nabla^2 \mathbf{u} + \mathbf{g} - \nabla.\langle \mathbf{u}'\mathbf{u}' \rangle \tag{2}$$

Here ρ is the density, p is the static pressure, $\mathbf{u}$ is the mean velocity and $\mathbf{u}'$ is the turbulent velocity fluctuation. The latter are related to the instantaneous velocity $\mathbf{U}$ as

$$\mathbf{U} = \mathbf{u} + \mathbf{u}' \tag{3}$$

It is assumed that the timescale of the turbulent velocity fluctuation $\mathbf{u}'$ is much smaller than the timescale of the mean velocity $\mathbf{u}$.

The use of eddy-viscosity models to express the Reynolds stresses in term of the mean quantities is not well suited for swirling flow, see Pope (2000). The skewness of the flow violates the eddy-viscosity assumption that the shear stresses and the velocity gradients have the same direction, as pointed out by Kitoh (1991). Various sources of turbulence, i.e. strain rates, are not represented by the eddy viscosity models. Also, the assumption of isotropic turbulence overstates the shear stresses and the radial diffusion of momentum, see Murphy *et al.* (2007).

Therefore a Reynolds stress model (RSM) is used, in which the Reynolds stresses $\langle \mathbf{u}'\mathbf{u}' \rangle$ are provided by transport equations. One of the advantages of the model is that the production terms of the Reynolds stresses can be represented exactly. Therefore, the strain rates associated with streamline curvature and flow skewness, both important in swirling flow, are incorporated in the production of turbulence, see Hanjalic (1999). Moreover, anisotropic behavior of the turbulent flow can be accounted for by the separate transport equations for the Reynolds stresses.

In the present research the SSG Reynolds stress model of Speziale *et al.* (1991) is used. Contrary to other models, this model uses a quadratic pressure-strain relation. This RSM is recommended for swirling flows, e.g. by Cullivan *et al.* (2003) and Chen and Lin (1999). To close the SSG model, a seventh transport equation is included, namely for the dissipation rate.

The Reynolds stress transport equation for an incompressible, isothermal flow is given by

$$\frac{\partial \langle u_i' u_j' \rangle}{\partial t} + \langle u_k \rangle \frac{\partial \langle u_i' u_j' \rangle}{\partial x_k} + \frac{\partial T_{ijk}}{\partial x_k} = P_{ij} + R_{ij} - \varepsilon_{ij} \tag{4}$$

Index notation is used here for convenience. In equation (4) the Reynolds stress flux tensor T_{ijk} is modeled by the gradient-diffusion model of Daly and Harlow (1971):

$$T_{ijk} = \left(\nu \delta_{kl} + C_s \frac{k}{\varepsilon} \langle u_k' u_l' \rangle \right) \frac{\partial \langle u_i' u_j' \rangle}{\partial x_l} \tag{5}$$

The constant $C_s = 0.22$ and k is the turbulent kinetic energy. P_{ij} is the production tensor which gives the

C_{s1}	C_{s2}	C_{r1}	C_{r2}	C_{r3}	C_{r4}	C_{r5}
1.7	-1.05	0.9	0.8	0.65	0.625	0.2

Table 1: Constants of rapid pressure tensor R_{ij} in SSG turbulence model.

Reynolds stresses generated by the mean flow velocity gradients. It transfers kinetic energy from the mean velocity field to the fluctuation velocity field. The production tensor is given by

$$P_{ij} = -\langle u_i' u_k' \rangle \frac{\partial \langle u_j \rangle}{\partial x_k} - \langle u_j' u_k' \rangle \frac{\partial \langle u_i \rangle}{\partial x_k} \tag{6}$$

The pressure-strain tensor R_{ij} models the redistribution of the energy among the Reynolds stresses and is often split into two contributions; the slow pressure-strain or return-to-isotropy tensor $R_{ij}^{(s)}$ and the rapid pressure-strain tensor $R_{ij}^{(r)}$. In the SSG the $R_{ij}^{(s)}$ tensor is given by

$$R_{ij}^{(s)} = -\varepsilon \left[C_{s1} a_{ij} + C_{s2} \left(a_{ik} a_{kj} - \frac{1}{3} a_{kl} a_{kl} \delta_{ij} \right) \right] \tag{7}$$

Here the constants $C_{s1} = 1.7$ and $C_{s2} = $ -1.05. The normalized anisotropy tensor a_{ij} is defined as

$$a_{ij} = \frac{\langle u_i' u_j' \rangle}{k} - \frac{2}{3} \delta_{ij} \tag{8}$$

Evidently, $R_{ij}^{(s)}$ is quadratic in the anisotropy tensor. The rapid pressure-strain tensor is given by

$$\begin{aligned} R_{ij}^{(r)} = & -C_{r1} P a_{ij} + \\ & C_{r2} k S_{ij} - \\ & C_{r3} k S_{ij} \sqrt{a_{kl} a_{kl}} + \\ & C_{r4} k \left(a_{ik} S_{jk} + a_{jk} S_{ik} - 2/3\, a_{kl} S_{kl} \delta_{ij} \right) + \\ & C_{r5} k \left(a_{ik} \Omega_{jk} + a_{jk} \Omega_{ik} \right) \end{aligned} \tag{9}$$

P is the production of turbulent kinetic energy given by

$$P = \langle u_l' u_k' \rangle \frac{\partial \langle u_l \rangle}{\partial x_k} \tag{10}$$

Furthermore, S_{ij} is the mean strain rate tensor, defined by

$$S_{ij} = \frac{1}{2} \left(\frac{\partial \langle u_i \rangle}{\partial x_j} + \frac{\partial \langle u_j \rangle}{\partial x_i} \right) \tag{11}$$

and Ω_{ij} is the mean vorticity tensor, defined by

$$\Omega_{ij} = \frac{1}{2} \left(\frac{\partial \langle u_i \rangle}{\partial x_j} - \frac{\partial \langle u_j \rangle}{\partial x_i} \right) \tag{12}$$

The constants of the pressure tensor R_{ij} in the SSG model are given in table 1. Finally, the dissipation tensor ε_{ij} is modeled as

$$\varepsilon_{ij} = \frac{2}{3} \delta_{ij} \varepsilon \tag{13}$$

Here ε is the dissipation of turbulent kinetic energy. For flows with high Reynolds numbers equation (13) is valid due to local isotropy (Pope, 2000). A separate transport equation for ε is part of the turbulence model. This equa-

tion is given by

$$\frac{\partial \varepsilon}{\partial t} + u_k \frac{\partial \varepsilon}{\partial x_k} = \frac{\partial}{\partial x_k}\left[\left(\nu \delta_{kl} + C_\varepsilon \frac{k}{\varepsilon}\langle u'_k u'_l\rangle\right)\frac{\partial \varepsilon}{\partial x_l}\right] \quad (14)$$
$$+ C_{\varepsilon 1}\frac{P\varepsilon}{k} - C_{\varepsilon 2}\frac{\varepsilon^2}{k}$$

Here the constant are $C_\varepsilon = 0.18$, $C_{\varepsilon 1} = 1.45$ and $C_{\varepsilon 2} = 1.83$.

In the experimental setup a flow straightener is mounted. To model the effects of the elimination of the swirl on the upstream flow field the flow straightener is numerically modeled as a porous region. The porous region is characterized by its porosity γ and the momentum loss term S_m. In the porous domain the single-phase flow equations are given by

$$\nabla.(\gamma \mathbf{u}) = 0 \quad (15)$$

$$\gamma\frac{\partial(\mathbf{u})}{\partial t} + \gamma \mathbf{u}.\nabla \mathbf{u} = -\gamma\frac{\nabla p}{\rho} + \gamma \nu \nabla^2 \mathbf{u} + \gamma \mathbf{g} \quad (16)$$

$$- \gamma \nabla.\langle \mathbf{u}'\mathbf{u}'\rangle + \frac{\gamma}{\rho}\mathbf{S}_m \quad (17)$$

At the interfaces between the fluid and the porous regions a jump in porosity is present. Across the interface the mass and the momentum fluxes are conserved. The porosity γ is defined as the fraction of the volume occupied by the fluid. For this flow straightener the porosity is $\gamma = 0.2667$. The reduction in flow area leads to a substantial increase in velocity. The momentum loss term S_m represents the inertial loss contribution, which depends on the square of the fluid velocity

$$S_m = -\mathbf{K}_{loss}\frac{\rho}{2}|\mathbf{u}|\mathbf{u} \quad (18)$$

The axial loss coefficient of $\mathbf{K}_{loss}$ is estimated from pressure drop measurements and pipe flow theory. Also the transverse components of the parameter $\mathbf{K}_{loss}$ are set a factor ten higher than the axial component to ensure the suppression of the radial and azimuthal velocity components. The loss parameter $\mathbf{K}_{loss}$ is given by

$$\mathbf{K}_{loss} = \begin{bmatrix} 120 & 0 & 0 \\ 0 & 120 & 0 \\ 0 & 0 & 12 \end{bmatrix} [m^{-1}] \quad (19)$$

Two-phase flow

The high volume fraction of the dispersed oil phase demands the use of the two-fluid model for the calculation of the two-phase flow. This two-fluid model is also called the Euler-Euler model. The model is obtained by volume or time-averaging of the two-phase flow, in which it
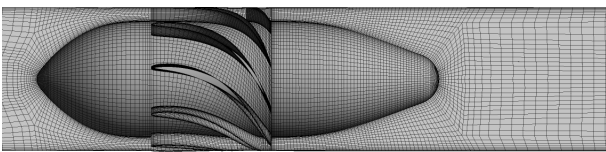
Figure 3: Mesh on the surface of the ISE and on the plane through the axis on the separator. 1.4M hexahedral elements are used for the mesh.

is assumed that the averaging volume is large enough or the averaging time scale is long enough to obtain a meaningful average of the non-uniformities in the flow. For a thorough derivation the reader is referred to Prosperetti and Tryggvason (2007) or Drew (1983). In the resulting model both phases are represented as interpenetrating fluids, with only the volume fraction indicating the relative fractions of the phases at that location. For both phases separate continuity and momentum equations part of the model. These equations are coupled by an interfacial momentum transfer term M. The continuity equation and the momentum equations for phase k are given by

$$\frac{\partial \alpha_k}{\partial t} + \nabla \cdot (\alpha_k \mathbf{u}_k) = 0 \quad (20)$$

$$\rho_k \alpha_k \frac{D\mathbf{u}_k}{Dt} = -\alpha_k \nabla p + \nabla \cdot (\alpha_k \sigma) + \alpha_k \rho_k \mathbf{g} \quad (21)$$

$$+ \rho_k \nabla \cdot (\alpha_k\langle \mathbf{u}'_k \mathbf{u}'_k\rangle) + \mathbf{M}_k \quad (22)$$

Here α_k is the volume fraction of phase k and the material derivative is defined as

$$\frac{D\mathbf{u}_k}{Dt} = \frac{\partial \mathbf{u}_k}{\partial t} + (\mathbf{u}_k \cdot \nabla)\mathbf{u}_k \quad (23)$$

Both phases share the same pressure field and therefore the phase subscript of the pressure is dropped. The viscous stress tensor is given by

$$\sigma = \mu_k(\nabla \mathbf{u}_k + (\nabla \mathbf{u}_k)^T) \quad (24)$$

M_k is the interfacial momentum transfer, which is the fluid dynamics force acting on phase k. Here surface tension effects are neglected and therefore $M_w = -M_o$, where the subscripts w and o indicate water and oil, respectively.

The momentum transfer term models the physics of the interaction of the phases. Currently, only the drag force is incorporated. In the derivation of the drag force the water phase is defined as continuous and the oil phase as dispersed. The expression for the drag force acting on the water phase is given by

$$M_w = \frac{3}{4}\frac{C_D}{D}\rho_w \alpha_o \mid \mathbf{u}_o - \mathbf{u_w}\mid(\mathbf{u}_o - \mathbf{u}_w) \quad (25)$$

The C_D is the drag coefficient and D is the diameter of the oil droplets. The drag law formulations by Schiller and Naumann (1933) and by Ishii and Zuber (1979) are considered in the present study. The correlation of Schiller and Naumann (1933) is defined by

$$C_D = \frac{24}{Re_D}(1 + 0.15Re_D^{0.687}) \quad (26)$$

Here Re_D is the Reynolds number based on the relative velocity:

$$Re_D = \frac{\rho_w \mid \mathbf{u_o} - \mathbf{u_w}\mid D}{\mu_w} \quad (27)$$

This correlation is applicable to spherical droplets for Reynolds numbers up to 1000. However, equation (26) does not take into account the hinderance effect other droplets have on the movement of a droplet.

In the expression by Ishii and Zuber this effect is modeled by basing the Reynolds number on the mixture viscosity. The viscosity of the water in equation (27) is therefore

replaced by

$$\mu_m = \mu_w(1-\alpha_o)^{-2.5\frac{\mu_o+0.4\mu_w}{\mu_o+\mu_w}} \qquad (28)$$

As a droplet moves through the fluid it will induce a motion of the continuous phase and thereby deform the surrounding fluid. When other droplets are present in this surrounding fluid they will be subjected to this deformation as well. Due the Laplace pressure, the surrounding droplets will resist deformation more than the continuous fluid, leading to a higher perceived viscosity experienced by the moving droplet. Therefore the drag for these dense systems is modeled by assuming similarity to the single droplet case and increasing the viscosity.

In addition to the pressure field, in the two-phase computation both phases share the turbulence field, that is at a certain location the Reynolds stresses and the turbulent dissipation are identical for both phases. Since the phases will separate the use of a different turbulence model for the dispersed phase is not advised. As for the single-phase flow here the SSG model is used to model the turbulence in both phases.

Computational method

The governing equations were solved using the commercial CFD package Ansys CFX 12.1, which uses a cell-centered finite-volume method. The CFX solver uses a co-located grid in which the discrete values of the pressure and velocity components are computed at the same location. The spatial and temporal discretizations are second-order accurate.

A computational mesh has been generated which consists of 1.4 million hexahedral elements. Figure 3 shows the mesh on the surface of the ISE and on the plane through the axis of the separator.

Near the walls the mesh is refined in order to capture the near wall behavior of the flow. To reduce the computational requirements wall functions are employed to represent the flow structure in the region adjacent to the wall. Wall functions use empirical relations to impose the wall shear stress at the nodes next to the wall, which are all located outside the viscous sublayer.

At the inlet the bulk axial velocity u_b is 2 m/s, leading to a flow rate of 56.5 m^3/hr. At the oil outlet a mass flow boundary condition of 30wt% of the inlet flow is imposed. At the water outlet an averaged reference pressure of 0 Pa is imposed. The density of the water and the oil is 1067.8 kg/m^3 and 869 kg/m^3, respectively. A mono-dispersed oil phase is assumed with a droplet diameter $D = 100~\mu$m. The dynamic viscosity of the the water and the oil is 1.183×10^{-3} kg/ms and 8.690×10^{-3} kg/ms, respectively.

The transient simulations are run until an operational state is established. In this operational state the mean velocity **u** varies in a periodic fashion around some final mean value. After this state has established, the time-averaged values of the mean velocity and other quantities are calculated using sufficient time steps to capture several periods of the periodic solution.

SINGLE-PHASE FLOW RESULTS

Downstream of the ISE a strongly swirling flow is present. The generation of the swirling flow is accompa-
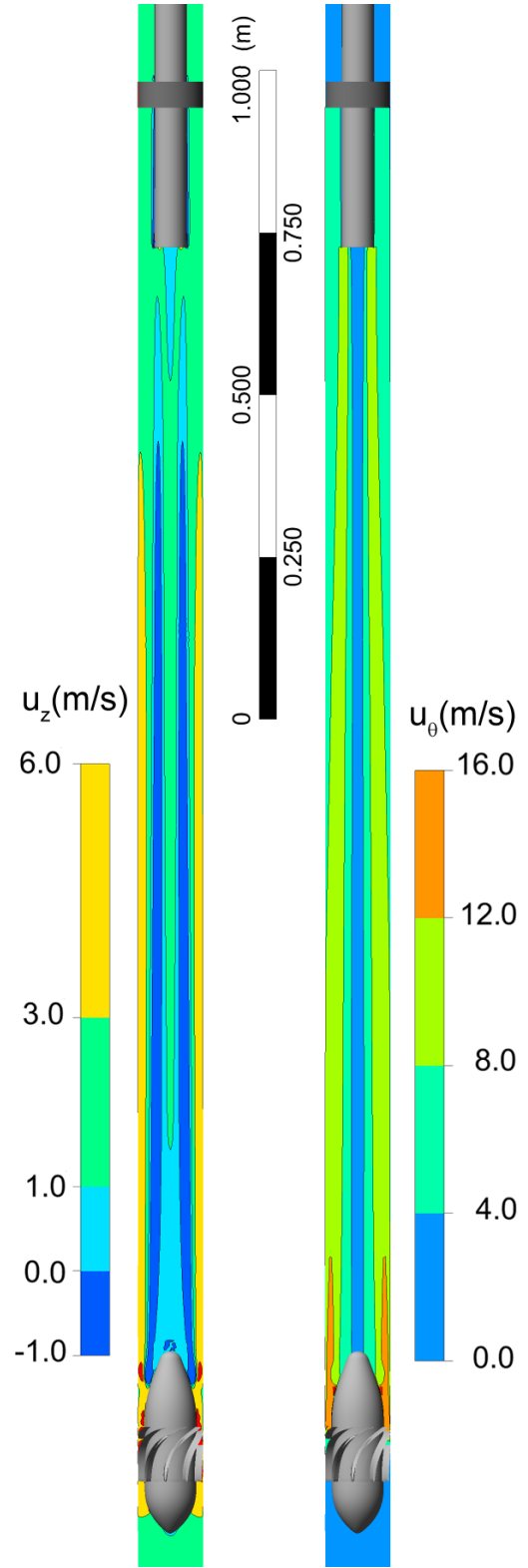
Figure 4: Contours of time-averaged velocities on plane through the axis of the separator for flow of single-phase water: axial velocity (left) and azimuthal velocity (right).

nied by a pressure drop in the axial direction of 1.5×10^5 Pa. For the calculation of this pressure difference, the pressure is averaged over the cross-sectional planes just up- and just downstream of the ISE.

The time-averaged axial and azimuthal velocity on a plane through the axis of the separator are seen in figure 4. In the plot of the axial velocity, an annular region of re-
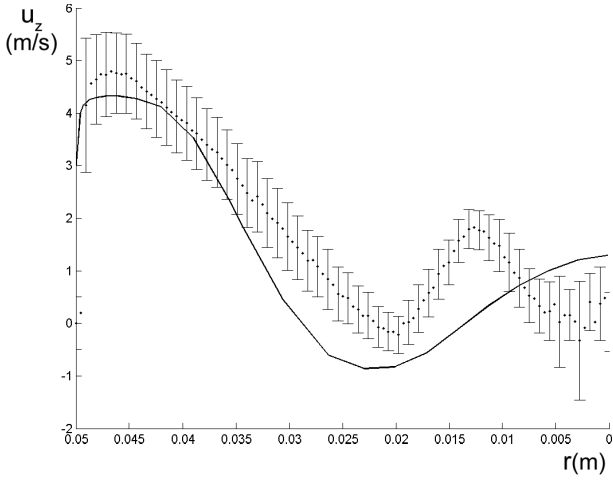
(a) Axial velocity
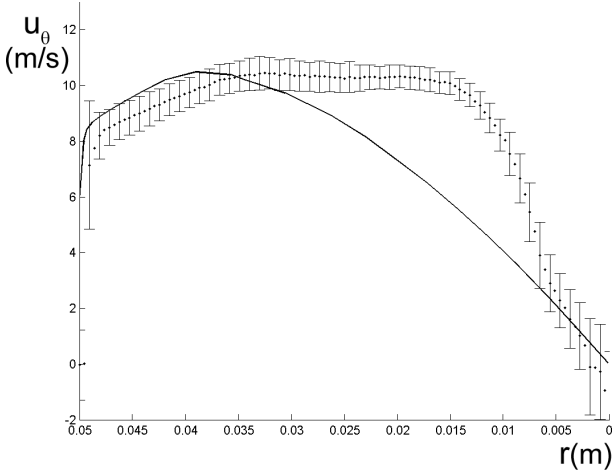
(b) Azimuthal velocity

Figure 5: Comparison of radial distribution of time-averaged axial and azimuthal velocity at 0.44 m downstream of the ISE of numerical (solid) and experimental (dotted) results, error bars give standard deviation of measurements around mean value. Results for half the pipe diameter are shown.

(a) Axial velocity

(b) Azimuthal velocity

Figure 6: Comparison of radial distribution of time-averaged axial and azimuthal velocity at 1.395 m downstream of the ISE of numerical (solid) and experimental (dotted) results, error bars give standard deviation of measurements around mean value. Results for half the pipe diameter are shown.

versed flow can be seen surrounded by a regions with positive axial velocity near the pipe wall and one around the center of the pipe, resulting in a W-shaped radial distribution of the axial velocity. This reversed flow pattern has been observed before (Mattner *et al.*, 2002; Ko, 2005). In downstream direction, the axial velocity decreases in the region near the pipe wall and becomes less negative in the annular reversed flow region. In the region at the center of the pipe the axial velocity increases further downstream. Just upstream of the pick-up tube a distinct change in flow pattern is obversed. In the center a decrease in the axial velocity is seen, while the axial velocity increases in the region near the inner wall of the pick-up tube. Still further downstream, inside the pick-up tube, the W-shaped radial distribution of the axial velocity is recovered. Furthermore, a second reversed flow region is observed in the region next to the outer surface of the pick-up tube. All three effects are features of the swirling flow and are not seen in case of non-swirling flow. The porous region emulating the flow straightener is indicated by the dark grey ring in the figure 4. Due to the obstruction of the flow

the axial velocity experiences a sharp increase inside the flow straightener.

The highest azimuthal velocity can be seen just downstream of the ISE, reaching velocities up to 16 m/s. Initially, the azimuthal velocity decreases rapidly, but further downstream the rate of decay of the swirl decreases. The azimuthal velocity remains higher than 8 m/s for most of the separator volume. In downstream direction the location of the maximum in the radial distribution of the azimuthal velocity moves towards the center of the pipe. Near the pick-up tube the flow converges, leading to centrifugal accelerations of 600 g near the pick-up tube opening.

Although obscured by the time-averaging, a mild vortex core precession of the flow is seen, that is a low-amplitude time-dependent motion of the vortex core around the geometrical axis of the pipe. The vortex core precessing is strongest just aft of the ISE, further downstream it decreases. The reduction in vortex core precessing may be attributed to the pick-up tube which appears to have a stabilizing effect on the flow.

The numerical and experimental results for the radial distribution of the time-averaged axial and azimuthal velocity along a line through the center in the cross-sectional plane at z = 0.44 m and 1.395 m downstream of the ISE are compared in the figures 5 and 6, respectively.

Currently, in the experimental setup a gas core with a diameter of about 10 mm is present. This more or less stagnant gas core is likely to considerably influence the velocity profile of the liquid phases near the center. Moreover, for the LDA system it is difficult to measure through the gas core. Since the optical transition between the PMMA pipe wall and the water causes refraction, measurements are only done along lines passing through the center of the pipe. Therefore, only the velocity distributions for half the pipe diameter, from the pipe wall to the center are presented here.

The numerical results predict the axial flow pattern well, except for the 10 mm near the center as can be observed in figure 5(a). Both the predicted high axial velocity near the wall and the reversed flow region are confirmed by the experiments. In the center the experiments show a second local minimum, while the numerical results show a local maximum in axial velocity. Moreover, the experiments show an overall higher axial velocity and therefore a higher mass flow compared to the mass flow prescribed in the numerical simulations. This may be explained by asymmetries in the flow field in the experimental setup. The axial velocity on the other side of the gas core should therefore be lower than the axial velocity found in the computation.

The azimuthal velocity in figure 5(b) shows good agreement in the near wall region. Further inward, the experiments show a much higher azimuthal velocity, indicating a relatively narrow region with strong axial vorticity. In the results of the numerical simulation the vorticity is at a lower level and is distributed over a larger region.

Further downstream, at z = 1.395 m, the agreement is very satisfactory for radial locations above 20 mm. Closer to the center the differences become large. While the numerical solution indicates the end of the annular reversed flow region, the experiments show a further decrease in axial velocity of the reversed flow compared to the situation at the upstream station at z = 0.44 m. Furthermore, the experiments show a higher peak in the azimuthal velocity. The maximum is located closer to the center compared to the upstream situation, leading to a much larger velocity gradient.

Apart from the region near the center of the pipe, there is good qualitative agreement between the measurements and the results from numerical flow simulations. However, the influence of the gas core on the velocity field is unknown and is very likely to contribute to the differences in the results. Efforts will be made in the future to remove the gas core.

TWO-PHASE FLOW RESULTS

Simulations of two-phase flow have been carried out to study the oil-water flow in the separator and to assess the predicted separation efficiency for different drag law formulations. The inlet oil volume fraction is set to 0.25, representing a feed from a high watercut oil field. The mass flow split through the oil outlet is again set to 0.3. The mass fraction of oil at the inlet is lower than 0.3, therefore this mass flow setting will likely result in
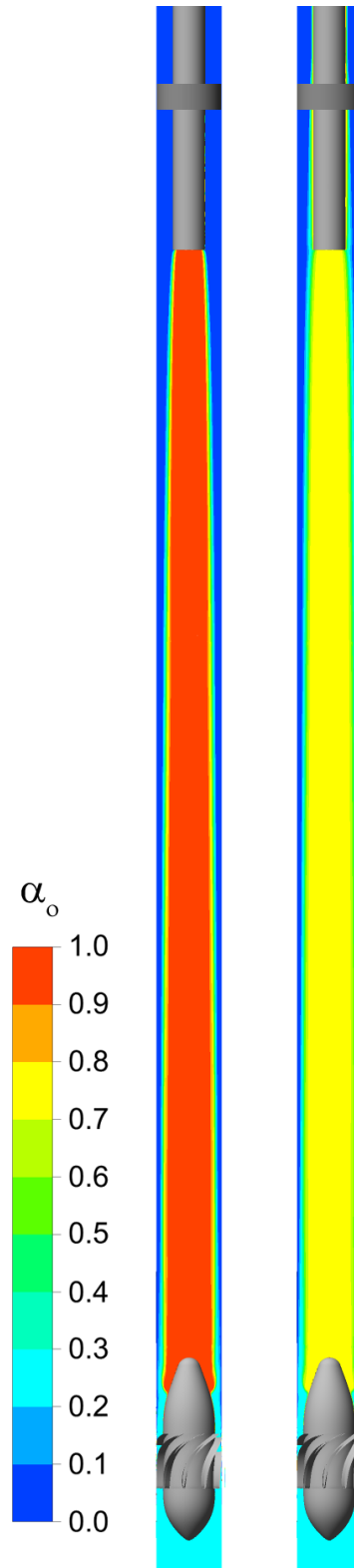
Figure 7: Contours of time-averaged oil volume fraction on plane through the axis of the separator for Schiller-Naumann (left) and Ishii-Zuber (right) drag laws. Inlet volume fraction is 25%.

cleaner water at the water outlet rather than purer oil at the oil outlet. The drag law correlation of Schiller and Naumann (1933) and that of Ishii and Zuber (1979) are used in the modeling of the interfacial drag between the oil and water phase.

The solution indeed shows the successful bulk separation

of the phases. The oil volume fraction in the separator is shown in figure 7, the left subfigure shows the results for the Schiller-Naumann drag law and the right subfigure shows the results for the drag law by Ishii and Zuber. A large difference in the distribution of the volume fraction is observed. For the Schiller-Naumann case, a large central region of pure oil can be seen. Oil will accumulate in the separator, leading to a hold-up of 42%. Almost all the oil is captured by the pick-up tube. The distribution of the oil volume fraction is different for the case for which the Ishii-Zuber drag law has been applied. Also in this case oil accumulates in the center of the separator leading to a hold-up of 38%. However, the oil volume fraction only reaches a value of about 80%. The oil volume fraction does not appear to increase to values higher than this 80%. Also some oil can be seen to spill over the pick-up tube, flowing towards the water outlet.

The reason for this behavior can be found in the definition of the mixture viscosity μ_m in equation (28). The ratio of mixture viscosity to water viscosity is given as function of the oil volume fraction α_o in figure 8. The mixture viscosity is increasing rapidly as the oil volume fraction increases above 0.6. For instance, at an oil volume fraction of 0.80 the mixture viscosity is already 40 times as high as the water viscosity. Since M_k increases with the mixture viscosity, the resulting velocity difference between the oil and the water will become very small. Therefore, further separation is prevented and the oil volume fraction is limited. Ishii and Zuber claim their drag relation can be used for dispersed volume fractions up to 0.95 if the dispersed phase is a gas or liquid. However, in a real application it is likely that at lower oil volume fractions coalescence between the droplets will occur. At a certain point phase inversion will occur and water will become the dispersed phase. However, in the current drag formulation the oil is treated as the dispersed phase, regardless of the value of the volume fraction.

It appears that the Schiller-Naumann drag law will over-estimate the radial velocity of the dispersed phase since it cannot account for the mutual interferences of droplets moving towards the center of the pipe. Moveover, the Ishii-Zuber drag law will impose a maximum oil volume fraction due to its inability to incorporate phase inversion.

(a) z = 0.44 m

(b) z = 1.395 m

Figure 9: Comparison of radial distribution of time-averaged axial water velocity at z = 0.44 m and z = 1.395 m for single-phase flow (solid with dots), two-phase flow with Schiller-Naumann drag law (dashed) and two-phase flow with Ishii-Zuber drag law (solid).

The separation efficiency is defined as the ratio of the oil mass flow rate through the oil outlet to the oil mass flow rate at the inlet. When the Schiller-Naumann drag relation is applied the separation efficiency is 98%. The separation efficiency for the case in which the Ishii-Zuber relation is used is lower, as expected: 89%. Another important result from the simulation is the oil volume fraction at the water outlet, this is 0.7% and 4% when using the Schiller-Naumann and Ishii-Zuber drag law, respectively. Current experimental results indicate the separation efficiency to be about 65%. Therefore, it appears that in both cases the numerical simulations substantially overestimate the separation efficiency. This may partially be attributed to discrepancies in the input parameters of the numerical simulations and those of the experiments. For instance, the mass flow split in the experiments is lower than the one in the numerical simulations and the droplet sizes at inlet differ. However, the main reason for the difference in separation efficiency is

Figure 8: The ratio of mixture viscosity μ_m to water viscosity μ_w given as function of the oil volume fraction α_o

expected to be the effect of turbulence on the segregation of the dispersed phase which is not taken into account. Therefore, a suitable turbulent dispersion model should be incorporated in the interfacial momentum transfer term in future work.

The radial distribution of time-averaged axial water velocity for single-phase flow, two-phase flow with the Schiller-Naumann drag law and with the Ishii-Zuber drag law at z = 0.44 m and z = 1.395 m are shown in figure 9. The difference between the axial velocity of the phases is negligible compared to the magnitude of the axial velocity. Therefore only the water velocity is shown here. At z = 0.44 m the differences in axial water velocity obtained for the three flow simulations is small. The differences in the azimuthal water velocity are even smaller and are therefore not shown here. It appears that the introduction of a second phase has little effect on the axial velocity field. The similar velocity distribution for both two-phase flow simulations indicate that only the radial movement of the oil phase is affected by the higher drag coefficient of the Ishii-Zuber drag relation. In the axial and azimuthal direction the differences in the velocity of the oil and the water is only a fraction of the total velocity. So any changes in these slip velocities will be hardly visible. Furthermore, due to the high Reynolds number of these flows, the effect of the higher viscosity of the oil on the velocity field is likely to be small. Although the velocity fields are very similar, the single-phase flow simulation showed a 10% higher pressure drop over the ISE cause by the higher density of the water compared to the mixture.

Further downstream, at z = 1.395 m, the differences in velocity are larger. This difference can be explained by changes in the volume flow split. Although the mass flow split is set to 0.3 in all simulations, the volume flow split differs due to changes in composition of the mixture at the outlet. The largest quantity of oil is extracted through the oil outlet in the two-phase flow case with the Schiller-Naumann drag law. Consequently, the highest axial water velocities can be seen for that case. The opposite is true for the single-phase flow simulation, leading to the lowest axial water velocities in the center region of the pipe. Since the volume rates at the inlet are equal for all three cases the axial velocities in the near wall region show to opposite behavior.

CONCLUSIONS

An in-line oil-water separator has been designed and is investigated for both single- and two-phase flow. The separator consists of an internal swirl element (ISE), which uses vanes to generate the swirling flow by deflecting the flow. Downstream a pick-up tube is placed to collect the separated oil stream. In the separator a strongly swirling flow is seen with an annular reversed flow region.

The predicted single-phase flow field has been compared to LDA measurements of the flow in the experimental setup of the separator at Delft University of Technology. The agreement between numerical and experimental results is satisfactory in the region near the wall. However, near the center of the pipe large differences are seen. In the experimental setup an gas core was observed, which negatively influences the comparison.

Two-phase flow simulations have been carried out to study the flow field of an oil-water mixture in the separator. In addition, different drag laws were employed to investigate their effect on the flow field and on the separation efficiency. In the region downstream of the ISE the oil accumulates, leading to an oil hold-up of about 40%. The use of the drag law by Schiller and Naumann results in a core of pure oil, which is subsequently extracted with little spill-over. In the two-phase flow simulation which used the drag law by Ishii and Zuber the oil volume fraction in the separator did not increase beyond about 80%. Considerable spill-over was seen for this case. The two-phase flow simulations overestimate the separation efficiency by more than 20% when compared to the experimental results. Finally, the velocity field in the two-phase flow simulation was found to be very similar to that resulting from the single-phase flow computation.

ACKNOWLEDGEMENTS

REFERENCES

BELT, R. (2007). *On the liquid film in inclined annular flow*. Ph.D. thesis, Delft University of Technology.

BRADLEY, D. (1965). *The Hydrocyclone*. Pergamon Press.

CHEN, J. and LIN, C. (1999). "Computations of strongly swirling flows with second-moment closures". *International Journal for Numerical Methods in Fluids*, **30**, 493–508.

CULLIVAN, J. *et al.* (2003). "Understanding the hydrocyclone separator through computational fluid dynamics". *Transactions Institution of Chemical Engineers A*, **81**, 455–466.

DALY, B. and HARLOW, F. (1971). "Transport Equations in Turbulence". *Physics of Fluids*, **13**, 2634–2649.

DELFOS, R. *et al.* (2004). "A design tool for optimising axial liquid-liquid hydrocyclones". *Minerals Engineering*, **17(5)**, 721–731.

DERKEN, J. (2003). "Separation performance predictions of a stairmand high-efficiency cyclone". *American Institute of Chemical Engineers Journal*, **49(6)**, 1359–1371.

DIRKZWAGER, M. (1996). *A New Axial Cyclone Design for Fluid-Fluid Separation*. Ph.D. thesis, Delft University of Technology.

DREW, D. (1983). "Mathematical modeling of two-phase flow". *Annual Review of Fluid Mechanics*, **15**, 261–291.

HANJALIC, K. (1999). "Second-Moment Turbulence Closures for CFD: Needs and Prospects". *International Journal of Computational Fluid Dynamics*, **12(1)**, 67–97.

HOEKSTRA, A.J. (2000). *Gas Flow Field and Collection Efficiency of Cyclone Separtors*. Ph.D. thesis, Delft University of Technology.

ISHII, M. and ZUBER, M. (1979). "Drag coefficient and relative velocity in bubbly, droplet or particulate flows". *AIChE J*, **25**.

KHAROUA, N. *et al.* (2010). "Hydrocyclones for de-oiling applications-a review". *Petroleum Science and Technology*, **28**, 738–755.

KITOH, O. (1991). "Experimental study of turbulent

swirling flow in a straight pipe". *Journal of Fluid Mechanics*, **225**, 445–479.

KO, J. (2005). *Numerical modelling of highly swirling flows in a cylindrical through-flow hydrocyclone*. Ph.D. thesis, Royal Institute of Technology.

MANNINEN, M. and TAIVASSALO, V. (1996). "On the mixture model for multiphase flow". Tech. rep., Technical Research Centre of Finland.

MATTNER, T. *et al.* (2002). "Vortical flow. part 1. flow through a constant-diameter pipe". *Journal of Fluid Mechanics*, **463**, 259–291.

MURPHY, S. *et al.* (2007). "Prediction of strongly swirling flow within an axial hydrocyclone using two commercial CFD codes". *Chemical engineering science*, **62**, 1619–1635.

NOROOZI, S. and HASHEMABADI, S. (2009). "CFD simulation of inlet design effect on deoiling hydrocyclone separation efficiency". *Chemical Engineering and Technology*, **32(12)**, 1885–1893.

PALADINO, E. *et al.* (2007). "Developing multiphase models for liquid-liquid hydrocyclone flow". *6th International Conference on Multiphase Flow*, S6 Wed C 37.

POPE, S.B. (2000). *Turbulent Flows*. Cambridge University Press.

PROSPERETTI, A. and TRYGGVASON, G. (2007). *Computational Methods for Multiphase Flow*, chap. Averaged equations for multiphase flow, 237–282. Cambridge University Press.

SCHILLER, L. and NAUMANN, A. (1933). "Uber die grundlegenden berechnungen bei der schwerkraft aufbereitung". *Zeitschrift des Vereines Deutscher Ingenieure*, **77**, 318.

SPEZIALE, C. *et al.* (1991). "Modelling the pressure-strain correlation of turbulence: an invariant dynamical systems approach". *Journal of Fluid Mechanics*, **227**, 245–272.

8th International Conference on CFD in Oil & Gas, Metallurgical and Process Industries
SINTEF/NTNU, Trondheim NORWAY
21-23 June 2011

CFD11-122

CFD SIMULATION OF A HIGH TEMPERATURE FURNACE

Jozsef NAGY, Andras HORVATH, Christian JORDAN, <u>Michael HARASEK</u>[1][*]

[1]Institute of Chemical Engineering, Vienna University of Technology, Getreidemarkt 9/166, A-1060

Vienna, AUSTRIA

[*] E-mail: mharasek@mail.zserv.tuwien.ac.at

ABSTRACT

This work deals with the simulation of a high temperature furnace for burning of fire clay, which is heated by six wall mounted burners. Both the fluid dynamics inside the burners and the processes inside the furnace are investigated in detail. The burners themselves are simulated separately and the results are used as boundary and initial conditions in the simulation of the full furnace. For the simulation radiation and combustion have to be included into the model. Also the thermal diffusion inside the walls and other solid parts inside the furnace is included. The development steps are presented of the model and an overview over the preliminary results made so far. By combination of several models, questions like the feasibility of oxygen enrichment in the burners can be answered.

Keywords: CFD, combustion, fluid-solid simulation, fire clay, swirl .

NOMENCLATURE

Greek Symbols
τ Time scale, $[s]$.
κ Weighting factor for turbulent mixing, $[-]$.
ρ Mass density, $[kg/m^3]$.
ν Kinematic viscosity, $[m^2/s]$.
λ Thermal conductivity, $[W/(mK)]$.

Latin Symbols
$\mathbf{u}$ Velocity vector, $[m/s]$.
$\mathbf{g}$ Acceleration of gravity, $[m/s^2]$.
$\mathbf{F}$ Volumetric force density, $[kg/(m^2 s^2)]$.
Y Molar species concentration, $[-]$.
R Source term of species, $[kg/(m^3 s)]$.
h Enthalpy, $[J]$.
S Source term of sensible enthalpy, $[kgJ/(m^3 s)]$.
T Temperature, $[K]$.
c_p Specific heat at constant pressure, $[J/(kgK)]$.

Sub/superscripts
c Chemical.
mix Mixing, due to turbulence.
turb Turbulence.
i Species 'i'.
react Reaction.
rad Radiation.
s Sensible enthalpy.

INTRODUCTION

The combined calculation of fluid flow and combustion at high temperatures is a challenging task for *Computational fluid dynamics* (Baukal and Gershtein, 2001). The problem setting discussed in this work deals with the processes inside a high temperature furnace used in the burning process of industrial fire clay. Measurement of process phenomena like the shape and length of the flame or the fluid movement inside the furnace is a very difficult task during industrial production. Simulation of the processes can help visualize and compare different operating conditions. These investigations are done in an ongoing industrial project in cooperation with Rath AG (Vienna, Austria). Scope of the work is to give an overview over the methods and procedures used for the simulation as well as achievements and preliminary results so far in the project.

The simulation of the high temperature burning process of fire clay also poses various difficulties. One has to consider the distribution of temperature in both the fluid and the solid phase (e.g. clay, furnace walls). One cannot simply assume constant boundary conditions on the solid surface, as the walls of the burning furnace consist of different layers of refractory bricks, which themselves are placed in a certain alignment. Thus the diffusion of heat in the solid has to be fully considered in the simulation. Also the flow of the fluid is highly swirled in some regions, which introduces additional difficulties to the simulation.

Also the transport of the sensible enthalpy due to convection, diffusion, turbulence and radiation in the fluid has to be considered.

The chemical reaction of the burning process that is still taking place in the volume of the furnace itself has to be modeled. The process of investigation is a non-premixed combustion inside the burners and a partially premixed combustion inside the furnace. An adequate chemistry solver in Open-FOAM for this problem is the PaSR (Partially Stirred Reactor) chemistry model developed at Chalmers University (Tao *et al.*, 2004; Iudiciani, 2009).

A complex algorithm has to be used that is able to handle these processes. Adequate spatial resolution has to be guaranteed with a mesh, that sufficiently resolves fluid and solid regions. The simulation is split into two separate parts: first a single burner is simulated in FLUENT, second the results of this simulation are used as boundary conditions for the actual simulation of the furnace.

The open source CFD software OpenFOAM allows modifi-

cation of the source code to control all important aspects of the solution procedure. Also it can be highly parallelized in order to reduce calculation time. A solver was assembled in OpenFOAM out of existing solvers (OpenCFD Limited, 2011), that takes account of all these issues.

The first step of the simulation is the assumption of a flow with hot gas without chemical reactions in the furnace. This assumes full burnout inside the burners. The burners themselves are simulated separately and the values at a certain predefined surface are used as boundary conditions in the simulation of the full furnace. However this has to be corrected in the second step and chemical reactions have to be added to the burning process.

As a benchmark case for the simulation of the non-premixed swirling methane-air burners the well known TECFLAM flame is used. The flame was simulated with the solver assembled in OpenFOAM and results are compared to experimental data (V.Bergmann *et al.*, 1998; Landenfeld *et al.*, 1998; Böckle *et al.*, 2000b,a). For validation reasons measurements were executed in an industrial furnace. Multiple temperature probes were installed in both the fluid phase. These results can be compared to the simulation results.

One important question is, if it is reasonable to enrich the inlet air of the burners with oxygen thus reducing the amount of nitrogen to be heated up to save energy and also increasing the temperature of the flame. This question can be answered with the model built up in the steps of the project presented in this work.

Numerical studies of mesh independency and the investigation of different discretization schemes were conducted. However presenting the results here would exceed the acceptable limits of the article.

MODEL DESCRIPTION

Governing equations

The newly assembled OpenFOAM solver uses a segregated approach for the solution of the governing differential equations. The mesh has to be divided into separate fluid and solid regions with individual meshes, that communicate through special interface boundary conditions. The regions are solved consecutively for the transient transport equations. The PaSR chemistry solver for combustion in the fluid region in the OpenFOAM version 1.7 is time dependent. The solver first solves the chemical reaction(s) using the PaSR model (Tao *et al.*, 2004).

At high temperatures and highly turbulent conditions in our investigation turbulence is a dominating factor for combustion the other one being the finite-rate chemistry. The underlying assumption of this model is, that it treats a constant volume (each single cell in the mesh) as a partially stirred reactor regarding combustion, where reactions only occur in a fraction of its volume. This is done by a weighting factor κ, that is given by

$$\kappa = \frac{\tau_c}{\tau_{mix} + \tau_c} \qquad (1)$$

Here, the chemical reaction and micro-mixing time scale are the parameters, that determine the degree of turbulent mixing and chemical reaction. If $\tau_{mix} << \tau_c$ the value for κ reduces to the laminar case of 1. Further details of the model can be found in (Tao *et al.*, 2004).

Since the code is assuming a compressible fluid the next equation to solve is the continuity equation.

$$\frac{\partial \rho}{\partial t} + \nabla \cdot (\rho \mathbf{u}) = 0 \qquad (2)$$

For the velocity-pressure coupling in OpenFOAM an internal PISO-loop is used (OpenCFD Limited, 2011), for which the momentum equation is used:

$$\frac{\partial \rho \mathbf{u}}{\partial t} + \nabla \cdot (\rho \mathbf{u}\mathbf{u}) = -\nabla p + \\ \rho \mathbf{g} + \nabla \rho \nu [(\nabla \mathbf{u}) + (\nabla \mathbf{u})^T] + \mathbf{F}_{\text{turb}} \qquad (3)$$

The turbulence term $\mathbf{F}_{\text{turb}}$ can be modeled in different ways, for example via the k-ε model or Reynolds-Stress Method (RSM). Detailed description of these models can be found in the literature (Launder and Spalding, 1974; Launder, 1989; Launder and Spalding, 1972) and will not be discussed in detail. With the calculated values of velocity, each of the species Y_i present in the reaction is transported according to

$$\frac{\partial \rho Y_i}{\partial t} + \nabla \cdot (\rho \mathbf{u} Y_i) = \nabla \rho \nu (\nabla Y_i) + \\ R_{\text{turb}} + \kappa R_{\text{react}} \qquad (4)$$

Here additionally to advection and diffusion source terms due to turbulence and the chemical reaction are used. κ is the factor from equation 1. For the transport of the sensible enthalpy h_s the following equation is used

$$\frac{\partial \rho h_s}{\partial t} + \nabla \cdot (\rho \mathbf{u} h_s) = \\ S_{\text{turb}} + \kappa S_{\text{react}} + S_{\text{rad}} \qquad (5)$$

Here source terms are introduced by turbulence, reaction and radiation. The temperature is internally calculated out of the value of the sensible enthalpy h_s.

In the solid phase the diffusion of temperature has to be solved. The equation is given by

$$\frac{\partial \rho c_p T}{\partial t} = \Delta(\lambda T). \qquad (6)$$

TECFLAM FLAME

The TECFLAM flame (see figure 1) is used as a benchmark for models in OpenFOAM. For the TECFLAM burner air is run through a swirl generator producing an overall swirl number of 0.9. This swirled flow is both transporting oxygen to the flame and stabilizing the combustion region (V.Bergmann *et al.*, 1998; Landenfeld *et al.*, 1998; Böckle *et al.*, 2000b,a). The flame was intensively investigated and detailed experimental data is available for the comparison with simulation results.

A 60° wedge of the geometry was implemented using periodic boundary conditions. The reason for this periodic three dimensional approach is the need to depict turbulence with a three dimensional flow field. The mesh for OpenFOAM consists of 567308 hexahedral cells with an additional region of solid (industrial steel) as the wall of the burning chamber.

For turbulence modeling the k-ε model is used (Frassoldati *et al.*, 2005). In later steps different turbulence models will also be investigated (e.g. the Reynolds stress model called 'LRR' or Large Eddy Simulation). The simulations are conducted for a swirl number 0.9 and an air/fuel ratio of 1.2 of the 150 kW burner. Inlet values are calculated from the power and inlet surfaces, which were received from the authors of (V.Bergmann *et al.*, 1998; Landenfeld *et al.*, 1998;

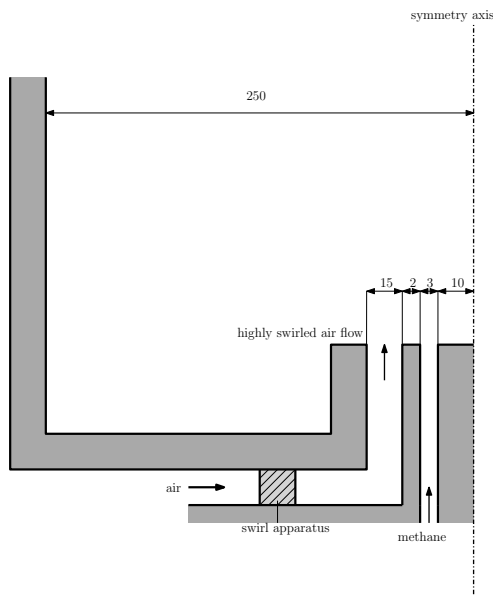Böckle *et al.*, 2000b,a). The OpenFOAM simulation is tran-

Figure 1: Schematic sketch (not to scale) of the geometry of the TECFLAM burner (dimensions in mm)
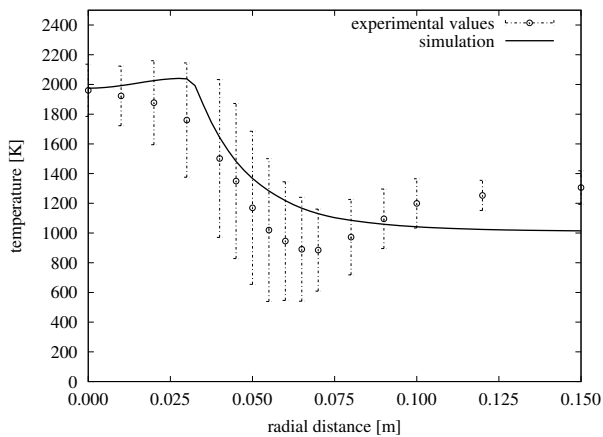

Figure 2: Radial temperature distribution inside the TECFLAM burner 0.09 m above the gas exit
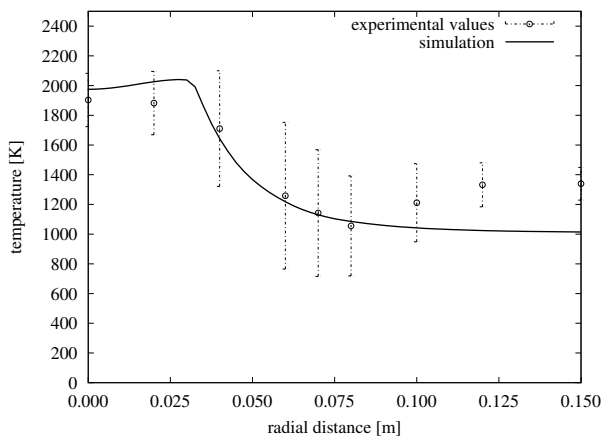

Figure 3: Radial temperature distribution inside the TECFLAM burner 0.12 m above the gas exit

sient and 2 s of burning process has been simulated, however after 0.75 s the flame is stable in shape.

In the first 5 ms an initial flow field is calculated without combustion above the inlet surfaces. After this the inlet temperature of methane and air is set to 800 K for 3 ms and combustion is started. Then the inlet temperatures are set back to 300 K and the simulation is carried out with a Courant number of 0.3 until 2 s.

In figures 2 and 3 one can see the radial temperature distribution at a height of 0.09 m and 0.12 m, respectively. Simulation results lie within these error intervals until a radial distance of 0.1 m. A small local maximum appears at 0.03 m and the minimum at around 0.06-0.08 m is 'smeared'. However temperature values can be depicted at this stage in the direction of the axial velocity within the measured variances. The errors of highest magnitude at this stage are done by using a mean value for the magnitude of the axial and tangential velocity at the inlet of air. In a future simulation a more detailed inlet distribution for velocity will be used in order to be able to depict the TECFLAM flame in a more detailed way.

SIMULATION OF THE HIGH TEMPERATURE FURNACE

Furnace geometry
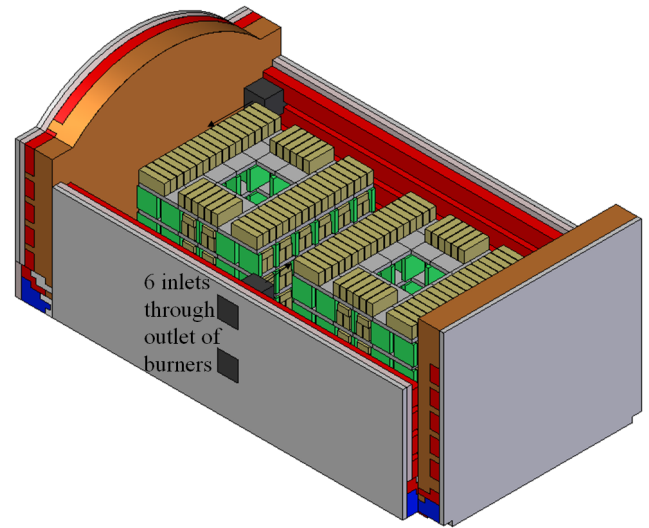
Figure 4: Implemented geometry of the high temperature furnace

The investigated geometry is a high temperature furnace for burning high density fire clay. The geometry was created and assembled in Solid Edge V20. Colors in figure 4 do not represent the actual colors of the different materials. The construction is built of materials with different specific heat and thermal conductivity. The different layers are not implemented brick by brick, but regions of the same material are combined into one volume and these volumes are put together in the software to build up the geometry. Fire clay is stacked onto two wagons, that are pushed into the furnace before the burning process. The platforms of these wagons also have a layered design in order to insulate the high temperature region around the fire clay bricks from near ambient conditions below the trolleys. This insulation is achieved by a labyrinth sealing. In figure 4 the roof construction and some of the furnace layers are not shown in order to see the wagons and the bricks on them.

Also a structure of purple and green bricks can be seen. This structure is needed, because the burning process is accomplished at 1900-2000 K by methane combustion. At these temperatures the bricks are close to the the yield point and a shelf system is used to separate the bricks and prevent deformations due to their own weight. Three bricks are stored within one of each pocket of the structure. There are pockets with open and closed back wall. Also a rectangular hole in the middle of the holding structure can be seen. This hole is maintained throughout the wagon itself and connects to the gas outlet of the furnace. In the lower part of figure 5 two volumes can be seen, that lead out of the bottom part of the wagons. These are the off gas ducts. The six black boxes in figure 4 represent the six burners of the same type. The surfaces of these boxes connected to the region of gas inside the furnace are used as inlet surfaces of the flow exiting the burners. In figure 5 the two wagons, the bricks and the air in between the bricks are shaded gray in oder to show the location of the fire clay bricks relative to the furnace walls and wagons.
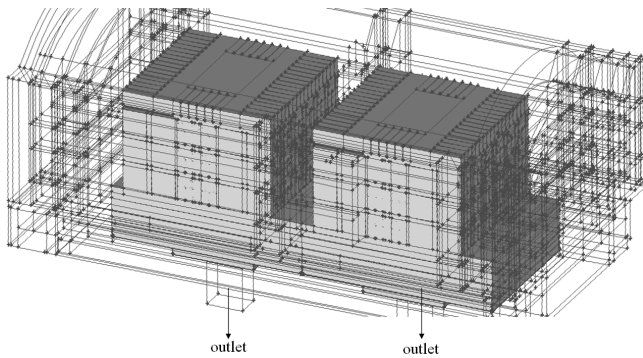
Figure 5: Geometry of the high temperature furnace created for meshing

The grid for the domain is created by importing the geometric data into GAMBIT 2.4.6 and by cutting the gas region and the layers of the wall as well as the bricks into approximately 2500 separated volumes suitable for hexahedral meshing. 15.500.000 hexahedral cells are used for the mesh.

Burner geometry
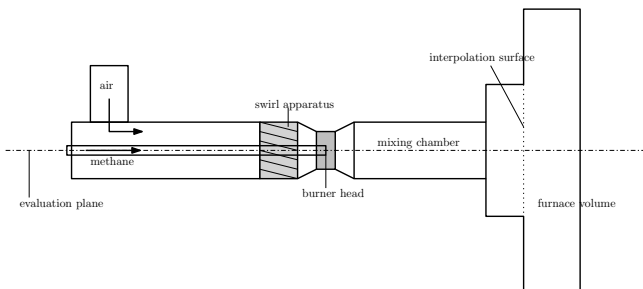
Figure 6: Schematic sketch (not to scale) of the burner geometry

The geometry of the burner is implemented separately. A schematic sketch is shown in figure 6. On the left hand side air is supplied to the burner from the top side reaching a swirl apparatus, that is creating a highly turbulent flow of the hot gas in order to increase combustion efficiency. In the middle of the burner a small tube introduces methane into

the flow. After the swirling apparatus (swirling number 0.9) these flows merge and react creating the high temperature flame used in the burning process of the fire clay. Two surfaces are indicated in figure 6. A horizontal line symbolizes the evaluation plane used for plots shown in following sections, and a vertical line at the end of the burner geometry shows the interpolation surface, that is used to transform data from the burner simulation to the simulation of the furnace. A small part of the furnace volume is included into the domain in order to move the outlet away from the inner domain of the burner. The mesh was created in GAMBIT. It consists of 5.5 million hexahedral cells.

Burning process
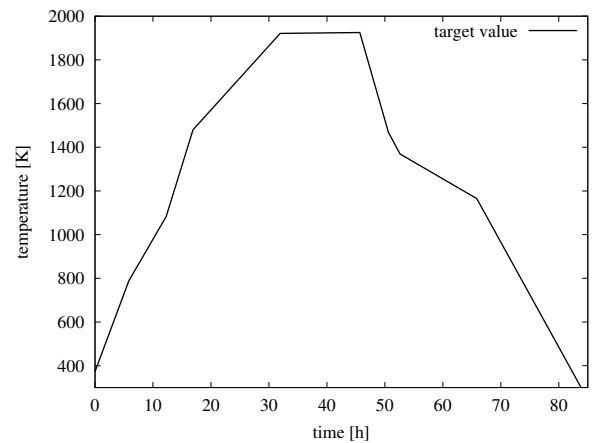
Figure 7: Target values for temperature during the burning process

The burning process lasts over several days and the simulation was set up to the conditions shown in figure 7. For that reason a small part of the burning curve is selected and further investigated. Figure 7 shows the entire burning curve. These are the target values, that regulate the temperature inside the furnace. Temperature sensors are located in the volume of the furnace and monitor the temperature. The simulations are conducted in the last part of the heating-up period between 17 h and 32 h. In this segment the burners are under full load and highest temperatures are reached at maximum methane flow rate.

Simulation of the burner

The simulation of the burner itself is done in FLUENT 6.3.26 with the three dimensional solver. As the flame is highly swirled the RSM turbulence model is used with the Eddy dissipation Model (EDM) for combustion with a methane-air-two-step mechanism (Fluent 6.3.26 User's Guide). Other combustion models are numerically too extensive and would increase the calculation time by unreasonable amounts. Radiation is modeled with the discrete ordinates method with 4x4 rays with one iterations every 11 flow iteration. Figure 8 shows a quarter of the mesh on the interpolation surface described in chapter *'Burner geometry'*. Here a hexahedral mesh can be seen with a diagonal in each cell surface shown. Figure 9 shows the simulation results of velocity magnitude inside the burner. Velocity values are high, where methane is introduced into the combustion chamber and where the swirling apparatus creates the swirl of the gas. One can also see, that alongside the walls the swirl increases the velocity and that the core region is mostly stagnant.

In figure 10 one can see the temperature distribution inside the burner. An adiabatic boundary condition was used on the wall. The design of the burner creates a cold layer alongside the wall created by freshly introduced air, that is cooling the stone placed around the burner preventing it from temperatures outside its specification.

Figure 11 shows the molar concentration of methane. Is not fully combusted at the interpolation surface, which means, that the combustion reactions still occur in the volume of the furnace.

The values of velocity, temperature, species and other values are evaluated on the interpolation surface and used as boundary conditions for the simulation of the furnace.

Conclusions of this simulation are the fact, that the flame reaches well into the furnace, where 30 % of available

Figure 8: Quarter if the mesh on the interpolation surface shown in figure 7
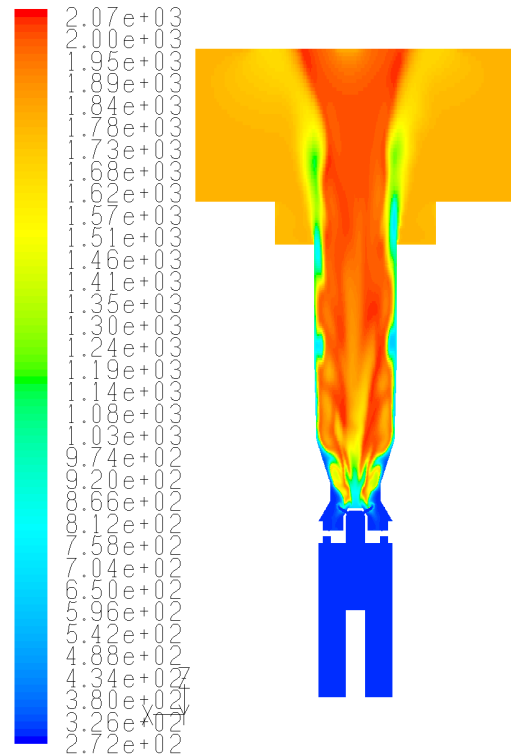
Figure 10: Temperature (in K) in the burner on the evaluation plane shown in figure 7
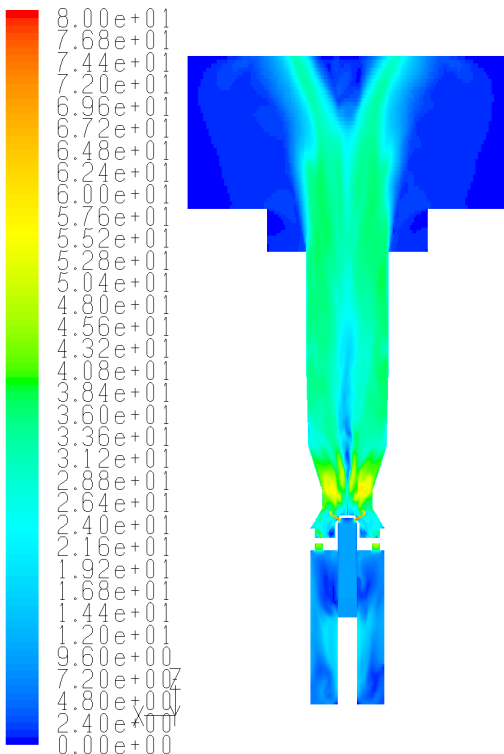
Figure 9: Velocity magnitude (in m/s) in the burner on the evaluation plane shown in figure 7
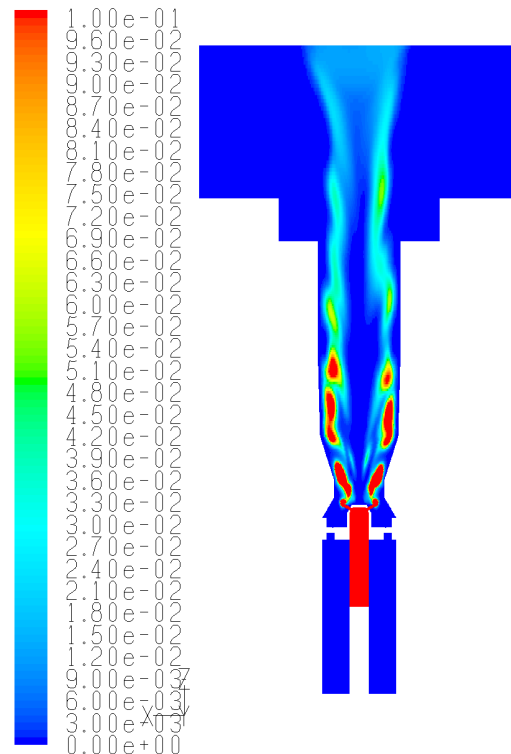
Figure 11: Molar fraction of methane (v/v) in the burner on the evaluation plane shown in figure 7

methane reacts.

High temperature flow simulation of the furnace

The standard OpenFOAM solver chtMultiRegionSimple-
Foam (OpenCFD Limited, 2011) is used and extended by the
C++ object for radiation. This is a steady-state solver and
intentions with it are first results showing reasonable charac-
teristics in the flow field and thus the correct advective and
radiative transport of temperature. No combustion is used at
this stage, which introduces deviation to the simulation in-
cluding chemistry as combustion is still occurring outside of
the burner volume (see chapter *'Simulation of high tempera-
ture flow including combustion'*). As this is a first test of the
solver simulation results of the burner are taken and averaged
over the inlet surface. The high core temperature and the
swirl are neglected, but for the advection of the gas coming
out of the burners in the furnace volume, this is an adequate
first estimate. For that reason a mean velocity of 6.6 m/s and
a mean temperature of 1742 K are used as simplified bound-
ary conditions. Since the swirl is neglected and thus no con-
siderable entries in the off-diagonal elements of the stress
tensor appear at this stage the k-ε turbulence model is used.
As the used mean value of inlet temperature is in the middle
region of the investigated time and temperature interval in
this case an initial temperature of 1600 K is patched into the
calculation domain. A boundary temperature of 473 K on
the outer wall of the most outer solid domains (mean mea-
sured temperature of the outer wall of the furnace) is set.
At the outlet (see figure 5) pressure is set to ambient pres-
sure. For the radiation the discrete ordinates method 'fv-
DOM' (OpenCFD Limited, 2011) is used with 2x2x4 rays
and 5 iterations every 20 iteration of the flow field. Since the
geometry is very complex, 400000 iterations are done with
the steady-state solver to ensure convergence. The simula-
tion was carried out on 32 CPU in a parallel way.
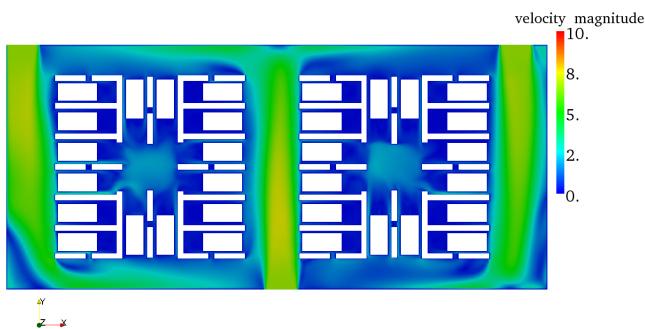
Figure 12: Velocity magnitude (in m/s) on the plane at the
height of the middle of the upper burners

In figure 12 one can see the plot of velocity magnitude on
the plane at the height of the upper burners inside the fluid
region. One can see the three burners, where gas enters the
volume of investigation, continuing in a forward direction
and hitting the opposite wall. At this point the gas is diverted
and flows along the opposite wall in the direction of the op-
posite burner(s). Also fluid is flowing in the middle of the
structure placed on top of the wagons. Yet one can see, that
through the pockets of the holding structure containing the
bricks with closed back wall air cannot flow through in an
amount as through the pockets with opened back wall. Also
one can see an increased flow of gas in the middle section
of the holding structure as fluid is flowing in the negative

z-direction through the hole inside the wagon and in the di-
rection of the outlet.

Figure 13 shows the resulting temperature plot on the same
plane. One can see again, that the hot gas is moving in
a forward direction and is redirected by the opposing wall.
However the asymmetric location of the burners results in an
asymmetric distribution of velocity magnitude and tempera-
ture.

Conclusions drawn from this initial simplified simulations
are, that a completely closed back wall of a fire clay hold-
ing pockets is disadvantageous in comparison to a pocket
with partially opened back wall. Also the flow field is de-
picted *reasonably* and the *convective and radiative transport
of temperature* is assured. However an *average value for in-
let values* on the inlet surface is too rough and a better *ex-
port/import procedure* between burner and furnace simula-
tion has to be used.

Interpolation of results for boundary conditions

As the burner is simulated in FLUENT and the furnace is
simulated in OpenFOAM and mean values are not adequate
for the depiction of the flow in the furnace an interpolation
script is created in Python, that is able to transform results on
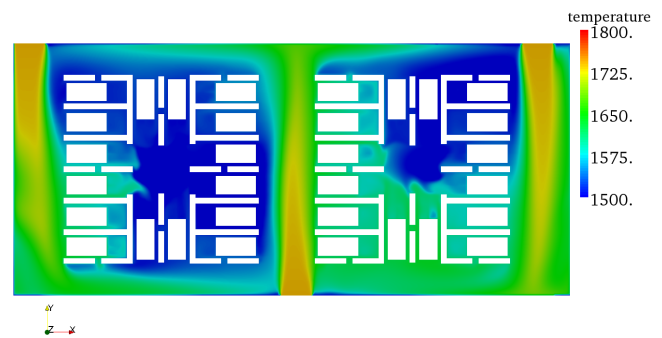

Figure 13: Temperature (in K) on the plane at the height of
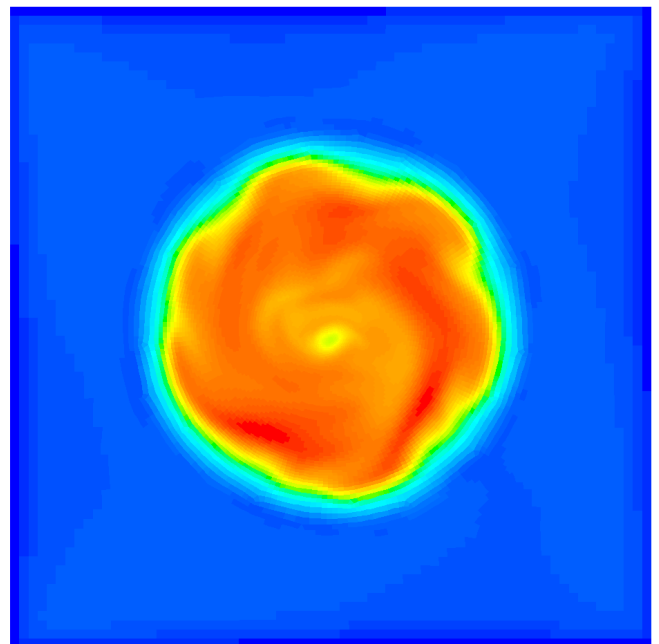the middle of the upper burners

Figure 14: Fine resolution of velocity magnitude on the in-
terpolation plane in FLUENT (between 0 and 33 m/s)

arbitrary surfaces within arbitrary meshes in FLUENT and is able to interpolate them onto another arbitrary surface in an OpenFOAM mesh as boundary conditions. This is an important bridge between the commercial and the open source software.

The script checks the results written out in FLUENT on a certain surface if the cell coordinates are within the coordinates of a given cell surface element in the OpenFOAM boundary. The values, that are within the OpenFOAM cell are averaged and written as value for the cell. This is done for every cell on the OpenFOAM surface mesh. In the next step the list is reorganized in the correct order, that OpenFOAM is using, as mesh numbering does not have to be in a structured way. In the last step different orientation of coordinates are corrected for velocity and the Reynolds-stress tensor and the list of boundary condition values are written into a list, that can be used as input for OpenFOAM.

Simulation of high temperature flow including combustion

Simulation with 20.9 % O_2 (air)

The simulation of the furnace in OpenFOAM is extended by the chemistry C++ object in OpenFOAM using the PaSR model (see chapter *'Model Description'*). For combustion a single reaction mechanism is used.

$$CH_4 + 2O_2 \longrightarrow CO_2 + 2H_2O \qquad (7)$$
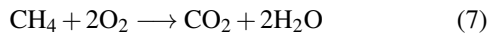
At this stage we are not interested in the concentrations of NO_x and CO a single equation reaction mechanism is used for the depiction of the heat generation due to combustion. The gas, that is introducing O_2 into the mixing chamber of the burner in the FLUENT simulation (see figure 6) is fresh air with 20.9 % O_2. In this case the interpolated temperature and other field values out of this burner simulation are used. Initial temperatures at the interpolation surface reach up to and beyond 2000 K, thus the operationg conditions at the
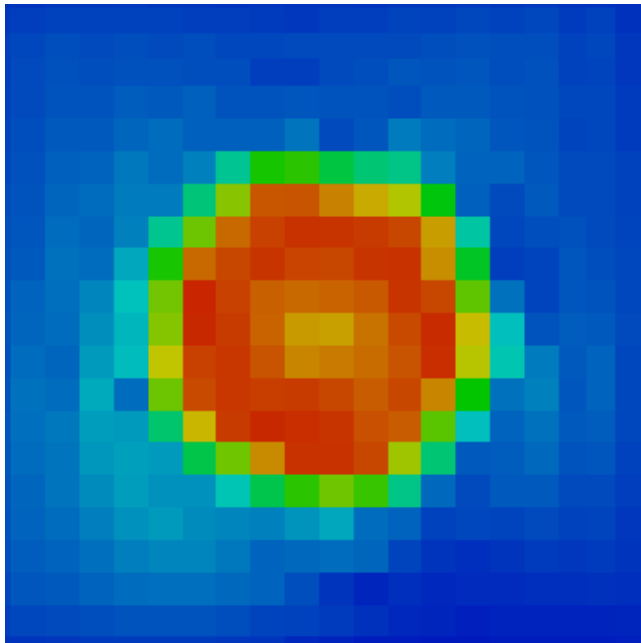
very end of the shown time interval of investigation shown in chapter , where temperature values lie around 1800 K can be investigated. For that reason in this case the temperature inside the furnace is initialized by 1800 K. Initially air was patched in the furnace volume. In this case the Reynolds-Stress Model 'LRR' (OpenCFD Limited, 2011) is used for modeling turbulence. The switch to this model is essential in order to connect the simulation with the simulation of the burner and in order to depict the correct swirl of the flame. The same fvDOM radiation modeling as in chapter *'High temperature flow simulation of the furnace'* is further used here. Boundary conditions on the outer wall are the same as used previously. Presented results are shown for the simulated time of 1.5 s, where a Courant number of 0.3 is used. Also in this case a 32 fold parallelization of the calculation was used.
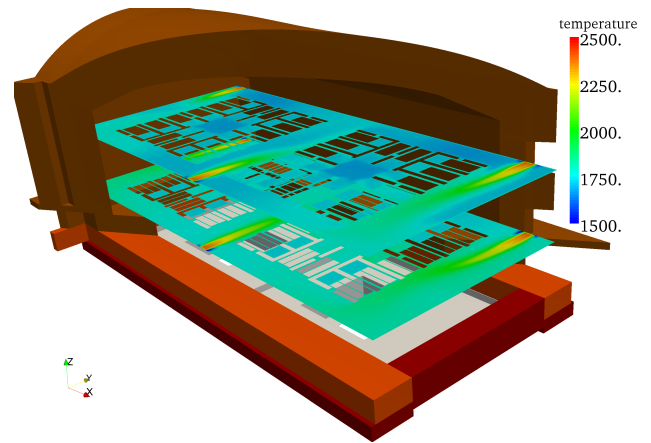
Figure 16: Furnace geometry with temperature distribution on two surfaces at the height of the middle of the burners

Figure 16 shows parts of the wall of the furnace with the temperature distribution on two surfaces in the fluid region. The two surfaces are at the height of the middle of the burner outlet surfaces.
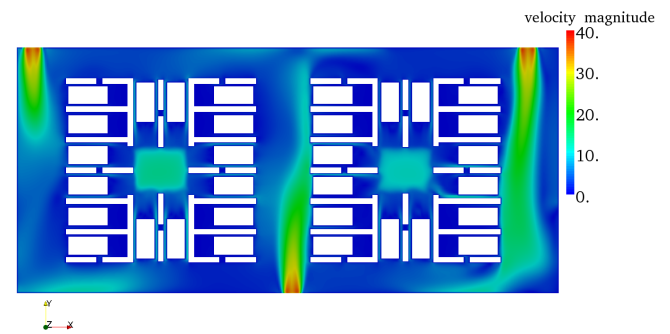

Figure 17: Velocity magnitude (in m/s) on the plane at the height of the middle of the upper burners

In figure 17 one can see, that the pockets with closed back wall are still not flushed with gas as one could already see in the previous chapter. In the pockets with partially opened back wall gas flows by the bricks at increased velocity thus resulting in a higher heat transfer rate into the bricks compared to the closed pockets.

Figure 18 shows the temperature distribution. One can see, that the poorly ventilated pockets do not reach the same temperature values as the ones with opened back wall. The asymmetric middle burner is causing an asymmetric distri-

Figure 15: Coarse resolution of velocity magnitude on the inlet surface in OpenFOAM (between 0 and 33 m/s), interpolation from FLUENT-mesh to OpenFOAM by averaging

bution of velocity magnitude and other field values.

Figure 19 shows the molar fraction of methane. Combustion of methane is still carried on in the furnace, yet at approximately 0.5 m after the burners no methane can be found. This can indicate the length of the flame under these conditions.

Simulation with 25 % O₂

The furnace simulation is conducted under the same conditions as in the previous chapter only with different boundary conditions on the burner inlet surfaces. One important question, that can be answered at this stage of the simulation of the furnace is, whether it is useful to enrich the air with additional O_2 up to a level of 25 % molar concentration of O_2. In the industrial production this will increase the the combution rate and reduce inert N_2, that has to be heated up during the process. Thus the volume flux can be reduced and higher tempratures can be achieved theoretically. This may reduce the duration of the burning process. For the simulation all the settings are the same in the burner as in the previous chapter with the difference of the molar fraction of N_2 and O_2 and the values of inlet velocity.

In figure 20 one can see the difference of temperature due to O_2 enrichment plotted on the interpolation surface of the burner simulation. In the 20.9 % case one can clearly see the cool layer alongside the wall, that is dissappearing in the case of 25 % O_2. Thus the brick surfaces around the burner are experiencing temperature values up to 600 K higher than in the first case. These values may lie over the specification values of the material.

In figure 21 one can see in the plot of velocity magnitude the reduction of the volume flow coming out of the burners. Also the flame velocity drops more rapidly after the burner exit.

Figure 22 shows the resulting temperature distribution at the changed operating condition. At 25 % O_2 temperature drops

more rapidly after the burner, however the overall temperature is rising. In overall a rise of about 50 K can be found due to the changes made.

In figure 23 the molar fraction of methane is completely different in comparison to figure 19. Methane is almost completely combusted after the burner exit and residual quantity of methane is of one magnitude lower than in the previous case. This is due to the lower velocities and higher temperature inside the burner. Thus also the length of the flame is significantly reduced.

As a conclusion of the comparison between the two investigated operating conditions one can say, that, as expected, with the same methane load the temperature is increased by approximately 50 K inside the furnace and the gas consumption could be lowered in order to reach the same desired temperature by the burning process. Yet this advantage is not worth the *increased temperature values alongside the burner walls* are , as this phenomenon is likely to damage the apparatus and to reduce the life time of the equipment. Here, with these initial simulation values one can clearly say, that O_2
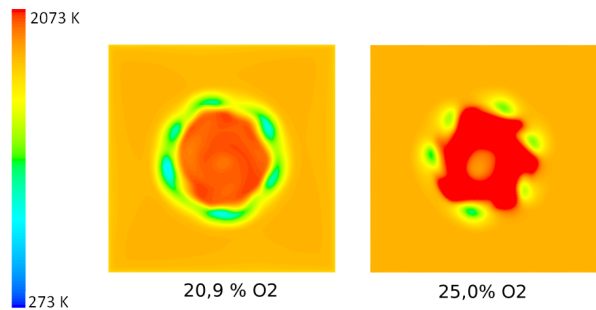
Figure 20: Temperature (in K) on the interpolation surface in the case with 20.9 % O_2 and 25 % O_2
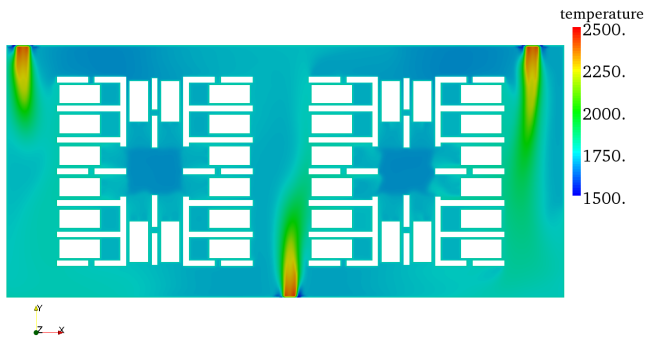
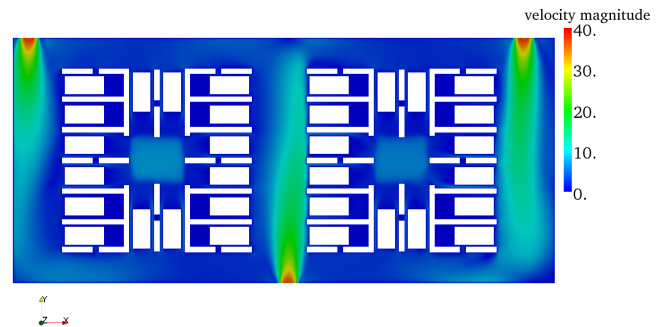Figure 18: Temperature (in K) on the plane at the height of the middle of the upper burners

Figure 21: Velocity magnitude (in m/s) on the plane at the height of the middle of the upper burners

Figure 19: Molar fraction of methane (v/v) on the plane at the height of the middle of the upper burners
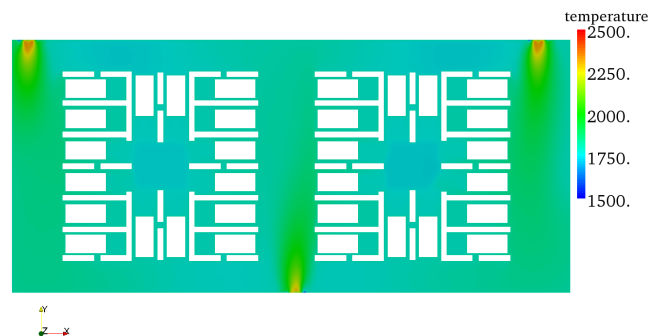
Figure 22: Temperature (in K) on the plane at the height of the middle of the upper burners

enrichment with the currently operating burners is not recommended.

CONCLUSION

In this work results and experience of the simulation of a high temperature furnace for the process of burning fire clay made in an ongoing industrial project are presented. The model is built up and first results are presented. The advective and the radiative heat transport together with combustion are included. Both the burners and the volume of the furnace are simulated. Results from the simulation of the burner are exported and imported into the simulation of the furnace as boundary conditions. For this an interpolation script was created.

Conclusions so far:

1. Combustion takes place outside the burner inside the furnace.

2. The asymmetric location of the burner can lead to an asymmetric distribution of heat. Thus fire clay bricks may be treated with different temperatures at different locations

3. Pockets containing fire clay to be burnt, that cannot be flushed with gas, do not seem to show the desired high temperatures, that can be found elsewhere in the fluid region.

4. According to our simulation results the enrichment of oxygen during the burning process is not a reasonable step with the current burners.

ACKNOWLEDGMENTS

FURTHER WORK

Next steps will include the sophistication of the model. On the one hand more detailed combustion modeling with more than one reaction will be used. The thermal transport from air to the bricks will be investigated as well as the temperature distribution at different points of time of the burning process. Also geometric variations will be simulated like a different distribution of bricks or a potential relocation of the middle burners.

REFERENCES

BAUKAL, C. and GERSHTEIN, V. (2001). *Computational fluid dynamics in industrial combustion*. CRC Press.

BöCKLE, S. *et al.* (2000a). "Simultaneous single-shot laser-based imaging of formaldehyde, oh and temperature in turbulent flames". *Proceedings of the Combustion Institute*, vol. 28, 279–286. Elsevier.

BöCKLE, S. *et al.* (2000b). "Single-shot laser-induced fluorescence imaging of formaldehyde with xef excimer excitation". *Applied Physics B*, **70**, 733–735.

FRASSOLDATI, A. *et al.* (2005). "Determination of NO$_x$ emmisions from strong swirling confined flames with an intergrated cfd-based procedure". *Chemical Engineering Science*, **60**, 2851–2869.

IUDICIANI, P. (2009). "A modified version of the reactingFoam tutorial for LES". URL http://www.tfd.chalmers.se/~hani/kurser/OS_CFD_2009/PieroIudiciani/IudicianiFinalSlides.pdf.

LANDENFELD, T. *et al.* (1998). "Laserdiagnostic and numerical studies of strongly swirling natural-gas flames". *Symposium (International) on Combustion*, **27(1)**, 1023–1029.

LAUNDER, B. (1989). "Second-moment closure and its use in modelling turbulent industrial flows". *Journal for Numerical Methods in Fluids*, **9(8)**, 963–985.

LAUNDER, B. and SPALDING, D. (1972). *Lectures in Mathematical Models of Turbulence*. Academic Press, London.

LAUNDER, B. and SPALDING, D. (1974). "The numerical computation of turbulent flows". *Computer Methods in Applied Mechanics and Engineering*, **3(2)**, 269–289.

Fluent 6.3.26 User's Guide ().

OpenCFD Limited (2011). "OpenFOAM source code". URL http://www.openfoam.com/.

TAO, F. *et al.* (2004). "A phenomenological model for the prediction of soot formation in diesel spray combustion". *Combustion and Flame*, **136**, 270–282.

V.BERGMANN *et al.* (1998). "Application of spontaneous raman and rayleigh scattering and 2d lif for the characterization of a turbulent CH$_4$/H$_2$/N$_2$ jet diffusion flame". *Applied Physics B*, **66**, 489–502.

Figure 23: Molar fraction of methane (v/v) on the plane at the height of the middle of the upper burners

8th International Conference on CFD in Oil & Gas, Metallurgical and Process Industries
SINTEF/NTNU, Trondheim Norway
21-23 June 2011

CFD11-124

PARCEL-BASED APPROACH FOR THE SIMULATION OF GAS-PARTICLE FLOWS

Stefan RADL[1]*, Charles RADEKE[2], Johannes G. KHINAST[2,3], Sankaran SUNDARESAN[1]

[1]Department of Chemical and Biological Engineering, Princeton University, Princeton, NJ

[2]Research Center Pharmaceutical Engineering GmbH, Graz, Austria

[3]Institute for Process and Particle Engineering, Graz University of Technology, Graz, Austria

* E-mail: sradl@princeton.edu

ABSTRACT

We focus on a parcel-based approach, similar to the one used by O'Rourke and Snider, 2010, which tracks the motion of a so-called "parcel" of particles. We derive a scaling law for a linear-spring dashpot interaction model that enables tracking of clouds of particles through DEM-based simulation of (scaled) pseudo-particles. This guarantees convergence to a DEM-based simulation of the unscaled system, i.e., a system where all the individual particles are tracked. We use a BGK-like relaxation term to model collisions between particles in dilute regions of the flow field. This combined approach is implemented in an in-house code that runs on GPUs (Radeke et al., 2010), and is used to study a granular jet impinging on a plane surface, as well as a simple shear flow. We find that a BGK-type relaxation model is necessary when using parcel-based approaches for capturing some prominent flow features.

Keywords: Discrete element method, simulation, granular impinging jet, shear flow.

NOMENCLATURE

Latin Symbols

c	Damping coefficient of primary particles, [kg/s].
C	Constant in the filter function.
d	Diameter, [m].
e_p	Coefficient of restitution.
E	Young's modulus, [N/m²].
f	Particle distribution function.
$\mathbf{F}$	Force, [N].
g_0	Radial distribution function.
G	Filter function.
h	Switch-off function.
k	Stiffness of primary particles, [N/m].
K	Constant.
m	Mass, [kg].
N	Number of particles in a parcel.
p	Pressure, [N/m²].
P	Probability distribution function.
R	Radius, [m].
r_{32}	Sauter mean radius of primary particles, [m].
t	Time, [s].
T	Granular temperature, [m²/s²].
$\mathbf{T}$	Torque, [N·m].
U	Initial velocity, [m/s].
$\mathbf{v}$	Velocity, [m/s].
y	Vertical distance, [m].

Greek Symbols

α	Scaling ratio.
β	Size ratio of colliding particles.
δ	Overlap, [m].
Δ	Dimensionless filter length.
ϕ	Volume fraction.
γ	Shear rate, [1/s].
η	Damping function.
κ	Exponent.
λ	Experimental parameter for the scattering angle.
μ	Friction coefficient.
Π	Dimensionless parameter.
θ	Scattering angle, [rad].
ρ	Particle density, [kg/m³].
$\boldsymbol{\sigma}$	Stress, [N/m²].
τ	Shear stress [N/m²].
τ_D	Relaxation time, [s].
$\boldsymbol{\omega}$	Rotation rate, [rad/s].

Sub/superscripts

*, *'	Dimensionless quantities.
BGK	Bhatnagar–Gross–Krook.
CP	Close packed.
eff	Effective.
el	Elastic.
eq	Equilibrium.
fluct	Fluctuation.
half	Half.
impact	At impact.
jet	Jet.
model	Modeled term.
n	Normal direction.
t	Tangential direction.
off	Value at switch-off.
p	Parcel.
prim	Primary particle.

PP	Particle-particle.
PW	Particle-wall.
roll	Rolling.
sample	At sample position.
0	Reference value.

INTRODUCTION

Discrete Particle Models (DPM), aim at tracking individual particles, or parcels thereof, in the flow domain. By using this approach, the treatment of a granular assembly made up by particles with different, size, density, shape, or composition is straightforward. Particle-based methods offer the possibility to include complex particle-wall interactions, the handling of rare events, as well as to extend the method to gas-particle-droplet systems (Link et al., 2009; O'Rourke et al., 2009; Zhao et al., 2009). Interest in the latter systems has been recently motivated by the pharmaceutics industry (Radeke and Khinast, 2011; Radeke et al., 2010), and also by classical applications like coking (typically performed in fluidized beds, see Darabi et al., 2010; Radmanesh et al., 2008), or catalyst impregnation. When using a DPM, two major approaches can be chosen: First, each particle in the system can be tracked. In this case, relatively simple models based on instantaneous ("hard-sphere" model), or enduring collision dynamics ("soft-sphere" model, recently summarized by Cleary, 2009) can be employed. The soft-sphere approach is more general, and allows also for the simulation of dense regions with enduring contacts, and is usually referred to as "Discrete Element Method" (DEM).

Second, the particle population can be represented by so-called "parcels" of particles, i.e., a cloud of particles, and hence the name parcel-based approach. Another way of interpreting such an approach is to think of a (discrete) approximation of the particle distribution function by test particles. For gas-solid flows, Andrews and O'Rourke, 1996, proposed the so-called "Multi-Phase Particle-In-Cell" (MP-PIC) approach, which is a parcel-approach. MP-PIC has been applied widely to fluidized beds, sedimentation, hopper flow, as well as other dense granular flows (O'Rourke et al., 2009; O'Rourke and Snider, 2010; Snider, 2001; Snider, 2007). In principle, a parcel-based approach does not require a second-phase to be present; however, MP-PIC requires an implicit coupling to the fluid phase due to stability reasons. The MP-PIC approach does not track collisions between particles directly, but employs a simple "particle pressure" model to prevent particles from becoming close-packed. Instead of modeling particle interaction forces with a particle pressure, Patankar and Joseph, 2001, explored the use of a simple soft-sphere model (without friction) in conjunction with a parcel-based method for a relatively small system. A similar approach was taken by Sakai et al., 2010; Sakai and Koshizuka, 2009, as well as Mokhtar et al., 2011.

Only recently Bierwisch et al., 2009 have shown that a parcel-based approach with contact detection, when using appropriately scaled interaction parameters, yields simulation results independent of the number of particles making up the parcel. Bierwisch et al., 2009 showed that

this scaling must be based on identical (i) particle density, (ii) coefficient of restitution, (iii) friction coefficients, and (iv) Young's modulus for their Hertzian repulsion force model. The scaling proposed by Bierwisch et al., 2009 yields stresses in the quasi-static regime, and parcel velocities in all regimes, that are scale independent. However, the analysis of Bierwisch et al., 2009, is based on a single collision, and studies on parcel behavior in dense to moderately dense systems (i.e., for particle volume fractions between 0.05 and 0.50) are still lacking.

Our first objective is to provide a scaling for the parameters of a DEM-based (linear spring-dashpot) model, such that stresses and velocities in the quasi-static flow regime are scale independent. Our second objective is to establish a method that takes the effect of sub-parcel collisions, not directly tracked when using a parcel-based approach, into account. We base our method on the ideas of O'Rourke and Snider, 2010. However, we aim at a strategy that is consistent with DEM, i.e., that yields a "pure" DEM-based simulation in a situation where only one particle is in the parcel. Our third objective is to demonstrate the effect of the proposed scaling and the sub-parcel collision model on the dynamics of two granular flows. Our simulations are based on an in-house code running on graphic processing units (GPUs).

MODEL DESCRIPTION

Dense Region

When using a parcel-based approach, one has to prevent over-packing in dense regions either with an (indirect) particle pressure model (Andrews and O'Rourke, 1996), or a model based on the direct detection of particle collisions (e.g., the strategy followed by Patankar and Joseph, 2001). In our model we have chosen to account for collisions by using a linear spring-dashpot model (see Eqns. 1-2), which is well established for granular dynamics. The details of our implementation are provided in Radeke et al., 2010, and here we only provide the most essential model equations. For our present work we included a spring-dashpot-slider model in the tangential direction (see Eqn. 2), as well as a rolling friction model between particles, and particles and the wall (see Eqns. 3-5; $\mathbf{v}_{roll}$ is a "rolling velocity" as defined by Luding, 2008).

$$\mathbf{F}_{ij,n} = k_n \cdot \delta_n \cdot \mathbf{n} + c_n \cdot \dot{\delta}_n \cdot \mathbf{n} \qquad (1)$$

$$\mathbf{F}_{ij,t} = \min\left(\mathbf{F}_{ij,n} \cdot \mu, \ k_t \cdot \delta_t \cdot \mathbf{t} + c_t \cdot \dot{\delta}_t \cdot \mathbf{t}\right) \qquad (2)$$

$$\mathbf{F}_{roll} = -\mu_{roll} \cdot \mathbf{F}_n \cdot \mathbf{v}_{roll} / |\mathbf{v}_{roll}| \qquad (3)$$

$$\mathbf{v}_{roll} = -R_{eff} \cdot [\mathbf{n} \times \boldsymbol{\omega}_1 - \mathbf{n} \times \boldsymbol{\omega}_2] \qquad (4)$$

$$\mathbf{T}_{roll} = R_1 \cdot \mathbf{n} \times \mathbf{F}_{roll} \qquad (5)$$

The central question when using a DEM-based model for the parcel-based approach is how to connect particle interaction parameters with parcel interaction parameters. Specifically, we ask the question, how

spring stiffness and damping coefficient must be scaled, when a parcel with a diameter $d_p = \alpha \cdot d_{prim}$ is used in the simulation (α is the ratio of the parcel diameter to the primary particle diameter).

In the following we describe the details on such a scaling that yields identical stresses for dense granular flow using the linear spring-dashpot model (Eqns. 1-5).

Scaling of Interaction Parameters

We base our analysis on equal energy densities in the original, and the coarse-grained system. This means that the density of the particles, as well as the translational velocity must be invariant. Also, the total rotational kinetic energy of the original and coarse-grained particles must be identical. The following analysis is valid for a linear spring-dashpot model with frictional slider, and is similar to the analysis for a Hertzian interaction model by Bierwisch et al., 2009. Since we base our analysis on an effective mass and radius for the collision, it is valid for both particle-wall, as well as for particle-particle collisions with arbitrary size ratios of the primary particles (i.e., the particles in the original system). Our analysis does not include differences in particle densities; however, an extension to these systems can be easily done in analogy to particle size differences.

We start with the differential equation for the overlap in normal direction from Newton's equation of motion:

$$m_{eff} \cdot \ddot{\delta}_n = k_n \cdot \delta_n + c_n \cdot \dot{\delta}_n. \qquad (6)$$

Here the effective mass is:

$$m_{eff} = \frac{m_i \cdot m_j}{(m_i + m_j)} = \frac{4\pi}{3} \frac{R_i^3 \cdot \rho_p \cdot \beta^3}{1 + \beta^3}. \qquad (7)$$

The effective radius is

$$R_{eff} = \frac{R_i \cdot R_j}{(R_i + R_j)} = \frac{R_i \cdot \beta}{1 + \beta}. \qquad (8)$$

Inserting these expressions, and using the dimensionless variables $\delta_n^* = \delta_n / R_i$, $\dot{\delta}_n^* = \dot{\delta}_n / v_0$, and $t^* = t/(R_i/v_0)$, as well as approximating Young's modulus with $E \approx k_n/R_i$ yields:

$$K_1 \cdot \ddot{\delta}_n^* = \frac{k_n \cdot \delta_n^*}{R_i \cdot \rho_p \cdot v_0^2} + \frac{c_n}{R_i^2 \cdot \rho_p \cdot v_0} \cdot \dot{\delta}_n^*, \qquad (9)$$

with $K_1 = 4\pi \cdot \beta^3 / [3(1 + \beta^3)]$. Thus, our scaling is based on the dimensionless (normal) overlap for the translational motion of a particle, with the reference length being the parcel diameter in the parcel approach and the particle diameter in the original unscaled problem, i.e., the relative overlap will remain invariant when scaling the system. From Eqn. 9 the following dimensionless parameters can be identified:

$$\Pi_1 = \beta, \ \Pi_2 = k_n / (R_i \cdot \rho_p \cdot v_0^2),$$
$$\Pi_3 = c_n / (R_i^2 \cdot \rho_p \cdot v_0) \qquad (10)$$

Π_1 requires a constant ratio of the radii of the colliding particles or parcels. This ratio will remain constant, as long as each parcel is made up by the same number of

particles N. Π_2 requires that $k_n / R_i = const$, since we require also the density and the reference velocity v_0 to be invariant. This is in agreement with the simulation results of Chialvo et al., 2010, which found that the pressure scales with k_n/R in a monodisperse, quasi-static granular flow.

Also, the stresses will be identical during scaling. This is because the ratio of the elastic normal forces in the original and scaled system is given by $F_{ij,n}^{el\,\prime} / F_{ij,n}^{el} = (k_n \cdot \alpha) \cdot (\delta_n^* \cdot \alpha \cdot R_i) / [k_n \cdot \delta_n^* \cdot R_i] = \alpha^2$. (our analysis was based on invariant non-dimensional overlaps δ_n^*). Since the macroscopic contact stress is given by the sum of the dyadic product of contact forces and the distances between two particles in a control volume (see Latzel et al., 2000, for details on the evaluation of stress tensors), the stresses are invariant when using this scaling in the dense regime.

Π_3 requires that $c_n / R_i^2 = const$, i.e., c_n scales with α^2, which results in an invariant coefficient of restitution when scaling the system, as well as a damping force that scales with α^2. Finally, it is easy to see that the already dimensionless friction coefficients μ and μ_{roll} must be kept constant when scaling the system.

Dilute Region

Previous Work

To take collisional effects between the particles in a parcel into account, O'Rourke and Snider, 2010, proposed a relaxation of the particle distribution function f to an equilibrium distribution f_{eq} in a BGK-like fashion (in our discrete approximation, f is represented by parcels having individual velocities **v**). Thus, they set:

$$\frac{\partial f}{\partial t} = \frac{f_{eq} - f}{\tau_D} \qquad (11)$$

to take into account particle collisions. O'Rourke and Snider, 2010, suggested the following correction to the parcel velocity to take collisions of particles within the parcel into account:

$$\mathbf{v}' = \frac{\mathbf{v} + (\delta t/(2\tau_D)) \cdot \overline{\mathbf{v}}}{1 + (\delta t/(2\tau_D))} \qquad (12)$$

Here, δt is the computational time step, and the mass-averaged particle velocity $\overline{\mathbf{v}}$ is given by a summation over parcels p near the parcel under consideration:

$$\overline{\mathbf{v}} = \sum_p (N \cdot m_{prim} \cdot \mathbf{v}) / \sum_p (N \cdot m_{prim}), \qquad (13)$$

where m_{prim} is the mass of primary particles, and N is the number of particles in each parcel. O'Rourke and Snider, 2010, proposed Eqns. 14 to 16 for calculating the damping time τ_D.

$$g_0(\phi_p) = \frac{\phi_{p,CP}}{\phi_{p,CP} - \phi_p + eps} \qquad (14)$$

$$\eta = (1 + e_p)/2 \qquad (15)$$

$$\frac{1}{\tau_D} = \frac{8 \cdot \sqrt{2}}{3 \cdot \pi} \cdot \frac{\phi_p}{r_{32}^3} \cdot g_0(\phi_p) \cdot \eta \cdot (1-\eta) \cdot$$

$$\frac{\sum_p N \cdot (d_{prim}/2 + r_{32})^4 \cdot (\mathbf{v} - \overline{\mathbf{v}})^2}{\sum_p N \cdot (d_{prim}/2 + r_{32})^2 \cdot \sqrt{(\mathbf{v} - \overline{\mathbf{v}})^2}} \qquad (16)$$

Here *eps* is a small number (taken to be 10^{-5}), r_{32} is the local Sauter-mean radius, and d_{prim} is the (primary) particle diameter of the particles making up the parcel. Eqn. 16 is based on the kinetic theory of granular flow with corrections for particle inelasticity, as well as local particle volume fraction. Also, one can take frictional contacts between particles into account by using an effective coefficient of restitution as proposed by Jenkins and Berzi, 2010. However, it should be kept in mind that the velocity relaxation proposed by O'Rourke and Snider, 2010, applies for an approach where collisions between parcels are not detected; when such collisions are detected, as in our present study, one must modify Eqn. 16 to avoid overdamping.

Modified Relaxation Model for Parcel Velocities

The equation for the collision frequency proposed by O'Rourke and Snider, 2010, models the effect of collisions between particles in different parcels. However, since we are already accounting for collisions between parcels in our implementation (via the spring-dashpot model), we need to model only collisions that occur with a frequency $1/\tau_{D,model}$, i.e.,

$$1/\tau_{\text{D,model}} = 1/\tau_D - 1/\tau_{\text{D,p}}. \qquad (17)$$

Assuming that the latter collision frequency between parcels follows the expression in Eqn. 16, and by requiring that the fluctuation velocities of particles and parcels are identical, one obtains:

$$1/\tau_{\text{D,model}} = 1/\tau_D (1 - 1/\alpha). \qquad (18)$$

Hence, the frequency of collisions $1/\tau_{D,model}$ that requires modeling in addition to the "resolved" collisions of the parcels, is somewhat lower in our model than the one proposed by O'Rourke and Snider, 2010. Note, that Eqn. 18 is consistent with a "full" simulation of the original system, where all particles are tracked, i.e., $\alpha = 1$ and $1/\tau_{D,model}$ equals zero.

Furthermore, we have to consider a correction in the dense limit, where parcel-parcel collisions become more frequent, and Eqn. 16 is no longer valid. This is because in the limit of close packing, contact forces due to enduring contacts (calculated directly with the spring-dashpot model) will already lead to a velocity relaxation. Thus, we have to reduce the modeled collision frequency at a certain volume fraction $\phi_{p,off}$ to avoid the divergence of $1/\tau_{D,model}$ at $\phi_p = \phi_{p,CP}$. We do this by multiplying Eqn. 18 with a factor $h(\phi_p)$ that approaches zero when ϕ_p equals $\phi_{p,CP}$:

$$h(\phi_p) = \min\left(1, \left[\frac{\phi_{p,CP} - \phi_p}{\phi_{p,CP} - \phi_{p,off}}\right]^{\kappa_{off}}\right) \qquad (19)$$

Here κ_{off} is an exponent that controls how fast the collision frequency model is switched off. We choose κ_{off} to be 8 for a rapid switch off, and $\phi_{p,off} = 0.60$. This rather abrupt switch off is motivated by the publications of Silbert et al., 2007, Reddy and Kumaran, 2007, as well as Chialvo et al., 2011. These authors show that there is an abrupt switch between an inertial regime (where the model given by Eqns. 14 and 18 is appropriate) and a quasi-static regime, for which a more complex rheological model has to be used (in our case the DEM-based model shown in Eqns. 1-5).

In summary, our modified relaxation model is consistent with a DEM-based simulation in the dense regime, and with a "full" DEM-based simulation in case the original system is modeled, i.e., a situation where α equals 1. In the dilute limit, and when the parcel size is much larger than the particle size, our relaxation model is identical to the model based on kinetic theory shown in O'Rourke and Snider, 2010.

Local Particle Volume Fraction and Velocity

For the relaxation of parcel velocities, one needs to know the local mean particle volume fraction ϕ_p, as well as the mean velocity of the parcels $\overline{\mathbf{v}}$. Previous work (e.g., O'Rourke and Snider, 2010) used a Cartesian grid for this purpose. This requires an interpolation of particle volume and velocity from and to this grid. We, however, reconstruct ϕ_p and $\overline{\mathbf{v}}$ from a spatial filtering on a spherical domain surrounding each parcel. Our filter function has the form:

$$G(R) = \begin{cases} C_2 + (R_0/R)^2 & R < (R_i + R_j) \cdot \Delta_{BGK} \\ 0 & R \geq (R_i + R_j) \cdot \Delta_{BGK} \end{cases}, \qquad (20)$$

with parameters C_2, and R_0 chosen such that the integral of $G(R)$ in a spherical domain is unity. This filter guarantees that the mean quantities are evaluated at the center of the parcel. For our simulations we choose $\Delta_{BGK} = 3$, i.e., filtering was performed in a sphere with a diameter three times the parcel diameter.

RESULTS

Granular Jet

Cheng et al., 2007, have experimentally investigated the normal impact of 0.050 mm to 2.1 mm glass and brass particles (monodispers and spherical) on a circular disc. They showed that the characteristic scattering angle θ_{half} of the rebounding particles is influenced by the ratio of particle and jet diameter d_p/d_{jet}:

$$\theta_{half} = \text{atan}\left(\lambda \cdot 2 \cdot d_p / d_{jet}\right) \qquad (21)$$

with $\lambda = 1.05 \pm 0.05$. Thus, for a small particle-to-jet ratio the granular jet behaves like a liquid without a scattering of particle velocities. When using our parcel-approach, the goal is that only the size of the primary particles should affect the scattering angle, and not the parcel diameter itself.

We performed simulations using (i) an unscaled system (i.e., the interaction parameters in Eqns. 1-5 were not

changed with parcel size); (ii) a scaled system (scaling based on the dimensionless parameters displayed in Eqn. 10), but without relaxation model; as well as (iii) a scaled system with the relaxation model shown in Eqn. 18. Also, a simulation of the original system, for which the motion of the primary particles was calculated directly, was performed. The simulation parameters are listed in Table 1. The damping coefficient c_n was calculated from the coefficient of restitution (see Luding, 2008), and we set $c_t = c_n$.
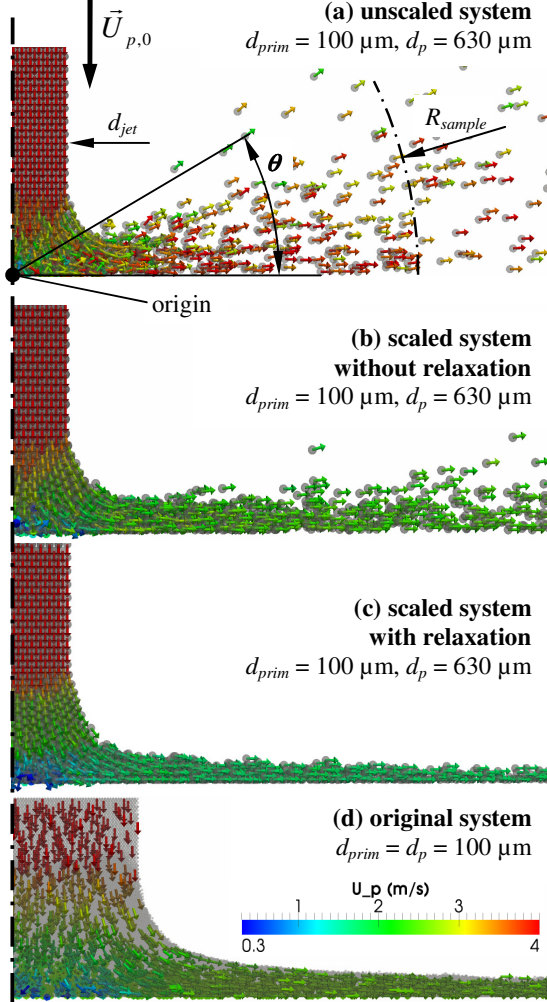
Figure 1: Particle velocities near the impact region of a granular jet. The jet (which has a circular cross section with diameter d_{jet}) impacts the planar surface under an angle of $\theta_{impact} = \pi/2$.

The scattering patterns of these three systems are shown in Figure 1a-c; a magnified version of a slightly smaller region near the impact point for the original system is shown in Figure 1d. Here we show front views of the particle jet, which approaches the planar surface from the top. For the results displayed in Figure 1 we have chosen the scaling factor α as 6.3, i.e., we have grouped 250 single particles into one parcel.

As can be easily seen from Figure 1a, the unscaled system represents a case with a much larger (effective) particle diameter, and the characteristic scattering angle is much larger than that observed in the original system (see Figure 1d). This behavior is expected, since we do

not perform any scaling, and the scattering angle is in good agreement with the experimental results of Cheng et al., 2007 (see the comparison of simulation results for the unscaled system indicated by dots with the correlation indicated by the bold line in Figure 3).

Table 1: Parameters for the granular jet simulations.

Parameter	*Value*
d_{jet}	7.3 [mm]
y_{jet}	25 [mm]
d_{jet} / d_p	3.5; 14.6; 29.2; 73
d_p	0.10 - 2.19 [mm]
$U_{p,0}$	1 - 8 [m/s]
ϕ_p	0.60
ρ_p	2500 (glass)
e_p	0.75, 0.95
μ_{PP}	0.10
μ_{PW}	0.15
μ_{roll}	0.01
k_n	306 [N/m]
k_t	88 [N/m]
R_{sample}	63.5 [mm], 20 [mm]

Appropriate scaling of the system significantly lowers the scattering angle (see Figure 1b), even in the case no relaxation is employed. However, some scattering of parcels still occurs. Employing the BGK-like relaxation (Figure 1c) finally yields a parcel behavior similar to the one observed in the original system with 250-times more particles.
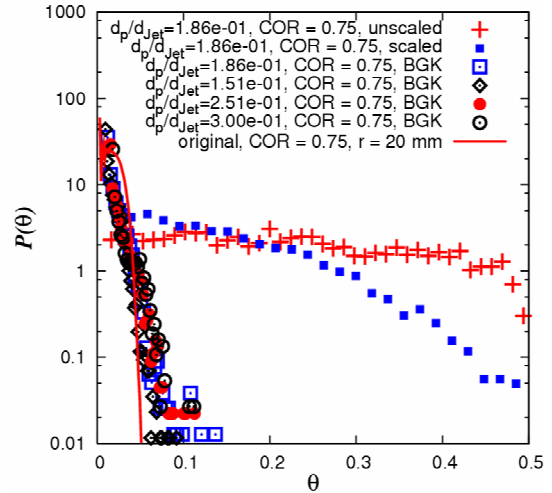
Figure 2: The scattering angle distribution - comparison of the original system (red line), with results using the parcel approach (symbols).

To quantify the effect of the BGK-like relaxation, we compare the distribution of particle scattering angles in Figure 2. Specifically, we plot the number density distribution $P(\theta)$ of the scattering angle θ (i.e., the angle measured between the impact surface and the particle position as illustrated in Figure 1a). To calculate $P(\theta)$, we only consider particles located at a radial distance of $R_{sample} = 63.5 \pm 2.5$ mm from the origin, as per Cheng et

al., 2007; for the original system, though, we set R_{sample} = 20 ± 2.5 mm, since we were unable to simulate the full system. As can be seen from Figure 2, the unscaled and scaled systems give a wide distribution of scattering angles, with scattering half angles θ_{half} (defined as $\int_0^{\theta_{half}} P(\theta)d\theta = 0.5$) of 0.28 and 0.14, respectively. This result is in distinct contrast to the very narrow distribution of the original system (shown by the red line in Figure 2). However, when we employ the relaxation model, all simulations using a larger parcel diameter (see the symbols for different values of d_p/d_{jet} in Figure 2) agree reasonably well with behavior of the original system. The improved agreement of the BGK cases indicates the importance of the relaxation model in replicating the behavior of the much smaller particles within a parcel.
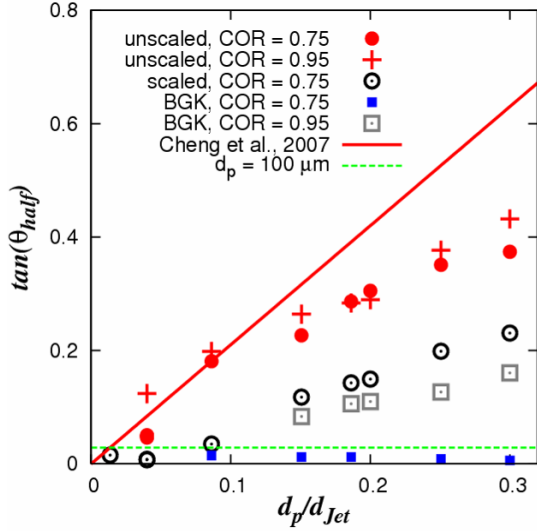
Figure 3: The scattering half angle θ_{half} as a function of dimensionless parcel size (symbols represent simulation results, lines are theoretical predictions).

In Figure 3 we show a summary of our results for the granular jet for various scalings, expressed as d_p/d_{jet}. Clearly, when the system is unscaled (filled circles and crosses), the parcels behave like large particles. In this systems the scattering half angle is close to the correlation established by Cheng et al., 2007, and given in Eqn. 21. For the unscaled system we find that the coefficient of restitution has no significant effect at large dimensionless parcel diameters. Only for the smallest system studied (i.e., d_p/d_{jet} = 0.04) there is a large relative difference for our results involving $e_p = 0.75$ and $e_p = 0.95$. The cause for this behavior is unclear, as previous computational studies (e.g., that of Huang et al., 2010) could not afford to simulate that large systems (the simulations for d_p/d_{jet} = 0.04 required us to track 0.97 million particles) and the experiments of Cheng et al., 2007, only included particles that had a coefficient of restitution equal to 0.75.

The scaled system using the BGK-like relaxation model (blue filled squares in Figure 3) shows a more realistic behavior, as we obtained the small scattering angles typical for a system made up by particles of 100 µm (the scattering angle for 100 µm particles as expected from

Eqn. 21 is shown as green dashed line Figure 3). Our simulation results for the original system are indicated by the leftmost black circle at d_p/d_{jet} = 0.0137. These simulations involved already 2.7 million particles in a domain half the size as the one used for the other cases. Our results when using the relaxation model (blue filled squares in Figure 3) are somewhat below the expected results from Eqn. 21, as well as our simulations of the original system. This behavior is also visible in Figure 2, where the simulation results using the BGK relaxation do not match perfectly with the original system (red line in Figure 2). It seems that the chosen expression for the relaxation time slightly over-predicts the collision frequency, even though we already subtract the collision frequency between parcels. More work, and possibly a more suitable model, is required to explain this difference, and to make the scattering angles in both systems collapse. Another explanation could be that the switch off particle volume fraction of $\phi_{p,off}$ = 0.60 in our simulations is somewhat too high. Indeed, simulations with lower values for $\phi_{p,off}$ showed that such a parameter adjustment could be used to improve the collapse. However, there is no rationale for choosing a different value for $\phi_{p,off}$, and hence we suggest to first improve the collision frequency model, rather than to perform a parameter fit.

Simple Shear

We performed simple shear flow simulations using a cubic box of particles. Lees-Edwards boundary conditions (LEBCs, Lees and Edwards, 1972) were employed on two sides of the box, whereas on the other four sides periodic boundaries were set. The LEBCs impose a steady shear motion on the particles. Stresses, fabric tensors, velocities, as well as particle rotation rates were recorded during the simulation, and then averaged over the box. Stresses were probed by calculating the contact and streaming stress tensor for each particle, and then summing up the contributions from each particle. A similar procedure was employed for the fabric tensor (results not shown). Both procedures (i.e., for the stress and the fabric) follow the work of Latzel et al., 2000. The granular temperature in the system was estimated by calculating the velocity fluctuation tensor $\underline{\underline{\mathbf{v}^2_{p,fluct}}}$, and then setting

$$T = tr\left(\underline{\underline{\mathbf{v}^2_{p,fluct}}}\right)\Big/3 \, . \qquad (22)$$

The velocity fluctuations were calculated from the instantaneous particle velocity and the local average velocity. The latter was calculated under the assumption of a linear velocity profile.

Similar to the granular jet, we performed shear flow simulations in (i) an unscaled system (i.e., the interaction parameters for the contact model were not changed with parcel size); (ii) a scaled system (scaling based on Eqn. 10), but without relaxation model; as well as (iii) a scaled system with relaxation model. For our simulations we used the same particle interaction parameters as shown in Table 1, except for μ_{roll}, which was set to zero. Simulations were performed with ϕ_P =

0.55, $e_p = 0.75$, and the shear rate was chosen such that $\gamma* = \gamma \cdot d_{prim} \big/ \sqrt{k/(\rho_p \cdot d_{prim})} = 10^{-4}$ was constant. Systems with different parcel sizes where investigated by holding the box size (0.015 m) and the primary particle diameter (d_{prim} = 100 µm) constant, and grouping between 4 and 8192 particles into one parcel. Also, a limited number of simulations were performed with $\phi_P = 0.62$ to show the system behavior in the quasi-static flow regime. Each of these simulations involved approximately 4,000 parcels in a box of variable size to investigate the effect of the parcels size.

Granular Temperature

Already previous work (Benyahia and Galvin, 2010) showed that the granular temperature in a wall-bounded shear flow dramatically increases with parcel size. This finding is expected, since a simple calculation based on the kinetic theory of granular flow would predict that (see, e.g., Sangani et al., 1996):

$$\frac{T}{(\gamma \cdot d_p)^2} = \frac{1 + \pi/12 \cdot [1 + 5/(8 \cdot \phi_p \cdot g_0)]^2}{15 \cdot (1 - e_p)} \qquad (23)$$

Here g_0 is the radial distribution function at contact, for which we use the expression in Eqn. 15. Thus, by just scaling the particle diameter, and performing a naive DEM-based simulation leads to a significant overestimation of the granular temperature in the system.
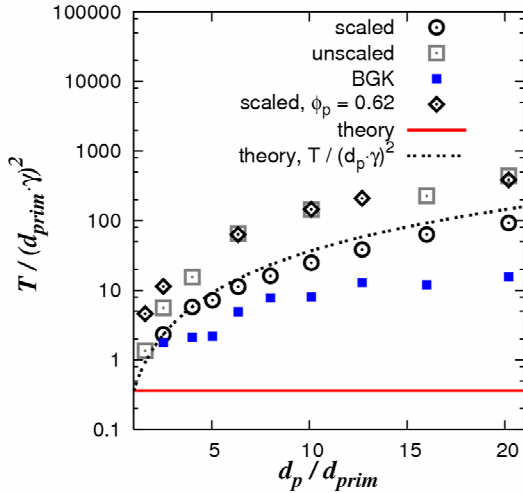
Figure 4: Granular temperature scaled by the velocity fluctuation in the original system ($d_{prim} \gamma)^2$ (symbols represent simulation results, lines are theoretical predictions, $\phi_P = 0.55$ unless otherwise stated).

The results for the granular temperature (made dimensionless with the shear rate and the primary particle diameter d_{prim}) are shown in Figure 4. The red bold line represents the expected granular temperature of the original system for $\phi_P = 0.55$ estimated from Eqn. 23, which should remain constant when using the relaxation model. Also, we have included a line representing the theoretical prediction using Eqn. 23 for the increase in granular temperature in the simulations without relaxation model (i.e., the scaled and unscaled system should behave like a system consisting of large

particles, and the granular temperature should increase proportional to $(d_p/d_{prim})^2$). Clearly, the results for the scaled system and $\phi_P = 0.55$ agree reasonably well with the theory of Sangani et al., 1996, which slightly overpredicts the granular temperature. The unscaled system, as well as the scaled system with $\phi_P = 0.62$ shows a higher granular temperature, but the same principal trend as the theoretical prediction of Sangani et al., 1996. This is because the unscaled system represents a case with a higher coefficient of restitution - this increase can be easily understood by inspection of Eqn. 23. The scaled system with $\phi_P = 0.62$ is in the quasi-static regime, for which the theory of Sangani et al., 1996, is no longer applicable.

The simulations using the BGK-like relaxation in Figure 4 show a lower granular temperature, i.e., the system behavior is closer to the theoretical prediction of the original system (bold red line). Still the granular temperature is significantly overpredicted using the relaxation model given by Eqns. 14 and 18. Thus, the relaxation to the local mean velocity is too week to dampen the velocity fluctuations of the parcels. Also, the scaled granular temperature increases with parcel size, indicating that the dependency of the current relaxation model on the parcel size is too weak.

Stresses
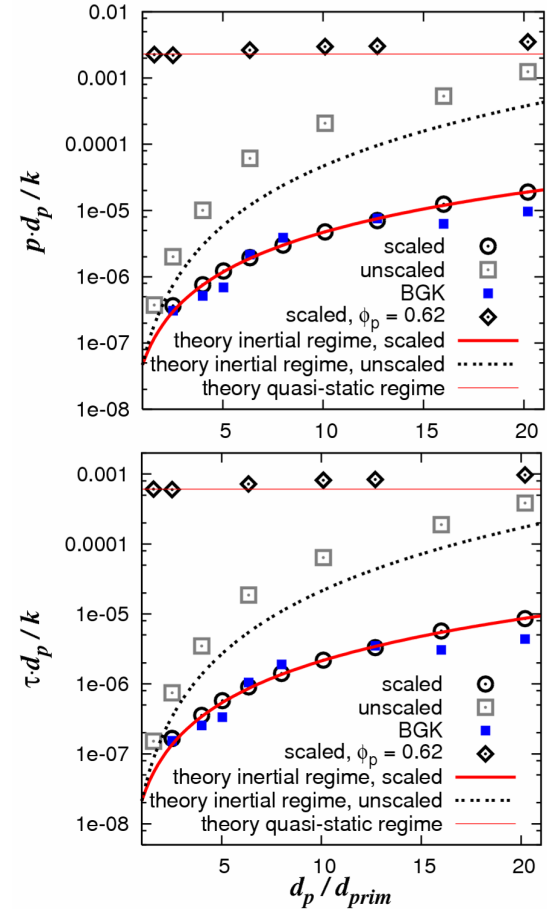
Figure 5: Pressure (top) and shear stress (bottom) for different parcel diameters and filter sizes in a scaled and unscaled system, as well as a in a system with BGK-like relaxation (symbols represent simulation results, lines are theoretical predictions, $\phi_P = 0.55$ unless otherwise stated).

The results for the sum of contact and streaming stresses are shown in Figure 5. Here we have defined the pressure as $p = (\sigma_{xx} + \sigma_{yy} + \sigma_{zz}) / 3$, and the shear stress τ is the stress component pointing in the shearing direction and acting on the surface normal to the gradient direction (the other shear stress components are much smaller).

As can be seen from Figure 5, with increasing parcel size both pressure and shear stress dramatically increase for the systems with $\phi_P = 0.55$. This is explained with the fact that these systems correspond to a system with a higher dimensionless shear rate $\gamma^{*\prime}$, in case we define this dimensionless shear rate with $\gamma^{*\prime} = \gamma \cdot d_p / \sqrt{k / (\rho_s \cdot d_p)}$, i.e., we use the parcel diameter instead of the primary particle diameter. Thus, $\gamma^{*\prime}$ increases with $(d_p/d_{prim})^{3/2}$ in the unscaled system, and with (d_p/d_{prim}) in the scaled system since our scaling is based on k/d_p = const. As our simulations were performed with $\mu_{PP} = 0.1$, and $\gamma^{*\prime} < 10^{-2}$, the systems with $\phi_p = 0.55$ were in the inertial regime, and the systems with $\phi_p = 0.62$ were in the quasi-static regime (for an exact regime definition refer to Chialvo et al., 2011). Previous studies, and simple theory tells us that pressure and shear stress scale with the dimensionless shear rate squared in the inertial regime (at constant volume fraction and friction coefficient). In the quasi-static regime the stresses are expected to remain constant, and only a moderate increase for $\gamma^{*\prime} > 10^{-3}$ (which corresponds to $d_p/d_{prim} > 10$ in our scaled system) is anticipated due to a regime transition into an intermediate flow regime (see the findings of Chialvo et al., 2011). We have included lines showing the expected trends for the stresses in the quasi-static and inertial flow regime in Figure 5 (see the red solid lines).

As can be seen, the simulation results for the scaled system agree well with the expected scalings in the inertial and quasi-static regime. For the latter regime our simulation results for the stresses (black diamonds in Figure 5) slightly increase with parcel size above d_p/d_{prim} = 10 due to the transition to an intermediate flow regime. This increase has also been observed by Chialvo et al., 2011, for flows at different dimensionless shear rates.

Also the results for the unscaled system with $\phi_p = 0.55$ follow the theoretical predictions for flow in the inertial flow regime; however, they show somewhat higher stresses. This is explained by the fact that for the unscaled system also the coefficient of restitution increases with parcel size, which results in higher granular temperature and stresses.

In case the BGK-like relaxation is applied, the sum of contact and streaming stress stays nearly unaffected (see the filled blue boxes in Figure 5), and only for $d_p/d_{prim} > 15$ a rather small drop in the stresses is observed. Thus, even in case we perform a BGK-like relaxation, the stresses do not significantly change compared to a scaled system.

CONCLUSION

Even though parcel-based approaches have been in use for more than fifteen years since the pioneering work of Andrews and O'Rourke, 1996, there is still a strong need to analyze the basic features of this simulation approach. Recent literature highlights this need (see the work of Benyahia and Galvin, 2010; Benyahia and Sundaresan, 2011).

In this work we performed a relaxation of parcel velocities to a local mean velocity to account for collisions of particles making up the parcels. We claim that such a relaxation is necessary in any DEM-based simulation that uses bigger (pseudo) particles, and has the ambition to model the original system consisting of a much higher number of primary particles. Even in cases where a proper scaling of particle interaction parameters is performed (i.e., a scaling like the one proposed by Bierwisch et al., 2009, or the one presented in this work for the linear spring-dashpot model), a relaxation seems necessary. Thus, our simulations involving the relaxation model gave a nearly parcel-sized independent behavior for a granular jet impinging on a planar surface, while simulations without relaxation did not.

The challenge for parcel-based methods is to correctly compute the collision rate, the granular temperature and the inter-parcel stress in a dilute to moderately dense region. Our simulations for a simple shear flow in the inertial regime agree with the kinetic theory of granular flow that predicts a massive increase in granular temperature and stress with parcel size when no relaxation is used. For the stress this is explained with the higher dimensionless shear rate when parcels are used, i.e., the shear rate increases with $(d_p/d_{prim})^{3/2}$ in an unscaled system, and with d_p/d_{prim} in a system with scaled interaction parameters to yield identical behavior in quasi-static granular flow. Thus, there is no easy way of scaling parcel interaction parameters to yield identical flow behavior in the inertial flow regime. For the quasi-static flow regime, however, scaling is less problematic and we observe a nearly constant stress in our shear flow simulations. Only the transition to an intermediate flow regime, as defined by Chialvo et al., 2011, will lead to an increase in the stresses in a correctly scaled system.

For simple shear flow in the inertial regime the use of the relaxation model based on O'Rourke and Snider, 2010, used in a slightly modified form in our work, leads to a granular temperature for the parcel-based approach closer to the original system, but this is not true for the stress. It is still unclear how one can obtain an identical stress for flows in the inertial regime when using a parcel-based approach. Clearly, more work is required, especially in connection with the relaxation model, which is subject of ongoing work.

ACKNOWLEDGEMENT

APPENDIX

List of animation files:

(A1) "1000k_boxLEBC_PrincetonLogoMix.avi"
(simple shear of 10^6 particles in a box with Lees-Edwards boundary conditions)

REFERENCES

ANDREWS, M.J. and O'ROURKE, P.J., (1996), "The multiphase particle-in-cell (MP-PIC) method for dense particulate flows", *International Journal of Multiphase Flow*, **22**, 379-402.

BENYAHIA, S. and GALVIN, J.E., (2010), "Estimation of Numerical Errors Related to Some Basic Assumptions in Discrete Particle Methods", *Industrial & Engineering Chemistry Research*, **49**, 10588-10605.

BENYAHIA, S. and SUNDARESAN, S., (2011), "Do We Need Sub-grid Scale Corrections for Both Continuum and Discrete Gas-Particle Flow Models", *(Submitted for Publication)*.

BIERWISCH, C., KRAFT, T., RIEDEL, H., and MOSELER, M., (2009), "Three-dimensional discrete element models for the granular statics and dynamics of powders in cavity filling", *Journal of the Mechanics and Physics of Solids*, **57**, 10-31.

CHENG, X., VARAS, G., CITRON, D., JAEGER, H.M., and NAGEL, S.R., (2007), "Collective behavior in a granular jet: Emergence of a liquid with zero surface tension", *Physical Review Letters*, **99**, 188001-1-188001-4.

CHIALVO, S., SUN, J., and SUNDARESAN, S., (2010), "Rheology of simple shear flows of dense granular assemblies in different regimes", APS DFD Meeting, Long Beach, California, American Physical Society.

CHIALVO, S., SUN, J., and SUNDARESAN, S., (2011), "Bridging the rheology of granular flows in three regimes", *(Submitted for Publication)*.

CLEARY, P.W., (2009), "Industrial particle flow modelling using discrete element method", *Engineering Computations*, **26**, 698-743.

DARABI, P., POUGATCH, K., SALCUDEAN, M., and GRECOV, D., (2010), "Agglomeration of Bitumen-Coated Coke Particles in Fluid Cokers", *International Journal of Chemical Reactor Engineering*, **8**, A122.

HUANG, Y.J., CHAN, C.K., and ZAMANKHAN, P., (2010), "Granular jet impingement on a fixed target", *Physical Review e*, **82**, 031307-1-031307-8.

JENKINS, J.T. and BERZI, D., (2010), "Dense inclined flows of inelastic spheres: tests of an extension of kinetic theory", *Granular Matter*, **12**, 151-158.

LATZEL, M., LUDING, S., and HERRMANN, H.J., (2000), "Macroscopic material properties from quasi-static, microscopic simulations of a two-dimensional shear-cell", *Granular Matter*, **2**, 123-135.

LEES, A.W. and EDWARDS, S.F., (1972), "Computer Study of Transport Processes Under Extreme Conditions", *Journal of Physics Part C Solid State Physics*, **5**, 1921-1929.

LINK, J.M., GODLIEB, W., TRIPP, P., DEEN, N.G., HEINRICH, S., KUIPERS, J.A.M., SCHONHERR, M., and PEGLOW, M., (2009), "Comparison of fibre optical measurements and discrete element simulations for the study of granulation in a spout fluidized bed", *Powder Technology*, **189**, 202-217.

LUDING, S., (2008), "Cohesive, frictional powders: contact models for tension", *Granular Matter*, **10**, 235-246.

MOKHTAR, M.A., KUWAGI, K., TAKAMI, T., HIRANO, H., and HORIO, M., (2011), "Validation of the Similar Particle Assembly (SPA) Model for the Fluidization of Geldart's Group A and D Particles", *AIChE Journal (Accepted)*.

O'ROURKE, P.J. and SNIDER, D.M., (2010), "An improved collision damping time for MP-PIC calculations of dense particle flows with applications to polydisperse sedimenting beds and colliding particle jets", *Chemical Engineering Science*, **65**, 6014-6028.

O'ROURKE, P.J., ZHAO, P., and SNIDER, D., (2009), "A model for collisional exchange in gas/liquid/solid fluidized beds", *Chemical Engineering Science*, **64**, 1784-1797.

PATANKAR, N.A. and JOSEPH, D.D., (2001), "Modeling and numerical simulation of particulate flows by the Eulerian-Lagrangian approach", *International Journal of Multiphase Flow*, **27**, 1659-1684.

RADEKE, C. and KHINAST, J.G., (2011), "Wet Mixing of Powders - a Large Scale GPU Implementation", *(in Preparation)*.

RADEKE, C.A., GLASSER, B.J., and KHINAST, J.G., (2010), "Large-scale powder mixer simulations using massively parallel GPU architectures", *Chemical Engineering Science*, **65**, 6435-6442.

RADMANESH, R., CHAN, E., and GRAY, M.R., (2008), "Modeling of mass transfer and thermal cracking during the coking of Athabasca residues", *Chemical Engineering Science*, **63**, 1683-1691.

REDDY, K.A. and KUMARAN, V., (2007), "Applicability of constitutive relations from kinetic theory for dense granular flows", *Physical Review e*, **76**, 061305.

SAKAI, M. and KOSHIZUKA, S., (2009), "Large-scale discrete element modeling in pneumatic conveying", *Chemical Engineering Science*, **64**, 533-539.

SAKAI, M., SHIBATA, K., KAWASAKI, V.M., and KOSHIZUKA, S., (2010), "Numerical Simulation of a Bubbling Fluidized Bed by the Coarse Grain Modeling of DEM (in Japanese)", *Journal of the Society Powder Technology Japan*, **47**, 17-25.

SANGANI, A.S., MO, G.B., TSAO, H.K., and KOCH, D.L., (1996), "Simple shear flows of dense gas-solid suspensions at finite Stokes numbers", *Journal of Fluid Mechanics*, **313**, 309-341.

SILBERT, L.E., GREST, G.S., BREWSTER, R., and LEVINE, A.J., (2007), "Rheology and contact lifetimes in dense granular flows", *Physical Review Letters*, **99**, 068002-1-068002-4.

SNIDER, D.M., (2001), "An incompressible three-dimensional multiphase particle-in-cell model for dense particle flows", *Journal of Computational Physics*, **170**, 523-549.

SNIDER, D.M., (2007), "Three fundamental granular flow experiments and CPFD predictions", *Powder Technology*, **176**, 36-46.

ZHAO, P., O'ROURKE, P.J., and SNIDER, D., (2009), "Three-dimensional simulation of liquid injection, film formation and transport, in fluidized beds", *Particuology*, **7**, 337-346.

8th International Conference on CFD in Oil & Gas, Metallurgical and Process Industries
SINTEF/NTNU, Trondheim Norway
21-23 June 2011

CFD11-125

A CFD STUDY OF ENTRAINED-FLOW GASIFIERS USING TWO FEED TYPES

Vikram SREEDHARAN[1]* , **Bjørn H. HJERTAGER[2]**, **Tron SOLBERG[1]**

[1] ...

[2] ...

...

ABSTRACT

A computational fluid dynamics (CFD) model for gasification within two different types of gasifiers have been developed for two different kinds of feedstock. This model captures the important physical and chemical processes that occur during gasification. An Euler-Lagrange formulation has been used, assuming dilute flow (volume fraction of particle/droplet phase less than 10%), with use of the discrete phase model (DPM). The first gasifier involves gasification of coal in an entrained-flow coal gasifier. Two different reduced chemical kinetics schemes have been considered for the coal gasification model. The second gasifier deals with gasification of heavy oil. The CFD predictions for the two gasifiers have been compared with experimental data.

Keywords: Particle tracking, reactive flows, heat and mass transfer, energy and environment, coal, heavy oil, gasification, chemical reactors.

NOMENCLATURE

Greek Symbols

ρ	Mass density, [kg/m^3].
μ	Dynamic viscosity, [kg/m.s].
ε	Turbulence dissipation, [m^2/s^3].

Latin Symbols

f	Mixture fraction, [-].
h	Specific enthalpy, [J/kg].
k	Turbulence kinetic energy, [J/kg].
Nu	Nusselt number, [-].
P	Pressure, [Pa].
Pr	Prandtl number, [-].
Sc	Schmidt number, [-].
T	Temperature, [K].
$\mathbf{u}$	Velocity, [m/s].
Y	Mass fraction, [-].

Sub/superscripts

g	Gas.
p	Particle.
k	Phase k.
i	Index i.
j	Index j.

INTRODUCTION

Among the different types of gasifiers in widespread use, entrained-flow gasifiers are popular for the gasification of coal and petcoke, in particular, for power generation and production of synthetic fuels. This type has also been utilized for the gasification of heavy oil, for instance in the Shell gasification process (SGP) and in Texaco gasification studies. The entrained-flow gasifier is characterized by high operating temperatures (in excess of 1400°C) and an operating pressure ranging from 20 to 70bar. These high temperatures are necessary to ensure high carbon conversion despite the short residence time of the feedstock within the reactor. In entrained-flow gasifiers the fine coal particles react with steam and oxygen flowing co-currently. The operating temperature of these gasifiers exceeds the ash melting temperature of the coal feedstock (Higman and Burgt, 2008). This ensures a high carbon conversion of the coal and destruction of tars and oils as well as low methane content of the resulting synthesis gas (syngas). Entrained-flow gasifiers have a relatively high oxygen prerequisite, and the raw syngas has high sensible heat content. Virtually all types of coal can be used in this type of gasifier, though it is often not economically viable to use high moisture and high ash content coals. The ash produced in entrained-flow gasifiers consists of a black, fine, inert, gritty material.

The flexibility of feedstock type, the widespread availability of coal, increased environmental concerns and fluctuations in the price of natural gas are factors which have contributed to gasification emerging as an attractive option for power generation, when used in the context of technologies like integrated gasification combined cycle (IGCC) plants. Gasification is also widely used for the synthesis of chemicals such as methanol, ammonia, industrial gases, Fischer-Tropsch products and clean fuel gas (Higman and Burgt, 2008).

In the present work, two entrained-flow gasifiers using different feeds have been studied. The first gasifier is

based on a numerical study by Ajilkumar et al (2009), in which the feedstock is a sub-bituminous coal with a completely defined composition (proximate and ultimate analysis). In the second gasifier, the feedstock is heavy oil as experimentally investigated by Ashizawa et al (2005). Attention is given to the different chemical reaction schemes describing the gasification, i.e., devolatilization, char combustion and the gas-phase reactions for the different feedstock. Furthermore, turbulent multiphase (dilute) flow with combustion is the focus here, with the use of an appropriate model for radiation.

THEORETICAL FORMULATION

Gasification involves a number of complex physical and chemical processes such as turbulence, multiphase flow, heat transfer, mass transfer and chemical reactions. When a feedstock is introduced into the reactor at high temperature, usually with air or oxygen as a carrier, a number of physical and chemical processes occur within the gasifier. Quite often, to obtain the benefit of savings in space and energy, gasification takes place at high pressures. If the feedstock used is a dry feed coal, the volatile portion in the coal particles is consumed during devolatilization and the resulting char is burned or gasified.

In an entrained-flow gasifier, the coal particles would mainly follow the gas flow which is represented typically as a dilute flow regime. In this regime, the volume occupied by the particles and the particle-particle interactions are assumed to be negligible. A criterion used in the CFD software FLUENT for dilute flow is that the particle volume fraction should be less than 10%.

Multiphase Flow

A discrete phase model (DPM) is appropriate for multiphase flows where the dispersed phases are dilute. The continuous gas phase is described in an Eulerian formulation by solving conservation equations for mass, momentum and energy, while the dispersed phases are described in a Lagrangian formulation by tracking the exchange of mass, momentum and energy for individual particles.

Continuous Phase

Turbulent reactive flow taking place in the continuous gas phase can be described by Favre-averaged balance equations for mass, momentum and energy. The governing transport equations can be written in a generalized form using Cartesian tensor notation as

$$\frac{\partial}{\partial t}\left(\rho\Phi\right)+\frac{\partial}{\partial x_j}\left(\rho u_j\Phi\right)=$$
$$\frac{\partial}{\partial x_j}\left(\frac{\mu_t}{\sigma_\Phi}\frac{\partial\Phi}{\partial x_j}\right)+S_\Phi+S_{\Phi P} \tag{1}$$

Here, the dependent variable $\Phi = 1, u_i, h, Y_k k, \varepsilon$ represents a variable such as mass, momentum, energy, species,

turbulent kinetic energy and turbulent kinetic energy dissipation rate, respectively. S_Φ is the standard source term in the governing equations and $S_{\Phi P}$ is the source term taking into account the interaction with the dispersed particle phase. The turbulent eddy viscosity

$$\mu_t = \rho C_\mu \frac{k^2}{\varepsilon} \tag{2}$$

is determined from a standard $k - \varepsilon$ turbulence model.

Discrete Phase

The mass conservation equation for the discrete phase particle (solids or droplets) takes the following form

$$\frac{dm_p}{dt}=\frac{dm_1}{dt}+\frac{dm_2}{dt}+\frac{dm_3}{dt}+\frac{dm_4}{dt}+\frac{dm_5}{dt}+\frac{dm_6}{dt} \tag{3}$$

Where, $m_1 - m_6$ are the mass of gas originating from the chemical reactions (11) - (16).

The trajectory of the discrete phase particles are determined from Newton's second law of motion. The force balance on the particle can be written as

$$\frac{du_{pi}}{dt}=F_D\left(u_{gi}-u_{pi}\right)+g_i\frac{\left(\rho_p-\rho_g\right)}{\rho_p}+$$
$$\frac{\rho_g}{2\rho_p}\frac{d}{dt}\left(u_{gi}-u_{pi}\right)+\left(\frac{\rho_g}{\rho_p}\right)u_{pj}\frac{\partial u_{gi}}{\partial x_j} \tag{4}$$

Here, the particle inertia is balanced by the drag, the gravity, the virtual mass and the force due to the pressure gradient acting on the particle. For a rigid spherical particle, the drag is defined by

$$F_D=\frac{18\mu_g}{\rho_p d_p^2}\frac{\text{Re}\,C_D}{24} \tag{5}$$

The drag coefficient is determined from the Schiller and Naumann model correlation,

$$C_D=\begin{cases}24\left(1+0.15\text{Re}^{0.687}\right)\!\big/\text{Re} & \text{Re}\le1000\\ 0.44 & \text{Re}<1000\end{cases} \tag{6}$$

Energy conservation (thermal) for the discrete phase particle can be written as

$$\frac{d(m_p c_p T_p)}{dt}=A_p\frac{\lambda Nu}{d_p}\left(T_g-T_p\right)+$$
$$A_p\varepsilon_a\left(Q_R-\sigma_B T_p^4\right)+\sum_{k=1}^{6}\dot{m}_k\Delta h_k \tag{7}$$

Where, the rate of change of thermal energy of a particle is balanced by the convective and radiative heat transfer and heat due to devolatilization and chemical surface reactions. The convective heat transfer coefficient is determined from the Ranz and Marshall's Nusselt correlation, i.e.

$$Nu = \frac{hd_p}{k_\infty} = 2.0 + 0.6 \, \text{Re}_d^{1/2} \, \text{Pr}^{1/3} \qquad (8)$$

Gasification of Coal

The gasification process can be broken down into the following simple sub-processes for ease of modeling. Coal (either dry feed or slurry feed) undergoes the following sub-processes during gasification.

Passive Heating

The coal particles are heated till the vaporization/devolatilization temperature is reached. There is no mass transfer or chemical reaction during this stage. When the coal particles reach a certain temperature, say the vaporization temperature, moisture is released. Accordingly, the moisture behaves as a source for the gas phase. Meanwhile, energy is taken out from the gas phase to supply the latent heat of vaporization.

Devolatilization

A phenomenological model needs to be constructed based on data from experiments used to characterize the coal. This model can then be used to predict the yields of some major gas components while preserving a strict elemental balance to determine stoichiometry. The main species included in the devolatilization model are CH_4, CO_2, CO, O_2, H_2, H_2S, N_2 and H_2O. The release of volatiles from the coal can be represented as:

$$C_{m01}H_{m02}O_{m03}N_{m04}S_{m05}Ash_{m06}Mois_{m07} \rightarrow$$

$$C_{m11}H_{m12}O_{m13}N_{m14}S_{m15}Mois_{m17} + C_{m21}Ash_{m26} \qquad (9)$$

The kinetic devolatilization rate is determined from the Kobayashi model with two competing rates. The weighted rate of devolatilization is given by

$$\frac{dm_v}{dt} = \left(m_{p,0} - m_a \right)$$

$$\left(\alpha_1 R_1 + \alpha_2 R_2 \right) \exp\left(-\int_0^t (R_1 + R_2) dt \right) \qquad (10)$$

Here $R_1 = A_1 \exp(E_1/RT_p)$ and $R_2 = A_2 \exp(E_2/RT_p)$ are the competing rates that control the devolatilization over different temperature ranges. The first yield factor α_1 is the fraction of volatiles as determined by proximate analysis representing devolatilization at low temperature. The second yield factor α_2 is taken as unity, which is the yield of volatiles at high temperature.

Volatiles Oxidation, Char Combustion and Gasification

After all the volatiles have been released, oxidation of volatiles, char combustion and gasification takes place until all the char is consumed or the particles flow out of the reactor. The chemical reactions include volatile oxidation (combustion), char combustion (oxidation),

char-steam gasification, char-carbon dioxide gasification and char-hydrogen gasification, followed by the gas phase reactions. Volatiles oxidation/combustion for oxygen-rich conditions are described by,

$$C_{m11}H_{m12}O_{m13}N_{m14}S_{m15}$$

$$+ \left(m_{11} + \frac{m_{12}}{4} - \frac{m_{13}}{2} + m_{15} \right) O_2 \xrightarrow{k1} \qquad (11)$$

$$m_{11}CO_2 + \frac{m_{12}}{2} H_2O + m_{15}SO_2 + \frac{m_{14}}{2} N_2$$
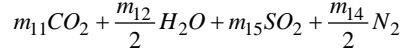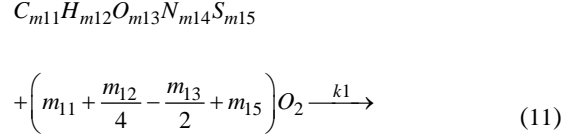
Using the expression for the partial oxidation of volatiles from Chen et al (2000), the chemical reaction for volatiles oxidation/combustion for oxygen-lean conditions, i.e. $\phi < \left(m_{11} + \frac{m_{12}}{4} - \frac{m_{13}}{2} + m_{15} \right)$ are described by,

$$C_{m11}H_{m12}O_{m13}N_{m14}S_{m15} + \phi O_2 \xrightarrow{k2}$$

$$m_{11} \left(\alpha_1 CO_2 + \alpha_2 CO \right)$$

$$+ \left(\frac{1 - \alpha_1}{2} (m_{12} - 2m_{15}) \right) H_2$$

$$+ \frac{\alpha_1}{2} (m_{12} - 2m_{15}) H_2O \qquad (12)$$

$$+ m_{15}H_2S + \frac{m_{14}}{2} N_2$$
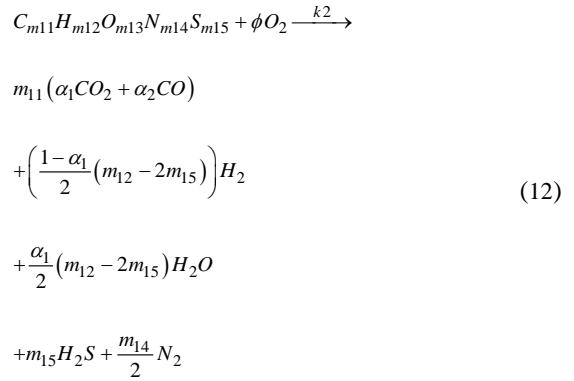
Table 1: Stoichiometric coefficient values.

Parameter	Coal M	Heavy Oil
m11	1.366	2.02
m12	4.9	3.79
m13	0.426	0.01
m14	0.102	0.0169
m15	0.013	0.0456

If we substitute the values in Table 1 in chemical equations (11) and (12), we get the complete and partial oxidation relations for the released volatiles for coal and heavy oil.

Carbon monoxide and hydrogen are produced during the gasification of char particles. The performance of a gasifier is determined primarily by the char gasification reaction. The following reactions have been included in the model

$$C + \frac{1}{2} O_2 \xrightarrow{k3} CO \qquad (13)$$

$$C + H_2O \xrightarrow{k4} CO + H_2 \qquad , \qquad (14)$$

$$C + CO_2 \xrightarrow{k5} 2CO \qquad (15)$$

$$C + 2H_2 \xrightarrow{k6} CH_4 \qquad (16)$$
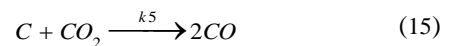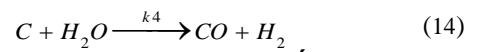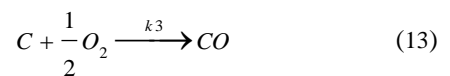
The heterogeneous surface reactions are determined by a kinetics-diffusion limited reaction rate as

$$\frac{dm_p}{dt} = -A_p p_{ox} D_0 \frac{R}{(D_0 + R)} \qquad (17)$$

Where the diffusion-rate coefficient is defined by

$$D_0 = C_1 \frac{\left[\frac{(T_p + T_\infty)}{2} \right]^{0.75}}{d_p} \qquad (18)$$
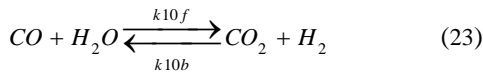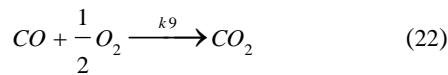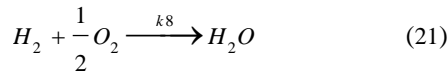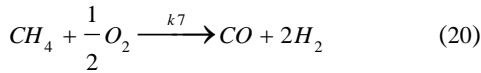
and the kinetic rate for the chemical reactions (13)-(16) are defined by,

$$R = C_2 e^{-(E/RT_p)} \qquad (19)$$

The multiple surface reactions model is used in conjunction with the surface combustion model detailed here.

Gas Phase Reactions

The continuous phase is modeled by using global reactions to describe gas phase chemistry. A set of reduced chemical reaction kinetics appropriate for gasification studies has been used in this analysis The following reaction paths have been considered for this model

$$CH_4 + \frac{1}{2} O_2 \xrightarrow{k7} CO + 2H_2 \qquad (20)$$

$$H_2 + \frac{1}{2} O_2 \xrightarrow{k8} H_2O \qquad (21)$$

$$CO + \frac{1}{2} O_2 \xrightarrow{k9} CO_2 \qquad (22)$$

$$CO + H_2O \underset{k10b}{\overset{k10f}{\rightleftharpoons}} CO_2 + H_2 \qquad (23)$$

The gas phase reactions are modelled by combining laminar finite-rate chemical kinetics and eddy-dissipation turbulence-chemistry interaction. The reaction rate of chemical species i due to chemical reaction $R_{i,r}$, is taken as the sum of the reaction rates over r reactions that the species may take part in, i.e.

$$R_i = \sum_r R_{i,r} \qquad (24)$$

The effective reaction rate $R_{i,r}$ is the smaller of the laminar finite-rate and the eddy-dissipation reaction rates. The laminar finite-rate reaction rate is given by

$$R_{i,r} = M_i \left(\upsilon''_{i,r} - \upsilon'_{i,r} \right) k_r \prod_j \left[C_{j,r} \right]^{\left(\eta'_{j,r} + \eta''_{j,r} \right)} \qquad (25)$$

Here, $\upsilon'_{i,r}$ and $\upsilon''_{i,r}$ are stoichiometric coefficients for reactant i and product i respectively, in reaction r. $C_{j,r}$ is the molar concentration of species j in reaction r. $\eta'_{i,r}$ and $\eta''_{i,r}$ are rate exponents for reactant species j and product species j respectively, in reaction r. The Arrhenius expression is then defined by

$$k_r = A_r T_g^{n_r} \exp\left(\frac{E_r}{RT_g} \right) \qquad (26)$$

Where, A_r is the pre-exponential factor, n_r is the temperature exponent, and E_r is the activation energy.

The eddy-dissipation reaction rate is given by the smaller, or limiting value of the two expressions below,

$$R_{i,r} = \upsilon'_{i,r} M_i A \rho \frac{\varepsilon}{k} \min_R \left(\frac{Y_R}{\upsilon'_{R,r} M_R} \right) \qquad (27)$$

$$R_{i,r} = \upsilon'_{i,r} M_i A B \rho \frac{\varepsilon}{k} \frac{\sum_P Y_P}{\sum_P \upsilon''_{P,r} M_P} \qquad (28)$$

Here, Y_R is the mass fraction of a particular reactant R, and Y_P is the mass fraction of any product species, P. A and B are empirical constants.

The values of the pre-exponential coefficient and the activation energies for the numbered chemical reactions to determine the reaction rates are given in Table 2. Scheme 1 represents the chemical kinetics scheme used in Ajilkumar et al (2009) adapted from the sub-schemes of Chen et al (2000) for the heterogeneous reactions and Watanabe and Otaka (2006) for the gas-phase reactions, whereas Scheme 2 represents a modification of the chemical kinetics scheme as laid out in Wu et al (2010).

Table 2: Chemical kinetics reaction rates.

Eq. #	A_r	E_r (J/kmol)	n_r	$\prod_j \left[C_{j,r} \right]^{\left(\eta'_{j,r} + \eta \right)}$	Source
Scheme 1					
(k1)	2.119e11	2.027e8	0	$[Vol]^{0.2}[O_2]^{1.3}$	FLUENT 12.1
(k2)	4.4e11	1.25e8	0	$[Vol]^{0.2}[O_2]^{1.3}$	Jones & Lindstedt (1988)
(k3)	0.052	6.1e7	-	-	Chen et al (2000)
(k4)	0.0782	1.15e8	-	-	Chen et al (2000)
(k5)	0.0732	1.125e8	-	-	Chen et al 2000)
(k8)	6.8e15	1.68e8	0	1	Watanabe & Otaka (2006)
(k9)	2.2e12	1.67e8	0	1	Watanabe & Otaka (2006)
(k10f)	2.75e10	8.38e7	0	1	Watanabe & Otaka (2006)
(k10b)	2.65e-2	3.96e3	0	1	Watanabe & Otaka (2006)

Scheme 2					
(k1)	2.119e11	2.027e8	0	$[Vol]^{0.2}[O_2]^{1.3}$	FLUENT 12.1
(k2)	4.4e11	1.25e8	0	$[Vol]^{0.2}[O_2]^{1.3}$	Jones & Lindstedt (1988)
(k3)	0.052	6.1e7	-	-	Chen et al (2000)
(k4)	0.0782	1.15e8	-	-	Chen et al (2000)
(k5)	0.0732	1.125e8	-	-	Chen et al (2000)
(k6)	6e-7	7.53e7	-	-	Govind & Shah (1984)
(k7)	4.4e11	1.25e8	0	$[CH_4]^{0.5}[O_2]^{1.25}$	Jones & Lindstedt (1988)
(k8)	2.5e16	1.68e8	-1	$[H_2]^{0.5}[O_2]^{2.25}[H_2O]^{-1}$	Jones & Lindstedt (1988)
(k9)	3.16e12	1.67e8	0	$[CO]^{1.5}[O_2]^{0.25}$	Wu et al (2010)
(k10f)	5e12	2.83e8	0	$[CO]^{0.5}[H_2O]^{1}$	Callaghan (2006)
(k10b)	9.5e10	2.39e8	0	$[CO_2]^{1}[H_2]^{0.5}$	Callaghan (2006)

Gasification of Heavy Oil

For the heavy oil case, an eddy dissipation model has been used in combination with the discrete phase method (DPM) in FLUENT. This model includes an inert heating phase, droplet evaporation, volatiles oxidation, gasification (and/or combustion) and gas-phase reactions. The gas-phase reactions are similar to that used in the coal gasification case.

MODEL DESCRIPTION

Gasifier 1

The first gasifier is a tubular coal gasifier studied numerically by Ajilkumar et al (2009). A schematic of the gasifier layout is given in Figure 1. The gasifier has a length of 1m and a nominal diameter of 0.072 m. . The computational mesh consists of 72 x 1000 quadrilateral control volumes. The discrete phase method in FLUENT 12.1 was used for the CFD simulation.
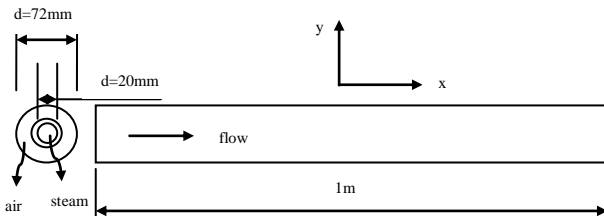
Figure 1: Schematic of gasifier geometry.

As given in Ajilkumar et al (2009), the design coal feed rate is 2.4kg/hr (or 6.67e-04kg/s). The mass of air corresponding to a gasifier air ratio of 0.409 is 0.00334kg/s.. There are two streams entering the gasifier, the first being the air stream entering the inlet for the coal feed (0.000667kg/s), hence acting as a carrier gas for the coal particles. The other is the air stream entering through the outer inlet of the tubular coal gasifier (0.0027kg/s). The coal inlet stream was preheated to 400K and the outer stream to 600K. . The operating pressure for this model is 2.0MPa.

The proximate and ultimate analysis for the Australian black coal (coal M) used for this study is given in Table 2.

Table 2: Coal M - proximate and ultimate analyses.

	(Wt. %)
Proximate analysis	
Moisture	4.2
Fixed Carbon	56.2
Volatile Matter	30.9
Ash	8.7
Ultimate analysis	
Carbon	76.3
Hydrogen	5.31
Nitrogen	1.54
Oxygen	7.31
Sulfur	0.46

Flow and Heat Transfer Models

The standard k-ε model was used for modeling turbulence in the continuous phase, and stochastic tracking was implemented for the steady-state model of the gasifier to simulate particle motion and turbulent dispersion. The SIMPLE algorithm was used to implement the pressure-velocity coupling with second-order upwind discretization. The coal particles were assumed to fit a Rosin-Rammler size distribution with a minimum size of 4μm and a maximum of 140, with an average of 54.5μm. The spread parameter was 2.51 and 6 discrete particle sizes were considered. Conductive, convective and radiative heat transfer was assumed between the gases, particles and reactor walls. The scattering property of the particles due to radiation is assumed to be isotropic and the standard P1 model has been used for the purpose of modeling radiative heat transfer. This model is based on the expansion of radiation intensity into an orthogonal series of spherical harmonics. The weighted-sum-of-gray-gases-model (wsggm) was used to calculate the absorption coefficient of the gas phase.

Gasifier 2

The second gasifier is a heavy oil gasifier studied experimentally by Ashizawa et al. (2005). The length of the gasifier is 3m and the nominal diameter is 0.3m. The computational domain consists of one-quarter of the gasifier taking symmetry into account. The mesh for this geometry consists of 160 x 48 x 8 hexahedral control-volumes The discrete phase method in FLUENT 12.1 was used for the CFD simulation. Figure 2 is a representation of the mesh employed for the CFD calculations.

The oil droplets were assumed to have a Rosin-Rammler size distribution with a minimum size of 4μm and a maximum of 150, with an average of 40μm. The

spread parameter was 1.2 and 10 discrete particle sizes were considered. The feed rate corresponds to an oxygen ratio of 0.39. The operating pressure used in this model is 1.9MPa.
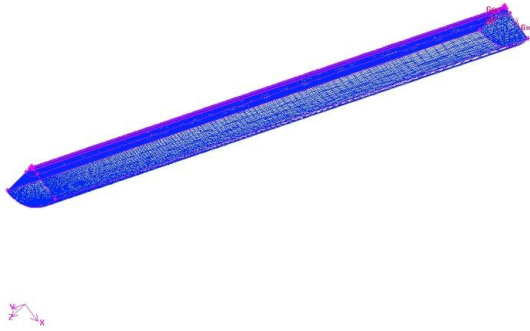

Figure 2: Computational mesh used for heavy oil gasifier.

RESULTS AND DISCUSSION

Gasifier 1 – Scheme 1

Using the first chemical kinetics scheme, comprising the heterogeneous reaction rates Chen et al (2000) and the gas-phase reaction rates of Watanabe and Otaka (2006), we can obtain the following contour plots for the temperature and velocity distributions within the gasifier (Figure 3 and Figure 4).
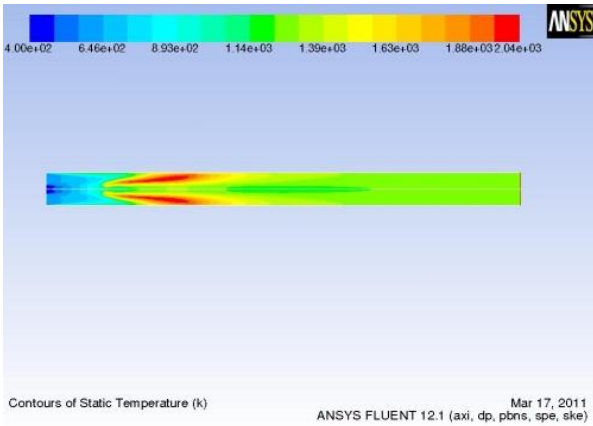
Figure 3: Gasifier 1 – Scheme 1: Temperature contour plot.
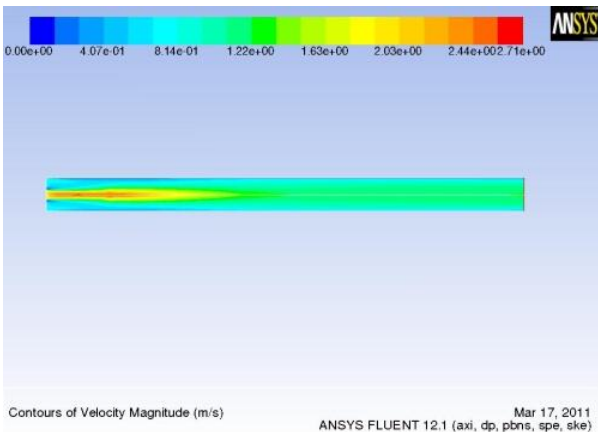
Figure 4: Gasifier 1 – Scheme 1: Velocity contour plot.

From Figures 3 and 4, it is seen that the maximum temperature within the gasifier is about 2042K and it occurs about 0.2m downstream of the inlet. The maximum velocity is estimated to be 2.71m/s and occurs along the gasifier axis.

It is seen from the contour plots for the species mole fractions depicted in Figure 5 and Figure 6 that the carbon monoxide mole fraction at the gasifier outlet varies between 17% and 20%, whereas that of hydrogen is around 11%. The peak values of the mole fractions for carbon monoxide and hydrogen are 31.4% and 16%, respectively.
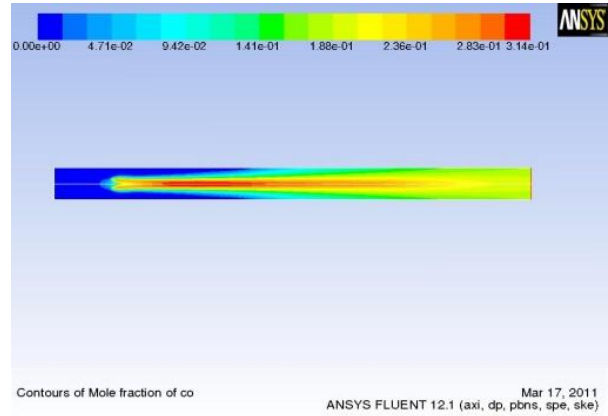
Figure 5: Gasifier 1 – Scheme 1: CO mole fraction contour.
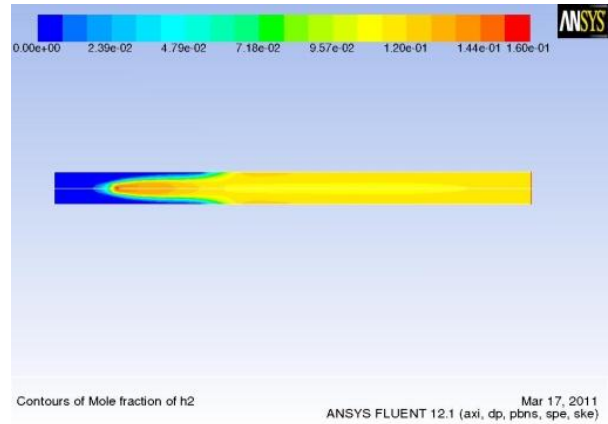
Figure 6: Gasifier 1 – Scheme 1: H_2 mole fraction contour.

Gasifier 1 – Scheme 2

Using the second chemical kinetics scheme comprising the heterogeneous reaction rates of Chen et al (2000) and the gas-phase reaction rates of Wu et al (2010) and Callaghan (2006), we can obtain the following contour plot for the temperature distribution within the gasifier (Figure 7). The velocity contour plot is not depicted since it is almost identical to the plot obtained with the first scheme.

From Figure 7, it is seen that the maximum temperature within the gasifier is about 2040K which is very close to that obtained with the first scheme, and at an almost identical location within the gasifier.
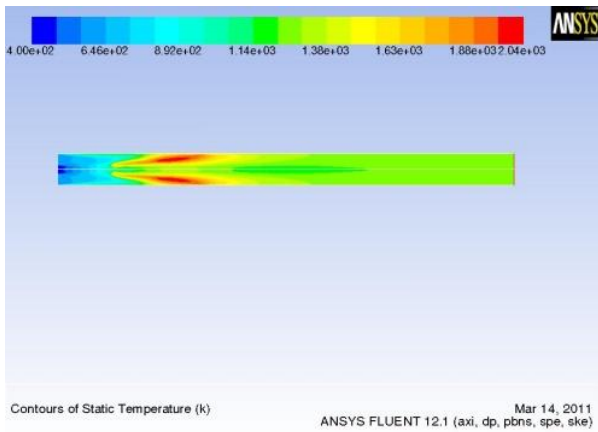
Figure 7: Gasifier 1 – Scheme 2: Temperature contour plot.

It is seen from the contour plots for the species mole fractions depicted in Figure 8 and Figure 9 that the carbon monoxide mole fraction at the gasifier outlet varies between 21% and 23%, whereas that of hydrogen is around 8%. The peak values of the mole fractions for carbon monoxide and hydrogen are 31.4% and 14.9%, respectively.
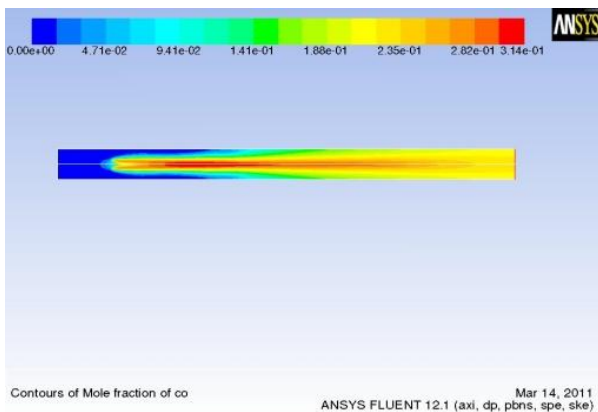
Figure 8: Gasifier 1 – Scheme 2: CO mole fraction contour.
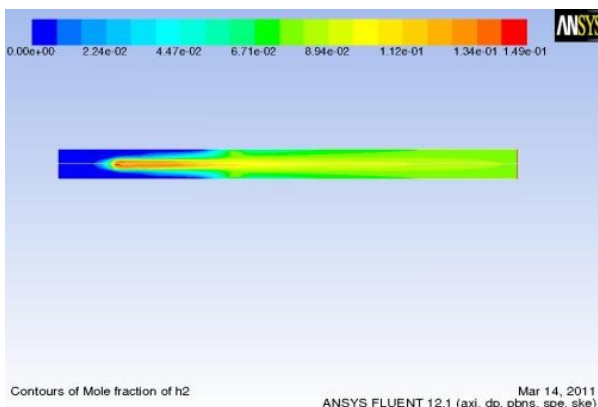
Figure 9: Gasifier 1 – Scheme 2: H_2 mole fraction contour.

Figure 10 shows the temperature profile obtained along the gasifier flow direction, passing through the region in the gasifier where the maximum temperature is experienced. A comparison of the experimental data from Watanabe and Otaka (2006), the results of

Ajilkumar et al (2009), and the two schemes used in this study can be seen.
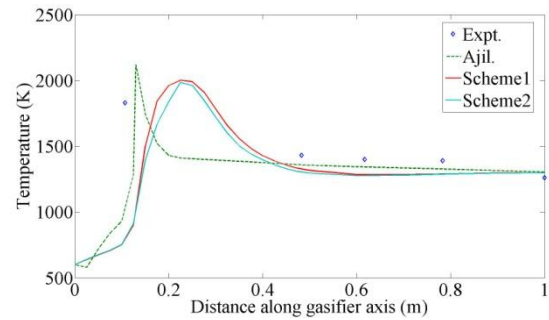
Figure 10: Gasifier 1: Axial temperature profiles.

It can be observed from Figure 10 that the agreement with experimental results is very good for all the CFD studies depicted with the correct temperature trend being captured in the axial direction. The peak temperatures observed with the two schemes differ from that obtained by Ajilkumar et al (2009) by about 80K, with a slight shift in the location of the observed maximum. The difference in the numerical predictions may be due to uncertainties in the inlet flow conditions. On further analysis it has been determined that the peak temperature occurs at about 0.02m before that observed for the experimental data as opposed to 0.05m later (as seen in the fig.) when two-way turbulence coupling is included in the model.
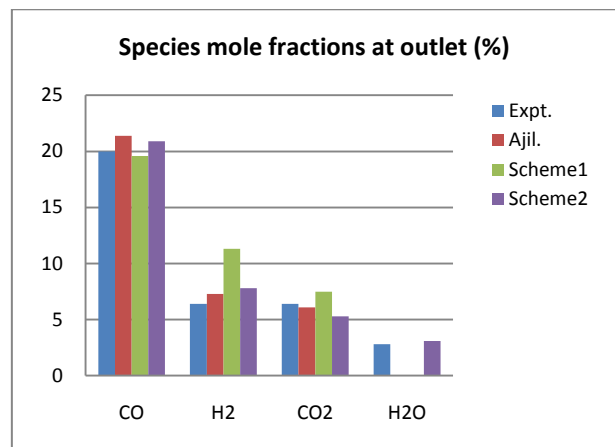
Figure 11: Gasifier 1: Species outlet mole fractions (%).

From Figure 11 it is seen that Scheme 2 performs better than Scheme 1 in predicting the mole fraction percentages of the major species at the gasifier outlet. Scheme 2 performs as well as the Ajilkumar et al (2006) model, with the added advantage of depicting the water vapour mole fraction. The species outlet mole fraction error varies between 2% for carbon monoxide and 76.5% for hydrogen in the case of scheme 1, with this scheme being unable to predict the outlet mole fraction for water vapour. The species outlet mole fraction error varies between 4.5% for carbon monoxide and 21.8% for hydrogen in the case of scheme 2.

The species mole fractions of carbon dioxide and carbon monoxide along the gasifier axis for the two chemical

kinetics schemes compared with Ajilkumar et al (2009) yields Figure 12.
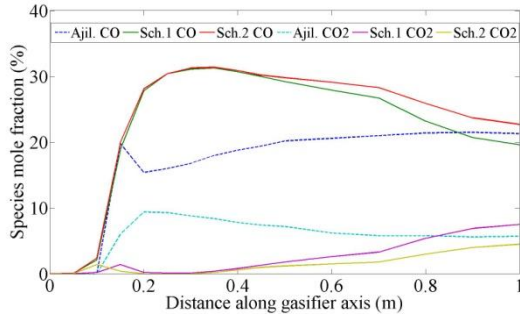
Figure 12: Gasifier 1: Axial CO & CO_2 mole fractions (%).

It is seen that the outlet mole fractions of both schemes are similar and so is the trend along the gasifier axis for the mole fractions of the two species. However, it is seen that a distance of 0.2 to 0.3m from the inlet that the peak value for the species mole fraction for carbon monoxide is observed for the two schemes whereas a "dip" is observed in the same region by Ajilkumar et al (2009). This trend seems to be reversed in the case of carbon dioxide at the same axial distance downstream of the inlet. This difference needs to be looked at in detail and investigated further. Furthermore, it can be seen from Figure 12 that eddy dissipation is the predominant mixing mechanism closer to the gasifier inlet, while the finite-rate chemistry plays a greater role further downstream, and is especially pronounced near the gasifier outlet.
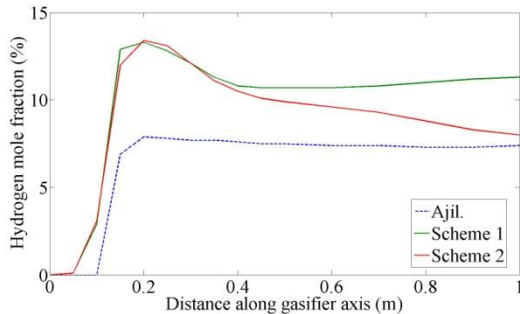
Figure 13: Gasifier 1: Axial hydrogen mole fraction (%).

From Figure 13 it is seen that the hydrogen mole fraction predicted by scheme 1 is high when compared to the predictions of the other two CFD models. Scheme 2 produces results that shows good agreement with experimental data, and can be deemed more suitable than scheme 1. Again, it is seen that eddy dissipation is the stronger mixing mechanism near the combustion (and gasification) zone, with the finite rate chemistry becoming a larger factor downstream in the flow.

Gasifier 2

The model for heavy oil gasification has been developed in similar manner to the coal gasification model. The following temperature and velocity contours have been obtained for the gasifier geometry given in Ashizawa et al (2005).
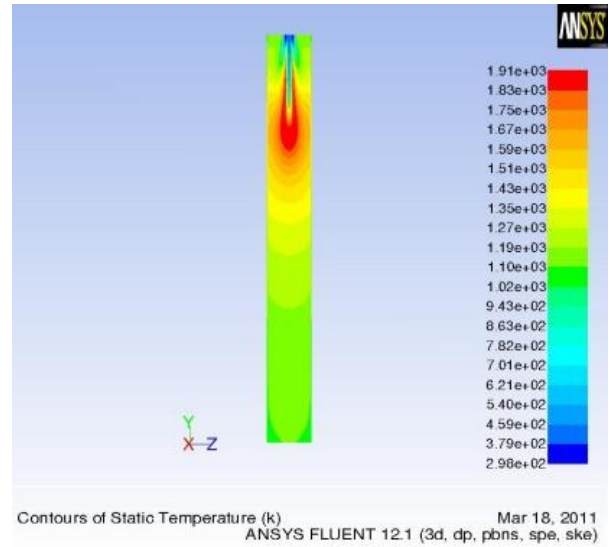
Figure 14: Gasifier 2: Temperature contour plot.

From Figure 14 it is seen that the peak temperature along the gasifier axis is approximately 1910K with its location between 0.6 and 0.9m from the inlet. The temperature of the product gas at the outlet is estimated to be less than 1100K. From Figure 15, it is observed that the maximum velocity within the gasifier is 20.6m/s, close to the point of injection of the heavy oil.
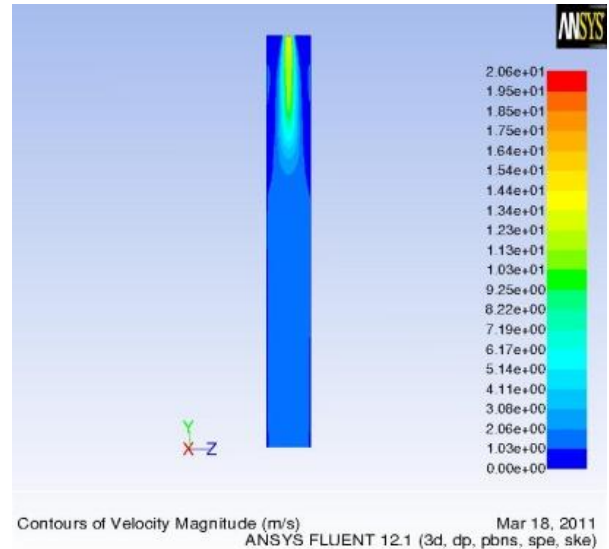
Figure 15: Gasifier 2: Velocity contour plot.

Figures 16 and 17 illustrate the species mole fractions of the two main components forming the product syngas makeup – carbon monoxide and hydrogen, respectively.

It is seen from Figure 16 that the maximum carbon monoxide mole fraction observed with this model is 37.2%, which also happens to be the gasifier outlet mole fraction for this species. From Figure 17, it is seen that the peak hydrogen mole fraction percentage predicted is 35.7%.
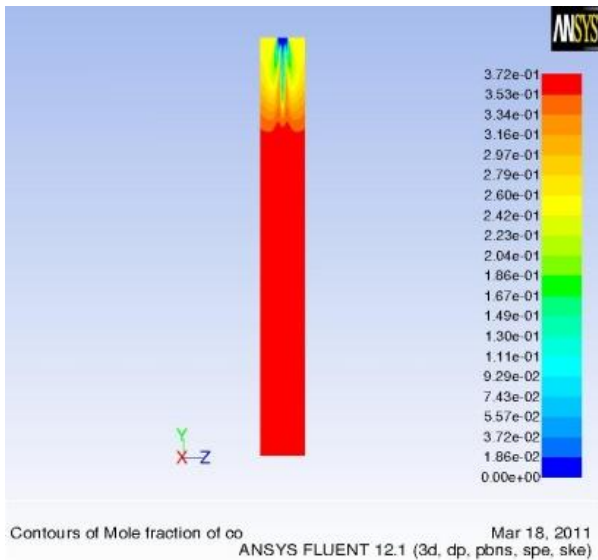
Figure 16: Gasifier 2: CO mole fraction contour plot.
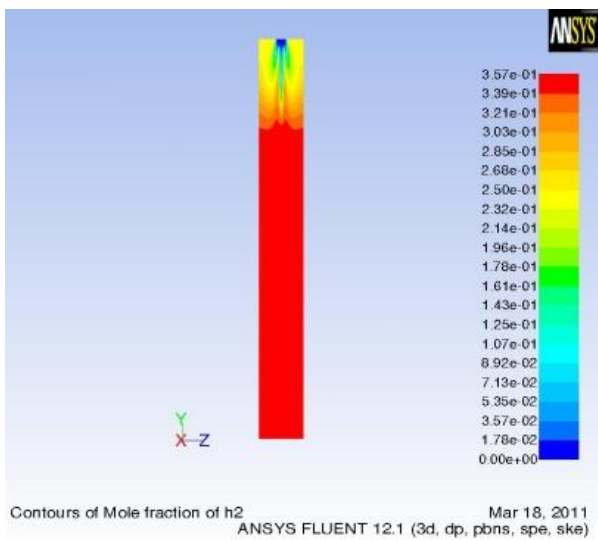
Figure 17: Gasifier 2: H_2 mole fraction contour plot.

From Figure 18, it is observed that there is good agreement of the predicted axial distribution of temperature when compared to the experimental values obtained by Ashizawa et al (2005).
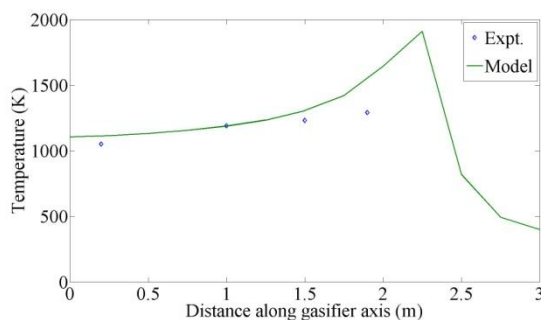

Figure 18: Gasifier 2: Axial temperature distribution.

From Figure 19, it is seen that the predictions of the CFD model are in good agreement with the experimental data as it pertains to species mole fractions at the outlet. The largest difference is seen in the species

mole fraction of water, where the value predicted by the CFD model is 18.6% as compared to 13.6% in the experiment of Ashizawa et al (2005). The smallest difference is observed in the mole fraction of methane – 0.05% for the experiment and 0.04% is the model prediction.
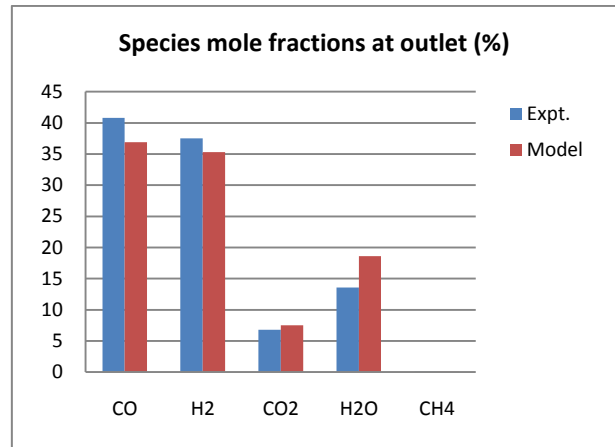
Figure 19: Gasifier 2: Outlet species mole fractions.

CONCLUSION

Two different CFD models have been presented in this study. The first is used to model the physical and chemical processes occurring within an entrained-flow coal gasifier. Two different chemical kinetics schemes have been considered for coal gasification, and the predictions compared with that of Ajilkumar et al (2009) and the experimental results of Watanabe and Otaka (2006).

From the predictions obtained with the first model, it is seen that both schemes yield good results with respect to temperature distribution within the gasifier. The peak temperature observed with both the schemes is approximately 2040K. However, it is also seen that the first scheme produces a gentle temperature gradient in the region of combustion/gasification as compared to the second chemical kinetics scheme. This difference could be worth investigating in future studies comparing the two chemical kinetics schemes.

For gasifier 1, it is also observed that scheme 2 produces more accurate results when investigating the gasifier outlet species mole fractions. The over-prediction of hydrogen and the non-prediction of water vapour is a small concern with scheme 1. It was also observed that eddy dissipation is the dominant mixing mechanism close to the combustion region, while the finite rate chemistry seems to play a larger role as the flow begins to near the gasifier outlet.

From the predictions of temperature distribution and species mole fractions at the gasifier outlet, it can be concluded that the performance of scheme 2 makes it a suitable candidate for use in future studies of coal gasification.

The second model deals with the gasification of heavy oil in an entrained-flow gasifier. This CFD model produces estimates that agree well with both the temperature and outlet species mole fraction data of Ashizawa et al (2005). Further refinement of this model might be possible by investigating different reaction schemes (and chemical kinetics), considering other turbulence models (including LES) and by using more complex radiation and heat transfer models.

ACKNOWLEDGEMENTS

REFERENCES

AJILKUMAR, A., SUNDARARAJAN, T. and SHET, U.S.P., (2009), "Numerical modelling of a steam-assisted tubular coal gasifier", *Int. J. Therm. Sci.*, **48**, 308-321.

ASHIZAWA, M., HARA, S., KIDOGUCHI, K. and INUMARU, J., (2005), "Gasification characteristics of extra-heavy oil in a research-scale gasifier", *Energy*, **30,** 2194-2205.

CALLAGHAN, C.A., (2006), "Kinetics and Catalysis of the Water-Gas-Shift Reaction: A Micro Kinetic and Graph Theoretic Approach", Ph.D. Dissertation, Department of Chemical Engineering, Worcester Polytechnic Institute, U.S.A.

CHEN, C., HORIO, M. and KOJIMA, T., (2000), "Numerical simulation of entrained flow coal gasifiers. Part I: modeling of coal gasification in an entrained flow gasifier", *Chem. Eng. Sci.*, **55**, 3861-3874.

GOVIND, R. and SHAH, J., (1984), "Modeling and Simulation of an Entrained Flow Coal Gasifier", *AIChE J.*, **30 (1)**, 79-92.

HIGMAN, C. and VAN DER BURGT, M., "Gasification", Second Ed. 2008, Elsevier Science.

JONES, W.P. and LINDSTEDT, R.P. (1988), "Global Reaction Schemes for Hydrocarbon Combustion", *Combust. Flame*, **73**, 233-249.

WATANABE, H. and OTAKA, M., (2006), "Numerical simulation of coal gasification in entrained flow coal gasifier", *Fuel*, **85**, 1935-1943.

WU, Y., SMITH, P.J., ZHANG, J., THORNOCK, J.N. and YUE, G., (2010), "Effects of turbulent mixing and controlling mechanisms in an entrained flow coal gasifier", *Energy Fuels*, **24 (2)**, 1170-1175.

8th International Conference on CFD in Oil & Gas, Metallurgical and Process Industries
SINTEF/NTNU, Trondheim Norway
21-23 June 2011

CFD11-126

IMPLEMENTATION OF THE QUADRATURE METHOD OF MOMENTS IN A 3D CFD PIPE GEOMETRY FOR GIBBSITE PRECIPITATION

Kieran Hutton[1,3,*] **, Darrin W. Stephens**[1]**, Iztok Livk**[2]

[1] CSIRO Mathematics, Informatics & Statistics, Clayton, VIC 3168, Australia

[2] CSIRO Light Metals Flagship (CPSE)/Parker Centre, Waterford, Perth, WA 6152, Australia

[3] CSIRO Light Metals Flagship/Parker Centre, Clayton, VIC 3168, Australia

* E-mail: kieran.hutton@csiro.au

ABSTRACT

Keywords:

INTRODUCTION

NOMENCLATURE

β
ε
γ
γ
η
ν
σ
ω
ψ

et al
et al

Quadrature Method of Moments

$$\frac{dn\,L}{dt} = \frac{L}{\int}\int_{}^{L} \frac{k^a\left(\left(L\,-\,\lambda\,\right)^{-}\,\lambda\,\right)}{\left(L\,-\,\lambda\,\right)^{-}} n\left(\left(L\,-\,\lambda\,\right)^{-}\right) n(\lambda) d\lambda$$

$$-\,n(L)\int_{}^{\infty} k^a\left(L\,\,\lambda\,\right) n(\lambda) d\lambda$$

$$+\int_{L}^{\infty} \beta\left(L\middle|\lambda\right) k^b\left(\lambda\right) n\left(\lambda\right) dv - k^b\left(L\right) n(L)$$

ω

$$\frac{dn\,L}{dt} = G\frac{dn\,L}{dL} + \delta\,L - L_{crit}\,B_U$$

$$\frac{dm_k}{dt} = -\sum_{i=}^{N} \omega_i \sum_{j=}^{N} \omega_j \left(L_i + L_j\right)^k \psi\,\,k^a\left(L_i\,\,L_j\right)$$

$$-\sum_{i=}^{N} L_i^k \omega_i \sum_{i=j}^{N} \psi\,\,k^a\left(L_i\,\,L_j\right)\omega_j + \sum_{i=}^{N} k^a\left(L_i\right)\overline{\beta}\left(L_i\,\,L_j\right)\omega_i$$

$$-\sum_{i=}^{N} L_i^k k^a\left(L_i\right)\omega_i + \sum_{i-}^{N} kL^{k-}\,G\omega_i + L_{crit}^k B_U$$

ψ

et al

et al   *et al*

et al

et al.

et al

et al

MODEL DESCRIPTION

Additional Variables and Mass Fractions

$$k^a = \sqrt{\frac{\varepsilon}{\nu}}\left(L_i + L_j\right)$$

$$\psi = \cfrac{}{+ \quad \times \quad ^- \quad \eta \quad \left(\cfrac{\left(\gamma \quad U_{tip}\right)}{\left(G \quad L\right)}\right)}$$

Model Kinetic Equations

Geometry and Initial Conditions

Figure 1:

$$A = \frac{C}{+ J}$$

$$G = k_G \quad \left(\frac{-\Delta E_G}{RT}\right)\frac{\left(A - A\right)}{C}$$

et al   *et al,*
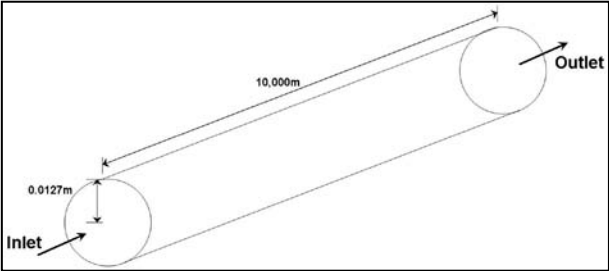
$$B_U = K_N \sigma \quad \gamma M$$

RESULTS AND DISCUSSION

Table 1:

Quantity	Value	Units
γ		
η		

Table 2:

Moment No.	Raw (m^k)	Scaled (μm^k)
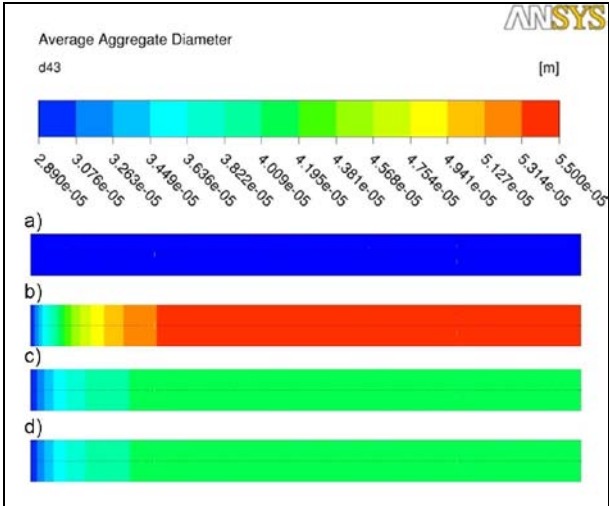
Figure 2:

Addition of Physics

μ

μ

et al.
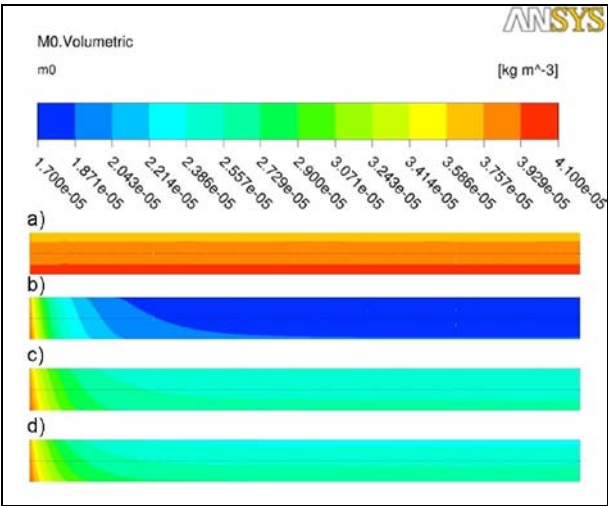
Figure 3:

Effect of Process Variables

Case 2.1 – Effect of Changing Temperature
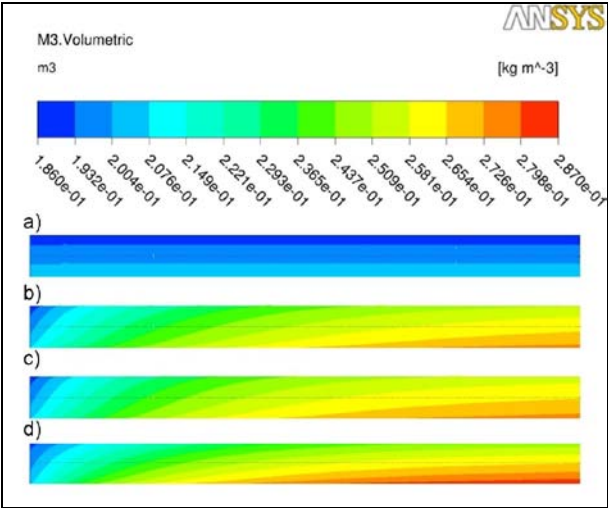
Figure 5:
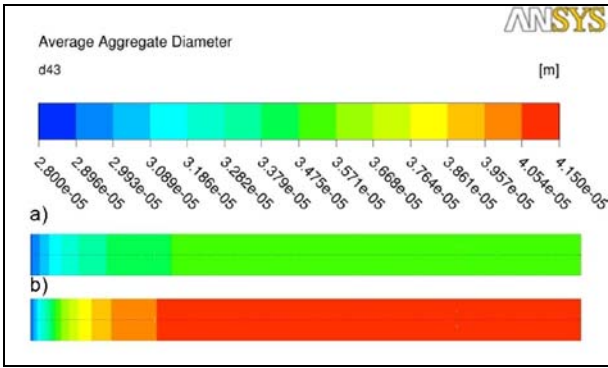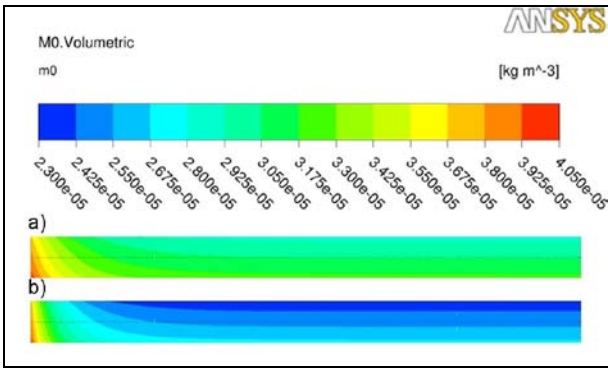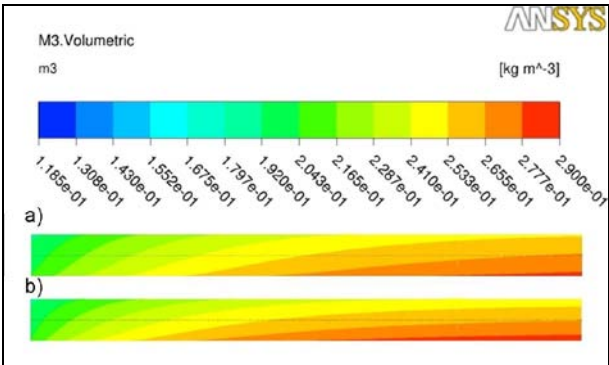
Figure 4:
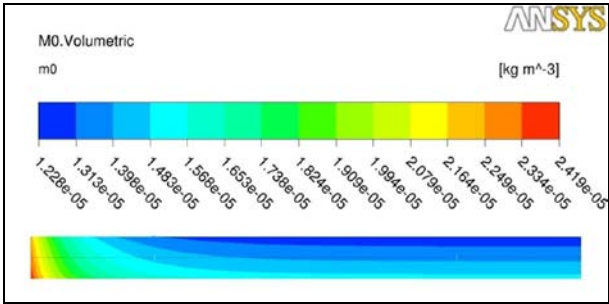
Figure 6:
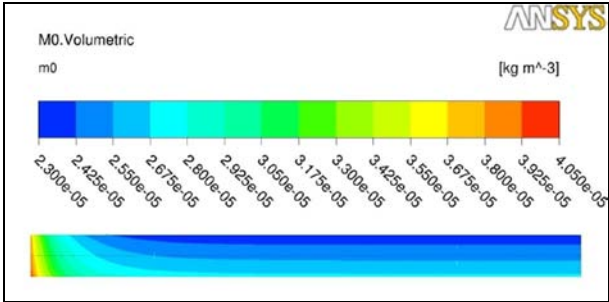
Figure 9:

Figure 7:

Figure 10:

Case 2.2 – Effect of Initial Suspended Solids Concentration
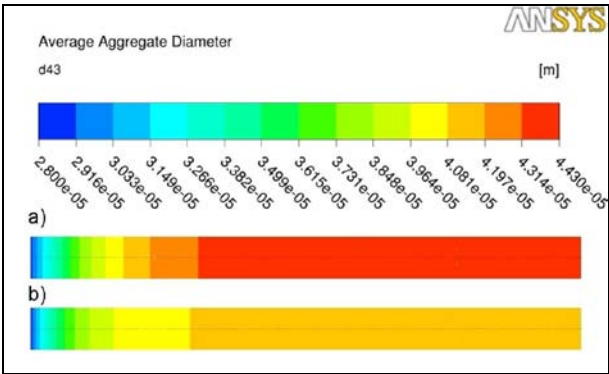
Figure 8:
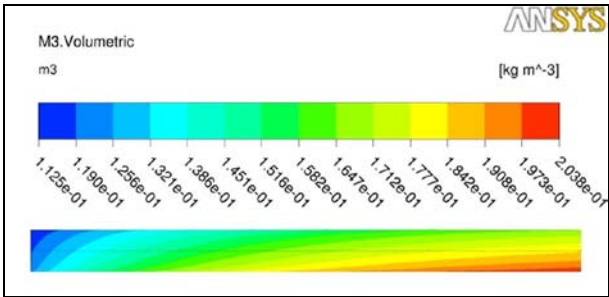
Figure 11:
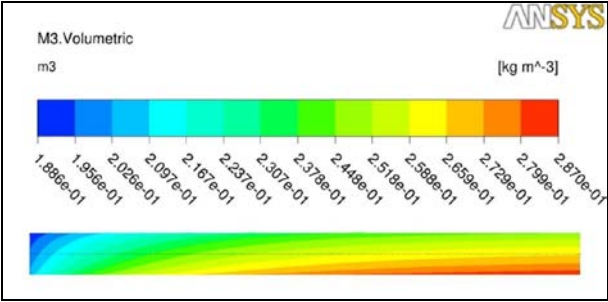
Figure 12:

CONCLUSION

REFERENCES

Proceedings   of   the   3rd   International Symposium   on   Agglomeration

Annalew   der   Physik

AIChE J

CHEMECA 2010

Chemical   Engineering Science

Chem Eng Technol

AICheJ

Chem. Eng Sci

Journal of Colloid and Interface Science

Aerosol Science and Technology

Journal   of   Crystal Growth

Proceedings of 4th International Alumina Quality Workshop

Zeitschrift   fur   Physikalische Chemie

Trans Cambridge Philos. Soc

Light Metals

8th International Conference on CFD in Oil & Gas, Metallurgical and Process Industries
SINTEF/NTNU, Trondheim NORWAY
21-23 June 2011

CFD11-127

EFFICIENT SOLUTION METHOD FOR THE STOKES EQUATIONS WITH VARIABLE VISCOSITY AND PERIODIC BOUNDARY CONDITIONS

Joost S.B. VAN ZWIETEN[1*]**, Martin B. VAN GIJZEN**[1]**, C. (Kees) VUIK**[1]**, Jan VAN MALE**[2]**,**

J.G.E.M. (Hans) FRAAIJE[3]

[1] DIAM, TU DELFT, 2628CD Delft, THE NETHERLANDS

[2] Culgi B.V., 2333BD Leiden, THE NETHERLANDS

[3] Leiden Institute of Chemistry, Leiden University, 2333CC Leiden, THE NETHERLANDS

* E-mail: joostvanzwieten@gmail.com

ABSTRACT

An efficient solution method for the incompressible Stokes equations on a regular grid with shear periodic boundaries and variable viscosity is proposed.

The Stokes equations are decomposed in two unidirectionally coupled systems. In case the viscosity is homogeneous, we apply a technique based on Fourier transforms to solve the subsystems. We extend this approach to shear periodic boundary conditions, in which case a modified Fourier transform is used. For variable viscosities the constant problem serves as an efficient preconditioner. Results show that the proposed method converges up to ten times faster than conventional methods for three dimensional systems with moderate viscosity contrasts. For two dimensional systems the difference is even higher. The rate of convergence is almost independent of the grid size which makes it ideal for large grids. The memory foot print is small and independent of the number of iterations.

Keywords: process industry, polymer production, Stokes equations, variable viscosity, regular grid.

INTRODUCTION

In this paper, we are concerned with the solution of the incompressible Stokes problem,

$$-\nabla \cdot \left(\nu \left(\nabla \boldsymbol{u} + \nabla^T \boldsymbol{u} \right) \right) + \nabla p = \boldsymbol{f}, \qquad (1)$$

$$\nabla \cdot \boldsymbol{u} = 0, \qquad (2)$$

where ν denotes the variable viscosity, $\boldsymbol{u}$ the velocity, p the pressure and $\boldsymbol{f}$ the body force or molecule interactions.

The application that sparked our interest in solving the Stokes equations is polymer reactor dynamics. Polymers are synthesised in a reaction process where monomers, say A and B, form polymers of different composition, e.g. AAABAABABBBBABBB. The solubility of the reaction products may lead to accumulation of mass into microdomains that are rich in either A or B. The resulting morphology of microdomains is a key determining factor of the mechanical properties of the plastic created in the reactor. The overall goal is to understand the factors that influence the morphology formation through a combination of experiments and theory, such that the reaction process can be influenced to yield products with the desired properties.

In a polymer reactor, the morphology formation is influenced by several factors like the reactivity of the monomers, their diffusion constants, solubility and the temperature. A stirring or shearing motion inside a reactor can be described by the Stokes equations, since the length and time scales are such that inertia plays almost no role. Shear will deform the phase separated microdomain droplets. Simultaneously, the droplet surface tension will hinder deformation of the droplets under shear. The latter effect is described by the body force or Korteweg force $\boldsymbol{f}$ in Equation (1). The viscosity ν of the droplets may be different from the continuous phase, leading to different flow behaviour.

Dynamic density functional theory (DDFT) was developed to model the time evolution of an inhomogeneous spatial distribution of molecules by integrating a diffusion-convection equation. (Fraaije *et al.*, 1997) DDFT is a mean-field theory that is based on a statistical thermodynamics model of both chain conformation entropy and physical energy interactions. The Stokes equations are solved independently from the DDFT diffusion-convection equation. That is, the DDFT molecule densities result in a viscosity ν and a body-force (Korteweg force) $\boldsymbol{f}$ which are both position dependent and used as input for the Stokes equations. Solving the Stokes equations results in a velocity vector-field $\boldsymbol{u}$ which in turn is used in the DDFT diffusion-convection equation. The pressure p is discarded.

The (continuous) DDFT equations are commonly solved on a rectangular grid. The reasons for this are mostly of practical nature. The grid is typically spaced such that molecules extend over several grid points. This way, the influence of chain architecture and chemical composition can be modelled directly. Simulating, for instance, a whole reactor where polymers are created is infeasible, simply because a grid with the necessary detail would be enormous. Therefore, only a small portion of the whole domain is simulated. Since this subdomain lacks real boundaries it is natural to assume that the fluid is periodic in the neighbourhood of the subdomain. Indeed, in molecular simulations, periodic boundary conditions are widely used to minimise finite size artefacts of the simulation domain. When using periodic boundaries, the domain is surrounded by an infinite amount of regularly packed images of itself.

To model a stirring or shearing motion, we employ a grid based equivalent of the Lees-Edwards boundary conditions known from particle simulations. (Allen and Tildesley, 1994) A constant velocity difference across a boundary in one direction is imposed on the periodic domain. The boundary velocity difference results (through the Stokes equations)

in a non-uniform velocity gradient in the domain. Also, the periodic boundary becomes shifted, i.e. the periodic virtual images of the domain are shifted with an amount that increases over time.

The Stokes equations are discretised using first order finite difference methods on an equidistant staggered grid. The pressure and viscosity nodes are located at the center of the grid cells. The velocity nodes are centered at the faces of the cells, such that the direction of the velocity coincides with the normal of the face. The discretisation yields the following system,

$$\mathscr{L}\boldsymbol{u} + \mathscr{G}p = \boldsymbol{f}, \tag{3}$$

$$\mathscr{G}^T u = 0, \tag{4}$$

where $\mathscr{L}$ is a symmetric positive semi-definite vector Laplace operator, $\mathscr{G}$ a gradient operator and $\mathscr{G}^T$ a divergence operator. See Appendix A for the discretised equations. Due to the periodic boundary conditions, the Stokes equations have a null space spanned by a constant pressure and constant velocities, i.e. the Stokes equations can be solved up to a constant.

In the following section we define the notation used in this paper. In the third section we describe a method for reducing the Stokes equations in two unidirectionally coupled subsystems. The fourth and fifth sections are devoted to the solution method for these subsystems for the two-dimensional Stokes equations. In the sixth section we extend the theory to three dimensions. We conclude with numerical experiments of the proposed solution method.

NOTATION

In this paper we use the following notation:

$d \in \{2,3\}$ The number of dimensions.

$\boldsymbol{L} \in \mathbb{R}^d$ The size of the domain.

$\Omega = [0, L_1] \times \cdots \times [0, L_d]$ The domain.

$\boldsymbol{N} \in \mathbb{N}^d$ The number of nodes.

$(\boldsymbol{h}_j)_k = \delta_{jk} L_j / N_j$ The unit cell vector.

$\|\boldsymbol{h}_j\|_2$ The cell width.

X The pressure grid nodes: $X = \{0, \|\boldsymbol{h}_1\|_2, \ldots, (N_1 - 1)\|\boldsymbol{h}_1\|_2\} \times \cdots \times \{0, \|\boldsymbol{h}_d\|_2, \ldots, (N_d - 1)\|\boldsymbol{h}_d\|_2\}$.

$X_\infty = \{\boldsymbol{nd} : \boldsymbol{n} \in \mathbb{Z}^d\}$ The infinitely extended grid.

X_{u_j} The u_j velocity nodes: $X_{u_j} = \{x + \frac{1}{2}\boldsymbol{h}_j : x \in X\}$.

$\Xi = \{0, 1, \ldots, N_1\} \times \cdots \times \{0, 1, \ldots, N_d\}$ The frequency grid.

Variables on a discrete grid X or X_∞ are denoted as functions, e.g. the pressure on X is the function $p : X \to \mathbb{R}$. Linear operators are denoted in calligraphic font. We omit parentheses in the following cases: $\mathscr{G}^T \mathscr{G}p(\boldsymbol{x})$ is equal to $(\mathscr{G}^T \mathscr{G}p)(\boldsymbol{x})$ and component j of the Laplacian of u is denoted by $\mathscr{L}\boldsymbol{u}(\boldsymbol{x})_j$ instead of $((\mathscr{L}\boldsymbol{u})(\boldsymbol{x}))_j$. Note that this notation does not introduce ambiguity.

NULL SPACE REDUCTION IN TWO DIMENSIONS

We use the null space reduction method, see Benzi *et al.* (2005) and their references, to reduce the Stokes equations in two unidirectionally coupled subsystems.

The conservation of mass (4) restricts the solution space of the velocity to the divergence-free subspace, $\boldsymbol{u} \in \ker \mathscr{G}^T$. Assuming the columns of some matrix $\mathscr{Z}$ span this subspace, $\mathrm{col}\,\mathscr{Z} = \ker \mathscr{G}^T$, then the velocity can be written in terms of $\mathscr{Z}$ as $\boldsymbol{u} = \mathscr{Z}w$. Substitution into (3) yields

$$\mathscr{L}\mathscr{Z}w + \mathscr{G}p = \boldsymbol{f}, \tag{5}$$

and (4) is satisfied automatically.

Note that the number of velocity unknowns is $2N_1N_2$. Recall from linear algebra that the direct sum of the null space and row space of $\mathscr{G}^T$ equals the total space $\mathbb{R}^{2N_1N_2}$. Equation (5) can be separated by projection onto both subspaces,

$$\mathrm{proj}_{\ker \mathscr{G}^T}(\mathscr{L}\mathscr{Z}w + \mathscr{G}p - \boldsymbol{f}) = 0, \tag{6}$$

$$\mathrm{proj}_{\mathrm{row}\,\mathscr{G}^T}(\mathscr{L}\mathscr{Z}w + \mathscr{G}p - \boldsymbol{f}) = 0. \tag{7}$$

Solving both equations solves (5). The projections are effectively the same as left multiplication with the matrices $\mathscr{Z}^T$ and $\mathscr{G}$, respectively, yielding the system

$$\mathscr{Z}^T \mathscr{L}\mathscr{Z}w + \mathscr{Z}^T \mathscr{G}p = \mathscr{Z}^T \boldsymbol{f}, \tag{8}$$

$$\mathscr{G}^T \mathscr{L}\mathscr{Z}w + \mathscr{G}^T \mathscr{G}p = \mathscr{G}^T \boldsymbol{f}. \tag{9}$$

Since the columns of $\mathscr{Z}$ and $\mathscr{G}$ are orthogonal, $\mathscr{Z}^T \mathscr{G} = 0$ and (8) becomes

$$\mathscr{Z}^T \mathscr{L}\mathscr{Z}w = \mathscr{Z}^T \boldsymbol{f}, \tag{10}$$

a square system to be solved for the velocity w in the divergence-free subspace. Finally, (9) is to be solved for the pressure p using the solution of (10). It is easy to verify that both subsystems are symmetric positive semidefinite.

Construction of a basis for the null space

For general, unstructured grids, finding a basis or a spanning set of vectors for $\ker \mathscr{G}^T$ is not trivial. Furthermore, it is advantageous to construct a sparse basis, or, even better, a basis such that $\mathscr{Z}^T \mathscr{L}\mathscr{Z}$ is sparse, since this affects the amount of work in solving the velocity subsystem (10). Fortunately, for the equidistant grid which we use to discretise the Stokes equations, it turns out to be very easy, as we will show now. Figure 1 shows a fragment of the staggered grid with a grid numbering relative to some (pressure) node $\boldsymbol{r} \in X$. The divergence at the reference point $\boldsymbol{r}$ is given by

$$\mathscr{G}^T(\boldsymbol{r}) = $$
$$z_1\left(\boldsymbol{r} + \tfrac{1}{2}\boldsymbol{h}_1\right) - z_1\left(\boldsymbol{r} - \tfrac{1}{2}\boldsymbol{h}_1\right) + z_2\left(\boldsymbol{r} + \tfrac{1}{2}\boldsymbol{h}_2\right) - z_2\left(\boldsymbol{r} - \tfrac{1}{2}\boldsymbol{h}_2\right). \tag{11}$$

We use a heuristic approach for constructing one divergence free velocity vector z, i.e. we want $\mathscr{G}^T z = 0$. Fix $\boldsymbol{r} \in X$ and let $z_1\left(\boldsymbol{r} + \tfrac{1}{2}\boldsymbol{h}_1\right) = -\|\boldsymbol{h}_2\|_2^{-1}$, the velocity node directly to the right of $\boldsymbol{r}$. This affects two nodes at which the divergence is computed, $\boldsymbol{r}$ and $\boldsymbol{r} + \boldsymbol{d}_1$. The divergence of z at $\boldsymbol{r}$ can be made zero by setting $z_2\left(\boldsymbol{r} + \tfrac{1}{2}\boldsymbol{h}_2\right) = \|\boldsymbol{h}_1\|_2^{-1}$, among others. This solves the divergence at $\boldsymbol{r}$, but introduces a new defect at $\boldsymbol{r} + \boldsymbol{h}_2$. This is resolved by setting $z_1\left(\boldsymbol{r} + \tfrac{1}{2}\boldsymbol{h}_1 + \boldsymbol{h}_2\right) = \|\boldsymbol{h}_2\|_2^{-1}$, which, in return, affects the divergence at $\boldsymbol{r} + \boldsymbol{h}_1 + \boldsymbol{h}_2$. Both this and $\boldsymbol{r} + \boldsymbol{h}_1$ can be solved simultaneously by setting $z_2\left(\boldsymbol{r} + \boldsymbol{h}_1 + \tfrac{1}{2}\boldsymbol{h}_2\right) = -\|\boldsymbol{h}_1\|_2^{-1}$ introducing no other defects.
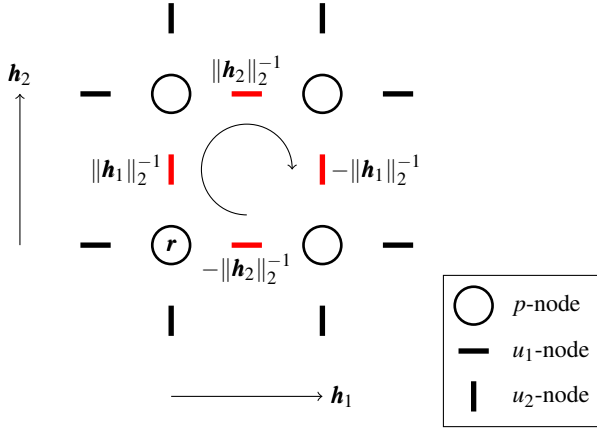
Figure 1: Illustration of one basis vector for the divergence free velocity subspace $\ker \mathscr{G}^T$. The non-zero elements are marked red

Summarising, the constructed divergence free vector $\boldsymbol{z}$, $z_1 : X_{u_1} \to \mathbb{R}$ and $z_2 : X_{u_2} \to \mathbb{R}$, is given by

$$
z_1(\boldsymbol{x}) = \begin{cases} -\|\boldsymbol{h}_2\|_2^{-1} & \boldsymbol{x} = \boldsymbol{r} + \frac{1}{2}\boldsymbol{h}_1 \\ \|\boldsymbol{h}_2\|_2^{-1} & \boldsymbol{x} = \boldsymbol{r} + \frac{1}{2}\boldsymbol{h}_1 + \boldsymbol{h}_2 \quad \boldsymbol{x} \in X_{u_1}, \quad (12) \\ 0 & \text{otherwise,} \end{cases}
$$

and

$$
z_2(\boldsymbol{x}) = \begin{cases} \|\boldsymbol{h}_1\|_2^{-1} & \boldsymbol{x} = \boldsymbol{r} + \frac{1}{2}\boldsymbol{h}_2 \\ -\|\boldsymbol{h}_1\|_2^{-1} & \boldsymbol{x} = \boldsymbol{r} + \frac{1}{2}\boldsymbol{h}_2 + \boldsymbol{h}_1 \quad \boldsymbol{x} \in X_{u_2}, \quad (13) \\ 0 & \text{otherwise.} \end{cases}
$$

It can be shown that there exists no sparser vector than $\boldsymbol{z}$. Translating this vector by every possible offset $\boldsymbol{r} \in X$ yields a set of $N_1 N_2$ vectors which span the divergence free velocity subspace $\ker \mathscr{G}^T$. This set contains exactly one redundant vector, i.e. by removing one vector from the set it becomes linearly independent, hence a basis for $\ker \mathscr{G}^T$. However, as will become apparent below, it is advantageous to keep the extra vector.

The basis vectors constructed above are in fact pure rotations, illustrated in Figure 1, and the transposed null space operator $\mathscr{Z}^T$ is a discrete curl operator. This is no surprise since the divergence of the curl of any function is zero. The discrete curl operator, following the derivation above, is given by

$$
\mathscr{Z}^T = \operatorname{curl}_{12} \boldsymbol{u}(\boldsymbol{x}) = \frac{u_1\left(\boldsymbol{x} + \frac{1}{2}\boldsymbol{h}_2 + \boldsymbol{h}_1\right) - u_1\left(\boldsymbol{x} + \frac{1}{2}\boldsymbol{h}_2\right)}{\|\boldsymbol{h}_1\|_2}
$$
$$
- \frac{u_2\left(\boldsymbol{x} + \frac{1}{2}\boldsymbol{h}_1 + \boldsymbol{h}_2\right) - u_2\left(\boldsymbol{x} + \frac{1}{2}\boldsymbol{h}_1\right)}{\|\boldsymbol{h}_2\|_2}, \quad \boldsymbol{x} \in X. \quad (14)
$$

Note that the reference point $\boldsymbol{x}$ is not located at the center of rotation but at the lower left corner.

SOLVING THE PRESSURE SUBSYSTEM

Although the pressure subsystem (9) is to be solved after the velocity subsystem (10), we will start with a solution technique for the former, as the derivation is easier and can be used for the latter.

The pressure subsystem that follows from applying the null space reduction to the Stokes equations is a discrete Poisson problem. Fast solution techniques exist for this type of problem on a rectangular grid with Dirichlet or periodic boundary conditions, based on a combination of Fourier transforms

and a method to solve a (circulant) tridiagonal system (Chen, 1987). The latter can be solved using a Fourier transform as well. The principle behind these so called 'Fast Poisson Solvers' is the convolution theorem, which relates convolutions in the spatial domain to products in the frequency domain and vice versa. In this section we derive a Fast Poisson Solver generalise the Fourier transform and convolution theorem for sheared periodic boundary conditions, based on the work of Brucker *et al.* (2007).

The (shear) periodic boundary conditions for the pressure imply a repetition of the pressure p in every direction on an infinitely extended grid. Let $\mathscr{P}_{\boldsymbol{s}} p$ denote this extension of the pressure, formally defined by

$$
\mathscr{P}_{\boldsymbol{s}} p (\boldsymbol{x} + \boldsymbol{n} L + n_1 s_2 \boldsymbol{h}_2) = p(\boldsymbol{x}), \quad \boldsymbol{x} \in X, \ \boldsymbol{n} \in \mathbb{Z}^2. \quad (15)
$$

The periodic extension in absence of shearing is denoted by $\mathscr{P}_0$. This representation of the pressure allows us to write the pressure subsystem, Equation (9), as

$$
\sum_{j=1}^2 \frac{-2\mathscr{P}_{\boldsymbol{s}} p(\boldsymbol{x}) + \mathscr{P}_{\boldsymbol{s}} p(\boldsymbol{x} + \boldsymbol{h}_j) + \mathscr{P}_{\boldsymbol{s}} p(\boldsymbol{x} - \boldsymbol{h}_j)}{\|\boldsymbol{h}_j\|_2^2} = g(\boldsymbol{x}),
$$
$$
\boldsymbol{x} \in X_\infty, \quad (16)
$$

where g contains all constant terms of Equation (10), including the divergence free velocity w,

$$
g = \mathscr{G}^T \boldsymbol{f} - \mathscr{G}^T \mathscr{L} \mathscr{Z} w. \quad (17)
$$

Normal periodicity

We start with a derivation of a Fast Poisson Solver for normal periodicity, i.e. $\boldsymbol{s} = 0$.

Definition 1. The two-dimensional Fourier transform of $p : X \to \mathbb{R}$, denoted by $\mathscr{F}p$, is defined by

$$
\mathscr{F}p(\boldsymbol{\xi}) := \sum_{\boldsymbol{x} \in X} p(\boldsymbol{x}) \phi(\boldsymbol{\xi}, \boldsymbol{x}), \quad \boldsymbol{\xi} \in \Xi. \quad (18)
$$

with the Fourier basis functions $\phi(\boldsymbol{\xi}, \boldsymbol{x})$ defined by

$$
\phi(\boldsymbol{\xi}, \boldsymbol{x}) = e^{-2\pi i \left(\frac{\xi_1 x_1}{L_1} + \frac{\xi_2 x_2}{L_2}\right)}. \quad (19)
$$

Note that the periodic extension of the pressure $\mathscr{P}_0 p$ can be represented by a discrete Fourier series,

$$
\mathscr{P}_0 p(\boldsymbol{x}) = (\#X)^{-1} \sum_{\boldsymbol{\xi} \in X} \hat{p}(\boldsymbol{\xi}) \overline{\phi(\boldsymbol{\xi}, \boldsymbol{x})}, \quad \boldsymbol{x} \in X_\infty, \quad (20)
$$

where $\#X$ denotes the number of elements in set X and equals $N_1 N_2$.

Substituting the two-dimensional discrete Fourier representations of p and g into the Poisson equation, Equation (16), yields

$$
\sum_{\boldsymbol{\chi} \in \Xi} \hat{p}(\boldsymbol{\chi}) \hat{k}(\boldsymbol{\chi}) \overline{\phi(\boldsymbol{\chi}, \boldsymbol{x})} = \sum_{\boldsymbol{\zeta} \in X} \hat{g}(\boldsymbol{\zeta}) \overline{\phi(\boldsymbol{\zeta}, \boldsymbol{x})}. \quad (21)
$$

with

$$
\hat{k}(\boldsymbol{\xi}) = \sum_{j=1}^2 \frac{-2 + e^{2\pi i \frac{\xi_j}{L_j}} - e^{2\pi i \frac{\xi_j}{L_j}}}{\|\boldsymbol{h}_j\|_2}, \quad \boldsymbol{\xi} \in \Xi. \quad (22)
$$

Multiplying both sides of (21) with a Fourier basis function of frequency $\boldsymbol{\xi} \in \Xi$ and applying orthogonality of the Fourier

basis functions to eliminate both sums yields the following system of equations,

$$\hat{p}(\boldsymbol{\xi})\hat{k}(\boldsymbol{\xi}) = \hat{g}(\boldsymbol{\xi}), \quad \boldsymbol{\xi} \in \Xi. \tag{23}$$

Hence, we can solve the pressure subsystem by applying a Fourier transform to g, solving Equation (23) for $\hat{p}$ and applying an inverse Fourier transform to the result. The complexity of the Fast Fourier Transform (FFT), a class of efficient algorithms for computing the Fourier transform, is $O(\#X \log \#X)$. The complexity of solving the pressure subsystem via (23) is $O(\#X \log \#X)$ as well.

From Fourier analysis is known that a product of functions in frequency domain is equal to a convolution in spatial domain, where the convolution is defined as

Definition 2. The periodic convolution of p and $k : \Xi \to \mathbb{R}$, denoted by $p \circledast k : X_\infty \to \mathbb{R}$, is defined by

$$(p \circledast k)(\boldsymbol{x}) := \sum_{\boldsymbol{y} \in X} \mathscr{P}_0 p(\boldsymbol{x} - \boldsymbol{y}) \mathscr{P}_0 k(\boldsymbol{y}), \quad \boldsymbol{x} \in X_\infty. \tag{24}$$

We conclude that Equation (10) can be written as a convolution

$$p \circledast k = g, \tag{25}$$

where k is the default five-point stencil for the Laplace operator.

Shear periodicity

We now attempt to generalise the convolution for shearing and derive a shear convolution theorem.

Definition 3. The shear periodic convolution of p and $k : X \to \mathbb{R}$, denoted by $p \circledast_{\boldsymbol{s}} k : X_\infty \to \mathbb{R}$, is defined by

$$(p \circledast_{\boldsymbol{s}} k)(\boldsymbol{x}) := \sum_{\boldsymbol{y} \in X} \mathscr{P}_{\boldsymbol{s}} p(\boldsymbol{x} - \boldsymbol{y}) \mathscr{P}_{\boldsymbol{s}} k(\boldsymbol{y}), \quad \boldsymbol{x} \in X_\infty. \tag{26}$$

Note that the shear periodic extensions of p and k are used.

When $s_2 = 0$, i.e. there is no shearing, the shear periodic convolution is equal to the ordinary two-dimensional periodic or circular convolution.

Using the definition of the shear periodic convolution, we can write the Poisson equation as

$$p \circledast_{\boldsymbol{s}} k = g, \tag{27}$$

where k is the default five-point stencil for the Laplace operator. Equation (27) is a generalisation of (25).

The ordinary convolution theorem would follow from substitution of the Fourier inverses of $\hat{p}$ and $\hat{k}$ for $\mathscr{P}_0 p$ and $\mathscr{P}_0 k$, respectively, and applying orthogonality, as is done in the previous section. However, the inverse Fourier transform does not satisfy the periodic extension (15) in case of shearing. To overcome this problem, we use the modified Fourier transform of Brucker *et al.* (2007). An informal derivation of this Fourier transform follows.

Figure 2a shows a partition of the infinitely extended grid with shear amount $s_2 = 2$, i.e. every repetition is shifted two nodes upwards with respect to the left. If it is possible to shift every column down by $s_2 x_1 L_1^{-1}$, see Figure 2b, then the result is ordinary periodic in every direction and we could use the procedure for normal periodicity described above to solve the problem. From Fourier theory it is known that a shift in spatial domain corresponds to multiplication with a

linear phase in frequency domain. First transform the second axis,

$$\tilde{p}(x_1, \xi_2) = \sum_{x_2=0}^{L_2-1} p(x_1, x_2) e^{-2\pi i \frac{\xi_2 x_2}{L_2}}, \tag{28}$$

and multiply with a linear phase,

$$\check{p}(x_1, \xi_2) = \tilde{p}(x_1, \xi_2) e^{2\pi i \frac{\xi_2 s_2 x_1}{L_1 L_2}}. \tag{29}$$

A backwards Fourier transform yields an interpolated grid which is normal periodic, see Figure 2c. At this point we could apply the theory described above. As this involves another Fourier transform over the second axis, we combine the shear compensation in Fourier space with the ordinary two-dimensional Fourier transform which yields

Definition 4. The two-dimensional shear Fourier transform of $p : X \to \mathbb{R}$, denoted by $\mathscr{F}_{\boldsymbol{s}} p : \Xi \to \mathbb{C}$, is defined by

$$\mathscr{F}_{\boldsymbol{s}} p(\boldsymbol{\xi}) := \sum_{\boldsymbol{x} \in X} p(\boldsymbol{x}) \phi_{\boldsymbol{s}}(\boldsymbol{\xi}, \boldsymbol{x}), \quad \boldsymbol{\xi} \in \Xi. \tag{30}$$

with the shear Fourier basis functions $\phi_{\boldsymbol{s}}(\boldsymbol{\xi}, \boldsymbol{x})$ defined by

$$\phi_{\boldsymbol{s}}(\boldsymbol{\xi}, \boldsymbol{x}) = e^{-2\pi i \left(\frac{\xi_1 x_1}{L_1} + \frac{\xi_2 x_2}{L_2} - \frac{\xi_2 x_1 s_2}{L_1 L_2} \right)}. \tag{31}$$

Note that this definition is a generalisation of the ordinary two-dimensional Fourier transform since $\phi_0 = \phi$.

Two analogous interpretations of this Fourier transform are worth mentioning. First, the Fourier basis functions $\phi_{\boldsymbol{s}}$ are equal to the normal basis functions on a transformed spatial coordinate system.

$$\phi_{\boldsymbol{s}}(\boldsymbol{\xi}, \boldsymbol{x}) = \phi\left(\boldsymbol{\xi}, \left[x_1, x_2 + s_2 x_1 L_1^{-1}\right]\right). \tag{32}$$

Second, collecting the terms for x_1 and x_2 in the exponent of $\phi_{\boldsymbol{s}}(\boldsymbol{\xi}, \boldsymbol{x})$ and comparing with the original basis functions reveals a transformation of the frequencies,

$$\phi_{\boldsymbol{s}}(\boldsymbol{\xi}, \boldsymbol{x}) = \phi\left(\left[\xi_1 - s_2 \xi_2 L_1^{-1}, \xi_2\right], \boldsymbol{x}\right). \tag{33}$$

Before we can prove the convolution theorem for shear periodicity, we state some necessary properties of the shear Fourier transform.

Theorem 1. *Properties of the shear Fourier transform in two dimensions.*

1. *The inverse shear Fourier transform is given by*

$$p(\boldsymbol{x}) = \mathscr{F}_{\boldsymbol{s}}^{-1} \hat{p}(\boldsymbol{x}) = (\#X)^{-1} \sum_{\boldsymbol{\xi} \in \Xi} \hat{p}(\boldsymbol{\xi}) \overline{\phi_{\boldsymbol{s}}(\boldsymbol{\xi}, \boldsymbol{x})}. \tag{34}$$

2. *The inverse shear Fourier transform satisfies the periodic extension (15), i.e. $\mathscr{P}_{\boldsymbol{s}} p = \mathscr{F}_{\boldsymbol{s}}^{-1} \mathscr{F}_{\boldsymbol{s}} p$.*

3. *The shear Fourier basis functions are orthogonality. Let $\boldsymbol{\xi}, \boldsymbol{\zeta} \in \Xi$. Then*

$$\sum_{\boldsymbol{x} \in X} \phi_{\boldsymbol{s}}(\boldsymbol{\xi}, \boldsymbol{x}) \overline{\phi_{\boldsymbol{s}}(\boldsymbol{\zeta}, \boldsymbol{x})} = 0 \iff \boldsymbol{\xi} \neq \boldsymbol{\zeta}, \tag{35}$$

For a proof of these properties we refer to Van Zwieten (2011).

Theorem 2. *The shear periodic convolution of vectors p and $k \in \mathbb{R}^{N_1 \times N_2}$ is equivalent to multiplication in shear Fourier domain,*

$$\mathscr{F}_{\boldsymbol{s}}(p \circledast_{\boldsymbol{s}} k) = \mathscr{F}_{\boldsymbol{s}} p \mathscr{F}_{\boldsymbol{s}} k. \tag{36}$$

(a) Grid with shear periodic boundaries. Every repetition of the domain is shifted two nodes upward in the second (vertical) direction along the first (horizontal) direction.

(b) Correction of the shear periodicity to normal periodicity by shifting horizontal lines down with a correct amount.

(c) Interpolation of the shear-corrected grid, see Figure 2b, onto the regular grid. The result is a normal grid with normal periodicity.

Figure 2: Illustration of the shear periodic boundaries and the shear correction and interpolation stage.

Proof. Substitute the inverse shear Fourier transforms of p and k into the convolution and use orthogonality to eliminate one of the three summations over X. $\qquad\square$

Applying Theorem 2 to the pressure subsystem, Equation (27), yields

$$\hat{p}(\boldsymbol{\xi})\hat{k}(\boldsymbol{\xi}) = \hat{g}(\boldsymbol{\xi}), \quad \boldsymbol{\xi} \in \Xi, \tag{37}$$

where $\hat{p}$, $\hat{k}$ and $\hat{g}$ are the shear Fourier coefficients of p, k and g, respectively.

We can compute a shear Fourier transform efficiently using two one-dimensional Fast Fourier Transforms and a vector vector operation in between. The vector vector operation has no impact on the complexity of the transformation. Hence, the complexity of solving the Poisson with shear periodic boundary conditions via (37) is $O(\#X \log \#X)$.

An alternative method is found by replacing the inner Fourier transform by a direct solver for a tri-diagonal circulant matrix. See Chen (1987).

SOLVING THE VELOCITY SUBSYSTEM

The solution method for the velocity subsystem depends on the homogeneity of the viscosity. In the first subsection we explain how to solve the subsystem for homogeneous viscosity using the convolution theorem. In the second subsection we describe a solution method for the general case.

Homogeneous viscosity

We showed that the scalar Laplace operator, $\mathscr{G}^T\mathscr{G}$, can be written as a convolution. The same applies to $\mathscr{Z}$ and $\mathscr{L}$, if the viscosity is homogeneous. For $\mathscr{Z}$ this it due to the fact that we keep the redundant basis vector. It is easy to verify that any product and sum of convolution operators is again a convolution operator, which implies that $\mathscr{Z}^T\mathscr{L}\mathscr{Z}$ is a convolution operator,

$$\mathscr{Z}^T\mathscr{L}\mathscr{Z}w = w \circledast_s k, \tag{38}$$

and we can use the convolution theorem, Theorem 2, to find a solution.

An alternative method is found by replacing the inner Fourier transform by a direct solver for penta-diagonal circulant matrices, see Chen (1987).

Inhomogeneous viscosity

When the viscosity is inhomogeneous, we cannot write the vector Laplace operator $\mathscr{L}$ as a convolution, because the viscosity depends on the position. We have to use an iterative solver to find a solution to the velocity subsystem. Since this system is symmetric positive semi-definite, the method of choice is the Conjugate Gradient solver. This method has a small memory foot print.

If the viscosity is only slightly varying in position, we assume that the problem with homogeneous viscosity is very close to the inhomogeneous problem. We propose to use the homogeneous problem, for which we derived a solution method based on the convolution theorem, as a preconditioner for the Conjugate Gradient solver. The performance of this solver is examined in the section on numerical experiments.
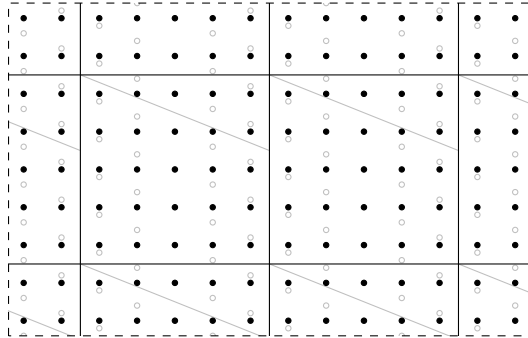
EXTENSION TO THREE DIMENSIONS

The null space reduction, described above, is independent of the number of dimensions, i.e. applies to the three dimensional without modification. The basis for the null space, however, needs to be extended to three dimensions. We define such a basis in the second subsection. In the first subsection we define the shear Fourier transform, which is a natural extension from the two dimensional version. Finally, the reduced vector Laplace operator $\mathscr{Z}^T \mathscr{L} \mathscr{Z}$ operates on a divergence free velocity vector w with two components instead of one. In the last subsection we explain how to solve this system using the convolution theorem.

Shear Fourier transform

Definition 5. The three-dimensional shear periodic extension of $p : X \to \mathbb{R}$, denoted by $\mathscr{P}_s p : X_\infty \to \mathbb{R}$, is defined by

$$\mathscr{P}_s p \left(\boldsymbol{x} + \boldsymbol{n}L + \sum_{j=2}^{3} n_1 s_j \boldsymbol{h}_j \right) = p(\boldsymbol{x}), \quad \boldsymbol{x} \in X, \quad \boldsymbol{n} \in \mathbb{Z}^3. \tag{39}$$

Definition 6. The three-dimensional shear Fourier transform of $p : X \to \mathbb{R}$, denoted by $\mathscr{F}_s p : \Xi \to \mathbb{C}$, is defined by

$$\mathscr{F}_s p(\boldsymbol{\xi}) := \sum_{\boldsymbol{x} \in X} p(\boldsymbol{x}) \phi_s(\boldsymbol{\xi}, \boldsymbol{x}), \quad \boldsymbol{\xi} \in \Xi. \tag{40}$$

with the shear Fourier basis functions $\phi_s(\boldsymbol{\xi}, \boldsymbol{x})$ defined by

$$\phi_s(\boldsymbol{\xi}, \boldsymbol{x}) = \mathrm{e}^{-2\pi i \left(\Sigma_{j=1}^{3} \frac{\xi_j x_j}{L_j} - \Sigma_{j=2}^{3} \frac{\xi_j x_1 s_j}{L_1 L_j} \right)}. \tag{41}$$

The shear periodic convolution, Definition 3, the shear Fourier properties, Theorem 1, and the convolution theorem, Theorem 2, apply to the above defined periodic extension and Fourier transform without modification.

Construction of a basis for the null space

The null space operator for two dimensions is equal to the discrete curl operator. Because of the sparsity and regularity of this operator, we would like to obtain a similar operator for three dimensions. The three-dimensional curl operator is given by

$$\mathrm{curl}_{jk}\boldsymbol{u}(\boldsymbol{x}) = \frac{u_j\left(\boldsymbol{x} + \frac{1}{2}\boldsymbol{h}_k + \boldsymbol{h}_j\right) - u_j\left(\boldsymbol{x} + \frac{1}{2}\boldsymbol{h}_k\right)}{\|\boldsymbol{h}_j\|_2}$$
$$- \frac{u_k\left(\boldsymbol{x} + \frac{1}{2}\boldsymbol{h}_j + \boldsymbol{h}_k\right) - u_k\left(\boldsymbol{x} + \frac{1}{2}\boldsymbol{h}_j\right)}{\|\boldsymbol{h}_k\|_2}. \tag{42}$$

which is very similar to the two-dimensional version, the difference being that there are three planes jk with $j,k \in \{1,2,3\}$ in which rotations can occur/are defined.

It seems natural, but is incorrect, to define the transposed null space operators as

$$\left(\mathscr{Z}^T \boldsymbol{u}\right)_1 = \mathrm{curl}_{12}\boldsymbol{u}, \tag{43}$$

and

$$\left(\mathscr{Z}^T \boldsymbol{u}\right)_2 = \mathrm{curl}_{23}\boldsymbol{u}. \tag{44}$$

The former consists of all rotations in the plane orthogonal to the third axis and does not depend on u_3. As in the two-dimensional case, there exists no sparser set of vectors. As noted above, the rank of $\mathscr{Z}$ should equal twice the number of pressure unknowns/nodes minus two. Comparing $\mathscr{Z}$ with

the two-dimensional $\mathscr{Z}$ yields there are $2N_3$ redundant/linear dependent columns in $\mathscr{Z}$. Hence the rank of $\mathscr{Z}$ is too small, and the columns of $\mathscr{Z}$ do not span the divergence free velocity space.

We can add the missing vectors, but this would break the regularity, which is a requirement for using the convolution theorem. Instead, we use

$$\left(\mathscr{Z}^T \boldsymbol{u}\right)_1 = \mathrm{curl}_{12}\boldsymbol{u} + \mathrm{curl}_{13}\boldsymbol{u}, \tag{45}$$

and

$$\left(\mathscr{Z}^T \boldsymbol{u}\right)_2 = \mathrm{curl}_{21}\boldsymbol{u} + \mathrm{curl}_{23}\boldsymbol{u}. \tag{46}$$

Velocity subsystem

The velocity subsystem (10) can be written in terms of multiple convolutions as

$$\left(\mathscr{Z}^T \mathscr{L} \mathscr{Z} w\right)_j = w_1 \circledast_s k_{j1} + w_2 \circledast_s k_{j2} = \left(\mathscr{Z}^T \boldsymbol{f}\right)_j,$$
$$j \in \{1,2\}. \tag{47}$$

Applying the convolution theorem, Theorem 2, yields #X decoupled 2×2-systems,

$$\hat{w}_1(\boldsymbol{\xi})\hat{k}_{j1}(\boldsymbol{\xi}) + \hat{w}_2(\boldsymbol{\xi})\hat{k}_{j2}(\boldsymbol{\xi}) = \hat{g}_j(\boldsymbol{\xi}), \quad \boldsymbol{\xi} \in \Xi, \quad j \in \{1,2\}, \tag{48}$$

where $\hat{w}_j = \mathscr{F}_s(w_j)$, $\hat{k}_{jn} = \mathscr{F}_s(k_{jn})$ and $\hat{g}_j = \mathscr{F}_s\left(\left(\mathscr{Z}^t \boldsymbol{f}\right)_j\right)$. These systems are solved explicitly by

$$\begin{bmatrix} \hat{w}_1(\boldsymbol{\xi}) \\ \hat{w}_2(\boldsymbol{\xi}) \end{bmatrix} = \frac{1}{\det\hat{\boldsymbol{k}}(\boldsymbol{\xi})} \begin{bmatrix} \hat{k}_{22}(\boldsymbol{\xi}) & -\hat{k}_{12}(\boldsymbol{\xi}) \\ -\hat{k}_{21}(\boldsymbol{\xi}) & \hat{k}_{11}(\boldsymbol{\xi}) \end{bmatrix} \begin{bmatrix} \hat{g}_1(\boldsymbol{\xi}) \\ \hat{g}_2(\boldsymbol{\xi}) \end{bmatrix}, \tag{49}$$

if the determinant, given by

$$\det\hat{\boldsymbol{k}}(\boldsymbol{\xi}) = \frac{1}{\hat{k}_{11}(\boldsymbol{\xi})\hat{k}_{22}(\boldsymbol{\xi}) - \hat{k}_{12}(\boldsymbol{\xi})\hat{k}_{21}(\boldsymbol{\xi})}, \tag{50}$$

is non-zero, which is true for $\boldsymbol{\xi} \neq 0$.

NUMERICAL EXPERIMENTS

Test problems

The first test problem is a droplet of oil in water. Oil and water repel each other but entropy ensures that a finite (trace) amount of water is present in the oil phase and vice versa. Upon increasing repulsion, the demixing of the phases decreases and the droplet interface becomes more narrow. Prior to the test run, the droplet is equilibrated using DDFT without any shear. The test solves the Stokes equations for the first time step only. This is a suitable limiting case: subsequent time steps are somewhat simpler to solve since one can use the solution from a previous time step as an initial guess. Figure 3 illustrates the system after a few shear time steps.

The second test problem is a symmetric A8B8 block copolymer melt, a simplified model system. The A and B blocks repel each other which leads to phase separation but since the blocks are covalently linked, finite size domains are formed in contrast to the macroscopic phase separation seen in the first test problem. This system will have the tendency to form lamellae but as is illustrated in Figure 4, the initial stages of demixing result in a rather chaotic picture. Compared to the first test problem, this one has lots of interface and hence a finite body-force and viscosity that both vary throughout the domain.
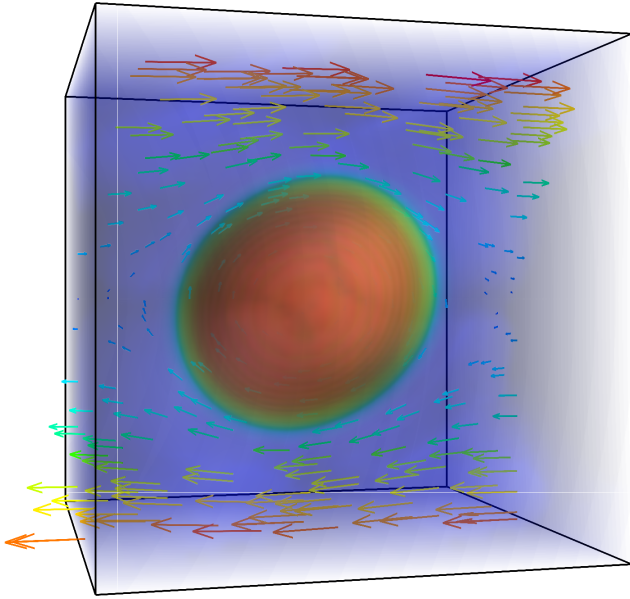
Figure 3: Volume rendering of an oil droplet suspended in water. Red means a high oil density and transparent/blue a high water density.
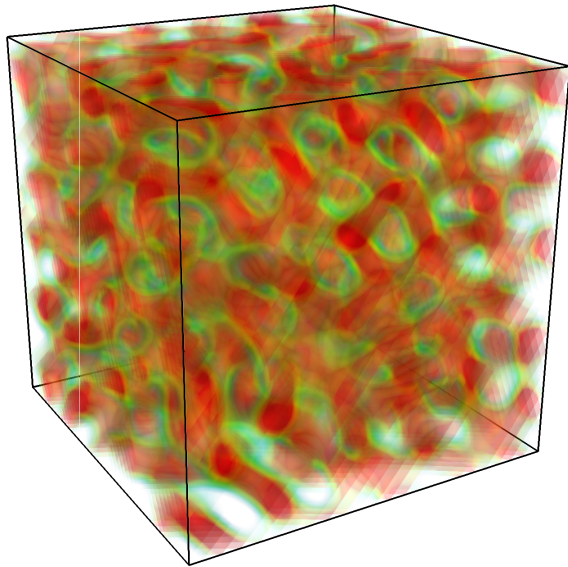
Figure 4: A typical snapshot of the initial stages of microphase separation in a symmetric A8B8 polymer blend. Red means a high density of A molecules, while the transparent/greenish parts indicate a high density of B molecules.

Compared methods

We compare the solution technique described above with two methods from the literature. The first is a MINRES, a solver for (general) symmetric systems, with diagonal preconditioning,

$$\mathscr{M} = \begin{bmatrix} \tilde{\mathscr{L}} & \mathscr{O} \\ \mathscr{O} & \tilde{\mathscr{S}} \end{bmatrix}. \tag{51}$$

Here, the vector Laplace operator is approximated by the diagonal. The Schur complement is approximated by the inverse viscosity,

$$\tilde{\mathscr{S}}p(\boldsymbol{x}) = \frac{-2}{\nu(\boldsymbol{x})}p(\boldsymbol{x}). \tag{52}$$

The second method is based on GCR with a triangular preconditioner, see Benzi *et al.* (2005) and their references,

$$\mathscr{M} = \begin{bmatrix} \mathscr{L} & \mathscr{G} \\ \mathscr{O} & \tilde{\mathscr{S}} \end{bmatrix}. \tag{53}$$

The inverse of $\mathscr{L}$, computed every GCR iteration, is solved approximately using CG with a tolerance slightly stricter than the residual norm of GCR at the current iteration. The approximation for the Schur complement is equal to the one used in MINRES.

Results

The physical domain size $\boldsymbol{L}$ is constant, which implies that the cell widths vary inversely with $\boldsymbol{N}$. All grids considered are square. The viscosity ratio is defined as the ratio between the maximum and minimum values of the viscosity. The three methods, the null space method with Fourier preconditioner, the MINRES method with diagonal preconditioner and the GCR method with block triangular preconditioner, are compared in terms of the number of floating point operations (flops) needed to find a solution with an accuracy of at least 10^{-8} times the norm of the initial residual.

Table 1 shows numerical results for the first test problem, the oil droplet, in two dimensions for various grid sizes $\boldsymbol{N}$ and viscosity ratios. For this test problem, the oil droplet has, naturally, the highest viscosity.

A viscosity ratio of 1 refers to the homogeneous viscosity case. The null space method with Fourier preconditioner needs a single iteration to solve the problem, since the preconditioner is the exact inverse of the discretised Stokes equations. For ν-ratio > 1 this is no longer true and the solver requires several iterations to reach the accuracy. This difference between homogeneous and inhomogeneous is clearly visible in Figure 5, where the viscosity ratio is varied while the grid size is kept constant. The other methods are not susceptible to this viscosity difference, however, they require a lot more work than the null space method.

Varying the grid size while keeping the viscosity ratio constant has only a small effect on the amount of work for the null space method, see Table 1 and Figure 6. The other two methods are much more sensitive to the number of unknowns. This indicates that, at least for small viscosity ratios, the null space method is superior to the other two methods for large grids. For the investigated problems, the null space method is up to a hundred times faster than the other two methods.

Table 2 shows the numerical results for the second test problem, the diblock copolymer melt. The null space method behaves very similar to the oil droplet problem. The influence of the grid size on the amount of work is small and

increasing the viscosity ratio has a substantial impact on the performance. The other two methods, however, require more work compared to the oil droplet, especially for large viscosity ratios. Figure 7 shows that all methods are almost equally sensitive to increasing viscosity ratios.

Table 3 shows the results for the diblock copolymer melt problem which has evolved a couple of time steps using the DDFT method, hence has a shear periodicity. The null space method seems insensitive to the shear periodicity. The GCR and MINRES methods perform slightly better for high viscosity ratios and large grids compared the the normal periodic case.

Table 4 shows the results for the oil droplet in a three-dimensional domain. The trends of all methods are similar to the two dimensional case. However, the null space method is more susceptible to big viscosity ratios. Nevertheless, the null space method outperforms the other two methods.

CONCLUSION

In this paper we developed a method for solving the Stokes equations on a regular structured grid with variable viscosity and shear periodic boundary conditions. The method consists of a reduction of the Stokes equations in two unidirectionally coupled systems, both symmetric positive semi-definite, and an iterative solver with an efficient preconditioner and a small memory foot print.

The convolution theorem holds for shear periodic boundaries using a generalisation of the Fourier transform. Shear periodic convolutions can be computed and inverted using ordinary Fast Fourier Transforms and vector vector operations.

The complexity of the proposed method scales linearly with the degrees of freedom. For realistic viscosity ratios the proposed method is up to a hundred times faster compared to two conventional methods. A large viscosity ratio gives a substantial performance penalty. Further research is needed to decrease the influence of the viscosity.

The null space method for three dimensions performs worse than the two-dimensional version. This might be a result of a suboptimal basis for the null space of the divergence operator, used in the reduction of the Stokes equations. Further research is needed to find an optimal basis for the null space.

Table 1: Amount of work needed to solve the oil droplet problem in two dimensions for various grid sizes and viscosity ratios.

grid size	v-ratio	work (flops/dof)		
		null	gcr	minres
16×16	1	$6.03 \cdot 10^1$	$7.41 \cdot 10^3$	$5.41 \cdot 10^3$
16×16	10	$1.29 \cdot 10^3$	$1.05 \cdot 10^4$	$1.52 \cdot 10^4$
16×16	100	$2.88 \cdot 10^3$	$2.62 \cdot 10^4$	$1.82 \cdot 10^4$
32×32	1	$6.57 \cdot 10^1$	$1.08 \cdot 10^4$	$1.15 \cdot 10^4$
32×32	10	$1.54 \cdot 10^3$	$1.71 \cdot 10^4$	$2.90 \cdot 10^4$
32×32	100	$4.03 \cdot 10^3$	$3.66 \cdot 10^4$	$3.31 \cdot 10^4$
64×64	1	$6.90 \cdot 10^1$	$1.58 \cdot 10^4$	$1.96 \cdot 10^4$
64×64	10	$1.68 \cdot 10^3$	$2.82 \cdot 10^4$	$5.16 \cdot 10^4$
64×64	100	$5.52 \cdot 10^3$	$4.85 \cdot 10^4$	$5.90 \cdot 10^4$
128×128	1	$8.03 \cdot 10^1$	$2.86 \cdot 10^4$	$4.09 \cdot 10^4$
128×128	10	$1.97 \cdot 10^3$	$6.35 \cdot 10^4$	$1.12 \cdot 10^5$
128×128	100	$6.45 \cdot 10^3$	$1.03 \cdot 10^5$	$1.26 \cdot 10^5$
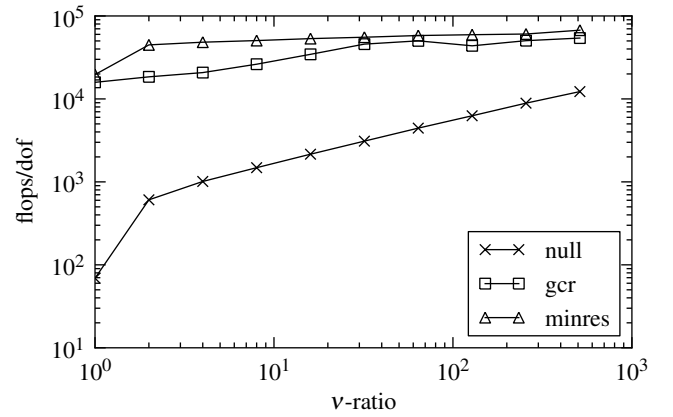
Figure 5: Amount of work needed to solve the oil droplet problem in two dimensions for various viscosity ratios with grid size $N = 64 \times 64$.
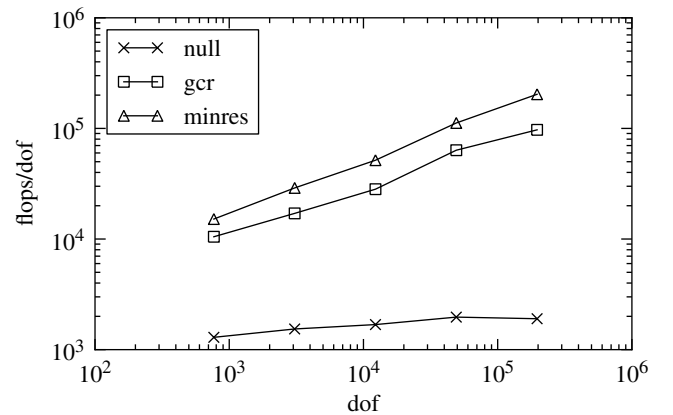
Figure 6: Amount of work needed to solve the oil droplet problem in two dimensions for various grid sizes with viscosity ratio $v = 10$.

Table 2: Amount of work needed to solve the diblock copolymer melt problem in two dimensions for various grid sizes and viscosity ratios.

grid size	v-ratio	work (flops/dof)		
		null	gcr	minres
16×16	1	$6.03 \cdot 10^1$	$8.34 \cdot 10^3$	$5.81 \cdot 10^3$
16×16	10	$1.35 \cdot 10^3$	$1.48 \cdot 10^4$	$2.50 \cdot 10^4$
16×16	100	$2.41 \cdot 10^3$	$3.69 \cdot 10^4$	$4.10 \cdot 10^4$
32×32	1	$6.57 \cdot 10^1$	$1.21 \cdot 10^4$	$1.28 \cdot 10^4$
32×32	10	$1.67 \cdot 10^3$	$2.22 \cdot 10^4$	$4.80 \cdot 10^4$
32×32	100	$3.27 \cdot 10^3$	$5.92 \cdot 10^4$	$8.20 \cdot 10^4$
64×64	1	$6.90 \cdot 10^1$	$1.58 \cdot 10^4$	$2.24 \cdot 10^4$
64×64	10	$1.89 \cdot 10^3$	$4.12 \cdot 10^4$	$8.49 \cdot 10^4$
64×64	100	$5.66 \cdot 10^3$	$1.65 \cdot 10^5$	$1.96 \cdot 10^5$
128×128	1	$8.03 \cdot 10^1$	$3.21 \cdot 10^4$	$4.92 \cdot 10^4$
128×128	10	$2.20 \cdot 10^3$	$8.55 \cdot 10^4$	$1.84 \cdot 10^5$
128×128	100	$6.29 \cdot 10^3$	$3.18 \cdot 10^5$	$3.95 \cdot 10^5$
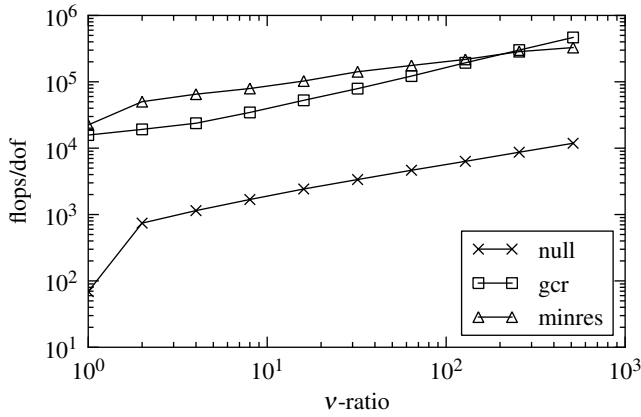
Figure 7: Amount of work needed to solve the diblock copolymer melt problem in two dimensions for various viscosity ratios with grid size $N = 64 \times 64$.

Table 4: Amount of work needed to solve the oil droplet problem in three dimensions for various grid sizes and viscosity ratios.

grid size	v-ratio	work (flops/dof)		
		null	gcr	minres
$16 \times 16 \times 16$	1	$1.28 \cdot 10^2$	$1.13 \cdot 10^4$	$1.35 \cdot 10^4$
$16 \times 16 \times 16$	10	$3.04 \cdot 10^3$	$1.90 \cdot 10^4$	$3.56 \cdot 10^4$
$16 \times 16 \times 16$	100	$9.59 \cdot 10^3$	$4.22 \cdot 10^4$	$4.98 \cdot 10^4$
$32 \times 32 \times 32$	1	$1.41 \cdot 10^2$	$1.85 \cdot 10^4$	$2.49 \cdot 10^4$
$32 \times 32 \times 32$	10	$3.38 \cdot 10^3$	$3.27 \cdot 10^4$	$6.75 \cdot 10^4$
$32 \times 32 \times 32$	100	$1.01 \cdot 10^4$	$7.63 \cdot 10^4$	$9.24 \cdot 10^4$
$64 \times 64 \times 64$	1	$1.50 \cdot 10^2$	$2.71 \cdot 10^4$	$3.82 \cdot 10^4$
$64 \times 64 \times 64$	10	$3.60 \cdot 10^3$	$4.45 \cdot 10^4$	$1.15 \cdot 10^5$
$64 \times 64 \times 64$	100	$1.21 \cdot 10^4$	$9.26 \cdot 10^4$	$1.66 \cdot 10^5$

Table 3: Amount of work needed to solve the diblock copolymer melt problem in two dimensions with shear periodicity for various grid sizes and viscosity ratios.

grid size	v-ratio	work (flops/dof)		
		null	gcr	minres
16×16	1	$6.03 \cdot 10^1$	$8.78 \cdot 10^3$	$8.22 \cdot 10^3$
16×16	10	$1.41 \cdot 10^3$	$1.72 \cdot 10^4$	$2.50 \cdot 10^4$
16×16	100	$2.58 \cdot 10^3$	$6.00 \cdot 10^4$	$4.75 \cdot 10^4$
32×32	1	$6.57 \cdot 10^1$	$1.18 \cdot 10^4$	$1.70 \cdot 10^4$
32×32	10	$1.73 \cdot 10^3$	$2.94 \cdot 10^4$	$4.50 \cdot 10^4$
32×32	100	$4.48 \cdot 10^3$	$9.50 \cdot 10^4$	$8.94 \cdot 10^4$
64×64	1	$6.90 \cdot 10^1$	$1.90 \cdot 10^4$	$3.04 \cdot 10^4$
64×64	10	$1.89 \cdot 10^3$	$4.66 \cdot 10^4$	$8.08 \cdot 10^4$
64×64	100	$5.19 \cdot 10^3$	$1.62 \cdot 10^5$	$1.53 \cdot 10^5$
128×128	1	$8.03 \cdot 10^1$	$3.98 \cdot 10^4$	$6.52 \cdot 10^4$
128×128	10	$2.20 \cdot 10^3$	$1.01 \cdot 10^5$	$1.78 \cdot 10^5$
128×128	100	$6.29 \cdot 10^3$	$3.39 \cdot 10^5$	$3.30 \cdot 10^5$

REFERENCES

ALLEN, M.P. and TILDESLEY, D.J. (1994). *Computer Simulation of Liquids*. Clarendon Press, Oxford.

BENZI, M. *et al.* (2005). "Numerical solution of saddle point problems". *Acta numerica*, **14**, 1–137.

BRUCKER, K.A. *et al.* (2007). "Efficient algorithm for simulating homogeneous turbulent shear flow without remeshing". *Journal of Computational Physics*, **225(1)**, 20–32.

CHEN, M. (1987). "On the solution of circulant linear systems". *SIAM Journal on Numerical Analysis*, **24(3)**, 668–683.

FRAAIJE, J.G.E.M. *et al.* (1997). "The dynamic mean-field density functional method and its application to the mesoscopic dynamics of quenched block copolymer melts". *J. Chem. Phys.*, **106**, 4260–4269.

VAN ZWIETEN, J.S.B. (2011). *Efficient solution methods for the incompressible Stokes problem*. Master's thesis, Delft University of Technology. To appear on `http://ta.twi.tudelft.nl/nw/users/vuik/numanal/zwieten_joost_eng.html`.

APPENDIX A

For reference, the discretised operators used in this paper. The discrete gradient operator is defined by

$$\mathscr{G}p(\boldsymbol{x})_j = \frac{\mathscr{P}_s p\left(\boldsymbol{x}+\frac{1}{2}\boldsymbol{h}_j\right) - \mathscr{P}_s p\left(\boldsymbol{x}-\frac{1}{2}\boldsymbol{h}_j\right)}{\|\boldsymbol{h}_j\|_2},$$
$$\boldsymbol{x} \in X_{u_j}, \quad j \in \{1,\ldots,d\}. \quad (54)$$

Transposing this operator yields the discrete divergence operator,

$$\mathscr{G}^T\boldsymbol{u}(\boldsymbol{x}) = \sum_{j=1}^{d} -\frac{\mathscr{P}_s u_j(\boldsymbol{x}+\frac{1}{2}\boldsymbol{h}_j) - \mathscr{P}_s u_j(\boldsymbol{x}-\frac{1}{2}\boldsymbol{h}_j)}{\|\boldsymbol{h}_j\|_2},$$
$$\boldsymbol{x} \in X. \quad (55)$$

For the Laplace operator we define an intermediate operator, for ease of notation. Let $\mathscr{H}_j$ be defined by

$$\mathscr{H}_j\boldsymbol{u}(\boldsymbol{x})_k = \mathscr{P}_s v(\boldsymbol{x})\left(\mathscr{G}\boldsymbol{u}_j(\boldsymbol{x})_k + \mathscr{G}\boldsymbol{u}_k(\boldsymbol{x})_j\right). \quad (56)$$

Then the discrete vector Laplace operator is defined by

$$\mathscr{L}\boldsymbol{u}(\boldsymbol{x})_j = \mathscr{G}^T\mathscr{H}_j\boldsymbol{u}(\boldsymbol{x}), \quad \boldsymbol{x} \in X, \quad j \in \{1,\ldots,d\}. \quad (57)$$

The missing values for the viscosity are approximated by four neighbours,

$$v(\boldsymbol{x}+\tfrac{1}{2}\boldsymbol{h}_j+\tfrac{1}{2}\boldsymbol{h}_k)$$
$$= \frac{v(\boldsymbol{x})+v(\boldsymbol{x}+\boldsymbol{h}_j)+v(\boldsymbol{x}+\boldsymbol{h}_k)+v(\boldsymbol{x}+\boldsymbol{h}_j+\boldsymbol{h}_k)}{4},$$
$$\boldsymbol{x} \in X, \quad j,k \in \{0,\ldots,d\}, \quad j \neq k. \quad (58)$$

NUMERICAL SIMULATION OF SINGLE ELONGATED BUBBLE PROPAGATION IN INCLINED PIPES

Jinsong HUA* , Morten LANGSHOLT and Christopher LAWRENCE

Institute for Energy Technology, Department of Process and Fluid Flow Technology

PO Box 40, No-2027 Kjeller, NORWAY

* E-mail: jinsong.hua@ife.no

ABSTRACT

Keywords:

NOMENCLATURE

Greek Symbols
α
ε
θ
κ
μ
ρ
σ
$\sigma_k \;\; \sigma_\varepsilon \;\; \sigma_\omega$

ω

Latin Symbols
$C_\mu \quad C \qquad C$
C
D
$\mathbf{F}_{ST}$
g
G_k
G_ω
k
p
R_{LC}
S_{ij}
t
$\mathbf{u}$
U_m
U_d

Sub/superscripts
b
G
in
L
t
w

INTRODUCTION

$k \;\; \varepsilon \;\; \omega$

$$U_{in} = U_L$$

FORMULATIONS AND NUMERICAL METHOD

CFD Model

$$L$$

$$D$$

$$U_b$$

$$U_w$$

$$U_w =$$

$$U_w = -U_b$$

$$U_{in} \qquad\qquad U_L$$

$$U_{in} = U_L$$

$$U_{in} = U_L - U_b$$

g

$L \quad D =$

Figure 1:

Continuity equation
$$\nabla \cdot (\mathbf{u}) =$$

Momentum equation
$$\frac{\partial \rho \mathbf{u}}{\partial t} + \nabla \cdot (\rho \mathbf{u} \mathbf{u}) = -\nabla p + \nabla \cdot \left[\mu \left(\nabla \mathbf{u} + \nabla \mathbf{u}^T \right) \right]$$
$$+ \mathbf{F}_{ST} + (\rho - \rho_L) \mathbf{g}$$

$\mathbf{F}_{ST}$

$$\mathbf{F}_{ST} = \sigma \kappa \nabla \alpha$$

σ κ

n

$$\kappa = \nabla \cdot n \qquad n = \frac{\nabla \alpha}{|\nabla \alpha|}$$

Volume fraction equation

$$\frac{\partial \rho \alpha}{\partial t} + \nabla \cdot (\rho \mathbf{u} \alpha) =$$
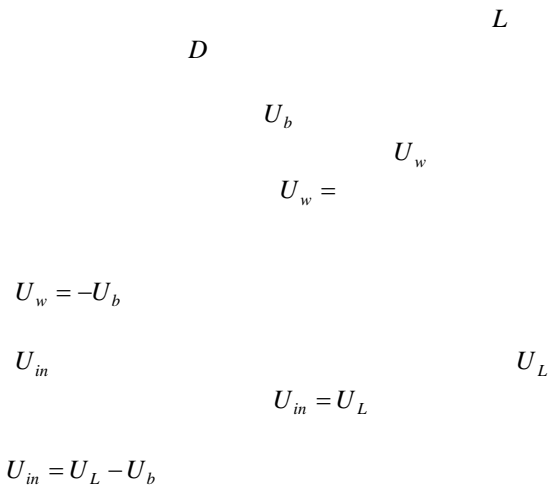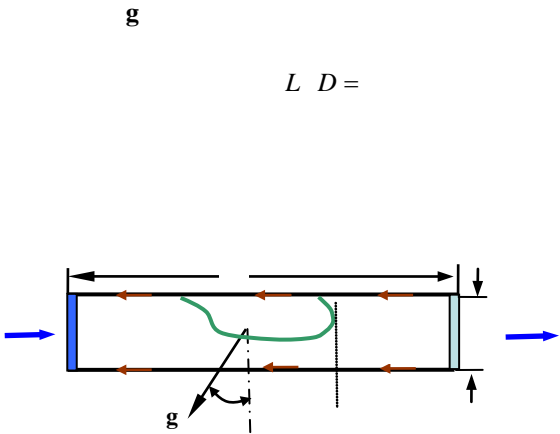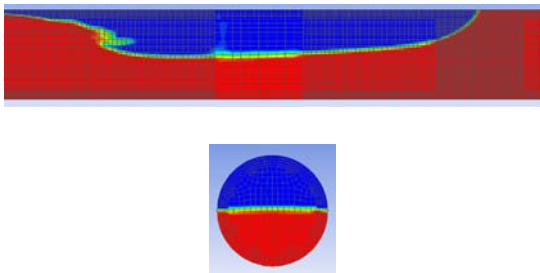
Figure 2:

Governing Equations

α

ρ μ

$$\rho = \rho_G \cdot \alpha + \rho_L \cdot (-\alpha)$$
$$\mu = \mu_G \cdot \alpha + \mu_L \cdot (-\alpha)$$

α

$G \qquad L$

Moving Reference Frame

$$\frac{\partial \rho \mathbf{u}}{\partial t} + \rho \frac{dU_b}{dt} + \nabla \cdot (\rho \mathbf{u} \mathbf{u}) = -\nabla p$$
$$+ \nabla \cdot \left[\mu \left(\nabla \mathbf{u} + \nabla \mathbf{u}^T \right) \right] + \mathbf{F}_{ST} + (\rho - \rho_L) \mathbf{g}$$

Turbulence Models

k-• turbulence model

ε

$$\frac{\partial \rho k}{\partial t} + \nabla \cdot (\rho \mathbf{u} k) = \nabla \cdot \left[\frac{\mu + \mu_t}{\sigma_k} (\nabla k) \right]$$

$$+ \ G_k - \rho \varepsilon$$

$$\frac{\partial \rho \varepsilon}{\partial t} + \nabla \cdot (\rho \mathbf{u} \varepsilon) = \nabla \cdot \left[\frac{\mu + \mu_t}{\sigma_\varepsilon} (\nabla \varepsilon) \right]$$

$$+ \frac{\varepsilon}{k} \ C \ G_k - C \ \rho \varepsilon$$

G_k

μ μ_t

σ_k σ_ε

C C

$$\mu_t = \rho C_\mu k \quad \varepsilon$$

$$G_k = \ \mu_t S_{ij} S_{ij} \qquad S_{ij} = -\left(\frac{\partial u_j}{\partial x_i} + \frac{\partial u_i}{\partial x_j} \right)$$

k

$$\frac{\partial \rho k}{\partial t} + \nabla \cdot (\rho \mathbf{u} k) = \nabla \cdot \left[\left(\mu + \frac{\mu_t}{\sigma_k} \right) (\nabla k) \right]$$

$$+ \ G_k - Y_k$$

$$\frac{\partial \rho \omega}{\partial t} + \nabla \cdot (\rho \mathbf{u} \omega) = \nabla \cdot \left[\left(\mu + \frac{\mu_t}{\sigma_\omega} \right) (\nabla \omega) \right]$$

$$+ \ G_\omega - Y_\omega \ + D_\omega$$

G_k

G_ω ω Y_k

Y_ω k ω

D_ω

RESULTS AND DISCUSSION

Inclined Pipes with Stagnant Liquid

Bubble propagation speed and shape

Shear stress transport k-• turbulence model

Figure 3:

$$U_{b\,ver} = \quad gD$$

$D >$
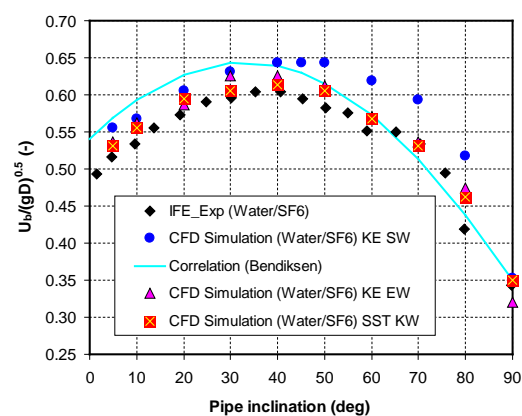
Figure 4:

$$U_{b\,hor} = \quad gD$$

$$U_b = U_{b\,hor} \quad \theta + U_{b\,ver} \quad \theta$$
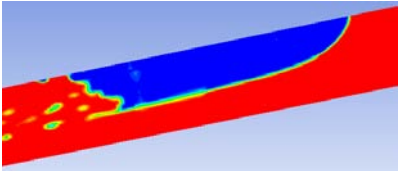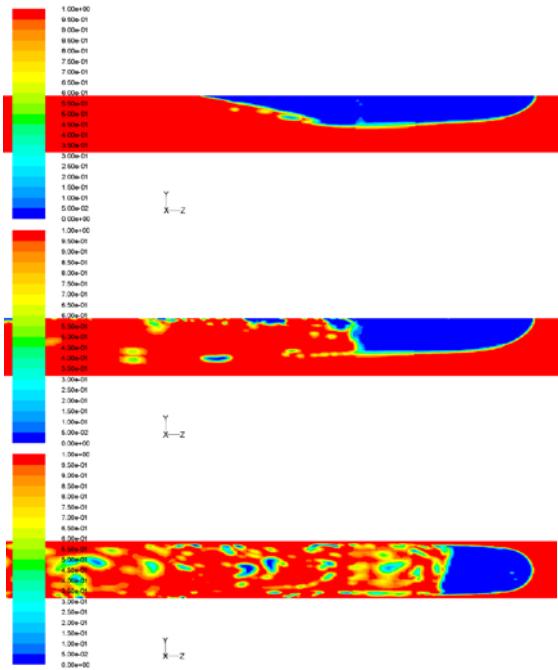
Figure 5:

Velocity field around the bubble
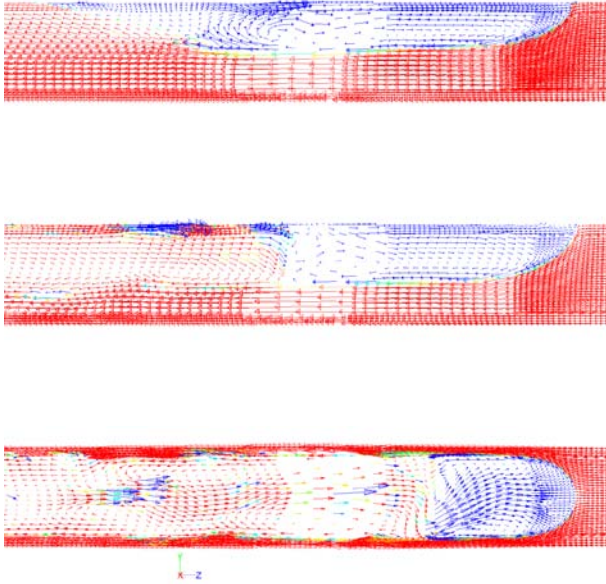
Figure 6:
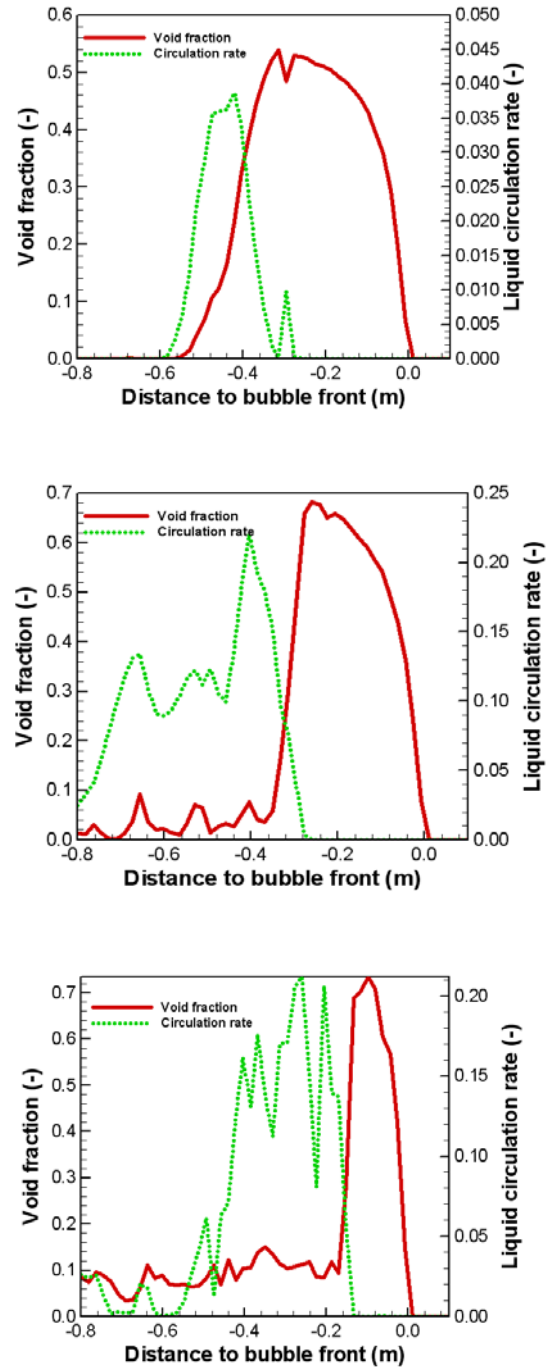
Figure 7:

R_{LC}

FL_{down}

FL_{up}

$$R_{LC} = FL_{up} \quad FL_{down} - FL_{up}$$

Wall shear stress
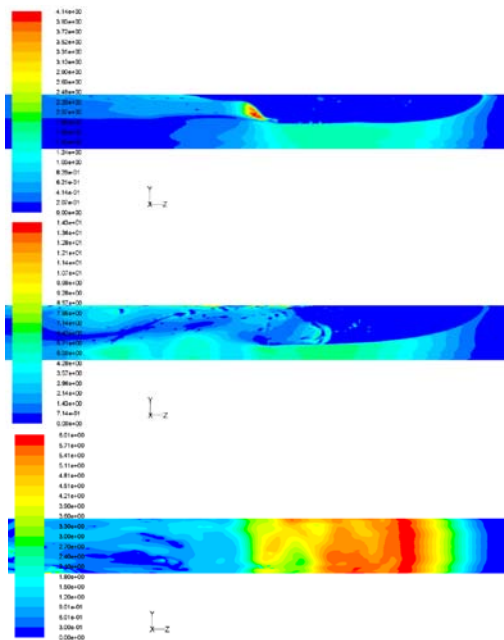
Figure 8:
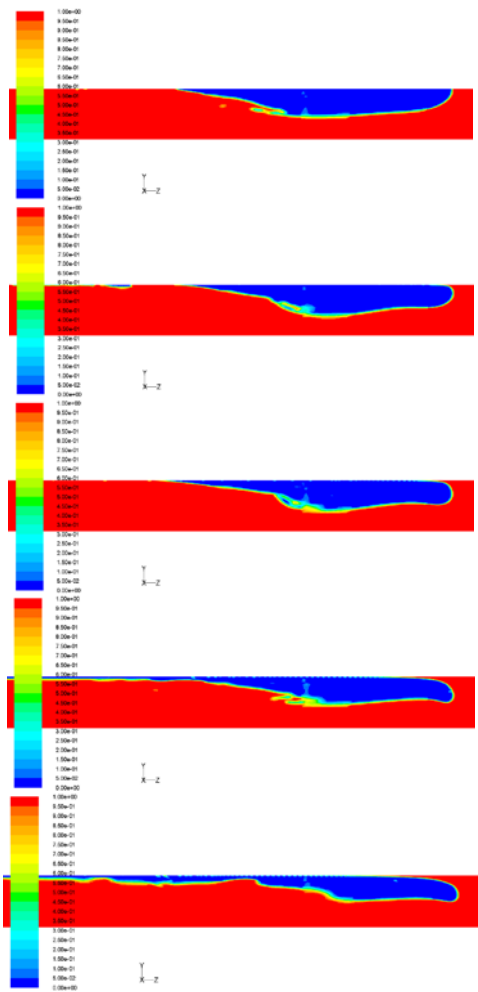
Figure 9:

Inclined Pipes with Flowing Liquid
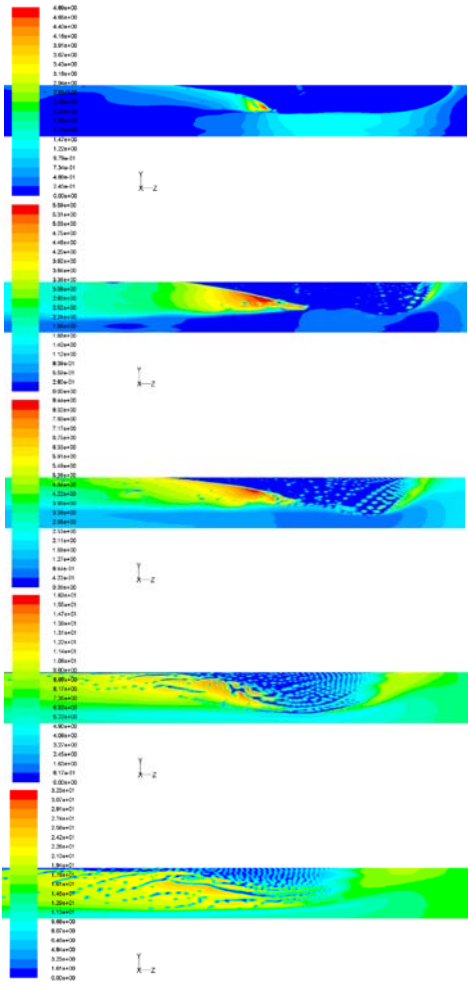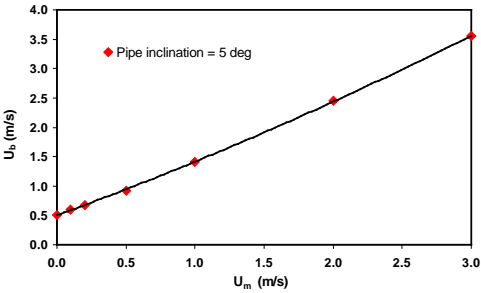
Figure 11:

CONCLUSION

Figure 10:

$$U_b = C\ U_m + U_d$$
$$C$$

$$U_b = \quad + \quad U_m \cdot U_m + \quad \cdot gD$$
$$C = \quad + \quad U_m$$

Engineering Analysis with Boundary Elements
30

J. Comput. Phys. **227**

Int. J. Heat Mass Transfer **24**

ACKNOWLEDGEMENT

Computer Methods in Applied Mechanics and Engineering **3**

AIAA Journal, **32**

REFERENCES

Chem. Eng. Sci. **61**

Int. J. Multiphase Flow **10**

J. Fluid Mechanics **31**

Multiphase Science and Technology **20**

Proc. R. Soc. Lond. A, **200**

8th International Conference on CFD in Oil & Gas, Metallurgical and Process Industries
SINTEF/NTNU, Trondheim NORWAY
21-23 June 2011

CFD11-129

AN IMPROVED ROE SOLVER FOR THE DRIFT-FLUX TWO-PHASE FLOW MODEL

Gunhild Allard REIGSTAD[1], **Tore FLÅTTEN**[2*]

[1]NTNU Department of Energy and Process Engineering, 7491 Trondheim, NORWAY

[2]SINTEF Energy Research, 7465 Trondheim, NORWAY

[*] E-mail: tore.flatten@sintef.no

ABSTRACT

This paper concerns the numerical solution of a hyperbolic system of conservation laws describing two-phase flow in a pipeline. The selected model is a one dimensional drift-flux model consisting of two mass conservation equations, one momentum conservation equation and one slip function relating the velocities of each phase. The approximate Riemann solver of Roe (1981) is used due to its robustness and relative simplicity, and an improved Roe solver compared with the one shown in Flåtten and Munkejord (2006) is presented. Along with the model, some relevant numerical examples are presented to illustrate the accuracy and robustness of the method.

Keywords: Multiphase pipe flow, Drift-flux model, Roe scheme
.

NOMENCLATURE

Greek Symbols

α_k Volume fraction, $[-]$.
β Wave strength, $[-]$.
Δx Grid length, $[m]$.
ε Minimum gas volume fraction in the moving Gauss curve, $[-]$.
Φ Slip relation, $[m/s]$.
η Dynamic viscosity, $[Pa\,s]$.
κ Compressibility parameter, $[m^5/kg\,s^2]$.
λ Eigenvalue of the flux Jacobi matrix, $[m/s]$.
μ Position of initial maximum point in the moving Gauss cuve, $[m]$.
μ_g Partial derivative of slip relation with respect to gas volumetric mass, $[m^4/kg\,s]$.
μ_ℓ Partial derivative of slip relation with respect to liquid volumetric mass, $[m^4/kg\,s]$.
μ_v Partial derivative of slip relation with respect to gas phase velocity, $[-]$.
θ Measure of the smoothness of a characteristic component of the solution, $[-]$.
ρ_k Mass density, $[kg/m^3]$.
$\breve{\rho}$ Pseudo mass, $[kg/m^3]$.
σ Deviation in the moving Gauss curve, $[m]$.
ζ Partial derivative of slip relation with respect to liquid phase velocity, $[-]$.

Latin Symbols

$A(q)$ Flux Jacobi matrix.
$\widehat{A}_{i-1/2}$ Linearised Roe matrix.
$\mathscr{A}^{\pm}\Delta Q_{i-1/2}$ Fluctuations.
c Speed of sound, $[m/s]$.
$\mathscr{E}$ Measure of error in numerical calculation, $[-]$.
$f(q)$ Vector of fluxes.
F_w Wall friction momentum source, $[kg/m^2\,s^2]$.
$\widetilde{F}$ Higher-order correction flux.
I_k Volumetric momentum, $[kg/m^2\,s]$.
K Constant used in the Zuber-Findlay slip relation, $[-]$.
m_k Volumetric mass, $[kg/m^3]$.
n Convergence order, $[-]$.
p Pressure, common for both phases, $[Pa]$.
q Vector containing the conserved variables.
Q_i Vector containing the discrete conserved variables.
r Right eigenvector.
R Right eigenvector matrix.
$s(q)$ Vector of sources.
s Wave speed, $[m/s]$.
S Variable used in the Zuber-Findlay slip relation, $[m/s]$.
v_k Velocity, $[m/s]$.
$\mathscr{W}$ Wave.

Sub/superscripts

0   Indicator of reference state.
g Gas phase.
i Cell index.
k Indicator of phase, l=liquid, g=gas.
ℓ Liquid phase.
L Grid on the left hand side of a grid interface.
p Wave number.
R Grid on the right hand side of a grid interface.

INTRODUCTION

The selected pipe flow model for two phase flows has many applications, including oil and gas transport, nuclear engineering, CO_2 capture and storage and the modelling of heat exchangers. The numerical solution is obtained using an approximate Riemann solver of Roe (1981). This is a convenient upwind finite volume method due to its robustness and relative simplicity. The solver is also easily extended to second-order accuracy for smooth solutions through the wave-limiter approach of LeVeque (2007). The use of a finite volume method ensures that physically conserved variables are also numerically conserved.

The parameter vector approach suggested by Roe (1981) to obtain the solver requires a certain level of algebraic sim-

plicity of the equation system. The slip relation and the thermodynamic closure relations in a drift-flux model generally have a complex structure which makes the approach unfeasible.

Toumi and Caruge (1998) used a weak formulation of the approximate Riemann solver of Roe in order to overcome this challenge. In this approach the Jacobian matrix is made dependent on a smooth path linking the left and right states of a grid interface in addition to the states themselves. The Roe solver was applied on a three-dimensional drift-flux model. Romate (1997) established a matrix satisfying the Roe conditions by a numerical approach . Based on an intermediate condition dependent on the left and right states, the Jacobian matrix was identified and its eigenvalues and eigenvectors were calculated. The Jacobian matrix was then represented by the eigenvector matrix, its inverse and the matrix containing the eigenvalues of the Jacobian matrix along its diagonal. By modifying the diagonal matrix, the Roe conditions could be satisfied.

In a previous work (Flåtten and Munkejord, 2006), an alternative approach for constructing an analytical Roe solver for the drift-flux model was presented. Herein, the problem was divided into a convective and a pressure part, allowing us to treat the Roe-averaging of the slip relation and the thermodynamic density relations as separate problems. However, the approach required the introduction of two separate Roe-averages of the velocities of each phase.

In the current paper, the approach has been improved such that there are unique Roe-averages for the phase velocities. Along with the improved method, numerical examples relevant for industrial challenges related to multiphase pipeline transport are presented. These illustrate the accuracy and robustness of the method.

THE DRIFT-FLUX MODEL

The drift-flux model consists of two equations for conservation of mass, one for each phase, and one equation for the conservation of total momentum as shown in equations (1) to (4).

$$\frac{\partial \boldsymbol{q}}{\partial t} + \frac{\partial \boldsymbol{f}(\boldsymbol{q})}{\partial x} = \boldsymbol{s}(\boldsymbol{q}) \tag{1}$$

$$\boldsymbol{q} = \begin{bmatrix} \rho_g \alpha_g \\ \rho_\ell \alpha_\ell \\ \rho_g \alpha_g v_g + \rho_\ell \alpha_\ell v_\ell \end{bmatrix} = \begin{bmatrix} m_g \\ m_\ell \\ I_g + I_\ell \end{bmatrix} \tag{2}$$

$$\boldsymbol{f}(\boldsymbol{q}) = \begin{bmatrix} \rho_g \alpha_g v_g \\ \rho_\ell \alpha_\ell v_\ell \\ \rho_g \alpha_g v_g^2 + \rho_\ell \alpha_\ell v_\ell^2 + p \end{bmatrix} = \begin{bmatrix} I_g \\ I_\ell \\ I_g v_g + I_\ell v_\ell + p \end{bmatrix} \tag{3}$$

$$\boldsymbol{s}(\boldsymbol{q}) = \begin{bmatrix} 0 \\ 0 \\ -F_w \end{bmatrix} \tag{4}$$

The volume fractions satisfy:

$$\alpha_\ell + \alpha_g = 1 \tag{5}$$

Thermodynamic submodel

The drift-flux model presented above is based on the assumption of isentropic and isothermal flow. Hence dynamic mass and energy transfer between the phases are neglected. A result of this assumption is that the pressure may be found as:

$$p = p(\rho_\ell) = p(\rho_g) \tag{6}$$

Thus, the thermodynamic model relates the phase density to the common pressure according to equation (7).

$$\rho_k = \rho_{k,0} + \frac{p - p_{k,0}}{c_k^2} \tag{7}$$

The variables $p_{k,0}$ and c_k^2 are defined in equation (8) and (9) respectively.

$$p_{k,0} = p(\rho_{k,0}) \tag{8}$$

$$c_k^2 \equiv \frac{\partial p}{\partial \rho_k}(p_{k,0}) \tag{9}$$

For convenience, the model is implemented in the form of equation (10), where the variable ρ_k^0 is defined by equation (11)

$$p_k = c_k^2(\rho_k - \rho_k^0) \tag{10}$$

$$\rho_k^0 = \rho_{k,0} - \frac{p_{k,0}}{c_k^2} \tag{11}$$

Hydrodynamic submodel

In addition to the equations (1) to (4), an equation relating the liquid and gas velocities to each other is needed. The slip relation is defined as $\Phi = v_g - v_\ell$, and in general it is presented on the form:

$$v_g - v_\ell = \Phi(m_g, m_\ell, v_g) \tag{12}$$

In the present work, two different slip relations are implemented, the no slip relation, eq. (13), and the Zuber-Findlay slip relation, eq. (14).

$$\Phi = 0 \tag{13}$$

$$\Phi = \frac{(K-1)v_g + S}{K\alpha_\ell} \tag{14}$$

The Zuber-Findlay slip relation is valid for slug and bubbly flow regimes, and K and S are flow dependent constants. The models are implemented because of their simplicity. However, as the slip relation for the various flow regimes may be far more complex, use of the analytic expression for the slip relation is avoided in the derived Roe averages used in this work.

THE ROE NUMERICAL SCHEME

If the flux functions are smooth in all independent variables such that the partial derivatives exists, the equation system in equation (1) may be written in a quasi-linear form as in equation (15).

$$\frac{\partial \boldsymbol{q}}{\partial t} + \boldsymbol{A}(\boldsymbol{q})\frac{\partial \boldsymbol{q}}{\partial x} = \boldsymbol{s}(\boldsymbol{q}) \tag{15}$$

The Roe scheme is based upon a replacement of the Jacobi matrix $\boldsymbol{A}$, with a matrix $\widehat{\boldsymbol{A}}$ containing averaged values for each grid interface. Hence the non-linear system is approximated by a locally linearised system:

$$\frac{\partial \hat{\boldsymbol{q}}}{\partial t} + \widehat{\boldsymbol{A}}_{i-1/2}\frac{\partial \hat{\boldsymbol{q}}}{\partial x} = \boldsymbol{s}(\hat{\boldsymbol{q}}) \tag{16}$$

In Flåtten and Munkejord (2006), the Jacobian matrix, $\boldsymbol{A}$, was derived as:

$$\boldsymbol{A} = \frac{1}{\breve{\rho}} \begin{bmatrix} m_g m_\ell \mu_g + \zeta m_\ell v_g & m_g m_\ell \mu_\ell - m_g v_\ell & m_g \\ -(m_g m_\ell \mu_g + \zeta m_\ell v_g) & m_g v_\ell - m_g m_\ell \mu_\ell & \zeta m_\ell \\ a_{31} & a_{32} & a_{33} \end{bmatrix} \tag{17}$$

where

$$a_{31} = \kappa \check{\rho} \rho_\ell + 2 m_g m_\ell \mu_g (v_g - v_\ell) + (\zeta m_\ell - m_g) v_g^2 \\ - 2\zeta m_\ell v_g v_\ell \tag{18}$$

$$a_{32} = \kappa \check{\rho} \rho_g + 2 m_g m_\ell \mu_\ell (v_g - v_\ell) \\ - (\zeta m_\ell - m_g) v_\ell^2 - 2 m_g v_g v_\ell \tag{19}$$

$$a_{33} = 2(m_g v_g + \zeta m_\ell v_\ell) \tag{20}$$

The variables μ_g, μ_ℓ and μ_v are partial derivatives of the slip function with respect to gas volumetric mass, liquid volumetric mass and gas phase velocity respectively (see eq. (21) to eq. (23)). ζ is the partial derivative of the gas velocity with respect to liquid velocity (see eq. (24)).

$$\mu_g = \left(\frac{\partial \Phi}{\partial m_g} \right)_{m_\ell, v_g} \tag{21}$$

$$\mu_\ell = \left(\frac{\partial \Phi}{\partial m_\ell} \right)_{m_g, v_g} \tag{22}$$

$$\mu_v = \left(\frac{\partial \Phi}{\partial v_g} \right)_{m_g, m_\ell} \tag{23}$$

$$\zeta = \left(\frac{\partial v_\ell}{\partial v_g} \right)_{m_g, m_\ell} \tag{24}$$

The pseudo mass $\check{\rho}$ is defined as:

$$\check{\rho} = m_g + \zeta m_\ell \tag{25}$$

κ is defined as:

$$\kappa = \frac{1}{(\partial_p \rho_g) \rho_\ell \alpha_g + (\partial_p \rho_\ell) \rho_g \alpha_\ell} \tag{26}$$

In accordance with the Jacobian matrix, the linearised matrix, $\widehat{A}$, is defined as:

$$\widehat{A} = \frac{1}{\hat{\check{\rho}}} \begin{bmatrix} \hat{a}_{11} & \hat{a}_{12} & \hat{m}_g \\ -\hat{a}_{11} & -\hat{a}_{12} & \hat{\zeta} \hat{m}_\ell \\ \hat{a}_{31} & \hat{a}_{32} & \hat{a}_{33} \end{bmatrix} \tag{27}$$

where

$$\hat{a}_{11} = \hat{m}_g \hat{m}_\ell \hat{\mu}_g + \hat{\zeta} \hat{m}_\ell \hat{v}_g \tag{28}$$

$$\hat{a}_{12} = \hat{m}_g \hat{m}_\ell \hat{\mu}_\ell - \hat{m}_g \hat{v}_\ell \tag{29}$$

$$\hat{a}_{31} = \hat{\kappa} \hat{\check{\rho}} \hat{\rho}_\ell + 2 \hat{m}_g \hat{m}_\ell \hat{\mu}_g (\hat{v}_g - \hat{v}_\ell) + (\hat{\zeta} \hat{m}_\ell - \hat{m}_g) \hat{v}_g^2 \\ - 2 \hat{\zeta} \hat{m}_\ell \hat{v}_g \hat{v}_\ell \tag{30}$$

$$\hat{a}_{32} = \hat{\kappa} \hat{\check{\rho}} \hat{\rho}_g + 2 \hat{m}_g \hat{m}_\ell \hat{\mu}_\ell (\hat{v}_g - \hat{v}_\ell) - (\hat{\zeta} \hat{m}_\ell - \hat{m}_g) \hat{v}_\ell^2 \\ - 2 \hat{m}_g \hat{v}_g \hat{v}_\ell \tag{31}$$

$$\hat{a}_{33} = 2(\hat{m}_g \hat{v}_g + \hat{\zeta} \hat{m}_\ell \hat{v}_\ell) \tag{32}$$

The $\widehat{A}_{i-1/2}$ matrix has to fulfil three conditions :

Condition 1 $\widehat{A}_{i-1/2}$ *must be diagonalisable and have real eigenvalues*

Condition 2 $\widehat{A}_{i-1/2} \to f'(\bar{q})$ *as $Q_{i-1}, Q_i \to \bar{q}$*

Condition 3 $\widehat{A}_{i-1/2}(Q_i - Q_{i-1}) = f(Q_i) - f(Q_{i-1})$

Condition 1 ensures that system (16) is hyperbolic. Condition 2 is required in order for the method to be consistent with the original conservation law. The last condition is proposed

based on a desire of having $\mathcal{W}^p$ as an eigenvector of $\widehat{A}_{i-1/2}$ if the states Q_{i-1} and Q_i are connected by a single wave $\mathcal{W}^p = Q_i - Q_{i-1}$ in the true Riemann solution. For the particular expressions for fluctuations selected in this work (see eq. (71)), it will also guarantee that the numerical method is conservative. (LeVeque, 2007)

According to Theorem 2 in Flåtten and Munkejord (2006), the Roe matrix system can be divided into sub-systems in order to simplify the derivation of the averaged variables. The selected sub-systems are:

Equations for conservation of mass

$$\widehat{A}_m = \frac{1}{\hat{\check{\rho}}} \begin{bmatrix} \hat{m}_g \hat{m}_\ell \hat{\mu}_g + \hat{\zeta} \hat{m}_\ell \hat{v}_g & \hat{m}_g \hat{m}_\ell \hat{\mu}_\ell - \hat{m}_g \hat{v}_\ell & \hat{m}_g \\ -(\hat{m}_g \hat{m}_\ell \hat{\mu}_g + \hat{\zeta} \hat{m}_\ell \hat{v}_g) & \hat{m}_g \hat{v}_\ell - \hat{m}_g \hat{m}_\ell \hat{\mu}_\ell & \hat{\zeta} \hat{m}_\ell \\ 0 & 0 & 0 \end{bmatrix} \tag{33}$$

$$f_m(q) = \begin{bmatrix} m_g v_g \\ m_\ell v_\ell \\ 0 \end{bmatrix} \tag{34}$$

with the corresponding equation for Roe condition 3:

$$\widehat{A}_m(Q^R - Q^L) = f_m(Q^R) - f_m(Q^L) \tag{35}$$

In equation (35), the condition in cell *i* is labelled with R as it is on the right hand side of the cell interface. Similarly the condition in cell (*i*-1) is labelled with L. This notation will be used in the rest of this section.

Equations for conservation of momentum

Gas momentum convection

$$\widehat{A}_g = \frac{1}{\hat{\check{\rho}}} \begin{bmatrix} 0 & 0 & 0 \\ 0 & 0 & 0 \\ \hat{a}_{g,31} & \hat{a}_{g,32} & 2 \hat{m}_g \hat{v}_g \end{bmatrix} \tag{36}$$

$$f_g(q) = \begin{bmatrix} 0 \\ 0 \\ m_g v_g^2 \end{bmatrix} \tag{37}$$

where

$$\hat{a}_{g,31} = 2 \hat{m}_g \hat{m}_\ell \hat{v}_g \hat{\mu}_g + (\hat{\zeta} \hat{m}_\ell - \hat{m}_g) \hat{v}_g^2 \tag{38}$$

$$\hat{a}_{g,32} = 2 \hat{m}_g \hat{m}_\ell \hat{v}_g \hat{\mu}_\ell - 2 \hat{m}_g \hat{v}_g \hat{v}_\ell \tag{39}$$

The Roe condition number 3 for the gas momentum conservation equations is expressed as:

$$\widehat{A}_g(Q^R - Q^L) = f_g(Q^R) - f_g(Q^L) \tag{40}$$

Liquid momentum convection

$$\widehat{A}_l = \frac{1}{\hat{\check{\rho}}} \begin{bmatrix} 0 & 0 & 0 \\ 0 & 0 & 0 \\ \hat{a}_{l,31} & \hat{a}_{l,32} & 2 \hat{\zeta} \hat{m}_\ell \hat{v}_\ell \end{bmatrix} \tag{41}$$

$$f_l(q) = \begin{bmatrix} 0 \\ 0 \\ m_\ell v_\ell^2 \end{bmatrix} \tag{42}$$

where

$$\hat{a}_{l,31} = -(2 \hat{m}_g \hat{m}_\ell \hat{v}_\ell \hat{\mu}_g + 2 \hat{\zeta} \hat{m}_\ell \hat{v}_g \hat{v}_\ell) \tag{43}$$

$$\hat{a}_{l,32} = -(2 \hat{m}_g \hat{m}_\ell \hat{v}_\ell \hat{\mu}_\ell + (\hat{\zeta} \hat{m}_\ell - \hat{m}_g) \hat{v}_\ell^2) \tag{44}$$

The 3rd Roe condition expressed as:

$$\widehat{A}_l(Q^R - Q^L) = f_l(Q^R) - f_l(Q^L) \tag{45}$$

Pressure terms

$$\widehat{\boldsymbol{A}}_{\mathrm{p}} = \begin{bmatrix} 0 & 0 & 0 \\ 0 & 0 & 0 \\ \hat{\kappa}\hat{\rho}_\ell & \hat{\kappa}\hat{\rho}_{\mathrm{g}} & 0 \end{bmatrix} \tag{46}$$

$$\boldsymbol{f}_{\mathrm{p}}(\boldsymbol{q}) = \begin{bmatrix} 0 \\ 0 \\ p \end{bmatrix} \tag{47}$$

with Roe condition number 3 expressed as:

$$\widehat{\boldsymbol{A}}_{\mathrm{p}}(\boldsymbol{Q}^{\mathrm{R}} - \boldsymbol{Q}^{\mathrm{L}}) = \boldsymbol{f}_{\mathrm{p}}(\boldsymbol{Q}^{\mathrm{R}}) - \boldsymbol{f}_{\mathrm{p}}(\boldsymbol{Q}^{\mathrm{L}}) \tag{48}$$

Derivation of averaged parameters

Derivation of $\hat{\alpha}_\ell$, $\hat{\alpha}_{\mathrm{g}}$, $\hat{\rho}_\ell$ and $\hat{\rho}_{\mathrm{g}}$

The averaged volume fractions, $\hat{\alpha}_\ell$, $\hat{\alpha}_{\mathrm{g}}$, and densities, $\hat{\rho}_\ell$ and $\hat{\rho}_{\mathrm{g}}$, are found from the Roe condition 3 applied on the pressure sub-system, eq. (48). As in Flåtten and Munkejord (2006), $\hat{\kappa}$ is set equal to

$$\hat{\kappa} = \frac{1}{(\widehat{\partial_{\mathrm{p}}\rho_{\mathrm{g}}})\hat{\rho}_\ell\hat{\alpha}_{\mathrm{g}} + (\widehat{\partial_{\mathrm{p}}\rho_\ell})\hat{\rho}_{\mathrm{g}}\hat{\alpha}_\ell} \tag{49}$$

This leads to the equation

$$\frac{\hat{\rho}_\ell(m_{\mathrm{g}}^{\mathrm{R}} - m_{\mathrm{g}}^{\mathrm{L}}) + \hat{\rho}_{\mathrm{g}}(m_\ell^{\mathrm{R}} - m_\ell^{\mathrm{L}})}{(\widehat{\partial_{\mathrm{p}}\rho_{\mathrm{g}}})\hat{\rho}_\ell\hat{\alpha}_{\mathrm{g}} + (\widehat{\partial_{\mathrm{p}}\rho_\ell})\hat{\rho}_{\mathrm{g}}\hat{\alpha}_\ell} = p^{\mathrm{R}} - p^{\mathrm{L}} \tag{50}$$

For $\widehat{\partial_{\mathrm{p}}\rho_{\mathrm{k}}}$ the expression suggested by Flåtten and Munkejord (2006) is used:

$$\widehat{\partial_{\mathrm{p}}\rho_{\mathrm{k}}} = \begin{cases} \frac{\rho_{\mathrm{k}}^{\mathrm{R}} - \rho_{\mathrm{k}}^{\mathrm{L}}}{p^{\mathrm{R}} - p^{\mathrm{L}}} & p^{\mathrm{R}} \neq p^{\mathrm{L}} \\ (\partial_{\mathrm{p}}\rho_{\mathrm{k}})^{\mathrm{L}} & p^{\mathrm{R}} = p^{\mathrm{L}} \end{cases} \tag{51}$$

Entering the expression for $\widehat{\partial_{\mathrm{p}}\rho_{\mathrm{k}}}$ into equation (50), the requirement for the averaged variables can be expressed as:

$$\begin{aligned} &\hat{\rho}_\ell(m_{\mathrm{g}}^{\mathrm{R}} - m_{\mathrm{g}}^{\mathrm{L}}) + \hat{\rho}_{\mathrm{g}}(m_\ell^{\mathrm{R}} - m_\ell^{\mathrm{L}}) \\ &= \hat{\rho}_{\mathrm{g}}\hat{\alpha}_\ell(\rho_\ell^{\mathrm{R}} - \rho_\ell^{\mathrm{L}}) + \hat{\rho}_\ell\hat{\alpha}_{\mathrm{g}}(\rho_{\mathrm{g}}^{\mathrm{R}} - \rho_{\mathrm{g}}^{\mathrm{L}}) \end{aligned} \tag{52}$$

This equation is satisfied by arithmetic averages for volume fractions and densities:

$$\hat{\alpha}_\ell = \frac{1}{2}(\alpha_\ell^{\mathrm{L}} + \alpha_\ell^{\mathrm{R}}) \tag{53}$$

$$\hat{\alpha}_{\mathrm{g}} = \frac{1}{2}(\alpha_{\mathrm{g}}^{\mathrm{L}} + \alpha_{\mathrm{g}}^{\mathrm{R}}) \tag{54}$$

$$\hat{\rho}_\ell = \frac{1}{2}(\rho_\ell^{\mathrm{L}} + \rho_\ell^{\mathrm{R}}) \tag{55}$$

$$\hat{\rho}_{\mathrm{g}} = \frac{1}{2}(\rho_{\mathrm{g}}^{\mathrm{L}} + \rho_{\mathrm{g}}^{\mathrm{R}}) \tag{56}$$

Here, it was used that:

$$m_{\mathrm{k}} = \rho_{\mathrm{k}}\alpha_{\mathrm{k}} \tag{57}$$

Derivation of $\hat{\mu}_{\mathrm{g}}$, $\hat{\mu}_\ell$ and $\hat{\mu}_{\mathrm{v}}$

In Flåtten and Munkejord (2006), the derivation of averaged volumetric masses and velocities from the set of equations in (35) resulted in the criteria:

$$\hat{\mu}_{\mathrm{g}}(m_{\mathrm{g}}^{\mathrm{R}} - m_{\mathrm{g}}^{\mathrm{L}}) + \hat{\mu}_\ell(m_\ell^{\mathrm{R}} - m_\ell^{\mathrm{L}}) + \hat{\mu}_{\mathrm{v}}(v_{\mathrm{g}}^{\mathrm{R}} - v_{\mathrm{g}}^{\mathrm{L}}) = \Phi^{\mathrm{R}} - \Phi^{\mathrm{L}} \tag{58}$$

In the Roe scheme presented here we will use this as a starting point. Hence the averages derived in Flåtten and Munkejord (2006) may be kept:

$$\hat{\mu}_{\mathrm{g}} = \begin{cases} \frac{\Phi(m_{\mathrm{g}}^{\mathrm{R}}, m_\ell^{\mathrm{L}}, v_{\mathrm{g}}^{\mathrm{L}}) - \Phi(m_{\mathrm{g}}^{\mathrm{L}}, m_\ell^{\mathrm{L}}, v_{\mathrm{g}}^{\mathrm{L}})}{m_{\mathrm{g}}^{\mathrm{R}} - m_{\mathrm{g}}^{\mathrm{L}}} & \text{for} \quad m_{\mathrm{g}}^{\mathrm{L}} \neq m_{\mathrm{g}}^{\mathrm{R}} \\ \mu_{\mathrm{g}}(m_{\mathrm{g}}^{\mathrm{L}}, m_\ell^{\mathrm{L}}, v_{\mathrm{g}}^{\mathrm{L}}) & \text{for} \quad m_{\mathrm{g}}^{\mathrm{L}} = m_{\mathrm{g}}^{\mathrm{R}} \end{cases} \tag{59}$$

$$\hat{\mu}_\ell = \begin{cases} \frac{\Phi(m_{\mathrm{g}}^{\mathrm{R}}, m_\ell^{\mathrm{R}}, v_{\mathrm{g}}^{\mathrm{L}}) - \Phi(m_{\mathrm{g}}^{\mathrm{R}}, m_\ell^{\mathrm{L}}, v_{\mathrm{g}}^{\mathrm{L}})}{m_\ell^{\mathrm{R}} - m_\ell^{\mathrm{L}}} & \text{for} \quad m_\ell^{\mathrm{L}} \neq m_\ell^{\mathrm{R}} \\ \mu_\ell(m_{\mathrm{g}}^{\mathrm{R}}, m_\ell^{\mathrm{L}}, v_{\mathrm{g}}^{\mathrm{L}}) & \text{for} \quad m_\ell^{\mathrm{L}} = m_\ell^{\mathrm{R}} \end{cases} \tag{60}$$

$$\hat{\mu}_{\mathrm{v}} = \begin{cases} \frac{\Phi(m_{\mathrm{g}}^{\mathrm{R}}, m_\ell^{\mathrm{R}}, v_{\mathrm{g}}^{\mathrm{R}}) - \Phi(m_{\mathrm{g}}^{\mathrm{R}}, m_\ell^{\mathrm{R}}, v_{\mathrm{g}}^{\mathrm{L}})}{v_{\mathrm{g}}^{\mathrm{R}} - v_{\mathrm{g}}^{\mathrm{L}}} & \text{for} \quad v_{\mathrm{g}}^{\mathrm{L}} \neq v_{\mathrm{g}}^{\mathrm{R}} \\ \mu_{\mathrm{v}}(m_{\mathrm{g}}^{\mathrm{R}}, m_\ell^{\mathrm{R}}, v_{\mathrm{g}}^{\mathrm{L}}) & \text{for} \quad v_{\mathrm{g}}^{\mathrm{L}} = v_{\mathrm{g}}^{\mathrm{R}} \end{cases} \tag{61}$$

Derivation of $\hat{m}_{\mathrm{g}}$, $\hat{m}_\ell$, $\hat{v}_{\mathrm{g}}$ and $\hat{v}_\ell$

Inserting (58) into the first row of the equation system (35) gives the following condition:

$$\begin{aligned} &\hat{m}_{\mathrm{g}}\hat{m}_\ell\left(\hat{\zeta}(v_{\mathrm{g}}^{\mathrm{R}} - v_{\mathrm{g}}^{\mathrm{L}}) - (v_\ell^{\mathrm{R}} - v_\ell^{\mathrm{L}})\right) + \hat{\zeta}\hat{m}_\ell\hat{v}_{\mathrm{g}}\left(m_{\mathrm{g}}^{\mathrm{R}} - m_{\mathrm{g}}^{\mathrm{L}}\right) \\ &- \hat{m}_{\mathrm{g}}\hat{v}_\ell\left(m_\ell^{\mathrm{R}} - m_\ell^{\mathrm{L}}\right) + \hat{m}_{\mathrm{g}}\left(m_\ell^{\mathrm{R}}v_\ell^{\mathrm{R}} - m_\ell^{\mathrm{L}}v_\ell^{\mathrm{L}}\right) \\ &= \hat{\zeta}\hat{m}_\ell\left(m_{\mathrm{g}}^{\mathrm{R}}v_{\mathrm{g}}^{\mathrm{R}} - m_{\mathrm{g}}^{\mathrm{L}}v_{\mathrm{g}}^{\mathrm{L}}\right) \end{aligned} \tag{62}$$

A second equation is found by adding the equations for Roe condition 3 for the gas and liquid momentum, eq. (40) and eq. (45), and using equation (58):

$$\begin{aligned} &2\hat{m}_{\mathrm{g}}\hat{m}_\ell(\hat{v}_{\mathrm{g}} - \hat{v}_\ell)\left(\hat{\zeta}(v_{\mathrm{g}}^{\mathrm{R}} - v_{\mathrm{g}}^{\mathrm{L}}) - (v_\ell^{\mathrm{R}} - v_\ell^{\mathrm{L}})\right) \\ &+ \left((\hat{\zeta}\hat{m}_\ell - \hat{m}_{\mathrm{g}})\hat{v}_{\mathrm{g}}^2 - 2\hat{\zeta}\hat{m}_\ell\hat{v}_{\mathrm{g}}\hat{v}_\ell\right)\left(m_{\mathrm{g}}^{\mathrm{R}} - m_{\mathrm{g}}^{\mathrm{L}}\right) \\ &- \left((\hat{\zeta}\hat{m}_\ell - \hat{m}_{\mathrm{g}})\hat{v}_\ell^2 + 2\hat{m}_{\mathrm{g}}\hat{v}_{\mathrm{g}}\hat{v}_\ell\right)\left(m_\ell^{\mathrm{R}} - m_\ell^{\mathrm{L}}\right) \\ &+ 2\left(\hat{m}_{\mathrm{g}}\hat{v}_{\mathrm{g}} + \hat{\zeta}\hat{m}_\ell\hat{v}_\ell\right)\left(m_{\mathrm{g}}^{\mathrm{R}}v_{\mathrm{g}}^{\mathrm{R}} + m_\ell^{\mathrm{R}}v_\ell^{\mathrm{R}} - m_{\mathrm{g}}^{\mathrm{L}}v_{\mathrm{g}}^{\mathrm{L}} - m_\ell^{\mathrm{L}}v_\ell^{\mathrm{L}}\right) \\ &= \left(\hat{m}_{\mathrm{g}} + \hat{\zeta}\hat{m}_\ell\right)\left(m_{\mathrm{g}}^{\mathrm{R}}(v_{\mathrm{g}}^{\mathrm{R}})^2 + m_\ell^{\mathrm{R}}(v_\ell^{\mathrm{R}})^2 - m_{\mathrm{g}}^{\mathrm{L}}(v_{\mathrm{g}}^{\mathrm{L}})^2 - m_\ell^{\mathrm{L}}(v_\ell^{\mathrm{L}})^2\right) \end{aligned} \tag{63}$$

By inserting (62) into (63), the equation may be simplified to:

$$\begin{aligned} &\hat{v}_{\mathrm{g}}^2\left(m_{\mathrm{g}}^{\mathrm{R}} - m_{\mathrm{g}}^{\mathrm{L}}\right) - 2\hat{v}_{\mathrm{g}}\left(m_{\mathrm{g}}^{\mathrm{R}}v_{\mathrm{g}}^{\mathrm{R}} - m_{\mathrm{g}}^{\mathrm{L}}v_{\mathrm{g}}^{\mathrm{L}}\right) + m_{\mathrm{g}}^{\mathrm{R}}(v_{\mathrm{g}}^{\mathrm{R}})^2 - m_{\mathrm{g}}^{\mathrm{L}}(v_{\mathrm{g}}^{\mathrm{L}})^2 \\ &+ \hat{v}_\ell^2\left(m_\ell^{\mathrm{R}} - m_\ell^{\mathrm{L}}\right) - 2\hat{v}_\ell\left(m_\ell^{\mathrm{R}}v_\ell^{\mathrm{R}} - m_\ell^{\mathrm{L}}v_\ell^{\mathrm{L}}\right) + m_\ell^{\mathrm{R}}(v_\ell^{\mathrm{R}})^2 - m_\ell^{\mathrm{L}}(v_\ell^{\mathrm{L}})^2 = 0 \end{aligned} \tag{64}$$

The equation may be satisfied by the averages:

$$\hat{v}_{\mathrm{g}} = \frac{\sqrt{m_{\mathrm{g}}^{\mathrm{L}}}v_{\mathrm{g}}^{\mathrm{L}} + \sqrt{m_{\mathrm{g}}^{\mathrm{R}}}v_{\mathrm{g}}^{\mathrm{R}}}{\sqrt{m_{\mathrm{g}}^{\mathrm{L}}} + \sqrt{m_{\mathrm{g}}^{\mathrm{R}}}} \tag{65}$$

and

$$\hat{v}_\ell = \frac{\sqrt{m_\ell^{\mathrm{L}}}v_\ell^{\mathrm{L}} + \sqrt{m_\ell^{\mathrm{R}}}v_\ell^{\mathrm{R}}}{\sqrt{m_\ell^{\mathrm{L}}} + \sqrt{m_\ell^{\mathrm{R}}}}. \tag{66}$$

By reformulating equation (62) to:

$$\begin{aligned} &\hat{\zeta}\hat{m}_\ell\left(\hat{m}_{\mathrm{g}}(v_{\mathrm{g}}^{\mathrm{R}} - v_{\mathrm{g}}^{\mathrm{L}}) + \hat{v}_{\mathrm{g}}(m_{\mathrm{g}}^{\mathrm{R}} - m_{\mathrm{g}}^{\mathrm{L}}) - (m_{\mathrm{g}}^{\mathrm{R}}v_{\mathrm{g}}^{\mathrm{R}} - m_{\mathrm{g}}^{\mathrm{L}}v_{\mathrm{g}}^{\mathrm{L}})\right) \\ &- \hat{m}_{\mathrm{g}}\left(\hat{m}_\ell(v_\ell^{\mathrm{R}} - v_\ell^{\mathrm{L}}) + \hat{v}_\ell(m_\ell^{\mathrm{R}} - m_\ell^{\mathrm{L}}) - (m_\ell^{\mathrm{R}}v_\ell^{\mathrm{R}} - m_\ell^{\mathrm{L}}v_\ell^{\mathrm{L}})\right) = 0 \end{aligned} \tag{67}$$

it is seen that the conservation of mass is satisfied by the averages:

$$\hat{m}_g = \sqrt{m_g^L m_g^R}, \qquad (68)$$

$$\hat{m}_\ell = \sqrt{m_\ell^L m_\ell^R} \qquad (69)$$

when $\hat{v}_g$ and $\hat{v}_\ell$ are given by eq. (65) and (66).

NUMERICAL ALGORITHM

The numerical algorithm is similar to the one selected in Flåtten and Munkejord (2006). It is based on Godunov's method, applied on non-linear systems and with the use of limiters in order to increase the accuracy of smooth solutions (LeVeque, 2007):

$$Q_i^{n+1} = Q_i^n - \frac{\Delta t}{\Delta x}(\mathscr{A}^- \Delta Q_{i+1/2} + \mathscr{A}^+ \Delta Q_{i-1/2}) \qquad (70)$$
$$- \frac{\Delta t}{\Delta x}(\widetilde{F}_{i+1/2} - \widetilde{F}_{i-1/2}) + \Delta t\, s(Q_i^n)$$

The source term has here been added on the right hand side of the equation for simplicity reasons. This will make the overall algorithm first order accurate. Using e.g. a Strang splitting algorithm to handle this term would increase the overall order of accuracy to two.

The fluctuations $\mathscr{A}^\pm \Delta Q_{i-1/2}$ are found as:

$$\mathscr{A}^\pm \Delta Q_{i-1/2} = \sum_{p=1}^m (s_{i-1/2}^p)^\pm \mathscr{W}_{i-1/2}^p \qquad (71)$$

where

$$(s_{i-1/2}^p)^+ = \max(0, s_{i-1/2}^p) \qquad (72)$$

$$(s_{i-1/2}^p)^- = \min(0, s_{i-1/2}^p) \qquad (73)$$

$$s_{i-1/2}^p = \hat{\lambda}_{i-1/2}^p \qquad (74)$$

As mentioned earlier, the selected fluctuations will give a conservative method due to condition 3. (LeVeque, 2007)

The waves, $\mathscr{W}_{i-1/2}^p$, may be calculated from the eigenvectors of the Roe matrix $\widehat{A}_{i-1/2}$:

$$Q_i - Q_{i-1} = \sum_{p=1}^m \mathscr{W}_{i-1/2}^p = \sum_{p=1}^m \beta_{i-1/2}^p \hat{r}_{i-1/2}^p \qquad (75)$$

$$\beta_{i-1/2} = \widehat{R}_{i-1/2}^{-1}(Q_i - Q_{i-1}) \qquad (76)$$

The correction flux is defined in equation (77) with the limited wave $\widetilde{\mathscr{W}}_{i-1/2}^p$ defined as in equation (78).

$$\widetilde{F}_{i-1/2} = \frac{1}{2}\sum_{p=1}^m |s_{i-1/2}^p|\left(1 - \frac{\Delta t}{\Delta x}|s_{i-1/2}^p|\right)\widetilde{\mathscr{W}}_{i-1/2}^p \qquad (77)$$

$$\widetilde{\mathscr{W}}_{i-1/2}^p = \phi(\theta_{i-1/2}^p)\mathscr{W}_{i-1/2}^p \qquad (78)$$

$$\theta_{i-1/2}^p = \frac{\mathscr{W}_{I-1/2}^p \cdot \mathscr{W}_{i-1/2}^p}{\mathscr{W}_{i-1/2}^p \cdot \mathscr{W}_{i-1/2}^p} \qquad (79)$$

where

$$I = \begin{cases} i-1 & s_{i-1/2}^p \geq 0 \\ i+1 & s_{i-1/2}^p < 0 \end{cases} \qquad (80)$$

The monotonized central-difference limiter (MC limiter), eq. (81), was chosen.

$$\phi(\theta) = \max(0, \min((1+\theta)/2, 2, 2\theta)) \qquad (81)$$

Table 1: Initial data for the Riemann problem

Quantity	Symbol (unit)	L	R
Volumetric mass:			
Phase 1	m_1	3.17123	2.70708
Phase 2	m_2	3.38324	4.0434
Total volumetric momentum	$I_1 + I_2$	3.71816	3.5629

Table 2: Equation of state parameters for the Riemann problem

	Phase 1	Phase 2
ρ_o^k	0.0	0.0
Sonic speeds, c_k		
Case 1: $c_1 = c_2$	$\sqrt{6}$	$\sqrt{6}$
Case 2: $c_1 < c_2$	1	4
Case 2: $c_1 > c_2$	4	1

NUMERICAL RESULTS

The numerical results from three different cases are presented. All cases are simulated with a CFL number of 0.5. (CFL $= \max_j |\lambda_j| \frac{\Delta t}{\Delta x}$. λ_j is the j-th eigenvalue of the Jacobian matrix, A, Δt is the length of the time step and Δx is the size of the grid cells.) The phase velocities are related by the no-slip relation in the two first cases. In the third case, the Zuber-Findlay slip relation is used. This is also the only case where wall friction is included. In the two first cases the friction is neglected, e.g. $F_w = 0$.

Case: A Riemann problem

The case is found in Banda *et al.* (2010) and has initial data with a single discontinuity. A no-slip relation is assumed for the gas and liquid velocities and the simulation is performed in a tube that is 2m long. Initial data and parameters related to the equation of state are shown in table 1 and table 2 respectively. The case results are shown for three different assumptions on the sonic speeds of the two phases. In the first simulation, the sonic speeds are set equal. In the following two simulations they differ.
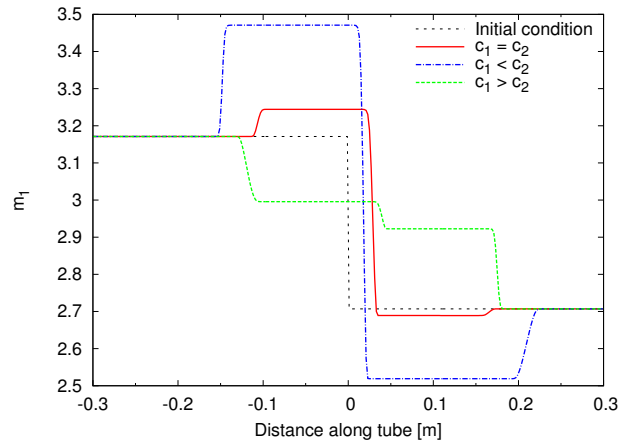
Figure 1: Riemann problem - Phase 1 volumetric mass

The results at $t = 0.06$s are presented in figure 1 to figure 4. The discontinuity is initially positioned at $x = 0$m and for

clarity, the figure only shows the section of the tube containing waves. The simulation is run with 1000 grid cells.

Compared to the results in Banda *et al.* (2010), the waves have similar shapes and the results seem reasonable. However, the position of the wave-fronts and the amplitudes of the momentum waves differ. The largest differences are seen for the two cases $a_1^2 > a_2^2$ and $a_1^2 < a_2^2$. For these cases, the pressure levels presented in the article are wrong compared to the published initial data. It seems therefore that the authors of the article have presented results for the two cases that do not
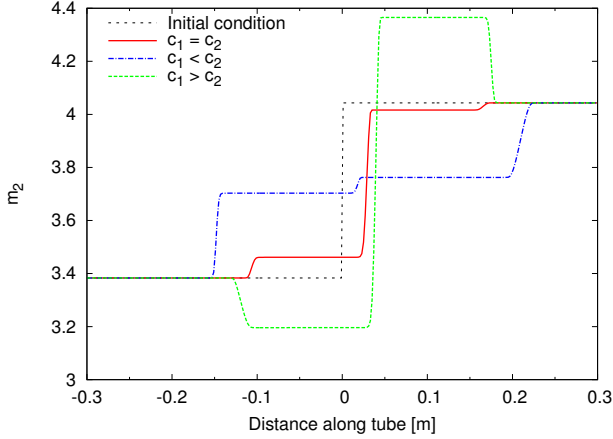
Figure 2: Riemann problem - Phase 2 volumetric mass
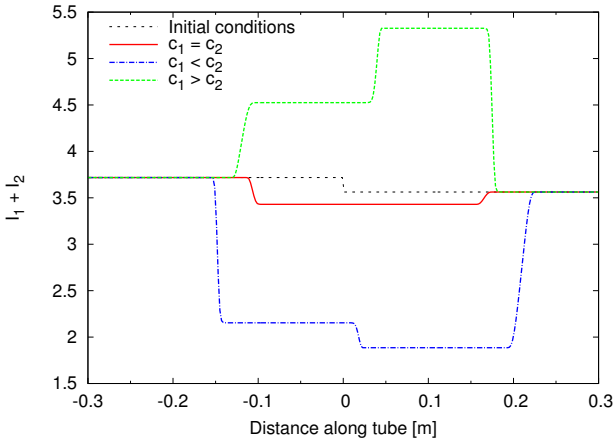
Figure 3: Riemann problem - Total volumetric momentum
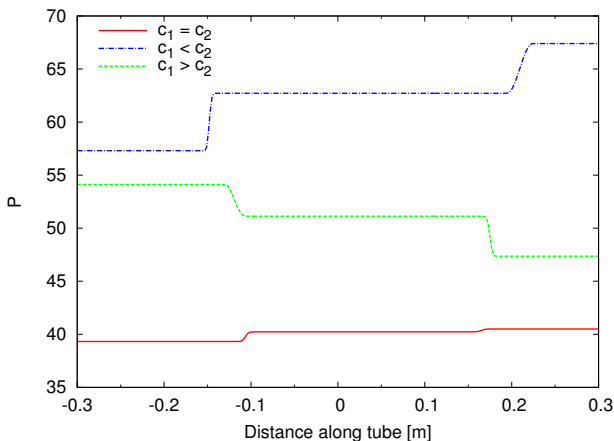
Figure 4: Riemann problem - Pressure

Table 3: Initial data for the moving Gauss curve

Quantity	Symbol (unit)	
Gas volume fraction	α_g (-)	$\alpha_{g,0}$
Pressure	p (kPa)	100
Gas velocity	v_g (m/s)	100
Liquid velocity	v_ℓ (m/s)	100

Table 4: Equation of state parameters for the moving Gauss curve case

	c_k (m/s)	ρ_o^k (kg/m³)
Gas (g)	$\sqrt{10^5}$	0
Liquid (l)	1000	1000

correspond with the data they provide. This is most likely the reason for the discrepancies that are observed.

Case: Moving Gauss curve - Investigation of model accuracy

The convergence order of smooth solutions has been verified using a constructed test case found in Munkejord *et al.* (2009). The initial volume fraction profile in a 12 meter long tube is according to equation (82), and it is moving along the tube with the speed of the liquid and vapour.

$$\alpha_{g,0} = (1 - 2\varepsilon)\exp\left(-\frac{(x-\mu)^2}{2\sigma^2}\right) + \varepsilon \qquad (82)$$

where $\varepsilon = 1 \times 10^{-12}$, $\mu = 6$m and $\sigma = 0.42$m.

The simulation is run for 0.03 seconds with periodic boundary conditions. As seen in table 3, the fluid velocity in the pipe is 100 m/s. Hence at the end of the simulation time, the analytical solution is a volume fraction profile which is symmetric around $x = 9$m. This is shown as the analytical result in figure 5 and figure 6. The parameters presented in table 4 were used in the equation of state for the simulation.

The results presented in figure 5 and figure 6 illustrate the differences in the results introduced by the MC limiter. The main difference is the accuracy obtained when using the MC limiter, even for a fairly low number of grid cells. This is the main reason for the focus on the very small region in figure 6. The figures also show that while the original simulation is symmetric around $x = 9$m, the results from the simulation with limiter are nonsymmetrical. This is due to the nature of the limiter method (Munkejord *et al.*, 2009).

The convergence order is calculated by finding the error in the calculated gas volume fraction as (Munkejord *et al.*, 2009):

$$||\mathscr{E}(\alpha_g, \Delta x)||_1 = \Delta x \sum_{\forall j} |\alpha_{g,j} - \alpha_{g,\text{ref},j}| \qquad (83)$$

The error for two simulations with grid size Δx_1 and Δx_2 are then compared in order to determine the convergence order (Munkejord, 2005):

$$n = \frac{\ln[||\mathscr{E}(\alpha_g, \Delta x_2)||_1 / ||\mathscr{E}(\alpha_g, \Delta x_1)||_1]}{\ln[\Delta x_2 / \Delta x_1]} \qquad (84)$$

Table 5 shows the estimated errors and convergence order for selected grid sizes. As expected, the numerical scheme with limiter approaches an order of 2, while the scheme without limiter approaches an order of 1.

Table 5: Convergence order calculated from simulation results

Δx	Without limiter		With MC limiter	
	$\|\|\mathscr{E}(\alpha_g)\|\|_1$	n	$\|\|\mathscr{E}(\alpha_g)\|\|_1$	n
0.015	1.109×10^{-1}		1.571×10^{-3}	
0.0075	5.852×10^{-2}	0.92	4.077×10^{-4}	1.95
0.00375	3.011×10^{-2}	0.96	1.028×10^{-4}	1.99
0.001875	1.528×10^{-2}	0.98	2.598×10^{-5}	1.98
0.0009375	7.695×10^{-3}	0.99	6.525×10^{-6}	1.99

In order to compare the performance of the Roe scheme, simulation results were also obtained using the FORCE scheme (see e.g. Toro (2009, Ch. 18.2) or Chen and Toro (2004)). Among the three-point centered difference schemes, FORCE is regarded as the optimal scheme (Chen and Toro, 2004). Simulations were run at different grid cell sizes in order to achieve an error estimate equivalent to the one obtained by the largest grid cell size when using the Roe scheme without limiter. For each simulation the CPU time consumption as reported from the program was registered. The results are shown in table 6. They show that for this case, the Roe scheme both with and without limiter is far more efficient regarding CPU time consumption than the FORCE scheme.
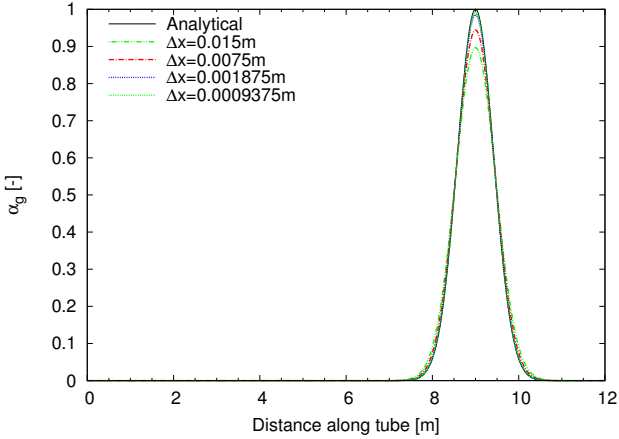
Figure 5: Gas volume fraction profile at $t = 0.03s$ - Roe scheme without limiter
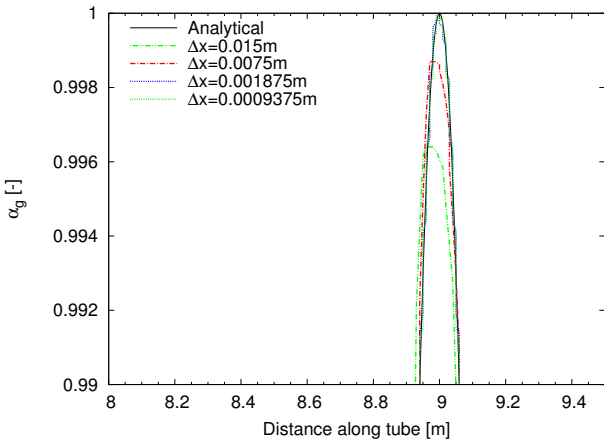
Figure 6: Gas volume fraction profile at $t = 0.03s$ - Roe scheme with MC limiter

Table 7: Equation of state parameters for the pipe flow problem

	c_k (m/s)	ρ_o^k (kg/m³)
Gas (g)	$\sqrt{10^5}$	0
Liquid (l)	1000	999.9

Case: Pipe flow

In the pipe flow case, a pipe which is 1000m long is initially filled with stagnant liquid at a pressure of 1bar. A small gas fraction of $\alpha_g = 1 \times 10^{-5}$ flows with a velocity corresponding to the slip relation (14). The relation is used with K as a constant of value 1.0. S is expressed as a function of the volume fraction:

$$S = S(\alpha_g) = \frac{1}{2}\sqrt{1 - \alpha_g} \tag{85}$$

At the outlet boundary, the pressure is kept constant at 1bar. At the pipe inlet, the flow rate of gas and liquid are varied:

- *Inlet liquid flow rate:* increased linearly from zero to 12.0kg/s from $t = 0$s to $t = 10$s, kept constant from $t = 10$s to $t = 175$s.

- *Inlet gas flow rate:* increased linearly to 0.08kg/s from $t = 0$s to $t = 10$s, kept constant to $t = 50$s, decreased linearly to 1×10^{-8}kg/s from $t = 50$s to $t = 70$s and kept constant for the rest of the simulation until $t = 175$s.

The equation of state parameters used in the case are found in table 7. In this case, wall friction is also included. This is modelled as

$$F_w = \frac{32 v_m \eta_m}{d^2} \tag{86}$$

where v_m is the mixture velocity defined as

$$v_m = \alpha_g v_g + \alpha_\ell v_\ell \tag{87}$$

η_m is the dynamic mixture viscosity defined as

$$\eta_m = \alpha_g \eta_g + \alpha_\ell \eta_l \tag{88}$$

d is the tube diameter, set to 0.1m. The constants η_g and η_l are set to $\eta_g = 5 \times 10^{-6}$Pa s, $\eta_l = 5 \times 10^{-2}$Pa s. Results for the time $t = 175$s is presented in figure 7 to figure 10. The results correspond well with the ones presented in Flåtten and Munkejord (2006).

CONCLUSION

A simplified analytical Roe scheme for a drift-flux, two-phase flow model is derived. The work in based on a previous work, Flåtten and Munkejord (2006), where the simplification is to introduce only one set of averaged velocities for each phase. The robustness of the scheme, and the possibility of extending to second order accuracy for smooth solutions by introducing wave-limiters are illustrated by the three different numerical examples presented.

ACKNOWLEDGEMENT

Table 6: Comparison of CPU consumption for FORCE vs Roe numerical schemes

	$\Delta x [m]$	$\|\|\mathscr{E}(\alpha_g)\|\|_1$	CPU consumption $[s]$	Relative Error $[-]$	Relative consumption $[-]$
Roe scheme without limiter	0.015	1.109×10^{-1}	1.347×10^2	1	1
Roe scheme with MC limiter	0.015	1.571×10^{-3}	1.545×10^2	0.0142	1.147
	0.001875	1.526×10^{-1}	6.754×10	1.376	50.14
FORCE	0.001290	1.099×10^{-1}	1.415×10^4	0.990	105.0
	0.0009375	8.213×10^{-2}	2.677×10	0.740	198.7

REFERENCES

BANDA, M.K. *et al.* (2010). "Coupling drift-flux models with unequal sonic speeds". *Mathematical and Computational Applications*, **15(4)**, 574–584.

CHEN, G.Q. and TORO, E.F. (2004). "Centered difference schemes for nonlinear hyperbolic equations". *Journal of Hyperbolic Differential Equations*, **1(3)**, 531–566.

FLÅTTEN, T. and MUNKEJORD, S.T. (2006). "The approximate Riemann solver of Roe applied to a drift-flux two-phase flow model". *ESAIM Mathematical Modelling and Numerical Analysis*, **40**, 735–764.

LEVEQUE, R.J. (2007). *Finite volume methods for hyperbolic problems*. 6th ed. Cambridge University Press.

MUNKEJORD, S.T. (2005). *Analysis of the two-fluid model and the drift-flux model for numerical calculation of two-phase flow*. Ph.D. thesis, Norwegian University of Science and Technology.

MUNKEJORD, S.T. *et al.* (2009). "A musta scheme for a nonconservative two-fluid model". *SIAM Journal of Scientific computing*, **31(4)**, 2587–2622.

ROE, P.L. (1981). "Approximate riemann solvers, parameter vectors, and difference schemes". *Journal of Computational Physics*, **43(2)**, 357–372.

ROMATE, J.E. (1997). "An approximate riemann solver for a two-phase flow model with numerically given slip relation". *Computers & Fluids*, **27(4)**, 455 – 477.

TORO, E.F. (2009). *Riemann sovers and numerical methods for fluid dynamics*. 3rd ed. Springer.

TOUMI, I. and CARUGE, D. (1998). "An implicit second-order numerical method for three-dimensional two-phase
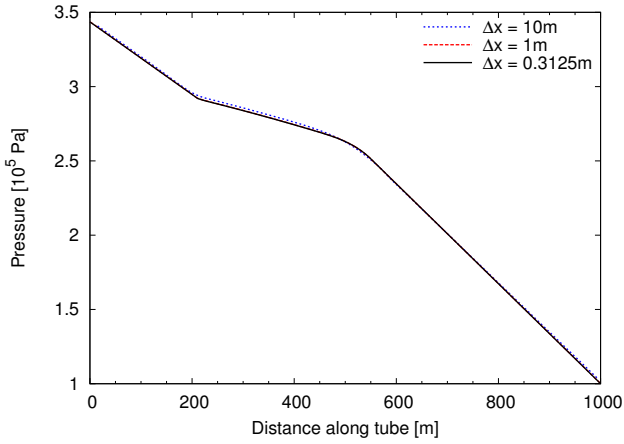
Figure 7: Pipe flow case - Pressure
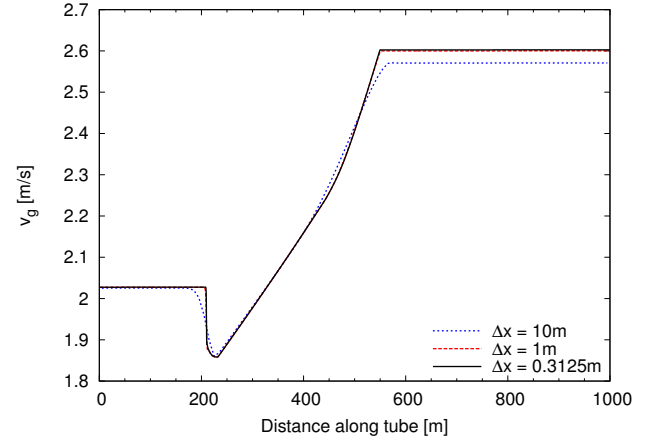
Figure 9: Pipe flow case - Gas velocity
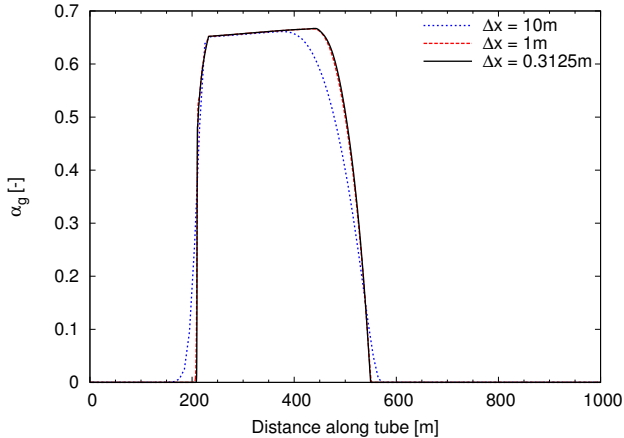
Figure 8: Pipe flow case - Gas volume fraction
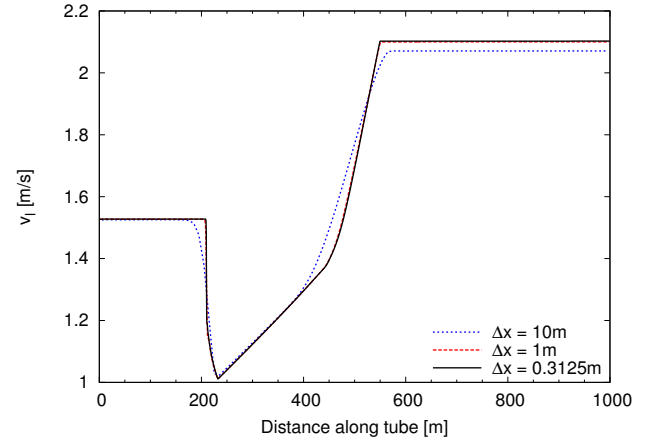
Figure 10: Pipe flow case - Liquid velocity

flow calculations". *Nuclear Science and Engineering*, **130**, 213–225.

APPLICATION OF THE LEAST-SQUARES METHOD TO THE MULTISCALE TRANSPORT EQUATION IN POROUS MEDIA

Federico SPORLEDER[1*], **Pablo M. DUPUY**[2†]

[1]NTNU Department of Chemical Engineering, 7491 Trondheim, NORWAY

[2]CSIRO Mathematics, Informatics and Statistics, 3169 Clayton South VIC, Australia

[*] E-mail: federico.sporleder@nt.ntnu.no
[†] E-mail: pablo.dupuy@csiro.au

ABSTRACT

During the last two decades characterization capabilities of porous media have been transformed by advances on computation and visualization technologies. It is now possible to obtain a fairly good visualization of the microstructure by computer tomographies. Discrete, diffusion or fluid flow simulations can be run in these domains obtaining traditional experimental characterization parameters. However, the characterization itself has not suffered a significant change because our models have not been updated. On this regard, new models are needed to achieve better up-scaling. A multi-scale approach for up-scaling renders into a model that keeps track of different phenomena happening at different scales and that is coupled in all scales simultaneously imposing great challenges for the solution method. In this work we study the suitability of a high-order least-square method for the solution of a multi-scale transport equation for porous media. Our results show that the method is particularly well suited for the solution of the equation that models 1D transport with reactions depending strongly on the scale, even in the presence of a multi-scale coupling term.

Keywords: Chemical reactions, pore size distribution, LSQ .

NOMENCLATURE

Greek Symbols

ξ Pore scale size, $[m]$

ε Porosity, $[m^3/m^3]$; $\varepsilon(\xi)d\xi$ is the probability density function for the porosity, $[m^3/m^3]$

ϕ Concentration, $[mol/m^3]$; $\phi(\xi)d\xi$ is the probability density function for the concentration, $[m^3/m^3]$

Ω Domain of the problem

Γ Boundary of the problem domain

Latin Symbols

q Discharge or superficial velocity, $[m/s]$; $q(\xi)d\xi$ is the probability density function for the discharge, $[m/s]$..

h   Inter-pore-scale redistribution; $h(\xi_1, \xi_2)d\xi_1 d\xi_2$ is the double probability density function for the inter-scale discharge, $[1/s]$.

A Porosity definition arbitrary constant, $[1/m^3]$.

V Discharge definition arbitrary constant, $[1/ms]$.

L Redistribution definition arbitrary constant, $[m]$.

M Concentration definition arbitrary constant, $[1]$.

R Concentration definition arbitrary constant, $[m]$.

S Model source term; $S(\xi)d\xi$ is the source distribution per scale, $[mol/sm^3]$.

X Solution functional space.

Y Residual functional space.

$\mathbf{A}$ Matrix of the discrete problem.

$\mathbf{w}$ Generic function.

$\mathbf{f}$ Generic solution.

$\mathbf{F}$ Source vector for discrete problem.

$\mathbf{L}$ Operator matrix.

$\mathbf{W}$ Weight matrix.

$\mathbf{G}$ Source vector.

$\mathbf{b}$ Solution vector for discrete problem.

$\mathbf{D}$ Derivative operator matrix.

$\mathbf{H}$ Identity operator matrix.

$\mathbf{I}$ Integral operator matrix.

$\mathscr{B}$ Trace operator.

$\mathscr{E}$ Equation.

$\mathscr{J}$ Norm-equivalent functional.

$\mathscr{L}$ Problem operator.

Sub/superscripts

f Upper domain limit.

0   Lower domain limit.

h Index h.

k Index k.

q Index q.

j Index j.

INTRODUCTION

Theories for studying porous media were first formulated as early as the end of the eighteen century, after the volume fraction concept was introduced for describing mud. Half a century later, one of the most basic laws for saturated porous solids was established by Henry Darcy, i.e. the flow velocity of the liquid in a porous solid is proportional to the pressure gradient. Since then, increasingly more complex theories for predicting the proportionality constant have arisen, incorporating the capillary force and considering deformable media with the definition of the consolidation problem (De Boer, 1992).

Studies on the water-soil characteristic curve (Durner, 1994), experimental characterization techniques such as gas adsorption or mercury porosimetry (Navas *et al.*, 2010; Jaroniec and Kaneko, 1997; Abell *et al.*, 1999), and the popularization of pore networks (Zhang and Seaton, 1994; Held and Celia, 2001; Oren and Bakke, 2002; Blunt *et al.*, 2002; Piri and Blunt, 2005; Ahrenholz *et al.*, 2008; Sholokhova *et al.*,

2009) have consolidated the concept of coexisting pores of different sizes, which can be better represented with a pore size distribution, e.g. see (Dullien, 1991).

Indeed, there are many different phenomena that will be affected by the pore size, as for example the physical principles of any of the experimental methods mentioned before. At the same time, heterogeneous reactions and the pore hydraulic resistivity are expected to depend strongly with the pore size. Therefore there is a clear need for adopting models that are able to capture and use the information on the pore size distribution in an efficient way.

The multi-scale transport equation for porous media (MSTE) was proposed as an extension of approaches considering a finite number of groups (Chen, 1989; Bouffard and Dixon, 2001). One internal coordinate was recently introduced (Dupuy and Schwarz, 2011) to the continuity problem for accounting the multi-scale transport of species and the scale-dependent physics. Furthermore, the MSTE defines an inter-pore redistribution function h that makes the equation open and requires further research to find the most adequate closure or model.

However, the incorporation of one internal coordinate to the transport equation introduces one extra dimension in complexity. Not only all the main variables depend now on the pore scale, but also the partial differential equation system becomes an integro-partial differential equation system. This brings problems at the time of choosing the most suitable solution method.

Several numerical methods have been developed for solving integro–differential equations in other areas of science. Examples are the neutron transport equation (Duderstadt and Hamilton, 1976) and the population balance equation (Ramkrishna, 2000). Most of these methods are designed to eliminate the integral terms from the equations. In recent years, the work by (Dorao and Jakobsen, 2005), (Patruno, 2010) and (Sporleder *et al.*, 2011) has shown the capability of the least-squares method (LSQ) to solve the integro-differential form of the equations directly. This spectral method is based on the idea that under certain conditions minimizing the residual of the equations defined with the numerical solution is equivalent to minimizing the error, i.e., the distance between the numerical solution and the exact solution (Jiang, 1998). This reformulation of the equations as a minimization problem is independent of the equations at hand, and therefore it allows for flexible and general–purpose programming. Besides, the method uses a measure of the residual as a built-in error estimator, and presents semi-analytical solutions, as the minimizing function is expanded in a family of basis functions. When combined with the finite or spectral element approach (Gerritsma and De Maerschalck, 2010), it is capable of solving large problems in arbitrary geometries, using unstructured meshes.

The scope of the present work leaves aside how to find the kernels of the MSTE as well as possible comparisons with experiments. Instead, we focus on the suitability of the LSQ to solve the MSTE. The analysis will make use of the manufactured solution method for a one-dimensional steady–state case. The extension to more complex problems is straight–forward.

The objective of this paper is to propose the LSQ for the solution of the MSTE for porous media and explain its implementation. The model, the solution method and the numerical example are given in the following three sections.

MODEL

Traditionally, the transport of a given species with concentration ϕ convected by plug flow through a porous media without diffusion in one dimension (z) can be written as:

$$\varepsilon v \frac{\partial \phi(z)}{\partial z} = S(z) \qquad (1)$$

where v is the advective velocity, ε is the void (or fluid) porosity and the right hand side is a source term. However, this approach is not able to capture all the degrees of freedom present in real porous media and the two-porosity model has been a successful first extension towards a more scale-size-related approach. Recently, a multi-scale approach has been introduced as a generalization to this concept based on the pore scale (Dupuy and Schwarz, 2011).

The term pore size has been used loosely in the literature and needs to be addressed first. In our framework, it is a characteristic length that represents the pore scale. Some authors (Dullien, 1991) proposed to define the pore size as twice the hydraulic radius. Other definitions may be used. Regardless of the choice, a consitent definition of a pore as a unity is required. Most pore networks agree on the definition of these elementary units. Each pore will therefore have a volume. In the MSTE, all the void volume is assigned to pores, and the concept of throat (Oren and Bakke, 2002; Blunt *et al.*, 2002; Piri and Blunt, 2005) is not needed. This is different to some pore network strategies.

Let us define ξ as the pore size, and $\varepsilon(\xi)d\xi$ as the total volume of the pores of sizes between ξ and $\xi + d\xi$ per volume unit. We will indicate the permeability of a pore of size ξ with $k(\xi)$, the advective velocity of the fluid at the scale ξ as $v(\xi)$, and the discharge (or slip velocity) for the same scale as $q(\xi) = \varepsilon(\xi)v(\xi)$.

Recent works (Dupuy and Schwarz, 2011) introduced the concept of the redistribution function $h(\xi_1 \rightarrow \xi_2)$ as the discharge from pores of size ξ_1 into pores of sizes ξ_2. This is a measure of the mixing between pores of different scales.

The $\varepsilon(\xi)d\xi$ and $q(\xi)d\xi$ are the probability density functions for porosity and discharge. Their definition is sometimes clarified by defining the cumulative distribution function, $F_\varepsilon(\xi) = \int_0^\xi \varepsilon(\hat{\xi})d\hat{\xi}$ and $F_q(\xi) = \int_0^\xi q(\hat{\xi})d\hat{\xi}$. $F_\varepsilon(\xi)$ is dimensionless and represents the porosity of a solid media obtained by considering all the pores of size smaller or equal to ξ.

The multi-scale transport for a tracer in all the pores assuming one dimension (z) and steady state case can be written as (Dupuy and Schwarz, 2011):

$$q(z,\xi) \cdot \frac{\partial \phi(z,\xi)}{\partial z} = S(z,\xi) + \int [\phi(z,\hat{\xi}) - \phi(z,\xi)]h(z,\hat{\xi} \rightarrow \xi)d\hat{\xi}$$
$$\phi(z = z_\Gamma, \xi) = \phi_\Gamma(\xi). \qquad (2)$$

With $\phi_\Gamma(\xi)$ a boundary condition. The left hand side and first term of the right hand side of the equation 2 are the convection per scale and the source per scale and present no major interaction between scales. However, the integral on the right hand side couples different scales and makes impossible to solve the problem for each scale independently. It should be pointed out that advection can be happening at different speeds ($\frac{\partial q}{\partial \xi} \neq 0$) and the source term can also be written independently for each pore-size.

THE LEAST-SQUARES METHOD

The LSQ reformulates any given well-posed set of equations as a minimization problem. As the MSTE could be taken as part of a more complex model, we present the method in a general manner, for a non-linear set of equations.

Let us write the problem to be solved as follows:

Find $\mathbf{f} \in X(\Omega)$ such that:

$$\mathcal{L}\mathbf{f} = \mathbf{g} \quad \text{in } \Omega \qquad (3)$$
$$\mathcal{B}\mathbf{f} = \mathbf{f}_\Gamma \quad \text{on } \Gamma \qquad (4)$$

where Ω is the domain of the system, Γ is the boundary of the domain, $\mathcal{L}$ is a functional operator, and $\mathcal{B}$ is the trace operator. $\mathbf{f}$ is the approximating function, which in the ideal case coincides with the exact solution to the problem.

Equation 4 represents the equations of the boundary conditions, while equation 3 represents the main equations of the problem. For example, taking equation 2 we find:

$$
\begin{aligned}
\mathbf{f} &= \phi_i \\
\mathbf{g} &= S_i \\
\mathcal{L}\bullet &= q \cdot \frac{\partial \bullet}{\partial z} - \int \bullet h(z, \hat{\xi} \to \xi) d\hat{\xi} + \bullet \int h(z, \hat{\xi} \to \xi) d\hat{\xi} \\
\mathcal{B}\bullet &= \bullet
\end{aligned}
\qquad (5)
$$

A norm equivalent functional can defined as follows:

$$\mathcal{J}(\mathbf{f}) \equiv \frac{1}{2} \| \mathcal{L}\mathbf{f} - \mathbf{g} \|^2_{Y(\Omega)} + \frac{1}{2} \| \mathcal{B}\mathbf{f} - \mathbf{f}_\Gamma \|^2_{Y(\Gamma)} . \qquad (6)$$

The functional $\mathcal{J}(\mathbf{f})$ is a measure of the residual of an aproximating function $\mathbf{f} \in X(\Omega)$. If the approximating function is the exact solution, the functional becomes zero. The residual of the boundary equations is included in equation 6 to allow a weak imposition of the boundary conditions. That is, we allow the use of spaces $X(\Omega)$ that are not constrained to satisfy these conditions.

It is assumed that the problem is well-posed and that the operators $\mathcal{L}$ and $\mathcal{B}$ conform a continuous mapping of the function space $X(\Omega) \times X(\Gamma)$ on the space $Y(\Omega) \times Y(\Gamma)$. Under these conditions, a norm equivalence between the norm of the residual and the norm of the error is established. That is, finding a function $\mathbf{f} \in X(\Omega)$ that minimizes the functional $\mathcal{J}(\mathbf{f})$ is equivalent to finding the approximating function in $X(\Omega)$ which is closest to the exact solution to the problem. Therefore, the least squares method is based on finding an $\mathbf{f} \in X(\Omega)$ such that this functional is minimized. The reader is refered to (Bochev and Gunzburger, 2009) for more details on the mathematical formalism.

Solution procedure

Using variational analysis, minimizing the functional $\mathcal{J}(\mathbf{f})$ is equivalent to finding $\mathbf{f} \in X(\Omega)$ such that:

$$\lim_{\varepsilon \to 0} \frac{d}{d\varepsilon} \mathcal{J}(\mathbf{f} + \varepsilon \, \mathbf{w}) = 0 \qquad \forall \mathbf{w} \in X(\Omega) \qquad (7)$$

where $X(\Omega)$ is the space of admissible functions.

We use the L^2 norm defined as $\| \bullet \|^2_{Y(\Omega)} = \langle \bullet, \bullet \rangle = \int_\Omega \bullet \bullet \, d\Omega$ for simplicity. Using $\mathcal{E}(\mathbf{f}) = \mathcal{L}\mathbf{f} - \mathbf{g}$ to represent the equations, we express the norm equivalent functional as:

$$\mathcal{J}(\mathbf{f}) \equiv \frac{1}{2} \langle \mathcal{E}(\mathbf{f}), \mathcal{E}(\mathbf{f}) \rangle \qquad (8)$$

Here, we leave aside the equations for the boundary conditions. The extension of the solution procedure to these is straight-forward.

In practice, we restrict the search of the minimizing function to a finite–dimensional function space such that $\mathbf{f}_P \in X_P(\Omega) \subset X(\Omega)$ and $X_P(\Omega) = span\{\varphi_0, ..., \varphi_P\}$:

$$\mathbf{f}_P^e = \sum_{j=0}^{N_p - 1} \mathbf{b}_j^e \varphi_j^e \qquad (9)$$

$$\mathbf{f}_P = \bigcup_{e=1}^{N_e} \mathbf{f}_P^e \qquad (10)$$

Equation 7 yields then the equivalent problem: find $\mathbf{f}_P \in X_P(\Omega)$ such that:

$$\left\langle \frac{\partial \mathcal{E}}{\partial \mathbf{f}} \mathbf{w}, \mathcal{E}(\mathbf{f}_P) \right\rangle = \mathcal{G} = 0 \, , \quad \forall \mathbf{w} \in X_P(\Omega) \qquad (11)$$

Here, $\frac{\partial \mathcal{E}}{\partial \mathbf{f}}$ is the operator obtained by dividing the different equations by the different variables. It can be divided in rows which represent each equation, and in columns which represent the operator affecting each variable in each equation. That is,

$$\mathbf{f} = \begin{bmatrix} f_1 & \dots & f_v & \dots & f_{N_v} \end{bmatrix}^T$$

$$
\mathcal{E}\frac{\partial \mathcal{E}}{\partial \mathbf{f}} = \begin{bmatrix}
\frac{\partial \mathcal{E}_1}{\partial \mathbf{f}_1} & \cdots & \frac{\partial \mathcal{E}_1}{\partial \mathbf{f}_v} & \cdots & \frac{\partial \mathcal{E}_1}{\partial \mathbf{f}_{N_v}} \\
\cdots & \cdots & \cdots & \cdots & \cdots \\
\frac{\partial \mathcal{E}_c}{\partial \mathbf{f}_1} & \cdots & \frac{\partial \mathcal{E}_c}{\partial \mathbf{f}_v} & \cdots & \frac{\partial \mathcal{E}_c}{\partial \mathbf{f}_{N_v}} \\
\cdots & \cdots & \cdots & \cdots & \cdots \\
\frac{\partial \mathcal{E}_{N_c}}{\partial \mathbf{f}_1} & \cdots & \frac{\partial \mathcal{E}_{N_c}}{\partial \mathbf{f}_v} & \cdots & \frac{\partial \mathcal{E}_{N_c}}{\partial \mathbf{f}_{N_v}}
\end{bmatrix}
\qquad (12)
$$

where N_v is the number of variables and N_c is the number of equations.

For linear problems, $\frac{\partial \mathcal{E}}{\partial \mathbf{f}} \mathbf{w} = \mathcal{L}\mathbf{w}$, and the problem is reduced to finding $\mathbf{f}_P \in X_P(\Omega)$ such that:

$$\mathcal{A}(\mathbf{f}_P, \mathbf{w}) = \mathcal{F}(\mathbf{w}) \, , \quad \forall \mathbf{w} \in X_P(\Omega) \qquad (13)$$

where

$$
\begin{aligned}
\mathcal{A}(\mathbf{f}, \mathbf{w}) &= \langle \mathcal{L}\mathbf{f}, \mathcal{L}\mathbf{w} \rangle \\
\mathcal{F}(\mathbf{w}) &= \langle \mathbf{g}, \mathcal{L}\mathbf{w} \rangle
\end{aligned}
\qquad (14)
$$

For non-linear problems, a seed solution $\mathbf{f}_P^*$ is proposed, and the Newton-Raphson method is used to iterate until the minimizing solution is found. This method is based on the expansion in Taylor series of $\mathcal{G}$ around $\mathbf{f}_P^*$, and yields the following equivalent problem: find $\delta \mathbf{f}_P = \mathbf{f}_P - \mathbf{f}_P^* \in X_P(\Omega)$ such that:

$$\left\langle \frac{\partial}{\partial \mathbf{f}} \left(\frac{\partial \mathcal{E}}{\partial \mathbf{f}} \mathbf{w} \right)^* \delta \mathbf{f}_P, \mathcal{E}(\mathbf{f}_P^*) \right\rangle$$
$$+ \left\langle \frac{\partial \mathcal{E}^*}{\partial \mathbf{f}} \delta \mathbf{f}_P, \frac{\partial \mathcal{E}^*}{\partial \mathbf{f}} \mathbf{w} \right\rangle + \left\langle \mathcal{E}(\mathbf{f}_P^*), \frac{\partial \mathcal{E}^*}{\partial \mathbf{f}} \mathbf{w} \right\rangle = 0 \, , \quad \mathbf{w} \in X_P(\Omega) \quad (15)$$

The first term is usually set to zero (Winterscheidt and Surana, 1994; Codd, 2001). This term is dominated by the others near the solution. Furthermore, the absence of this term simplifies greatly the computation and does not affect the method, only the way in which the solution is looked for.

The equivalent problem to be solved is to find $\mathbf{f_P} \in X_P(\Omega)$ such that equation 13 is fulfilled, with:

$$\mathscr{A}(\mathbf{f},\mathbf{w}) = \langle \frac{\partial \mathscr{E}^*}{\partial \mathbf{f}} \mathbf{f}, \frac{\partial \mathscr{E}^*}{\partial \mathbf{f}} \mathbf{w} \rangle$$

$$\mathscr{F}(\mathbf{w}) = \langle \frac{\partial \mathscr{E}^*}{\partial \mathbf{f}} \mathbf{f}^* - \mathscr{E}(\mathbf{f}^*), \frac{\partial \mathscr{E}^*}{\partial \mathbf{f}} \mathbf{w} \rangle \tag{16}$$

Comparing equation 16 to equation 14, this procedure is equivalent to linearizing the equations using the Newton-Raphson method and then applying the least-squares method to the resulting linear problem $\frac{\partial \mathscr{E}^*}{\partial \mathbf{f}} \mathbf{f} = \frac{\partial \mathscr{E}^*}{\partial \mathbf{f}} \mathbf{f}^* - \mathscr{E}(\mathbf{f}^*)$. The Picard method (also known as fixed point or direct substitution method) has also been used to linearize the equations (Sporleder *et al.*, 2010).

The algebraic set of equations corresponding to the equivalent problem is found expanding the approximate solution (equation 9). The internal products are approximated numerically using quadrature rules. Thus, the system of algebraic equations is given as follows:

$$\mathbf{Ab} = \mathbf{F} \tag{17}$$

where $\mathbf{b}$ is the vector of coefficients of the expansion in equation 9, and where:

$$\mathbf{A} = \mathbf{L}^T \mathbf{WL}$$
$$\mathbf{F} = \mathbf{L}^T \mathbf{WG}$$

$\mathbf{L}$ is called the problem operator matrix, $\mathbf{W}$ is a diagonal matrix built with the quadrature weights and $\mathbf{G}$ is called source vector. The three can be subdivided analogously to equation 12:

$$\mathbf{G} = \begin{bmatrix} G_1 & \dots & G_c & \dots & G_{N_c} \end{bmatrix}^T$$

$$\mathbf{L} = \begin{bmatrix} L_{11} & \dots & L_{1v} & \dots & L_{1N_v} \\ \dots & \dots & \dots & \dots & \dots \\ L_{c1} & \dots & L_{cv} & \dots & L_{cN_v} \\ \dots & \dots & \dots & \dots & \dots \\ L_{N_c1} & \dots & L_{N_cv} & \dots & L_{N_cN_v} \end{bmatrix} \tag{18}$$

where:

$$[L_{cv}]_{qk} = \left(\frac{\partial \mathscr{E}_c}{\partial \mathbf{f}} \right)_v^* \varphi_k(\mathbf{r_q})$$

$$[G_c]_q = \frac{\partial \mathscr{E}_c^*}{\partial \mathbf{f}} \mathbf{f}_P^*(\mathbf{r_q}) - \mathscr{E}_c(\mathbf{f}_P^*(\mathbf{r_q})) \tag{19}$$

Here, $\mathbf{r_q}$ is the quadrature point q.

NUMERICAL EXAMPLE

As shown in equation 5, the MSTE is linear when solved for $\phi(z, \xi)$. The equation presents a derivative, an identity and an integral operator applied to ϕ. In matricial form:

$$\mathbf{L} = \mathbf{C_1 Dz} + \mathbf{C_2 H} + \mathbf{I_h} \tag{20}$$
$$\mathbf{G} = \mathbf{S} \tag{21}$$

with:

$$[\mathbf{C_1}]_{qj} = \delta_{qj} q(z_q, \xi_q)$$
$$[\mathbf{C_2}]_{qj} = \delta_{qj} \int h(z_q, \xi_q \to \hat{\xi}) d\hat{\xi}$$
$$[\mathbf{S}]_q = S(z_q, \xi_q)$$

where δ_{qj} is the Kronecker delta. The other matrices, namely $\mathbf{D_z}$, $\mathbf{H}$, and $\mathbf{I_h}$ are called operator matrices.

$\mathbf{D_z}$ is called the derivative operator matrix in z, and is defined as follows:

$$[\mathbf{D_z}]_{qj} = \frac{\partial \varphi_j}{\partial z}(z_q, \xi_q) \tag{22}$$

$\mathbf{H}$ is the identity operator matrix, and is defined as follows:

$$[\mathbf{H}]_{qj} = \varphi_j(z_q, \xi_q) \tag{23}$$

$\mathbf{I_h}$ is the integral operator weighted with h, and is defined as follows:

$$[\mathbf{I_h}]_{qj} = -\int h(z_q, \xi_q \to \hat{\xi}) \varphi_j(z_q, \hat{\xi}) d\hat{\xi}$$
$$= -\sum_k h(\xi_q \to s_k) \varphi_j(z_q, s_k) \omega_k \tag{24}$$

Here, we define new quadrature points and weights such that s_k exists within the integration boundaries for each row of the integral operator matrix.

We select the case of flow through a column for our numerical example. A one meter column filled with a packed bed of rocks has a porosity per scale given by $\varepsilon(\xi)$. Liquid is introduced from the top which percoles down the column at a given discharge per scale given by $q(\xi)$. The pore-scale redistribution, h is assumed proportional to the discharges.

In the manufacturing solution method we propose a solution $\phi(\xi, z)$ and calculate analitically the value of the source. For this problem the chosen functionalities and values are:

$$\varepsilon(\xi) = A(\xi - \xi_0)(-\xi + \xi_f) \tag{25}$$
$$q(\xi) = V \varepsilon(\xi) \xi^2 \tag{26}$$
$$h(z, \hat{\xi} \to \xi) = q(\hat{\xi}) q(\xi) / L \tag{27}$$
$$\phi(z, \xi) = 10 \sin(z)(1 - M Log(\xi/R)) \tag{28}$$
$$S(z, \xi) = 10 AV \cos(z) \xi^2 (\xi - \xi_0)(\xi_f - \xi)(1 - M Log[\xi/R]) +$$
$$A^2 MV^2 (360L)^{-1} \xi^2 (\xi - \xi_0)(\xi - \xi_f) \sin(z) \times \dots$$
$$\left(-81\xi_0^5 + 175\xi_0^4 \xi_f - 175\xi_0 \xi_f^4 + \dots \right.$$
$$81\xi_f^5 + 60\xi_0^4 (3\xi_0 - 5\xi_f) Log\left[\frac{\xi_0}{\xi}\right] + \dots$$
$$\left. 60(5\xi_0 - 3\xi_f)\xi_f^4 Log\left[\frac{\xi_f}{\xi}\right] \right) \tag{29}$$

with $A = 1/500$ mm^{-3}, $V = 0.001$ m/mm^{2}s, $M = 1$, $R = 2\xi_f$, $L = 10^{-5}$ m^2/s and pore scale limits $\xi_0 = 1$ mm and $\xi_f = 10$ mm.

The selected model was based on physical cases. The porosity expands from 1 mm to 10 mm pore size. Pore sizes might be extended to various order of magnitudes below one millimetre if the rock presents internal porosity or fractures. However, for a pack of solid bodies 1 mm can be a reasonable magnitude. The pore space has a maximum at 5.5 mm, and a total porosity of 24% (note that this is very close to the

ideal close pack porosity of $\frac{\pi}{18}$). The discharge q will in general depend with the permeability, the porosity and a factor that scales directly with the pore size (the square of the diameter is for pipes). The redistribution discharge follows the model of symmetric mixing with length characteristic length L. Measurements and previous calculations on the redistribution matrix have shown some similarity with this model, (Dupuy *et al.*, 2011).

Results

The Gauss–Lobatto–Legendre quadrature rule was used to approximate the integrals in z, while the Gauss–Legendre quadratures were used for ξ. The solution was approximated using a nodal expansion based on Lagrange polynomials defined at the zeros of these quadratures. The problem was coded in MATLAB, and its direct solver was used for the calculations.

Both the discharge, $q(\xi)$ and the porosity, $\varepsilon(\xi)$ do not depend on the position along the column. Plot of the distribution and cumulative distribution for these two functions are given in Figure 1.
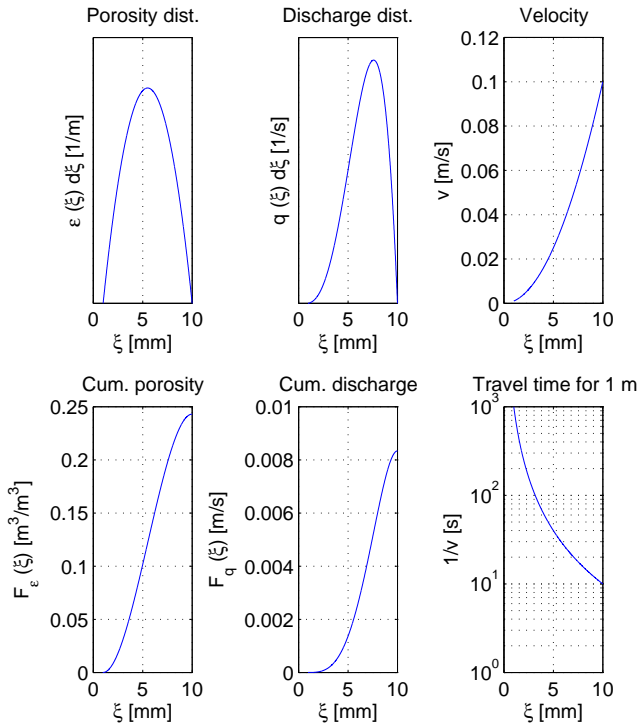
Figure 1: Left column: porosity distribution (top) and cumulative porosity distribution (bottom). Middle column: discharge distribution (top) and cumulative discharge distribution (bottom). Right column: velocity per channel (top), and 1-metre residence time (bottom)

The solution is shown in Figure 2. As the liquid flows down the column ϕ increases due to reactions happening inside the pores. Despite the source term is very different for different pore sizes (negative for large pores and positive for small pores, see Figure 3) the tracer ϕ is exchanged between different pores scales tending to level out the differences. However the increase is larger for the small pores at all the length of the column (z values). The source term (Figure 3) behaves differently for different pore scales. Large amounts of ϕ are generated for pores smaller than 5 mm, while a sink is observed in the largest pores. This behaviour for the source term mimic two competing reactions. It models the case of a

species that is a product of an heterogeneous reaction but is a reactant of a reaction taking place in the liquid bulk. Heterogeneous reactions depend strongly of the surface to volume ratio which is much larger for small pore scales. At the same time the reactant is consumed in the larger pores in this case as the bulk reaction that consumes ϕ becomes more dominant.
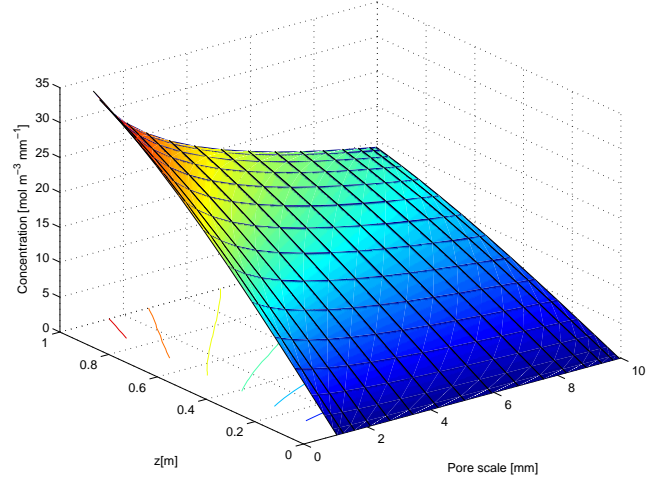
Figure 2: Solution $\phi(z, \xi)$.
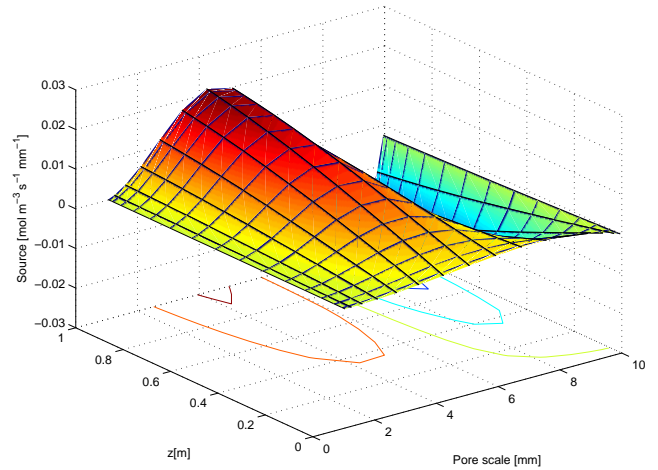
Figure 3: Source term $S(z, \xi)$.

Finally, the polynomial order for both dimensions was varied from 5 to 12 to analyze the accuracy of the numerical solution. Figure 4 shows the L^2 norm of the error. It can be seen that the error is reduced with an exponential convergence rate. This follows the behavior of the norm of the residual, due to the norm equivalence mentioned when presenting the LSQ. The norm of the residual, shown in Figure 5, decreases until reaching a point of limiting accuracy, close to numerical precision. The existance of norm equivalence provides the numerical method with a built-in error estimator. In finite and spectral element versions of the method, the norm of the residual can be used to design hp-adaptivity strategies that optimize the grid used.

For completeness, the condition number versus the order of the approximation is shown in Figure 6. This number increases steeply with the order, reaching values over 10^{12}. The condition number depends mostly on the fill-up of the matrix. The use of an element approach will reduce drastically this number. Larger models that use the MSTE are also

expected to have lower condition numbers.
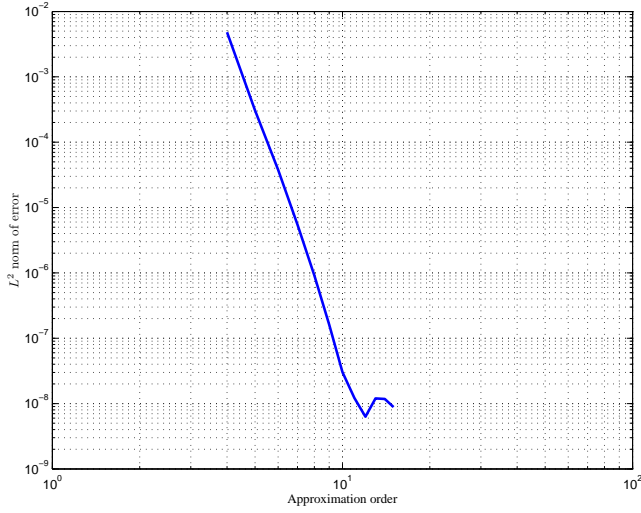
Figure 4: L^2 norm of the error vs. order of the approximation
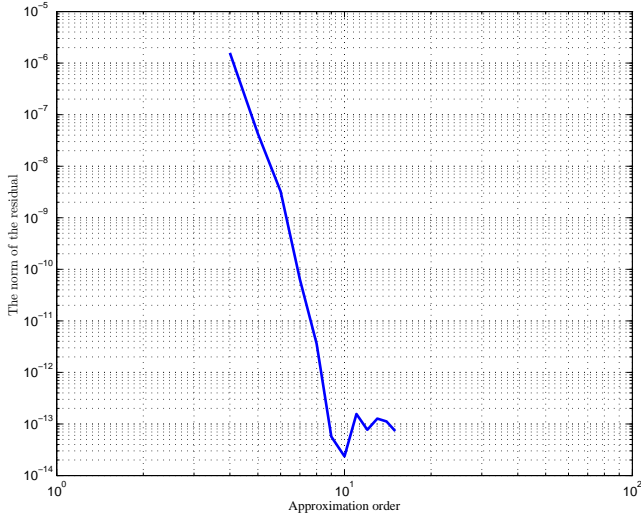
Figure 5: L^2 norm of the residual vs. order of the approximation
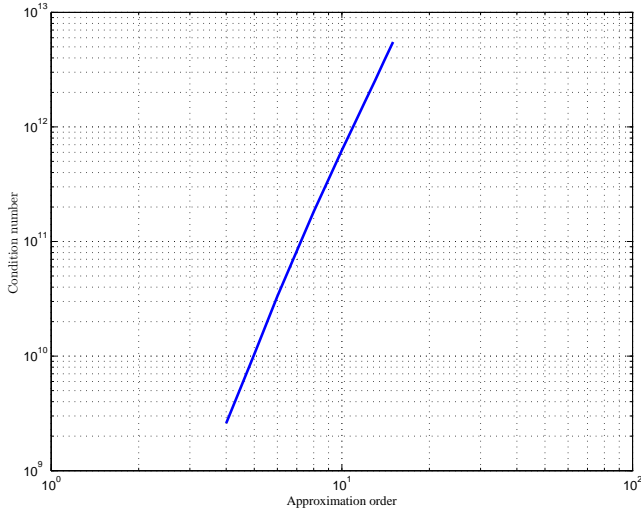
Figure 6: Condition number vs. order of the approximation

CONCLUSION

The conclusions of this paper are:

- The LSQ is well suited for the solution of the multiscale transport equation for porous media, achieving exponential convergence in the method order.

- A method has been described and can now be applied for the solution of transport and reactions problems in porous media.

The combination of the MSTE with LSQ enables a set of new physics that now can be modelled. We have shown how the specific discharge, and therefore, the advecting velocity can be different at different scales, having travelling times between the smallest and the largest pore scales that vary two order of mangitude. The cumulative distribution function of any variable, such as the tracer concentration can be recovered at any point of the domain. Furthermore, having a source term that works as sink and as source depending on the pore scale is also possible enabling the modelling of the competition between heterogeneous rections and reactions occuring in the liquid bulk. Finally, the incorporation of a redistribution tems add the complexity of an integral term that binds physics happening at different scale loosing the locality behavior proper of a normal transport equation and still this can be fully captured by the LSQ also with exponential convergency.

Future work still remains on the area of finding the most adequate kernels that best represent different porous media. Mainly empirical studies of the redistribution function need to be done.

REFERENCES

ABELL, A.B. *et al.* (1999). "Mercury intrusion porosimetry and image analysis of cement-based materials". *Journal of Colloid and Interface Science*, **211(1)**, 39 – 44.

AHRENHOLZ, B. *et al.* (2008). "Prediction of capillary hysteresis in a porous material using lattice-boltzmann methods and comparison to experimental data and a morphological pore network model". *Advances in Water Resources*, **31(9)**, 1151–1173.

BLUNT, M.J. *et al.* (2002). "Detailed physics, predictive capabilities and macroscopic consequences for pore-network models of multiphase flow". *Advances in Water Resources*, **25(8-12)**, 1069–1089.

BOCHEV, P.B. and GUNZBURGER, M.D. (2009). *Least-Squares Finite Element Methods*. Springer.

BOUFFARD, S.C. and DIXON, D.G. (2001). "Investigative study into the hydrodynamics of heap leaching processes". *Metallurgical and Materials Transactions B-Process Metallurgy and Materials Processing Science*, **32(5)**, 763–776.

CHEN, Z.X. (1989). "Transient flow of slightly compressible fluids through double-porosity, double-permeability systems âĂŤ a state-of-the-art review". *Transport in Porous Media*, **4**, 147–184. 10.1007/BF00134995.

CODD, A.L. (2001). *Elasticity-Fluid Coupled Systems and Elliptic Grid Generation (EGG) based on First-Order Sytem Least Squares (FOSLS)*. Ph.D. thesis, University of Colorado.

DE BOER, R. (1992). "Development of porous media theories – a brief historical review". *Transport in Porous Media*, **9**, 155–164. 10.1007/BF01039634.

DORAO, C. and JAKOBSEN, H. (2005). "Application of the Least Square Method to Population Balance Problems". *Computers and Chemical Engineering*, **30**, 535–547.

DUDERSTADT, J.J. and HAMILTON, L.J. (1976). *Nuclear Reactor Analysis*. Wiley.

DULLIEN, F.A.L. (1991). "Characterization of porous-media - pore level". *Transport in Porous Media*, **6(5-6)**, 581–606.

DUPUY, P.M. and SCHWARZ, M.P. (2011). "A multiscale transport equation". *Transport in Porous Media*, **Under review.**

DUPUY, P.M. *et al.* (2011). "Pore scale definition and computation from tomography data". *Computer Physics Communications*, **Accepted manuscript.**

DURNER, W. (1994). "Hydraulic conductivity estimation for soils with heterogeneous pore structure". *Water Resources Research*, **30(2)**, 211–223.

GERRITSMA, M.I. and DE MAERSCHALCK, B. (2010). *Advanced Computational Methods in Science and Engineering*, vol. 71 of *Lecture Notes in Computational Science and Engineering*, chap. Least-Squares Spectral Element Methods in Computational Fluid Dynamics, 179–227. Springer-Verlag Berlin Heidelberg.

HELD, R.J. and CELIA, M.A. (2001). "Pore-scale modeling and upscaling of nonaqueous phase liquid mass transfer". *Water Resources Research*, **37(3)**, 539–549.

JARONIEC, M. and KANEKO, K. (1997). "Physicochemical foundations for characterization of adsorbents by using high-resolution comparative plots". *Langmuir*, **13(24)**, 6589–6596.

JIANG, B.N. (1998). *The least-squares finite element method: theory and applications in computational fluid dynamics and electromagnetics*. Springer.

NAVAS, J. *et al.* (2010). "Pore characterization methodology by means of capillary sorption tests". *Transport in Porous Media*, 1–19.

OREN, P.E. and BAKKE, S. (2002). "Process based reconstruction of sandstones and prediction of transport properties". *Transport in Porous Media*, **46(2-3)**, 311–343.

PATRUNO, L. (2010). *Experimental and numerical investigations of liquid fragmentation and droplet generation for gas processing at high pressures*. Ph.D. thesis, Norwegian University of Science and Technology.

PIRI, M. and BLUNT, M.J. (2005). "Three-dimensional mixed-wet random pore-scale network modeling of two- and three-phase flow in porous media. i. model description". *Physical Review E*, **71**.

RAMKRISHNA, D. (2000). *Population Balances, Theory and Applications to Particulate Systems in Engineering*. Academic Press.

SHOLOKHOVA, Y. *et al.* (2009). "Network flow modeling via lattice-boltzmann based channel conductance". *Advances in Water Resources*, **32(2)**, 205–212.

SPORLEDER, F. *et al.* (2010). "Simulation of chemical reactors using the least-squares spectral element method". *Chemical Engineering Science*, **65**, 5146–5159.

SPORLEDER, F. *et al.* (2011). "Model based on population balance for the simulation of bubble columns using methods of the least square type". *Chemical Engineering Science*, **Accepted manuscript.**

WINTERSCHEIDT, D. and SURANA, K.S. (1994). "p-version least squares finite element formulation fot two-dimensional, incompressible fluid flow". *International Journal for Numerical Methods in Fluids*, **18**, 43–69.

ZHANG, L. and SEATON, N.A. (1994). "The application of continuum equations to diffusion and reaction in pore networks". *Chemical Engineering Science*, **49(1)**, 41–50.

STUDY OF THE STEEL/SLAG INTERFACE INSTABILITY AND THE INFLUENCE OF INJECTED GAS IN THE CONTINUOUS CASTING OF STEEL

Z Kountouriotis[1], K Pericleous[1*], G Djambazov[1], JF Domgin[2], P Gardin[2]

[1] Centre for Numerical Modelling and Process Analysis, University of Greenwich, UK
[2] ArcelorMittal Research, BP 30320, 57283 Maizieres-les-Metz Cedex, France

*Corresponding author, e-mail: k.pericleous@gre.ac.uk

ABSTRACT

Keywords:

NOMENCLATURE

Greek Symbols

δt

ε

μ

ρ

σ

Latin Symbols

A

Cd

$\mathbf{g}$

$\mathbf{u}$

$\bar{\mathbf{u}}$

$\mathbf{u}'$

k

V

Sub/superscripts

p

f

m

l

INTRODUCTION

k

$$f = Min\left(\frac{\Delta \bullet \varepsilon}{\kappa}\right)$$
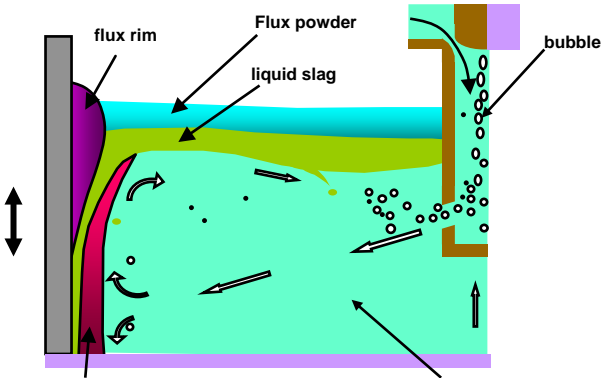
Figure 1:
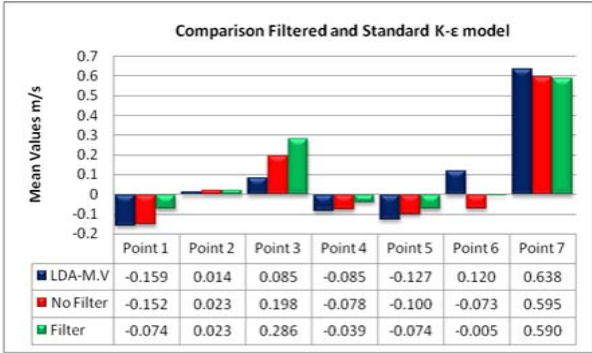
Figure 2:

MODEL DESCRIPTION

ϕ

ϕ

CFL

Continuity equation

$$\frac{\partial \rho}{\partial t} + \nabla \cdot \left(\rho \mathbf{u} \right) =$$

CDM

S   *CDM*

Momentum equation

$$\frac{\partial}{\partial t} (\rho \mathbf{u}) + \nabla \cdot \left(\rho \mathbf{u} \mathbf{u} \right) = \nabla \cdot \left(\mu \nabla \mathbf{u} \right) - \nabla p + \mathbf{S}$$

ϕ ϕ

$\mathbf{u}$ p •

μ $\mathbf{S}$

$$Q = C \cdot q \cdot \left(- \phi_{down} \right) \cdot \phi_{up}$$

Free surface -The Counter Diffusion Method

Q

C

$(1\text{-}\phi_{down})$

ϕ_{up} q

$$q = \left| \mathbf{u} \cdot n \right| \cdot A$$

$$\frac{D\left(\rho \right)}{Dt} + \nabla \cdot \left(\mathbf{u} \right) =$$

n

$$\frac{\partial}{\partial t} (\rho \mathbf{u}) + \nabla \cdot \left(\rho \mathbf{u} \mathbf{u} \right) = \nabla \cdot \left(\mu \nabla \mathbf{u} \right) - r \nabla p + \mathbf{S}$$

r ∇p

$$r = \left\{ + \phi \left(\frac{\rho_m}{\rho_f} - \right) \right\}^{-}$$

et a.

ρ_f ρ_m

ρ

μ

ϕ U_p

$$\mu = \mu_f + \phi \left[\left(\mu_m \frac{\rho_f}{\rho_m} \right) - \mu_f \right]$$

$$m_p \frac{d\mathbf{u}_p}{dt} = \left(\rho_p - \rho_l \right) \mathbf{g} V_p - - \rho_l V_{slip} \left| \mathbf{u}_p - \mathbf{u} \right| \frac{\pi d}{} Cd - - m_p \frac{\rho_l}{\rho_p} \frac{d\mathbf{u}_p}{dt}$$

$\mathbf{T}$

μ_f μ_m

$$\rho = \rho_f + \phi \left(\rho_m - \rho_f \right)$$

$$\mathbf{u}_p = \left(\mathbf{u}_p + \mathbf{S}_u \cdot \delta_t\right) \ \left(\ + \mathbf{F} \cdot \delta_t\right) \ where$$

$$\mathbf{F} = \quad \cdot Cd \cdot \rho_l \cdot \mathbf{V}_{slip} \ \left(d_p \cdot \rho_f\right)$$

$$\mathbf{S}_u = F \cdot \mathbf{u}_p + \left(\rho_p - \rho_l\right) \cdot \mathbf{g} \ \ \rho_f$$

$$\rho_f = \rho_p + - \rho_l$$

$$\mathbf{V}_{slip} = \mathbf{u}_p - \mathbf{u}$$

$\mathbf{F}$ $\mathbf{S}_u$

Cd

$\cdot t$

Figure 3:

$\mathbf{u}$

$\mathbf{u}'_l$

$\overline{\mathbf{u}}_l$

a)0.5m/s   b)0.8m/s   c)1.018m/s

Figure 4:

$\mathbf{u}'_l$

$\overline{\mathbf{u}}_l = \quad m \ \ s$

$= \sqrt{\quad \cdot} \quad k$
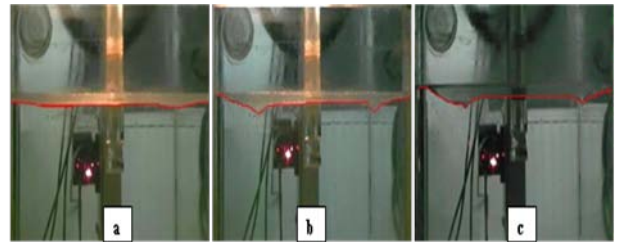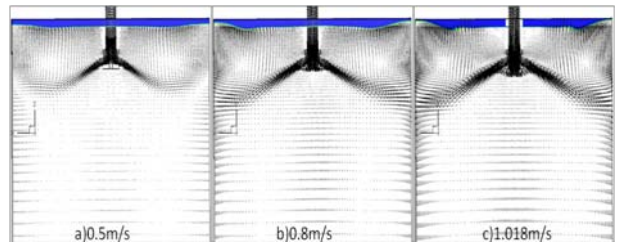
RESULTS

Oil and gas qualitative observations
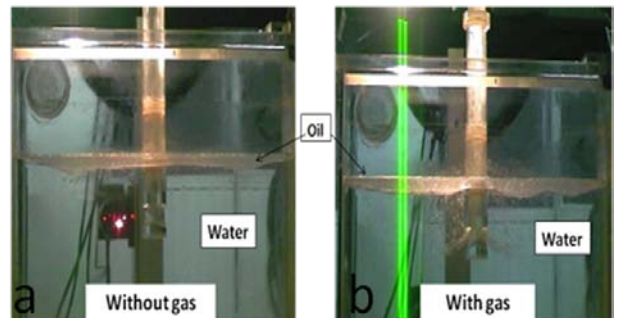
Figure 5:
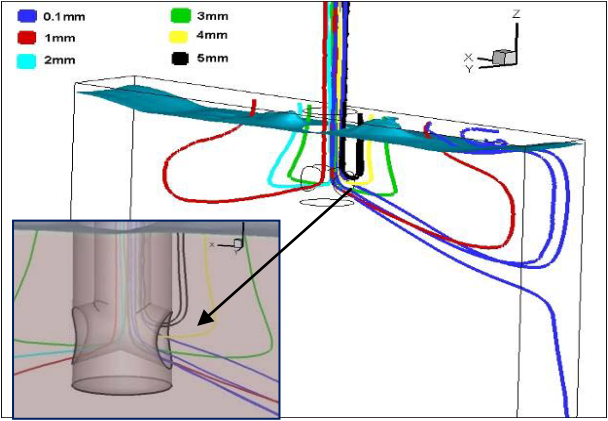
Figure 6:
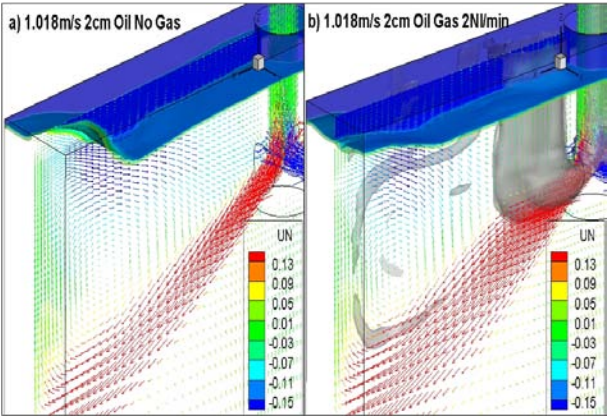
Figure 7:

Quantitative comparisons

Figure 8:

$$k = -u'\, t$$

$k)$
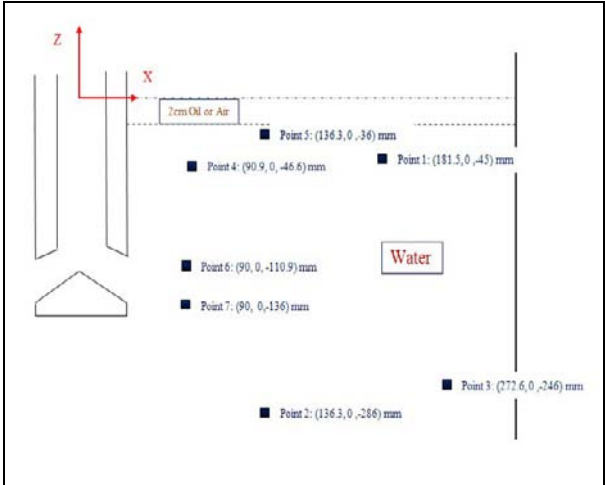
$$\sigma = \sqrt{\ u\ t\ +-k}$$

$u(t)$

var
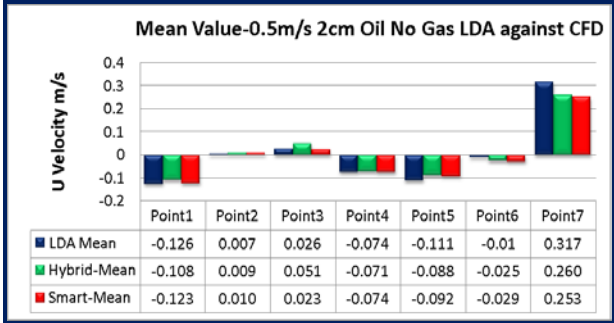
Figure 9a:
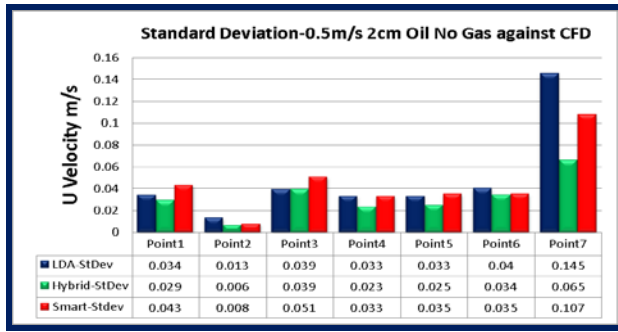
Figure 9b:

Influence of oil and gas on meniscus stability
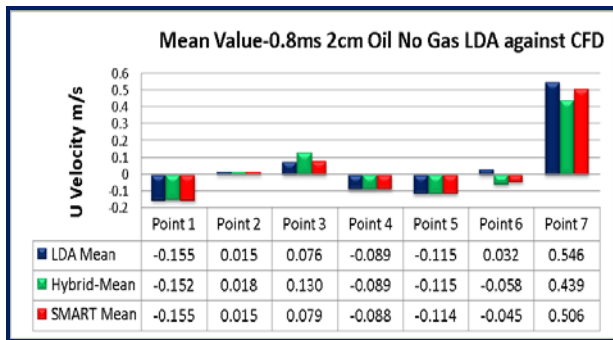
Figure 10a:
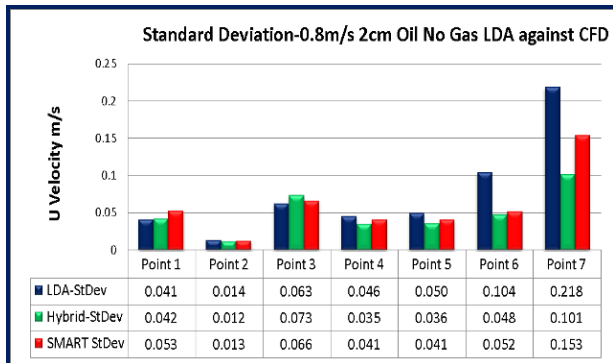
Figure 11:
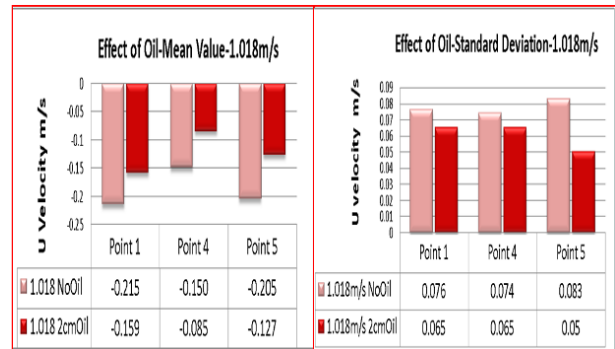
Figure 10b:
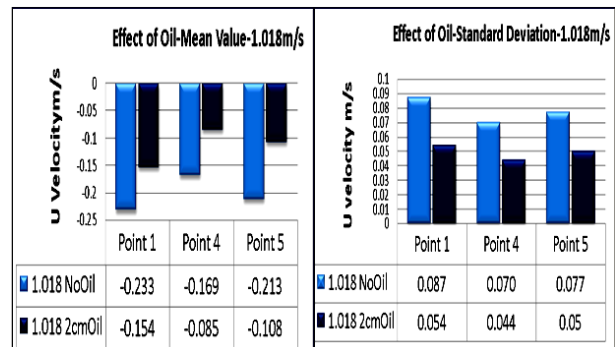
Figure 12:

Spectral analysis
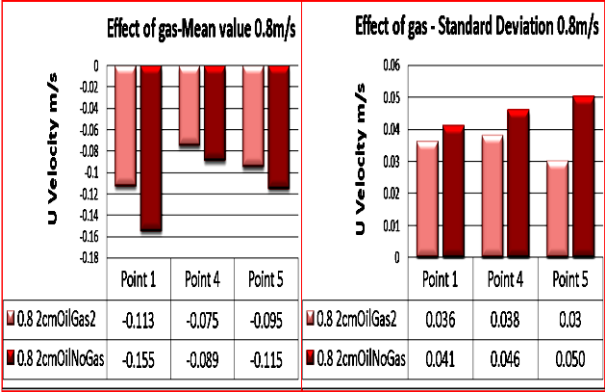
Figure 13:
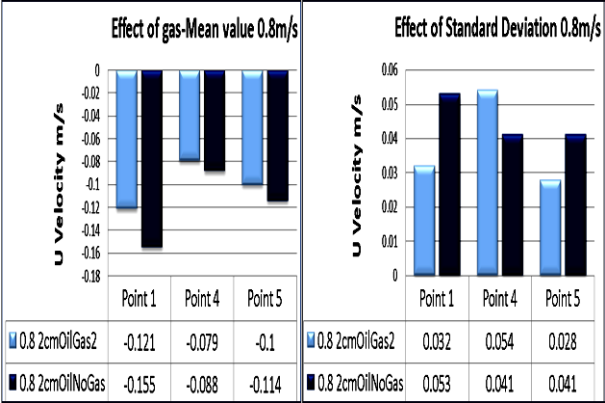
Figure 14:
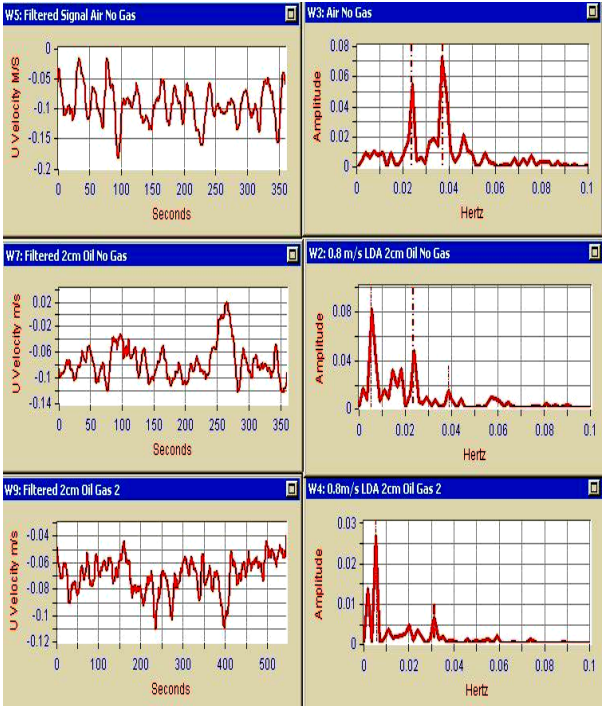
Figure 15:   *Vin*

Flow oscillation analysis
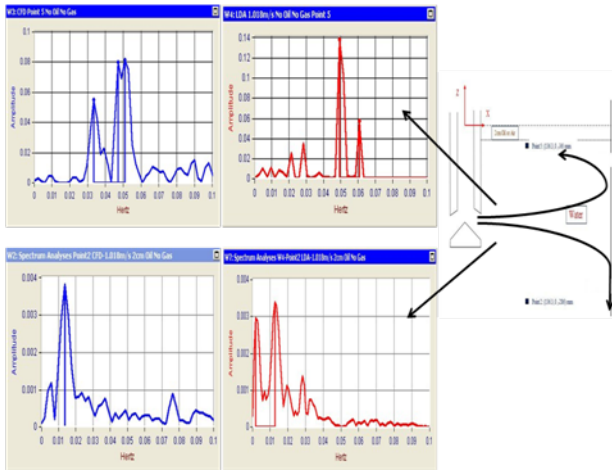
Figure 16:

Application to an industrial caster
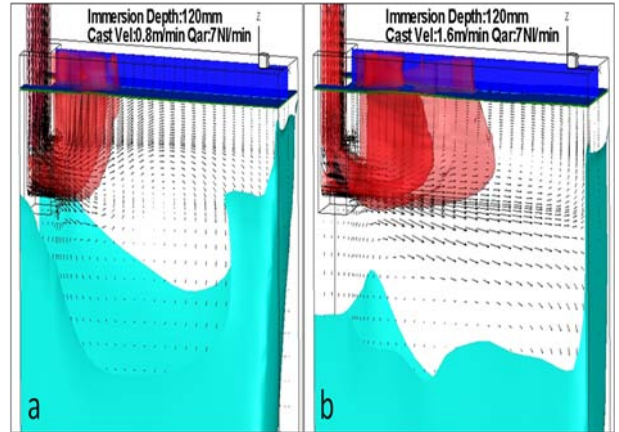
Figure 17:
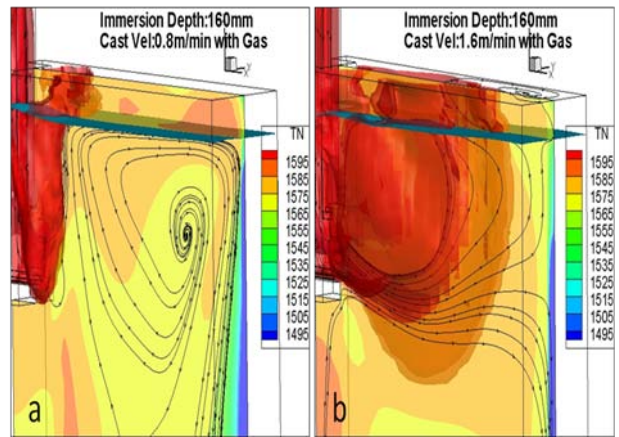
Sub-meniscus Velocity Control
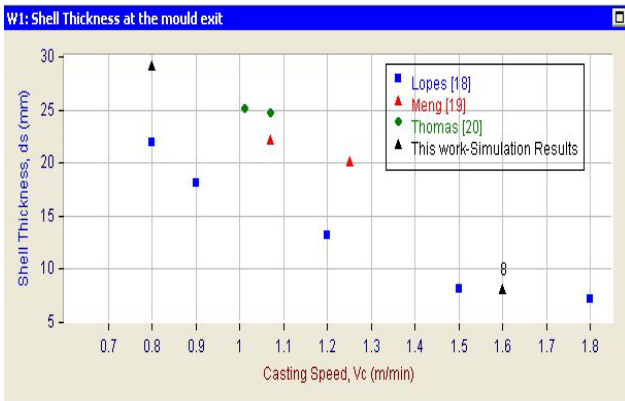
Figure 18:

Figure 19:

CONCLUSIONS

REFERENCES

” *Revue De Metallurgie*

Proc. Int. Cong. on Stencils

J. Stencils **5,**

”
Journal of Comp.l Physics

” *The
Encyclopedia of Materials: Science and Technology*

”. *Fifth
International Conference on CFD in the Process
Industries*

” *ISIJ International*

” *Second
International Conference on CFD in the Minerals and
Process Industries*

”. *4th European Continuous Casting Conference,*

*International
Journal of Heat and Fluid Flow*

”
International Journal for Numerical Methods in Fluids
8

Advances in Computational Mathematics

” *ASME, Transactions, Series I - Journal
of Fluids Engineering*
“Aspects of
computer-simulation of liquid-fuelled combustors”,
Journal of Energy

”

”. *AISTech*

Z. Kountouriotis, K. Pericleous, G. Djambazov, J.F. Domgin, P. Gardin

POPULATION BALANCE MODELLING OF ISOTHERMAL BUBBLY-CAP FLOWS USING TWO-GROUP AVERAGED BUBBLE NUMBER DENSITY APPORACH

S.C.P. Cheung[1]* , G.H. Yeoh[2,3] , J.Y. Tu[1], E. Krepper[4] and D. Lucas[4]

[1] SAMME, RMIT University, Victoria 3083, AUSTRALIA

[2] ANSTO, Kirrawee DC, NSW 2232 AUSTRALIA

[3] SMME, University of New South Wales, Sydney, NSW 2052 AUSTRALIA

[4] Forschungszentrum Rossendrof e.V., P.O. Box 510 119, 01314 Dresden, GERMANY

* E-mail: chipok.cheung@rmit.edu.au

ABSTRACT

NOMENCLATURE

Greek Symbols

-
-
-
- μ
- μ_T
-
-

Latin Symbols

D_b

F

F

F

F

F

g

K

n

R

$\tilde{}$

Sub/superscripts

g

j j

l

INTRODUCTION

Keywords:

FORMULATION OF TWO-GROUP MODEL

Two-group average bubble number density equation

$$D = \sqrt{\frac{\sigma}{g\Delta\rho}}$$

$$D = \sqrt{\frac{\sigma}{g\Delta\rho}}$$

$$\frac{\partial n}{\partial t} + \nabla \cdot \vec{v}^{\,g} n = \sum_j R_j + R_j$$

$$\frac{\partial n}{\partial t} + \nabla \cdot \vec{v}^{\,g} n = \sum_j R_j + R_j$$

$$n \qquad\qquad \vec{v}^{\,g} \qquad\qquad \gamma^{RC} \qquad K^{RC}$$

$$\alpha^g = \alpha^g + \alpha^g$$

Bubble mechanistic models

$$\phi^{TI} = \gamma^{TI} \frac{\alpha^g \quad -\alpha^g}{D_b \quad \alpha_{TI} \quad -\alpha^g} \frac{\varepsilon^l}{} \times$$

$$-K^{TI} \frac{\sigma}{\rho^l D_b \quad \varepsilon^l}$$

$$\gamma^{TI} \qquad K^{TI}$$

	Group -1	Inter-group	Group-2
Coalescence	Random collision	Wake entrainment	Wake entrainment
Breakup		Turbulent impact	
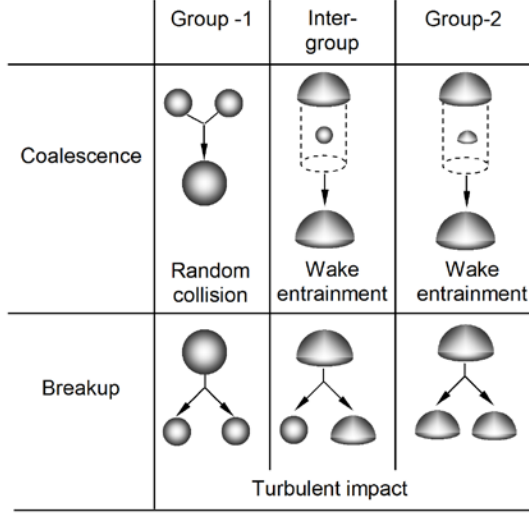
Figure 1:

$$\phi^{WE} = -\gamma^{WE} \frac{\alpha^g \alpha^g \quad v_{axial} \quad -v^l}{D_b \quad D_b} \times$$

$$\left\{ -K^{WE} \frac{\rho^l}{\sigma} \frac{\varepsilon^l}{} - \left(\frac{D_b \quad D_b}{D_b \quad +D_b} \right) \right\}$$

$$v_{axial} \qquad v^l$$

$$\gamma^{WE} \qquad K^{WE}$$

$$\sum_j R_j \quad +R_j \quad = \phi^{RC} + \phi^{TI} + \phi^{WE} + \phi^{TI} \qquad\qquad \phi^{TI}$$

$$\phi^{RC} \quad \phi^{TI} \qquad \phi^{WE}$$

$$\phi^{TI} = \gamma^{TI} \frac{\alpha^g \quad -\alpha^g}{D_b \quad \alpha_{TI} \quad -\alpha^g} \frac{\varepsilon^l}{} \times$$

$$\left(-K^{TI} \frac{\sigma\{ D_b \quad -D_b \quad + \quad D_b \quad -D_b \}}{\rho^l D_b \quad \varepsilon^l} \right)$$

$$\gamma^{TI} \qquad K^{TI}$$

$$\sum_j R_j \quad = \phi^{WE} + \phi^{TI}$$

$$\phi^{RC} = -\gamma^{RC} \frac{\alpha^g}{D_b \quad \alpha_{RC} \quad -\alpha^g} \frac{\varepsilon^l}{} \times$$

$$-K^{RC} \frac{D_b \quad \rho^l \quad \varepsilon^l}{\sigma}$$

$$\phi^{WE} = -\gamma^{WE} \frac{\alpha^g \quad v_{axial} \quad -v^l}{D_b} \times$$

$$\left\{ -K^{WE} \frac{D_b \quad \rho^l \quad \varepsilon^l}{\sigma} \right\}$$

$$\phi^{TI} = \gamma^{TI} \frac{\alpha^g \quad -\alpha^g \quad \varepsilon^l}{D_b \quad \alpha_{TI} \quad -\alpha^g} \times$$

$$\left(-K^{TI} \frac{\sigma}{\rho^l D_b \quad \varepsilon^l} \right)$$

$$\gamma^{WE} \quad \gamma^{TI} \quad K^{WE} \quad K^{TI}$$

$$F = -F^{gl} = F_D + F_L + F_W + F_T$$

$$F = -F^{gl} = F_D + F_L + F_W + F_T$$

THREE FLUID MODEL

$$\frac{\partial \rho^g \alpha^g}{\partial t} + \nabla \cdot \rho^g \alpha^g \vec{v}^g = -\dot{m}$$

$$\frac{\partial \rho^g \alpha^g}{\partial t} + \nabla \cdot \rho^g \alpha^g \vec{v}^g = \dot{m}$$

$$\dot{m}$$

$$\omega$$

$$\varepsilon$$

EXPERIMENTAL DETAILS

$$\frac{\partial \rho^g \alpha^g \vec{v}^g}{\partial t} + \nabla \cdot \rho^g \alpha^g \vec{v}^g \vec{v}^g = -\alpha^g \nabla P +$$

$$\alpha^g \rho^g \vec{g} + \nabla \cdot \left[\alpha^g \quad \mu^g + \mu_T^g \quad \nabla \vec{v}^g + \vec{v}^g {}^T \right] -$$

$$\dot{m} \vec{v}^g + F^{gl}$$

$$\frac{\partial \rho^g \alpha^g \vec{v}^g}{\partial t} + \nabla \cdot \rho^g \alpha^g \vec{v}^g \vec{v}^g = -\alpha^g \nabla P +$$

$$\alpha^g \rho^g \vec{g} + \nabla \cdot \left[\alpha^g \quad \mu^g + \mu_T^g \quad \nabla \vec{v}^g + \vec{v}^g {}^T \right] +$$

$$\dot{m} \vec{v}^g + F^{gl}$$

$$\frac{\partial \rho^l \alpha^l}{\partial t} + \nabla \cdot \rho^l \alpha^l \vec{v}^l =$$

$$\frac{\partial \rho^l \alpha^l \vec{v}^l}{\partial t} + \nabla \cdot \rho^g \alpha^l \vec{v}^l \vec{v}^l = -\alpha^l \nabla P + \alpha^l \rho^l \vec{g}$$

$$+ \nabla \cdot \left[\alpha^l \quad \mu^l + \mu_T^l \quad \nabla \vec{v}^l + \vec{v}^l {}^T \right] + F + F$$

$$F \qquad\qquad F$$

NUMERICAL SCHEME
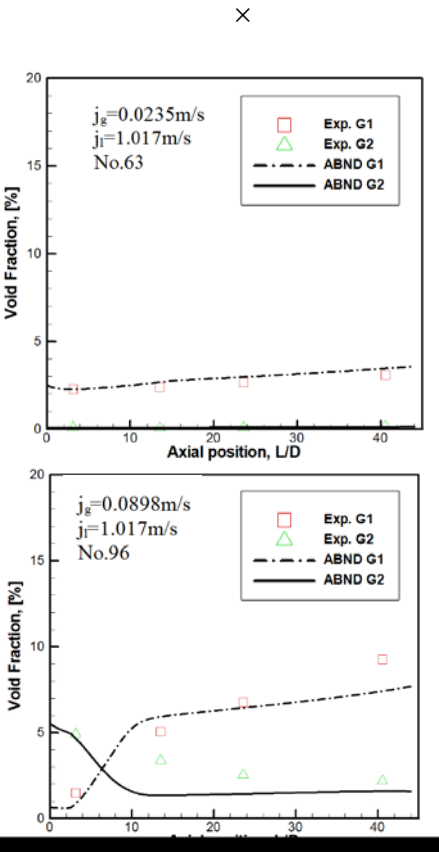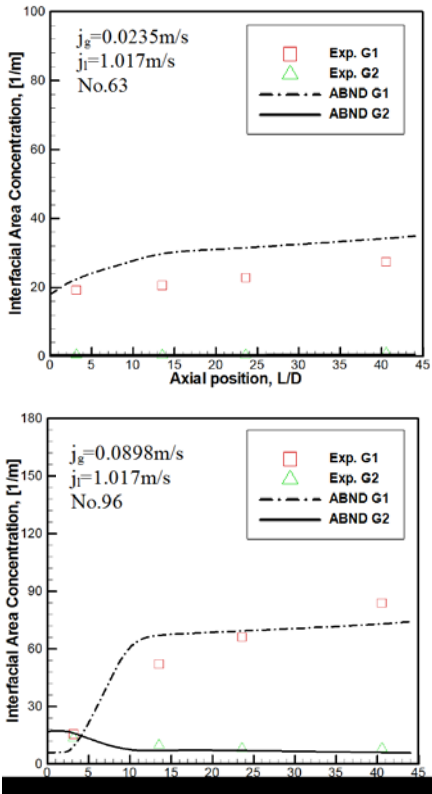
Figure 3:

Axial evolution of flow structure

Figure 2:

RESULTS

(a)
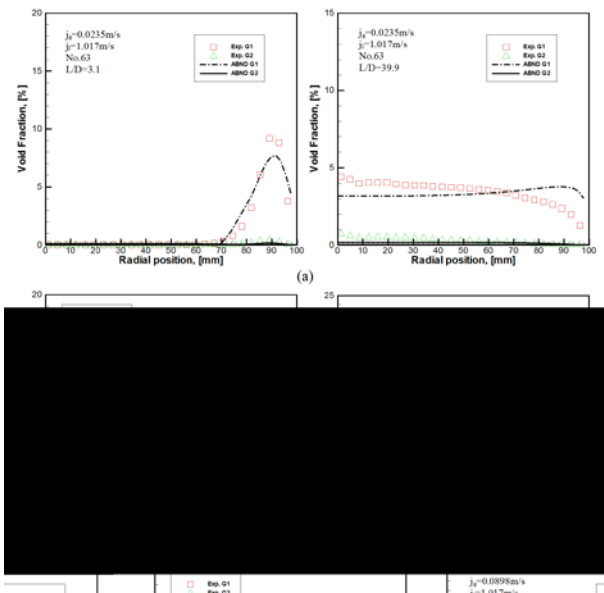
Figure 4:

Local flow structure

(a)

(b)
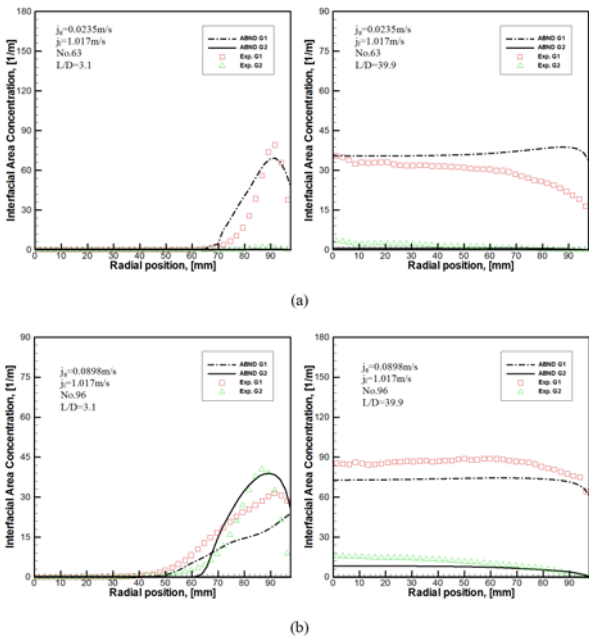
Figure 5:

CONCLUSION

Int. J. Therm. Sci. 49

Int. J. Multiphase Flow

Int. J. of Heat and Mass Transfer,

Nuc. Eng. Des.

Third Int. Conference on Multiphase Flow

ACKNOWLEDGMENT

Trans. JSME

REFERENCES

Int. J. Heat Mass Transfer

Chem. Eng. Comm.

Int. J. Heat Mass Transfer

Fifth Int. Conference on Multiphase Flow

, Appl. Sci. Res.

Chem. Eng. Sci.

Int. J. Multiphase Flow

Proc. of Third Symp. on Two-Phase Modeling and Experimentation

Int. J. Heat Mass Transfer

Nuc. Eng. Des.

J. Comp. Multiphase Flows

Nuc. Eng. Des.

J. Comp. Multiphase Flows

ON THE MODELLING OF ANODIC BUBBLES IN HALL-HÉROULT CELLS

Kristian Etienne EINARSRUD[1*] ,**Stein Tore JOHANSEN[2]**

[1] ...

[2] ...

...

ABSTRACT

Recent progress on the modelling of gas evolving anodes in the production of primary aluminium is presented. The proposed model is a multiscale approach in which molecular species are produced and transported through a supersaturated electrolyte. Sub grid bubbles are allowed to form through nucleation and the resulting bubble population evolves through mass transfer and coalescence. As sub grid bubbles reach a certain size they are transferred to a macroscopic phase which evolution is governed by a volume of fluid method.

The current work describes the underlying theory and motivation for the proposed model. Finally, the model is used to describe electrolysis on laboratory scale, showing the potential of the suggested approach.

Keywords: ...

NOMENCLATURE

A complete list of symbols used, with dimensions, is required.

Greek Symbols

α Phase fraction, [-].

Γ_{ij} Coalescence kernel, [m^3/s].

γ_{eg} Surface tension, [N/m].

μ_i Dynamic viscosity, [kg/m.s].

υ Stochiometric number, [-].

Ω_{ij} Collision frequency, [m^3/s].

φ Electrical potential, [V].

ρ_i Mass density, [kg/m^3].

ρ_p Pore density, [%].

σ_i Electrical conductivity, [Ω^{-1} m^{-1}].

Latin Symbols

A_i Area, [m^2].

b_i Birth rate, [1/s].

C Concentration, [kg/m^3].

D_{bub} Bubble diameter, [m].

D Diffusivity, [m^2/s].

d_i Death rate, [1/s].

F Faraday's constant, [C/mol].

f_{nuc} Nucleation frequency, [1/s].

$\mathbf{j}$ Current density, [A/m^2].

K Mass transfer factor, [m^5/kg.s].

$\dot{m}$ Mass rate, [kg/s].

$\dot{M}$ Mass flux, [kg/m^2.s].

M_{CO_2} Molar mass of CO$_2$, [kg/mol].

n_i Number density, [1/m^3].

N_p Number of active pores, [#].

P_{ij} Coalescence probability, [-].

Re Reynolds number, [-].

S Generic source term, [-].

Sc Schmidt number, [-].

Sh Sherwood number, [-].

t Time, [s]

$\mathbf{u}$ Velocity, [m/s].

V_i Volume, [m^3]

Sub/superscripts

$cell$ Cell property.

CO_2 Dissolved CO$_2$.

e Electrolyte.

g Gas (resolved).

G Ghost class.

M Largest subgrid bubble

i,j,k Population bin indices

Abbreviations

FFT   Fast Fourier Transform

UDF   User Defined Function

UDM   User Defined Memory

UDS   User Defined Scalar

VOF   Volume Of Fluid

INTRODUCTION

Industrial production of primary aluminium is carried out in aluminium reduction cells by the Hall-Héroult process in which alumina (Al_2O_3) is dissolved in an electrolyte consisting mainly of molten cryolite (Na_3AlF_6) (Thonstad et al. 2001). By means of an externally imposed electric field, ions are transported through the electrolyte before reaching the electrodes where chemical reactions occur. A sketch of an industrial cell is shown in figure 1.

The net (simplified) reaction in the Hall-Héroult cell can be written as

$$\frac{1}{2}Al_2O_{3(d)} + \frac{3}{4}C_{(s)} \rightarrow Al_{(l)} + \frac{3}{4}CO_{2(g)} \qquad (1)$$
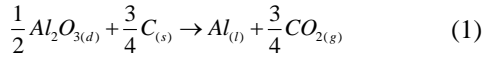
where the solid carbon is supplied from the anode. Due to the negligible electrical conductivity of gaseous CO_2, the presence of bubbles effectively screens the anode surface, thus decreasing its active area and increasing the overall cell voltage (cf. Cooksey et al. (2009)). As a result, the specific energy consumption increases. As bubbles are responsible for as much as 10% of the cell voltage, the potential energy savings from increased knowledge of bubble formation and evolution are significant, thus motivating the current work.

The Hall-Héroult cell has a strong dynamic nature due to buoyant bubbles and MHD flow. Hence, it should come as no surprise that the cell voltage varies with time. There are several sources to these variations, ranging from high frequency ripples in the DC current applied to the cell; to low frequency MHD-instabilities creating large scale wave motion of the metal pad. A special frequency band ranging from 0.5 to 5 Hz has been credited to bubbles and the resulting signal is commonly denoted as bubble noise (cf. for instance Kalgraf et al. (2007) and references therein and Wang and Tabereaux (2000)).
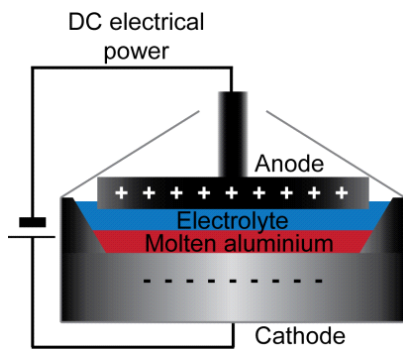
Figure 1: Industrial reduction cell consisting of an anode, a cathode and an electrolyte. Electrochemical reactions of the raw-material (alumina) occur within the electrolyte yielding molten aluminium. The cell is powered by an external DC energy source.

The relation between gas coverage and bubble noise has recently been studied by Kiss (2006), by means of a quasi 2D Lagrangian model. The study shows that the nature of the bubble noise is highly dependent on the number of bubbles present. A regular pattern is observed for single bubbles, corresponding to its growth, while the presence of several bubbles results in random like fluctuations, a combined effect of growing, coalescing and detaching bubbles. However, under certain conditions, bubbles can manifest a concerted movement due to very big gas pockets sweeping alongside the anode, engulfing lesser bubbles in their motion.

A detailed experimental description of growth and evolution of single bubbles is given by Xue and Øye (1995), identifying three distinct stages. Initially, spherical or semi spherical bubbles in the range 0.4-0.6 mm are nucleated and grow due to mass transfer. As the inter-bubble distance decreases smaller bubbles begin to merge by coalescence, forming flattened spheroids. In the final stage, large bubble sheets of the size of the anode are formed, which, due to buoyancy, detach and release from the anode, marking the end of one bubble cycle.

The final stage and its influence on the hydrodynamics of the cell has been studied recently (Einarsrud (2010)) by means of a VOF model. The present work sets out to describe a framework which extends the VOF approach so that initial stages, and thus a complete description of gas evolving anodes, can be treated.

In the following, each of the phenomena required for a general framework are treated, followed by a qualitative validation based on a measurements performed on a lab scale anode.

MODEL DESCRIPTION

Generation and Transport of CO_2

It is an undisputed experimental fact that small gaseous bubbles predominantly form on specific nucleation sites, a phenomenon which relies upon the presence of CO_2, which is formed on the anode surface by some chemical reaction. The anode reaction is assumed to be given by the half reaction

$$\frac{3}{2}O^{2-} + \frac{3}{4}C \rightarrow 3e^- + \frac{3}{4}CO_2, \qquad (2)$$
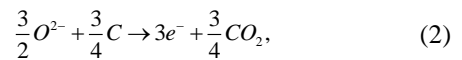
which is assumed to be instantaneous. Oxygen is present through alumina which is added at regular intervals in order to keep concentrations uniform and within a given operational interval (cf. Grjotheim and Kvande (1993)). Carbon is present through the anode which is consumed as it reacts, typically at a rate of 1 cm per 24 hours. This process is however much slower than the typical time scales considered for bubbles.

Hence, as a first approximation is it reasonable to assume that the production of CO_2 is controlled only by the presence of electrical charge, i.e. Faraday's law (in kg/s)

$$\dot{m}_{CO_2} = \frac{M_{CO_2}\mathbf{j} \cdot \mathbf{A}}{\upsilon F}. \qquad (3)$$

Although the literature agrees upon the fact that molecular CO_2 is produced on the anode surface, the path taken by dissolved CO_2 is somewhat disputed. As

sketched in figure 2, two possibilities exist, namely transport through pores in the anode or through the bath.

Both processes rely on the fact that either the anode or the bath operates as a gas reservoir, i.e. either of the two is supersaturated with molecular gas. Although both transport mechanisms have been used for general electrolysis applications, it appears as though the anode transport scenario has become the most common for aluminium applications, possibly due to the conclusion of Poncsák et al. (1999) stating that storage and diffusion of gas inside the electrolyte plays a negligible role in the aluminium reduction cell. This is based upon the fact that CO_2 has a relatively small diffusivity in the bath and that the anode is known to have a porosity of 10-30% (Grjotheim and Kvande (1993)), suggesting that it can contain a corresponding amount of gas.

A direct consequence of the anode transport model is that a non-porous anode cannot develop into a gas evolving electrode. Nevertheless, successful electrolysis experiments have been performed using so-called glassy anodes (cf. for instance Leistra and Sides (1988)). In addition no plausible mechanism explaining the physics resulting in a supersaturated anode is given, i.e. by which physical principles the gas moves through the anode and back to bubble nuclei, rather than leaving the anode altogether. This suggests that the anode transport hypothesis may be physically unsound.

In a real process (excluding glassy anodes), both bath and anodic gas transport are most likely present and the dominating mode will vary from process to process, depending upon operational parameter. From a modelling perspective one mode can be included in the other by adjusting the mass transfer parameters accordingly, yielding the two transport mechanisms equivalent. The choice of model thus becomes of a practical nature based on predictive power, numerical stability, compatibility with other models and computational cost.
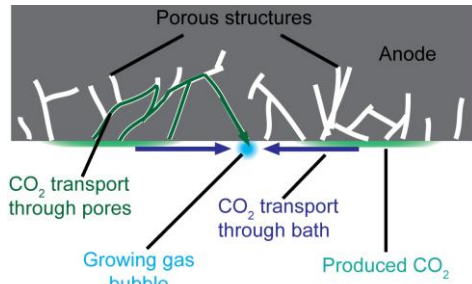
Figure 2: Sketch of the two possibilities for transport of molecular CO_2.

Due to a higher predictive power (possibility to treat glassy anodes), and direct relation to fluid flow, the bath transport model is chosen. In this case, the concentration of dissolved CO_2 is governed by the following advection-diffusion equation

$$\frac{\partial C_{CO_2}}{\partial t} + \nabla \cdot \left(\mathbf{u} C_{CO_2} - D_{eff} \nabla C_{CO_2} \right) = S^p - S^n - S^{dmt}, \qquad (4)$$

where $\mathbf{u}$ is the bath velocity and D_{eff} is the effective diffusivity. The source- and sink terms on the right hand side represent production (as of equation 3) nucleation of gaseous bubbles and direct mass transfer to existing bubbles, respectively.

Nucleation of Gaseous Bubbles

Little is known regarding nucleation in Hall-Héroult cells, regarding both experimental and theoretical investigations. A phenomenological description can however be extracted from the overall information found in the literature. Considering matters of operational importance, i.e. large to moderate voltage oscillations, one finds that small to moderate sized systems exert a periodic release of large bubbles. Large bubbles are created in a semi-continuous fashion through the successive coalescence and growth of lesser bubbles down to some minimal bubble size (typical diameter of 0.4-0.6 mm) found to originate from the anode surface in a steady manner (cf. Xue and Øye (1995)).

The detailed behavior of single bubbles during electrolysis (although not aluminium-electrolysis) has been described by Gabrielli et al. (1989), showing how single bubbles form periodically on specific sites on the electrode. As in the study of Xue and Øye, Gabrielli et al. find enhanced gas evolution at higher current densities, which is as expected, as more (molecular) gas is produced as of equation 3.

Both of the above studies find a linear relation between voltage and time during the initial growth of bubbles (before coalescence occurs), which corresponds to a linear increase in the projected bubble area. This suggests that the bubble radius should follow a growth-law of the form

$$D_{bub} \propto \sqrt{t}, \qquad (5)$$

which is the classical result of Scriven (1959), describing the growth of bubbles in supersaturated solutions. This is the basis for the model used by Jones et al. (1999a), to describe non classical nucleation; a form of nucleation occurring at low degrees of supersaturation with a negligible energy barrier.

In addition to the expected growth law, the linear voltage growth starts shortly after the release of a bubble (cf. Xue and Øye and Einarsrud and Sandnes (2011)), as shown in figure 3.
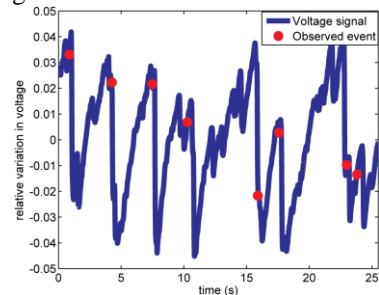
Figure 3: Measured voltage signal (solid line) and observed escaping bubbles (circles).

The short time between release and generation of new bubbles suggests that low to moderate levels of supersaturation are sufficient to initiate bubble nucleation. This indicates that nucleation in Hall-Héroult cells relies upon a steady production of gas, rather than abrupt flashing of bubbles expected from classical nucleation. That is, *non-classical* nucleation appears to phenomenologically describe steady state nucleation in Hall- Héroult cells.

The main requirement for non classical nucleation is that gas cavities exist on the anode surface prior to nucleation events. These gas cavities can be remnants of classical nucleation events or from the preparation of the anode and are thus dependent on the surface porosity and wetting properties of the bath. As a simple model, the number of active pores in a computational cell, N_p, is given as

$$N_p = \gamma_a \rho_p \frac{A_{cell}}{A_{p0}}, \qquad (6)$$

where γ_a is an activation parameter, ρ_p is the pore density and A_{cell} and A_{p0} are the cell- and the pore areas, respectively. The pore area is given by the mean pore diameter and the pore density as a linear distribution.

Mass Transfer to Bubbles

The general result for the mass flux to a rigid sphere for combined modes of mass transfer in a supersaturated solution is

$$\dot{M} = \frac{D}{D_{bub}} Sh \left(C_{CO_2} - C_{CO_2,s} \right) = \frac{D}{D_{bub}} Sh \Delta C_{CO_2}, \qquad (7)$$

where $Sh=2$ for the case of diffusive mass transfer in a quiescent fluid. The Sherwood number can incorporate advective effects through dependence on the Reynolds number, typically through a relation on the form

$$Sh = a + b \, \mathrm{Re}^c \, Sc^d. \qquad (8)$$

Assuming isobaric expansion of ideal gas bubbles, and mass fluxes given as for rigid spheres, the rate of change of mass is

$$\dot{m} = f_1 D_{bub} Sh D \Delta C_{CO_2} = 3 \rho_g f_2 D_{bub}^2 \frac{dD_{bub}}{dt} \qquad (9)$$

for a bubble with surface and volume

$$A_{bub} = f_1 D_{bub}^2 \qquad V_{bub} = f_2 D_{bub}^3. \qquad (10)$$

The solution of equation (9) is

$$D_{bub}(t) = \sqrt{K \Delta C_{CO_2} t} \qquad (11)$$

with

$$K = \frac{2}{3} \frac{ShD}{\rho_g} \frac{f_1}{f_2}. \qquad (12)$$

As shown by Jones et al. (1999b), this is equivalent to the solution of Scriven (1959), if the Sherwood number is chosen as

$$Sh = 2.0 + \sqrt{2.0 \mathrm{Re} \, Sc}, \qquad (13)$$

which thus serves as a theoretical minimum.

As shown by Jones et al. (1999b), non classical nucleation is analogous to bubble growth. Hence, the time required for a bubble to reach its detachment diameter is

$$t_d = \frac{D_{bub,d}^2}{K \Delta C_{CO_2}}, \qquad (14)$$

where the detachment diameter $D_{bub,d}^2$ is assumed to be equal to the smallest observed bubble diameter. Combined with the number of active pores, the nucleation frequency in a given computational cell is

$$f_{nuc} = \frac{N_p}{t_d} = \frac{N_p K \Delta C_{CO_2}}{D_{bub,d}^2}, \qquad (15)$$

which serves as the rate at which gas bubbles are created on the anode surface.

Considering Lagrangian-type bubbles, further growth is easily treated by a source term as of equation 9. For macroscopic VOF-bubbles, the mass transfer term is written as

$$S^{dmt} = D_{eff} \left(\nabla \alpha_g \cdot \nabla C_{CO_2} \right), \qquad (16)$$

which is a formidable numerical challenge due to steep gradients in the proximity of the VOF-bubble.

Fortunately, the effect of mass transfer is significant only for small bubbles, while larger bubbles evolve mainly through coalescence. This can be seen from the voltage curve of one bubble cycle (figure 4), where coalescence induced oscillations occur only after an initial (linear) growth regime. Furthermore, as seen from the figure below, the average voltage rate *decreases* after the initial linear regime,
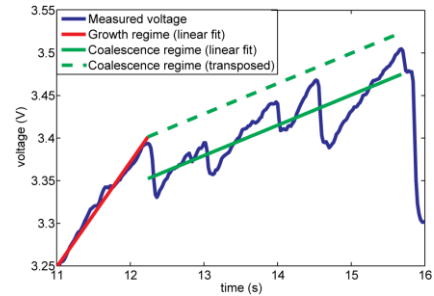
Figure 4: Measured voltage signal (blue) and linear fit to growth regime (red) and coalescence regime (green).

suggesting that the contribution due to mass transfer has decreased.

Due to the apparent presence of two different voltage regimes, multiple scales present in the problem as well as the challenges related to growing VOF-bubbles, a multi-scale approach is suggested in which phase growth by mass transfer is allowed only for sub-grid spherical bubbles while macroscopic bubbles are allowed to evolve only by coalescence and sources due to mature sub grid bubbles.

Dispersed Gas Treatment

The sub grid bubbles are treated by means of a population balance model (PBM). As the existing model implemented in FLUENT is not compatible with the

VOF model a tailored model is developed for the current application. In essence, a PBM is a model which deals with entities forming a population. Assuming that N_i bubbles of class i are present in a volume V, the conservation of the i-th bubble number density reads

$$\frac{1}{V}\frac{dN_i}{dt} = \frac{dn_i}{dt} = b_i - d_i, \qquad (17)$$

where b_i and d_i represent birth- and death rates for the i-th bubble class. Classes are denoted by indices

$$i = [1, 2, ..., M]. \qquad (18)$$

In order to span a large range of bubbles using few classes, an exponential discretization based on volume is used, relating neighbouring classes by

$$V_{i+1} = qV_i, \qquad (19)$$

as sketched in figure 5. In the current application, $q=2$.

Evolution by Coalescence

The net evolution of the bubbly flow in a Hall-Héroult cell can in essence be described as a one way process; lesser bubbles coalescing and growing to form larger ones. Hence, a simplification can be made for the population balance, assuming that effects due to bubble breakup (on the subgrid level) are negligible. Following Hounslow et al. (1998), a *finite* population undergoing coalescence is described by

$$\frac{dn_i}{dt} = \frac{1}{2}\sum_{j}^{M}\sum_{k}^{M}\Gamma_{kj}n_k n_j \xi_{ijk} - n_i(1-\delta_{iM})\sum_{j}^{M}\Gamma_{ij}n_j, \qquad (20)$$

where Γ_{ij} is the discrete coalescence kernel and ξ_{ijk}, defined as

$$\xi_{ijk} = \begin{cases} \frac{V_k + V_j}{V_i} & \text{if} \quad V_{i-1/2} \le V_k + V_j < V_{i+1/2} \\ 0 & \text{otherwise} \end{cases} \qquad (21)$$

as of Suttner and Yorke (2001), ensures conservation of numbers and mass.
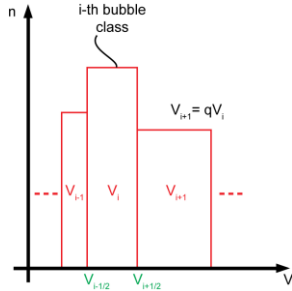
Figure 5: Sketch of discrete bubble distribution.

The factor $1-\delta_{iM}$, δ_{iM} being a Kronecker delta function, ensures conservation of the largest bubble class, M.
The coalescence kernel is written as

$$\Gamma_{ij} = \Omega_{ij} P_{ij} g(\alpha), \qquad (22)$$

where the collision frequency Ω_{ij} and coalescence probabilities P_{ij} are given by Luo (1993), assuming that coalescence is driven by intertial subrange turbulence. $g(\alpha)$ is a distribution function included to prevent over compactation of dispersed bubbles above a phase fraction α_{max}.

Evolution by Mass Transfer

Although coalescence is present at all stages of a bubble cycle, the initial stages are believed to be governed by mass transfer. Following Hounslow et al. (1998), a growing population can be described by

$$\frac{dn_i}{dt} = \frac{G_V^{i-1}n_{i-1}}{V_i - V_{i-1}} - \frac{G_V^{i}n_i}{V_{i+1} - V_i}, \qquad (23)$$

where the first term represents growth into and the second term represents growth out of the i-th bubble class and G_V^{i} is the corresponding growth rate.

Assuming again an isobaric expansion of an ideal gas, the growth rate can be expressed as

$$G_V^{i} = \frac{dV_i}{dt} = K_2 \Delta C_{CO_2} V_i^{\frac{1}{3}}, \qquad (24)$$

with

$$K_2 = \frac{3}{2}f_2^{\frac{2}{3}}K. \qquad (25)$$

Coupling to Macroscopic Bubbles

Considering a population of M bubble classes, the transition to the continuous phase can be treated by extending the population with an additional bubble class, which represents the smallest possible concentration of the continuous phase. As the additional bubble class is not a true entity of the population it is denoted a ghost class, with subscript G. The volume of a ghost bubble is determined by

$$V_G = qV_M = V_{M+1}, \qquad (26)$$

which is analogous to the PBM treatment, thus replacing the largest class M.

The number density of ghost bubbles is not determined by a transport equation, but from the volume fraction of the continuous phase, i.e.

$$n_G = \frac{\alpha_g}{V_G}, \qquad (27)$$

From the above two definitions, the hybrid nature of the ghost class is evident. Its rate of change is analogous to that of the PBM classes, and is given as

$$\dot{n}_G = K_2 \Delta C_{CO_2} n_M \left(\frac{V_M^{1/3}}{V_G - V_M} \right) + \frac{1}{2}\sum_{j}^{M}\sum_{k}^{G}\Gamma_{kj}n_k n_j \xi_{Gjk} \qquad (28)$$

where the first term is due to mass transfer and the second is due to coalescence and engulfment, including both bubble-bubble- and bubble-continuous phase interactions.

Considering water model experiments (cf. Fortin et al. (1984) and Einarsrud (2010)) and the lab scale experiments of Xue and Øye (1995) it is clear that there is a significant difference in the behavior of micro- and macroscopic bubbles. While small bubbles remain close to stationary in the immediate neighborhood of the anode surface (moving randomly due to coalescence and secondary fluid flow), large bubbles sweep longside the anode with velocities in the order of 0.3 m/s, engulfing smaller bubbles as they move, suggesting high collision frequencies and large coalescence probabilities. Moreover, due to the small size of the sub-grid bubbles and their affinity to the anode surface, it is reasonable expect that are located deep in the boundary layer as sketched in figure 6.

Following Chesters (1991), the generic form of the coalescence kernel is

$$\Gamma_{ij} = k u_{rel} \frac{\left(D_{bub,i} + D_{bub,j}\right)^2}{4} P_{ij}. \qquad (29)$$

where k is a geometric factor and u_{rel} is the typical relative velocity between the two colliding particles. Based on the above discussion, the PBM-ghost coalescence kernel is approximated to

$$\Gamma_{iG} = \frac{\pi}{4} |\mathbf{u}| \left(D_{bub,i} + D_{bub,G}\right)^2, \qquad (30)$$

that is the typical relative velocity is taken as the local fluid velocity and the coalescence probability is set to unity.

The rate of change of the ghost class serves as a mass source for the continuous gas phase, defined as

$$S_g = \rho_g V_G \dot{n}_G. \qquad (31)$$

Thus, once an entity of the population has evolved to the ghost class, it is transferred to the continuous gas phase from which the VOF model handles the further evolution.

Coupling to Fluid Flow

Equation 17 describes the uncoupled PBM. In the current work, a one way coupling to the fluid flow is adopted, resulting in an advection diffusion equation of the form

$$\frac{\partial n_i}{\partial t} + \nabla \cdot \left(f(\mathbf{u})n_i - D_{PBM,i} \nabla n_i\right) = b_i - d_i, \qquad (32)$$

where $f(\mathbf{u})$ is an advection function and $D_{PBM,i}$ is a diffusivity.
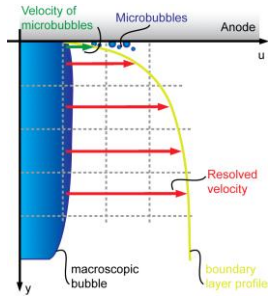
Figure 6: Boundary layer profile, resolved velocity and typical velocity where bubbles are located.

COMPLETE MODEL

In addition to the dissolved gas and dispersed bubbles treated so far, the continuous flow and electromagnetic fields must be treated. As shown in figure 7, all fields considered are to some extent coupled.

Governing Equations

The evolution of continuous phases is governed by a phase fraction equation on the form

$$\frac{\partial}{\partial t}\left(\alpha_k \rho_k\right) + \nabla \cdot \left(\alpha_k \rho_k \mathbf{u}\right) = S_k, \qquad (33)$$

where a source on the form of equation 33 is present for the gaseous phase. A single flow field is shared between

the phases, governed by the incompressible Navier-Stokes equations, that is, gas expansion is neglected.

Faraday's law (equation 3) requires an electrical current as input. This is obtained from Ohm's law reading

$$\mathbf{j} = -\sigma \nabla \varphi, \qquad (34)$$

where σ is the electrical conductivity and φ is the electrical potential. Induction currents are neglected as these typically are small in electrolytes. The electrical potential is determined by the Laplace equation resulting from the requirement of current conservation.

Given the local current density, the production term in equation 4 reads

$$S^p = \frac{M_{CO_2} \mathbf{j} \cdot \mathbf{A}_{cell}}{\nu_e F V_{cell}}. \qquad (35)$$

The sink due to nucleation is obtained from equation 15

$$S^n = f_{nuc} \frac{\rho_g V_1}{V_{cell}} = \frac{N_p K \Delta C_{CO_2}}{D_1^2} \frac{\rho_g V_1}{V_{cell}}, \qquad (36)$$

with a corresponding source term on the form

$$S^n = \frac{f_{nuc}}{V_{cell}} \qquad (37)$$

for the smallest bubble class.

Finally, the sink term due to mass transfer is given by an appropriate sum over the terms in equation 27, resulting in

$$S^{dmt} = \sum_{i=1}^{M} K_2 \Delta C_{CO_2} n_i \left(\frac{V_i^{1/3}}{V_{i+1} - V_i}\right) \rho_g \left(V_{i+1} - V_i\right). \qquad (38)$$
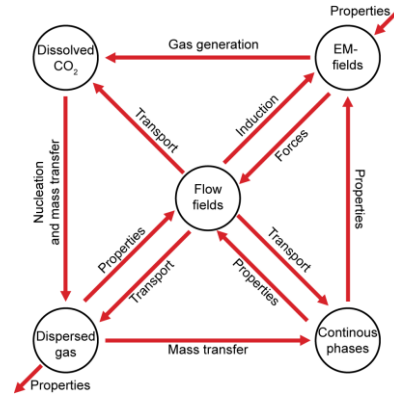
Figure 7: Sketch of elements in complete model and their interaction.

The population is evolved by means of equation 34, with birth and death terms given by the combination of equations 20 and 27.

Turbulence is modelled in the continuous phases by means of the realizable k-ε model.

Fluid Properties

As a first approximation, all hydrodynamic properties are assumed to be constant in each phase, mixture cells being treated by default arithmetic averaging.

Due to the negligible electrical conductivity of gas, microscopic bubbles are allowed to influence the

electrolyte conductivity. Following Bruggeman (1935), the electrolyte conductivity is

$$\bar{\sigma}_e = \sigma_g \alpha_{PBM} + \sigma_e \left(1 - \alpha_g\right)^{3/2}, \qquad (39)$$

where

$$\alpha_{PBM} = \sum_{i=1}^{M} n_i V_i \qquad (40)$$

is the dispersed gas void fraction. Correspondingly, the mixture conductivity is

$$\sigma = \sigma_g \alpha_g + \bar{\sigma}_e \left(1 - \alpha_g\right)^{3/2}. \qquad (41)$$

Treatment in FLUENT

Each of the model equations (i.e species and electrical potential) are solved as a UDS in FLUENT, while their coupling and the determination of properties is performed by means of a library of user defined functions (UDF). Buffer quantities are stored as UDMs. The flow is initialized by means of the DEFINE INIT()-macro, where all initial parameters and anode properties are fixed.

Source terms are updated either at the end of each iteration using the DEFINE ADJUST()-macro or at the end of each time step using the DEFINE EXECUTE AT END()-macro.
Properties are updated in the following order:

- Á Update phase fractions stored in memory.
- Á Calculate electromagnetic fields.
- Á Calculate source and sink terms due to mass transfer.
- Á Calculate source and sink terms due to coalescence.
- Á Calculate gas sources due to nucleation.

Calculated source and sink terms are passed to the governing equations through the DEFINE SOURCE()-macro, while fluid properties are updated through DEFINE DIFFUSIVITY()- and DEFINE PROPERTY()- macros, based on stored phase fractions.

Simulations are performed using the pressure based solver where gradients are computed with a Green-Gauss cell based method and pressure velocity coupling is performed by the PISO algorithm with default correction factors for neighbor-skewness. The multiphase nature of the flow is treated by means of the explicit VOF model, discretized using the Geo-reconstruct-scheme with surface tension activated. UDS equations are discretized using the QUICK scheme, while the remaining equations are discretized with the first order upwind method. The multigrid solver is set to a V-cycle for UDS equations for increased convergence rate.

Time advancement is performed using the first order implicit scheme with a constant time step of 0.0005 s. All other settings are kept at their default values.

Values for the various parameters used in the simulations are given in table 1.

Table 1: Modelling conditions.

Parameter	Units	Value
ρ_g	kg/m^3	0.435
ρ_e	kg/m^3	2070
μ_g	kg/m.s	$1.79 \cdot 10^{-5}$
μ_e	kg/m.s	$2.69 \cdot 10^{-3}$
σ_g	$\Omega^{-1} m^{-1}$	$1 \cdot 10^{-12}$
σ_e	$\Omega^{-1} m^{-1}$	200
γ_{eg}	N/m	0.1
D_i	m^2/s	$1 \cdot 10^{-7}$
A_{p0}	m^2	$2.25 \cdot 10^{-8}$
$A_{cell}{}^*$	m^2	$1.60 \cdot 10^{-5}$
$V_{cell}{}^*$	m^3	$1.60 \cdot 10^{-8}$
$D_{bub,1}$	m	$5 \cdot 10^{-4}$
q	-	2
M	-	5
$/\mathbf{j}/$	A/m^2	8000
K	m^5/kg.s	$1.1 \cdot 10^{-6}$
$C_{CO_2,s}$	kg/m^3	0.1

[*] Values refer to cells adjacent to reaction zone on anode surface.

All simulations are performed using FLUENT version 13.0 (ANSYS Inc., Canonsburg) running on a HP Z800 workstation equipped with two W5590 processors, running at 3.33GHz and 24 GB of RAM. The operating system is Windows Vista Enterprise 64-bit.

CASE STUDY

In the following, the proposed model is applied to a lab scale electrolysis cell described by Eick et al. (2011).

In the experiments a 10 by 10 cm anode was made from industrial carbon and placed in a cylindrical graphite lined crucible lined with Si_3N_4SiC with inner diameter 230mm. The anode was fixed to a steel rod so that the anode-cathode distance could be varied. Two of the sides of the anode where fitted with Si_3N_4-plates in order to force gas bubbles to escape in a preferred direction. The anode was slightly tilted to enhance gas escape further. A simplified sketch of the experimental setup is shown in figure 8.
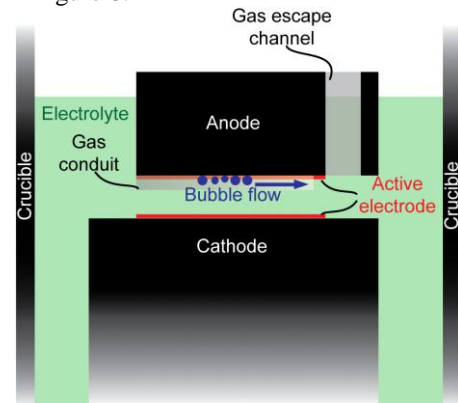
Figure 8: Sketch of experimental cell. A gas conduit forces bubbles to escape through a designated gas

escape channel. The active electrode regions with dimensions 10 by 10 cm is shown in red.

The cell voltage was logged at 50Hz using a CR23X multilogger from Campbell Scientific, UK, with resolution 1.6 μV and an accuracy of 25 μV, resulting in characteristic voltage curves as shown in figure 3.

As a reference case, experiments performed with current density 8000 A/m^2 with an anode-cathode spacing 4 cm. On average the dominant frequency in the voltage signal was 0.35 Hz, with lesser frequencies present on an interval of 0.2 – 1 Hz. Bubbles where responsible for fluctuations of $\pm$3 % of the mean voltage. These values serve as a basis for a qualitative comparison for the proposed model.

A typical voltage curve obtained from the simulations is shown in figure 9, while typical bubble behavior is shown in figure 10.
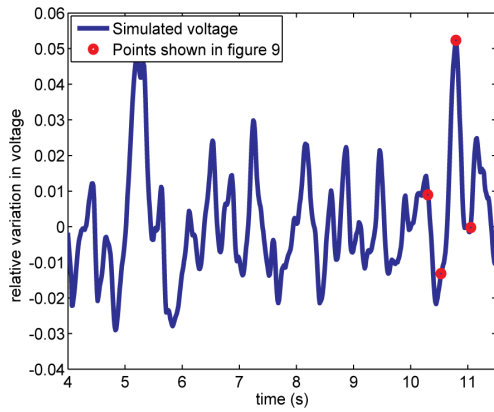
Figure 9: Typical simulated absolute voltage variation around mean value. Red circles show voltage at times shown in figure 10.
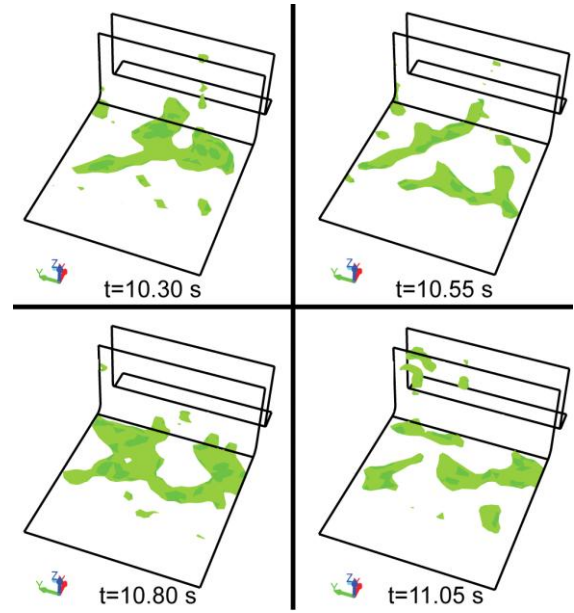
Figure 10: Typical simulated bubble coverage under anode. Figure shows active anode region and part of the gas escape channel with iso-surfaces of the bubbles at four subsequent times.

As seen from figure 9, the simulated voltage signal shows fluctuations of the same magnitude as those obtained experimentally, suggesting that the total gas coverage is treated appropriately. The FFT of the simulated signal shows a higher dominating frequency, 1.4 Hz, with lesser frequencies present on an interval of 0.2-2.3 Hz, suggesting that the gas evolution (for the simulated interval) is too fast. The overall shape of the voltage curve does however compare well to the expected behaviour; a slow net increase with superimposed, lesser fluctuations followed by an abrupt decline in voltage as large bubbles escape from the electrode surface.

As seen from figures 9 and 10, there is a close relation between large gas coverage fractions and peaks in the voltage fluctuations, as expected from the low conductivity of bubbles and confirmed experimentally by Einarsrud and Sandnes (2001).

Although the predicted frequency does not match the ones obtained in experiments exactly, it is within the expected range for bubble noise reported in the literature.

Several factors influence the numerical results which could explain the difference in frequencies compared to experiments, the most important being:

Stable experimental conditions were obtained by running electrolysis for 24 hours prior to experiments. Such a preparation is not feasible for a transient simulation (limited to tens of seconds flow time), meaning that for instance concentration and velocity fields not necessarily are comparable in the two cases, potentially resulting in different rates of mass transfer.

Furthermore, the concentration of reacting species, in particular Al_2O_3 is known to influence critical parameters such as the solubility of CO_2 and the gas-electrolyte contact angle. Although the correlation is evident, the literature lacks models quantitatively describing the coupling. Thus, the influence on the gas evolution can only be determined implicitly though a parametric study.

In addition to the uncertainty related to physical properties of the system at hand, a large degree of uncertainty is related to the Sherwood number governing the mass transfer. The voltage curves shown in figure 9 are obtained using a constant Sherwood number. In a real setting, the Sherwood number would vary in different regions of the cell, resulting in either increased or decreased mass transfer (and hence bubble evolution) depending on local flow properties. Moreover, the form of the Sherwood number (as of equation 13) is highly dependent upon local flow features, and different empirical relations can result in typical time scales differing by several orders of magnitude as shown by Kolev (2007), chapter 12.

MHD effects are neglected in the current work. However, the electrical currents passing through the cell will set up magnetic fields which in turn result in Lorentz forces acting primarily on the electrolyte. As shown recently by Bojarevics and Roy (2011), the motion of anodic bubbles can, at least in an industrial setting, be significantly influenced by the Lorentz forces, either working with or against buoyancy, depending on the relative directions of the fields.

The distribution of *active* pores is believed to be a crucial parameter for gas evolution, as it will dictate the dynamics of the smallest bubbles. A smaller number of active pores will result in fewer nucleation sites and thus fewer bubbles. On the other hand, this implies that the concentration of CO_2 will *increase,* thus promoting increased mass transfer. A large number of active pores would result in a larger quantity of small bubbles, thus promoting increased coalescence.

Hence, it is clear that either case can result in enhanced gas evolution, but through different mechanisms. Although data for the porosity of anodes is accessible in the open literature, the distribution of (and condition for) *active* pores is not. Thus, the influence of pore density on global flow phenomena must be determined by a parametric study.

Finally, typical frequencies are hard to define as the measured voltage signal is the result of the collective bubble behaviour under the anode, exerting random like fluctuations except under special conditions where self organization occurs, as described by Kiss (2006). Different frequencies can dominate in different modes of self organization, even under (close to) identical operating conditions, as seen in Einarsrud and Sandnes (2011), thus strengthening the need for long simulation times, in order to capture possible variations.

CONCLUSIONS AND OUTLOOK

This paper develops and describes models and constitutive relations that are intended for the simulation of anodic bubbles in Hall-Héroult cells, ranging from the generation of molecular gas species through Faraday's law and subsequent bubble nucleation, to the evolution of macroscopic bubbles by means of a VOF formalism. The coupling between macro- and micro scales is performed by means of a population balance model.

Molecular gas is assumed to supersaturate the electrolyte in the current approach, differing from previously proposed models where the electrodes act as gas reservoirs. One benefit of the current assumption is that it opens for the possibility to treat glassy anodes. Furthermore, transport processes can be described through known phenomenological models. Finally, it allows for complete coupling to a sub-grid PBM model which allows for a coarser resolution compared to pure VOF approach in the electrolyte.

In addition, the model is physically sound, with no need of ad hoc hypothesis.

A validation of the model is performed comparing essential features of a simulation to lab scale electrolysis experiments. The overall similarity is good, simulations showing increasing voltage as bubbles grow and coalesce before a sharp drop as bubbles escape at the anode edge. The magnitude of the voltage oscillations correspond well to that expected, bubbles accounting for variations of ± 3 % around the mean voltage. The bubble evolution is however somewhat too fast compared to the experimental results. The frequencies obtained from simulations are however within the expected range for anodic bubble noise, suggesting that the relevant physics qualitatively can be represented by the proposed model and the simplified parameters given in table 1.

A quantitative validation of the proposed model can be obtained only through simulations with flow time sufficiently long for fields to stabilize and for self organization to settle, in addition to a parametric study to determine a set of parameters (i.e. mass transfer and distribution of active pores) which adequately describes the rate of gas escape.

The above two points will be the main issue of future research.

REFERENCES

THONSTAD J., FELLNER P., HAARBERG G. M., HíVES J., KVANDE H., STERTEN Å., (2001),

Aluminium Electrolysis - Fundamentals of the Hall-Héroult Process, 3rd edition. Aluminium-Verlag.

COOKSEY M.A., TAYLOR M.P. AND CHEN J.J.J., (2008) "Resistance Due to Gas Bubbles in Aluminium Reduction Cells", *Journal of Metals*, Vol. 2, pp. 51-57.

KALGRAF K., JENSEN M. AND PEDERSEN T.B., (2007), "Theory of bubble noise, bath height and anode quality", *Light Metals*, pp. 357-361.

WANG X. AND TABEREAUX A.T., (2000) "Anodic Phenomena - observations of anode overvoltage and gas bubbling during aluminium electrolysis", *Light Metals*, pp. 1-9.

KISS L.I. (2006) "Transport processes and bubble driven flow in the Hall-Héroult cell", 5th Int. Conf. on CFD in Proc. Ind., CSIRO, Melbourne, Australia, pp. 1-7.

EINARSRUD K. E., (2010) "The effect of detaching bubbles on aluminium-cryolite interfaces: A numerical and experimental study*", Met. Trans. B*., Vol. 41:3, pp. 560-573.

GRJOTHEIM K. and KVANDE H., (1993) Introduction to aluminium electrolysis, 2nd edition. Aluminium Verlag.

PONCSÁK S., KISS L. I. and BUI R.T., (1999) "Mathematical modelling of the growth of gas bubbles under the anode in the aluminium electrolysis cells", *Light Metals (Met. Soc.),* pp. 57-72.

LEISTRA J. A. and SIDES P. J., (1988) "Hyperpolarization at Gas Evolving Electrodes - II.", *Electrochimica Acta*, Vol. 33:12, pp. 1761-1766.

GABRIELLI C., HUET F., KEDDAM M., MACIAS A. and SAHAR A., (1989) "Potential drops due to an attached bubble on a gas-evolving electrode." *Journal of Applied Electrochemistry*, Vol. 19, pp. 617-629.

SCRIVEN L. E., (1959) "On the dynamics of phase growth." *Chemical Engineering Science*, Vol. 10:1, pp. 1-18.

JONES S.F., EVANS G. M. and GALVIN K. P., (1999a) "Bubble nucleation from gas cavities - a review." *Advances in Colloid and Interface Science*, Vol. 80, pp. 27-50.

EINARSRUD K. E. and SANDNES E., (2011) "Anodic voltage oscillations in Hall-Héroult cells", *Light metals*, pp. 555-560.

JONES S. F., EVANS G. M. AND GALVIN K. P., (1999b) "The cycle of bubble production from a gas cavity in a supersaturated solution." *Advances in Colloid and Interface Science*, Vol. 80, pp. 51-84.

HOUNSLOW M. J., RYALL R. L. AND MARSHALL V. R., (1998) "A Discretized Population Balance for Nucleation, Growth and Aggregation." *AIChE Journal*, Vol. 34:11, pp. 1821-1832.

SUTTNER G. AND YORKE H.W., (2001) "Early dust evolution in protostellar accreation disks", *The Astrophysical Journal*, Vol. 551, pp. 461-477.

LUO H., (1993) "Coalescence, Breakup and Liquid Circulation in Bubble Column Reactors." PhD Thesis 105, Norwegian Institute of Technology (NTH).

FORTIN S., GERARD M. AND GESING A.J., (1984) "Physical Modelling of Bubble Behaviour and Gas Release from Aluminium Reduction Cell Anodes." *Light Metals*, pp. 721-741.

CHESTERS A.K., (1991) "The Modelling of Coalescence Processes in Fluid-Liquid Dispersions: A Review of Current Understanding." *Chemical Engineering Research and Design*, Vol. 69a, pp. 259-270.

BRUGGEMAN D.A.G., (1935) "Berechnung verschiedener physikalischer Konstanten von heterogenen Substanzen. I. Dielektrizitätskonstanten und Leitfähigkeiten der Mischkörper aus isotropen Substanzen." *Annalen der Physik*, Vol. 416:7, pp. 636-664.

KOLEV N. I., (2007), Multiphase Flow Dynamics 3: Turbulence, Gas Absorption and Release, Diesel Fuel Properties. Springer Verlag.

BOJAREVICS V., ROY A., (2011) "Bubble Transport by Electro-Magnetophoretic Forces at Anode Bottom of Aluminium Cells", *Light Metals* pp. 549-554.

EICK I., ROSENKILDE K., SEGATZ M. GUDBRANDSEN H., SOLHEIM A., SKYBAKMOEN E. AND EINARSRUD K.E. (2011) "Bubble release behaviour at lab cell anode down to very low ACD" To be published at the 10th Australasian Aluminium Smelting Technology Conference, Launceston,Tasmania.

8th International Conference on CFD in Oil & Gas, Metallurgical and Process Industries
SINTEF/NTNU, Trondheim NORWAY
21-23 June 2011

CFD11-136

UNSTRUCTURED MESH OF A DISC USING MULTIPLE TRANSFINITE MAPPINGS

Federico SPORLEDER[1]*, **Carlos A. DORAO**[2]†, **Hugo A. JAKOBSEN**[3]‡

[1]NTNU Department of Chemical Engineering, 7491 Trondheim, NORWAY

[2]NTNU Department of Energy and Process Engineering, 7491 Trondheim, NORWAY

[3]NTNU Department of Chemical Engineering, 7491 Trondheim, NORWAY

* E-mail: federico.sporleder@chemeng.ntnu.no
† E-mail: carlos.dorao@ntnu.no
‡ E-mail: hugo.a.jakobsen@chemeng.ntnu.no

ABSTRACT

A large number of problems of relevance in engineering can be modeled as occurring in a cylindrical domain. The use of cylindrical coordinates fails when considering asymmetric phenomena, and the singularity present at the axis in most cases hampers the use of spectral methods.

We analyze the use of transfinite mappings to generate meshes on a cylinder, which allows for the use of Cartesian coordinates. This well-known technique has previously been used to generate discoball type of meshes. We show how these become ill-conditioned for problems of relevant size.

This work focuses in particular on the use of multiple mappings to generate the needed meshes. We present two meshes, the square center grid and the curved center grid, and document a readily implemented procedure to generate them. These mappings allow us to build meshes for a disc of any size and make use of a center region of variable size.

The three meshes are tested using the least squares spectral element method. Although both multi-mapped meshes yield results comparable to an undeformed square mesh, the curved center mesh proved to be the best option.

Keywords: numerical analysis , cylindrical domain , least squares , spectral element , transfinite mapping , mesh generation , simulation .

NOMENCLATURE

Greek Symbols
ε low-value constant.
ε_{min} Minimum accuracy.
ε_{num} Numerical precision.
Ω Problem domain.
$\partial\Omega$ Boundary of the problem domain.
φ_j Basis function.

Latin Symbols
C Problem variable.
g Problem source term.
$\mathscr{S}$ Generalized domain.
$\mathscr{R}$ Physical domain.
$\mathscr{F}$ Biunivalent mapping.
$\mathscr{U}$ Transfinite mapping.
$R_e xt$ External radius of disc.
A_c Area of the central region.
$R_i nt$ Radius of the curves in the internal region.
$\mathscr{L}$ Operator.
$\mathbf{f}$ Solution vector.

$\mathbf{h}$ Source vector.
$\mathbf{h}_\Gamma$ Source vector for the boundary conditions.
$\mathscr{J}$ Norm-equivalent functional.
$\mathbf{v}$ Test function vector.
$\mathbf{b}_j$ Coefficient of the approximating solution.
$\mathscr{M}$ Mapping.
u Problem variable.
v Problem variable.
C_a Analytic solution.

Sub/superscripts
o Outer region.
e Element.
P Belonging to reduced search space.

INTRODUCTION

Most of the phenomena relevant to engineers can be modeled using second order differential equations. Examples of these are the Navier–Stokes equations, and the convection–diffusion and convection–conduction equations. The simplest second order equation that can be formulated is the Poisson equation, of the form:

$$\Delta C = \nabla^2 C = g \tag{1}$$

We will take this equation to represent any second-order model for simplicity.

The cylindrical coordinate system is traditionally used for cylindrical domains:

$$\frac{\partial^2 C}{\partial r^2} + \frac{1}{r}\frac{\partial C}{\partial r} + \frac{1}{r^2}\frac{\partial^2 C}{\partial \theta^2} + \frac{\partial^2 C}{\partial z^2} = g(r,\theta,z) \tag{2}$$

When considering this equation in a model, with $r \in [0,R]$, $\theta \in [0,2\pi]$ and $z \in [0,L]$, two issues arise:

1. Two boundary conditions are required for each direction.

2. The equation is singular for $r = 0$.

The first issue traditionally implies the assumption of axial symmetry, as only information on the border of the cylinder is usually available. Examples of this are the wall concentration inside a tubular membrane, the temperature at the wall of a heat exchanger tube, or the velocity field in a pipe flow. The axial symmetry is expressed as:

(a) Disco-ball mesh   (b) Square center mesh   (c) Curved Center mesh
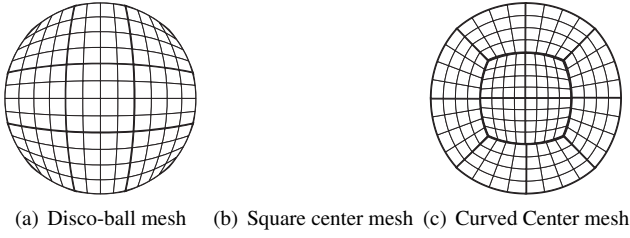
Figure 1: Meshes of a disc.

$$\frac{\partial C}{\partial r}\bigg|_{(r=0)} = 0 \ , \ \frac{\partial \bullet}{\partial \theta} = 0 \tag{3}$$

The second issue, on the other hand, could be tackled in a relatively simple manner by multiplying equation (2) by r^2. Nevertheless, it yields a trivial equation $(0 = 0)$ when considering axial symmetry, yielding an under-determined system of equations. The traditional way of coping with the singularity in the finite difference and finite volume methods is the addition of a constant of very low value, ε, to r:

$$(r+\varepsilon)\frac{\partial^2 C}{\partial r^2} + \frac{\partial C}{\partial r} + (r+\varepsilon)\frac{\partial^2 C}{\partial z^2} = (r+\varepsilon)g(r,z) \tag{4}$$

Here, we have considered axial symmetry, and we have multiplied equation (2) by r. For $r = 0$, the second term becomes zero, and the equation can be solved. For some spectral methods, however, this procedure can severely affect the convergence. Recent publications propose different alternatives to overcome the singularity (Fernandino *et al.*, 2007). Nevertheless, the use of cylindrical coordinates still implies the assumption of axial symmetry.

Both issues are overcome when considering a Cartesian coordinate system:

$$\frac{\partial^2 C}{\partial x^2} + \frac{\partial^2 C}{\partial y^2} + \frac{\partial^2 C}{\partial z^2} = g(x,y,z) \tag{5}$$

In this way, we are able to describe fully asymmetric phenomena (such as turbulence in a pipe flow, for example) and we eliminate the singularity. This idea is not new and to do so, it is necessary to define a mesh in a disc. A mapping is defined to generate the grid, which is then extended to the cylindrical domain. An example of such mesh is the disco–ball type of mesh, shown in Figure 1(a). This grid can be found already in Gordon and Hall (1973) for a disc and in Gordon and Thiel (1982) for a cylinder. Instead of mapping every point of a square reference domain to the physical circular domain (as in the polar mapping), the authors show that it is enough to trace the points at the border and interpolate for the rest. It is an inexpensive, widely used procedure, which we will refer to as transfinite mapping. In recent years, Heinrichs (2004) uses the disco-ball mapping for a unit disc with spectral collocation schemes. The use of the disco-ball mesh, however, can affect the convergence of a spectral method. This is due to the high deformation at the corners of the reference domain, as will be shown.

In this work, we analyze two alternative meshes that can be used instead. These are unstructured meshes that can be used with any finite or spectral element method. Both use multiple mappings to trace different regions of a disc: a central region and four external regions identical but for a rotation.

The first multi-mapped grid is defined with a square central region of variable size and four regions defined with the directions the square's diagonals (see Figure 1(b)). Bouffanais (2007) uses a similar grid for the simulation of shear-driven swirling flows using a spectral element method. The other grid is defined by curving the sides of the central square (see Figure 1(c)). This is done to improve the condition at the corners, as will be discussed in the work. The latter mesh was used in Sporleder *et al.* (2011b) with the least squares spectral element method (LS-SEM) as part of a 4D grid. A similar mesh, not generated using transfinite mapping, can be found in Boules (2001), where finite elements is used. Mavriplis (1996) shows also a similar grid in an example of block structured grids.

The article presents in detail the mappings needed to generate the meshes for a disc. The mappings are presented for the most general case. Discs of all sizes can be mapped, and the size of the center region is variable. The extension to the cylindrical case is straight–forward. We take the LS-SEM as the test subject, and the Poisson problem as the test case. The results obtained are representative of what would be obtained using other spectral methods with physical models.

The objective of this work is to document a readily implemented procedure to generate the meshes and analyze their performance. Section MESHES OF A DISC presents the transfinite mappings for the disco-ball and the multi-mapped meshes. Section TEST CASE gives a brief description of the LS-SEM, and how the mappings reflect on the method. The performance for each mesh is analyzed in section NUMERICAL TESTS. The conclusions are drawn in section CONCLUSION.

MESHES OF A DISC

In order to map a unit square domain $\mathscr{S}$ onto a disc domain $\mathscr{R}$, it would be necessary to define a vector–valued function $\mathscr{F} : \mathscr{S} \to \mathscr{R}$ that traces $\mathscr{R}$ in an univalent manner. An example is the well–known polar mapping:

$$[x \ , \ y] = \mathscr{F}(s,t) = [r\cos(\theta) \ , \ r\sin(\theta)] \tag{6}$$

Here, $[s,t]$ are the generalized coordinates, i.e. the coordinates on $\mathscr{S}$. Every point $[s,t]$ traces one point in $[x,y]$, and vice-versa.

Gordon and Hall (1973) explain how a transfinite interpolatory mapping of $\mathscr{S}$ induces a natural curvilinear system on $\mathscr{R}$. This implies that in practice it is enough to build an univalent function $\mathscr{U} : \mathscr{S} \to \mathscr{R}$ that matches $\mathscr{F}$ on the boundary. Thus, it is not necessary to know $\mathscr{F}$, but just its functionality for the domain borders. In this work, we employ the bilinear transfinite Lagrange interpolant of $\mathscr{F}$, for simplicity. For this case, $\mathscr{U}$ is expressed as:

$$\begin{aligned}
\mathscr{U}(s,t) = (1-s)\mathscr{F}(0,t) + s\mathscr{F}(1,t) + (1-t)\mathscr{F}(s,0) \\
+ t\mathscr{F}(s,1) - (1-s)(1-t)\mathscr{F}(0,0) \\
- (1-s)t\mathscr{F}(0,1) - s(1-t)\mathscr{F}(1,0) - st\mathscr{F}(1,1)
\end{aligned} \tag{7}$$

The reader is referred to Gordon and Hall (1973) for further detail on the obtainment of equation (7).

This section will present the mappings of the borders of the reference domains for the three cases analyzed. The reference domain will be considered to be a unit square, and the origin of the reference system is placed at the bottom-left vertex. The center of the mapped disc for all cases will be located at $[R_{ext} \ , \ R_{ext}]$, with R_{ext} being the disc radius.
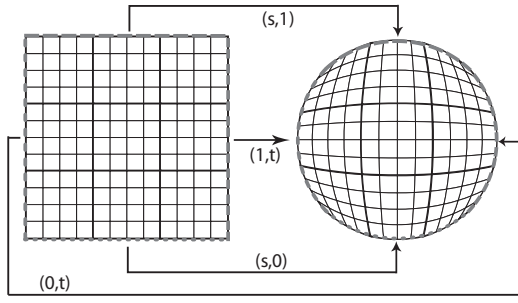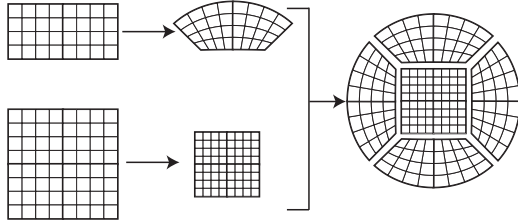
Figure 2: Disco-ball type of mapping.

Figure 3: Mappings for the square center mesh.

Disco-ball grid

To generate this mesh, the borders of the reference square are traced to equal quarters of the perimeter of the disc, as shown in Figure 2. The borders are traced as follows:

$$
\begin{aligned}
\mathscr{F}_1(s,0) &= \begin{bmatrix} R_{ext}\cos\pi(0.5s+1.25) \\ R_{ext}\sin\pi(0.5s+1.25) \end{bmatrix} \\[2mm]
\mathscr{F}_1(s,1) &= \begin{bmatrix} R_{ext}\cos\pi(-0.5s+0.75) \\ R_{ext}\sin\pi(-0.5s+0.75) \end{bmatrix} \\[2mm]
\mathscr{F}_1(0,t) &= \begin{bmatrix} R_{ext}\cos\pi(0.5t-0.25) \\ R_{ext}\sin\pi(0.5t-0.25) \end{bmatrix} \\[2mm]
\mathscr{F}_1(1,t) &= \begin{bmatrix} R_{ext}\cos\pi(-0.5t+1.25) \\ R_{ext}\sin\pi(-0.5t+1.25) \end{bmatrix} \quad (8)
\end{aligned}
$$

where R_{ext} is the radius of the cylindrical domain. The resulting mesh presents a high deformation for the corners regions of the reference square. These can reach angles close to $180°$.

Square center grid

This multi-mapped grid is built considering five different regions, as seen in Figure 3. Each region is mapped using transfinite mapping, analogously to the disco-ball mesh. The mapping of the central region is trivial, and will not be discussed. The four external regions differ only on a rotation. The mapping for the top quarter is given as:

$$
\begin{aligned}
\mathscr{F}_{2o}(s,0) &= \begin{bmatrix} (2s-1)b \\ b \end{bmatrix} \\[2mm]
\mathscr{F}_{2o}(s,1) &= \begin{bmatrix} R_{ext}\cos\pi(-0.5s+0.75) \\ R_{ext}\sin\pi(-0.5s+0.75) \end{bmatrix} \\[2mm]
\mathscr{F}_{2o}(0,t) &= \begin{bmatrix} -t(R_{ext}\cos\frac{\pi}{4}-b)-b \\ t(R_{ext}\cos\frac{\pi}{4}-b)+b \end{bmatrix} \\[2mm]
\mathscr{F}_{2o}(1,t) &= \begin{bmatrix} t(R_{ext}\cos\frac{\pi}{4}-b)+b \\ t(R_{ext}\cos\frac{\pi}{4}-b)+b \end{bmatrix} \quad (9)
\end{aligned}
$$

where b is half of the side length of the center region.
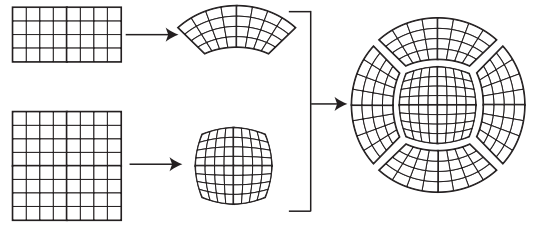
Figure 4: Mappings for the curved center mesh.

It may be of interest to define the area of the center region so as to have an equal density of points as in an outer quarter. Assuming the latter has $N_1 \times N_2$ nodes and the center region $N_2 \times N_2$ nodes, the central area A_c can be calculated following equation (10).

$$
A_c = \frac{\pi R_{ext}^2}{1+4\frac{N_2}{N_1}} \quad (10)
$$

In this grid, the most ill-conditioned elements have a maximum angle of $135°$, and are placed on the inner corners of the outer quarters.

Curved center grid

In this grid, the sides of the center square are replaced by curved sides which yield corner angles of $120°$. Figure 4 shows mappings used for this mesh. The mapping of the curved center region is shown in equation (11):

$$
\begin{aligned}
\mathscr{F}_{3i}(s,0) &= \begin{bmatrix} R_{int}\cos\frac{\pi}{6}(s+8.5) \\ R_{int}\sin\frac{\pi}{6}(s+8.5)+a \end{bmatrix} \\[2mm]
\mathscr{F}_{3i}(s,1) &= \begin{bmatrix} R_{int}\cos\frac{\pi}{6}(-s+3.5) \\ R_{int}\sin\frac{\pi}{6}(-s+3.5)-a \end{bmatrix} \\[2mm]
\mathscr{F}_{3i}(0,t) &= \begin{bmatrix} R_{int}\cos\frac{\pi}{6}(-t+6.5)+a \\ R_{int}\sin\frac{\pi}{6}(-t+6.5) \end{bmatrix} \\[2mm]
\mathscr{F}_{3i}(1,t) &= \begin{bmatrix} R_{int}\cos\frac{\pi}{6}(t-0.5)-a \\ R_{int}\sin\frac{\pi}{6}(t-0.5) \end{bmatrix} \quad (11)
\end{aligned}
$$

where R_{int} is the curvature radius of the sides and $a = R_{int}(\cos\frac{\pi}{12}-\sin\frac{\pi}{12})$.
The mapping of the upper quarter is given as:

$$
\begin{aligned}
\mathscr{F}_{3o}(s,0) &= \begin{bmatrix} R_{int}\cos\frac{\pi}{6}(-s+3.5) \\ R_{int}\sin\frac{\pi}{6}(-s+3.5)-a \end{bmatrix} \\[2mm]
\mathscr{F}_{3o}(s,1) &= \begin{bmatrix} R_{ext}\cos\frac{\pi}{2}(-s+1.5) \\ R_{ext}\sin\frac{\pi}{2}(-s+1.5) \end{bmatrix} \\[2mm]
\mathscr{F}_{3o}(0,t) &= \begin{bmatrix} -t(R_{ext}\cos\frac{\pi}{4}-c)-c \\ t(R_{ext}\cos\frac{\pi}{4}-c)+c \end{bmatrix} \\[2mm]
\mathscr{F}_{3o}(1,t) &= \begin{bmatrix} t(R_{ext}\cos\frac{\pi}{4}-c)+c \\ t(R_{ext}\cos\frac{\pi}{4}-c)+c \end{bmatrix} \quad (12)
\end{aligned}
$$

where $c = R_{int}\sin\frac{\pi}{12}$. The area of the center region A_c is related to R_{int} as follows:

$$
A_c = R_{int}^2 \left(\frac{\pi}{3} + 4\sin^2\frac{\pi}{12} - 4\cos\frac{\pi}{12}\sin\frac{\pi}{12} \right) \quad (13)
$$

Equation (10) can be used to define the center area that yields the same density of nodes in the central and outer parts.

TEST CASE

This section presents the LS-SEM in a general and simplified manner. The reader is referred to (Bochev and Gunzburger, 2009) for more details.

The least squares methods (the spectral method, and the finite elements and spectral elements versions) were originally formulated for linear partial differential equations. Extension of the theory to non-linear equations such as the Navier-Stokes equations can be found in (Bochev and Gunzburger, 2009). The method has been successfully applied to other non-linear equations, as reviewed by Kayser-Herold and Matthies (2005) and Gerritsma and De Maerschalck (2010). The method has also been used to solve integro-differential equations, such as the neutron transport equation (Manteuffel and Ressel, 1998) and the population balance equation (Dorao and Jakobsen, 2008; Sporleder *et al.*, 2011a).

The great majority of works present calculations based on first-order systems of equations. This is done to relax the regularity requirements and to keep the condition number of the system in reasonable values (Jiang, 1998). Systems of higher order have also been solved (Sporleder *et al.*, 2010; Surana *et al.*, 2007).

The section is focused on the part that the mappings have on the method. We first present the basic idea behind any least square method, and we continue by showing relevant implementation issues regarding the LS-SEM.

The least squares method

The idea behind least squares method is independent of the equations at hand. Let us write an abstract problem as:

$$\mathscr{L}\mathbf{f} = \mathbf{h} \quad \text{in } \Omega \tag{14}$$

$$\mathscr{B}\mathbf{f} = \mathbf{h}_\Gamma \quad \text{on } \partial\Omega \tag{15}$$

where Ω is the domain of the system (in our case, $\mathscr{R}$), $\partial\Omega$ is its boundary, $\mathscr{L} : X(\Omega) \to Y(\Omega)$ is a linear partial differential operator, and $\mathscr{B} : X(\partial\Omega) \to Y(\partial\Omega)$ is the trace operator. Equation (15) represents the equations of the boundary conditions, while equation (14) represents the main equations of the problem.

It is assumed that the problem is well-posed and that the operators $\mathscr{L}$ and $\mathscr{B}$ conform a continuous mapping of the function space $X(\Omega) \times X(\partial\Omega)$ on the space $Y(\Omega) \times Y(\partial\Omega)$. Under these conditions, a norm-equivalence can be established between the solution space X and the residual space Y (Bochev and Gunzburger, 2009). This equivalence implies that small residual norms correspond to small error norms, and vice-versa. We can then define the so-called least squares functional:

$$\mathscr{J}(\mathbf{f}) \equiv \frac{1}{2} \parallel \mathscr{L}\mathbf{f} - \mathbf{h} \parallel_{Y(\Omega)}^2 + \frac{1}{2} \parallel \mathscr{B}\mathbf{f} - \mathbf{h}_\Gamma \parallel_{Y(\partial\Omega)}^2 \tag{16}$$

Due to the existence of norm equivalence, solving the abstract problem in equations (14)–(15) is now equivalent to finding the $\mathbf{f} \in X(\Omega)$ that minimizes $\mathscr{J}(\mathbf{f})$.

Solution Procedure

From a practical point of view it is convenient to choose solution and residual function spaces that make the residual norms easy to calculate. Here, we consider $Y(\Omega)$ to be $L^2(\Omega)$, i.e. the space of functions which are continuous in the domain, with $\parallel \bullet \parallel_{L^2(\Omega)}^2 = \langle \bullet, \bullet \rangle_{L^2(\Omega)} = \int_\Omega \bullet \bullet \, d\Omega$.

The minimization procedure yields the equivalent problem of finding $\mathbf{f} \in X(\Omega)$ such that (Gerritsma and De Maerschalck, 2010):

$$\langle \mathscr{L}\mathbf{f}, \mathscr{L}\mathbf{v} \rangle_{L^2(\Omega)} + \langle \mathscr{B}\mathbf{f}, \mathscr{B}\mathbf{v} \rangle_{L^2(\partial\Omega)} =$$
$$\langle \mathbf{h}, \mathscr{L}\mathbf{v} \rangle_{L^2(\Omega)} + \langle \mathbf{h}_\Gamma, \mathscr{B}\mathbf{v} \rangle_{L^2(\partial\Omega)} \ , \ \forall \mathbf{v} \in X(\Omega) \tag{17}$$

The integrals in equation (17) are approximated using quadrature rules for simplicity. The discrete problem is found by reducing the search of the minimizing function to a finite–dimensional function space such that $\mathbf{f}_P \in X_P(\Omega) \subset X(\Omega)$ and $X_P(\Omega) = span\{\varphi_0, ..., \varphi_P\}$.

Most authors base both the expansion and the quadrature rule on Legendre polynomials over the interval $[-1, 1]$ (Gerritsma and De Maerschalck, 2010). The multi-dimensional basis functions are obtained doing tensor products of the 1D bases. The spectral (and finite) element method consists in sub-dividing the computational domain Ω into N_e non-overlapping sub-domains Ω_e, called spectral elements. The solution is approximated in each element using N_p basis functions, such that:

$$\mathbf{f}_P = \bigcup_{e=1}^{N_e} \mathbf{f}_P^e \quad , \quad \mathbf{f}_P^e = \sum_{j=0}^{N_p-1} \mathbf{b}_j^e \varphi_j^e \tag{18}$$

where $\mathbf{b}_j^e$ are the coefficients of the expansion for the spectral element e.

Mappings

In order to map from the generalized domain $\mathscr{S} = [-1, 1]^d$ where the basis functions are defined to the physical domain Ω_e, we use the mapping $\mathscr{M} : \mathscr{S} \to \Omega_e$. Let us define $J(\mathscr{M})$ as the Jacobian of the mapping, and $|J(\mathscr{M})|$ as its determinant. The mappings affect the derivative and integral operators in $\mathscr{L}$ and the integrals of the internal products in equation (17), as follows:

$$\int_{\mathscr{S}} d\mathscr{S} = \int_{\Omega_e} |J(\mathscr{M})| \, d\Omega_e \tag{19}$$

$$\hat{\nabla}\varphi_i = \nabla\varphi_i \cdot J(\mathscr{M}) \tag{20}$$

where $\hat{\nabla}$ is the gradient operator defined in the generalized coordinates.

NUMERICAL TESTS

This section presents numerical experiments that test the performance of the LS-SEM presented in section TEST CASE with the grids presented in section MESHES OF A DISC. For this, we took a 2D Poisson problem with Dirichlet conditions at the boundary of the disc. The problem was re-casted into a system of first-order equations, as shown in equation (22). The reader is referred to (Jiang, 1998; Sporleder *et al.*, 2010) for more details on the reasons.

$$u - \frac{\partial C}{\partial x} = 0$$
$$v - \frac{\partial C}{\partial y} = 0 \tag{21}$$
$$\frac{\partial u}{\partial x} + \frac{\partial v}{\partial y} = h(x,y)$$
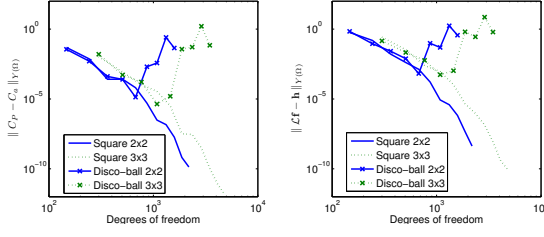
Figure 5: Accuracy test for the Poisson problem with the disco-ball grid.

For this case:

$$\mathbf{f} = \begin{bmatrix} C & u & v \end{bmatrix}^T$$
$$\mathbf{h} = \begin{bmatrix} 0 & 0 & h(x,y) \end{bmatrix}^T \qquad (22)$$
$$\mathscr{L} = \begin{bmatrix} -\frac{\partial \bullet}{\partial x} & \bullet & 0 \\ -\frac{\partial \bullet}{\partial y} & 0 & \bullet \\ 0 & \frac{\partial \bullet}{\partial x} & \frac{\partial \bullet}{\partial y} \end{bmatrix}$$

The analytical solution considered is given in equation (23).

$$C_a(x,y) = \cos\frac{\pi}{2}(x^2 + y^2) \qquad (23)$$

The Gauss–Lobatto–Legendre (GLL) quadrature rule was used for the integrals in the equivalent problem. Lagrange interpolants through the GLL-nodes were used as basis functions. The problem was coded in MATLAB, and its direct solver was used to solve the problem.

Four parameters were taken to analyze the performance: the norm of the residual $\| \mathscr{L}\mathbf{f}_P - \mathbf{h} \|_{L^2(\Omega)}$, the norm of the error $\| C_P - C_a \|_{L^2(\Omega)}$, the condition number of the matrix of the discrete problem and the wall-time of the calculations. An undeformed square grid was used as reference.

One element was used for each region of the multi-mapped grids. For the disco–ball and square grids, 2 and 3 elements in each direction were used. The same number of basis functions was used in both directions. The results differ in degrees of freedom, i.e. the number of basis functions used. The smallest problem considered used 4 Lagrange interpolants in each direction. The results are extensible to cases where the number of elements is varied.

Disco-ball grid

Figure 5 compares the accuracy of the disco-ball grid and the undeformed square mesh for increasing degrees of freedom. Both the norm of the error and the norm of the residual are shown.

Ideally, the two grids would yield similar results. Exponential convergence rates with increasing order of approximation would be expected both for the norm of the error and the norm of the residual. Nevertheless, the disco-ball grid reaches a point of limiting accuracy for 8 interpolants. The accuracy is further reduced for higher orders. This poor performance is due to the high deformations of the corner points in the disco-ball mesh. These affect the Jacobians used in equations (19)–(20), which in time affects the condition number of the matrix.

As can be seen in Figure 6, the condition number increases exponentially with the degrees of freedom of the problem, but for the disco-ball this occurs in a much steeper manner.
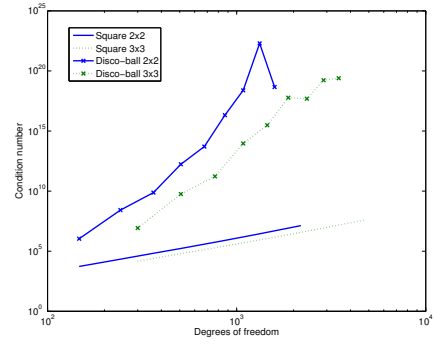
Figure 6: Condition number obtained for the disco-ball grid. The results for the undeformed square mesh are included.
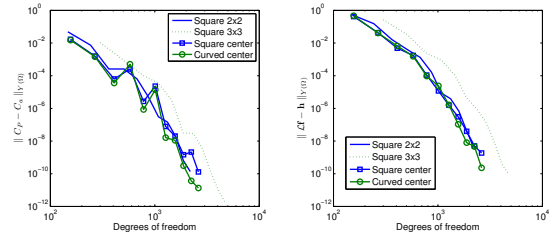
Figure 7: Accuracy test for the Poisson problem with the multi-mapped grids.

Comparing Figures 5 and 6, we see that the following rule–of–thumb applies:

$$\varepsilon_{min} \sim \kappa \, \varepsilon_{num} \qquad (24)$$

where ε_{min} is the minimum error achievable, ε_{num} is the numerical precision (usually 10^{-16}) and κ is the condition number. With 8 interpolants, the accuracy is limited by the condition number rather than by the order of the approximation. For higher orders, the condition number reaches 10^{16}, and the accuracy is lost.

It is interesting to notice the correspondence between the norm of the error and the norm of the residual in Figure 5. This is due to the norm–equivalence mentioned in section TEST CASE. The norm of the residual can be thus used as an error estimator built in the LS-SEM.

Multi-mapped grids

Figure 7 shows the norm of error and norm of residual obtained for the multi-mapped grids. The results are comparable to the undeformed mesh case.

The improvement in the performance is due to the low deformations that the mappings used cause. The condition number obtained for these cases is comparable to the condition number of the square mesh, as shown in Figure 8.

The square center grid has nodes which have higher deformations than those in the curved center grid. Therefore, the accuracy of the latter is expected to be better. Figure 9 shows the ratio between the norm of the error in both cases. The curved center grid proved to perform more accurately.

The generation of the curved center grid is more computationally demanding than the square center grid case. This can be seen in Figure 10, where the ratio between the wall time in both cases is shown. For larger problems the time spent in mesh generation becomes negligible. This ratio decreases asymptotically to one with the degrees of freedom.
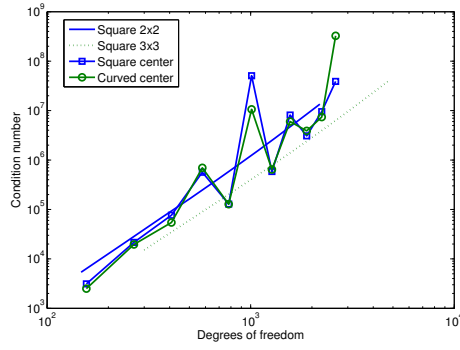
Figure 8: Condition number obtained for the multi-mapped grids. The results for the undeformed square mesh are included.
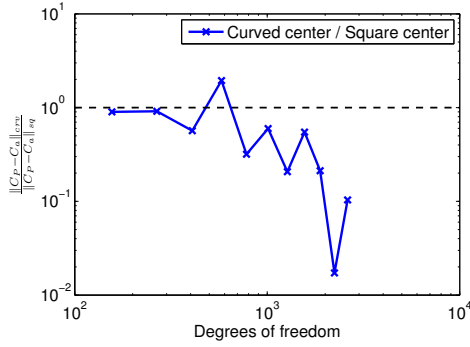
Figure 9: Ratio of the L^2 norms of difference obtained for the multi-mapped grids.
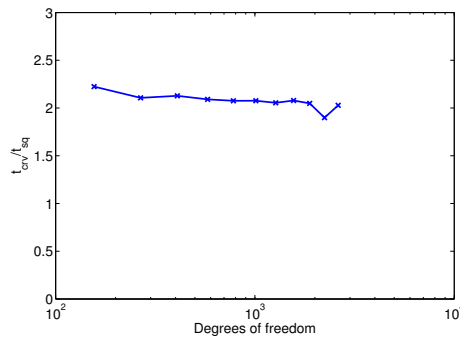
Figure 10: Ratio of the wall time spent for the multi-mapped grids.

CONCLUSION

In this work, we analyzed the use of transfinite mappings to generate meshes on a disc as an alternative to the use of polar coordinates. We documented in detail how to construct well-known disco-ball mesh defining a single mapping, and the square and curved center grids using multiple mappings.

The presented mappings allow us to build meshes for a disc of any size. The multi-mapped meshes make use of a center region of variable size and four external regions that are identical but for a rotation, and therefore only two mappings are actually needed.

The meshes were tested using the LS-SEM. We showed how the disco-ball mesh becomes ill-conditioned for problems of relevant size. Contrarily, the results obtained with the multi-mapped grids were comparable to those obtained with an undeformed square mesh. The curved center grid proved to yield more accurate results than the square center grid, but the latter took less time to generate. However, the mesh generation time becomes negligible for large non-linear problems, and therefore the curved center grid arises as the most attractive option. The results found with the LS-SEM are representative of other spectral element methods.

The meshes on the disc can be extended to full cylindrical grids. The use of the multi-mapped meshes allows for the simulation of asymmetric physical phenomena in cylindrical domains (such as turbulent flow in a pipe or two-phase flow in bubble columns) using spectral methods, without the need of recurring to mesh generation softwares.

ACKNOWLEDGEMENT

REFERENCES

BOCHEV, P.B. and GUNZBURGER, M.D. (2009). *Least-Squares Finite Element Methods*. Springer.

BOUFFANAIS, R. (2007). *Simulation of shear-driven flows: Transition with a free surface and confined turbulence*. Ph.D. thesis, École Polytechnique Fédérale de Lausanne.

BOULES, A.N. (2001). "On the least-squares conjugate-gradient solution of the finite element approximation of burger's equation". *Applied Mathematical Modelling*, **25**, 731–741.

DORAO, C.A. and JAKOBSEN, H.A. (2008). "hp-adaptive least squares spectral element method for population balance equations". *Applied Numerical Mathematics*, **58**, 563–576.

FERNANDINO, M. *et al.* (2007). "Jacobi galerkin spectral method for cylindrical and spherical geometries". *Chemical Engineering Science*, **62**, 6777 Ű 6783.

GERRITSMA, M.I. and DE MAERSCHALCK, B. (2010). *Advanced Computational Methods in Science and Engineering*, vol. 71 of *Lecture Notes in Computational Science and Engineering*, chap. Least-Squares Spectral Element Methods in Computational Fluid Dynamics, 179–227. Springer-Verlag Berlin Heidelberg.

GORDON, W.J. and HALL, C.A. (1973). "Construction of curvilinear co-ordinate systems and applications to mesh generation". *International Journal for Numerical Methods in Engineering*, **7**, 461–477.

GORDON, W.J. and THIEL, L.C. (1982). "Transfinite mappings and their application to grid generation". *Numerical Grid Generation*, **-**, 171–233.

HEINRICHS, W. (2004). "Spectral collocation schemes on the unit disc". *Journal of Computational Physics*, **199**, 66–86.

JIANG, B.N. (1998). *The least-squares finite element method: theory and applications in computational fluid dynamics and electromagnetics*. Springer.

KAYSER-HEROLD, O. and MATTHIES, H.G. (2005). "Least-squares FEM literature review". Tech. Rep. 2005-05, Technical University Braunschweig.

MANTEUFFEL, T.A. and RESSEL, K.J. (1998). "Least-squares finite-element solution of the neutron transport equation in diffusive regimes". *SIAM J. Numer. Anal.*, **35**, 806–835.

MAVRIPLIS, D.J. (1996). *Handbook of computational fluid dynamics*, chap. Mesh generation and adaptivity for complex geometries and flows, 417–459. Academic Press. London.

SPORLEDER, F. *et al.* (2010). "Simulation of chemical reactors using the least-squares spectral element method". *Chemical Engineering Science*, **65**, 5146–5159.

SPORLEDER, F. *et al.* (2011a). "Model based on population balance for the simulation of bubble columns using methods of the least square type". *Chemical Engineering Science*, **Accepted manuscript.**

SPORLEDER, F. *et al.* (2011b). "Study of dispersed phase model for the simulation of a bubble column". A. Kuzmin (ed.), *Computational Fluid Dynamics 2010*. Springer-Verlag Berlin Heidelberg.

SURANA, K.S. *et al.* (2007). "k-version least squares finite element processes for 2-D generalized newtonian fluid flows". *International Journal for Computational Methods in Engineering Science and Mechanics*, **8**, 243–261.

8th International Conference on CFD in Oil & Gas, Metallurgical and Process Industries
SINTEF/NTNU, Trondheim Norway
21-23 June 2011

CFD11-137

CFD MODELING OF SILICA FUME FORMATION DURING REFINING OF SILICON METAL

Jan Erik OLSEN[1] , Mari NÆSS & Gabriella TRANELL[2]*

[1] SINTEF Materials and Chemistry, 7465 Trondheim, NORWAY

[2] NTNU Department of Material Science & Engineering, 7491 Trondheim, NORWAY

* E-mail: Jan.E.Olsen@sintef.no

ABSTRACT

Silica fume is formed at the metal surface during oxidative ladle refining of silicon. For the plant operators this is a potential health risk. The phenomenon has been studied by standard conservation laws and modules available in most commercial CFD tools. The work has not resulted in any new models or break throughs for the CFD community, but it demonstrates the applicability of CFD to study industrial challenges. The analysis unveils which parameter influence the fuming rate most significantly. It also demonstrates that by applying a lid on top of the ladle, the fuming rate can be reduced considerably.

Keywords: CFD, refining, fuming, reactions.

NOMENCLATURE

Greek Symbols
ρ Mass density, [kg/m^3].
μ Dynamic viscosity, [kg/m.s].

Latin Symbols
A pre exponential factor [m/s]
D diffusion [m/s^2]
E activation energy [J/mol]
H enthalpy [J/mol]
J diffusion flux [kg/s m^2]
p Pressure, [Pa].
R total production rate [kg/s m^3]
Sc   Schmidt number []
$\dot{r}$ reaction rate [mol/s m^3]
v Velocity, [m/s]
Y mass fraction []

Sub/superscripts
g gas
i index
l liquid
m mass
s solid
T thermal
t turbulent
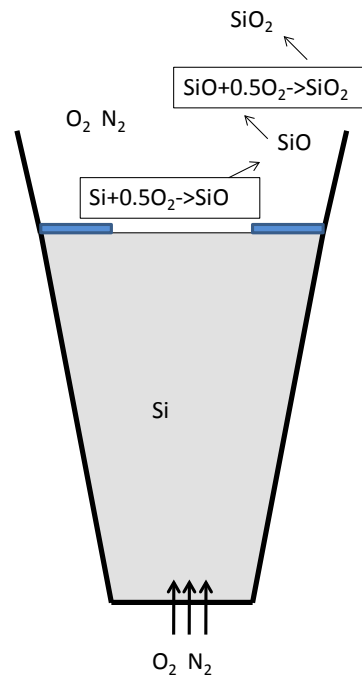
Figure 1: Silicon ladle refining process indicating steps towards fume formation. Top layer of slag is indicated in blue.

INTRODUCTION

Formation of silica fume from the ladle in which metal is refined into its final specifications is an environmental issue of importance for the working environment in the production plant. In layman-term fume is often known as dust. It is formed when metal reacts with oxygen. For silicon production, silica fume (SiO_2) is produced when silicon metal (Si) reacts with oxygen (O_2).

Silicon is produced in a submerged arc furnace. The metal is tapped from the furnace into a ladle for refining. The refining is conducted by injecting a mixture of air and pure oxygen at the bottom of the ladle. The oxygen reacts with the metal and the impurities, and the amount of impurities is reduced according to product specification. At the ladle surface, metal also reacts with oxygen present in the air

surrounding the ladle. This reaction produces silica fume as illustrated in Figure 1.

The formation of silica fume follows is slightly more complicated than in the figure and it is believed to follow four chemical reactions and phase transitions. At the metal surface, oxygen reacts with metal and forms SiO as a gas species above the metal surface:

$$Si(l) + \frac{1}{2}O_2(g) \rightarrow SiO(g) \qquad (I)$$
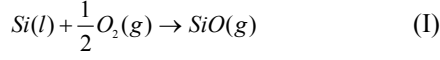
SiO-gas moves into the bulk gas by convection and diffusion where it reacts with oxygen to form silica in gas form by the following two reactions:

$$SiO(g) + O_2(g) \rightarrow SiO_2(g) + O(g) \qquad (II)$$

$$SiO(g) + O(g) + M \rightarrow SiO_2(g) + M \qquad (III)$$
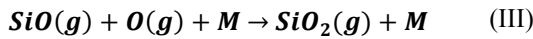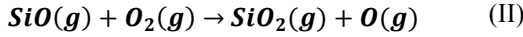
where M denotes any radicals such as a catalyst. The gas molecules will cluster and form solid silica also considered as dust in this context. It is still unclear whether this goes via a liquid state (Chagger, *et al.*,1996), but for now we combine this into one reaction/transition:

$$SiO_2(g) \rightarrow SiO_2(s) \qquad (IV)$$
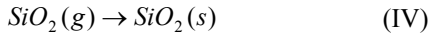
The first of these reactions is exothermic and produces additional heat at an already hot metal surface. This feeds the second and third reaction which is endothermic. The clustering of gaseous SiO_2 in Reaction IV is highly exothermic.

The reaction rates of reaction I, II and IV are not well known. Reaction IV is very fast compared to the other reactions and as long as we use a faster kinetics in the calculations, the result is not sensitive to this. For reaction II we have two estimates from the literature {Andersson, 2011;Chagger, 1996}. Both estimates are comparable and we will use the estimate of Andersson (2011) for this modelling attempt. Reaction I is the reaction of which we now the least. We will therefore tune this reaction rates to match the measured fuming rate at production plants.

Measured values of fuming indicate a typical fuming rate of 3-8 kg/h(Næss, *et al.*,2011). In order to establish whether the amount of metal at the interface was a limiting factor, a multiphase model was applied to estimate the flow rate of metal towards the surface. An Eulerian-Lagrangian model(Olsen and Cloete,2010) was applied to simulate the flow conditions in the ladle for typical gas rates and ladle geometries. The model is not perfect since it does not accurately account for the high gas fractions observed in the process, but it should at least give estimates which are of the correct order of magnitude. The results indicate a metal flow towards the surface far above 100 kg/s. When comparing this to the observed fuming rate, it could be concluded that there is an unlimited amount of metal available for the reaction. This fact allows for a simplified modeling concept, since we may assume that the metal surface is

a wall with an infinite amount of silicon. We may thus apply a single phase modelling concept for the analysis.
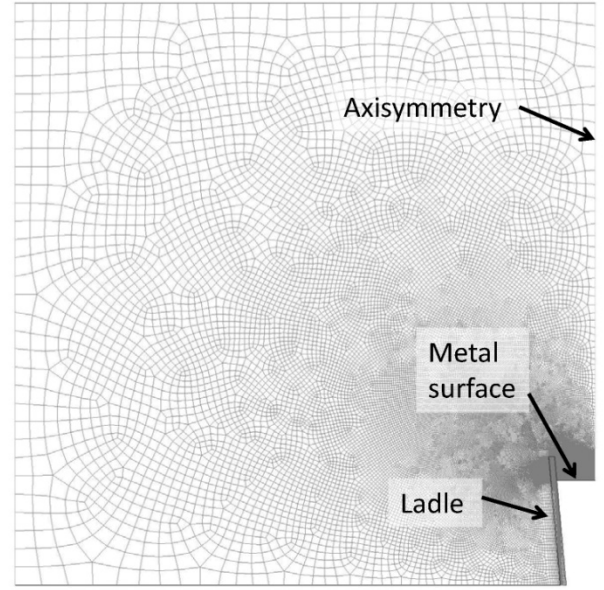
Figure 2: Modelling geometry with ladle and surrounding gas volume.

MODEL DESCRIPTION

The model describing the fuming process is a steady state, single phase model with axis symmetry. It accounts for turbulence, radiation and chemical reactions, in addition to the obvious conservation of mass, momentum and energy. The modelling concept is implemented in Fluent 13.

Species conservation and reaction kinetics

The gas phase is modelled as multicomponent mixture material with the following species: O_2, O, N_2, SiO and SiO_2 and $SiO_2(s)$ $SiO_2(s)$ is the fume (or dust) and in reality it is tiny particles (50-60nm(Næss, *et al.*,2011)) and not part of the gas mixture. However, for modelling simplicity we will assume that it is a part of the gas mixture. The species conservation is mathematically accounted for by

$$\frac{\partial}{\partial t}(\rho Y_i) + \nabla \cdot (\rho \vec{v} Y_i) = -\nabla \cdot \vec{J}_i + R_i + S_i \qquad (1)$$

where ρ is gas density, v is gas velocity, Y_i, J_i, R_i and S_i are the mass fraction, diffusion flux, net reaction rate and mass transfer from other phases for species i. The diffusion flux accounts for molecular, turbulent and thermal diffusion:

$$\vec{J}_i = -\left(\rho D_{i,m} + \frac{\mu_t}{Sc_t}\right)\nabla Y_i - D_{T,i}\frac{\nabla T}{T} \qquad (2)$$

Here $D_{i,m}$ and $D_{i,T}$ are the molecular and thermal diffusion coefficients for species i. Sc_t is the turbulent Schmidt number.

Although the reaction between liquid silicon and oxygen, Reaction I, is a heterogeneous multiphase reaction, we treat it as a wall reaction where silicon, Si, is a site species on the metal surface. The other reactions are gas phase reactions. The reaction rates are

given by the Arrhenius equation and the rate coefficients are found in Table 1.

Conservation of mass, momentum and energy

Conservation of mass and momentum are taken care of by the continuity equation and Navier Stokes equation. Turbulence is accounted for by the standard k-ε model. Tests showed that other RANS models do not significantly affect the results. These models are well known and described in many text books(White,1991).

The conservation of energy is modelled with the standard energy equation and added terms for reaction sources and sinks and radiation. For radiation we use the DO-model (discrete ordinates).

Boundary conditions and material properties

The metal in the ladle is accounted for by applying a given temperature on the walls in contact with the ladle material and the gas phase. This temperature is typically 1450-1650°C. At the metal surface a site species of Si with an infinite amount is prescribed for Reaction I. The chosen ladle has an inner bottom diameter of 1m. It is 2.2m tall and filled up to 1.8m with metal.

The gas region extends radially outwards for 10m where a pressure inlet is specified with ambient conditions. The top is situated 10m above the floor with a pressure outlet condition. For the floor we apply an adiabatic wall. All walls are given an emissivity of 0.95 for the radiation modelling, except for the metal surface. Pure silicon has a low emissivity of around 0.17(Rulison and Rhim,1995).

Material properties are the standard properties for the species involved under the assumption that they are ideal gases. Mixture properties are derived from the principle of mass weighing between the species. The diffusion coefficients are found from the kinetic theory of gases.

Table 1: Reaction kinetics for Reaction I and IV

	A	E [cal/mol]	ΔH [kJ/mol]
$Si(l) + \frac{1}{2}O_2(g) \rightarrow SiO(g)$	5.0E8	195984	-161
$SiO + O_2 \rightarrow SiO_2 + O$	1.0E13	6500	38
$SiO + O + M \rightarrow SiO_2 + M$	2.5E15	4370	-469
$SiO_2(g) \rightarrow SiO_2(s)$	1.0E15	1000	-791

Numerical setup

An axis symmetric grid of 53000 cells was applied. It was refined towards the metal surface with a grid size of 1mm. A proper grid dependence study was not performed, but it was verified that a grid with 212000 cells did not alter the results. This was performed by

splitting all cells into 4 by grid refinement of the entire domain.

First order schemes were applied for all equations except the momentum equations and species conservation equations which were calculated with a second order upwind algorithm. The pressure-velocity coupling was performed with the SIMPLE scheme.

Although residuals were checked for convergence, it was found that the fuming rate did not level out at the standard residual limits. Simulations were run until no further changes in fuming rate were observed.
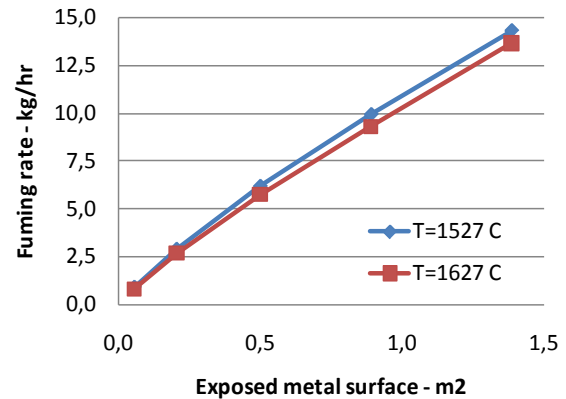
Figure 3: Effect of exposed metal surface and ladle temperature on fuming rate.
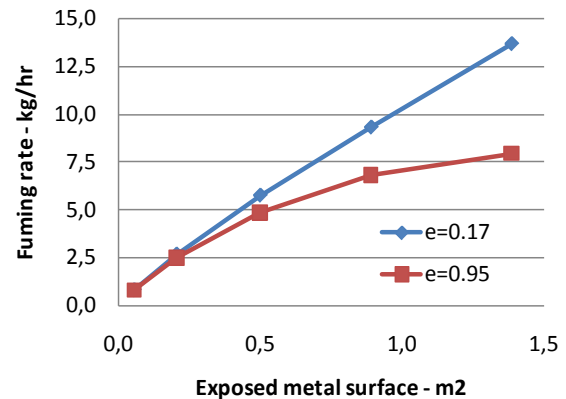
Figure 4: Effect of exposed metal surface and metal surface emissivity on fuming rate.

RESULTS

A study was conducted to check whether a lid on top of the ladle would reduce the fuming rate. However, first a sensitivity analysis was performed. As suspected, the exposed area of metal was the most significant parameter. This is the area on top of the metal not covered by slag.

One would also expect the ladle temperature to affect the fuming rate. This effect was much less than expected. As seen in Figure 3, the fuming rate is much more sensitive to the exposed metal surface than the ladle temperature. Increasing the ladle temperature by 100°C gives a small, almost insignificant, decrease in fuming rate. This is contradictory to the reaction

kinetics which yields higher reaction rates at higher temperatures. However, more than reaction rates determine the overall fuming rate. The authors believe that the temperature effect on diffusion and/or convection counteract the effect of the reaction rate.

The results were more sensitive towards the emissivity of the exposed metal surface. It was originally assumed to be 0.17. This has been measured on a stagnant and clean silicon surface. The real surface is quite dynamic with stirring activity and pollutants are present. Thus it was investigated if a metal surface emissivity of 0.95 would alter the fuming rate. The results presented in Figure 4indicate that the metal surface emissivity significantly influences the fuming rate. Especially as the exposed metal area approaches its maximum value.

For the ongoing study it was chosen to use the case with a ladle temperature of 1527°C, a metal surface emissivity of 0.17 and exposed metal surface area of 0.5m^2 as a reference case. For this case we see the temperature distribution in Figure 5 and the oxygen distribution in Figure 6. There are high temperatures close to the ladle, but they drop very sharply, especially on the sides were no reaction occurs. Note that this is the static temperature. Radiation will make all exposed surfaces and equipment feel a much higher temperature. The oxygen concentration is seen to decrease towards the metal surface. This is due to the oxygen consumption of the fuming reactions. In Figure 7 we see how the oxygen flows towards the metal surface. Diffusion and natural convection drives the oxygen up along the outside of the ladle and down towards the metal surface along the centre axis. The concentration of fume (or dust) is illustrated in Figure 8. The highest concentration is seen close to the metal surface and towards the internal wall of the ladle.

In order to study the effect of putting a lid on top of the ladle, the geometry was made flexible with segments on top of the ladle which could switch between the status of *wall* and *interior*. The first of these represents a lid segment. With this flexibility it was possible to study different sizes of the lid and whether it covering the centre or edges of the ladle surface. The lid configurations are illustrated in Figure 9.

Figure 6: Mass fraction of oxygen close to metal surface
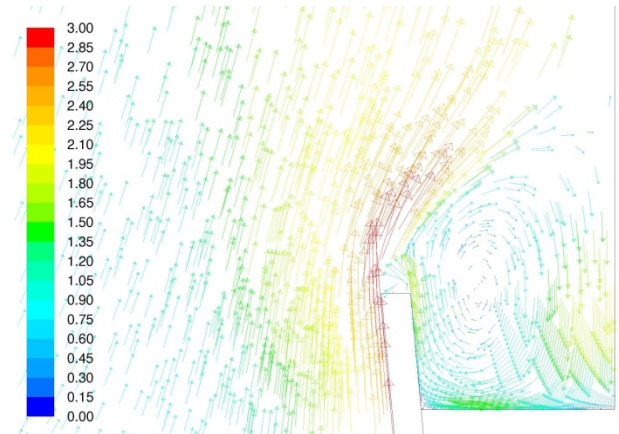
Figure 7: Velocity vectors colored by velocity magnitude (m/s) close to ladle and metal surface.
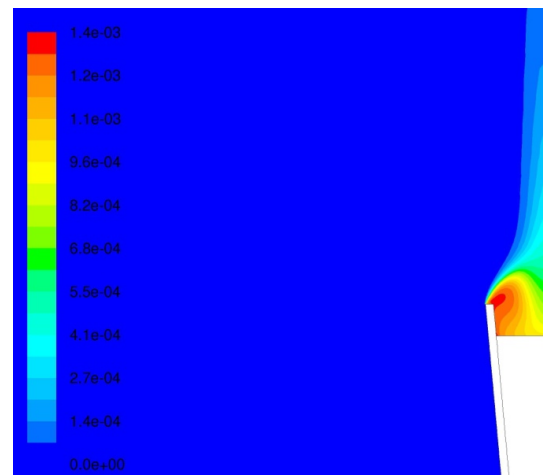
Figure 8: Distribution of fume (dust) seen as mass fraction of SiO$_2$.

Figure 5: Contour plot of temperatures in centigrade.

The results of the simulations indicate a significant reduction in fuming when a lid is applied. This is seen in Figure 10 where the relative fuming rate is plotted as a function of lid coverage for both centre lid and edge lid. The relative fuming rate is the fuming rate with a lid normalized with the fuming rate without lid (the reference case). Figure 10 shows that a centre lid is more efficient than an edge lid in terms of fume reduction. This can be explained by the flow pattern. The edge lid does not directly block the flow of oxygen seen for the reference case without lid (Figure 7). Thus it may not prevent the oxygen flow towards the metal surface. For a small edge lid, fuming may actually increase as seen in Figure 10. The flow pattern for a small edge lid is shown in Figure 11. For a centre lid, the oxygen flow is directly blocked as seen in Figure 12.
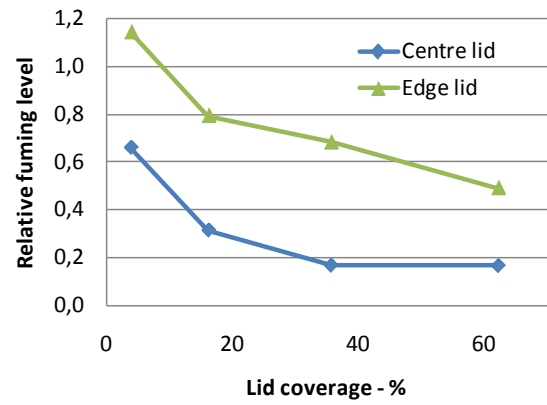
Figure 10: Effect of lid on fuming rate relative to case without lid.

Figure 11: Velocity vectors colored by velocity magnitude (m/s) for ladle with edge lid.

Figure 9: Potential lid configurations. Centre lid at top and edge lid at bottom.
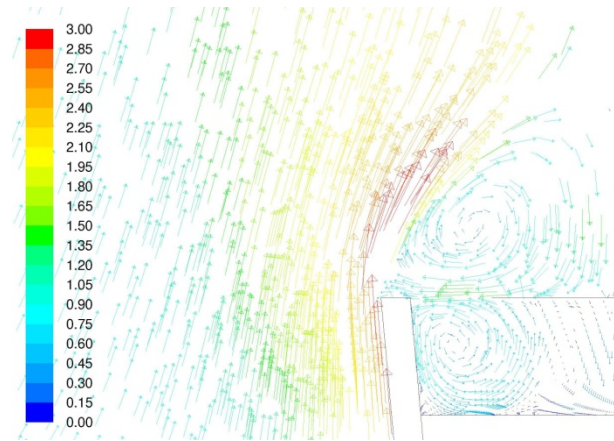
Figure 12: Velocity vectors colored by velocity magnitude (m/s) for ladle with centre lid.

CONCLUSION

A model for estimating the fuming rate from oxidative ladle refining of silicon is presented. Due to limited knowledge on the underlying reaction kinetics, the reaction rates where estimated based on related, but not exactly similar reaction mechanisms, and on model tuning with observed reaction rates. This limits the models applicability towards proper estimation of the fuming rates, but it allows for running parametric study to understand the qualitative influence of certain parameters such as process temperature and ladle design. The metal surface was also assumed to be a wall with infinite amount silicon available for the fuming reactions. This was shown to be a realistic assumption by an Eulerian-Lagrangian multiphase model for bubble columns. However, the wall of silicon has no nitrogen flowing through it as we have in the real process.

With these assumptions and limitations it was found that the exposed metal surface area was the most significant parameter for the fuming rate. Ladle temperature was almost insignificant while metal surface emissivity was more important. Applying a lid on top of the ladle blocks the oxygen flow and will reduce the fuming rate. A centre lid is more efficient than an edge lid.

In order to better understand the fuming issue under ladle refining of silicon it is critical to provide better estimates on the reaction rates for both of the reactions responsible for the fuming. This is difficult to achieve experimentally, but it could be studied with such disciplines as molecular dynamics and quantum chemistry. For the modelling of fuming during silicon ladle refining to be more robust, the following features needs to be added into the modelling concept:

- Reaction kinetics
- Realistic value of metal surface emissivity
- Nitrogen flux through metal surface

REFERENCES

CHAGGER, H.K. *et al.*(1996) The formation of SiO2 from hexamethyldisiloxane combustion in counterflow methane-air flames. *Twenty-Sixth Symposium (International) on Combustion, Vols 1 and 2*, 1859-1865

ANDERSSON, S. (2011) To be published

NÆSS, M.K., TRANELL, G.M., OLSEN, J.E. & KAMFJORD, N.E.(2011) *Mechanisms and kinetics of liquid silicon oxidation during industrial refining*,

OLSEN, J.E. & CLOETE, S. (2010) Eulerian-Lagrangian Methods for Modeling of Gas Stirred Vessels with a Dynamic Free Surface.in *7th Int.Conf. on Multiphase Flow (ICMF 2010),* Tampa, USA.

RULISON, A.J. & RHIM, W.K.(1995) Constant-Pressure Specific-Heat to Hemispherical Total Emissivity Ratio for Undercooled Liquid Nickel, Zirconium, and Silicon. *Metall Mater Trans B* **26**, 503-508

SINGH, S.K., SCHLUP, J.R., FAN, L.T. & SUR, B.(1988) Modeling of Thermal-Oxidation of Silicon. *Ind Eng Chem Res* **27**, 1707-1714

WHITE, F.M.(1991) *Viscous Fluid Flow*. McGraw-Hill.

8th International Conference on CFD in Oil & Gas, Metallurgical and Process Industries
SINTEF/NTNU, Trondheim NORWAY
21-23 June 2011

CFD11-140

DIRECT NUMERICAL SIMULATION OF TWO-FLUID FLOWS WITH A LEVEL-SET METHOD

Kateryna VORONETSKA[1][*], **Guillaume VINAY**[†], **Anthony WACHS**[‡], **Jean-Paul CALTAGIRONE**[2][§]

[1]IFP Energies nouvelles, Fluid Mechanics Department, 1-4 avenue de Bois-Préau,

92852 Rueil-Malmaison, FRANCE

[2]Université Bordeaux 1, Institut d'Ingénierie Mécanique, TREFLE, 16 avenue Pey-Berland, 33607

Pessac, FRANCE

[*] E-mail: kateryna.voronetska@ifpen.fr
[†] E-mail: guillaume.vinay@ifpen.fr
[‡] E-mail: anthony.wachs@ifpen.fr
[§] E-mail: calta@ipb.fr

ABSTRACT

In the petroleum industry flows of non-miscible fluids are frequently met, especially for the separation process in production. The presented work is dedicated to the simulation of two-phase dispersed flow. The Level-Set method was chosen to describe precisely the interface and the interactions between phases. Incompressible Navier-Stokes equations are solved thanks to the Operator-Splitting method. It allowed us to split the problem into three sub problems (advection, diffusion and degenerated Stokes) and to use a specific solution method for each of them. When it comes to the processing of discontinuity at the interface, we chose the CSF method. It is a global method since it is based on the update of the whole set of data that show a shift at the interface. 2D parallel simulations called "phase inversion" were performed to study in detail the separation process.

Keywords: level-set, bubble and droplet dynamics, phase inversion.

NOMENCLATURE

Greek Symbols
ϕ Level-Set function.
κ Curvature, $[1/m]$.
τ Fictitious time, $[s]$.
$\Delta\tau$ Fictitious time step, $[s]$.
ρ Density, $[kg/m^3]$.
μ Dynamic viscosity, $[Pas]$.
σ Surface tension coefficient, $[N/m]$.
δ_ε Regularized form of the Dirac function.
ρ_w Density of water, $[kg/m^3]$.
ρ_o Density of oil, $[kg/m^3]$.
μ_w Dynamic viscosity of water, $[Pas]$.
μ_o Dynamic viscosity of oil, $[Pas]$.

Latin Symbols
$\mathbf{n}$ Normal to the interface.
$\mathbf{u}$ Velocity, $[m/s]$.
t Physical time, $[s]$.
p Pressure, $[Pa]$.
$\mathbf{D}$ Deformation rate.
$\mathbf{g}$ Gravity vector, $[m/s^2]$.
H_ε Regularized form of the Heaviside function.
Δx Cell size, $[m]$.
Δt Discrete time step, $[s]$.
L Characteristic size of the domain, $[m]$.

D Diameter, $[m]$.
$\mathscr{R}e$ Reynolds number.
$\mathscr{W}e$ Weber number.
$\mathscr{C}a$ Capillary number.
$\mathscr{L}a$ Laplace number.

Sub/superscripts
ε Interface fictive thickness.

INTRODUCTION

The study of multi-phase flows is a major subject for fluid mechanics research. Applications are numerous, the petroleum industry shows great interest for this kind of flows, especially in the separation process for production. Because of the complexity of multi-phase flows during this process, we have used a numerical approach to study the emulsion zone. This zone is a continuous phase in which a great number of dispersed inclusions interact. The main physical mechanisms, such as coalescence or breakage, occur in this area.

There are two possible approaches to model this type of flow. In the first one, the flow is described from a macroscopic point of view. In this case, local phenomena (breakage or coalescence of droplets, phase slip, local compaction) are modeled thanks to analytic or empiric laws. In the second approach, the flow is simulated on a drop scale and the objective is to describe precisely the interface and the interactions between phases.

In our study, we did not care about macroscopic events that characterize the flow in an industrial petroleum separator. We used instead the second approach to model a two-phase dispersed flow. We worked at the drop scale to study the water/oil separation process in the emulsion zone. We considered that such a model would enable us to evaluate the influence of this specific zone on the global hydrodynamic behavior.

Various interface recognition methods exist. We mostly paid attention to methods that are able to detect even strong topology changes at the interface. We chose the Level-Set method to describe precisely the interface.

When it comes to the processing of discontinuity at the interface, we chose the CSF method.

Navier-Stokes incompressible equations are solved thanks to the Operator-Splitting method.

The main purpose of our work was thus to develop a direct numerical simulation code that is able to model a liquid/liquid two-phase flow and study precisely the effects of

drops coalescence or breakage. To validate our work, we chose the phase inversion test.
Our code is developed under the framework of the full MPI open source platform PELICANS.

NUMERICAL MODELING OF A TWO-PHASE FLOW

To model a two-phase flow, it is necessary to choose an appropriate interface tracking method and to develop a solver for Navier-Stokes incompressible equations to compute the velocity and pressure values. Also, a coupling method, able to handle the discontinuous quantities at the interface, has to be implemented.

In our case, we considered non-miscible, newtonian and homogeneous fluids; density and viscosity are constant in each phase.

Level-Set method

Among all methods for interface tracking, we focused on methods that are able to deal with high topology changes at the interface. We finally chose the Level-Set (Osher and Sethian, 1988) to describe precisely the interface.

Level-Set method principle is to define a scalar function ϕ which value at a given point is an image of the distance between this point and the interface. ϕ can therefore be considered as the description of a variety of level sets. One level is defined by the set of points where ϕ is constant. When ϕ is null, the distant to the interface is null and the level set is the interface itself.

For each point in the space, the sign of the Level-Set function indicates immediately on which side of the interface the point is.

In addition, the main idea in defining the Level-Set method is the direct access to the interface geometrical local characteristics, i.e. the normal $\boldsymbol{n}$ and the curvature κ (1).

$$\boldsymbol{n} = \frac{\nabla \phi}{\|\nabla \phi\|} \qquad \kappa = \nabla \cdot \left(\frac{\nabla \phi}{\|\nabla \phi\|} \right) = \nabla \cdot \boldsymbol{n} \qquad (1)$$

The interface evolution in a given velocity field $\boldsymbol{u}$, is governed by the purely transport equation (2).

$$\frac{\partial \phi}{\partial t} + (\boldsymbol{u} \cdot \nabla) \, \phi = 0 \qquad (2)$$

Particular attention must be paid to this transport equation. Some problems may arise when the Level-Set method is developed (spreading and stretching of the level sets). A re-distancing algorithm (Sussman *et al.*, 1994) must be applied to keep ϕ as the algebraic distance to the interface. The algorithm is based on the iterative solution of equation (3).

$$\frac{\partial \Phi}{\partial \tau} = \text{sign}(\phi)(1 - \|\nabla \Phi\|) \qquad (3)$$

where τ is a fictitious time. The sign function was defined in an identical manner to (Peng *et al.*, 1999). We solved (3) until steady state was reached. We then replaced ϕ by Φ. In practice, for each physical time step Δt, several iterations of the re-distancing algorithm are required to ensure the good distribution of level sets.

Remark :
In the validation test cases presented below, the re-distancing algorithm was used only for the Rider and Kothe test (Rider and Kothe, 1995).

Operator splitting algorithm

The interface tracking Level-Set method was then coupled with an operator splitting algorithm (Glowinski, 2003) to solve the Navier-Stokes incompressible equations (4).

$$\rho(\phi) \left(\frac{\partial \boldsymbol{u}}{\partial t} + (\boldsymbol{u} \cdot \nabla) \boldsymbol{u} \right) = -\nabla p + \nabla \cdot (2\mu(\phi)\boldsymbol{D})$$
$$- \sigma \kappa(\phi) \delta_\varepsilon(\phi) \nabla \phi + \rho(\phi) \boldsymbol{g} \qquad (4)$$
$$\nabla \cdot \boldsymbol{u} = 0$$

where $2\mu(\phi)\boldsymbol{D}$ is the stress tensor.
This method allowed us to split the problem into three sub-problems (advection, diffusion and degenerated Stokes) and to apply an appropriate solving method to each of them.
The viscous term was assembled implicitly in the linear system. For discretization of the divergence of the stress tensor

$$\nabla \cdot (2\mu(\phi)\boldsymbol{D}) = \begin{pmatrix} (\mu u_x)_x + \left(\mu \frac{u_x + v_y}{2} \right)_y \\ (\mu v_y)_y + \left(\mu \frac{u_y + v_x}{2} \right)_x \end{pmatrix} \qquad (5)$$

as well as for the curvature term, we used central differencing in identical manner to (Sussman *et al.*, 1994).

Continuum surface force (CSF) method

As said above, the fact of considering non-miscible fluids led us to the concept of interface. The separation layer stands for an interface through which physical properties of both fluids change drastically. To deal with the variation of properties at the interface, we defined density $\rho(\phi)$ and viscosity $\mu(\phi)$ according to the following equations (6).

$$\rho(\phi) = \rho_o + (\rho_w - \rho_o) H_\varepsilon(\phi)$$
$$\mu(\phi) = \mu_o + (\mu_w - \mu_o) H_\varepsilon(\phi) \qquad (6)$$

In the CSF approach (Brackbill *et al.*, 1992), the regularized form of the Heaviside function $H_\varepsilon(\phi)$ (7) is smoothed on two nodes approximately on each side of the interface.

$$H_\varepsilon(\phi) = \begin{cases} 0 & \phi < -\varepsilon \\ \frac{1}{2} \left(1 + \frac{\phi}{\varepsilon} + \frac{1}{\pi} \sin\left(\frac{\pi \phi}{\varepsilon} \right) \right) & |\phi| \leq \varepsilon \\ 1 & \phi > \varepsilon \end{cases} \qquad (7)$$

where ε is the smoothing parameter that defines the interface fictive thickness. The thickness is $\varepsilon = \frac{3}{2} \Delta x$, where Δx stands for the cell size.

The expression of the surface tension has been added as a source term in the momentum equation (first equation in (4)), following CSF model : $-\sigma \kappa(\phi) \delta_\varepsilon(\phi) \nabla \phi$. For this formulation the regularized Dirac function is defined as follows :

$$\delta_\varepsilon(\phi) = \frac{\mathrm{d} H_\varepsilon(\phi)}{\mathrm{d}\phi} = \begin{cases} 0 & |\phi| > \varepsilon \\ \frac{1}{2\varepsilon} \left(1 + \cos\left(\frac{\pi \phi}{\varepsilon} \right) \right) & |\phi| \leq \varepsilon \end{cases}$$

FINITE VOLUME METHOD

Discretization consists in dividing the computational domain in a finite number of volumes. A centered control volume, on which are integrated the equations to solve, is associated to each variable. A staggered grid is adopted to integrate the discretized form of the continuity momentum and Level-Set

transport equations. The velocity components are located at the cell faces whereas pressure and Level-Set function are cell centered.

We have chosen the TVD Lax-Wendroff scheme with a Superbee flux limiter (Sweby, 1984) for the spatial discretization of the advection term in the momentum equation.

When it comes to the convective terms in the transport equation (2) and in the Hamilton-Jacobi equation (3), a high order scheme to get suitable results is required. We therefore implemented the 5th order WENO scheme (Jiang and Shu, 1996).

Transient terms are discretized thanks to the explicit 1st order Euler scheme for the Navier-Stokes equations and thanks to the 2nd order Runge-Kutta scheme for the interface transport. The discrete time step Δt was calculated to satisfy the stability condition given in (Kang *et al.*, 2000).

The general algorithm to simulate a two-phase flow is given hereunder:

- Interface initialization with the Level-Set function ϕ.

- At each time step ($n = 1, 2, \ldots$) :

  1. Computation of the interface geometrical properties as well as density $\rho(\phi)$ and viscosity $\mu(\phi)$.

  2. Solution of Navier-Stokes with the operator splitting algorithm.
     - Solution of the advection-diffusion problem. Gravity and surface tension terms are computed here.
     - Solution of the degenerated Stokes problem (Poisson's equation for the variable coefficient (Liu *et al.*, 2000)).

  3. Solution of the transport equation for the Level-Set function using the velocity computed at step 2.
     - Application of the re-distancing algorithm.
     - Update of the Level-Set function ϕ.

Running a direct numerical simulation tool for a two-phase flow requires a considerable computation power. This is the reason why we developed our tool on the PELICANS platform [1].

PELICANS is a software platform developed by IRSN (Institut de Radioprotection et de Sureté Nucléaire). It enables the development of complex and powerful simulation tools thanks to an efficient parallelization.

Our numerical tool is already able to process 3D simulations.

VALIDATION TEST CASES

Single vortex problem

To validate our simulation tool, we ran lots of academic tests. In particular, we validated the interface transport with the Rider and Kothe configuration (Rider and Kothe, 1995) (stretching of a circle in a shear velocity field) that demonstrated how well the Level-Set method is able to handle the development of very thin filaments (Fig. 1).

If the grid is not accurate enough, the classical Level-Set method can show distorted results because of the mass loss. On the contrary, the Level-Set method combined with re-distancing algorithm tends to make the interface thicker because of a mass conservation problem.

---

[1] PELICANS `https://gforge.irsn.fr/gf/project/pelicans/`

(a)   *(b)*
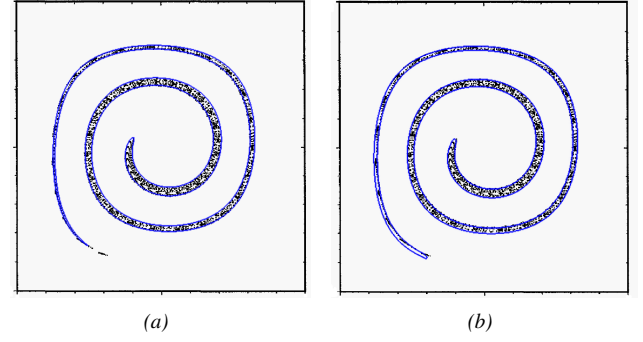
Fig. 1: Results for the single vortex problem on a 256×256 grid (blue line) with *(a)* Level-Set method, *(b)* Level-Set method with re-distancing algorithm. Analytical solution (black dots) (Rider and Kothe, 1995).

To illustrate this phenomenon, Fig. 2 shows the percentage of mass loss (Level-Set method) or gain (Level-Set method with re-distancing algorithm) as a function of the simulation time for different grids.

(a)

(b)
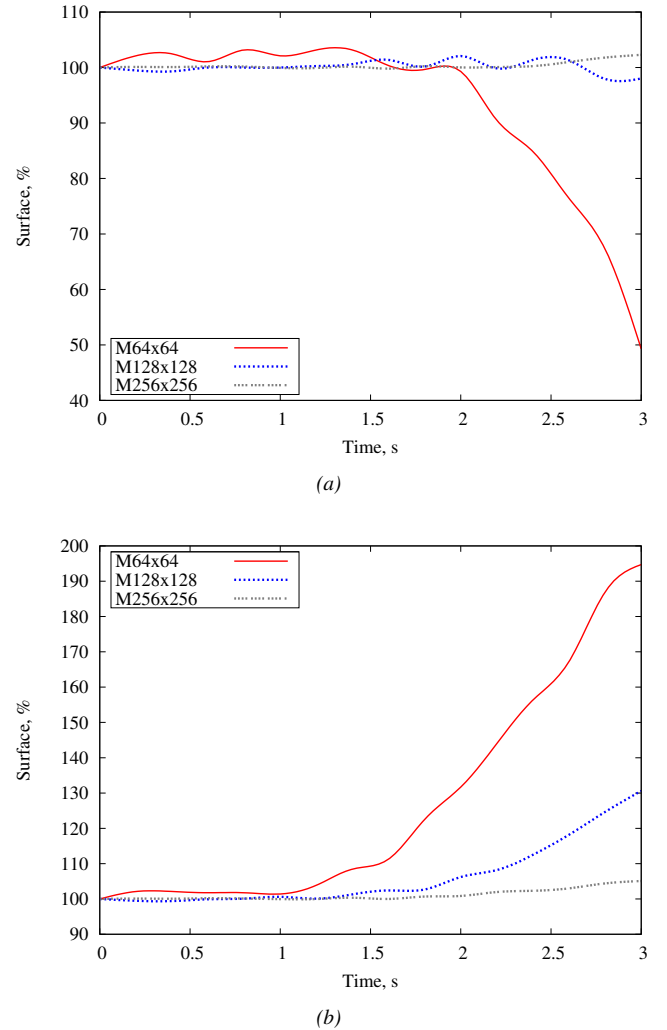
Fig. 2: Results of mass conservation for the single vortex problem *(a)* Level-Set method, *(b)* Level-Set method with re-distancing algorithm.

We observe that the coarser the grid, the more we have problem with the mass conservation.

The static bubble test

The static bubble simulation is the first academic test to verify the convergence and the consistency of numerical methods for the treatment of discontinuities at the interface. The bubble interface is a circle. Initially, the velocity field is null. In the absence of gravitational forces, the theoretical solution of this test case is given by the Laplace law.

Theoretically, no velocity field should arise during the simulation. Practically though, numerical errors, due to the scheme discretization and the treatment of discontinuities, create numerical velocities called spurious currents. They accumulate with time and tend to gather nearby the interface. In the static bubble simulation, capillary forces prevail. It is thus appropriate to verify if the surface tension term is correctly implemented. In this case, evaluation of the spurious currents amounts to evaluation of the error.

Numerous parameter choices exist in the literature for the static bubble simulation (Vincent and Caltagirone, 2004), (Desjardins *et al.*, 2008), (Smolianski, 2005), etc. We have tested several combinations of the parameters.

$\mathscr{L}a$	12	120	1200	12000	120000
$\mathscr{C}a$	$4.87 \cdot 10^{-5}$	$4.87 \cdot 10^{-5}$	$4.93 \cdot 10^{-5}$	$6.46 \cdot 10^{-5}$	$5.61 \cdot 10^{-5}$

Tab. 1: Dependence of parasitic currents on the Laplace number for a static bubble simulation on a 32×32 mesh.

Some error results are given in Tab. 1. They have been obtained with the (Desjardins *et al.*, 2008) parameters where

$$\mathscr{C}a = \frac{u\mu}{\sigma} \quad (8)$$

is the capillary number and

$$\mathscr{L}a = \frac{\sigma \rho D}{\mu^2} \quad (9)$$

the Laplace number. These results show that the capillary number $\mathscr{C}a$ remains quite constant despite the great changes of the Laplace number $\mathscr{L}a$.

The mesh convergence was studied with $\mathscr{L}a = 12000$ and is given in the Tab. 2.

Mesh	16×16	32×32	64×64	128×128
$\mathscr{C}a$	$7.99 \cdot 10^{-5}$	$3.22 \cdot 10^{-5}$	$1.51 \cdot 10^{-5}$	$5.54 \cdot 10^{-6}$

Tab. 2: Dependence of parasitic currents on mesh spacing for a static bubble simulation with $\mathscr{L}a = 12000$.

The here-above results allow us to conclude that the surface tension term is correctly implemented. The spurious currents, represented by the capillary number, remain very small and should not affect the accuracy of further simulations.

Poiseuille two-phase flow

We also used one-phase and two-phase Poiseuille tests (Vincent *et al.*, 2004a) to verify the implementation of the viscous term.

The Poiseuille two-phase flow is a horizontal stratified flow of two fluids in between two parallel walls. The gravity and the surface tension forces are neglected.

We have reached the stationary solution after a number of iterations starting from a zero velocity field. Fig. 3 shows the obtained velocity profile for the 31×31 grid compared with the theoretical solution.
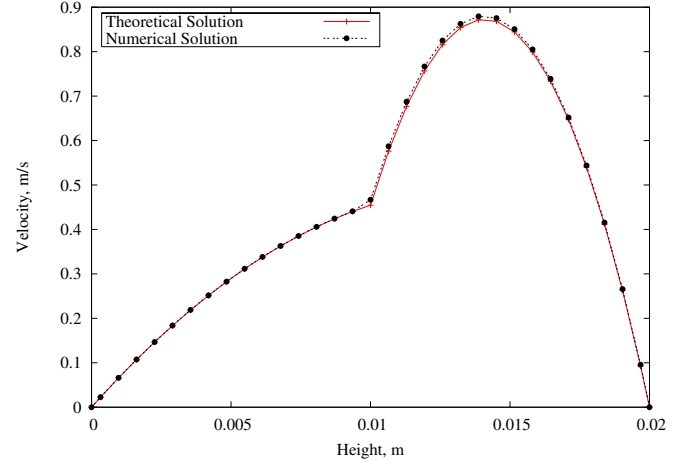
Fig. 3: Level-Set simulation of the two-phase flow in between parallel walls on a 31×31 grid. Comparison between numerical and theoretical solutions.

The mesh convergence is given in Tab. 3, where $\|e\|_\infty = \left\| u^{theo} - u^{num} \right\|_\infty$ and confirms the good results of Fig. 3.

Mesh	17×17	31×31	63×63
$\|e\|_\infty$	$2.74 \cdot 10^{-2}$	$1.22 \cdot 10^{-2}$	$4.57 \cdot 10^{-3}$

Tab. 3: Evolution of the error on velocity with different mesh spacing.

Validation tests conclusion

The results of the three academic tests presented above and the comparison with their analytic solution are satisfactory. They allow us to move forward with confidence to the application simulation : the phase inversion.

APPLICATION CASE : PHASE INVERSION IN A CLOSED BOX

After the validation process, we could finally carry out the application simulation.

We focused on the processes of coalescence and breakage in a two-phase flow. We considered the inversion phase test (Vincent *et al.*, 2004b), (Labourasse *et al.*, 2007) as the most appropriate to describe both phenomena at the same time. This test consists in defining an initial state where a light fluid (oil) is immersed in a heavier one (water) in a closed box.

The typical non-dimensional parameters of this simulation are the Reynolds number

$$\mathscr{R}e = \frac{\rho_w u L}{2\mu_w} \quad (10)$$

and the Weber number

$$\mathscr{W}e = \frac{\rho_w u^2 L}{2\sigma} \quad (11)$$
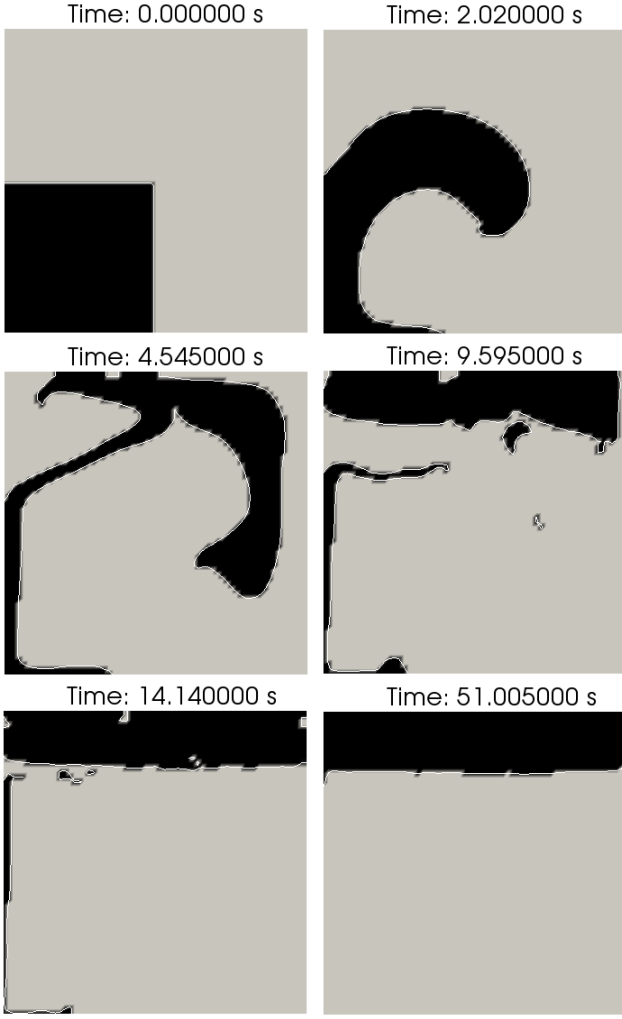
Fig. 4: Time evolution of the phase inversion problem (oil/water) in a closed box with $\mathscr{R}e = 550$, $\mathscr{W}e = 537$ and for 64×64 grid.

where $u = \dfrac{\rho_w - \rho_o}{\rho_w}\sqrt{\dfrac{gL}{2}}$ is the characteristic velocity.
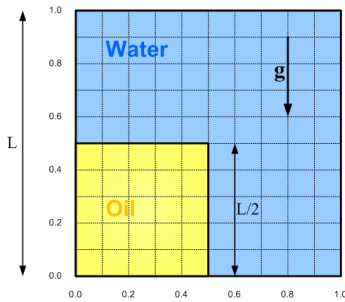
Fig. 5: Initial configuration of the oil/water phase inversion problem.

The two-phase flow is generated by means of a square oil inclusion (with a side equal to $L/2$) initially located in a bottom corner of a square cavity (with a side equal to $L = 1m$) filled of water (Fig. 5).

During the simulation, the light fluid (black in Fig. 6), under the gravity influence, tends to go up and distort. Some oil droplets escape in the continuous water phase, which illustrates the breakage phenomenon (Fig. 6 at time
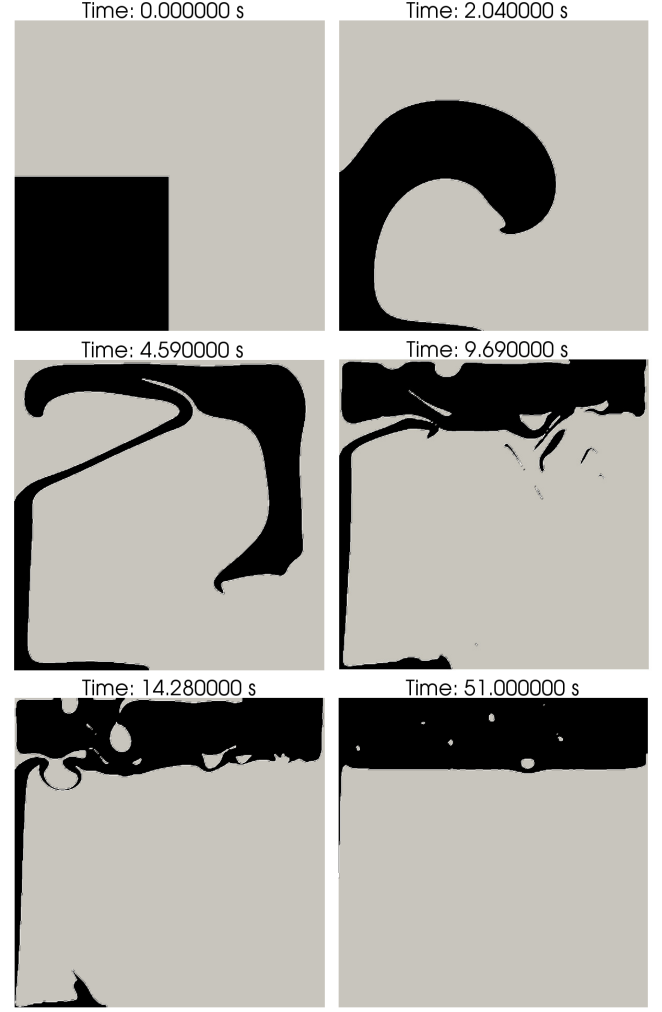
Fig. 6: Time evolution of the phase inversion problem (oil/water) in a closed box with $\mathscr{R}e = 550$, $\mathscr{W}e = 537$ and for 256×256 grid.

$T = 9.69s$). Then, oil reaches the top of the box enclosing some water drops. At final state, the coalescence effect has gathered most water drops and we obtain two continuous separated phases.

We carried out several simulations in the order to show the influence of the surface tension during the phase inversion test and to illustrate the accuracy of the simulations with regard to the grid size. We have thus tried the two sets of parameters reported in Tab. 4 and two different grids : 64×64 and 256×256.

Density, ρ_w [kg/m^3]	Viscosity, μ_w [Pa s]	Surface tension, σ [N/m]	$\mathscr{R}e$	$\mathscr{W}e$
1000	0.2	0.045	550	537
1000	0.2	1.0	550	24

Tab. 4: Reynolds and Weber number of the two simulated phase inversion problems.

Firstly, Fig. 4 and Fig. 6 illustrate the simulation results respectively for a 64×64 grid and a 256×256 grid and both
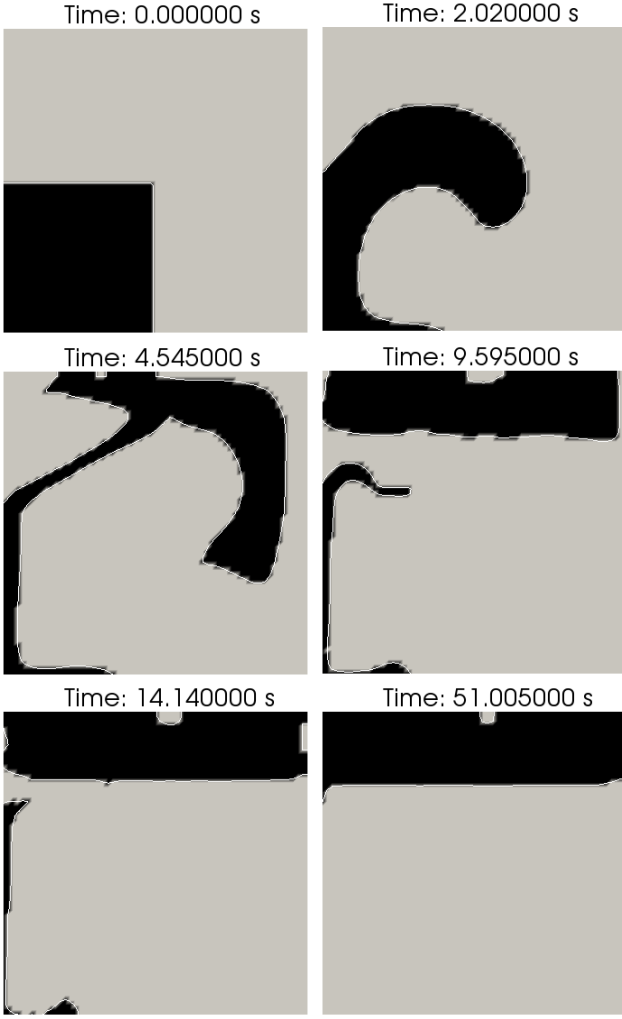
Fig. 7: Time evolution of the phase inversion problem (oil/water) in a closed box with $\mathcal{R}e = 550$, $\mathcal{W}e = 24$ and for 64×64 grid.

Fig. 9: Time evolution of the phase inversion problem (oil/water) in a closed box with $\mathcal{R}e = 550$, $\mathcal{W}e = 24$ and for 256×256 grid.

Fig. 8: Results of mass loss for the phase inversion problem $\mathcal{W}e = 537$.
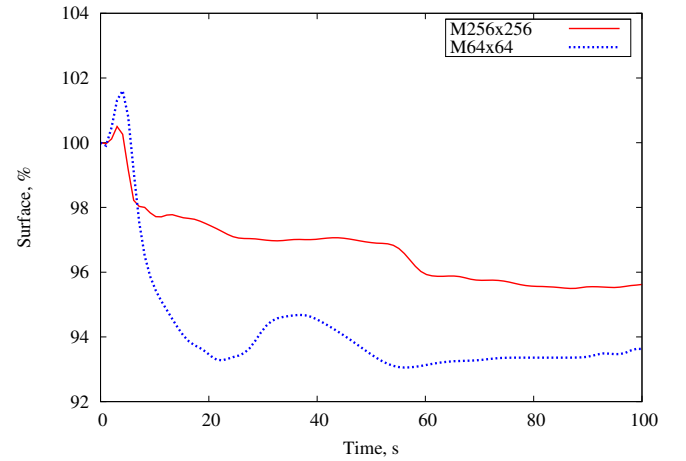
Fig. 10: Results of mass loss for the phase inversion problem $\mathcal{W}e = 24$.

for $\mathcal{R}e = 550$ and $\mathcal{W}e = 537$.

In the same manner, Fig. 7 and Fig. 9 illustrate the simulation results for the same grids but for $\mathcal{R}e = 550$ and $\mathcal{W}e = 24$.

The results of the second simulation ($\mathcal{W}e = 24$) correspond to what we expected. A high value of surface tension

strengthens the fluid cohesion and therefore limits the phenomenon of breakage during the phase inversion, meaning that drops are obviously larger when the surface tension is high.

Meanwhile, for both sets of parameters, we can see that the 64×64 grid simulation is not accurate enough to render the small scale phenomena during the inversion phase process.

Fig. 8 and Fig. 10 show the mass loss as a function of the physical time for both 64×64 and 256×256 grids and for respectively $\mathscr{W}e = 537$ and $\mathscr{W}e = 24$. For these simulations, the Level-Set method was used without re-distancing algorithm. We observe that the mass loss is greater for the 64×64 grid. For the 256×256 grid, we only loose 7 % (Fig. 8) and 4 % (Fig. 10) of the total initial mass, which is reasonable for further studies.

Remark :
We imposed no specific treatment at walls for the Level-Set function.

CONCLUSION

The results of two phase inversion tests have been presented in this paper. Each of them shows dynamics that look natural, and the comparison between the two of them, after modification of the Weber number, is consistent with physics principles.
We can conclude that the Level-Set method is relevant to track the interface in the context of direct numerical simulation of a two-phase flow. It allows us to consider the use of this method for the study of more complex physical processes.
The phase inversion that we have simulated can be described through three successive steps: the initial state with two continuous phases separated by a single interface, the dispersed phase and the final state with again two continuous phases. Thanks to this phase inversion problem we illustrated both breakage and coalescence phenomena.
These tests are thus a decisive step before we move toward the simulation of a real emulsion in which thousands of oil droplets are dispersed in a continuous water phase. The objective of such a simulation will be to evaluate the influence of the physical fluid properties on the time evolution of the separation front.

REFERENCES

BRACKBILL, J. *et al.* (1992). "A continuum method for modeling surface tension". *Journal of Computational Physics*, **100**, 335–354.

DESJARDINS, O. *et al.* (2008). "An accurate conservative level set/ghost fluid method for simulating turbulent atomization". *Journal of Computational Physics*, **227**, 8395–8416.

GLOWINSKI, R. (2003). *Numerical methods for fluids (Part 3)*. P.G. Ciarlet and J.L. Lions, North-Holland, Elsevier.

JIANG, G. and SHU, C. (1996). "Efficient implementation of Weighted ENO schemes". *Journal of Computational Physics*, **126**, 202–228.

KANG, M. *et al.* (2000). "A boundary condition capturing method for multiphase incompressible flow". *Journal of Scientific Computing*, 323–360.

LABOURASSE, E. *et al.* (2007). "Towards large eddy simulation of isothermal two-phase flows: Governing equations and a priori tests". *Journal of Multiphase Flow*, **33**, 1–39.

LIU, X.D. *et al.* (2000). "A boundary condition capturing method for Poisson's equation on irregular domains". *Journal of Computational Physics*, **160**, 151–178.

OSHER, S. and SETHIAN, J. (1988). "Fronts propagating with curvature-dependent speed : Algorithms based on Hamilton-Jacobi formulations". *Journal of Computational Physics*, **79**, 12–49.

PENG, D. *et al.* (1999). "A PDE-based fast local level set method". *Journal of Computational Physics*, **155**, 410–438.

RIDER, W. and KOTHE, D. (1995). "Stretching and tearing interface tracking methods". *12th AIAA Computational Fluid Dynamics Conference*. San Diego, California, United States.

SMOLIANSKI, A. (2005). "Finite-Element/Level-Set/Operator-Splitting (FELSOS) approach for computing two-fluid unsteady flows with free moving interfaces". *International Journal for Numerical Methods in Fluids*, **48**, 231–269.

SUSSMAN, M. *et al.* (1994). "A level set approach for computing solutions to incompressible two-phase flow". *Journal of Computational Physics*, **114**, 146–159.

SWEBY, P. (1984). "High resolution schemes using flux limiters for hyperbolic conservation laws". *SIAM Journal of Numerical Analysis*, **21**, 995–1105.

VINCENT, S. and CALTAGIRONE, J.P. (2004). "Test-case number 10: Parasitic currents induced by surface tension". *Multiphase Science and Technology*, **16**, 69–74.

VINCENT, S. *et al.* (2004a). "Test-case number 14: Poiseuille two-phase flow". *Multiphase Science and Technology*, **16**, 97–100.

VINCENT, S. *et al.* (2004b). "Test-case number 15: Phase inversion in a closed box". *Multiphase Science and Technology*, **16**, 101–104.

A MULTI-PURPOSE OPEN SOURCE CFD-DEM APPROACH

Christoph GONIVA[1*], Christoph KLOSS[1], Alice HAGER[1], Gijsbert WIERINK[3] and Stefan PIRKER[1,2]

[1] Christian Doppler Laboratory on Particulate Flow Modelling

[2] Institute of Fluid Mechanics and Heat Transfer

both Johannes Kepler University, Altenbergerstr. 69, 4040 Linz, Austria

[3] Research Group of Mechanical Process Technology and Recycling

Aalto University - School of Science and Technology, Espoo, Finland

* E-mail: christoph.goniva@jku.at

Keywords: CFD-DEM, fluidised bed, fictitious domain

ABSTRACT

In this paper we present a multi-purpose CFD-DEM framework to simulate coupled fluid-granular systems. The motion of the particles is resolved by means of the Discrete Element Method (DEM), and the Computational Fluid Dynamics (CFD) method is used to calculate the interstitial fluid flow. The focus of this paper is to show the ability of this coupled CFD-DEM framework to handle different scales and physical phenomena.

Firstly, with "approach A" we show the applicability of the coupling framework for flows, where the particle sizes are significantly smaller than the CFD grid. The motion of an incompressible fluid phase in the presence of a secondary particulate phase is then governed by a modified set of Navier-Stokes-Equations accounting for the volume fraction α occupied by the fluid, and a momentum exchange term $\mathbf{R}_{pf}$.

Secondly, with "approach B" we show the applicability of the coupling framework to the case of large particles and fine computational grids using the fictitious domain / immersed boundary method. In the first step the incompressible Navier-Stokes equations are solved over the whole domain. The next task is to correct the bodies' velocities in the affected cells (i.e. those cells, which are covered by the immersed bodies). Finally a correction-operation is applied to account for the divergence-free condition of the flow field.

Both approaches are successfully tested against analytics as well as experimental data. Application examples of the coupling are shown, ranging from to floatation and fluidised beds (approach A) to sedimentation (approach B).

Concluding, we show the versatility and applicability of the open source CFD-DEM framework (CFDEM, 2011) which is based on the DEM code LIGGGHTS (LIGGGHTS, 2011) and the open source CFD toolbox OpenFOAM® (OpenCFD Ltd., 2009). LIGGGHTS and an initial release of the CFD-DEM coupling are available for public download.

NOMENCLATURE

Greek Symbols

α volume fraction

ν kinematic viscosity

μ_c Coulomb friction coefficient

ρ density

τ stress tensor

Latin Symbols

c damping coefficient

C_d drag coefficient

d diameter

$\mathbf{R}$ momentum source term

$\mathbf{F}$ force exerted on a single particle

$\mathbf{g}$ gravity constant

k stiffness

$\mathbf{K}$ momentum exchange Coeff.

m mass

p pressure

$\mathbf{u}$ velocity

$\Delta \mathbf{u}_p$ relative particle velocity at contact point

Re   Reynolds number

V volume

$\mathbf{x}$ position

$\Delta \mathbf{x}$ particle overlap at contact point

Sub/superscripts

d   drag

f   fluid

n   normal to contact point

p   particle

t   tangential to contact point

INTRODUCTION

Many flows in nature as well as industry are particulate flows. During the last decades several strategies to numerically describe granular flows have been developed. Hereby two main approaches can be found: the continuum approach and the discrete approach.

In a continuum approach the multitude of particles is considered as an artificial continuum and is based on the solution of the underlying conservation equations using Computational Fluid Dynamics (CFD) techniques (Gidaspow 1992).

The discrete approach does not rely upon continuum mechanics. It rather describes the motion of each particle individually, with a special treatment of eventual collisions. The most important discrete model is the Discrete Element Method (DEM) and its derivatives.

In industrial application, single phase 'dry' granular flow rarely occurs. In the vast majority of natural or industrial processes concerning granular materials, a secondary fluid phase, such as air, is present and its effects like fluidization (aeration of particles by gas injection) play an important role. In some cases, such as pneumatic conveying, the fluid phase controls particle movement, but particle-particle interactions may still be an important issue that cannot be neglected, whereas in other applications, such as hopper discharge, the particle flow induces fluid flow.

A promising approach to model such coupled granular-fluid systems is a coupled CFD-DEM approach. Reviews on DEM and the CFD-DEM technique have been published by Zhu et al. (2007, 2008). Recently Kloss et al. (2009) presented a CFD-DEM coupling approach along with experimental validation for two commercial software packages for DEM and CFD respectively. Yet, due to shortcomings of the commercial software packages this approach is limited to shared memory machines.

In this paper we will describe a CFD-DEM approach based on the Open Source software packages OpenFOAM® (OpenCFD Ltd., 2009) and LIGGGHTS (LIGGGHTS, 2011). We show the versatility of this coupling routine and the applicability to a variety of particle laden flows. Therefore several applications along with validation work are presented. A basic version of this coupling is provided and maintained by the authors via a dedicated web page (CFDEM, 2011).

MODEL DESCRIPTION

DEM Method

The Discrete Element Method was introduced by Cundall and Strack (1979). A very brief description of the method will be provided in this section. Further details on the contact physics and implementation issues are available in the literature (e.g. Campbell (1990); Zhou et al. (1999); Bertrand et al. (2005)). In the frame of the DEM, all particles in the computational domain are tracked in a Lagrangian way, explicitly solving each particle's trajectory, based on the force balance

$$m_p \ \ddot{x}_p = F_{p,n} + F_{p,t} + F_{p,f} + F_{p,b} \ , \tag{1}$$

where $F_{p,n}$ is the normal particle-particle contact force, $F_{p,t}$ is the tangential particle-particle contact force. $F_{p,f}$ is the force that the fluid phase exerts on the particles, which will be described in further detail later. Other body forces like gravity, electrostatic or magnetic forces are subsumed into $F_{p,b}$. Similar balances are necessary

for the particles' angular momentum which are not stated here for the sake of shortness.

Each physical particle is mathematically represented by a sphere, another geometrically well-defined volume or a combination of them. The translational and angular accelerations of a sphere are based on the corresponding momentum balances. Generally, the particles are allowed to overlap slightly. The normal force tending to repulse the particles can then be deduced from this spatial overlap Δx_p and the normal relative velocity at the contact point, $\Delta u_{p,n}$.
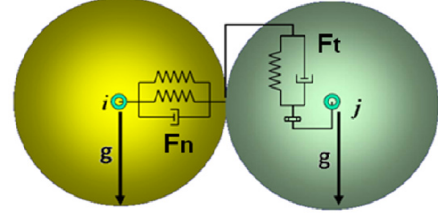
Figure 1: Simple spring-dashpot model

The simplest example is a linear spring-dashpot model, shown in Fig. 1. In the frame of this model, the normal force is given by

$$F_{p,n} = -k_n \Delta x_p + c_n \ \Delta u_{p,n} \ . \tag{2}$$

The magnitude of the tangential contact force can be written as:

$$F_{p,t} = min\left\{ \left| k_t \int_{t_{c,0}}^{t} \Delta u_{p,t} dt + c_t \Delta u_{p,t} \right|, \ \mu_c \ F_{p,n} \right\} . \tag{3}$$

where $\Delta u_{p,t}$ is the relative tangential velocity of the particles in contact. The integral term represents an incremental spring that stores energy from the relative tangential motion, representing the elastic tangential deformation of the particle surfaces that happened since the time when particles touched at $t = t_{c,0}$. The second part, the dashpot, accounts for the energy dissipation of the tangential contact. The magnitude of the tangential force is limited by the Coulomb frictional limit, where the particles begin to slide over each other.

The strength of the DEM lies in its ability to resolve the granular medium at the particle scale, thus allowing realistic contact force chains and giving rise to phenomena induced by particle geometry combined with relative particle motion, such as particle segregation by percolation. Thereby, it is able to capture many phenomena, describe dense and dilute particulate regimes, rapid flow as well as slow flow and equilibrium states or wave propagation within the granular material.

Thanks to advancing computational power, the DEM has become more and more accessible lately. On actual desktop computers, simulations of up to a million particles can be performed. On very large clusters, the trajectories of hundreds of millions of particles can be computed.

DEM solver "LIGGGHTS"

LIGGGHTS is an open source software for modelling granular material by means of the Discrete Element Method (LIGGGHTS, 2011). LIGGGHTS stands for

'LAMMPS Improved for General Granular and Granular Heat Transfer Simulations' and is based on LAMMPS ('Large Atomic and Molecular Massively Parallel Simulator'), a successful open source Molecular Dynamics code by Sandia National Laboratories for massively parallel computing on distributed memory machines (see Plimpton, 1995). LAMMPS is a parallel particle simulator at the atomic, meso, or continuum scale. If coarse-grained granular particles are simulated, this method is termed DEM as in the previous section. LAMMPS offers implementations for both linear (Hooke) and non-linear (Hertz) granular potentials. LIGGGHTS improves these features for granular simulations, comprising geometry import from CAD files and a moving mesh capability, features for particle insertion and packing, multiple contact models, non-spherical particle handling by means of the multi-sphere method, a bonded particle model, wall-stress analysis and wear prediction, and a 6 degree-of-freedom capability for rigid bodies. Both LIGGGHTS and LAMMPS run on single processors or in parallel using message-passing techniques and a spatial-decomposition of the simulation domain. The code is designed to be easy to modify or extend with new functionality.

Both LIGGGHTS and LAMMPS are distributed as open source codes under the terms of the GPL.

CFD-DEM Method - Approach A

This approach "A" is applicable to those cases where particle sizes are smaller than the computational grid, thus the particles are assumed to not completely fill a cell.

Fluid flow

The motion of an incompressible fluid phase in the presence of a secondary particulate phase is governed by a modified set of Navier-Stokes-Equations, which can be written as:

$$\frac{\partial \alpha_f}{\partial t} + \nabla \cdot \left(\alpha_f \mathbf{u_f} \right) = 0 \, , \tag{4}$$

$$\frac{\partial \left(\alpha_f \mathbf{u_f} \right)}{\partial t} + \nabla \cdot \left(\alpha_f \mathbf{u_f} \mathbf{u_f} \right) = -\alpha_f \nabla \frac{p}{\rho_f} - \mathbf{R_{pf}} + \nabla \cdot \tau \, . \tag{5}$$

Here, α_f is the volume fraction occupied by the fluid, ρ_f is its density, $\mathbf{u_f}$ its velocity, and $\tau = \nu_f \nabla \mathbf{u_f}$ is the stress tensor for the fluid phase. $\mathbf{R_{pf}}$ represents the momentum exchange with the particulate phase which is calculated for each cell where it is assembled from the particle based drag forces.

For solving above equations a pressure based solver using PISO pressure velocity coupling is used.

CFD-DEM coupling

The coupling routine consists of several steps:
 (1) The DEM solver calculates the particles positions and velocities.
 (2) The particles positions and velocities are passed to the CFD solver.
 (3) For each particle, the corresponding cell in the CFD mesh is determined.
 (4) For each cell, the particle volume fraction as well as a mean particle velocity is determined.
 (5) Based on the particle volume fraction, the fluid forces acting on each particle are calculated.
 (6) Particle-fluid momentum exchange terms are assembled from particle based forces by ensemble averaging over all particles in a CFD cell.
 (7) The fluid forces acting on each particle are calculated and sent to the DEM solver and used within the next time step.
 (8) The CFD solver calculates the fluid velocity taking into account local volume fraction and momentum exchange.
 (9) Additional equations such as species concentration can optionally be evaluated.
 (10) The routine is repeated from (1).

Usually DEM time steps need to be set an order of magnitude smaller than CFD time steps due to high particle collision dynamics and requirements on maximum particle overlap for particle collision modelling when using soft-sphere approach. As the coupling routine on one hand and extremely small time steps for the CFD calculation on the other hand would really slow down the simulation, the fluid-particle forces on DEM side are kept constant in between the coupling steps. This approach can save computational time, as coupling interval can be decoupled from usually short DEM time step sizes. Needless to say that this is limited and as a rule of thumb at least every 5-200 DEM time steps a coupling time step is required.

Additionally it might be desirable to use CFD time steps smaller than the coupling interval, thus either reduce the computation time spent on calculation of coupling properties or allow the CFD side to better resolve fluid flow (or other properties such as radiation and temperature). For those cases it is possible to temporally under-relax the momentum exchange fields on the CFD side. This helps to reduce discontinuities in the exchange fields and thus improves convergence behaviour.

From the above list of calculations necessary to realise the coupling it becomes obvious that for the calculation of the volume fraction (Step 4) it is necessary to interpolate the particles' volumes, a Lagrangian property, from the DEM side to the volume fraction field, which is defined on the fixed Eulerian grid of the CFD simulation.
A very simplified approach for this transformation is to simply sum up the volume of those particles whose centres are located in a CFD cell. We will further refer to this approach as "centered" volume fraction calculation. This approach can lead to erroneous results due to artificially inhomogeneous volume fraction field when particle size approaches cell size.
Another approach, further referred to as "divided" volume fraction calculation, is to resolve a particle by a series of distributed marker points and thus evenly

apportion the particle's volume to all cells being (partly) covered. This on one hand helps to smoothen exchange fields without artificially enlarging spatial influence of a particle, but on the other hand its applicability is limited. When particles completely cover a cell and thus volume fraction approaches one, this method is no longer applicable.

One possible approach to overcome this problem was proposed by Link et al. (2005) where the spatial region of influence is artificially enlarged and thus exchange fields are smeared out. Being very efficient for structured grids this approach is hardly applicable on arbitrary unstructured grids used within this study.

A very similar approach was tested by the authors. It will further be referred as "big particle" volume fraction calculation. For this approach the particles are treated as essentially bigger, but porous particles having the original volume. The determination of the cells covered by the particle can then here be done recursively and in a way which is suitable also for arbitrary structured grids.

Once the particle volume fraction is calculated it is possible to evaluate each particle's contribution to particle-fluid momentum exchange which is mostly established by means of a drag force depending on the granular volume fraction.

For numerical reasons the momentum exchange term is split-up into an implicit and an explicit term using the cell-based ensemble averaged particle velocity $\langle \mathbf{u_p} \rangle$:

$$\mathbf{R_{pf}} = \mathbf{K_{pf}}\left(\mathbf{u_f} - \langle \mathbf{u_p} \rangle\right), \tag{6}$$

where

$$\mathbf{K_{pf}} = \frac{\left|\sum_i \mathbf{F_d}\right|}{V_{cell} \cdot \left|\mathbf{u_f} - \langle \mathbf{u_p} \rangle\right|}. \tag{7}$$

For the calculation of $\mathbf{K_{pf}}$ many different drag correlations have been proposed during the recent years (Zhu et al. (2007) Tsuji et al. (2008) and Kafui et al. (2002)). A widely used model was proposed by Di Felice (see Zhu et al. (2007)):

$$\mathbf{F_d} = \frac{1}{2}\rho_f\left(\mathbf{u_f} - \mathbf{u_p}\right)\left|\mathbf{u_f} - \mathbf{u_p}\right|C_d\frac{d_p^2\pi}{4}\alpha_f^{(2-\chi)}, \tag{8}$$

$$C_d = \left(0.63 + \frac{4.8}{\sqrt{\mathrm{Re}_p}}\right)^2, \tag{9}$$

$$\chi = 3.7 - 0.65\exp\left[-\frac{\left(1.5 - \log_{10}\mathrm{Re}_p\right)^2}{2}\right], \tag{10}$$

$$\mathrm{Re}_p = \frac{\rho_f d_p \alpha_f\left|\mathbf{u_f} - \mathbf{u_p}\right|}{\mu_f}. \tag{11}$$

An alternative drag model, for mono-disperse particles, which gives very similar results was introduced by Gidaspow (1992) which is a combination of the Wen and Yu (1966) model and the Ergun (1952) equation.

For $\alpha_f > 0.8$ momentum exchange is calculated as:

$$\mathbf{K_{pf}} = \frac{3}{4}C_d\frac{\alpha_f\left(1 - \alpha_f\right)\left|\mathbf{u_f} - \mathbf{u_p}\right|}{d_p}\alpha_f^{-2.65}, \tag{12}$$

$$C_d = \frac{24}{\alpha_f\,\mathrm{Re}_p}\left[1 + 0.15\left(\alpha_f\,\mathrm{Re}_p\right)^{0.687}\right], \tag{13}$$

$$\mathrm{Re}_p = \frac{\left|\mathbf{u_f} - \mathbf{u_p}\right|d_p}{\nu_f}, \tag{14}$$

Whereas for $\alpha_f \leq 0.8$ the Ergun equation is used:

$$\mathbf{K_{pf}} = 150\frac{\left(1 - \alpha_f\right)^2\nu_f}{\alpha_f d_p^2} + 1.75\frac{\left(1 - \alpha_f\right)\left|\mathbf{u_f} - \mathbf{u_p}\right|}{d_p}. \tag{15}$$

More recently a drag relation based on lattice Boltzmann simulations was proposed by Koch and Hill (2001):

$$\mathbf{F_d} = \frac{V_p\beta}{\varepsilon_p}\left(\mathbf{u_f} - \mathbf{u_p}\right), \tag{16}$$

$$\beta = \frac{18\mu\left(1 - \alpha_f\right)\alpha_f^2}{d_p^2}\left(F_0\left(\alpha_p\right) + \frac{1}{2}F_3\left(\alpha_p\right)\mathrm{Re}_p\right), \tag{17}$$

with $F_0\left(\alpha_p\right)$ being defined for $\alpha_p = 1 - \alpha_f < 0.4$

$$F_0\left(\alpha_p\right) = \frac{1 + 3\sqrt{\frac{\alpha_p}{2}} + \frac{135}{64}\alpha_p\ln\left(\alpha_p\right) + 16.14\alpha_p}{1 + 0.681\alpha_p - 8.48\alpha_p^2 + 8.16\alpha_p^3}, \tag{18}$$

and for $\alpha_f \geq 0.4$

$$F_0\left(\alpha_p\right) = \frac{10\alpha_p}{\left(1 - \alpha_p\right)^3}, \tag{19}$$

further

$$F_3\left(\alpha_p\right) = 0.0673 + 0.212\alpha_p + \frac{0.0232}{\left(1 - \alpha_p\right)^5}. \tag{20}$$

Besides the drag force resulting from a relative velocity between the particle and the fluid, other forces, neglected in this work, may be relevant too. These may stem from the pressure gradient in the flow field (pressure force), from particle rotation (Magnus force), particle acceleration (virtual mass force) or a fluid velocity gradient leading to shear (Saffman force). The modular implementation of the CFD-DEM coupling allows to easily implement additional forces and superpose all forces acting on a particle. An example for additional particle forces will be presented in the example on floatation modelling.

CFD-DEM Method - Approach B

This approach "B" is applicable to those cases where particle sizes are bigger than the computational grid, thus the particles are assumed to cover at least ten cells. In this approach the particulate phase is represented by a fictitious domain method (Patankar et al., 2000) where only one velocity and pressure field for both phases exists. Those regions covered by a particle have the same velocity as the particle itself.
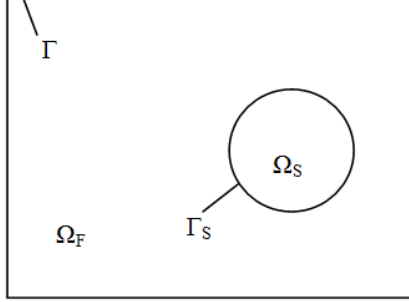
Figure 1: Sketch of particle domain and fluid domain.

Fluid flow

The governing equations of the fluid domain are the incompressible Navier-Stokes equations which guarantee the conservation of momentum and mass, combined with boundary and initial conditions. These equations hold on the whole domain $\Omega = \Omega_F + \Omega_S$. The equations of motion for the particles and the surrounding fluid as well as the boundary and initial conditions can be summarised as follows (Shirgaonkar 2008):

$$\rho_f \frac{\partial \mathbf{u_f}}{\partial t} + \rho_f (\mathbf{u_f} \cdot \nabla)\mathbf{u_f} = -\nabla p + \mu \nabla^2 \mathbf{u_f} \text{ in } \Omega_F, \quad (21)$$

$$\nabla \cdot \mathbf{u_f} = 0 \text{ in } \Omega_F, \quad (22)$$

$$\mathbf{u_f} = \mathbf{u}_\Gamma \text{ on } \Gamma, \quad (23)$$

$$\mathbf{u_f} = \mathbf{u_p} \quad \text{and} \quad \sigma \cdot \hat{\mathbf{n}} = t_{\Gamma_S} \text{ on } \Gamma_S, \quad (24)$$

$$\mathbf{u_f}(x, t = 0) = \mathbf{u}_0(x) \text{ in } \Omega_F. \quad (25)$$

The time-discretized form of (Eqn. 21) is given by

$$\rho_f \frac{\hat{\mathbf{u}}_\mathbf{f} - \mathbf{u_f}^{n-1}}{\Delta t} + \rho_f(\mathbf{u_f}^{n-1} \cdot \nabla)\mathbf{u_f}^{n-1} = -\nabla \tilde{p} + \mu \nabla^2 \mathbf{u_f}^{n-1}. \quad (26)$$

Here $\tilde{p}$ denotes an estimated value for the pressure, which will later on be corrected (PISO), $\hat{\mathbf{u}}_\mathbf{f}$ is the interim solution, $\mathbf{u_f}^{n-1}$ is the solution at the previous time step. For correcting $\tilde{p}$ one uses a Poisson-equation for the pressure.
The next step consists of correcting the velocity in the particle domain to the velocity taken from the DEM-data or an input-file, which yields the current velocity $\tilde{\mathbf{u}}_\mathbf{f}$. Technically speaking this is equivalent to adding a

force term f to the Navier-Stokes equations, which fulfils

$$\rho_f \frac{(\tilde{\mathbf{u}}_\mathbf{f} - \hat{\mathbf{u}}_\mathbf{f})}{\Delta t} = f. \quad (27)$$

The divergence-free condition for the velocity over the whole domain is violated now. In order to fix this, the following correction-operation is applied to the velocity:

$$\mathbf{u_f}^n = \tilde{\mathbf{u}}_\mathbf{f} - \nabla \phi. \quad (28)$$

Here $\mathbf{u_f}^n$ is the final solution, ϕ a scalar field. As one wants to end up with $\nabla \cdot \mathbf{u_f}^n = 0$, we get the following Poisson equation for ϕ:

$$\nabla^2 \phi = \nabla \cdot \tilde{\mathbf{u}}_\mathbf{f}. \quad (29)$$

Correcting the velocity as described above is equivalent to adding an additional force-term to the Navier-Stokes equations.

CFD-DEM coupling

Generally the force on a particle is given by

$$\int_{\Omega_S} \eta(x, y, z, t) dV = \int_\Omega \eta(x, y, z, t) \xi(x, y, z, t) dV, \quad (30)$$

where

$$\xi = \begin{cases} 1 & \text{if } (x, y, z) \in \Omega_S \\ 0 & \text{else} \end{cases} \quad (31)$$

η consists of the viscous component

$$\eta = \rho v_f \nabla^2 \mathbf{u_f}^{n-1}, \quad (32)$$

and the pressure-component

$$\eta = -\nabla p^{n-1}. \quad (33)$$

The coupling routine consists of several steps:
(1) The DEM solver calculates the particles positions and velocities.
(2) The particles positions and velocities are passed to the CFD solver.
(3) A first fluid flow field is calculated.
(4) For each particle, the corresponding cells in the CFD mesh are determined.
(5) Particle velocity is corrected in those cells covered by the particle.
(6) The fluid forces acting on each particle are calculated and sent to the DEM solver and used within the next time step.
(7) The flow field is corrected to be divergence free.
(8) Additional equations such as species concentration can optionally be evaluated.
(9) The routine is repeated from (1).

CFD-DEM solver

The method presented here treats the fluid and particle calculations in two strictly separated codes. This allows for taking advantage of independent code development on either side.

The interaction is realised by exchange fields being evaluated in a predefined time interval, where the codes work in a sequential manner. Both the CFD and the DEM code do their calculations in parallel using Message Passing Interface (MPI) parallelisation. Also data exchange between the codes is realised using MPI functionality.

The CFD-DEM approach described above was implemented within an open source environment. The DEM simulations are conducted by the DEM code LIGGGHTS (LIGGGHTS, 2011) and the CFD simulations are conducted by a solver realised within the open source framework of OpenFOAM® (OpenCFD Ltd., 2009). The coupling routines are collected in library providing a modular framework for CFD-DEM coupling with the C++ codes LIGGGHTS and OpenFOAM®. Both, a selection of coupling routines as well as example solvers are provided at a dedicated web page maintained by the authors (www.cfdem.com).

RESULTS

In this section the CFD-DEM model approaches "A" and "B" described in the previous sections are applied to a selection of test cases.

Single spout fluid bed

This test case was originally investigated by Link et al. (2005) and has been excessively investigated during the recent years, e.g. Buijtenen et al. (2011). It is therefore an ideal candidate for checking the CFD-DEM framework using approach A, described in this paper. For volume fraction calculation the "divided" approach was used. The fluid particle momentum exchange is calculated applying the drag correlation of Koch and Hill (2001).

Geometry

The geometry of the single spout fluidized bed is depicted in Fig. 2, the Numerical settings are listed in Table 1.
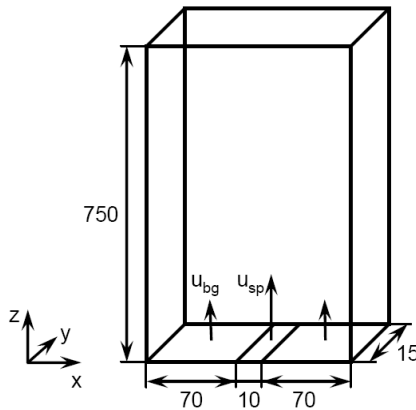
Figure 2: Sketch of the pseudo 2-D spout fluidized bed geometry.

Table 1: Numerical settings.

Property	Value	Unit
N_x	29	-
N_y	2	-
N_z	250	-
t_{end}	20	s
N_p	2.45e4	-

Material properties

The physical and model parameters of the glass beads and the fluid are given in Table 2.

Table 2: Material properties / boundary conditions.

Property	Value	Unit
material	glass/air	-
d_p	3.0	mm
ρ_f	1	kg/m^3
ρ_p	2505	kg/m^3
ν_f	1.8e-5	m^2/s
e_{p-p}	0.97	-
e_{p-w}	0.97	-
μ_{p-p}	0.1	-
μ_{p-w}	0.1	-
u_{bg}	1.5	m/s
u_{sp}	30	m/s

Where e denotes the coefficient of restitution for particle-particle and particle-wall contact. Accordingly, μ denotes the coefficient of friction.

In Figure 3 the time averaged vertical flux of the granular phase at z=0.13 is depicted. The results obtained with the model presented in this paper are in very good accordance to data published by Link et al. (2005). Both simulation results slightly differ from experimental data.
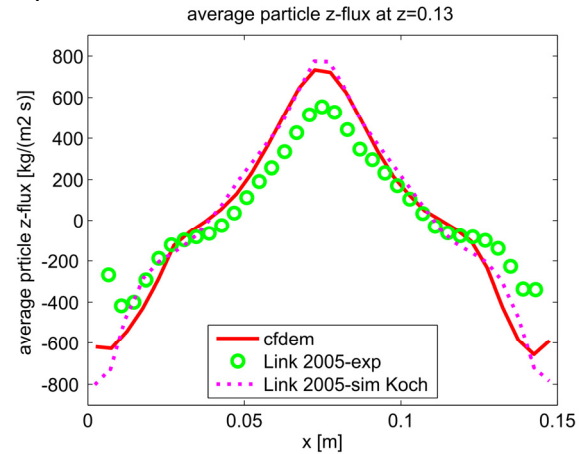
Figure 3: Vertical time averaged flux at z=0.13. Results compared to simulation and experimental data achieved by Link et al. 2005.

Settling of two discs

In this test case the detailed motion and the flow around of two settling disks is calculated using the CFD-DEM framework (approach B). In literature (Patankar et al. (2000)) three states have been defined, namely drafting, kissing and tumbling. The computational domain is a 2D box with 2 x 6 cm and fixed wall boundary conditions. Material properties and particle staring positions x_p are set according to Table 3.

Table 3: Material properties.

Property	Value	Unit
d_p	0.25	cm
ρ_p	1.5	g/cm^3
ρ_f	1	g/cm^3
ν_f	0.1	cm^2/s
x_{p1}	(1, 4.5)	cm
x_{p2}	(1, 5)	cm
g	(0, 981)	cm^2/s

In Figure 4 this behaviour and the fluid flow is illustrated. Fig. 5 and 6 show the position of the two particles (y-direction) as well as the settling velocities. First, the two particles settle without influencing each other. As soon as the following particle reaches the wake of the leading particle, it accelerates (drafting). At t ~ 0.15s, the two particles collide (kissing). Until this point the behaviour of the particles is predictable, only in the last stadium, the so called tumbling, a strict prediction is not possible.
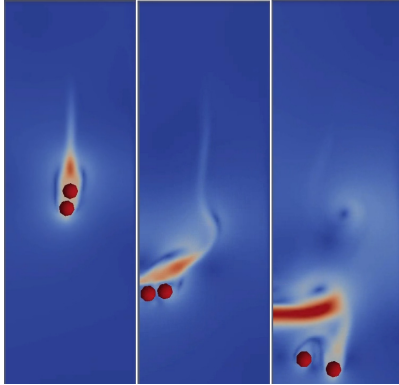
Figure 4: Drafting (left), kissing (middle), tumbling (right), appellation according to Patankar et al. (2000).
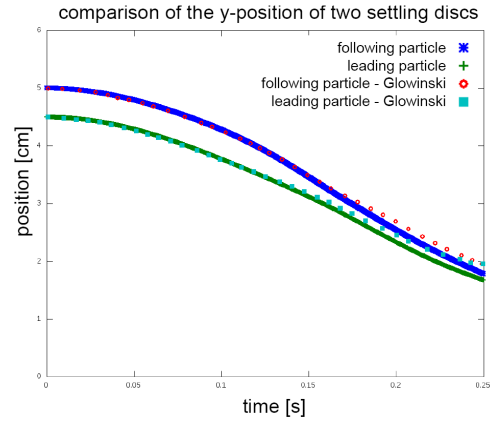
Figure 5: Simulated y-position of two settling discs, compared to data from Glowinski et al. (2000).
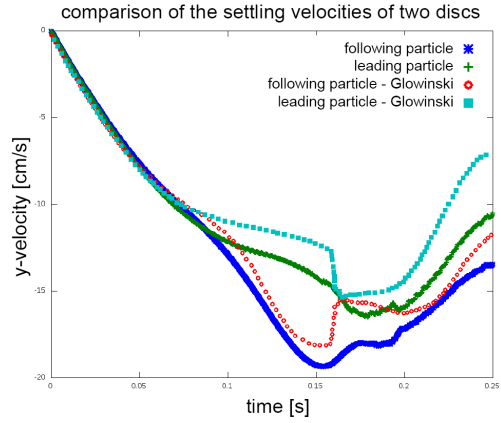
Figure 6: Simulated y-velocity of two settling discs, compared to data from Glowinski et al. (2000).

Floatation

Mineral froth flotation is a widely used method for beneficiation of primary as well as secondary resources. Flotation is a physico-chemical separation process where surface chemical properties of suspended bubbles and particles are exploited to generate bubble-particle aggregates. Stable aggregates rise to the surface of the flotation cell or column and the target mineral can be recovered from the froth concentrate. The study of bubble-particle interaction forms the very basis of flotation science and research, as kinetics at this scale determine flotation efficiency. Momentum coupling and unification of physical and chemical forces are key parts of detailed modelling of bubble-particle interaction. (Wierink and Heiskanen, 2010a; Wierink and Heiskanen, 2010b) In this section we show that this can be achieved using the CFDEM modelling framework.

After sufficient contact time between bubble and particle, attachment forces can cause film rupture and three-phase contact to form (Dobby and Finch, 1987; Schulze, 1983). The main attachment forces are the capillary and hydrodynamic forces and can be evaluated based on physic-chemical properties of the system, such as surface tension and contact angle (see Fig. 1) (Schulze, 1983).
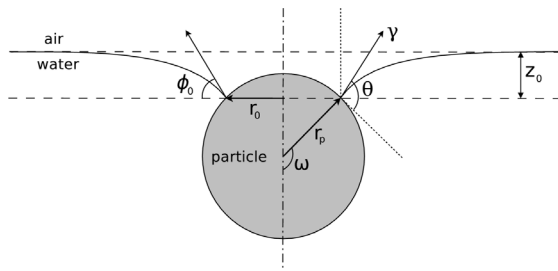
Figure 7: A spherical particle attached to a gas-liquid interface, with contact angle θ and particle radius r_p (after Schulze, 1983).

The preliminary results of simulation of bubble-particle interaction using CFDEM is shown in Fig. 8. The model approach A, extended for two phase flow (Volume of Fluid method) is used. The contact angle is 66°, surface tension is 70 mN/m, particle density and diameter are 3000 kg/m3 and 100 μm, respectively. The results show that computation of detailed three-phase interaction is feasible with the CFD-DEM approach. The structure of the attachment forces may be improved, however, the modelling framework proves stable and to yield promising first results.
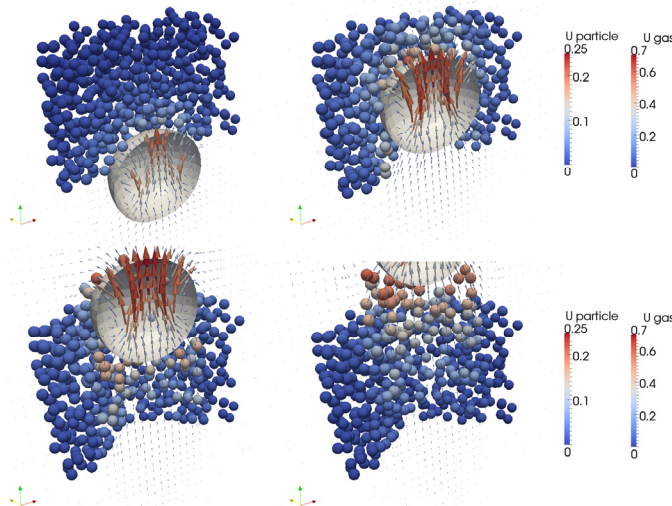
Figure 8: 1mm air bubble rising in water with 1000 particles of 100μm (clipped at the bubble centre), Tree phase, 4-way coupled flow including three phase contact model (particle-gas-water).

CONCLUSION

The diversity of fluid-granular processes demands a variety of different solution techniques to picture them by means of numerical simulations. The flexible and modular approach of the CFD-DEM framework (CFDEM (2011)) presented in this paper allows its application to a wide range of problems. First validation cases give very promising results. Due to the underlying codes for the CFD and DEM calculations the coupling can be run in parallel on distributed memory clusters. Further validation work as well as model development is planned by the authors. A basic version of the coupling framework presented here is available for download.

REFERENCES

BERTRAND, F., LECLAIRE, L.-A. and LEVECQUE, G. (2005): "DEM-based models for the mixing of granular materials", *Chemical Engineering Science*, **60**, 2517 – 2531

van BUIJTENEN, M. S., van DIJK, W. J., DEEN, N. G., KUIPERS, J.A.M., LEADBEATER, T. and PARKER, D.J. (2011) ,"Numerical and experimental study on multiple-spout fluidized beds", *Chemical Engineering Science*, doi:10.1016/j.ces.2011.02.055

CAMPBELL, C. S. (1990): "Rapid Granular Flows", *Annual Rev. Fluid Mech.*, **22**, 57-92.

CFDEM (2011). "CFDEM- Open Source CFD, DEM and CFD". URL http://www.cfdem.com.

CUNDALL, P.A. and STRACK, O.D. (1979): "A discrete numerical model for granular assemblies." *Geotechnique*, **21**, 47-65

DOBBY, G.S. and FINCH, J.A. (1987), "Particle size dependence in flotation derived from a fundamental model of the capture process". Int. J. Miner. Process. 21, 241-260.

ENWALD, H., PEIRANO, E., ALMSTEDT, E. (1996): "Eulerian Two-Phase Flow Theory Applied to Fluidization." *Int. J. of Multiphase Flow*, **22**, 21-66

ERGUN, S. (1952): "Fluid Flow through Packed Columns." *Chem. Eng. Prog.*, 48(**2**):89

GIDASPOW, D., BEZBURUAH, R., DING, J. (1992): "Hydrodynamics of Circulating Fluidized Beds, Kinetic Theory Approach", in Fluidization VII, *Proceedings of the 7th Engineering Foundation Conference on Fluidization*

GLOWINSKI, R., PAN, T.-W., HESLA, T.I., JOSEPH, D.D. and PERIAUX, J., (2000): "A fictitious domain approach to the direct numerical simulation of incompressible viscous flow past moving rigid bodies: applicatioin to particulate flow.", *J. Comput. Phys.*, **169**, 363-426

GONIVA, C., KLOSS, C., and PIRKER, S. (2009), Towards fast parallel CFD-DEM: An Open-Source Perspective, *Proc. of Open Source CFD International Conference*, Barcelona, November 12-13.

GONIVA, C., KLOSS, C., HAGER, A. and PIRKER, S. (2010), An Open Source CFD-DEM Perspective, *Proc. of OpenFOAM Workshop, Gothenburg*, June 22.- 24.

KAFUI, K.D., THORNTON, C., ADAMS, M. J. (2002): "Discrete particle-continuum modelling of gas–solid fluidised beds", *Chemical Engineering Science*, 57, 2395 – 2410

KLOSS, C., GONIVA, C., AICHINGER, G. and PIRKER, S. (2009): "Comprehensive DEM-DPM-CFD simulations: Model synthesis, experimental validation and scalability", *Proceedings Seventh International Conference on CFD in the Minerals and Process Industries*, CSIRO, Melbourne, Australia, December 9-11

C. KLOSS, C. GONIVA, S. PIRKER (2010): "Open Source DEM and CFD-DEM with LIGGGHTS and OpenFOAM®", *Proc. Open Source CFD International Conference* , Munich, 4th - 5th November 2010

KOCH, D.L., HILL, R. J. (2001): "Inertial effects in suspension and porous-media flows.", Annual Review of Fluid Mechanics, 33, 619

KUNII, D., LEVENSPIEL, O. (1992): "Fluidization Engineering", 2nd ed., *Butterworth-Heinemann series in chemical engineering* ISBN 0-409-90233-0

LIGGGHTS (2011). "LAMMPS Improved for General Granular and Granular Heat Transfer simulations". URL http://www.liggghts.com.

LINK, J.M. and CUYPERS, L.A. and DEEN, N.G. and KUIPERS, J.A.M. (2005): "Flow regimes in a spout-fluid bed: a combined experimental and simulation study.", *Chemical Engineering Science*, 60 (13). pp. 3425-3442. ISSN 0009-2509

MATUTTIS, H.G., LUDING S. and HERRMANN, H.J. (2000): "Discrete element simulations of dense packings and heaps made of spherical and non-spherical particles", *Powder Technology*, **109**, 278–292

OpenCFD Ltd. (2009). "OpenFOAM - The open source CFD toolbox". URL http://www.openfoam.com.

PATANKAR, N.A., SINGH, P., JOSEPH, D.D., GLOWINSKI, R. and PAN, T.-W., (2000): "A new formulation of the distributed lagrange multiplier/ fictitious domain method for particulate flows.", *Int. J. Multiphase Flow*, **26**, 1509-1524

PLIMPTON, S. J. (1995), "Fast Parallel Algorithms for Short-Range Molecular Dynamics", J. Comp. Phys., 117, 1-19 (LAMMPS homepage: http://lammps.sandia.gov).

SANDIA (2009): "LAMMPS User Manual", http://lammps.sandia.gov/doc/Manual.html, Sandia National Laboratories, USA

SCHULZE, H.J. (1983). Physico-chemical elementary processes in flotation, vol. 4 of *Developments in Mineral Processing*. Elsevier, Amsterdam, The Netherlands.

SHIRGAONKAR, A.A., MACIVER, M.A. and PATANKAR, N.A., (2008): "A new mathematical formulation and fast algorithm for fully resolved simulation of self-propulsion", *J. Comput. Phys.*, **160**, 2366-2390

WEN, C.-Y. and YU, Y. H. (1966), "Mechanics of Fluidization", *Chem. Eng. Prog. Symp.Series*, **62**:100

TSUJI, T., YABUMOTO, K. and TANAKA, T. (2008): "Spontaneous structures in three-dimensional bubbling gas-fluidized bed by parallel DEM–CFD coupling simulation", *Powder Technology*, **184**, 132–140

WIERINK, G.A., HEISKANEN, K. (2008), "Momentum coupling in flotation modelling". In: *Proc. Computational Modelling '08*, Cape Town, South Africa, November 11-12, 2008.

WIERINK, G.A. and HEISKANEN, K. (2010a), "Modelling bubble-particle interaction with dynamic surface tension". *Minerals Engineering* **23**(11-13), 973-978.

WIERINK, G. and HEISKANEN, K. (2010b), "On kinetic coupling in meso-scale phenomena in mineral froth flotation". In: *Proc. XXV IMPC*, Brisbane, Australia, 6-10 September 2010, pp. 3395-3401.

ZHOU, Y.C., WRIGHT, B.D., YANG, R.Y., XU, B.H., YU, A.B. (1999): "Rolling friction in the dynamic simulation of sandpile formation", *Physica A*, **269**, 536-553

ZHU, H.P., ZHOU, Z.Y., YANG, R.Y., YU, A.B. (2007): "Discrete particle simulation of particulate systems: Theoretical developments", *Chemical Engineering Science*, **62**, Issue 13, July 2007, Pages 3378-3396

ZHU, H.P., ZHOU, Z.Y and YANG, R.Y., YU, A.B. (2008): "Discrete particle simulation of particulate systems: A review of major applications and findings", Chemical Engineering Science, 63, 5728-5770

8th International Conference on CFD in Oil & Gas, Metallurgical and Process Industries
SINTEF/NTNU, Trondheim Norway
21-23 June 2011

CFD11-142

APPLICATION OF A COMBINED CFD/EXPERIMENTAL APPROACH TO QUANTIFYING EROSION RATE

Christopher B. SOLNORDAL[1]*** , **Chong Y. WONG**[2]***

[1] CSIRO Mathematics, Informatics and Statistics, Clayton, Victoria, AUSTRALIA

[2] CSIRO Process Science and Engineering, Highett, Victoria, AUSTRALIA

* E-mail: chris.solnordal@csiro.au

ABSTRACT

A new method for predicting erosion rate involves measuring the profile of a cylindrical surface before and after erosion, generating erosion rate data for impact angles from 0° to 90° in a single experiment. An empirical equation is then fitted to the data and used in CFD models for erosion rate prediction. In the current work this method was used to produce an erosion rate model for coarse sand in air, impacting an aluminium surface. The model was then used to predict erosion rates on a geometrically different experimental system - a flat plate with central hole. The erosion model predicts initial erosion rates within 50% of experiment, while later erosion rates are predicted to within 25%. It is postulated that the erosion incubation period is affecting initial accuracy, and that if this effect is taken into account then predicted erosion rates would fall to even lower levels.

Keywords: erosion, incubation, erosion modelling, cylinder, flat plate, CFD.

NOMENCLATURE

Greek Symbols
α particle impact angle, [radian].
β cylinder angle, [radian].
ε Turbulence energy dissipation rate, [m^2/s^3].
ϕ Empirical angle in Eq. (4), [radian].
μ viscosity, [$kg.m/s^2$].
θ approach angle, [radian].
ρ gas density, [kg/m^3].
ρ_{surf} density of surface material, [kg/m^3].
ρ_p particle density, [kg/m^3].
σ_k Turbulent Prandtl number for k, [-].
σ_ε Turbulent Prandtl number for ε, [-].

Latin Symbols
a empirical coefficient in Eq. (4), [-].
A area, [m^2].
b empirical coefficient in Eq. (4), [-].
C_1 coefficient in k-ε turbulence model, [-].

C_2 coefficient in k-ε turbulence model, [-].
C_μ coefficient in k-ε turbulence model, [-].
C_D drag coefficient, [-].
d particle diameter, [m].
d_N N% of solid material is smaller than d_N [m].
D pipe diameter, [m].
e erosion rate, [kg surface/kg impact].
E erosion rate density, [kg surface/m^2/s].
E_L linear erosion rate, [m/s].
$f(\alpha)$ wear function, [-].
F_B particle force due to buoyancy, [$kg.m^2/s^2$].
F_D particle force due to drag, [$kg.m^2/s^2$].
g acceleration due to gravity, [m^2/s].
G_0 bulk mass flow rate of particles, [kg/s].
k kinetic energy of turbulence, [m^2/s^2].
K empirical coefficient in Eq. (1), [-].
$\dot{m}$ mass impact rate of particles, [$kg/m^2/s$].
m_p particle mass, [kg].
n empirical coefficient in Eq. (1), [-].
p pressure, [N/m^2].
PVF particle volume fraction, [-].
r radius, [m].
Re Reynolds number, [-].
Stk Stokes number, [-].
t time, [s].
$\mathbf{u}$ gas velocity, [m/s].
$\mathbf{u'}$ fluctuating component of gas velocity, [m/s].
U particle impact velocity, [m/s].
U_0 gas bulk (or approach) velocity, [m/s].
U_S gas/particle slip velocity, [m/s].
v_p particle velocity, [m/s].
w empirical coefficient in Eq. (4), [-].
x empirical coefficient in Eq. (4), [-].
y empirical coefficient in Eq. (4), [-].
z empirical coefficient in Eq. (4), [-].

INTRODUCTION

Erosion causes significant damage in a wide variety of engineering and process equipment, and can lead to catastrophic failure of components if susceptible equipment is not regularly monitored and maintained. In the oil and gas industry the production of sand in gas wells is a case in point. Despite the prevalence of sand

screens, finer sand passes into the well base pipe and causes erosion in components on the surface (McLaury *et al.*, 2000). Furthermore, the screens themselves can fail due to erosion by the formation sand, leading to even higher levels of coarse sand production (Arukhe *et al.*, 2005). In the down well environment it is very difficult to monitor the existence and degree of erosion. Consequently, gas wells tend to be conservatively designed to reduce the likelihood of failure by erosion.

Failure by erosion could be avoided if a reliable method for predicting erosion life was available. Development of erosion models has been going on since at least 1960 when Finnie (Finnie, 1960) proposed an empirical equation for predicting the rate of erosive wear caused by particles impacting a ductile surface. Finnie's equation had the form

$$e = \frac{E}{\dot{m}} = K\,U^{\,n} f(\alpha) \qquad (1)$$

where e is the erosion rate, E is the erosion rate density, $\dot{m}$ is the local mass rate of impacting particles on a surface, K is a scaling coefficient, U is the impact velocity, n is the impact velocity power law coefficient that typically varies between 1.8 and 2.3 for ductile materials (Lester *et al.*, 2010), and $f(\alpha)$ is the dimensionless wear function that describes the impact angle effect of wear rate.

Eq. (1) shows that wear rate is primarily influenced by the impact velocity and impact angle of the striking particle. Other factors relating to the physical properties of the particle and surface are embodied in the empirical coefficients of the equation, and so a new set of coefficients must be determined for each particle/surface pair.

Since Finnie's work, thousands of papers have been published attempting to reliably quantify erosion rate. In 1995 Meng and Ludema presented an exhaustive review of the work to that time (Meng and Ludema, 1995). They found that, of more than 5000 papers reviewed, over 300 equations for predicting erosive wear had been proposed, made up of over 100 different particle and surface properties. They concluded that models attempting to predict wear from a theoretical basis were generally less reliable than empirical models such as that of Finnie (Finnie, 1960). However, the empirical models were only valid within the range of operation that they had been developed.

An empirical model requires a mathematical function that can represent typical erosion behaviour, and a set of experimental data to fit that mathematical function to. Equation (1) for instance has two empirical coefficients that can be adjusted to fit the equation to a set of data.

To generate a set of erosion rate data for a particular particle/surface pair it is necessary to accurately measure erosion rate for a known particle impact velocity and impact angle. Traditionally this task was performed using many combinations of impact velocity and angle, by, for example, bombarding a flat plate with

a particle stream at different approach angles (Kleis and Kulu, 2008). This approach is time consuming and limits data sets to a relatively few specific points.

Recently at CSIRO's laboratories in Melbourne, Australia, Lester (Lester *et al.*, 2010) developed a method of generating erosion rate data at multiple combinations of impact velocity and impact angle in a single experiment. The method involves bombarding a cylindrical surface with particles, thus ensuring impact angles vary depending on where on the surface the erosion is taking place. Using this method, Lester was able to predict erosion on a cylindrical surface at a velocity intermediate to the two velocities at which the erosion rate data were derived with an accuracy of up to ±1%. These predicted values are in stark contrast to others in the literature which are often an order of magnitude away from measured values, especially for complex geometries (Wallace *et al.*, 2004). However, Lester's method has not yet been tested in predicting erosion rate in a geometry different to that used in the erosion rate data experiment.

In this paper CSIRO's methodology (Lester *et al.*, 2010) was used to generate an erosion model to predict the erosion of an aluminium surface impacted with sand. Experimental measurements of erosion rate were then taken on a geometrically different system – a flat aluminium plate with a single central hole – and the erosion model then used to predict erosion in this different system. Comparisons between measured and predicted erosion rates are made, and their implications discussed.

METHODOLOGY

Approach

The aim of the current work is to apply Lester's approach for quantifying erosion rate to a geometrically different system, as might be encountered in an industrial problem. The tasks to accomplish this aim are outlined here.

- *Generate erosion rate data* by impacting an aluminium cylinder in cross-flow with silica sand particles at three different nominal velocities: 30, 60 and 80 m/s. Perform these experiments using the techniques of Lester *et al.* (2010).
- *Create an erosion sub-model* by fitting a mathematical function to the erosion rate data. The sub-model can then be used in calculations within a CFD framework.
- *Predict erosion rates in a different geometry,* in this case an aluminium plate with a single bevelled hole in its centre, impacted with silica sand suspended in air, at a nominal velocity of 80 m/s. Use CFD in conjunction with the erosion sub-model.
- *Experimentally measure erosion* on the plate in the aluminium plate-with-hole experiment.
- *Compare* and contrast the predicted and measured erosion rates for the plate-with-hole experiment.

Generation of Erosion Rate Data

Surface erosion is caused by the impact of particles, and the degree of erosion has been shown to primarily be caused by the local impact velocity, U, and impact angle, α. As a particle strikes a surface it will generally do so at a different velocity and angle to that of the approaching fluid, so that $U \neq U_0$, $\alpha \neq \theta$ (Figure 1). This is because the local curvature of fluid streamlines approaching the surface can affect the path of the solid particle.
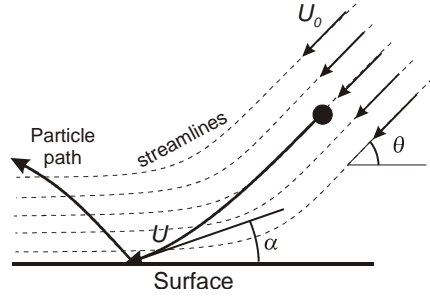
Figure 1: Particle impacting a surface, general case.
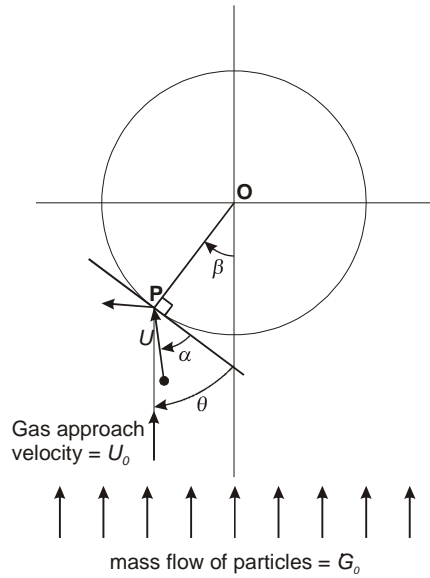
Figure 2: Particle impacting a cylindrical surface, general case.

Earlier methods of generating erosion rate data involved impacting a flat surface with particles approaching from a given angle, and so required many experiments to give a comprehensive data set. The approach of Lester (Lester *et al.*, 2010) dramatically reduces the number of experiments required to generate a data set by impacting a cylindrical, rather than a flat surface. Figure 2 shows how the impact angle varies depending on the location of the impact point, P, on the cylindrical surface.

To generate a set of erosion rate data for silica sand impacting aluminium, a cylindrical aluminium sample was positioned in cross-flow in a wind tunnel seeded with silica sand. The cylinder was exposed to a known quantity of silica sand suspended in air travelling at a nominal velocity of 80 m/s. The profile of the cylinder was measured before and after the experiment, thus giving a linear erosion rate, E_L, as a function of cylinder angle, β, as defined in Figure 2.

In the most general case there is no simple way to determine the impact velocity and impact angle occurring for a given location on the cylinder, and so in Lester's work CFD is used to determine these values. However, the sand used in the current work was a relatively coarse silica sand with $d_{10} = 150$ μm, $d_{50} = 223$ μm, and $d_{90} = 350$ μm (where 10 wt% of the sample is less than or equal to d_{10}, and so on). For particles of this size suspended in air the Stokes number of the system is expected to be much greater than 1, meaning that the particle path is not affected by the fluid streamlines around the cylinder and $\alpha = \theta = \pi/2 - \beta$, $U = U_0$ (Figure 3). Therefore the impact velocity and impact angle is known at any location on the cylinder surface, and can be directly associated with the linear erosion rate there.
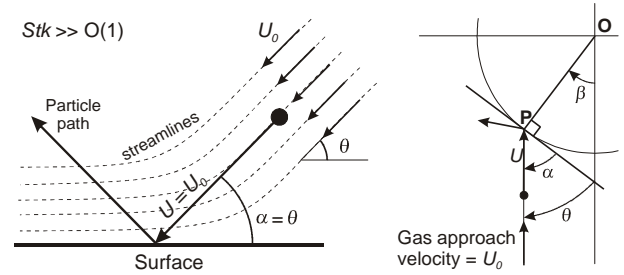
Figure 3: Particle impacts for *Stk* >> O(1).

By further assuming a uniform distribution of sand in the apparatus, the local average particle impact rate, $\dot{m}$, can be calculated under these conditions as

$$\dot{m} = \frac{4G_0}{\pi D^2} \cos\beta \qquad (2)$$

where G_0 is the overall mass flow rate of sand through the pipe, and D is the pipe diameter. The erosion rate can then be directly determined from the linear erosion rate so that

$$e = \frac{E}{\dot{m}} = \frac{\rho_{surf} E_L}{\dot{m}} \qquad (3)$$

where ρ_{surf} is the density of the surface material, in this case aluminium with density 2700 kg/m^3.

Creation of an Empirical Erosion Sub-Model

Creation of an empirical erosion sub-model involves the fitting of a mathematical function to experimentally generated erosion rate data. The commonly used form of the mathematical function was shown in Eq. (1) and was first used by Finnie (Finnie, 1960). More recently, Chen proposed using Finnie's equation with the wear function shown in Eq. (4) (Chen *et al.*, 2004). This wear function fits the current erosion rate data with reasonable accuracy.

$$f(\alpha) = \begin{cases} a\alpha^2 + b\alpha & ; \quad \alpha \leq \phi \\ x\cos^2\alpha \sin(w\alpha) + y\sin^2\alpha + z & ; \quad \alpha > \phi \end{cases} \qquad (4)$$

In Eq. (4) *a*, *b*, *w*, *x*, *y*, *z* and ϕ are all coefficients that can be adjusted to attain a good fit to the erosion rate data set.

EXPERIMENTAL APPARATUS

The experimental apparatus used in the current work was a purpose-built wind tunnel that allowed seeding of the air flow with silica sand. The same tunnel was used for both generation of the erosion rate data set (using a cylindrical sample) and for measurement of erosion on the new geometry (using the aluminium plate with a central hole).

The apparatus consisted of an open-circuit wind tunnel driven by a 75 kW blower, with a circular cross-section of diameter 101 mm (4"), see Figure 4. The wind tunnel had three main legs: an initial horizontal leg in which particulate material could be presented to the flow; a vertical test section which allowed the particulates to distribute evenly in the tunnel, and then a horizontal return leg to a cyclone and bag house for particle collection. The cleaned air then returned to atmosphere.
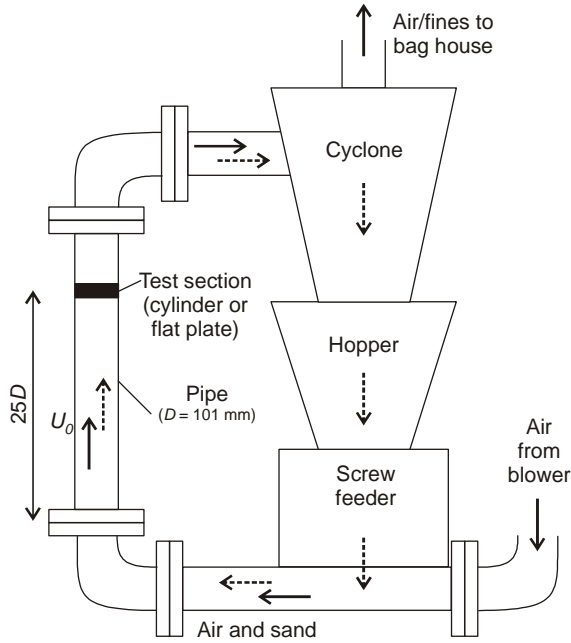
Figure 4: Experimental apparatus.

To ensure an even distribution of particles in the test section, the test plate was located approximately 25 diameters downstream of the initial elbow. Laser Doppler anemometer experiments by Kuan showed that a distance of 9D was required to produce a uniform field of 100 μm particles downstream of a 90° bend (Kuan *et al.*, 2007), so 25D was expected to be adequate for the current work. Observation of erosion patterns for samples located centrally in the tunnel showed a symmetrical distribution, thus confirming the uniform presentation of particulates.

The cylinder used for generating the erosion rate data set had a diameter of 10 mm and was 50 mm long. The test plate consisted of a single rectangular aluminium plate, 56 mm long × 24 mm wide × 2 mm thick, with a central 8 mm diameter hole. The hole had a slightly bevelled edge that was thought to contribute significantly to the erosion rate around the hole. Both samples were made from aluminium at 98.4% purity.

EXPERIMENTAL PROCEDURE

Prior to the flat plate experiment, the surface profile of the test plate was accurately measured using a Sheffield Discovery II D-8 Coordinate Measurement Machine (CMM). The CMM has a measurement uncertainty of ±1 μm and each measurement point has a spatial repeatability of ±5 μm. The spatial repeatability of each point was obtained over 4 measurement runs with the sample removed and re-positioned after each run sequence. Measurements were taken after the sample had been equilibrated in a temperature-controlled room (22°C) after several hours to avoid any thermal expansion effects.

The aluminium test plate was then mounted with its flat face normal to the gas stream in the test section of the pipe erosion rig (Figure 4). The blower was used to provide a steady air velocity through the rig of 80 m/s, while the flow was laden with silica sand. A total of 100 kg of sand was run through the rig at a nominal rate of 0.030 kg/s, giving a mean particle volume fraction of 1.73×10^{-5}. Thus the sand stream was very dilute and particle-particle interaction was expected to be minimal.

The test plate was once again positioned in the CMM for surface profile analysis after 50 kg and then after 100 kg of sand had passed through the equipment. The measured surface profiles were then compared to that predicted using the CFD model.

MATHEMATICAL MODEL

The erosion sub-model Eq. (1), in combination with Chen's wear function Eq. (4) (Chen *et al.*, 2004), was incorporated into a CFD framework to allow simulation of the flow around the experimental plate, and hence prediction of the erosion rate on the plate. The simulation was performed using the commercial software ANSYS CFX-12, which solves the Reynolds averaged Navier-Stokes equations. The model used an isothermal, steady state, single phase Eulerian simulation to represent the air flow, while simulation of sand particles was performed using Lagrangian particle tracking techniques.

Eulerian Equations

The air flow field was determined by solving the Reynolds averaged Navier-Stokes equations for air (ANSYS, 2009) Eqs. (5) and (6).

$$\frac{\partial}{\partial t}(\rho) + \nabla \cdot (\rho \mathbf{u}) = 0 \qquad (5)$$

$$\frac{\partial}{\partial t}(\rho \mathbf{u}) + \nabla \cdot (\rho \mathbf{u}\mathbf{u}) = -\nabla p + \nabla \cdot \left(\mu \left(\nabla \mathbf{u} + \rho \overline{\mathbf{u'}\mathbf{u'}} \right) \right) + \rho g \qquad (6)$$

All source terms of momentum (apart from buoyancy, denoted by the term ρg) were neglected.

The presence of Reynolds stress terms on the right hand side of Eq. (6) mean that the above equations are not closed. To obtain values for the Reynolds stress terms and close the equation set the standard k-ε turbulence model was used (Launder and Spalding, 1974), with

constants given as $C_1 = 1.44$; $C_2 = 1.92$; $\sigma_k = 1.0$; $\sigma_\varepsilon = 1.3$; $C_\mu = 0.09$ (Launder and Sharma, 1977).

Lagrangian equations

The distribution of sand impacting the test piece was estimated using the Lagrangian particle tracking technique as a post-processing step. This was possible as the dilute sand stream was found to have a negligible effect on the gas distribution through the system, so one way coupling between gas and solids was adequate. The starting position of representative sand tracks was specified to be randomly distributed over a small patch of the flow inlet, and the path these particles took through the air was determined by performing a force balance on each particle, Eq. (7).

$$m_p \frac{dv_p}{dt} = F_D + F_B$$
$$= \frac{1}{2} C_D \rho A |U_S| U_S + \frac{\pi}{6} d_p{}^3 (\rho_p - \rho) g \qquad (7)$$

In Eq. (7) the drag and buoyancy on the particle are represented by F_D and F_B respectively, and their values are expanded out on the right hand side of the equation. The drag coefficient, C_D, was determined using the correlation of Schiller and Naumann (Schiller and Naumann, 1933), as constrained by ANSYS (ANSYS, 2009), Eq. (8).

$$C_D = \max\left(\frac{24}{\text{Re}} \left(1 + 0.15 \, \text{Re}^{0.687}\right), \quad 0.44 \right) \qquad (8)$$

Eq. (7) was solved analytically for v_P. From this, the particle displacement was determined from integration of v_P with respect to t. Further details of these equations are given by ANSYS (ANSYS, 2009).

The effect of gas turbulence on the paths of particles was investigated and found to be insignificant for the coarse sand used in the current work.

Geometry, Mesh and Boundary Conditions

The experimental apparatus was modelled as a 90° segment of the pipe, utilizing both longitudinal symmetry planes to reduce computational effort. The geometry extended 15 pipe diameters both upstream and downstream of the test piece (Figure 5 (a)). A hexahedral mesh was imposed on the geometry, with substantial mesh refinement around the plate to allow high resolution of erosion rates to be predicted on the plate surface. A total of approximately 567,000 mesh elements were used. Figure 5 (c) and (d) shows the surface mesh on the aluminium plate. Detail around the central hole shows that its bevelled edge is captured in the geometry.

The model had a simple set of boundary conditions. A single inlet was modelled using a Dirichlet boundary (constant normal inlet velocity equal to 80 m/s, with moderate turbulence parameters corresponding to a turbulence intensity of 5%). The downstream outlet was modelled using a constant pressure condition equal to atmospheric pressure. All walls were modelled as no-slip boundaries with mesh refinement near their surface.
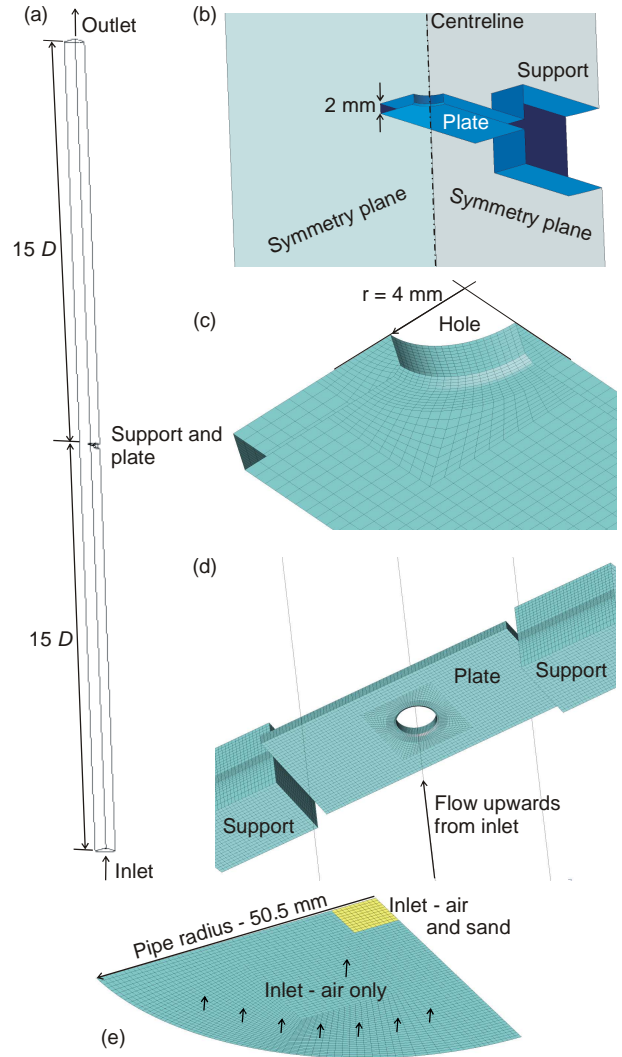
Figure 5: CFD model geometry and surface mesh.

Calculation Details

Calculation of the gas flow was very stable and converged in approximately 150 iterations. Simulation of the sand distribution was performed using 10^6 particle tracks to ensure a uniform impact distribution on the plate. The cumulative impact rate, impact velocity and impact angle of each track was summed for each mesh element on the plate surface, and these data used in conjunction with Eqs. (1) and (4) to determine the erosion rate on the plate.

RESULTS

Erosion Model

Having measured the erosion loss of the cylindrical sample under nominal bulk flow conditions corresponding to $U_0 = 80$, 60 and 30 m/s, the linear erosion rates for these three conditions are shown in Figure 6 (a). Note the high resolution of the data, with data points present at approximately 0.5° intervals around the cylinder.

Using the transformation equations Eq. (2) and (3), the data were re-cast to give erosion rates as a function of particle impact angle, for each of three impact velocities. These data are shown in Figure 6 (b).

(a)

(b)
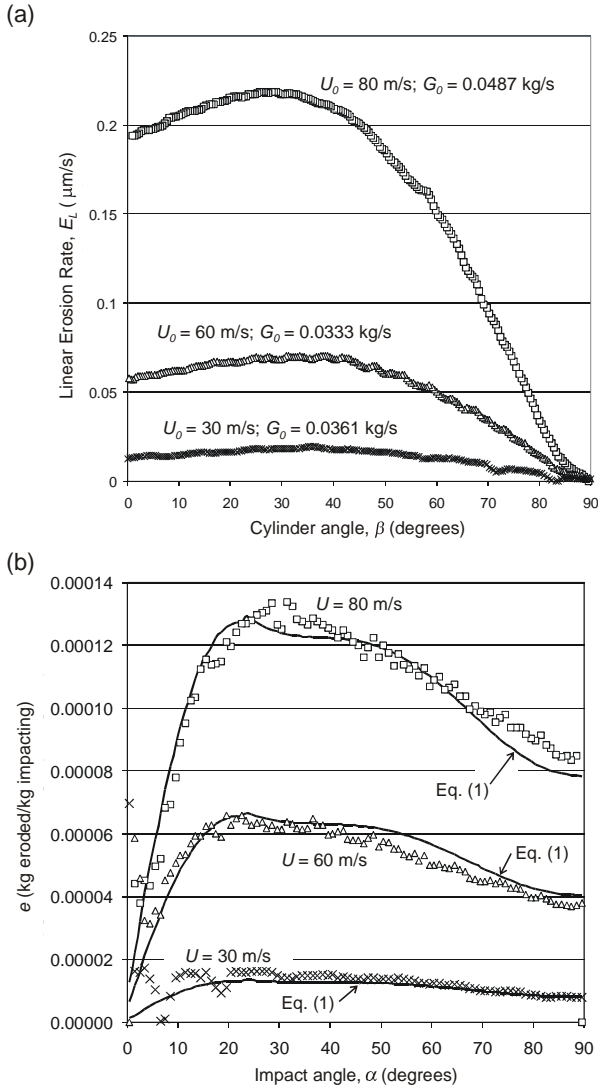
Figure 6: (a) Raw data set for linear erosion rate of aluminium by silica sand. (b) Reduced data showing erosion sub-model equation fit (Eq. (1) and (4)).

Table 1: Best-fit coefficients for erosion sub-model using Eqs. (1) and (4).

coefficient	value	coefficient	value
K	5.04×10^{-9}	x	0.4
n	2.3	y	-0.9
a	-7	z	1.556
b	5.45	φ	0.4014 radian
w	-3.4		(= 23°)

The erosion sub-model represented by Eqs. (1) and (4) was then fitted to the experimental data set, giving a best fit curve shown as a solid line in Figure 6 (b). Note that the same set of empirical coefficients fits the data at all three impact velocities, suggesting that the sub-model should be applicable for all impact velocities between 30 and 80 m/s. The best-fit coefficients for the model are shown in Table 1, with α and φ in Eq. (4) are expressed in radians.

CFD prediction

Incorporating the erosion sub-model into the CFD model of the flat plate experiment, it was possible to predict the erosion rate on the flat plate surface. Results

for the CFD simulation are shown in Figure 7 and Figure 8.

Figure 7 shows the speed and velocity distribution around the plate and through the central hole. The speed increases to approximately 180 m/s as it accelerates through the hole, while the bluff plate has recirculation zones formed behind it, as expected. Figure 8 (a) demonstrates the predicted paths of sand particles using the Lagrangian tracking approach. The model predicts the vast majority of the sand particles impacting the plate at 80 m/s, and at an angle at or close to 90°.

(a)

(b)
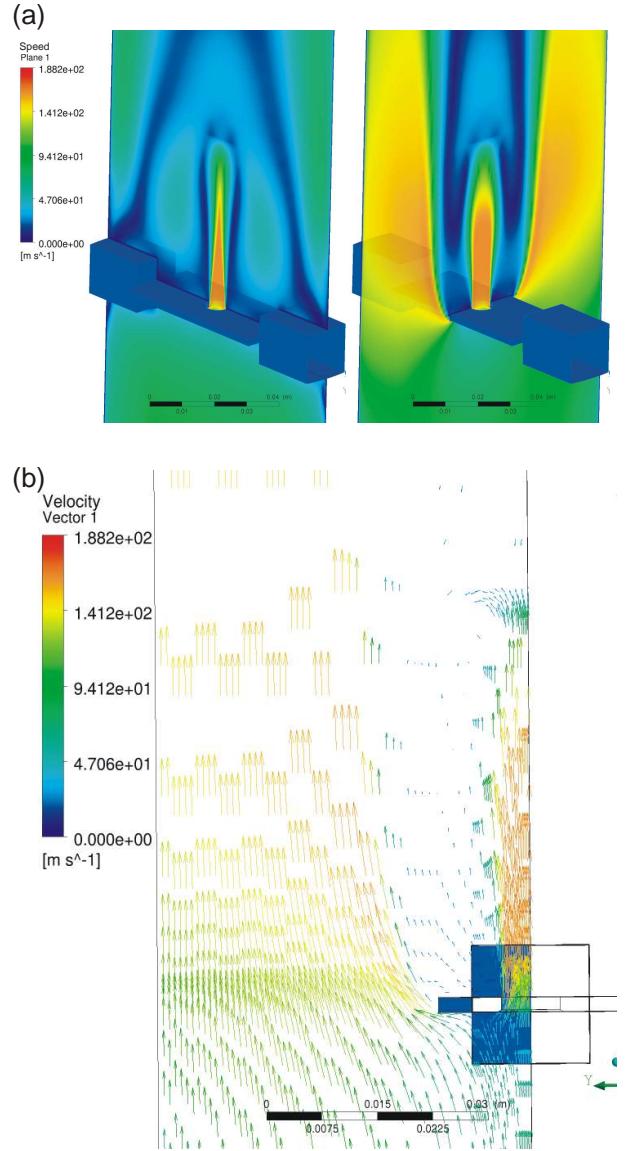
Figure 7: CFD prediction of (a) speed distribution, and (b) velocity distribution, around flat plate.

Tracks that hit the bevelled edge of the hole deflect towards a central point, while tracks that miss the plate entirely pass straight through the hole or around the plate.

The erosion distribution on the plate and around the central hole is shown (with surface grid) in Figure 8 (b), and then in close-up in Figure 8 (c). While there are some fluctuations in the predicted intensity of erosion rate, generally the distribution is shown to be axisymmetric around the hole centreline.

through the experimental erosion rig (points in Figure 9). The bevelled edge is shown in the pre-erosion state, and it is clear that as the surface is eroded, the bevelled edge becomes rounded.

Figure 9 also shows the surface profiles predicted using the CFD model. These profiles are determined from the predicted erosion rate data in units $M.L^{-2}.T^{-1}$ (Figure 8 (b), (c)) divided by the density of the plate surface material, giving a linear erosion rate in units $L.T^{-1}$. The linear erosion rate is used to calculate the new plate surface a given time after the erosion commences, assuming the erosion takes place perpendicular to the existing surface.
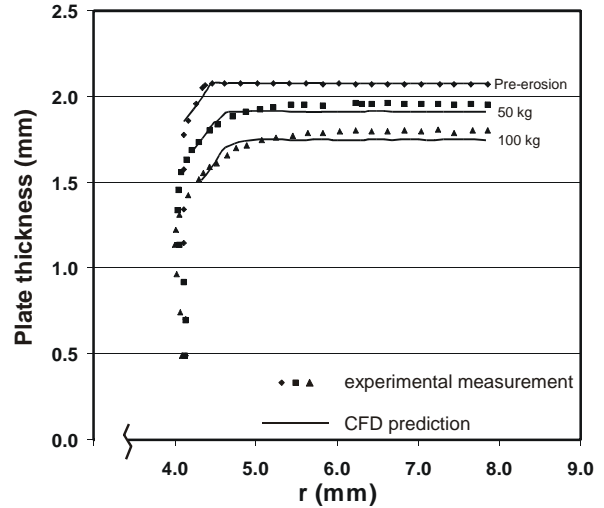
Figure 9: Experimental measurement of hole profile, together with CFD prediction (solid lines).

DISCUSSION

Accuracy of the Model Predictions

As shown in Figure 9, the CFD model over-predicts the rate of erosion on the flat part of the test plate, while slightly under-predicting the erosion rate on the bevelled edge. Regarding the flat surface of the plate, the profiles after 50 kg of impacting material and 100 kg of impacting material are both over-predicted by approximately the same amount numerically, suggesting that there is error in predicting the initial rate of erosion. It is known that erosion mechanisms typically have an incubation period, during which impacting material roughens and work hardens the surface, but no surface material is yet ejected (McCabe *et al.*, 1985). The computer model does not currently take into account this incubation period. It is recommended that a method of allowing for incubation be incorporated into the model, and that further experimental observations be made to allow investigation of the model's accuracy without incubation as a confounding variable.

The discrepancy on the bevelled edge arises from the method used to calculate the surface location. The calculation of the surface profile assumes erosion always takes place perpendicular to the surface (Figure 10 (a)), however the experimental data shows a rounding of the edge of the hole as it is eroded away (Figure 10 (b)).

Figure 8: CFD prediction of (a) sand particle tracks impacting flat plate; (b) erosion rate distribution on flat plate; (c) erosion rate around hole.

Comparison of Experimental and Predicted Erosion Profile

Figure 9 shows the experimentally measured surface profiles of the plate before the experiment, and then after 50 kg and then 100 kg of sand have been passed
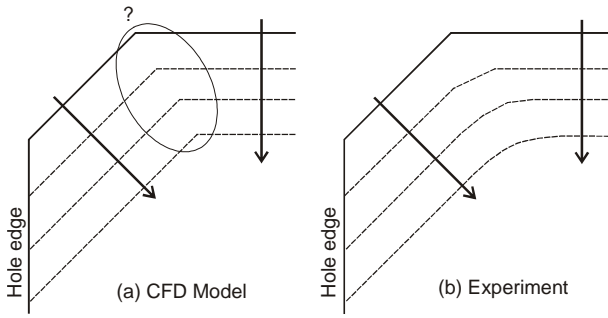
Figure 10: Schematic representation of erosion of sharp edge.

This is probably due to wear being caused by a combined effect of erosion from both surfaces that make up the edge, so the erosion rate at the edge is accentuated and the profile becomes smooth. The CFD model does not account for this behaviour, and so the edge is predicted to remain sharp.

The accuracy of the model prediction for the 50 kg impact profile on the flat surface is approximately 50%, while that of the 100 kg impact profile is 25%. If the incubation time is taken into account, it appears that the accuracy of this second profile would be substantially improved. However, even without incubation adjustments, the current results both compare favourably to those generated by others in the literature, where a 40% agreement is considered excellent (Zhang *et al.*, 2007) and anything within an order of magnitude is considered acceptable (McCasland *et al.*, 2004).

The most accurate result shown in previous literature that could be found was that of Lester (Lester *et al.*, 2010) who achieved an accuracy from their model of between 1 and 10%. Lester's work generated erosion rate data on a cylinder impacted by a sand/water slurry in cross-flow at velocities of 2.5 and 4.5 m/s. They then used their erosion rate model to predict erosion on the same cylinder at the intermediate velocity of 3.6 m/s. The excellent accuracy they achieved is believed to be due to their use of the same geometry for all the work. In contrast, the current work intentionally used a different geometrical configuration to test the erosion model's accuracy. This is an important point, since Lester's method of generating the erosion rate data using a cylinder is efficient and accurate, but most engineering applications will have a different geometry to a cylinder in cross-flow. It is recommended that even more complex geometries be investigated in the future to test the accuracy of any given model.

Stokes Number assumption

One of the key assumptions in the model as presented here was that the Stokes number of the flow was substantially larger than one. This assumption allowed the use of Eqs. (2) and (3) to simplify the impact rate, impact angle and impact velocity relationships. To test this assumption a simple CFD simulation was performed using a two-dimensional slice model of the cylinder in cross-flow. The simulation was set up with similar conditions to that of the test plate CFD model, and sand particles tracked through the solution using a variety of particle sizes. The results are shown in Figure 11 for

particle sizes ranging from 1 µm up to 20 µm in diameter.

As expected, the 1 µm particles follow the streamlines of the air and do not impact the cylinder at all. For the 5, 10 and 15 µm particles there is a decreasing effect of air on the particle paths as the Stokes number increases. Using 20 µm particles, the particle paths are unaffected by the gas streamlines around the cylinder, and impact the surface directly. Therefore, the use of the silica sand sample in this work, with a d_{10} of 150 µm, is large enough to prevent any Stokes number effects from coming into play.
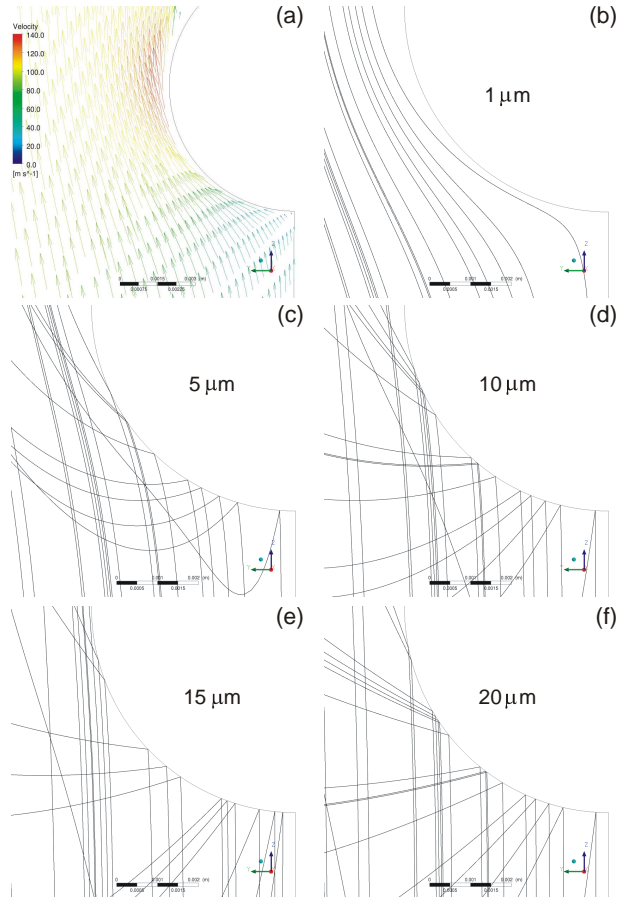
Figure 11: Two-dimensional CFD analysis of flow around a 10 mm cylinder, bulk velocity of 80 m/s. (a) velocity field; (b - f) paths of 1, 5, 10, 15 and 20 µm sand particles.

Particle Size Distribution

As is evident from Eq. (1), the empirical model formulation does not explicitly account for the size of impacting particles. Therefore, it is desirable that the particle sample used in the calibration experiments resemble that expected in the environment that is to be modelled as closely as possible. For situations with high Stokes Number (where the erodent is relatively coarse, and suspended in a gas) it is only necessary that the calibration material be of a similar size to that expected in the environment of interest. However, with fine erodents and/or in slurry suspensions, erosion will be caused by a range of particle sizes hitting the same location at different velocities and angles. In this case it is necessary to take into account erosion caused by all

particle sizes, and it is necessary to match the entire particle size distribution from the environment of interest in the calibration experiment. The authors are further developing the method to account for such situations.

Underlying the methodology is the assumption that the same amount of erosion will be caused by a given mass of erodent, irrespective of its particle size. This assumption could break down in situations where geometry is complex and flows recirculate. In this situation stratification of different sized particles may occur so that erosion is only caused by a specific subset of the entire size distribution. Further investigation of the current model under complex flow conditions will shed light on the extent of this limitation.

Particle-Particle Interaction

In the calibration work and environment being modelled, the average particle volume fraction (PVF) was below 10^{-4} (Table 2), which is well within the accepted "dilute phase" range of PVF < 0.01 (Faeth, 1987). This is true even when calculating the maximum PVF using the CFD model. It was therefore assumed that particle-particle interactions are minimal and do not affect the erosion rate appreciably. At higher particle concentrations it would be necessary to allow for such interactions, and further work should be performed to determine an upper limit of particle volume fraction for the technique.

The very dilute nature of the particle flows also means that particle impact conditions at the three velocities (30, 60 and 80 m/s) are comparable, despite the difference in PVF.

Table 2: Particle volume fraction for each calibration experiment.

Velocity	Mass flow rate	Sand particle volume fraction	
		Average	Maximum
30 m/s	0.03 kg/s	4.62×10^{-5}	4.90×10^{-5}
60 m/s	0.03 kg/s	2.31×10^{-5}	
80 m/s	0.03 kg/s	1.73×10^{-5}	

Other limitations of the model

As was the case with Lester's work (Lester *et al.*, 2010), it is important that the generated erosion model be used only at impact rates within its range of calibration. As shown by Lester, interpolation between calibration velocities can yield results of very high accuracy. However, it is unknown how accurate results will be with extrapolation to velocities beyond the range of calibration.

A more accurate equation fit may yield better results. The curve-fit of Eqs. (1) and (4) to the data in Figure 6 (b) is accurate to within approximately ±10% for impact angles greater than 25° and at the higher impact velocities. At low angles and/or low velocities the errors increase. Therefore the accuracy of predictions cannot be expected to be better than about ±10%. The number of adjustable coefficients in Chen's equation (Chen *et*

al., 2004) is nine, allowing for considerable control over the fitted curve, but also making it difficult to achieve an optimal fit. A different functional form, or else a mathematically rigorous fitting algorithm such as those available in Mathematica 7.0 could lead to a better curve fit, and hence a more accurate representation of the erosion rate calibration data (Lester *et al.*, 2010).

The current curve fit shown in Figure 6 (b) under-predicts the experimental calibration data for the conditions of 80 m/s at 90° by approximately 7%. Therefore, a better curve fit would predict a greater erosion rate and hence decrease the accuracy of the predicted profiles shown in Figure 9. However, once incubation effects are included in the model, the overall effect of using a better curve fit is expected to be that of improved accuracy in predictions.

Finally, predicting the accuracy of the change in surface profile will be greatly improved if the surface profile was updated in the CFD model. The mesh resolution on the surface would need to be higher than that used here to get a clearer indication of the profile development over time.

CONCLUSIONS

An erosion sub-model based on the experimental methods of Lester (Lester *et al.*, 2010), in conjunction with the mathematical functional form of Chen (Chen *et al.*, 2004), was generated for coarse silica sand impacting aluminium when suspended in air. The erosion sub-model was implemented in a CFD framework to investigate the erosion rate on a flat plate with central hole. Comparison is made between prediction and experiment.

It is found that the erosion sub-model can predict the initial erosion rate to within 50%, while later erosion rates are predicted to within 25% of experimental data. It is postulated that the erosion incubation period is affecting the accuracy of the results, and that if this effect is taken into account then predicted erosion rates will be significantly more accurate. The current work shows how this method can be applied to geometries different to that used in model calibration, and still achieve results of reasonable accuracy.

Future work should involve allowance in the model for the erosion incubation period, and investigations of more complex geometries relevant to a variety of industrial and engineering problems.

ACKNOWLEDGMENTS

REFERENCES

ANSYS, (2009), ANSYS-CFX12.0 User Manual. Pittsburgh, USA, ANSYS Inc.

ARUKHE, J., UCHENDU, C. and NWOKE, L., (2005). "Horizontal screen failures in unconsolidated, high permeability sandstone reservoirs: reversing the trend, SPE 97299", SPE Annual Technical Conference and Exhibition, Dallas, TX, USA.

CHEN, X., MCLAURY, B.S. and SHIRAZI, S.A., (2004), "Application and experimental validation of a computational fluid dynamics (CFD)-based erosion prediction model in elbows and plugged tees", Computers & Fluids 33(10): 1251-1272.

FAETH, G.M., (1987), "Mixing, Transport and Combustion in Sprays", Progress in Energy and Combustion Science 13(4): 293-345.

FINNIE, I., (1960), "Erosion of surfaces by solid particles", Wear 3(2): 87-103.

KLEIS, I. and KULU, P., (2008), Solid Particle Erosion, Springer-Verlag.

KUAN, B., YANG, W. and SCHWARZ, M.P., (2007), "Dilute gas-solid two-phase flows in a curved 90 degree duct bend: CFD simulation with experimental validation", Chemical Engineering Science 62(7): 2068.

LAUNDER, B.E. and SPALDING, D.B., (1974), "The numerical computation of turbulent flows", Computer methods in applied mechanics and engineering 3: 269-289.

LAUNDER, D.E. and SHARMA, B.T., (1977), "Application of the Energy Dissipation Model of Turbulence to the Calculation of Flow near a Spinning Disc", Letters in Heat and Mass Transfer 1(2): 131-138.

LESTER, D.R., GRAHAM, L.A. and WU, J., (2010), "High precision suspension erosion modeling", Wear 269(5-6): 449-457.

MCCABE, L.P., SARGENT, G.A. and CONRAD, H., (1985), "Effect of Microstructure on the Erosion of Steel by Solid Particles", Wear 105(3): 257-277.

MCCASLAND, M., BARRILLEAUX, M., RUSSELL, R., SCHNEIDER, D. and LUCE, T., (2004). "Predicting and Mitigating Erosion of Downhole Flow-Control Equipment in Water-Injector Completions, SPE 90179", SPE Annual Technical Conference and Exhibition, Houston, Texas, Society of Petroleum Engineers, 6.

MCLAURY, B.S., SHIRAZI, S.A. and BURDEN, T.L., (2000), "Effect of entrance shape on erosion in the throat of chokes", Journal of Energy Resources Technology-Transactions of the ASME 122(4): 198-204.

MENG, H.C. and LUDEMA, K.C., (1995), "Wear Models and Predictive Equations - Their Form and Content", Wear 181: 443-457.

SCHILLER, L. and NAUMANN, A., (1933), "Fundamental calculations in gravitational processing", Zeitschrift Des Vereines Deutscher Ingenieure 77: 318-320.

WALLACE, M.S., DEMPSTER, W.M., SCANLON, T., PETERS, J. and MCCULLOCH, S., (2004), "Prediction of impact erosion in valve geometries", Wear 256(9-10): 927-936.

ZHANG, Y., REUTERFORS, E.P., MCLAURY, B.S., SHIRAZI, S.A. and RYBICKI, E.F., (2007), "Comparison of computed and measured particle velocities and erosion in water and air flows", Wear 263: 330-338.

EFFECT OF NATURAL CONVECTION ON THE HEAT TRANSFER FOR A COLD SPOT IN A SUBSEA PIPELINE DURING SHUT-IN

Bente Helgeland SANNÆS[1]*

[1] Statoil, Porsgrunn, NORWAY

* E-mail: bhsa@statoil.com

ABSTRACT

Subsea pipelines are often insulated in order to keep the temperature of the flowing fluids high enough to avoid the appearance of hydrates or wax. Sometimes the insulation is damaged causing the steel of the pipe to be exposed to the cooler surroundings creating a cold spot.

The heat transfer from such a cold spot is much larger than from the insulated pipe. In a shut-down situation this will cause the fluid at the cold spot to cool more than the fluid in the insulated parts of the pipe. The worst case for the location of a cold spot is a section in a horizontal pipe. In case of an inclined pipe, the cooled fluid will flow away from the cold spot in exchange for warm fluid. In the case of a horizontal pipe the cooled fluid will circulate locally due to the natural convection arising from the density difference caused by the cooling. Such a horizontal pipe with a cold spot has been simulated using ANSYS Fluent 12.1.

Keywords: CFD, natural convection, cold spot.

NOMENCLATURE

A complete list of symbols used, with dimensions, is required.

Greek Symbols
α Thermal diffusivity, [m/s^2].
β Thermal expansion coefficient, [1/K].
ρ Mass density, variable [kg/m^3].
ρ_0 Mass density, constant [kg/m^3].
τ Time constant, [s].
λ Laminar viscosity, [W/(m·K)].
μ_{eff} Effective viscosity (sum of laminar and turbulent), [kg/(m·s)].
λ Thermal conductivity, [W/(m·K)].
λ_{eff} Effective thermal conductivity (sum of laminar and turbulent), [W/(m·K)].

Latin Symbols
C_p Specific heat, [J/(kg·K)].
L Characteristic length, [m].
P Pressure, [Pa].
T Temperature, variable [K].
T_0 Initial temperature, constant [K].
U Characteristic velocity, [m/s].

$\mathbf{u}$ Velocity, [m/s].

Pr Prandtl number, [-].
Ra Rayleigh number, [-].

INTRODUCTION

Subsea pipelines are insulated in order to keep the temperature of the flowing fluid(s) high enough to avoid the appearance of hydrates or wax during flow conditions. Sometimes the insulation is damaged causing the steel of the pipe to be exposed to the surrounding subsea cold water creating a cold spot. The heat transfer from such a cold spot is much larger than from the insulated pipe. For a flowing fluid a small cold spot is not considered to cause significant problems. In a shut-down situation the fluid inside the pipe will be stagnant. The same fluid will thus be exposed to large heat transfer for an extended time. This will cause the fluid inside the cold spot to enter the hydrate or wax regime much faster after start of the shut-in than the fluid in the insulated sections.

In this case the heat transfer is governed by natural convection, and to our knowledge, there exists no engineering correlation that can be used to accurately predict the heat transfer rate in this type of geometry. Therefore the use of CFD seems to be the only way to predict cool down times at shut-in. Mme et al. (2009) and Mme (2010) have studied a very similar problem in detail. They measured as well as calculated with CFD the local temperature decrease due to a cold spot on a 70 mm diameter pipe at several positions along the pipe and at different cross sectional positions. The measurements were performed for 3 different

inclinations: 2°, 45° and 88°. They found that most heat was lost from a cold spot when the pipe was close to horizontal. Two other relevant studies that are also cited by Mme are Taxy et al. (2004) who used CFD to evaluate the impact of cold spots of subsea equipment, and Aarnes et al. (2005) who carried out a full scale cool down test of a Christmas tree (X-Tree) in order to verify the insulation design.

Our simulations were compared with those measurements. Based on the findings from these simulations a larger diameter pipe, representative of a field application, was simulated.

MODEL DESCRIPTION

The governing equations for free convection flow are the conservation equations for mass, momentum, and energy. The effect of density variation due to temperature changes is incorporated through the use of the Boussinesq approximation. The density only changes with temperature – not with pressure. In addition, the density change is small, and considered to affect only the momentum balance. In the Boussinesq approximation the effect of the density difference due to temperature is modelled as

$$(\rho - \rho_0)g \approx -\rho_0 \beta (T - T_0)g \qquad (1)$$

where the thermal expansion coefficient is defined as

$$\beta = -\frac{1}{\rho}\left(\frac{\partial \rho}{\partial T}\right) \qquad (2)$$

The Boussinesq approximation is only valid when

$$\beta (T - T_0) \ll 1 \qquad (3)$$

This approximation can be used to simplify the equations considerably. The simplified equations are shown in Equation (4) through (6).

$$\nabla \cdot \mathbf{u} = 0 \qquad (4)$$

$$\rho_0 \frac{\partial \mathbf{u}}{\partial t} + \rho_0 \mathbf{u} \cdot \nabla \mathbf{u}$$
$$= -\nabla P + \mu_{eff} \nabla^2 \mathbf{u} - \rho_0 \mathbf{g} \beta (T - T_0) \qquad (5)$$

$$\frac{\partial T}{\partial t} + \mathbf{u} \cdot \nabla T = \frac{\lambda_{eff}}{\rho_0 C_p} \nabla^2 T \qquad (6)$$

Physical properties

The Mme (2010) experiments were performed in a 70 mm inner diameter steel pipe. The liquid in the pipe was water. The cold spot was 3 diameters long and was placed near the middle of the pipe. The long end was 1.25 m and the short end was 0.75 m long. The long end was always lower than the cold spot. This will be referred to as the downstream side of the cold spot as the cold (i.e. heavier) water will flow in that direction. All experiments were run at atmospheric conditions. The pipe and the cold spot are shown schematically in Figure 1.
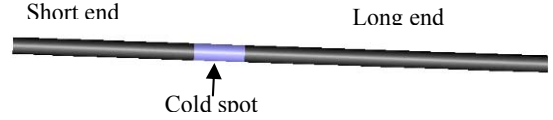
Figure 1: Schematic of the experimental pipe with the cold spot shown as blue.

The cold spot was cooled by circulating cold water (10 °C) around the pipe. For comparison the cases with 2° inclination and 40 °C initial temperature difference between the cooling water and the water in the test pipe were used. The material properties for the water are taken from Mme and reproduced in Table 1.

Table 1: Material properties of water.

ρ	998	kg/m^3
μ	1.003·10^{-3}	kg/(m·s)
λ	0.6	W/(m·K)
C_p	4182	J/(kg·K)
β	4.53·10^{-4}	1/K

Mme estimated the external heat transfer coefficient to 3513 W/(m^{2}K). He found that the external heat transfer coefficient was hard to determine. Three different methods were tried, and the averaged value was chosen. The values varied from 3150 to around 4000 W/(m^{2}K). No measure of the uncertainty was given. The comparison between measurements and simulations will be influenced by the uncertainty in the determination of the external heat transfer coefficient.

Even though the velocities in the system will remain small, the Rayleigh number defined in Equation (7) is typically larger than 10^9. This indicates that the flow is turbulent.

$$Ra = \frac{\rho g \beta \Delta T L^3}{\mu \alpha} \qquad (7)$$

The temperature difference is the difference between the bulk liquid temperature and the wall temperature on the cold spot. Thus the temperature difference will decrease with time as the liquid cools down.

Mme performed CFD analyses using Fluent 6.3. The simulation results using the k-ε-epsilon turbulence model and the LES model were compared with the experimental data. He found that the LES model compared significantly better to the experiments than the k-ε-epsilon model. Based on this he recommended the use of LES.

Simulation set-up

The simulations were performed using ANSYS Fluent 12.1. Due to the symmetry of the system, only one half of the pipe was modelled setting the central plane as a symmetry plane. The wall boundary conditions for the flow were no-slip. For the insulated parts of the pipes the thermal wall conditions were set to heat convection through an insulated wall. The wall was modelled as a thick wall (steel plus insulation) with heat transfer properties resembling an insulated wall. The convection setting of ANSYS Fluent was used for the heat transfer

of the wall. The outside was set to room temperature. Mme had used adiabatic conditions for these walls. The two settings were compared for identical cases, and no noticeable difference was seen. The thermal wall boundary for the cold spot was set using the convection setting of ANSYS Fluent. The outside temperature was set equal to the cooling water temperature of 10 °C. The heat transfer coefficient that had been estimated by Mme was used. The wall thickness and thermal material properties of the steel wall were given by Mme (2010). The LES turbulence model that is available in ANSYS Fluent 12.1 was used without modifications of any parameters.

The temperature in the positions where measurements were available was monitored as a function of time in order to enable comparisons.

Grid dependency test

Mme used a uniform hexahedral grid with cell sizes 3 mm in all directions. This was therefore used as the starting point of this study, although it was chosen to stretch the grid slightly towards the centres of end pipes. The longest grid cells were about twice as long as the shortest. The results agreed reasonably well with the previous results by Mme. To check for grid dependencies, the grid was refined to 2 mm hexahedral in the cross section while keeping the longitudinal discretisation. The results showed a more rapid cooling for the refined grid (see Figure 6). Thus the grid was further refined to 1 mm uniform hexahedral grid cells in the pipe cross section. This resulted in even more rapid cooling. It was assumed that the largest influence of the grid was close to the outer boundaries, especially on the cold spot. A grid with a boundary layer was therefore made. The outmost layer was set to 0.35 mm thickness with cells increasing with a growth factor of 1.1 for 15 cell rows. The inner part of the pipe was meshed with maximum 1.75 mm tetrahedral mesh, giving wedge shaped 3-dimensional grid elements. The cooling times for the two finest meshes were nearly identical, and it was thus concluded that a grid independent solution had been found.

The grids are shown in a cross sectional plane in Figure 2 to Figure 5.
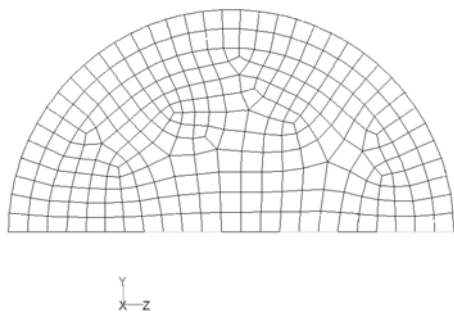
Figure 2 Cross sectional mesh for 3 mm grid size.
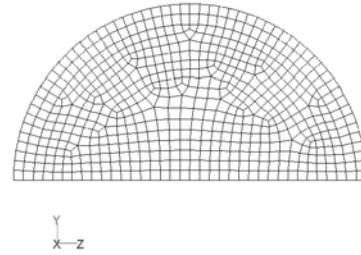
Figure 3 Cross sectional mesh for 2 mm grid size.
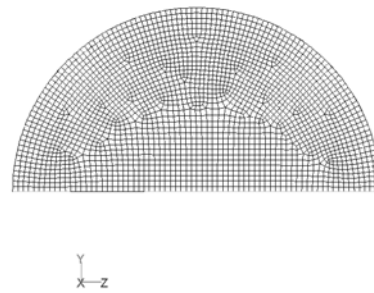
Figure 4 Cross sectional mesh for 1 mm grid size.
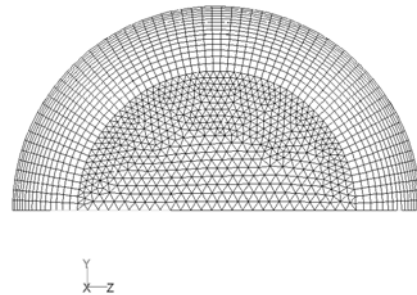
Figure 5 Cross sectional mesh with boundary layer and tetrahedral core.

Following the guidelines for solving high Rayleigh numbers flow from ANSYS Fluent User's Guide (2009) the time constant of the flow was determined as

$$\tau = \frac{L}{U} \sim \frac{L^2}{\alpha} \left(\Pr \mathrm{Ra} \right)^{-1/2} = \frac{L}{\sqrt{g\,\beta \Delta T L}} \qquad (8)$$

The User's Guide advice was to set the time step to

$$\Delta t \approx \frac{\tau}{4} = 0.15\,s \qquad (9)$$

The mean temperature for the total volume was used as an indicator for the amount of heat removed from the system. Figure 6 shows the mean temperature as a function of time for the different grids that were used. For the coarser grids less heat is removed from the system causing a slower cooling process than for the fine grids.
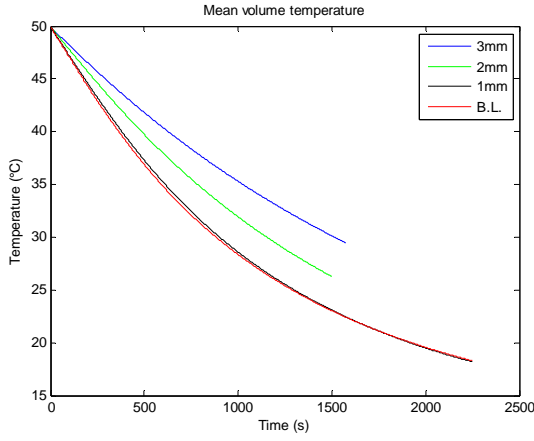
Figure 6 The mean temperature of the water being cooled in the pipe is shown for the four grids tested.

Mme (2010) reported measurements from 7 positions in the pipe. All the reported measurements were taken in the longest pipe section which was slightly lower than the cold spot. The positions of the measurement points are shown in Figure 7.
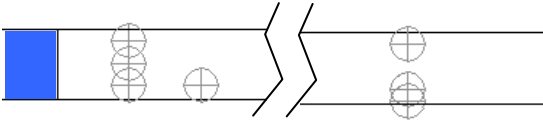
Figure 7 Positions of measurement points. The cold spot is marked in blue. The points are located 1, 2, and 16 diameters to the right of the cold spot.

One set of measurements were taken 1 diameter downstream of the cold spot. The measured temperature was reported at three cross sectional positions: one in the lower part (14 mm above the bottom of the pipe), one in the centre, and one in the upper part (12 mm below the top of the pipe).

Figure 8, Figure 9, and Figure 10 show the measurement together with the results from the simulations. In Mme (2010) the results from the simulations were only reported for the central position. Fairly good agreement was seen by Mme in his simulations for both the k-ε and LES turbulence models. The current simulations show that the results for the central and high positions are quite close to the experimental data for the 3 mm mesh, but that the cooling is too fast for the finer meshes. Obviously the results on the finest grid are expected to give the best representation of the physical model. The conclusion thus is that the model gives faster cooling than the experiment.

For the measurement at the low point (Figure 8) it is seen that the measured temperature falls about 10 °C almost instantly. The temperature gradient then becomes smaller. The results from the 3mm mesh simulation has a gradient that is very similar to the measurement, but the instant fall is much smaller. The finer grid cases give steeper gradients. Generally, it is seen that the finer the grid is, the steeper the gradient becomes.

This is in agreement with the more rapid cooling for the cases with the fines grids.
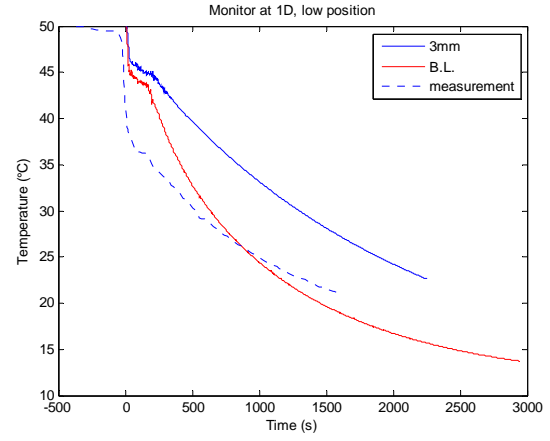
Figure 8 Comparison of measured and simulated temperatures at axial position 1D downstream of the cold spot and cross sectional position 0.2D, which is 14 mm above the bottom of the pipe.
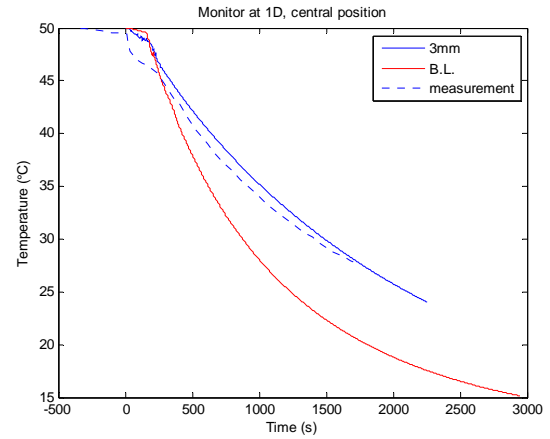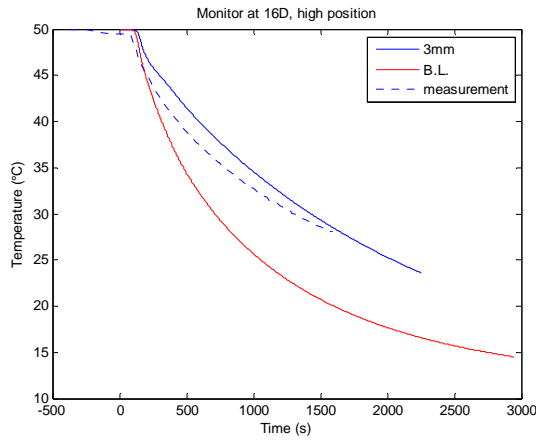

**Figure 9** Comparison of measured and simulated temperatures at axial position 1D downstream of the cold spot and in the cross sectional centre of the pipe.
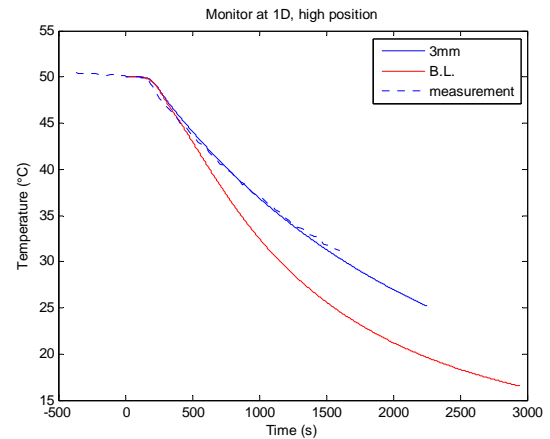
Figure 10 Comparison of measured and simulated temperatures at axial position 1D downstream of the cold spot and cross sectional position 0.83D, which is 12 mm below the top of the pipe.

One measurement was reported at 2 diameters downstream of the cold spot. This is located in the lower part of the pipe. Figure 11 shows the measurements 14 mm above the bottom for three positions downstream of the cold spot. By comparing with the measurements at 1D it is seen that the

temperature falls rapidly in all three points, but the steepness and size of the fall reduce with distance from the cold spot. The gradients after the initial fall are comparable.

Figure 12 shows the measurement and the simulations at the 2D position. The results are comparable to those at 1D.

Neither of the simulations was able to capture the magnitude of the rapid temperature decrease in the low point. All the simulations showed a qualitative agreement with the measurement, i.e. an abrupt temperature decrease followed by a short period with very small temperature gradient which in turn increased again.
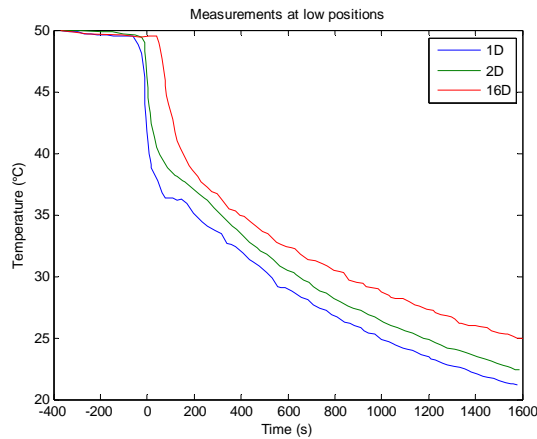
Figure 11 Measured temperatures at three positions along the pipe. The behaviour is similar but shifted in time.
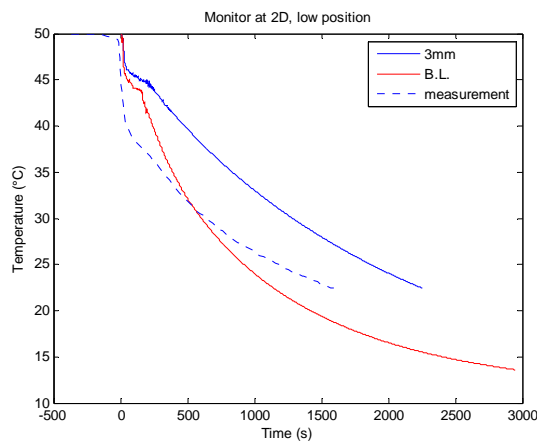
Figure 12 Comparison of measured and simulated temperatures at axial position 2D downstream of the cold spot and 14 mm above the bottom of the pipe.

Near the end of the pipe the measurements were reported at two positions near the bottom of the pipe and one position near the top. The position was 16 diameters (1.12 m) downstream of the cold spot. This point is thus 13 cm away from the closed end. The bottom positions were 14 and 3 mm above the bottom. Figure 13 and Figure 14 show the measurements and simulations in these two points.

The simulations for these points showed a better agreement with the fast temperature decrease than the simulated results at 1 and 2 diameters downstream of the cold spot.

When comparing the simulated results at 16 diameters with the results at 1 and 2 diameters it is seen that the temperature after 75 seconds is lower at the 16 diameters position. This differs from the measurements which are shown in Figure 11. The cause of this was studied in detail and it was found that in the simulations the cold fluid flowed along the bottom of the pipe below the measurement point. Figure 16 and Figure 17 show how the cold front flows down the pipe, reaches the end, and starts filling the pipe with cold fluid. When the cold fluid reaches the end of the pipe it starts filling the pipe from the bottom. The temperature levels are horizontal thus the lowest point will cool first and the higher points will be cool when the warm fluid has been displaced. Figure 20 shows how most of the cold flow passes below the measurement points at 1 and 2 diameters downstream of the cold spot.
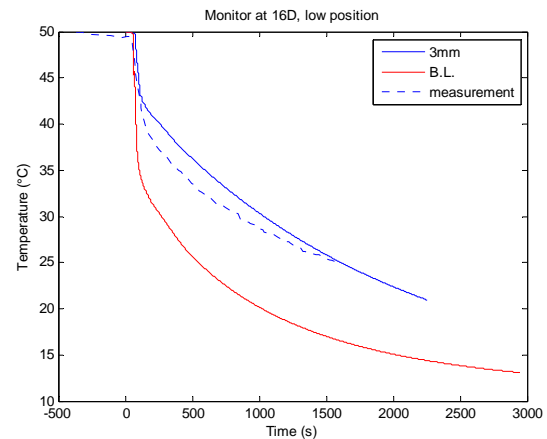
Figure 13 Comparison of measured and simulated temperatures at axial position 16D downstream of the cold spot and 14 mm above the bottom of the pipe.
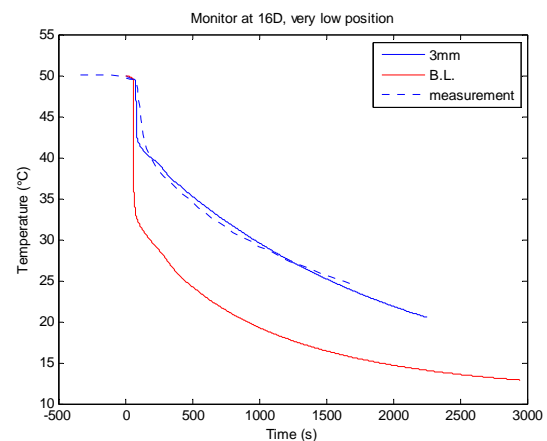
Figure 14 Comparison of measured and simulated temperatures at axial position 16D downstream of the cold spot and 3 mm above the bottom of the pipe.

Figure 15 shows the simulated results at 16 diameters downstream of the cold spot and near the top of the pipe. The agreement is fairly good although the grid independent solution shows a too rapid cooling also for this point.

Figure 15 Comparison of measured and simulated temperatures at axial position 16D downstream of the cold spot and 12 mm below the top of the pipe.

All the comparisons of the measured and simulated temperatures show that the simulations with the fine grids result in too rapid cooling. This may indicate that the estimated value of the external heat exchange coefficient is too large. Simulations with a smaller external heat exchange coefficient and fine grids can be performed to study this in more detail.

RESULTS

The cooling of the wall at the cold spot sets up circulation of the fluid in the pipe due to the density difference between cold and warm fluids. Figure 17 and Figure 18 show the temperature profiles in the symmetry plane for three different times. The figures show the pipe inclined at 2°. Initially the cold liquid falls to the bottom of the pipe where it flows towards the low end. The content of the pipe is cooled gradually maintaining a vertical temperature gradient.
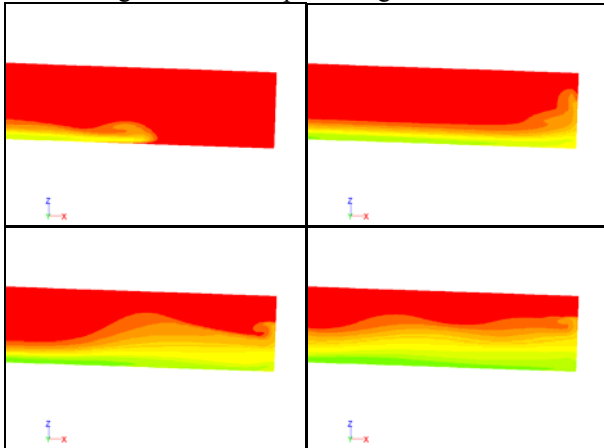
Figure 16 Temperature profiles in the symmetry plane showing the cold front flowing towards the bottom end of the pipe and hitting the end wall. The profiles are shown at 60, 70, 80, and 95 seconds.
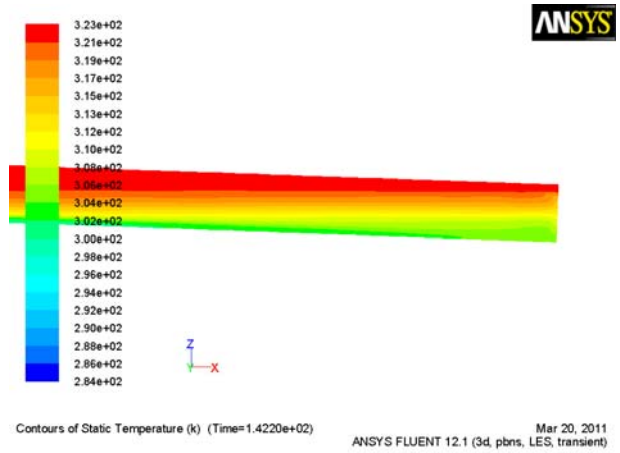
Figure 17 Temperature profile in the symmetry plane after 142 seconds.
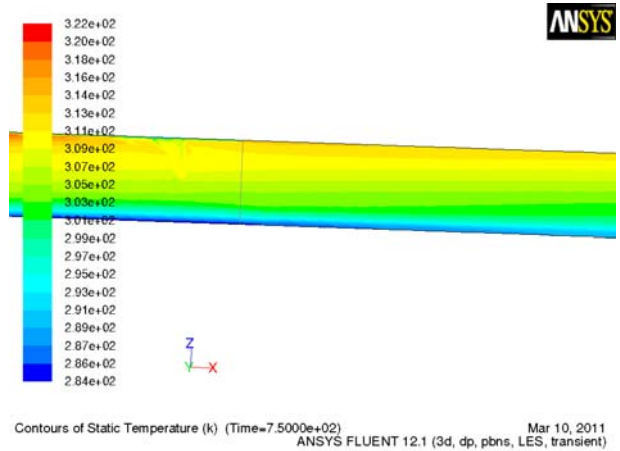
Figure 18 Temperature profile in the symmetry plane after 750 seconds.

Figure 19 shows the temperature in the cross sectional plane at the centre of the cold spot after 2250 seconds. There is a clear vertical temperature gradient. The fluid near the wall is much colder than the fluid in the core. The effect of the cold water falling along the wall can be seen in the profiles.
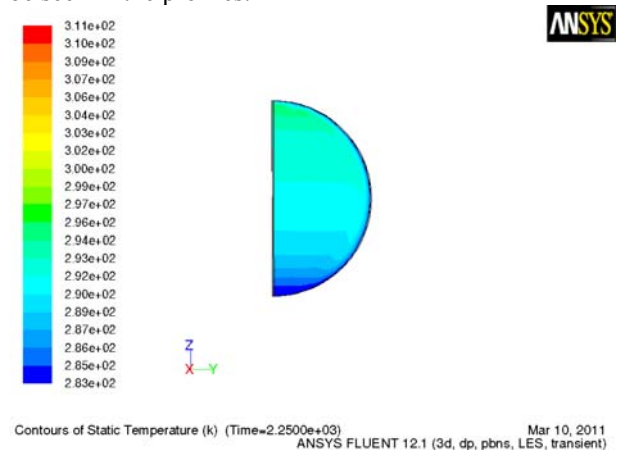
Figure 19 Temperature profile in the cross section at the midpoint of the cold spot after 2250 seconds.

Figure 20 and Figure 21 show the velocity vectors in the symmetry plane at two different locations. The velocity decreases with time due to reduced driving force for the heat exchange. In Figure 20 the low measurement points at 1 and 2 diameters downstream of

the cold spot are shown. It can be seen that most of the cold flow is below the measurement points. This is the reason why the sudden temperature decreases seen in the measurements at these points are not captured by the simulations. Figure 21 shows the cold front approaching the measurement point 16 diameters downstream of the cold spot. The flow reaches the end of the pipe just 1 diameter further downstream the pipe. The thickness of the cold layer then increases and the cold fluid reaches the measurement point. The sudden temperature decrease is thus captured better for the measurement points near the end of the pipe.
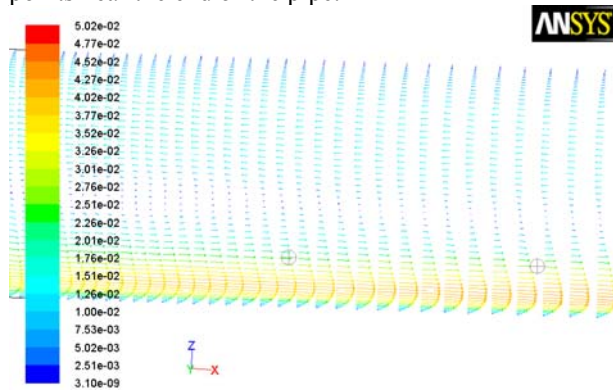
Figure 20 Velocity vectors in the symmetry plane after 90 seconds. Most of the flow is below the measurements points at 1 and 2 diameters downstream of the cold spot.
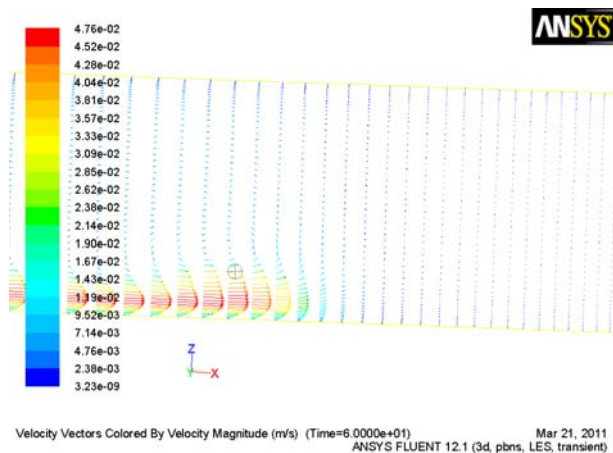
Figure 21 Velocity vectors in the symmetry plane showing the cold front flowing towards the bottom end of the pipe at 60 seconds. The 16 diameter measurement point is shown.

Simulation of a field application

In a field application the internal fluid can be either a compressed gas or any type of oil. In a multiphase flow line it will be a mixture of gas and liquid. The liquid phase can be oil, water, or an oil-water mixture. For the simulations only the simpler single phase cases have been considered. In a shut-down situation the liquid will be at the bottom and the gas at the top of the pipe. It is assumed that the single phase results will describe the outer limits of the results, with two- or three phase situations in between.

The simulations were set up with a cold spot positioned in a horizontal pipe. The pipe diameter used in the simulations was 8"=0.186 m. The cold spot was 3 diameters long. The mesh was made with a boundary layer with an outer layer with thickness 2 mm. The layer

thickness grew with a factor 1.1 for 10 layers. The core was meshed using a 10 mm tetrahedral mesh. This gave wedge shaped 3 dimensional elements. The resulting mesh in shown in Figure 22.
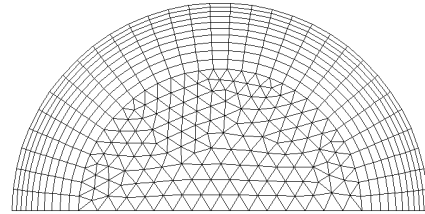
Figure 22 The mesh used for the field application.

The heat transfer coefficient towards the surroundings was set to 230 W/(m·K). The pipe walls were modelled as bare steel and insulated steel. Both wall types allow for heat transfer to the colder surroundings. Due to the lack of insulation the heat transfer is much larger from the cold spot than from the insulated part of the pipe.

The pipeline length was around 30 diameters. This is long compared to the cold spot although it is relatively short compared to a real life situation. In a real life situation, though, the pipe will typically not be horizontal nor will it be completely straight. The results are still considered valuable despite of the shortcomings of the model.

The Boussinesq approximation was used to account for the density changes due to falling temperatures. The Rayleigh number was seen to be large, and thus the LES turbulence model was used.

The time step was calculated using Equations (8) and (9), and was set to 0.06 s.

The effect of the thickness of the outer cell layer of the boundary layer was studied by refining this to 1 mm and 0.1 mm and keeping the boundary layer thickness constant. The core was refined to 5 and 2 mm tetrahedral mesh, respectively. The refined meshes are shown in Figure 23.
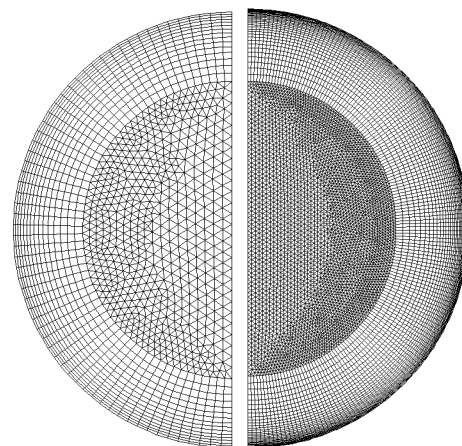
Figure 23 Refined meshes for the field application.

Figure 24 shows the mean temperature of the gas for various thicknesses of the outer cell layer. There is no noticeable effect of refining the boundary layer. It is therefore concluded that the solution is grid independent.
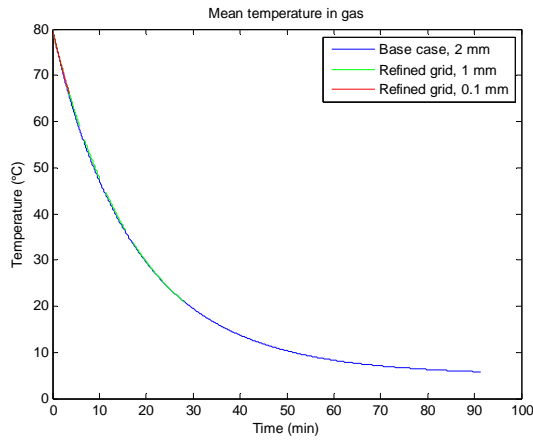
Figure 24 Mean gas temperature for different grid sizes.

The effect of the natural convection on the cooling time of the fluid in a pipeline with a cold spot during a shut-down situation was studied. The result for the mean temperature of the total domain for the natural convection simulation was compared to a similar simulation with constant density and thus without natural convection. The result is shown in Figure 25. The increased cooling due to the internal circulation of fluid is significant. For this case the cooling time is reduced to around ¼ of the cooling time of a non-flowing fluid.
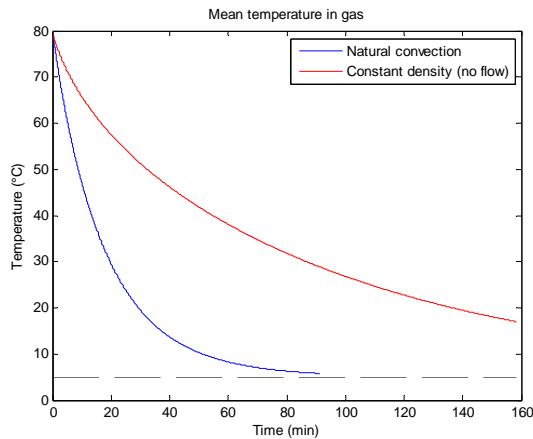
Figure 25 Comparison between mean temperature in gas for a system with natural convection and a non-flowing system. The natural convection enhances the cooling of the fluid in the pipeline significantly.

The effect of damage to or removal of the insulation on a small portion of the pipeline was studied. The results for the mean temperature in the total domain for cooling of natural gas at 50 bar in the case of a shut in with and without a cold, uninsulated spot on the pipeline are shown in Figure 26. These are compared with the results for oil. Due to the much higher heat capacity of the oil it cools much slower than the gas. The gas in the fully insulated pipe also cools much faster than the oil.
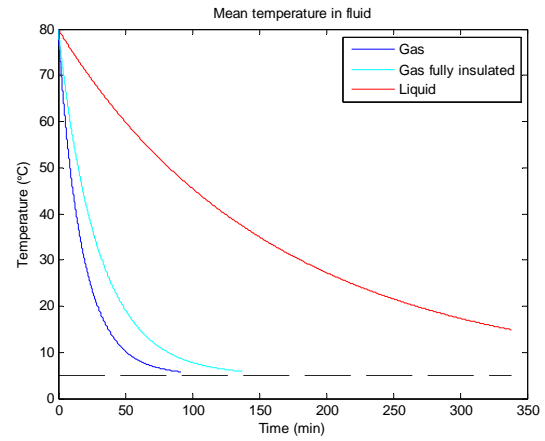
Figure 26 Comparison between mean temperature for gas and oil in a transport pipeline with a cold spot during a shut-in situation. The mean temperature for gas in a fully insulated pipeline is included.

Figure 27 and Figure 28 show how the temperature profile is developing with time. The cold fluid will initially fall along the wall and then start filling the bottom of the pipe. During this process it will constantly exchange heat with the warm fluid. The size of the recirculation zone will be determined by the extension of the cold layer on the bottom. During the filling only the warm fluid that has seen cold fluid on the bottom will recirculate towards the cold spot. The bottom of the pipe will eventually be filled with cold fluid all the way to the end of the domain. The whole domain will then contain recirculating fluid.
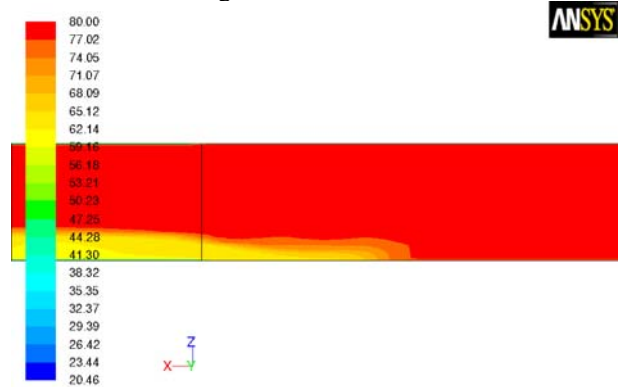
Figure 27 Temperature profile in the symmetry plane when the fluid has started cooling. The cold spot is to the left of the vertical line.
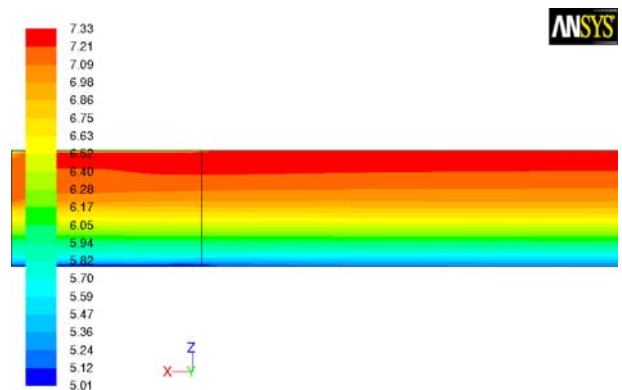
Figure 28 Fluid temperature after the cooled fluid has reached the end of the simulation domain and started to recirculate.

Figure 29 and Figure 30 show end views of the temperature profiles inside the cold spot. The effect of the falling cold liquid at the wall can be seen clearly in both figures.
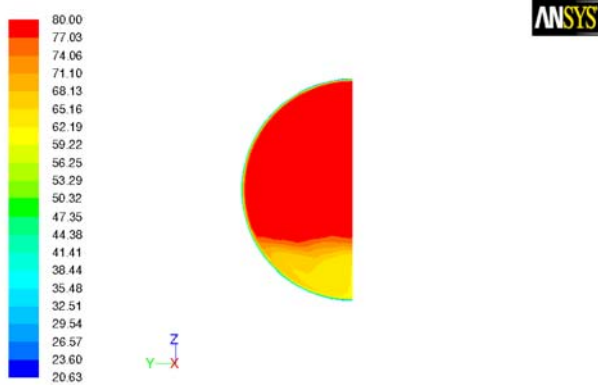
Figure 29 End view of the temperature profile inside the cold spot during the initial stages of the cooling, i.e. long before the fluid enters the end of the domain.
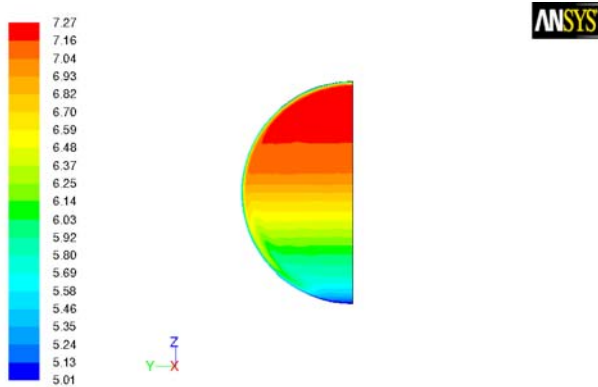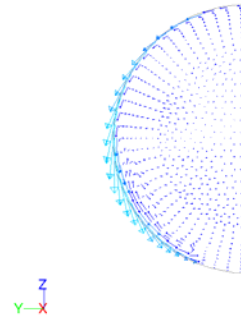

Figure 30 End view of the temperature profile inside the cold spot after the fluid has reached the end of the simulation domain and recirculates.

Figure 31 and Figure 32 show the velocity vectors in a cross sectional plane inside the cold spot during the initial cooling and at a later stage. The legends of the figures are identical. In the initial stage there is a recirculation in the cold fluid zone. When this zone has become more stable this recirculation moves upwards, and the magnitude of the flow is reduced. Both figures show that the cold fluid follows the wall as it falls due to density differences.
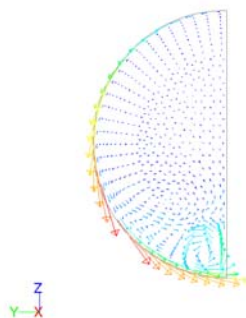
Figure 31 Velocity vectors in a cross sectional plane inside the cold spot during the initial cooling of the fluid.

Figure 32 Velocity vectors in a cross sectional plane inside the cold spot after the fluid has reached the end of the simulation domain and recirculates.

For a field application it is useful to have an estimate of how fast the fluid cools. If the gas temperature falls below the critical temperature for hydrate appearance, hydrates can be formed. In the worst scenario, these can block the pipeline. It is therefore important to get good estimates of the cooling time in order to avoid shut-in times that can have a potential of hydrate creation.

Locally, the fluid will be cooled faster than what is indicated in the mean temperature plot in Figure 26. This may cause local hydrate appearance earlier than expected from the volume averaged results. The mean wall temperature on the cold wall and the insulated wall are thus compared in Figure 33. The temperature on the cold spot falls quickly, and much faster than on the insulated part of the pipe.
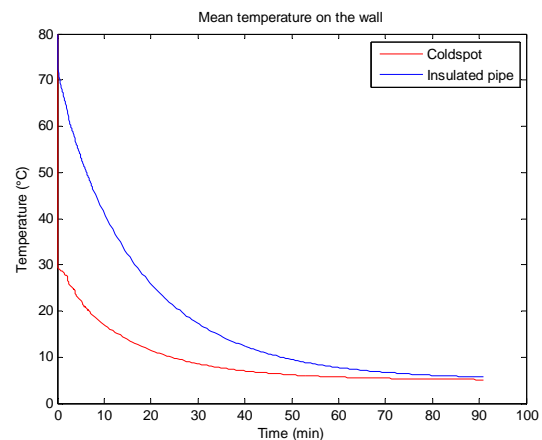
Figure 33 Mean temperature on cold spot and insulated part of pipe as a function of time.

The fluid at the wall is constantly exchanged with warmer fluid. Figure 34 shows how the temperature of a fluid element released near the top of the pipe decreases as it flows along the cold wall and then how it is increasing after the element re-enters the bulk liquid. The figure shows that the element circulates several times.
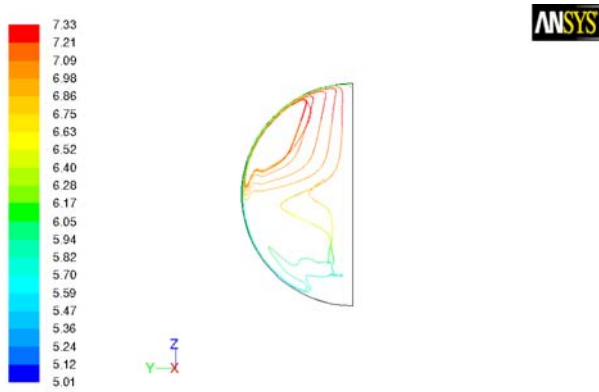
Figure 34 The flow path and temperature variation of a fluid element released near the top centre of the pipe.

CONCLUSION

The experimental data of Mme et al. (2009) and Mme (2010) were compared with CFD simulations with ANSYS Fluent to increase our understanding of the most important parameters in the modelling. The advice to use the LES turbulence model was followed. It was found the grid size near the wall influences the solution significantly. It is thus advised that a grid independent solution should be sought in order to get correct answers for the heat transfer and fluid temperatures.

In a shut-in situation the cooling time of the fluid inside the pipe is usually calculated using correlations and 1-dimensional models. If the insulation of a pipe has been damaged in some location(s) this will increase the local heat transfer. We have found that the effect of natural convection on cooling time is significant. The effect of the increased heat transfer due to natural convection and the proposed shut-in time should be considered in the planning of a shut-in of a pipeline with damaged insulation.

FUTURE WORK

We found that the grid resolution was important for the results when using the LES turbulence model. Mme (2010) advised the use of the LES model over the k-ε-model. Based on our findings on the grid independence for the LES model it is suggested that a grid independent solution for the k-ε-model should be sought and compared with the experimental results and the simulation results for the LES model.

The grid independent solution showed a poorer agreement with the data than the coarse grid solution. It is suggested that the cause of this is studied to increase the understanding of modelling of natural convection.

Mme found that the cooling time depended on the inclination of the pipe. Transportation pipelines are usually not perfectly horizontal. It is thus suggested that the effect of inclination on the cooling of transportation pipelines is studied further.

ACKNOWLEDGEMENT

REFERENCES

ANSYS Fluent 12.0, (2009), "User's Guide".

BEJAN, A., (1984), "Convection Heat Transfer", *John Wiley and Sons*, New York.

MME, U., JOHANSEN, S.T., SARKAR, S., MOE, R., GOLDSZAL, A. and LADAM, Y., (2009), "Flow and heat transfer in pipe caused by localised cold spot", *Progress in Computational Fluid Dynamics*, **9** (6-7), 409-416.

MME, U., (2010), "Free convection flow and heat transfer in pipe exposed to cooling", *PhD thesis, Norwegian University of Science and Technology*.

TAXY, S. and LEBRETON, E. (2004), "Use of computational fluid dynamics to investigate the impact of cold spots on subsea insulation performance", *Offshore Technology Conference*, Houston, Texas, U.S.A.

AARNES, K.A. and LESGENT, J. (2005), "Thermal Design of a Dalia SPS Deepwater Christmas Tree-Verified by Use of Full-Scale Testing and Numerical Simulations", *Offshore Technological Conference,* Houston, U.S.A

8th International Conference on CFD in Oil & Gas, Metallurgical and Process Industries
SINTEF/NTNU, Trondheim Norway
21-23 June 2011

CFD11-144

LIGGGHTS Open Source DEM: Models, Features, Parallelism and Quality Assurance

Christoph KLOSS[1], Christoph GONIVA[1], Stefan AMBERGER[1] and Stefan PIRKER[1,2]

[1]Christian Doppler Laboratory on Particulate Flow Modelling

[2]Institute of Fluid Mechanics and Heat Transfer

both Johannes Kepler University,

Altenbergerstr. 69, 4020 Linz, Austria

* E-mail: christoph.kloss@jku.at

ABSTRACT

$\mathbf{u}$
$\Delta\mathbf{u}$

$\mathbf{x}$

Sub/superscripts

INTRODUCTION

Keywords:

NOMENCLATURE

Greek Symbols
δ
μ
ρ

Latin Symbols

$\mathbf{F}$
$\mathbf{g}$

$$F_n = -k_n \delta_n + c_n \Delta u_n$$

$$F_t = min\left\{ \left| k_t \int_{t_c}^{t} \Delta u_t \, dt + c_t \Delta u_t \right|, \mu \, F_n \right\}$$

Δ

δ

DISCRETE ELEMENT METHOD (DEM)

Basic idea of soft-particle DEM

μ

$t = t_{c,0}$

$$m_i \ddot{x}_i = F_{i,n} + F_{i,t} + F_{i,f} + F_{i,b}$$

$F_{i,n}$

$F_{i,t}$

F

F

The concept of neighbour lists

δ

Δu

Ft

i

j

g

Fn

g

$$\|x_i - x_j\| < r_i + r_j + s$$

Figure 1

Δ
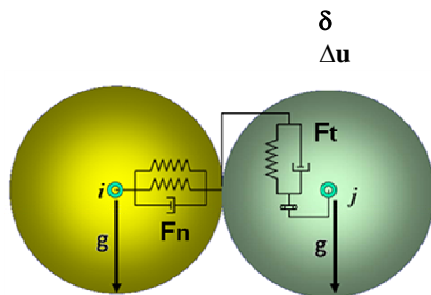
$$N_{verlet} = \frac{s}{v_{max}\,\Delta t}$$

Contact Laws

Triangulated wall handling

•

•

•

THE OPEN SOURCE DEM CODE LIGGGHTS

•

•

•

MODEL OVERVIEW

•

•

•
•
•
•
•

•
•

•
•

$$h_{ij} = \frac{k_i\, k_j}{k_i + k_j} \sqrt{A_{c,ij}}$$

$$A_{c,ij} = -\frac{\pi}{} \frac{\left(c_{ij} - r_i - r_j\right)\left(c_{ij} + r_i - r_j\right)\left(c_{ij} - r_i + r_j\right)\left(c_{ij} + r_i + r_j\right)}{c_{ij}}$$

$$c_{ij} = \delta_{n,ij} - r_i - r_j$$
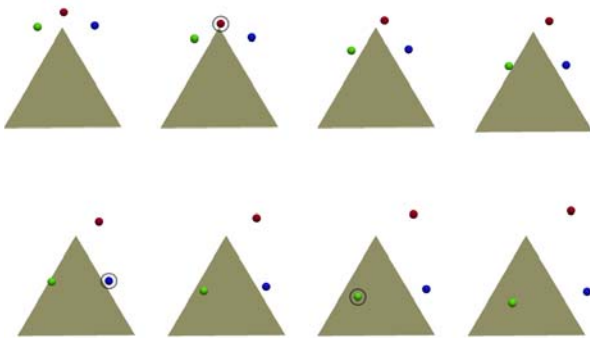
Figure 2:

Simple heat conduction model

Figure 3:

6 degree-of-freedom model for rigid bodies

$$m_i\, c_{p,i} \frac{dT_i}{dt} = \sum_j q_{ij} + q_{src,i}$$

$$q_{ij} = h_{ij}\left(T_j - T_i\right)$$
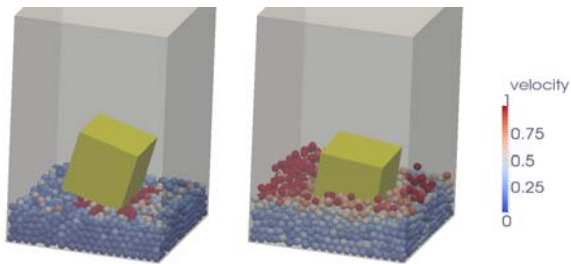
Figure 4:

Figure 5: (

PARALLELLISM

Parallelism as implemented in LAMMPS
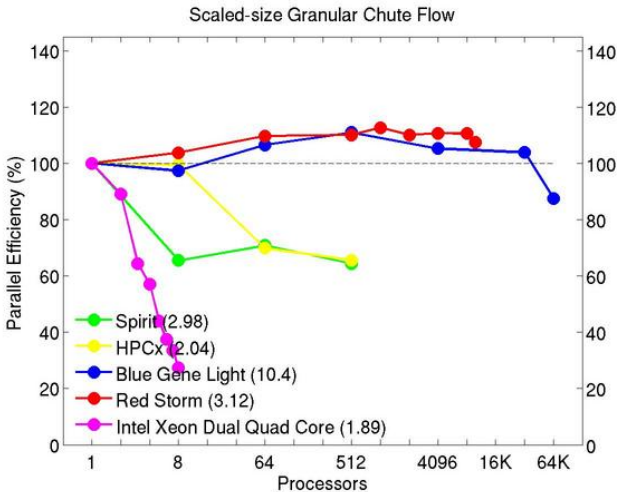
Dynamic Load Balancing

Scalability without dynamic load-balancing

Perform the decomposition with orthogonal cuts in x-, y- and z-direction so that these cuts divide the particle entity equally.
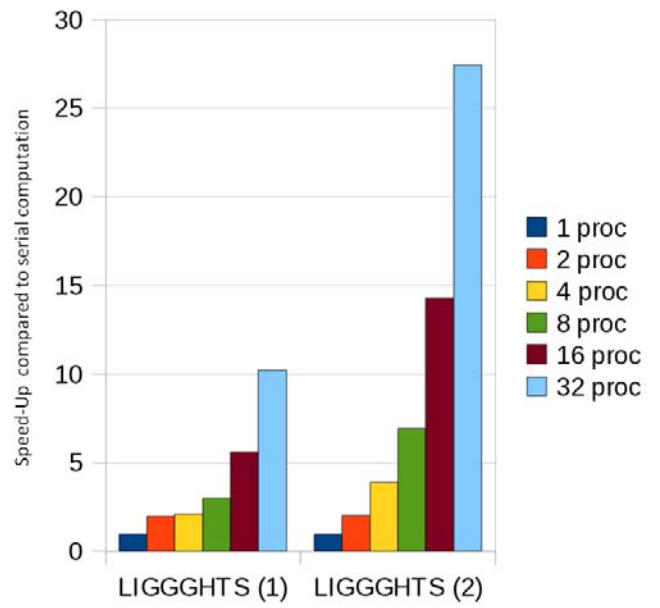
Figure 6: (

Dynamic Load Balancing Test Case
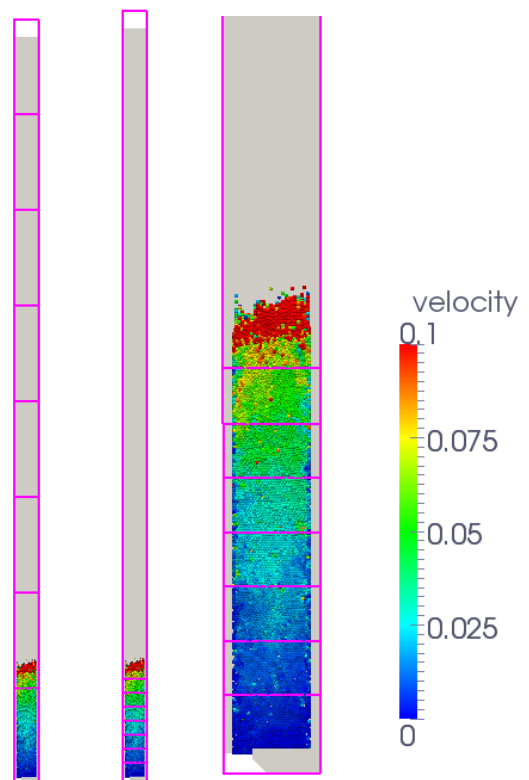
Figure 7:
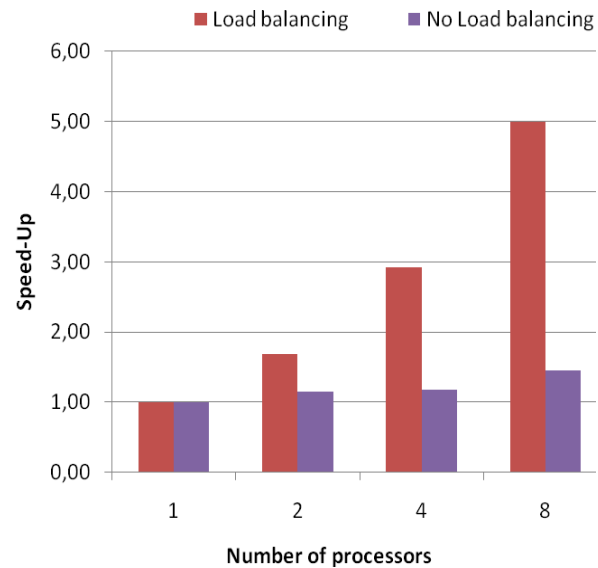
Figure 8:
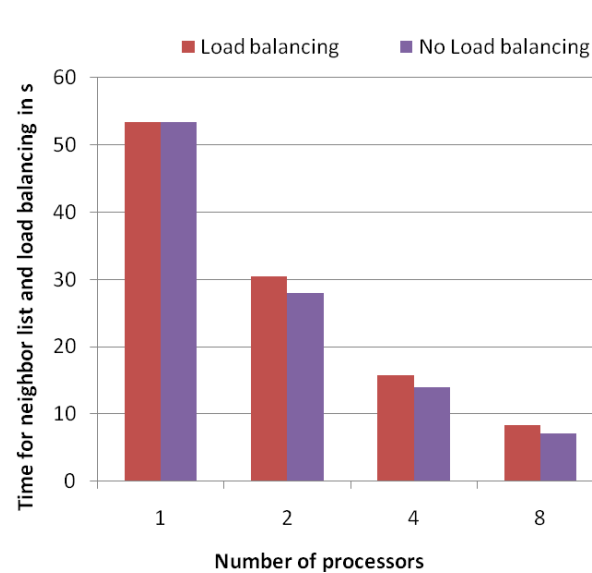
Figure 9:
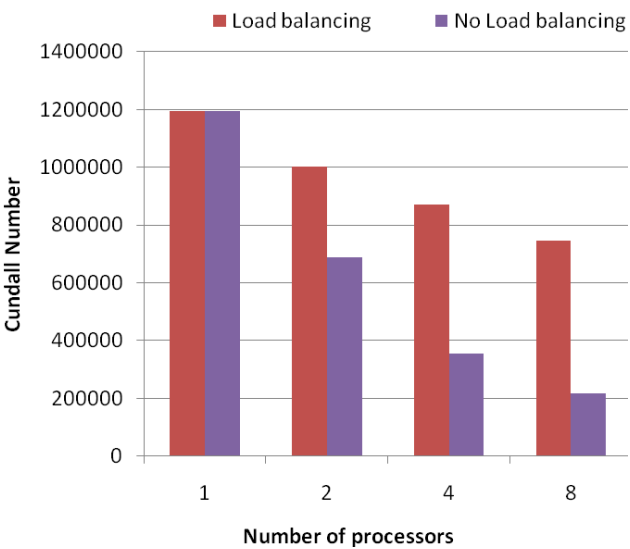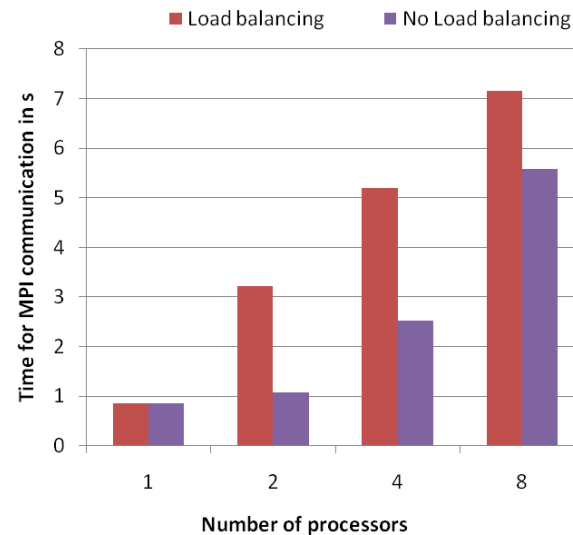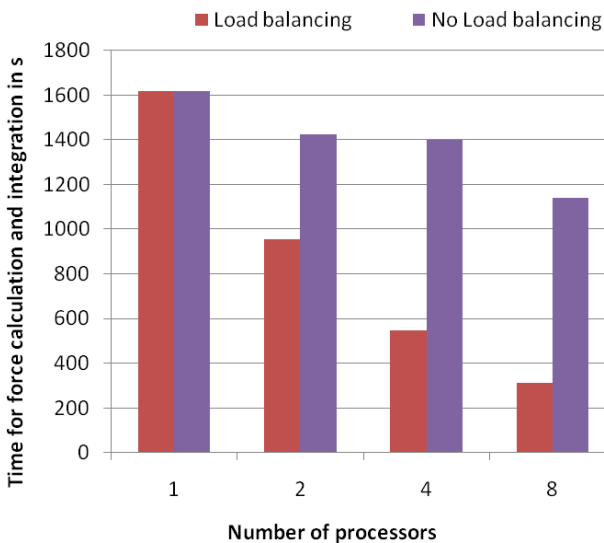
Figure 10:

Figure 11:

Figure 12:

QUALITY ASSURANCE
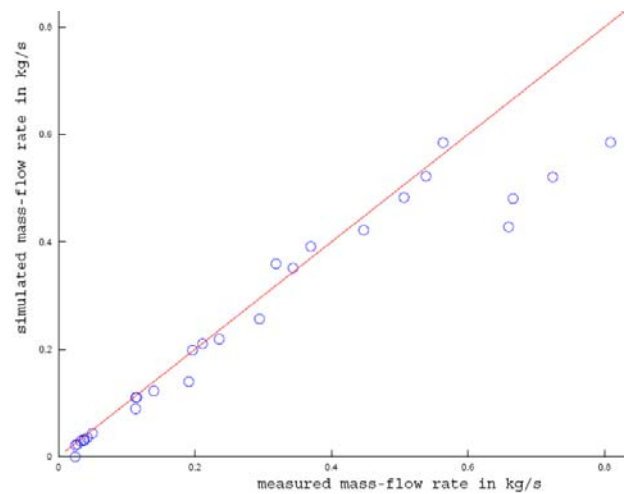
Figure 14:
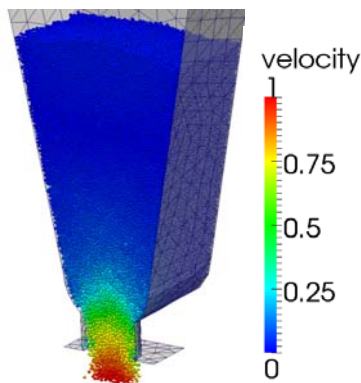
CONCLUSION

Experimental Validation – Hopper Flow

REFERENCES

The Mathematical Theory of Non-Uniform Gases

Chem. Eng. Sci

Geotechnique

Figure 13:

J. Comp. Meth. Appl. Engnrg.,

Proc. 5th Intl. Conf. on Discrete Element Methods

Proc. Open Source CFD International Conference

Proc. Open Source CFD International Conference

Int. J. for Num.Meth. Eng

An introduction to Granular Flow

Chemical Engineering Science

J. of Information and Software Technology

", Phys. Rev

Powder Technology

Chemical Engineering Science

8th International Conference on CFD in Oil & Gas, Metallurgical and Process Industries
SINTEF/NTNU, Trondheim NORWAY
21-23 June 2011

CFD11-145

INVESTIGATIONS OF TRANSITIONAL FLOWS USING IMAGE BASED HEMODYNAMICS

Kristian VALEN-SENDSTAD[1]*, **Mikael MORTENSEN**[2], **Kent-André MARDAL**[1], **Bjørn Anders PETTERSSON REIF**[2], **Hans Petter LANGTANGEN**[1]

[1]Center for Biomedical Computing at Simula Research Laboratory, P.O.Box 134, N–1325 Lysaker, Norway

[2]Norwegian Defence Research Establishment (FFI), 2027 Kjeller, Norway

* E-mail: kvs@simula.no

ABSTRACT

We investigated the complexity of blood flow in intracranial aneurysms in terms of the frequency spectrum of pointwise velocity and pressure fluctuations. The investigations were performed using high-resolution computational fluid dynamics (CFD) simulations for patient-specific middle cerebral artery (MCA) aneurysms, using realistic inflow profile. Through these simulations, the study confirmed that complex transitional flow can occur in intracranial aneurysms. In particular, we found fluctuations of the order of 500-1000 Hz.

Keywords: CFD, aneurysms, hemodynamics, turbulence.

NOMENCLATURE

Greek Symbols
ρ Mass density, $[kg/m^3]$
μ Dynamic viscosity, $[kg/s]$
ν Kinematic viscosity, $[m^2/s]$
ω Angular frequency, $[1/s]$
ε Dissipation rate, $[m^2/s^3]$.

Latin Symbols
D Diameter, $[m]$.
Hz Frequency, $[1/s]$.
k Turbulent kinetic energy, $[m^2/s^2]$.
l^+ Viscous lenght scale, $[m]$.
Δl Mean cell length , $[m]$.
p Pressure, $[Pa]$.
S Shear deformation rate, $[1/s]$.
t^+ Viscous time scale, $[s]$.
u Velocity, $[m/s]$.
u_* Friction velocity, $[m/s]$.
$\bar{u}$ Mean velocity, $[m/s]$.
u' Fluctuating velocity, $[m/s]$.

Sub/superscripts
i Index i.
j Index j.

Figure 1: An example of cerebral arteries with an aneurysm. Courtesy of (Lucien Monfils, 2008). The aneurysm can be identified as the spherically shaped object in the center of the image.

INTRODUCTION

Cardiovascular diseases, like cerebral strokes, are among the main causes of death in the developed world. Although the exact cause is unknown, these diseases have been related to heavy alcohol consumption, smoking, high blood pressure etc. (Eden *et al.*, 2008; Brisman *et al.*, 2006; Weir, 2002;
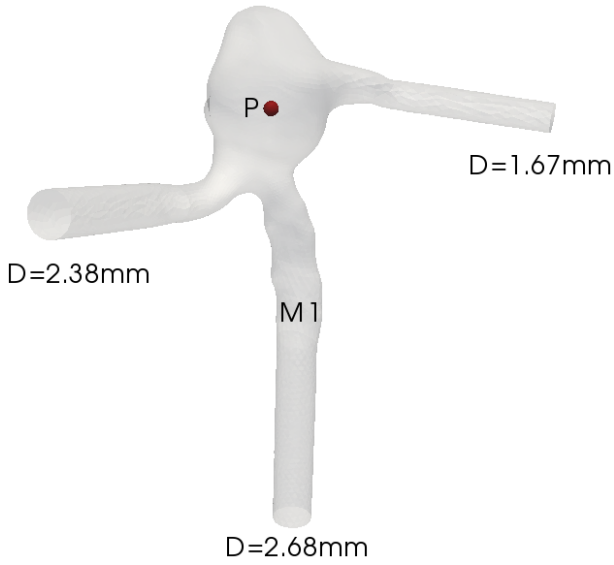
Figure 2: Patient-specific geometry (aneurysm A) used in this study illustrated as a 20% opaque surface. The sphere indicate where the velocity and pressure have been measured.
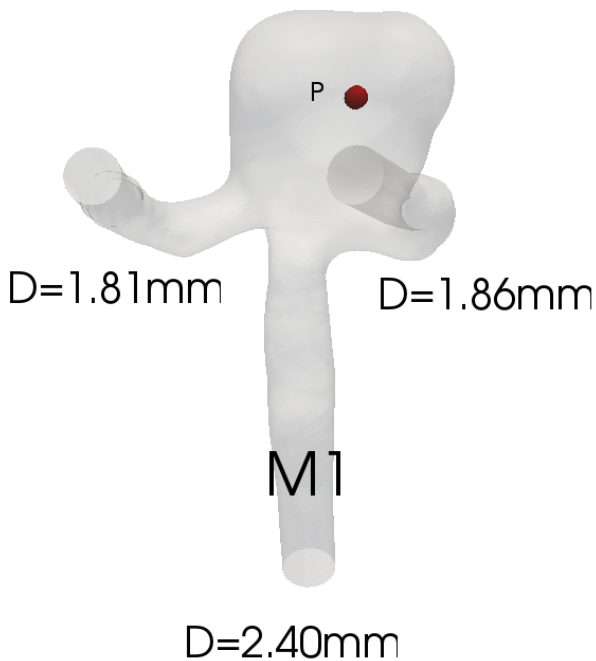

Figure 3: Patient-specific geometry (aneurysm B) used in this study illustrated as a 20% opaque surface. The sphere indicate where the velocity and pressure have been measured.

Schievink, 1997; Humphrey, 2001). In this study we will focus on a particular type of stroke, namely the rupture of an aneurysm. An aneurysm is a damaged part of a blood vessel which bulges out and an example is shown in Figure 1. The rupture results in a bleeding in the subarachnoid space that surrounds the brain. It is therefore called *subarachnoid hemorrhage* (SAH). This particular type of stroke is particularly dangerous - it results in death within 30 days in 50% of cases. The estimated incidence of SAH is roughly 1/10000 people annually (Brisman *et al.*, 2006). Aneurysms pose a particular challenge to clinicians since around 6% of the general population will develop such aneurysms within a life-time, but only few of these rupture. While a rupture is usually a catastrophic event for the individual, treatment is both costly and risky, and should only be performed when necessary.

The exact mechanisms behind initiation, growth, and rupture of intracranial aneurysms are unknown. What is known is that arteries remodel themselves according to flow conditions (Chien, 2007; Fung, 1984). For example, blood vessels thicken if blood pressure rises, they are lengthened with axial loads, and they increase internal diameter with high values of wall shear stress (WSS). In addition, if the WSS exceeds a limit of 40 Pa, the endothelial cells in the vessel wall are believed to be damaged, and an aneurysm might form (Davies *et al.*, 1986; Fry, 1968).

Sounds or bruits in the vasculatory system at the range of 1-1kHz have been reported by clinicians (Kurokawa *et al.*, 1994), and peaks at high frequencies are believed to be associated with sick blood vessels. Most blood flow simulations are performed at a resolution where rapid fluctuations can not be captured. The purpose of this study is therefore to perform flow simulations at higher resolution in time. We extend the study (Valen-Sendstad *et al.*, 2011a) where one aneurysm was studied, with another aneurysm and compare the flow in the two aneurysms. Therefore, the results from aneurysm in Figure 2 are included here as well. We also discuss the wall shear stress oscillations induced by the flow.

Blood flow in cerebral arteries is a complex phenomenon. As blood is a suspension of plasma and extremely flexible cells, it shows both nonlinear and visco-elastic behavior. Furthermore, blood vessels are compliant and the flow of blood is pulsatile. Turbulence has previously been shown to occur in both the aorta (Khanafer *et al.*, 2007) and in a stenosed carotid artery (Lee *et al.*, 2008). Audible sound, which implies turbulence, has successfully been recorded from saccular aneurysms in dogs (Sekhar *et al.*, 1990) and people (Ferguson, 1970). Even though one may argue that the blood flow is immensely complex, the resolution of the medical data is limited to slightly less than 1 mm in space and 1/20 s in time. Hence, it is important to find a model that capture only the relevant features. The current work will address the presence of turbulent flow in middle cerebral artery (MCA) aneurysms and their potential usage in understanding cerebral strokes. We assume that blood is Newtonian, use rigid walls, and perform a Direct Numerical Simulation (DNS), including all characteristic scales of the flow. The turbulence is thus not modeled, but resolved within a very fine spatial mesh and short time step. The objective of the present study is to determine if turbulent flow can occur in intracranial MCA aneurysms, and to determine the effects on the aneurysm wall.

METHODOLOGY

Imaging and Patient Data

MCA aneurysms from patients treated at the Department of Neurosurgery, University Hospital of North Norway during the period 2006 to 2008 were used for the patient-specific modeling. The selected aneurysms have been used in a previous study (Valen-Sendstad *et al.*, 2011b) and it was known to the authors that the two chosen aneurysms exhibited complex flow and relatively high values of vorticity. The aneurysm geometries are shown in Figures 2 and 3 and are hereby denoted aneurysm A and B. The aneurysms were retrieved by searching for MCA aneurysms in an aneurysm quality register. Three-dimensional imaging of the intracranial arteries and the aneurysm was obtained by computed tomography angiography. The patient-specific geometries were recreated on a computational mesh (Vascular Modeling Toolkit). We included as much as possible from the vessel to create realistic inlet and outlet conditions. In addition, the vessels have been extrapolated with a length of 10 diameters to reduce the boundary artifacts influencing the flow. Three computational mesh sizes consisting of 1.0, 3.1 and 5.5 million tetrahedrons were used for aneurysm A, and 2.0, 4.0 and 8.0 million tetrahedrons for aneurysm B. In order to assess whether or not the flow field was properly resolved, the grid resolution was quantified in terms of the viscous length scale, computed as

$$l^+ \equiv \frac{u_* \Delta l}{v}. \tag{1}$$

Here, Δl is a local length scale that represents the averaged extent of the tetrahedron grid cell $\Delta l = 12/\sqrt{2}\Delta_{\text{Vol}}^{1/3}$, where Δ_{Vol} is the tetrahedron volume. The friction velocity, u_*, is given as

$$u_*^2 = \frac{\mu}{\rho}(S_{ij}S_{ij})^{1/2}, \quad S_{ij} = \frac{1}{2}\left(\frac{\partial u_i}{\partial x_j} + \frac{\partial u_j}{\partial x_i}\right), \tag{2}$$

where S_{ij} is the shear deformation rate, u_i is a component of the fluid velocity and Einstein's summation convention is used for repeated indices. If $l^+ = 1$, then the average grid size Δl equals the viscous length scale which is the smallest spatial scale at which turbulent fluctuations can persist. Since we are not considering an almost unidirectional flow the usual classifications of the viscous scales in three different spatial dimensions are not straightforward (Durbin and Reif, 2001; Pope, 2000; Wilcox, 2002). Instead we have assumed that $l^+ \sim O(1)$ in any direction is sufficient as an indication of a proper grid resolution. Inside the aneurysm dome $l^+ \sim 2$ on the finest meshes. Similarly, we computed

$$t^+ \equiv \frac{v}{u_*^2}, \tag{3}$$

where t^+ is the smallest time scale in a turbulent flow. In our simulation $t^+ \leq 2.2$ for the finest mesh sizes. In all our models, the parent artery is the M1 segment of the MCA artery. The diameters (D) of the M1 segment were 2.4 and 2.68 mm. With a mean inflow velocity (U) of 0.75 m/s the corresponding mean Reynolds number (UD/v) was 527 and 589, where the kinematic viscosity is $v = \mu/\rho$. With a heart rate of 60 beats per minute, the angular frequency (ω) is 0.002 π/ms, and the Womersley numbers, $D/2(\omega/v)^{1/2}$, were 1.8 and 2.0.

Computational Fluid Dynamics Simulations

To simulate the flow, we solved the Navier-Stokes equations (Durbin and Reif, 2001; White, 1999) for incompress-
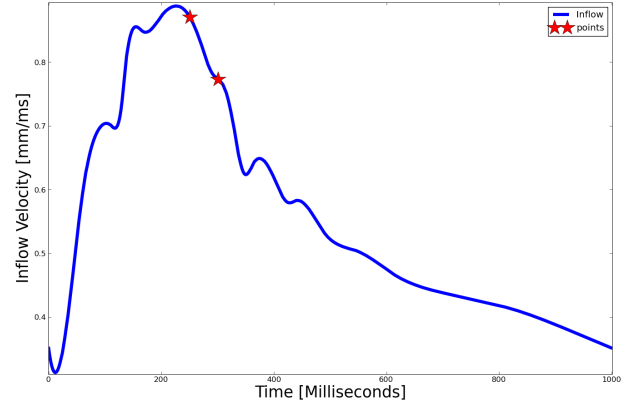

Figure 4: The figure shows the inflow velocity profile used for both aneurysms, with red points indicating the time from where the subsequent figures are made at T1 = 250 and T2 = 300, milliseconds.

ible Newtonian flow, using the numerical solver CDP, developed at Stanford University. CDP uses a second order accurate node–based finite volume discretization in space and advances the equations in time using a second order accurate fractional step method (Goda, 1979). The blood density and viscosity were set to $\rho = 1025\text{kg/m}^3$ and $\mu = 0.0035\text{Pa}\cdot\text{s}$, respectively. The time step was set in reference to the smallest mesh sizes and varied from 0.1, 0.05, to 0.025 milliseconds. Since the smallest viscous scales of the flow can be assumed to be resolved, no explicit turbulence model was applied. We simulated 13 and 10 heartbeats for aneurysm A and B, respectively, but due to (zero velocity) initial conditions used on the first cycle, we do not include the first cycle for the reported values. The simulations were performed on 32 CPUs, and each cardiac cycle required 12 hours of computational time for the finest mesh and time step.

Boundary Conditions

Figure 4 shows the waveform from a patient of equivalent age, which was used as the inflow boundary condition. The values have been adjusted to fit the values obtained by (Krejza *et al.*, 2005) where the MCA velocities of 335 people were measured. It should be noted that any transition occurring inside the aneurysm is most likely caused by local flow conditions rather than pre-determined inflow boundary conditions. On the outlets we used a non-reflecting boundary condition with an equal flux division between the daughter vessels. This particular choice was made since the pressure drop in the main cerebral arteries such as the MCA is dominated by the resistance in the complex downstream vasculature, cf. (Alastruey *et al.*, 2007; Vignon-Clementel *et al.*, 2006). The computed flow is obviously sensitive to the choice of boundary conditions, and the results will therefore be conditional on the outflow boundary conditions. Tests revealed, however, that the main finding in the current study, which is that the flow shows transition to turbulence, does not change.

Turbulence quantities

An instantaneous velocity component, u_i, can be decomposed as,

$$u_i = \bar{u}_i + u_i^{'},$$

where $\bar{u}_i$ and $u_i^{'}$ are the mean and fluctuating velocity components, respectively, in the x_i direction. The specific turbulent

Figure 7: The top half of the figure shows velocity measurements of the velocity components u_1, u_2 and u_3 for aneurysm A in the probe location indicated in Figure 2. The bottom half of the figure is the corresponding pressures at this location.
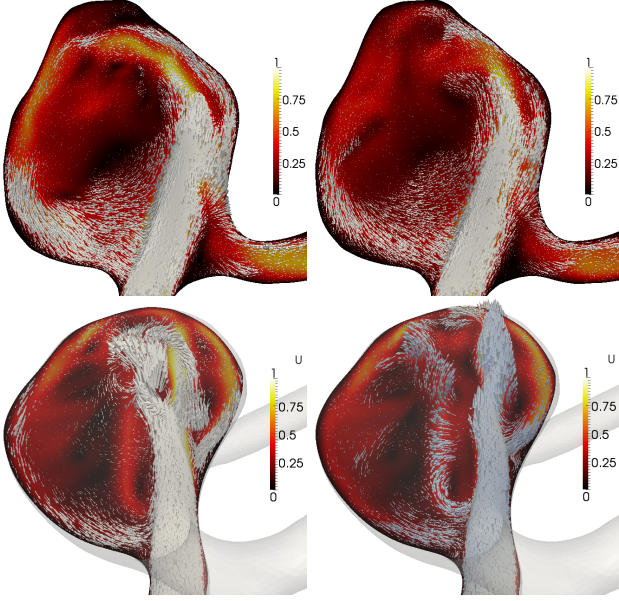
Figure 5: Flow patterns visualized as a slice through the aneurysm dome with arrows indicating flow direction at times T1-T2. In aneurysm A (top), the direction and magnitude of the velocity vectors changes significantly both in the center of the dome and in the high curvature regions near the wall. Recirculation zones also appear and disappear with time, in the latter regions. In aneurysm B (bottom), the flow impinges with an angle more normal to the aneurysm dome which sets up two vortices of different sizes.
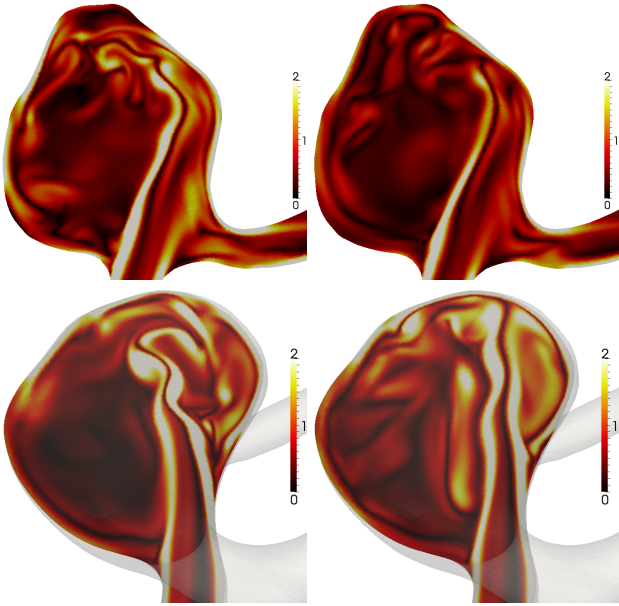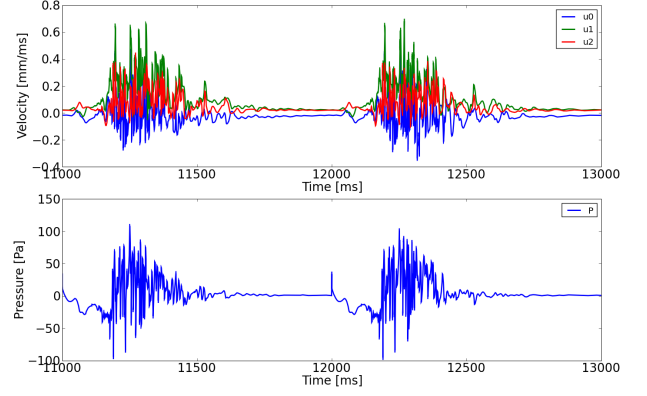
kinetic energy k is defined as:

$$k = \frac{1}{2}\overline{(u_i' u_i')} \qquad (4)$$

where the overline represents ensemble (phase) averaged quantities.

Convergence Tests

To assess whether or not the resolutions in both space and time are sufficient, we also measured the integral of the (pseudo) dissipation rate (E) within the computational domain,

$$E = \int_{\Omega} \varepsilon \, d\Omega,$$

where $\varepsilon = \nu(\overline{\frac{\partial u_i}{\partial x_j} \frac{\partial u_i}{\partial x_j}})$. For the two finest meshes with the time step set to 0.05 milliseconds, E varied with less than 1% between the meshes. Combined with $l^+ \sim 2$ and $t^+ \leq 2.2$, we considered this to be sufficient evidence that all spatial and temporal scales were adequately resolved.

RESULTS

The simulations were started from a zero velocity flow field by imposing a mass flux at the inlet. Since this procedure is somewhat unphysical and makes the first flow–through different from the rest, we did not use the first cycle for computing turbulence quantities reported later in this section.

Flow

Figure 5 shows the computed velocity fields at T1-T2 indicated in Figure 4 from the last cycles. The corresponding magnitude of vorticity (enstrophy) is visualized in Figure 6, which illustrates highly complex turbulent flow which are dampened towards diastole (at the end of the cardiac cycle). Measurements in point P from aneurysm A from the last two cycles, with velocity components u_1, u_2 and u_3 are shown at the top in Figure 7, and corresponding pressure fluctuations at the bottom. The peak pressure fluctuations are at roughly 200 Pa which corresponds to 1.5 mmHg, at a frequency of 100 Hz. The flow patterns in both aneurysms are highly complex and completely changes character during one heart

Figure 6: The magnitude of the vorticity (enstrophy) $\left[\frac{1}{ms}\right]$ is visualized as a slice through the aneurysm dome at times T1-T2. Aneurysm A at top and B at the bottom.
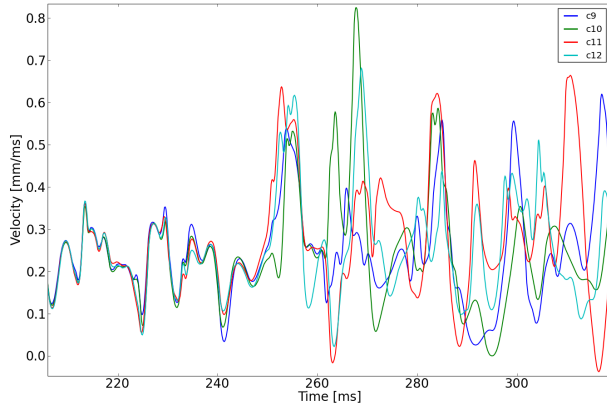
Figure 8: The u_1 velocity component is shown for aneurysm A from the last four cycles for a small period of time where the legends c9, c10, c11, c12 indicate the cycle number. The values are nearly identical until peak systole (at t=226ms), but differ as the inflow decelerates.

cycle with transition from fully laminar to transitional, turbulent and back to fully laminar again. At the beginning of a heart cycle the flow is completely laminar. However, the flow is quickly building complexity, which is clearly illustrated by the probe plots from aneurysm A in Figure 8. During the initial stages the flow starts to oscillate with frequencies in the range of $\mathcal{O}(10)$ Hz, but the flow is clearly laminar as the probe plots from different cycles lie on top of each other. As the flow reaches its peak at about 220 ms the probe plots from different cycles start to diverge and frequencies on the order of 500 - 1000 Hz are clearly visible in Figure 8. These frequencies are associated with unstable non-laminar chaotic flow and is a clear indication of transition to turbulence taking place near and after peak systole (at t=226 ms in Figure 4). Figures 9 and 10 shows the turbulent kinetic energy in the aneurysm dome computed from the last 12 and 10 cycles in aneurysm A and B, respectively. Although they exhibit pointwise highly different turbulent kinetic energy magnitude and spectrum, this figure clearly shows that there is no turbulence neither at the beginning nor the end of the cycle. It also shows that turbulence is not generated until after peak systole as the flow starts to decelerate.

The flow in both configurations studied enters the aneurysm dome like a jet into a confined space. The jet hits the opposing wall and sets up strong shear layers that promotes transition to turbulence through Kelvin-Helmholtz type instabilities. The jet starts to oscillate as small vortices build up and around peak systole the jet is observed to be oscillating violently. In Figure 11 we can see how the vortices impinge on the aneurysm wall creating regions of stagnation and making the WSS change rapidly in both direction and magnitude at times T1 and T2.

DISCUSSION

In an experiment performed four decades ago, acoustic recordings of aneurysms were performed with a small microphone on the end of a catheter during craniotomy surgeries (Ferguson, 1970). Bruits (sound) were found to be present in 10 of 17 of the aneurysms, and occurring during the deceleration phase of the cardiac cycle. These bruits had dominant frequencies of 460 ± 130 Hz, caused by a non–laminar phenomenon.
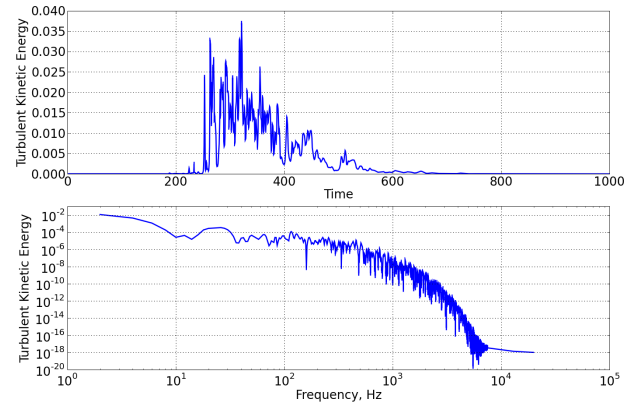

Figure 9: The top half of the figure shows the average turbulent kinetic energy based on 12 cycles for aneurysm A, and the bottom half of the figure is the frequency spectrum.
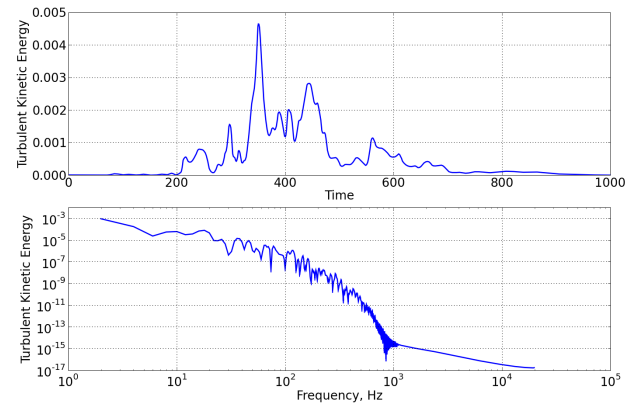

Figure 10: The top half of the figure shows the average turbulent kinetic energy based on 10 cycles for aneurysm B, and the bottom half of the figure is the frequency spectrum.
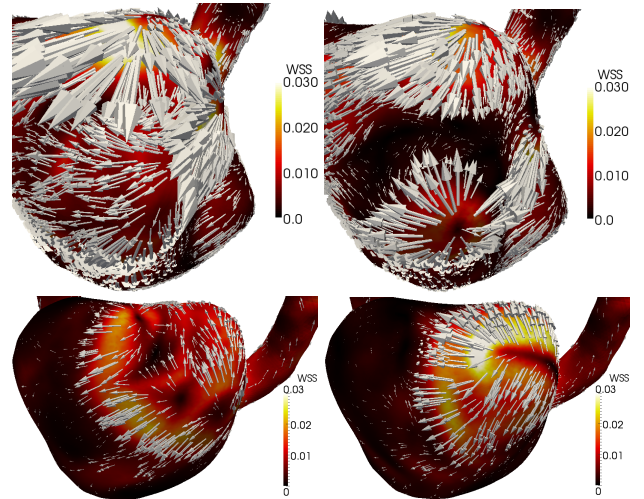

Figure 11: Aneurysm A (top): WSS$[\frac{g}{ms^2mm}]$ at times T1-T2 at the back side of where the flow impinges. At the top of the aneurysm dome, the WSS magnitude and direction changed several times during a heartbeat. Aneurysm B (bottom): WSS the top of the aneurysm dome where the flow impinges. In the figure to the left, there are at lest three visible stagnation point, where in the figure to the right, there is only one.

In the current study, there are three main reasons why the flow in some aneurysms exhibited a non–laminar behavior. Firstly, the volume of the aneurysm domes are relatively large. As the blood entered the dome, the increased volume resulted in less confinement of the jet and the flow therefore had an increased tendency to become more unstable. Secondly, strong shear forces developed due to the large velocity gradients, as the high speed flow entered the dome. This caused the flow field to undergo shear induced instabilities of the Kelvin-Helmoltz type. Thirdly, these instabilities resulted in a series of (primary) vortices which dominates the dynamics of the jet. After these impinge on the aneurysm wall they lead to an unsteady separation, cf. (Popiel and Trass, 1991). All three effects contribute to an increased likelihood for transition to turbulence.

The present study has been limited to a Newtonian description of the blood, but the effects on the flow are believed to be small for arteries in the vicinity of the Circle of Willis (Lee and Steinman, 2007). We have also assumed rigid, impermeable walls when the actual process involves an interaction between the blood flow and the surrounding tissue. The relative wall displacement in MCA aneurysms has previously been shown to be 10-15% (Bazilevs *et al.*, 2010). The outflow boundary conditions, however, have been shown to describe the outflow properly (Alastruey *et al.*, 2007).

CONCLUSION

We have demonstrated computationally that non–laminar turbulent flow can be present in a intracranial aneurysms, which is consistent with experimental results first reported decades ago (Ferguson, 1970). The turbulent flow resulted in both increased WSS magnitude, and WSS frequency. The peak pressure fluctuations were 1.5 mmHg, with dominant frequencies of 100 Hz. The flow exhibits multiple flowregimes that can not be captured well by any turbulence model. Consequently, turbulent flow and its subsequent effects on the arterial wall, should be considered in future simulations to describe the blood flow adequately.

ACKNOWLEDGEMENTS

REFERENCES

ALASTRUEY, J. *et al.* (2007). "Modelling the Circle of Willis to assess the effects of anatomical variations and occlusions on cerebral flows". *Journal of Biomechanics*, **40(8)**, 1794–1805.

BAZILEVS, Y. *et al.* (2010). "Computational vascular fluid–structure interaction: methodology and application to cerebral aneurysms". *Biomechanics and Modeling in Mechanobiology*, **9**, 481–498. URL `http://dx.doi.org/10.1007/s10237-010-0189-7`.

BRISMAN, J.L. *et al.* (2006). "Cerebral Aneurysms". *N Engl J Med*, **355(9)**, 928–939. `http://content.nejm.org/cgi/reprint/355/9/928.pdf`, URL `http://content.nejm.org`.

CHIEN, S. (2007). "Mechanotransduction and endothelial cell homeostasis: the wisdom of the cell". *Am J Physiol Heart Circ Physiol*, **292(3)**, H1209–1224. `http://ajpheart.physiology.`
`org/cgi/reprint/292/3/H1209.pdf`, URL `http://ajpheart.physiology.org/cgi/content/abstract/292/3/H1209`.

DAVIES, P.F. *et al.* (1986). "Turbulent fluid shear stress induces vascular endothelial cell turnover in vitro". *Proc. Natl. Acad. Sci. USA*, **83**, 2114–2117.

DURBIN, P. and REIF, B.A.P. (2001). *Statistical Theory and Modeling for Turbulent Flows*. Wiley & Sons.

EDEN, S. *et al.* (2008). "Gender and ethnic differences in subarachnoid hemorrhage". *Neurology*, **71**, 731–735.

FERGUSON, G.G. (1970). "Turbulence in human intracranial saccular aneurysms". *Journal of Neurosurgery*, **33(5)**, 485–497. `http://thejns.org/doi/pdf/10.3171/jns.1970.33.5.0485`, URL `http://thejns.org/doi/abs/10.3171/jns.1970.33.5.0485`.

FRY, D.L. (1968). "Acute Vascular Endothelial Changes Associated with Increased Blood Velocity Gradients". *Circ Res*, **22(2)**, 165–197. `http://circres.ahajournals.org/cgi/reprint/22/2/165.pdf`, URL `http://circres.ahajournals.org/cgi/content/abstract/22/2/165`.

FUNG, Y.C. (1984). *Biodynamics: Circulation*. Springer-Verlag.

GODA, K. (1979). "A multistep technique with implicit difference schemes for calculating two- or three-dimensional cavity flows". *Journal of Computational Physics*, **30(1)**, 76–95.

HUMPHREY, J.D. (2001). *Cardiovascular Solid Mechanics*. Springer.

KHANAFER, K.M. *et al.* (2007). "Turbulence significantly increases pressure and fluid shear stress in an aortic aneurysm model under resting and exercise flow conditions". *Annals of vascular surgery*, **21(1)**, 67–74.

KREJZA, J. *et al.* (2005). "Age and Sex Variability and Normal Reference Values for the VMCA/VICA Index". *AJNR Am J Neuroradiol*, **26(4)**, 730–735. `http://www.ajnr.org/cgi/reprint/26/4/730.pdf`, URL `http://www.ajnr.org/cgi/content/abstract/26/4/730`.

KUROKAWA, Y. *et al.* (1994). "Noninvasive detection of intracranial vascular lesions by recording blood flow sounds". *Stroke*, **25(2)**, 397–402. `http://stroke.ahajournals.org/cgi/reprint/25/2/397.pdf`, URL `http://stroke.ahajournals.org/cgi/content/abstract/25/2/397`.

LEE, S.W. and STEINMAN, D.A. (2007). "On the relative importance of rheology for image-based CFD models of the carotid bifurcation". *J Biomech Eng*, **129**, 273–8.

LEE, S.E. *et al.* (2008). "Direct numerical simulation of transitional flow in a stenosed carotid bifurcation". *Journal of Biomechanics*, **41(11)**, 2551–2561.

Lucien Monfils (2008). "Angiography of an aneurysm in a cerebral artery". URL `http://commons.wikimedia.org/wiki/File:Aneurysem.jpg`.

POPE, S.B. (2000). *Turbulent Flows*. Cambridge University Press.

POPIEL, C.O. and TRASS, O. (1991). "Visualization of a free and impinging round jet". *Experimental Thermal and Fluid Science*, **4(3)**, 253–264. URL `http://www.sciencedirect.com/science/article/B6V34-47X2FMS-1V/2/a88ce7132aaeb59d6d13be6baccb43b8`.

SCHIEVINK, W.I. (1997). "Intracranial Aneurysms". *N Engl J Med*, **336(1)**, 28–40. `http://content.nejm.`

org/cgi/reprint/336/1/28.pdf, URL http://content.nejm.org.

SEKHAR, L. *et al.* (1990). "Acoustic recordings from experimental saccular aneurysms in dogs". *Stroke*, **21(8)**, 1215–1221. http://stroke.ahajournals.org/cgi/reprint/21/8/1215.pdf, URL http://stroke.ahajournals.org/cgi/content/abstract/21/8/1215.

VALEN-SENDSTAD, K. *et al.* (2011a). "Direct numerical simulation of transitional flow in a patient–specific mca aneurysm". Submitted to Journal of Biomechanics.

VALEN-SENDSTAD, K. *et al.* (2011b). "A quantitative characterization of differences in flow patterns in ruptured versus unruptured mca aneurysms". Submitted to Stroke.

Vascular Modeling Toolkit (). "Vascular Modeling Toolkit". http://vmtk.org/.

VIGNON-CLEMENTEL, I.E. *et al.* (2006). "Outflow boundary conditions for three-dimensional finite element modeling of blood flow and pressure in arteries". *Computer Methods in Applied Mechanics and Engineering*, **195(29-32)**, 3776 – 3796. Absorbing Boundary Conditions, URL http://www.sciencedirect.com/science/article/B6V29-4H4T0NX-1/2/6b79330f0a6ef0ac9ad2889950126116.

WEIR, B. (2002). "Unruptured intracranial aneurysms: a review". *Journal of Neurosurgery*, **96(1)**, 3–42. http://thejns.org/doi/pdf/10.3171/jns.2002.96.1.0003, URL http://thejns.org/doi/abs/10.3171/jns.2002.96.1.0003.

WHITE, F.M. (1999). *Fluid Mechanics, 4th ed.* McGraw-Hill, International Editions.

WILCOX, D.C. (2002). *Turbulence Modeling for CFD*. D C W Industries.

NUMERICAL MODELLING OF OIL SPILL RESPONSE ACTIONS, FLOATING BOOM

Kameleh AGHAJANLOO[1]*, Moharam Dolatshahi Pirooz[1]

[1] School of Civil Engineering, College of Engineering, University of Tehran, Tehran, Iran

* E-mail: aghajanloo@ut.ac.ir

Latin Symbols

D_s

h_s

f

f_c

g

h

p $\qquad\qquad$ x

q $\qquad\qquad$ y

Q_s

T_B

T_E

T_G $\qquad\qquad$ T_B $\quad$ T_E

u $\qquad\qquad\qquad$ x

v $\qquad\qquad\qquad$ y

z

Sub/superscripts

$j =$ $\qquad\quad$ x $\quad$ y $\qquad$.

x $\qquad$ x $\qquad$.

y $\qquad$ y $\qquad$.

INTRODUCTION

ABSTRACT

Keywords:

NOMENCLATURE

Greek Symbols

ρ_o

ρ_w

τ_b

τ_s

υ_t

ξ

Tidal Currents Hydrodynamic Module

Continuity equation

$$\frac{\partial \xi}{\partial t} + \frac{\partial p}{\partial x} + \frac{\partial q}{\partial y} = \frac{\partial z}{\partial t}$$

X Direction Momentum equation

$$\frac{\partial p}{\partial t} + \frac{\partial}{\partial x}\left(\frac{p}{h}\right) + \frac{\partial}{\partial y}\left(\frac{pq}{h}\right) = \frac{\partial}{\partial x}\left(\upsilon_t \frac{\partial p}{\partial x}\right) + \frac{\partial}{\partial y}\left(\upsilon_t \frac{\partial p}{\partial y}\right)$$

$$- gh\frac{\partial \xi}{\partial x} - \frac{\tau_{bx}}{\rho_w} + \frac{\tau_{sx}}{\rho_w} - f_{cx}$$

Y Direction Momentum equation

$$\frac{\partial q}{\partial t} + \frac{\partial}{\partial x}\left(\frac{pq}{h}\right) + \frac{\partial}{\partial y}\left(\frac{q}{h}\right) = \frac{\partial}{\partial x}\left(\upsilon_t \frac{\partial q}{\partial x}\right) + \frac{\partial}{\partial y}\left(\upsilon_t \frac{\partial q}{\partial y}\right)$$

$$- gh\frac{\partial \xi}{\partial y} - \frac{\tau_{by}}{\rho_w} + \frac{\tau_{sy}}{\rho_w} - f_{cy}$$

Oil Slick Dynamic Module

MODEL DISCRIPTION

Dynamic equation of oil slick

$$\frac{\partial h_s}{\partial t} + \frac{\partial}{\partial x_j}\left(h_s v_j\right) - \frac{\partial}{\partial x_j}\left(D_s \frac{\partial h_s}{\partial x_j}\right) = \pm Q_s$$

Slick spreading function

$$D_s = gh_s \frac{\left((\rho_w - \rho_o)\rho_o\right)}{f\rho_w}$$

Boundary Conditions

Oil Weathering Module

THE MODEL IMPLEMENTATION

A simple case study

Table 1:

		kg/m^3
	$°C$	cP
		$°C$
		$°C$
		g/mol
	$°$	g/m^3
	$°$	Pa
		$dyne/m$

Mesh Generator

$$\Delta x = \Delta y = \quad m$$

$$\Delta t =$$

$$\frac{\partial h_s}{\partial t} + \frac{\partial}{\partial x_j}\left(h_s v_j\right) - \frac{\partial}{\partial x_j}\left(D_s \frac{\partial h_s}{\partial x_j}\right) = \pm Q_s$$
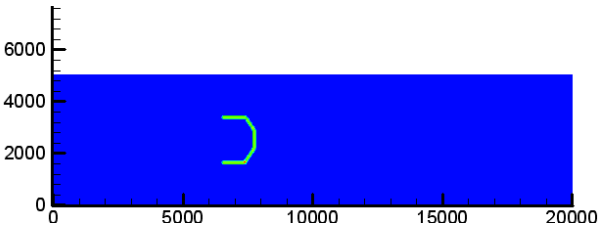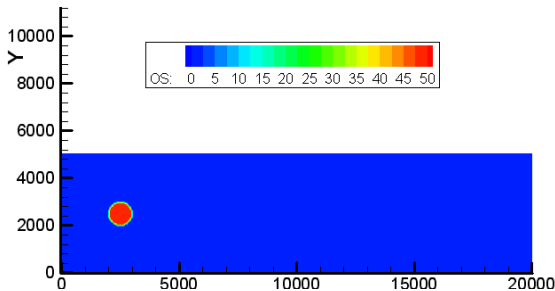
Figure 4:

Figure 1:

Figure 5:
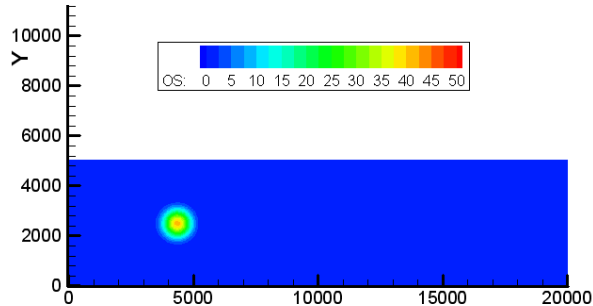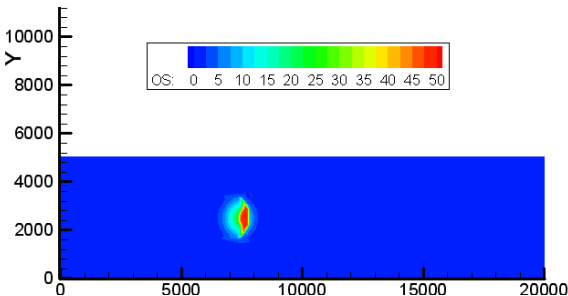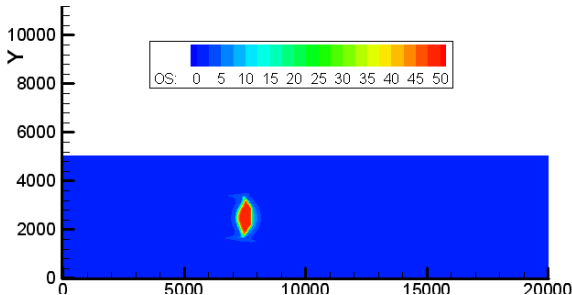
Figure 2:
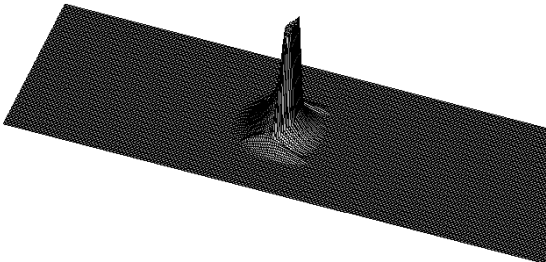
Figure 5:
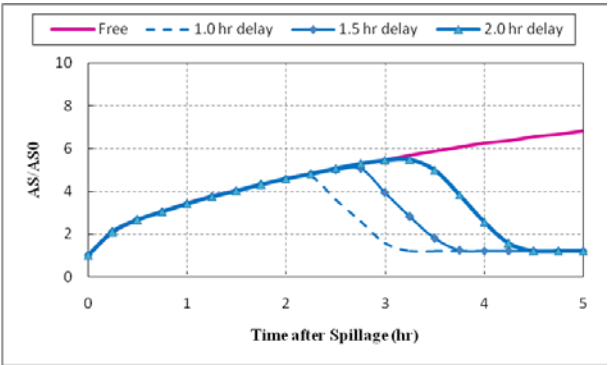
Figure 3:

Figure 7:

Figure 8:

Real Word Applications

Figure 9:

$$\Delta x = \Delta y = \quad km$$
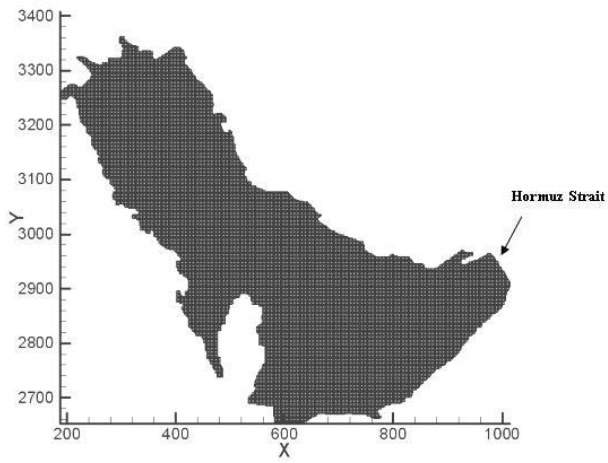
Figure 10:
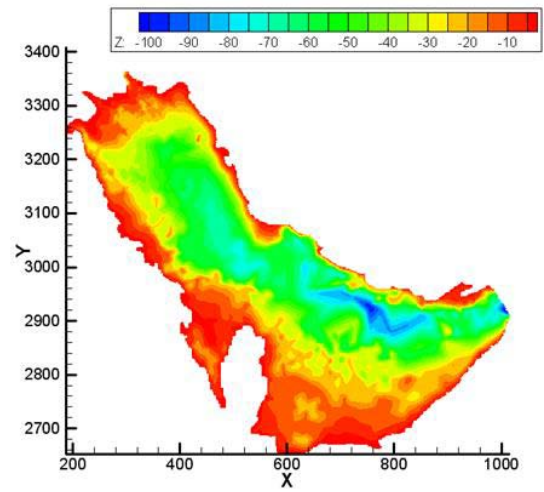
Figure 11:
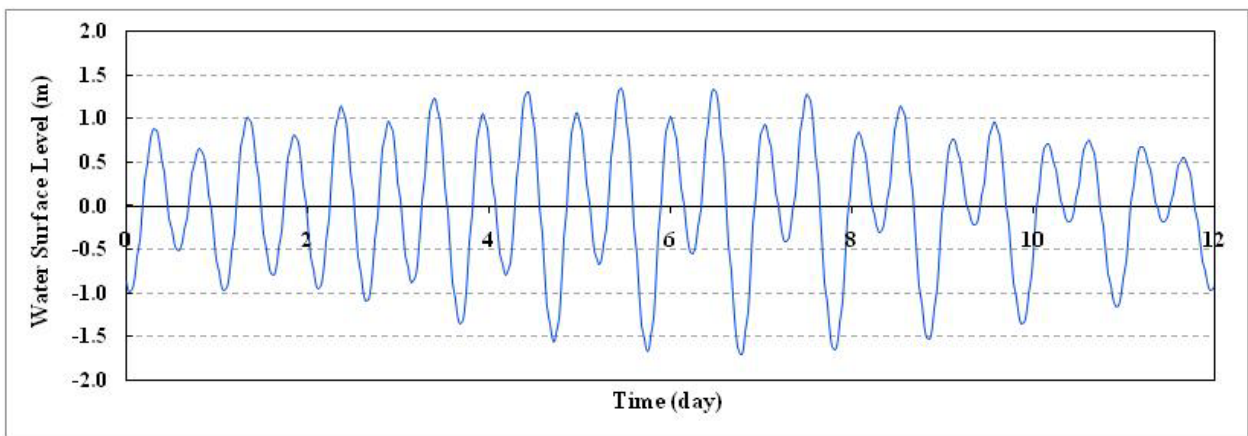
Fig 12:
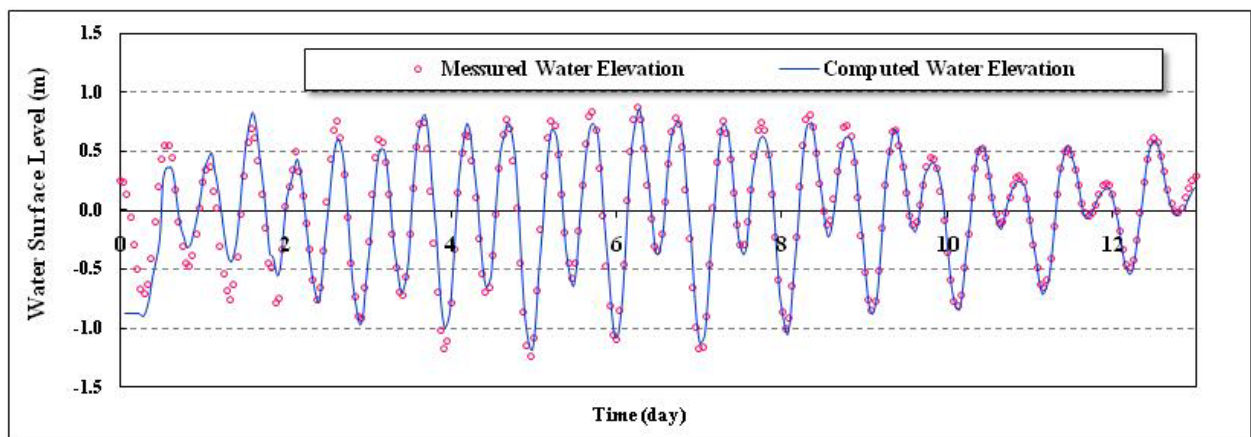
Fig 13:
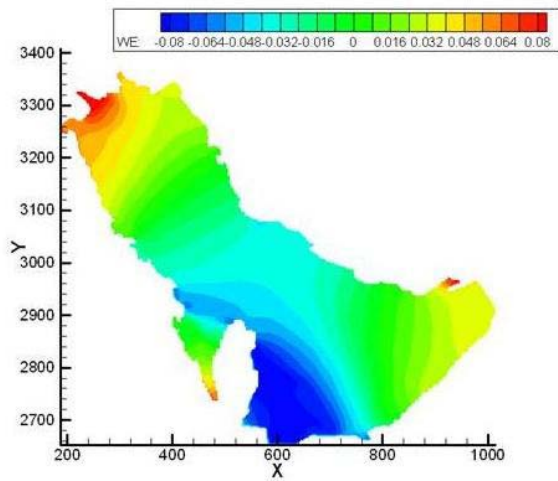
Figure 14:
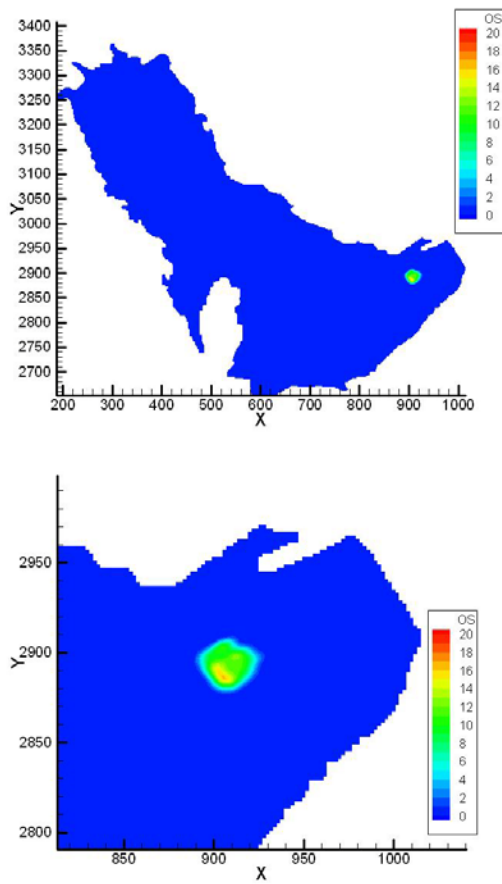
Figure 15:
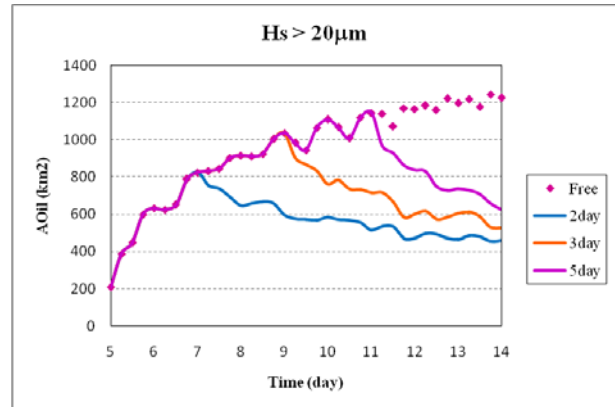
Figure 16:
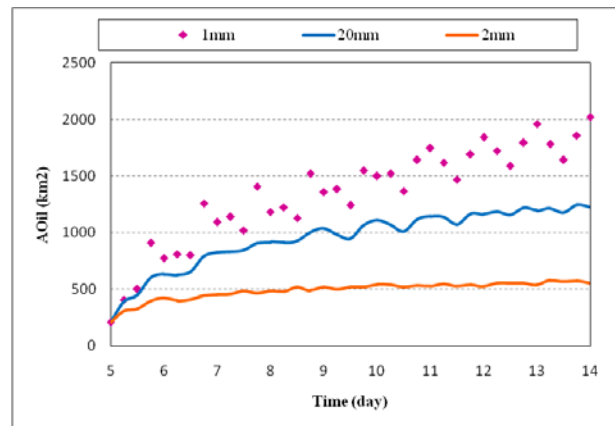
Figure 17:

CONCLUSION

Process Saf. Environ. Prot. **86,**

J. Hydro. Res. **1 (2),**

REFERENCES

J. Hazardous Materials **107**

Proc. Conf. of Mechanics of Oil Slicks

Water Res. **11**

Arctic Marine Oil Spill Program Technical Seminar

Spill Sci. & Technol. Bull. **8(4)**

8th International Conference on CFD in Oil & Gas, Metallurgical and Process Industries
SINTEF/NTNU, Trondheim Norway
21-23 June 2011

CFD11-147

INVESTIGATION OF TWO-PHASE SLUG FLOW IN A RISER USING PHYSICAL AND NUMERICAL SIMULATIONS

Mukhtar ABDULKADIR, Valente, HERNANDEZ-PEREZ, Ian S. LOWNDES* and Barry J. AZZOPARDI

Ú¦[&^••Áæ}åÁÓ}çã¦[}{^}œÁÒ}*ã}^^¦ã}*ÁÜ^•^æ&@ÁÖãçãɿã[}ÉÁO̓œæ&̃|ç̂ÁÁ-ÁÒ}*ã}^^¦ã}*ÁÊW]ãç^¦•ãĉÁ̂-ÁÞ[œã}*@æ{Á

W]ãç^¦•ãĉÁÚæ\ÉÁÞ[œã}*@æ{ÁÁÞÕÏÁGÜÖÉÁW]ãc^åÁSã}*å[{Á

ÊÒÁ̈ æa̅|̅ӕ̅̈ 岸̧́ å^•O[œã}*@æ{Èæ&È-\Á

ABSTRACT

Experimental investigations can prove to be expensive, risky and limited by the existing available techniques. In any industrial set-up time is always at premium and in an area where information is limited realistic and timely predictions are important. This paper presents the results of experimental and CFD studies of slug flow in a vertical riser using validated models.

An Electrical Capacitance Tomography (ECT) unit was used to monitor an air - silicone oil mixture flowing in a vertical 67 mm diameter riser. This enables the measurement of the instantaneous distribution of the flow phases over the cross - section of the pipe. The ECT sensor has two circumferential rings of electrodes, 89 mm apart (also known as twin - plane sensors) which enabled the determination of the rise velocity of any observed Taylor bubbles and liquid slugs.

The simulations were carried out using the commercial software package Star - CD and Star - CCM+, which is designed for numerical simulation of continuum mechanics problems. The model consisted of a cylindrical 67 mm internal diameter and 6 m vertical pipe. A butterfly mesh structure was employed in the computational domain. Air and silicone oil were used as the model fluids. The condition of two-phase slug flow was simulated with the Volume of Fluid (VOF) model, taking into consideration turbulence effects using the standard $k - \varepsilon$ model. The simulation predictions were validated both qualitatively and quantitatively against the experimental data and were then used to obtain further insights into the characteristics of slug flow.

A reasonably good agreement can be observed for the results of the experiment and computational fluid dynamics (CFD) based on the time series of void fraction. As was done for the experimental conditions, more information about the slug parameters for this particular case were obtained from the time series of void fraction, such as the dominant frequency, and therefore comparisons of the experimental results and CFD computations were also performed in terms of the Probability Density Function (PDF) of the time series and the Power Spectral Density (PSD). The study demonstrates the potential of Computational Fluid Dynamics (CFD) as a design tool.

Keywords: CFD, ECT, VOF, Slug flow, air - silicone oil, riser.

NOMENCLATURE

A	Area [m^2]
F	Frequency [Hz]
ε_g	Void fraction [-]
ε_{gs}	Void fraction in the liquid slug [-]
ε_{TB}	Void fraction in the Taylor bubble [-]
V_{TB}	Structure velocity [m/s]
L_{SU}	Length of the slug unit [m]
L_S	Length of the liquid slug [m]
L_{TB}	Taylor bubble length [m]
k	Kinetic energy of turbulence [m^2/s^2]
n	number of phases [-]
u	Velocity [m/s]
i, j	Space directions
q	Phase index

INTRODUCTION

The occurrence of slug flow in a vertical riser is a very common phenomenon under normal operating conditions of a two-phase flow facility, such as in an oil production riser. Considerable amount of research has been devoted to the study of this two-phase flow regime (Dumitrescu (1943); Moissis and Griffith (1962); Nicklin *et al.* (1962); White and Beardmore (1962); Brown (1965); Akagawa and Sekoguchi (1966); Wallis (1969); Collins *et al.* (1978); Fernandes *et al.* (1983); Mao and Dukler (1985); Mao and Dukler (1991); Barnea and Brauner (1993); DeJesus *et al.* (1995); Pinto and Campos (1996); Clarke and Issa (1997); van Hout *et al.* (2002); Taha and Cui (2006) among others. A critical review of this topic is given by Fabre and Line (1992). However, there remains much to investigate and understand of the flow pattern.

One of the features of the slug flow pattern is an acceleration of the liquid phase which results in the

transition of fast liquid slugs, which carry a significant amount of liquid with high kinetic energy. It is potentially hazardous to the structure of the system due to the strong oscillating pressure levels produced from the liquid slug as well as the mechanical momentum of the slugs. It is therefore important to predict the flow behaviour. Empirical correlations and mechanistic models have been presented in the literature. These are one-dimensional approaches that cannot fully characterise the flow. The limitations of the one-dimensional models can be overcome using CFD. Successful applications of CFD in multiphase flow are highly dependent on the flow pattern under study, as different models are used for different flow patterns. As understood, multidimensional models in CFD must be generally able to capture the physics in all flow regimes. These models require to be validated in order to be applied confidently. CFD code validation requires experimental data that characterise the distributions of parameters within large flow domains.

In this work some slug flow parameters are determined using experiments and CFD.

EXPERIMENTAL METHODOLOGY

The experimental investigations were carried out on an inclinable pipe flow rig within the Chemical Engineering Laboratories of University of Nottingham. The details of the experimental facility can be found elsewhere, (e.g. Azzopardi et al (1997), Geraci et al. (2007a) and Geraci et al. (2007b), Hernandez-Perez et al (2008), and Abdulkadir et al. (2010)). In brief: the experimental test section of the facility consists of a transparent acrylic pipe of 6 m length and 0.067 m internal diameter. The test pipe section may be rotated on the rig to allow it to lie at any inclination angle of between -5 to 90° to the horizontal. For the experiments reported in this paper the rig test pipe section was mounted as a vertical riser

(an inclination of 90° to the horizontal). It is worthy of mention that full-experimentation in risers of this magnitude and other larger ones is expensive and therefore a more cost-effective approach for exploring the behaviour of two-phase flow in these risers is by using validated CFD codes.

The resultant flow patterns created for the range of air - silicone oil injection circulation flow rates studied were recorded using electrical capacitance tomography (ECT). A detailed description of theory behind the ECT technology can be found elsewhere, for example, Hammer (1983), Huang (1995), Zhu *et al.* (2003) and Azzopardi *et al.* (2010). The use of two such circumferential rings of sensor electrodes, located at a specified distance apart (also known as twin - plane sensors), enabled the determination of the rise velocity of any observed Taylor bubbles and liquid slugs. The twin - plane ECT sensors were placed at a distance of 4.4 and 4.489 m upstream of the air - silicone oil mixer injection portal located at the base of the riser. A flow chart of the various experimental measurements recorded and the parameter calculations performed to characterise the observed slug flows are presented in Table 1. Parallel to the experiments, CFD calculations were carried out. The aim of the numerical simulations is the validation of prediction of the slug flow with the existing multiphase flow models, built in the commercial code Star-CD and Star-CCM+.

CFD MODEL

The commercial CFD software Star-CD and Star-CCM+ are used to simulate the motion of the Taylor bubbles rising in a flowing liquid through a vertical 67 mm internal diameter and 6 m height riser. In discretizing the computational domain, the Star-CD code uses the Finite Volume method.

Table 1: Table of Flowchart for experimental measurement used to obtain the parametric characterisation of the slug flow regime

Direct physical measurement		Data processing method	Parametric Output 1	Parametric Output 2
Instrument	Data			
ECT	Time series of void fraction	PDF of void fraction	Flow pattern, $\varepsilon_{gs}, \varepsilon_{TB}$, frequency	Lengths of liquid slug and Taylor bubble, symbols of parameter set
		PSD – Power Spectral Density	Frequency, symbols of parameter set	
		Cross-correlation	Structure velocity, symbol	
		Image reconstruction	Contours of phase distribution	3D structures

The movement of the gas-liquid interface is tracked based on the distribution of α_{G_1}, the volume fraction of gas in a computational cell, where $\alpha_G = 0$, in the liquid cell and $\alpha_G = 1$ in the gas phase, Hirt and Nichols (1981). Therefore, the gas - liquid interface exists in the cell where α_G lies between 0 and 1.

Computational domain

In order for the simulation to produce meaningful results, it was important to ensure that the geometry of the flow domain represented that of the experimental arrangement. Hence, a full 3-Dimensional domain, as shown in Figure 1, was considered based on the fact that the flow simulated has been found to be axisymmetric according to the experimental works of Azzopardi et al. (2010) and Hernandez-Perez et al. (2011). They employed conductance wire mesh sensor (WMS) to look at the flow distribution in a 67 mm internal diameter and 6 m vertical pipe (same as the one used in this study). They concluded that the classical Taylor bubble shape is rarely obtained when the pipe diameter is increased.
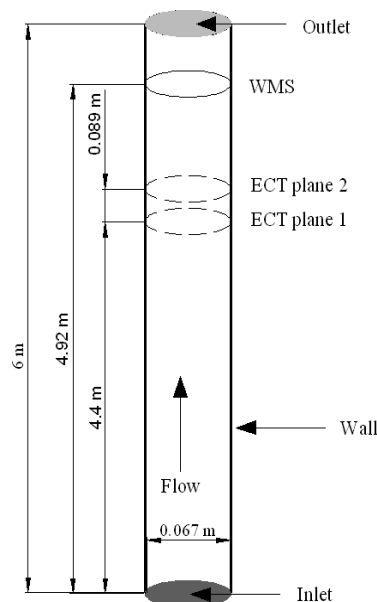
Figure 1: 3-D geometry of the computational domain showing the measurement locations and instrumentation.

In this work, two CFD measurement sections were placed at positions similar to those of the experimental work, namely, 4.4 m and 4.489 m, the two electrical capacitance tomography (ECT) planes. Air and silicone oil are supplied at the inlet section of the pipe, then the two - phase mixture flowed along the pipe, and is finally discharged through the outlet at atmospheric pressure. The relevant fluids properties are shown in Table 2.

Table 2: Properties of the fluids

Fluid	Density (kg/m³)	Viscosity (kg/ms)	Surface tension (N/m)
Air	1.18	0.000018	
Silicone oil	900	0.0053	0.02

Gas – liquid mixing section

In the experimental set up, it was ensured that the mixing section of the air and silicone oil phases took place in such a way as to reduce flow instability. Flow stability was achieved by using a purpose built mixing device, providing maximum time for the two-phase to develop. The mixing device is made from PVC pipe as shown in Figure 2.The silicone oil enters the mixing chamber from one side and flows around a perforated cylinder. There, air is introduced through a large number of 3 mm diameter orifices. Thus, gas and liquid could be well mixed at the test section entry. Inlet volumetric flow rates of liquid and air are determined by a set of rotameters.

As for the CFD, at the inlet, a velocity-inlet boundary type is used in which the mixture velocity and the liquid volume fraction are specified. The velocity profile is assumed to be uniform. This approach requires no additional experimental knowledge about the slugs in order to set up the numerical simulation. This is also similar to the way the experimental work has been carried out.
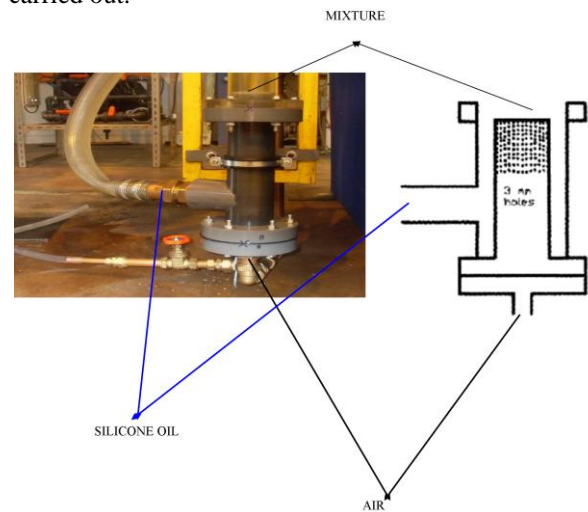
Figure 2: Gas liquid mixing section

Grid generation

It has been reported by Hernandez-Perez *et al.* (2011) and confirmed in this study that the mesh has a great influence on the solver convergence and solution of every CFD simulation. It is important to keep high mesh quality standards to ensure convergence and the accuracy of the simulation. The model geometry was built and meshed with Star-CD, then imported into Star-CCM+, where the computation and post-processing of the results were performed. The name of the mesh employed is known as butterfly grid. In this grid, a Cartesian mesh is used in the centre of the pipe combined with a cylindrical one around it. It requires multiple blocks but generally has the best grid quality in terms of orthogonality and mesh density. The construction of this mesh requires a more elaborated procedure, but it can be automated by implementing a macro in the Star-CD software. Details can be found in Hernandez-Perez *et al.* (2011).

The mesh density selected was based on the grid convergence study carried out in this work and Hernandez-Perez (2008), where a mesh with 500,000

cells for an inclined pipe of 6 m length and 38 mm diameter was found to be adequate for an inlet flow condition that consists of liquid and gas superficial velocities of 0.7 m/s and 1.6 m/s, respectively. However, in the present work, lower velocities are used.

Governing equations

The motion of an incompressible two-phase slug flow under isothermal conditions has been considered as the flow scenario in the present work. The Volume of Fluid (VOF) method, based on the Eulerian approach, implemented in the commercial CFD package Star-CCM+ is used in the numerical simulation. In addition, Star-CCM+ (2009) uses a High Resolution Interface Capturing Scheme (HRIC) based on the Compressive Interface Capturing Scheme for Arbitrary Meshes (CISCAM) introduced by Ubbink (1997) and enhanced by Muzaferija and Peric (1999). The body forces in the momentum equation consist of gravitational force and surface tension. Surface tension along an interface arises as a result of attractive forces between molecules in a fluid. In the VOF method, surface tension is introduced by adding a momentum source. The momentum equation, equation (2), is dependent on the volume fractions of all phases through the properties ρ and μ.

The mass, momentum and volume fraction conservation equations for the two-phase flow through the domain are represented as:

$$\frac{\partial \rho}{\partial t} + \frac{\partial \rho u_i}{\partial x_i} = 0 \qquad (1)$$

$$\frac{\partial \rho u_j}{\partial t} + \frac{\partial \rho u_i u_j}{\partial x_i} = -\frac{\partial P}{\partial x_j} + \frac{\partial}{\partial x_i}\mu\left(\frac{\partial u_i}{\partial x_j} + \frac{\partial u_j}{\partial x_i}\right) + \rho g_j + F_j$$
(2)

Where, P, g and F indicate, respectively, the pressure, the gravitational acceleration and the external force per unit volume. The momentum equation, shown above, is dependent on the volume fractions of all phases through the properties density (ρ) and viscosity (μ). For a two-phase flow system, if the phases are represented by the subscripts 1 and 2 and the volume fraction of phase 2 is known, the ρ and μ in each cell are given by the following equation:

$$\rho = \alpha_2 \rho_2 + (1-\alpha_2)\rho_1, \mu = \alpha_2 \mu_2 + (1-\alpha_2)\mu_1 \quad (3)$$

The interface between the two phases can be traced by solving the continuity equation for the volume fraction function:

$$\frac{\partial \alpha_q}{\partial t} + \frac{u_i \partial(\alpha_q)}{\partial x_i} = 0 \qquad (4)$$

Where u_i and x_i denote, respectively, the velocity component and the co-ordinate in the direction i (i =1, 2 or 3), t, being the time; and through the resolution of the momentum equation shared by the two considered fluids.

The primary-phase volume fraction will be computed based on the prevailing condition: the volume fraction equation for the primary phase in equation (4) will be obtained from the following equation:

$$\sum_{q=1}^{n} \alpha_q = 1 \qquad (5)$$

The continuum surface force (CSF) model proposed by Brackbill *et al.* (1991) was used to model the surface tension. With CSF model, the addition of surface tension to the VOF model calculation results in a source term in the momentum equation (2).

Solving these sets of equations has been done using a software package Star-CCM+. For the calculation of fluxes at control volume faces required by the VOF model, a second order discretization scheme was used, as recommended by the Star-CD (2009) code documentation.

Turbulence model

As the Taylor bubbles rises through the liquid, even in low flow rates, a developing film is created around the bubble and a wake at its tail. Therefore, turbulence must be considered in the numerical simulation. The accuracy of CFD solutions for turbulent flows can be affected by turbulence modelling, especially because of the complex features of the flow. According to Versteeg and Malalasekera (2007), it has been recognised by CFD users that, the choice of turbulence models used to represent the effect of turbulence in the time-averaged mean-flow equations represents one of the principal sources of uncertainty of CFD predictions. In order to simulate turbulence, the standard k-ε model, Launder and Spalding (1974), which requires that the flow is fully turbulent, was used for several reasons; the model is computationally-efficient, is implemented in many commercial codes, the pipe geometry is not complicated and it has demonstrated capability to simulate properly many industrial processes, including multiphase flow Ramos – Banderas *et al.* (2005), Cook and Behnia (2001) among others

Boundary and initial conditions

Once the mesh was generated, the boundaries of the computational domain were specified. All wall conditions were assumed to be no slip boundary. The no slip condition (v = 0) is the appropriate condition for the velocity component at solid walls. At the inlet, velocities for both phases were prescribed as superficial velocities: liquid 0.05 m/s and gas 0.34 m/s. The phases were clearly defined with the primary phase as oil and the secondary phase as air. The volume fraction and density of each phase were both prescribed at the inlet. The inlet values for turbulent kinetic energy, k, and its dissipation rate, ε, are estimated with the following equations proposed by Launder and Spalding (1974):

$$k_{in} = \frac{3}{2}I^2 U_{in}^2 \qquad (6)$$

$$\varepsilon_{in} = 2k_{in}^{3/2}/d \qquad (7)$$

$$I = \frac{0.16}{\mathrm{Re}^{1/8}} \qquad (8)$$

Where d is the pipe diameter, and I the turbulence intensity for fully developed pipe

Close to the wall, the standard wall function approach also based on the Launder and Spalding (1974) was employed to predict accurately the flow close to the walls. At the outlet, the remaining variables are

transported out of the computational domain with zero average static pressure so that the mass balance is satisfied. Operating conditions were specified as being standard atmospheric pressure (101.3 kPa) and temperature 20°C. Gravity effects are accounted for and the acceleration due to gravity to be -9.81 m/s^2 on the vertical.

Solution algorithm

In order to numerically solve the system of governing partial differential equations, discretisation of the equations has been carried out using a Finite Volume Method (FVM) with an algebraic segregated solver and co-located grid arrangement, as implemented in Star-CCM+(2009). In this grid arrangement, pressure and velocity are both stored at cell centres. Details of the discretisation (FVM) can be found elsewhere (e.g. Versteeg and Malalasekera (2007) and are hence omitted here. Since Star-CCM+ uses a segregated solver for VOF, the continuity and momentum equations need to be linked. Various techniques are reported in the literature. However, the SIMPLE algorithm, which stands for Semi-Implicit Method for Pressure-Linked Equations, Patankar and Spalding (1974), is applied to control the overall solution because of its good performance to find a fast converged solution. In addition, the iterative solver was speeded up tremendously by using an Algebraic Multigrid (AMG) technique to yield a better convergence rate.

All simulations in this work are performed under time dependent conditions. For the time dependent solution scheme, the main controlling factor is the time step. The time step was set to 2×10^{-4} seconds. This was became necessary in order to give a small number of time steps as possible whilst maintaining a smoothly converging solution. If a large time step is chosen, then the solution changes too much and is therefore likely to diverge. Inside each time interval iterations are carried out to resolve the transport equations for that time step. As long as the time step is small enough to get convergence, the smaller the time step, the fewer iterations, per time step are required. For this iteration process to converge, it may be necessary to control the change of the variables from one iteration to the next. This is achieved with under relaxation factors. Under relaxation factors of 0.3, 0.7 and 0.8 respectively were applied on pressure, momentum and turbulence kinetic energy parameters, as recommended by Star-CCM+ (2009).

An assessment of the degree to which the solution is converged can be obtained by plotting the residuals errors for each equation at the end of each time step. For a well-converged simulation, the maximum residual obtained was set to be around 10^{-4}; it is possible that a residual increases after any particular time step, but it does not necessarily imply that the solution is diverging. It is usual for residuals to occasionally get larger, such as at the beginning of a run.

Mesh independence study:

One of the most significant factors influencing the computation time is the size of the computational grid specified by the user. Mesh independence means that the

converged solution obtained from a CFD calculation is independent of the grid density. In practice, mesh independence is indicated when further mesh refinement yields only small, insignificant changes in the numerical solution.
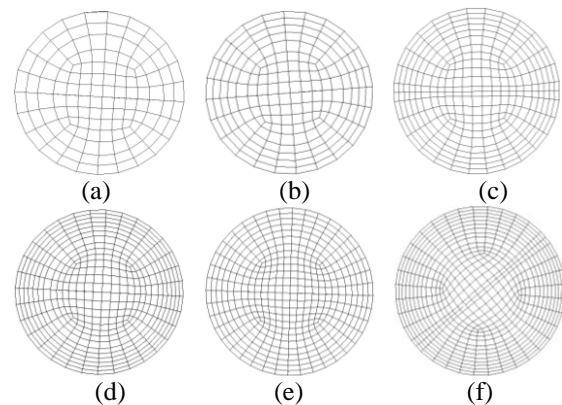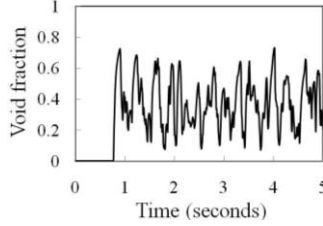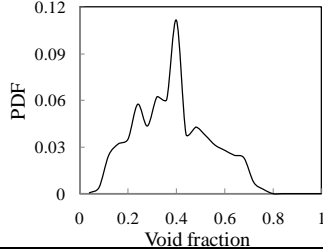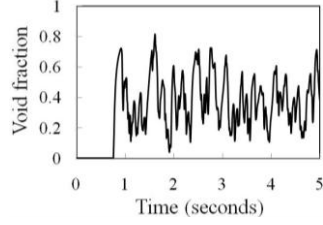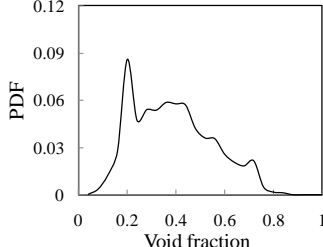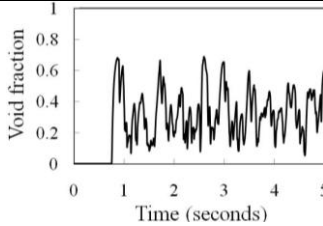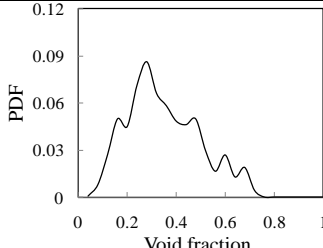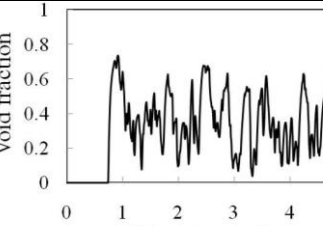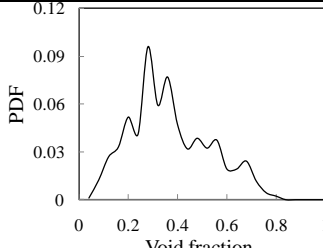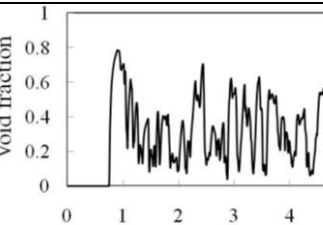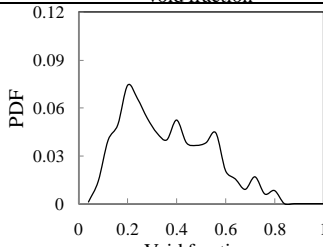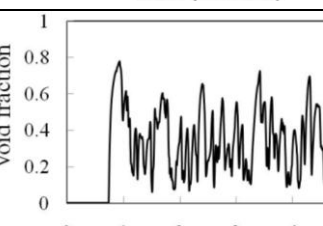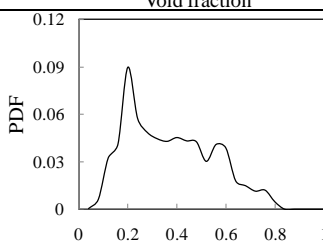
Figure 3: cross-sectional view of different sizes of computational grid used for mesh independent study (a) 26400 cells (b) 36000 cells (c) 54600 cells (d) 76800 cells (e) 84000 cells (f) 102600 cells
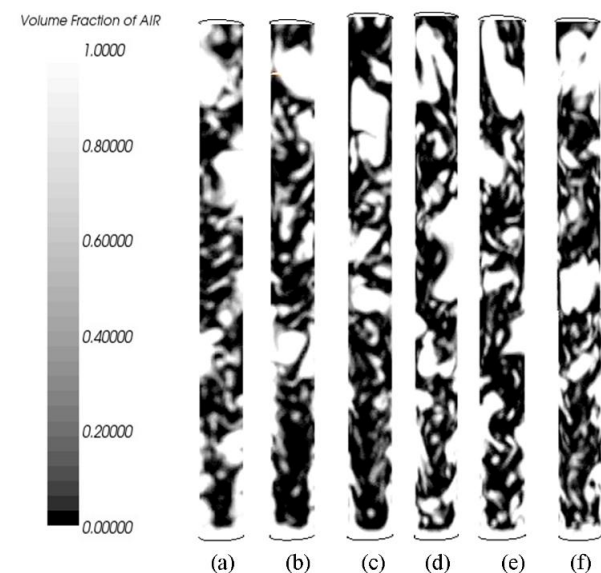
Figure 4: Contour plots of void fraction for different mesh densities (a) 26400 cells (b) 36000 cells (c) 54600 cells (d) 76800 cells (e) 84000 cells (f) 102600 cells

In order to identify the minimum mesh density to ensure that the solution is independent of the mesh resolution, a mesh sensitivity analysis has been carried out in the construction and analysis of the CFD model. In the mesh independence study, a computational domain of 1m length was used as this length is sufficient to carry out a test on the performance of the mesh with quite reasonably computational effort. Six 3-Dimensional meshes were investigated in the present study as shown in Figure 3 and the results of the study are presented in both Table 3 and Figure 4 for the general case of a vertical riser and a suitable grid resolution has been found.

Table 3: The results of obtained from the CFD mesh independence studies

Number of cells	Time series of void fraction	PDF of void fraction
26400		
36000		
54600		
76800		
84000		
102600		

An insight into the effect of mesh density can be obtained from the contours of phase distribution in a longitudinal sectional view at the centre of the pipe, at a time when the flow, injected as a homogeneous two-phase mixture with a uniform velocity profile, has travelled from the inlet to the outlet section, Figure 3. This shows that bubbles are formed as the flow moves upwards, with a sharper gas - liquid interface as the mesh density is increased. However, no clear difference in terms of the flow pattern can be established.

In order to quantify the effect of the mesh density, the time series of cross sectional average void fraction has been recorded at a plane located at 0.5 m from the inlet for a time interval of 5 seconds. Results are presented in Table 3. In order to determine the time series of void fraction, the following procedure similar to that used by Hernandez - Perez (2008) was performed: a cross-sectional plane is defined at the measurement location, and the Area-Weighted Average value of the void fraction is calculated. The cross-sectional average void

6

fraction is computed by dividing the summation of the product of the air volume fraction and facet area by the total area of the surface as follows:

$$\frac{1}{A}\int \varepsilon A = \frac{1}{A}\sum_{i=1}^{n} \varepsilon |A_i|$$

(9)

What we can see from Table 3 is that the times that it takes for the leading Taylor bubbles to arrive to the measuring section are: 0.692, 0.679, 0.651, 0.625, 0.624, and 0.625 seconds for the six meshes in order of increasing mesh density. The differences between these arrival times are small, in particular between the two bigger mesh densities (0.16 %). As the time increases and the intermittent flow pass though the measuring section, it became difficult to compare the time series directly. In view of this development, we decided to use statistical tools, Probability density function (PDF). In this case the graphs of probability density function (PDF) have been obtained and it can be observed that they vary with mesh density for all cases.

It is concluded that the PDFs of the predicted void fractions for the 84000 and 102600 cells are quite similar. For the range of mesh sizes studied, the void fraction was observed to fluctuate over the range, 0.05 and 0.8, whilst the minimum and maximum peak PDF are given by 0.074 and 0.117, respectively. However, for the PDF of void fraction for the 84000 and 102600 cells, the void fraction is the same, 0.2 whilst the height of the peak of the PDF are 0.074 and 0.09 for the 102600 and 84000 cells, respectively. Therefore, it can be concluded that the mesh with 84000 cells is adequate, as the change in the results produced is very small when the number of cells is increased to 102600, and it requires less computational effort than the one of 102600. Since the simulation involves a 6 m pipe, we decided to multiply the selected mesh size, 84000 cells by 6 to produce approximately 500,000 cells.

RESULTS AND DISCUSSION

The comparison between the results obtained from the CFD and experiment will be based on time series of void fraction, probability density function (PDF) of void fraction and power spectral density (PSD) of void fraction. A stop watch will be used to verify the time that it took the first bubble to arrive at the measurement section. This will be carried out at same liquid and gas superficial velocities of 0.05 and 0.34 m/s, respectively.The model fluid is air-silicone oil.

Comparison between the Computational fluid dynamics (CFD) and experiment

The PDF of void fraction both for the CFD and experiment predict the same flow pattern as slug flow, according to the definition of Costigan and Whalley (1996). According to them, slug flow is a flow pattern characterised by a PDF graph with two peaks, one at lower void fraction (liquid slug) and the other one at higher void fraction, Taylor bubble.

From Figure 5, it is interesting to observe that the CFD simulation is able to mimic the appearance of the first Taylor bubble (leading) as observed from the experiment. From the plot of the time series of void fraction for the CFD, the Taylor bubble first got to the measurement location from the mixing section in about 5.1 seconds whilst for the experiment, 5.7 s. A time interval of 5.2 seconds was recorded using a stop watch. The % time delay is 1.9 and 9.6 for the CFD and experiment, respectively. The % delay can be attributed to the uncertainty in taking measurements of the time the Taylor bubble departs the mixing section and reached the measurement location.

The contours of phase distribution as shown in Figure 6 (a) - (b) and Figure 7 (a) - (b) for the Taylor bubble obtained from both the CFD and experiment show a reasonably good agreement. It is worth mentioning that the CFD as shown in Figure 8 (a) - (b) is able to replicate what is happening at the tail of the Taylor bubble (wake), a feat that cannot be achieved with the experiment. Three regions can be observed from the velocity profiles in Figure 8(a) - (b): the Taylor bubble, falling film and the wake region. From the plot, the Taylor bubble can be seen moving vertically upwards whilst the liquid film on the other hand, downwards due to the action of gravity and the shape of the nose of the Taylor bubble. A similar observation was reported by Mao and Dukler (1991), van Hout et al. (2002) and Legius *et al.* (1995) who all worked on vertical pipes using air and water as the model fluid. The falling film with some entrained bubbles drop into the wake region and a vortex region is created. The liquid film and some of the entrained bubbles are subsequently carried upwards by the incoming gas phase. This behaviour is similar to that observed by Fernandes et al. (1983) and Shemer *et al*. (2004) that the rising bubbles in the liquid slug rise from entrainment of gas from the Taylor bubble base.
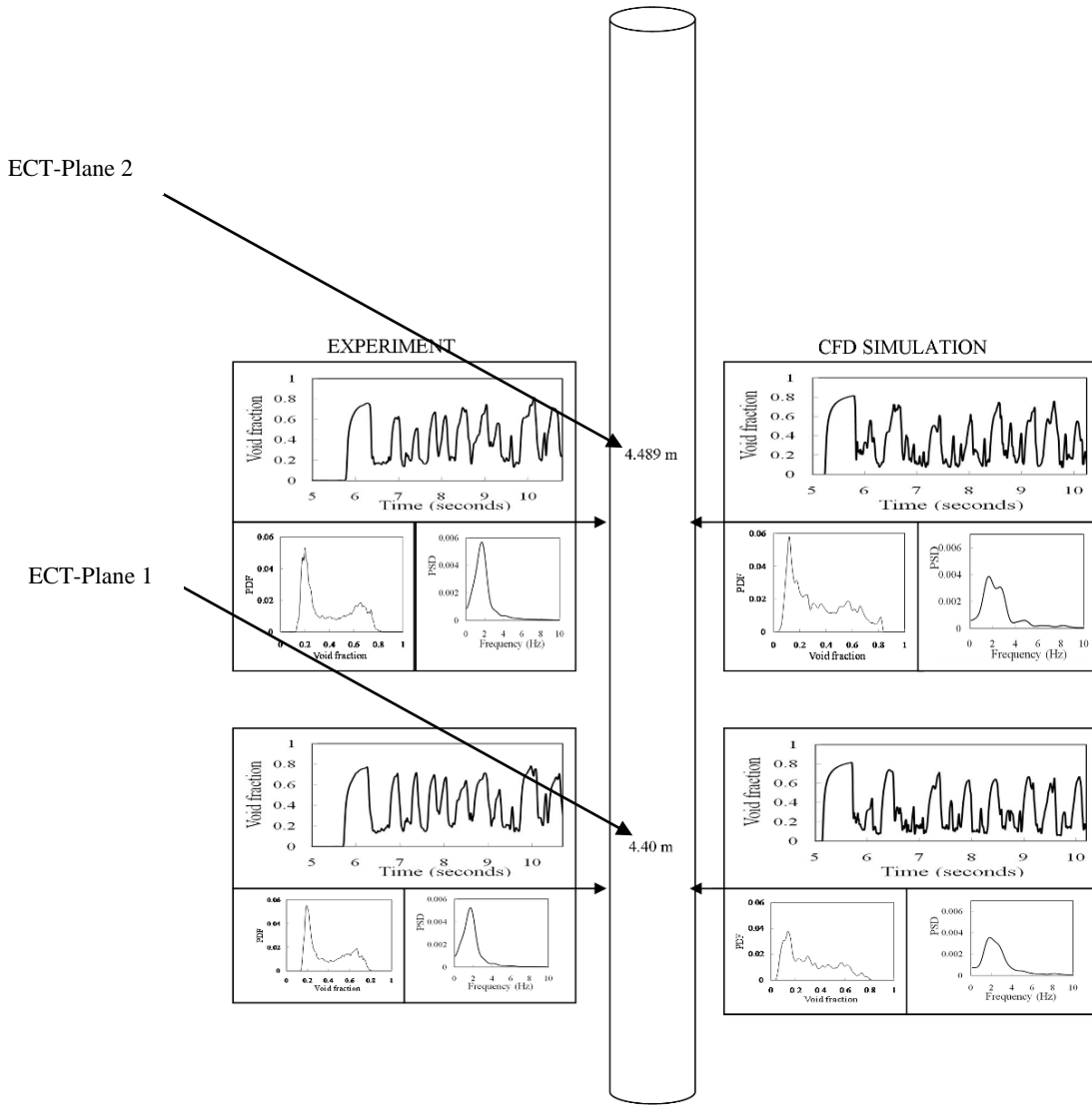
Figure 5: Comparison between experimental data and CFD simulation results (same method of introducing the liquid into the flow domain)

(a)   (b)

Figure 6: comparison of contours of phase distribution, same inlet velocity condition for (a) CFD (b) ECT. The liquid and gas phases are represented by dark and light colours, respectively

Much of this entrained gas is swept around a vortex in the Taylor bubble wake and re-enters the bubble. This agreement suggest that the CFD simulation can be considered to be useful for obtaining other flow parameters that characterize the internal structure of the flow that are difficult to measure experimentally, such as the velocity field and phase distribution.

(a)   (b)
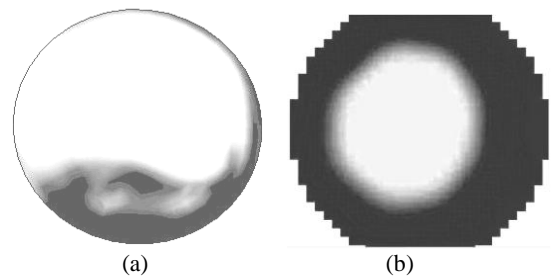
Figure 7: Contours of phase distribution (cross-sectional void fraction of air) for the Taylor bubble obtained from (a) CFD (b) ECT. Screen shots taken at liquid and gas superficial velocity of 0.05 and 0.34 m/s, respectively.
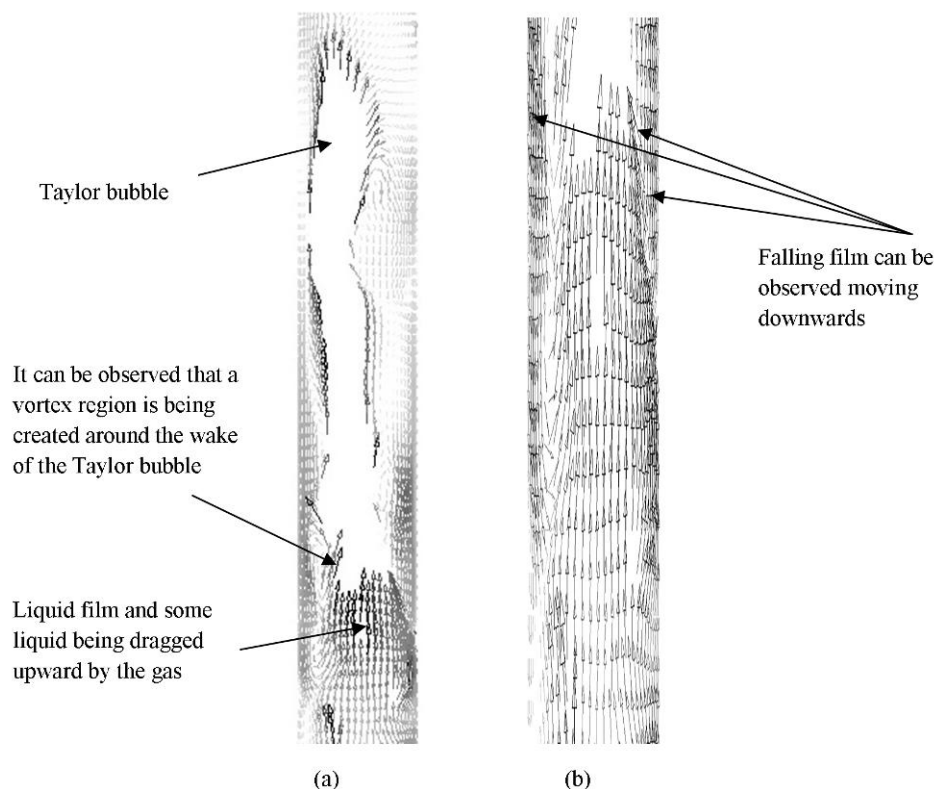
Figure 8: velocity profile around the (a) Taylor bubble (b) Wake region of the Taylor bubble for liquid and gas superficial velocity of 0.05 and 0.34 m/s, respectively obtained from CFD

The experiment was carried out with the pipe first full of liquid, before injecting air (gas), as was done for the CFD. This was done to give us confidence in our results; by comparing like with like.

CONCLUSION

A comparison between the results obtained from the CFD simulation and experiments has been carried out and the following conclusions can be drawn:

1) Á This work also confirms the results reported in the literature for the characteristics of slug flow.

2) Á A reasonably good agreement was obtained, and the CFD simulation can be used to characterize the slug flow parameters with confidence. However, further parametric CFD studies might be required to close the gap between CFD simulations and the experimental results.

ACKNOWLEDGEMENTS

REFERENCES

ABDULKADIR, M., HERNANDEZ-PEREZ, V., SHARAF, S., LOWNDES, I. S. & AZZOPARDI, B. J., (2010). Experimental investigation of phase distributions of an air-silicone oil flow in a vertical pipe. World Academy of Science, Engineering and Technology (WASET), 61, 2010, 52-59

AZZOPARDI, B. J., (1997). Drops in annular two-phase flow. International Journal of Multiphase Flow 23, S1-S53.

AZZOPARDI, B. J., ABDULKAREEM, L.A., SHARAF, S., ABDULKADIR, M., HERNANDEZ-PEREZ, V., & IJIOMA, A., (2010). Using tomography to interrogate gas-liquid flow. In: 28th UIT Heat Transfer Congress, Brescia, Italy, 21-23 June.

AKAGAWA, K., & SAKAGUCHI, T., (1966). Fluctuation of void fraction in gas-liquid two-phase flow. Bulletin JSME, 9, 104-110

BARNEA, D., & BRAUNER, N., (1993). A model for slug length distribution in gas-liquid slug flow. International Journal of Multiphase Flow, 19, 829-838

BRACKBILL, J.U., KOTHE, D.B., & ZEMACH, C. (1992). A continuum method for modelling surface tension, Journal of Computational Physics, 100, 335-354.

BROWN, R. A. S., (1965). The mechanics of large gas bubbles in tubes: I. Bubble velocities in stagnant liquids. Canadian Journal of Chemical Engineering, 43, 217-223

BUGG, J.D., MACK, K. & REZKALLAH, K.S., (1998). A numerical model of Taylor bubbles rising through stagnant liquid in vertical tubes. International Journal of Multiphase Flow, 24, 271–281.

CLARKE, A. & ISSA, R. I., (1997), A numerical model of slug flow in vertical tubes. *Computers and Fluids*, 26, 4, 395-415.

COLLINS, R., DE MORAES, F. F., DAVIDSON, J. F., & HARRISON, D., (1978), The motion of a large gas bubble rising through liquid flowing in a tube. *Journal of Fluid Mechanics*, 89, 497-514.

COOK, M. & BEHNIA, M., (2001), Bubble motion during inclined intermittent flow. International Journal of Multiphase Flow, 22, 543 - 551.

COSTIGAN, G., & WHALLEY, P. B., (1996), Slug flow regime identification from dynamic void fraction measurements in vertical air-water flows. *International Journal of Multiphase Flow*, 23, 263-282

DAVIES, R.M. & TAYLOR, G.I., (1950), The mechanics of large bubbles rising through extended liquids and through liquids in tubes. *Proceedings of the Royal Society*, A 200, 375-395

DEJESUS, J.D., AHMAD, W., & KAWAJI, M., (1995), Experimental study of flow structure in vertical slug flow. *Advances in Multiphase Flow*, 31, 105-118

DUMITRESCU, D. T. (1943), Stromung an einer luftblase in senkrechten rohr Z angrew *Math Mech*, 23, 139-149

FABRE, J., & LINE, A., (1992), Modelling of two-phase slug flow. *Annual Review of Fluid Mechanics*, 24, 21-46

FERNANDES, R. C., SEMIAT, R., & DUKLER, A.E., (1983), Hydrodynamics model for gas-liquid slug flow in vertical tubes. *AIChE Journal*, 29, 981-989

GERACI, G., AZZOPARDI, B. J., & VAN MAANEN, H. R. E., (2007a), Inclination effects on circumferential film distribution in annular gas/ liquid flows, *AIChE Journal*, 53, 5, 1144-1150.

GERACI, G., AZZOPARDI, B. J., & VAN MAANEN, H .R .E. (2007b), Effects of inclination on circumferential film thickness variation in annular gas/ liquid flows. *Chemical Engineering Science*, 62, 11, 3032-3042.

HERNANDEZ-PEREZ, V., (2008), Gas-liquid two-phase flow in inclined pipes. *PhD thesis*, University of Nottingham.

HERNANDEZ-PEREZ, V., ABDULKADIR, M., & AZZOPARDI, B. J., (2011), Grid generation issues in the CFD modelling of two-phase flow in a pipe. *The Journal of Computational Multiphase Flow,3,13-26*

HAMMER, E. A., (1983),Three –component flow measurement in oil/ gas/ water mixtures using capacitance transducers. *PhD thesis*, University of Manchester

HIRT, C. W. & NICHOLS, B. D., (1981), Volume of Fluid (VOF) Method for the Dynamics of Free Boundaries, *Journal of Computational Physics*, 39, 201.

HUANG, S. M., (1995), Impedance sensors-dielectric systems. In R. A. Williams, and M. S. Beck (Eds.). *Process Tomography*, Cornwall: Butterworth-Heinemann Ltd.

LAUNDER, B. & SPALDING, D., (1974), The numerical computation of turbulent flows, *Computer Methods in Applied Mechanics and Engineering*, 3, 269-289.

LEGIUS, H.J.W.M., NARUMO, T.J. & VAN DEN AKKER, H.E.A., (1995), Measurements on wave propagation and bubble and slug velocities in concurrent upward two-phase flow. *Two Phase Flow Modelling and Experimentation*, Editizioni ETS, 907-914

MAO, Z. S., & DUKLER, A.E., (1985), Brief communication: Rise velocity of a Taylor bubble in a train of such bubbles in a flowing liquid. *Chemical Engineering Science*, 40, 2158-2160

MAO, Z. S. & DUKLER, A. E., (1991), The motion of Taylor bubbles in vertical tubes. II. Experimental data and simulations for laminar and turbulent flow, *Chemical Engineering Science*, 46, 2055-2064.

MAO, Z. S. & DUKLER, A. E., (1990), The motion of Taylor bubbles in vertical tubes. I. A numerical investigation for the shape and rise velocity of Taylor bubbles in stagnant and flowing liquid, *Journal of computational physics*, 91, 132-160.

MOISSIS, R., & GRIFFITH, P., (1962), Entrance effects in two-phase slug flow. *ASME Journal of Heat Transfer*, 366-370

MUZAFERIJA, S. & PERIC, M., (1999), Computation of free surface flows using interface-tracking and interface-capturing methods, Chap.2 in O. Mahrenholtz and M. Markiewicz (eds.), Nonlinear Water Wave Interaction, *Computational Mechanics Publication,* WIT Press, Southampton

NICKLIN, D. J., WILKES, J. O., & DAVIDSON, J. F., (1962), Two-phase flow in vertical tubes. *Transaction of Institution of Chemical Engineers*, 40, 61-68

PATANKAR, S.V. & SPALDING, D.B., (1972), A calculation procedure for heat, mass and momentum transfer in three dimensional parabolic flows", *Int. J. of Heat and Mass Transfer*, 15, 1787.

PINTO, A. M. F. R. & CAMPOS, J. B. L. M., (1996), Coalescence of two gas slugs rising in a vertical column of liquid, *Chemical Engineering Science*, 51, 45-54

RAMOS – BANDERAS, A., MORALES, R.D., SANCHEZ – PEREZ, R., GARCIA – DEMEDICES, L. & SOLORIO – DIAZ, G, (2005), Dynamics of two – phase downwards flow in submerged entry nozzles and its influence on the two – phase flow in the mold. International Journal of Multiphase flow, 31, 643-665.

SHEMER, L., GULITSKI, A., & BARNEA, D., (2004), Velocity field in the Taylor bubble wake measurements in pipes of various diameters, *24nd European Two-phase Flow Group Meeting*, Geneva

STAR-CD Version 4.10 & STAR-CCM+ Documentation, (2009), CD-adapco

TAHA, T., & CUI, Z.F., (2006). CFD modelling of slug flow in vertical tubes. *Chemical engineering science*, 61, 676-687

UBBINK, O., (1997), Numerical prediction of two fluid systems with sharp interfaces, *PhD thesis*, University of London

VAN HOUST, R., BARNEA, D., & SHEMER, L., (2002), Translational velocities of elongated bubbles in continuous slug flow. *International Journal of Multiphase flow*, 28, 1333-1350.

VERSTEEG, H.K. & MALALASEKERA, W., (2007), An Introduction to Computational Fluid Dynamics: the Finite Volume Method. 2nd ed. Pearson Educational Limited.

WALLIS, G. R., (1969), One- dimensional two-phase flow. McGraw-Hill, New York

WHITE, E. T. & BEARDMORE, R. H., (1962), The velocity of rise of single cylindrical air bubbles through liquids contained in vertical tubes. *Chemical Engineering Science*, 17, 351-361.

ZHU, K., MADHUSUDANA RAO, S., WANG, C., & SUNDARESAN, S., (2003), Electrical capacitance tomography measurements on vertical and inclined pneumatic conveying of granular solids. *Chemical Engineering Science*, 58, 4225-4245

GPU-ACCELERATED LARGE-SCALE CFD-DEM COUPLING SIMULATION OF THREE-DIMENSIONAL GAS-SOLID FLUIDIZED BED

Feiguo CHEN[1*]**, Wei GE**[1] **and Jinghai LI**[1]

[1] State Key Laboratory of Multi-Phase Complex System, Institute of Process Engineering, Chinese Academy of Sciences, Beijing 100190, CHINA

* E-mail: fgchen@home.ipe.ac.cn

ABSTRACT

INTRODUCTION

Keywords:

NOMENCLATURE

Greek Symbols

•

μ

•

•

Latin Symbols

C

d

$\mathbf{f}$

g

I

m

Re

$\mathbf{T}$

t

V

$\mathbf{v}$

Sub/superscripts

cl

D

i $i.$

p

$$C_D = C_D\, \varepsilon^{-}$$

$$\frac{\partial(\varepsilon\rho)}{\partial t} + \nabla\cdot(\varepsilon\rho\,\mathbf{u}) =$$

$$\frac{\partial(\varepsilon\rho\,\mathbf{u})}{\partial t} + \nabla\cdot(\varepsilon\rho\,\mathbf{uu}) = -\varepsilon\nabla p + \nabla\cdot(\varepsilon\ ) + \varepsilon\rho\ +$$

$$\mathbf{u}\ \bullet_g\ p\qquad\bullet$$

MODEL DESCRIPTION

EQUATIONS FOR PARTICLE MOTION AND GAS PHASE

$$m_i\frac{d\mathbf{v}_i}{dt} = \mathbf{f}_{ci} + \mathbf{f}_{Di} + m_i\mathbf{g}$$

$$I_i\frac{d\bullet_i}{dt} = \mathbf{T}_i$$

$\mathbf{f}$

$\mathbf{f}$

$\mathbf{T}$

$\mathbf{v}\ \bullet\qquad I$

$m\,\mathbf{g}$

$\mathbf{F}$

$\mathbf{f}$

$$\mathbf{F}\ = \frac{\displaystyle\sum_{i\in cell}^{V}\mathbf{f}}{\Delta V_{cell}}$$

NUMERICAL METHOD

$\mathbf{F}$
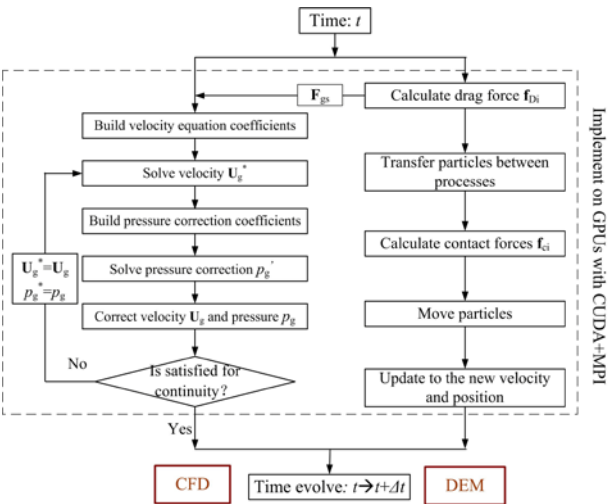
Figure 1:

$$C_D = \begin{cases} \dfrac{1}{Re_{cl}}\left(+\quad Re_{cl}\ \right) & Re_{cl} < \\[2ex] & Re_{cl} \ge \end{cases}$$

$$Re_{cl} = \frac{\varepsilon\rho_g d_{cl}}{\mu_g}U$$

d

$$d_{cl} = d_p\frac{A\rho_p}{\rho_{sus}}$$

Table 1:

μ

d

d

N

t

t

Region division   Sub-region

Figure 2:

RESULTS

x
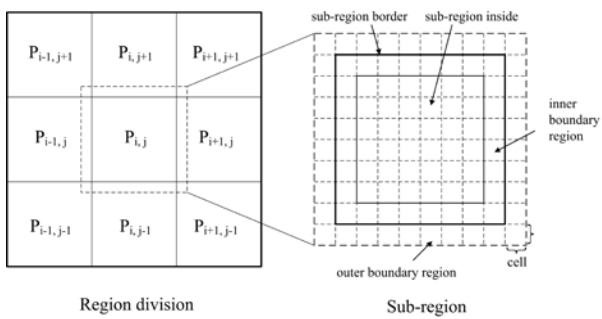
Figure 3:
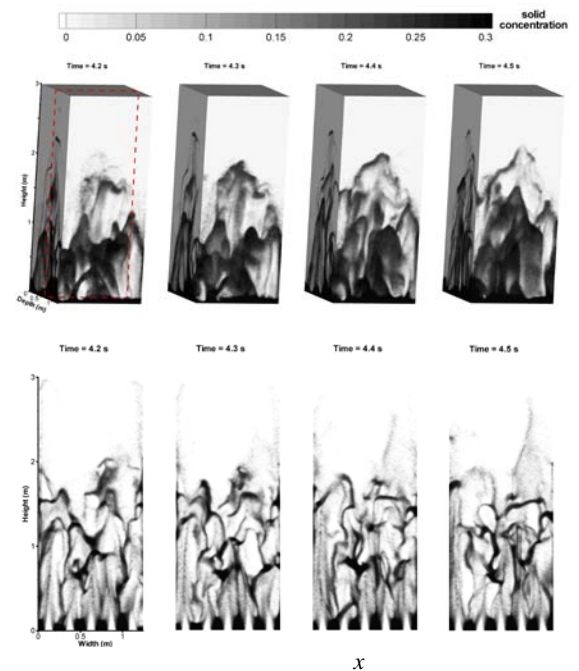
Powder Technology **207**

Chemical Engineering Science **57**

Table 2:

International Journal of Heat and Mass Transfer **15**

Engineering Chemistry and Metallurgy **14**

Chemical Engineering Science **64**

Powder Technology **184**

CONCLUSIONS

Powder Technology **77**

Chemical Engineering Progress Symposium Series **62**

Chemical Engineering Science **65**

ACKNOWLEDGEMENT

Petroleum Processing and Petrochemicals **32**

Powder Technology **139**

REFERENCES

Powder Technology **184**

Science in China Series B: Chemistry **52**

Chemical Engineering Science **62**

Geotechnique **29**

Chemical Engineering Science **63**

Chemical Engineering Science **51**

COMPARISON OF CFD TOOLS FOR MULTIPHASE FLOW APPLICATIONS

Aditya SINGH[1], Raghu MENON[2], Ruud HENKES[3]*

[1] Shell Projects & Technology, Amsterdam, the Netherlands

[2] Shell Projects & Technology, Bangalore, India

[3] Shell Projects & Technology, Amsterdam, the Netherlands, and

Delft University of Technology, the Netherlands

* E-mail: Ruud.Henkes@shell.com

ABSTRACT

Multiphase flows are prevalent in a wide range of applications in several processes that are important to the oil and gas industry. Computational Fluid Dynamics (CFD) is increasingly utilized to understand, design, optimize, scale-up and improve multiphase processes in upstream and downstream applications. Various commercially available CFD software packages such as ANSYS-CFD, STAR-CD, StarCCM+, Ansys-CFX etc are typically used for such simulations. In addition to commercial software, a few open source CFD tools have become available in the recent past, with OpenFOAM being the most important one.

In the present study, the performance of OpenFOAM version 1.5 for multiphase flow applications was compared with the commercial software packages ANSYS-CFD and STAR-CD. The objective of the study is to apply different CFD tools to the same cases and to assess the performance of OpenFOAM compared to the commercial software. From the results, we conclude that OpenFOAM version 1.5 is not yet able to capture the gas-liquid interface accurately in the VOF simulation of a Taylor bubble. Further, in the case of the bubble column simulation, the predicted flow profiles do not resemble those obtained from experiments. In addition, options available for the computational models are also still limited in OpenFOAM. Thus, although the concept of OpenFOAM is of much interest for industrial users, significant improvements are still required in the OpenFOAM code before it can be used widely to model multiphase flows of general interest to the oil and gas industry.

Keywords: CFD, OpenFOAM, multiphase flow, bubble column, Taylor bubble.

NOMENCLATURE

Greek Symbols

ρ mass density, [kg/m^3].

μ dynamic viscosity, [kg/ms].

σ surface tension, [N/m]

Latin Symbols

U velocity, [m/s].

g acceleration due to gravity [m/s^2]

D column diameter [m]

v rise velocity [m/s]

Eö Eötvös Number, $g\rho D^2/\sigma$

Mo Morton Number, $g\mu^4/\sigma^3\rho$

Sub/superscripts

r relative

b bubble

INTRODUCTION

Multiphase flows, such as for gas and liquid, occur in a wide range of applications in several processes that are important to the oil and gas industry. Both experimental and computational methods help to better understand multiphase flows, enabling improved designs of equipment and processes. Computational Fluid Dynamics (CFD) is often used to gain detailed insights into the flow physics. CFD is increasingly being utilized within the oil and gas industry to design, optimize, scale-up and improve processes with applications that span upstream to downstream areas.

Commercially available CFD software packages, such as ANSYS-CFD, STAR-CD, StarCCM+, and Ansys-CFX, are currently used for CFD simulation of multiphase flows. Each tool has its own strengths and weaknesses. Models available in these codes for multiphase flows still need to be developed further to reach a stage where they can be truly predictive and will not require extensive validation and calibration. The limitation with the commercial tools is that access is limited to the underlying CFD code through sub-routines or User-Defined Functions.

Two commonly implemented methods of modelling multiphase flows in commercially available CFD software are the Euler-Euler model and the Volume of Fluid (VOF) (Hirt and Nichols, 1981 and Youngs, 1982). In the Euler-Euler method or Two-Fluid method (Pfleger and Becker, 2001) the different phases are treated as interpenetrating continua with momentum and heat exchange between them. Each phase has its own set of momentum and energy equations. Depending on their volume fraction, each phase is classified either as a continuous phase or as a dispersed phase. The VOF approach represents two or more immiscible fluids by

solving a single momentum equation and by tracking the volume fraction of each of the fluids throughout the domain.

OpenFOAM is an open source C++ library that solves time-dependent, three-dimensional flows. The advantage of this code over the commercial codes is that it is open source which gives the user the flexibility to customize it as per the requirement of a given problem. Furthermore, the development does not need to be done from scratch because a framework is provided to build on. Apart from this flexibility, OpenFOAM is available free of charge under the terms of the GNU Public License, which is a significant incentive in this cost constrained world. These factors have been the motivation for evaluating capabilities of OpenFOAM for multiphase gas-liquid flows of interest to the oil and gas industry. All the results discussed and the conclusions drawn in this work are based on OpenFOAM version 1.5. Á

The objectives of this study are to:
• Assess the capabilities of OpenFOAM for modelling multiphase flows, specifically two-phase gas-liquid flows.
• Evaluate the performance of OpenFOAM against commercial software packages such as ANSYS-CFD and STAR-CD in terms of accuracy and robustness using both the Euler-Euler and Volume of Fluid (VOF) approaches.
• Identify improvements required in closing gaps and bringing OpenFOAM to the level of current commercial software used for gas-liquid flow modelling.

This study is meant to give the readers some impressions on the capabilities of CFD tools for applied multiphase flows, with emphasis on the OpenFoam performance. The study follows a pragmatic approach, i.e. from an experienced industrial CFD user perspective. It is not meant to provide benchmarking results, i.e. with detailed analysis of the numerical methods and extensive grid refinement. We used versions of the various tools as available at the moment that this study was undertaken. This study thus gives only a 'snap-shot' overview. It is recommended to repeat the considered industrial cases when new versions are available and to track the improvements that are continuously being made in the CFD tools.

OPENFOAM

OpenFOAM is a library of C++ modules designed to build solvers for three-dimensional time-dependent problems such as fluid flow and solid mechanics. OpenFOAM is a C++ library, used primarily to create executables, known as applications. The applications fall into two categories: solvers, that are each designed to solve a specific problem in continuum mechanics, and utilities, that are designed to perform tasks that involve data manipulation. OpenFOAM contains numerous solvers and utilities covering a wide range of problems. In addition, the user can create custom solvers and utilities through C++ programming. This is a key feature of OpenFOAM, differentiating it from proprietary CFD software.

OpenFOAM is supplied with pre- and post-processing

capabilities. The overall structure of OpenFOAM is shown in Figure 1. In OpenFOAM all flow scenarios in continuum mechanics are classified under the following ten broad categories:
• Basic
• Incompressible flows
• Compressible flows
• Multiphase flows
• Direct Numerical Simulation and Large Eddy Simulation
• Combustion
• Heat transfer
• Electromagnetism
• Stress analysis of solids
• Finance
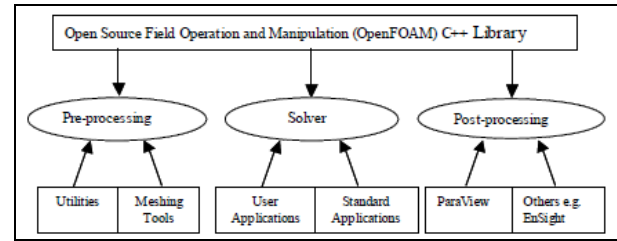
Figure 1: Overview of the OpenFOAM structure (from OpenFOAM User Guide version 1.5).

Each of these categories has a few solvers which simulate different physics or different approaches to the same physics. There are many tutorial cases available which cover almost all the solvers provided by OpenFOAM.

One of the features of OpenFOAM, which gives a lot of flexibility, is that the computer coding of the differential equation resembles the actual equation to a great extent. For example

$$\frac{\partial \rho U}{\partial t} + \nabla \cdot (\rho U U) - \nabla . \mu \nabla U = -\nabla p \qquad (1)$$

can be written in OpenFOAM code as

```
solve
(
fvm::ddt(rho, U)
+ fvm::div(phi, U)
- fvm::laplacian(mu, U)
= =
- fvc::grad(p)
);
```

Here the terms fvm::ddt(), fvm::div(), fvm::laplacian() and fvc::grad() are functions which carry out the respective operations on the variable matrix, as shown in Equation 1.

EULER-EULER METHOD

In the Euler-Euler approach (Pfleger and Becker, 2001), the different phases are treated mathematically as interpenetrating continua. Since the volume of a certain phase cannot be occupied by another phase, the concept of the phase volume fraction is introduced. These volume fractions are assumed to be continuous functions of space and time and their sum is equal to one at a particular point in space. In OpenFOAM the model is

the same but it has been implemented in a slightly different way. The details of the model and its implementation in OpenFOAM have been discussed thoroughly by Rusche (2002).

The physics of the bubble column is generally solved by the Euler-Euler method. Therefore this problem has been chosen in the present study. The bubble column has been simulated in ANSYS-CFD and in OpenFOAM. We kept as much similarity as possible between the set-up of the cases in the two simulations tools. The solver in OpenFOAM for multiphase flows using the Euler-Euler method is called *TwoPhaseEulerFoam*.
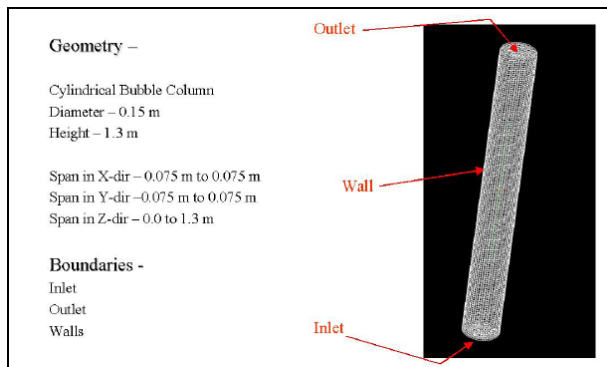
The Bubble Column Setup

The bubble column case has the specifications given in Table 1. The parameters shown in that table were among the ones which could be kept identical between ANSYS-CFD and OpenFOAM. Henceforth this case will be referred to as the baseline case. The QUICK scheme was used for discretization of the momentum equation to have higher accuracy and consistency with the ANSYS-CFD case. The geometry of the bubble column is shown in Figure 2.

Table 1: CFD model specifications for the bubble column

Specification	Description
Column diameter	0.15 m
Column height	1.3 m
System	Air-water
Gas superficial velocity	0.038 m/s
Sparging area	100 %
Numerical scheme for momentum eq.	QUICK
Two-phase model	Euler-Euler
Drag force (ANSYS-CFD default method)	Schiller-Neumann
Average bubble size	5 mm
Lift and virtual mass forces	Not-considered
Time step	0.025 seconds
Total simulation time	20 seconds
Number of cells	65000
Turbulence model	RNG k-ε (Yakhot & Smith 1992)

Figure 2: Geometry of the CFD model for the bubble column.

In OpenFOAM there is a time directory by the name "0" which is present in the case directory. Within the directory there is an ASCII file for each of the variables being solved in this case. The variables that are solved in this case are:

α – volume fraction of the discrete phase which is air in this case.

k – turbulent kinetic energy

ε – turbulent dissipation rate

p – pressure

U_a – velocity of the discrete phase i.e. air

U_b – velocity of the continuous phase i.e. water

Each of the files contains the value of the corresponding variable for all the boundary patches in the geometry, which for our case are the Inlet, Outlet and the Wall.

Generally two kinds of boundary conditions can be assigned for the variables, which are "fixed value" or "zero-gradient". There are other types of boundary conditions also available for specific kinds of flows. A detailed description of the boundary conditions is given in the OpenFOAM User Guide.

The boundary condition for k as well as ε is provided in terms of the actual values of these variables rather than in terms of turbulent intensity and length scale as done in the commercial software. Besides, it is also very important to initialize the volume with some appropriate values of k and ε so that OpenFOAM does not crash. The boundary conditions applied for the different variables in OpenFOAM and ANSYS-CFD are given in the Table 2. HD stands for Hydraulic diameter.

The outlet condition for U_a has been set as Inlet-outlet, which is a special kind of boundary condition, provided by OpenFOAM. It switches the value of the variable between a fixed value and zero-gradient based on the flow direction. For U_a it means that if the value of U_a is such that the flow is going out of the domain then it will be zero-gradient and if the flow is coming into the domain then it will be forcibly set to zero. This has been done to replicate the degassing boundary condition. The degassing boundary condition is one which allows only the gas to go out and retains the liquid in the domain. In spite of this, the degassing boundary condition does not completely get imposed because the value for U_b has been set to zero-gradient, which means that the solver will not maintain the condition that no water goes out of the domain.

Apart from the numerical scheme for the momentum equation all default schemes of the *TwoPhaseEulerFoam* solver was used. The default schemes and settings were obtained from the tutorial cases of *TwoPhaseEulerFoam* solver.

Table 2: Boundary conditions for bubble column

	Inlet	Outlet	Wall
p	Zero-gradient	0 Pa	Zero-gradient
U_a	0.038 m/s	Inlet-Outlet	No-slip
U_b	0 m/s	Zero-gradient	No-slip
k	7.22e-4 m²/s²	Zero-gradient	Zero-gradient
ε	3.66e-6 m²/s³	Zero-gradient	Zero-gradient
α	1	Zero-gradient	Zero-gradient

OpenFOAM

	Inlet	Outlet	Wall
p	Zero-gradient	0 Pa	Fluent Default
U_a	0.038 m/s	degassing	No-slip
U_b	0 m/s	degassing	No-slip
k	I = 5% ; HD = 0.15 m	I = 5% ; HD = 0.15 m	Fluent Default
ε	I = 5% ; HD = 0.15 m	I = 5% ; HD = 0.15 m	Fluent Default
α	1	Fluent default	Fluent Default

ANSYS-CFD (FLUENT)

There are a number of turbulence models available in OpenFOAM which can be used. For the solver named *TwoPhaseEulerFoam* only the standard *k-ε* by Launder & Sharma (1974) model is available and has been specifically hard-coded. This is because the turbulence models available with OpenFOAM have been written based on the velocity of the continuum, which is unique for single-phase flows whereas the turbulence for the two-phase flows is calculated based on the velocity of the continuous phase.

VOLUME OF FLUID METHOD

One of the classical cases which is a good test of the Volume of Fluid (VOF) approach is the simulation of the rising Taylor bubble.

The VOF model can deal with two or more immiscible fluids by solving a single set of momentum equations and tracking the volume fraction of each of the fluids throughout the domain. The VOF method by Hirt and Nichols (1981) and Youngs (1982) transports the local volume fraction of one of the fluids, a property varying sharply from 0 to 1 across the interfacial region, to update the position of the interface. However, unlike the Level Set approach by Sethian & Osher (1988), the VOF method usually involves a step of effective interface reconstruction. This step is based on the local volume fraction and the orientation of its gradient. Interfaces are then generally reconstructed using a piecewise linear interpolation proposed by Scardovelli and Zaleski (1999). Typical applications include the prediction of the jet breakup, the motion of large bubbles in a liquid, the motion of liquid after a dam break and the steady or transient tracking of any liquid-gas interface.

The feasibility of rigorously modelling the fluid mechanics of a Taylor gas bubble in a stagnant liquid-filled vertical pipe was examined by, among others, Tomiyama et al. (1994). The simulation was carried out using the VOF method. They also carried out experiments for the Taylor bubble shape under a wide range of Eö ($=g\rho D^2/\sigma$) and Mo ($=g\mu^4/\sigma^3\rho$) using sucrose solution and air at room temperature and atmospheric pressure. These two dimensionless numbers reflect the variation of the surface tension and of the liquid viscosity. It was confirmed by the experiments that the bluntness of the nose of the bubble, the flatness of the tail of the bubble and the thickness of the liquid film around the bubble were strongly affected by the two dimensionless numbers. The calculated terminal rising velocities and bubble shapes agreed fairly well with all the measured ones, which indicates that the effects of drag force, buoyancy and surface tension force on the bubble were well predicted by the CFD simulations.

The dedicated solver in OpenFOAM for VOF simulation is called *InterFoam*. The version of *InterFoam*, which also has turbulence models in it, is called *RasInterFoam*. The detailed description of the implementation of the VOF model in OpenFOAM is described by Rusche (2002).

Taylor Bubble Setup

The Taylor bubble case as simulated here has the specifications given in Table 3. MUSCL was used for

discretizing the momentum equation to have more accuracy and to have consistency with the simulations done in ANSYS-CFD. Figure 3 shows the geometry for the Taylor bubble CFD model.

The different variables being solved for the VOF approach in OpenFOAM are as follows:

γ – volume fraction of the liquid phase
k – turbulent kinetic energy
ε – turbulent dissipation rate
p_d – dynamic pressure.
U – velocity of the continuum

The values of these variables at the boundaries are given in Table 4. The boundary conditions in STAR-CD are similar to ANSYS-CFD in all respect with default settings retained wherever possible. Apart from the numerical scheme for the momentum equation all the other default schemes of the *RasInterFoam* solver were used.

Table 3: CFD model specifications for Taylor bubble case.

Specification	Description
Column diameter	0.28 m
Column height	3.05 m
System	Air-water
Gas inlet velocity	1 m/s for 0.3 sec
Numerical scheme for momentum eq.	MUSCL
Two phase model	VOF
Time-step	0.0001 sec
Number of cells	~1x10^6
Turbulence model	RNG k-ε
Surface tension	0.072 N/m
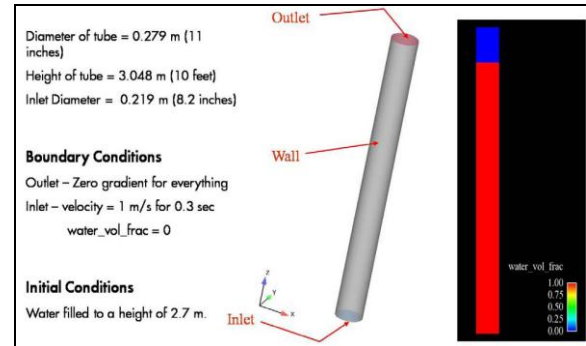
Figure 3: Geometry of the Taylor bubble CFD model. The figure on the right shows the level of liquid (red).

Table 4: Boundary conditions for bubble column

	Inlet	Outlet	Wall
γ	0	Inlet-Outlet	Zero-gradient
pd	Zero-gradient	0	Zero-gradient
k	1e-7 m²/s²	Zero-gradient	Zero-gradient
ε	0.1 m²/s³	Zero-gradient	Zero-gradient
U	1 m/s for 0.3 s	Zero-gradient	0

OpenFOAM

	Inlet	Outlet	Wall
γ	0	Fluent Default	Fluent Default
pd	Zero-gradient	0	Fluent Default
k	I = 5% ; HD = 0.28 m	I = 5% ; HD = 0.28 m	Fluent Default
ε	I = 5% ; HD = 0.28 m	I = 5% ; HD = 0.28 m	Fluent Default
U	1 m/s for 0.3 s	Fluent Default	0

ANSYS-CFD (FLUENT) and STAR-CD

Interface Capturing Method in OpenFOAM

The interface capturing technique is a very important part of the VOF methodology. In ANSYS-CFD the equation for γ is solved using a so-called geo-reconstruct (Rider & Kothe, 1998) discretization scheme whereas in OpenFOAM the following transport equation is solved.

$$\frac{\partial \gamma}{\partial t} + \nabla \cdot (\gamma \boldsymbol{U}) + \nabla \cdot (\boldsymbol{U}_r \gamma (1-\gamma)) = 0 \qquad (2)$$

Here U_r is a velocity field which is included to compress the interface to maintain its sharpness. The detailed description of the method of compressing the interface is given in Ruche (2002). The philosophy here is to use the extra term in the equation for γ to artificially compress the interface and to use bounded convective schemes to maintain the values for γ between 0 and 1.

RESULTS AND DISCUSSION

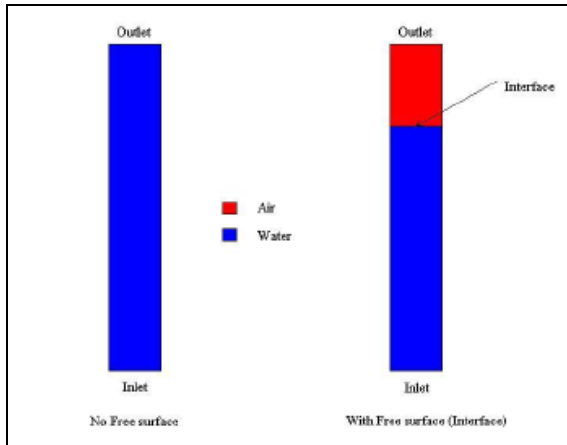## Euler-Euler Simulation for the Bubble Column

The simulation for the bubble column in OpenFOAM was done with two different boundary conditions. In one of the boundary conditions the column is fully filled with liquid, without the presence of a free surface, and in the other one there is a column of air above the liquid column so that there is a free surface in the simulation domain. This approach has been taken to see the effect of the free surface existing in the simulation domain. These two types of boundary conditions are shown in Figure 4. The condition in which there is a column of air will be referred to as the case with free board and the other one will be referred to as the case without free board.

Figure 4: Two approaches for the bubble column simulation.

Case without free board

The comparison of the holdup of air after 20 sec of analysis time between ANSYS-CFD and OpenFOAM is shown in Figure 5. The holdup in the ANSYS-CFD simulation is uniform throughout the column whereas in OpenFOAM we see local jumps in the holdup. In ANSYS-CFD the simulation after 20 sec of analysis time had reached a steady state whereas in OpenFOAM the flow still shows transient behaviour.

Figure 6 clearly shows that the velocity profile and the holdup profile with OpenFOAM are not homogeneous, neither along the height coordinate, nor in radial direction, which is in contrast to the ANSYS-CFD case without free board. The velocity of the air in OpenFOAM is higher than that predicted by ANSYS-CFD. The overall holdup predicted by OpenFOAM is about 8.5% whereas ANSYS-CFD predicts an overall holdup of 9.8%. The experiments show that the holdup is homogeneous throughout the domain both radially and along the height as predicted by ANSYS-CFD but the overall holdup is 20%. Thus both ANSYS-CFD and OpenFOAM underpredict the overall holdup by ~50%.

Case with free board

For the case with the free board the boundary condition at the outlet and the initial condition for α is different from what is given in Table 2. The outlet boundary condition for U_a and U_b is zero-gradient and a portion of the domain is initialized with $\alpha = 1$ at the top of the column. The height of the free board can be 10-15% of the total height of the column. This kind of initialization can be done using the *SetFields* utility in OpenFOAM. Figure 7 shows the comparison of results between the ANSYS-CFD case without free board and OpenFOAM case with free board. The other difference between the two cases is that ANSYS-CFD has the turbulence model on whereas OpenFOAM has the turbulence model off because the turbulence model was diverging with the free board simulation.

Figure 7 shows that with the free board condition OpenFOAM results improve considerably and become close to the results of ANSYS-CFD. This is further endorsed by the graphs of the holdup profile and the velocity magnitude of air profiles at different heights along the column in Figure 8. The velocity profile is predicted very well in terms of values as well as homogeneity. The holdup values are still not homogeneous but the overall average has increased and is now closer to the value predicted by ANSYS-CFD. The solution with OpenFOAM reaches a steady state after about 20 sec of analysis time, which is the same as found in ANSYS-CFD.

A comparison of Figure 6 and Figure 8 clearly shows that the free board boundary condition is causing the results to improve significantly. In the boundary condition without the free board the solution is unstable, does not reach a steady state and is highly inhomogeneous whereas all these characteristics are removed if the free board condition is applied. This shows that there is some problem in OpenFOAM caused by the outlet boundary condition. In ANSYS-CFD we have the provision of applying the degassing boundary condition whereas in OpenFOAM this kind of a boundary condition is not available. The outlet boundary condition used for this model in OpenFOAM is a special kind of boundary *InletOutlet*. The *InletOutlet* condition allows only the air to leave through the outlet, and it prohibits any inflow of air into the domain through the outlet.
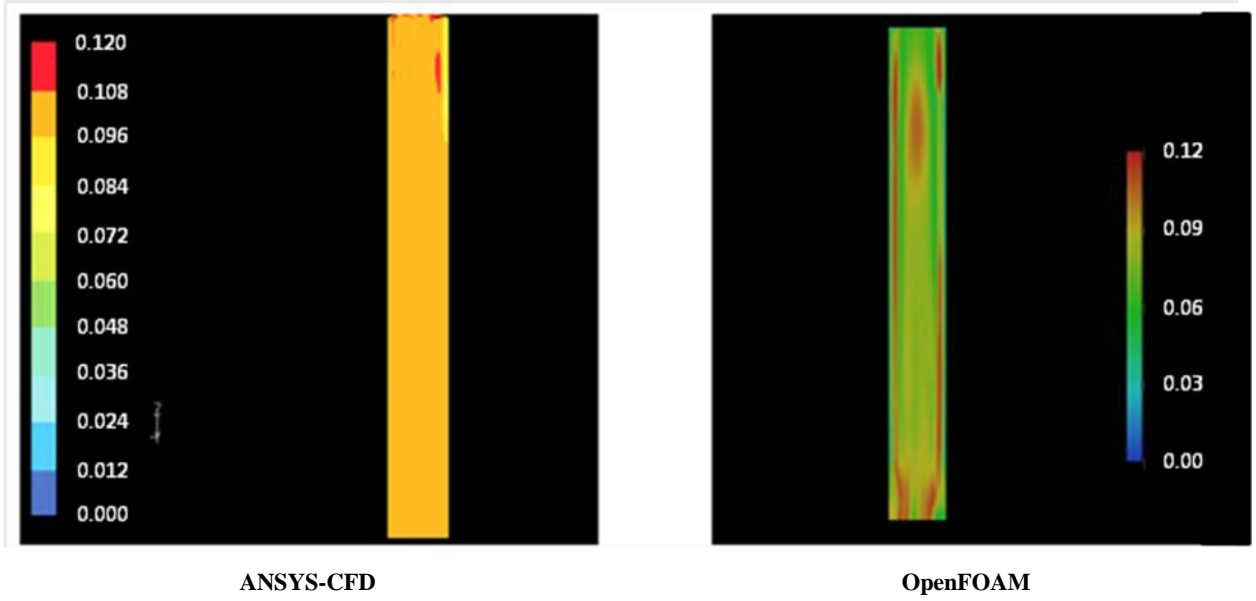
ANSYS-CFD   **OpenFOAM**

Figure 5: Comparison of the air holdup (α) contours in the bubble column simulations with ANSYS-CFD and OpenFOAM.
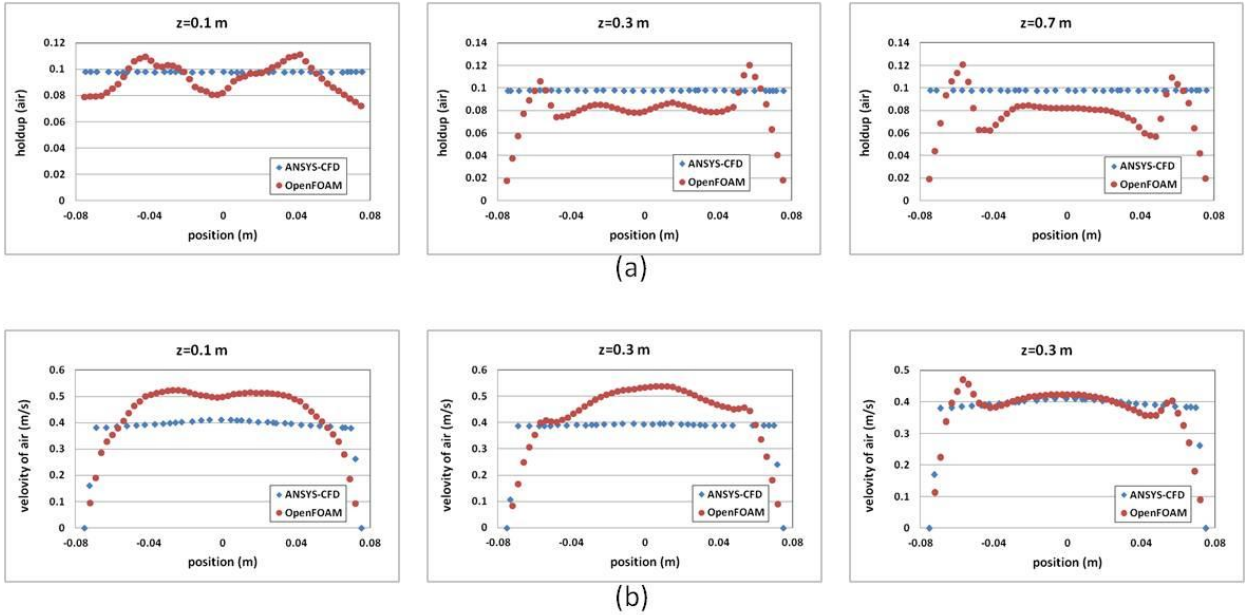
Figure 6: Comparison of the (a) air holdup and (b) the axial velocity of air at different sampling locations along the height of the column for cases without free board.

The turbulence model in OpenFOAM does not work in the case with free board. It may be due to a problem with the turbulence models at the interface because of the way the two-fluid turbulence model works. The turbulence equations have some source terms based on the gradient of the volume fraction implemented in OpenFOAM. These terms become very large near the interface and this can lead to numerical instabilities. The other term**,** which may become unstable due to the same large gradients, is the turbulent dispersion term driven by the gradient of volume fraction. A description of these numerical difficulties is given in Ruche (2002).

VOF Simulation for the Taylor Bubble

A comparison is made between the results for the VOF simulations for the Taylor bubble as obtained with OpenFOAM, STAR-CD, and ANSYS-CFD.

The shape of the Taylor bubbles in Figure 9 shows that OpenFOAM version 1.5 is not able to capture the features adequately. The surface of the bubble is uneven in OpenFOAM, whereas it is very smooth in ANSYS-CFD and in STAR-CD. This may be due to the difference in the numerical discretization scheme that is used for solving the volume fraction equation. OpenFOAM uses the interface-capturing technique as discussed earlier, ANSYS-CFD uses the geo-reconstruct scheme and STAR-CD uses HRIC (High Resolution Interface Capturing) by Muzaferija and Peric (1998). This shows that the geo-reconstruct scheme is able to

(a) ANSYS-CFD
          (b) OpenFOAM

Figure 7: Comparison of air holdup (α) contours: (a) ANSYS-CFD without free board and with turbulence (b) OpenFOAM with free board and no turbulence

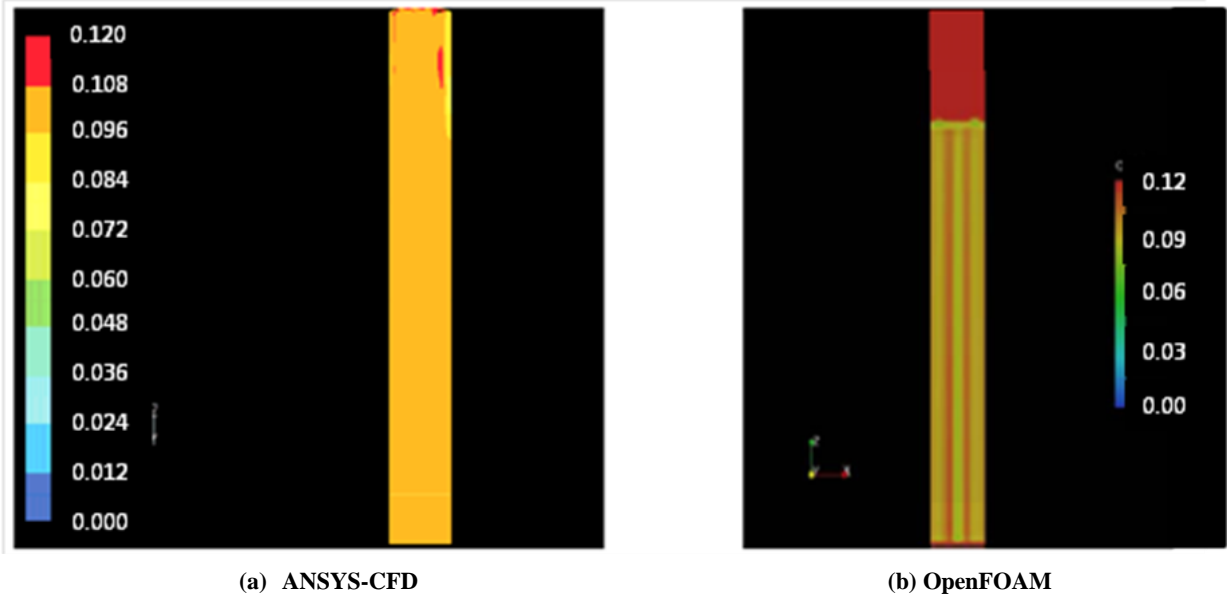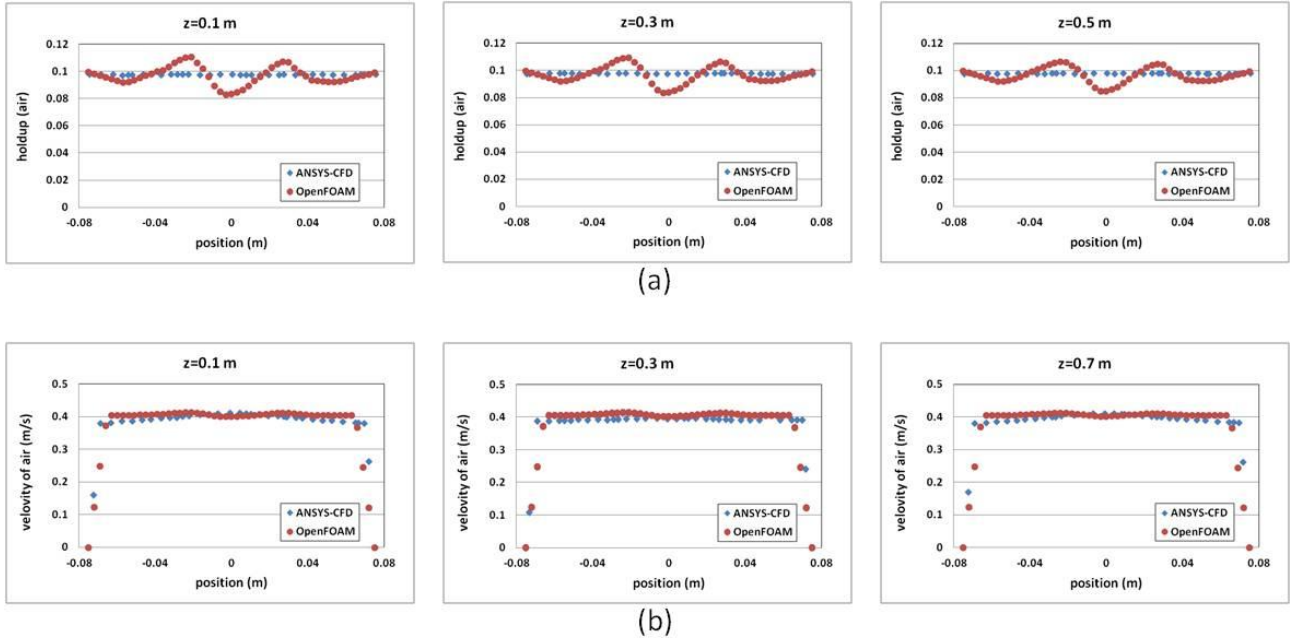
Figure 8: Comparison of the (a) air holdup and (b) the axial velocity of air at different sampling locations along the height of the column for ANSYS-CFD case with free board and OpenFOAM case without free board.

capture the interface better than the other methods. OpenFOAM version 1.5 does not have the geo-reconstruct scheme. The results from STAR-CD have very few trailing bubbles as compared to OpenFOAM and ANSYS-CFD. The number of trailing bubbles is so large in OpenFOAM that later on the bubble disintegrates completely as shown in Figure 11.

Figure 10 shows the rise velocity of the Taylor bubble; here the bubble surface has been identified as the iso-surface with a value of the γ = 0.5. To calculate the velocity of the bubble the vertical height of the centroid of the bubble from the base of the column was monitored with time. The centroid of the bubble was calculated by taking the area average of the height over the bubble surface. The ratio of the change in height to

change in time has been plot in Figure 10. The analytical expression for the rise velocity of a single Taylor bubble is $v_b = 0.328\sqrt{gD}$, which has been derived in the work by Davies & Taylor (1950) and Dumitrescu (1943) (here g is the gravitational acceleration and D is the column diameter). According to this expression the rise velocity of the bubble for this case should be 0.56 m/s. All the three CFD tools predict a lower value of about 0.45 m/s for the terminal rise velocity of the bubble (see Figure 10). The difference might be due to the inclusion of the effect of the trailing bubbles. However, from the finding that there are very few trailing bubbles in the STAR-CD results, whereas it still predicts a lower terminal velocity, it may be argued that the trailing bubbles may not be the only reason for the deviation in the terminal velocity. Other reasons might be insufficient resolution

of the numerical mesh and/or weaknesses of the discretization scheme of the volume fraction equation. More investigation needs to be carried out to find out the real cause of such behaviour.

Due to the inability of OpenFOAM to capture the interface in a smooth manner the bubble finally disintegrates completely after 4.15 seconds as is shown in Figure 11. This demonstrates that OpenFOAM version 1.5 does not properly simulate Taylor bubbles.
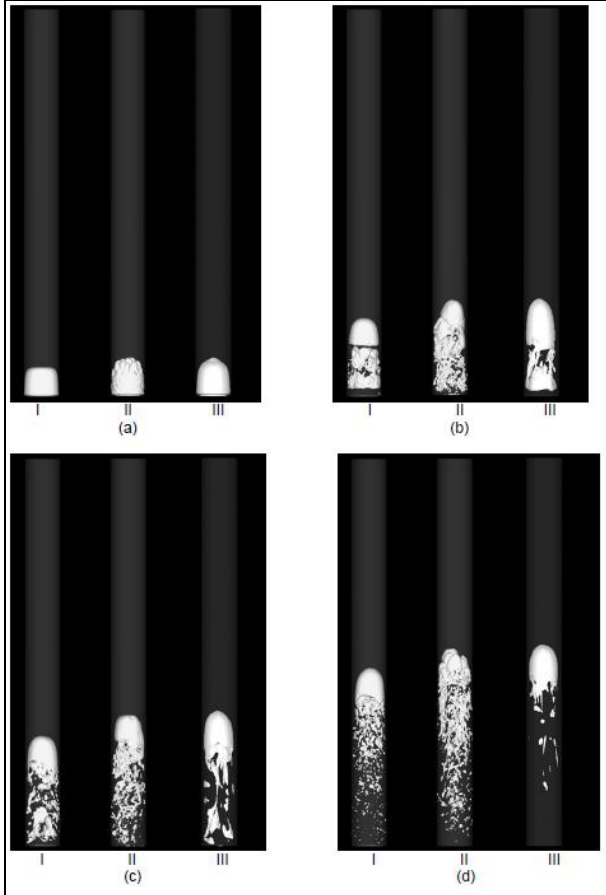
Figure 9: Comparison of the shape of the Taylor bubble as obtained with three CFD tools, (I) ANSYS-CFD (II) OpenFOAM (III) STAR-CD, at four different instances (a) 0.3 sec (b) 1.0 sec (c) 1.5 sec (d) 2.5 sec
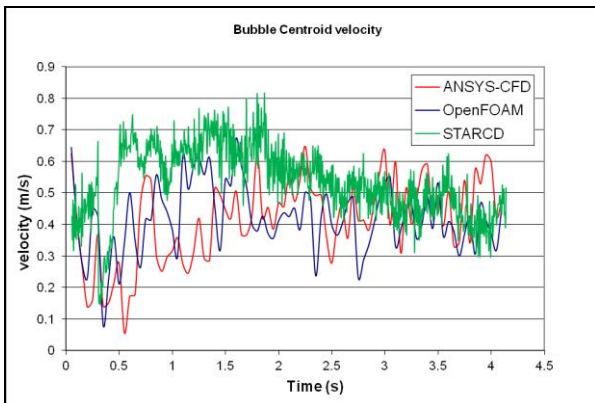
Figure 10: Centroid velocity of the Taylor bubble.

CONCLUSION

Based on the results of this study, it can be concluded that OpenFOAM version 1.5 has limited capabilities to model multiphase flows of interest to the oil and gas industry. In the latest release of OpenFOam (version 1.7), the *InterFoam* and *RasInterFoam* solvers have been merged, but not much has changed in the *TwoPhaseEulerFoam* solver.

The flexible and open structure of OpenFOAM gives the user many options to improve and customize this CFD tool. With the capabilities in version 1.5, OpenFOAM cannot yet compete with the commercial software for multiphase flow modeling, such as ANSYS-CFD and STAR-CD. With the ongoing development of OpenFOAM, however, it is likely that future versions of the software will overcome the shortcomings identified in this study.
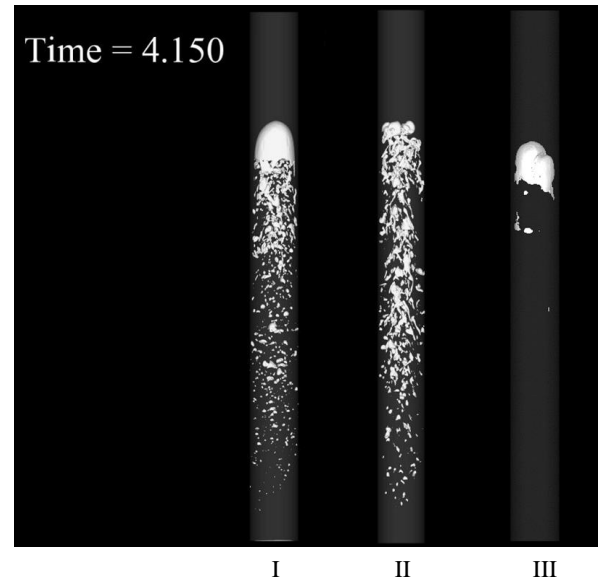
Figure 11: Iso-surface of Volume fraction of liquid = 0.5 (I) ANSYS-CFD (II) OpenFOAM (III) STAR-CD.

The key findings for OpenFOAM version 1.5 are summarized below:

1. Á In OpenFOAM various turbulence models are available for the simulation of single phase flows. Unlike this, the solver for the Euler-Euler method only has the standard *k-ε* model available. The other turbulence models, such as the RNG *k-ε*, still have to be coded. The VOF model in OpenFOAM can already use the other turbulence models.

2. Á The Euler-Euler approach available in OpenFOAM version 1.5 is not as well implemented as in ANSYS-CFD. The predictions of the gas holdup are not good for conditions without free board and require further improvement. This may be due to the difficulty in handling the exit boundary condition or lack of ability of OpenFOAM to dampen unstable behaviour of the numerical solution. The case with the free board gives much better results, but it crashes when the turbulence model is switched on. Further investigation has to be done to find out the cause of this crash.

3. Á The VOF model available in OpenFOAM version 1.5 is not able to capture the interface of the Taylor

bubble in a physically viable manner. It is not ready at this point to simulate slug and churn flows. The higher order interface capturing schemes such as the HRIC and PLIC (geo-reconstruct) are not available in OpenFOAM.

4.Á It is recommended to recalculate the industrial cases used in this study for the latest release of OpenFOAM (version 1.7), and also for future releases of both OpenFOAM and the commercial tools. It is also recommended to carry out successive grid refinement.

REFERENCES

DAVIS R.M. and Sir TAYLOR G., (1950), "The mechanics of large bubbles rising through extended liquids and through liquids in tubes", *Proc. Roy. Soc.*, 200, 375-390.

DUMITRESCU D.T., (1943), "Strömung an einer Luftblase im senkrechten Rohr", *Z. Angw. Math. Mech.*, 23, 139-149.

HIRT C.W. and NICHOLS B.D., (1981), "Volume of Fluid (VOF) method for the dynamics of free boundaries", *J. Comput. Phys.,* 39, 201–225.

LAUNDER B. E. and SHARMA B. I., (1974), "Application of the Energy Dissipation Model of Turbulence to the Calculation of Flow near a Spinning Disc", *Letters in Heat and Mass Transfer*, 1(2), 131-138.

MUZAFERIJA S. and PERIC M., (1998), "Computation of free-surface flows using interface-tracking and interface capturing methods," in Mahrenholtz O, Markiewicz M. (eds.), *Nonlinear Water Wave Interaction, Computational Mechanics Publications*, Southampton.

OSHER S. and SETHIAN J. A., (1988), "Fronts propagating with curvature dependent speed: Algorithms based on Hamilton-Jacobi formulation", *Jour. Comp. Phys.,* 79, 12–49.

PFLEGER D. and BECKER S., (2001), "Modelling and simulation of the dynamic behaviour in a bubble column", *Chemical Engineering Science*, 56, 1737-1747.

RIDER W.J. and KOTHE D.B., (1998), "Reconstructing volume tracking", *J. Comput. Phys.,* 141, 112–152.

RUSCHE, H., (2002), "Computational Fluid Dynamics of Dispersed Two-Phase Flows at High Phase Fractions", *PhD Thesis*, *Imperial College of Science, Technology & Medicine Department of Mechanical Engineering).*

SCARDOVELLI R. and ZALESKI S., (1999), "Direct numerical simulation of free-surface and interfacial flow" *Annu. Rev. Fluid Mech.*, 31,567-603.

TOMIYAMA A., SOU A. and SAKAGUCHI T., (1994), "Numerical simulation of a Taylor bubble in a stagnant liquid inside a vertical pipe"*, JSME International Journal, Series B (Fluid and Thermal Engineering)*, 39 (3), 517-24.

YAKHOT V. and SMITH L. M., (1992), "The Renormalization Group, the ε-Expansion and Derivation of Turbulence Models", *J. Sci. Comput.*, 7, 35-61.

YOUNGS D.L., (1982), "Time-dependent multi-material flow with large fluid distortion. In: Morton, K.W., Baynes, M.J. (Eds.)", *Numerical Methods for Fluid Dynamics. Academic Press, New York*, 273-285.

8th International Conference on CFD in Oil & Gas, Metallurgical and Process Industries
SINTEF/NTNU, Trondheim NORWAY
21-23 June 2011

CFD11-150

CFD MODELING OF TAPPING PROCESS IN FERROMANGANESE FURNACES

Mehdi KADKHODABEIGI[1][*], **Halvard TVEIT**[2][†], **Stein Tore JOHANSEN**[3][‡]

[1]NTNU Department of Materials Science and Engineering, 7491 Trondheim, NORWAY

[2]Elkem Thamshavn, 7301 Orkanger, NORWAY

[3]SINTEF Materials and Chemistry, 7465 Trondheim, NORWAY

[*] E-mail: mehdi.kadkhodabeigi@material.ntnu.no
[†] E-mail: halvard.tveit@elkem.no
[‡] E-mail: stein.t.johansen@sintef.no

ABSTRACT

For the stable operation of a submerged arc furnace, precise controlled tapping of the molten products is an important factor. In this study tapping of slag and metal from submerged arc furnaces used for ferromanganese (FeMn) production is investigated. An in-depth understanding of the melt flows and heat transfer in the furnace is essential in order to identify the governing conditions on the tapping process. Therefore a comprehensive computational fluid dynamics (CFD) model of an industrial size furnace is described which is able to predict the melt flows in the furnace heart, temperature distribution in the melt and the furnace wall refractories and flow rates of slag and metal during furnace tapping. The model addresses multiphase fluid flow; conjugate heat transfer, natural convection, turbulent flow through porous beds inside the furnace and high resolution grid. Using the modified $k - \varepsilon$ turbulence model for porous media, the effect of fluid flows around coke particles is taken into account. The results show that the tapping flow rate is mainly dependent on the initial level of slag and metal inside the furnace. The model also predicts that the slag-metal and gas-slag interfaces are tilted towards the furnace taphole. The results of the model are in good agreement with industrial measurements for total weight of slag and metal tapped in a given time interval. These results show validity of the developed model.

Keywords: CFD, Submerged arc furnace, Tapping process, Multiphase fluid flow, Turbulence model for porous media .

NOMENCLATURE

ρ Density, $[kg/m^3]$
μ Dynamic viscosity, $[kg/ms]$
μ_t Turbulent viscosity, $[kg/ms]$
ε Porosity of the bed
β Thermal coefficient of volumetric expansion, $[1/K]$
λ Thermal conductivity, $[W/m.K]$
σ_T Turbulent Prandtl number of enthalpy
$(\lambda_{diss})_{XX}$ Apparent conductivity in longitudinal direction
$(\lambda_{diss})_{YY}$ Apparent conductivity in transverse direction
α Permeability of the bed
$\mathbf{u}$ Velocity, $[m/s]$
T Temperature, $[K]$
p Pressure, $[Pa]$
g Gravity acceleration, $[m/s^2]$
k Turbulent kinetic energy, $[m^2/s^2]$
C_μ Turbulent model constant
C_2 Inertial resistance

d_p Particle diameter, $[m]$
c_p Specific heat, $[J/kgK]$
D_F Furnace diameter, $[m]$
D_E Electrodes diameter, $[m]$
D_T Taphole diameter, $[m]$
H_F Considered height of furnace, $[m]$
H_T Taphole height, $[m]$
L Taphole lenght, $[m]$
h   Slag or metal height, $[m]$

INTRODUCTION

High carbon ferromanganese is commercially produced by carbothermic reduction of manganese ores, primarily in electric submerged arc furnaces. Recently built furnaces for the production of ferromanganese have capacities of 75-90 MVA. The produced metal typically contains around 78% Mn and 7% C, and the slag around 40% MnO (high-MnO slag practice). An increasing part of the metal is refined to medium or low carbon ferromanganese (Olsen *et al.*, 2007). Electric furnaces used in the production of manganese alloys are generally circular and have three electrodes, each connected to a separate electrical phase. The electrodes are submerged in the burden and the electric current run through the area bellow the electrode tips where electrical energy is converted to heat. Produced slag and metal may be tapped simultaneously from the same taphole, or separately in different slag and metal tapholes arranged at a vertical distance of 0.5-1.0 *m*. A ferromanganese producing furnace is schematically shown in Figure 1.

Stable operation of submerged arc furnace is required to reduce energy consumption in the furnace. Stability of furnace operation is highly dependent on the quality of tapping process. Tapping of melt from the furnace is directly connected to the furnace inside conditions. To maintain the furnace inside in good condition, in addition to different operational issues, it is necessary to clarify the drainage behavior of molten metal and slag in the hearth. Therefore the melt flow behavior should be understood precisely.

The furnace heart consists of metal layer and an overlaying coke bed zone. The coke bed starts approximately at the tip of the submerged electrodes down in the furnace. In this area there will be a bed of oxide coke, slag and metal (Olsen *et al.*, 2007). Due to the different densities of coke, slag and metal the various layers are often described in the literature as consisting of separate layers, as illustrated in Figure 2(A) Olsen *et al.* (2007). However from excavation of a single-phase pilot scale furnace Tangstad (1996) and Tangstad *et al.* (2001)

and industrial furnaces Barcza *et al.* (2001), Tangstad (1999), Ringdalen and Eilertsen (2001), Olsen and Tangstad (2004) it has been proven that coke is present all the way down to the metal layer. Often "dry" bed of coke is present at the top of the coke bed area. The slag to coke ratio increases with decreasing distance to the metal layer, as illustrated in Figure 2 Olsen *et al.* (2007). The coke bed is "forced" into the slag layer by the weight of the overburden. The viscosities of slag and metal are also largely different; the molten slag is usually several orders of magnitude more viscous. Since the coke bed zone is often packed with coke particles, so that the liquids inside this zone can only flow throughout the void space between the particles. Hence, the tapping process is often idealized as the drainage of immiscible liquids from a packed-bed reservoir.

Flow of molten slag and metal in a FeMn furnace is very similar to melt flows in a blast furnace (BF) heart (Ashrafian and Johansen, 2006). There are several researches available in the literature about flow of molten slag and metal in the blast furnace heart. Throughout the pioneering experiments about tapping process in the blast furnaces (Fukutake and

Okabe, 1976), it was shown that during the tapping period, the slag surface tilts towards the taphole resulting in an early discharge of the furnace gases and remaining of relatively large amounts of slag in the furnace. These observations were furthermore completed in other studies (Tanzil *et al.*, 1984) where it was observed that the slag-metal interface may also tilt towards the taphole. Simultaneous to the tapping of the overlaying slag layer, the metal layer is also entrained into the taphole from levels well below the taphole level. Different flow regimes in tapping of the slag and metal from the blast furnace heart are schematically shown in Figure 3.
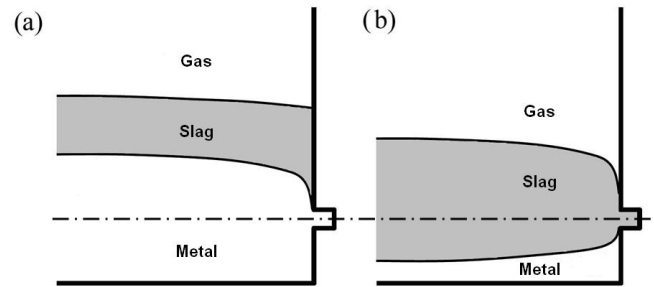

Figure 3: Different flow regimes in tapping of stratified fluids from a packed bed reservoir while the metal height is above (a) or bellow (b) the taphole level.

In fluid mechanics, the entrainment of immiscible liquids during the tapping of one or the other is a well-known phenomenon. In many applications, it is necessary to predict the maximum rate of withdrawal of a fluid with desired properties which can be attained before fluid from a different level also begins to flow (Turner, 1973). The behavior of fluid flow in the channels due to existence of point and line sinks in the end wall of channel at different levels from the interface between the two layers have been investigated in previous works (Craya, 1949) and (Huber, 1960). Further improvements of the theory of the withdrawal from a two-layer fluid through a line sink were carried out through works done by (Hocking and Forbes, 2001), (Tyvand, 1992) and (Stokes *et al.*, 2003).

In the case of tapping from a ferromanganese furnace, existence of metal, slag and gas as three separate phases in the system, interaction of different phases with a packed bed of solid particles in the slag and coke bed zones and unknown shape for the coke bed, are just examples which show how complex the system is. Drainage rates as well as the viscosity of the working liquids are often quite high. The complex flow behavior through the furnace heart is, therefore a result of the simultaneous action of inertial, buoyancy and viscous forces, including the geometrical effects represented by the packed bed.

Tapping of slag and metal from the FeMn furnaces could be idealized as the drainage of immiscible liquids from a packed bed reservoir. This problem was revisited by (Ashrafian and Johansen, 2006) through developing a simple two-dimensional CFD model. Their model includes a non-porous metal zone and porous slag and gas zones, where the porosity and particles size are evenly distributed in these zones. The aim of their work was to study the behavior of metal and slag flows while tapping from a packed bed reservoir as the furnace hearth. The influence of density and viscosity ratios of slag and metals as well as the packed bed characteristics on the onset of entrainment of the lighter liquid into the taphole was studied in their work. They found
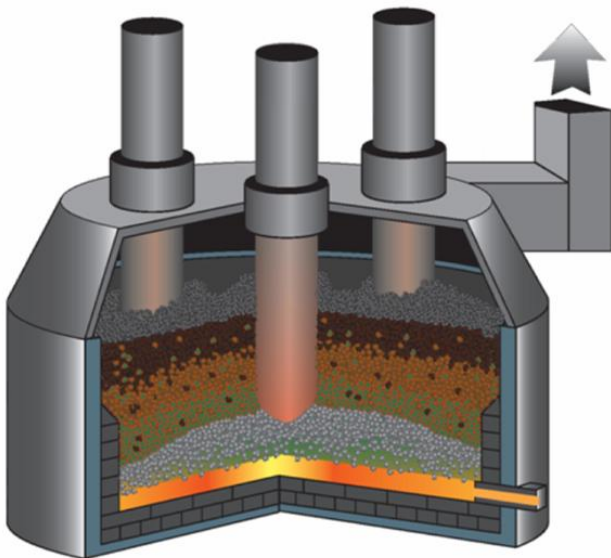

Figure 1: Schematic view of a ferromanganese production furnace showing furnace body, electrodes, off-gas system and charge materials (Tangstad, 2011).
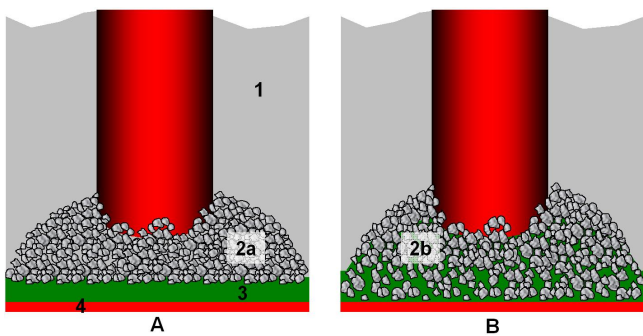

Figure 2: Possible coke bed configurations. A) Separate coke bed, slag layer and metal layer. B) Coke bed mixed with slag and separate metal layer. 1-pre-reduction zone, 2a-coke bed with small amount of slag, 2b-coke bed with increasing amount of slag towards the metal layer, 3-slag layer, 4-metal layer Olsen *et al.* (2007).

that buoyancy effects are the underlying parameter in determining the onset of the simultaneous tapping. Also they concluded that in the absence of packed bed, the viscosity ratio was found out to have no influence on the tapping behavior while with the presence of the packed-bed the tapping behavior is drastically changed. Their results show that onset of entrainment of the lighter liquid as well as the gas-liquid interface into the taphole is advanced, leading to the considerable amounts of the lighter liquid to be remained in the reservoir.

In spite of the investigations described above, a general description of the flow behavior during the tapping of slag and metal from the submerged arc furnaces is difficult to obtain, due to the complexity of the real system and simplifications and assumptions made in the numerical models. The current study aims to develop a new three-dimensional numerical model to resolve the complex flow structures and heat transfer within the heart of a FeMn furnace. Therefore our model is restricted to the high temperature zone of the furnace.

MODEL DESCRIPTION

The current model is built based on an industrial size furnace and uses multiphase Computational Fluid Dynamics (CFD) techniques together with refined computational grid and applies a set of mathematical equations for turbulent flow-heat transfer in porous media. Moreover, the flow pattern and heat transfer are described and analyzed in more details to extend the knowledge on the liquid slag and metal flows. Physical properties of coke bed zone such as porosity, permeability and particles size as well as the most probable coke bed structure have been selected based on both the available literature and industrial information about the furnace inside conditions.

Model Geometry

Since the model is restricted on the high temperature zone of the furnace including metal layer and the coke bed, only 1 *m* from the furnace bottom is considered in the geometry of the model. In order to study the heat distribution in the lower part of the furnace, the geometry includes the furnace refractory walls both side wall and bottom wall. The furnace geometry has been selected based on an industrial size FeMn furnace with the specifications listed in Table 1.

Table 1: Detailed geometry of the FeMn production furnace used in CFD modeling.

D_F (m)	H_F (m)	D_E (m)	D_T (m)	L (m)	H_T (m)
11	1	2	0.10	0.6	0.4

The high temperature zone of the furnace is treated as symmetric about the plane defined by the hearth centerline and the taphole, so only one half of the furnace needs to be modeled. The furnace geometry including different zones is shown in Figure 4.

The coke bed zone is divided into two different zones called fine coke bed, the zones located under the electrodes, and coarse coke bed which includes the rest of coke bed zone (see Figure 5). Physical properties of the prescribed zones, slag and metal are given in Table 2. Surface tension for the metal is equal to 1.17 *N/m* (Shin *et al.*, 2010), for the slag is 0.5 *N/m* and metal - slag interfacial tension is equal to 0.6 *N/m* (Ashrafian and Johansen, 2006).

The furnace wall refractory thickness is considered 1.6 *m* at the bottom and 0.6 *m* at the furnace side wall. It was assumed that the wall refractory is made of normal carbon bricks used in constructing submerged arc furnaces (Scheepers, 2008) and therefore the material properties of the bricks were chosen upon to the available information.

Model governing equations

Metal, slag and gas are the immiscible phases available in the model of the FeMn producing furnace. The interfaces between these phases are tracked by VOF method. The conservation equations for mass and momentum in isotropic porous medium, resistance against fluid flows in an isotropic porous medium are written in coordinate free tensor notation as:
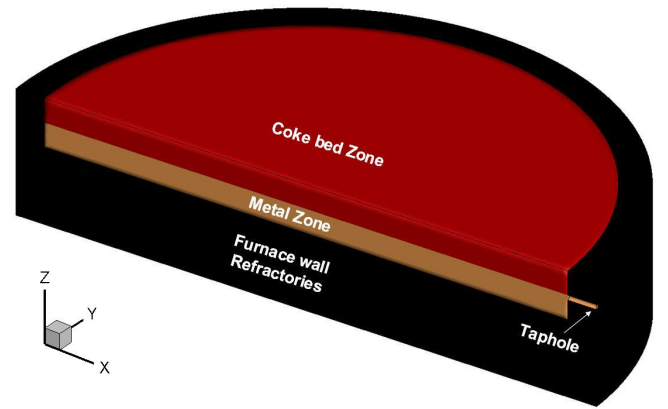

Figure 4: Geometry of the FeMn production furnace including the slag and metal zones as well as wall refractories.
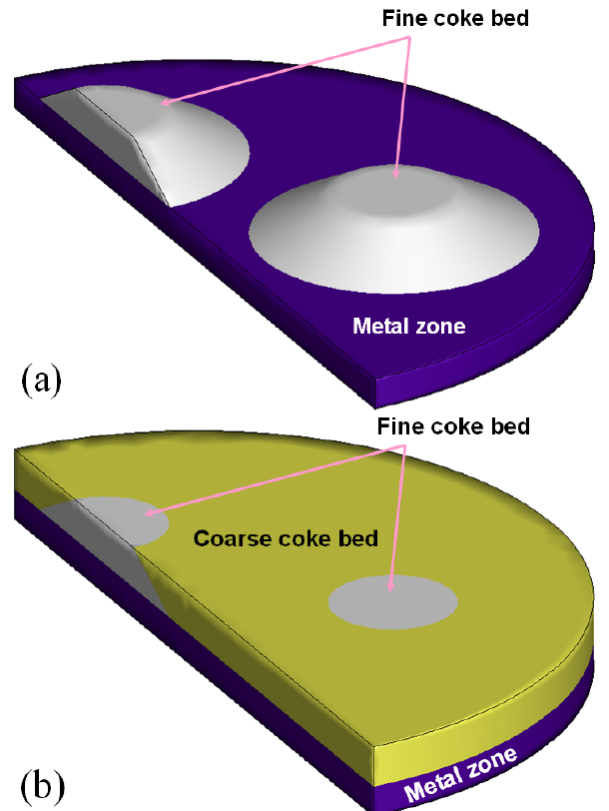

Figure 5: Coke bed zone laid over the metal layer in the furnace heart, the fine coke bed (a) and the coarse coke bed (b).

Table 2: Physical properties of slag and metal in different zones used in CFD modeling of the FeMn production furnace (Olsen *et al.*, 2007), (Shin *et al.*, 2010) and (Eramet, 2010)

Zone	ρ_f	μ	λ_f	ε	c_{pf}	d_p
Metal	6100	0.005	40	1	791	-
Coarse coke bed	3000	0.1	3	0.3	1800	0.05
Fine coke bed	3000	0.1	3	0.5	1800	0.015

$$\frac{\partial \varepsilon \rho}{\partial t} + \nabla \cdot (\varepsilon \rho \mathbf{u}) = 0 \tag{1}$$

$$\frac{\partial \varepsilon \mathbf{u}}{\partial t} + \nabla \cdot (\varepsilon \rho \mathbf{u}\mathbf{u}) - \nabla \cdot \left[\mu_{eff} \varepsilon (\nabla \mathbf{u} + (\nabla \mathbf{u})^T) \right] = \\ -\varepsilon \nabla (p + \frac{2}{3}\rho k) + \varepsilon \rho g \beta (T - T_{ref}) - \varepsilon \mathbf{R} \tag{2}$$

$$\rho = \sum_\kappa \varepsilon_\kappa \rho_\kappa / \sum_\kappa \varepsilon_\kappa \tag{3}$$

$$\mu = \sum_\kappa \varepsilon_\kappa \mu_\kappa / \sum_\kappa \varepsilon_\kappa \tag{4}$$

The scalar equation for the propagation of the liquid fraction has similar form as Equation (1). The effective and turbulent viscosities are defined as follows:

$$\mu_{eff} = \mu + \mu_t \tag{5}$$

$$\mu_t = \rho C_\mu \frac{k^2}{\varepsilon} \tag{6}$$

The model is a generalization of Darcy's Law, commonly used for flows in porous media, and of the Reynolds-averaged Navier Stokes equations, with an eddy viscosity accounting for the turbulent effects. The last term in Equation (2) represents the resistance to flow in porous media. Based on the well-known Ergun's equation (Ergun, 1952), the resistance force for flow through a bed of particles is given by:

$$\mathbf{R} = \frac{150\mu}{d_p^2} \frac{(1-\varepsilon)^2}{\varepsilon^3} \mathbf{u} + \frac{1.75\rho}{d_p} \frac{(1-\varepsilon)}{\varepsilon^3} |\mathbf{u}|\mathbf{u} \tag{7}$$

The defined resistance in the Ergun's equation for each component can be written as:

$$\mathbf{R}_i = -(\frac{\mu}{\alpha} \cdot \mathbf{u}_i + C_2 \frac{1}{2}\rho |\mathbf{u}|\mathbf{u}_i) \tag{8}$$

$$\alpha = \frac{d_p^2}{150} \frac{\varepsilon^2}{(1-\varepsilon)^3} (Permeability) \tag{9}$$

$$C_2 = \frac{3.5}{d_p} \frac{(1-\varepsilon)^3}{\varepsilon^3} (Inertial Resistance) \tag{10}$$

The turbulent viscosity is determined by applying the k-ε model modified by (Nakayama and Kuwahara, 1999) in which an extra source term, comparing to normal fluid flow, due to solid particles is added into the equations solved for kinetic energy and its dissipation within the turbulence model. This model allows unified treatments for the liquid iron flow over the entire hearth. Assuming thermal equilibrium between the fluid and solid matrix of packed bed, for saturated rigid porous media, the energy equations for the fluid and solid phases can be written as ((Guo *et al.*, 2008)):

$$\rho_f c_{pf} \frac{\partial T}{\partial t} + \rho_f c_{pf} \nabla \cdot (\mathbf{u}T) - \nabla \cdot \left[\left(\lambda_f + \frac{c_{pf}\mu_t}{\sigma_T} \right) \nabla T \right] = 0 \tag{11}$$

$$\rho_s c_s \frac{\partial T}{\partial t} - \nabla \cdot (\lambda_s \nabla T) = 0 \tag{12}$$

Integration of the two microscopic energy equations yields the energy equation:

$$\left(\varepsilon \rho_f + (1-\varepsilon)\rho_s c_s \right) \frac{\partial T}{\partial t} + \varepsilon \rho_f c_{pf} \nabla \cdot (\mathbf{u}T) = \nabla \cdot \{\lambda_p \cdot \nabla T\} \tag{13}$$

Where λ_p is a modified thermal conductivity which can be expressed as:

$$\lambda_p = \left[\varepsilon \lambda_f + (1-\varepsilon)\lambda_s + \varepsilon \frac{c_{pf}\mu_t}{\sigma_T} \right] + \lambda_{tor} + \lambda_{dis} \tag{14}$$

The apparent conductivity tensors, λ_{tor} and λ_{dis}, are introduced to describe the tortuous molecular diffusion and the thermal dispersion, respectively.

$$\left(\varepsilon \rho_f c_{pf} + (1-\varepsilon)\rho_s c_s \right) \frac{\partial T}{\partial t} + \varepsilon \rho_f c_{pf} \nabla \cdot (\mathbf{u}T) = \\ \nabla \cdot \left\{ \left[\left(\varepsilon \lambda_f + (1-\varepsilon)\lambda_s + \varepsilon \frac{c_{pf}\mu_t}{\sigma_T} \right) + \lambda_{tor} + \lambda_{dis} \right] \cdot \nabla T \right\} \tag{15}$$

This equation is similar in format to the generic advection diffusion equation that governs the energy transport in the fluid flow through porous media except for a modified thermal conductivity.

These extra terms in the effective conductivity are usually prescribed in normalized forms. λ_{tor}/λ_f decreases by increase of, Peclet number, *Pe*, or decrease of λ_s/λ_f Guo *et al.* (2008). The Peclet number is defined as follows:

$$Pe = \frac{\rho_f c_{pf} d_p \varepsilon |\mathbf{u}|}{\lambda_f} \tag{16}$$

With increasing *Pe*, the contribution due to thermal dispersion dominates that due to tortuosity. Therefore the tortuosity term can be neglected.

The thermal dispersion is non-isotropic, with a higher level in the longitudinal flow direction than in the transverse direction Guo *et al.* (2008). Empirical correlations in terms of the Peclet number and porosity for longitudinal and transverse dispersion are respectively as follows (Kuwahara and Nakayama (1999)):

$$\frac{\left(\lambda_{dis} \right)_{XX}}{\lambda_f} = 2.7 \frac{Pe_p}{\varepsilon^{1/2}} \tag{17}$$

$$\frac{\left(\lambda_{dis} \right)_{YY}}{\lambda_f} = 0.052 \left(1-\varepsilon \right)^{1/2} Pe_p \tag{18}$$

where Pe_p is a modified Peclet number, given by:

$$Pe_p = Pe \left(1-\varepsilon \right)^{1/2} \tag{19}$$

In the computation, the longitudinal direction aligns with the local velocity vector, which changes with location.

Numerical method and boundary conditions

The numerical computations were performed with the commercial CFD package FLUENT 6.3.26 which is a finite volume based software. To construct liquid-liquid and gas-liquid interfaces in the system, the Volume Of Fluid (VOF) method together with the CICSAM scheme, suitable for fluids with big viscosity difference, was chosen. The software provides a solver for a standard set of Navier-Stokes equations for fluid flow and heat transfer. The additional source terms for the modified turbulence and heat transfer model are introduced using user defined functions (UDF's) to the software. The mesh generated for the model is arranged in such a way that the resolution is high in regions where velocities or temperature tends to vary greatly, e.g., near taphole and in the radial direction. The total number of grid points is about 600 000.

For boundary conditions it is assumed that both the slag and metal production happen in the fine coke bed zone. Based on industrial data an average production rate of 200 *ton/day* for slag and 330 *ton/day* for metal, have been considered as the mass source terms in the fine coke bed zone. Pressure on the taphole surface is set as the atmospheric pressure condition. On the slag surface, a constant pressure and temperature of 1450°C were specified. The pressure term is considered to account the effect of charge weight on the slag and hence metal zones. At the wall, a no-slip condition exists on the hot face of the refractory walls. The standard log law wall function is applied for the velocity. The thermal boundary layer is modeled using the thermal law-of-the-wall function. Temperatures at the cold face of the refractory and the furnace bottom are explicitly specified. The upper surface of the refractory wall is adiabatic. The computational grid developed for CFD modeling is presented in Figure 6.
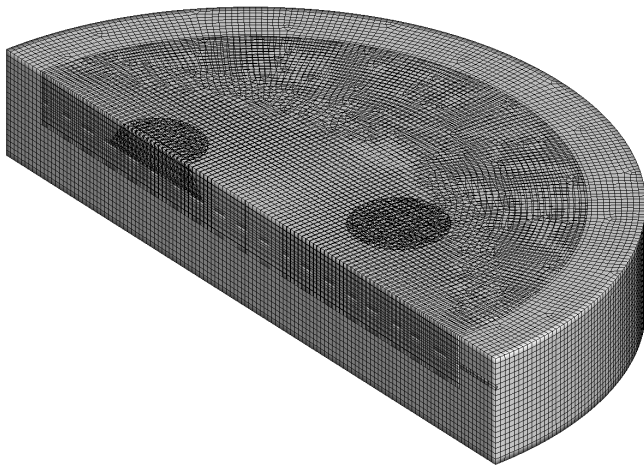

Figure 6: Computational grid of the FeMn furnace geometry including the high temperature zone of the furnace and the wall refractory.

RESULTS AND DISCUSSIONS

Melt flows in the furnace heart

The predicted results show there are two different flow zones in the furnace, which can be separated by the interfacial boundary between the slag and metal layers. The fluid velocity in the metal layer is always more than that in the slag layer. Resistance created by the low permeable coke bed zone against the high viscosity slag flow is the main reason for low fluid velocity in the coke bed zone. Figure 7 shows the velocity vectors in the slag and metal layers for the vertical central plane of the furnace.
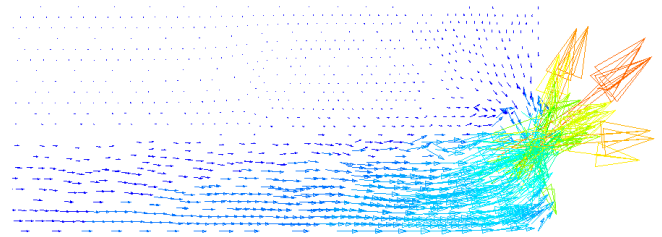
Figure 7: Velocity vectors in the central vertical plane of the furnace, y=0, showing higher velocity magnitude in the metal layer comparing with flow of highly viscous slag in the coke bed zone ($V_{max} = 0.5m/s$).

The slag velocity magnitude also varies between the fine coke bed and coarse coke bed zones. Reduced size of coke particles in the fine coke bed zone leads to formation of a less permeable region and hence higher resistance against fluid flow in this zone. This phenomenon is shown in Figure 8.
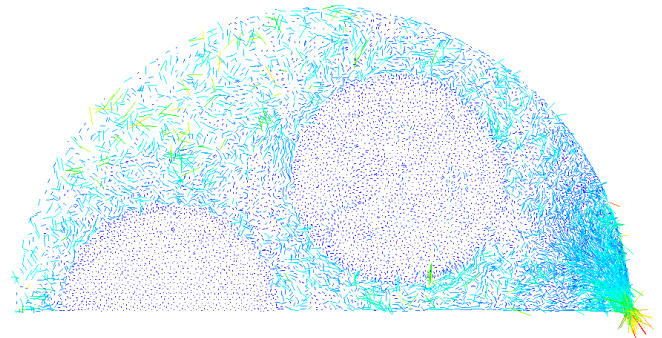
Figure 8: Velocity vectors in the central horizontal plane of the furnace, z=0.5 *m*, showing higher velocity magnitude for the slag in the coarse coke bed zone comparing to the slag flow in the fine coke bed zone ($V_{max} = 0.04m/s$).

The metal flows towards the furnace taphole even when the metal height is bellow the taphole level. Evolution of the slag and metal flows towards the taphole is shown in Figure 9.

As it can be seen from this figure, by start of tapping process the direction in the metal zone is towards the furnace taphole, even in the zone close to the furnace bottom, and metal is the only phase which goes through taphole. As the tapping proceeds the metal flow towards the taphole is disturbed due to flow of slag phase in the same direction and also decreased metal height. By time passing the metal flow is restructured through formation of recirculation loops in the zone close to the furnace bottom. In this situation the metal flow rate from the taphole decreases and slag is the main phase which occupies the taphole. At the final stage the gas phase also entrains towards the taphole while the slag height in the furnace is still above the taphole level. In this situation the tapping rate of both the slag and metal from the furnace taphole drops. Figure 10 shows the situation where the slag and metal are getting tapped from the furnace and the gas phase has entrained the melt flows.

Temperature distribution in the furnace heart

The melt flow pattern determines the temperature distribution in the liquid phases. High efficiency heat transfer is made by

the bulk flow advection, turbulent diffusion and thermal dispersion, which strongly depend upon the fluid velocity. Temperature distribution in the slag and metal as well as furnace wall refractory is shown in Figures 11 and 12. Results of the model considering the melt flows in the furnace heart, Figure 11, show that the temperature is basically uniform over a large portion of the melt pool, while the change in temperature is mostly restricted to the near-wall regions or those corner regions of the refractory-hot metal interface. As it can

be seen from this figure the metal temperature in the furnace and close to the taphole zone is higher than the opposite side in vicinity of the furnace wall. This is in one hand due to high thermal conductivity of molten metal which leads to higher heat transfer from hot metal to the cold wall refractory. In the other hand it is caused because of low melt velocity in this zone and hence decreased heat transfer efficiency due to bulk flow advection and turbulent diffusion. This phenomenon is not seen in the coke bed zone due to very low thermal conductivity of molten slag which flows in this zone.
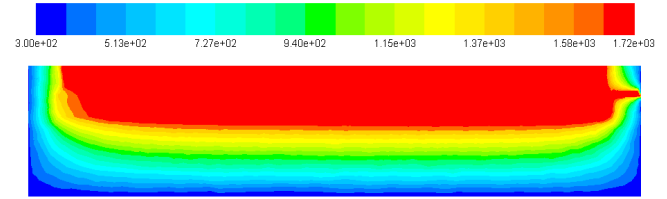
Figure 11: Temperature distribution ($^\circ$K) in the high temperature melt zone of the furnace as well as wall refractory in the central vertical plane of the furnace.
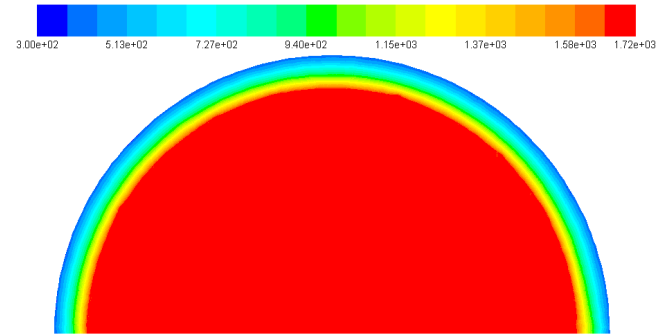
Figure 12: Temperature distribution ($^\circ$K) in the high temperature melt zone of the furnace as well as wall refractory in the horizontal plane located over the slag surface.

The temperature profile along the vertical centreline of the furnace is shown in Figure 13. In the solid refractory region, between $z = 0$ and $z = 1.6m$, the temperature gradient is inversely proportional to the thermal conductivity of the construction material. Overall, the thermal conduction across the solid refractory dominates the entire heat transfer from hot melts to the surrounding.

Figure 14 represents the same temperature profile when it is only restricted to the metal and coke bed zones. As it is seen from this figure there is a linear temperature gradient in the metal zone while a change in the slope of this linear gradient at the slag - metal interface, approximately at $z = 2.1m$, is clear. It is also seen that there is a linear temperature gradient in the coke bed zone and there is very small or no temperature gradients in the upper part of the slag zone.

This result show that there is a distinct temperature difference between slag and metal phases which can be used to make distinguish between these phases in the situation where slag and metal are simultaneously tapped from FeMn furnaces.

The temperature profile in the slag and metal phases along the horizontal centerline of the furnace is presented in Figures 15 and 16.

The temperature profile in the metal zone shows that there is a temperature gradient while moving in the vertical direction in this zone. In fact due to higher temperature in the
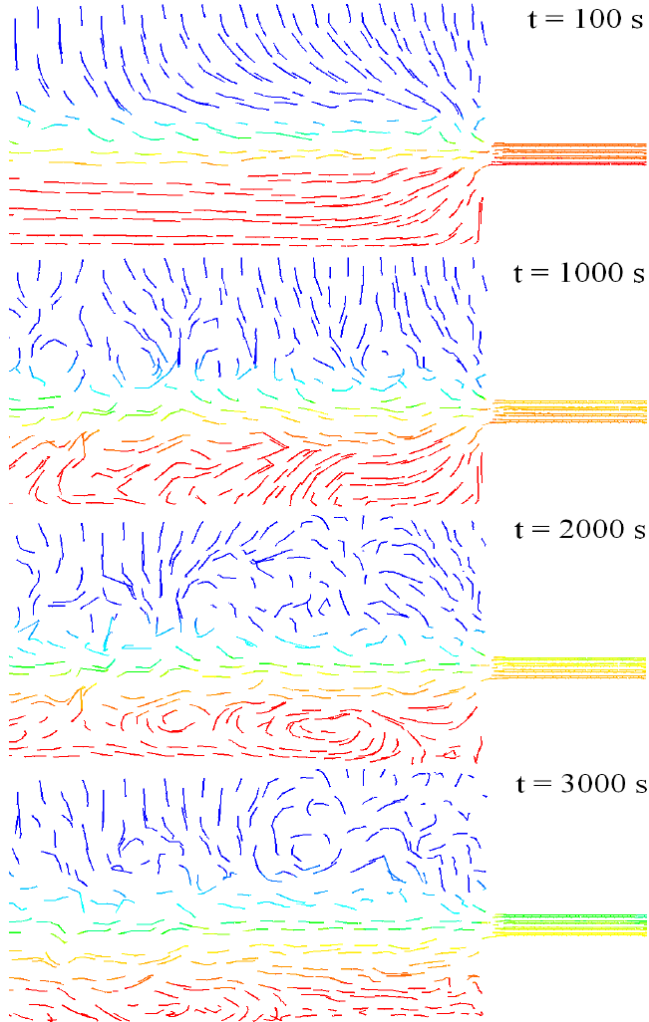

Figure 9: Evolution of the pathlines of the slag and metal flows in the high temperature zone of the furnace in vicinity of the taphole colored by volume fraction of metal.
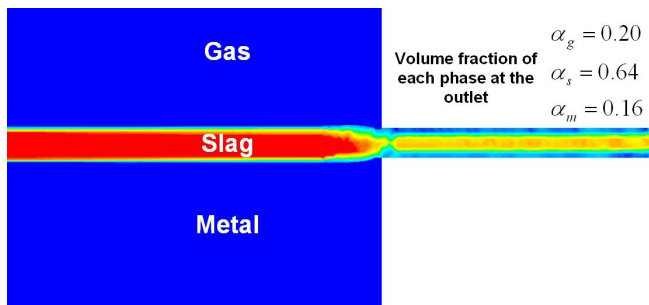

Figure 10: Volume fraction of different phases, in vicinity of furnace taphole, in the FeMn furnace during tapping process showing simultaneous flow of metal and slag through the taphole while the gas phase has entrained the melt flows.

slag, the metal temperature increases as the vertical distance to the slag-metal interface decreases. There is also a temperature gradient in the horizontal direction showing that the metal temperature close to the taphole region is higher than the opposite side in the furnace.

In the coke bed zone where slag exists, the melt temperature is mostly constants along the horizontal centerline and there
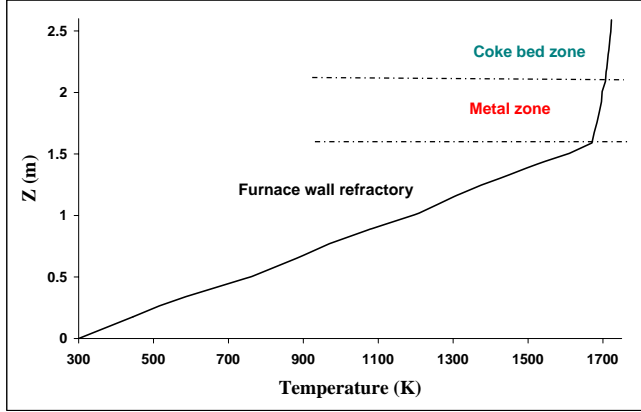
Figure 13: Temperature profile along the vertical centerline of the furnace, $x = 5.5m$, showing the temperature gradients in both wall refractory and molten phases.
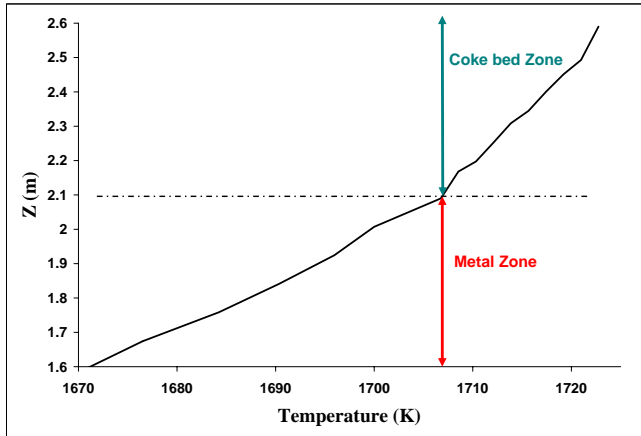
Figure 14: Temperature profile along the vertical centerline of the furnace, $x = 5.5m$, showing the temperature gradients only inside the molten phases.
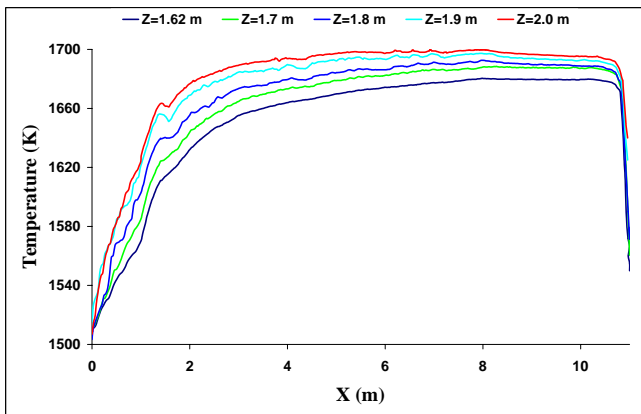
Figure 15: Temperature profile along the horizontal centerline of the furnace, parallel to the furnace bottom, showing the temperature gradients in the metal zone.

is rapid changes in the temperature close to the wall refractory. It is also clear that close to the wall refractory, the melt temperature in the taphole region is higher than the opposite side in the furnace.

Effect of buoyancy on the melt temperature profile

In the presented results the fluid density change due to thermal expansion, buoyancy effect, has been ignored in the model. Thermal coefficient of volumetric expansion for the metal is $1.65 \times 10^{-4} K^{-1}$ (Shin *et al.*, 2010) and for slag is equal to $6.4 \times 10^{-6} K^{-1}$. Considering the buoyancy effect in the melt leads to a changed temperature profile in the furnace. Figure 17 shows comparison between temperature profile along the vertical centreline of the furnace with and without considering the buoyancy effect. The effect of buoyancy on the temperature profile is more clear when it is restricted to the zone including the melts (see Figure 18).

From these figures it is seen that in the case where no buoyancy is considered, temperature changes significantly in the metal layer, whereas it is not the case when the buoyancy is included. It is also seen that the buoyancy force is negligible for the case of a liquid with a low thermal expansion coefficient, such as slag. In this case, the turbulence/dispersion makes very little difference to the calculated result. However,
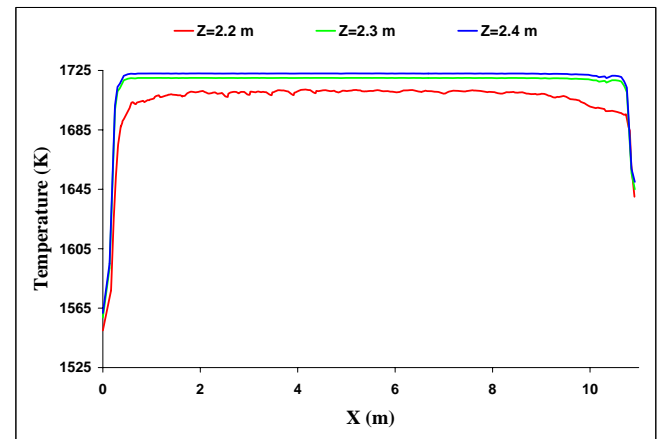
Figure 16: Temperature profile along the horizontal centerline of the furnace, parallel to the furnace bottom, showing the temperature gradients in the slag.

Figure 17: Comparison between the temperature profile along the vertical centerline of the furnace, $x = 5.5m$, in two situations with and without considering the buoyancy effect in the melt.

the contribution of turbulence/dispersion has been found to be much stronger when a stagnant zone due to natural convection exists. Presence of coke particles would generate additional turbulence and thermal dispersion compared with the metal layer where there is no particle in it.

Investigation of the effect of slag and metal height on the tapping parameters

One of the main parameters which can influence tapping of slag and metal from FeMn furnaces, is the volume of the melts inside the furnace heart. The initial levels of molten products in the furnace heart in one hand determines the hydrostatic pressure in the furnace as a deriving force for tapping of the melts. In the other hand it influences the composition of slag and metal in the tapped melts. In the current research the effect of slag and metal height on the tapping flow rate from the prescribed size FeMn furnace is investigated. The case studies which have been considered in this research are listed in Table 3.

Table 3: List of the case studies which have been investigated in the current research.

h \ Case No.	Case 1	Case 2	Case 4	Case 4
Metal Height (m)	0.4	0.5	0.6	0.7
Slag Height (m)	0.6	0.5	0.4	0.3

During tapping process the metal height in the furnace gradually decreases and therefore the coke bed zone which is floating on the metal layer, will descend as well. In order to consider the vertical movement of porous coke bed, several zones in form of layers located on top of each other have been considered in the model. The physical properties of each layer changes from non-porous to a porous zone as it is filled with slag. Since modeling of a moving porous bed is somehow difficult and because this method is applied only to a very narrow region at the slag-metal interface, it seems that this simplification does not affect the accuracy of the model significantly.

Tapping flow rate from the FeMn furnace in the case where the slag and metal heights are equal to 0.5m is shown in Figure 19. It is seen from this figure that metal flow rate is quite high by the start of tapping and it decreases to a constant level

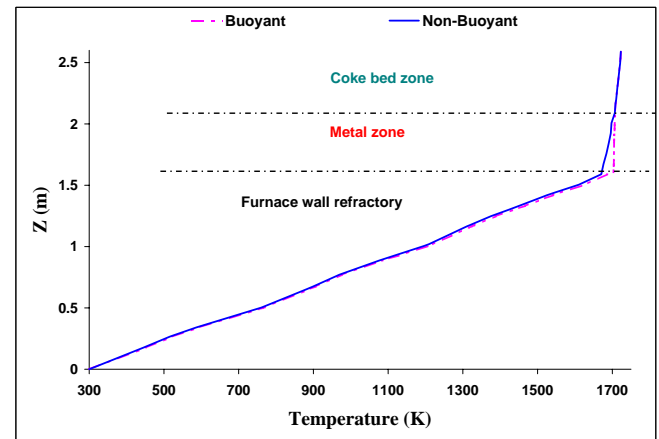Figure 18: Comparison between the buoyant and non-buoyant temperature profiles along the vertical centerline of the furnace, $x = 5.5m$, in the zone where molten phases do exist.

as tapping process proceeds. The slag has a much less tapping rate, comparing to metal, at the beginning but it slowly increases to a higher and constant amount and finally it decreases to a lower rate again. The resultant total flow rate from the furnace shows a decreasing behavior.
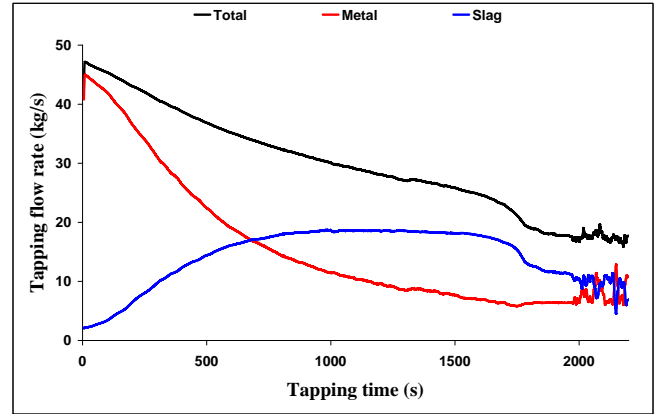
Figure 19: Tapping flow rate from the FeMn furnace in the situation where the slag and metal heights are both equal to 0.5m.

The tapping weight for this case is shown in Figure 20. The result show that the metal weight increases with a faster rate at the beginning and it reaches to a more flat level as the metal tapping rate decreases. The slag tapping weight shows an increasing behavior up to the time when its tapping rate drops to a much lower level and after that it has a much slower increase rate. The total tapping weight follows a pattern very similar to the metal weight.
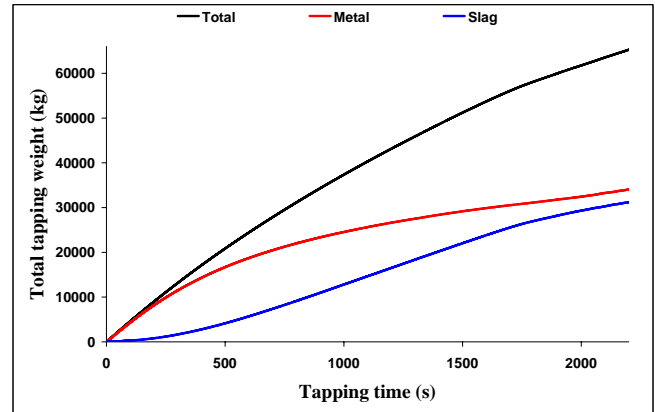
Figure 20: Tapping weight from the FeMn furnace in the situation where the slag and metal heights are both equal to 0.5m.

The tapping rate of metal for different case studies is presented in Figure 21. The results show that the flow rate of metal which is tapped from the furnace is directly related to the initial metal height. As tapping process continues, the tapping flow rate decreases to a level which is almost constant in all case studies. Evolution in the total weight of the metal which is tapped from the furnace is shown in Figure 22.

The slag flow rate as a function of tapping time is presented in Figure 23. The most interesting result is that the slag height is detrimental parameter for tapping flow rate of slag only if the metal height is above the taphole level. In this situation the higher the slag height the higher the tapping flow

rate of slag, although the flow rate difference is not significant. In the situation where the metal height is lower than the taphole level, $MH = 0.4m$, the slag height is highest among the case studies but the slag flow rate is the lowest.

The main reason for this phenomenon is that the metal flow through the furnace taphole acts as a deriving force to evacuate the overlaying high viscosity slag when the slag reaches to the taphole.

Comparing the results of model with industrial measurements

Figure 24: Comparison between the results provided by the model and industrial data from one week operation of the same furnace size as the model.

In order to check validity of the predicted results by the model, using of industrial measurements is an essential step. Industrial data from operation of a FeMn furnace with the same size as the model have been provided by one of the industrial partner of the project (Eramet Norway). These data have been taken from one week of normal furnace operation. Comparison between the model results and industrial measurements is shown in Figure 24. The points represent the industrial measurement of the metal weight after each tapping.

This comparison shows that the model covers the industrial data in its range. The main result is that the model predicts a metal height of $0.5m \mp 0.05m$ inside the furnace. Considering the fact that taphole level is at $z = 0.45m$, the model prediction shows that the metal height in the furnace just before the start of tapping is always above the taphole level.

Figure 21: Metal flow rate during tapping of the FeMn furnace in the situation where the metal heights ranges from $0.4m$ - $0.7m$.
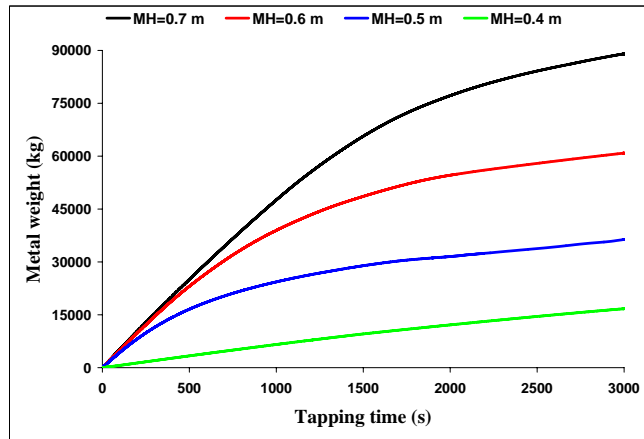
Figure 22: Metal weight increase during tapping of the FeMn furnace in the situation where the metal heights ranges from $0.4m$ - $0.7m$.
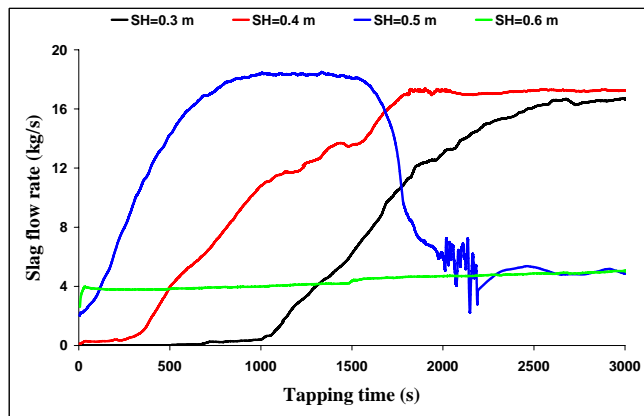
Figure 23: Slag flow rate during tapping of the FeMn furnace in the situation where the slag heights ranges from $0.3m$ - $0.6m$.

CONCLUSION

Tapping process in ferromanganese (FeMn) production furnaces was investigated. A 3D multiphase model for the high temperature zone of the furnace was developed. The furnace geometry was taken from an industrial size FeMn furnace. The developed model is based on Computational Fluid Dynamics (CFD) techniques and it considers slag and metal flows and heat transfer in the furnace heart. The model shows that there is a distinct temperature difference between molten slag and metal inside the furnace. Also the metal temperatures in the different regions over the furnace bottom are different. The temperature in the slag zone is evenly distributed except for a narrow region at the slag-metal interface where the slag temperature is influenced by metal. The tapping flow rate for different phases including slag and metal was predicted by the model for a number of different cases. The results indicate that since the permeability of the coke bed is low, the metal below the taphole level is able to drain during the tapping process. Decreased coke bed permeability can make this phenomenon more significant. Comparison between the model predictions and industrial tests can be used to estimate the true metal height inside a furnace.

REFERENCES

ASHRAFIAN, A. and JOHANSEN, S.T. (2006). "Tapping of stratified liquids from a packed bed". *5th International Conference on CFD in the Process Industries*. Melbourne, Australia.

BARCZA, N.A. *et al.* (2001). "The dig-out of a 75 mva high carbon ferromanganese electric smelting furnace". *Proceedings of the 37th Electric Furnace Conference, INFACON IX*. Quebec, Canada.

CRAYA, A. (1949). "Theoretical research on the flow of non-homogeneous fluids". *La Houille Blanche*, **4**, 44–55.

ERAMET (2010). "Core drilling of femn furnaces". *Eramet Norway internal report (2010)*.

ERGUN, S. (1952). "Fluid flow through packed columns". *Chemical Engineering Progress*, **48**, 89–94.

FUKUTAKE, T. and OKABE, K. (1976). "Experimental studies of slag flow in the blast furnace hearth during tapping operation". *Transactions ISIJ*, **16**, 309–316.

GUO, B.Y. *et al.* (2008). "Cfd modelling of liquid metal flow and heat transfer in blast furnace hearth". *ISIJ International*, **48**, 1676–1685.

HOCKING, G.C. and FORBES, L.K. (2001). "Supercritical withdrawal from a two-layer fluid through a line sink if the lower layer is of finite depth". *Journal of Fluid Mechanics*, **428**, 333–348.

HUBER, D.G. (1960). "Irrotational motion of two fluid strata towards a line sink". *Journal of Engineering Mechanics Division of American Society of Civil Engineering*, **86**, 71–86.

KUWAHARA, F. and NAKAYAMA, A. (1999). "Numerical determination of thermal dispersion coefficients using a periodic porous structure". *Journal of Heat Transfer*, **121**, 160–163.

NAKAYAMA, A. and KUWAHARA, F. (1999). "A macroscopic turbulence model for flow in a porous medium". *Journal of Fluids Engineering*, **121**, 427–433.

OLSEN, S.E. and TANGSTAD, M. (2004). "Silicomanganese production - process understanding". *Proceedings of the 10th International Ferroalloys Congress, INFACON X*. Cape Town, South Africa.

OLSEN, S.E. *et al.* (2007). "The high carbon ferromanganese process - coke bed relations". *Tapir Academic Press*. Trondheim, Norway.

RINGDALEN, E. and EILERTSEN, J. (2001). "Excavation of a 54 mva hc-ferrochromium furnace". *Proceedings of the 9th International Ferroalloys Congress, INFACON IX*. Quebec, Canada.

SCHEEPERS, E. (2008). "Fingerprint of submerged - arc furnace, optimising energy consumption through data mining, dynamic modelling and computational fluid dynamics". *Dr.-ing thesis, Printpartners Ipskamp*. Enschede, The Netherlands.

SHIN, M. *et al.* (2010). "Surface tension and density of femn alloys". *Presentation of TOFA 2010, Discussion Meeting on Thermodynamics of Alloys*. Porto, Portugal.

STOKES, T.E. *et al.* (2003). "Unsteady free-surface flow induced by a line sink". *Journal of Engineering Mathematics*, **47**, 137–160.

TANGSTAD, M. (1996). "Production of manganese ferroalloys". *Dr.-ing thesis, MI-Report 1996:49, NTH*. Trondheim, Norway.

TANGSTAD, M. (1999). "Excavation of femn furnaces in 1994 and 1995". *Elkem internal report (1999)*. Trondheim, Norway.

TANGSTAD, M. (2011). "Presentation of roma-project (resource otimization in the material industry) a typical co-operation project in norway". *Pyro 2011*. Johanesburg, South Africa.

TANGSTAD, M. *et al.* (2001). "Simn production in a 150 kva pilot scale furnace". *Proceedings of the 9th International Ferroalloys Congress, INFACON IX*. Quebec, Canada.

TANZIL, W.B.U. *et al.* (1984). "Experimental model study of the physical mechanisms governing blast furnace hearth drainage". *J. Stencils*, **24**, 197–205.

TURNER, J.S. (1973). "Buoyancy effects in fluids". *Cambridge University Press*. Cambridge, England.

TYVAND, P.A. (1992). "Unsteady free-surface flow due to a line source". *Journal of Physics of Fluids A*, **4**, 671–676.

THE APPLICATION OF COMPUTATIONAL FLUID DYNAMICS (CFD) AND OVEN DESIGN OPTIMISATION IN THE BRITISH BREAD-BAKING INDUSTRY

Zinedine KHATIR[1*], Harvey Thompson[1], Nik Kapur[1], Vassili Toropov[1,2], Joe Paton[1] and Malcolm Lawes[1]

[1] School of Mechanical Engineering, University of Leeds, LS2 9JT, UNITED KINGDOM

[2] School of Civil Engineering, University of Leeds, LS2 9JT, UNITED KINGDOM

* E-mail: z.khatir@leeds.ac.uk

ABSTRACT

Rising energy costs and changing legislation are bringing the need for more efficient baking processes into much sharper focus. Forced convection ovens use convective heat transfer from air impingement jets to bake bread. Air impingement bread-baking ovens are complex systems used to entrain thermal air flow. In this paper, Computational Fluid Dynamics (CFD) is combined with an optimization framework in order to develop a tool for the rapid generation of forced convection oven designs. A design parameterization of a three-dimensional generic oven model is carried out to enable optimization, for a wide range of oven sizes and flow conditions, to be performed subject to appropriate objective functions measuring desirable features such as, for example, temperature uniformity throughout the oven. Optimal Latin Hypercubes for surrogate model building and model validation points are constructed using a permutation genetic algorithm and design points are evaluated using CFD. Surrogate models are built using a Moving Least Squares (MLS) approach. A series of optimizations for various oven sizes and flow conditions are performed using a genetic algorithm with responses calculated from the surrogates. This approach results in a set of optimized designs, from which appropriate oven designs for a wide range of specific applications can be inferred. It is found that for the particular oven design and objective function under investigation, the optimized design is obtained with a dimensionless nozzle-to-surface distance $H/D = 6.82$, nozzle diameter $D = 20$mm and an operating jets velocity $u_{noz} = 38.12$ m/s under baking temperature of 240 ^{o}C. Under these conditions baking time can be reduced by 5-10%, subsequently resulting in energy savings of a similar magnitude.

Keywords: CFD Application, Optimisation, Bread-Baking Industry, Energy Efficiency.

NOMENCLATURE

Greek Symbols
α Thermal diffusivity, $K/(\rho\, c_p)$, [m²/s].
ΔT_s Temperature difference between the top of bread average temperature and baking chamber, [K].
ρ Mass density, [kg/m³].
ν Kinematic viscosity, [m²/s].
μ Dynamic viscosity, [kg/m.s].
σ_T Temperature functional for minimization, [K].
σ_i Standard deviation of minimum distance of DOE_i
θ Closeness-of-fit parameter.

Latin Symbols
AFR   Air fuel ratio, [-].
Bi   Biot number, $(h_cL)/K$, [-].
c_p Specific heat, [J/(kgK)].
D   Nozzle jet diameter, [m].
DOE_i Design of experiment i, $i=b, m, v$.
DV_i Design variable $i=1, 2, 3$.
F   Objective function.
$\vec{g}$ Acceleration due to gravity, [m²/s].
H/D   Dimensionless nozzle-to-surface distance, [-].
h_c Convective heat transfer coefficient, [W/(m²K)].
L   Characteristic length, [m].
K   Thermal conductivity, [W/(mK)].
L_{ij} Distance between points i and j in Latin Hypercube.
Nu   Nusselt number, $(h_cD)/K$, [-].
p   Pressure, [Pa].
R   Correlation coefficient.
Re   Reynolds number, $(u_{noz} D)/\nu$, [-].
r_i Normalized distance from the current point to model building point i.
S   Nozzle to nozzle spacing, [m].
u   Velocity, [m/s].
u_i Velocity components in the ith coordinate direction x_i, [m/s].
U   Pseudo-potential energy of *DoE* points.
w_i Weighting factor of the *DoE* build point i.
x_i i^{th} coordinate direction, [m].
u_{noz} Nozzle velocity, [m/s].
V   Volume, [m³].

Sub/superscripts
i   Index *i*.
j   Index *j*.
b   Model building *DOE*.
m   Combined model *DOE*.
v   Model validation *DOE*.

INTRODUCTION

Commercial bread baking is a complex process of simultaneous heat, water and water vapour transport within the dough/bread in which heat is supplied by ovens. Two types of oven are commonly used in the commercial baking industry; indirect fired ovens and forced convection (or direct fired) ovens. Forced

convection ovens are the focus of the present study and are based on hot air jet impingement technologies that have been used extensively in order to dry coated products, paper and textiles (Ikin and Thompson 2007). Within forced convection baking ovens, heat is transferred to the dough/bread via conduction, convection and radiation and the relative importance of each mode is determined by the air temperature and velocity of the impinging air jets, (Martin 1977).

Uniformity of air temperature and velocity across the width of an industrial baking oven is vital to ensure an even distribution of heat transfer to each loaf and therefore maintaining constant product quality. In order to ensure this uniformity is maintained in jet impingement bread ovens, high air pressure is created in the plenum that feeds the banks of nozzles. If nozzle design could be optimised such that the air is distributed uniformly across the oven width, product quality could potentially be maintained whilst altering the oven settings to reduce oven energy use.

CFD is increasingly being used to predict airflows for many applications in the food industry (Norton and Sun, 2006). The capability of CFD modeling to predict temperature distribution within the oven, which has an important influence on final bread quality, is demonstrated in Khatir *et al.* (2010, 2011).

Studies have shown that the ratio of distance between the air jet and impinged surface to nozzle diameter (commonly referred to as the dimensionless ratio *H/D* where *D* is the nozzle jet diameter) is optimum for heat transfer when in the range of 6-8 (Sarkar and Singh, 2004). Previous optimisation studies in bread baking have altered the temperature profile along the length of the oven to reduce moisture loss (Therdthai *et al.*, 2002), optimised temperature, heat transfer coefficient and bread radius (i.e. dough shape) for improving product quality (Purlis, 2011), and used multi-objective optimization and control vector parameterization approaches to optimize product quality for ratios of different heat sources (Hadiyanto *et al.,* 2009, 2011).

This paper specifically combines high fidelity CFD analysis and experimentation within a formal optimization framework in order to develop a novel optimization tool that can be used to improve oven efficiency. Since product quality is dependent on the uniformity in a baking oven, this will be the focal point of the current work. This work aims to investigate the viability of doing this using an approach used that searches for optimal combinations of oven geometrical and operating parameters; such as nozzle diameter *D*, ratio between the air jet diameter and impinged surface distance *H/D* and nozzle jet velocity u$_{noz}$.

MODEL DESCRIPTION

Following Khatir *et al.* (2011), air flows in the oven are analysed using the steady-state Reynolds Averaged Navier-Stokes (RANS) equations for three-dimensional flow. For steady state flows the continuity and momentum equations written in the RANS format are:

$$\frac{\partial}{\partial x_i}(\rho u_i) = 0 \qquad (1)$$

$$\frac{\partial}{\partial t}(\rho u_i) + \frac{\partial}{\partial x_i}(\rho u_i u_j) = -\frac{\partial p}{\partial x_i} + \frac{\partial}{\partial x_j}\left[\mu\left(\frac{\partial u_i}{\partial x_j} + \frac{\partial u_j}{\partial x_i} - \frac{2}{3}\delta_{ij}\frac{\partial u_l}{\partial x_l}\right)\right] \qquad (2)$$

$$+ \rho \vec{g} + \frac{\partial}{\partial x_i}\left(-\rho \overline{u_i' u_j'}\right)$$

where ρ and u_i are the air density and velocity components in the ith coordinate direction x_i respectively, p is pressure and $\vec{g}$ is the acceleration due to gravity. The last term of Eq. (2) represents the turbulent stresses that requires additional closure equation(s) to be solved. Turbulence is modeled using the realizable k-ε transport model as in Khatir *et al.* (2011, 2010) and Boulet *et al.* (2010). The turbulence is described with two additional variables *k* (turbulent kinetic energy) and ε (turbulent dissipation) that enables the computation of the turbulent stress and the turbulent viscosity. The realizable *k*–ε model is an improvement of the standard *k*– ε model that can be useful for flows in complex geometries, and consists of the following two transport equations:

$$\frac{\partial}{\partial x_j}(\rho k u_j) = \frac{\partial}{\partial x_j}\left[\left(\mu + \frac{\mu_t}{\sigma_k}\right)\frac{\partial k}{\partial x_j}\right] + G_k - \rho\varepsilon \qquad (3)$$

$$\frac{\partial}{\partial x_j}(\rho \varepsilon u_j) = \frac{\partial}{\partial x_j}\left[\left(\mu + \frac{\mu_t}{\sigma_\varepsilon}\right)\frac{\partial \varepsilon}{\partial x_j}\right] + \rho C_1 S_\varepsilon \qquad (4)$$

$$- \rho C_2 \frac{\varepsilon^2}{k + \sqrt{\nu\varepsilon}}$$

In Eq. (3), the term G_k represents the turbulence energy production by means of the velocity gradient. The negative term represents the energy dissipation. For Eq. (4), the first production term (the second term on the right-hand side of Eq. (4)) is related to the spectral energy transfer (and does not contain the term G_k). The turbulent viscosity μ_t is obtained from the turbulent energy *k* and the dissipation. The terms σ_k, σ_ε, C_1, C_2, are model parameters, with the following given values $\sigma_k = 1.0$, $\sigma_\varepsilon = 1.2$, $C_1 = \max[0.43, \frac{\eta}{\eta + 5}]$, $\eta = S\frac{k}{\varepsilon}$, $S = \sqrt{2S_{ij}S_{ij}}$, $C_2 = 1.9$.

The energy equation is also solved and takes the form:

$$\frac{\partial}{\partial x_i}(u_i \rho c_p T) = \frac{\partial}{\partial x_j}\left(K\frac{\partial T}{\partial x_j}\right) \qquad (5)$$

where c_p, *T* and *K* are the specific heat capacity, temperature and thermal conductivity of the air, respectively.

Second order upwind schemes are used for all flow variables and solutions are computed using the SIMPLE algorithm (Patankar and Spalding, 1972). The continuity, momentum, turbulence transport and energy equations (1)-(5) are solved computationally using ANSYS FLUENT 13.0.

A surrogate modeling approach is adopted for the optimization study. Such approaches have been successfully used recently for the design optimization of jet pumps (Fan *et al.*, 2011, Eves *et al.,* 2010). Design of experiments (DoE) is carried out using Optimal Latin Hypercube containing build and validation points. This is achieved via a permutation genetic algorithm (Narayanan *et al.,* 2007), applied to the multi-objective problem of optimizing the uniformity of model building point, model validation point, and combined DoEs. The optimality criterion for each DoE is defined by the

Audze-Eglais method (Toropov *et al.,* 2007) shown in Eq. (6) with the objective function defined by Eq. (7):

$$U = \sum_{i=1}^{P} \sum_{j=i+1}^{P} \frac{1}{L_{ij}} \qquad (6)$$

$$F = W_b U_b + W_v U_v + W_m U_m \qquad (7)$$

where U is a pseudo-potential energy of *DOE* points, L_{ij} is the distance between points i and j where $i \neq j$, F is the objective function to be minimized, W are weighting factors, and, b, v, m denote model building, model validation and merged *DOEs* respectively.

Surrogate models were built using a Moving-Least-Squares (MLS) method where the weighting of points in the regression coefficients calculation are determined using a Gaussian decay function:

$$w_i = \exp(-\theta\, r_i^2), \qquad (8)$$

where w_i is the weighting of the *DoE* build point i, r_i is the normalized distance from the current point to model building point i, and θ is a closeness-of-fit parameter. This parameter is optimized to maximize the R^2 value for the obtained surrogate model, as calculated on the validation *DoE*. The surrogate is then rebuilt using the combined building and validation *DoEs*. Global optimization is performed using a genetic algorithm (GA) with responses calculated using the surrogate models.

CFD Validation Study

The oven analysed is based on a typical industrial type direct-fired, forced convection oven. A schematic representation of the impingement jet configuration is shown in Fig. 1.
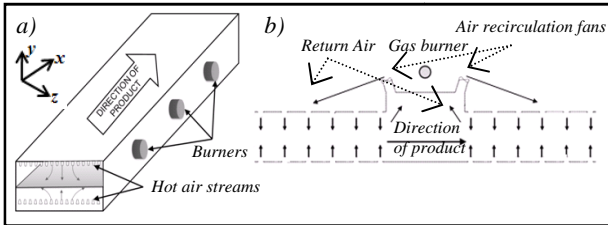
Figure 1: Three-zone direct fired oven: *a)* Overview of the oven; *b)* Simplified schematic showing the mechanism for distributing air through the nozzles for a single zone

Due to geometric and physical symmetry, only the flow field within the solution domain characterized in Fig. 2 together with the boundary conditions is solved numerically.

The geometry shown in Fig. 2*b)* is composed of flow openings, symmetry planes and walls as in Banooni and Mujumdar, (2009). For flow openings a combination of velocity inlet and pressure outlet types are used, with temperature and convective heat transfer defined along the walls (see Table 1).

Grid independency analysis is undertaken for both grid cell numbers and grid distributions where values of the temperature functional σ_T is defined as:

$$\sigma_T = \sqrt{\frac{\int_V (T_i - T_{Zone})^2\, dV}{\int_V dV}} \qquad (9)$$

are analyzed, where V is the volume of the baking domain, T_{zone} the air-jet temperature in the baking

chamber set at 513 K. Results for H/D=6 and D=14mm are outlined in Fig. 3.
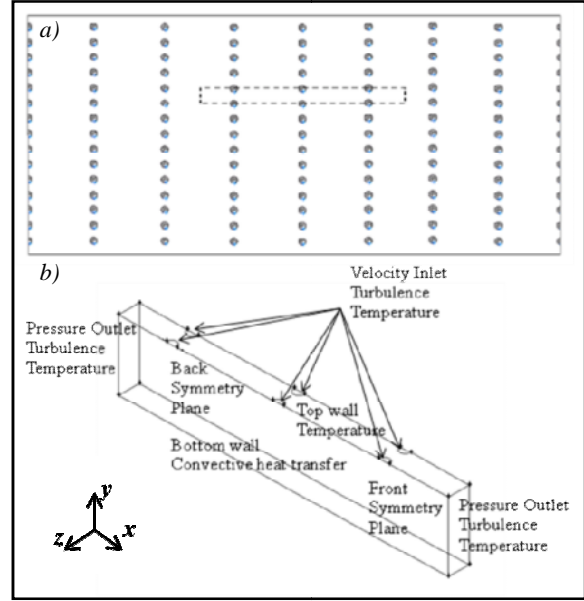
Figure 2: Geometry of the oven baking chamber showing the solution domain and the boundary conditions: *a)* Plane-view of section of oven being analysed; *b)* Solution domain and boundary conditions.

Table 1: Summary of boundary conditions.

Modelled equation	Inlet	Outlet	Wall
Energy	T=513 K	T=513 K	(Top) T=513 K (Bottom) h_c=10 W/(m^{2}K)
Momentum	V_{in}= u_{noz}	Gauge pressure P = 0 Pa	No-slip
Turbulence			Wall function
Length scale	l_{scale}=5×10^{-4}	l_{scale}=5×10^{-4}	
Intensity	I=2%	I=2%	
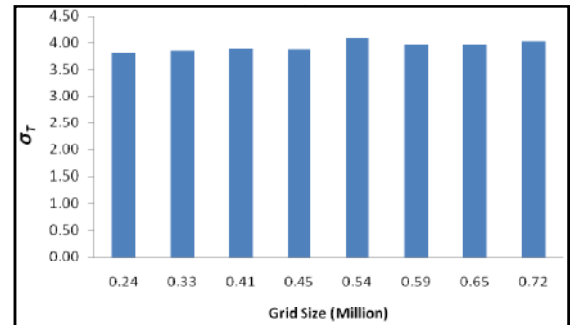
Figure 3: Grid independency: Temperature Functional, σ_T (Eq.(4)) vs. grid size.

Optimization Results

The oven is parameterized by two geometric, DV_1=D and DV_2=H/D and one operating design variable DV_3=u_{noz} as indicated in Fig. 4. with a fixed nozzle to nozzle distance spacing S=200mm.

A 30 point Optimal Latin Hypercube *DOE* is constructed with three dimensions using the approach described earlier. Of the 30 points, 20 are building points and 10 are validation points. Equal weights are used in Eq. (2). The levels of the Latin Hypercube are then scaled to correspond to the ranges:

5mm≤DV_1≤20mm; 2≤DV_2≤10; and 8m/s≤DV_3≤40m/s. The distribution of points in normalized design variable space is shown in Fig. 5.
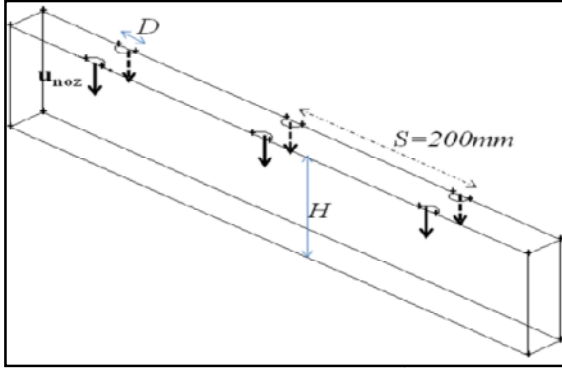
Figure 4: Generic model of oven with design variables: nozzle jet diameter *D*, jet velocity u$_{noz}$ and distance *H* between bottom impinged surface and nozzle jet, with nozzle to nozzle distance spacing *S*=200mm.

Values of standard deviation of minimum distances σ_b, σ_v and σ_m for building, validation and merged *DOEs* are found to be σ_b=0.87, σ_v=1.12 and σ_m=1.02 respectively. Figure 6 confirms the uniform scattering of the cloud of design points.

An initial CFD mesh is morphed to match each set of design variables. This is achieved by altering the location of boundary nodes of the bottom plate, as well as the rounded nozzle jet diameter as indicated in Figs. 2 and 4 via a script using GAMBIT mesh software. Mesh checks and smoothing ensure mesh quality is maintained. CFD analysis is performed at each design point using the approach outlined above.
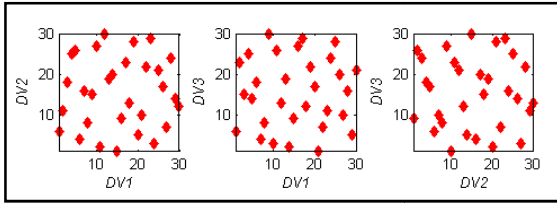
Figure 5: Distribution of design points in design variable space.
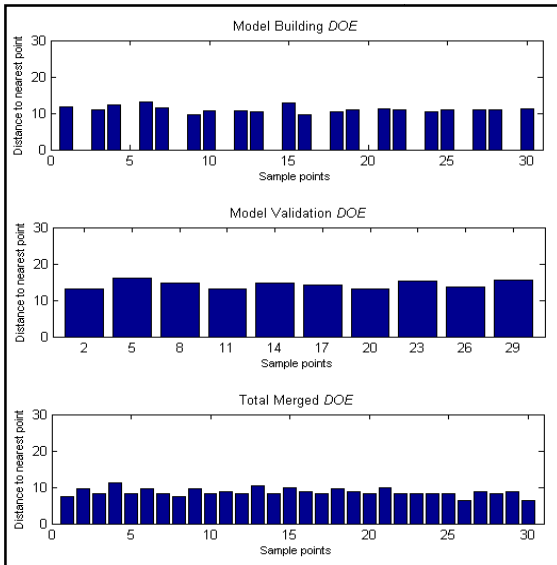
Figure 6: Sample points minimum distance plot for model building, validation and total merged *DOEs*.

Of primary importance in bread-baking is ensuring good temperature uniformity within the baking chamber to ensure high quality bread. Such a uniformity assessment can be measured via the temperature functional σ_T as defined by Eq.(4). The temperature functional σ_T values are extracted from the CFD data. MLS approximations of the response is then constructed, using a second order base polynomial and the 20 model building points. The closeness of fit parameter in Eq. (3) is optimized using the 10 model validation points. MLS surfaces gave equally good agreement with building and combined *DOEs* (R^2 values of 0.92 and 0.91 for *DOE$_b$* and *DOE$_m$* respectively). However there was a slight difference in agreement with the validation points (R^2 values of 0.81) due to the complexity of the flow field and the use of relatively few design points. Nevertheless the current level of approximation is acceptable within the optimisation framework.

The optimization problem was formulated in order to minimize the objective function σ_T. A genetic algorithm (GA) was used to find a global minimum with fitness evaluations carried out by the surrogate models. The GA produced a design which, as predicted by the surrogate model, would reduce temperature difference between the top of the bread (i.e. bottom wall plate in our 3D CFD generic model) and the baking chamber temperature. Results were obtained as follows: *D*=20mm, *H/D*=6.82 and u$_{noz}$=38.12m/s with a σ_T =1.16 from the surrogate model which σ_T surface response is represented in Fig. 7. Note that the *H/D* value of 6.82 is within the range of 6-8 that has been proposed by previous studies (Gardon and Akfirat, 1966; Sarkar and Singh, 2004). The corresponding ratio *S/D* of 10 is in fairly accurate agreement with the analysis carried out by Attalla and Specht, (2009).
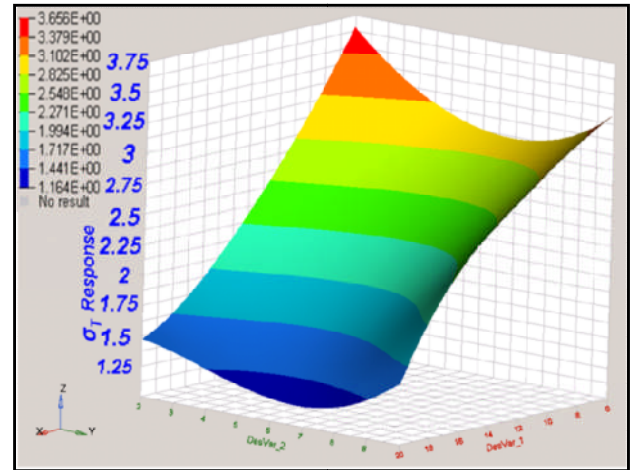
Figure 7: Surface response of surrogate model.

A CFD study was made of the optimized design and showed good agreement with the surrogate model with a σ_T =1.22 which is within 5% of the surrogate's prediction. The use of the CFD model for thermal air flow analysis and energy efficiency assessment is considered next.

Thermal Airflow Analysis and Energy Efficiency

Thermal Airflow Analysis

The complexity of the air flow field within such systems is emphasized in Fig. 8 where multiple recirculation and vortical structures are clearly demonstrated by the pathlines coloured by velocity magnitude. This is also
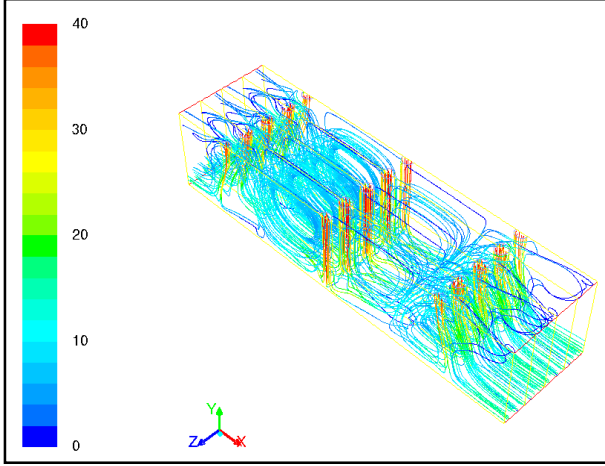
Figure 8: Pathlines coloured by velocity magnitude.

seen through contour plot of velocity magnitude on the front surface plane in Fig. 9.
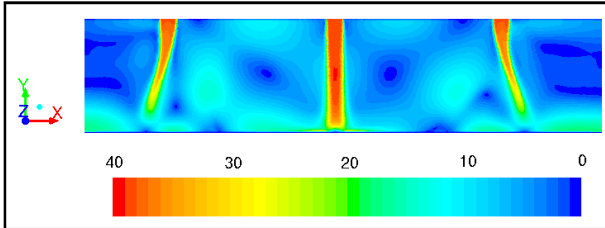
Figure 9: Contour plot velocity magnitude on the front surface plane.

As already mentioned, a value of σ_T =1.22 is obtained implying a uniform temperature within the baking chamber. This is further confirmed by Fig. 10 where various contour plots of temperature are shown. A difference of temperature ΔT_s of 10^oC between the
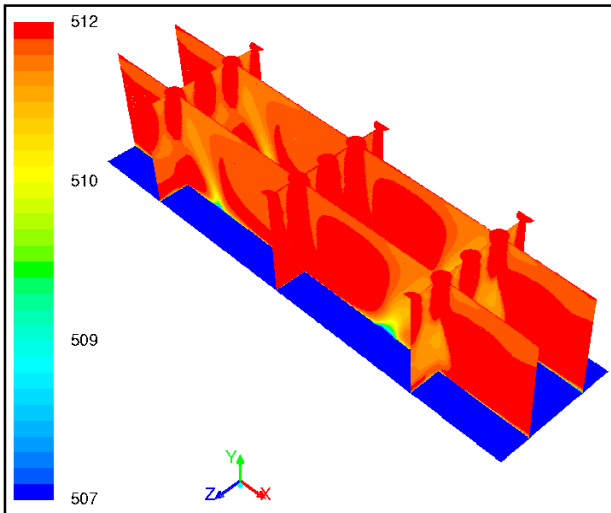
Figure 10: Contour plots of temperature emphasizing temperature uniformity within the baking chamber.

average temperature of top of bread and baking chamber temperatures is obtained. This is an important aspect of the baking process as this will allow the bread to cook efficiently.

Energy Efficiency

The density of the dough/bread is assumed to be constant with value ρ=330 kg/m^3 and a thermal diffusivity α=2.165x10^{-6}m^2/s (Wong *et al.,* 2007) with a loaf of bread of 0.25m length, 0.10m width and 0.12m height (i.e. mass of a loaf bread of around 1kg) and a convective heat transfer coefficient h_c=10 W/(m^{2}K) (Zhang and Datta, 2006) It is also assumed that bread is cooked when its core temperature reaches 85-90 ^{o}C (Purlis, 2011).

Complex models predicting the baking process have been developed previously by other authors (Zhang and Datta, 2006; Bollada, 2008, Jefferson *et al.,* 2007), however this paper uses a simplified heat transfer model showing the rate of temperature rise within the bread and does not incorporate moisture content and volume change. It is used to illustrate the scope of energy savings possible within the bread-baking industry.

Following the analysis for plane wall heat conduction with convection as described by Incropera *et al.* (2006) the temperature inside of the dough/bread is modelled by the one-dimensional heat equation:

$$\frac{\partial^2 T}{\partial x^2} = \frac{1}{\alpha}\frac{\partial T}{\partial t} \tag{10}$$

for 0≤*x*≤L, 2L=0.25m with the following initial conditions, T(*x*,0) = 30 °C and boundary conditions, $\frac{\partial T}{\partial x}\big|_{x=0} = 0$ and $-K\frac{\partial T}{\partial x}\big|_{x=L} = h_c[T(L,t) - T_\infty]$ where $T_\infty = 513\ K$. The approximate solution of Eq. (10) given by Incropera *et al.* (2006, p.273) is used to compute the cooking time for various values of ΔT_s, difference between the temperature of top of bread and the baking chamber temperature (i.e. $\Delta T_s = T(L,t) - T_\infty$). Calculated cooking times for various values ΔT_s are summarized in Figs. 11 and 12. ΔT_s=0°C represents the surface of the bread being at the same temperature of the oven, and giving the maximum driving force for heat conduction into the bread (initially at a temperature of 30 °C).
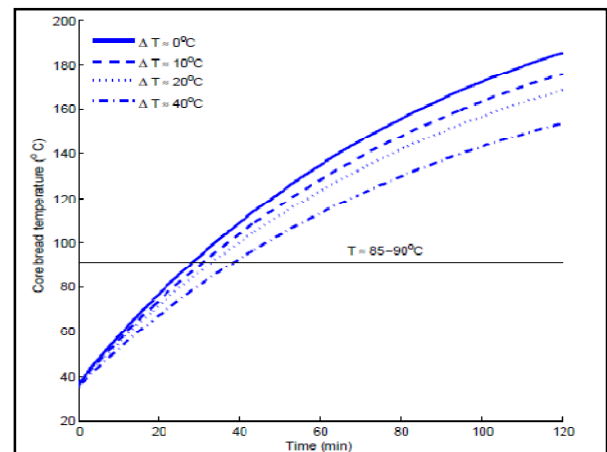
Figure 11: Cooking time vs. core-bread temperature for various values of ΔT_s, difference between the average temperature of top of bread and the baking chamber temperature.
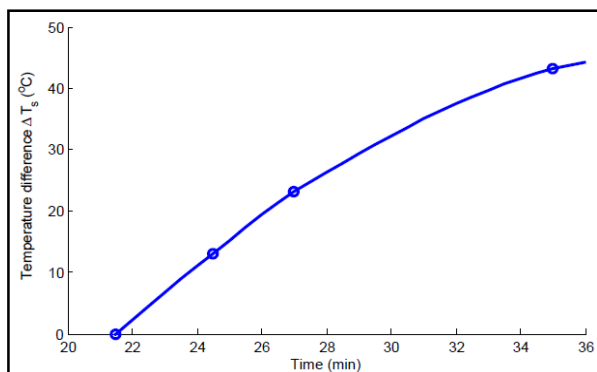
Figure 12: Cooking time vs. ΔT_s for the core-bread to reach a temperature of 85-90 ^{o}C initially at a temperature of 30 ^{o}C.

Thus, the optimum design would allow the bread to cook in around 24 minutes, that is 2.5 minutes more than the ideal case $\Delta T_s=0^o$C and about 3 and 10 minutes less than for $\Delta T_s=20^o$C and $\Delta T_s=40$ ^{o}C respectively. For practical bread-baking applications a value of 10°C for ΔT_s is usually acceptable. This would lead to a 5-10% reduction in baking time that results in increased plant efficiency for values of ΔT_s in the region of 15-20 ^{o}C.

CONCLUSION

High fidelity flow analysis has been combined with a formal optimization framework in order to optimize a set of ovens with various geometric and jet velocities configurations. An initial oven design is parameterized into three key design variables and a number of designs are produced using an Optimal Latin Hypercube design of experiments. Each design is evaluated using CFD analysis and Moving Least Squares surrogate models of temperature uniformity are built. CFD results emphasize the complexity of the thermal airflow behaviour of such industrial systems, thus demonstrating CFD to be a powerful design tool. Finally optimization using a genetic algorithm is performed with the aim of reducing the effective baking time of the bread, and hence improve the energy efficiency of the process. The use of CFD within an optimisation framework, where a suitable objective function is chosen to represent the desired outcome, allows efficient use of computational resource. The choice of objective function is crucial in determining what constitutes an optimal design; the challenge is to interpret the physical parameters (velocities, temperatures, etc) from the CFD solution in a way that links with the objective function of choice. Current ongoing work is focused on developing a range of objective functions for energy efficiency or manufacturability within the break baking oven.

Acknowledgements

REFERENCES

ATTALLA, M. and SPECHT, E., (2009) "Heat transfer characteristics from in-line arrays of free impinging jets", *Heat and Mass Transfer*, **45**(5), 537-543.

BOLLADA, P.C., (2008) "Expansion of elastic bodies with application in the bread industry" *Mathematical and Computer Modelling,* **48**(7-8), 1055-1067.

EVES, J., FAN, J., TOROPOV, V.V., THOMPSON, H.M., KAPUR, N., COPLEY, D. and MINCHER, A., (2010), "Design Optimization of Supersonic Jet Pumps using High Fidelity Flow Analysis", *13th AIAA/ISSMO Multidisciplinary Analysis and Optimization Conference*, 13 – 15 September 2010, Forth Worth, Texas, *AIAA 2010-9366.*

FAN, J., EVES, J., THOMPSON, H.M., TOROPOV, V.V., KAPUR, N., COPLEY, D. and MINCHER, A., (2011), "Computational fluid dynamic analysis and design optimization of jet pumps" *Computer & Fluids*, doi:10.1016/j.compfluid.2010.10.024.

GARDON, R. and AKFIRAT, J.C., (1966), "Heat Transfer Characteristics of Impinging Two-Dimensional Air Jets", *Journal of Heat Transfer*, **88**(1), 101-107.

HADIYANTO, BOOM, R.M., STRATEN, G. VAN, VAN BOXTEL, A.J.B. and ESVELD, D.C., (2009), "Multi-Objective Optimization to Improve the Product Range of Baking Systems", *Journal of Food Process Engineering*, **32**(5), 709-729.

HADIYANTO, H., ESVELD, D.C., Boom, R.M., STRATEN, G. VAN and BOXTEL, A.J.B. VAN, (2008), "Control vector parameterization with sensitivity based refinement applied to baking optimization", *Food and Bioproducts Processing*, **86**(C2), 130-141.

INCROPERA, F.P. DEWITT, D.P, BERGMAN, T.L. and LAVINE, A.S., (2006), *Fundamentals of Heat and Mass Transfer*, 6th Edition, John Wiley & Sons.

IKIN, J.B. and THOMPSON, H.M., (2007), "Drying air-induced disturbances in multi-layer coating systems" *Chemical Engineering Science*, **62**(23), 6631-6640.

JEFFERSON, D.R., LACEY, A.A. and SADD, P.A., (2007) "Crust density in bread baking: Mathematical modelling and numerical solutions", *Applied Mathematical Modelling*, **31**(2), 209-225.

KHATIR, Z., PATON, J., THOMPSON, H., KAPUR, N., TOROPOV, V., LAWES, M. and KIRK, D., (2011), "Computational fluid dynamics (CFD) investigation of air flow and temperature distribution in a small scale bread-baking oven", *Applied Energy*, doi:10.1016/j.apenergy.2011.02.002.

KHATIR, Z., PATON, J., THOMPSON, H., KAPUR, N., TOROPOV, V., LAWES, M. and KIRK, D., (2010), "Thermal Management in Commercial Bread Baking - CFD investigation of thermal air flow in a small scale bread-baking oven", *Proceedings of the 1st PRO-TEM Network Conference - Sustainable Thermal Energy Management 2010 (SusTEM2010 Conference)*, Newcastle, UK, 2-3 November, 146-155.

BOULET, M., MARCOS, B., DOSTIE, M. and MORESOLI, C., (2010), "CFD modeling of heat transfer and flow field in a bakery pilot oven", *Journal of Food Engineering*, **97**(3), 393-402.

MARTIN, H., (1977), "Heat and Mass Transfer between Impinging Gas Jets and Solid Surfaces", *Advances in Heat Transfer*, **13**, 1-60.

NARARYANAN, A., TOROPOV, V.V., Wood, A.S. and CAMPEAN, I.F., (2007), "Simultaneous model building and validation with uniform designs of experiments", *Engineering Optimization*, **39**(5), 497–512.

BANOONI, S. and MUJUMDAR A.S., (2009), "Mathematical Modeling of Bread Baking in an Impingement Oven", In *Mathematical Modeling of Industrial Transport Processes,* Peng Xu, Zhonghua Wu and A.S Mujumdar (Editors), TPR Group NUS, Singapore, 173-189.

NORTON, T. and SUN, D.-W., (2006), "Computational fluid dynamics (CFD) - an effective and efficient design and analysis tool for the food industry: A review", *Trends in Food Science & Technology*, **17** (11), 600-620.

PATANKAR, S.V. and SPALDING, D.B., (1972), "A calculation procedure for heat, mass and momentum-transfer in three-dimensional parabolic flows", *International Journal of Heat and Mass Transfer*, **15**(10), 1787-1806.

PURLIS, E., (2011), "Bread baking: Technological considerations based on process modelling and simulation", *Journal of Food Engineering*, 2011, **103**(1), 92-102.

SARKAR, A. and SINGH, R.P., (2004), "Air impingement technology for food processing: visualization studies", *LWT - Food Science and Technology*, **37**(8), 873-879.

THERDTHAI, N., ZHOU, W. and ADAMCZAK, T., (2002), "Optimisation of the temperature profile in bread baking", *Journal of Food Engineering*, **55**(1), 41-48.

TOROPOV, V.V., BATES, S.J., and QUERIN, O.M., (2007) ,"Generation of Extended Uniform Latin Hypercube Designs of Experiments", In *Proceedings of the 9th International Conference on the Application of Artificial Intelligence to Civil, Structural and Environmental Engineering*, B.H.V. Topping (Editor), Civil-Comp Press, Stirlingshire, Scotland.

WONG, S.-Y., ZHOU, W. and Hua, J. (2007), "CFD modeling of an industrial continuous bread-baking process involving U-movement", *Journal of Food Engineering*, **78**(3), 888-896.

ZHANG, J. and DATTA, A.K. (2006), "Mathematical modeling of bread baking process", *Journal of Food Engineering*, **75**(1), 78-89.

8th International Conference on CFD in Oil & Gas, Metallurgical and Process Industries
SINTEF/NTNU, Trondheim Norway
21-23 June 2011

CFD11-152

CFD SIMULATION OF SLAG DROPLET FORMATION BY A SPINNING DISC IN DRY SLAG GRANULATION PROCESSES

Yuhua PAN[1]*, **Peter J. WITT**[2], **Benny KUAN**[2] and **Dongsheng XIE**[1]

[1] CSIRO Process Science and Engineering, Box 312, Clayton South, VIC 3169, AUSTRALIA

[2] CSIRO Mathematics, Informatics and Statistics, Box 312, Clayton South, VIC 3169, AUSTRALIA

* E-mail: Yuhua.Pan@csiro.au

ABSTRACT

A transient three-dimensional CFD model has been developed, using the ANSYS/CFX modelling package, to simulate breakup of a liquid slag film by a spinning disc. Owing to centrifugal forces, the slag film disintegrates into ligaments and droplets after leaving the spinning disc. The computational domain is a region extending from the disc edge to a finite outer boundary, in which the slag film first deforms into ligaments and then breaks up into droplets. Partial differential equations governing turbulent multiphase flows with free surfaces were numerically solved for each fluid phase (liquid slag and air). The free surface was modelled with the continuum surface force method. The developed CFD model was applied to predict the droplet size distributions which, as a means of model validation, were compared with those of slag granules obtained from dry slag granulation experiments carried out at CSIRO. The influence of liquid slag surface tension coefficient on the droplet size distribution was investigated.

Keywords: Spinning disc, dry slag granulation, CFD modelling, simulation, free surface flow, multiphase flow, droplet formation.

NOMENCLATURE

Greek Symbols

α_3 Constant in turbulence model, [–]
β' Constant in turbulence model, [–]
β_3 Constant in turbulence model, [–]
ϕ Disc diameter, [m]
μ Dynamic viscosity, [kg.m^{-1}.s^{-1}]
μ_t Turbulent viscosity, [kg.m^{-1}.s^{-1}]
θ Azimuthal (angular) coordinate, [rad]
ρ Density, [kg.m^{-3}]
$\sigma_{\omega 2}$ Prandtl number for ω in transformed k-ε model, [–]
$\sigma_{\omega 3}$ Prandtl number for ω in SST turbulence model, [–]
σ_{k3} Prandtl number for k in SST turbulence model, [–]
ω Turbulence eddy frequency, [s^{-1}]

Latin Symbols

$\mathbf{C}_{\alpha\beta}$ Interphase momentum transfer term, [kg.m^{-2}.s^{-2}]
$\mathbf{F}_g$ Body force vector due to gravitation, [kg.m^{-2}.s^{-2}]

F_1 First blending function in turbulence model, [–]
$\mathbf{F}_s$ Surface tension force vector, [kg.m^{-2}.s^{-2}]
k Turbulence kinetic energy, [m^2.s^{-2}]
p Pressure, [kg.m^{-1}.s^{-2}]
P_k Production rate of k, [kg.m^{-1}.s^{-3}]
r Volume fraction, [–]
R Radius of disc, [m]
t time, [s]
$\mathbf{u}$ Velocity vector, [m.s^{-1}]
y Radial coordinate, [m]
z Vertical (axial) coordinate, [m]

Sub/superscripts

α, β Fluid phase identity (liquid slag or air)

INTRODUCTION

Slags are high volume by-products from the iron and steel industry. Each year, about two million tonnes of slags are produced in Australia, with some hundred millions of tonnes produced globally. Currently these slags are either air cooled in slag pits or water granulated. A large amount of waste heat contained in the molten slag is not recovered. Water granulation also consumes a large amount of fresh water and may cause possible air and ground water pollution due to sulphur emission.

Dry slag granulation using a spinning disc is emerging as an attractive alternative to conventional processes. In this new approach, molten slag is atomised using a spinning disc to produce fine slag droplets which are quenched with air to produce solidified glassy granules. Simultaneously heat released is recovered to produce hot air at 500-600 °C that can be used at the plant for drying, preheating or steam generation. Compared to wet granulation processes, the dry process also saves water and minimises sulphur emission and possible pollution.

The concept of spinning disc dry slag granulation was first proposed in the 1980s. Recent work at CSIRO has

led to a significant breakthrough in process design by overcoming several major difficulties (Xie and Jahanshahi, 2008). A new integrated dry granulation and heat recovery process has been demonstrated via a prototype pilot plant. The new process has been scaled up to a semi-industrial scale (treating slags at up to 100 kg.min^{-1}) and used to collect data for a CFD model, which will then be used for further scale up to full industrial size with plant trials to be conducted in 2-3 years (Xie, 2011).

Dry slag granulation on a spinning disc involves complex fluid dynamics, heat transfer as well as phase transformation. In this process, molten slag is poured onto a spinning disc, where it spreads outwards, under centrifugal forces, to become a liquid film. The film collapses, at or past the edge of the disc, into a number of ligaments and breaks up into fine droplets. The fluid flow is accompanied by simultaneous slag cooling and significant changes in slag properties such as viscosity. It is important to understand slag spreading on a spinning disc and the subsequent droplet formation process as the size of the slag droplets determines the rate of heat transfer, hence droplet cooling and solidification.

Formation of a continuous liquid film on a spinning disc has been extensively studied previously (e.g., Matar et al., 2006, Sisoev et al., 2003ab, Bhatelia et al., 2009). The film thickness is determined by the disc spinning rate. But most of these studies deal with isothermal systems with no heat transfer or phase transformation and, thus, are not directly applicable to the flow of molten slag on a spinning disc.

While there has been a large body of published studies on liquid film flow over a spinning disc, little has been published on ligament formation and subsequent breakup of the ligaments to produce liquid droplets from the disc. Limited studies to date (e.g., Wu et al., 1997, Lasheras and Hopfinger, 2000, Shinjo and Umemura, 2010) were focused on ligament formation by a liquid jet/nozzle and subsequent necking and breakup to form droplets. In the case of the atomisation of molten slags by a spinning disc, it is obvious that the mechanism of ligament formation and breakup differ significantly from liquid jets.

In order to understand slag atomisation by a spinning disc and effects of key process parameters, efforts have been made to develop a suitable CFD model to simulate the process. In a previous paper (Pan et al., 2010), CFD modelling techniques were applied to predict slag spreading to form a continuous film on a spinning disc and the formation of a solid frozen slag layer at the disc surface. A steady-state two-dimensional (2D) CFD model was established, using the ANSYS/CFX modelling package, and successfully applied to simulate free surface flow, solidification of a slag layer and heat transfer in the slag and the disc. The 2D slag film model can be used to calculate slag film thickness at the disc edge, which has a significant effect on the sizes of the slag droplets produced.

In the present work, a transient three-dimensional (3D) CFD model has been developed, using the ANSYS/CFX modelling package, to simulate breakup of the slag film after leaving the spinning disc into droplets under centrifugal force. The slag film thickness at the disc edge predicted by our earlier 2D slag film model was used as an input to the 3D model and the droplet formation and droplet sizes are calculated and compared with experimental data available from dry slag granulation experiments carried out at CSIRO.

MODEL FORMULATION

General Assumptions

In order to mathematically simulate breakup of a liquid slag film after leaving a spinning disc, the following general assumptions have been made:

- A stable liquid film with a fixed radial mass flow rate (tapping rate) and uniform temperature is maintained at the edge of the disc, which is defined as an inlet of the computation domain;

- In the vicinity of the disc, the air flow is influenced only by the spinning disc and the motion of liquid slag;

- To reduce computational effort, a computation domain only includes limited portions of the disc side wall face and air near the disc side wall. A consequence of this is that any perturbations on liquid free surface on the disc are neglected as we assume that they are much smaller than the perturbations experienced by the liquid leaving the disc;

- Heat transfer and slag solidification are neglected but a rim formed by a layer of solidified slag over which liquid slag flows as a film is considered;

- Periodical symmetry about the axis of the spinning disc is assumed.

Governing Equations

In this work the liquid slag and air flow is modelled as a three-dimensional, transient and two-phase free surface flow problem. The following partial differential equations (PDEs) governing multiphase flows are solved numerically.

Continuity Equation

Separate PDEs are considered for mass conservation of both the incompressible liquid slag and air phases:

$$\frac{\partial(r_\alpha \rho_\alpha)}{\partial t} + \nabla \cdot (r_\alpha \rho_\alpha \mathbf{u}_\alpha) = 0 \qquad (1)$$

Momentum Equations

Separate velocity fields are obtained by solving the following momentum equation for each phase.

$$
\frac{\partial(r_\alpha \rho_\alpha \mathbf{u}_\alpha)}{\partial t} + \nabla \cdot [r_\alpha (\rho_\alpha \mathbf{u}_\alpha \mathbf{u}_\alpha)] = -r_\alpha \nabla p_\alpha
$$
$$
+ \nabla \cdot [r_\alpha (\mu + \mu_t)(\nabla \mathbf{u}_\alpha + (\nabla \mathbf{u}_\alpha)^T)] + \mathbf{F}_g + \mathbf{F}_s + \mathbf{C}_{\alpha\beta} \tag{2}
$$

where, $\mathbf{F}_s$ is an additional momentum source due to surface tension, which is approximated by using the Continuum Surface Force (CSF) method (Brackbill et al., 1992); and $\mathbf{C}_{\alpha\beta}$ is the interphase drag force that is calculated using the Grace drag model (Grace and Weber, 1982). Other symbols appearing in the above equations and in the subsequent sections (including those in equations, figures and tables) are defined in NOMENCLATURE.

Turbulence Equations

Turbulence effects are accounted for by using a homogeneous turbulence model, which is a phase weighted extension of the single phase Shear-Stress-Transport (SST) model. The SST model is described by the following equations for transport of turbulent kinetic energy and turbulent eddy frequency, respectively.

$$
\frac{\partial(\rho k)}{\partial t} + \nabla \cdot (\rho \mathbf{u} k) = \nabla \cdot \left[\left(\mu + \frac{\mu_t}{\sigma_{k3}} \right) \nabla k \right]
$$
$$
+ P_k - \beta' \rho k \omega \tag{3}
$$

$$
\frac{\partial(\rho \omega)}{\partial t} + \nabla \cdot (\rho \mathbf{u} \omega) = \nabla \cdot \left[\left(\mu + \frac{\mu_t}{\sigma_{\omega 3}} \right) \nabla \omega \right]
$$
$$
+ (1 - F_1) 2\rho \frac{\nabla k \nabla \omega}{\sigma_{\omega 2} \omega} + \alpha_3 \frac{\omega}{k} P_k - \beta_3 \rho \omega^2 \tag{4}
$$

Further details of the constants and terms in the above equations can be found elsewhere (ANSYS inc., 2009).

Computational Domain

Figure 1 schematically illustrates the computation domain considered in the present modelling work. It is three-dimensional in space extending, in the radial (y) direction, from the disc side wall face to a sufficient finite distance from the disc to allow formation of liquid slag ligaments and droplets. In the vertical (z) direction the domain extends upward and downward from the liquid slag (film) inlet sufficient distance so that the air flow has a negligible influence on liquid slag flowing off the disc. In the azimuthal (θ) direction, the angle θ is determined by test computations such that at least two liquid ligaments formed are covered by the computation domain, with rotational periodicity boundary conditions applied to the faces bounding the computation domain in this direction. The θ direction is also the disc spinning direction. The disc side wall face is a cylindrical surface with a radius of 25 mm, i.e., the disc radius. (The disc is

flat and has a diameter of 50 mm and a thickness of 10 mm but is excluded from the computation domain.) As has been observed from experiments and simulated in the previous modelling work (Pan et al., 2010), a solid slag layer is normally formed on the top face of the disc with a thin film of liquid slag flowing over it. The solid slag layer normally extrudes beyond the disc edge by about 2 to 5 mm. Therefore, this part of extruded solid slag layer (rim) is included in the computation domain as a solid wall (i.e., "Solid slag upper face" and "Solid slag lower face" shown in Figure 1).

The domain was discretised into nearly 640,000 vertex-centred cells comprising of tetrahedral, pyramid, prism and hexahedral elements. For numerical stability and accuracy over 532,000 hexahedral elements were used and concentrated in the region of ligament and droplet formation. Mesh refinement was used to find a balance between accuracy and computational run time. Typical element sizes range from 0.1 mm to 0.75 mm.
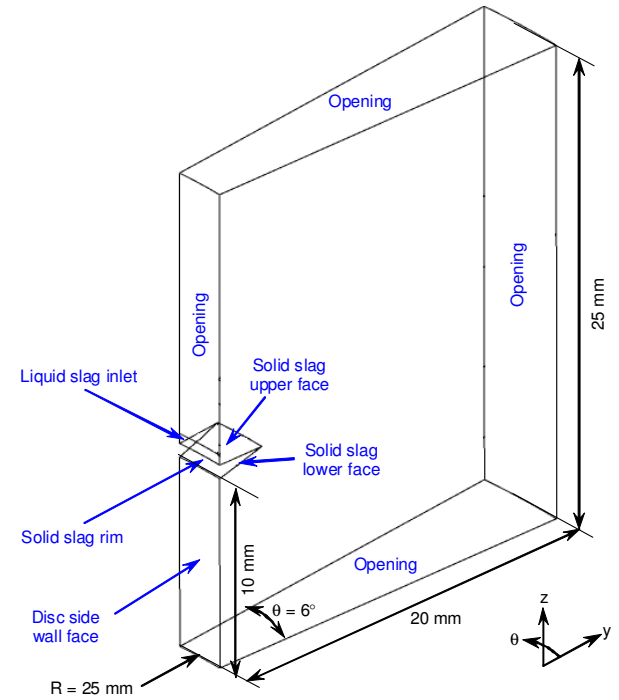
Figure 1: Schematic diagram of three-dimensional computation domain.

Initial and Boundary Conditions

Initial Condition

A transient CFD model is used to simulate breakup of liquid slag and formation of ligaments and droplets. As an initial condition, all simulations start with a layer of liquid slag film already spreading over the upper face of the solid slag rim. This slag film has a uniform radial velocity equal to that calculated from the slag tapping rate and a uniform tangential velocity equal to that of the edge of the spinning disc, whereas the velocity in the vertical z-direction is set to zero.

Boundary Conditions

No-slip conditions are applied to all solid wall faces such as disc side wall face and solid slag upper and lower faces shown in Figure 1, which are rotating in the θ direction; all openings are set as pressure boundaries (with opening pressure equal to zero) over which air can leave or enter the domain. Zero gradient conditions are applied to variables at these boundaries. In the θ-direction, rotational periodical conditions are applied to the faces bounding the domain in this direction. At the liquid slag inlet, a radial velocity is set at a value equivalent to the slag tapping rate and a tangential velocity equal to the rotating velocity of the disc edge. In this work, the thickness of the liquid slag film at the disc edge (inlet) is set to 0.52 mm, which was predicted by the previously developed 2D CFD Model (Pan et al., 2010) for a slag tapping rate of 5 kg/min and a disc spinning speed of 2000 RPM. These settings give overall inlet liquid Reynolds number and Weber number (all based on inlet film thickness) of 10 and 78, respectively.

Material Properties

Table 1 gives the thermophysical properties of liquid slag and air used in the present modelling work.

Table 1: Material thermophysical properties.

Property	Unit	Liquid slag	Air
Density	kg.m⁻³	2590 [a]	1.185 [c]
Dynamic viscosity	Pa.s	0.7 [b]	1.831×10^{-5} [c]
Surface tension coefficient	N.m⁻¹	0.478 [a]	-

a: Inaba et al. (2004), b: Purwanto et al. (2005),
c: http://users.wpi.edu/~ierardi/FireTools/air_prop.html

Solution Method

The governing equations expressed by Eqs. (1) through (4) together with the initial and boundary conditions described in the preceding sections were solved numerically using the commercial CFD package ANSYS/CFX 12 (ANSYS Inc., 2009). A second order backward Euler method was used for integration on the transient terms with a typical time step of 0.001 to 0.005 milliseconds. A scheme approaching second order was used for spatial discretisation of convective terms in the equations.

RESULTS AND DISCUSSION

Prediction of Droplet Formation and Size Distribution

Figure 2 shows the CFD model predicted process of liquid slag film breakup, formation of ligaments and their breakup into droplets, for one type (geometry) of spinning disc (Type A). In this figure, the liquid domains (film, ligaments and droplets) are represented by iso-surfaces of liquid volume fraction at a value of 0.37. This value was obtained by volume-averaging the integral of liquid volume fraction along the droplet's radius. Strictly speaking, different iso-surface values of liquid volume fraction should be applied to map different shapes of liquid domains. In the present case, for instance, 0.5 can be used for liquid films presumably with flat surfaces, about 0.44 for ligaments with cylindrical surfaces and around 0.37 for droplets with spherical surfaces. However, for simplicity of processing the simulation results and that a primary interest of this step is to predict the size of droplets in the system, 0.37 was used for mapping all liquid domains in Figure 2.

It can be seen from Figure 2 that, under the given operating conditions (i.e., slag tapping rate and disc spinning speed), the liquid slag film completely breaks up into droplets in less than 20 ms. During the first few milliseconds waves or ripples were formed on the surface of the liquid film. They propagate outwards towards the edge of the film forming a ring. After about 6 ms the ring detaches from the bulk film and travels outward. The liquid slag film deforms into ligaments during 6 to 12 ms, and the ligaments break up into droplets in a further distance in the radial direction. During this initial period (i.e., 0 to 12 ms) two such liquid rings are formed. These rings are relatively thick and thus they eventually break up into large droplets but in a greater distance beyond the radial extent of the computational domain. Therefore, in this initial period the modes of rupture of a liquid slag film by a spinning disc can be regarded as two-fold: (1) ring formation and (2) ligament formation. The ring formation takes place first followed by the ligament formation which quickly becomes a dominant mode. (It should be mentioned here that, unlike the second ring formation, the first ring formation may also be associated with, to a certain extent, an initial assumption that a layer of liquid slag film already exists on top of the solid slag rim. In the future, this effect will be investigated by removing the initial slag film.) Roughly 18 ms later, the ligaments completely break up into droplets at about 10 mm away from the disc edge. After 20 to 30 ms the slag film breakup process essentially reaches a pseudo-steady state.

With the developed CFD model one can predict the size distributions of the formed droplets under different operating conditions. Figure 3 illustrates an example of the approach used for evaluating the size distribution of slag droplets sampled from the simulation results between 20 to 30 ms and the results are given in Figure 4. The droplet size (diameter) was manually measured from the plots like the sampling region shown in Figure 3. From Figure 4 very fine droplets are produced under the operating condition given. More than 90 wt. % of the droplets are smaller than 0.5 mm in diameter, as indicated by the curve showing cumulative weight fraction (CWF). A maximum weight fraction (WF) of the droplets falls between 0.3 and 0.325 mm size range. The model has also been used to investigate influences of liquid slag surface tension on the droplet size distribution.
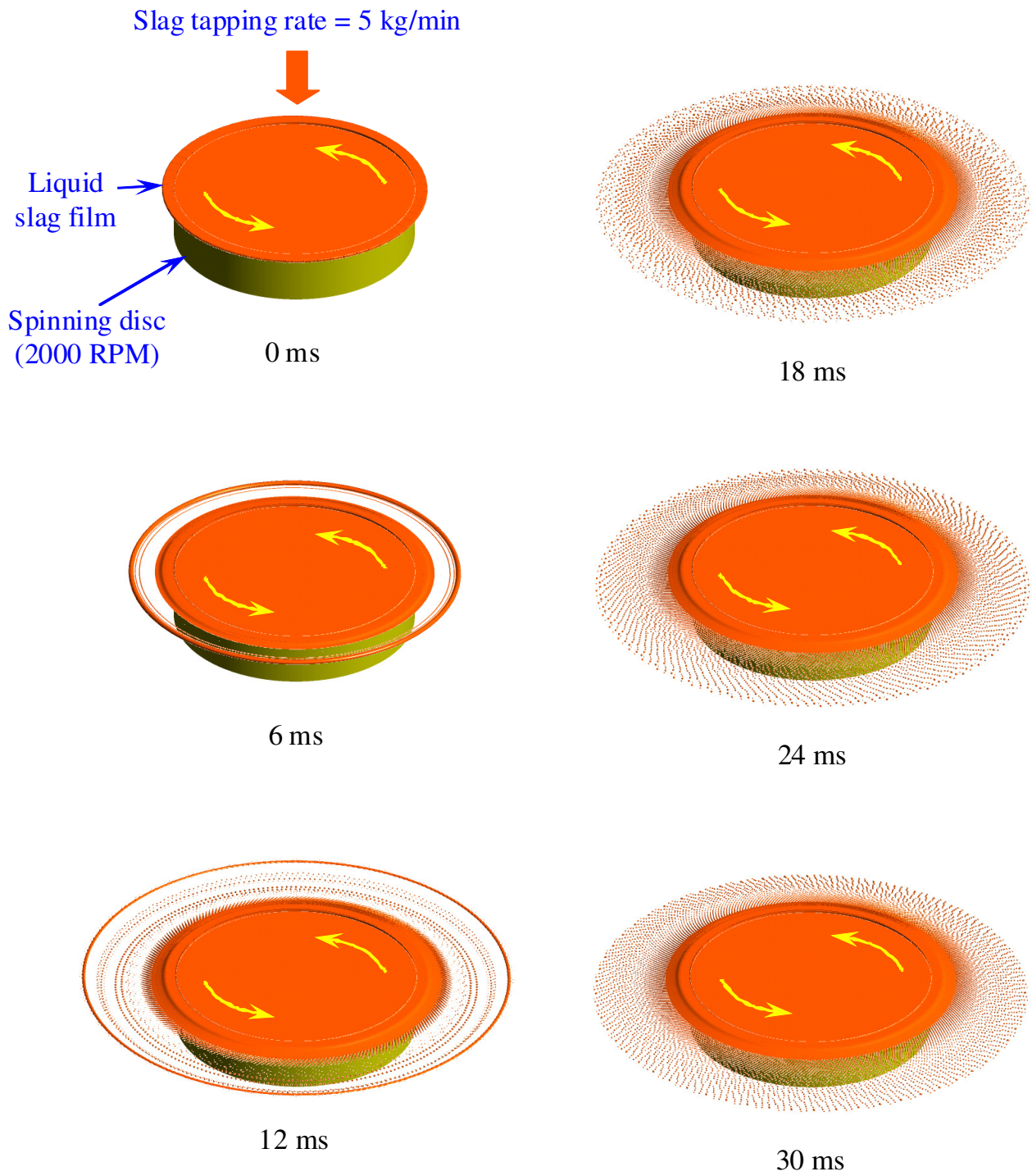
Figure 2: Predicted process of liquid slag film break-up and formation of rings, ligaments and droplets by a spinning disc.
(Disc type: A, Liquid slag tapping rate: 5 kg.min^{-1}, Disc spinning speed: 2000 RPM)
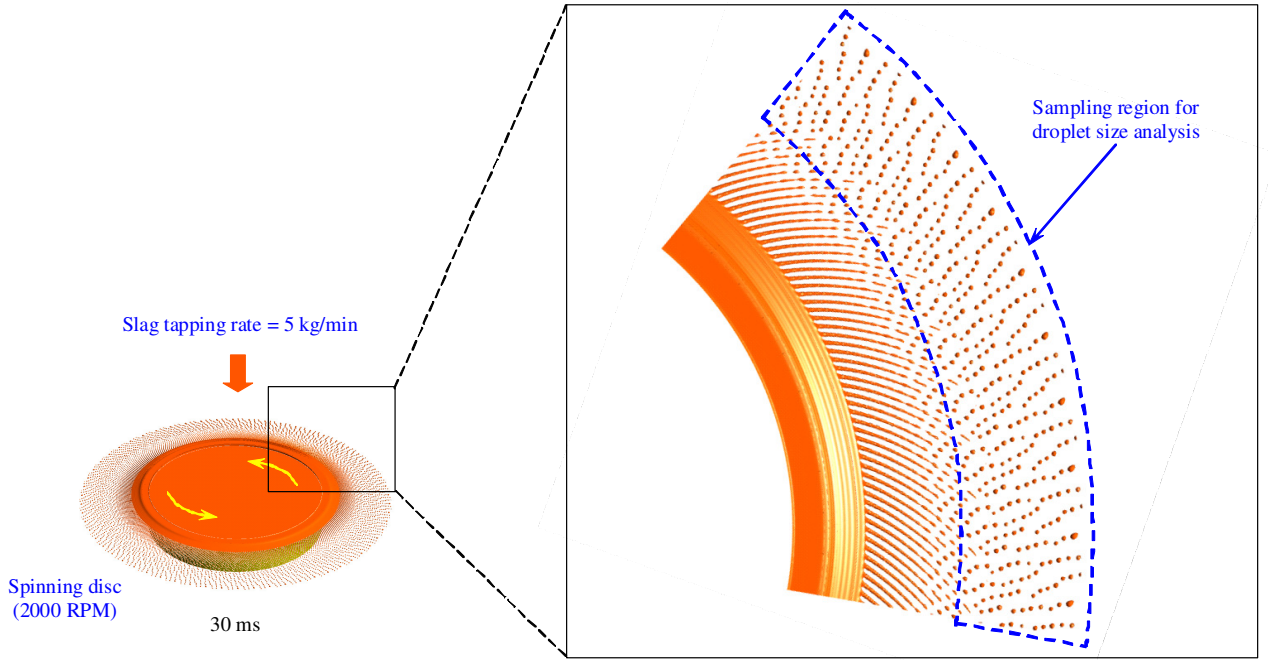
Figure 3: Sample of droplets for size distribution analysis. (Disc type: A, Liquid slag tapping rate: 5 kg.min^{-1}, Disc spinning speed: 2000 RPM, Time: 30 ms)

Influence of Surface Tension on Droplet Size Distribution

Figure 5 shows a comparison of the predicted size distributions of the droplets formed from liquid slag with different surface tension coefficients. It can be seen from this figure that, as shown by the WF data, a decrease in the liquid surface tension coefficient results in the formation of a greater number of smaller droplets. Table 2 gives a comparison of mean diameter (MD) and standard deviation (SD) of droplet size distributions predicted for different surface tension coefficients. A smaller liquid surface tension coefficient leads to a smaller MD but with a comparable SD. This phenomenon can be easily explained by referring to the Weber number, which represents the ratio of inertia force to surface tension force. For the same inertia force, i.e., the same disc spinning speed and tapping rate, liquid with a smaller surface tension coefficient will be stable as small droplets.

Table 2: Comparison of MD and SD of droplet size distributions for different surface tension coefficients.

Liquid slag surface tension coefficient	Mean Diameter (MD)	Standard Deviation (SD)
0.478 N.m^{-1}	0.292 mm	0.063 mm
0.239 N.m^{-1}	0.265 mm	0.082 mm
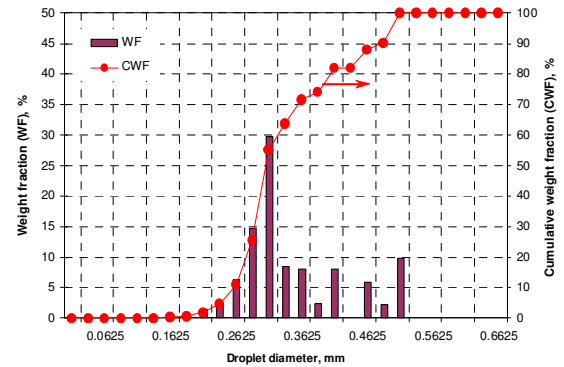
Figure 4: Predicted droplet size distributions. (Disc type: A, Liquid slag tapping rate: 5 kg.min^{-1}, Disc spinning speed: 2000 RPM, Time: 20 – 30 ms)
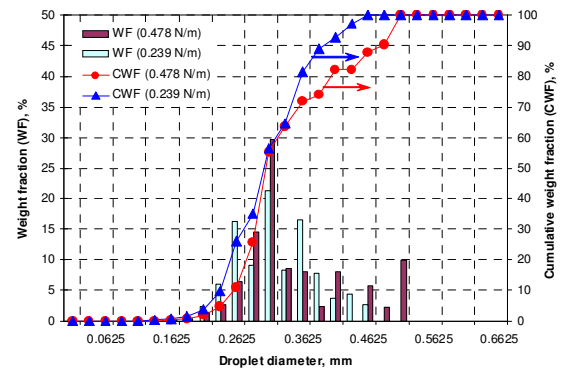
Figure 5: Influence of liquid slag surface tension coefficient on droplet size distribution. (Disc type: A, Liquid slag tapping rate: 5 kg.min^{-1}, Disc spinning speed: 2000 RPM, Time: 20 – 30 ms)

Model Validity

In order to verify the validity of the developed CFD model, we also compared the model predictions with experimental observations and measurements. Figure 6 illustrates a qualitative comparison between a video image obtained from an earlier liquid slag atomisation experiment using a different spinning disc (Type B) and that simulated by the CFD model for the same conditions. It can be seen from this figure that the CFD model qualitatively captures the key features of ligament formation and their breakup into droplets as observed in the experiment. Although it should be noted the length of the ligaments is shorter in the model than observed in experiments. This is because the CFD model has a limitation of resolving very thin ligaments, resulting in relatively premature breakup.

Slag tapping rate = 2 kg/min

(a) Experimental observation
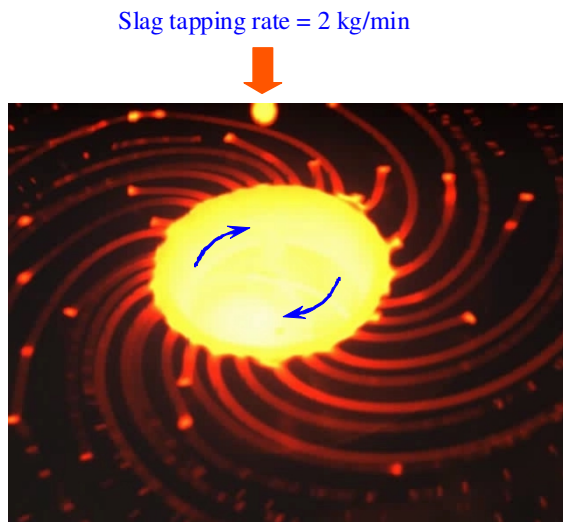
Slag tapping rate = 2 kg/min
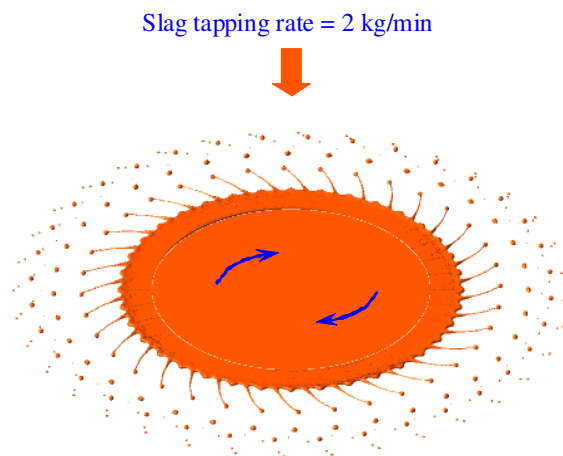
(b) CFD simulation

Figure 6: Qualitative comparison between experimental observation and CFD simulation on liquid slag breakup by a spinning disc and formation of ligaments and droplets. (Disc type: B, Liquid slag tapping rate: 2 kg.min^{-1}, Disc spinning speed: 1780 RPM)

Figure 7 shows a quantitative comparison between droplet size distributions measured from the laboratory experiments and predicted by CFD simulations. This figure demonstrates that the predicted droplet size distributions (WF and CWF) agree very well with the measurements except for the large size range (e.g., > 1.2 mm). One reason that the CFD model can not capture very large droplets (e.g., diameter > 1.2 mm) is that such large droplets likely form through ring breakup in the early period and in a greater distance beyond the radial extent of the computation domain, which is restricted primarily by the limitation of computing resources in the present work.
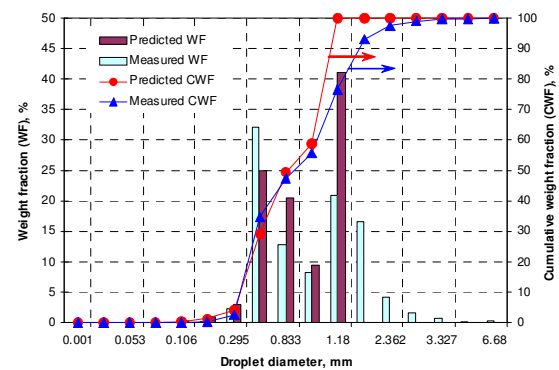
Figure 7: Quantitative comparison between droplet size distributions measured from laboratory experiments and predicted by CFD simulations on liquid slag breakup by a spinning disc and formation of ligaments and droplets. (Disc type: B, Liquid slag tapping rate: 2 kg/min, Disc spinning speed: 1780 RPM)

CONCLUSIONS

A transient three-dimensional CFD model for simulating the flow of liquid slag from a spinning disc and its breakup into ligaments and droplets has been developed. Comparison of the predicted results shows a qualitative agreement with video images of the process. Predicted droplet size distributions are in a quantitative agreement with those measured from a laboratory experimental set-up. The modelling results demonstrate that the process of liquid slag film breakup by a spinning disc into droplets takes place via two modes in time. One is the initial short-time (milliseconds) ring formation and breakup into droplets; the other the ligament formation and breakup into droplets which is the dominant mode afterwards. The CFD model was also used to assess the effect of liquid slag surface tension on the droplet size distribution showing that decreasing surface tension results in smaller mean droplet diameters with a similar standard deviation.

ACKNOWLEDGMENT

REFERENCES

ANSYS Inc., 2009, ANSYS CFX User Manual, Release 12.0.

BHATELIA, T.J., UTIKAR, R.P., PAREEK, V.K., TADE, M.O., (2009), "Characterizing liquid film thickness in spinning disc reactors", *Seventh Int. Conf. CFD Min. Pro. Ind.*, CSIRO, Melbourne, Australia, 9-11 December.

BRACKBILL, J.M.; KOTHE, D.B. and ZEMACH, C., (1992), "A continuum method for modelling surface tension", *J. Computational Physics*, **100**, 335-354.

GRACE, J.R. and WEBER, M.E., (1982), "Hydrodynamics of drops and bubbles", *Handbook of Multiphase Systems*, ed. G. Hetsroni, Hemisphere.

http://users.wpi.edu/~ierardi/FireTools/air_prop.html

INABA, S.; KIMURA, Y.; SHIBATA, H. and OHTA, H., (2004), "Measurement of physical properties of slag formed around the raceway in the working blast furnace", *ISIJ International*, **44**, No. 12, 2120-2126.

LASHERAS, J.C., HOPFINGER, E.J., (2000), "Liquid jet instability and atomization in a coaxial gas stream", *Annu. Rev. Fluid Mech.*, **32**, 275-308.

MATAR, O.K., SISOEV, G.M., LAWRENCE, C.J., (2006), "The flow of thin liquid films over spinning discs", *The Canadian J. Chem. Eng.*, **84**, 625-642.

PAN, Y., WITT, P.J., and XIE, D., (2010), "CFD simulation of free surface flow and heat transfer of liquid slag on a spinning disc for a novel dry slag granulation process", *Progress in Computational Fluid Dynamics*, **10,** 292-299.

PURWANTO, H., MISUOCHI, T., AKIYAMA, T., (2005), "Prediction of granulated slag properties produced from spinning disk atomizer by mathematical model", *Mat. Trans.*, **46**(6), 1324-1330.

SHINJO, J., UMEMURA, A., (2010), "Simulation of liquid jet primary breakup: Dynamics of ligament and droplet formation", *In. J. Multiphase Flow*, **36**, 513-532.

SISOEV, G.M., MATAR, O.K., LAWRENCE, C.J., (2003a), "Modelling of film flow over a spinning disk", *J. Chem. Tech. Biotech.*, **78**, 151-155.

SISOEV, G.M., MATAR, O.K., LAWRENCE, G.J., (2003b), "Axisymmetric wave regimes in viscous liquid film flow over a spinning disk", *J. Fluid Mech.*, **495**, 385-411.

WU, P.K., KIRKENDALL, A., FULLER, R.P., (1997), "Breakup processes of liquid jets in subsonic crossflows", *J. Prop. Power*, **13**(1), 64-73.

XIE, D. and JAHANSHAHI, S., (2008), "Waste Heat Recovery from Molten Slags", *International Congress on Steel 2008 (ICS2008)*, 6-8 October 2008, Gifu, Japan.

XIE, D., (2011), "Turning molten slag into green cement", *The Chemical Engineer TCE*, No. 837, March, 40-41.

8th International Conference on CFD in Oil & Gas, Metallurgical and Process Industries
SINTEF/NTNU, Trondheim NORWAY
21-23 June 2011

CFD11-153

POROUS AND VISCOUS FLOW MODELING ON THE STUDY OF CYST DEVELOPMENT IN THE HUMAN SPINAL CORD

Ida Norderhaug DRØSDAL[1]*, **Victor HAUGHTON**[2], **Kent-André MARDAL**[3], **Karen-Helene STØVERUD**[4]

[1]Center for Biomedical Computing, Simula Research Laboratory, 1325 Lysaker, NORWAY

[2]Department of Radiology, University of Wisconsin, 600 Highland Ave, Madison WI 53792, USA

[3]Center for Biomedical Computing, Simula Research Laboratory, 1325 Lysaker, NORWAY

[4]Center for Biomedical Computing, Simula Research Laboratory, 1325 Lysaker, NORWAY

* E-mail: i.n.drosdal@gmail.com

ABSTRACT

In this study, we apply an incremental pressure correction scheme to a coupled Navier-Stokes-Darcy problem in order to model porous and viscous flow in and around the human spinal cord. Simulations show that the central canal, a narrow channel in the spinal cord which is usually only partly present in most adults, has a profound effect on pressure distributions within the spinal cord – an effect that can be of importance in the study of cyst formation in the cord. The numerical method was verified using the method of manufactured solutions, showing that the simple operator splitting scheme produces reliable results in this complex case.

Keywords: coupled porous and viscous flow, cerebrospinal fluid flow, syringomyelia development .

NOMENCLATURE

Greek Symbols

ρ Mass density, $[kg/m^3]$
σ Cauchy stress tensor, $[Pa/(kg/m^3)]$
ν Kinematic viscosity, $[m^2/s]$
μ Dynamic viscosity, $[kg/m \cdot s]$
ϕ Porosity, $[1]$

Latin Symbols

n   Normal vector, $[1]$
t   Tangent vector, $[1]$
ê   Unit vector, $[1]$
u   Volume-averaged fluid velocity, $[m/s]$
f   Volume forces, $[N/(kg/m^3)]$
p Pressure, $[Pa]$
K Intrinsic permeability, $[m^2]$

Sub/superscripts

v Viscous domain
p Porous domain
x x-direction
y y-direction

INTRODUCTION

In this study, we address the development of cysts in the spinal cords of patients suffering from the Chiari Malformation (see Figure 1). The Chiari Malformation is a medical condition characterized by the herniation of the cerebellar tonsils into the spinal canal. Chiari is often accompanied by syringomyelia: a condition where fluid-filled cysts form in the spinal cord. Syringomyelia is a serious condition affecting the central nervous system.

It is not fully understood why the cysts form, but prevailing theories suggest that they are a result of abnormal flow of cerebrospinal fluid (CSF) (Levine, 2004; Greitz, 2006). CSF is the fluid surrounding the brain and spinal cord. It flows in a periodic manner up and down the spinal canal, driven by the expansion and contraction of the brain with each heartbeat. A Chiari malformation disrupts the flow between the spinal canal and cranium, resulting in abnormal flow patterns. This has been demonstrated by magnetic resonance imaging (MRI) (cf. e.g. Quigley *et al.* (2004); Haughton *et al.* (2003)).

In recent years, computational fluid dynamics (CFD) has been introduced as a tool in the study of flow-induced cyst formation in Chiari patients. CSF flows both inside the spinal cord and in the surrounding CSF space (see Figure 1). Existing models either describe the CSF space flow (Roldan *et al.*, 2009; Linge *et al.*, 2010; Loth *et al.*, 2001) or the flow within the spinal cord (Støverud *et al.*, 2011). However, to our knowledge, none of these consider the coupling between these two domains. In this study we take coupling into account, using a coupled viscous and porous model to simulate CSF flow in the spinal canal. We assume rigid walls, thus neglecting the viscoelasticity of the cord and the elasticity of the channel walls.

The use of this model necessitates an efficient solver for the coupled Navier-Stokes-Darcy system. As a result, we develop and verify an incremental pressure correction scheme applied to this problem.

Our simulations indicate that the spinal cord central canal affects pressure distributions within the spinal canal. The cen-
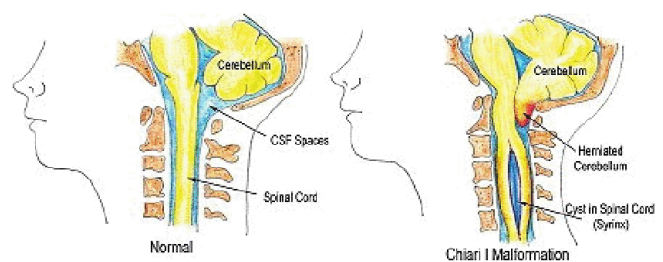

Figure 1: Illustration of Chiari Malformation accompanied by syringomyelia.

tral canal is a narrow channel in the center of the spinal cord. This is fully intact in infants, but occludes with age. Remaining segments of the central canal will be present in an estimate of 30-70% of adults in the ages 20 to 70 (Yasui *et al.*, 1999). If these segments alter pressure distributions in the spinal canal, this could be important to take into account in further studies of syringomyelia development.

MODEL DESCRIPTION

We model CSF flow in a segment of the spinal canal containing an open central canal. The spinal cord is modeled as a porous medium saturated in the fluid of the adjacent CSF space and central canal. The central canal is occluded in both ends, only letting in fluid through the spinal cord tissue. The flow into the domain is oscillatory with a period of one heartbeat.

Figure 2: Model domain. The lighter area is the viscous domain, Ω_v, representing the CSF space and the central canal. The darker area is the porous domain, Ω_p, representing the tissue of the spinal cord.

The model domain is a simplified, rectangular, 2D representation of the spinal canal (see Fig 2). In this problem a cylindrical description would be preferable, but, as we intend to later apply the model to more complicated domains, we keep cartesian coordinates.

The domain, Ω, is divided into a viscous and a porous domain, Ω_v and Ω_p, respectively. The CSF space and central canal comprises the viscous domain, Ω_v, and is governed by the Navier-Stokes equations

$$\frac{\partial \mathbf{u}}{\partial t} + \mathbf{u} \cdot \nabla \mathbf{u} = \nabla \cdot \sigma(\mathbf{u}, p) + \mathbf{f} \tag{1}$$

$$\nabla \cdot \mathbf{u} = 0. \tag{2}$$

Here σ is the Cauchy stress tensor, $\sigma(\mathbf{u}) = 2\nu\varepsilon(\mathbf{u}) - \frac{1}{\rho}pI$, $\varepsilon(\mathbf{u}) = \frac{1}{2}(\nabla \mathbf{u} + \nabla \mathbf{u}^T)$. The volume force, $\mathbf{f}$, is set equal to zero. We eliminate gravity by assuming that this is balanced by the hydrostatic pressure. As a result, pressure describes only the dynamic pressure. This simplification is, however, not true during sudden movements such as standing up.

The cord tissue is referred to as the porous domain, Ω_p, and is governed by a non-stationary Darcy's law

$$\frac{1}{\phi}\frac{\partial \mathbf{u}}{\partial t} = -\frac{1}{\rho}\nabla p - \nu K^{-1}\mathbf{u}. \tag{3}$$

$$\nabla \cdot \mathbf{u} = 0. \tag{4}$$

The two domains are coupled at the interfaces ($\Gamma = \Omega_v \cap \Omega_d$) by mass conservation, continuity of normal stress and the Beavers-Joseph-Saffman condition (Beavers and Joseph, 1967; Saffman, 1973)

$$\mathbf{u}_v \cdot \mathbf{n} = \mathbf{u}_p \cdot \mathbf{n}, \tag{5}$$

$$2\mu\mathbf{n} \cdot \varepsilon(\mathbf{u}_v) \cdot \mathbf{n} - p_v = -p_p, \tag{6}$$

$$2\mathbf{n} \cdot \varepsilon(\mathbf{u}_v) \cdot \mathbf{t} = \alpha K^{-1/2}\mathbf{u}_v \cdot \mathbf{n}. \tag{7}$$

Here $\mathbf{n}$ is the unit normal vector pointing out of the porous domain.

Flow into and out of the domain is through the top and bottom boundaries. To simulate a central canal occluded at both ends, boundary flow is allowed through the CSF space only. This flow is given a parabolic profile and a flow rate varying sinusoidally in time with a period of one heartbeat. The usual no-slip boundary conditions are applied for the channel walls. The domain boundary, $\partial\Omega$, is divided into a viscous and a porous boundary, $\partial\Omega_v = \partial\Omega \cup \Omega_v$ and $\partial\Omega_p = \partial\Omega \cup \Omega_p$, respectively. The viscous boundary is further divided into walls, $\partial\Omega_{walls}$, and a flow boundary, $\partial\Omega_{flow}$. In this terminology, the boundary conditions translate to

$$\mathbf{u} = 0 \quad \text{on} \quad \partial\Omega_{walls}, \tag{8}$$

$$\mathbf{u} = u_0 f(\mathbf{x})\sin(2\pi t)\hat{\mathbf{e}}_y \quad \text{on} \quad \partial\Omega_{flow}, \tag{9}$$

$$\mathbf{u} \cdot \mathbf{n} = 0 \quad \text{on} \quad \partial\Omega_p, \tag{10}$$

where u_0 is the flow amplitude, and $f(\mathbf{x})$ the flow profile on $\partial\Omega_{flow}$. This is zero in the central canal, and parabolic in the CSF spaces.

Model parameters

The dimensions of the spinal canal are patient specific, highly irregular and vary along the length of the canal. In Loth *et al.* (2001), data from the visual human project was used to create an overview of the spinal canal dimensions. Based on these investigations we choose to use a spinal canal radius of 1.4 cm and cord radius of 1.0 cm in our simple model. We use an estimated central canal radius of 0.05 cm. The tissue of the spinal cord may be described as a porous medium of low permeability. Its properties are similar to brain tissue. Porosity and permeability of brain tissue have been measured by in vitro infusion tests. In our simulations we use porosity $\phi = 0.2$ (Nicholson and Philips, 1981) and permeability $K = 1.4 \cdot 10^{-15} \text{ m}^2$, derived from Smith and Humphrey (2007).

The properties of CSF are similar to water (Bloomfield *et al.*, 1998). In the model we use the viscosity and density of water at 37°C.

Flow velocities in the CSF space have been measured by cine MRI. Based on data by Loth *et al.* (2001), we use an amplitude $u_0 = 4.0 \text{ cm/s}$ and a period of 1 s.

The model parameters are summarized in Table 1.

METHODS

We use the finite element method (FEM) to solve the model equations. The implementation is done using the FEniCS toolkit (Logg and Wells, 2010).

Due to the fact that most Stokes elements are unstable for Darcy flow and vice versa, numerical methods for Darcy-Stokes type equations have been studied to a large extent in recent years (cf. e.g. Karper *et al.* (2008); Xie *et al.* (2008); Juntunen and Stenberg (2009)). In this work we take a rather

Table 1: Model parameters.

Canal dimensions:	
Spinal canal radius [cm]	1.40
Spinal cord radius [cm]	1.00
Central canal radius [cm]	0.05
Length of channel segment [cm]	10.00
Spinal cord properties:	
Porosity	0.2
Permeability [m^2]	1.4×10^{-15}
CSF properties:	
Mass density [kg/m^3]	1.0×10^3
Dynamic viscosity [$kg/(m \cdot s)$]	7.0×10^{-4}
Flow properties:	
Peak velocity, u_0 [cm/s]	4.0
Period [s]	1.0

simple approach, where we use an incremental pressure correction scheme with continuous quadratic elements for the velocity and continuous linear elements for the pressure. Initial tests suggest that this simple and efficient method is both accurate and robust with respect to discretization parameters. However, in order to obtain accurate results in our model problem, we needed to use small time steps. In fact, larger time steps introduced completely different flow characteristics. This method will be compared with a fully coupled solver in the near future.

Numerical scheme

In the incremental pressure correction scheme (IPCS), a tentative velocity is computed using the pressure value from the last time step. This is then projected onto the space of divergence free vector fields.

The scheme is implemented in the following weak formulation: for each time step, n, find $u^n \in V$, $p^n \in Q$ by

1. Compute a tentative velocity u^*:

$$F(u^*,v) = \frac{1}{\Delta t}\left\langle u^* - u^{n-1}, v \right\rangle_{\Omega_v} + \frac{1}{\phi \Delta t}\left\langle u^* - u^{n-1}, v \right\rangle_{\Omega_p}$$
$$+ \left\langle \nabla u^* \cdot u^{n-1}, v \right\rangle_{\Omega_v} - \frac{1}{\rho}\left\langle p^{n-1}, \varepsilon(v) \right\rangle_{\Omega}$$
$$+ 2\nu \left\langle \varepsilon(u^*), \varepsilon(v) \right\rangle_{\Omega_v} + \frac{\nu}{K}\left\langle u^*, v \right\rangle_{\Omega_p}$$
$$+ \alpha \nu K^{-1/2}\left\langle u_v^* \cdot t, v_v \cdot t \right\rangle_{\Gamma}$$
$$= 0$$

2. Compute the corrected pressure, p^n

$$\left\langle \nabla p^n, \nabla q \right\rangle_{\Omega} = \left\langle \nabla p^{n-1}, \nabla q \right\rangle_{\Omega} - \frac{\rho}{\Delta t}\left\langle \nabla \cdot u^*, q \right\rangle_{\Omega_v}$$
$$- \frac{\rho}{\phi \Delta t}\left\langle \nabla \cdot u^*, q \right\rangle_{\Omega_p}$$

3. Compute the corrected velocity, u^n

$$\left\langle u^n, v \right\rangle_{\Omega} = \left\langle u^*, v \right\rangle_{\Omega} - \frac{\Delta t}{\rho}\left\langle \nabla(p^n - p^{n-1}), v \right\rangle_{\Omega_v}$$
$$- \frac{\phi \Delta t}{\rho}\left\langle \nabla(p^n - p^{n-1}), v \right\rangle_{\Omega_p}$$

where $V = \{v \in H^2(\Omega)\}$, $Q = \{q \in H^1(\Omega)\}$. This weak formulation assumes slip boundary conditions on the Darcy domain and Dirichlet velocity boundary conditions on the entire boundary.

Scheme verification

The numerical scheme was verified using the method of manufactured solutions. The equations were generalized by adding a volume force and allowing the solution to be compressible. The implemented scheme was then tested by inserting the following analytical solution into the equations

$$\mathbf{u} = \cos(k_x x)\hat{\mathbf{e}}_x + \sin(k_y y)\hat{\mathbf{e}}_y,$$
$$p = cos(2\pi t). \tag{11}$$

This was done on a simpler domain. The channel length and radius were the same as in the model problem, but instead of a complex splitting of the domain into porous and viscous regions, the domain was split in half with a porous region on the left and a viscous region on the right. To match slip boundary conditions in the Darcy domain, k_x and k_y was chosen to give $\mathbf{u} \cdot \mathbf{n} = 0$ on the boundaries. This test case does not match the Beavers-Joseph-Saffman condition. This was taken into account by adding an interface term to the volume force.

The L2-averaged error was computed for time steps in the range $\Delta t = 1.0 \cdot 10^{-1}$ s to $\Delta t = 2.5 \cdot 10^{-2}$ s, combined with mesh resolutions of $\Delta x = 1.0 \cdot 10^{-2}$ cm to $\Delta x = 2.5 \cdot 10^{-3}$ cm and $\Delta y = 1.0 \cdot 10^{-1}$ cm to $\Delta y = 2.5 \cdot 10^{-2}$ cm. These values were chosen to match the CFL condition. The computations were done on a crossed mesh, meaning that each cell of dimension $\Delta x \times \Delta y$ was divided into four triangles by taking the diagonals over the cell corners. The errors in velocity were of the order 10^{-6} cm/s to 10^{-5} cm/s for all the mentioned discretizations. The errors in the pressure was of the order 10^{-3} Pa. We did, however, not get a clear convergent behavior.

Discretization parameters and accuracy of model problem

When solving the model problem, a time step, Δt, of $5 \cdot 10^{-4}$ s was necessary to obtain reasonable stable results. The solution was more stable with respect to the spatial discretization, where we used a crossed mesh with $\Delta x = 0.01$ cm and $\Delta y = 0.1$ cm.

Several key velocity and pressure values were sampled to measure stability with respect to the discretization parameters. The key velocities were the axial velocities in the centers of the CSF spaces and central canal. Two key pressure values were sampled in the upper part of the domain, one in the central canal and one in the CSF space. The difference in key velocities and pressure when going from $\Delta t = 5 \cdot 10^{-4}$ s to $\Delta t = 1 \cdot 10^{-4}$ s, was of the order of 0.01 cm/s for the velocity and 0.01 Pa for pressure. Further refinement of the mesh did not give a significant change in the solution.

The accuracy in these discretization parameters was also tested against the test problem described under scheme verification. This gave L2-averaged errors of order 10^{-5} cm/s in velocity and 0.1 Pa in pressure.

RESULTS

Our model indicates that an open segment of the central canal increases pressure gradients across the spinal cord. In the absence of the central canal, the pressure is constant with respect to the radial direction (Figure 3). The introduction of a central canal segment sets up pressure gradients between the CSF spaces and the central canal (Figure 4). A slice in the radial plane (Figure 5), displays constant pressure across the CSF spaces and constant gradients over the cord tissue.

These figures show the pressure when the gradients are maximal. This occurs at the same time as the CSF flow changes direction.
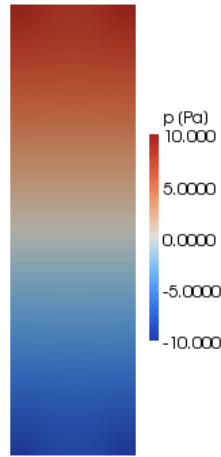
Figure 3: Pressure plot over domain with no central canal. This corresponds to the plot in Figure 4, without the central canal.
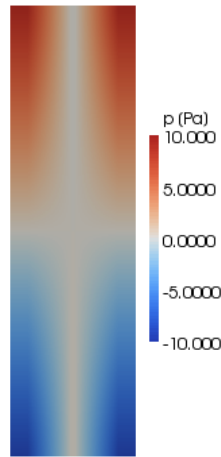
Figure 4: Pressure plot over domain when velocity changes direction from upwards to downwards.

The gradient over the cord is proportional to the axial distance from the channel center (Figure 6). This shows that the gradients are largest near the occlusion of the central canal. Furthermore, a longer central canal opening will result in larger pressure gradients. Due to the choice of coordinates, the gradients have opposite sign at each end. This will be reversed when the flow changes to the opposite direction.

CONCLUSIONS

In this study, we have used a coupled porous and viscous model to simulate CSF flow in and around the human spinal cord to obtain greater insight into the problem of cyst formation in the spinal cords of Chiari patients. Our simulations indicate that the presence of an open segment of the central canal increase pressure gradients over the spinal cord.

Furthermore, tests of the numerical scheme show that the simple incremental correction scheme applied to this coupled Navier-Stokes-Darcy flow produces reliable results.

REFERENCES

BEAVERS, G.S. and JOSEPH, D.D. (1967). "Boundary conditions at a natural permeable wall". *Jour. of Fluid Mechanics*, **30**, 197–207.

BLOOMFIELD, I.G. *et al.* (1998). "Effects of proteins, blood cells and glucose on the viscosity of cerebrospinal fluid". *Pediatr Nerosurg*, **28**, 246–251.

GREITZ, D. (2006). "Unraveling the riddle of syringomyelia". *Nerosurg Rev*, **29**, 251–264.

HAUGHTON, V. *et al.* (2003). "Peak systolic and diastolic CSF velocity in the foramen magnum in adult patients with Chiari I malformations and in normal control participants". *Am. J. Neuroradiol.*, **24**, 169–176.

JUNTUNEN, M. and STENBERG, R. (2009). "Analysis of finite element methods for the Brinkman problem". *Calcolo*, **47(3)**, 129–147.

KARPER, T. *et al.* (2008). "Unified finite element discretizations of coupled Darcy-Stokes flow". *Numerical methods for partial differential equations*, **25(2)**, 311–326.

LEVINE, D.N. (2004). "The pathogenesis of syringomyelia associated with lesions at the foramen magnum: a critical review of existing theories and proposal of a new hypothesis". *J Neurol Sci*, **220**, 3–21.
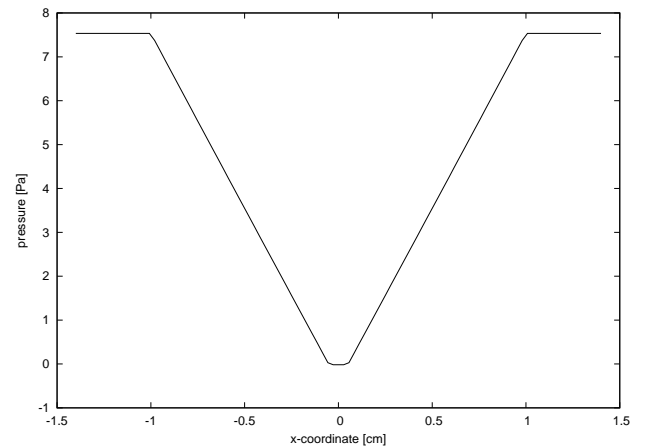
Figure 5: Typical pressure distribution in a slice in the radial direction. This plot is a slice of Figure 4, taken across the canal, one centimeter from the top of the domain.
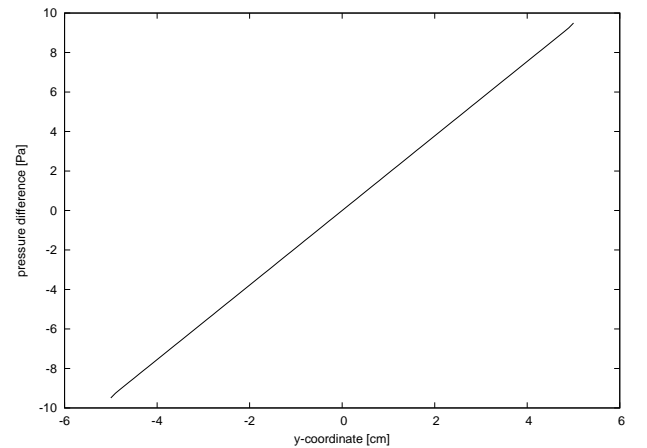
Figure 6: Pressure difference between the CSF space and central canal along the length of the channel. This is taken at the same time as Figure 4. The channel ranged from $y = -5$ cm to $y = 5$ cm.

LINGE, S.O. *et al.* (2010). "CSF flow dynamics at the craniovertebral junction studied with an idealized model of the subarachnoid space and computational flow analysis". *Am. J. Neuroradiol.*, **31**, 185–192.

LOGG, A. and WELLS, G.N. (2010). "DOLFIN: Automated finite element computing". *Transactions on Mathematical Software*, **37(2)**.

LOTH, F. *et al.* (2001). "Hydrodynamic modeling of cerebrospinal fluid motion within the spinal cavity". *ASME J. Biomech. Engrg.*, **123**, 71–73.

NICHOLSON, C. and PHILIPS, J.M. (1981). "Ion diffusion modified by tortuosity and volume fraction in the extracellular microenvironment of the rat cerebellum". *J. Physiol.*, **321**, 225–257.

QUIGLEY, M.F. *et al.* (2004). "Cerebrospinal fluid flow in foramen magnum: Temporal and spatial patterns at MR imaging in volunteers and in patients with Chiari I malformation". *Radiology*, **232**, 229–236.

ROLDAN, A. *et al.* (2009). "Characterization of CSF hydrodynamics in the presence and absence of tonsillar ectopia by means of computational flow analysis". *Am. J. Neuroradiol.*, **30**, 941–946.

SAFFMAN, P.G. (1973). "On the boundary conditions at the interface of a porous medium". *Studies in Applied Mathematics*, **1**, 93–101.

SMITH, J.H. and HUMPHREY, J.A.C. (2007). "Interstitial transport and transvascular fluid exchange during infusion into brain and tumor tissue". *Microvascular Research*, **73**, 58–73.

STØVERUD, K.H. *et al.* (2011). "CSF flow in Chiari I and syringomyelia from the perspective of computational fluid dynamics". *The Neuroradiology Journal*, **24(20-23)**.

XIE, X. *et al.* (2008). "Uniformly-stable finite element methods for Darcy-Stokes-Brinkman models". *J. Comput. Math*, **26(3)**, 437–455.

YASUI, K. *et al.* (1999). "Age-related morphologic changes of the central canal of the human spinal cord". *Acta Neuropathol*, **97**, 253–259.

IMPLEMENTATION OF THE SECTIONAL QUADRATURE METHOD OF MOMENTS IN FLUENT

John C. Morud[1]*

[1] SINTEF Materials and Chemistry, 7465 Trondheim, NORWAY

* E-mail: john.morud@sintef.no

ABSTRACT

An implementation of the Sectional Quadrature Method of Moments (SQMOM) has been made in the CFD code FLUENT 12.0. The SQMOM method, which is a hybrid between the Method of Classes and the QMOM methods, consists of dividing the size distribution of the secondary phase into coarse sections and solve transport equations for the moments of each section. Two different quadrature rules based on previous literature were implemented.

Keywords: CFD, fluid mechanics, hydrodynamics, two-phase, multi-phase, droplets, films, quadrature, moments, population balance.

NOMENCLATURE

Greek Symbols
α Volume fraction, [-]
β Daugther distribution from breakup, [-]
Γ Breakup kernel, $[1/m^3 \cdot s]$
χ Parameter in equation 11
μ Normalized moment in equations, 11/12
ψ Parameter in equation 11
ρ Density, $[kg/m^3]$
σ Parameter in equation 11

Latin Symbols
a_{rs} Aggregation kernel, $[1/m^3 \cdot s]$
B_k Birth term, $[m^k/m^3 \cdot s]$
d Droplet diameter, [m]
D_k Death term, $[m^k/m^3 \cdot s]$
f_{rs} Discrete aggregation kernel, $[1/m^3 \cdot s]$
M_k Moment of distribution, $[m^k/m^3]$
m_k Moment per fluid mass, $[m^k/kg]$
$\dot{m}_{ji}$ Mass exchange rate between sections, $[kg/m^3 \cdot s]$
n Droplet size distribution, $[(droplets/m^3)/m]$
S Source term
t Time, [s]
u Velocity, [m/s]
w Quadrature weights, $[droplets/m^3]$

Sub/superscripts
a Aggregation
br Breakup
$\overline{()}$ Overbar. Moment of quantity
$cont$ Continuity equation
i Section index
j Index for quadrature point in section
k Moment k

INTRODUCTION

In many multiphase applications the behaviour of the flow is critically dependent on the size of the dispersed phase. Frequently, the use of an average particle size is sufficient for fluid flow simulations. However, there are a number of applications where one should consider the complete particle size distribution. One such application is high pressure gas-liquid separation (scrubbers) where there is a small amount of low surface tension liquid in a gas flow. The motivation for the work in this paper stems from such applications. However, most of the methodology is directly applicable to general multiphase flows.

There are a number of possible strategies for population balance simulations. One way is by treating the dispersed phase as Lagrangian particles and track them throughout the flow field. The Lagrangian approach is particularly applicable in breakup dominated flows, since breakup events are easy to handle in such frameworks. Also aggregation events are possible to handle by counting and computing particle statistics in the numerical mesh. Another approach is to apply a quadrature rule to the integrals occurring in the population balance and track information in an Eulerian fashion. Among such methods are the Method of Classes (Ramkrishna, (2000)); Galerkin methods; the method of Least Squares (Jiang (1998), Dorao and Jakobsen (2005)); Orthogonal Collocation techniques and moment methods (McGraw (1997)). This paper is about the implementation of a particular moment method, the Sectional Quadrature Method of Moments (SQMOM) in FLUENT. The paper is heavily inspired by the work of Attarakih *et. al.* (2009).

The SQMOM method is a hybrid between the Method of Classes and the Quadrature method of Moments (QMOM). In the Method of Classes the particle size distribution is divided into a number of particle classes, each of a narrow size range. Each class is then tracked in an Eulerian fashion. The Method of Classes is straightforward, but requires a large number of classes to be accurate. On the other hand, the QMOM method tracks moments of the complete distribution. Closure is obtained by constructing a quadrature rule from the moments and applying this to the integrals occurring in the population balance equation. The QMOM method is of high order, but tends to become very ill-conditioned when the number of moments is large. The idea behind the SQMOM method is thus to combine the advantages of both methods by dividing the size distributions into coarse classes, denoted "sections", and applying the QMOM method to each section using a low number of moments for each section (typically three to four moments per section).

The paper is organized as follows: First the transport equations for the moments are developed, as well as the SQMOM quadrature rules and source term handling. Then, the implementation of the method as FLUENT User Defined Functions (UDF) is discussed. Finally, an example simulation is shown, followed by a summary/conclusion. We will in the following denote fluid particles as "droplets" although the general framework is also applicable to bubbles or solid particles.

MODEL DESCRIPTION

Droplet distribution

The droplet size distribution at a given point in time and space, $n(d)$, is illustrated in Figure 1. Thus, within an infinitesimal size range between droplet size d [m] and $d+\partial d$ [m], the concentration of droplets is $n(d)\,\partial d$ [droplets/m³].
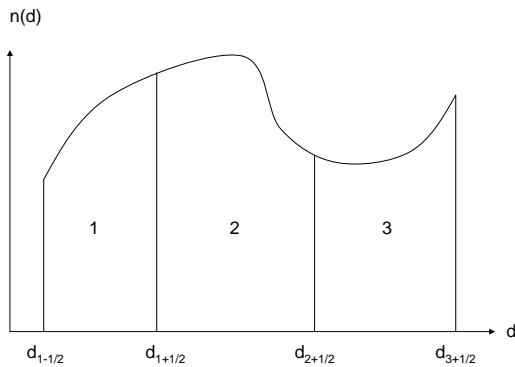
Figure 1: Droplet size distribution.

Three size sections for illustration.

In the SQMOM method, the droplet size distribution is divided into size ranges – called sections – and moments are taken within each of these sections. In this

sense, the SQMOM method is a hybrid between the method of classes and the quadrature method of moments (QMOM). If we use a single moment for each section and a large number of sections we have the method of classes. On the other hand, if we use a single section and a large number of moments for this section we have the QMOM method.

Transport equations

Using the FLUENT Eulerian model, we define each droplet size section as a separate (secondary) Eulerian phase. A transport equation may be written for the droplet size distribution within each section:

$$\frac{\partial n^i}{\partial t} + \nabla \cdot \left(u^i n^i \right) = S^i \tag{1}$$

where n^i is the size distribution within droplet size section i, u^i is the velocity of the section and S^i is a source term resulting from the birth and death of droplets due to breakup and aggregation. Note that the sections have individual velocity fields.

Moments of the distribution

Define moment k of droplet size section i as

$$M_k^i = \int_{d_{i-1/2}}^{d_{i+1/2}} d^k n(d)\,\partial d \tag{2}$$

Thus, for section i:

- M_0^i is the number of droplets per m³,
- the ratio M_1^i / M_0^i is the arithmetic mean droplet size,
- M_2^i is proportional to the droplet surface area per m³ and
- M_3^i is proportional to the volume of droplets per m³ in the section.

In order to fit the format of the FLUENT user-defined-scalar (UDS) equation, it is also useful to define the moment per mass of section "i" (specific moment):

$$m_k^i = \frac{M_k^i}{\rho^i \alpha^i} \tag{3}$$

Note that the third specific moment is simply a constant, and we do not need to solve a transport equation for it (More correctly, the Eulerian mass balances for the secondary phases **are** the transport equations for the third moment).

$$m_3^i = \frac{6}{\pi \rho^i} \tag{4}$$

Also note that the Sauter mean diameter is given as

$$d_{32}^i = \frac{m_3^i}{m_2^i} \tag{5}$$

We also need to define the moment k of the source term in size section i:

$$\bar{S}_k^i = \int_{d_{i-1/2}}^{d_{i+1/2}} d^k S^i \partial d \qquad (6)$$

Moment transport equations

Taking moment k of the transport equation 1 results in

$$\frac{\partial M_k^i}{\partial t} + \nabla \cdot \left(u^i M_k^i \right) = \bar{S}_k^i \qquad (7)$$

Introducing the moments per mass, we can write this in the standard form for a UDS transport equation:

$$\frac{\partial \alpha^i \rho^i m_k^i}{\partial t} + \nabla \cdot \left(\alpha^i \rho^i u^i m_k^i \right) = \bar{S}_k^i \qquad (8)$$

We may also introduce a diffusion term. In the present work, no diffusion has been included.

The SQMOM quadrature rule

In the SQMOM method, a quadrature rule is constructed from the moments. That is, an integral of any function, say $f(d)$, over the droplet distribution in section i is approximated as a discrete sum:

$$\int_i f(d) n(d) \partial d \approx \sum_{j=1}^N f\left(d_j^i \right) w_j^i \qquad (9)$$

For each size section i we thus have discrete droplet sizes d_j^i (j=1,2,3...), and corresponding weights w_j^i. These are constructed by requiring that selected moments M_k^i are preserved, i.e. that for selected k:

$$M_k^i = \int_{d_{i-1/2}}^{d_{i+1/2}} d^k n(d) \partial d = \sum_{j=1}^N \left(d_j^i \right)^k w_j^i \qquad (10)$$

From a modeling/intuitive point of view it is useful to think of the quadrature rule (d_j^i, w_j^i) as a discrete droplet size distribution. That is, we think of the quadrature for size section i as consisting of droplet sizes d_j^i [m], j=1,2,... in concentrations w_j^i [droplets/m^3].

In the current work, two different quadrature rules have been implemented:
- Four-moments per size section. That is, we require that moments M_0^i, M_1^i, M_2^i and M_3^i are preserved. This is a special case of the general N-moment rule.
- The three-moment equal-weight rule by Attarakih *et. al.* (2009). In this quadrature, moments M_0^i, M_1^i and M_3^i are preserved. In this rule, the number of droplets, the arithmetic average droplet size and droplet mass are all conserved, but droplet surface area is not exactly conserved.

The general N-moment quadrature rule may be computed by the algorithm of Wheeler (1974).

However, in the four-moment and three-moment rules above, analytical closed-form expressions for the quadrature rules exist (Attarakih *et. al.* (2009)). The rules are listed in the following.

Four-moment quadrature rule

Analytical formulas for calculating the quadrature in the four-moment case are (From Attarakih *et. al.* (2009)):

$$d_{1,2}^i = -\frac{1}{2}\psi \mp \frac{1}{2}\sqrt{\psi^2 - 4\chi}$$

$$w_{1,2}^i = \left(\frac{\sigma}{\tilde{d} - d_{1,2}} \right)_i^2 \frac{M_0^i}{1 + \left[\sigma / \left[\tilde{d} - d_{1,2} \right] \right]_i^2}$$

where $\qquad\qquad (11)$

$$\psi = \left(\frac{\hat{\mu}_1 \hat{\mu}_2 - \hat{\mu}_3}{\sigma^2} \right)_i, \chi = \left(\frac{\hat{\mu}_1 \hat{\mu}_3 - \hat{\mu}_2^2}{\sigma^2} \right)_i$$

$$\sigma^2 = \left(\hat{\mu}_2 - \hat{\mu}_1^2 \right)_i, \hat{\mu}_k = \frac{M_k^i}{M_0^i}, \tilde{d} = \hat{\mu}_1$$

Three-moment equal-weight rule

Analytical formulas for the three-moment case are (From Attarakih *et. al.* (2009)):

$$d_{1,2}^i = \hat{\mu}_1^i \mp \frac{1}{\sqrt{3}} \sqrt{\frac{\hat{\mu}_3^i}{\hat{\mu}_1^i} - \left(\hat{\mu}_1^i \right)^2}$$

$$w_{1,2}^i = \frac{1}{2} M_0^i \qquad (12)$$

According to Attarakih *et. al.* (2009), the loss in accuracy of using this rule compared to the full four-moment quadrature is minimal.

Source terms

The source term of the droplet transport equation (1) may be written as the sum of four terms, birth and death of droplets due to breakup and coalescence (aggregation)[1]:

$$S = \underbrace{D_{br}}_{\substack{\text{Death by} \\ \text{breakup}}} + \underbrace{B_{br}}_{\substack{\text{Birth by} \\ \text{breakup}}} + \underbrace{D_a}_{\substack{\text{Death by} \\ \text{aggregation}}} + \underbrace{B_a}_{\substack{\text{Birth by} \\ \text{aggregation}}} \qquad (13)$$

The first term is the death of droplets due to droplet breakup, which is assumed to be proportional to the droplet concentration, n, and a breakup frequency, Γ [s^{-1}]. The breakup frequency is a function of the droplet diameter and possibly other quantities like the turbulence intensity.

$$D_{br} = -\Gamma(d) n(d) \qquad (14)$$

Taking the kth moment of this term and applying the quadrature rule we get

---

[1] In some applications growth terms should also be included

$$\bar{D}^i_{br,k} = \int_i d^k \left(-\Gamma(d)n(d)\right)\partial d$$
$$\approx -\sum_{j=1}^{N} \left(d^i_j\right)^k \Gamma\left(d^i_j\right) w^i_j \qquad (15)$$

The second term is the birth by breakup. It is assumed that the daughter particles resulting from a breakup have a size distribution $\beta(d\,|\,d')$ where d' [m] is the diameter of the parent droplet and d [m] is the diameter of a daughter particle. The birth by breakup term for diameter d is thus found by integrating over all larger particles d'.

$$B_{br} = \int_d^{\infty} \Gamma(d')\beta(d\,|\,d')n(d')\partial d' \qquad (16)$$

Taking the k'th moment and interchanging the order of the integrals:

$$\bar{B}^i_{br,k} = \int_i d^k \left(\int_d^{\infty} \Gamma(d')\beta(d\,|\,d')n(d')\partial d'\right)\partial d =$$
$$\int_{d_{i-1/2}}^{\infty} \Gamma(d')\left(\int_{d_{i-1/2}}^{\min(d_{i+1/2},d')} d^k\beta(d\,|\,d')\partial d\right)n(d')\partial d' \qquad (17)$$

We thus define the moments of the daughter distribution

$$\bar{\beta}^i_k(d') = \int_{d_{i-1/2}}^{\min(d_{i+1/2},d')} d^k\beta(d\,|\,d')\partial d , \qquad (18)$$

and apply the quadrature rule to get

$$\bar{B}^i_{br,k} = \sum_{q=i}^{N_{sections}} \left(\sum_{j=1}^{N} \Gamma\left(d^q_j\right)\bar{\beta}^i_k\left(d^q_j\right)w^q_j\right) \qquad (19)$$

When it comes to aggregation/coalescence of droplets, it is possible to write a closed form expression for these terms in terms of the quadrature points and weights, as described in Attarakih *et. al.* (2009). Alternatively, we may think of the quadrature rule as a discrete droplet size distribution and compute the aggregation terms by considering all pairs of droplet sizes in this distribution. The latter is closer to the way that the aggregation term is actually implemented, so this is what is described here:

1. For each section, define vectors for the quadrature points and weights, where N is the number of quadrature points per section.

$$\mathbf{d}^i = [d^i_1, d^i_2, \ldots d^i_N]$$
$$\mathbf{w}^i = [w^i_1, w^i_2, \ldots w^i_N] \qquad (20)$$

2. Stack the quadrature points for all sections into global vectors

$$\mathbf{d}' = [\mathbf{d}^1, \mathbf{d}^2 \ldots \mathbf{d}^{Nsections}]$$
$$\mathbf{w}' = [\mathbf{w}^1, \mathbf{w}^2 \ldots \mathbf{w}^{Nsections}] \qquad (21)$$

3. Pick all pairs of droplets d'_r, d'_s from these global vectors where $s \geq r$. The rate of aggregation of these droplets are

$$f^a_{rs} = \begin{cases} \dfrac{1}{2} a_{rs} w'_r w'_s & s = r \\[2mm] a_{rs} w'_r w'_s & s > r \end{cases} \qquad (22)$$

where a_{rs} is the aggregation kernel for droplet pairs of sizes d'_r and d'_s.

4. For moment k: Subtract $\left(d'_r\right)^k f^a_{rs}$ from the source term of the section that d'_r belongs to, subtract $\left(d'_s\right)^k f^a_{rs}$ from the section that d'_s belongs to, and add $\left(d'_{r+s}\right)^k f^a_{rs}$ to the section that the combined particle
$$d'_{r+s} = \left(d'^3_r + d'^3_s\right)^{1/3} \text{ belongs to.}$$

The section mass balance (continuity)

The mass balance for section i may be written as

$$\frac{\partial \alpha^i \rho^i}{\partial t} + \nabla \cdot \left(\alpha^i \rho^i u^i\right) = \sum_{j=1}^{N} \left(\dot{m}_{ji} - \dot{m}_{ij}\right) + S^i_{cont} \qquad (23)$$

This equation and the interaction with the momentum equation are handled automatically by the Eulerian model in FLUENT. However, we need to provide functions for the mass exchange terms, $\dot{m}_{ij}$, from phase i to phase j. The mass exchange is related to the third moment as:

$$\sum_{j=1}^{N} \left(\dot{m}_{ji} - \dot{m}_{ij}\right) = \frac{\pi}{6} \rho^i \bar{S}^i_3 \qquad (24)$$

Thus, contributions to the mass exchange terms are easily calculated together with the computation of the moment source terms as long as one is careful to keep track of the direction of the mass exchange.

IMPLEMENTATION DETAILS

There are a number of FLUENT User Defined Functions (UDF) involved, which are described in the following:

-   One secondary phase is defined for each size section.
-   For each size section, one User Defined Scalar equation (UDS) is defined for each moment that is tracked, except for the third moment which is handled by the mass balance (continuity). For example, for the four-moment quadrature we thus need three UDS equations per section.
-   The system is solved by time stepping (transient).
-   A DEFINE_ADJUST calculates the quadratures, the mass exchange terms and the

source terms once at the start of each time step. Apart from efficiency, we are thus sure that we compute the quadrature based on consistent/converged moments. The results are written into User Defined Memory (UDM) in linear form as coefficients Sc and Sp where the source terms are defined as S(M)=Sc+Sp·M. However, by default we simply use Sp=0, which has proved to work satisfactorily.

- A DEFINE_MASS_TRANSFER routine for the mass balance returns the appropriate m_{ij} by fetching the value from User Defined Memory.

- A common DEFINE_SOURCE routine for all the moment equations. The equation number is used for identifying which is the current equation and the appropriate value is fetched from User Memory.

- The breakup and aggregation kernels $\Gamma(d)$ and $a(d)$ and the daughter distribution $\beta(d|d')$ are made as separate routines considered to be user input for the particular system to be modeled. That is, it is up to the user to code the appropriate kernels.

EXAMPLE CALCULATION

As an example, we simulate the flow in a simple backward-facing step geometry, as shown in Figure 2. The purpose is just to demonstrate the methodology; the geometry is not taken from any particular application.
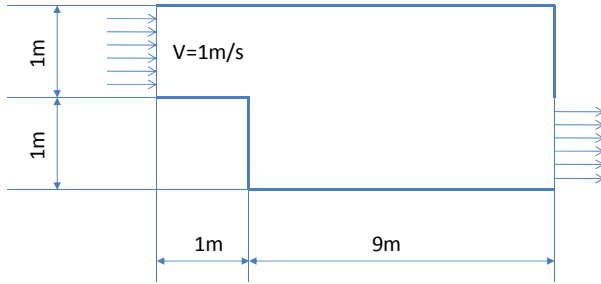
Figure 2: Backward facing step geometry for example (Not in scale).

Assumptions:
- Two droplet size sections, "section 1"=[0-0.5mm] and "section 2"=[0.5-1.0mm]
- Breakup kernel $\Gamma(d)=kd^3$ with k=1 [mm^{-3}s^{-1}] and aggregation kernel a=0 (no aggregation).
- The daughter distribution from breakup is taken from the example by Attarakih *et. al.* (2009).

$$\beta(d \mid d') = \frac{6d^2}{d'^3} \qquad (25)$$

- Input volume fractions 1% of "section 1" and 1% of "section 2".
- Flat inlet droplet size distributions within each section, i.e. inlet $n(d)=c_1$ within "section 1" and $n(d)=c_2$ within "section 2". The constants are determined by requiring the 1% inlet volume fractions above. The moments from this distribution was used both as inlet boundary conditions and for initializing the flow domain.
- Inlet flow velocity 1 m/s, turbulence intensity 10% and using the mixture k-ε model.
- No gravity. In a real application, one would normally turn gravity on.

Using the three-moment quadrature, the system was simulated for 200 seconds which corresponds to about 10 times the residence time.

Some results are presented in the following. The plots are chosen for the purpose of demonstration, and the plots show more or less the moments themselves:
- Number of droplets per m^3 for a section. This is the zeroth moment M_0.
- The arithmetic average particle diameter is simply the ratio of the first and zeroth moments, M_1/M_0.
- The volume fraction of a section is proportional to the third moment.

The plots are in terms of the physical interpretations.

Figure 3 shows the calculated flow field at t=200 sec. The flow looks as expected, with a recirculation zone behind the step.
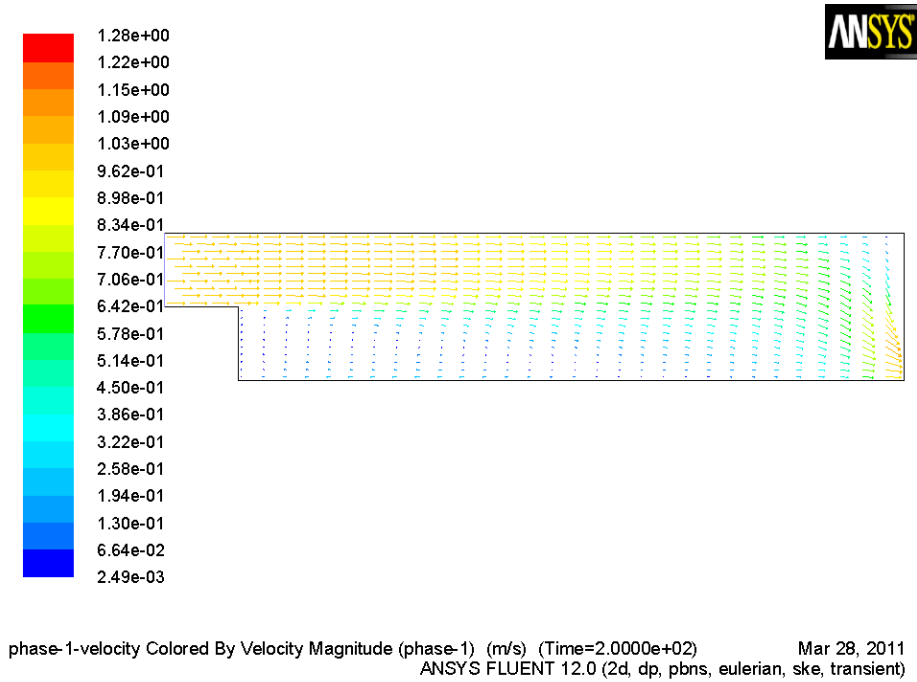
Figure 3: Mixture velocity field [m/s].

Figure 4 shows the volume fraction of droplets in "section 1", which is the [0-0.5mm] droplet range. There is an accumulation of the size range behind the step.
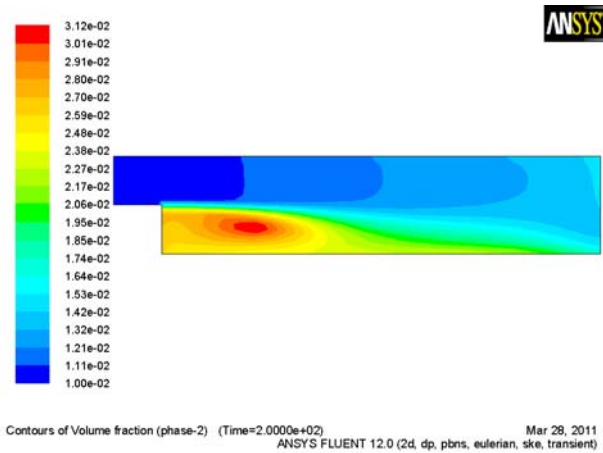
Figure 4: Volume fraction of section 1 (0-0.5mm size range).

Figure 5 shows the number of droplets of "section 1" ([0-0.5mm]) per m^3. This shows the same trend, there is an accumulation of this size range behind the step.
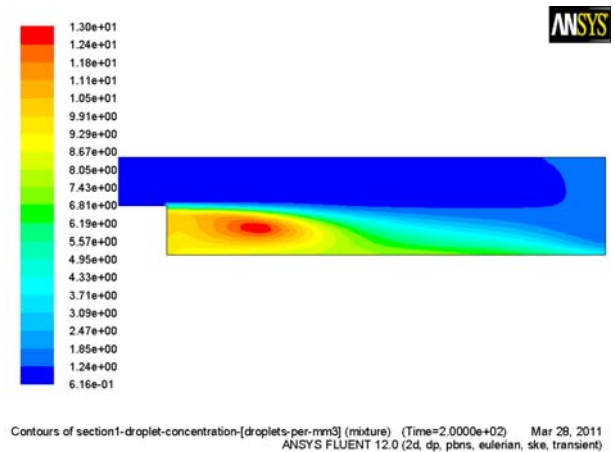
Figure 5: Number of section 1 (0-0.5mm) droplets per mm^3.

Figure 6 shows the arithmetic mean droplet size of "section 1" ([0-0.5mm]). At the inlet, the arithmetic mean size is 0.25 mm as expected due to assumption of flat $n(d)$-distribution within the size range. Due to droplet breakup, the arithmetic mean size is lower behind the step.
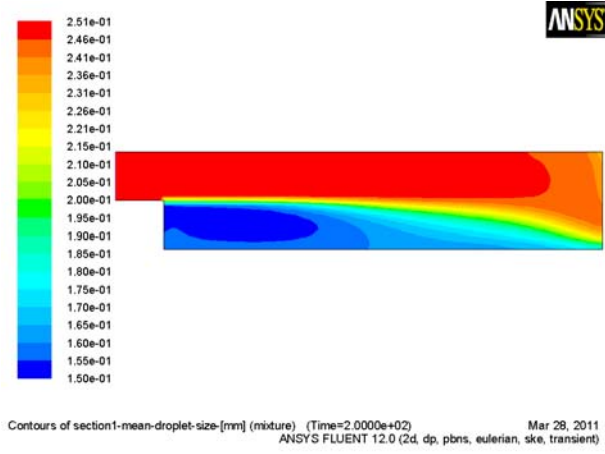
Figure 6: Arithmetic mean droplet size [mm] for section 1 .

Figure 7 shows the volume fraction of "section 2", which is the [0.5-1.0mm] droplet range. The volume fraction of the size range is decreasing along the flow due to breakup (mass transfer to "section 1").
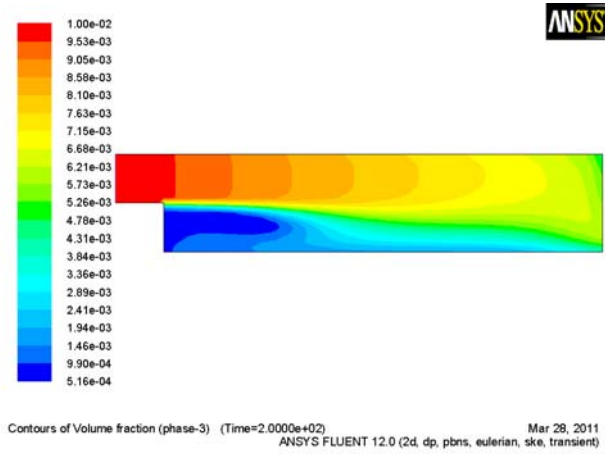
Figure 7: Volume fraction of section 2 (0.5-1.0mm range).

Figure 8 shows the number of droplets of "section 2" ([0.5-1.0mm]) per m^3. It is interesting that the number of droplets in this size range is actually *increasing* along the flow right after the inlet. With hindsight, this is understandable, since many of the initial droplet breakups in the size range ends up as smaller droplets in the same size range. We will get an increase as long as the birth rate of daughter particles in "section 2" is larger than the death rate of their parents, i.e. as long as

$$\int_{0.5mm}^{1.0mm} \Gamma(d)\,\overline{\beta}_0^2\,n(d)\,\partial d > \int_{0.5mm}^{1.0mm} \Gamma(d)\,n(d)\,\partial d \quad (26)$$

$\underbrace{\phantom{\int_{0.5mm}^{1.0mm} \Gamma(d)\,\overline{\beta}_0^2\,n(d)\,\partial d}}_{\substack{\text{Birth rate of daughter particles} \\ \text{in "section 2" due to breakup}}}$ $\underbrace{\phantom{\int_{0.5mm}^{1.0mm} \Gamma(d)\,n(d)\,\partial d}}_{\substack{\text{Death rate of particles in} \\ \text{"section 2" due to breakup}}}$

It is a simple exercise to show that this is indeed the case for the inlet size distribution in this example.
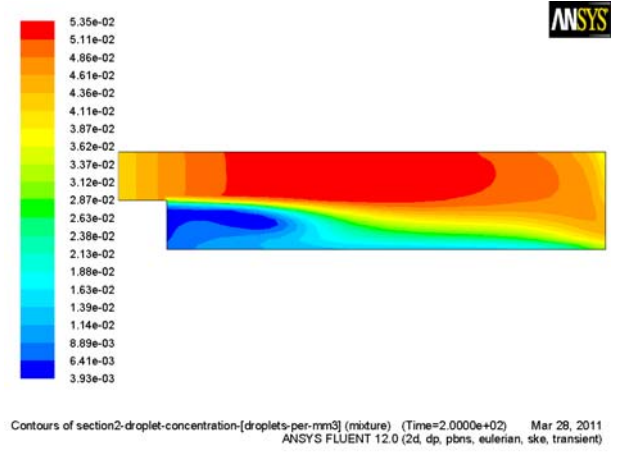
Figure 8: Number of section 2 (0.5-1.0mm) droplets per mm^3.

Figure 9 shows the arithmetic mean droplet size of "section 2" ([0.5-1.0mm]). At the inlet, the arithmetic mean size is 0.75 mm as expected due to assumption of flat n(d)-distribution within the size range. Due to droplet breakup, the arithmetic mean size of the size range is decreasing along the flow.
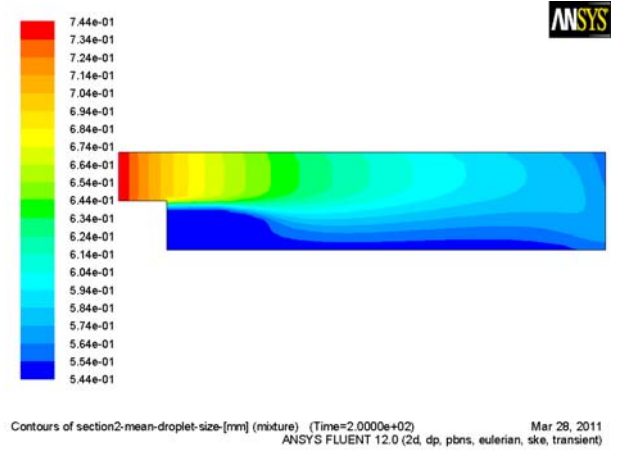
Figure 9: Arithmetic mean droplet size [mm] for section 2 .

Finally, Figure 10 shows the mass transfer from "section 2" ([0.5-1.0mm] size range) to "section 1" ([0-0.5mm] size range). It is interesting to note that the mass transfer rate does actually have a maximum inside the domain. Initially, a substantial part of droplet breakup in "section 2" ends up as smaller droplets in the same size range and thus is not transferred to "section 1". Further breakup eventually ends up in "section 1".
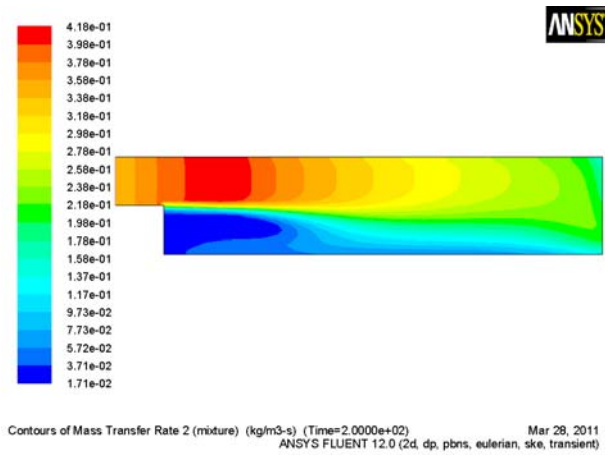
Figure 10: Mass transfer rate $[kg/m^3 \cdot s]$ from section 2 to section 1.

DISCUSSION

The FLUENT 12.0 default solver appears to solve the SQMOM equations without difficulties when using a time stepping scheme. However, there are some important details/observations:

- The three-moment quadrature appears to be much more robust/stable than the four-moment quadrature for the example case.
- It is essential to compute the quadrature based on consistent/converged moments. The only possibility is thus to compute at the beginning of each time step. If the moments are not converged, it is likely that the code will take the square root of a negative number when computing quadratures. The source terms may be linearized for improved stability, but constant values worked satisfactorily for the example case.
- By looking at the expression for the three-moment quadrature of Attarakih *et. al.* (2009), it is clear that the quadrature points for a section may fall outside the size range of a section even for a valid size distribution. This is not necessarily a problem for smooth kernels, but one should guard against negative values for the first section (Negative diameters were never observed in the test runs, but it is easy to construct examples where this could happen).
- It is wise to scale the moment equations for better numerical properties. In the current case, we have used mm-units for the droplet size distribution and m-units for the flow. That is, we use d [mm], w [droplets/mm^3] and n [(droplets/m^3)/mm].

CONCLUSION

An implementation of the Sequential Method of Moments (SQMOM) has been made in FLUENT 12.0. Two different quadrature rules based on the article by Attarakih *et. al.* (2009) were implemented, one conserving the first four moments M_0, M_1, M_2 and M_3 and the other conserving the three moments M_0, M_1 and M_3. Thus, both quadratures conserve mass.

The three-moment quadrature appears to be much more robust than the four-moment quadrature.

The implementation appears to work properly as long as one ensures that the moments are properly converged at one time step before proceeding to the next. Attempts to compute the quadrature based on poorly converged moments are not recommended.

REFERENCES

ATTARAKIH, M.M., BART, H.J., and FAQIR, N.M. (2004), "Numerical solution of the spatially distributed population balance equation describing the hydrodynamics of interacting liquid-liquid dispersions", *Chemical Engineering Science*, **59**, 2567-2592.

ATTARAKIH, M.M., DRUMM, C. and BART, H.J., (2009), "Solution of the population balance equation using the sectional quadrature method of moments (SQMOM)", *Chemical Engineering Science*, **64**, 742-752.

DORAO, C.A. and JAKOBSEN, H.A. (2005), Application of the least square method to population balance problems. *Computers and Chemical Engineering*, **30**, 535-547.

JIANG, B. (1998), The Least-Square Finite Element Method: Theory and Applications in Computational Fluid Dynamics and Electromagnetics. Springer, Berlin. ISBN 3-540-63934-9.

MARCHISIO, D.L., VIGIL, R.D. and FOX, R.O. (2003). "Implementation of the quadrature method of moments in CFD codes for aggregation–breakage problems". *Chemical Engineering Science*, **58**, 3337 – 3351.

McGRAW, R. (1997), "Description of aerosol dynamics by the quadrature method of moments", *Aerosol Science and Technology*, **27**, 255-265.

RAMKRISHNA, D. (2000), Population balance-Theory and Applications to Particulate Processes in Engineering. Academic Press, San Diego.

WHEELER, J.C., (1974), "Modified moments and Gaussian quadratures", *Rocky Mountain Journal of Mathematics*, **4**, 287-296.

8th International Conference on CFD in Oil & Gas, Metallurgical and Process Industries
SINTEF/NTNU, Trondheim Norway
21-23 June 2011

CFD11-155

DE-MIXING OF BINARY PARTICLE MIXTURES DURING UNLOADING OF A V-BLENDER

Gerald G. PEREIRA[*], **Paul W. CLEARY**

CSIRO Mathematics, Informatics and Statistics, Private Bag 33, Clayton South, AUSTRALIA

* E-mail: Gerald.Pereira@csiro.au

ABSTRACT

The V-blender is an industrial batch mixing device which is used to blend granular mixtures in the food, household products and pharmaceuticals industries. The mixing characteristics of this device have been previously studied experimentally and numerically using the Discrete Element Method (DEM). When emptying the device de-mixing of this granular mixture occurs due to segregation produced by the flow. This reverses some fraction of the mixing produced by the blender. In this study we consider the de-mixing that occurs when the particles flow out of the device. We begin with close to a perfectly mixed state and measure the change in particle homogeneity during discharge. In this initial study we consider only the simplest case of a binary mixture with components only differing by size. The extent of de-mixing is evaluated as a function of the size ratio of the mixture components. Different unloading scenarios are considered.

Keywords: DEM, segregation, de-mixing, unloading.

INTRODUCTION

Mixing and segregation in granular media is not only of fundamental scientific interest in itself but also has a myriad of industrial applications that range from pharmaceuticals, food processing, plastics and household products. In some applications mixing is required and the quality of the final product depends on the degree of mixing of the constituent materials. In other cases, separation of granular materials according to some material property is desirable.

Computer modelling of granular media can be advantageous in understanding the flow within a processing device and hence optimizing its efficiency. The discrete element method (DEM) technique is now established as a useful simulation tool that can provide detailed information not easily measured in experiments.

The V-blender is a batch mixing device where each arm has a cylindrical cross-section (Cleary and Sinnott, 2008). There is typically an access port at the bottom of the V-blender for filling and discharge of the particulates. The V-blender normally rotates about a horizontal axis passing through the middle of the device and mixing of particles occurs in the ensuing shearing bulk flow. A snap-shot of a typical V-blender geometry is show in Fig. 1. Figure 1a is in the *y-z* plane, with the gravity vector pointing in the negative *y* direction. Figure 1b rotates the V-blender so that we are looking down one of the arm's axis.

Discrete Element Method (DEM) studies of the mixing flow in the V-blender have previously been considered in some detail (Kuo *et al.*, 2002, Cleary and Sinnott, 2008). Kuo *et al.* (2002) validated their DEM models against positron emission particle tracking (PEPT) measurements and observed the flow exhibited two phases: a separation phase as material splits into two streams and flows along the arms of the V-blender and a re-combination phase where the streams come together at the bottom of the blender. They showed that mass transfer from one arm to the other occurs during separation of the streams. Cleary and Sinnott (2008) considered the critical issue of scale up from the laboratory scale (1.864 litre blender) to the process scale (210 litre blender). They found mixing time increased as the V-blender size increased (by a factor of 3.78 from lab scale to process scale).
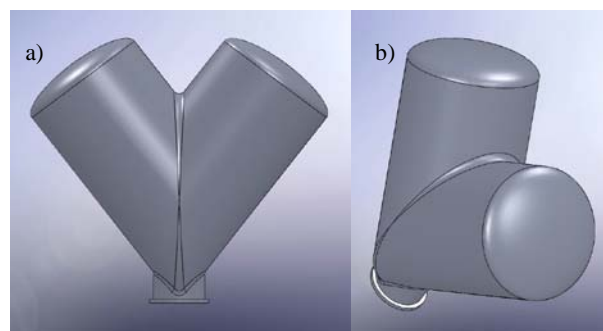
Figure 1: Snap-shots of V-blender. a) Front on and b) down an axis of one of the cylindrical arms.

After the mixing process is complete, the V-blender is emptied through the bottom exit port by removing the cover. In this emptying process, de-mixing can occur due to either the shear during flow within the V-blender and/or due to flow into the collection device. In this paper, we explore the degree of de-mixing that occurs in both parts of the discharge process. Initially, we consider the case of de-mixing just due to discharge from the V-blender and subsequently we consider the de-mixing due to two different collection procedures. The first collection procedure is collection in a cylindrical container placed directly under the exit port while the second collection procedure is via a flat, sloping chute into a cylindrical container. These two procedures are (probably) the most common one can implement and we should be able to infer important characteristics of de-mixing from them. Another

important aspect of the de-mixing process is how the degree of de-mixing varies with particle size. To understand this we focus only on binary sized particles and vary the size ratio between simulations.

MODEL DESCRIPTION

We use the Discrete Element Method (DEM) to model the flow of particles out of the V-blender and into the collection and transfer devices. DEM models particulate systems whose motions are dominated by collisions. It follows the motion of every particle or object in the flow and models each collision between the particles and between the particles and their environment (such as the blender). This study is performed using the DEM code described in Cleary (2004, 2009).

Simulation Parameters

We are interested here in coarse mm scale particles, which are representative of some foods, grains, household products and some plastic feed stocks. It is well known that particles segregate based on differences in size, density or shape (Rosato *et al.*, 1988, Ottino and Khakhar, 2000). Here we will concentrate on particles which differ in size. Furthermore, although in general there will be a continuous distribution of particle sizes, we will explore a simple system considering only a binary mixture of particle sizes (with equal volumes of each type of particle). The particles are spherical in shape, have a mean size of 2.75 mm and the ratio of sizes of each constituent varies from 1.75 up to 4 (see Table 1 for number of particles and size ratios). The particle density is 1500 kg/m^3 and the blender is initially filled to 50% of its volume. We simulate a laboratory scale V-blender which has an arm length of 0.23 m and an internal volume of 1.864 litres with a vertex angle of 75 degrees. This means the mass of particles in the mixer is around 0.78 kg. The coefficients of restitution are 0.7 for particle-particle collisions and 0.85 for particle-wall (steel) collisions. The friction coefficient was 0.5 for particle-particle contacts and 0.4 for particle-wall contacts. The spring stiffness used was 1000 N/m. In each of the simulation cases discussed in the following sections we initially have to fill the V-blender. This is done by rapid filling (from a virtual inflow) and takes an initial 0.8 seconds. All our quantitative measures begin from the start of the filling period and we can check, with our mixing measures, that the mixture is comparatively homogenous at the beginning of the outflow from the V-blender.

Simulation Measures

We use a variety of measures to quantify the degree of segregation during the outflow of granular particles from the V-blender. Specifically:

Qualitative pictures: The DEM technique constantly updates all the particles' positions and velocities. By colouring particles according to their radius we can obtain a qualitative picture of the amount of de-mixing during the flow out of the V-blender.

Sample Planes: We can place sample planes at various positions to monitor the types, velocities and numbers of particles flowing through these locations.

Centroids: We measure the centre of mass (or centroid) of each type of particle throughout each simulation. Each component (*x, y, z*) of the centre-of-mass can be independently evaluated and the degree of separation of these components, for each particle type, yields information on the amount of segregation.

Homogeneity mixing measure: This quantitative measure of segregation involves looking at the distribution of local averages of the particle radius. This is done using a small characteristic volume at an array of locations throughout the domain. If the binary mixture is perfectly mixed then the distribution is a uni-modal Gaussian peaked at the mass weighted average of the particles. If the particles are completely de-mixed, then the distribution is bi-modal with peaks centered on the radius of each particle type. The segregation state that is computed falls between these two limits. The theory behind this measure can be found in Cleary (1998). It differs from the earlier measures in that it does not depend on any spatial direction just measuring the local homogeneity of the particle mixture.

CASE 1: FLOW OUT OF V-BLENDER

We first consider the flow out of the V-blender without any collection apparatus. This allows us to quantify segregation purely arising from the flow within the V-blender and when discharging through the exit port. For this case we have considered four different size ratios.

Figure 2 displays the particle distributions for a size ratio of 1.75. In this case the particles sizes are 2 mm and 3.5 mm. According to our homogeneous mixing measure, at the beginning of the outflow the mixture is perfectly mixed. After the first 0.7 seconds (Fig. 2a) of discharge the mixture appears to have not de-mixed to any significant extent. There appears to be a small excess of larger (red) particles on the top (free) surface. After a further 1.8 seconds (and close to the end of the outflow, Fig. 2b) the remaining mixture appears to be only marginally de-mixed, with larger particles predominantly in the centre of the outflow stream.

Fig. 3a shows the *y*-component of the centroid location for the two sizes of particles. It decreases continuously with time as the particles discharge and the remaining particles are progressively lower in the domain. There is a small but observable difference in centroid position between the two particle types, with the smaller particles (black curve) slightly below the one for the larger particles (green curve), except at the very end. This indicates that the finer particles are on average lower in the system and that there is a small amount of de-mixing of the different particle types during outflow. The mass flow rate data for the upper sample plane (just under the V-blender exit) is shown in Fig. 3b. It indicates that the smaller particles discharge at a faster rate than the larger particles for much of the emptying process. Towards the end when the supply of remaining finer particles is dwindling, the mass flow rate of coarser particles then dominates. This is in keeping with Fig. 2, which shows larger particles had collected at the top of the particle bed during emptying. The sample planes data for the

second sample plane, which is 6 cm below the first sample plane, shows similar characteristics. The average outflow rate for this ratio is 0.32 kg/s and is the smallest of all the size ratios (see Table 1).
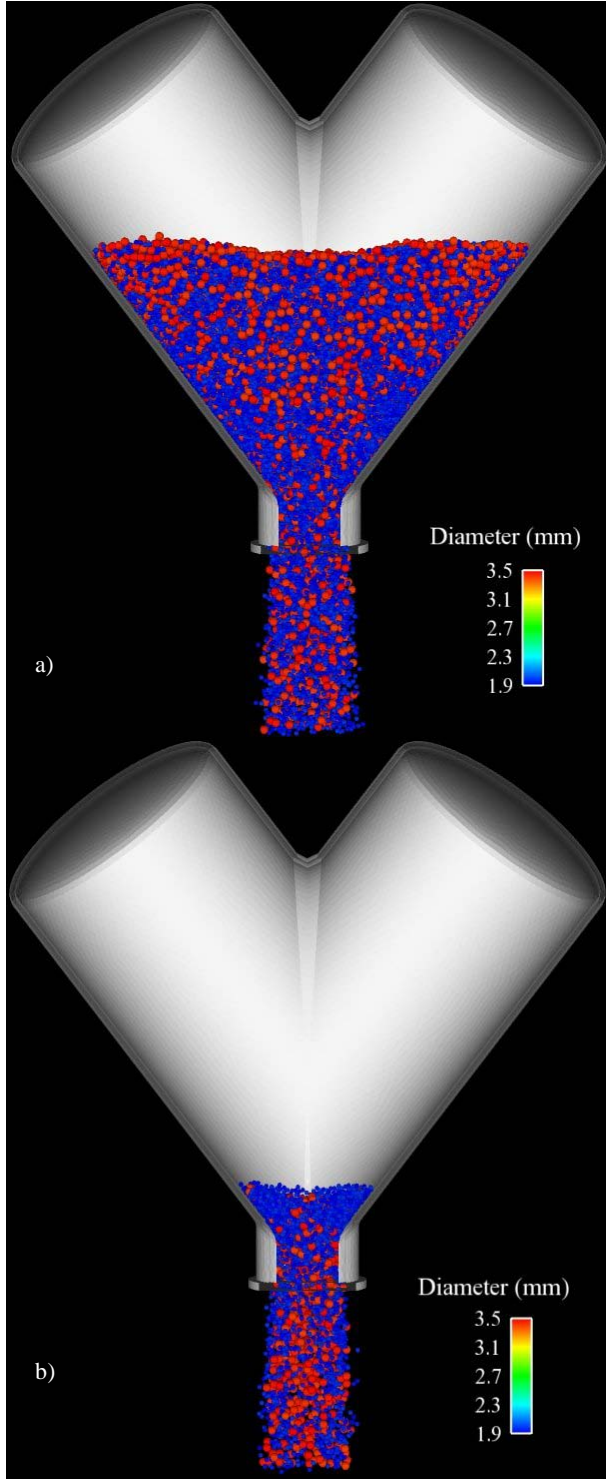
Figure 2: Discharge from the V-blender for a size ratio of 1.75. Smaller particles are coloured blue while larger particles are coloured red. After (a) 0.7 s of outflow, and (b) 2.5 s of outflow.

Next we consider outflow for largest of the particle size ratios. Figure 4 shows snapshots of the particle distribution at two times during the outflow. Here light blue represents the smaller particles while red represents the larger particles. After the first 0.5 seconds of outflow (Fig. 4a), we observe that a layer of larger particles has

accumulated at the top surface. During the remainder of the outflow this process continues and by approximately 1.5 seconds of outflow (Fig. 4b) the larger particles form a distinct layer at the top and in the centre of the outflow stream.
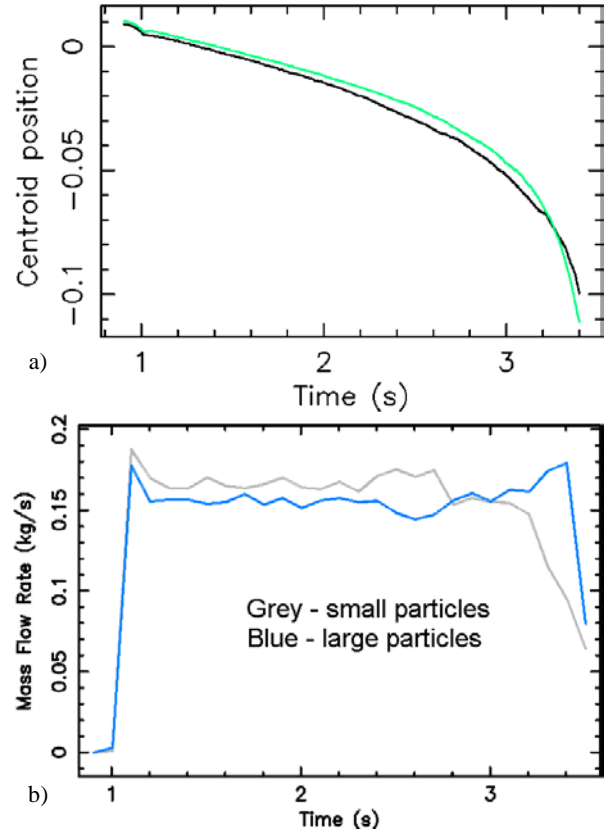
Figure 3: a) *Y*-component of centroid position of large (green) and small (black) particles as a function of time, and b) mass flow rate through the upper sample plane as a function of time.

The segregation process occurring here is related to particle size and commonly occurs in granular media with differing particle sizes. For example see Pereira *et al.* (2011) where segregation due to percolation was observed in the shearing avalanching layer of a binary granular mixture placed in a slowly rotating drum. This *percolation* mechanism occurs generally when small particles slip through the voids created by the larger particles. As a result, a layering of particles occurs with smaller particles found, in larger concentration, lower in the bed and larger particles found higher in the bed. As the emptying proceeds the top surface becomes inclined towards the discharge port. As particles roll down this sloped surface, the smaller (blue) particles can easily percolate down through the gaps (interstitial voids) between the larger particles. As a result, larger particles segregate to the top of the mixture while smaller particles become more concentrated underneath. This mechanism becomes stronger and faster as the particle size-ratio increases which explains what we have observed in these two cases. This leads to a high concentration of large particles on the free surface directly above the exit hole. Hence the larger particles are funnelled through the middle of the outflow stream, as observed in Fig. 4b.
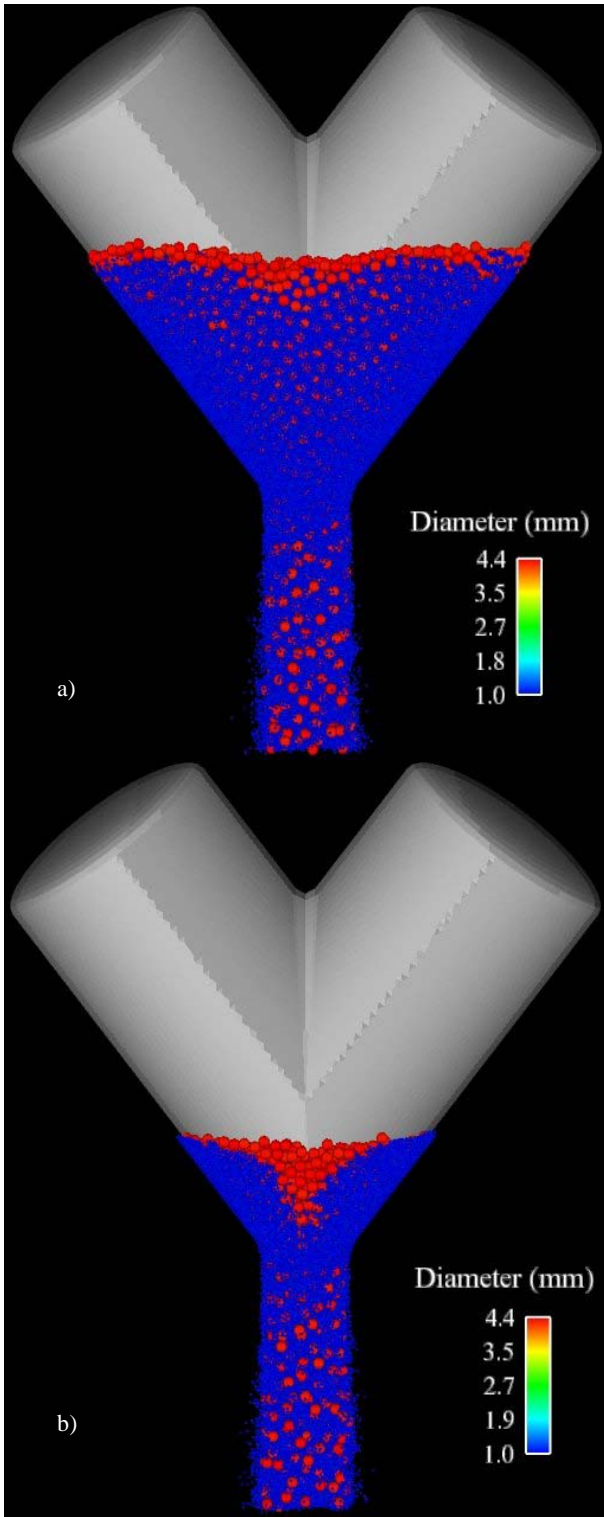
Figure 4: Discharge from the V-blender for size ratio of 4. Smaller particles are coloured light blue while larger particles are coloured red. After (a) 0.5 s of outflow, and (b) 1.5 s of outflow.

The mass flow rates for this case are shown in Fig. 5. The smaller particles (grey curve) again pass through the sample planes faster in the early stages of the outflow. The larger particle flow rate (blue curve) is again only highest once the fine particles are substantially removed from the blender and the large particle rich region of particles at the top of the bed reach the discharge port and flow out. This agrees with the percolation mechanism for de-mixing, since the smaller particles are found lower in the particle bed and hence closer to the

exit. The flow rate difference between the two particle sizes has increased from (on average) 0.32 kg/s, for the simulation with a particle size ratio of 1.75 to 0.45 kg/s for the simulation for a particle size ratio of 4. The discharge time is shorter at 2.1 s for the size ratio of 4 than for the size ratio of 1.75 which was 2.7 s. Table 1 shows that there is a gradual decrease in the discharge time (and correspondingly an increase in flow rate) as the particle size ratio increases. This is likely to be due to the ability of particles to rearrange within the entrance the outflow stream and flow out of the exit. For very small particles this is much easier than for large particles. In general, the discharge process for large size ratio leads to greater de-mixing.
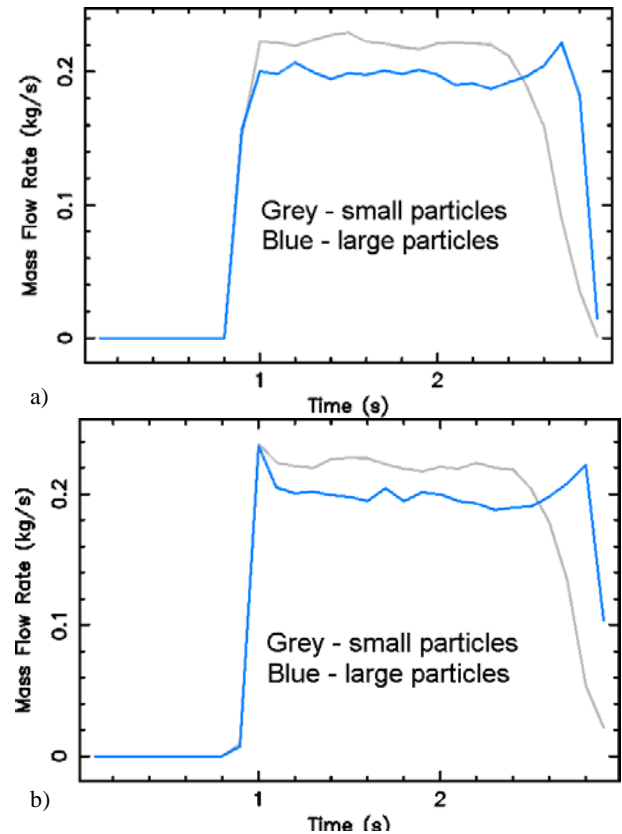
Figure 5: a) Mass flow rate through the upper sample plane as a function of time. b) Same as a) but for lower sample plane (6 cm below upper plane).

The homogenous measure quantifies the degree of de-mixing for all the particles in the simulation domain. As emptying progresses, the number of particles present decreases until the end when there are no particles remaining. The homogenous measure for the four particles size ratios are given in Table 2. This data is taken near the end of the simulation, where there are not many particles left, so there is a large statistical fluctuation, but to be consistent with other cases, we have decided this is the best time to compare this measure. There is an increase in the segregation percentage with increasing size ratio (from 1.75 to 4), although the decrease from 3 to 4 is probably not a systematic trend but more due to the small number of particles sampled. However, as will become apparent later, these segregation percentages are quite low.

Table 1: Number of particles**,** outflow time and outflow rate for the various particle size ratios simulated.

Size ratio	1.75	2	3	4
# particles	8×10^4	9.3×10^4	2.1×10^5	4.3×10^5
Outflow time (s)	2.8	2.6	2.2	2.1
Flow rate (kg/s)	0.32	0.33	0.38	0.45

In this case, where only the flow within the blender is considered, de-mixing is due to percolation of small particles through the shear flow that occurs along the sloping upper surfaces of the bed. This effect increases with increasing particle size ratio.

Table 2: Homogenous segregation measure, as a percentage where 0% corresponds to well mixed and 100% corresponds to completely segregated, for all the cases simulated.

Particle size ratio	No collector	Cylindrical collector	Chute into cylinder
1.75	.5	14	17
2	1	22	50
3	45	76	99
4	26	86	97

CASE 2: FLOW INTO CYLINDRICAL VESSEL

We next consider flow from the V-blender into a cylindrical container directly under the exit. The radius of cylindrical container is 15 cm and its bottom is 11 cm below the exit of the V-blender. Four particle size ratios from 1.75 to 4 were again considered. Fig. 6 shows the particle distributions at different times for the size ratio of 2. During the first 0.9 seconds of outflow (Fig. 6a) a small heap of particles forms below the V-blender exit. While the heap is small it does not show a significant amount of de-mixing. In contrast to the de-mixing due to percolation within the blender, which is due to percolation in the shearing layer, the initial formation of the heap occurs with a large amount of energy being dissipated which randomly re-arranges the particle distribution. Hence, the particles in the heap remain relatively well mixed.

Once a large heap has been established (Fig. 6b), particles no longer collide and rebound from the cylinder base, but rather fall into the heap, where they collide with other particles, dissipate their incoming kinetic energy and push other particles down the free surface slope. Small particles in this avalanching flow will also percolate through the avalanche layer, concentrating larger particles (red) along or near the upper surface. As discharge progresses and the heap becomes larger, the avalanching region that produces segregation increases in length leading to increasing segregation. Hence, during the later stages of the discharge process de-mixing in the collection container increases. When the blender is empty (Fig. 6c) the final heap shows that a reasonable amount of de-mixing has occurred, with more large particles on the upper surface.
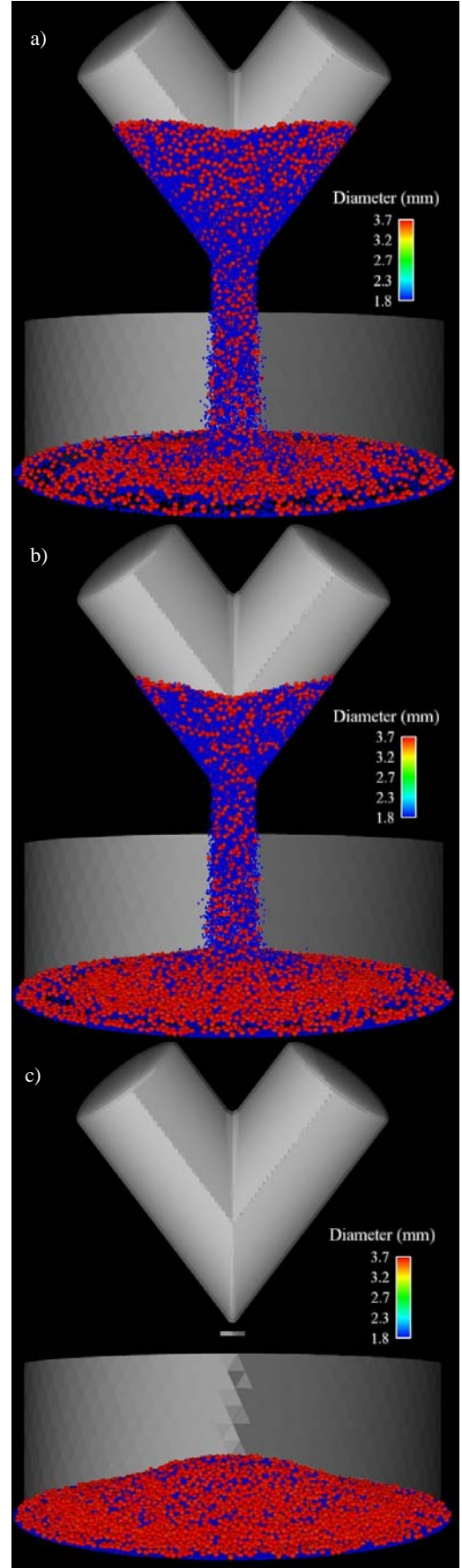
Figure 6: Flow out of V-blender into a cylindrical container for a particle size ratio of 2 at three different stages during the emptying process. Smaller particles are coloured blue while larger particles are coloured red. After outflow of (a) 0.9 s, (b) 1.8 s, and (c) 3.5 s .

Figure 7a shows the relative *y*-component of the centroid for both particle sizes over time. The overall *y*-component of centre-of-mass of all particles was subtracted from the centroids of each set of particles to give a relative displacement. The relative centroids both start at zero and have a zero difference since the material is initially well mixed. Once the outflow begins, (after 0.8 s) the difference between the relative centroids increases. This is due to the percolation mechanism occurring in the flow within the V-blender. Once the particles have formed a heap in the cylindrical container, further de-mixing occurs also due to percolation of particles flowing down the heap surface. The maximum amount of separation between the two curves is only about 11 mm or about 4 average particle diameters.

Figure 7b shows the homogeneity measure as a function of time. It correlates quite well with the centroid measure with an increase in degree of segregation (de-mixing) once the outflow begins. The amount of segregation becomes constant once the flow out of the V-blender has ceased. The amount of segregation once all flow has ceased is 21%.
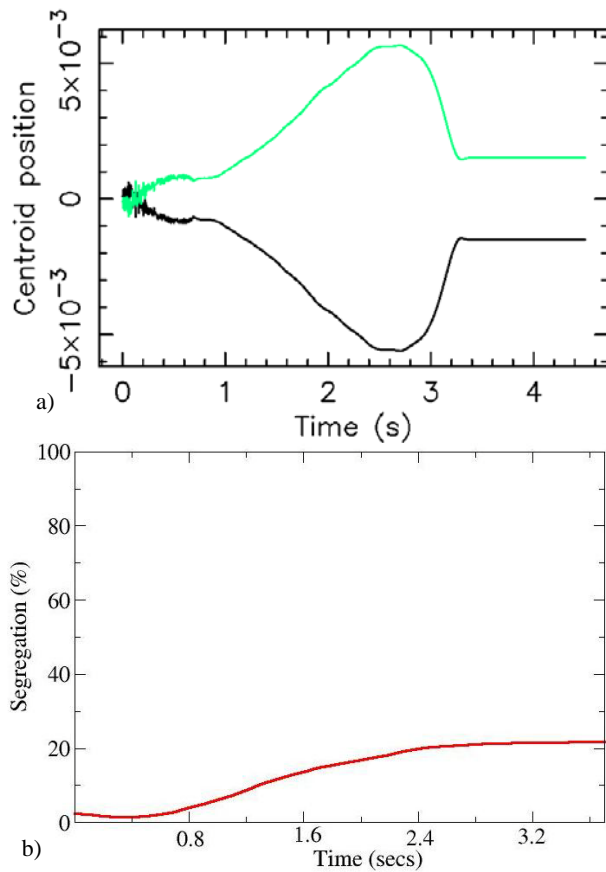
Figure 7 a) Relative *Y*-centroid position for the outflow into a container for a particle size ratio of 2. Larger particles are shown by the green curve and black corresponds to the smaller particles. b) Homogeneity measure for size ratio of 2. The first 0.8 s is for filling the V-blender. Outflow begins at 0.8 s.

Figure 8 shows the particle distribution at three different times during the outflow for a size ratio of 4. The initial distribution of particles is partially de-mixed. In fact from our homogenous mixing measure (see Fig. 9) it is around 15% at 0.8 s (at the beginning of outflow). This

comes about from the fact that there is large size ratio between the particles and almost any flow process involving these granular particles will result in some de-mixing.
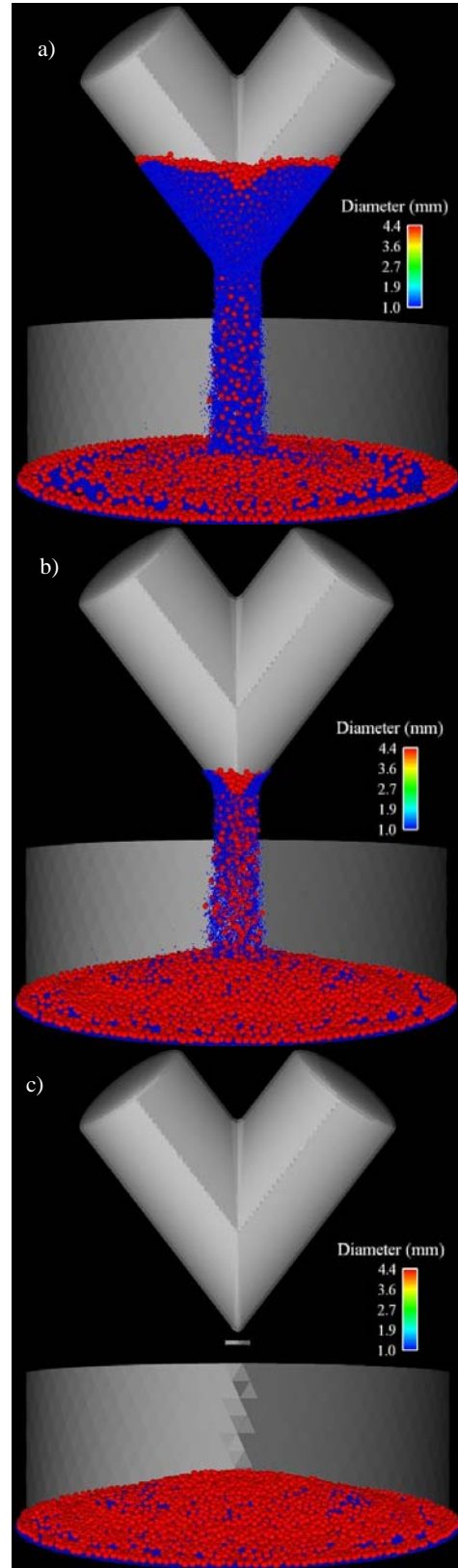
Figure 8: Flow out of V-blender into a cylindrical container for a particle size ratio of 4 at three different times during outflow. Smaller particles are coloured light blue while larger particles are coloured red, after outflow for: (a) 0.95 s, (b) 1.95 s, and (c) 2.95 s.

The general characteristics of the outflow from the V-blender are again similar to the previously described cases. Due to a large difference in particle sizes, percolation of the small particles through the surface shear layer results in a layer of large particles forming on the top surface (Fig. 8a). Particles that empty into the cylindrical container initially rebound of the bottom surface and splatter and form a layer on the cylindrical container's bottom. Once a heap has begun to form in the cylinder, particles roll along the sloped surface of the heap and again percolation of the smaller particles results in a layer of larger particles on the upper surface of the heap (Fig. 8b). The larger particles are more concentrated in the middle of the outflow stream. This is because the surface layer of larger particles flows radially inwards to the vertical centre-line of the blender and then flows vertically downwards towards the discharge port. By the time the flow has ended (Fig. 8c) there is a reasonable amount of de-mixing of the heap visible, with larger particles forming a thick surface layer and smaller particles concentrated in the middle of the bed.

The centroid data shows that particles de-mix as outflow proceeds with a shape similar to Fig. 7b. In comparison to the case with size ratio 2 (Fig. 7b), the difference between the two curves is larger by roughly 50%. The difference rises to nearly 19 mm (about 7 average particle diameters) compared to 11 mm (4 average particles) for size ratio 2. This indicates the degree of segregation increases (approximately linearly) with the increase in size ratio. The homogenous mixing measure (Fig. 9) for this case corroborates this finding, with the segregation rising to 85% by the completion of the outflow.
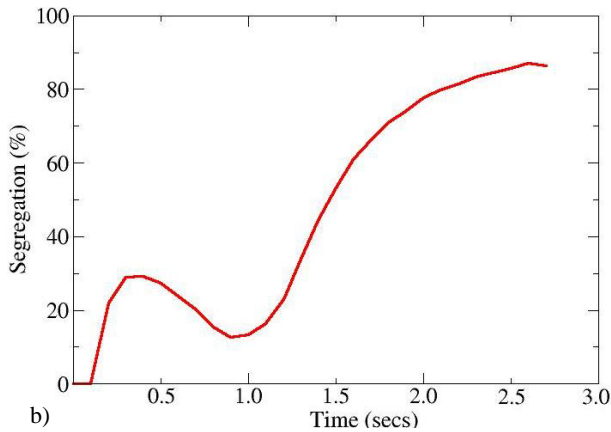
Figure 9: Homogeneity measure for size ratio of 4. The first 0.8 s is for filling the V-blender. Outflow begins at 0.8 s

These results show that when particles flowing out from a V-blender are collected in a container directly below the exit, the amount of de-mixing is enhanced, primarily due to percolation of smaller particles within surface shearing layers of the heap that forms in the collection device. Table 2, shows the homogeneity measure increases from 14% (for particle size ratio of 1.75) up to 86% segregated (for particle size ratio 4), which yields an almost six-fold increase in segregation with an approximate doubling of the size ratio. Table 3 gives the

maximum difference in the *y*-component of the particle centroids for each size ratio simulated. Here we see a linear increase in this value (with particle size ratio). Both these measures indicate, for this case, the extent of de-mixing is enhanced significantly for larger differences between the particles which make up the granular mixture.

Table 3: Maximum difference (mm) between *y*-component of particle centroids for Case 2 and Case 3.

Particle size ratio	Cylindrical collector	Chute into cylinder
	Max diff (mm)	Max diff (mm)
1.75	10	15
2	11	17
3	17	26
4	19	28

CASE 3: FLOW VIA A CHUTE

We now consider the case where the particles flow down a chute from the V-blender into a cylindrical container. The end of the chute is slightly offset from the centre of the container which is the same as in the previous case. The chute angle is 45 degrees and aligned with the *z*-axis. The particles travel along the chute for about 15 cm before dropping a short distance vertically into the container. This arrangement significantly reduces the vertical free fall heights and therefore the kinetic energy available for driving percolation in avalanching surface layers of the heap. It however also introduces a third opportunity for shear induced percolation in the flow along the chute. So the question is which is the more important effect?

Figure 10 displays snapshots of the particle distribution for this case with a particle size ratio of 2. The flow in and from the V-blender is similar to the previous cases. Once out of the V-blender, the particles now flow along the flat chute surface. They accelerate and there is shear induced by the frictional resistance of the chute. The larger (red) particles strongly segregate to the top of the flowing layer and come to rest closer to the walls of the cylinder (Fig. 10a). Due to the horizontal component of the velocity generated by the chute, the heap that forms in the receiving container is asymmetrical in shape (Fig. 10b). The avalanching flow to the left is much stronger leading to strong percolation of finer particles down into the heap. By the completion of the discharge, the heap that forms is significantly de-mixed, with many more of the larger, red particles on the upper surface and on the left side of the heap (Fig. 10c). This is in contrast to the previous case (flow into a cylinder without a chute) where the heap forms quite a symmetrical particle distribution (about the centre of the cylinder).
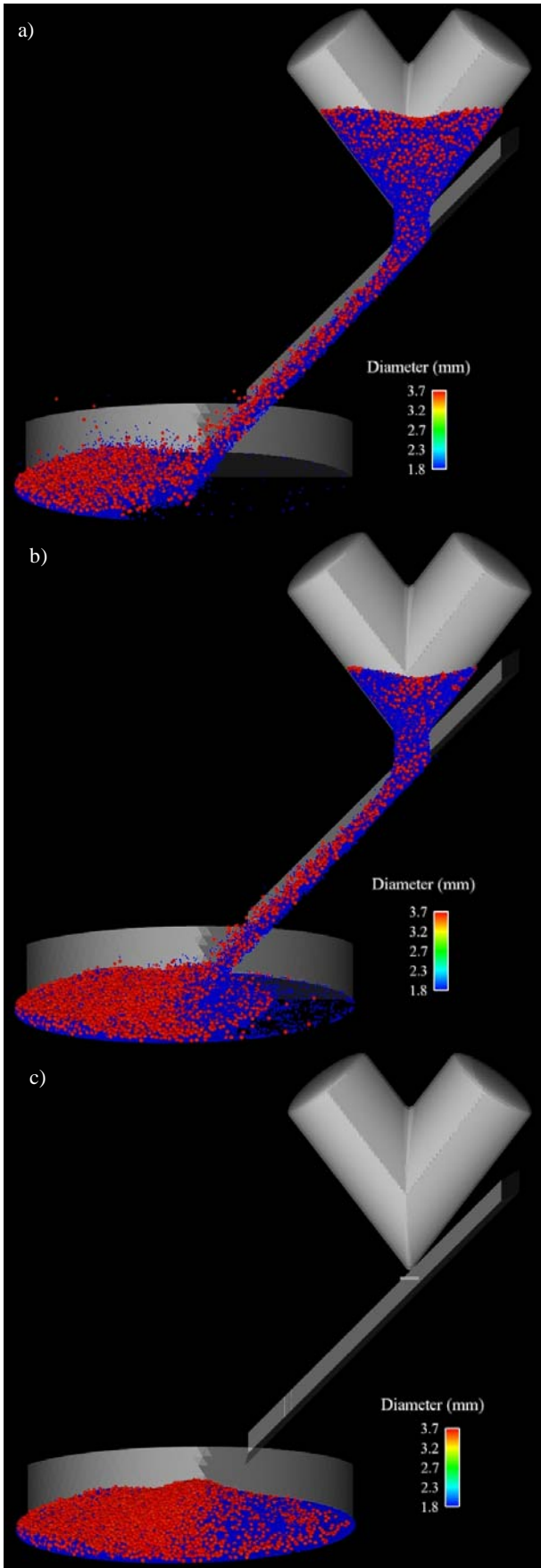
The shape of the *y*-centroid curves are similar to Case 2, with larger particles segregating to higher positions in the particle beds while the smaller particles tend to flow earlier and are located lower in the system. The maximum relative separation of the centroids is about 17 mm (about 6 average particle diameters). This is higher than for Case 2 (and for that matter also Case 1). This is an interesting observation, since one could argue that much of the segregation induced by the chute should be along the direction of the chute (so both horizontal and vertical segregation occurs). In contrast, when particles drop vertically into the cylinder (Case 2) vertical segregation only occurs. A complete understanding of this observation requires further explanation and investigation. The final separation of the *y*-centroids is around 5 mm (2 particle diameters). Table 4 gives the separation between the *z*-component of the centroid (between the two particle types) for all particle ratios. (Recall, the chute is aligned with the *z*-axis). For the cylindrical case, these differences are negligible for all particles size ratios. But for this case it is large – around 19 mm or 6-7 particle diameters. Note, the *x*-centroid shows no significant variation between particle types.
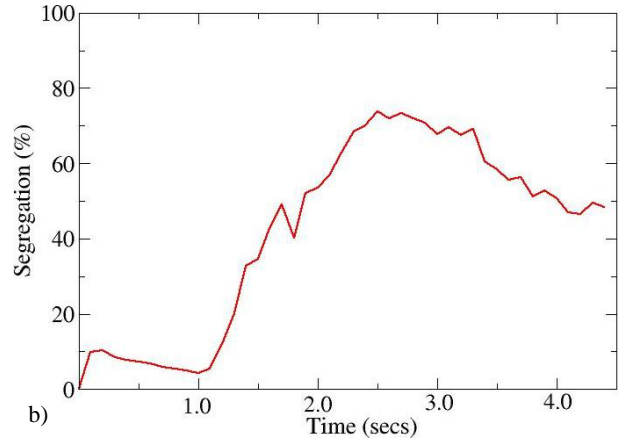
Figure 11: Homogeneity measure for size ratio of 2. The first 0.8 secs is for filling the V-blender. Outflow begins at 0.8 s.

The homogenous measure (Fig. 11) has a different shape compared to Fig. 7b. For the flow directly into the cylinder the increase in segregation was quite gradual, whereas for the chute case the segregation measure increases dramatically once particles begin flowing along the chute (at 1 s). The peak degree of segregation is around 70% occurring at 2.5 s. This indicates that segregation due to flow along the chute surface is significant and rapid. Later the degree of segregation decreases back to around 50% when flow is complete suggesting that the avalanche flow in the heap is actually helping to partially re-mix the particles. This final degree of segregations compares to about 20% for Case 2 where particles just fall directly into the container. The inclusion of any chute in the system is very deleterious to preserving the mixed state of the particles.

Figure 12 shows the particle distribution for size ratio of 4. The behaviour is quite similar to that described for the lower size ratio shown in Fig. 10. However, now there seems to much more rebound of particles off the cylinder base, when flowing into the cylinder (Fig. 12a).

Figure 10: Flow out of V-blender via chute into a cylindrical container for a particle size ratio of 2 at different times. Smaller particles are coloured blue while larger particles are coloured red. (a) After 1.0 s of outflow, (c) after 2.0 s and (d) after 3.5 s of outflow.
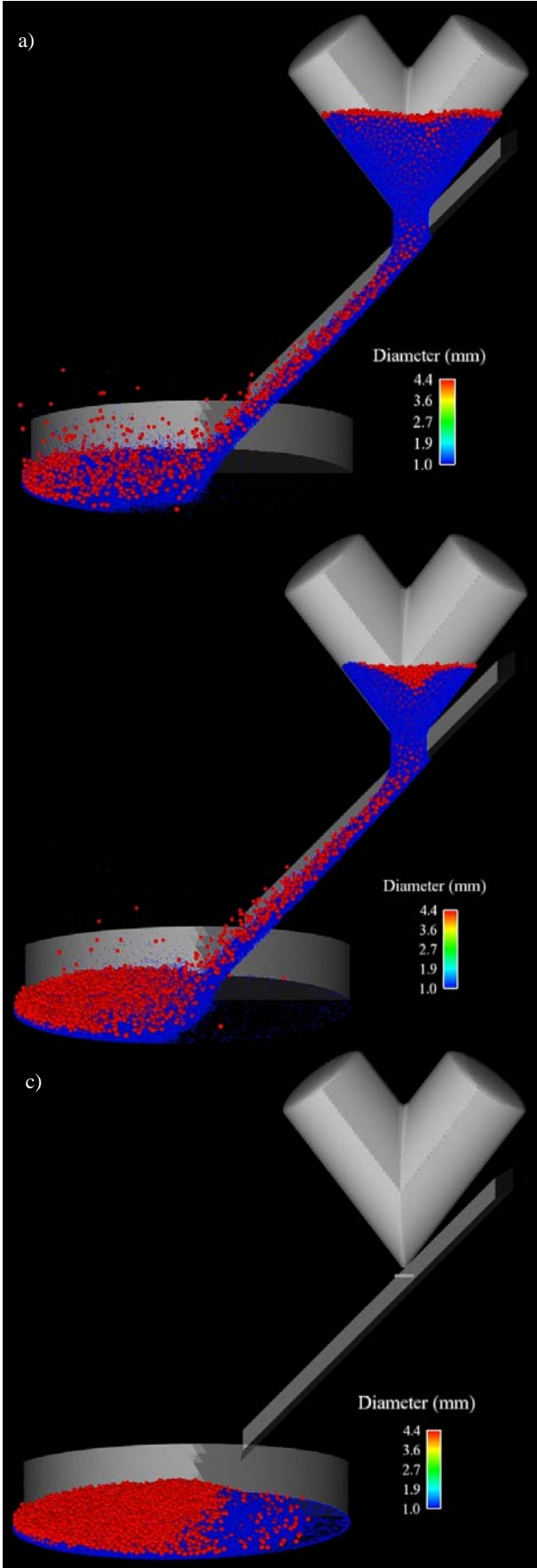
Figure 12: Flow out of V-blender via chute into a cylindrical container for a particle size ratio of 4 at different times during the outflow. Smaller particles are coloured blue while larger particles are coloured red. (a) After 0.5 s of outflow, (c) after 1.35s and (d) after 2.75 s of outflow.

In this process the larger particles come to rest closer to the container wall (Fig. 12b). When the particles come to rest the heap again has an asymmetrical shape with significant concentrations of larger (red) particle in the surface layer of the heap and more on the left side of the picture (Fig. 12c). The smaller particles (blue) are not only underneath the larger particles, but also have re-bounded further from the far wall of the cylindrical container and now appear in higher concentration on the right side of the cylinder (underneath the chute). This asymmetry in the distribution of particles in the heap is shown up quantitatively in the *z*-component of the centroids (Fig. 13a).

Table 4 gives the maximum difference in the *z*-component of the centroid, between the two particle types, for both Case 2 and Case 3. Flow without a chute shows negligible differences but with a chute the difference is large varying between 6 particle diameters (size ratio of 1.75) up to 9 particle diameters (size ratio of 3). One other interesting aspect of the *z*-centroid curves (Fig. 13a) is that the positions of the particles change during the simulation. Initially more small particles are located near the far wall of the cylinder, but they then are shifted, due to more large particles entering the cylinder and displacing the smaller particles which were adjacent to the far cylinder wall.
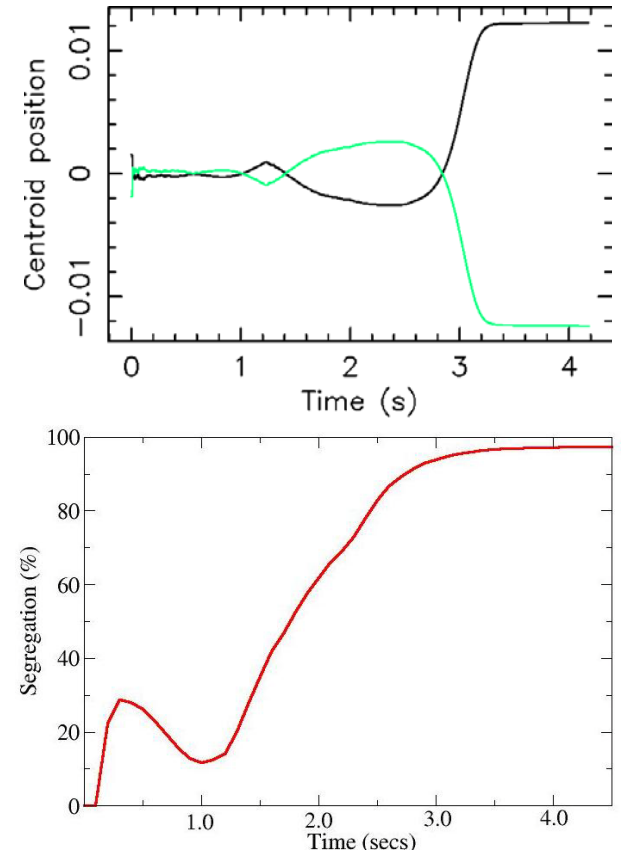
Figure 13: a) Relative *z*-centroid position for the outflow into a container for a particle size ratio of 4. Larger particles are shown by the green curve and black corresponds to the small particles. b) Homogeneity measure for size ratio of 4. The first 0.8 s is for filling the V-blender. Outflow begins at 0.8 s.

The *y*-centroid data has a similar form to those already discussed. The peak centroid separation increases to 28

mm or around 10 average particle diameters which is significantly higher than for the size ratio of 2. Table 3 shows the maximum difference in the *y*-component of the centroid for all the particle size ratios simulated. For this Case, as with Case 2, we see a gradual increase (again roughly linear) in this value with increasing particle size ratio. This suggests the segregation that occurs must be due to percolation.

Table 4: Maximum difference (mm) between *z*-component of particle centroids for Case 2 and Case 3.

Particle size ratio	Cylindrical collector Max diff (mm)	Chute into cylinder Max diff (mm)
1.75	0.01	19
2	0.4	21
3	1	27
4	0.6	25

The homogenous measure for this case (Fig. 13b) starts at about 15% segregated at the beginning of the outflow (at 0.8 s). Once particles roll along the chute (after 1 s) the segregation increases rapidly up to around 90% by 2.6 s. After this, it asymptotes to about 97%. Table 2 gives the final value of the homogeneity measure for all the particle size ratios simulated. In general, for this Case as with Case 2, we see a gradual increase of this measure with increasing particle size ratio. Comparing this measure between Case 2 and Case 3, for the same particle size ratio, we see Case 3 generally yields higher values (and thus more de-mixing). However, while de-mixing via a chute can yield more segregation of particles, it also produces a highly energetic outflow, which ultimately can tend to re-mix particles (as observed in the later stages of the flow shown in Figs. 12 and 13). Table 3 also shows that segregation between the two particle types increases with size ratio. Table 4 shows that the chute introduces additional segregation (in the *z*-direction). In summary, the flow of particles into a cylinder via a chute leads to significantly higher amounts of de-mixing than for flow in any configuration that is without a chute. As with the other cases the extent of de-mixing increases with the size ratio of particles.

CONCLUSION

In this study we have considered the de-mixing due to outflow from a V-blender, using the DEM method. We have considered three different cases, so as to clearly understand which parts of the outflow contribute to de-mixing and to what extent. The V-blender, itself, is made up of sloping walls which lead to the exit port (see Fig. 1). The outflow that results from this geometry is predominantly shear flow. The top (free) surface of the particle bed becomes inwardly sloped towards a point vertically above the exit port. Shearing flow then leads to smaller particles percolating through the voids created by the larger particles. As a result, smaller particles concentrate lower in the particle bed and hence tend to exit the V-blender earlier than the larger particles. This percolation driven de-mixing has been seen many times

before in a variety of granular devices (e.g., see Pereira *et al.*, 2011).

Once the granular mixture has exited the V-blender, it needs to be collected in a suitable container. We investigated two collection procedures, firstly by simply dropping into a cylindrical container and secondly by being transferred via a sloping chute into a cylindrical container. In each case, both flows introduce additional de-mixing of the granular mixture. When falling directly into a cylindrical container, de-mixing occurs due to percolation along the sloped surfaces of the collecting heap. When an additional chute is introduced into the transfer process, quite a violent flow may result, with particles being sheared along the flat surface of the chute as well as in the gradually forming heap.

In general, all our segregation measures point to an increase in segregation with particle size ratio. This agrees with our hypothesis that the mechanism behind the de-mixing is percolation. It is clear any transfer schemes which introduce a shearing flow into the system will increase de-mixing. In the light of this observation, it appears the best transfer strategy is to allow the mixture to directly flow into the collection device. In addition, it is clear the presence of the sloped heap surface produces more de-mixing. One possible strategy to investigate in future work, to inhibit de-mixing, is to flatten out the heap, via a gentle shaking of the cylindrical container.

REFERENCES

CLEARY, P.W, (1998), "Predicting charge motion, power draw, segregation, wear and particle breakage in ball mills using discrete element methods", *Minerals Eng.,* **11**, 1061–1080

CLEARY P.W., (2004), "Large scale industrial DEM modelling", *Eng. Comput.*, **21,** 169-204.

CLEARY P.W., (2009), "Industrial particle flow modelling using discrete element method", *Eng. Comput.*, **26,** 698-743.

CLEARY P.W., SINNOTT M.D., (2008), "Assessing mixing characteristics of particle-mixing and granulation devices", *Particuology*, **6,** 419-444.

KUO H.P., KNIGHT P.C., PARKER D.J., TSUJI Y., ADAMS M.J., SEVILLE J.P.K., (2002), "The influence of DEM simulation parameters on the particle behaviour in a V-mixer", *Chem. Eng. Sci.,* **57**, 3621-3638.

OTTINO J.M., KHAKHAR D.V., (2000), "Mixing and segregation of granular materials", *Ann. Rev. Fluid Mech.,* **32**, 55-91.

PEREIRA G.G, PUCILOWSKI S., LIFFMAN K., CLEARY P.W., (2011), "Streak patterns in binary granular material in a rotating drum", *Appl. Math. Modelling*, **35,** 1638-1641.

ROSATO A., STRANDBOURG K.J., PRINZ F., SWENDSEN R.H., (1988), "Why the Brazil nuts are on top – size segregation of particulate matter by shaking", *Phys. Rev. Lett.,* **58**, 1038-1040.

PREDICTION OF PERMEABILITY FOR DEM GENERATED PACKINGS OF SPHERICAL AND NON-SPHERICAL PARTICLES USING SPH AND LB

Gerald G. PEREIRA* , Pablo M. DUPUY, Paul W. CLEARY, Gary W. DELANEY

CSIRO Mathematics, Informatics and Statistics, Private Bag 33, Clayton South, AUSTRALIA

* E-mail: Gerald.Pereira@csiro.au

ABSTRACT

Understanding how the permeability of a porous media changes as a function of solid fraction or pore geometry is vital in many significant areas such as oil recovery, groundwater flow or flow in biological materials. Here we construct sample porous media using particle packings generated using the Discrete Element Method (DEM). We use a number of different arrangements of solid particles with different shapes to make up the porous media. They are (i) spherical and mono-disperse, (ii) spherical and poly-disperse and (iii) non-spherical blocky particles (cuboidal). We then simulate the flow of a viscous liquid through the solid packing using the Smoothed Particle Hydrodynamics (SPH) and Lattice Boltzmann (LB) methods. Comparisons of flow and permeability predictions as well as computational time of both methods are then made.

Keywords: DEM, SPH, LB, porous media, permeability.

NOMENCLATURE

A complete list of symbols used, with dimensions, is required.

Greek Symbols
- Porosity or liquid (void) fraction, $[m^3/m^3]$.

Latin Symbols
- k Permeability, $[m^2]$.
- d Grain diameter, $[m]$.

INTRODUCTION

For creeping fluid flow through a porous medium, the flow rate is given by the driving force, its viscosity and a parameter related to the topology of the solid matrix, known as the permeability, k. Different mathematical techniques have been adopted for this calculation. However, as the Reynolds number for a pore increases, the validity of the Darcy model becomes invalid. For the general solution of such porous media fluid flow (independent of the Reynolds regime) different computational fluid dynamic approaches have been proposed. This, in turn, yields an estimate of the medium's permeability.

Examples of numerical techniques used to determine permeability of porous media include the random walk method (Schwartz *et al*, 1994), finite difference methods (Zhan *et al*, 2011), finite element methods (Arns *et al*, 2002), pore network models (Blunt *et al*, 2002) with realistic connectivity of the pore space and Lattice Boltzmann methods (Ahrenholz *et al*, 2008, Chai *et al*, 2010, Lin *et al*, 2005, Pan *et al*, 2006). Although there have been numerous other numerical works to evaluate the permeability of porous media, the main aims of this paper is to compare the performance of two techniques, namely the Lattice Boltzmann (LB) method and Smoothed Particle Hydrodynamics (SPH) method for predicting the fluid flow in computationally generated media. We use computationally generated media since it is more realistic than simple geometries previously studied (Pereira *et al*, 2010), but still controllable (e.g. to obtain a particular porosity). To our knowledge, there have been limited studies using the SPH technique to model permeability of realistic porous media, while the LB method is (probably) now recognized as the most efficient method for this specific problem. We present a qualitative comparison of the fluid velocity field and a quantitative comparison of the permeability, between the LB and SPH methods.

Beyond determining the nature of the fluid flow and estimation of the permeability, such modelling can be used to study mixing processes, chemical reactions and multiphase behaviour in pores, chaos, and enhanced effective diffusivity. The methods used in this study are described in the next section, followed by a discussion of the flows for four different solid particle packings. We then evaluate the permeability for each of the packings and compare the LB and SPH predictions. Finally, we discuss the relative merits of the methods, the limitations of the present study and also directions for future investigation.

MODEL DESCRIPTION

We use the DEM method, to generate the initial granular packing. This is then used as the basis for our porous medium and flow through the system is simulated using the SPH and LB techniques, separately. Here we briefly describe each method in sequence.

### Packing generation using DEM

To generate the granular packings for use in the flow simulations, we utilise DEM and a dynamic particle expansion technique. This kind of technique has been

widely employed in the study of granular packings (Lubachevsky & Stillinger, 1990) and full details of this approach are given in Delaney & Cleary (2010). Here we will briefly outline the technique.

We initially seed our DEM particle generation with particles in a unit periodic box at random positions and with random orientations. The particles are initially a fraction of their final sizes, with a packing fraction less than 20%. The particles are frictionless and have unit density.

The packing process proceeds by uniformly increasing the size of the particles at a constant volumetric growth rate, while imposing a condition of constant kinetic energy. Interactions between particles are modeled using a fully dynamic linear spring Discrete Element Method (DEM) (Cundall & Strack, 1979). At each iteration we obtain the contact locations and linear overlaps between particles and hence solve for the forces and torques on each particle. Further details of our DEM technique are given in Cleary (2004, 2009). Particle growth continues until a final jammed configuration of the particles is reached. Packings with different final densities and degrees of ordering can be achieved by adjusting the growth rate used.
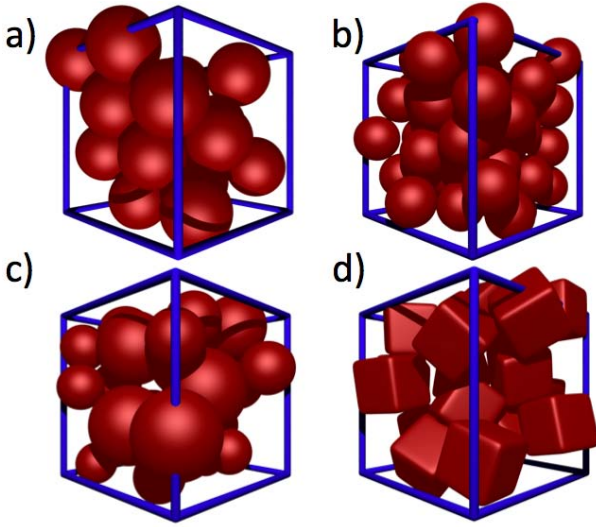
Figure 1: Images of the four packings used in the flow simulations. The packings consist of (a) 20 mono-disperse spheres with a porosity of 0.31, (b) 50 mono-disperse spheres with a porosity of 0.38, (c) 25 poly-disperse spheres with a porosity of 0.37, and (d) 20 cubic particles with a porosity of 0.46.

Here we consider four packings that cover a range of possible densities and structural characteristics that can be found in real granular systems. Images of the packings are shown in Figure 1:

- Packing (a) contains 20 mono-disperse spheres at a high packing fraction of 0.69 ($\bullet$ = 0.31). This is the most ordered packing we consider, with a packing fraction above the random close packing limit and with some degree of crystalline ordering. Packings around this density level and with similar degrees of ordering are commonly found where a system

has undergone certain types of shearing or vibration over a long period of time.

- Packing (b) is a random packing of 50 mono-disperse spheres with a packing fraction of 0.62 ($\bullet$ = 0.38). Random packings around this density are commonly found where spherical grains are quickly poured into a container.
- Packing (c) is a random packing of 25 poly-disperse spheres with a packing fraction of 0.63 ($\bullet$ = 0.37). The spheres diameters are uniformly random with a diameter ratio between the smallest and largest of 2:1. As most systems in nature do not consist of purely mono-disperse grains, it is important to consider the effect of polydispersity on permeability.
- Packing (d) is a random packing of 20 cubic particles at a packing fraction of 0.54 ($\bullet$ = 0.46). Particle shape is a key determining factor in defining the shape of the pores within a granular system and thus can strongly affect the permeability. In generating this packing the orientations of the particles were fixed in random directions so as to avoid the generation of a perfectly ordered system with near unit density. The particles were represented in the simulation using super-elliposids defined by the equation:

$$\left(\frac{x}{a}\right)^m + \left(\frac{y}{b}\right)^m + \left(\frac{z}{c}\right)^m = 1, \tag{1}$$

where $a=b=c$ and $m=10$. This produces a particle shape very close to an exact cube. For simplicity in discretising the surface for use in the flow simulations, the shape of the particles was assumed to be a cube. See Cleary (2004, 2009) for more details and examples of these particle shapes.

SPH Method

The SPH method is reviewed in detail by Monaghan (2005). We give here only details which are required for this particular application. The SPH continuity equation, taken from Monaghan (1994) is:

$$\frac{d\rho_a}{dt} = \sum_b m_b (\mathbf{v}_a - \mathbf{v}_b) \bullet \nabla W_{ab} \tag{2}$$

where m_b is the mass of particle b, ρ_a is the density of particle a with velocity $\mathbf{v}_a$. Here W($\mathbf{r}$,h) is a C^2 spline based interpolation or smoothing kernel with radius $2h$ that approximates the shape of a Gaussian function. We denote the position vector from particle b to particle a by $\mathbf{r}_{ab} = \mathbf{r}_a - \mathbf{r}_b$ and let $W_{ab} = W(\mathbf{r}_{ab}, h)$ be the interpolation kernel with smoothing length h evaluated at distance $|\mathbf{r}_{ab}|$. This form of the continuity equation is Galilean invariant (since the positions and velocities appear only as differences), has good numerical conservation properties and is not affected by free surfaces or density discontinuities.

The SPH method used here is quasi-compressible and an equation of state is used to specify the relationship between particle density and fluid pressure. A form suitable for incompressible fluids is:

$$P = P_0 \left[\left(\frac{\rho}{\rho_0} \right)^{\gamma} - 1 \right] \qquad (3)$$

where P_0 is the magnitude of the pressure and ρ_0 is the reference density (Monaghan, 1994). For water and similar fluids $\gamma = 7$.

The momentum equation for each particle a is:

$$\frac{d\mathbf{v}_a}{dt} = \mathbf{g} - \sum_b m_b \left[\begin{array}{c} \left(\dfrac{P_b}{\rho_b^2} + \dfrac{P_a}{\rho_a^2} \right) \\ - \dfrac{\xi}{\rho_a \rho_b} \dfrac{4\mu_a \mu_b}{(\mu_a + \mu_b)} \dfrac{\mathbf{v}_{ab}\mathbf{r}_{ab}}{\mathbf{r}_{ab}^2 + \eta^2} \end{array} \right] \nabla_a W_{ab} \qquad (4)$$

where P_a and μ_a are pressure and viscosity of particle a and $\mathbf{v}_{ab} = \mathbf{v}_a - \mathbf{v}_b$. Here ξ is a calibration factor for the viscosity (Cleary, 1998), η is a small parameter used to smooth out the singularity at $r_{ab} = 0$ and $\mathbf{g}$ is body force.

The pressure scale factor P_0 is given by:

$$\frac{g P_0}{r_0} = 100 V^2 = c^2 \qquad (5)$$

where V is the characteristic or maximum fluid velocity and c is the speed of sound. This means that the sound speed is ten times the characteristic speed. This ensures that the density variation is less than 1% and that the flow is close to incompressible. The speed of sound is much less than the actual (physical) speed of sound so as to increase the numerical time-step.

As two particles approach each other, their relative velocity is negative (as is the gradient of the kernel) so that there is a positive contribution to $d\rho_a / dt$. If this rate of change is positive then the density of particle a rises. This leads to a positive pressure that pushes the particles apart again. If two particles move apart, then their densities decrease creating a negative pressure that pulls the particles back towards each other. This interplay of velocity and density/pressure ensures that the particle remains "on average" equally spaced and that the density is close to uniform, so that the fluid is close to incompressible.

To simulate confined or partially confined fluid flow, such as is typically found in industrial and geophysical fluid flows, the modelling of physical boundaries is important. Boundaries in SPH can be modelled in a range of ways, but here we use approximately evenly spaced SPH particles at which a Lennard-Jones style penalty force (a very steep polynomial potential relating the force with the displacement into the boundary) is applied in the normal direction. In the tangential direction, the boundary particles are included in the summation for the shear stress using equation (4) (with the pressure gradient term set to zero) to give non-slip boundary conditions on the walls.

LB Method

The Lattice Boltzmann (LB) method is a numerical method widely applied to fluid flow problems including, but not limited to, simulations of fluid flowing through porous media (Ahrenholz *et al.* 2008, Chai *et al.* 2010,

Lin *et al.* 2005, Pan *et al.* 2006). However, LB methods for fluid flow simulations are not based on a discretization of the mass and momentum conservation equations as in the SPH and other CFD methods, but instead use a discretisation of the Boltzmann transport equation. A multiscale expansion, usually referred to as the Chapman-Enskog expansion, provides the mathematical grounds for extending results from the Boltzmann equation to the macroscopic variables of density, pressure and velocity. Two characteristics present in most of the Lattice Boltzmann schemes are the discretization of the domain into a fixed lattice of nodes and the discretization of the internal coordinate, i.e., the velocity vector into q discrete velocities $\vec{e} = \{\vec{e}_0, \vec{e}_1, \vec{e}_2, ..., \vec{e}_i, ..., \vec{e}_{q-1}\}$. For each velocity i, the following equation is solved

$$\frac{\partial f_i(\vec{r},t)}{\partial t} + \vec{e}_i \cdot \nabla f_i(\vec{r},t) = \Omega(\vec{f},\vec{r},t) + F_i \qquad (6)$$

The terms on the right hand side are the collision operator and external forcing terms, see (Succi, 2001 and d'Humières *et al.* 2001).

Different implementations, forcing terms and sets of discrete velocities were tested. For the results reported for comparison with the SPH model results and convergence test a set of 13 discrete velocities introduced by d'Humières *et al.* (2001) were used. A cubic voxel has 6 faces, 12 edges and 8 vertices defining the three first layers of its neighbourhood. The widely used D3Q19 model uses the first two layers of neighbours; the D3Q13 model uses only the second layer. The space of 13 discrete velocity vectors is generated by having one null and 12 vectors pointing towards each voxel edge. Note that all the 12 non-trivial discrete velocities have the same length.

The collision operator (•) is defined by imposing some constraints on how given moments of the population distribution will change during collisions. The following 13 moments are considered by d'Humières et al. (2001).

$$M = \begin{pmatrix} e_0^0 & e_1^0 & \cdots & e_{q-1}^0 \\ e_{0,x} & e_{1,x} & \cdots & e_{q-1,x} \\ e_{0,y} & e_{1,y} & \cdots & e_{q-1,y} \\ e_{0,z} & e_{1,z} & \cdots & e_{q-1,z} \\ \frac{13}{2}e_0^2 - 12e_0^0 & \frac{13}{2}e_1^2 - 12e_1^0 & \cdots & \frac{13}{2}e_{q-1}^2 - 12e_{q-1}^0 \\ 3e_{0,x}^2 - e_0^2 & 3e_{1,x}^2 - e_1^2 & \cdots & 3e_{q-1,x}^2 - e_{q-1}^2 \\ e_{0,y}^2 - e_{0,z}^2 & e_{1,y}^2 - e_{1,z}^2 & \cdots & e_{q-1,y}^2 - e_{q-1,z}^2 \\ e_{0,x}e_{0,y} & e_{1,x}e_{1,y} & \cdots & e_{q-1,x}e_{q-1,y} \\ e_{0,y}e_{0,z} & e_{1,y}e_{1,z} & \cdots & e_{q-1,y}e_{q-1,z} \\ e_{0,x}e_{0,z} & e_{1,x}e_{1,z} & \cdots & e_{q-1,x}e_{q-1,z} \\ e_{0,x}\left(e_{0,y}^2 - e_{0,z}^2\right) & e_{1,x}\left(e_{1,y}^2 - e_{1,z}^2\right) & \cdots & e_{q-1,x}\left(e_{q-1,y}^2 - e_{q-1,z}^2\right) \\ e_{0,y}\left(e_{0,z}^2 - e_{0,x}^2\right) & e_{1,y}\left(e_{1,z}^2 - e_{1,x}^2\right) & \cdots & e_{0,y}\left(e_{q-1,z}^2 - e_{q-1,x}^2\right) \\ e_{0,z}\left(e_{0,x}^2 - e_{0,y}^2\right) & e_{1,z}\left(e_{1,x}^2 - e_{1,y}^2\right) & \cdots & e_{q-1,z}\left(e_{q-1,x}^2 - e_{q-1,y}^2\right) \end{pmatrix} \cdot \begin{pmatrix} f_0 \\ f_1 \\ \vdots \\ f_{q-1} \end{pmatrix} \qquad (7)$$

The first four moments are defined as the fluid density and three components of the fluid momentum. In addition, 13 definitions are given for the moments of an equilibrium distribution such that the Chapman-Enskog expansion ensures that the Navier-Stokes set of

equations is solved (see d'Humières *et al*., 2001). The equilibrium distribution and therefore its moments depend only on the fluid density, three components of the fluid momentum and speed of sound. The collision operator is built such that each distribution moment will relax towards the equilibrium distribution moments. Note that the four first moments will remain unchanged because they are the same.

Some of the main advantages of the Lattice Boltzmann methods are that the scheme provides compact stencils making computations more local and therefore efficient and that the equations to solve are linear (making a notable difference to the Navier-Stokes equations which are non-linear) and no pressure updating step is required.

A proper Chapman-Enskog expansion will show that for low Mach number the solution method is second order in the number of lattice nodes meaning that duplicating the nodes used to discretize a channel will reduce the error by a factor of four. However, the Chapman-Enskog expansion of the main equations ensures the second order convergence if boundary conditions are not considered, i.e. depending on the boundary conditions the method can be either first or second order.

As for SPH, the (in)compressibility constraint is obtained by the density, but with the difference that in the (weakly) compressible Lattice Boltzmann schemes the equation of state is an ideal gas with fixed sound speed. For this reason there are two possible ways of obtaining permeability independent of compressible gas effects: one approach suggests using very low pressure gradients such that the variations in density are very small, e.g. below 1% percent as in the previous method. Another approach is using an incompressible Lattice Boltzmann model where the inertial-density is treated as a constant everywhere, but the sum of the particle population is redefined to be linked with the pressure instead (He and Luo, 1997).

Boundary conditions need to be implemented in this porous media application. For a vertical wall located between two nodes a half-way bounce back will give the correct, second order convergence in all cases. A full bounce back, while easier to implement, will give a second order convergence for steady state flows, but degraded results during a transient simulation. Lastly, if the wall is not located half-way between the nodes, or is not aligned with the lattice, the difference between the correct solution considering the actual angle and sub-grid location of the wall and the solution of one of the methods mentioned before will degrade the solution method. However, if the topological model of the domain is unknown at a level comparable with the lattice space, there is no possible way of describing the position and shape of the wall below the voxelization limit, usually constrained by the resolution of imaging methods or tomography scans. This makes the full bounce-back approach an attractive alternative for studying permeability of real porous media where no transient results are of interest. Its implementation requires inverting the direction of all distributions in the boundaries nodes.

The LB simulations were performed using in-house code based on either of the following libraries: Palabos, parallel lattice Boltzmann library (http://www.lbmethod.org/palabos/); and Sailfish, optimized for modern multi-core systems, especially GPUs (Graphics Processing Units) (http://code.google.com/p/sailfish-cfd/).

FLUID FLOW IN POROUS MEDIA

In each case the porous media was filled to saturation with fluid (we modelled a fluid with density 1000 kg/m^3 and viscosity of 1 Pa.s) and the flow was simulated using a driving body force of 4.9 N/kg in the negative *z* direction. In principal we would like to simulate an infinitely large porous media. Clearly, computationally this is not possible and the next best option, to mitigate any domain boundary effects, is to use periodic boundary conditions on a cubic domain. The flow was allowed to reach steady state by monitoring the kinetic energy as a function of time. Only when this quantity has stabilised sufficiently can we be considered to be in the steady state regime. The steady state flow patterns and the steady state average flow velocity are reported and compared. They are also used in the prediction of the porous media permeability. An important question we must address is the particle size (or lattice spacing size) for both fluid flow methods. Previously (Pereira, 2011) we had determined suitable particle size resolutions for SPH simulations when we considered flow around an ordered array of spheres. As always, there is a trade off between computational time and accuracy. Using our previous study as an indication, in this study, we use an SPH fluid particle size of 0.1mm. (The cubic domain has side length 1cm.) Thus we have 100 particles across a side and in total of the order of half a million fluid particles in the SPH simulation. For the LB simulations, Fig. 2 indicates convergence is achieved above 200 lattice sites per side. For this study we quote results for this value (i.e., 200 lattices sites per side). In future, we intend to make a more detailed resolution study and comparison between the two methods. This is a computationally time consuming task.

Validity of LB for permeability calculation

The first step in our study is to validate independently the permeability results calculated from both techniques. Previously (Pereira *et al*, 2011) considered the permeability of a simple cubic packing of spheres using the SPH technique for a variety of porosities. They compared their SPH derived permeabilities with the theoretical results of Hasimoto (1959) and Zick and Homsy (1982) and found excellent agreement.
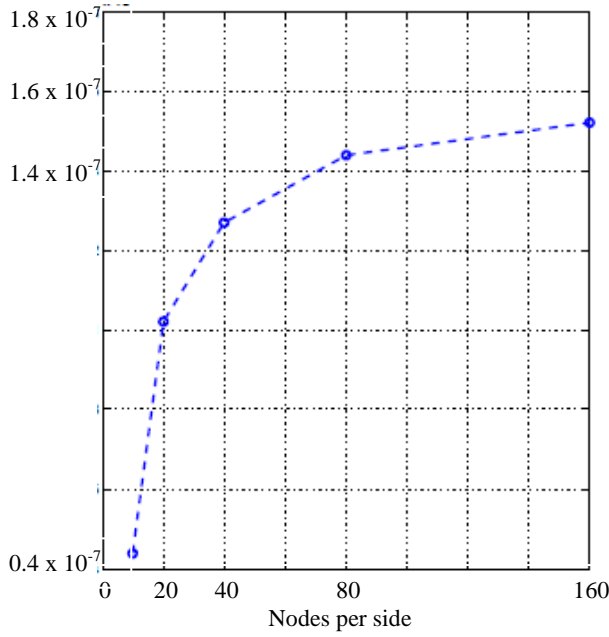
Figure 2: LB permeability convergence for a simple cubic packing of spheres at a porosity of 0.46.

We now do the same for LB concentrating on a porosity of 0.47. Figure 2 shows the convergence of the LB prediction of the permeability for increasing resolution of the lattice nodes. The permeability for a resolution of 160 is 1.55×10^{-7} m^2. This compares with the SPH value of 1.3×10^{-7} m^2 and theoretical value of 1.2×10^{-7} m^2. The LB is reasonably different to the other two values which are quite close. However, we note that the true value is not known and all three are estimates. Thus it is not possible to say which one is more right. We can only assume that clustered values are more likely to be correct when pairs or more of the methods agree closely. The closeness of the predictions gives us confidence in the implementation of LB for evaluating permeabilities of porous media.

The low Mach number Lattice Boltzmann simulations are dimensionless, and the simulations were run using a D3Q13 distribution with multiple relaxation time giving a kinematic viscosity of 0.01 in a domain of 200 nodes per side. A constant acceleration field of 10^{-6} was used with a naive implementation of the forcing term. For comparison with the SPH simulations we matched the domain size (to 1 cm) and kinematic viscosity (to 0.001 m^2/s), leading to a Reynolds number of Re ≈ 1. The corresponding SPH simulations were run for a Reynolds number range of Re $= 10^{-3} - 10^{-1}$ (Pereira *et al*, 2011). All these Reynolds numbers are in the laminar regime, so they should converge to the same steady-state solutions.

Fluid flow for 20 mono-disperse spheres

The first DEM generated porous media case to be considered is a random mono-disperse distribution of spherical particles (packing a). This geometrical domain contains 20 spheres. The domain length is one centimetre and the porosity is 0.31.
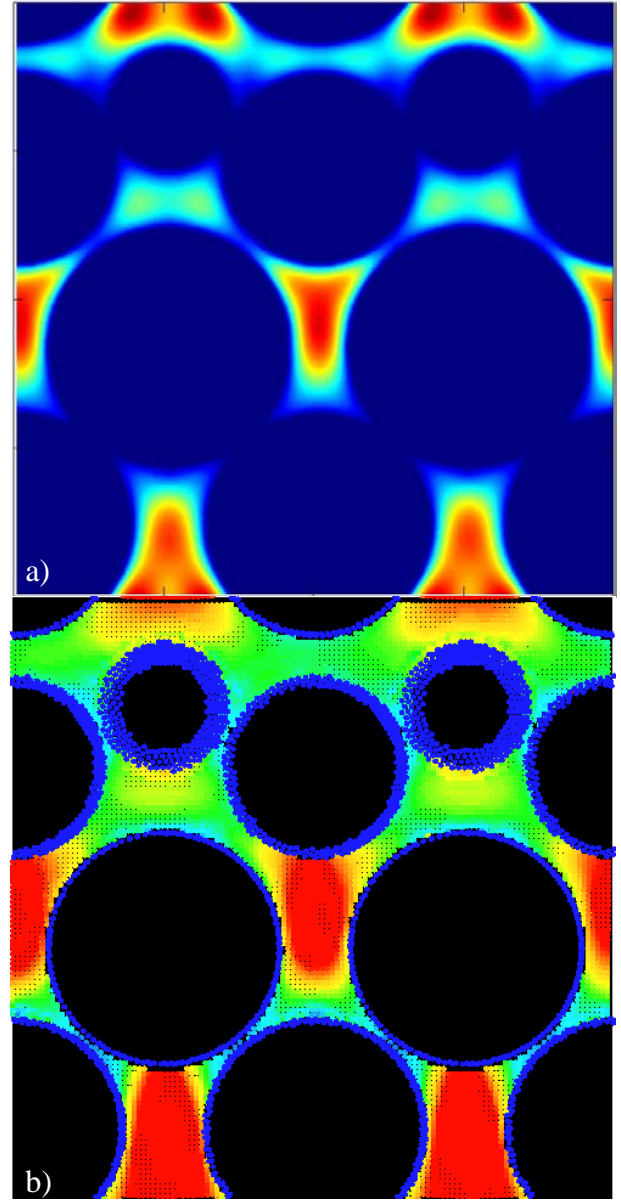
Figure 3: Fluid flow for packing a with 20 mono-disperse spheres per unit volume from (a) Lattice Boltzmann and (b) SPH simulations. Both plots are for an *x-z* slice of 0.1 mm thickness, at *y*=0. The colour scale, which represents the fluid speed, runs from blue (0.0 mm/s) to red (1.24 mm/s).

Figure 3 shows the flow in one vertical slice at *y*=0. The body force vector points in the negative *z* direction. A large circle results when the slicing plane intersects a sphere close to the prime meridian, while smaller circles occur when the sectioning plane is well off the centre of the sphere. The colour map shows the fluid speed with red being the highest value of the speed within the cubic domain (not just within the slice). Note that in the LB plot (Fig. 3a) the blue colour represent all lattice points with zero velocity (including solid particles) while for the SPH plot (Fig. 3b) the internal solid particles are represented as black (while boundary solid particles are blue, since they are stationary). The packing in this case is relatively ordered and, as a result, the fluid velocity plots appear quite ordered, with alternating regions of high and low flow.

The snapshots given in Fig. 3 are for steady state flow conditions, which we can determine by monitoring the

stabilisation of the kinetic energy as a function of time. By conservation of mass, through any horizontal cross-section (*x-y* plane) the mass flow rate must be a constant. Hence fluid must speed up in narrow pores and slow down in wider regions. This can be clearly seen in Fig. 3, where, for example, the high velocity streams adjacent to the top two pores slows down as the pore space widens. Qualitatively, there appears to be excellent agreement between the LB and SPH results – regions of high velocity (most notably in between solid particles) correlate well between plots.

Fluid flow for 50 mono-disperse spheres

The absolute velocity for an *x-z* slice at *y*=0 is shown in Figure 4 for the 50 mono-size sphere packing b. This structure is more disordered than the previous case and also has a larger porosity of 0.38. Most of the velocities plotted here are much lower than the maximum velocities for the whole cubic domain. Hence the velocities displayed are generally of a bluish hue. Possibly this domain presents a channelling effect due to the interconnection of large spaces. Overall there seems to be good qualitative agreement between LB and SPH velocity plots. Both have an absence of maximum velocity regions in this slice and mostly bluish coloured regions.

Fluid flow for 25 poly-disperse spheres

Packing c has 25 poly-disperse spheres and a porosity of 0.37. The flow through the *y*=0 slice of this porous media is shown in Figure 5. Here different circle sizes might mean different sphere sizes.

The LB simulation (Fig. 5a) again shows the effect of channelling where the highest velocities are not seen in the slicing plane. However, the SPH simulation (Fig. 5b) does display the largest velocity (red colour) within the domain. Hence this represents a difference between the LB and SPH simulations.

We believe the reason for this difference between SPH and LB is that the SPH and LB are using different discretizations for this particular simulation. The LB result displayed in Fig. 5a is for 200 lattice points along each edge. However, the SPH discretization is for 100 lattice points along each edge. This difference means that around each spherical particle there is a small error created (due to using a cube to approximate a smooth curve) in the fluid volume fraction (porosity), which can amount to a few percent overall.

To ensure the porosities of the LB and SPH simulations are similar, we reduced the solid particle radii slightly, by half to one SPH particle spacing. This means that whereas in the LB simulations particles will be in contact, in the SPH simulations there will be a gap. For example, see the large sphere in the bottom left hand corner of the LB simulation (Fig. 5a). This sphere is in contact with the larger sphere above it at an angle of approximately 45 degrees. In contrast in the SPH case (Fig. 5b) these two spheres are clearly not in contact. As a consequence, this allows easier movement of fluid

throughout the domain and hence higher fluid velocities for the SPH simulation.
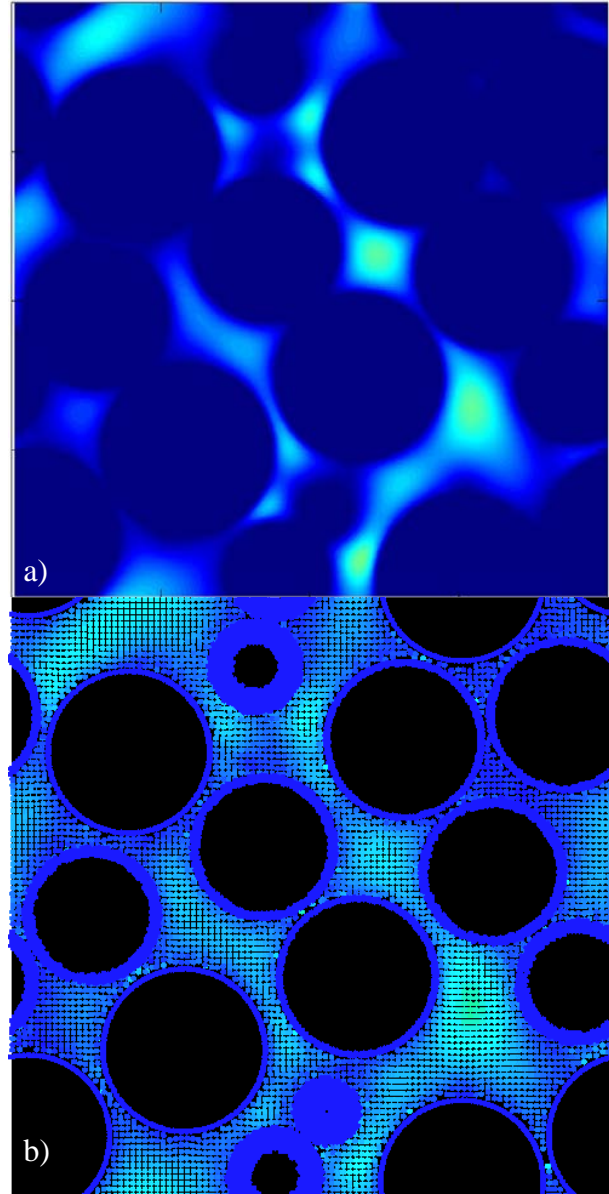
Figure 4: Fluid flow for packing b with 50 mono-disperse spheres per unit volume from (a) Lattice Boltzmann and (b) SPH simulations. Both plots are for an *x-z* slice of 0.1 mm thickness, at *y*=0. The colour scale, which represents the fluid velocity, runs from blue (0.0 mm/s) to red (1.77 mm/s).

Since there are small spheres in the geometrical domain, they can occupy interstitial voids left by the large spheres. This notably reduces the possibility of finding large pores and can contribute to reducing the degree of ordering of the structure compared to the 20 sphere case. This, together with the presence of large bodies, can increase the average flow velocities compared with the previous cases.
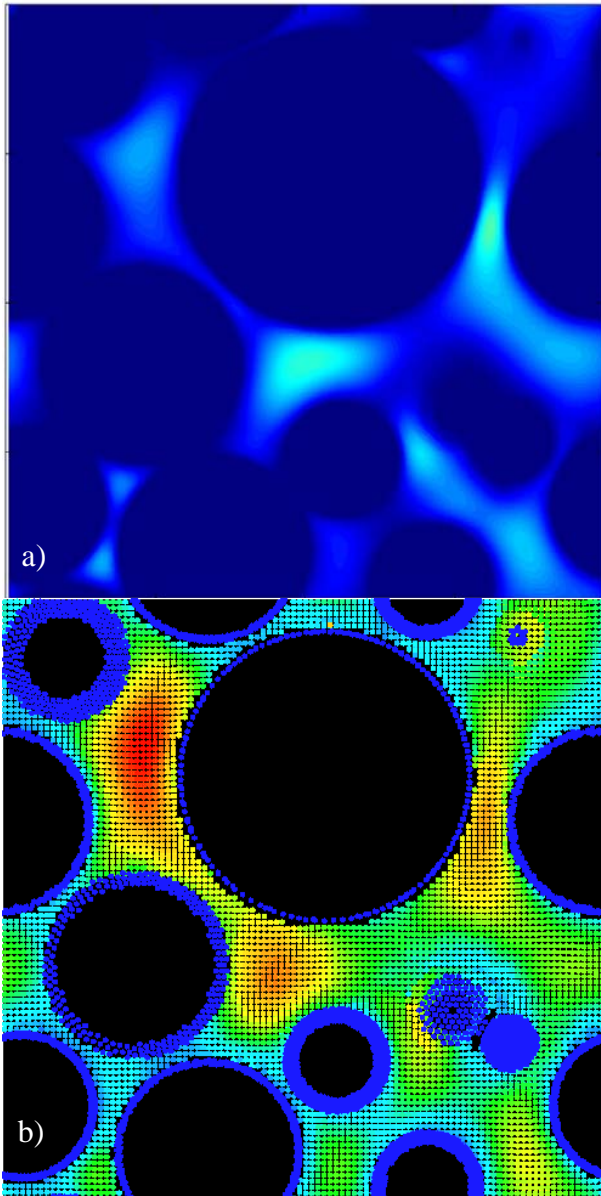
Figure 5: Fluid flow for packing c with 25 poly-disperse spheres per unit volume from (a) Lattice Boltzmann and (b) SPH simulations. Both plots are for an *x-z* slice of 0.1 mm thickness, at *y*=0. The colour scale, which represents the fluid velocity, runs from blue (0.0 mm/s) to red (1.66 mm/s).

Figure 6: Fluid flow for packing d with 20 randomly oriented cubes per unit volume from (a) Lattice Boltzmann and (b) SPH simulations. Both plots are for an *x-z* slice of 0.1 mm thickness, at *y*=0. The colour scale, which represents fluid velocity, runs from blue (0.0 mm/s) to red (1.5 mm/s).

Fluid flow for 20 mono-disperse cubes

Packing d has 20 mono-disperse cubes. Figure 6 shows the fluid flow in the *y*=0 slice. The intersection of the slice with the particles produces a pattern of randomly oriented polygons. For both LB and SPH high velocity regions are observed within this slice and overall both techniques agree relatively well in this case. We see a channel of high fluid velocity running down the right-hand side of the domain. This location of this region matches quite well between the two techniques.

As the pore geometry for this case allows for channel flow we would expect higher average flow velocities, in comparison to the previous cases simulated. This channelling effect is due to the anisotropy of the pack.

PERMEABILITY OF SAMPLE POROUS MEDIA

In the previous section we have presented the flow diagrams for four different computationally generated porous media from the two simulation techniques implemented (LB and SPH) in this study. In general, the comparisons were encouraging but were of a qualitative nature. Now we move to a more quantitative comparison. Obtaining the permeability of a porous medium is not only a good quantitative comparison, but also is of significant importance in real world applications such as ground-water flow, oil recovery or flow in biological materials..

Since we are in the laminar regime, we assume that the flow can be approximated as a Darcy flow. Hence we estimate the permeability by

$$k = \frac{\mu}{\rho F_b}\langle U_z \rangle \qquad (8)$$

where k is the permeability, F_b is the body force per unit mass applied and the quantity in the angular brackets represents the average z-component of the superficial velocity at steady state conditions. The superficial velocity is obtained from the z-component of the steady state velocity via $U_z = \varepsilon u_z$, where u_z is the steady state fluid velocity. The predicted permeabilities for each packing and using each method are given in Table 1. A correlation used by Sheikhzadeh *et al.* (2005), is also given for the spherical cases. For the polydisperse case, we use d_{10} as an equivalent diameter obtained when 10% of solid material is smaller than d_{10}. In most cases this will be smaller than the mean diameter and has been used before for correlating the permeability (Sheikhzadeh *et al.*, 2005).

Table 1: Permeabilities calculated by the SPH and LB methods and an empirical correlation by Sheikhzadeh *et al.* (2005).

Case	• Porosity	LB k (m²)	SPH k (m²)	k $\frac{d^2 \, •^3 (1-•)^{-2}}{180}$
20 mono spheres	0.31	0.7×10^{-8}	3.4×10^{-8}	0.5×10^{-8}
50 mono spheres	0.38	0.6×10^{-8}	1.1×10^{-8}	0.6×10^{-8}
25 poly spheres	0.37	1.1×10^{-8}	4.1×10^{-8}	0.4×10^{-8}
20 mono cubes	0.46	1.1×10^{-8}	3.5×10^{-8}	-

We generally find that the SPH permeability results are larger than the LB permeability results by a factor of 2 to 5. The lowest permeability for both the LB and SPH techniques is the 50 mono-disperse spheres while the largest permeability is the 20 mono-disperse cubes (for the LB simulation) and the 25 poly-disperse spheres (SPH simulation). The 50 mono-disperse sphere case represents the most number of solid grains. As a consequence the solid grains, themselves, are small which in turn means the gap between grains is very small. Thus fluid will find it difficult to flow through these narrow gaps and hence the permeability will be small. The 25 mono-disperse cube case was the case we noticed a channel of fluid flowing down the right side (see Fig. 6). The presence of this channel provides an easy pathway for fluid flow and hence a larger permeability. The 25 poly-disperse sphere case is an interesting one. In this case, the combination of smaller and larger grains tends to reduce the number of large gaps, since the smaller spheres tend to fill these gaps. Hence we would expect the fluid would find it more difficult to flow through this medium and hence a

smaller permeability results. In this case the SPH simulation gives a larger permeability and the reason, we believe, for this is the slightly smaller grain size used. In future work we intend to refine our SPH setup to properly simulate this case. In general, the LB permeability values correspond quite well to Sheikhzadeh estimates, except possibly for the 25 polydisperse spheres, where it is 2-3 times larger. However, we must note there is not a large variation in the Sheikzadeh estimate (between the three values) and hence we can only regard these, at best, as correct in their order of magnitude.

COMPUTATIONAL COSTS

All the Lattice Boltzmann cases were run using a 200x200x200 lattice domain. Successive test simulations run up to 500 nodes per side showed a general increase in the permeability. However, after 200 nodes per side this increase was small and asymptoted to the limiting value. The permeability value for all the tested cases does not produce an increase larger than 5%. A current limitation of Sailfish is that there is no support for multi cores. However 200 nodes per side with a D3Q13 distribution fitted perfectly into the device memory (Tesla S2050). Under these optimum conditions, convergence of the results was achieved within 15 minutes. For the larger test problems (400 nodes per side), the code written using Palabos was used and single CPU simulation using more than 10GB of RAM required about 24 hrs to reach steady state. All the SPH simulations were run for a 100x100x100 lattice domain. This corresponds to roughly half-a-million particles and takes of the order of 3-4 weeks to reach steady state on a single cpu core (Xeon 5450).

The agreement in permeability values between the SPH and LB simulations is slightly disappointing. In general the permeability values obtained from the SPH simulations are larger than the permeability values obtained from the LB simulations (and the Sheikzadeh estimates). There are a number of reasons for this:

1) Although the SPH simulations have run for a long time, they had not reached steady state conditions. This means our current estimates for the average fluid velocity are somewhat over-estimated and consequently the permeability values from the SPH simulations will be overestimated.
2) The LB simulations are generally observed to underestimate the actual permeability for lower resolutions. The results for the permeability are for the lowest resolution attempted (200x200x200) and consequently we would generally expect to be lower than the actual permeability value. Preliminary calculations allow us to estimate that the discrepancy in the permeability when choosing 200 nodes per site and twice this value is of the order of 5%.

For this specific type of problem, the LB technique is much computationally faster than the SPH technique. The finest resolution attempted for SPH (100x100x100) takes of the order of months to run to achieve steady

state conditions on a single core machine. In contrast, the LB achieves steady state conditions after a few hundred thousand iterations achieved in less than half an hour (wall-time) when the problem fits entirely in the GPU device memory (i.e. for a resolution of 200x200x200). While the LB method is much faster for this problem, it might be the case that for variants (such as if the solid grains begins to change with time as in heap-leaching or bio-leaching due to digestion, crystallisation or chemical reaction) the SPH method may be more suitable. This is a result of not needing to pre-define the domain for the duration of a simulation, i.e. its domain can easily change as a function of time and the addition of multiple coupled reaction-diffusion equations in SPH is straight forward.

CONCLUSION

The present study compares the predictions by the SPH and LB methods for flow through computationally generated porous media consisting of grains with selected size and shape distributions. To do this we use the DEM method to generate the initial packing of the solid grains. An advantage of both fluid dynamics methods is that they do not rely on a direct spatial discretization of the Navier-Stokes equations to a fixed grid. The LB method in fact does not solve the Navier-Stokes directly and SPH uses a smoothing kernel function to evaluate spatial derivatives in the Navier-Stokes equation. This is advantageous in dealing with complicated boundary problems, as we have in the case of a porous medium.

Generally the fluid flow comparisons between LB and SPH are good but the permeability comparisons show reasonable differences for some cases. It is therefore important to be aware of the assumptions and behaviour of the solution methods, which were addressed in detail in the previous section. In all cases, it is of interest to see how both methods agree without constraints in time. This will be explored in future work. This, however, is the first time (to our knowledge) that such a comparison has been made between the two techniques for a suitably realistic porous medium.

Beyond the present comparison in terms of fluid flow and estimation of the permeability, future work can also be directed towards the study of the mixing process in pores, chaos, and enhanced effective diffusivity. An SPH particle history can be used directly for obtaining this information, while the LB approach will require solving a convective-diffusion equation on top of the fluid flow simulation. This information cannot be obtained by experimental techniques. Additionally, SPH has shown a larger success for the simulation of free surface flow, while lattice Boltzmann will generally require the adoption of a multiphase or free surface model.

REFERENCES

AHRENHOLZ, B., TOLKE, J., LEHMANN, P., PETERS, A., KAESTNER, A., KRAFCZYK, M.

DURNER, W. (2008), "Prediction of capillary hysteresis in a porous material using lattice-Boltzmann methods and comparison to experimental data and a morphological pore network model" *Adv. in Water Res.*, **31**, 1151-1173.

ARNS, C.H., PINCZEWSKI, W.V., KNACKSTEDT, M.A., GARBOCZI, E.J., (2002), "Computation of linear elastic properties from microtomographic images: Methodology and agreement between theory and experiment", *Geophysics,* **67**, 1396-1405.

BLUNT, M.J., JACKSON, M.D., PIRI, M., VALVATNE, P.H., (2002), "Detailed physics, predictive capabilities and macriscopic consequences for pore-network models of multiphase flow", *Adv. Water Res.,* **25**, 1069-1089.

CHAI, Z. H., SHI, B. C., LU, J. H., GUO, Z. L. (2010), "Non-Darcy flow in disordered porous media: A lattice Boltzmann study", *Computers & Fluids*, **39**, 2069-2077.

CLEARY P, (1998), "Modelling confined multi-material heat and mass flows using SPH*" Appl. Math. Model.*, **22**, 1061.

CLEARY P.W., (2004), "Large scale industrial DEM modelling", *Eng. Comput.*, **21,** 169-204.

CLEARY P.W., (2009), "Industrial particle flow modelling using discrete element method", *Eng. Comput.*, **26,** 698-743

CUNDALL P., STRACK O., (1979), "A discrete numerical model for granular assemblies", *Geotechnique*, **29**, 47-65.

DELANEY G.W., Cleary PW, (2010), "The packing properties of superellipsoids", Europyhsics Letters, 89, 34002.

D'HUMIERES D., BOUZIDI M., LALLEMAND P (2001), "Thirteen-velocity three-dimensional lattice Boltzmann model", Phys. Rev. E, **63**, 066702.

HASIMOTO H., (1959), "On the periodic fundamental solutions of the Stokes equations and their application to viscous flow past a cubic array of spheres", *J. Fluid Mech.*, **5,** 317-328.

HE, X., LUO, L.-S. (1997), "Lattice Boltzmann Model for the Incompressible Navier–Stokes Equation", *J. Stat. Phys.*, **88**, 927-944.

LIN, C. L., MILLER, J. D. & GARCIA, C. (2005), "Saturated flow characteristics in column leaching as described by LB simulation", *Min. Eng*., **18**, 1045-1051.

LUBACHEVSKY B. D. and STILLINGER F. H., (1990),., "Geometric properties of random disk packings" *J. Stat. Phys*., **60**, 561.

MONAGHAN J.J., (1994), "Simulating free surface flows with SPH", *J. Comput. Phys.* **110**, 39-406.

MONAGHAN J.J., (2005), "Smoothed particle hydrodynamics", *Rep. Prog. Phys.,* **68**, 1703-1759.

PAN, C., HILPERT, M. & MILLER, C. T. (2001), "Pore-scale modeling of saturated permeabilities in random sphere packings", *Phys. Rev. E*, **64**, 066702.

PAN, C. X., LUO, L. S. & MILLER, C. T. (2006), "An evaluation of lattice Boltzmann schemes for porous medium flow simulation" *Computers & Fluids*, **35**, 898-909.

PEREIRA, G.G., PRAKASH M., CLEARY, P.W., (2011), "SPH modeling of fluid at the grain level in a porous medium," *Appl. Math. Model.*, **35**, 1666-1670.

SCHWARTZ, L.M., AUZERAIS, F., DUNSMIR, J., MARTYS, N., BENTZ, D.P., TORQUATO, S., (1994), "Transport and diffusion in three dimensional composite media", *Physica,* **207A**, 28-36.

SHEIKHZADEH, G.A., MEHRABIAN, M.A., MANSOURI, S.H., SARRAFI, A. (2005), "Computational modelling of unsaturated flow of liquid in heap leaching—using the results of column tests to calibrate the model", *Int. J. Heat and Mass Transfer,* **48**, 279-292.

SUCCI, S., (2001), "The Lattice Boltzmann Equation For Fluid Dynamics and Beyond", Oxford, Oxford University Press.

ZICK A.A., HOMSY G.M., (1982), "Stokes flow through periodic array of spheres", *J. Fluid Mech.,* **115**, 13-26.

ZHAN X., SCHWARTZ, L., MORGAN, D., SMITH, W., TOKSOZ, N., (2008), "Numerical modelling of transport properties and comparison to laboratory measurements", *MIT Technical Report,* [Online @ http://www-eaps.mit.edu/erl/Zhan_2008_final.pdf.]

8th International Conference on CFD in Oil & Gas, Metallurgical and Process Industries
SINTEF/NTNU, Trondheim Norway
21-23 June 2011

CFD11-158

Towards a computational analysis of binary collisions of shear-thinning droplets

Christian Focke, **Dieter Bothe***

TUD Center of Smart Interfaces, 64287 Darmstadt, GERMANY

* E-mail: bothe@csi.tu-darmstadt.de

ABSTRACT

We investigate binary droplet collisions as a prototype elementary sub-process inside sprays and focus on shear-thinning liquids. The aim of these investigations is to develop semi-analytical descriptions for the outcome of droplet collisions. Such collision models can then be employed as closure terms for scale-reduced simulations.

Keywords: head on collision; lamella stabilization; free surface flow; VOF-Method.

NOMENCLATURE

Greek Symbols
- Delta distribution, [-].
- ρ Mass density, [kg/m^3].
- μ Dynamic viscosity, [kg/m.s].
- Curvature, [1/m^2].

Latin Symbols
- D Droplet diameter, [m].
- f Phase indicator function, [-].
- g Gravity, [m/s^2].
- t Time, [s].
- p Pressure, [Pa].
- **v** Velocity, [m/s].

Sub/superscripts
- Interface.
- 0 Initial value.
- c Continuous phase.
- d Disperse phase.
- t Time.

INTRODUCTION

To understand the influence of non-Newtonian shear-thinning fluid rheology on the flow inside the colliding drops, we employ direct numerical simulations (DNS) based on an extended Volume of Fluid method. The simulations are then analyzed according to the role of viscosity and its influence on the shape and temporal evolution of the collision complex. Detailed energy balances are used to distinguish different collision phases. This allows identifying the dominant flow phenomena which lead to viscous dissipation during the droplet interaction. In order to compare collisions of shear-thinning fluid with shear independent viscosity we find, that in all considered cases of head-on collisions an effective constant viscosity can be found, which leads to the same collision dynamics. This effective viscosity is neither the mean nor the minimum viscosity, but can be estimated on the basis of the DNS results. The aim is to derive laws for a prediction of this effective viscosity.

MODEL DESCRIPTION

The numerical method employed here is based on the Volume-of-Fluid (VOF) method by Hirt and Nichols, (1981). The VOF method solves the Navier-Stokes equations for an incompressible transient two-phase flow. The fundamental idea of this method is to capture the interface position implicitly by means of a phase indicator function, i.e. a scalar function $f = f(t, x)$ with, say, $f = 1$ in the dispersed phase and $f = 0$ in the continuous phase. Due to the absence of phase change, the transport of f is governed by the advection equation

$$\partial_t f + \nabla \cdot (f\mathbf{v}) = 0 \,. \tag{1}$$

Therefore, the VOF-method inherently conserves phase volume. This an important issue especially if the long term behavior of solutions is to be studied, where other methods like Level Set or Front tracking could lose too much of the droplet volume. In the Finite Volume (FV) discretization scheme employed here, the cell centered value of f corresponds to the phase fraction inside a computational cell. Based on these values, an approximation of the interface normal can be computed as

$$\mathbf{n} = \frac{\nabla f}{\|\nabla f\|} \,. \tag{2}$$

Combination of the fractional volume of the dispersed phase with the interface normal then allows an interface reconstruction with the so-called PLIC method (Rider and Kothe, 1998). This reconstruction of the phase geometry inside the computational cells creates important subgrid-scale information. The reconstructed interface is employed for an accurate convective transport of the phase indicator.

Once the phase distribution is known, a one-field formulation of the Navier-Stokes system is possible in which the interfacial momentum jump condition acts as a source term in the momentum equations. It reads as

$$\bullet\, \partial_t \mathbf{v} + \bullet\,(\mathbf{v}\cdot\nabla)\mathbf{v} + \nabla p = \mu\bullet\,\mathbf{v} + \bullet\,g + \bullet\,\bullet\,\mathbf{n}\bullet. \qquad (3)$$

where the material properties • and μ refer to the phase dependent values. The local values of the density are determined by

$$\bullet = f \bullet_d + (1-f)\bullet_c. \qquad (4)$$

The computation of cell viscosities at the interface is different for different parts of the stress. For the viscous normal stress which corresponds to elongational flow, the viscosities are calculated by arithmetic means. The off-diagonal part of the stress, corresponding to shear flow, involves also harmonic means. More precisely, the shear stress is computed at the cell vertices and done as follows. First, a mean cell viscosity is computed using the respective phase fractions as weights. Then, face viscosities are calculated as the arithmetic mean of adjacent cell values. Next, two harmonic mean, each from two neighboring face values, are determined and, finally, the minimum of these is chosen as the corner viscosity. The surface tension is incorporated using the conservative CSS model (Lafaurie et al., 1994), whereas the normals are computed using eq. 2.

Lamella Stabilization

The results show that during collisions an extremely thin fluid lamella appears in case of large Weber numbers. This lamella has to be accounted for in any physically sound simulation and we apply a stabilizing algorithm to be able to keep the lamella from rupturing. A rupture of a collision lamella cannot be observed in binary droplet collisions (Tanguy and Berlemont, 2005, Qian and Law, 1997, Ashgriz and Poo, 1990). The simulations give a quantitative prediction of the resulting diameter of the droplet collision complex. The stabilizing algorithm enables us to compute collision results for reflexive separations with large Weber numbers. The surface tension is incorporated using the continuum surface stress (CSS) model. The algorithm of CSS smoothes the *f*-field using a 27 cell stencil. Subsequently a capillary pressure tensor is computed on the smoothed field again using a 27 cell stencil so that the surface tension in one cell is influenced by 125 cells. The stabilization algorithm corrects the capillary pressure tensor computation by avoiding artificial interactions of the two sides of the lamella. For the computation of the surface tension of one lamella side a modified *f*-field is used which contains only the one side of the lamella, as illustrated in Figure 1.
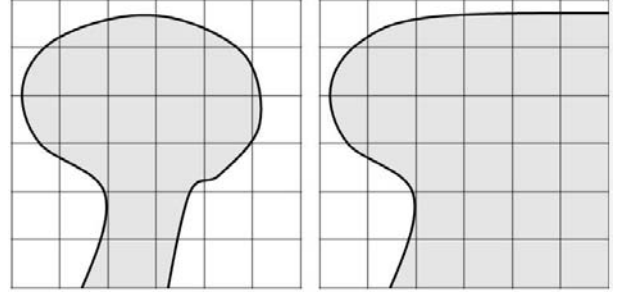
Figure 1: schematic of lamella stabilization, left: original *f*-field of rim and lamella, right: *f*-field used for surface tension computation of the left lamella side.

The surface tension of the opposite lamella side is computed in the same manner. In the rim area the original *f*-field is used. The surface tension forces are computed for the different fields and afterwards merged in an appropriate way. In order to distinguish both lamella sides and to allow for a correct *f*-transport, a minimum lamella thickness of two cells must be kept by filling the lamella with artificial liquid. Special care has to be taken for the amount of additional liquid to avoid considerable effects on the collision dynamics. In case of a head on collision of two drops, only the correction of the surface tension computation is needed. In case of an off-center collision or different drop diameter, a modest addition of artificial liquid is necessary.

The lamella stabilization is validated by comparison with experiments of Qian and Law (1997). The resolution of the simulation is 64 x 64 x 32 cells. Table 1 shows the maximum enlargement of the collision complex of Qian and Law (1997). The predicted collision complex size by *FS3D* shows a good agreement with the experimental data. The simulation shows, that the thin collision lamella appears at t • 0.45 ms and disappears at t • 0.7 ms.

Table 1: Maximum enlargement of the collision complex.

t [ms]	experiment D_{max}/D_0 [-]	deflection to experiment *FS3D*	deflection to experiment in Nikolopoulos et al. (2009)
0.10	3.08	2.9%	1.6%
0.50	4.55	8.1%	8.6%
0.73	4.86	1.2%	0.0%
0.95	4.54	3.5%	7.0%

The experiments by Qian and Law (1997) are also used as validation data by Nikolopoulos et al. (2009). Despite the fact that an adaptive local grid refinement is used, the collision lamella ruptures in the simulations. Table 1 shows that the ruptured lamella in Nikolopoulos et al. (2009) leads to a deflection of 7.0% at t = 0.95 ms. The prediction of the shape of the collision complex by *FS3D* shows good agreement with the experimental data as can be seen in Figure 2.

Figure 2: Off-center collision of water droplets. Upper row: experiment, below: *FS3D* with lamella stabilization.

With a resolution of 64 x 64 x 32 cells, 6.01 % artificial mass is added, with a resolution of 128 x 128 x 64 cells, 0.50 % mass is added. We assume that higher resolutions (512 x 512 x 256 cells are possible) will further reduce the mass added. Applying the lamella stabilization, the VOF-code is able to predict the correct outcome of such collisions.

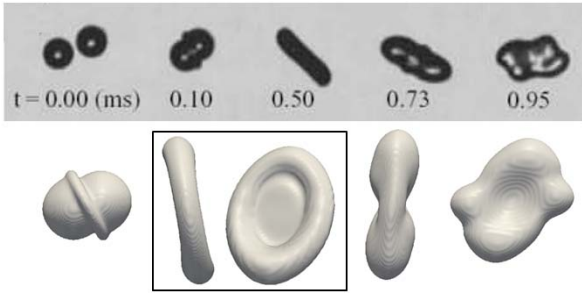### Validation for non-Newtonian Fluid Dynamics

In order to test the tangential movement of the interface in shear thinning fluids, a pressure driven two-phase steady laminar flow of a power-law fluid in contact with a Newtonian fluid between two stationary parallel planes of infinite extent was chosen. The predicted velocity profile in the gap was compared to the analytical solution of the governing equations by Chhabra and Richardson (1999). The numerical solution agrees very well with the analytical one, the error of the maximum velocity being below 1%.

In order to test the normal movement of the interface, the 2D Bretherton problem with a shear thinning continuus phase provides an appropriate test case. The Bretherton problem describes the displacement of a viscous Newtonian liquid by an inviscid gas bubble in a gap (Bretherton, 1961). For shear thinning rheology, the film thickness is described by Gutfinger and Talmadge, (1965) and Halpern and Gaver, (1994).

The simulation is performed with 512 x 64 cells in order to resolve the film with at least 4 cells. According to the analytical equation the film thickness for a Capillary number of Ca = 0.05 is $5.63 \cdot 10^{-5}$ m. *FS3D* predicts a film thickness of $5.70 \cdot 10^{-5}$ m. With only 1.3 % deviation the prediction of the film thickness is sufficiently accurate. For details of these validation cases see Focke and Bothe (2011).

For the validation of our numerical simulations, experimental results on binary droplet collisions from (Motzigemba et al., 2002) are used. The shear thinning liquid is an aqueous solution 2.8 weight% CMC sodium salt.

RESULTS

The simulations were performed on 16 Intel XEON Linux-Cluster cores with 4 GB main memory per core using Cartesian grids having about 8.4 million cells. Based on the symmetry of a binary droplet collision of two equal sized droplets, 3 symmetry planes were used in the simulations to reduce the computational effort.

The domain size is 1.4 x 1.4 x 7 cm³, the resolution is 256 x 256 x 128 cells. The predicted temporal evolution of the droplet collision complex diameter is shown in Figure 3.

The comparison of the time evolution between the DNS and the experimental results from (Motzigemba et al., 2002) show that the numerical simulation nearly captures the maximum collision complex diameter which is also attained at the correct time, but shows deviations in the contraction phase where the retraction of the collision complex seems to be faster than in the experiments. On the other hand, the range of uncertainties in the experimental measurements given in (Motzigemba et al., 2002) is +/- 10 % for the initial diameter D_0. Therefore, to investigate the sensitivity of the evolution of the collision complex w.r. t. errors in the initial diameter measurement, we performed simulations with a change in the initial diameter D_0 by +/- 10 %. This variation of the initial diameter leads to changes in the maximum complex diameter from 3.36 to 4.71 d/D_0, hence the maximum diameter of the experimental data is in range of the simulations.
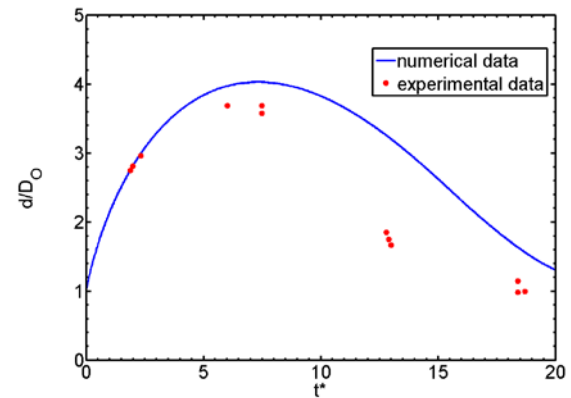
Figure 3: Dimensionless diameter of collision complex vs. dimensionless time t*=t/(D/U) for CMC-solution (2.8 wt%): Experiment versus simulation.

Comparison of Newtonian and non-Newtonian droplet collisions

In this section we study the question whether a non-Newtonian droplet collision can be modeled with a Newtonian effective viscosity. For this purpose a constant viscosity is to be found which results especially in the same collision complex diameter as for the shear-thinning fluid. Such an effective viscosity can be found by simulating the collisions with different Newtonian viscosities and then using interpolation. Table 2 shows the maximum collision complex diameter for different Newtonian viscosities.

Table 2: Resulting collision complex diameter for different constant viscosities.

μ [mPa s]	d_{max} / D_0 [-]
45	4.51
54	4.14
60	3.93
75	3.47
102	2.88

Here the effective viscosity turns out to be 54 mPa·s. The comparison of the evolution of the collision complex with the Newtonian liquids of the effective viscosity compared to the shear-thinning droplet collision shows that the full time evolution appears to be almost identical. Also, only minor differences can be found in the shapes of the collision complex as can be seen in Figure 4.
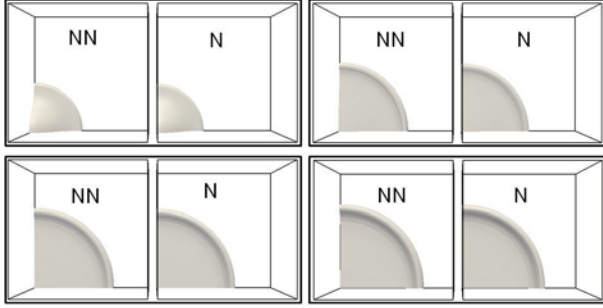
Figure 4: Shapes of the collision complex at different stages with shear-thinning fluid (NN) and a Newtonian fluid with adjusted viscosity (N) at 0.1, 0.2, 0.3, 0.4 ms

A difference can be found in the minimum thickness of the lamella. In the Newtonian case the thickness of the lamella is 4.8 µm, while in the non-Newtonian case the thickness of the lamella is 5.6 µm. A comparison of the velocity fields shows almost no difference.

The explanation lies in the fact that relatively small regions of high shear rate and reduced viscosity at the beginning of the collision are more important than the mean viscosity during the collision. The reason for this phenomenon can be seen in Figure 5 and is explained below.

Figure 5: Time evolution of different energy components during a binary collision.

Figure 5 shows the evolution of different components of the energy during the droplet collision. The influence of the viscosity on the collision is visible in the dissipated energy. Figure 5 reveals that most of the viscous dissipation takes place at the beginning of the collision. Further analyses show that during the initial collision, the viscous friction leads to dissipation due to shear. Subsequently, the dissipation due to elongati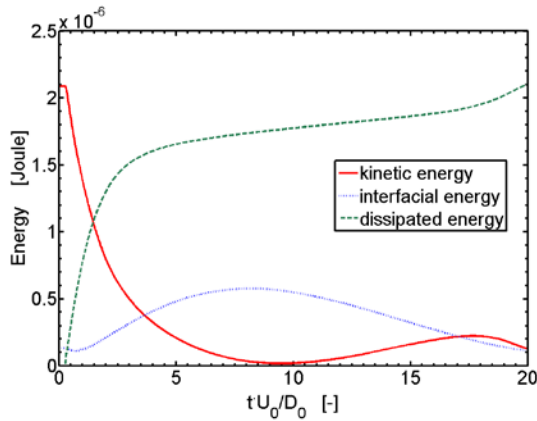on rises, while the shear part decreases. In later stages of the collision only surface- and inertia forces dominate the

collision dynamics. For further details see Focke and Bothe (2011).

CONCLUSION

Given that no rupture of the collision lamella occurs in the experiments, the numerical stabilization introduced above is an appropriate means to capture the collision dynamics with significantly reduced numerical effort. The stabilization on a symmetry plane gives reliable results for a lamella thickness even below 1 µm. Thereby, the lamella is resolved with 1/3 grid cell without observing any limitations at this size. In the case of an off-center collision of droplets with different diameter, the lamella stabilization has to be extended and validated for non-symmetric situations which is one of our present activities.

The droplet collisions with shear thinning liquid are compared to collisions of droplets with Newtonian rheology. A constant effective viscosity was found that produces the same collision complex diameter as the shear thinning liquid. The simulations show that even the temporal evolution and the shapes are almost the same. The temporal evolution of the viscous energy dissipation shows that viscous friction forces only influence the collision dynamics during the initial stage.

ACKNOWLEDGEMENTS

REFERENCES

Ashgriz, N. and Poo, J.Y., (1990), "Coalescense and separation in binary collisions of liquid drops", *Journal of Fluid Mechanics*, **221**, 183-204.

Bretherton, F.P., (1961), "The motion of long bubbles in tubes", *Journal of Fluid Mechanics*, **10**, 166-188.

Chhabra, R.P. and Richardson, J.F., (1999), "Non-Newtonian Flow in the Process Industries: Fundamentals and Engineering Applications", Butterworth-Heinemann.

Focke, C. and Bothe, D., (2011), "Computational Analysis of Binary Collisions of shear-thinning Droplets", *Journal of Non-Newtonian Fluid Mechanics*, accepted.

Gutfinger, C. and Tallmadge, J.A., (1965), "Films of non-Newtonian fluids adhering to flat plates", *AICHE Journal,* **11**, 403-413.

Halpern, D. and Gaver, P., (1994), "Boundary element analysis of the time-dependent motion of a semi-infinite bubble in a channel", *Journal of Computational Physics*, **115**, 366-375.

Hirt, C.W. and Nichols, B.D., (1981) "Volume of Fluid (VOF) Method for the Dynamics of Free Boundaries", *Journal of Computational Physics*, **39**, 201-225.

Lafaurie, B., Nardone, C., Scardovelli, R., Zaleski, S., Zanetti, G., (1994), "Modelling merging and fragmentation in multiphase flows with surfer" *Journal of Computational Physics*, **113**, 134-147.

Motzigemba, M., Roth, N., Bothe, D., Warnecke, H.-J., Prüss, J., Wielage, K., Weigand, B., (2002), "The Effect of Non-Newtonian Flow Behaviour on Binary Droplet Collisions: VOF-Simulation and Experimental Analysis", *Proc. 18th Annual Conf. Liquid Atomization and Spray Systems*, Zaragoza, Spain, November 9-11.

Nikolopoulos, N., Theodarakakos, A., Bergeles, G. (2009), "Off-centre binary collision of droplets: A numerical investigation", *International Journal of Heat and Mass Transfer*, **52**, 4160-4174.

Qian, J. and Law, C.K., (1997), "Regimes of coalescence and separation in droplet collision", *Journal of Fluid Mechanics*, **331**, 59-80.

Rider, W.J. and Kothe, D.B., (1998), "Reconstructing volume tracking", *Journal of Computational Physics*, **2**, 112–152.

Tanguy, S. and Berlemont, A., (2005), "Application of a level set method for simulation of droplet collisions", *International Journal of Multiphase Flow*, **31,** 1015-1035.

8th International Conference on CFD in Oil & Gas, Metallurgical and Process Industries
SINTEF/NTNU, Trondheim Norway
21-23 June 2011

CFD11-159

MAPPING OF THE OPERATING WINDOW OF A LAB SCALE BUBBLING FLUIDIZED BED REACTOR BY CFD AND DESIGNED EXPERIMENTS

Schalk CLOETE[1] & Shahriar AMINI[2]*

[1] NTNU Department of Energy and Process technology, Richard Birkelands Vei 3, 7034 Trondheim, NORWAY

[2] SINTEF Materials and Chemistry, Richard Birkelands Vei 3, 7034 Trondheim, NORWAY

* E-mail: Shahriar.Amini@sintef.no

ABSTRACT

CFD simulations were completed to map out the operating window of a lab-scale, pseudo-2D, bubbling fluidized bed reactor that will be constructed for CFD validation purposes. Simulations were carried out within the framework of the kinetic theory of granular flows (KTGF) using a two fluid model (TFM) approach. A central composite design was used to structure the simulation experiments, quantify the significance of factors and construct a model of reactor performance within a given parameter space. The parameter space was defined by four factors: gas feed rate, reactor operating temperature, bed height and solids fed rate. Of these four factors, the gas feed rate was found to be the most influential on reactor performance (degree of feed gas conversion achieved). A decrease in gas feed rate caused an increase in gas residence time and thereby facilitated better gas conversion. The bed height was the next most influential factor. Reactor performance was improved in taller beds also as a result of an increased gas residence time, but the beneficial effect of bed height was only about half of that caused by the gas feed rate. This could be explained by the substantial bubble growth observed in taller beds as opposed to the progressively smaller bubbles created by lower gas feed rates. Larger bubbles significantly decrease the quality of gas-solids contact and reduce the overall rate of reaction. The effects of reactor operating temperature and solids feed rate were also highly significant, but smaller than those of gas feed rate and bed height. Once the effects of these factors were quantified, a quadratic model of the response of reactor performance to changes in the four factors was constructed to serve as an operational map for the reactor. This map will be used as an initial operational guideline for operating the real reactor.

Keywords: CFD, kinetic theory of granular flows, two fluid model, bubbling fluidized bed, reactor, central composite design, designed experiments.

NOMENCLATURE

Main Symbol definitions:

Greek symbols:

α Volume fraction

ϕ_{gs} Interphase energy transfer (kg/m.s^3)

γ Dissipation rate (kg/m.s^3)

λ Bulk viscosity (kg/(m.s))

μ Viscosity (kg/(m.s))

Θ_s Granular temperature (m^2/s^2)

ρ Density (kg/m^2)

$\bar{\bar{\tau}}$ Stress tensor (kg/(m.s^2))

$\vec{\upsilon}$ Velocity vector (m/s)

∇ Gradient/Divergence (1/m)

Regular symbols:

d Diameter (m)

$\vec{g}$ Gravity vector (m/s^2)

H Bed height (m)

$\bar{\bar{I}}$ Identity tensor

$\vec{J}$ Diffusive flux (kg/(m^2.s))

K_{sg} Interphase momentum exchange coefficient (kg/(m^3.s))

k Diffusion coefficient (kg/m.s)

k Reaction rate constant (mol^{1-n}m^{3n-2}/s)

M Molar weight (kg/kmol)

N Number of moles (mol)

p Pressure (Pa)

R Universal gas constant (8.314 J/(K.mol))

R^H Heterogeneous reaction rate (mol/m^{3}s)

S Source term

V Volume (m^3)

Y Species mass fraction

x Mass fraction

Sub- and superscript definitions:

Greek symbols:

Θ_s Granular temperature

$\vec{\upsilon}$ Momentum

Regular symbols:

eq Equivalent

g Gas

gs Gas-solids

i Species i

n Reaction order

s Solids

INTRODUCTION

A fluidised bed reactor presents a highly coupled, non-linear system that is notoriously difficult to model. Difficulties begin with the complex hydrodynamic structures exhibited by these reactors. These flows are characterised by the formation of meso-scale structures which have a major influence on all the transport phenomena inside the reactor. The nature of these structures vary greatly depending on the fluidisation regime in which the reactor is operated. Secondly, the heat transfer and

resulting temperature distribution inside the reactor needs to be understood, especially in larger units. Local temperature will depend greatly on the local heat of reaction, the boundary conditions and the generally good mixing caused by the hydrodynamic behaviour of the bed. Finally, the reaction kinetics occurring inside these beds depends both on the surface reaction rate occurring on each individual particle (mostly an exponential function of temperature) and the quality of gas-solid contact (greatly influenced by the nature of the meso-scale structures characterising the reactor hydrodynamics). The three areas of hydrodynamics, heat transfer and reaction kinetics therefore interact and can give rise to numerous non-linear effects that are impossible to predict with standard engineering models.

For this reason, the framework of computational fluid dynamics (CFD) is selected as the modelling tool for studying these systems. The fundamental basis of the conservation of mass, species, momentum and energy through space and time on which CFD is based allows such non-linear interactions to be simulated directly. CFD also has the distinct advantage over physical experimentation that it is not subject to any physical limitations. This implies that any combination of design and operational variables can readily be simulated without any practical difficulties, making CFD the ideal tool for optimization and prototyping. The ease with which flow information can be extracted from a CFD simulation will also aid greatly in the proper understanding and appropriate utilisation of fluidized bed reactor systems.

In order to exploit these advantages, the current project was defined to improve CFD modelling of bubbling fluidized bed reactors. A lab-scale reactor will be constructed during this project for the purpose of CFD validation. The aim of the work presented in this paper is to use the CFD models available today to map the initial operating window of this reactor and ensure that the required reactor performance can indeed be achieved using the proposed design. The feasibility of using designed experiments in combination with CFD for this purpose will also be evaluated.

MODEL DESCRIPTION

Equation system

The CFD model was based on the standard Eulerian-Granular two fluid model (TFM) with closure laws from the kinetic theory of granular flows (KTGF).

Conservation equations

The conservation of mass,

$$\frac{\partial}{\partial t}\left(\alpha_g \rho_g\right) + \nabla \cdot \left(\alpha_g \rho_g \vec{\upsilon}_g\right) = \alpha_g S_g \tag{1}$$

$$\frac{\partial}{\partial t}\left(\alpha_s \rho_s\right) + \nabla \cdot \left(\alpha_s \rho_s \vec{\upsilon}_s\right) = \alpha_s S_s \tag{2}$$

momentum,

$$\frac{\partial}{\partial t}\left(\alpha_g \rho_g \vec{\upsilon}_g\right) + \nabla \cdot \left(\alpha_g \rho_g \vec{\upsilon}_g \vec{\upsilon}_g\right) = -\alpha_g \nabla p \\ + \nabla \cdot \overline{\overline{\tau}}_g + \alpha_g \rho_g \vec{g} + K_{sg}\left(\vec{\upsilon}_s - \vec{\upsilon}_g\right) + S_g^{\vec{\upsilon}} \tag{3}$$

$$\frac{\partial}{\partial t}\left(\alpha_s \rho_s \vec{\upsilon}_s\right) + \nabla \cdot \left(\alpha_s \rho_s \vec{\upsilon}_s \vec{\upsilon}_s\right) = -\alpha_s \nabla p - \nabla p_s \\ + \nabla \cdot \overline{\overline{\tau}}_s + \alpha_s \rho_s \vec{g} + K_{gs}\left(\vec{\upsilon}_g - \vec{\upsilon}_s\right) + S_s^{\vec{\upsilon}} \tag{4}$$

and species

$$\frac{\partial}{\partial t}\left(\alpha_g \rho_g Y_{g,i}\right) + \nabla \cdot \left(\alpha_g \rho_g \vec{\upsilon}_g Y_{g,i}\right) = \nabla \cdot \alpha_g \vec{J}_{g,i} + \alpha_g S_{g,i} \tag{5}$$

$$\frac{\partial}{\partial t}\left(\alpha_s \rho_s Y_{s,i}\right) + \nabla \cdot \left(\alpha_s \rho_s \vec{\upsilon}_s Y_{s,i}\right) = \nabla \cdot \alpha_s \vec{J}_{s,i} + \alpha_s S_{s,i} \tag{6}$$

were solved for both the gas and the solids phases. The source terms on the right hand side of these equations originate from heterogeneous reactions. No conservation of energy was included on the assumption that temperature variations are negligible in the small, well mixed reactor simulated here.

Closures

Only a partial description of the closure equations will be given here in a reference based format. For a full description of the equation set, refer to (Cloete, *et al.*,2011).

The solids stresses in equation (4) are modelled according to the kinetic theory of granular flows. Here, the motions of the particles are likened to motions of molecules in a gas. Just as uncorrelated molecular motions, quantified as the temperature, give rise to gas viscosity and pressure, uncorrelated particle motions, quantified as the granular temperature, are modelled to give rise to a granular viscosity and pressure. The granular temperature is written in conservation form as follows:

$$\frac{3}{2}\left[\frac{\partial}{\partial t}\left(\alpha_s \rho_s \Theta_s\right) + \nabla \cdot \left(\alpha_s \rho_s \vec{\upsilon}_s \Theta_s\right)\right] = \left(-p_s \overline{\overline{I}} + \overline{\overline{\tau}}_s\right) : \nabla \vec{\upsilon}_s \\ + \nabla \cdot \left(k_{\Theta_s} \nabla \Theta_s\right) - \gamma_{\Theta_s} + \phi_{gs} \tag{7}$$

Equation (7) was solved in its algebraic form by neglecting the convection and diffusion terms. This is a good assumption in slow moving, dense beds where the local generation and dissipation of granular temperature would far outweigh the contributions from convective and diffusive transport. The solids pressure and collisional dissipation of fluctuating energy were modelled according to (Lun, *et al.*,1984), while the inter-phase drag induced damping was modelled according to (Gidaspow, *et al.*,1992).

The solids stress tensor, responsible for the generation of granular temperature in equation (7) and for viscous momentum diffusion in equation (4) is written as follows:

$$\overline{\overline{\tau}}_s = \alpha_s \mu_s \left(\nabla \vec{\upsilon}_s + \nabla \vec{\upsilon}_s^T\right) + \alpha_s \left(\lambda_s - \frac{2}{3}\mu_s\right)\nabla \cdot \vec{\upsilon}_s \overline{\overline{I}} \tag{8}$$

Here, the shear viscosity was modelled to consist of three parts: kinetic and collisional (Gidaspow, *et al.*,1992) as well as frictional (Schaeffer,1987). The bulk viscosity was modelled according to (Lun, *et al.*,1984).

No turbulence modelling was included due to the fine mesh used and the relatively slow moving bubbling fluidized bed simulated.

The inter-phase momentum exchange coefficient in equations (3) and (4) was modelled according to (Syamlal, *et al.*,1993).

A heterogeneous reaction describing the reduction of Iron(III)oxide by methane was simulated:

$$CH_4 + 4Fe_2O_3 \rightarrow 8FeO + CO_2 + 2H_2O$$
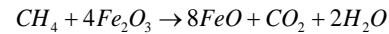
This is the primary reaction occurring in the reduction of the naturally occurring oxygen carrier material, Ilmenite. Kinetics of this reaction was experimentally determined by (Abad, *et al.*,2011) as being a first order reaction with the following Arrhenius type rate constant.

$$k = 9.8\exp\left(\frac{-135200}{RT}\right) \tag{9}$$

The rate constant was subsequently used to calculate the reaction rate per unit volume occurring in each cell based on the shrinking unreacted core model (Levenspiel,1999).

$$R^{H} = -\frac{1}{V}\frac{dN_{CH_4}}{dt} = \frac{6}{d_s}\alpha_s x_{Fe_2O_3}^{2/3} k\left(\frac{x_{CH_4}\rho_g}{M_{CH_4}}\right)^n \qquad (10)$$

The expression in equation (10) shows that the reaction rate depends on the following parameters:

- The surface area of solids available for reaction which is a function of the size of the grains on which the reaction takes place and the local solids volume fraction in the cell. The grain diameter in this study was 2.5 µm (Abad, *et al.*,2011).
- The degree of conversion of Fe_2O_3 which models the reduction of the surface area exposed by the shrinking unreacted core as the reaction progresses.
- The reaction rate constant which is a function of the type of reaction taking place and the temperature.
- The local reacting gas species concentration to some power (order of reaction). This reaction was found to be first order (Abad, *et al.*,2011).

Reactor performance will primarily depend on optimization of these parameters so as to result in the highest reaction rate economically achievable.

The calculated heterogeneous reaction rate is subsequently used to calculate mass, species and momentum source terms to be added to the conservation equations (equations (1) through (6)) as detailed in (Cloete, *et al.*,2011).

Simulation domain, boundary conditions and materials

The simulation domain consisted of a simple 2D planar geometry, 0.15 m in width and 1.8 m in height. The geometry is depicted in Figure 1.

Gas was injected through a velocity inlet modelled at the bottom face of the geometry. The velocity magnitude and the temperature with which the gas was injected were changed according to the experimental run in question. The gas always consisted of 100% methane. Gas density and viscosity were implemented as a function of temperature and chemical composition.

Solids were injected through a 2 cm velocity inlet with the velocity adjusted according to each experimental run. The solids were injected at a volume fraction of 0.6 and a chemical composition of 33% Fe_2O_3 and the balance inerts (calculated from (Abad, *et al.*,2011)). The solids had a density of 4250 kg/m^3 and a mean particle diameter of 250 µm.

Five possible solids outlets were considered (see Figure 1). The solids outlets were 2 cm in height and designated either as a wall or an atmospheric pressure outlet depending on the simulation run in question. For any given experiment, four of these outlets were walls and the remaining one a pressure outlet at atmospheric pressure.

The gas outlet was also modelled as an atmospheric pressure outlet.

Partial slip walls were included in the simulation according to the formulation of (Johnson and Jackson,1987). The specularity coefficient, representing the roughness of the wall, was set to 0.5. The regular walls and the four potential pressure outlets not utilized in any particular experimental run were given identical boundary conditions.

The geometry was meshed with square, structured computational cells, 20 particle diameters in width. A single level of hanging node adaptive grid refinement was then added up to the level of the solids outlet in order to better resolve the bubble structures in the bed. The resulting cell size of 10 particle diameters was previously found to easily achieve hydrodynamic grid independence but not complete reaction kinetic grid independence (Hommel, *et al.*,2011). The reaction kinetic grid independence observed on this particular grid size was not great, however, and should lead to correct quantitative predictions of reactor performance.
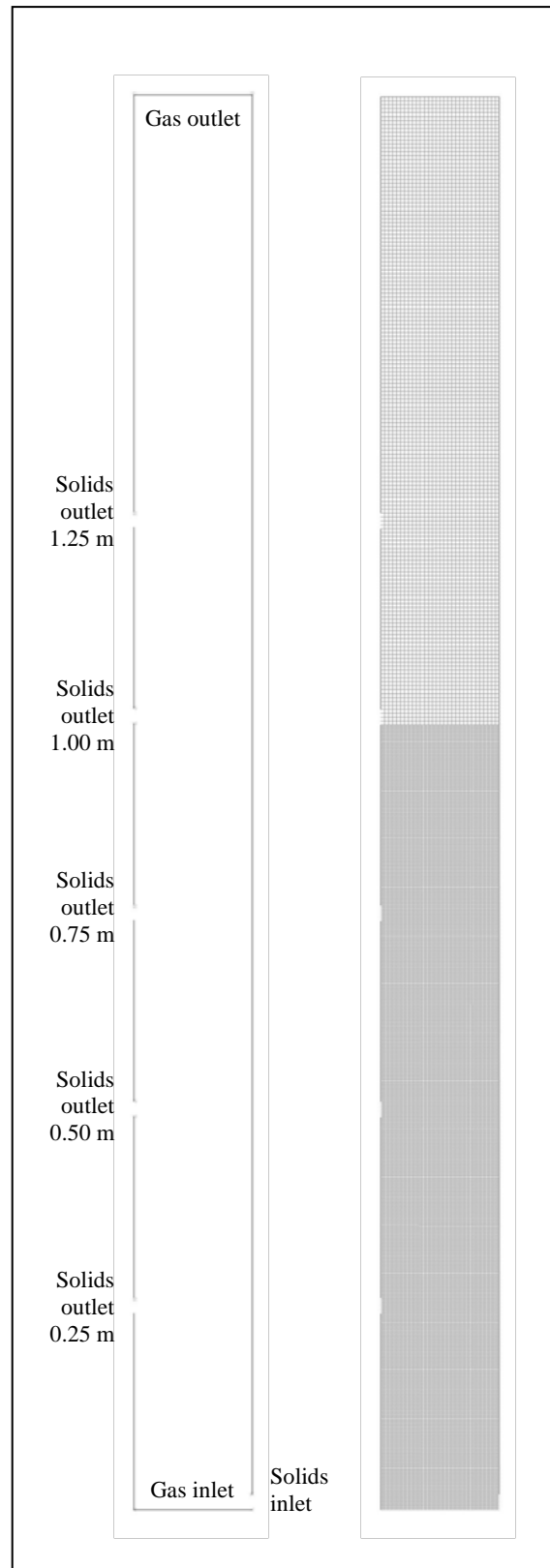
Figure 1: Simulated reactor geometry and mesh for a simulation with a 1 m bed height.

Solver settings

The commercial CFD package, FLUENT 12.1 was used as the flow solver to carry out the simulations. The phase-coupled SIMPLE algorithm (Patankar,1980) was selected for pressure-velocity coupling, while the QUICK scheme (Leonard and Mokhtari,1990) was employed for discretization of all remaining equations. 1st order implicit temporal discretization was used.

Operation and data extraction

Each of the 26 simulation runs were initialised with a fixed bed patched in at a volume fraction of 0.5 up to the location of the solids outlet. Simulations were then run on a non-refined grid until the average Fe_2O_3 mass fraction inside the bed levelled out. This was a slow process and typically required about 150 seconds of simulation time. Once this directive was achieved, the bed was refined up to the level of the solids inlet and the simulation was run for at least 10 seconds more, allowing for at least one clear pass of fresh reacting gas through the reactor.

From this point on, the mass flow rate of methane was collected on a horizontal line located at the bottom of the solids outlet (at the top of the bed). This fluctuating signal was collected for a minimum of 20 seconds and subsequently time-averaged in order to find the mean rate at which methane exits the reactor unreacted. This value was then normalised by the mass rate at which methane enters the reactor to facilitate easy comparison between experimental runs.

The unreacted methane performance measure hinders easy data interpretation, however, because of its exponential nature. If this performance measure can be linearised, data interpretation would be much easier. Additionally, the statistical methods employed in this study require linear performance measures in order to reliably quantify system performance.

Therefore, the exponential unreacted methane performance measure was linearised according to the height of the bed required to achieve that specific degree of conversion. This was accomplished by completing five simulations at different bed heights and establishing a relation between the bed height and the amount of unreacted methane. This relation is shown in Figure 2.
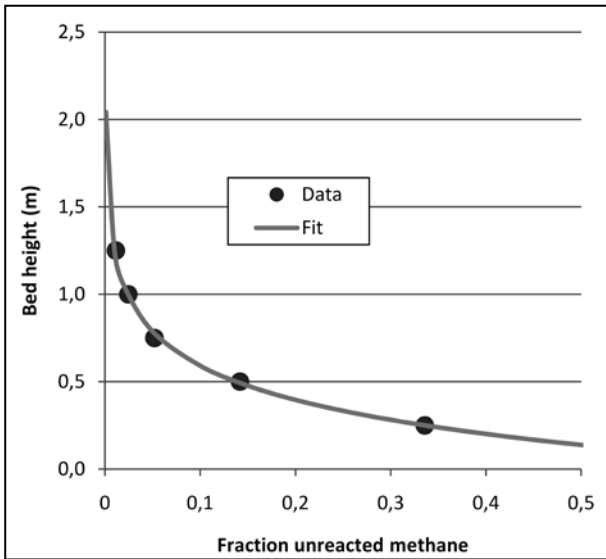
Figure 2: Relation between fraction unreacted methane and bed height.

It is shown that a very good fit is achieved. Using this fit, the fraction of unreacted methane performance measure extracted from any simulation can easily be converted to an equivalent bed height which is a linear and easily visualised performance measure. The relation between these two performance measures shown in Figure 2 is mathematically expressed as:

$$H_{eq} = \frac{\ln\left(x_{CH_4} - 4.315\text{E-}4\right) + 0.2005}{-3.560} \quad (11)$$

The experimental points in Figure 2 were calculated at a gas mass flow rate of 0.0024 kg/s, a temperature of 800°C and a solids mass flow rate of 0.5 kg/s. The equivalent bed height

given in equation (11) should therefore be interpreted as the bed height required to achieve a specific degree of methane conversion when operated under the aforementioned operating conditions.

RESULTS AND DISCUSSION

The simulation experiments were organised in the form of a central composite design (Montgomery,2001). This form of experimental design evaluates a number of independent variables, henceforth called 'factors', at five different values, henceforth called 'levels'. The response of a number of dependent variables to changes in these factors can then be quantified statistically and easily visualised. Design and analysis of the central composite design was carried out by means of the commercial software package STATISTICA 10. Four factors were considered in the design:

- The mass flow rate of methane entering the reactor
- The operating temperature of the reactor
- The height of the reactor bed
- The mass flow rate of solids to the reactor

The influence of variations in the four factors on the dependent variable of equivalent bed height will be determined and elaborated upon in the section.

Experimental results

A four factor central composite design requires 26 experiments to be performed. The specifications of these 26 experiments and the equivalent bed height returned by each run is summarised in Table 1.

Table 1: Results from the four factor central composite design.

Run	$\dot{m}_g$ (kg/s)	T (°C)	H (m)	$\dot{m}_s$ (kg/s)	x_{CH_4}	H_{eq} (m)
1	0.0016	750	0.50	0.3	0.0618	0.728
2	0.0016	750	0.50	0.7	0.0354	0.885
3	0.0016	750	1.00	0.3	0.0046	1.480
4	0.0016	750	1.00	0.7	0.0020	1.764
5	0.0016	850	0.50	0.3	0.0149	1.134
6	0.0016	850	0.50	0.7	0.0079	1.319
7	0.0016	850	1.00	0.3	0.0014	1.901
8	0.0016	850	1.00	0.7	0.0010	2.067
9	0.0032	750	0.50	0.3	0.5152	0.130
10	0.0032	750	0.50	0.7	0.3587	0.232
11	0.0032	750	1.00	0.3	0.1433	0.490
12	0.0032	750	1.00	0.7	0.0644	0.716
13	0.0032	850	0.50	0.3	0.3498	0.239
14	0.0032	850	0.50	0.7	0.1421	0.493
15	0.0032	850	1.00	0.3	0.0807	0.652
16	0.0032	850	1.00	0.7	0.0241	0.995
17	0.0008	800	0.75	0.5	0.0011	2.014
18	0.0040	800	0.75	0.5	0.2282	0.359
19	0.0024	700	0.75	0.5	0.1427	0.491
20	0.0024	900	0.75	0.5	0.0110	1.221
21	0.0024	800	0.25	0.5	0.3359	0.251
22	0.0024	800	1.25	0.5	0.0115	1.209
23	0.0024	800	0.75	0.1	0.7164	0.038
24	0.0024	800	0.75	0.9	0.0337	0.899
25	0.0024	800	0.75	0.5	0.0472	0.804
26	0.0024	800	0.75	0.5	0.0520	0.777

ANOVA

The first and foremost result given by a central composite design comes in the form of the analysis of variance (ANOVA). The ANOVA quantifies the significance of each factor on the chosen dependent variable. Both a linear and a

quadratic effect can be calculated for each factor as well as first order interaction effects between all factors. The percentage of the total variance in the design explained by each of these effects can be calculated from the ANOVA. Additionally, the significance of each effect can be quantified as a p-value. The p-value is calculated from the F-test which weighs the amount of explained variance (variance resulting from changing the level of the factor) against the amount of unexplained variance (variance resulting from human errors, round-off errors, averaging errors, data not well described by the chosen mathematical function or the presence of significant higher order interaction effects). The amount of unexplained variance is an indication of the amount of uncertainty in the design. A large amount of uncertainty reduces the confidence with which a specific effect can be classified as significant. Thus, if the ratio of explained to unexplained variance becomes small due to a large amount of unexplained variance, the significance of the effect reduces. This significance is measured by the p-value. Typically, a p-value of 0.05 or lower is regarded as significant. A p-value of 0.05 can be interpreted as follows: if this experiment was repeated 100 times with the same degree of error, the opposite of the currently predicted effect would occur 5 times. Thus, the predicted effect would occur 95 out of a 100 times.

ANOVA results are displayed in Table 2.

Table 2: Percentage of variance and significance of each effect in the design. 'L' denotes a linear effect, 'Q' a quadratic effect and 'by' an interaction effect. The significant effects are denoted in bold type.

Effect	Percentage of variance	p-value
$\dot{m}_g$ - L	**30.26**	**9.77E-09**
$\dot{m}_g$ - Q	**7.14**	**4.23E-03**
T - L	**10.90**	**1.91E-04**
T - Q	2.33	2.66E-01
H - L	**19.40**	**9.41E-07**
H - Q	0.49	8.10E-01
$\dot{m}_s$ - L	**9.78**	**4.56E-04**
$\dot{m}_s$ - Q	3.31	1.24E-01
$\dot{m}_g$ by T	2.62	2.14E-01
$\dot{m}_g$ by H	**4.83**	**3.34E-02**
$\dot{m}_g$ by $\dot{m}_s$	0.46	8.23E-01
T by H	0.15	9.40E-01
T by $\dot{m}_s$	0.62	7.61E-01
H by $\dot{m}_s$	1.12	5.85E-01
Error	6.59	

It is clear from Table 2 the linear effects caused by all four factors are highly significant. Only the gas mass flow rate has a significant quadratic effect, however, while some degree of quadratic behaviour can also be seen for the temperature and the solids mass flow rate. Only one significant interaction effect can be observed, that between the gas mass flow rate and the bed height. These significant effects will be the primary focus of further discussions.

Response surfaces

The central composite design creates a quadratic model which describes the variation of the equivalent bed height dependent variable inside the four factor parameter space considered in this design. This quadratic model can be used to construct response surfaces for easy visualization of the variation of the

dependent variable with two chosen factors anywhere within this parameter space. Four such response services are given in Figure 3 to Figure 6.
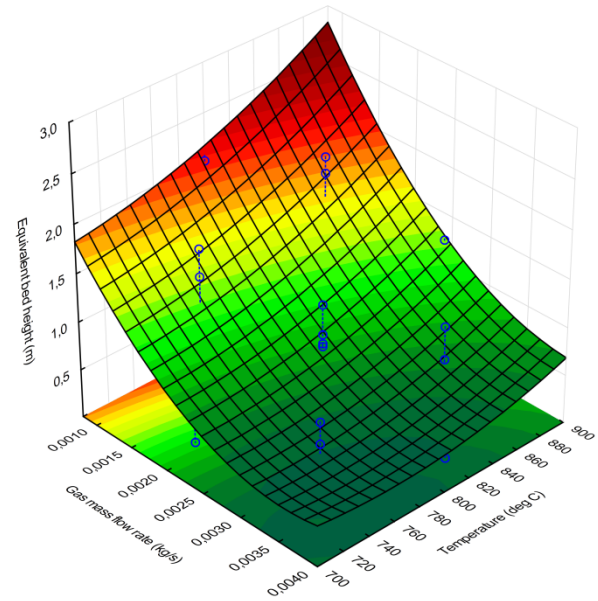
Figure 3: Response of the equivalent bed height to changes in gas mass flow rate and reactor operating temperature. The bed height and solids mass flow rate were kept constant at 0.75 m and 0.5 kg/s respectively.
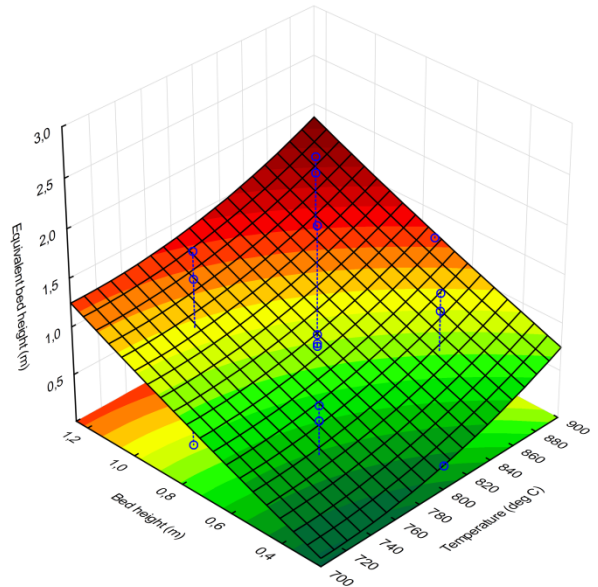
Figure 4: Response of the equivalent bed height to changes in reactor operating temperature and bed height. The solids mass flow rate and gas mass flow rate were kept constant at 0.5 kg/s and 0.0024 kg/s respectively.
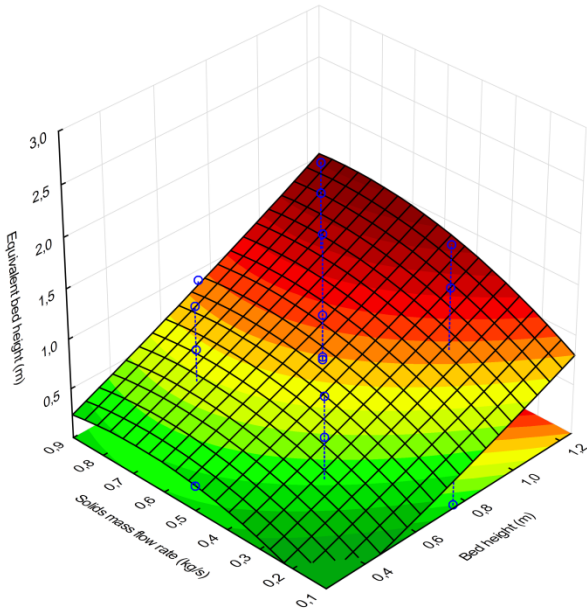
Figure 5: Response of the equivalent bed height to changes in bed height and solids mass flow rate. The gas mass flow rate and temperature were kept constant at 0.0024 kg/s and 800°C respectively.

Figure 6: Response of the equivalent bed height to changes in solids mass flow rate and gas mass flow rate. The temperature and bed height were kept constant at 800°C and 0.75 m respectively.

With the aid of the visual representations in Figure 3 to Figure 6, the significant effects identified in Table 2 can now be further discussed.

Detailed discussion of significant factors

The first and most significant factor in the design is the gas flow rate. Table 2 shows that this factor accounts for almost 40% of the variance inside of the design. When looking a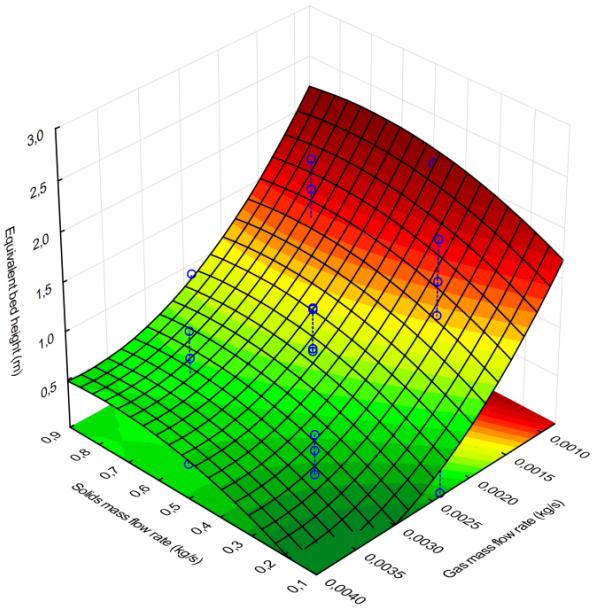t Figure 3 and Figure 6, it is clear that lower levels of this factor result in better reactor performance. This is primarily due to the longer gas residence times granted by lower gas feed rates. The gas residence time is inversely proportional to the gas feed rate, meaning that the residence time and resulting reactor performance will rapidly increase to infinity as the gas feed rate approaches zero. This is the main cause of the quadratic

response in Table 2. Figure 3 and Figure 6 also confirm that reactor performance increases more and more rapidly towards lower levels of the gas feed rate factor.

An additional influence on the steep increase in reactor performance towards lower levels of gas feed rate is the quality of gas-solids contact. Figure 7 illustrates this concept.
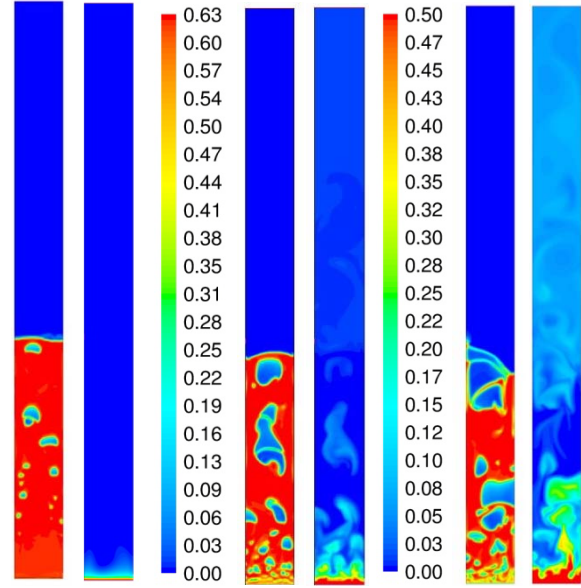
Figure 7: Snapshots of instantaneous solids volume fraction and methane mole fraction for a gas feed rate of 0.0008 (left), 0.0024 (middle) and 0.004 (right) kg/s. The colourmap on the left shows solids fraction and the one on the right shows methane mole fraction.

The increase in the quality of gas-solids contact with a decrease in the gas feed rate is evident from Figure 7. It is clear that the number and size of the bubbles decreases with the gas feed rate, thereby decreasing reactant slip and ensuring that more of the methane is converted.

The next factor is that of reactor temperature. The effect of this factor is actually surprisingly small and surprisingly linear (Table 2). The Arrhenius type reaction rate description used (equation (9)) ensures an exponential increase in reaction rate with an increase in temperature. In fact, the reaction rate constant increases with a factor of 17.3 from the lowest temperature (700°C) to the highest temperature (900°C) investigated. This ratio is much greater than that of the gas feed rate which increases only with a factor of five from the lowest to the highest level investigated. One would therefore expect that the degree of methane conversion would increase greatly and in an exponential fashion as the temperature is increased. However, when looking at Figure 3, it is clear to see that the effect of temperature is much smaller than that of gas feed rate.

The surprisingly low effect of temperature can be explained by the very important mass transfer limitation inside fluidised beds. Even if the reaction rate is very fast, the reactant must still be transported out of the bubble towards the dense emulsion phase. As the reaction rate becomes higher, this limitation becomes more and more dominant. This is illustrated in Figure 8, where it is clear to see that the reactant is slipping past the emulsion phase by means of some large bubbles at the high temperature. At the low temperature, however, the reacting gas can penetrate into the emulsion phase, thereby involving a much larger portion of the solids phase available for reaction. It can therefore be concluded that the lowest temperature investigated is limited by reaction kinetics, while the high temperature is limited more by mass transfer.

Another factor that plays a role reducing the improvement in reactor performance caused by higher temperatures is the reduction in fluidizing gas density. Gas density decreases with an increase in temperature, meaning that the volume flow rate will increase at a constant gas mass flow rate. Gas injected at a higher temperature will therefore have a lower residence time.
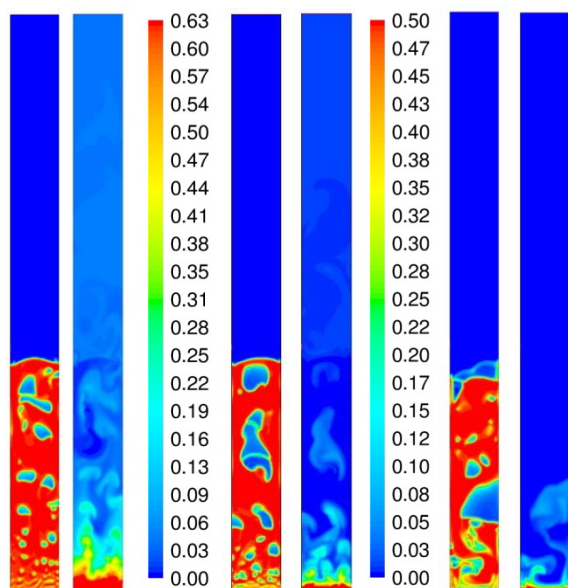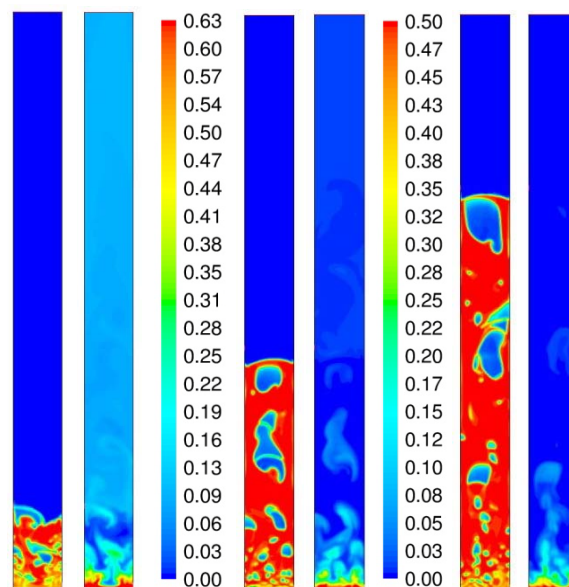

Figure 8: Snapshots of instantaneous solids volume fraction and methane mole fraction for a reactor temperature of 700 (left), 800 (middle) and 900 (right) degrees Celsius. The colourmap on the left shows solids fraction and the one on the right shows methane mole fraction.

Another observation from Figure 8 is the clear two-way coupling between the reaction kinetics and the hydrodynamics. Especially at high temperatures, the influence of hydrodynamics on reaction kinetics is clearly visible. The effect of reaction kinetics on hydrodynamics can also be seen from Figure 8. The particular reaction simulated produces 3 moles of gas for every mole of gas consumed. Faster reaction therefore produces more fluidising gas, creating larger bubbles are more reactant slippage. This effect contributes to reducing the ability of an increase in temperature to improve reactor performance.
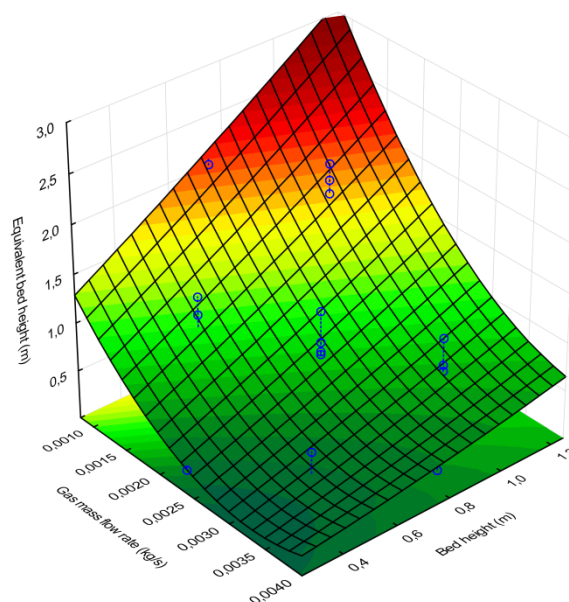
The third significant effect is that of bed height. It is to be expected that the relation between actual bed height and the equivalent bed height performance measure should be linear. Figure 4 and Figure 5 confirm this to be the case.

The effect of bed height is somewhat more than half the size of the effect from reactant feed rate. Both of these performance measures were changed with a factor of five from the lowest to the highest levels. This implies that a reactor scaling strategy based on an increase in reactor width at a constant gas feed rate (thereby decreasing the velocity at which the gas is injected) will be more efficient than a strategy of increasing the reactor height. Figure 9 illustrates the reason for this. Where a reactor width increase and the corresponding decrease in gas velocity will decrease the size of the bubbles and thereby increase the gas-solid contact (Figure 7), an increase in bed height will do just the opposite as illustrated in Figure 9. It is clear that there exists significant bubble growth along the height of the reactor. Therefore, the quality of gas solid contact decreases significantly towards the upper regions of the reactor. Naturally, a taller reactor would be more influenced by this effect than a shorter one, thereby reducing the effectiveness of reactor scaling by height.

Figure 9: Snapshots of instantaneous solids volume fraction and methane mole fraction for a bed height of 0.25 (left), 0.75 (middle) and 1.25 (right) m. The colourmap on the left shows solids fraction and the one on the right shows methane mole fraction.

It is also interesting to observe the moderately significant interaction effect between bed height and gas feed rate shown in Table 2. This effect can be visualised with the aid of Figure 10. Here it is clear that the effect of bed height is significantly smaller at high gas feed rates than it is at low gas feed rates. This characteristic can once again be explained with reference to the bubble structures formed in fluidised beds. At higher gas feed rates, the bubbles are large from the beginning and grow very rapidly along the height of the bed (Figure 7), thereby decreasing the effect of an increase in bed height. At lower gas feed rates, however, the bubbles are much smaller at the beginning and might even require some time to nucleate. The growth of these bubbles is therefore much slower along the height of the reactor and an increase in bed height is therefore more efficient.

Figure 10: Response of the equivalent bed height to gas mass flow rate and bed height.

The final significant effect discussed is that of solids feed rate. It is clear from Figure 5 and Figure 6 than an increase in solids

feed rate causes an increase in reactor performance. This is to be expected since an increase in solids feed rate will decrease the residence time of solids in the reactor and thereby decrease the degree of solids conversion. A lower degree of solids conversion will expose the larger surface area of the shrinking unreacted core to the reaction and thereby increase the reaction rate. This increasing reaction rate with the solids mass flow rate is illustrated in Figure 11.

Figure 11: Snapshots of instantaneous solids volume fraction and methane mole fraction for a solids feed rate of 0.1 (left), 0.75 (middle) and 0.9 (right) kg/s. The colourmap on the left shows solids fraction and the one on the right shows methane mole fraction.
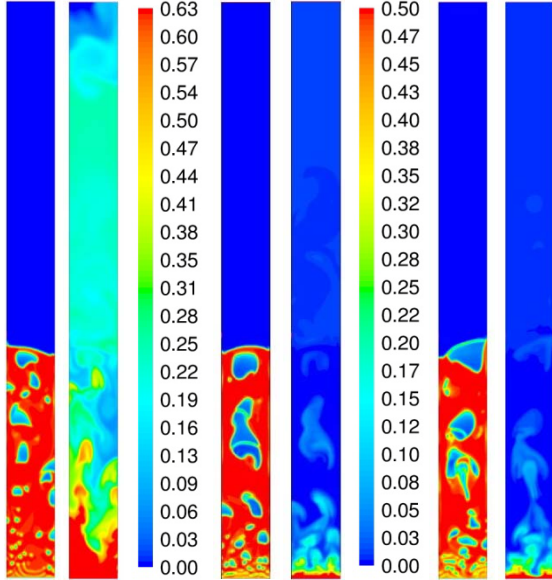
Even though the quadratic effect of solids feed rate is shown to be insignificant in Table 2, it is still visible in Figure 5 and Figure 6. Both figures show that virtually no reactor performance is lost as the solids feed rate is decreased from 0.9 to 0.5 kg/s. This can also be observed in Figure 11. The solids residence time and the degree of solids conversion will increase with a factor of $0.9/0.5 = 1.8$ in this case which will cause a decrease in reaction rate by a factor of only $1.8^{2/3} = 1.43$ according to equation (10). A further decrease in solids feed rate from 0.5 to 0.1 kg/s will cause a further factor of 5 increase in solids residence time and conversion. However, the degree of solids conversion achieved by the solids feed rate of 0.5 kg/s is already around 50%. Another five times increase in conversion is therefore not possible. Under these circumstances, the reactor experiences a strong decrease in reaction rate as the solids are reacted to completion, hence the dip in reactor performance shown at the lowest level of solids feed rate in Figure 5, Figure 6 and Figure 11.

Mapping of reactor operating window

The model constructed by the central composite design within the four factor parameter space can be used to give operational guidelines for achieving a pre-specified level of reactor performance. In this case, the required reactor performance will be set to that of an equivalent bed height of 0.75 m, equating to 5.7% unconverted methane (94.3% conversion). The area inside the parameter space where this level of reactor performance can be achieved can now be easily visualized for three factors at a time as shown in Figure 12 and Figure 13.
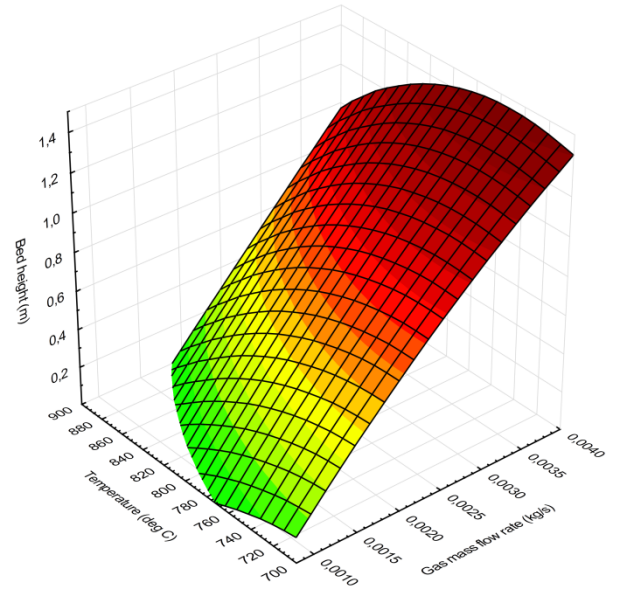
Figure 12: Reactor operating window described by the factors of gas mass flow rate, reactor temperature and bed height for achieving 94.3% conversion. The remaining factor, solids flow rate, is kept constant at a value of 0.5 kg/s.
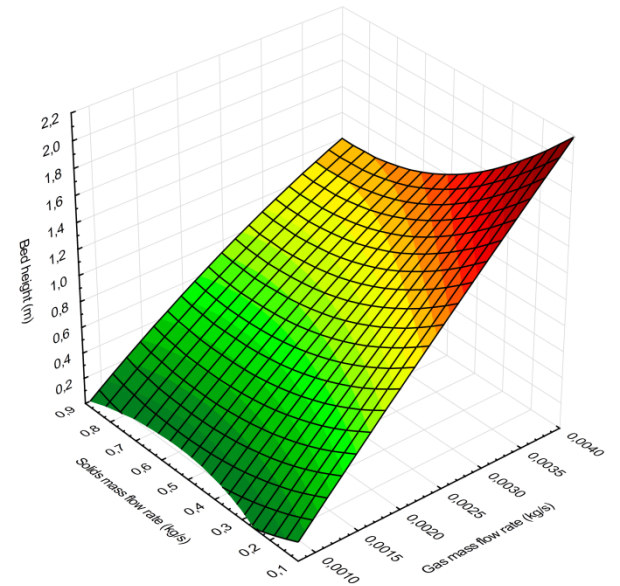
Figure 13: Reactor operating window described by the factors of gas mass flow rate, bed height and solids flow rate for achieving 94.3% conversion. The remaining factor, reactor temperature, is kept constant at a value of 800°C.

The model predicts that the desired reactor performance (94.3% conversion) can be achieved at any point on the surfaces in Figure 12 and Figure 13. Both figures again emphasize that gas feed rate and bed height are the dominant factors in this design, overshadowing the factors of reactor temperature and solids feed rate. This is a favourable conclusion for the current project, because the factors of reactor temperature and solids feed rate will practically be the most challenging to facilitate in the experimental reactor.

High temperature reactor operation is very challenging and it is therefore desired that the reactor be operated under as low temperatures as at all possible. Figure 12 shows that a decrease in reactor temperature can easily be compensated for by a slight decrease in gas feed rate or a slight increase in bed

height. The reactor can therefore safely be operated at 700°C or even lower. From a modelling perspective this should be done with caution, however, since the kinetic data was only determined for temperatures of 800°C and above.

It would also be beneficial for the experimental reactor operation if the solids feed rate could be kept to a minimum. Maintaining a high feed rate of solids will be practically difficult, because a sufficiently large stockpile of fresh solids has to be maintained to last for the duration of the experiment. These fresh solids also have to be heated up inside the reactor which would require very high heat fluxes for higher solids feed rates. Figure 13 shows, however, that the negative influence of a reduction in solids feed rate is practically negligible down to a solids feed rate of around 0.4 kg/s. Even beyond this number the loss in reactor performance can once again easily be compensated for by a slight decrease in gas feed rate or a slight increase in bed height, meaning that even solids feed rates as low as 0.1 kg/s can be accommodated.

Naturally, if this was an industrial case, the information in Figure 12 and Figure 13 could be used to formulate an informative cost curve for reactor operation. If a certain cost description could be linked to each operating variable, the point on the curve leading to the lowest operating costs can easily be identified. Seeing the wide range of variance available within each factor, such a cost optimization study can lead to some substantial financial benefits.

CONCLUSIONS

A modelling study was carried out to map out the operating window of a small scale, pseudo-2D reactor that will be constructed for the purpose of CFD validation. The reactor was simulated in 2D using the TFM KTGF approach.

Simulation experiments were carried out in the form of a four factor central composite design, quantifying the response of reactor performance to changes in gas feed rate, reactor temperature, bed height and solids feed rate. The central composite design was used to quantify the significance of the different factors and to construct a model of reactor performance within the parameter space investigated in this study.

The gas feed rate was identified as the most significant factor. Lower gas fed rates both increased the gas residence time in the reactor and increased the quality of gas-solids contact by creating smaller bubbles. Bed height was the next most significant factor in the design. An increase in bed height also increased the gas residence time, but the potential improvements were somewhat nullified by the significant bubble growth allowed by taller beds. These large bubbles reduced the quality of gas-solids contact, meaning that reactor improvement by increasing bed height was about half as effective as that resulting from reducing the gas feed rate.

An increase in operating temperature had a surprisingly small impact on reactor performance. Over the range of operating conditions investigated, the increase in temperature made the particles 17.3 times more reactive, but the resulting gain in overall reactor performance was about half that which could be achieved by a five times increase in bed height. This could be attributed to a significant bubble to emulsion mass transfer limitation that begins to dominate the overall conversion rate at higher temperatures.

Reactor performance could also be improved by increasing the solids feed rate, resulting in a lower degree of conversion and higher level of reactivity of the solid particles. It was shown, however, that this increase in performance quickly flattens out after a given value and any further increases in solids feed rate would not lead to significant increases in reactor performance.

For the purposes of the current project, the conclusion that the effects of operating temperature and solids feed rate were substantially smaller than that of gas feed rate and bed height was very encouraging. Practically speaking, an increase in operating temperature and solids feed rate will be much more

challenging to facilitate than a decrease in gas feed rate or an increase bed height. The reactor can therefore be safely operated at very low levels of operating temperature and solids feed rate, compensated for by small changes in the more significant factors of gas feed rate and bed height.

REFERENCES

ABAD, A. *et al.*(2011) Kinetics of redox reactions of ilmenite for chemical-looping combustion. *Chemical Engineering Science* **66**, 689-702

CLOETE, S., AMINI, S. & JOHANSEN, S.T.(2011) On the Effect of Cluster Resolution in Riser Flows on Momentum and Reaction Kinetic Interaction. *Powder Technology* **In press**

GIDASPOW, D., BEZBURUAH, R. & DING, J. in *7th Engineering Foundation Conference on Fluidization* 75-82 (1992).

HOMMEL, R., CLOETE, S. & AMINI, S.(2011) Numerical Investigations to quantify the effect of Horizontal Membranes on performance of a Fluidized Bed Reactor *International Journal of Chemical Reactor Engineering* **Under review**

JOHNSON, P.C. & JACKSON, R.(1987) Frictional-Collisional Contitutive Relations for Granular Materials, with Application to Plane Shearing. *Journal of Fluid Mechanics* **176**, 67-93

LEONARD, B.P. & MOKHTARI, S. (1990) ULTRA-SHARP Nonoscillatory Convection Schemes for High-Speed Steady Multidimensional Flow.in *NASA TM 1-2568 (ICOMP-90-12),* NASA Lewis Research Center.

LEVENSPIEL, O.(1999) *Chemical Reaction Engineering.* 3 edn, John Wiley & Sons.

LUN, C.K.K., SAVAGE, S.B., JEFFREY, D.J. & CHEPURNIY, N.(1984) Kinetic Theories for Granular Flow: Inelastic Particles in Couette Flow and Slightly Inelastic Particles in a General Flow Field. *Journal of Fluid Mechanics* **140**, 223-256

MONTGOMERY, D.(2001) *Design and Analysis of Experiments.* 5 edn, John Wiley and Sons.

PATANKAR, S.(1980) *Numerical Heat Transfer and Fluid Flow.* Hemisphere Publishing Corporation.

SCHAEFFER, D.G.(1987) Instability in the Evolution Equations Describing Incompressible Granular Flow. *Journal of Differential Equations* **66**, 19-50

SYAMLAL, M., ROGERS, W. & O'BRIEN, T.J.(1993) *MFIX Documentation: Volume 1, Theory Guide.*, National Technical Information Service.

8th International Conference on CFD in Oil & Gas, Metallurgical and Process Industries
SINTEF/NTNU, Trondheim NORWAY
21-23 June 2011

CFD11-160

INFLUENCE OF SUBCOOLING ON DENSITY WAVE OSCILLATIONS IN A HEATED PIPE

Dag STRØMSVÅG[1][*], **Leonardo C. RUSPINI**[2][†], **Maria FERNANDINO**[3][‡], **Carlos A. DORAO**[4][§]

[1]NTNU Department of Energy and Process Engineering, 7491 Trondheim, NORWAY

[2]NTNU Department of Energy and Process Engineering, 7491 Trondheim, NORWAY

[3]NTNU Department of Energy and Process Engineering, 7491 Trondheim, NORWAY

[4]NTNU Department of Energy and Process Engineering, 7491 Trondheim, NORWAY

[*] E-mail: dag@stromsvag.net
[†] E-mail: leonardo.c.ruspini@ntnu.no
[‡] E-mail: maria.fernandino@ntnu.no
[§] E-mail: carlos.dorao@ntnu.no

ABSTRACT

Boiling two-phase flow is found in many industrial applications such as boiling water reactors, two-phase flow heat exchangers and refrigeration systems. The physics of two-phase gas-liquid flow may lead to undesirable system instabilities, and in the literature density wave oscillations (DWO) are reported to be the most commonly two-phase instability phenomenon. In this work, the fundamental mechanisms of DWO and the influence of subcooling is investigated further by performing a numerical analysis using a one dimensional homogenous equilibrium flow model. The degree of subcooling is represented by the non-dimensional subcooling number N_{sub}. The literature presents two different points of view regarding the fundamental mechanism of DWO. The relative weight of either mechanism, mixture density or mixture velocity, is different depending on the level of subcooling. The results show that the change from mixture density to mixture velocity as the fundamental mechanism is a smooth transition for increased N_{sub}. The oscillation period of the modeled DWO grows continuously for increased subcooling number, and the period increases in a strong non-linear fashion at high values of N_{sub}. It is postulated that it is the transition towards a more mixture velocity dominated system pressure drop at higher subcooling numbers that causes the oscillation period to evolve as it does.

Keywords: two-phase flow, instabilities, density wave oscillations, transient simulation, numerical analysis.

INTRODUCTION

Boiling two-phase flow is found in many industrial applications such as boiling water reactors, two-phase flow heat exchangers and refrigeration systems. Unfortunately, boiling two-phase flow systems are accompanied by the possibility of thermally induced instabilities leading to oscillations in system flow rate and pressure. The consequences are mechanical vibrations and problems with system control. In extreme cases the heat transfer characteristics are disturbed so that the heat transfer surface may burn-out (dry-out, boiling crisis, critical heat-flux) (Boure *et al.*, 1973; Kakac and Bon, 2008).

Two-phase flow instabilities are divided into two main categories, namely *static* and *dynamic* instabilities. Static instability can be found when the steady state operating point of a system is of the unstable kind. Hence, when the system is subjected to a perturbation the flow will move asymptotically towards a new operating point not located in the vicinity of the original. The new operating point is a stable equilibrium operating point. Dynamic instability is related to the continuous interaction and delayed feedback that occurs between the inertia of the flow and the compressibility of the two-phase mixture (Boure *et al.*, 1973; Kakac and Bon, 2008).

Density wave oscillations (DWO) are classified as a dynamic instability, and result from multiple regenerative feedbacks between the flow rate, vapor generation and pressure. In other words, a temporary reduction of the inlet flow in a boiling system will increase the rate of enthalpy rise, thereby lowering the mixture density. This disturbance will propagate downstream and affect the channel pressure drop which will immediately be transmitted back to the inlet, causing additional changes to the inlet flow rate. For certain system conditions the resulting oscillations may become self-sustained with a constant period and amplitude (Boure *et al.*, 1973). DWO is in the literature reported as the most common type of two-phase flow instabilities (Boure *et al.*, 1973; Belblidia and Bratianu, 1979; Ding *et al.*, 1995; Kakac and Bon, 2008). However, in the literature we also find two opposing views on what is considered the fundamental mechanism of DWO. In what is often referred to as the classical description of DWO it is said that it is the variation in downstream mixture density that acts as the fundamental mechanism of the DWO phenomenon, and that the observed oscillations have a period that is about one to two times the boiling channel residence time (Boure *et al.*, 1973; Kakac and Bon, 2008). Rizwan-Uddin (1994) raised criticism towards this classical description. This last work shows that for the parameter space considered the emphasis should be on variations in mixture velocity rather than mixture density. Further, it is found that the modeled oscillations have a period closer to four times the channel residence time. In Ambrosini *et al.* (2000) it is possible to find an additional discussion related to the fundamental mechanisms of DWO. This work states evidence that support both the classical description of DWO and the contradicting view of Rizwan-Uddin (1994). The opposing views are according to Ambrosini *et al.* (2000) a result of the difference in the applied level of subcooling. The classical description is based on a low level of system subcooling, while the view of Rizwan-Uddin (1994) is considering high subcooling.

The operating conditions of a boiling channel system can be represented by what is defined as the phase-change number N_{pch} and the subcooling number N_{sub}. N_{pch} scales the rate of phase-change due to heat addition, while N_{sub} scales the level of subcooling (Saha *et al.*, 1976). Ishii and Zuber (1970) pro-

posed what is now a well known two-dimensional stability map for boiling systems where N_{pch} and N_{sub} are used as the x- and y-axis, respectively. For certain combinations of N_{pch} and N_{sub} the boiling system will experience self-sustained periodic oscillations. The operating points yielding such an oscillatory behavior comprise what is known as the stability threshold of the boiling channel system at hand.

The research presented in this paper is a contribution to the fundamental understanding of DWO and the influence of subcooling. The degree of subcooling is here given by the subcooling number N_{sub}, and its influence on DWO is investigated by comparing modeled self-sustained periodic oscillations found in different regions of parameter space.

MODEL DESCRIPTION

Modeled System

The modeled boiling channel system is shown in figure 1. The channel is a circular horizontal pipe heated with a constant uniform power q. The system is exposed to a constant externally imposed pressure drop given by the inlet- and exit reservoir pressure p_I and p_E, respectively. T_I represents the constant fluid inlet temperature. Two flow restrictions are placed at the channel inlet and exit, and represent sources of pressure drop located upstream and downstream of the boiling channel, respectively. The pressure drop across the inlet and exit restriction is proportional to the local dynamic pressure, where K_i and K_e are the respective proportionality constants. The parametric effect of inlet and exit restrictions has been investigated by numerous investigators (see Belblidia and Bratianu (1979)). An increase of the inlet restriction coefficient will add to the single-phase pressure drop, and hence increases the damping effect and stabilizes the system. The opposite is experienced when increasing the exit restriction coefficient. The exit restriction adds to the two-phase pressure drop, and a higher K_e will consequently have a destabilizing effect on the system.
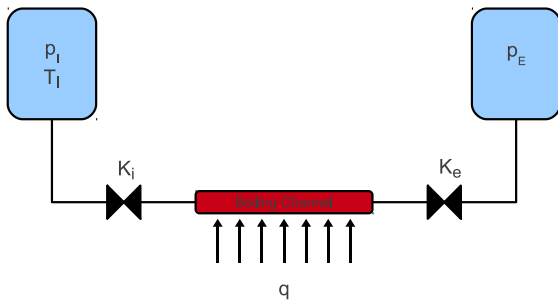

Figure 1: Schematic of the modeled boiling channel system.

Mathematical Model

Following Lahey and Podoski (1989), the following assumptions are made concerning the mathematical description of the system flow:

- One dimensional
- Horizontal
- Homogenous flow

- Thermodynamic equilibrium between phases
- Constant externally imposed pressure drop
- Constant inlet temperature
- Constant uniform heating

The model solves the conservation equation for mass, momentum and energy as given by:

$$\frac{\partial \rho_m}{\partial t} + \frac{\partial G}{\partial z} = 0 \tag{1}$$

$$\frac{\partial G}{\partial t} + \frac{\partial}{\partial z}\left(\frac{G^2}{\rho_m}\right) = -\frac{\partial p}{\partial z} - \left[\frac{f}{D} + \sum_j^N K_j \delta(z - z_j)\right]\frac{G^2}{2\rho_m} \tag{2}$$

$$\frac{\partial h_m}{\partial t} + \frac{G}{\rho_m}\frac{\partial h_m}{\partial z} = \frac{1}{A\rho_m}\frac{q}{L} \tag{3}$$

For single-phase flow, the friction factor f is obtained by applying the Colebrook pressure drop correlation. For the two-phase flow region, the friction factor is found using the Muller-Steinhagen and Heck (1986) pressure drop correlation. The sum of localized pressure drops is included to take into account the effect of the flow restrictions in the momentum equation. N represent the total number of valves and z_j their positions. In the energy equation, the friction dissipation and flow work terms are neglected, since they are, for the cases analyzed in this research, at least four orders below that of the heating source terms. In contrast to previous models, this work updates the mixture density according to the local mixture enthalpy assuming thermodynamic equilibrium. The influence of latter assumption over the results is discussed in Ruspini *et al.* (2011).

Numerical solver

The introduction of a significant diffusion by low-order methods can affect the numerical solution, describing inaccurately the modeled problem. High-order discretization reduces the numerical diffusion. The necessity of solving thermal-hydraulic problems with high accuracy is analyzed in Ambrosini and Ferreri (1998); Ruspini *et al.* (2009). Here, the system of equations is solved by applying the *Space-Time Least-Square Spectral Element Method* (ST-LQSEM), following Ruspini *et al.* (2009) and Ruspini *et al.* (2010). A detailed description of this numerical methods is given in de Maerschalck (2003); Deville *et al.* (2002).

Modeling Procedure

Steady state initial conditions are imposed by first solving the governing equations ignoring the time-dependent terms. A constant mass flux G and exit reservoir pressure p_E act as the system's boundary conditions. The steady state solution results in the necessary inlet reservoir pressure p_I, and the transient modeling is initiated using p_I and p_E as boundary conditions. Consequently, the system is exposed to an constant externally imposed pressure drop $\Delta p_{ext} = p_I - p_E$, and the transient response of the system from steady state can be investigated.

The modeled self-sustained periodic oscillations which are compared in this research are all found by using the same steady state mass flux and exit reservoir pressure. After choosing a desired subcooling number N_{sub} set by the fluid inlet temperature T_I, the phase-change number N_{pch} is varied by changing the applied power q until self-sustained periodic oscillations are observed. N_{pch} and N_{sub} are defined as in equation 4 and 5, respectively (Ishii and Zuber, 1970):

$$N_{pch} = \frac{q}{G_i A} \frac{\frac{1}{\rho_l} - \frac{1}{\rho_g}}{\frac{1}{\rho_l}(h_l - h_g)} \qquad (4)$$

$$N_{sub} = (h_l - h_{m,i}) \frac{\frac{1}{\rho_l} - \frac{1}{\rho_g}}{\frac{1}{\rho_l}(h_l - h_g)} \qquad (5)$$

RESULTS

The modeled results presented in this paper yield for the constant system conditions given in table 1, and are found following the modeling procedure described earlier.

Working fluid:	Water
Boiling channel length:	$L = 1$ m
Boiling channel diameter:	$D = 0.005$ m
Inlet restriction coefficient:	$K_i = 12$
Exit restriction coefficient:	$K_e = 4$
Exit reservoir pressure:	$p_E = 120$ kPa
Steady state mass flux:	$G = 400$ kg/m^{2}s

Table 1: Constant system conditions from which the modeled results are obtained.

The operating points for the modeled system are represented by their respective combination of the phase-change number N_{pch} and the subcooling number N_{sub}. Figure 2 shows the modeled $N_{pch} - N_{sub}$ stability map, where the red dots represent operating points that produced self-sustained periodic oscillations. Hence, the operating points are located on the stability threshold of the modeled system. In the *single-phase liquid* region of the stability map, the operating conditions are so that the boiling channel exit quality will be less than zero ($x_e < 0$). Hence, only single-phase liquid flow is present in the system. Operating points in the *stable region* located between the solid blue line ($x_e = 0$) and the stability threshold (red dots), yield a modeled system able to damp out the effect of a perturbation and return to its initial state. If one operates the modeled system in the *unstable region*, the system would, when subjected to a perturbation, produce diverging oscillations which in time will grow out of proportions.

The influence of subcooling on DWO will be investigated by comparing modeled self-sustained periodic oscillations for different values of N_{sub}. The operating points to be compared are given by the red dots in figure 2, and are therefore labeled with numbers signifying their relative degree of subcooling. These labels will in future be used to refer to the individual results and allow for an easier comparison.

Mixture Density vs. Mixture Velocity

Each of the operating points labeled in figure 2 showed a significant difference in the role played by the variation in mixture density and mixture velocity with respect to the modeled system pressure drop. This difference will be presented by showing how oscillations in the exit mixture density $\rho_{m,e}$ and in exit mixture velocity $u_{m,e}$ affect the exit restriction pressure drop Δp_e. Figure 3, 4 and 5 show the variations in Δp_e, $\rho_{m,e}$ and $u_{m,e}$ with respect to the their mean value for operating points 1, 5, and 11, respectively.

For operating point 1 where $N_{sub} < 1$, figure 3 shows that Δp_e varies almost completely in-phase with $\rho_{m,e}$. For operating point 5 where $N_{sub} \approx 3$, figure 4 shows that the variation
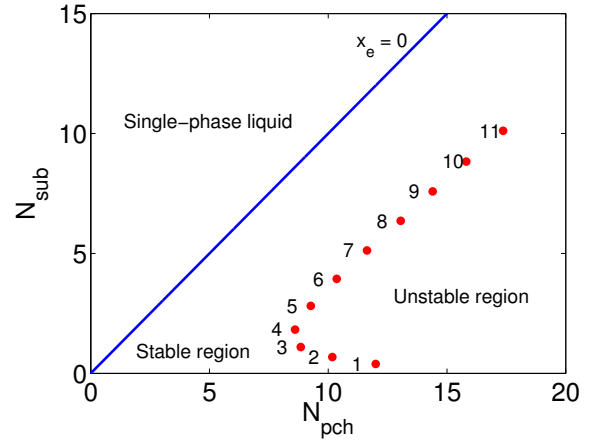

Figure 2: The modeled stability map. Red dots: operating points located on the stability threshold, and which produced modeled self-sustained periodic oscillations.

in Δp_e is still more in-phase with the variation in $\rho_{m,e}$. The above results are in accordance to the classical description DWO which states that mixture density should be regarded as the fundamental mechanism. Figure 5 shows modeled oscillations as found for operating point 11 where $N_{sub} \approx 10$. In this case, compared to the previous two, the exit restriction pressure drop is more in-phase with the variation in exit mixture velocity. Hence, mixture velocity is the fundamental mechanism of DWO for high subcooling numbers, as also stated by Rizwan-Uddin (1994) and Ambrosini *et al.* (2000).

In order to determine why mixture velocity acts as the fundamental mechanism for high subcooling numbers, we look at the relation governing the exit restriction pressure drop:

$$\Delta p_e = \frac{1}{2} K_e \rho_{m,e} u_{m,e}^2 \qquad (6)$$

Hence, Δp_e is proportional to the exit mixture density as well as to the square of the exit mixture velocity. This relation states that the exit restriction pressure drop is more sensitive to a change in $u_{m,e}$ than in $\rho_{m,e}$. As shown by figure 6 and 7, the oscillation amplitude of both $\rho_{m,e}$ and $u_{m,e}$ grows continuously with N_{sub}. However, because of the squared relationship between Δp_e and $u_{m,e}$, the variation in mixture velocity becomes dominating for high N_{sub} because of the relatively large amplitude. For low values of N_{sub} it is the variation in $\rho_{m,e}$ that causes the oscillation in Δp_e. This shift from a mixture density dominated exit restriction towards a more mixture velocity dominated exit restriction was shown earlier in figure 3, 4 and 5. In figure 3 we observe that $u_{m,e}$ barely changes, and it is therefore the presence of a variation in $\rho_{m,e}$ that causes the oscillation in Δp_e. In figure 4, the oscillation in $u_{m,e}$ grows noticeably stronger compared to figure 3, but the oscillation in $u_{m,e}$ is still not strong enough to fully control the exit restriction pressure drop which is still more in-phase with $\rho_{m,e}$. In figure 5 where $N_{sub} \approx 10$, the variation in $u_{m,e}$ is dominating the pressure drop even though the oscillation in $\rho_{m,e}$ also grows stronger compared to lower subcooling number cases. The latter is due to the squared relationship between Δp_e and $u_{m,e}$, and it seems as though there is a smooth change towards a more velocity dominated exit restriction as the subcooling number N_{sub} is increased.
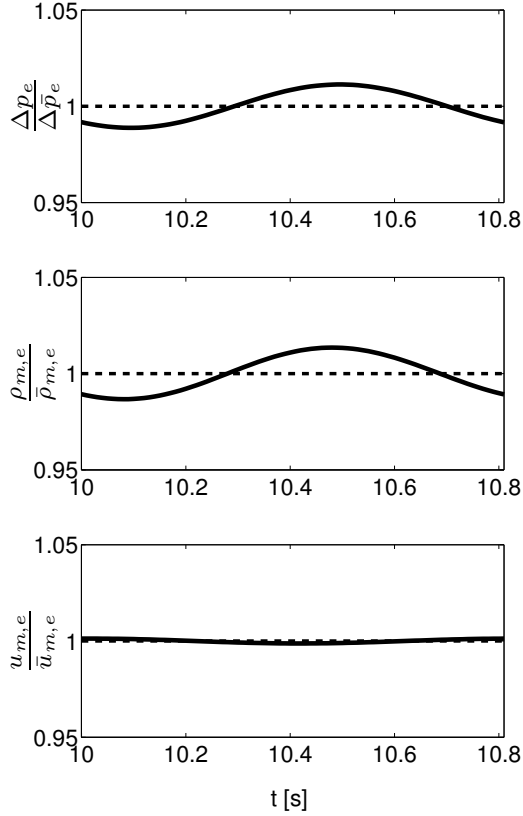
Figure 3: Operating point 1 ($N_{sub} < 1$): one periodic oscillation in exit restriction pressure drop Δp_e, exit mixture density $\rho_{m,e}$ and exit mixture velocity $u_{m,e}$ with respect to mean values.

Figure 4: Operating point 5 ($N_{sub} \approx 3$): one periodic oscillation in exit restriction pressure drop Δp_e, exit mixture density $\rho_{m,e}$ and exit mixture velocity $u_{m,e}$ with respect to mean values.

Oscillation Period and Residence Time

Another aspect of the influence of subcooling on DWO which was addressed in Rizwan-Uddin (1994) and also confirmed by Ambrosini *et al.* (2000), is the fact that the ratio between the oscillation period t_p and the mean boiling channel residence time $\bar{t}_r$ grows as the subcooling number increases. In the classical description of DWO yielding for low N_{sub}, t_p is believed to be approximately two times $\bar{t}_r$. Rizwan-Uddin (1994) found at high N_{sub} this ratio to be closer to four times. The labeled operating points shown in figure 2, show a significant difference in the observed oscillation period. Figure 8 shows how the oscillation period t_p evolves as the subcooling number increases. The oscillation period increases almost linearly up to $N_{sub} \approx 5$. From this point on, the t_p increases non-linearly. Hence, self-sustained periodic oscillations found for subcooling numbers sufficiently exceeding $N_{sub} = 10$ will have an oscillation period that grows out of proportions.

In contrast to the non-linear increase found in t_p for $N_{sub} < 5$, the positive slope of $\bar{t}_r$ decreases, as shown in figure 9. To the author it seems as though the mean boiling channel residence time move towards some unknown upper limit, however further modeling is needed to confirm this postulate. Figure 10 shows the change in the ratio of t_p and $\bar{t}_r$ as N_{sub} is increased. The non-linear growth in the latter figure is a natural consequence of the observed evolution in t_p and $\bar{t}_r$. However, it does not explain the observed ratio evolution.

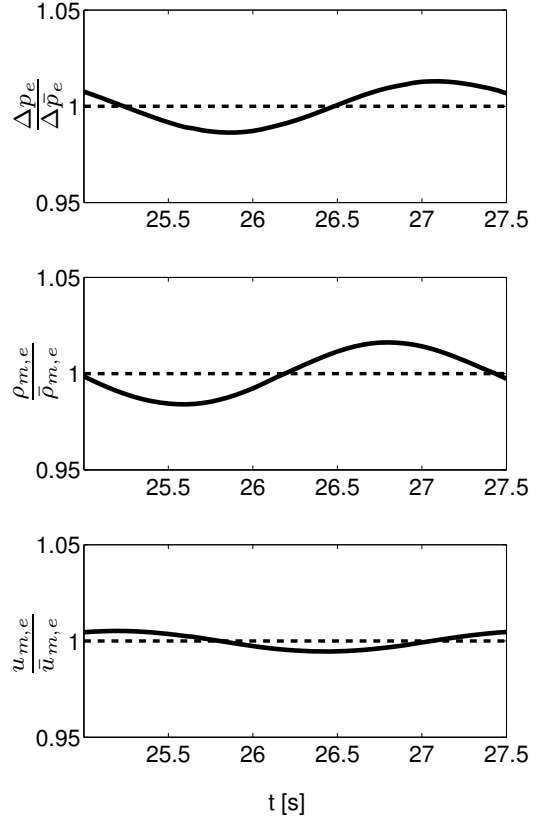In the literature it is explained that DWO is the result of a time delayed pressure drop caused by an earlier time flow perturbation. This change in system pressure drop produces regenerative feedback to the boiling channel inlet, and depending on system operating conditions, various oscillatory behaviors can be observed. In this work we have studied this change in downstream pressure drop by investigating the behavior of the exit restriction. The exit restriction is the most time delayed pressure drop source and will consequently have the biggest destabilizing effect on the modeled system. The dynamic behavior of the system, here represented by the oscillation period, is therefore assumed to be a result of how the exit restriction responds to changes in mixture density and mixture velocity. In figure 7 we showed that the amplitude of oscillations in exit mixture velocity increases exponentially beyond $N_{sub} \approx 5$, and consequently causes the exit restriction pressure drop to be controlled more by the variations in mixture velocity. If we combine this result with the fact that the positive slope of t_p shown in figure 8 changes from linear to non-linear at approximately the same limit of N_{sub}, we conclude that it is most likely the change towards a mixture velocity dominated system pressure drop that causes the oscillation period to increase as it does.

CONCLUSION

The influence of subcooling on density wave oscillations (DWO) in a heated pipe was investigated by comparing modeled self-sustained periodic oscillations for different subcooling numbers N_{sub}. The results show that:

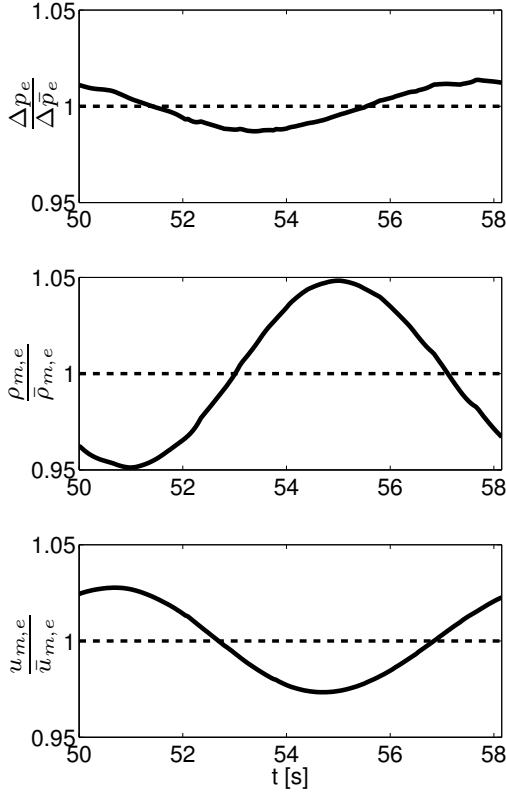1. For $N_{sub} < 1$ the exit restriction pressure drop oscil-

Figure 5: Operating point 11 ($N_{sub} \approx 10$): one periodic oscillation in exit restriction pressure drop Δp_e, exit mixture density $\rho_{m,e}$ and exit mixture velocity $u_{m,e}$ with respect to mean values.
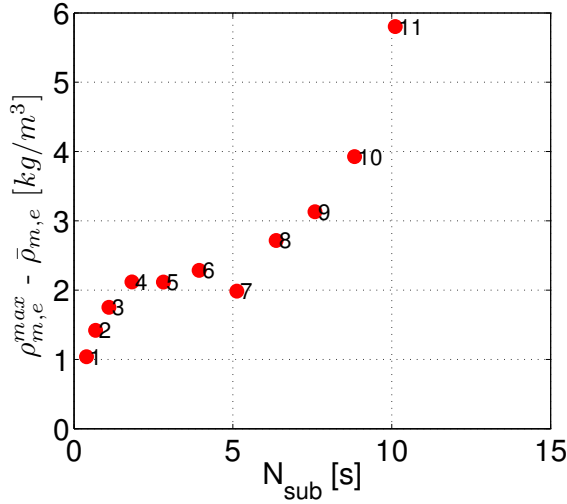
Figure 6: Amplitude of modeled self-sustained periodic oscillations in exit mixture density $\rho_{m,e}$ at different subcooling numbers N_{sub}.

lates close to in-phase with the variation in exit mixture density, and it is concluded that in this region of N_{sub} mixture density should be considered the fundamental mechanisms of DWO. At $N_{sub} \approx 10$ the variation in exit restriction pressure drop is strongly controlled by the variation in exit mixture velocity. Hence, for $N_{sub} > 10$
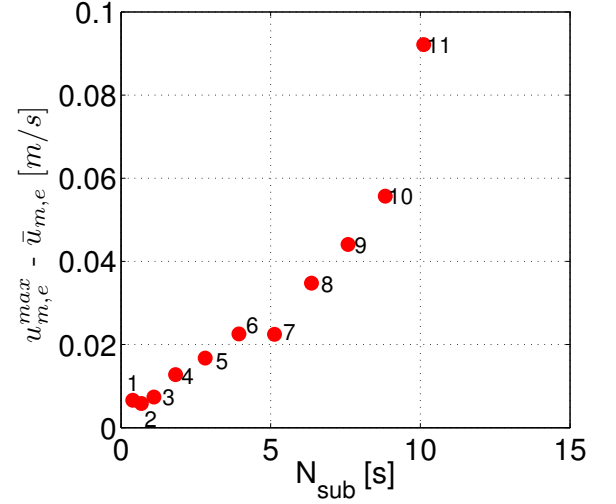
Figure 7: Amplitude of modeled self-sustained periodic oscillations in exit mixture velocity $u_{m,e}$ at different subcooling numbers N_{sub}.

Figure 8: Evolution of oscillation period t_p for modeled self-sustained periodic oscillations at different subcooling numbers N_{sub}.

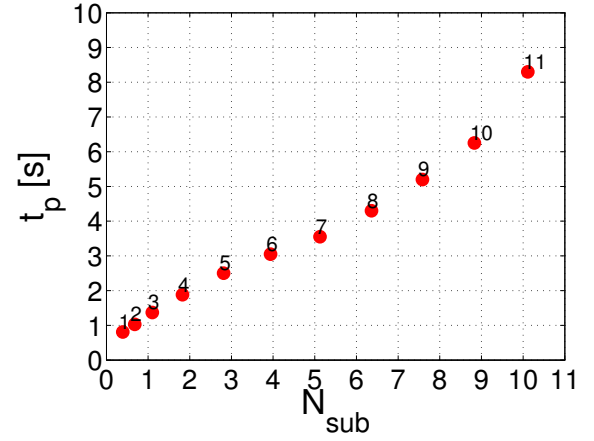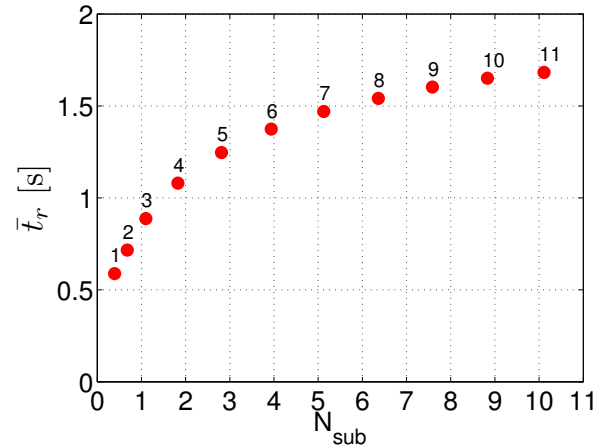Figure 9: Evolution of mean boiling channel residence time $\bar{t}_r$ for modeled self-sustained periodic oscillations at different subcooling numbers N_{sub}.
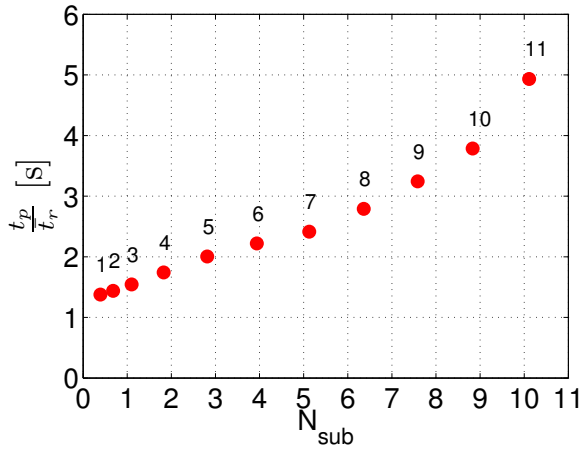
Figure 10: Evolution of the ratio between the oscillation period t_p and mean boiling channel residence time $\bar{t}_r$ for self-sustained periodic oscillations at different subcooling numbers N_{sub}.

mixture velocity can be considered as the fundamental mechanism of DWO.

2. With increasing N_{sub}, the oscillation amplitudes of both exit mixture density and exit mixture velocity grow continuously. Further, an increase of the subcooling number beyond $N_{sub} \approx 5$ results in an exponential growth in the same amplitudes. Because of the squared relationship that exists between the exit restriction pressure drop and the exit mixture velocity, the role of mixture velocity as the fundamental mechanism of DWO increases with a growing subcooling number. Based on the modeled results there seems to be a smooth change towards a more velocity dominated pressure drop with increasing N_{sub}.

3. The period of the modeled oscillations grows continuously with N_{sub}. For $N_{sub} > 5$ the oscillation period evolves non-linearly. This is believed to be due to the transition to exponential growth seen for the oscillation amplitude of exit mixture velocity in approximately the same level of N_{sub}. For $N_{sub} < 3$ the oscillation period is found to be about one or two times the mean boiling channel residence time, which is the same as that stated by the so-called classical description of DWO. At $N_{sub} \approx 10$ the oscillation period is found to be about five times the mean boiling channel residence time. The latter ratio is even higher than what is found in Rizwan-Uddin (1994).

REFERENCES

AMBROSINI, W. and FERRERI, J. (1998). "The effect of truncation error in the numerical prediction of linear stability boundaries in a natural circulation single phase loop." *Nuclear Engineering and Design*, **183(1-2)**, 53–76.

AMBROSINI, W. *et al.* (2000). "Linear and nonlinear analysis of density-wave instability phenomena". *Heat and Technology*, **18(1)**, 27–36.

BELBLIDIA, L. and BRATIANU, C. (1979). "Density-wave oscillations". *Annals of Nuclear Energy*, **6(7-8)**, 425–44.

BOURE, J. *et al.* (1973). "Review of two-phase flow instability". *Nuclear Engineering and Design*, **25(2)**, 165–192.

DE MAERSCHALCK, B. (2003). *Space-time Least-squares Spectral Element Method For Unsteady Flows*. Master's thesis, Technische Universiteit Delft.

DEVILLE, M. *et al.* (2002). "High-order methods for incompressible fluid flow." *Cambridge University Press*.

DING, Y. *et al.* (1995). "Dynamic instabilities of boiling two-phase flow in a single horizontal channel". *Experimental Thermal and Fluid Science*, **11(4)**, 327–342.

ISHII, M. and ZUBER, N. (1970). "Thermally induced flow instabilities in two phase mixtures". *Proceedings of the fourth international heat transfer conference*, **B5.11**.

KAKAC, S. and BON, B. (2008). "A review of two-phase flow dynamic instabilities in tube boiling systems". *International Journal of Heat and Mass Transfer*, **51(3-4)**, 399–433.

LAHEY, R. and PODOSKI, M. (1989). "On the analysis of varius instabilities in two-phase flows". *Multiphase Science and Technology*, 183–370.

MULLER-STEINHAGEN, H. and HECK, K. (1986). "A simple friction pressure drop correlation for two-phase flow in pipes". *Chemical Engineering and Processing*, **20(6)**, 297–308.

RIZWAN-UDDIN (1994). "On density-wave oscillations in two-phase flows". *International Journal of Multiphase Flow*, **20(4)**, 721–737.

RUSPINI, L. *et al.* (2009). "Simulation of a natural circulation loop using a least squares hp-adaptive solver". *Accepted to Mathematics and Computers in Simulation*.

RUSPINI, L. *et al.* (2011). "Study of density wave phenomena in boiling and condensing two-phase flow systems". *Nureth-14. International topical meeting on nuclear reactor thermal hydraulics*.

RUSPINI, L. *et al.* (2010). "Dynamic simulation of ledinegg instability". **2(5)**, 211–216.

SAHA, P. *et al.* (1976). "Experimental investigation of the thermally induced flow oscillations in two-phase systems". *Journal of Heat Transfer*, **98 Ser C(4)**, 616–622.

8th International Conference on CFD in Oil & Gas, Metallurgical and Process Industries
SINTEF/NTNU, Trondheim Norway
21-23 June 2011

CFD11-161

AUTONOMOUS INFLOW CONTROL DEVICE: CFD SIMULATIONS OF FLUID-STRUCTURE INTERACTION

Atle J. GYLLENSTEN[1*] , Vidar MATHIESEN[1]

[1] Statoil ASA, NORWAY

* E-mail: agy@statoil.com

ABSTRACT

In long horizontal oil wells, the volume fraction of oil often varies along the wellbore. This is caused either by uneven fluid inflow, leading to so called coning (of gas) or cresting (of water), or by heterogeneities in the reservoir. To account for this, Statoil has developed an inflow valve that is mounted in the production tubing, which has a self adjusting geometry that chokes back the flow of less viscous fluids and also promotes a more constant fluid flow rate. This valve has been modelled by using Fluent's 2D axisymmetric CFD solver. The challenge is to find the position of the free floating disc inside the valve that adjusts to the fluid flowing around it. This is done by simulating a number of disc positions, calculating the fluid forces acting on the disc and finding the position where the forces sum up to zero. The simulations have been compared to valve characteristics obtained by in-house experiments and it is found that the simulations capture the main features of the valve behaviour, and that for low viscous fluids the quantitative match is quite good.

Keywords: CFD, inflow control, horizontal oil well.

NOMENCLATURE

A complete list of symbols used, with dimensions, is required.

Greek Symbols
ρ Mass density, [kg/m^3].
μ Dynamic viscosity, [kg/m.s].

Latin Symbols
p Pressure, [Pa].
**u** Velocity, [m/s].

INTRODUCTION

Long horizontal wells with one or more branches have been used to maximize reservoir contact and improve well performance by Statoil and other oil companies for more than a decade. Frictional pressure drop and/or variation in permeability along the well trajectory will lead to a non-uniform inflow profile along the well. This may lead to early gas and/or water breakthrough, which will reduce the well performance and oil recovery significantly. The breakthrough will typically occur in the heel of the well (the start of the horizontal part) or in areas of permeability variations. Nowadays, passive inflow control is applied to delay the unwanted gas/water breakthrough. However, conventional inflow control will not stop the gas/water breakthrough. The new valve developed by Statoil will, in addition to delaying the breakthrough by ensuring a more constant fluid flow rate along the well, reduce the consequences of the breakthrough. The autonomous valve chokes the flow of low-viscous fluids and favours the more viscous fluid (i.e. oil).

The valve is developed, patented and piloted in the North Sea by Statoil. The valve is autonomous, i.e. the valve operates entirely without the need for interventions and it does not require electric or hydraulic power. Extensive tests have shown that the valve strongly reduces the inflow of gas in a reservoir which contains a light crude oil. In a reservoir which contains heavy crude oil the valve will reduce unwanted water production as well.

In principle, the valve acts much like a conventional condense steam trap (Seneviratne, 2007). It reacts to the flowing fluid and reduces the cross sectional area available for the flow when the unwanted fluid enters the valve.

Figure 1 shows how the fluid is flowing through the valve. Note that the disc is freely floating.
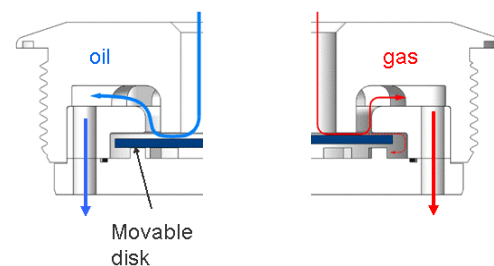
Figure 1: Illustration of the flow through the valve. Typical behaviour for oil (left), and gas (right).

The cross sectional area above the disc is governed by the disc position, and typically the gap between the disc

and the inner seat of the valve is in the order of one tenth, or even one hundredth, of a millimetre for normal fluids. This means that the velocities in this area are very high, which, according to the Bernoulli principle, leads to a low static pressure and hence creates a suction trying to close the valve even further.

It is this interaction between the floating disc and the fluid flow that makes the simulation of the autonomous valve non-trivial.

MODEL DESCRIPTION

The governing equations for the fluid flow through the valve are the well known steady-state incompressible Navier-Stokes equations without volumetric forces given in Equations (1) and (2).

Continuity equation
$$\nabla \cdot (\rho \mathbf{u}) = 0 \qquad (1)$$
Momentum equation
$$\nabla \cdot (\rho \mathbf{u} \mathbf{u}) = -\nabla p + \mu \nabla^2 \mathbf{u} \qquad (2)$$

Solution of the Navier-Stokes equations is not feasible for the involved flow. Therefore, the Reynolds-averaged Navier-Stokes (RANS) equations are used to describe the flow field. This requires closure relations for turbulence modelling. Where applicable, turbulence is modelled using the Realizable k-epsilon model, documented in the Fluent 6.3.26 Users guide.

Fluent 6.3.26 is used for the simulations, while Gambit 2.4.6 and Ansys Workbench 12.1 have been used for creating the grids.
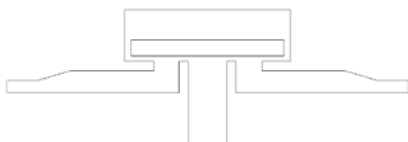
Geometry

An example of an actual valve is shown in Figure 2.
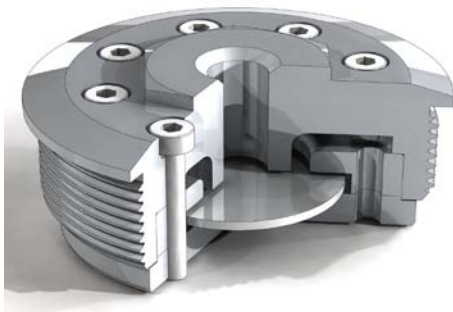
Figure 2: Looking inside the A-valve.

The geometry used for one of the simulated valves is shown in Figure 3.

Figure 3: Geometry outline (rotated 180° compared to Figure 2).

The outlet area is somewhat changed from the actual design to make the geometry axisymmetric. In this area velocities are low and the simplification should not have a significant influence on the results.

Grid

Hex grid is used in the high velocity zone below the disc, with a minimum of eight grid cells across this narrow gap. Away from this critical area, a pave mesh is used, growing with a factor of 1.05 from the smallest cell size.

Figure 4 and Figure 5 show one of the meshes used in the simulations in some detail.
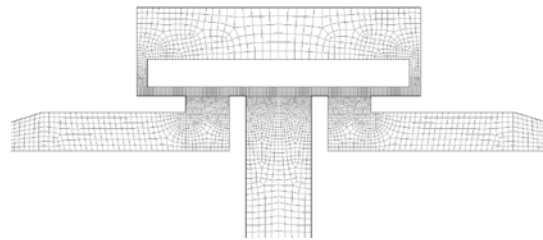
Figure 4: Grid in the main area.
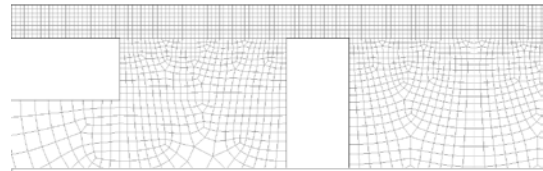
Figure 5: Grid in the tight channel.

Boundary conditions

We run simulations with a constant total relative pressure with respect to a reference pressure at the inlet and the outlet. For convenience, the outlet relative pressure is always set to zero, which means that negative relative pressures are reported in the high velocity areas.

Solver settings

We use the steady-state 2D axisymmetric model in order to reduce the required computational effort, which is important since the valve characteristics of a given fluid will typically require about 10 simulations.

The coupled solver has been used along with second-order schemes for all discretized derivatives. In order to have a robust solution strategy, simulations were started with the SIMPLE pressure-velocity coupling and first order discretization of the derivatives.

Finding the disc position

The challenge of modelling the valve is related to fact that we don't know the disc position *a priori*.

To model the valve characteristics with CFD simulations, the following methodology has been developed:

1. Create a grid for different disc positions (valve opening): 0.05mm, 0.1mm 0.2mm, 0.3mm, 0.5mm, 0.8mm, 1.3mm, 1.8mm and 2.5mm. The disc is assumed only to move vertically and to have no rotation.
2. Run simulation with a given (total) pressure difference and a given fluid for one of the geometries
   a. Check if the force acting on the disc is positive (the disc will open) or negative (the disc will closed)
   b. Run the simulation geometry with larger / smaller opening, depending on the result above. Repeat until the force acting on the disc changes sign (or we run out of disc positions)
   c. Interpolate so we can find the position where the force will be zero, and use this also to interpolate simulated flow rate at this position
3. Repeat step 2 with a new pressure difference

This procedure gives us the pressure drop as a function of flow rate, i.e., the valve characteristics, for the given fluid.

We have developed a Python script that runs simulations based on this algorithm. It reads a simple text inputfil (ini-file) specifying the simulation setup. The script is parallelized so that it can handle multiple fluids simultaneously.

In addition to the normal numerical convergence criteria, we judge the convergence of the simulations considered based on the stability of a mass flow monitor.

RESULTS

Simulations overview

Table 1 and Table 2 lists the types of valves and fluids used for the simulations.

Table 1: List of valve types and fluids used for the simulations. The greyish area denotes that comparison with experimental data exists.

VALVE TYPE	A	B-1	B-3	B-5	C
Gas		X	X	X	
Tap water, 10°C		X	X	X	
Oil 0.8cp					X
Water 0.3cp					X
Synthetic oil 1cp	X				
Synthetic oil 10cp	X				
Synthetic oil 100cp	X				
Synthetic oil 1000cp	X				

Table 2: List of fluid densities.

	DENSITY [kg/m3]
Gas	80
Tap water, 10°C	1000
Oil 0.8cp	750
Water 0.3cp	980
Synthetic oil 1cp	950
Synthetic oil 10cp	950
Synthetic oil 100cp	950
Synthetic oil 1000cp	950

Typical velocity and pressure distributions

Here we consider the C-valve where the fluid is a 0.8cp oil, the valve opening is 0.2mm and the pressure drop across the valve is 3 bars. Figure 6 shows the velocities through the entire valve while Figure 7 zooms in on the disc opening. It should be noted that, while the other valves shown above has the outlet on the same side as the inlet, the C-valve has the outlet radially outwards.
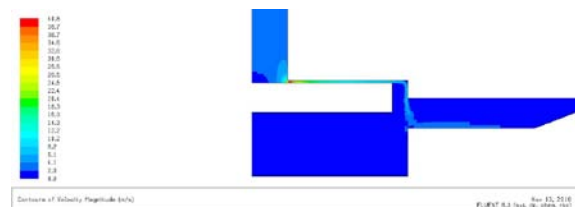
Figure 6: Velocity distribution for the C-valve. The inlet is at the top while the outlet is on the right.

As expected, there is a high velocity region in the tight channel and the velocity decreases radially outwards.
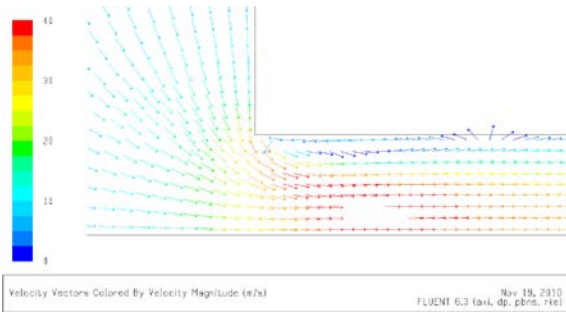
Figure 7: Velocity vectors for the C-valve, zoomed into the tight channel.

Figure 8 and Figure 9 show the pressure distribution through the valve.
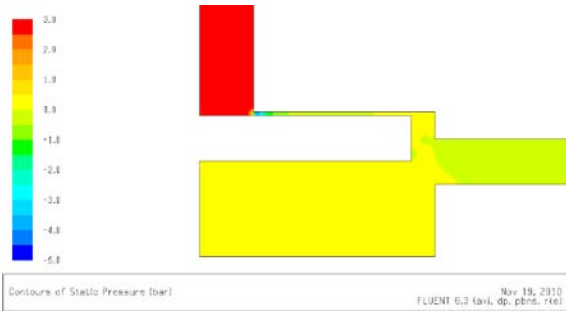
Figure 8: Pressure distribution for the C-valve. The inlet is at the top while the outlet is on the right.

Figure 9: Pressure distribution for the C-valve, zoomed into the tight channel.

The high velocity zone manifests itself by giving a low static pressure in the tight channel. We note that much of this is recovered as the flow slows down and that almost all of the pressure drop is lost over a radial distance of only 2mm, as can be seen from Figure 10.
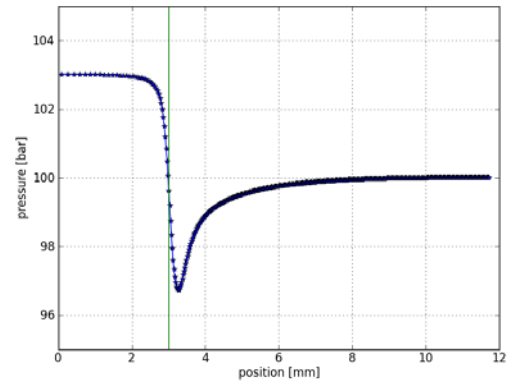
Figure 10: Static pressure along the disc from the center in the area of the tight channel. The green line denotes the start of the channel.

The effect of increasing viscosity

The main feature of the autonomous valve is that it chokes back fluids with low viscosity while fluids with a higher viscosity flow more easily. It is this counter-intuitive behaviour that gives the valve its flow control properties.phase separation properties.

Figure 11 shows that the CFD simulations capture this feature.
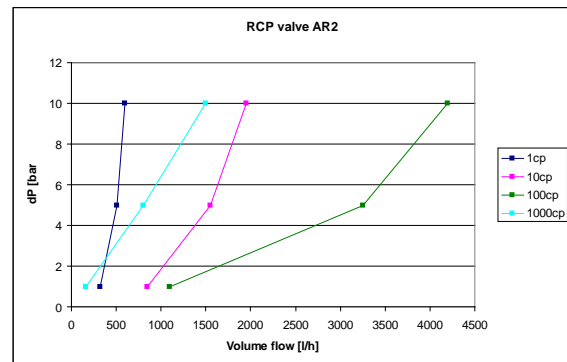
Figure 11: Valve characteristics for the A-valve for oils with various viscosities.

The reason that the 1000cp oil is more restrictive than the 100cp oil (or even the 10cp oil), is that the valve hits its maximum opening barrier and therefore has a fixed geometry.

The effect of increasing the pressure difference

In order to obtain a very uniform inflow, we would like the valve to choke when it is subject to a higher pressure drop. Figure 12 shows that this is in fact what happens. This effect leads to a relation between the flow rate and the pressure drop that can be described by a power function with an exponent larger than two.
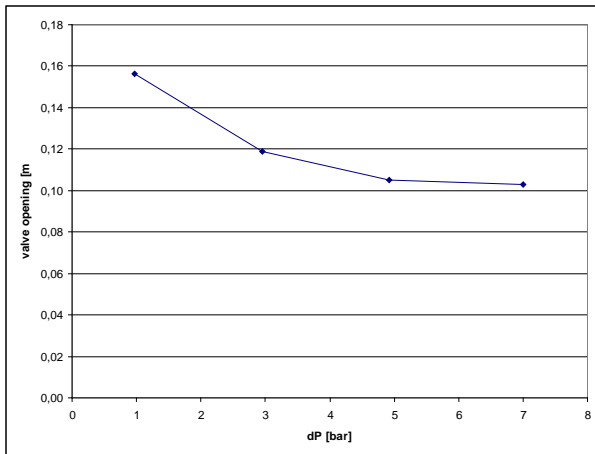
Figure 12: Valve opening as a function of pressure drop for the C-valve with water.

We also note that the actual valve opening is very small, in the order of 0.1mm, for a fluid with a low viscosity, for example water.

Comparison to experimental data

The simulations give a useful insight of the fluid flow through the valve, and is still the only way of getting a realistic estimate of the disc position.

However, simulated valve characteristics should match experimental data for actual use in the design process.

Obtaining experimental data

Statoil has facilities for testing inflow control devices like the autonomous valve in Porsgrunn. There are rigs for testing single phase fluids at low pressure conditions for design and development purposes, a rig for testing the effect of erosion, and one for testing the valve's ability to handle drilling mud. We also have a high pressure multiphase rig that we have used for testing the valve with live oil and various fluid mixtures. In addition to this, a new very high pressure – high temperature rig that is dedicated to inflow control will be used in near future.

The testing procedure is basically very simple. The valve is installed into a flow loop and the flow rate is adjusted to obtain a predefined pressure drop across the unit. A differential pressure gauge and a coriolis mass flow meter are used for this purpose. In addition, an absolute pressure gauge is needed.

When the flow and pressure have stabilized at the given test point, the flow is adjusted to match the next test pressure drop defined in the test matrix.

These test points then give the valve characteristic for the given fluid.

B valves for water

Figure 13 shows the comparison between experimental data and simulated data for three variants of the B-valve

using water as fluid. The B-1 has a 6mm inlet, B-3 has an 8mm inlet, while B-5 has a 10mm inlet.
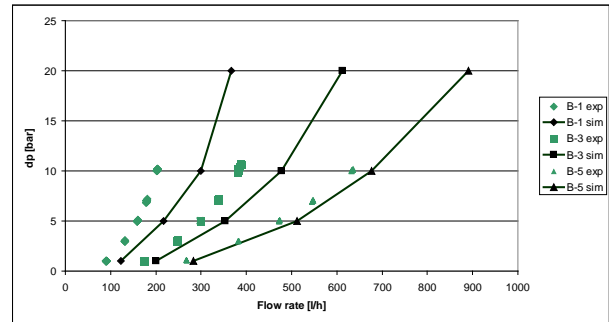
Figure 13: Comparison of experimental (in blue) and simulated (in green) valve characteristics for three different B-valves using water.

We see that for the valve with the largest inlet opening, B-5, the simulated curve has an excellent match to the experimental values. For the two other valves, the match is less good, but still acceptable.

B-valves for gas

The experimental data for gas have been obtained at 100bars and, as for the liquid cases, we assume that the flow is incompressible. Here, the match is less good than for water, see Figure 14. We notice that the experimental flow data for the B-5 valve flattens out for higher pressure drop, an untypical behaviour which is not well understood.
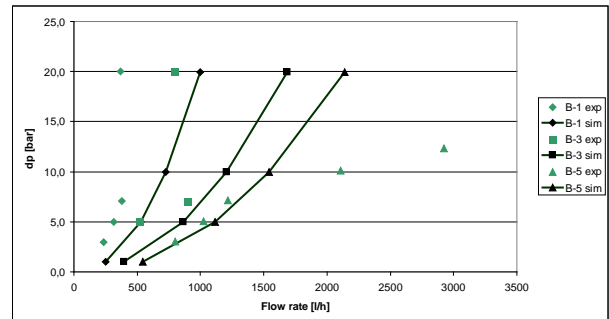
Figure 14: Comparison of experimental (in blue) and simulated (in green) valve characteristics for three different B-valves using gas.

Valve C for water and oil at reservoir conditions

The experimental data for Valve C have been obtained from the high pressure multiphase rig. This means that we have similar conditions to what is found in the reservoir.

Figure 15 shows that both the water characteristics and the oil characteristics are well predicted by the simulations, although the oil curve is somewhat overpredicted.
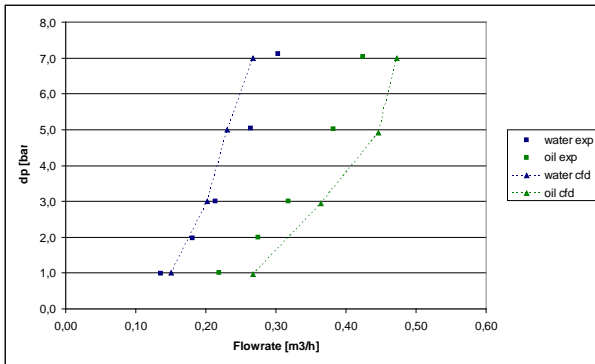
Figure 15: Comparison of experimental (in blue) and simulated (in green) valve characteristics for the C-valve using oil and water at reservoir conditions.

Future work

In order to have more manageable simulations, we want to move the disc dynamically using the moving mesh capability of Fluent.

CONCLUSIONS

The conclusions are:
1. The CFD simulations give useful insight of the flow in the valve
2. The CFD simulations capture the main features of the valve for liquids
3. The CFD simulations match the experimental data quite well for liquids with low viscosity.

REFERENCES

Fluent 6.3.26, (2006), *User's Guide.*

SENEVIRATNE, M. (2007), *A practical approach to water conservation for commercial and industrial facilities.* 1st ed. Butterworth-Heineman.

A MASSIVELY PARALLEL INCOMPRESSIBLE SMOOTHED PARTICLE HYDRODYNAMICS SIMULATOR MOTIVATED BY OILFIELD APPLICATIONS

Paul DICKENSON[1,2*] , William N DAWES[1]

[1] CFD Laboratory, Dept of Engineering, University of Cambridge, Trumpington Street, Cambridge, CB2 1PZ, UK

[2] Schlumberger Cambridge Research, High Cross, Madingley Road, Cambridge, CB3 0EL, UK

* E-mail: pd268@cam.ac.uk

ABSTRACT

Computational Fluid Dynamics (CFD) can improve understanding of multiphase flows in oilfield applications. Smoothed Particle Hydrodynamics (SPH) has been chosen for development with the aim of modelling rotating gas-liquid flows such as those found in separators and flow conditioners.

A new SPH simulator has been developed using the incompressible formulation and implemented for Graphics Processing Units (GPU). This combination offers reduced run times and reliable results even under the high accelerations seen in rotating fluid systems.

All significant computation occurs on the GPU, minimising costly data transfers. Neighbour searching, generation of the PPE matrix problem, and solution of the PPE are all performed in a massively parallel fashion. A new sparse matrix format is introduced for storage of the PPE matrix.

The new SPH simulator is demonstrated for simple development test cases. The results are correct to within 2% of analytical solutions and are obtained within short run times.

Keywords: Meshfree Methods, SPH, Separation and Mixing, Massively Parallel Computing.

NOMENCLATURE

Greek Symbols
γ Exponent in WCSPH equation of state.
ρ Density, [kg/m^3].
ρ_0 Reference density in WCSPH, [kg/m^3].
ω Smoothing function/kernel.

Latin Symbols
$\underline{A}$ Matrix of PPE coefficients.
B Coefficient in WCSPH equation of state.
$\underline{b}$ Array of PPE coefficients.
m Particle mass, [Kg].
p Pressure, [Pa].
$\underline{r}$ Position, [m].
t time, [s].
$\underline{u}$ Velocity, [m/s].
$\underline{x}$ Array of pressures in PPE.

Superscripts
n Current timestep
* Intermediate, after correct stage.

Subscripts
a Particle of interest.
b Neighbour particle.

INTRODUCTION

Multiphase flows occur in many high-value oilfield applications such as pumps, valves, separators and flow conditioners. Multiphase Computational Fluid Dynamics (MPCFD) can help increase our understanding of such devices and the multiphase flows within them.

Smoothed Particle Hydrodynamics (SPH) has been selected as a promising method for the simulation of oilfield devices. Its capabilities are a particularly good match to the gas-liquid free surface flows often seen in the oilfield. However, there is also much scope for further development of SPH making it an appealing target for research.

Rotating gas-liquid flows occur in devices of industrial importance such as separators, hydrocyclones and other flow conditioners. They are difficult to model using conventional CFD but are a good fit to the capabilities of SPH. Consequently there is both industrial and technical motivation to model rotating gas-liquid systems using SPH.

For SPH to be successful it must produce reliable results within feasible run times, even under the high accelerations of rotating systems. In this paper we introduce a new SPH simulator addressing the twin needs of short run times and accurate results. Early stage results are shown for simple test cases.

SMOOTHED PARTICLE HYDRODYNAMICS

Smoothed Particle Hydrodynamics (SPH) is a Lagrangian meshless particle method. Unlike most conventional fluid simulation methods, there is no Eulerian mesh. Instead the fluid of interest is modelled by a cloud of interpolation points with fluid properties distributed over these points using kernel functions. The

points have mass and so are commonly regarded as particles.

The Lagrangian nature of SPH means it can automatically handle topology changes and free surfaces. It also focuses computational resources on the fluid of interest. For example, only the liquid is modelled in a gas-liquid free surface flow. Consequently, SPH is particularly well suited to the simulation of energetic flows, free surface problems where the liquid dominates, and problems where the dominant fluid fills a small proportion of space.

SPH was first developed for astrophysical applications (Monaghan, 1988) but was soon adapted for environmental and engineering free surface flows (Monaghan, 1994). In recent years there has been renewed interest in the method for engineering problems. A good summary of recent SPH development and applications is given by Cleary et al (2007).

Weakly Compressible SPH

Astrophysical SPH simulators use a gaseous equation of state to describe the fluid. This type of simulator can be adapted to model liquids by using a stiffened equation of state (Monaghan, 1994). The resulting formulation is known as Weakly Compressible SPH (WCSPH). The most commonly used equation of state is shown in Equation 1, typically with $\gamma = 7$.

$$p = B\left[\left(\frac{\rho}{\rho_0}\right)^{\gamma} - 1\right] \quad (1)$$

The compressibility, and hence the speed of sound, are set by B such that the Mach number is approximately 0.01. This produces good results for many applications, particularly where the acceleration is low.

Like all compressible techniques, the timestep for a WCSPH simulator is a function of both the maximum fluid velocity and the sound speed. A high sound speed leads to a small timestep and consequently high computational cost. This problem becomes particularly severe when the fluid experiences high accelerations. A high sound speed is required to avoid unphysical compression of a liquid.

WCSH also suffers from oscillations in the pressure field caused by acoustic waves moving at far below the physical sound speed. These can echo around an enclosed chamber for many timesteps.

These problems of WCPPH motivated the development of a truly incompressible SPH formulation.

Incompressible SPH

An incompressible SPH formulation (ISPH) was proposed by Cummins and Rudman (1999). Density is a fixed value rather than a variable to be calculated. The velocity field is therefore divergence-free. To enforce this we solve the equation of motion using a three stage process.

Predict

First, the particle accelerations and velocities are predicted by solving the equation of motion without

pressure. The resulting velocity field will have locally non-zero divergence.

Solve

Secondly, the Pressure Poisson Equation (PPE, shown in Equation 2) is solved for pressure. This is the pressure required to enforce incompressibility by generating a divergence-free velocity field.

$$\nabla^2 p^{n+1} = \frac{\rho}{\Delta t}\nabla.\underline{u}* \quad (2)$$

Applying a projection method to the PPE generates a matrix problem of the form shown in Equation 3. **A** is a sparse matrix of coefficients, **b** is a dense vector of coefficients and **x** is a dense array of pressures. Each row of the matrix problem relates to one particle. The matrix problem is solved using an iterative linear solver.

$$\underline{A}\underline{x} = \underline{b} \quad (3)$$

Correct

Thirdly, the accelerations and velocities are corrected to include the effects of pressure and enforce incompressibility. The new particle positions are calculated using this corrected velocity.

The ISPH formulation requires more computational effort per timestep since we must solve a large matrix problem. However, the size of the timestep is no longer a function of sound speed and so larger steps are possible. This removes the conflict between compressibility and computational cost. It also removes the slow moving acoustic waves, so reducing noise.

ROTATING GAS-LIQUID FLOWS

Rotating gas-liquid flows occur in several important oilfield applications. These include separators, hydrocyclones and flow conditioners. They are also of relevance to other industries such as mining, food production and paper making.

Typically a rotating gas-liquid flow is formed when a mixture of gas and liquid is given a tangential velocity, either by an impeller or the geometry of the inlet. The resulting acceleration causes radial stratification giving a gas core and a liquid film on the wall. This is shown in cross section by Figure 1. Once stratified, the two phases can be handled separately.

Motivation

Rotating gas-liquid flows are industrially relevant. They
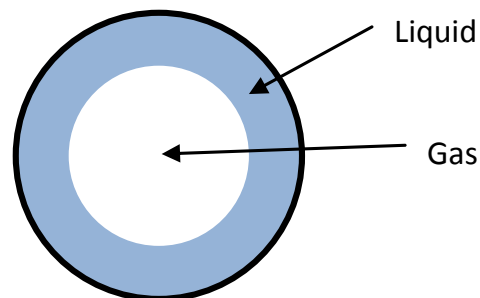
Figure 1: Cross section of a generic rotating gas-liquid system. Note radial separation of liquid and gas.

occur in valuable devices whose fundamental behaviour remains poorly understood. Such devices have often proved difficult to model using conventional CFD techniques. Hence they are an appealing target for a more novel simulation technique.

Rotating gas-liquid flows are well matched to the capabilities of SPH since they have a free surface. SPH needs development and demonstration, both of which are possible with rotating gas-liquid flows as an application.

This work is an academic-industrial collaboration. It is therefore important to develop a relevant but non-confidential test case for rotating gas-liquid flows. A simple example of such a test case is shown in Figure 2.
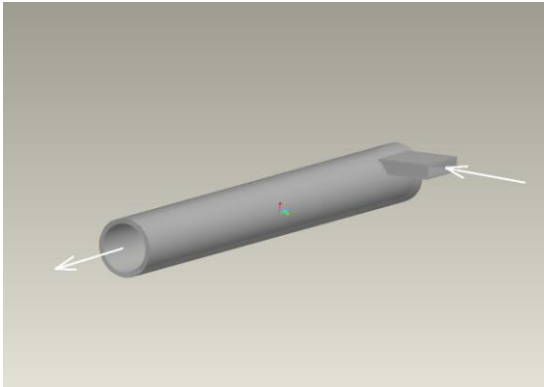
Figure 2: A simple non-confidential rotating flow test case. A mixture of gas and liquid enters through the tangential inlet (top right), swirls through the pipe section and exists bottom left.

Feasibility of Simulation

A study was conducted by the author (Dickenson, 2009) to test the feasibility of modelling a rotating gas-liquid flow using SPH. This suggested a free surface approximation would be valid for this case; the behaviour of the liquid dominates. This study also considered the likely computational cost and the SPH formulation required for this case.

Computational Cost

Consider a test case such as that shown in Figure 2 with dimensions typical of a relevant industrial device. The feasibility study suggested between 1 million and 7 million SPH particles would be required. Extrapolating from previous SPH simulations, the corresponding run times on a serial CPU would be between 3 and 29 days. As a consequence, any SPH simulation of this problem at realistic scale and resolution, and with an acceptable run time, will require some form of parallel computing.

WCSPH vs ISPH

The feasibility study considered which of the weakly compressible (WCSPH) or incompressible (ISPH) formulations would be required in this case. A weakly compressible simulator was tested with elevated gravity. It was clear the compressibility would be unacceptable under the accelerations present in rotating gas-liquid systems (Dickenson, 2009). Correcting this would require a very high sound speed, and consequently a small timestep and long run time. Instead we must use the truly incompressible (ISPH) formulation.

MASSIVELY PARALLEL COMPUTING

Massively parallel computing using Graphics Processing Units (GPU) was chosen as a good match to the simple data structures and high computation to memory ratio of SPH. GPU computing differs from traditional CPU computing in three main ways:

There is device-host operation. All commands and input data originate on the CPU (host). The GPU (device) has no operating system.

Algorithms must be parallel at the scale of elements in an array.

A much greater proportion of the silicon in a GPU is devoted to arithmetic logic.

Massively Parallel WCSPH

Several groups have demonstrated the acceleration of weakly compressible SPH (WCSPH) using GPU computing. For an example, see Crespo et al (2010). These implementations have seen a speed-up of up to 90x compared to serial CPU processing.

Challenges of Massively Parallel ISPH

Along with the challenges faced by massively parallel WCSPH, the implementation of massively parallel ISPH produces two additional, linked, challenges. These are to both set up and solve the PPE matrix problem on the GPU. This requires massively parallel implementation plus careful use of the limited GPU memory, as described in the next section

THE SPHIG SIMULATOR

SPHIG is a new 3D **S**moothed **P**article **H**ydrodynamics simulator using the **I**ncompressible formulation, implemented for **G**raphics Processing Units (GPU). The core ISPH algorithm is similar to that first developed by Cummins and Rudman (1999) and later refined by Lee (2007). The main novelty results from the combination of the incompressible formulation with massively parallel GPU computing. In this section we consider the main developments caused by this novelty.

Simulator Architecture

The simulator is composed of three separate pieces of software as shown in Figure 3. The pre-processor takes text files as inputs for geometry, initial conditions and simulator parameters. The three elements communicate via text files. The formats are such that the main simulator can receive input files from either the pre-processor or its own outputs. This allows restarts from any output timestep.

The pre-processor and main simulator are written in C/C++ with CUDA extensions to drive the GPU. The post-processor is written in Matlab.

Main Solver

The main SPHIG solver is shown schematically in Figure 4. Note how all the major computational
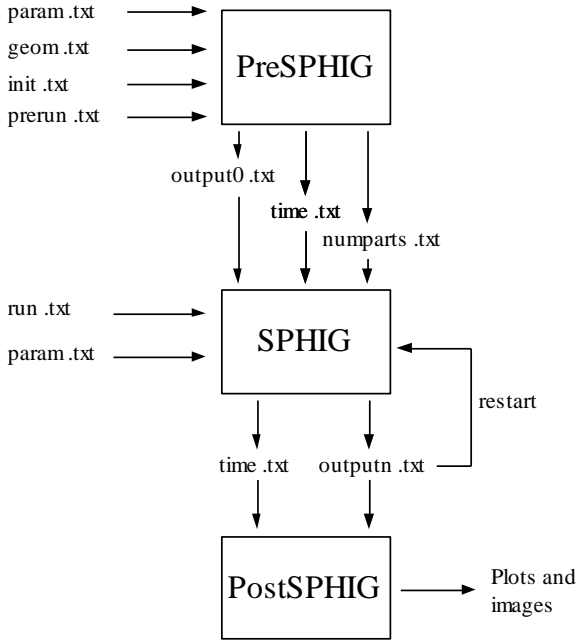
Figure 3: Overall SPHIG architecture showing pre-processor, main simulator and post-processor.
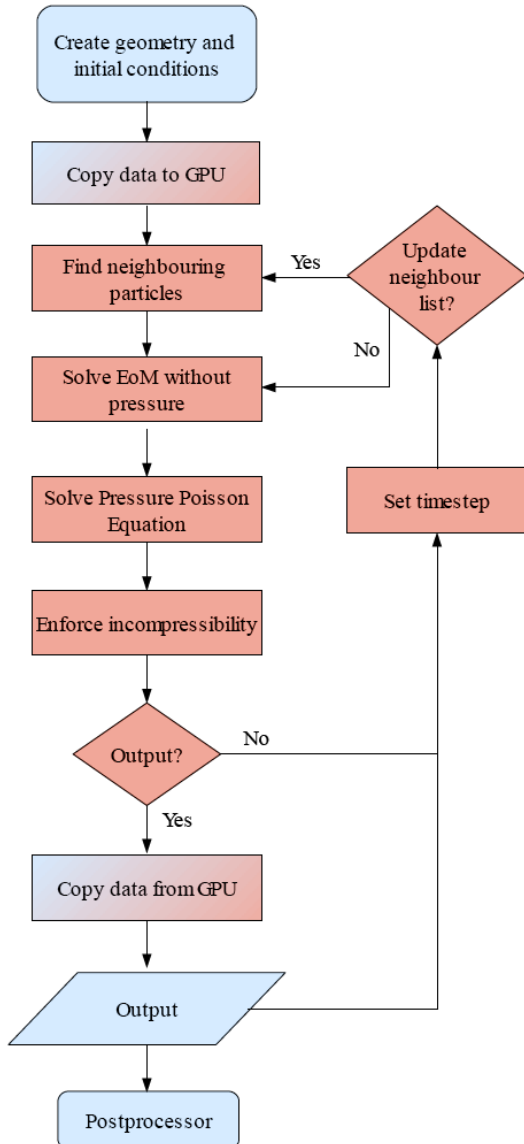
Figure 4: Flow diagram for main SPHIG solver. Blue processes occur on CPU, red are on GPU.

operations occur on the GPU with data only copied back to the CPU for output. This minimises slow device-host data transfers.

Neighbour Searching

At each timestep we must identify the neighbours for each particle. We use a hashing system to avoid searching all particles as potential neighbours at each timestep. First the domain is divided into a course hash grid and each particle placed in the correct hash cell. For each particle the relevant cells are then searched for potential neighbours.

The massively parallel neighbour searching algorithm used in SPHIG is similar to that mentioned in the documentation for the Particles example from the CUDA SDK (Green, 2008). However the algorithm is not implemented in the source code for that example.

Three neighbour searching arrays are maintained. CellID holds the hash cell identifier for each particle. CellCount holds the number of particles in each cell with one element per cell. PartsInCell stores the particle IDs for those particles present in each cell. The arrays are populated in a massively parallel fashion with one thread per particle. Atomic operations are required to avoid race conditions when multiple threads access the arrays simulatenously.

Boundary Conditions

Solid Walls

The solid wall boundaries in SPHIG simulations are formed from liquid particles fixed in space with velocity and acceleration forced to zero. The wall boundaries serve three purposes; to prevent penetration by liquid particles, to minimise kernel truncation away from the free surface, and to enforce a zero pressure gradient normal to the boundary.

The pressure at the wall particles adjacent to the liquid is free to vary during solution of the PPE, just like the pressure at a liquid particle. The "child" particles inside the wall have their pressure set to that of their "parent" particle on the surface (see Figure 5). As a consequence the pressure gradient inside the wall is always zero in the normal direction. The interconnectivity between parent and child particles is recorded during creation of the boundary by the preprocessor.

Free Surface

When solving the PPE, the value of pressure must be fixed at some point in the domain. The logical approach for a free surface problem is to set the pressure to zero at the free surface. All pressures in the simulation are then relative to atmospheric pressure.

To identify free surface particles we calculate the divergence of particle position, a measure of smoothing kernel truncation (Equation 4). Following Lee (2007), if the value is below 2.4 in 3D, the kernel is significantly truncated and so the particle is at the free surface.

$$\nabla . \underline{r} = \sum_{b} \frac{m_b}{\rho_b} \underline{r_{ab}} . \nabla \omega_a \qquad (4)$$
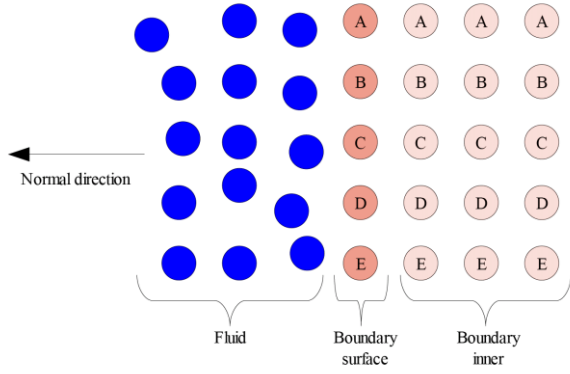
Figure 5: 2D cross section through a wall boundary showing fluid particles, parent particles at the boundary surface, and child particles inside the boundary. Child particles have pressure set equal to that of their parent labelled with the same letter.

Having identified a free surface particle, the pressure is forced to zero by setting the diagonal element of the relevant row of **A** to unity and the off diagonal elements to zero. The corresponding element of **b** is set to zero.

Solving the PPE

The Pressure Poisson Equation (PPE) is solved in the form **Ax**=**b** at the particle locations using a Bi-CGSTAB linear solver (see, for example Barrett et al, 1994). The matrix **A** is very large, perhaps 10^{12} elements. However, it is also very sparse; only approximately 0.01% of the elements are non-zero. Consequently a sparse matrix storage format is used to save memory.

SPHIG uses the SpeedIT library available from vratis.com. This includes a Bi-CGSTAB linear solver implemented for GPUs and accessible via low-level functions. It accepts inputs of the matrix **A** in Compressed Sparse Row (CSR) format and the array **b** in dense format. We must generate these formats during set up of the PPE problem.

PPE Set Up

It is necessary to set up the PPE matrix problem on the GPU in order to maximise the benefit of GPU computing. In particular, we must construct the sizeable matrix **A** in a massively parallel fashion.

Like most linear solvers, the SpeedIT Bi-CGSTAB solver expects the matrix **A** in Compressed Sparse Row (CSR) format. This format is illustrated for a small matrix in Equations 5 to 8. The *vals* array contains the values of all non zero elements, the *cidx* array contains the corresponding column indices for these non-zero values, and the *ridx* array contains the running number of the first non-zero element in each row. The final element of *ridx* gives the total number of non-zero elements in the matrix. Consequently the number of elements in *ridx* is equal to the number of rows plus one.

$$
\begin{bmatrix}
1.0 & 1.4 & 0.0 & 3.0 \\
0.0 & 1.0 & 0.0 & 0.0 \\
0.0 & 0.0 & 1.0 & 5.2 \\
7.1 & 0.0 & 0.0 & 1.0
\end{bmatrix} \tag{5}
$$

$$vals = [\ 1.0\ \ 1.4\ \ 3.0\ \ 1.0\ \ 1.0\ \ 5.2$$
$$7.1\ \ 1.0] \tag{6}$$

$$cidx = [\ 0\ \ 1\ \ 3\ \ 1\ \ 2\ \ 3\ \ 0\ \ 3\ ] \tag{7}$$

$$ridx = [\ 0\ \ 3\ \ 4\ \ 6\ \ 8\ ] \tag{8}$$

Unfortunately, the CSR format is inherently serial. The storage location of a non-zero value in the *vals* and *cidx* arrays depends on the number of preceding non-zero values. This is not suitable for massively parallel operation.

For SPHIG we use a new sparse matrix storage format, known here as pCSR, and covered by patent application number 1105576.1. pCSR again uses *vals*, *cidx* and *ridx* arrays but with a fixed number of elements allocated for each row of the matrix. This number of elements is equal to the maximum number of neighbours, obtainable by geometric arguments. Any spare elements not filled with non-zero values are then padded using zeros from that row. It has been found possible to repeatedly pad using a zero from the same location in the matrix. The matrix of Equation 5 is shown in pCSR format in Equations 9 to 11.

$$vals = [\ 1.0\ \ 1.4\ \ 3.0\ \ 1.0\ \ 0.0\ \ 0.0\ \ 1.0$$
$$5.2\ \ 0.0\ \ 7.1\ \ 1.0\ \ 0.0\ ] \tag{9}$$

$$cidx = [\ 0\ \ 1\ \ 3\ \ 1\ \ 0\ \ 0\ \ 2\ \ 3\ \ 0\ \ 0\ \ 3\ \ 1\ ] \tag{10}$$

$$ridx = [\ 0\ \ 3\ \ 6\ \ 9\ \ 12\ ] \tag{11}$$

In pCSR format the storage locations for values from each row are known before commencing computation. Hence it is suitable for massively parallel operation. It is also back compatible with the CSR format and so can be accepted by linear solvers expecting a matrix in CSR format. In SPHIG we build the matrix **A** in pCSR format using one thread per particle and hence per row.

TEST CASES

Even a highly abstracted rotating gas-liquid test case would be too complex for the development and testing of a code including novel features. Instead simple development test cases have first been used. These have known solutions for comparison to simulation results.

Hydrostatic

The hydrostatic test case used here is an open tank of square base 0.2m x 0.2m. It is filled with water to a depth of 0.2m. Particles are initially placed on a regular Cartesian grid. The test case geometry and initial particle locations are shown in Figure 6. The test case includes solid boundaries, bulk liquid and free surfaces; all important for more complex problems.
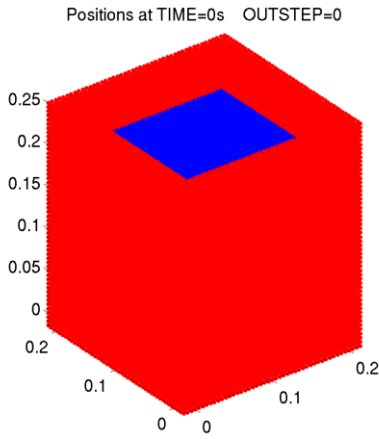
Figure 6: Initial particle positions for the hydrostatic test case. Boundary particles are red, water particles are blue. Axes are lengths in metres.

Figure 7: Pressure field in liquid after ten timesteps. Axes are lengths in metres, colour scale is pressure in Pa. Boundary particles are not shown.

When simulating the hydrostatic test case we should see no significant movement of water. There should be a hydrostatic pressure gradient in the liquid with zero pressure at the free surface. There should be a zero pressure gradient at the walls in the normal direction and there should be no unphysical artefacts at the free surface or boundaries.

The hydrostatic test case is also a good opportunity to test all the components of the code such as neighbour searching and the imposition of boundary conditions.

Inclined Hydrostatic

This test case uses the same geometry and initial conditions as the hydrostatic case. However, the acceleration due to gravity is inclined by 20 degrees to the vertical. This is akin to instantaneously tilting the tank at the start of the simulation.

When simulating the inclined hydrostatic test case we should see a hydrostatic pressure gradient inclined by 20 degrees to the horizontal. The liquid should flow towards the wall of the tank before reaching equilibrium with the free surface inclined at 20 degrees to the horizontal.

RESULTS AND DISCUSSION

Hydrostatic

The hydrostatic test case was first simulated using SPHIG for just one timestep. Checks were made of key intermediate variables such as kernel gradients, numbers of neighbours, accelerations and PPE coefficients. All were found to be correct in the bulk fluid, at the free surface, and at the solid boundaries. The only significant errors were found where the free surface meets the solid boundaries. These particles are not detected as free surface but do suffer kernel truncation.

Pressure Distribution

The test case was then simulated for ten timesteps, with several values of fixed timestep. At the first timestep the pressure at the bottom of the tank is overestimated by about 30%, then underestimated at the second timestep by about 15%. From the third timestep the pressure field is stable and within 2% of the analytical solution for the
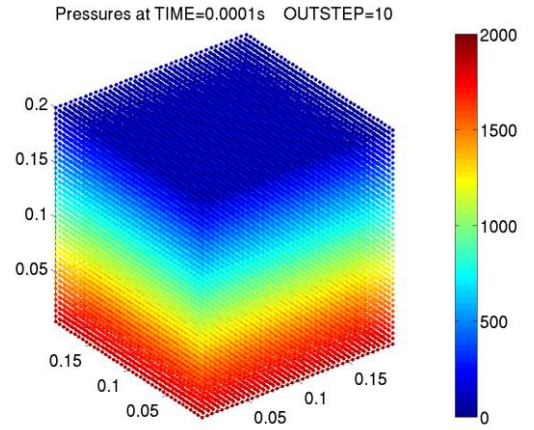
hydrostatic pressure gradient. Figure 7 shows the pressure field after ten timesteps.

During the first three timesteps the particles move to equilibrium positions slightly away from the initial starting positions on a grid. This process is driven by the pressure field, hence the initial over- and underestimates of pressure. Interestingly, this movement to equilibrium is independent of timestep; it always takes three steps. It should not be confused with the (much slower) acoustic waves observed in WCSPH simulations while the particles reach equilibrium. In fact it is on a similar timescale to physical oscillations at the true speed of sound.

Run times

A fixed timestep was used for these simulations. It is therefore difficult to make exact run-time comparisons between SPHIG and a serial WCSPH code. SPHIG must do more computation at each timestep but can take larger timesteps. How much larger a timestep determines the number of steps and hence the run-time. However, a conservative estimate of maximum timestep for SPHIG suggests the overall run-time is approximately 40 times shorter than for a serial WCSPH code. This will require confirmation after implementation of a variable timestep.

Memory Requirements

The memory requirements are significant even for this simple case, despite the use of a sparse matrix storage format. For each particle we require approximately 1250B of memory, mostly for storage of the PPE matrix. For this case of 100,000 particles, the memory usage is therefore approximately 125MB. This is entirely feasible with a typical GPU card but does place a limit on the maximum potential number of particles. For a card with 4GB memory it implies a maximum number of particles around 2.5million. This is considerable but still significantly less than the maximum number for a WCSPH solver where the PPE matrix need not be stored.

Free surface edges

If the hydrostatic test case is simulated for several hundred timesteps we see the effect of the errors at the

edges of the free surface, described above. Particles at this point slowly move into the boundary walls and eventually exit the system, forcing the simulation to end.

Since these particles are not detected as free surface, they do not have pressure set to zero in the PPE matrix problem. This implies the divergence of velocity is non-zero at these points with resulting non-physical particle movement through the walls.

To fix this problem we must reconsider the criteria for detection of free surface particles. The critical value for $\nabla.r$ was used directly from the work of Lee (2007). It may require tuning to fully detect all free surface particles. Increasing the critical value does of course increase the risk of false positives; particles from the bulk fluid incorrectly detected as free surface. It may also be advantageous to introduce a repulsive force boundary condition, further reducing penetration.
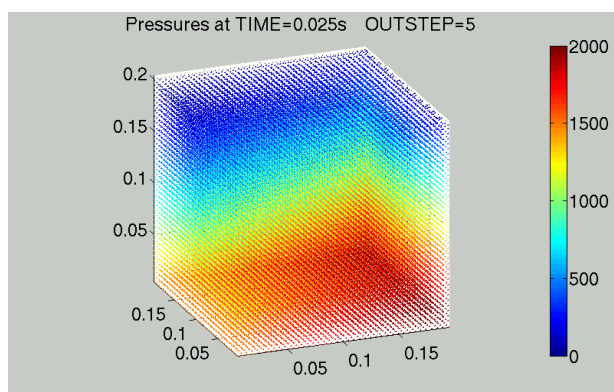
Figure 8: Pressure field in liquid after 0.025s (25 timesteps). Axes are lengths in metres, colour scale is pressure in Pa. Boundary particles are not shown.

Inclined Hydrostatic

The inclined hydrostatic test case was run for 0.1 seconds. The hydrostatic pressure distribution was established within 0.02 seconds, inclined at 20 degrees to the horizontal. The pressure distribution is shown in Figure 8.

After about 0.04 seconds the liquid began to flow due to the non-vertical gravitational acceleration. The free surface deformed. However, by 0.1 seconds the penetration of the walls had become severe, distorting the free surface and causing particles to move outside the tank. The free surface was therefore unable to achieve a new equilibrium position.

CONCLUSION

A new massively parallel ISPH simulator has been presented and demonstrated for simple development test cases. It has been possible to implement all elements needed for an ISPH simulator on the GPU with data only copied back for output. In particular, the challenges of massively parallel neighbour searching, setting up the PPE matrix, and solving the PPE have been overcome.

For the hydrostatic and inclined hydrostatic cases, the simulated pressure field closely matches the analytical solution. It is obtained within a few timesteps and without the unphysically slow acoustic waves seen in

WCSPH simulations. The results for longer duration and dynamic simulations are not yet satisfactory. Errors in the detection of free surface particles adjacent to the walls are causing penetration of the wall boundaries. In the inclined hydrostatic case, penetration occurs more rapidly than flow and so the free surface does not reach a new equilibrium position. A variable timestep will also be required for simulations involving significant flow.

The simulator described in this paper runs approximately 40 times faster than a typical WCSPH code. However, this must be verified once a variable timestep has been implemented. The GPU memory requirements are significant due to storage of the PPE matrix, placing a limit on the number of particles.

Overall, a massively parallel ISPH simulator for oilfield applications is feasible and promising but more work is required before complex problems can be simulated.

REFERENCES

BARRETT, R., BERRY, M., CHAN, T.F., DEMMEL, J., DONATO, J., DONGARRA, J., EIJKHOUT, V., POZO, R., ROMINE, C., van der VORST, H., (1994), "Templates for the Solution of Linear Systems: Building Blocks for Iterative Methods", SIAM, Philadelphia.

CLEARY, P.W., PRAKESH, M., HA, J., STOKES, N. and SCOTT, C., (2007), "Smoothed Particle Hydrodynamics: Status and Future Potential", *Progress in Computational Fluid Dynamics*, **7**(2/3/4).

CRESPO, A.J.C., DOMINGUEZ, J.M., BARREIRO, A., GOMEZ-GESTEIRA, M., (2010), "Development of a Dual CPU-GPU SPH Model", *5th International SPHERIC Workshop*, Manchester, June 2010.

CUMMINS, S. J. and RUDMAN, M., (1999), "An SPH Projection Method", *Journal of Computational Physics*, **152** (2): 584-607.

DICKENSON, P., (2009), "The Feasibility of Smoothed Particle Hydrodynamics for Multiphase Oilfield Systems", *Proc. Int. Conf. CFD in the Minerals and Process Industries*, CSIRO, Melbourne, Australia, 9-11 December.

GREEN, S., (2008), "CUDA Particles Documentation", Nvidia.

LEE, E., (2007), "Truly Incompressible Approach for Computing Incompressible Flow in SPH and Comparisons with the Traditional Weakly Compressible Approach", *PhD Thesis*, University of Manchester, September 2007.

MONAGHAN, J.J., (1988), "An Introduction to SPH", *Computer Physics Communications*, **48**(1):89-96.

MONAGHAN, J.J., (1994), "Simulating Free Surface Flows with SPH", *Journal of Computational Physics*, **110**(2):399-406.

8th International Conference on CFD in Oil & Gas, Metallurgical and Process Industries
SINTEF/NTNU, Trondheim NORWAY
21-23 June 2011

163

MODELING AND 3D SIMULATION OF PHYSICAL MASS TRANSFER AT SINGLE RISING GAS BUBBLES FOR MODERATE SCHMIDT NUMBERS

Stefan FLECKENSTEIN, Dieter BOTHE[1*]

[1]Center of Smart Interfaces, 64287 Darmstadt, GERMANY

[*] E-mail: bothe@csi.tu-darmstadt.de

ABSTRACT

In this contribution an unsplit subgrid-scale approach for simulation of mass transfer across deformable liquid interfaces is presented. Direct numerical simulation is used to obtain approximate solutions of the incompressible two-phase Navier-Stokes equations. Interface dynamics is accounted for by the Volume of Fluid method. Convergence behaviour of mass transfer for this method is investigated and compared to preceding approaches. The method is validated for mass transfer from bubbles using an exact solution for $Re < 1$ building on the Hadamard-Rybczynski velocity field. Numerical results are in good accordance with the exact solution and Sherwood numbers obtained from simulations match well with values calculated from correlations found in the literature.

Keywords: CFD, multiphase flow, mass transfer.

NOMENCLATURE

Greek Symbols
ρ Mass density, $[kg\, m^{-3}]$
η Dynamic viscosity, $[kg\, m^{-1} s^{-1}]$
σ Surface tension, $[kg\, s^{-2}]$
Ω Considered domain
Σ Phase boundary

Latin Symbols
f Volume fraction of the dispersed phase
p Pressure, $[Pa]$
u Velocity, $[m\, s^{-1}]$
c Molar concentration, $[mol\, m^{-3}]$
j Molar mass flux, $[mol\, m^{-2} s^{-1}]$
D Diffusion coefficient of chemical species, $[m^2\, s^{-1}]$
H Henry coefficient
Sh Sherwood number
Sc Schmidt number
n_Σ Interface normal vector pointing into Ω^d

Sub/superscripts
d Dispersed Phase
c Continuous Phase
i Index i
j Index j
k Index k

INTRODUCTION

Mass transfer at gas-liquid interfaces is encountered in various technical situations. These include oxygenation of waste water in bioreactors, carbon dioxide separation in power plants and liquid-liquid extraction among others. A special application are the widely used bubble column reactors, where an understanding of bubbly flows with mass transfer is important. Already the analysis of processes at single rising bubbles can provide crucial insight into significant characteristics, e.g. mass transfer and reaction rates. The involved phenomena range from small scale diffusion in interface vicinity to bubble bubble interaction and swarm behaviour in the macroscopic realm. Individual bubbles provide a suitable basic system, where the underlying local processes taking place in close vicinity of the bubble surface (i.e. transfer, mixing and reaction) can be studied in great detail.

As numerical methods and the computational power of available systems have improved over the years, direct numerical simulation (DNS) of flows around bubbles has become feasible. DNS can provide local data that would in many cases be inaccessible through experimental methods. Nevertheless these methods are not yet applicable to the whole range of relevant Schmidt numbers. This is due to the gap in scales on which hydrodynamics and mass transfer take place. The thickness of a concentration boundary layer remains a bottle neck in terms of resolution and effort spend, as it may be many times smaller than the length scale to be considered for computation of the velocity field. Typically the boundary layer thickness of the concentration field scales as $(Sc)^{-1/3}$ times the hydrodynamic length scale, where Sc denotes the Schmidt number, see (Asano, 2006). For aqueous systems Sc ranges up to several hundreds, e.g. $Sc \approx 370$ for oxygen solved in water at $25°C$. The gradient of species concentration may thus be very steep in the phase where the main resistance to mass transfer is situated, which in our setting is the liquid phase. An unaided numerical treatment of mass transfer would in this case imply to increase spatial resolution to a point where the boundary layer can be fully resolved – far beyond the resolution needed for accurate account of the hydrodynamics. This, however, is impractical or even nearly impossible to date, because of limited computational resources.

Mass transfer across deformable interfaces has already been investigated in the past by several authors. (Darmana *et al.*, 2006) have studied mass transfer coefficients of 3D bubbles rising in Newtonian fluids to obtain closure laws for simi-

lar systems, using a front tracking approach. Their simulations are carried out for low Schmidt numbers, assuming constant concentration inside the bubbles. In (Deshpande and Zimmerman, 2006) the characteristics of mass transfer from droplets at varying Reynolds numbers at different bubble shapes was investigated. Their numerical results are also compared to an empirical correlation for the Sherwood number from the literature. Hydrodynamics and mass transfer of bubbles and small bubble swarms is studied in (Radl *et al.*, 2007), where 2D simulations were carried out for Non-Newtonian fluids using a Semi-Lagrangian approach. There the interplay of mass transfer and the different bubble dynamics caused by different fluid properties is discussed. Simulations of mass transfer from rising bubbles in 2D and 3D employing the Volume of fluid method are presented in (Alke *et al.*, 2009, 2010). In these articles, computational techniques for high Schmidt number simulations and methods for conjugate mass transfer, which prohibit unphysical transfer of molar mass, are introduced. (Bothe *et al.*, 2010) finally applied these methods to reactive mass transfer and compared the obtained numerical data to experimental results.

Numerical methods developed for interfacial mass transfer must provide accurate integral and local data. In this article we present a VOF-based approach for simulating mass transfer of ideally diluted components from rising gas bubbles in liquids at realistic Schmidt numbers. We compare a directionally split and a directionally unsplit subgrid-scale (SGS) method for capturing the concentration boundary layer at the bubble interface at realistic Schmidt numbers for aqueous systems. Integral Sherwood numbers obtained from simulations are then compared to results from correlations found in the literature. The method is validated by comparison of local concentration profiles to an exact solution of the coupled hydrodynamic and reaction diffusion problem.

MODEL DESCRIPTION

Hydrodynamic model

In the following we will consider a bubble, represented by the domain $\Omega^d(t)$, which is totally immersed into an ambient liquid, filling the domain $\Omega^c(t)$. The interface of zero thickness separating $\Omega^d(t)$ and $\Omega^c(t)$ will be denoted by $\Sigma(t)$. Concerning the hydrodynamics, we assume

- incompressible bulk phases with constant density

- isothermal conditions

- negligible phase transfer

- fluids of constant viscosity

The governing equations are the standard two-phase Navier Stokes equations. Due to continuous velocity fields at the interface, the one field formulation

$$\rho \partial_t(u) + \rho(u \cdot \nabla)u = -\nabla p + \eta \Delta u + \rho g + \sigma \kappa n_\Sigma \delta_\Sigma, \quad (1)$$
$$\nabla \cdot u = 0, \quad (2)$$

applies in the entire domain Ω.

In this formulation the jump of momentum at the interface acts as a source term in the momentum balance (1). This term depends on the sum of local principal curvatures $\kappa = -\nabla \cdot n_\Sigma$ of the interface and the surface tension σ, which may be set to a constant value in the absence of surface active ingredients or thermal effects, e.g. Marangoni convection. Density ρ and viscosity η are local properties depending on

the respective phase, but which are constant within each bulk phase. Their values are given by

$$\rho = f\rho^d + (1-f)\rho^c,$$
$$\eta = f\eta^d + (1-f)\eta^c.$$

Here, the phase indicator function f represents the volume fraction of the dispersed phase in the considered domain. To account for bubble deformation and bubble movements, an additional transport equation for the volume fraction f,

$$\partial_t f + \nabla \cdot (fu) = 0, \quad (3)$$

is necessary. As this system of equations cannot be solved analytically, numerical schemes must be employed to obtain approximate solutions. In our simulations the Volume of Fluid method (VOF) by (Hirt and Nichols, 1981) is used to solve (3). This is done geometrically, i.e. we make use of information as interface positioning to determine the flux rate of volume fraction. The necessary data are gained from a piecewise linear reconstruction of the interface (PLIC), introduced by (Rider and Kothe, 1997). By this approach artificial blurring of the volume field f can be prevented.

The surface tension as needed in (1) is calculated via the continuum surface stress model (CSS) by (Lafaurie *et al.*, 1994). All transport equations are solved with a directionally split method where the order of the subsequent steps is alternated every cycle to prevent directional biases leading to skewed results.

The simulations are carried out with the inhouse code Free Surface 3D (*FS3D*) originally developed at ITLR by Rieber (Rieber and Frohn, 1999). For more information on *FS3D* see (Rieber, 2004).

Mass transfer

We consider a two-phase system containing a single chemical species k, with concentrations $c_k^d(t)$ and $c_k^c(t)$, that is transfered from dispersed to continuous phase. In addition to the assumptions already imposed on hydrodynamics, we consider only systems fullfilling the assumptions:

- dilute (two-phase) system

- no reactions

- no surface active ingredients

- local thermodynamical equilibrium at the interface

- conservation of molar mass

Then the resulting set of balance equations for species k with concentration $c_k(t)$ is

$$\partial_t c_k + \nabla \cdot (uc_k + j_k) = R_k, \quad \text{in } \Omega^c(t) \cup \Omega^d(t), \quad (4)$$

$$[j_k] = 0, \quad H_k = \frac{c_k^d}{c_k^c}, \quad \text{on } \Sigma(t). \quad (5)$$

Here, $[\phi]$ denotes the jump of a quantity ϕ across the interface Σ. The reaction term R_k, which accounts for all reactions in which species k is involved, represents in (4) the total molar mass production rate of this species. Since reactions are neglected in our considerations, R_k will be set to zero. Since we need to model the (area specific) molecular flux density j_k, suitable constitutive equations are necessary. Fick's law of diffusion is a suitable assumption for our ideally diluted system, hence

$$j_k = -D_k \nabla c_k, \quad (6)$$

where D_k is the (constant) diffusion coefficient of species k. The transfer condition in (5) is justified by conservation of mass and disregard of substances, that could possibly accumulate at the interface instead of being entirely transfered. Henry's law finally is warranted by local thermodynamical equilibrium at the interface. Initially at time t_0 the transfer species has constant concentration $c_k(t_0) > 0$ in the dispersed phase and $c_k(t_0) = 0$ elsewhere.

In *FS3D* scalar quantities are transported using a dimensionally split algorithm. This holds also true for species distribution. However, in this case we apply a two scalar approach to represent and store the mass of every single species. That is, we have

$$\phi_k^i(x) = \begin{cases} c_k(x), & x \in \Omega^i, \\ 0, & \text{else,} \end{cases}$$

where the concentration of species k is stored individually for each phase. This has the benefit of retaining information about the one-sided limits of concentrations within interface cells, enabling the application of the same methods that were used for the transport of the volume fraction. A consequence is, that unphyical mass transfer can be prevented and a sharp species distribution can be preserved in case of non-transfer species.

The described detachment of concentration fields in the respective phases implies the necessity of an explicit modeling of mass transfer between the phases and we get an additional source term in (4) for interface cells, transporting molar mass from ϕ_k^d to ϕ_k^c or vice versa. More information on this method can be found in (Alke *et al.*, 2009).

Sherwood number

An important measure for mass transport through liquid interfaces is the Sherwood number. Locally it may be defined as

$$Sh_{loc} = \left. \frac{\partial c}{\partial n_\Sigma} \right|_{x_\Sigma} \bigg/ \frac{c_\Sigma - c_\infty}{d} = \frac{\beta_{loc} d}{D}, \qquad (7)$$

also giving a local mass transfer coefficient β_{loc}. Note that the sign of the right hand side in (7) depends on the orientation of the surface normal n_Σ. An integral Sherwood number as an averaged total characteristic number of mass flux can then be calculated by integration over the whole interfacial area involved in molecular mass transfer, yielding

$$Sh = \frac{1}{|\partial V|} \int_{\partial V} Sh_{loc} dA = \frac{\beta d}{D_k}, \qquad (8)$$

analogously to (7) defining a macroscopic mass transfer coefficient $\beta = \dot{N}/(c_\Sigma - c_\infty)$ with the total molar mass flux $\dot{N}$. The quantities c_Σ and c_∞ are the molar concentrations at the interface and in the bulk, outside of the concentration boundary layer, respectively and d denotes the diameter of the considered bubble. Since in numerical calculations the gradient is usually not easily accessible from computed data, we use the macroscopic Sherwood number to obtain values in this case.

SPLIT AND UNSPLIT SUBGRID-SCALE MODEL

We first revisit the different approaches of the split and unsplit variant.

One dimensional model and dimensionally split method

We have already mentioned the problems of capturing the steep concentration gradient at the interface. One possibility

to accomplish this at relatively moderate cost and intermediate resolutions are subgrid-scale models, which have already been used in this context (Alke *et al.*, 2010). We build upon this and present here a three dimensional unsplit method to make use of such a subgrid-scale model. To recall the basic principles, we shortly outline the method and then proceed to extend it to multiple dimensions.

In (Alke *et al.*, 2010) a model for molecular mass transport in one phase adjacent to a phase boundary Σ was devised. The assumptions were a constant velocity tangential to Σ, unaffected of molecular distribution, and a diffusive species transport with constant diffusion coefficient D normal to the interface. This leads to a class of functions, describing the species distribution near the phase boundary:

$$c(x) = c_\Sigma \left(1 - erf\left(\frac{x}{\delta}\right)\right), \qquad (9)$$

where c_Σ is the species concentration at the interface, x the normal distance to Σ and δ denotes the local thickness of the concentration boundary layer. Given this approach, the concentration gradient at the interface is

$$\left. \frac{\partial c}{\partial x} \right|_\Sigma = \frac{2}{\sqrt{\pi}} \frac{1}{\delta} c_\Sigma. \qquad (10)$$

If a concentration value c can be computed for a known distance, the class of functions can be fitted to the local conditions. Newton's or similar methods are adequate to determine the boundary layer thickness δ in this way, resulting in fluxes through the local interface area for further use in numerical schemes.

In situations without phase change we have $[u] \cdot n_\Sigma = 0$ for the fluid velocity at Σ. Therefore, this model can be applied locally in every cell containing parts of the interface as a means to employ additional information. Note that within the two scalar frame work the concentration field used in (10) may vary according to the phase in which the main resistance to mass transfer is located.

Unsplit Method

In a single dimension the treatment of the coupled two-phase hydrodynamic and mass transport problem is numerically simple. Every quantity in normal direction to the interface is directly accessible after the interface has been located in a cell i. Figure 1 depicts this situation:

The interface is situated in cell i, concentration values for both continuous and dispersed phase are stored at cell centers x_i and x_{i+1}. To the right of Σ the concentration values are shown by the height of the shaded bars. Dispersed phase concentrations can been seen on the left of Σ. Continuous red and blue lines show an idealized analytic concentration profile as implied by the analytic subgrid model in the respective phase. F_i denotes the mass flux from disperse to continuous phase within a given cell. The essential issue here is to determine the distance from x_{i+1} to the interface by which the boundary layer thickness δ in the model can be estimated.

The problem remains to transfer this model correctly to higher dimensions, where scalar values are stored in fixed places that are typically not aligned with the interface normal direction n_Σ. In the one dimensional case displayed by Figure 1, n_Σ points exactly in x direction.

However, this problem can be circumvented by a dimensionally split approach, which consists of n one dimensional transport steps: A concentration gradient – with or without subscale input – is calculated for a direction x_i of a cell containing the interface if there is a neighbouring cell in that

direction which doesn't contain the phase boundary. The resulting fluxes from these gradients are then averaged according to their share of the outer normal direction. These fluxes then add up to the total mass flux through the interface.

Another possibility is given by an unsplit approach, which we want to propose with the following algorithm:

1. Exact localization of the PLIC surface in each cell containing the interface

2. Calculation of the centroid x_Σ of this area

3. Determining a suitable sampling point A along the normal n_Σ intersecting x_Σ and a concentration value φ_A in A

4. Employing the one dimensional subgrid-scale model to obtain a concentration gradient at the interface and calculate the resulting fluxes

To efficiently calculate a concentration value, we located a point A such that it always lies in a plane as shown in Figure 2. The figure shows a schematic sketch of dispersed and continuous phase in two dimensions. The situation is generic in the sense that concentrations $C_{i,j}$, $C_{i+1,j}$, $C_{i,j+1}$, $C_{i+1,j+1}$ in the continuous phase are nowhere in the desired normal direction. Additionally, an overly use of concentration values from interface cells should be avoided, because concentration values right in an interface cell may be regarded "contaminated" in situations with an underresolved concentration boundary layer as a consequence of the equilibrium assumption at Σ.

VALIDATION AND COMPARISON

Subsequently mentioned simulations were run in parallel on an Intel XEON computer cluster, consisting of 360 cores with 4GB memory each. The 3D simulations were carried out on 8 cores and lasted 4 ($Sc = 10$) and 4.5 ($Sc = 100$) days respectively with $0.3s$ simulated time. It has to be mentioned that in these simulations, surface tension was reduced to only 50% its original value in order to reduce the problem of parasitic currents. 2D simulations at highest resolution (1024×512 grid points) needed a total of 7 days to complete. Required simulation time of the presented unsplit method was lower than the time needed with the split method, as exchange of information among computational domains needed to be carried out only once for each species compared to three times for the split method in 3D simulations.
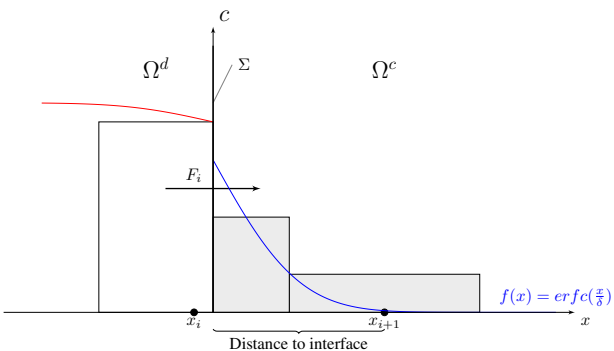
Validation of the unsplit method with exact solution

Figure 3 shows a concentration profile in normal direction of a species at the equator of a bubble with a diameter of 4mm. Plotted is the concentration in $mmol/l$ over distance to the interface in mm units. The Schmidt number in this example is $Sc = 1000$ and the flow around the bubble is in the low Reynolds number regime, $Re \approx 0.3$. The continuous line is the exact solution of the concentration distribution with the flow field given by the so called Hadamard-Rybczynski solution around a three dimensional rising bubble at low Reynolds numbers. The step function is a concentration profile obtained from numerical simulation of the coupled hydrodynamic and mass transfer problem with the same data as in the exact solution. The presented unsplit mass transfer method was used to compute mass flux through the interface. The considered domain is $1.6\,cm \times 1.6\,cm \times 1.6\,cm$, which was reduced to $1.6\,cm \times 0.8\,cm \times 0.8\,cm$ as we capitalized on the rotational symmetry of the problem. For computation we used an equidistant mesh with a cell width of $62.5\mu m$.

As can be seen, the numerical result is in good accordance with the exact solution. The concentration boundary layer is well resolved, although at greater distances from the interface we have slightly lower concentrations in the simulation than expected from the exact solution. Although the boundary layer is well captured, the agreement of the solutions far from the interface should be better at finer meshes. This is due to a somewhat increasing mass transfer rate at refined meshes, as discussed in a later section. This distribution at the interface does also quite well resemble the complemen-
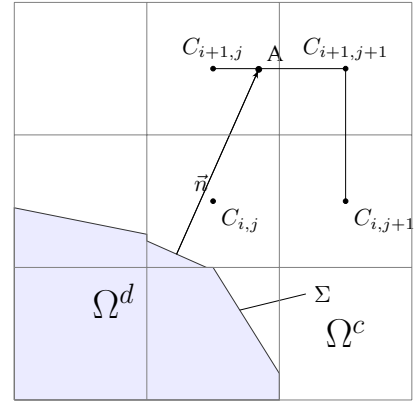

Figure 2: Location of a suitable sampling point A

Figure 1: Schematic view of one dimensional molar mass transfer through interface
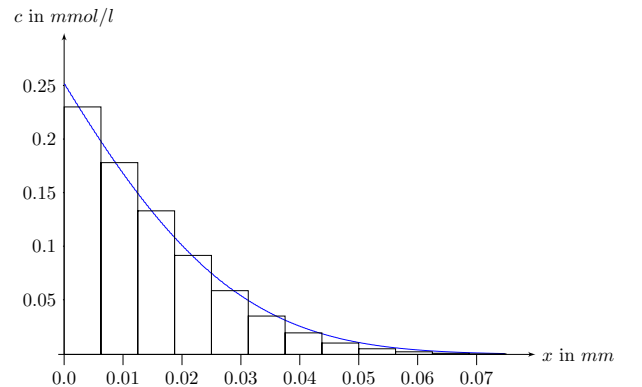

Figure 3: Comparison of numerical result and exact solution

tary error function that is at the core of the subgrid flux calculation. Note however, that the kind of flux calculation does not determine the qualitative behaviour of the concentration profile, but merely the level of transfered mass. At fine mesh sizes, this kind of profile can be qualitatively reproduced with other methods of mass flux calculations.

Convergence and comparison of methods

Mass transfer characteristics of the dimensionally split and unsplit method have been compared at different resolutions. A 2D rising bubble with 3mm diameter at $Sc = 10$ was considered at different resolutions. The decrease of initially normalized mass over time of the dispersed phase is shown in Figure 4 for different mesh sizes for the split and the unsplit approach.
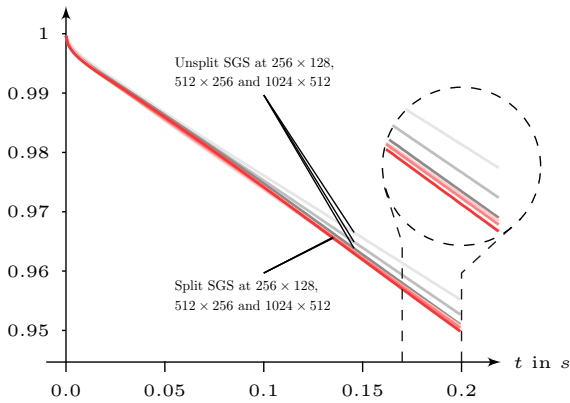

Figure 4: Comparison of decrease of total mass contained in dispersed phase (normalized with initial value) for different methods. Darker colours indicate higher resolutions.

Integral mass transfer of both, split and unsplit approach, converge to the same limit as resolution increases. The unsplit method starts at a lower level and gradually increases the transfered total species mass, whereas the split method is already close to its limit and does only increase slowly from its initially high mass transfer rates. This does not imply a general advantage of the dimensionally split method over the unsplit method. Other simulations at varying bubble sizes were carried out, where the split method led to the same increase of mass transfer from lower levels or finally even decreased a good deal from initially high transfer rates at low resolution. This behaviour is thus difficult to interpret as it is not known in advance what the split method's bias with respect to a "true" value might be.

Similar results were obtained for the same setting, but a higher Schmidt number, $Sc = 100$. In this case both methods alike showed a substantial increase of mass transfer with refined meshes. It has to be mentioned that the limit of the transfer rate was in this case only reached after an additional step of refinement – as expected because of an even thinner concentration boundary layer.

Figure 5 presents the same decrease of initially normalized molar mass contained in the dispersed phase as Figure 4. But now convergence of two different unsplit methods with increasing mesh resolution is displayed. One method is the discribed subgrid-scale model from the last paragraph, the other model does not use the subgrid information, but simply implements a linear calculation of the concentration gradient.

This comparison of convergence has already been performed in (Alke *et al.*, 2010) for the split subgrid-scale approach.
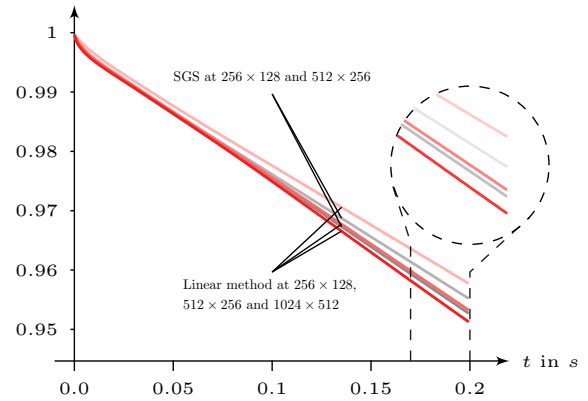

Figure 5: Convergence of mass transfer rate with increasing resolution. Depicted is the total mass contained in dispersed phase normalized with initial value.

The figure shows that the used subgrid-scale method creates higher mass fluxes at lower resolutions than the method applying a linear gradient. Nevertheless, both mass transfer rates converge to the same limit as mesh size is increased. Moreover, the subgrid-scale approach reaches realistic mass transfer rates at coarser grids compared to the linear approach. Thus the subgrid approach can save computational effort compared to an approach using a plain linear gradient.

Concentration profiles at different resolutions

A refinement of the used mesh, especially in close vicinity of the phase boundaries, can be beneficial to accuracy of both integral and local data. Particularly local concentration profiles can change markedly even if integral numbers already match. The change of local concentration profiles from one mesh to a doubly fine mesh can be seen in Figure 7 for an unsplit subgrid-scale method. Cross sectional views of the concentration profiles at varying angles are displayed: Two diagonal sections at angles 45° (side of oncoming flow) and 135° (wake sided section), and a horizontal cross section at 90°. Orientation and location of the cross sections can be seen in Figure 6, which depicts species concentrations around a 3*mm* bubble. To improve comparability of the profiles, the same fitted complementary error function is plotted in both figures, showing the right concentration value at the interface.

Again we assumed validity of Henry's law at the interface for all computations. However, with cells of finite thickness, the values represent averaged concentrations within the volume, which is why an exact reproduction of the interface concentration is usually not possible. The generic error function profile can be seen at high resolution for the horizontal section. For this view the profile is clearly sharper than at the coarser mesh, where the error function profile is still not rendered accurately. Moreover, for the finer mesh, the concentration at the phase boundary is higher, leading to increased mass transfer rates, as already mentioned in connection to convergence of the approximate solutions.

Since an orthogonal grid is used in the simulations, the computed diagonal profiles are stretched by a factor of $\sqrt{2}$ as can be seen in the cross sections at 45° and 135°. This implies fewer volumes in the boundary layer, although we have a steeper true concentration gradient in the incidental flow

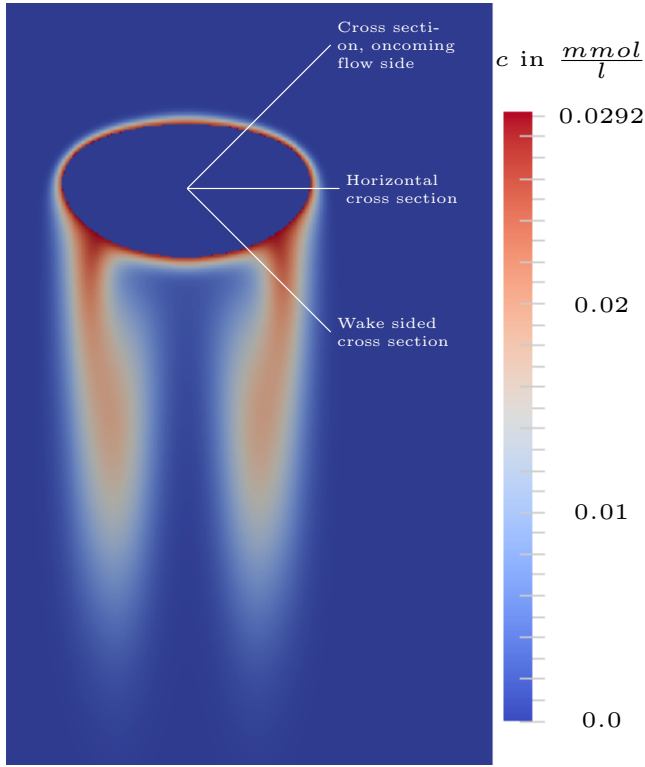region, aggravating the effects of underresolving the transfer region.

Figure 6: Molar concentrations around a rising bubble; detail from a simulation with resolution 1024×512.
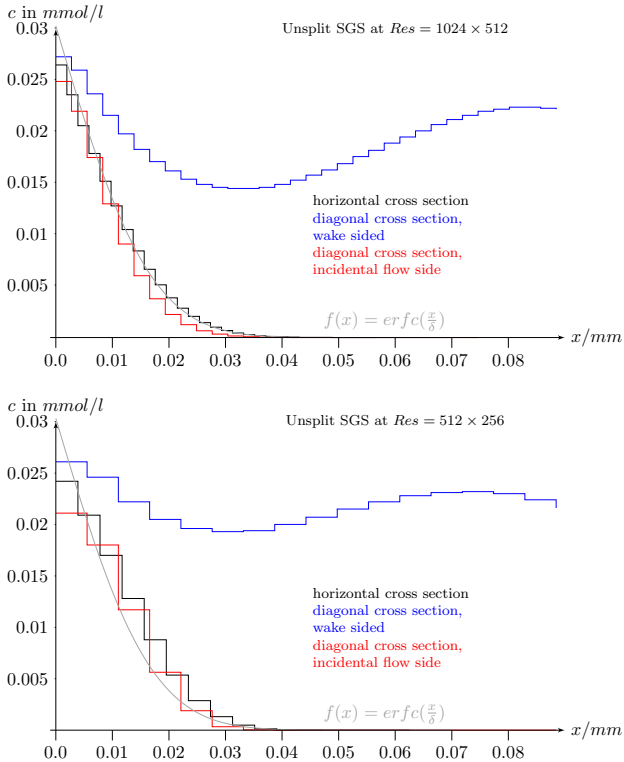

Figure 7: Concentration profiles at different angles; data obtained from simulations with the considered unsplit subgrid-scale approach.

The wake sided region, finally, is less flow and more diffusion dominated. Maximum concentration is already close to the equilibrium value at lower resolution and thus higher resolution will probably not boost this area's transfer contribution. The section though shows how the concentration profile is sharpened in the wake. The profiles at different resolutions indicate the formation of a vortex, cycling species mass from the interface into the wake and back again.

Comparison of Sherwood numbers

For different ranges of Reynolds and Schmidt numbers there is a vast amount of Sherwood correlations available, that predict mass transfer rates from bubbles. Many of those are unfortunately bound to small ranges of *Re* and *Sc* or were derived under limit assumptions as $Sc \to \infty$. We calculated and compared Sherwood numbers for different cases:
First a bubble rising in a Newtonian fluid with a diameter of $1.65mm$ at $Sc = 10$ and $Sc = 100$ with $Re = 19.8$ was considered. The obtained Sherwood numbers are compared to the results of the following correlations

$$Sh = 1 + (1 + 0.546(ReSc)^{2/3})^{3/4}, \qquad (11)$$

which is taken from (Clift *et al.*, 1978) and valid for $Re \to 0$ and arbitrary *Sc* and

$$Sh = 2 + 0.651 \frac{(ReSc)^{1.72}}{1 + (ReSc)^{1.22}} \qquad (12)$$

from (Oellrich *et al.*, 1973), which holds true for $Re \to 0$ and $Sc \to \infty$.
Moreover we did the same for the already mentioned bubble in the Hadamard-Rybczynski flow field, but now compare to the integral Sherwood number calculated by (8). The necessary data were given by the exact solution of the concentration field.
The results of these calculations are compiled in Table 1.

Table 1: Comparison of Sherwood numbers obtained from numerical simulations and theoretical values

Method	$Sc = 10$ $Re = 19.8$	$Sc = 100$ $Re = 19.8$	$Sc = 1000$ $Re = 0.29$
Split SGS	11.82	36.27	14.5
Unsplit SGS	10.8	28.1	13.83
Clift	10.4	29.8	–
Oellrich	11	30.6	–
Exact	–	–	13.40

From these data we can see that the Sherwood numbers in the first cases are in accordance with the correlations, the unsplit mass transfer method giving consistently lower numbers. This is not surprising after the comparison of mass transfer rates in the two dimensional case, done in a preceding section. For higher Schmidt numbers, however, numerically determined Sherwood numbers overpredict to a certain extent the theoretical value obtained from the exact solution.

CONCLUSION

A new unsplit subgrid-scale approach for transport of molar mass across phase boundaries is presented. The method accounts for the property of mass transfer being normal to the interface. It has been compared to older methods at $Sc = 10$ and $Sc = 100$ and an exact solution of a flow and concentration field around a gas bubble with $Sc = 1000$ and showed well overall accordance in local distribution of the

considered species. Furthermore, Sherwood numbers obtained from integral data were also close to the exact value and the results from correlations from the literature. In comparison to the considered dimensionally split method, the unsplit method gives consistently lower mass transfer rates. At fine meshes however, both methods tend to the same limit in the performed computations. The reason for this disparity might be the distance of the interface to a sampling point, at which the unsplit method computes a boundary layer thickness δ. The bigger this distance is, the less accurate are the calulation's predictions about the concentration gradient. As the split method does usually not use information in normal direction to the interface, it can employ values closer to the phase boundary. This effect should then be mainly noticeable in regions with extremely thin boundaries, i.e. the upper half of bubbles. In this case additional techniques to alleviate this problem might prove valuable. Moreover, in a further step the unsplit method can provide additional local information like boundary layer thickness, which are not directly accessible through a split approach.

ACKNOWLEDGEMENT

REFERENCES

ALKE, A., BOTHE, D., KRÖGER, M. and WARNECKE, H.J. (2009). "VOF-based simulation of conjugate mass transfer from freely moving fluid particles". *Computational Methods in Multiphase Flow V*, 157–168.

ALKE, A., BOTHE, D., WEIGAND, B., WEIRICH, D. and WEKING, H. (2010). "Direct numerical simulation of high Schmidt number mass transfer from air bubbles rising in liquids using the Volume-of-Fluid-Method". *Ercoftac Bulletin, special issue "Dispersed Multiphase Flow: From Micro- to Maco-Scale Numerical Modelling"*, **82**, 5 – 10.

ASANO, K. (2006). *Mass Transfer*. Wiley-VCH, Weinheim.

BOTHE, D., KRÖGER, M., ALKE, A. and WARNEKE, H.J. (2010). "A VOF-based Conservative Method for the Simulation of Reactive Mass Transfer from Rising Bubbles". *7th International Conference on Multiphase Flow*. Tampa, Florida.

CLIFT, J., GRACE, M. and WEBER, M. (1978). *Bubbles, Drops, and Particles*. Academic Press, New York.

DARMANA, D., DEEN, N.G. and KUIPERS, J.A.M. (2006). "Detailed 3D Modeling of Mass Transfer Processes in Two-Phase Flows with Dynamic Interfaces". *Chem. Eng. Technol.*, **29(9)**, 1027 – 1033.

DESHPANDE, K.B. and ZIMMERMAN, W.B. (2006). "Simulations of mass transfer limited reaction in a moving droplet to study transport limited characteristics". *Chem. Eng. Sci.*, **61(19)**, 6424 – 6441.

HIRT, C.W. and NICHOLS, B.D. (1981). "Volume of Fluid (VOF) Method for the Dynamics of Free Boundaries". *J. Comp. Phys.*, **39**, 201–225.

LAFAURIE, B., NARDONE, C., SCARDOVELLI, R., ZALESKI, S. and ZANETTI, G. (1994). "Modelling merging and fragmentation in multiphase flows with SURFER". *J. Comp. Phys.*, **113**, 134–147.

OELLRICH, H., SCHMIDT-TRAUB, H. and BRAUER, H. (1973). "Theoretische Berechnung des Stofftransports in der Umgebung einer Einzelblase". *Chem. Eng. Sci.*, **28**, 711 – 721.

RADL, S., TRYGGVASON, G. and KHINAST, J.G. (2007). "Flow and Mass Transfer of Fully Resolved Bubbles in Non-Newtonian Fluids". *AIChE*, **53(7)**, 1861 – 1878.

RIDER, W.J. and KOTHE, D.B. (1997). "Reconstructing volume tracking". *J. Comp. Phys.*, **141**, 141–112.

RIEBER, M. (2004). *Numerische Modelierung der Dynamik freier Grenzflächen in Zweiphasenstömungen*. Ph.D. thesis, Universität Stuttgart.

RIEBER, M. and FROHN, A. (1999). "A numerical study on the mechanism of splashing". *International Journal of Heat and Fluid Flow*, **20(5)**, 455 – 461.

ANALYSIS OF NON-ROUND PARTICULATE MIXING IN A PLOUGH SHARE MIXER USING DEM

Paul W CLEARY[1*]

[1] CSIRO Mathematics, Informatics & Statistics, Private Bag 33 Clayton South, AUSTRALIA

* E-mail: Paul.Cleary@csiro.au

ABSTRACT

A plough share mixer is a machine used for mixing particulate material. It consists of a horizontal cylindrical shell with a central shaft on which are located one or more plough shaped blades. The shaft and attached plough blades are rotated so that the blades impact the bed, digging in and lifting a portion of the bed from a trench in the path of the blade. Depending on the speed, the material can be pushed along the surface (like a bulldozer) or thrown high into the void space above the bed to fall back onto the bed surface some distance away. Each pass of a blade produces an increment of mixing. In this paper, we use the Discrete Element Method (DEM) to predict the mixing performance of a laboratory mixer 25% filled with rice grains. Previous modelling has approximated the particles as spherical, but now a highly accurate representation of the particle shape is used. The effect of particle shape on the flow characteristics and mixing performance of the mixer is assessed for a range of plough rotation rates. In particular, the ability of the blade to pick up and lift particles, the structure of the cloud of ballistic particles generated at higher speed and the shape of the mixing trench are analysed.

Keywords: DEM, mixing, particulates.

INTRODUCTION

Granular mixing is a critically important industrial process, occurring in applications ranging from blending on stockpiles in mineral processing to powder and grain mixing in pharmaceuticals and food processing. Mixing of particles can be performed using a wide variety of different devices. One class of mixers uses mechanical stirring by agitator to generate motion and therefore mixing in a particle bed.

The Discrete Element Method (DEM) is a computational method that allows the particles flows in such equipment to be simulated and the flow patterns and mixing rates to be predicted. DEM, in principle, provides the ability to optimise such equipment by evaluating design changes such as blade speed, the shapes of the blades, the number of blades, their angular off sets from neighbouring blades and the axial blade spacing.

DEM has been used to analyse the flow patterns in laboratory scale mixers of various types, such as V-blenders (Kuo at al. 2002; Lemieux et al., 2007, 2008) and bladed high shear mixers (Stewart et al., 2001a, b; Zhou et al. 2003; Kuo et al., 2004; Bertrand et al., 2005). DEM can and has been used to measure the progress of batch and continuous mixing (see Cleary and Sinnott, 2008) and to assess the effect of operating and equipment design changes on mixing performance.

One common device used at industrial scale is the ploughshare mixer. This has one or more blades attached via radial arms to a central shaft that rotates within the cylindrical mixing vessel. The blade somewhat resembles a chevron bent down the middle with the middle bend being the leading edge of the blade. The quality of mixing in such a device is controlled by the particle flow pattern generated by the motion of the blade(s) passing through the bed of material at the bottom of the mixing chamber.

Here we study mixing in a laboratory scale plough share mixer and consider the effect of particle shape on the flow and mixing performance. This configuration has previously been studied using DEM with rice that was approximated as spherical particles (Cleary et al., 2002; Cleary 2004; Cleary and Sinnott, 2008).

Cleary et al. (1998) showed that particle shape can have a critical impact on the prediction of mixing. In that study, salt cubes in a slowly rotating drum were approximated as spheres which gave too low an angle of repose and too little strength to the bed leading to slumping rather than avalanching. This incorrect prediction of the flow regime lead to errors in the mixing rate that are greater than an order of magnitude. Cleary and Metcalfe (2002) repeated this analysis using super-quadric particles in two dimensions and showed that the correct flow patterns were predicted and that the mixing rates were consistent with the experimental data. Motivated by these considerations, we re-visit the ploughshare mixer to investigate the effect of particle shape on the flow and mixing. The flow patterns are compared to those obtained for spherical particles. Mixing rates are assessed using a measure of local homogeneity and also using the centroids of particle groups based on their initial positions. The mixing performance using spherical and ellipsoidal particles are compared.

MODEL DESCRIPTION

The laboratory scale plough share mixer consists of a horizontal cylindrical shell of diameter 250 mm and length 450 mm. One or more plough blades (shown in Figure 1) are mounted on a shaft of diameter 30 mm located along the centreline of the shell. In this case, a single plough blade stirs a bed consisting of rice particles. The DEM plough share blade and containment vessel were constructed to exactly match the specifications of the laboratory mixer used in PEPT experiments (Laurent et al., 2000).

Previously (Cleary et al., 2002; Cleary 2004; Cleary and Sinnott, 2008) the rice particles were approximated as spherical. Since rice is poorly represented by spheres we now simulate the flow and mixing using super-quadric particles. This shape description is particularly well suited to grains. The rice has length 4-5 mm, super-quadric powers from 2.1 to 3.0 (reflecting their very ellipsoidal nature), intermediate and short axis aspect ratios between 0.4 and 0.5. An example of such a particle is shown in Figure 2. It should be noted that a major advantage of a super-quadric shape is that this is a single mathematical description of the particle (it is not created by gluing or compositing spherical sub-particles).
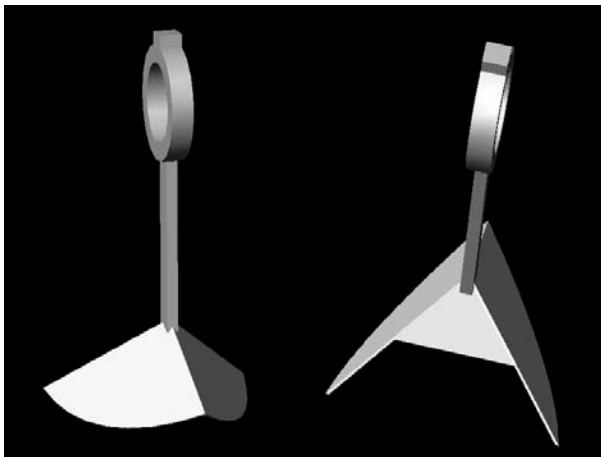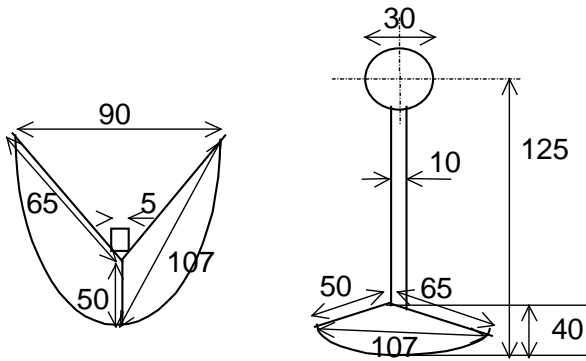
Figure 1: Sketches of the top view and side view of the plough (dimensions in mm) on the left and two views of the CAD model used in the DEM on the right.

The coefficient of restitution used was 0.5 and the friction coefficient was 0.4. A spring stiffness of 1000 N/m is required and gives average overlaps of 0.5% of the diameter. The mixer is filled to 25% by volume giving a bed made up of 280,000 particles and weighing 4.4 kg. This contrasts with around 103,000 particles when they were modelled as spheres. There are many less particles because a sphere occupies much less volume than an ellipsoid with the same length as the sphere radius.

Figure 2: Super-quadric particle with aspect ratios 2:1:1 representing a rice grain.

The particles are coloured according to their initial position, so that we can see the extent and nature of the mixing. In each radial cross section the particles in the left half and right half have different colours. These colours are also different on either side of the blade in the axial direction.

The DEM software used in this work is described in Cleary (2004, 2009). More details about super-quadric shaped particles and of other applications are also contained in these references.

MIXING OF ELLIPSOIDAL PARTICLES AT 4 HZ

Figure 3 shows the mixing in a single blade plough share mixer operated at 4 Hz and using the ellipsoidal rice shaped particles. The particles are coloured according to their initial position, so that we can see the extent and nature of the mixing. In each radial cross section the particles in the left half and right half have different colours. These colours are also different on either side of the blade in the axial direction. The blade starts on the near side of the mixer.

Figure 3a shows the mixer after 0.56 revs when the blade has risen above the initial surface level of the particles. It has pushed and lifted all the material that was in the path of the blade, leaving a clear trench behind the blade that is empty of particles. The particles near the periphery of the lifted mass, under the influence of gravity, are starting to flow down and away from the blade. The part of the bed lifted is very coherent and has a clearly defined free surface. This material is behaving like a deforming solid. There are very few particles splashed about by the impact of the blade with the bed. The motion is best characterised as a high speed bulldozing of the bed rather than as a high speed collision of the blade with individual particles. The very strong convective mixing effect of the blade is clearly visible with substantial amounts of blue and green material pushed from the front of the mixer into the rear. Similarly large amounts of yellow and red material are lifted into the air by the blade.
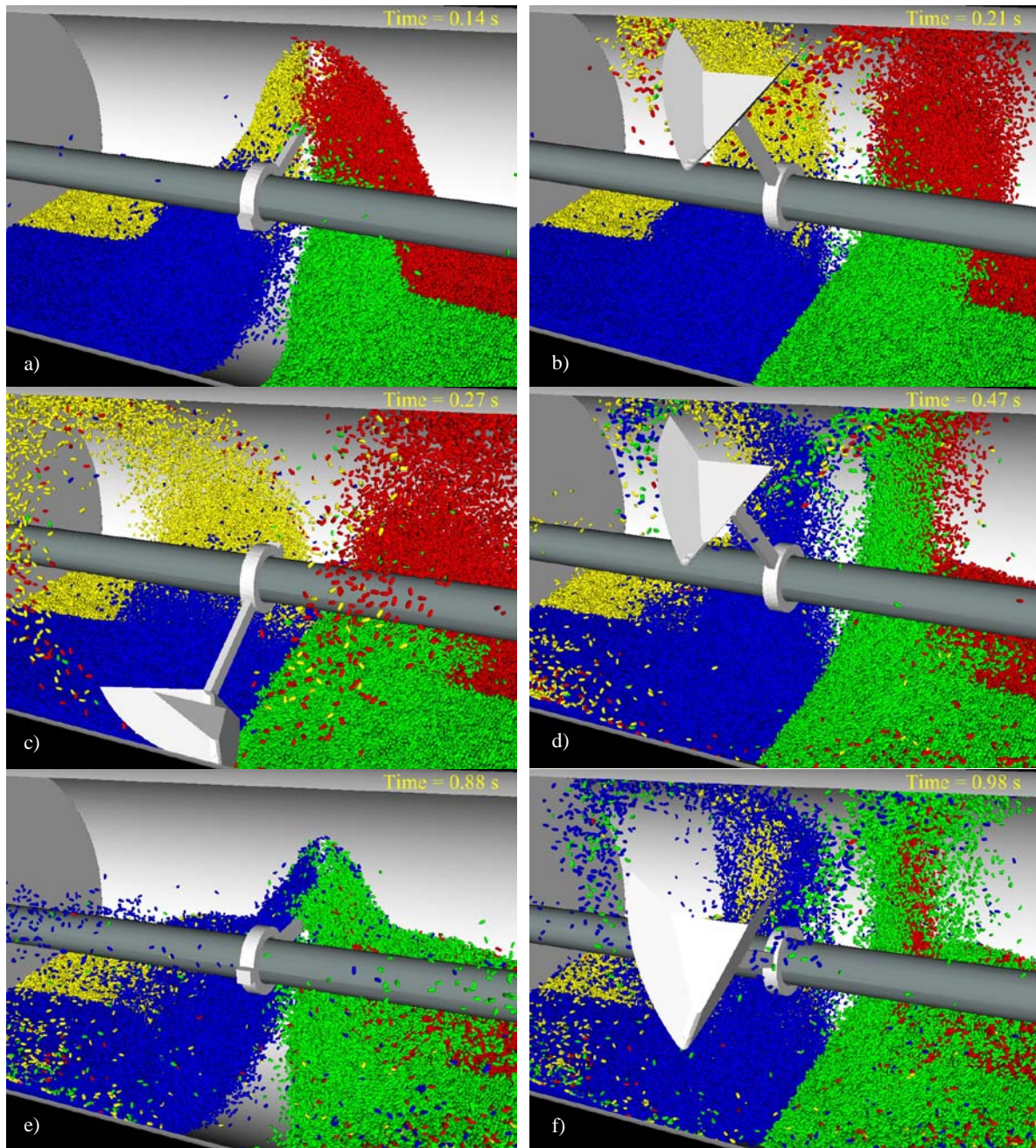
Figure 3: Single blade plough share mixer operating at 4 Hz with ellipsoidal rice particles at; a) 0.56 revs, b) 0.84 revs s, c) 1.08 revs, d) 1.88 revs, e) 3.52 revs and f) 3.92 revs.

In Figure 3b, (at 0.84 revs) the mass of particles that was lifted up have almost entirely lost contact with the blade. The ones closest to the blade maintain contact for the longest period and follow trajectories that are closest to the blade trajectory. Particles that are further away flow earlier from the mass being carried by the blade, tend to have slower velocities and move on trajectories that are lower and with more axial displacement. The band of particles flowing from each side of the blade remains quite coherent with a well defined structure which is wide near the bed and narrowing progressively as one moves above the bed and towards the tip of the blade. This shows that there is significant transport of the different colours to new parts of the mixer space but very little actual mixing between them. The sides of the trench behind the blade

have collapsed and particles have flowed back into the trench partially filling it, but the bed surface level remains lower than the initial bed surface location.

After 1.08 revs (shown in Figure 3c) material from the first blade pass has become much more dilute as the divergent trajectories of the particles cause them to be spread over progressively larger volumes. The leading material which is very close to the blade is sliding on the mixer shell and creates a coherent arc leading back towards the bed at the rear of the mixer. Significant axial displacement has now occurred for most of the ballistic particles. The blade tip is just about to enter the bed for its second revolution. Reasonable variation in the colours of the particles in the forward part of the ballistic bands indicates some mixing has occurred. There is little mixing of the colours in the wider but

slower moving parts of the lifted mass closer to the bed surface.

Figure 3d shows the situation after 1.88 revs. The ballistic material from the first pass of the blade has now fallen onto the surface of the bed at various distances from the plane of the blade passage. There is some modest mixing in the material that has come to rest on the shell at the front of the mixer. The passage of the blade has now lifted a second mass of particles into the air. The structure of the material flow around and from the blade is similar to that of the first pass, but in comparing Figures 3b and d we can observe that there is significantly less material being lifted on the second pass. The lifted bands are much narrower reflecting the much lower bed surface level in the path of the blade after the trench from the first blade pass only partially refills this region with particles. The material in these narrower bands is close to the blade and is thrown on the highest and widest trajectories. The parts of the bands from the first pass that are missing from the second are the slower material furthest from the blade, which falls from the mass much earlier and was less influenced by the blade. The amount of colour variation in the lifted mass is much higher for the second blade pass reflecting the presence of both colours on each side from the stretching of the bed produced by the first blade pass. The structure of the bed around the trench is very similar to the state at the comparable time of the previous blade pass (Figure 3b) indicating that the bed flow back into the trench is similar for each of the blade passes.

Figure 3e shows the flow at 3.88 revs as the blade is starting its fourth pass through the bed. The mass of material to be lifted is just being accelerated by the blade. After a few blade passes the shape of the free surface of the bed stabilizes, with the bed material removed by the blade being balanced by the material flow back along the free surface (which sits at the angle of repose) back into the trench left by the blade. Once this equilibrium is reached then each blade pass has the same effect on the bed and the amount of material lifted, the structure of the lifted bands of particles and their trajectories are the same. Each blade pass then makes an incremental change to the mixing state. The colour variation of material on the bed surface shows that there is already quite good re-distribution of the blue and green material across the top of the bed and that the surface material towards the front of the view is well mixed. This partially disguises a key problem with this mixer, which is the presence of large dead regions to either side of the blade induced trench. This was previously observed for spherical particles (Cleary et al., 2002; Cleary and Sinnott, 2008). Here the rice grain shaped material locks together better and steeper angles of repose mean that the trench is steeper and narrower and that the dead regions are now actually expanded in size.

Figure 3f shows the flow just before 4 revs are complete. The ballistic stream of particles flowing from the blade to the right now contains a good mix of green and red with some blue material. On the other side there is a good mix of blue and yellow material with some green. So in the agitated regions where the blade is able to transport the particles, the mixing is quite fast and works well. This leads to good mixing near the blade path and in surface regions further away, but not in the dead regions to either side.

EFFECT OF SHAPE ON FLOW AND MIXING

Figure 4 shows a comparison of the state of the system after 4 revolutions for plough speeds of 1.0, 2.25 and 4.0 Hz for both spherical particles (left) and ellipsoidal particles (right). The spherical particle solutions are from Cleary et al., (2002).

For a 1 Hz speed, the plough is unable to lift the particles into the air as it did for the 4 Hz speed. Instead it acts like a bulldozer and pushes through the bed moving from front to back. Each pass of the blade pushes particles from the forward side of the bed towards the back. After a couple of revolutions the bed shape reaches equilibrium with two piles visible at the back, one on each side of the plough blade. A trench leads from the front of the shell back towards the piles along the line of the axis of the plough. There is reasonable mixing between the blue and green particles at the back, but little mixing elsewhere. The initial quadrants of the different colour groups are strongly deformed by the bulldozing by the plough but there is little mixing. The mixing of the blue/green material at the back occurs because this material is dragged backwards by the plough, lifted slightly when the blade exits the bed and then falls back onto the surface of the yellow/red particles that were originally at the back.

The piles at the back are higher and the trench has much steeper sides for the ellipsoidal case compared to the spherical one. The depth of the trench is the same, but the angle of the trench is steeper so the shoulders at the edge of the trench are much closer to the plough blade than for the spherical case. This occurs because the spherical particle microstructure is quite weak, with the slope failing by particles rolling over each other leading to a very shallow angle of repose. For the ellipsoidal particles, the rolling mode of failure of the particle slopes is inhibited because they are not free to rotate. In order for the bed to fail, particles must slide over each other. This increases the strength of the bed to resist shear and leads to the much higher observed angle of repose. The increased steepness of the trench has important implications for the mixing performance of this ploughshare mixer, because the influence of the blade extends much less far in the axial directions than it did for the spherical particles. This means that the volume of material that the blade can agitate and therefore mixed is sharply reduced.

For the 2.25 Hz speed, similar differences are observed with the twin piles at the back being higher and more coherent in shape for the non-spherical particles. The trench is again steeper with the shoulders being closer to the plough blade. At this speed the plough is able to pick up material and throw it through the air. The volume of ballistic material thrown into the

air is increased for the ellipsoidal particles. They are also thrown on somewhat higher trajectories. This means that there is a little more material landing on the bed to either side of the plough path which will enhance the mixing. From these flow pictures it is not clear whether the increased mixing from this extra ballistic material will be more or less than the decrease in the mixing due to less particles being pushed by the plough along the narrower trench.

For the 4 Hz plough speed, compared to the predictions using spherical particles we observe that the streams of material lifted and thrown by the blade are more coherent and larger. The greater strength of the non-spherical material allows the blade effect to be felt

further from the blade. So more particles can be lifted and thrown out across the surface of the bed which is positive for mixing. The trench is again more coherent in shape and is longer lived reflecting the stronger bed material which takes longer to fail and flow back into the trench. This does not appear to affect the mixing simply delaying the re-filling of the trench. The sides of the trench are again much steeper which reduces the axial distance from which material can flow back in the trench and therefore increases the size of the dead regions to either side of the plough path. This is a negative for mixing performance arising from the ellipsoidal shape of the particles.
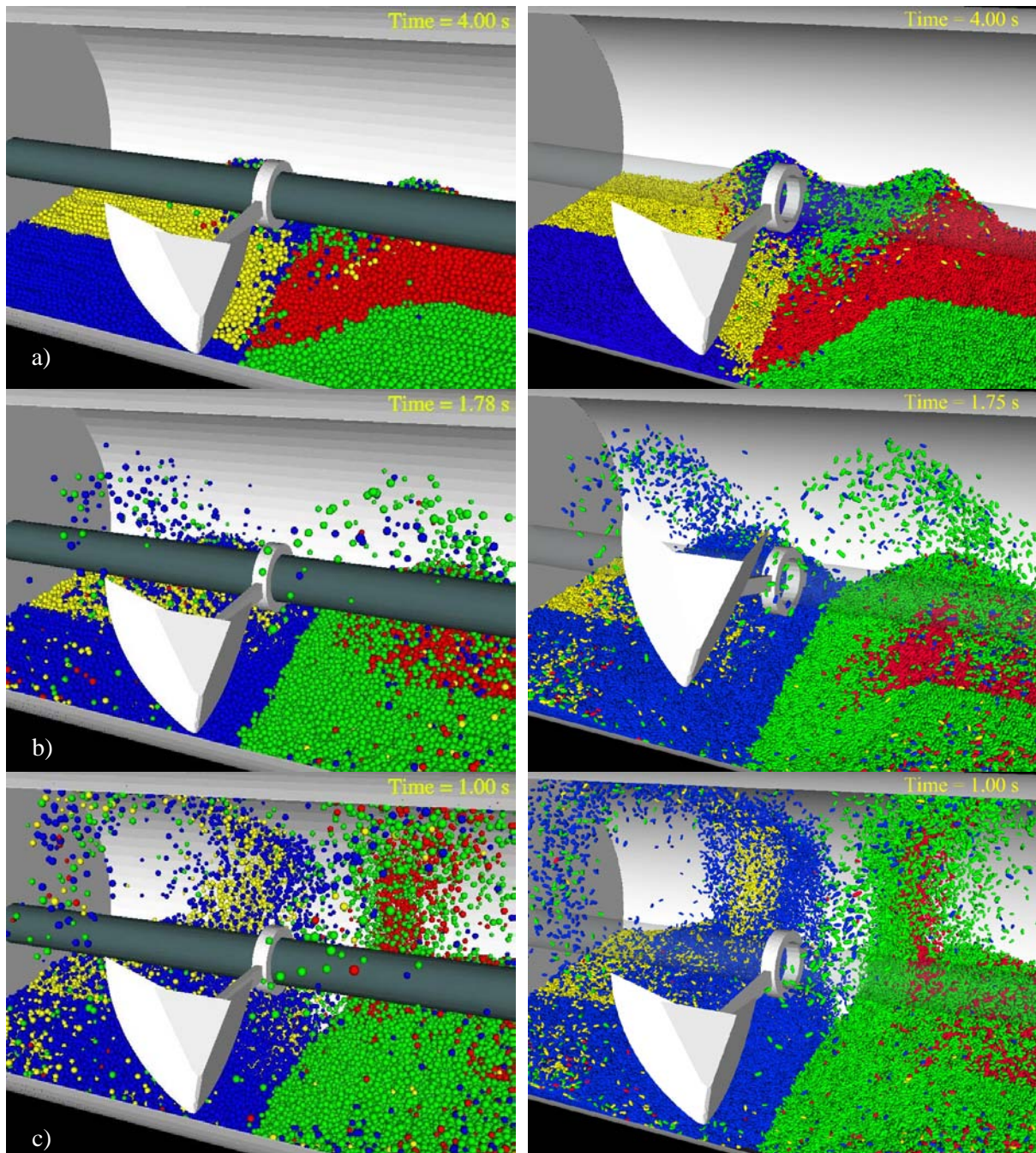
Figure 4: Comparison of the mixing after 4 revolutions between spherical (left column) and ellipsoidal (right column) particles for different speeds, a) 1 Hz, b) 2.25 Hz, and c) 4 Hz.

MIXING IN THE PLOUGH SHARE MIXER

The mixing can be measured in a number of ways. Here we use two methods:

- The distance of the centroids of each of the four colours from the overall center of mass characterises the degree of mixing. Initially, all the particles belonging to each colour are in one of the four quadrants of the mixer chamber. As the particles mix, some cross the blade path in the axial direction or change sides of the mixer in the blade motion direction. This mixing moves the centroid closer to the center of the mixer. The x- and z-components provides measure of radial and axial mixing.

- The homogeneity of the mixture can be measured using a local average of the particle colour index that is calculated at an array of locations in the mixer. The coefficient of variation of the distribution of these local averages also characterises the mixing/segregation state. The fully segregated and perfectly mixed limiting values can be used to normalise this and provide a % segregated measure as a function of time. See Cleary and Sinnott (2008) for details.

The % segregated (using the second measure) is shown for the three rotation rates Figure 5. The mixing rate is given by the rate of reduction in this measure. The results for the spherical particle cases are shown on the left and the ellipsoidal particle results are shown on the right. In all cases the mixing rate is highest early and progressively declines as the bed becomes progressively more mixed. The characteristic shape of these curves is similar for all cases, but there are important differences in the rates. For the spherical particle cases, the 4 Hz speed gives the fastest mixing with the 1 Hz speed producing the worst. After 200 revs the % mixed (which is equal to 1 - % segregated) is about 42%, 36% and 25%, respectively. It is clear that these curves will asymptote to non-zero values which means that there will be significant unmixed material remaining in dead regions at the ends of the mixer. The amount of unmixed material is also strongly rotation rate dependent. Based on the curves in figure 4 one might expect the 4 Hz case to reach a 60-70% mixed state, whilst one would not expect the 1 Hz case to only reach 30% mixed.

For the ellipsoidal cases, the mixing rates are all significantly reduced. The degree of mixing after 100 revolutions is quantified in Table 1. The largest reduction occurs for a speed of 4 Hz with a halving of the amount of mixing produced. The degree of deterioration for the lower speeds is only around 1/3. The best mixing is now obtained for an intermediate speed of 2.25 Hz. This is in contrast to the best mixing occurring for the highest speed when the particles were spherical. For spherical particles there was a reasonably strong increase in mixing with speed. However, for the non-round particles the degree of variation is much reduced so that they only differ by a few percent. The

very low levels of mixing achieved after 100 revolutions indicates that this is a poor mixing design with a chamber that is significantly too long for the plough. The design response is to include multiple blades (see Cleary 2004). DEM predictions on the width of the trench produced by the plough blade can provide critical information on the optimal spacing of these multiple blades.

Table 1: Degree of mixing after 100 revolutions.

Shape	1.0 Hz	2.25 Hz	4.0 Hz
Spherical	22%	30%	32%
Elliptical	15%	18%	16%

In order to understand the reasons for the strong deterioration in mixing for non-round particles we consider the *x* and *z*-components of the relative centroid position for each of the colour groups from the overall center of mass of the bed. The *x*-components for all the cases are shown in Figure 6 while the *z*-components are shown in Figure 7. The *x*-component is an indicator of the radial mixing. It drops rapidly and almost linearly for around 3-6 revolutions and then becomes almost constant. This behaviour is observed for all cases except for the 4 Hz spherical case, which has a much smoother and more gradual change. In the first rapid mixing stage, all the particles that are within the width of the plough influence (essentially the width of the trench) are rapidly mixed. Particles that are outside this distance cannot be mixed and so the radial mixing ceases because the fraction of particles that can be mixed have been mixed while the other are in the dead zones and cannot be mixed.

The z-component of the centroids measures the axial mixing and transport (Figure 7). For the spherical particle cases, the 1 Hz speed produces only very slow axial mixing, while the 2.25 Hz speed produces modest axial mixing. The 4 Hz speed produces much more axial motion. This axial motion is critical since it transports unmixed particles axially from the edges of the dead zones into the central mixing regions where the plough blade passes. So it is the limitation of the axial transport of unmixed particles that causes the second stage of very slow radial mixing (see in Figure 6). The radial mixing itself is inherently rapid, but to achieve radial mixing of dead region material it must be first transported into the central mixing zone – which is very slow.

For the ellipsoidal particles we can see that the rate of axial transport is significantly reduced. The early action of the plough pushes and throws material further from the plough axis so the centroids initially move further away from the center of the mixer. Then as the bed at the edges of the bed slowly fails there is a creeping type axial flow with a small number of particles moving towards and into the central trench with each blade pass. So it is the sharp deterioration of the axial transport that causes the strong reductions in the observed axial mixing (in Figure 6) and the overall strong reductions in the overall homogeneity of the mixture (Figure 5 and Table 1).
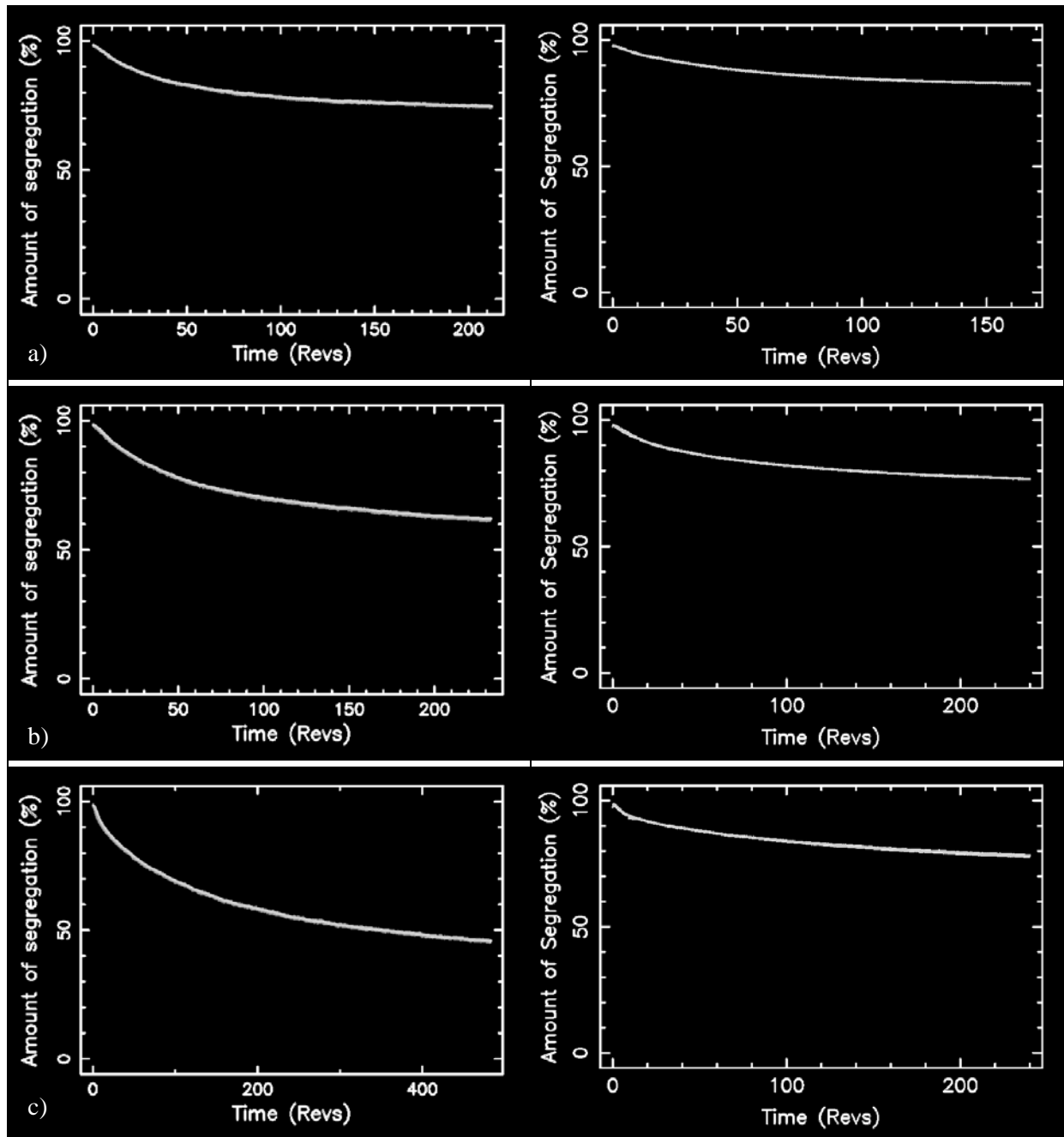
Figure 5: Progress of mixing for spherical (left column) and ellipsoidal (right column) particles for different speeds, a) 1 Hz, b) 2.25 Hz, and c) 4 Hz.

CONCLUSION

The mixing performance of a laboratory scale ploughshare mixer and its variation with particle shape has been investigated using DEM for a range of plough speeds. The key effects of the particles being non-round are:

- The central trench becomes narrower and steeper due to the higher angle of repose arising from the increased strength of the ellipsoidal material. This reduces the amount of material that the plough can agitate and mix.

- Particles are picked up more efficiently by the moving blade so that the ballistic streams are larger and more coherent.

- But ballistic material is thrown less far axially.

Mixing is poor in all cases with significant dead zones that cannot be mixed on either side of a narrow central mixing zone. For the ellipsoidal particles the best mixing per revolution was obtained for 2.25 Hz. It is slightly slower for 4 Hz and much slower for 1 Hz. However the amount of variation with speed was relatively small. This is quite different to what was observed for spherical particles where there was a fairly strong dependence on speed and the degree of mixing increased with speed. A comparison of mixing of spherical particles and rice shaped grains after 100 plough revolutions indicates:

- Mixing is significantly slower for particles with realistic shape

- Non-round shaped particles are less mobile during flow and so cannot mix as quickly.

- The size of the mixing zone is strongly reduced by the much steeper slope of the sides of the trench in the mixing zone.

- Idealising particles as spherical can lead to errors of up to 100% over-prediction of the mixing speed.

The radial mixing is quite fast and efficient, but the blade can only mix particles that are within the central mixing zone. The overall rate of mixing is then governed by the rate of axial transport of particles from the edges of the dead zones into the central mixing zones. For spherical particles the rate of transport is fairly slow but increases strongly with plough speed. This is the reason for the reasonably strong variation in overall mixing performance for higher speeds. However, for non-round particles, the axial transport into the central mixing zone is almost completely eliminated. This arises from the much stronger bed microstructure of the non-round particles. The significant reduction in the axial transport of non-round particles is the primary factor in the sharp reduction in their mixing rates compared to spherical particles.
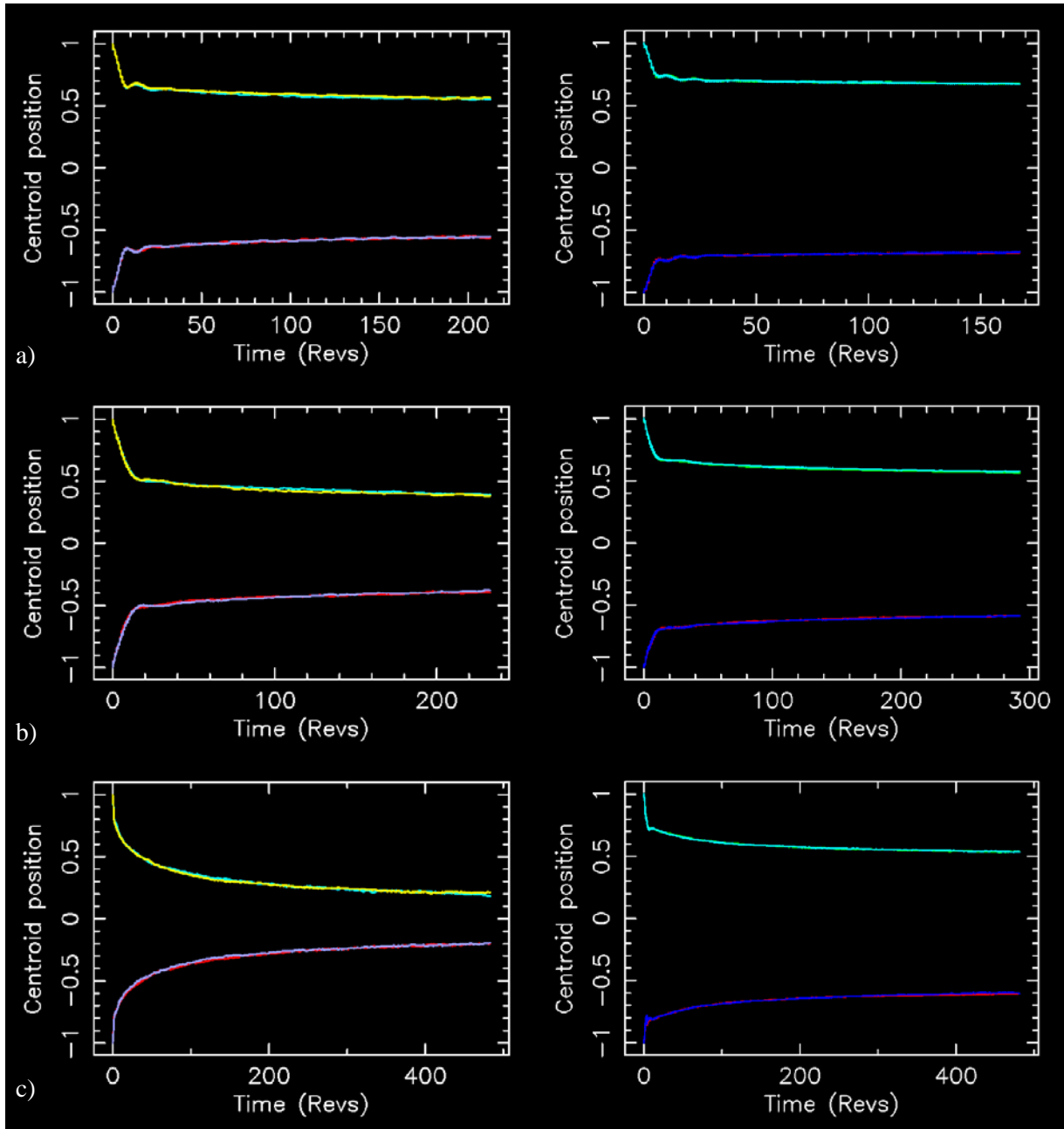
Figure 6: X-component of the centroid location of each colour group showing radial mixing for spherical (left column) and ellipsoidal (right column) particles for different speeds, a) 1 Hz, b) 2.25 Hz, and c) 4 Hz. Each of the four colours represents one of the 4 separately coloured domains. Since the configuration is symmetric only two curves are visible with the other two overlaying the first pair.
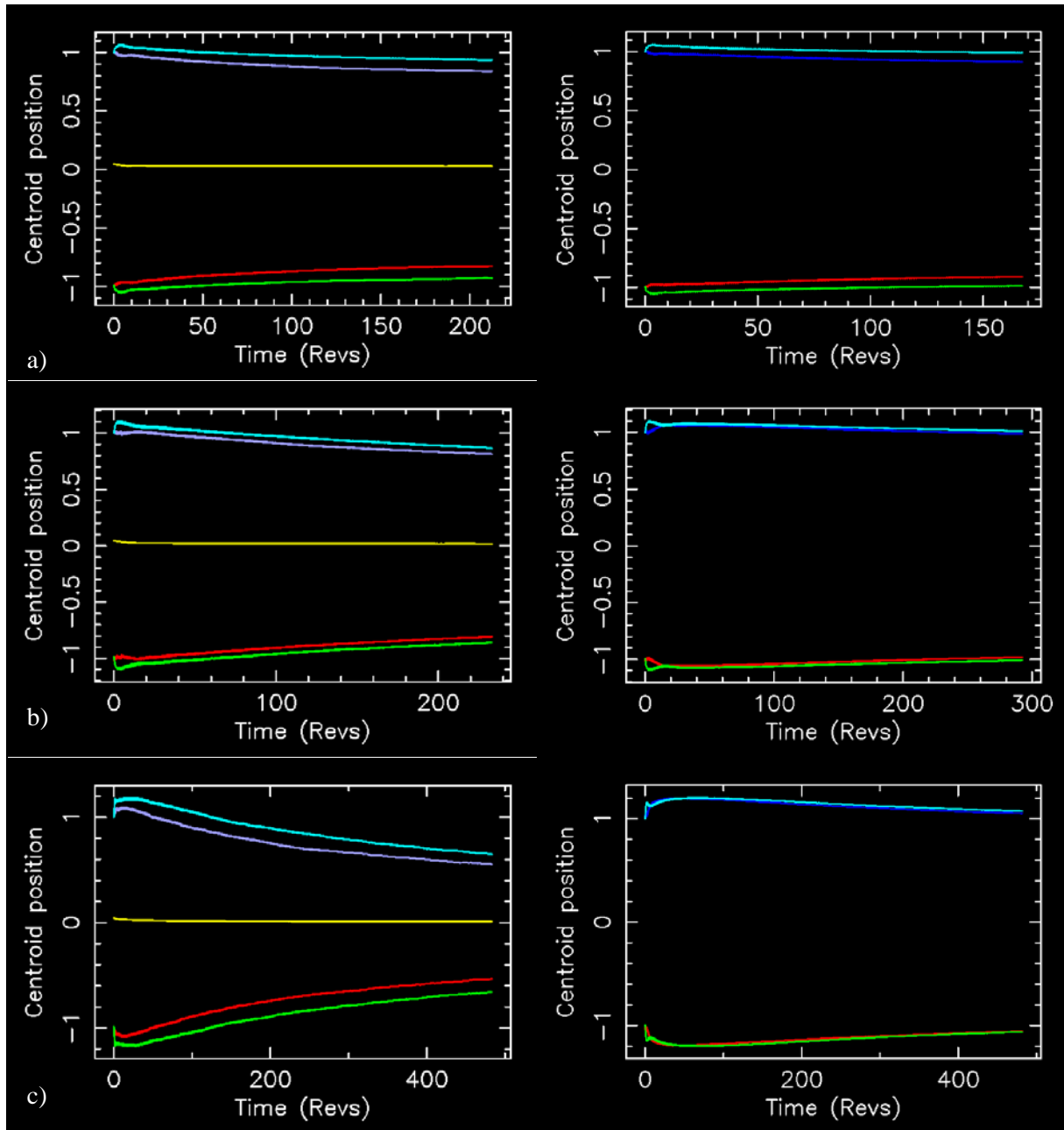
Figure 7: Z-component of the centroid location of each colour group showing axial mixing for spherical (left column) and ellipsoidal (right column) particles for different speeds, a) 1 Hz, b) 2.25 Hz, and c) 4 Hz. Each of the four colours represents one of the 4 separately coloured domains. The yellow curve shown in the spherical case is the overall center of mass of the bed.

REFERENCES

BERTRAND, F., LECLAIRE, L. A., and LEVECQUE, G. (2005), "DEM based models for the mixing of granular materials", Chem. Eng. Sci., 60, 2517-2531.

CLEARY, P.W., METCALFE, G. and LIFFMAN, K. (1998), "How well do discrete element granular flow models capture the essentials of mixing processes?", Applied Mathematical Modelling, 22, 995-1008.

CLEARY, P.W. and SAWLEY, M. (2002), "DEM modelling of industrial granular flows: 3D case studies and the effect of particle shape on hopper discharge", Applied Mathematical Modelling, 26, 89-111.

CLEARY, P.W. and METCALFE, G. (2002), "Quantitative comparison of mixing rates between DEM and experiment in a slowly rotating cylinder", Proc. World Congress of Particle Technology 4, 21-25 July, Sydney, CD paper 550.

CLEARY, P. W., LAURENT, B., and BRIDGEWATER, J., (2002), "DEM prediction of flow patterns and mixing rates in a ploughshare mixer", Proc. World Congress of Particle Technology 4, 21-25 July, CD paper 715.

CLEARY, P.W. (2004), "Large scale industrial DEM modelling", Engineering Computations, 21, 169-204.

CLEARY, P.W., and SINNOTT, M.D., (2008), "Assessing mixing characteristics of particle mixing and granulation devices", Particuology, 6, 419-444.

CLEARY, P. W., (2009), "Industrial particle flow modelling using DEM", Engineering Computations, 26(6), 698-743.

KUO, H.P., KNIGHT, P.C., PARKER, D.J., TSUJI, Y., ADAMS, M.J. and SEVILLE, J.P.K. (2002), "The influence of DEM simulation parameters on the particle behaviour in a V-mixer", Chemical Engineering Science 57, 3621-3638.

KUO, H.P., KNIGHT, P.C., PARKER, D.J., ADAMS, M.J. and SEVILLE, J.P.K. (2004), "Discrete element simulations of a high-shear mixer", Adv. Powder Tech. 15, 297-309.

LAURENT, B.F.C., BRIDGWATER J., and PARKER, D. J., (2000), "Motion in a particle bed stirred by a single blade", AIChE J. 46, 1723-1734.

LEMIEUX, M, BERTRAND, F., CHAOUKI, J. and GOSSELIN, P. (2007), "Comparative study of the mixing of free-flowing particles in a V-blender and a bin-blender", Chem. Eng. Sci. 62, 1783-1802.

LEMIEUX, M., LEONARD, G., DOUCET, J., LECLAIRE, L.A., VIENS, F., CHAOUKI, J. and BERTRAND, F. (2008), "Large-scale numerical investigation of solids mixing in a V-blender using the discrete element method", Powder Tech. 181, 205-216.

STEWART, R.L., BRIDGEWATER, J., ZHOU, Y.C. and YU, A.B. (2001b), "Simulated and measured flow of granules in a bladed mixer – a detailed comparison", Chemical Engineering Science 56, 5457-5471.

STEWART, R.L., BRIDGEWATER, J. and PARKER, D.J., (2001a), "Granular Flow over a flat-bladed stirrer", Chemical Engineering Science 56, 4257-4271.

ZHOU, Y.C., YU, A.B. and BRIDGEWATER, J., (2003), "Segregation of binary mixture of particles in a bladed mixer", J. Chem. Tech. and Biotech. 78, 187-193.

8th International Conference on CFD in Oil & Gas, Metallurgical and Process Industries
SINTEF/NTNU, Trondheim Norway
21-23 June 2011

CFD11-165

THREE DIMENSIONAL COUPLED DISCRETE ELEMENT-CFD MODELLING OF HIGH SPEED GAS-PARTICLE RACEWAY DYNAMICS

James E. Hilton[1] , Paul W. Cleary[1]*

[1] CSIRO Mathematics, Informatics & Statistics,

Private Bag 33 Clayton South, AUSTRALIA

* E-mail: james.hilton@csiro.au

ABSTRACT

The lateral injection of gas into a packed bed of particles can cause the formation of a vortical structure, or raceway, within the bed. This is characterised by an approximately elliptical region of high voidage around the injection site containing particles entrained by the gas driven around the base of the ellipse and falling back under gravity. This distinctive rapid circular motion gives the raceway its name. We computationally investigate this system using a coupled Discrete Element Model and pressure-gradient-force Navier-Stokes solution method. We show that raceway formation and stability are highly sensitive to inflow velocity and to particle shape, giving both an improved understanding of the fluid-gas flow interaction, as well as design optimisation strategies for specific industrial applications.

Keywords: DEM, Finite volume, particle injection, gas-particle dynamics

NOMENCLATURE

Greek Symbols

ε	voidage fraction
η	total viscosity
η_g	gas viscosity
η_t	turbulent viscosity
μ	particle friction
ρ_f	gas density
ρ_p	particle density
ρ_b	bulk particle density = $(1-\varepsilon)\rho_p$
τ	stress tensor
χ	empirical pressure correction factor
ω	particle spin vector

Latin Symbols

|	
A'	particle projected cross sectional area
C	particle damping coefficient
C_D	particle drag coefficient
d	particle diameter
$\mathbf{F}$	particle force
$\mathbf{f}$	particle to gas coupling body force
$\mathbf{g}$	gravitational acceleration
I	particle moment of inertia
k	particle spring constant
m	particle mass
p	pressure
r	particle radius
$\mathbf{S}$	rate of strain tensor
$\mathbf{S}_D$	square of rate of strain tensor
$\mathbf{T}$	particle torque
$\mathbf{u}$	interstitial gas velocity
$\mathbf{u}'$	superficial gas velocity
$\mathbf{v}$	particle velocity
V	particle volume
$\delta\mathbf{x}$	particle overlap

INTRODUCTION

Lateral high speed gas injection into a bed of packed particles has numerous industrial applications, such as catalyst regeneration in cross-flow reactors and combustion in blast furnaces. Of these, the blast furnace is, by far, the most commercially important application. Blast furnaces are predominantly used for pig iron smelting as a step in the steel making process. Around 50% of the 1.4 billion tons of steel produced in 2010 (U. S. Geological Survey, 2011) came from the smelting of 2.3 billion tons of iron ore in blast furnaces. This massive commercial scale has led to interest in the granular processes occurring within the furnace.

Gathering data within a blast furnace is a difficult challenge due to the very high operating temperatures and pressures. This is especially problematic around the blast area, where pre-heated air is injected into the base of the furnace through water-cooled copper tuyeres at pressures up to 4 bar. Temperatures within this region, called the bosh, range up 2200 degrees. A recent development has been the introduction of pulverised coal into the blast to reduce the coke consumption, and hence cost of operation (Mathieson *et al.*, 2005). The injection of hot blast into the particle bed within this region causes the formation of a raceway. A schematic diagram of the raceway and bosh in a blast furnace is shown in Fig. 1. The structure of this raceway is critical for stable operation as it distributes the hot gases required for the reduction reactions in the upper part of the furnace. The raceway is divided into several zones, including the physical void space adjacent to the tuyere, a surrounding region of circulating particles and a compact region beneath the raceway, called the "bird's nest". Raceway properties have been experimentally measured using methods such microwave reflection (Matsui *et al.*, 2005), and using samplers threaded through the tuyeres in a stopped furnace (Chung *et al.*, 1996).

The limited ability to collect data, as well as the difficulties associated with scale-up of experimental scale models, make computational simulations invaluable for understanding the dynamics within the raceway region. There

are several computational studies in the literature, which can be divided into two classes.
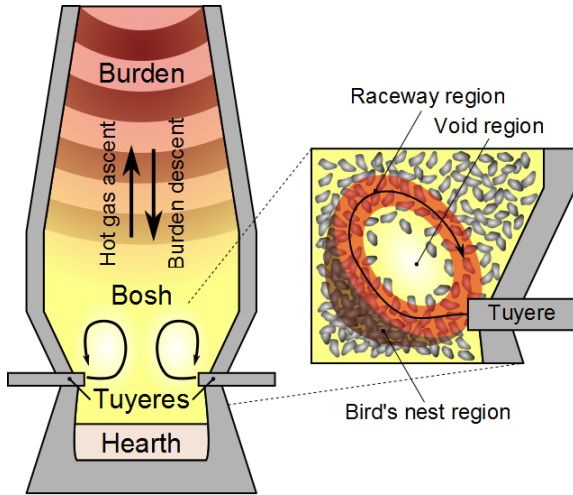
Figure 1: Left: schematic diagram of raceway formation within blast furnace. Scale of raceway has been enlarged for clarity. Right: regions within raceway zone.

The first class assumes a fixed raceway geometry, mainly based on measurements taken from pilot scale experimental models. One of the earliest models of this type was presented by McCarthy *et al.* (1983) based on pilot scale raceway geometries determined by Nakamura *et al.* (1977). The raceway used in the study was assumed to be an ellipse with a vertical long axis, with the tuyere located parallel to the base of the ellipse. The Navier-Stokes equations for gas flow in a porous bed were solved over a two dimensional domain containing the raceway geometry using a marker and cell method. The pressure gradient on the bed from the particles was calculated using the Ergun expression (Ergun, 1952), and turbulent terms were included using an effective viscosity formulation. Good matches to the experimental pressures from Nakamura's study were reported. A similar approach was used by Sugiyama *et al.* (1993). A much more recent study was undertaken by Shen *et al.* (2011), using a 'balloon' shaped raceway, based on previous raceway formation studies. The overall simulation approach was similar to that used by McCarthy *et al.*, where the raceway was assumed to be an empty zone surrounded by a porous region. A quasi-2D simulation domain was used, with a realistic tuyere model. The pressure gradient on the bed from the particles was calculated from the Ergun equation, although a different turbulence model, the eddy dissipation model, was used. A notable inclusion was the use of a one-way coupled tracer method to track the motion of pulverised coal particles injected into the gas stream, although the simulations did not take into account interactions between these coal particles.

The second class of method directly predicts the raceway geometry using coupled gas-solid methods. This is more difficult to simulate and fewer studies of this type have been carried out. Xu *et al.* (2000) carried out simulation of this type in a two dimensional bed using a coupled discrete element and gas model. Raceway formation was observed, but no sensitivity analysis of raceway form to gas injection velocity was undertaken. Vertical fluidisation was also reported in the bed at high gas velocities, which has not been reported elsewhere. A turbulence model was not used in the study. An in-depth model using a multiphase continuum gas-particle approach was carried out by Mondal *et al.* (2005). The multiphase constitutive relations for the granular material and gas were extended to take turbulence in the gas phase into account, which was incorporated using a k-$\bullet$ model. Realistic geometry was used for the domain of analysis, which was taken as a two dimensional slice across a blast furnace. The

size of the raceway was found to be proportional to the inflow velocity, and to the initial bed porosity. The raceway dimensions were found to be related to the fill height of the bed, suggesting pressure from the bed above can inhibit raceway formation. Coupled computational models based on a coupled DEM and Navier Stokes formulation are also presented by Umekage *et al.* (2005) and Yuu *et al.* (2005). The model presented by Umekage *et al.* (2005) shows good agreement with experimental data given by Matsui *et al.* (2005). A coupled model is also presented by Nouchi *et al.* (2005), which is used to investigate the stress distribution and abrasion of coke particles within the burden.

This study is of the second type using a coupled gas-solid method in three dimensions, with a LES based turbulence model. We explore the influence of gas inflow velocity and particle shape on raceway formation. Computational studies to date have only assumed a spherical particle shape for the burden, which is a major over-simplification. Coke consists of flat, angular particles and the iron ore can only be considered spherical if it is in pellet form, rather than sinter or lumps. We show that the shape of the particles plays a crucial role in bed dynamics in and around the raceway zone.

COMPUTATIONAL FORMULATION

Discrete Element Method

The Discrete Element Model (DEM) is a Lagrangian computational model for granular dynamics, first formulated by Cundall and Strack (1979). The positions and velocities of every particle in the system are updated at each time step according to a set of force relations. These include a collisional force, $\mathbf{F}_c$, determined from the overlap between neighbouring particles using a linear spring, dashpot and slider approximation. This force is the sum of a normal force $\mathbf{F}_n$ and a tangential force $\mathbf{F}_t$. The normal force is determined from the particle overlap $\bullet x$ and relative normal velocity $\mathbf{v}_n$:

$$\mathbf{F}_N = -k_n \delta x + C_n \mathbf{v}_n \qquad (1)$$

where k_n is the spring stiffness, which determines the maximum particle overlap (set to ~0.1% of the particle diameter) and C_n the normal damping coefficient, which gives the required coefficient of restitution. The tangential force is determined from a Coulomb friction limit and the relative surface tangential velocity $\mathbf{v}_t$:

$$\mathbf{F}_t = \min\left\{\mu\mathbf{F}_n, k_t \int \mathbf{v}_t dt + C_t \mathbf{v}_t\right\} \qquad (2)$$

where μ is the coefficient of friction, k_t the tangential spring stiffness and C_t the tangential damping coefficient. The linear and angular acceleration for each particle is numerically integrated to give the particle velocity and spin at each time step. These relations, for a particle i, are given as:

$$m_i \frac{\partial \mathbf{v}_i}{\partial t} = \mathbf{F}_{ci} + \mathbf{F}_D + \mathbf{F}_P + m_i g \qquad (3)$$

$$I_i \frac{\partial \bullet_i}{\partial t} = \mathbf{T}_{ci} + \mathbf{T}_D \qquad (4)$$

where m is the particle mass, $\mathbf{F}_D$ is the drag force from the gas on the particle and $\mathbf{F}_P$ the gas pressure gradient over the particle. These are given in the next section. The moment balance gives the rate of change of spin, $\bullet$, for a particle with moment of inertia I experiencing a rotational collisional force $\mathbf{T}_C$ and Stokesian rotational drag $\mathbf{T}_D$, which is also given in the next section.

The DEM method in this study uses a super-quadric formulation with a variable aspect ratio for the particle shape. This gives a wide, flexible, range of shapes which can be used to match physical particles. The range of particle shapes used

in this study is shown in Fig. 2. The particle cubicity is controlled using a shape parameter q, which gives shapes ranging from a sphere ($q = 2$) to a cube ($q \to \infty$). The particle semi-major axes, r_x, r_y and r_z can also be specified, so prolate and oblate shapes can also be simulated. DEM using non-spherical particles has been applied to a wide range of granular problems, and has been shown to strongly influence behaviour in several key industrial processes (Cleary, 2004, 2009).
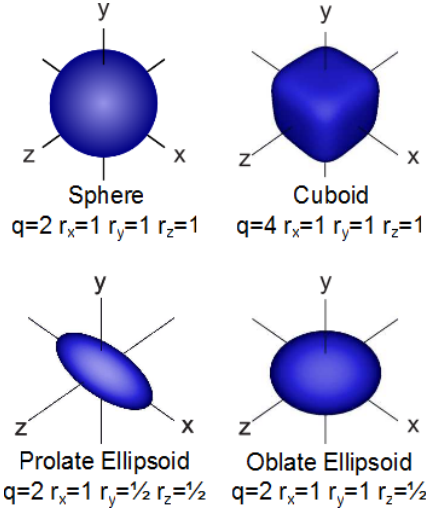
Figure 2: Super-quadric shape forms used in study, with cubicity parameter q and radii r_x, r_y and r_z.

CFD Formulation

We use the Navier-Stokes equations for gas phase through the bed with a wall-adapting local eddy-viscosity (WALE) turbulence formulation. The constitutive equations for gas flow model through a porous bed were derived by Anderson and Jackson (1967), and are given by Kafui (2002) in a 'pressure gradient force' form as:

$$\frac{\partial(\varepsilon \rho_G)}{\partial t} + \nabla \cdot (\varepsilon \rho_G \mathbf{u}) = 0 \qquad (5)$$

$$\frac{\partial(\varepsilon \rho_g \mathbf{u})}{\partial t} + \nabla \cdot (\varepsilon \rho_g \mathbf{u}\mathbf{u}) =$$
$$- \varepsilon \nabla p + \nabla \cdot (\varepsilon \bullet) - \mathbf{f}_{gp} + \varepsilon \rho_g \mathbf{g} \qquad (6)$$

where $\bullet$ is the bed porosity, $\bullet_g$ is the gas density, $\mathbf{u}$ the interstitial gas velocity, $\bullet$ is the stress tensor and $\mathbf{f}_{gp}$ is the force on the gas from the particles. These can be reformulated for the superficial gas velocity, $\mathbf{u}' = \bullet\mathbf{u}$, and assuming the gas density is constant. This gives a set of constitutive relations which can be used with incompressible flow methods, which are much less computationally expensive. Incompressible flow methods give a good flow approximation up to Mach numbers of around 0.3, which is around the maximum value in the systems under consideration here. The set of constitutive relations become:

$$\frac{\partial \varepsilon}{\partial t} + \nabla \cdot \mathbf{u}' = 0 \qquad (7)$$

$$\frac{\partial \mathbf{u}'}{\partial t} + \frac{1}{\varepsilon}(\mathbf{u}' \cdot \nabla)\mathbf{u}' + \mathbf{u}' \nabla \cdot \left(\frac{\mathbf{u}'}{\varepsilon}\right) =$$
$$- \frac{\varepsilon \nabla p}{\rho_g} - \frac{\nabla \cdot (\varepsilon \bullet')}{\rho_g} - \frac{\mathbf{f}_{gp}}{\rho_g} + \varepsilon \mathbf{g} \qquad (8)$$

where $\bullet'$ is the local stress tensor for the superficial velocity, given by:

$$\bullet' = -\eta \left(\nabla \frac{\mathbf{u}'}{\varepsilon} + \nabla \frac{\mathbf{u}'^T}{\varepsilon} \right) \qquad (9)$$

and $\bullet$ is the gas viscosity. The solution is integrated in time using a variation of the pressure correction method with Eq. (7) as a source term (Hilton *et al.*, 2010).

Turbulence is a key component of the model, as gas is injected into the bed at speeds of up to 120 m/s. We use a wall-adapting LES turbulence model called the WALE model. Most LES formulations require the distance to the nearest wall to be calculated and additional steps to be taken to give the correct turbulent viscosity scaling. The WALE model has the great advantage over other LES models that it gives the correct near-wall scaling without the need for any additional procedures (Nicoud and Ducros, 1999). LES type models calculate an addition viscous component, such that $\bullet = \bullet_g + \bullet_t$, where $\bullet_g$ is the gas viscosity and $\bullet_t$ is an addition turbulent viscous term. This additional viscous term is given by:

$$\eta_t = (C_W h)^2 \frac{(\mathbf{S}_D^2)^{\frac{3}{2}}}{(\mathbf{S}^2)^{\frac{5}{2}} + (\mathbf{S}_D^2)^{\frac{5}{4}}} \qquad (10)$$

where C_W is the WALE turbulence constant, set to 0.325 in our simulations, which is the default value used in the commercial code FLUENT, found to give good results over a wide range of flow types. The filter width, h, is set to the grid resolution. The tensors $\mathbf{S}$ and $\mathbf{S}_D$ are the strain rate tensor and the traceless symmetric part of the square of the strain rate tensor, respectively. These are given by:

$$\mathbf{S} = \frac{1}{2}\left(\nabla \frac{\mathbf{u}'}{\varepsilon} + \nabla \frac{\mathbf{u}'^T}{\varepsilon} \right) \qquad (11)$$

$$\mathbf{S}_D = \frac{1}{2}\left(\left[\nabla \frac{\mathbf{u}'}{\varepsilon}\right]^2 + \left[\nabla \frac{\mathbf{u}'^T}{\varepsilon}\right]^2 \right) - \frac{1}{3}\bullet\left[\nabla \frac{\mathbf{u}'}{\varepsilon}\right]^2 \qquad (12)$$

where $\bullet$ is the identity tensor. The WALE model has been shown to give very good results, conforming well to DNS simulations, for a range of standard test flow types including cylindrical pipe flow (Nicoud and Ducros, 1999) and flow past a wall mounted cube (Weickert *et al.*, 2010).

DEM and CFD coupling

The gas drag is the dominant coupling force in the system and other gas-particle forces, such as the Saffman (shear) lift force, the Magnus (rotational) lift force and Basset (gas acceleration) force, are considered small enough to be neglected. The drag force is given by:

$$\mathbf{F}_D = \tfrac{1}{2} C_D A' \rho_g |\mathbf{u}'|^2 \varepsilon^{-\chi} \mathbf{u}' \qquad (13)$$

where C_D is the drag coefficient, A' is the projected area of the particle incident to the gas velocity vector and $\bullet$ is a correction from Di Felice (1994) for the drag in multi-particle systems, given by:

$$\chi = 3.7 - 0.65 e^{-0.5(1.5 - \log \mathrm{Re})^2} \qquad (14)$$

The drag coefficient for particles of varying sphericity was taken from Holzer and Sommerfeld (2008), based on correlations to experimental data:

$$C_D = \frac{8}{\mathrm{Re}}\left(\frac{1}{\sqrt{\Phi'}} + \frac{2}{\sqrt{\Phi}} \right) + \frac{3}{\mathrm{Re}\sqrt{\Phi^{0.75}}}$$
$$+ \frac{1}{\Phi'} 0.42 \times 10^{0.4(-\log\Phi)^{0.2}} \qquad (15)$$

where the particle Reynolds number for a particle of diameter d is $Re = d \cdot_g | \mathbf{u}'|/\cdot$. The regular sphericity, $\cdot$, is the ratio between the surface area of the volume equivalent sphere and the surface area of the considered particle. The crosswise sphericity, $\cdot \cdot$, is the ratio between the cross-sectional area of the volume equivalent sphere, A, and the projected cross-sectional area of the considered particle perpendicular to the flow, A' giving $\cdot \cdot = A / A'$. The particles also have a Stokesian rotational drag, given by:

$$\mathbf{T}_D = \pi\eta d \cdot_r \qquad (16)$$

where the relative spin $\cdot_r = 0.5 (\nabla \times \mathbf{u}') - \cdot_p$ and $\cdot_p$ is the particle spin. The body force from the gas on the particles is given by:

$$\mathbf{f}_{gp} = \frac{1}{V}\sum_{i=i}^{n}\tfrac{1}{2}C_D A'_i \rho_g \varepsilon^{-(2-\chi)}|\mathbf{u}'-\mathbf{v}_i|^2(\mathbf{u}'-\mathbf{v}_i) \quad (17)$$

where n is the number of particles in the cell volume V.

The computational model accounts for the shape of the particle by calculating the projected area of each particle to the incident flow vector at each time step. This is carried out by calculating the visible rim of the super-quadric in the direction of the flow, projecting the rim onto a surface orthogonal to the flow and calculating the discretised polygonal area of this projection. The correct calculation of porosity is also essential for the correct dynamics within the bed (Hilton *et al.* 2010). The porosity in the simulations is calculated using a recursive octree approach, where each computational grid cell is recursively broken to match the surface of the super-quadric particle. The sum of the sub-cells within the super-quadric is used to calculate the volume fraction within the cell. The minimum sub-cell volume is 0.024% of the cell volume, and a further approximation to the form of the surface within the sub-cell is used to refine this volume calculation even further.

The gas flow equations are discretised onto a Cartesian grid, with velocity and forces defined on cell vertices and pressure, turbulent viscosity and voidage defined at cell centres. Finite difference stencils are used for the upwind terms, and incompressibility is enforced using a variation of the pressure correction method. Time integration is carried out using a second-order Runge-Kutta method. This model, without the turbulence component, has previously been applied to a wide range of gas-particle flows (Hilton *et al.* 2010, 2011, Delaney *et al.* 2011).

MODEL SET-UP

For the raceway model we simulated lateral gas injection into a rectangular bed of particles. This is a simplification of the complex geometry of a real blast furnace, but was chosen as we are concerned with only the influence of particle shape and inflow velocity, rather than the configuration of the enclosing geometry. Two types of geometry configurations were used in the simulations. The first was a three-dimensional box, as shown in Fig. *3*. The second was a slice across the bed with periodic boundary conditions in the z-direction, as shown in Fig. *4*. As we were only concerned with investigating the raceway dynamics, the system was considered cold and no heat model was used.

The domains were filled by creating a set of particles over a regular grid at the top of the domain and letting the particles freely fall under gravity. For simulations using non-round particles an additional random orientation was applied to the particles at the creation stage. Gas was injected into the particle beds through a square inflow at the base of the lower side wall of the domain. To match the flow conditions in an industrial blast furnace, and to ensure pressure balance within the domain, an outflow spanning the top of the domain was applied with a mass flux equal to the inflow. The gas injection was simulated using an inflow of square cross-section 7.5 ×

7.5 cm, located 17.5 cm from the base of the bed. A plug velocity profile was used over the inflow. Inflow speeds of 60 to 120 m/s were used in the simulations, matching the speed of real blast furnace inflows.

Table **1**: Simulation parameters for gas and particles

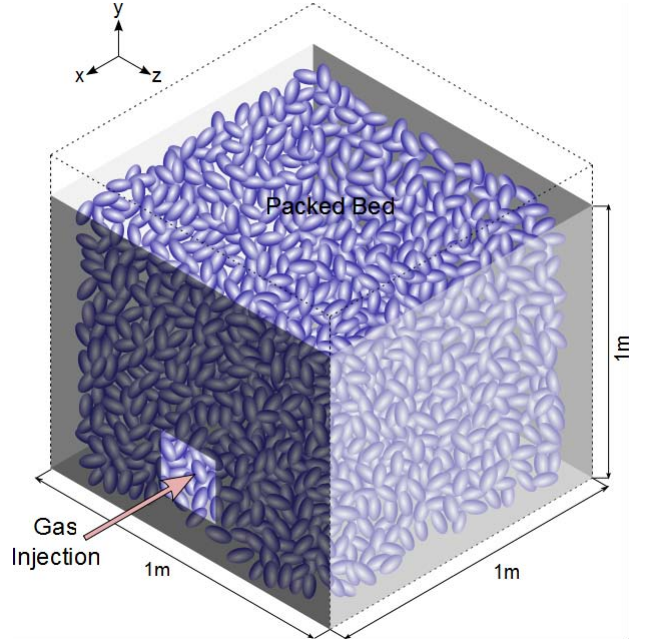| Parameter		Value
Gas viscosity	η_g	1.8×10^{-5} Pa
Gas density	ρ_g	1.2 kg/m^3
Gas turbulence constant	C_W	0.325
Particle density	ρ_p	600 kg/m^3
Particle friction	μ	0.3
Particle coefficient of restitution	e	0.5

Figure 3: Box set-up for full bed simulation
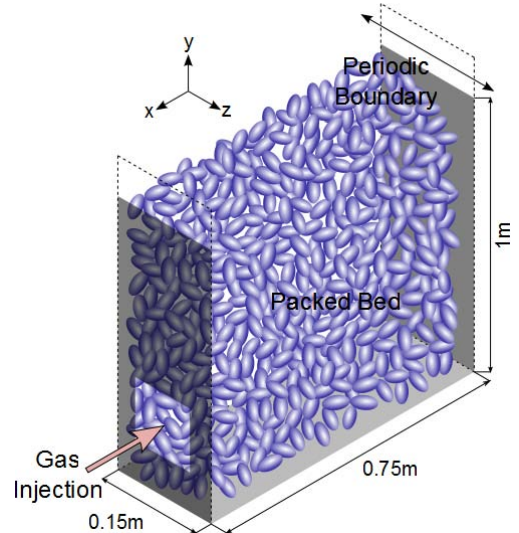
Figure 4: Slice set-up geometry with periodic boundary conditions in the z-direction.

Spherical particles and three types of non-spherical particle were used: cuboidal, prolate ellipsoidal and oblate ellipsoidal, as shown in Fig. 2. In this study the particles were chosen to be approximately mono-disperse, with the same volume as a spherical particle with diameter 14 mm. A ±1 mm variation in diameter was used to prevent any unphysical crystallisation effects in the packed bed. The parameters of the

particles used in the simulations are given in Table 1. The three-dimensional box geometry used around 500,000 particles, which was around 10 times as many particles as the slice set-up, giving a correspondingly large increase in simulation time. For this reason, the three-dimensional box set-up was run with only spherical particles and used to investigate how well the slice geometry compared to the fully three-dimensional box domain.

RESULTS

Full bed model with varying inflow speed

The full sized three dimensional model was run for 2 s at four different inflow velocities: 60, 80, 100 and 120 m/s. The spherical particle bed is shown in Fig. 5, overlaid with gas velocity streamlines.
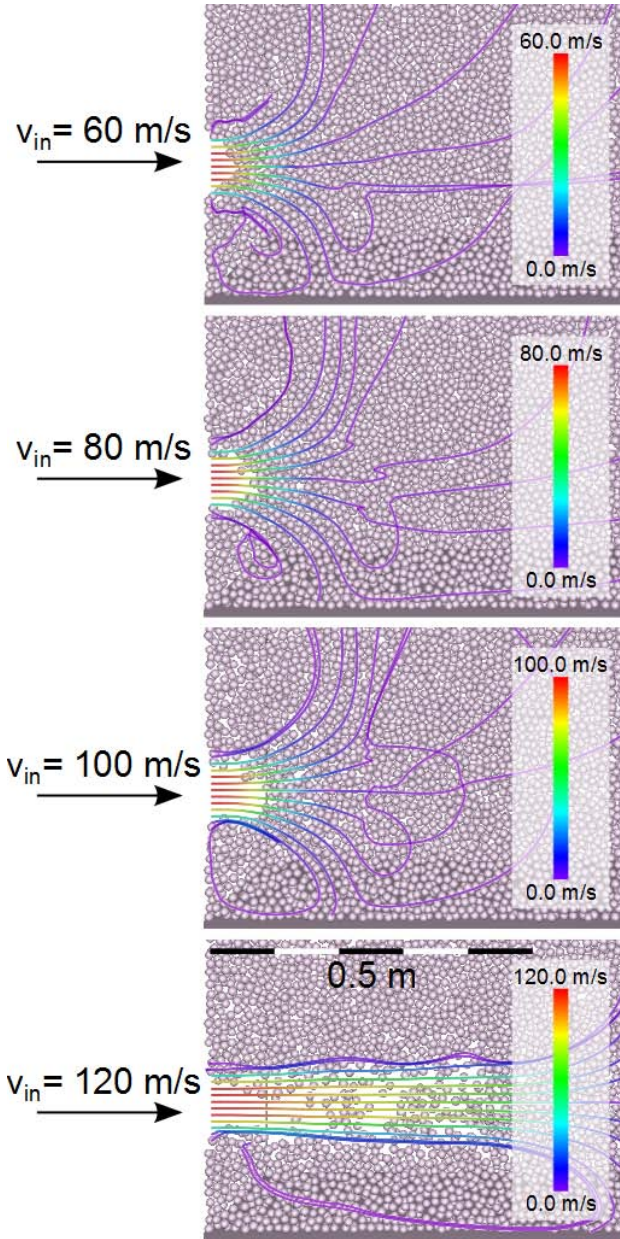

Figure 5 –Particles and gas velocity streamlines in the vicinity of the inflow shown over a 2D slice of the 3D cubical domain at steady-state for four inflow velocities. The streamlines are 3D and shaded by velocity magnitude. The streamlines have been projected onto the 2D slice of particles, and do not intersect in 3D space.

The formation of a voidage region is visible on the left hand side of each picture, adjacent to the inflow, at each of the inflow velocities. At 60, 80 and 100 m/s this voidage region is

formed almost immediately after the start of the simulation and remains in steady state for the duration of the simulation. In these cases the gas flow velocity fell rapidly as the jet penetrated from the void region into the particle bed. In contrast, for the 120 m/s case the voidage region rapidly grew until it reached a steady state length of around half the length of the domain. The voidage region in this case contained a large number of horizontally moving particles entrained by the gas stream, and resembled a horizontal fluidised bed. Due to this similarity with a fluidised bed we will refer to this state as 'lateral fluidisation'.

Particle circulation was observed for the 80, 100 and 120 m/s cases. A comparison between the steady state raceways are shown in Fig. 6 for the 80, 100 and 120 m/s cases. To allow visualisation of the actively moving particles in the domain, the particle opacity is set proportional to the particle velocity magnitude. The case with a gas inflow velocity of 60 m/s is not shown, as the particle bed remained static after the initial formation of the voidage region. The 80 and 100 m/s cases formed short raceways, of approximate length 0.1 m and 0.15 m, respectively. These were elliptical in form, and had sizes and dimensions in good agreement with experimentally observed raceways (Nakamura *et al.* 1977). Increasing the gas inflow velocity from 100 m/s to 120 m/s significantly increased the raceway size. The particle bed also showed significant lateral fluidisation, with a long particles plume of approximate length 0.5 m, and a very large increase in the overall size of the raceway circulation region.
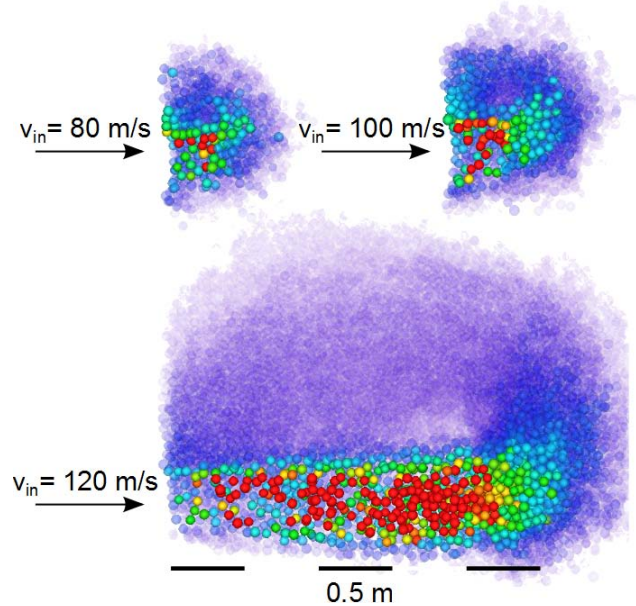
Figure 6 – Cross section of particle bed for comparison at steady-state for 80, 100 and 120 m/s gas inflow velocities. Particles are shaded by, and have an opacity proportional to, their velocity magnitude.

Bed slice model for different speeds and particle shapes

The slice model with periodic boundary conditions in the z-direction was run at four different inflow velocities: 60, 80, 100 and 120 m/s. In each case, four different particle shapes were used, spherical, cuboidal prolate and oblate ellipsoidal. These are shown schematically in Fig. 2. The spherical particles were used to compare to the full bed model to investigate the effects of imposing periodic boundary conditions.

A comparison between the steady state raceways for the different particle shapes is shown in Fig. 7 for the 80 m/s gas inflow velocity case. The particle opacity is proportional to the particle velocity magnitude allowing the raceway structure to
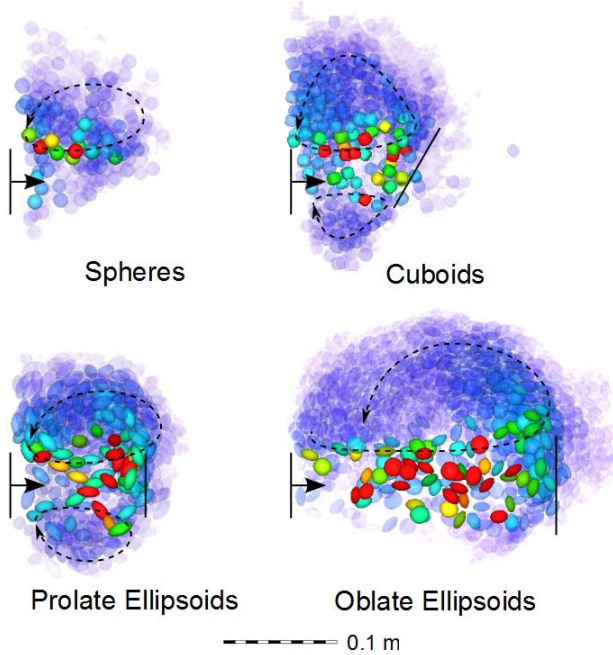
be visualised. Clear differences between the form of the raceway and dynamics within the raceway were observed for the differently shaped particles.

The spherical particles behaved in a similar fashion to the full bed simulation, forming a voidage region and a short raceway. The average velocities of the particles in the raceway region were slightly less in this case than in the full bed. The maximum particle velocities were, however, approximately the same value (at 2.0 m/s) and the overall length of the raceway region was the same (at 0.1 m). Overall this shows that the slice model gives a good approximation of raceway formation at a greatly reduced computational cost.

The cuboidal particles have approximately the same raceway length as the spherical particles but a very different raceway form. The particles preferentially align face-to-face giving an angular, rather than smoothly elliptical, raceway. This effect also causes the voidage region to end in a set of densely packed particles, aligned at approximately 30° to the vertical. The cuboidal particles also have a secondary smaller circulation region under the gas stream.

The prolate particles form two smooth elliptical rotation regions, with a larger upper raceway around the same length as the cuboid raceway length. Particles within the voidage region travel with their long axis aligned to the flow vector. This is expected from drag minimisation, as the particles tend to align to minimise their projected area in the flow direction. At the end of the voidage region particles impacting the bed experience torques tending to rotate them upward, causing a near-vertical alignment of the particles.

The oblate particles give the largest and most active raceway at a gas inflow velocity of 80 m/s. The bed shows lateral fluidisation and the path-lines of the particles do not follow a closed circuit. Particles circulate within a region away from the inflow, but new particles are also being drawn in from the bulk of the bed just above the inflow. At the end of the voidage region particles experience collisional torques tending to rotate them vertically, in the same manner as the prolate particles.
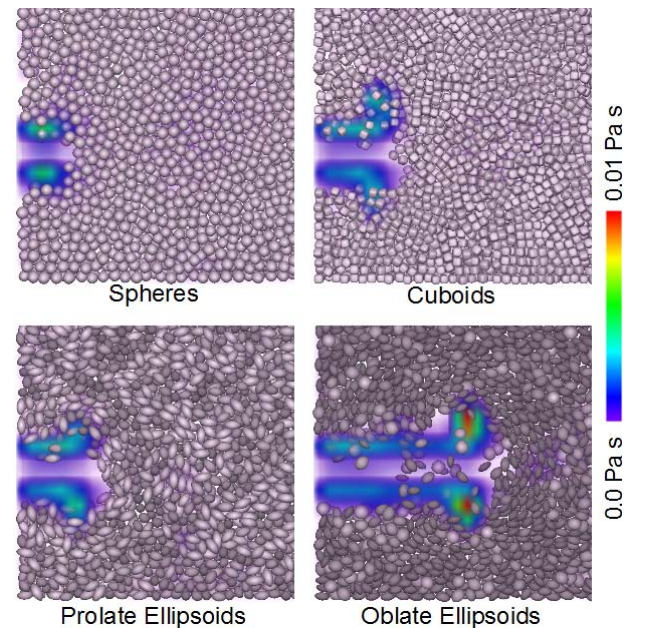
independent of particle shape. These forms can be approximately grouped in four categories, depending on the inflow velocity. These are, in order of increasing inflow velocity:

A. A small voidage region adjacent to inflow with no particle circulation. This is shown in Fig. 5 for the 60 m/s inflow velocity case.

B. An approximately elliptical circulation region above the inflow, along with a slightly larger voidage region. This is shown in Figs. 6 and 7 for the 80 m/s spherical particle cases.

C. Two circulation regions, with a second smaller circulation region below the inflow, along with a corresponding increase in the size of the voidage region. This is shown for the cuboids and prolate ellipsoids in Fig. 7 and the spheres in Fig. 6 for the 100 m/s case.

D. Lateral fluidisation of the bed giving a circulation region inside the bed, away from the inflow, along with a fast-moving plume of particles within a long voidage region. This is shown in Fig. 5 and 6 for the 120 m/s case, and Fig.7 for the oblate particles.

Table **2:** Category of dynamics observed for varying particle shape and inflow velocity, along with average packing fraction measured for initial beds with no inflow.

	Spheres	Cuboids	Prolate	Oblate
$v_{in} = 60$ m/s	A	A	A	B
$v_{in} = 80$ m/s	B	C	C	D
$v_{in} = 100$ m/s	C	D	D	D
$v_{in} = 120$ m/s	D	D	D	D
Packing fraction	0.64	0.73	0.70	0.69

The category of dynamics observed in all simulations are given in Table 2. Spheres show the full range of dynamics, whereas cuboidal and prolate skip the intermediate single circulation region stage as the gas inflow velocity is increased from 60 m/s to 80 m/s. Oblate particles show the largest sensitivity to the inflow velocity, laterally fluidising at a much lower velocity than the other particle shapes.

Figure 7 - Cross section of particle bed for different particle shapes at 80 m/s gas inflow velocities at *t* = 0.30 s. Approximate particle alignment axes are shown as solid lines at the end of the voidage regions.

Particle dynamics within the raceway

From the simulations at differing flow velocities we have observed common features of the form of the raceway

Figure 8 – Turbulent viscosity superimposed over particle beds at *t* = 0.30 s for 80 m/s gas inflow velocity.

From these simulations it is clear that the particle shape has a significant effect on the shape of the raceway and the behaviour of the particles in the raceway. The observed fluidisation behaviour is similar to dynamics in fluidised and laterally driven beds of non-spherical particles (Hilton *et al.* 2010, 2011). Cuboidal and prolate particles are found to have a lower fluidisation velocity than spherical particles, and oblate particles have a much lower fluidisation velocity than cubical and prolate particles. This behaviour arises due to two causes. The first is due to the packing density of the non-round particles, which is much greater than for spherical particles, causing a corresponding increase in the pressure gradient across the bed. The average packing fractions measured for the initial beds with no inflow are also given in Table 2. The second cause is the effect of the average particle area incident to the gas flow field. Oblate particles have the greatest net projected area, followed by prolate particles. Cuboidal particles have a similar projected area to spherical particles. Oblate ellipsoids have the greatest average area incident to the flow along with a larger packing density, and hence experience the greatest drag forces compared to the other particle shapes. This corresponds to the low velocity required to laterally fluidise the bed, compared to the other particle shapes.

The turbulent viscosity of the gas is shown in Fig. 8, superimposed over the particle bed for a gas inflow velocity of 80 m/s. The viscosity, given by Eq. (9), corresponds to regions of high strain rate in the gas within the bed. The oblate particle bed shows the greatest turbulence around the end of the voidage region. This is caused by an interesting effect due entirely to the particle shape. The particles preferentially lie horizontally after the filling of the bed, but are rotated into the vertical when driven to the end of the voidage region by the imposed gas flow. Alignment can clearly be seen in the prolate particles surrounding the end of the voidage region in Fig. 8. This causes the end of the voidage region to form a solid, packed plug composed of particles with the maximum possible projected area to the flow. This effect greatly enhances the horizontal fluidisation within the bed and causes the high gas strain rates. It is also highly likely that this effect is responsible for the creation and maintenance of the densely packed "bird's nest" region which has been found experimentally just outside the voidage region.

CONCLUSION

Three dimensional simulations of raceway formation in beds of shaped particles with a LES turbulence model have been carried out. The form and dynamics of the raceways were compared for four types of particle shapes. From these simulations, different types of raceway form were observed, which are common to all particle shapes investigated. Similar raceway forms have been observed in experimental studies including Nakamura *et al.* (1977) (category B or C) and Chung *et al.* (1996) (category D) as well as computational models including Xu *et al.* (2000) (category A and B), Yuu *et al.* (category D), Umekage *et al.* (category D) and Mondal *et al.* (2005) (category B or C). Raceway dimension found in the simulations closely match the dimensions found in each of these studies. However, few of these studies have shown the transition between different categories of raceway behaviour. Our simulations have shown that the form and dimensions of the raceway are both highly dependent on the gas inflow velocity.

Particle shape is also crucial to the form and the dynamics within the raceway. Generally, non-spherical particles undergo lateral fluidisation at a lower velocity than spherical particles. This is due to both a higher packing density and an increased average surface area incident to the flow in beds of these particles. Oblate, flat particles undergo strong lateral

fluidisation and form a long plume with a detached circulation region (category D) at the lowest inflow velocity of all the particle shapes considered here. The oblate particles also form a dense, aligned, packing surrounding the end of the voidage region. The large particle area incident to the flow increases the pressure gradient over this region and enhances the lateral fluidisation of the bed.

This study opens a range of possible avenues for potential future investigations. A mono-disperse particle distribution was used here to reduce the parameter space of the study, but it is likely that poly-dispersity in the granular material would affect the form of the raceway. Furthermore, granular pressure from the upper bed, which was restricted to a height of 1 m here, has been shown to influence raceway formation (Mondal *et al.*, 2005). Future studies will investigate both the influence of poly-dispersity and bed pressure on the dynamics and formation of the raceway. Our study has clearly highlighted, however, the inability of simple spherical particle models to adequately resolve the complex granular dynamics of such systems. These findings are of interest from both a fundamental point of view, in understanding fluid-gas flow interaction, as well as for design optimisation strategies for practical lateral gas-injection applications.

REFERENCES

ANDERSON, T.B. and JACKSON, R., (1967), "A fluid mechanical description of fluidised beds", *Industrial and Engineering Chemistry Fundamentals*, **6**, 527-539

CHUNG, J. K., HAN, J. W. and LEE, J. H., (1996), "Coke properties at tuyere level in blast furnace with pulverized coal injection", *Metals and Materials*, **2**, 1-7.

CLEARY, P.W., (2004), "Large scale industrial DEM modelling", *Engineering Computations*, **21**, 169-204

CLEARY, P.W., (2009), "Industrial particle flow modeling using discrete element method", *Engineering Computations*, **26**, 698-743

CUNDALL, P. A. and STRACK, O. D. L., (1979), "A discrete numerical model for granular assemblies", *Geotechnique*, **29**, 47-65

DELANEY G. W., HILTON J. E. and CLEARY P. W., (2011), "Definition of random loose packing for non-spherical grains", *Physical Review E, In Press*

Di FELICE, R., (1994) "The voidage function for fluid-particle interaction systems", *Int. J. Multiphase Flow*, **20**, 153-159

ERGUN, S., (1952), "Fluid flow through packed columns", *Chem. Eng. Prog.*, **48**, 89-94

HILTON, J. E., MASON, L. R. and CLEARY, P. W., (2010), "Dynamics of gas–solid fluidised beds with non-spherical particle geometry", *Chemical Engineering Science*, **65**, 1584-1596

HILTON, J. E., and CLEARY, P. W., (2011), "The influence of particle shape on flow modes in pneumatic conveying", *Chemical Engineering Science*, **66**, 231-240

HÖLZER, A. and SOMMERFELD, M., (2008), "New simple correlation formula for the drag coefficient of non-spherical particles", *Powder Technology*, **184**, 361-365

KAFUI, D. K., THORNTON and C. ADAMS, M. J., (2002), "Discrete particle-continuum fluid modelling of gas-solid fluidised beds", *Chem. Eng. Sci.*, **57**, 2395-2410

MATHIESON, J. G., TRUELOVE, J. S. AND ROGERS, H. (2005), "Towards an understanding of coal combustion in blast furnace tuyere injection", *Fuel*, **84**, 1229-1237.

MATSUI, Y., YAMAGUCHI, Y., SAWAYAMA, M., KITANO, S., NAGAI, N. and IMAI, T., (2006), "Analyses on blast furnace raceway formation by micro wave reflection gunned through tuyere", *ISIJ International*, **45**, 1432-1438

McCARTHY, M. J., TAGGART, I. J., PINCZEWSKI, W. V. and BURGESS, J. M., (1983), "Recirculating gas flow in the blast furnace raceway zone", *Eighth Australasian Fluid Mechanics Conference*, University of Newcastle, Australia, November 28 - December 2.

MONDAL, S. S., SOM, S. K., and DASH, S. K., (2005), "Numerical predictions on the influences of the air blast velocity, initial bed porosity and bed height on the shape and size of raceway zone in a blast furnace", *Journal of Physics D*, **38**, 1301-1307.

NAKAMURA, M., SUGIYAMA, T., UNO, T., HARA, Y. and KONDO, S., (1977), "Configuration of the raceway in the experimental furnace", *Tetsu to Hagane*, **63**, 28-36.

NICOUD, F. and DUCROSS, F., (1999), "Subgrid-scale stress modelling based on the square of the velocity gradient tensor", *Flow, Turbulence and Combustion*, **62**, 183-200.

NOUCHI, T., SATO, T., SATO, M., TAKEDA, K. and ARIYAMA T., (2006), "Stress Field and Solid Flow Analysis of Coke Packed Bed in Blast Furnace Based on DEM", *ISIJ International*, **45**, 1426-1431

SHEN, Y. S., GUO, B. Y., YU, A. B., AUSTIN, P. R. and ZULLI, P., (2011), "Three dimensional modelling of in-furnace coal/coke combustion in a blast furnace", *Fuel*, **90**, 728-738.

SUGIYAMA T., SHINOTAKE, A. and MATSUZAKI, C. (1993) "Numerical analysis offlow and r eaction in the raceway region of blast furnace", *Computer Aided Innovation of New Materials II*, 1761-1764.

UMEKAGE, T., YUU, S., and KADOWAKI, M., (2006), "Numerical simulation of blast furnace raceway depth and height, and effect of wall cohesive matter on gas and coke particle flows", *ISIJ International*, **45**, 1416-1425

U.S. GEOLOGICAL SURVEY, (2011), "Mineral commodity summaries 2011", *U.S. Geological Survey*, **198**, 85

WEICKERT, M., TEIKE, G., SCHMIDT, O. and SOMMERFELD, M., (2010), "Investigation of the LES WALE turbulence model within the lattice Boltzmann framework", *Computers and Mathematics with Applications*, **59**, 2200-2214.

XU, B. H., YU, A. B., CHEW, S. J. and ZULLI, P., (2000), "Numerical simulation of the gas-solid flow in a bed with lateral gas blasting", *Powder Technology*, **109**, 13-26

YUU, S., UMEKAGE, T., MIYAHARA, T., (2006), "Predicition of stable and unstable flows in blast furnace raceway using numerical simulation methods for gas and particles", *ISIJ International*, **45**, 1406-1415.

8th International Conference on CFD in Oil & Gas, Metallurgical and Process Industries
SINTEF/NTNU, Trondheim Norway
21-23 June 2011

CFD11-166

DUST DISPERSAL MODELLING ON A CONVEYOR CHUTE USING A COUPLED DISCRETE ELEMENT AND CFD METHOD

James E. Hilton[1] , Paul W. Cleary[1]*

[1] CSIRO Mathematics, Informatics & Statistics,

Private Bag 33 Clayton South, AUSTRALIA

* E-mail: James.Hilton@csiro.au

ABSTRACT

Airborne dust is a major concern in industrial processing plants, as long term exposure can result in occupational lung diseases as well as systemic intoxication. Even low exposure levels have been linked to a wide range of diseases. Furthermore, dust is a widespread environmental contaminant. Dust prediction methods for modelling dust generation and dispersal are therefore of significant importance in industrial processing. We present a coupled Discrete Element Method (DEM) and Navier-Stokes computational model to predict dust dispersal within a typical industrial conveyor transfer chute assembly. The dust concentration is modelled as a scalar field transported in the surrounding air. The dust concentration is advected and diffused by the coupled Navier-Stokes gas solver, allowing concentration levels within and around the assembly to be predicted.

Keywords: DEM, Finite volume method, dust, conveyor chute

NOMENCLATURE

Greek Symbols

ε	voidage fraction
η_g	gas viscosity
κ	dust flux constant
μ	particle friction
ρ_g	gas density
ρ_p	particle density
ρ_b	bulk particle density = $(1-\varepsilon)\rho_p$
τ	stress tensor
χ	empirical pressure correction factor
ω	particle spin vector

Latin Symbols

|	
C	particle damping coefficient
C_D	particle drag coefficient
d	particle diameter
F	particle force
$\mathbf{F}_d$	dust flux
f	particle to gas coupling body force
g	gravitational acceleration
I	particle moment of inertia
k	particle spring constant
L	system length scale
m	particle mass
p	pressure
p_s	static pressure
S	dust source
T	particle torque
u	interstitial gas velocity
u′	superficial gas velocity
$\mathbf{u}_r$	relative velocity = $\mathbf{u}' - \mathbf{v}_i$
v	particle velocity
V	particle volume
$\delta\mathbf{x}$	particle overlap

INTRODUCTION

Dust is a significant contaminant, both environmentally and for specific industrial settings, such as plants processing or handling granular materials. Types of dust found in processing plants include mineral dusts, such as coal and cement, metallic dusts, organic dusts, such as flour and cotton, and biological dust, such as mould and spores. Naturally occurring dusts include pollen, volcanic ash, and fine sand in sandstorms. Dust can be a significant health hazard. Fibrous dusts, such as asbestos and carbon fibre, are renowned for their detrimental effect on heath. Other types of dust directly cause health problems through overexposure, such as hard metal dusts, which may lead to diffuse pulmonary fibrosis, or dusts containing free crystalline silica, which causes the fatal, eponymous, disease silicosis. Even substances classified as innocuous may accumulate in the lungs into masses too large to be cleared through normal means. This process, known as 'dust overload' has been suggested as a precursor to tumour formation (Morrow 1992), leading to revised standards for these substances (WHO, 1999).

Dust pollution is also a significant concern to industrial operators, particularly in mines, bulk materials and mineral processing plants. Dust pollution can lead to revocation of the license to operate, regulatory difficulties in obtaining plant expansion approvals and heavy fines. Dust also presents a significant fire hazard as many fine particulates, especially organic and metallic powders, can burn. Rapid combustion of airborne dust is a significant explosion hazard.

Due to these major health and operational factors, modelling dust flow and contamination within processing plants should is a prime concern. Most models to date have been formulated by geophysics groups to simulate aeolian sand and sediment transport. Soil erosion, leading to dust formation, is a major problem, and many geophysical models include dust as a parameter (Gregory *et al.* 2004). Models directly predicting dust concentration rates include Harris *et al.* (2008, 2009), who use a Monte-Carlo technique to generate concentration profiles. The mean wind profile is,

however, considered fixed in their approach, and the simple geometry makes it unsuitable for industrial modelling applications. Li *et al.* (2008) give a two phase formulation, for a solid granular material phase and gas phase. Their method is compared, with good results, to experimental data, although the exact method of comparison used is unclear as the model is two-dimensional. Scott *et al.* (1995) give a theoretical model for saltation, finding that including the effects of saltation did little to change a simple power law form for suspended particle density derived by Budd (1966).

Particles transported by a gas fall into one of three transport modes depending on their size. These are suspension, saltation and creep. Particles in suspension constitute dust, and are the smallest particles in the system, with a diameter ~50 μm or smaller. At this size drag forces can balance gravitational forces, giving the particles long settling times. It should be noted that the actual particle diameter does not fully describe the state of the particle when airborne, so a more stringent limit is the particle aerodynamic diameter, defined as '*the diameter of a hypothetical sphere of density 1000 kg/m³ having the same terminal settling velocity in calm air as the particle in question, regardless of its geometric size, shape and true density*' (WHO 1999). At this upper limit, particles have a reasonably short settling time: a particle with aerodynamic diameter of 50 μm has a terminal velocity of 0.07 m/s. Dust contains particles down to micron sizes, however, where the terminal velocity is practically zero and the particles can be regarded as staying indefinitely airborne.
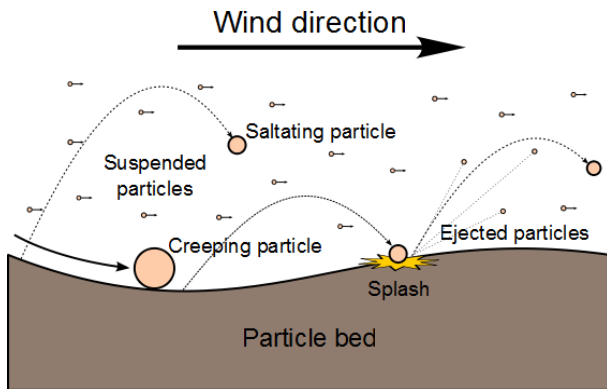
Figure 1 – The three transportation modes of particles in a gas: flow, creep, saltation and suspension. The bulk of suspended particles are ejected from the bed due to splash from saltating particles.

Saltating grains belong to the next size category. The motion of these grains are short parabolic jumps across the surface of the particle bed, as they get entrained by turbulent eddies near the surface of the bed, thrown upwards and fall back under gravity. A very important process is splash, where saltating particles knock other particles into the air on impact. The steady fall of saltating particles onto the surface of the bed is known as saltation bombardment. Crucially this, and *not* aerodynamic lift, is responsible for lofting smaller particles into the air to make up the suspended dust layer. This is due to the fact the cohesive forces dominate over lift forces at small particle sizes, and these cohesive forces are easily broken by the larger impacting grains (Shao *et al.* 1993). The correct understanding of saltation bombardment is therefore critical to correctly modelling dust formation. The final category is that of creeping particles. These are particles which roll along the surface of the bed, being too heavy to lift through aerodynamic forces. These particles have no effect on the saltating or suspended layers.

This sub-division into the three types of granular motion was first proposed by Bagnold in his seminal work on wind-driven granular motion (Bagnold, 1941). Bagnold gave the

dust emission flux (with units kg/m²s) from the surface of the bed, $\mathbf{F}_d$, as $\mathbf{F}_d \propto \mathbf{u}^{*3}$, where $\mathbf{u}^*$ is the bed shear velocity. The direction of the flux vector is orthogonal to the velocity vector. Although more complex models exist, it has been shown that this simple relation holds even when factors such as the saltation layer are taken into account (Scott *et al.* 1995). The relation was investigated experimentally by Shao *et al.* (1993), who confirmed the dependence on $\mathbf{u}^{*3}$ and gave a relation for dust flux emission, which we use in the model presented here. As their experimental findings are used for our computational model, we give a brief summary of their methodology and results.

Shao *et al.* (1993) carried out experiments using a wind tunnel with a rectangular cross section 1.15 m wide, 0.9 m high and of total length 6 m. Vertical dust collectors were located at the end of the wind tunnel. The granular material used in their study was red sand with a median particle diameter of 200 μm and the dust component was loose kaolin clay, with an average diameter of 2 μm. Three experiments were carried out. The first consisted of a 'pure dust' configuration in which a layer of kaolin clay 3 m long and 2 cm high was deposited 3 m from the dust collectors. The second consisted of a 'bombardment' configuration in which a 1 m long layer of sieved 210-530 μm diameter red sand was deposited upwind of a 2 m long layer of kaolin clay. This was designed to allow wind to pick up the larger particles, which would bombard the dust layer. The third consisted of a 'mixed' configuration where a layer of mixed, un-sieved, red sand and kaolin clay, with a 2:1 sand to dust ratio, was deposited in a 3 m long layer. The wind tunnel was run at four different wind speeds from 8.3 to 12.9 m/s.

For the 'pure dust' configuration, a rapid increase in dust flux at the start of the experiment was found, followed by an exponential decrease. The dust flux became negligible after around 200 s from the start of the experiment for all wind speeds. The experiment shows that aerodynamic forces alone cannot sustain a dust flux, and the initial dust flux was caused solely from a very small percentage of very loose particles removed from the top of the deposited bed. The remainder of the dust, below this loose layer, remains attached together as a fixed bed due to inter-particle cohesive forces.

In contrast, the 'bombardment' configuration gave sustained dust fluxes over the duration of the experiment many times higher than the initial dust fluxes found in the 'pure dust' configuration. For the two lowest wind speeds used, 8.3 and 9.8 m/s, the dust flux was constant over the entire nine minutes of experimental time. For the higher wind speeds the fluxes were constant until a rapid fall-off occurred at the end of the experiment. This was due to the supply of source material being used up, showing that the dust flux was limited by experimental conditions, rather than physical factors. The experiment confirmed that bombardment was the primary source of dust production. Furthermore, the experiment also showed that over short timescales the dust flux is constant and depends only on the relative wind speed.

The mixed configuration gave results similar to the 'pure dust' case, in which an initial dust flux exponentially fell to a negligible value over around 100 s. Similar results were reported with a mixture of ratio 1:1 sand to dust. The authors ascribe this to the sand particles being coated with dust particles, reducing the coefficient of restitution, and hence effect of saltation bombardment. The authors state that a much higher ratio of sand to dust would be required to give the same dust fluxes as the 'bombardment' configuration. Although mixtures with these ratios of 1:1 or 2:1 sand to dust are common in geophysical settings, they are uncommon in the industrial systems to which our method will be applied. The systems of interest have a much lower proportion of dust than granular material, so the findings from the 'bombardment' configuration can be used.

Shao *et al.* (1993) gave the following expression for the dust flux $\mathbf{F}_d$ from a fit to the experimental data values:

$$\mathbf{F}_d = \frac{k|\mathbf{u}_r|^{2.832}}{L} \qquad (1)$$

where $\mathbf{u}_r$ is the relative bed-gas velocity, L is a stream-wise length scale and:

$$k = 0.001\,e^{-3.88} \qquad (2)$$

Their findings confirm Bagnold's hypothesis that the dust emission flux $\mathbf{F}_d \propto \mathbf{u}^{*3}$ (their expression for the total flux, which was the subject of Bagnold's hypothesis, shows an even better match with $\mathbf{F}_t \propto \mathbf{u}_r^{2.926}$). In our model we make the assumption that the exponent is simply 3, in accordance with Bagnold's findings.

COMPUTATIONAL FORMULATION

Discrete Element Method

We use the Discrete Element Model (DEM) to simulate the granular dynamics of the large particles within the system. These include the particles which make up the fixed bed and the creeping particles. DEM is a Lagrangian formulation, first given by Cundall and Strack (1979), in which the positions and velocities of each particle is updated according to a set of force relations at each time step. The forces include a collisional force, $\mathbf{F}_c$, which is determined from the overlap between neighbouring particles. This force is the sum of a normal force $\mathbf{F}_n$ and a tangential force $\mathbf{F}_t$. The normal force is determined from the particle overlap δx and relative normal velocity $\mathbf{v}_n$ using a linear spring, dashpot and slider approximation:

$$\mathbf{F}_N = -k_n \delta x + C_n \mathbf{v}_n \qquad (3)$$

where k_n is the spring stiffness, which determines the maximum particle overlap and C_n the normal damping coefficient, which gives the required coefficient of restitution. The maximum overlap is set to ~0.1% of the particle diameter in our simulations. The tangential force is determined from a Coulomb friction limit and the relative surface tangential velocity between neighbouring particles $\mathbf{v}_t$:

$$\mathbf{F}_t = \min\left\{\mu\mathbf{F}_n, k_t\int\mathbf{v}_t dt + C_t\mathbf{v}_t\right\} \qquad (4)$$

where μ is the coefficient of friction, k_t the tangential spring stiffness and C_t the tangential damping coefficient. The linear and angular acceleration for each particle is numerically integrated to give the particle velocity and spin at each time step. These relations, for a particle i, are given as:

$$m_i \frac{\partial \mathbf{v}_i}{\partial t} = \mathbf{F}_{ci} + \mathbf{F}_D + \mathbf{F}_P + m_i g \qquad (5)$$

$$I_i \frac{\partial \boldsymbol{\omega}_i}{\partial t} = \mathbf{T}_{ci} + \mathbf{T}_D \qquad (6)$$

where m is the particle mass, $\mathbf{F}_D$ is the drag force from the gas on the particle and $\mathbf{F}_P$ the gas pressure gradient over the particle. These are given in the next section. The moment balance gives the rate of change of spin, $\boldsymbol{\omega}$, for a particle with moment of inertia I experiencing a rotational collisional force $\mathbf{T}_C$ and Stokesian rotational drag $\mathbf{T}_D$, which is also given in the next section. DEM has been applied and validated for a wide range of industrial processes (Cleary, 2004, 2009).

CFD Formulation

We use the Navier-Stokes equations for gas flow through a porous bed to simulate the global wind velocity within and over the particle bed. The Navier-Stokes equations in a porous

media were derived by Anderson and Jackson (1967), and given by Kafui (2002) in a 'pressure gradient force' form as:

$$\frac{\partial(\varepsilon\rho_G)}{\partial t} + \nabla\cdot(\varepsilon\rho_G\mathbf{u}) = 0 \qquad (7)$$

$$\frac{\partial(\varepsilon\rho_g\mathbf{u})}{\partial t} + \nabla\cdot(\varepsilon\rho_g\mathbf{u}\mathbf{u}) = \\ -\varepsilon\nabla p + \nabla\cdot(\varepsilon\boldsymbol{\sigma}) - \mathbf{f}_{gp} + \varepsilon\rho_g\mathbf{g} \qquad (8)$$

where ε is the bed porosity, ρ_g is the gas density, $\mathbf{u}$ is the interstitial gas velocity, $\boldsymbol{\sigma}$ is the stress tensor and $\mathbf{f}_{gp}$ is the force on the gas from the particles. These can be re-formulated for the superficial gas velocity, $\mathbf{u}' = \varepsilon\mathbf{u}$, and assuming the gas density is constant. In this application, the distributed dust within the gas phase is assumed to have a negligible effect on the gas density. This gives constitutive relations which can be used with incompressible flow methods, which are much less computationally expensive. The set of constitutive relations become:

$$\frac{\partial\varepsilon}{\partial t} + \nabla\cdot\mathbf{u}' = 0 \qquad (9)$$

$$\frac{\partial\mathbf{u}'}{\partial t} + \frac{1}{\varepsilon}(\mathbf{u}'\cdot\nabla)\mathbf{u}' + \mathbf{u}'\nabla\cdot\left(\frac{\mathbf{u}'}{\varepsilon}\right) = \\ -\frac{\varepsilon\nabla p}{\rho_g} - \frac{\nabla\cdot(\varepsilon\boldsymbol{\sigma}')}{\rho_g} - \frac{\mathbf{f}_{gp}}{\rho_g} + \varepsilon\mathbf{g} \qquad (10)$$

where $\boldsymbol{\sigma}'$ is the local stress tensor for the superficial velocity, given by:

$$\boldsymbol{\sigma}' = -\eta\left(\nabla\frac{\mathbf{u}'}{\varepsilon} + \nabla\frac{\mathbf{u}'^T}{\varepsilon}\right) \qquad (11)$$

and η is the gas viscosity. The solution is integrated in time using a variation of the pressure correction method with Eq. (7) as a source term (Hilton *et al.* 2010, 2011).

These gas flow equations are discretised onto a Cartesian grid, with velocity and forces defined on cell vertices and pressure, turbulent viscosity and voidage defined at cell centres. Finite difference stencils are used for the upwind terms, and incompressibility is enforced using a variation of the pressure correction method. Time integration is carried out using a second-order Runge-Kutta method.

Continuum dust model

The particles making up the saltation layer are not modelled as their influence on the system only manifests in the production of the dust flux. The dust, or suspended, layer is modelled as a continuum density distribution. The settling time of dust particles is considered much longer than the simulation time, so it is assumed that the dust remains airborne once produced. As the dust mass is conserved, the dust density field, ρ_d, obeys the Reynolds transport theorem over a control volume Ω:

$$\frac{d}{dt}\int_\Omega \rho_d d\Omega = -\int_{\partial\Omega}\rho_d\mathbf{u}'\cdot\partial\Omega + \int_\Omega S d\Omega \qquad (12)$$

Application of standard techniques for continuity equations of this type results in:

$$\frac{\partial\rho_d}{\partial t} = -\mathbf{u}'\cdot\nabla\rho_d + S \qquad (13)$$

where the assumption that the velocity field is incompressible has been used. Dust therefore is passively advected within the system by the superficial velocity field.

The source term is determined from Eq. (1) by assuming all dust produced in a time-step remains within the computational cell containing the source. This is reasonable as the CFD calculation is governed by a Courant–Friedrichs–Lewy condition, so no terms can be advected more than one computational cell per time-step. Mass flux into a computational cell is given by:

$$F_d = \frac{h^3}{L^2}\frac{\partial \rho_d}{\partial t} \qquad (14)$$

where h is the grid resolution. The rate of change of dust density, and hence source term, is given from Eq. (1), with approximation that the exponent is 3, by:

$$S = \frac{\partial \rho_d}{\partial t} = \frac{Cr|\mathbf{u}_r|^3}{h^3} \qquad (15)$$

where the length scale is chosen as the average particle radius, r, as it must be self-similar over the bed and be independent of the computational CFD parameters. Eq. (15) is only applied in cells which contain DEM particles.

The relative velocity, $\mathbf{u}_r$, is calculated as the difference between the superficial and DEM particle velocity, $\mathbf{u}_r = \mathbf{u}' - \mathbf{v}_i$. Each particle in a computational cell contributes to the total source term using Eq. (15). If a particle overlaps multiple computational grid cells, the total source for the particle is divided amongst the spanning cells. Each overlapping cell is updated with the source term multiplied by the fraction of particle within the cell. This ensures that the dust source term is accurately divided over the bed.

DEM and CFD coupling

The gas drag is the dominant coupling force on the creeping and bed particles. As suspended particles are modelled using a continuum approach, the Saffman (shear) lift force and the Magnus (rotational) lift force are neglected. The drag force is given by:

$$\mathbf{F}_D = \pi r^2 C_D \rho_g |\mathbf{u}'|^2 \varepsilon^{-\chi}\mathbf{u}' \qquad (16)$$

where C_D is the drag coefficient and $\bullet$ is a correction from Di Felice (1994) for the drag in multi-particle systems, given by:

$$\chi = 3.7 - 0.65 e^{-0.5(1.5-\log\mathrm{Re})^2} \qquad (17)$$

The drag coefficient was taken from Holzer *et al.* (2008), based on correlations to experimental data:

$$C_D = \frac{27}{\mathrm{Re}} + 0.42 \qquad (18)$$

where the particle Reynolds number for a particle of diameter d is $\mathrm{Re} = d \bullet_g |\mathbf{u}'|/\bullet$. The particles also have a Stokesian rotational drag, given by:

$$\mathbf{T}_D = \pi\eta d\bullet_r \qquad (19)$$

where the relative spin $\bullet_r = 0.5\,(\nabla\times\mathbf{u}') - \bullet_p$ and $\bullet_p$ is the particle spin. The body force from the gas on the particles is given by:

$$\mathbf{f}_{gp} = \frac{1}{V}\sum_{i=i}^{n}\tfrac{1}{2}C_D A'_i \rho_g \varepsilon^{-(2-\chi)}|\mathbf{u}_r|^2\mathbf{u}_r \qquad (20)$$

where n is the number of particles in the cell volume V. The body force is distributed in a similar manner to the distribution of the dust source term. This term is divided amongst cells spanning a particle using a weighting from the fraction of particle within the spanning cells.

RESULTS

Dust bed

As a first test case, the dust model was applied to a 10 cm × 10 cm bed of 1 mm diameter spherical particles, filled to a depth of 3 mm. This set up is shown in Fig. 2, and was chosen to model wind blowing over a flat bed of particle to show the ability of the method to simulate dust pick-up and concentration. The 1 mm DEM particles represent the creeping particles in the system, saltating particles are not directly simulated, as they produce of the dust, and the dust itself is modelled as a scalar field using Eq. (13). The properties for the particles and gas used in the simulations are given in Table 1. The boundary conditions were periodic in the x and z directions for both the gas flow and the particles. The particles were subject to a solid boundary, and the fluid was subject to a zero no-slip velocity boundary condition in the lower y-direction.

Table **1**: Simulation parameters for dust bed model

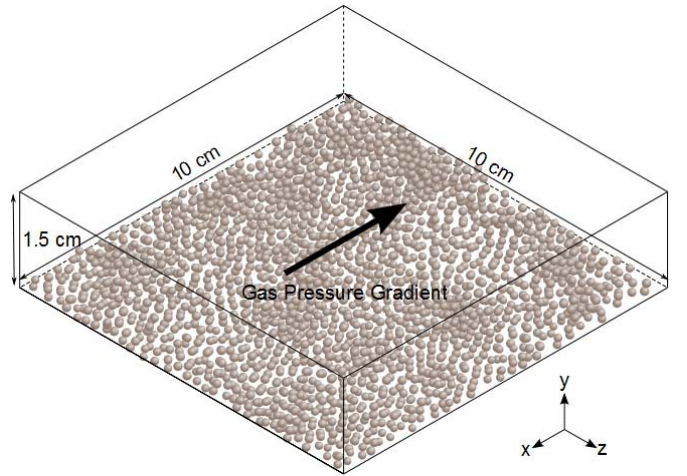| Parameter		Value
Gas viscosity	η_g	1.8×10^{-5} Pa
Gas density	ρ_g	1.2 kg/m³
Particle density	ρ_g	2700 kg/m³
Particle friction	μ	0.5
Particle coefficient of restitution	e	0.25
Particle diameter	d	1 mm
Grid resolution	h	2 mm

Figure 2 – Dust bed test set up with applied pressure gradient in the x –direction.

A gas pressure gradient was applied over the bed to provide the wind velocity. The pressure gradient was imposed by splitting the system pressure into a fluctuating and steady part, $p = p_f + p_s$. From Eq. (10) this gives:
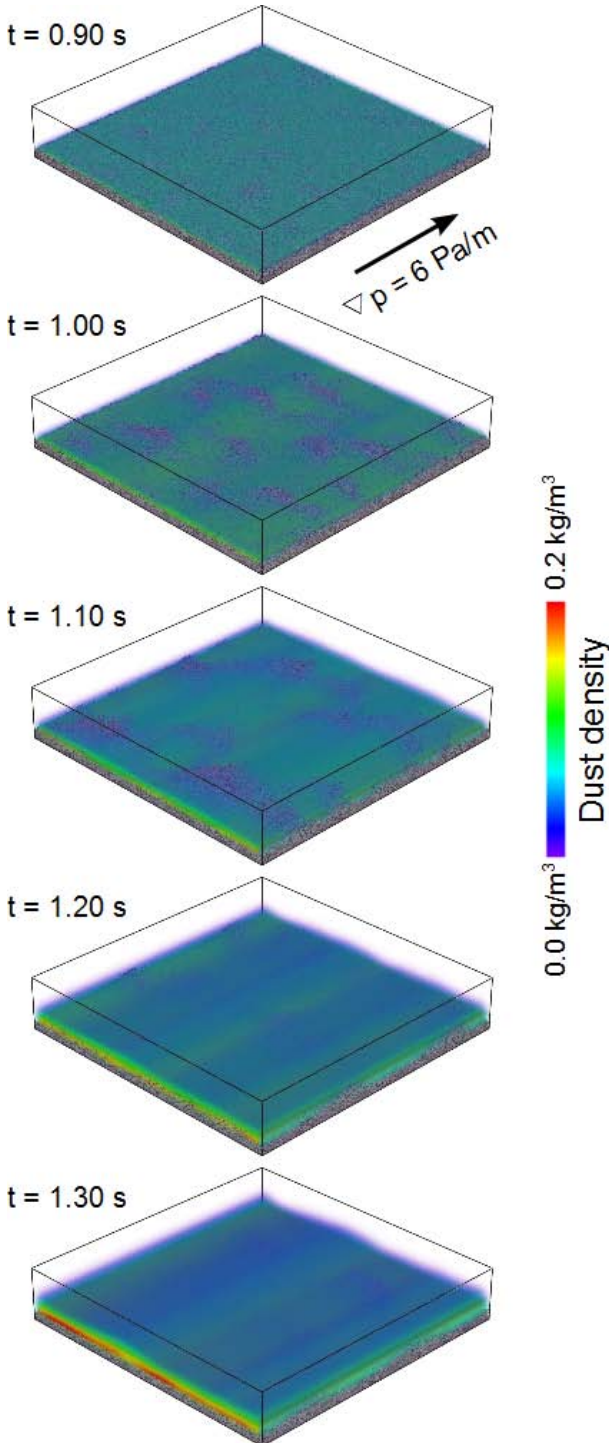
$$\frac{\partial\mathbf{u}'}{\partial t} + \frac{1}{\varepsilon}(\mathbf{u}'\cdot\nabla)\mathbf{u}' + \mathbf{u}'\nabla\cdot\left(\frac{\mathbf{u}'}{\varepsilon}\right) =$$
$$-\frac{\varepsilon\nabla p_f}{\rho_g} - \frac{\nabla.(\varepsilon\bullet')}{\rho_g} - \frac{\mathbf{f}_{gp}}{\rho_g} + \varepsilon\left(\mathbf{g} - \frac{\nabla p_s}{\rho_g}\right) \qquad (21)$$

such that the gradient of p_s gives a driving pressure gradient. This can easily be applied as a gas body force along with gravity, and is transparent to the periodic boundary conditions. Two cases with different pressure gradients were imposed, $\nabla p_s = 6$ Pa/m and $\nabla p_s = 12$ Pa/m. These represent the upper and lower ranges of the pressure gradients which were found to give creeping grains in this set-up. Below 6 Pa/m the grains were found to remain stationary, and above 12 Pa/m the

majority of the grains were airborne and filled the entire domain in a dilute state.

The simulations are shown in Fig. 3 for the $\nabla p_s = 6$ Pa/m case and Fig. 4 for the $\nabla p_s = 12$ Pa/m case. The dust density is shown as a coloured translucent field overlaying the particle bed. For the $\nabla p_s = 6$ Pa/m case, the upper layer of the particle bed started moving approximately 0.9 s into the simulation. At this time the average gas velocity over the particle bed was 4.2 m/s. Only a thin layer of dust was generated, adjacent to the top of the particle bed. Soon after the initiation of bed motion, at around 1 s, small ripples formed in the bed.

particles. They have a reversed profile compared to large scale dunes, with a steep downwind face and a shallow upwind slope. These act as an effective dust source, filling the region from their crest downwind to the next ripple. The ripples rapidly grew into larger ripples the length of the domain (in the z-direction) by 1.2 s. The formation of these ripples broke the vertical symmetry of the system, and caused vertical mixing of the dust into gas. Long-lasting striations in the dust layer appeared, which were caused by the underlying ripple dynamics in the bed below.


Figure 3 – Particles and dust density, shown as a translucent coloured field, for $\nabla p_s = 6$ Pa/m from initiation of bed motion at t = 0.9 s to t = 1.30 s

Ripples are precursors to dune formation, and form through particle drag and collision, rather than deposition of
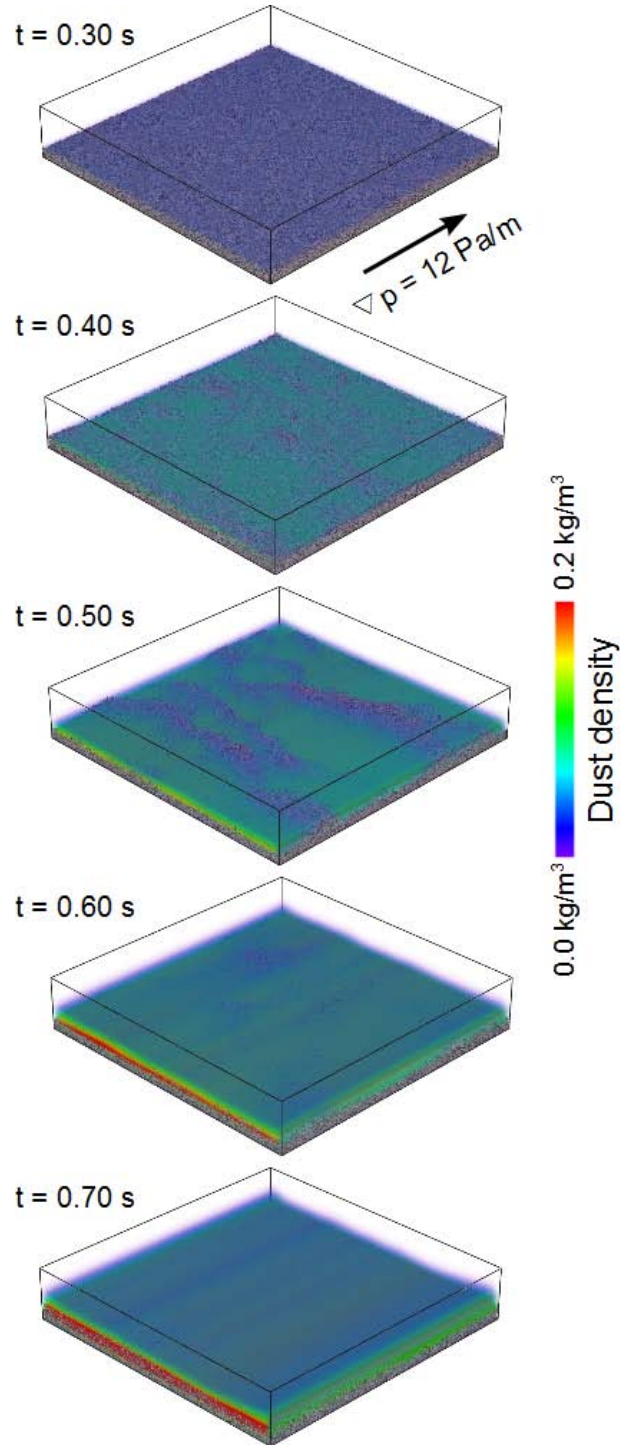
Figure 4 - Particles and dust density, shown as a translucent coloured field, for $\nabla p_s = 12$ Pa/m from initiation of bed motion at t = 0.3 s to t = 0.7 s

The $\nabla p_s = 12$ Pa/m case showed very similar dynamics to the $\nabla p_s = 6$ Pa/m case. Bed motion was initiated earlier, at 0.3

s into the simulation, but at the same gas velocity of 4.2 m/s. The particle bed formed long ripples orthogonal to the wind which grew vertically from the bed, rather than from smaller ripples merging together. The overall height and form of the dust layer is similar when compared to the $\nabla p_s = 6$ Pa/m case, although the maximum density of dust is higher in the $\nabla p_s = 12$ Pa/m case. This behaviour is expected as the form and height of the dust bed is a function of vertical mixing of the dust with the gas near the bed. As the overall ripple heights are the same in the two simulations the mixing, and hence the height of the dust layer, is the same. The dust flux is, however, proportional to the cube of the relative velocity between the bed and gas and is much higher in the $\nabla p_s = 12$ Pa/m case, giving a correspondingly greater maximum dust flux. In both cases the entire bed was covered by dust within 0.3 s of the initial bed movement.
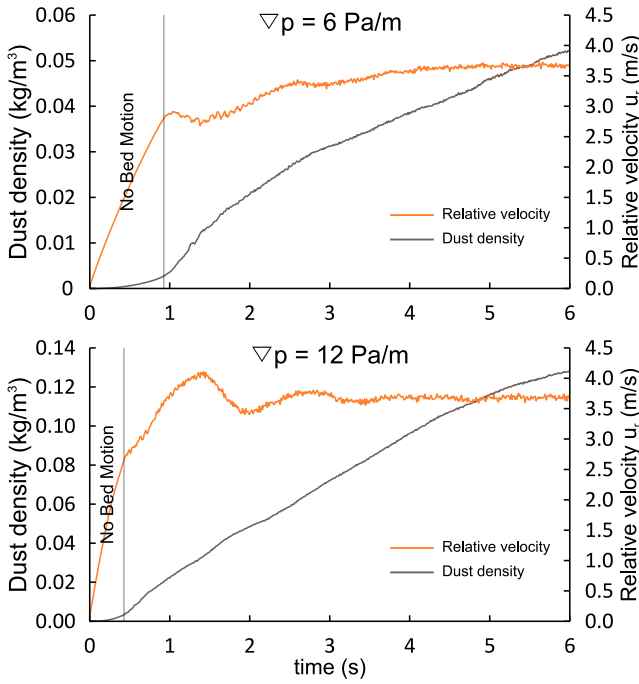

Figure 5 – Average relative velocity and integrated density plotted against time for $\nabla p_s = 6$ Pa/m and $\nabla p_s = 12$ Pa/m.

The dust density and average relative velocity are plotted against time in Fig. 5 for both simulations. The density in Fig. 5 was integrated vertically over a control volume the height of the simulation domain with dimension h in the x and z directions. The velocity average was calculated using this same control volume. The relative velocity in both simulations rose smoothly until bed motion was initiated at approximately 0.9 s for the $\nabla p_s = 6$ Pa/m case and 0.3 s for the $\nabla p_s = 12$ Pa/m case. Bed motion in both cases started at the same relative velocity of approximately 3 m/s. After this initial bed movement the relative velocity rose and settled around an average steady state velocity of 3.5 m/s for both case. The vertically integrated dust density rose exponentially before the initial bed motion, before settling to an approximately linear increase with time. The slope of this line is the average emitted dust flux, $\mathbf{F}_d$. The linear trend showed that the dust flux was constant for an approximately steady-state velocity field, as expected from Eq. (1).

Industrial conveyor chute

The dust model was applied to a large scale industrial conveyor chute system. The system is shown in Fig. 6, and consists of two conveyors transferring granular material through a drop of approximately 4 m and a turn of 90 degrees. The top conveyor tips material onto a spoon, where it is picked up by the second, lower, conveyor. The entire upper

assembly is enclosed within a head box, and the lower spoon is also covered. The relative motion in this case is between the moving particles and the stationary gas field, unlike the dust bed test case where the (initially) stationary particles were driven by the gas. Eq. (1) therefore still holds in this case, as it is dependent only on the relative velocity between the particles and gas. No expression similar to Eq. (1) exists for vertical particle motion, so Eq. (1) is assumed to hold at all orientations, in lieu of any further information.
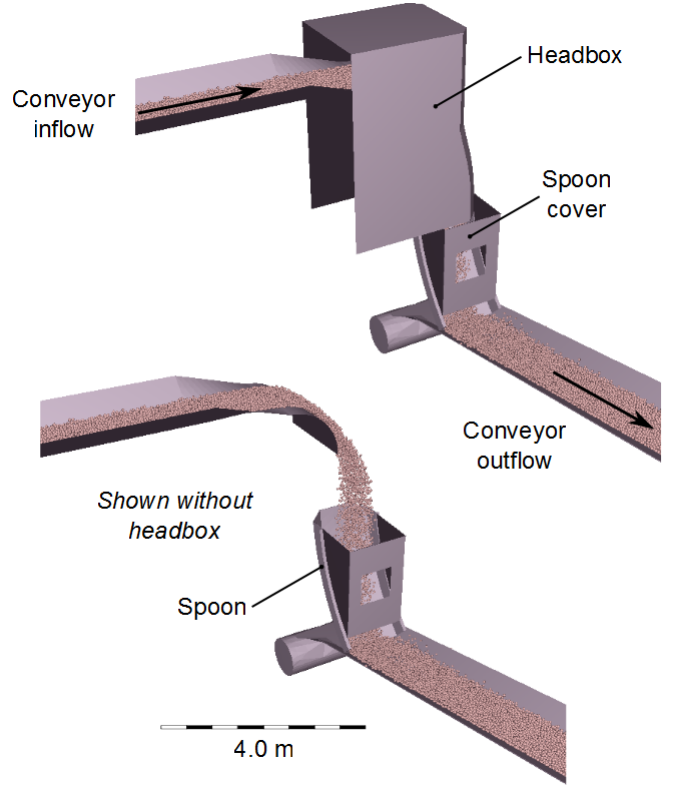

Figure 6 – Industrial chute system consisting of two conveyors at right angles transferring granular material over a drop of approximately 4 m. The lower pictures shows the assembly without the head box.

Table **2**: Simulation parameters for dust bed model

Parameter		Value
Gas viscosity	η_g	1.8×10^{-5} Pa
Gas density	ρ_g	1.2 kg/m^3
Particle density	ρ_p	2700 kg/m^3
Particle friction	μ	0.5
Particle coefficient of restitution	e	0.5
Particle diameter	d	3 - 4 cm
Grid resolution	h	5.55 cm

Simulations were run to predict the dust distribution within the head box and spoon cover. The creeping granular material was modelled using spherical particles from 3 – 4 cm in diameter, which were introduced using an inflow just above the upper conveyor. The parameters used for the particle and gas in the simulations are given in Table 2. Solid boundaries in the simulation were imposed using a zero-velocity no-slip condition on the gas velocity field. This was imposed by testing whether any of the geometry, which was made up of triangular elements, intersected with any of the computational grid cells. If so, the cell was marked and a zero velocity condition was imposed on the gas flow field at each time step.
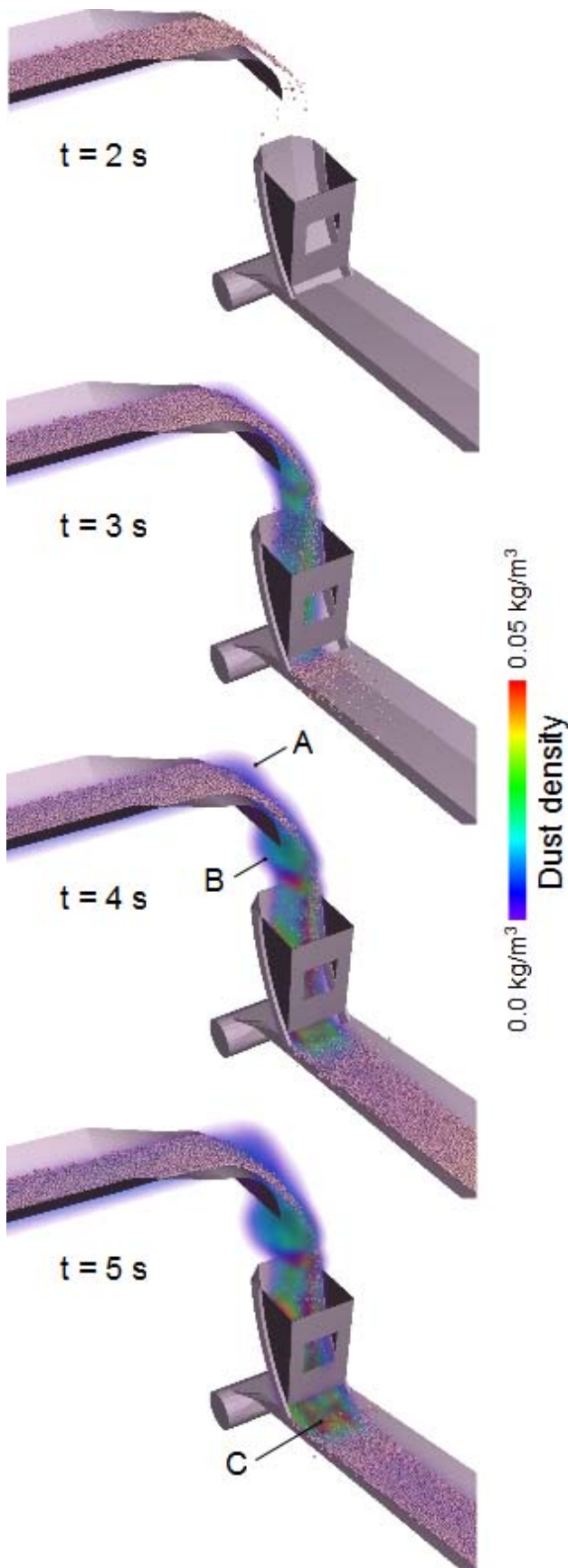
Figure 7 – Particle flow through a conveyor transfer chute from t = 2 s to 5 s generating dust. The dust density is shown as a translucent coloured field, . The head box is not shown for clarity.

The dust density distributions for the simulations are shown in Fig. 7. The head box is not shown in Fig. 7, to aid visualisation of the dust density distribution within the

assembly. Minimal amounts of dust were created by the transportation of the material along the belt as gas was dragged along at approximately the same speed as the particles, giving a relative velocity close to zero.

High dust densities were found to occur within the chute, as the granular material freely fell from the upper conveyor onto the spoon below. The regions of highest density within the chute were found at two locations, marked 'A' and 'B' in Fig. 7 and Fig. 8.
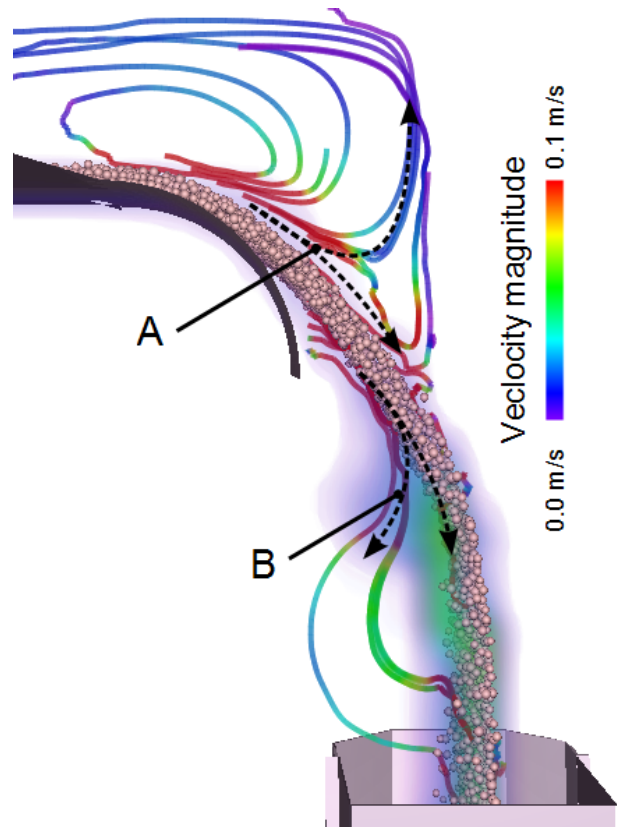

Figure 8 – Gas streamlines at t = 4 s showing flow separation between gas and particles in regions of high dust density.

The first location, 'A' was above the stream of particles, just after the end of the upper conveyor. The gas formed a vortex within the head box, drawing dust up from the falling particle stream. This vortex also confined the dust drawn from the particle stream inside the head box. The second location, 'B', was under the lip of the upper conveyor and occurred due to the particle stream overtaking the gas, which slowed due to confinement within the head box. The gas advected dust from the particle stream into a static dust cloud around 'B'. Region 'B' also experienced a high rate of dust production due to the large relative velocities between the gas and particles.

Fig. 9 shows a close up of dust production within the lower spoon region. Both the head box and spoon cover are not shown. The rate of dust generation here was much higher than other locations due to two factors. The first was due to backflow from the gas, which was confined by the spoon and spoon cover. The second was the high deceleration of the particles as they impacted the spoon. Both these mechanisms created a high relative velocity between the particles and gas, and hence a high rate of dust production. The rapidly falling, diffuse, particle stream also created highly transient gas velocities within the spoon, causing very effective mixing of the dust with the surrounding gas.

Dust escaped the system through the gap between the lower edge of the spoon cover and the particle bed on the lower conveyor. This location is marked 'C' in Fig. 7. A significant quantity of dust is transported out through this gap. At *t* = 6 s, the average dust concentration within the spoon is

0.1 kg/m^3, and the average dust concentration just outside at point 'C' is approximately 0.05 kg/m^3. The spoon cover therefore does not act as an effective dust barrier in this application.
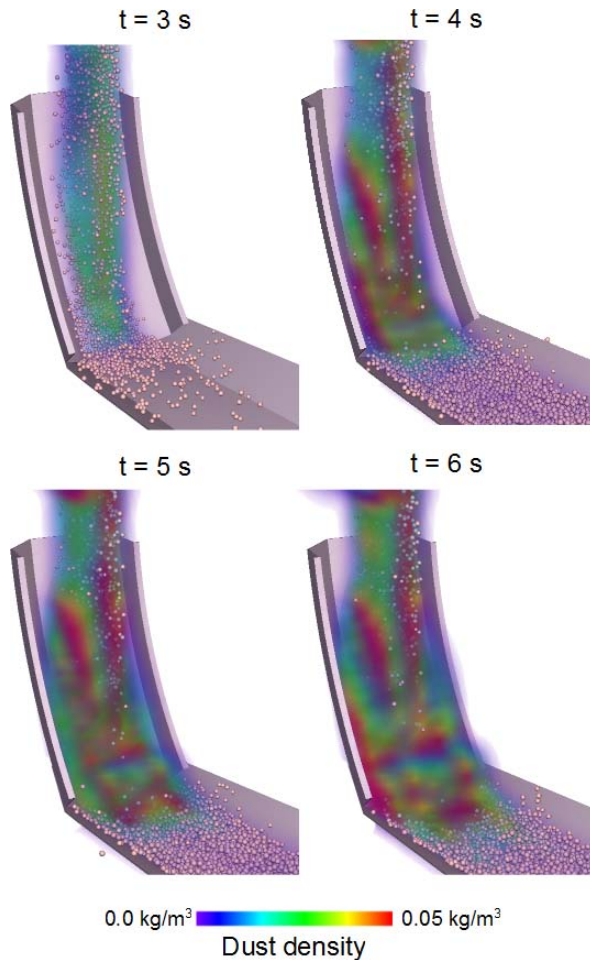
Figure 9 – Close up of particles and dust density within spoon from t = 3 s to t = 5 s. The head box and spoon cover are not shown for clarity.

CONCLUSION

A physically realistic dust model has been developed based on an empirical expression for dust flux, given by Eq. (1). This flux expression, along with the assumption that the dust remains suspended, allows the dust be regarded as a scalar density field. The field obeys an advection equation derived from the Reynolds transport theorem, given by Eq. (13). The model was incorporated into a combined DEM and CFD gas–particle computational method and applied to two systems. The first was a test case of a flat particle bed with an imposed horizontal gas pressure gradient. The full range of dynamics of the particle bed, from ripple formation to bed motion, was simulated. The dust model predicted the spatial dust distribution over the bed and correctly gave a constant dust flux for an approximately steady state velocity field.

The second system was an industrial conveyor chute transfer system. The model showed that the highest concentration of dust occurs where flow between the particle stream and gas field separate, which advects dust from the bed. The regions of highest dust production were found in areas of high relative velocity between the gas and particles. In this case, the region between the spoon and spoon cover had the highest rate of dust generation due to the rapid deceleration of the particles and strong counter-flow in the confined gas.

We have shown that this model can be used to predict dust production in large-scale industrial devices. This will allow optimisation of these devices to minimise dust pollution and hence health risks. The model also has a wide range of application in other areas such as modelling of aeolian dispersal of environmental dust and contaminants.

REFERENCES

ANDERSON, T.B. and JACKSON, R., (1967), "A fluid mechanical description of fluidised beds", *Industrial and Engineering Chemistry Fundamentals*, **6**, 527-539

BAGNOLD, R. A., *The physics of blown sand and desert dunes*, Methuen, 1941

BUDD, W. E., (1966), "The drifting of non-uniform snow particles", *Studies in Antarctic Meteorology*, **9**, 59-70

CLEARY, P.W., (2004), "Large scale industrial DEM modelling", *Engineering Computations*, **21**, 169-204

CLEARY, P.W., (2009), "Industrial particle flow modeling using discrete element method", *Engineering Computations*, **26**, 698-743

CUNDALL, P. A. and STRACK, O. D. L., (1979), "A discrete numerical model for granular assemblies", *Geotechnique*, **29**, 47-65

Di FELICE, R., (1994) "The voidage function for fluid-particle interaction systems", *Int. J. Multiphase Flow*, **20**, 153-159

ERGUN, S., (1952), "Fluid flow through packed columns", *Chem. Eng. Prog.*, **48**, 89-94

GREGORY, J. M., WILSON, G. R., SINGH, U. B. and DARWISH, M. N. (2004), "TEAM: integrated, process-based wind-erosion model", *Environmental Modelling and Software*, **19**, 205-215

HARRIS, A. R. and DAVIDSON, C. I., (2008), "Particle resuspension in turbulent flow: A stochastic model of individual soil grains", *Aerosol Science and Technology*, **42**, 613-628.

HARRIS, A. R. and DAVIDSON, C. I., (2009), "A Monte-Carlo model for soil particle resuspension including saltation and turbulent fluctuations", *Aerosol Science and Technology*, **43**, 161-173.

HILTON, J. E., MASON, L. R. and CLEARY, P. W., (2010), "Dynamics of gas–solid fluidised beds with non-spherical particle geometry", *Chemical Engineering Science*, **65**, 1584-1596

HILTON, J. E., and CLEARY, P. W., (2011), "The influence of particle shape on flow modes in pneumatic conveying", *Chemical Engineering Science*, **66**, 231-240

HÖLZER, A. and SOMMERFELD, M., (2008), "New simple correlation formula for the drag coefficient of non-spherical particles", *Powder Technology*, **184**, 361-365

KAFUI, D. K., THORNTON and C. ADAMS, M. J., (2002), "Discrete particle-continuum fluid modelling of gas-solid fluidised beds", *Chem. Eng. Sci.*, **57**, 2395-2410

LI, Y. and GUO, Y., (2008), "Numerical simulation of Aeolian dusty sand transport in a marginal desert region at the early entrainment stage", *Geomorphology*, **100**, 335-344

MORROW, P. E. (1992), "Dust overloading of the lungs: Update and appraisal", *Toxicol. appl. Pharmac.*, **113**, 1-12

SHAO, Y., RAUPACH, M. R. and FINDLATER, P. A., (1993), "Effect of saltation bombardment on the entrainment of dust by wind", *J. Geophysical Research*, **98**, 12719 – 12726

SCOTT, W. D., HOPWOOD, J. M., and SUMMERS, K. J., (1995), "A mathematical model of suspension with saltation", *Acta Mechanica*, **108**, 1-22

WORLD HEALTH ORGANIZATION, (1999), "Hazard prevention and control in the work environment: Airborne dust", WHO/SDE/OEH/99.14

ADVANCES IN THE SIMULATION OF MULTIPHASE FLOWS IN PIPELINES

Djamel LAKEHAL[1] , Mathieu LABOIS, Chidambaram NARAYANAN

[1] ASCOMP GmbH, 8005 Zurich, SWITZERLAND

Corresponding author's e-mail: lakehal@ascomp.ch

ABSTRACT

In this contribution we address the predictive performance of one class of Computational Multi-Fluid Dynamics (CMFD) methods for stratified, slug and annular flow regimes in horizontal pipes, with and without droplet entrainment. Within the Interface Tracking Techniques concept, use is made of the Level Set method to track free surface flows, combined with the Very-Large Eddy Simulation (VLES) approach to cope with turbulence. We will first discuss new results of transition from stratified to slug flow, which agree well with the data. We will then present other results of droplet entrainment in a stratified flow with lower water cut, which has long been tackled with lump-parameter models based on heuristic correlation for entrainment rates. While turbulence in these flows has long been addressed using RANS, we will show that other approaches are needed and are mature enough to be employed as viable alternatives to statistical approaches, including the filter-based approach, also known as VLES.

Keywords: VLES, Stratified Flow, Slug Flow, Entrainment

INTRODUCTION

Gas-liquid flows appear in various industrial processes and in the petroleum industry in particular, where mixture of gas with associated liquids (light and heavy components of oil, solid particles, hydrates, condensate and/or water) are produced and transported together. During their co-current flow in a pipe the sheared interfaces acquires various characteristic topologies or patterns (Badie, 2000, Hewitt, 2005). Understanding the transition from stratified flow to slug flow is important in hydrocarbon transportation systems, and as such it has constantly stimulated the research in this direction (Valluri et al., 2008). Slug flow is a commonly observed pattern in horizontal and upslope gas liquid flows. The regime is associated with large coherent disturbances, due to intermittent appearance of aerated liquid masses that fill the pipe cross-section and travel downstream. This causes large pressure fluctuations and variations in flow rates, which may in turn affect process equipments.

Earlier techniques for the prediction of slugs were based on various linear stability theories. The transition from stratified to slug flow regime has often been associated with the sudden growth of interfacial waves due to the Kelvin-Helmholtz instability (Taitel and Dukler, 1976; Barnea and Taitel, 1993), without accounting for wall shear and interfacial stress. The long-wave assumption is still adopted in the formulation of 1D lump parameter models, because it lends itself to integral momentum balance. Although the criteria for linear instability based on these theoretical investigations show good agreement with the data as to slug formation, the basic assumptions are still questionable (e.g. Lin and Hanratty, 1986).

Besides slug formation, the stratifying annular flow regime occurs in pipeline transport systems of natural gas and condensates, too. In this regime the liquid layer flowing on the wall is subject to droplet dispersion in the gas core. From the flow assurance standpoint, it is essential to understand the relationship between the continuous liquid film around the periphery and the thicker liquid pool at the bottom of the pipe (Brown et al., 2008). Until recently, droplet entrainment rates have long been determined with lump-parameter models based on heuristic correlations. In this mechanism, droplets are entrained from the film at the bottom of the pipe and are transported towards the upper part of the pipe where they deposit and form a liquid film which drains downwards towards the bottom. Thus, there is a process of continuous renewal and drainage of the film in the upper part of the pipe. Replenishment of the film by droplet deposition is then equal, in fully developed flow, to the deposition of the droplets on the surface (Anderson and Russell, 1970).

Interface Tracking Methods (ITM) have proven robust and accurate in predicting interfacial flows (Lakehal, 2008), revealing to some extent the occurrence events similar to KH-driven instabilities leading to sealing in pipe flows. We extend the prospect here by addressing slug formation and subsequent droplet entrainment. Use is made of ITM to bypass the limitations of phase-average models, in particular as to interphase friction, combined with large scale, time-dependent simulation to better capture turbulence anisotropy and/or non-homogeneity and its transient motion. This combination is arguably more interesting than using the two-fluid approach with k-ε model; this is now known as LEIS (Lakehal, 2010), short for Large Eddy & Interface Simulation, and is implemented in the CMFD code TransAT. LEIS could be used in conjunction with LES or VLES, short for Very-Large Eddy Simulation.

We discuss in particular the results of two-phase flow transition to slug in a 37 m long pipe under turbulent flow conditions. The data are from the WASP facility of Imperial College (Ujang, 2003; Ujang et al., 2006). Then we present first results of droplet entrainment and detachment in a low-water-holdup stratified pipe flow under strong interfacial shear conditions.

MODEL DESCRIPTION

Multiphysics Code TransAT©

The CMFD code TransAT© of ASCOMP is a multi-physics, finite-volume code based on solving multi-fluid Navier-Stokes equations on structured multi-block meshes. The grid arrangement is collocated and can thus handle more easily curvilinear skewed grids. The solver is pressure based (Projection Type), corrected using the Karki-Patankar technique for subsonic to supersonic compressible flows. High-order time marching and convection schemes can be employed; up to third order Monotone schemes in space. Multiphase flows can be tackled using (i) interface tracking techniques for both laminar and turbulent flows (Level Set, VOF with interface reconstruction, and Phase Field), (ii) N-phase, phase-averaged mixture model with Algebraic Slip, and (iii) Lagrangian particle tracking (one-to-four way coupling). As to the level set, use is made of the 3rd order Quick scheme for convection, and 3rd order WENO for re-distancing. Mass conservation is enforced using global and local mass-conserving schemes.

TransAT uses the Immersed Surfaces Technique (IST) to map complex system components into a simple rectangular Cartesian grid (e.g. figure 1). Near wall regions are treated by BMR (Block-based Mesh Refinement), a sort of geometrical multi-grid approach in which refined grid blocks or manifolds are placed where adequate and solved. The connectivity between blocks can be achieved in parallel (MPI) up to 8-to-1 cell mapping. The combination IST/BMR saves up to 70% grid cells in 3D and allows for conjugate-heat transfer modelling and solid body motion (e.g. debris).

On the VLES Strategy

VLES (Labois and Lakehal, 2011) also known as filter-based approach (Johansen et al., 2004) is based on the concept of filtering a larger part of turbulent fluctuations as compared to LES (as the name clearly implies). This directly implies the use of a more elaborate sub-grid modelling strategy than a zero-equation model like in LES. The V-LES implemented in TransAT is based on the use of $k - \varepsilon$ model as a sub-filter model. The filter width is no longer related to the grid size (~Δx); instead it is made proportional to a characteristics length-scale (Λ), which should be larger than (Δx), but necessarily smaller than the macro length-scale of the flow. Increasing the filter width beyond the largest length scales will lead to predictions similar to the output of RANS models, whereas in the limit of a small filter-width (approaching the grid size) the model predictions should tend towards those of LES. V-LES could thus be understood as a natural link between conventional LES and RANS. If the filter width is smaller than the length scale of turbulence provided by the RANS model, then larger turbulent flow structures will be able to develop during the simulation, provided that the grid resolution and simulation parameters are adequately set (in particular regarding time stepping and the order and accuracy of the time marching schemes employed).

For a more detailed presentation and a discussion on the values of the model constants, the reader can refer to Johansen et al. (2004) and Labois and Lakehal (2010). One of the key hypotheses in V-LES though is that the Kolmogorov equilibrium spectrum is supposed to apply to the sub-filter flow portion too.

On the Interface Tracking Concept

Interfacial flows refer to multi-phase flow problems that involve two or more immiscible fluids separated by sharp interfaces which evolve in time. Typically, when the fluid on one side of the interface is a gas that exerts shear (tangential) stress upon the interface, the latter is referred to as a free surface. ITM's are best suited for these flows, because the interface topology is accurately resolved. When the exact shape of the interfaces is not relevant one may resort to phase averaged approaches, where separate conservation equations are required for each phase with appropriate exchange forces. Both formulations can virtually deal with interfacial flows, but not with the same precision. ITM's are the cornerstone algorithms of the single-fluid formalism that solves a set of conservation equations with variable material properties (Lakehal *et al.* 2002). The strategy is rather accurate as it minimizes modelling assumptions.

SLUG FORMATION IN THE WASP FACILITY
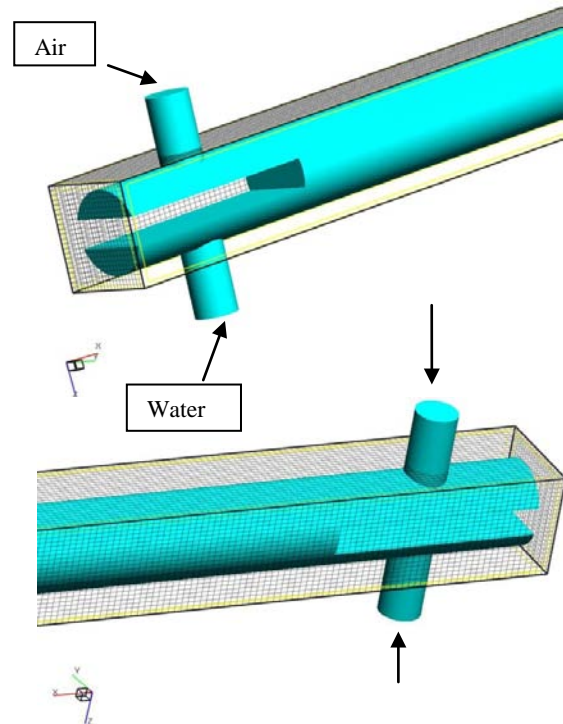
Description of the Test

Figure 1: Computational IST grid. The CAD file is immersed in a Cartesian grid. Air & water inflow are shown.

The experiments were performed at the Imperial College WASP facility with the test section mounted horizontally. Gas and water were fed from two different entries perpendicular to the main pipe (Fig. 1). Slugs were monitored from close to the point where they were first initiated until they decayed or exited the pipe. Twin-wire holdup probes were used to monitor the liquid level at a series of locations along the pipe.

Slugs were discriminated from large waves by measuring the velocity using cross correlation of the

outputs of successive probes (the waves travel at a lesser velocity that that of the mixture and slugs travel at a velocity higher than that of the mixture). The length of the stainless steel test section is 37 m and its diameter is 77.92 mm, the pressure at the outlet is 1 atm, and the temperature is 25

below a stratification plate at the bottom of the test-line and the gas is introduced above it. The superficial velocities of the two phases (air and water) are: U_{sL} = 0.611 m/s and U_{sG} = 4.64 m/s, respectively.

Problem Set-up for C*M*FD

Use was made here of the IST technique to mesh the pipe. The pipe CAD file was created using Rhinoceros software, and immersed into a Cartesian grid, as shown in Fig. 1. The 2D simulations were performed in a pipe of length 17m. The 3D simulations were performed in a shorter domain of 8m, consisting of 715.000 cells, then in a longer one of 16m, consisting of 1.200.000 cells. The simulation time for the 8m pipe simulation was 10 days on a low bandwidth Dell PC (2 nodes x 4 cores; Open MP parallel protocol) for 20s real time, and 53H on a high bandwidth 18 nodes IBM multicore computer (OpenMP parallel protocol).

The LEIS approach was employed here, with a filter width of 0.1D, combined with the Level-Set technique for interface tracking. Subscale modelling of turbulence was achieved with the k-ε model with filter width set equal to 0.1D (Labois and Lakehal, 2011). The inflow boundary conditions involve fixing the superficial gas and liquid velocities and the void fraction, as specified in the experiment. Specifically at the inflow, we have set the following values for the turbulent flow conditions: gas superficial velocity U_{sG} = 4.64 m/s; liquid superficial velocity U_{sL} = 0.611 m/s; void fraction = 50%. Initial flow disturbances based on the wall shear Reynolds number were applied in the entire flow domain to sustain turbulence.

Two-Dimensional Results

Figure 2 shows the measured liquid hold-up at different probe locations along the axis: 5.01m, 5.69m, 6.99m and 13.32m. The signals display distinct large-wave structures developing along the pipe that could in fact be considered as slug-structures (Ujang, 2003). While a traditional slug is a structure blocking the cross section of the pipe completely, large-wave structures with a length scale larger than the pipe diameter can also be termed as 'slugs'. The 3D simulations discussed next will help make the distinction between the different structures. Slugs or large-wave structures are captured around location x = 3m and beyond (results not shown here). The periodicity of slug occurrence is clearly visible from these locations (x > 5 m).

Figure 3 depicts the calculated water holdup in 2D at different probe locations along the axis, from 5.65 to 15m. While the signal is qualitatively similar to the measured one in terms of slug or large-wave structures intermittency, it is unclear whether slugs were indeed captured; various locations exhibit water holdup of about h_L/D = 0.8-0.9. Be it as it may, large surface perturbations were already captured upstream close to

the inflow, at x = 0.76m, while the experiment there shows liquid hold-up not exceeding h_L/D = 0.2. For the locations shown in the figure, the experiment and CFD provide a similar picture as to wave frequency.

Three-Dimensional Results

The objective of the 3D simulations was to reproduce a series of slugs travelling in the pipe. To address the effect of pipe length on the results, the flow was reproduced in two pipes with different lengths: 8 m and 16 m, using the same flow conditions.
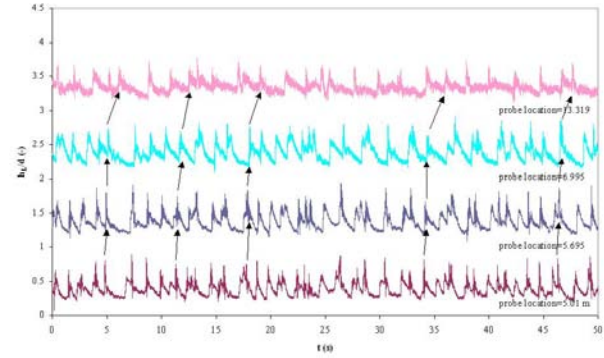

Figure 2: Measured liquid holdup for case U_{sL}= 0.611m/s and U_{sG}= 4.64m/s. Probe location from 5.01 to 13.319m.
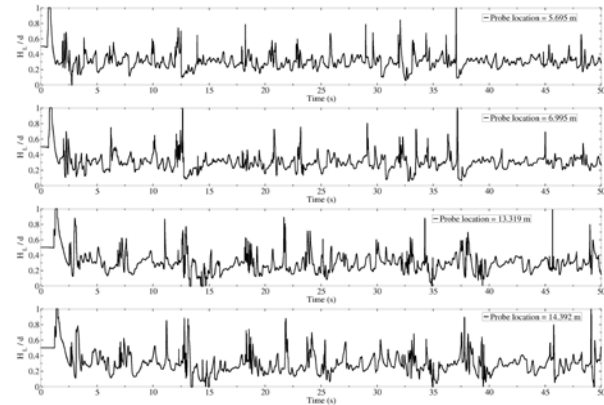

Figure 3: Calculated liquid holdup for case U_{sL}= 0.611m/s and U_{sG}= 4.64m/s. 2D (L=17m). Probe location from 5.7 to 14.4m
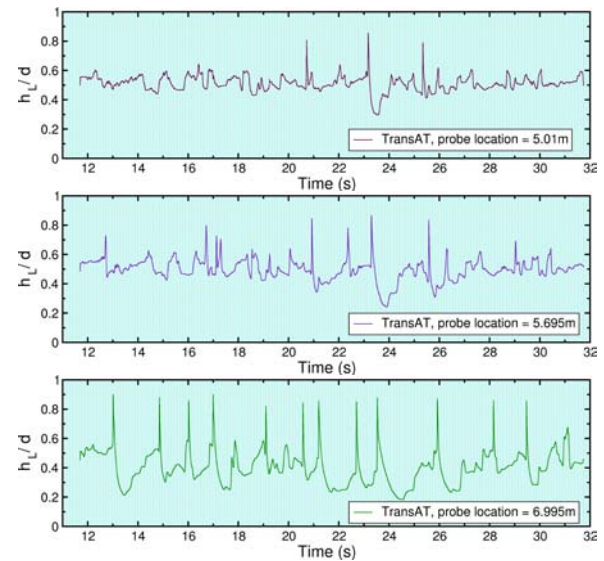

Figure 4: Calculated liquid holdup for case U_{sL}= 0.611m/s and U_{sG}= 4.64m/s. 3D (L=8m). Probe location from 5 to 7m.
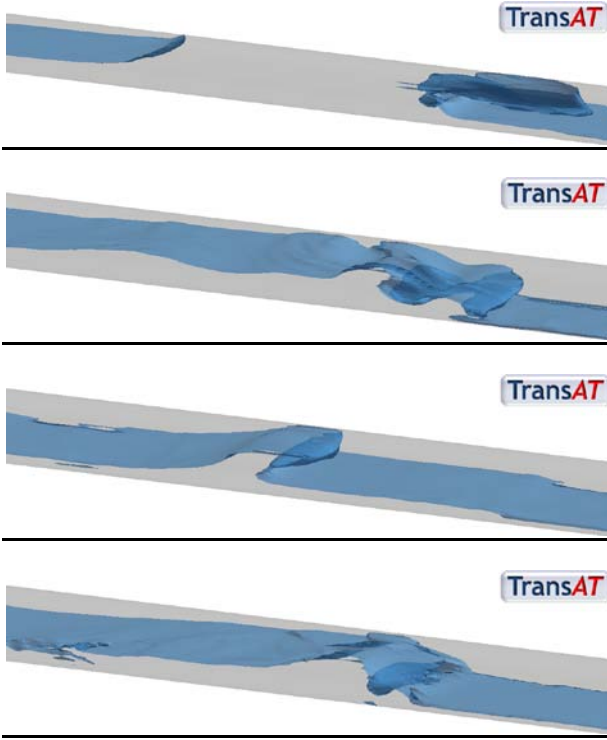
Figure 5: The formation of different types of slugs.

Figure 4 shows the development structures at different probe locations along the axis, at 5.01m, 5.695m and 6.995m. These were obtained from 3D simulations in the short pipe (L=8m). The distinct patterns at different locations show the variations in the slug frequencies. Slug frequency decays as the location of the probe is moved further downstream. Slugs or large-wave structures are predicted rather at downstream locations close to the pipe end: x = 7m, in contrast to the experiment and longer-pipe simulations, both indicating a shorter position for the early slugs. Further, in contrast to the 2D results discussed earlier, slugs or large disturbances of the surfaces are not predicted upstream close to the inflow, but rather downstream. These results are interpreted later on in terms of slug frequency, and compared to the longer pipe results.

Turning now to the 16m long pipe, the formation of the different types of slugs is well illustrated in Figure 5. The first panel exhibits a 'large-scale slug', which, in the experiments is often referred to as 'operation slug'. This slug is formed upstream (x < 3 m) and fills entirely the pipe ($h_L/D = 1$) with an average size of the order of 2-4 D. Although the lower panels do not show a 100% water holdup filling the pipe as in the first one, the liquid structures are travelling at a higher speed than the mean flow, which makes them 'slugs', independently from the liquid holdup. Here one observes that gas bubbles are caught inside the slug, which explains that the measured liquid hold up h_L/D is less than unity (usually h_L/D lays between 0.80 and 0.95).

The slug- or large-wave structures frequency results shown in Figure 6 are qualitatively similar to the structures observed in the experiment. The lines in green correspond to the 16m pipe simulations; the red

ones to the 8m simulations; both in 3D indeed. The shift in the frequency peak observed for the two simulations is clearly due to the difference in length of the pipes, as the outflow boundary condition has an important impact on the flow. The frequency of the slugs is measured as a function of the abscissa of the pipe. In the 16m case, better results are obtained as a peak frequency around 3.5m can be see), which is almost equal to the value delivered in the experiments.
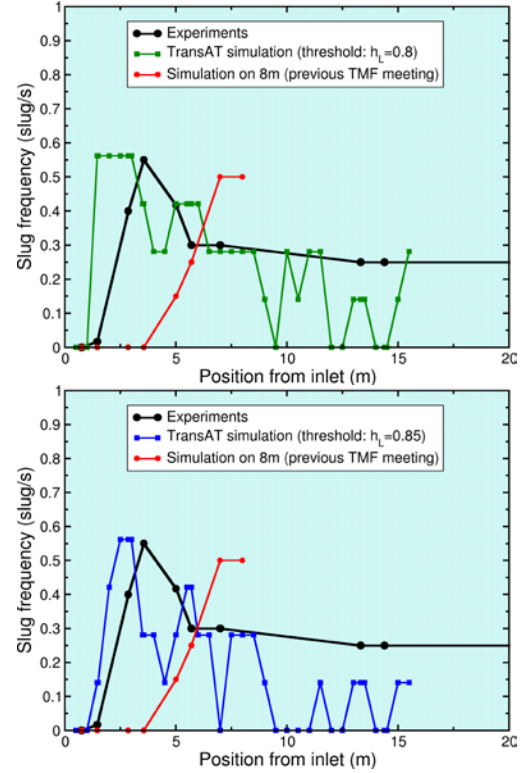

Figure 6: Comparison of experiment and simulations of slug frequency for 2 pipe lengths; L= 8m and 16m. Upper panel: threshold = 0.8; Lower panel: threshold = 0.85.

There is however a difference in terms of interpretation, when the frequency of slugs is evaluated based on a holdup h_L/D of 0.8 or 0.85. It is clear the simulation and measurement agree best for $h_L/D = 0.85$. Moreover, the evolution of the slug frequency along the axis of the pipe is in good agreement with the data, although the result suggests that the simulation time was not enough to acquire all the slugs with lower frequency (0.3 Slug/s). We thus conclude that the data could probably be better predicted with this size of the domain, but for longer simulation time.

DROPLET ENTRAINMENT AND DETACHMENT

Droplet entrainment and detachment has been simulated in a shorter tube, of diameter 0.5m and of length 5m, containing water at a low water holdup, i.e. $h_L/D = 0.14$. Water is injected at a velocity of 0.2m/s while air is injected at a bulk velocity of 20m/s. A splitter plate has been placed by purpose between the two phases for the first 16cm to help flow development and avoid raising issues with two-phase inlet conditions. To perform the simulations, V-LES has been used in order to capture the unsteady behaviour of the flow, in line with the

recommendations and *learnt-lessons* from the section presenting the 2D simulations, that three-dimensional effects are important for free surface deformations. All the more, 3D simulations increase the likelihood of correctly representing the zone of apparition of the first droplets including their size and shape. To be pragmatic though, it is clear that predicting droplets of the mm size would require a very dense grid, which is beyond reach of the available resources. To alleviate this limitation, one could rather resort to a time evolving, sheared, interfacial flow, using periodic boundary conditions (e.g. Gulati *et al.*, 2011).
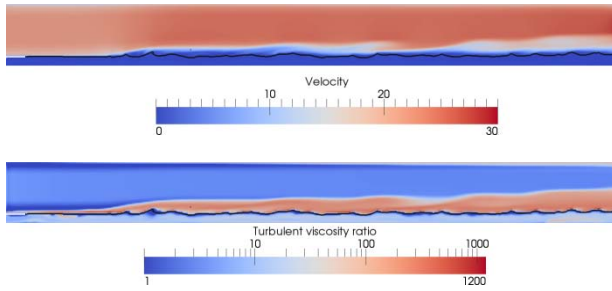

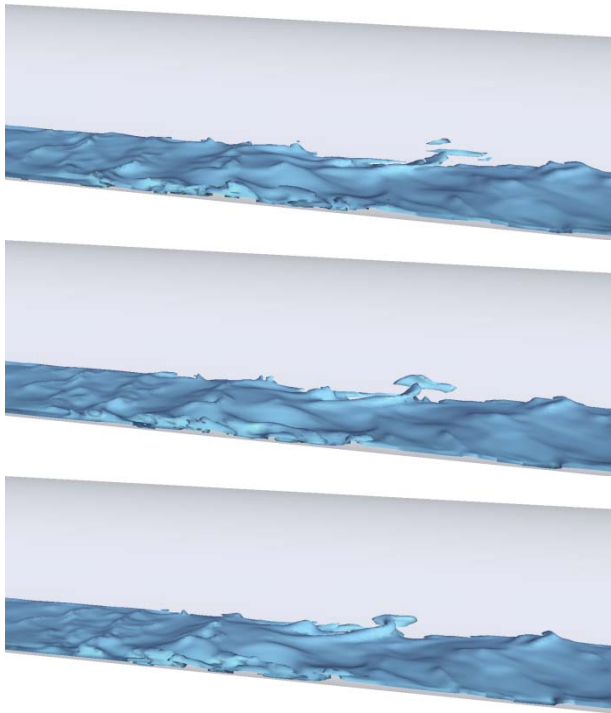Figure 7: Space evolution of the interfacial boundary layer

Figure 8: Surface deformations in the annular flow showing onset of droplet entrainment.

This flow is simulated on a grid consisting of 1.6 Mio cells, with regular cells of 1cm in all directions (580 along the pipe and 58 x 54 for the cross section). Use was made of the IST meshing technique introduced in an early section to represent the pipe inside a simple Cartesian grid. Only high order schemes were employed, for both space discretization and time marching (3rd order RK). Five days were necessary on a 16 core computer in order to simulate 2.6 s of real time.
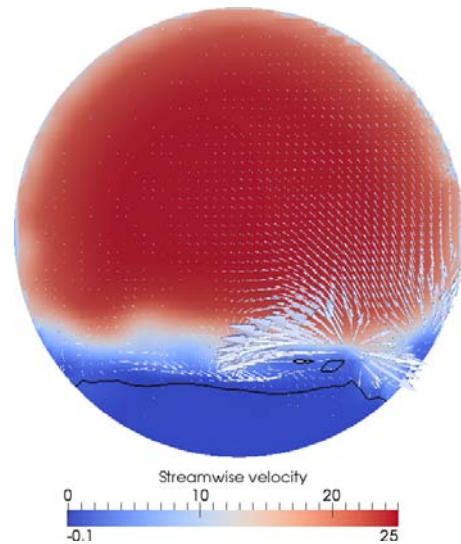

Figure 9: Surface deformations in the annular flow (cross sectional views) showing droplet formation & entrainment.

As was to be expected, the significant difference in velocity between the two phases results in an important shear at the interface, as shown in Fig. 7, displaying streamwise velocity contours and the corresponding turbulent eddy viscosity. The figure clearly shows the boundary layer evolution on top of the interface, which may evolve further to reach spatially fully developing conditions. Be it as it may, we can safely conclude that the computational parameters employed for this simulations are sufficient for the flow to develop (though probably not '*fully*') and return the main mechanisms of interface deformation and water droplet entrainment, as discussed next. The calculations show at least that the code is able to predict shear-induced fragmentation at the gas-liquid interface.

The same figure shows small amplitude perturbations at the surface, which finally results in droplet detachment, as can be clearly seen from the snapshots displayed in Fig. 8. These instabilities start growing downstream around x/D = 1.4 (55cm downstream of the separator plate), and the first droplet detachment occurs only around a streamwise location of 1.5m, corresponding to x/D = 3. These are then entrained in the turbulent air flow, as can be judged from the snapshots presented in Fig. 8. There are subjective reasons to think that the droplets are not well resolved by the grid such that they disappear from the computational domain. But this is actually not sure and further analysis is thus.

Figure 9 shows a cross-flow section highlighting surface deformations and the detachment of two droplets. The contours correspond to the streamwise velocity, which is shown to decay as the interface is approached. The liquid velocity is obviously too small to be displayed. Note that use was made of the near-interface turbulence damping model of Liovic and Lakehal (2007).

CONCLUSION

The development of large-wave structures in gas-liquid 3D pipe flows has been examined using detailed CMFD simulations combining the level set approach for

interface tracking and VLES for turbulence modelling. The investigation complements earlier other ones (e.g. Lakehal, 2008, 2010) which had shown that the approach predicts more details of the flow as compared to the Eulerian two-fluid model, even if this is still computationally expensive. Our predictions show that we can use the ITM approach for a one mile pipeline, using five million cells, which require one week of simulation on a 128 CPU cluster.

As to the first results discussed here, three-dimensional turbulent flows simulations clearly provide a better picture of the flow, in particular regarding the onset of slug formation and frequency, the latter being predicted in accord with the experiment. From a practical standpoint, the results show that today oil transport in portion of pipelines can be approached more rigorously. The information from detailed 3D simulations could actually be employed to calibrate coarse-grained 1D lumped parameter models, which fail under other conditions than straight pipes. But this sort of detailed simulations should be ultimately coupled with a 1D code like OLGA; it could then be activated in fixed critical regions, e.g. over a hill. The results of droplet entrainment are very encouraging, in that details of ligament formation and sheet breakup into droplets could be well reproduced by the simulations. The issue of grid refinement is still posed as to the prediction a cloud of droplets forming and dispersed by turbulence.

ACKNOWLEDGEMENTS

REFERENCES

ANDERSON, R.J., and RUSSEL, T.W.F. (1970), "Film formation in two-phase annular flow", *AIChE J.,* **16**, 26-633.

BADIE, S. (2000), "Horizontal stratifying/annular gas-liquid flow". *PhD Thesis*, University of London, London, UK.

BARNEA, D., and TAITEL, Y. (1993), "A Model for Slug Length Distribution in Gas Liquid Slug Flow", *Int. J. Multiphase Flow*, **19(4)**, 639-651

BROWN, L., HEWITT, G.F., HU, B., THOMSON, C.P., and VERDIN, P. (2008), "Predictions of droplet distribution in low liquid loading, stratified flow in a large diameter pipeline", *In Proc. BHR Conf.* Cannes, France, May 2008.

GULATI, S., BUONGIORNO, J., LAKEHAL, D., (2011), "LEIS of Liquid Entrainment in Turbulent Stratified Flow", In Proc. NURETH-14, Sep. 25-29, Toronto, Ontario, Canada.

HEWITT, G.F. (2005), "Three-phase gas-liquid-liquid flows in steady and transients states", *Nucl. Eng. Design*, **235**, 1303-1316.

JOHANSEN, S.T. , WU, J., and SHYY, W. (2004), "Filter-based unsteady RANS computations". *Int. J. Heat & Fluid Flow*, **25**, 10-21.

LABOIS, M. and LAKEHAL, D. (2011), "Very-Large Eddy Simulation (V-LES) of the Flow across a Tube Bundle", (DOI: 10.1016/j.nucengdes.2011.02.009), *Nucl. Eng. Design*.

LAKEHAL, D., MEIER, M., and FULGOSI, M., (2002), "Interface tracking for the prediction of interfacial dynamics and mass transfer in multiphase flows". *Int. J. Heat & Fluid Flow*, **23**, 242-255.

LAKEHAL, D., (2010), "LEIS for the prediction of turbulent multifluid flows for thermal hydraulics applications", *Nucl. Eng. Design*, **240**, 2096-2106.

LAKEHAL, D. (2008), "Large-scale simulation of stratified gas-liquid flow transition and slug in oil Pipes, *6th Int. Conf. CFD in Oil & Gas, Metallurgical & Process Industrie*s, SINTEF/NTNU, Trondheim NORWAY, 10-12 June 2008.

LIN, P.Y., and HANRATTY, T.J., (1986), "Prediction of the initiation of slugs with linear stability theory, *Int. J. Multiphase Flow,* **12**, 79–98.

LIOVIC, P. and LAKEHAL, D., (2007), "Multi-Physics Treatment in the Vicinity of Arbitrarily Deformable Fluid-Fluid Interfaces", *J. Comp. Physics*, **222**, 504-534.

SUSSMAN, M., SMEREKA, P., and OSHER, S., (1994), "A Level set approach for incompressible two-phase flow". *J. Comp. Physics*. **114**, 146-158.

TAITEL, Y and DUKLER, A.E, (1976), "A Model for Flow Regime Transitions in Horizontal and Near Horizontal Gas-Liquid Flow", *AlChE J.*, **22**, 47-55.

TRANSAT User Manual. ASCOMP GmbH Switzerland, 2010. www.ascomp.ch/transat.

UJANG, P.M., HALE, C.P., LAWRENCE, C.J., and HEWITT, G.F., (2006), "Slug initiation and evolution in two-phase horizontal flow." *Int. J. Multiphase Flow*, **32**, 527-552.

UJANG, P.M., (2003), "Studies of Slug Initiation and Development in Two-Phase Gas-Liquid Pipeline Flow" PhD Thesis, University of London, London, UK.

VALLURI, P, SPELT P.D.M., LAWRENCE, C.J. and HEWITT, G.F. (2008), "Numerical simulation of the onset of slug initiation in laminar horizontal channel flow ", *Int. J. Multiphase Flow*, **34**, 206-225.

8th International Conference on CFD in Oil & Gas, Metallurgical and Process Industries
SINTEF/NTNU, Trondheim Norway
21-23 June 2011

CFD11-168

UNDERSTANDING VISCOUS FLUID TRANSPORT AND MIXING IN A TWIN SCREW EXTRUDER

Paul W CLEARY[1*] and **Martin Robinson**[2]

[1] CSIRO Mathematics, Informatics & Statistics, Private Bag 33 Clayton South, AUSTRALIA

[2] University of Twente, NETHERLANDS

* E-mail: Paul.Cleary@csiro.au

ABSTRACT

The transport and mixing properties of a co-rotating twin screw extruder with both screw and kneading block elements is explored using the Smoothed Particle Hydrodynamics (SPH) method. The use of a Lagrangian method enables simulation of real extruders without the difficulties associated with extreme mesh deformation due to the conflicting rotation of the impellors and the small gaps between them. The cross-channel and down-channel fluid transport and mixing in both fully flighted screw elements and kneading blocks is analysed. The effect of parametric variations in both mixing elements on the nature of the fluid flow and the mixing are explored; specifically the effects of varying the screw pitch, kneading block stagger angle and gap size between the rotating elements.

Keywords: SPH, mixing, viscous liquid, Lagrangian.

INTRODUCTION

Twin screw extruders are popular devices in the food, polymer and other industries where the mixing of highly viscous fluids is required. While their use is widespread in industry, there is still a lack of understanding of the flow patterns and their effect on the mixing and fluid transport properties of the extruder.

The methodology used in this paper follows on from two previous papers by the authors. In Robinson et al. (2008) we presented 2D simulations of a Twin Cam mixer and successfully validated them against published FEM and experimental results. Robinson and Cleary (2011) analysed the mixing processes in a similar Twin Cam mixer and explored the effects of varying the impeller geometry and operating conditions. This paper extends the methodology developed in these papers to a more realistic 3D geometry, namely the Twin Screw Extruder.

In recent years there has been an increasing emphasis on the CFD modelling of Twin Screw Extruders (Connelly and Kokini, 2007; Rios et al. 1998; Cheng and Manas-Zloczower, 1998; Ishikawa et al. 2001, 2002; Kajiwara et al. 1996; Lawal and Kalyon 1995; Valette et al. 2008). These simulations provide a more detailed insight into the flow than experimental studies, and allow greater flexibility and reduced setup time in varying the geometry or the operational parameters.

The Finite Element Method (FEM) is the numerical technique most often applied to such systems. Connelly and Kokini (2007) and Bertrand et al. (2003) simulated a 2D cross-section of a Twin Screw Extruder. At low Reynolds numbers, the 2D assumption is valid for extruders containing only screw elements. However, the inclusion of kneading blocks creates a fully 3D flow field. Cheng and Manas-Zloczower (1998), Ishikawa et al. (2001), Kajiwara et al., Lawal and Kalyon (1995) and Valette et. al. (2008) all performed 3D simulations of a Twin Screw Extruder using FEM. However, all these authors simulate either the screw or kneading block element in isolation, whereas in this paper both elements are included at the same time allowing the interaction between them to be investigated.

The Smoothed Particle Hydrodynamics (SPH) method of Monaghan (2005) is used to simulate flow and mixing in the Twin Screw Extruder. SPH is a Lagrangian particle method for simulating fluid flow. Rather than using a fixed grid, the fluid variables are interpolated over particles which move with the fluid velocity. Each particle represents a volume of fluid, so it can have its own physical properties, and the advection is obtained automatically from the motion of the particles. SPH has proved to be a useful method for modelling many different classes of industrial applications. For example, Cleary et al. (2007) discusses the use of SPH in die casting, resin transfer moulding, pyrometallurgical processes with reactive solids, slurry flow in sag mills and the mixing of large particulate solids.

The primary advantages of using the SPH method over FEM for this application is that SPH naturally handles the use of complex, moving geometries and also fluid free-surfaces. The geometry of the Twin Screw Extruder contains a pair of intermeshing and rotating screws or kneading blocks within a stationary barrel-shaped outer channel. For an accurate FEM simulation, this would normally require re-meshing at every timestep, or the use of a method such as the Lagrange multiplier based fictitious domain method (Bertrand et al. 2003). Instead, SPH boundaries are constructed from

particles following the approach of Monaghan (2003). Moving components such as impellors can be included in a simulation by assigning the appropriate velocity to each boundary particle at each time based on its rigid body motion.

SPH METHOD

The SPH formulation used for this paper is identical to the one described in Robinson et al. (2008). It is a quasi-incompressible method that uses an equation of state given by Cole (1948) and evolves the particle densities using the SPH version of the continuity equation. The traditional cubic spline kernel is used to interpolate the fluid equations across the particles and the viscous term used is described by Monaghan (2005) The no-slip boundaries are modelled using a single layer of boundary particles and the sharp corners are modelled using a multiple-normal technique proposed by Monaghan (2003). Robinson et al. (2008) made a detailed comparison of the predictions of the SPH method to other numerical methods and to experiment for a two dimensional twin CAM mixer. The SPH method was more accurate in predicting the advection and mixing patterns in this mixer (which is equivalent to a single cross section of the three dimensional geometry used in this study). Further validation is also given in Cleary et al. (2007).

EXTRUDER AND ITS OPERATING CONDITIONS

The geometry of the twin screw extruder is based on the 2D cross-section depicted in Figure 1. The outer casing of the mixer is a double barrelled enclosure, containing two screw elements. Each element is a double flighted screw with a tip angle of $\alpha = 11.61$ degrees. The radius of each tip and the separations of the screw elements are chosen so that the minimum distance between them is 1.5 mm. The gap between the screw tips and the outer casing is 1.5 mm.
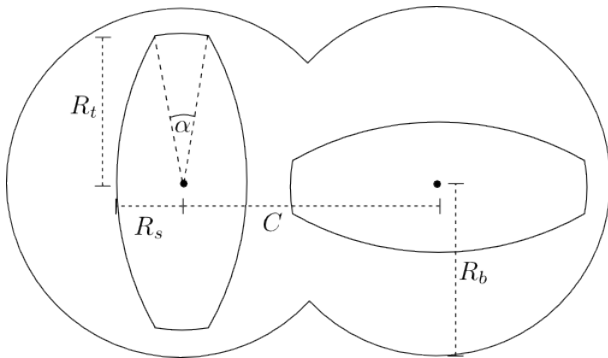
Figure 1: Cross-section of the Twin screw Extruder. $R_t = 25$ mm and $R_s = 13.75$ mm is the maximum and minimum radii of the screw elements. The centres of each barrel (and each screw element) are separated by $C = 40.25$ mm, and the radius of each barrel is $R_b = 26.5$ mm. The angle of each screw tip is set to $\alpha = 11.61$ degrees.

This cross-section can be used to generate two commonly used screw elements. The first is a fully-flighted (FF) screw, which is swept out by continuously rotating each screw cross-section while moving along

the rotation axis of the screw. The relevant parameters for this element are the screw pitch p and the extruder length L. The second type is the Kneading Blocks (KB), which is generated by rotating each cross-section in discrete jumps. The parameters for the KB are the block width d, the extruder length L and the block stagger angle β, which is the difference in rotation angle between subsequent blocks.

This paper examines the mixing due to these elements. The three base extruder geometries used are:

1. A combination extruder, with each screw element comprising a central Kneading Element (KE) section of length $L_{ke} = 137.53$ mm surrounded by two FF sections, both with length $L_{ff} = 66.67$ mm. Figure 2 shows this geometry.
2. Two FF mixer elements, each of length $L = 50$ mm. The pitch of each screw element is $p = 50$ mm.
3. Two KB elements of length $L = 75$ mm. The width of each kneading disc is $d = 12.5$ mm and each disc is rotated by $\beta = 30$ degrees relative to the previous disc.

In all cases the axis of rotation is chosen to be along the z-coordinate axis. The boundaries at either end of the extruder are periodic boundaries, and the fluid is transported by the rotational movement of the twin screw elements. The mixer is completely filled with a viscous fluid.
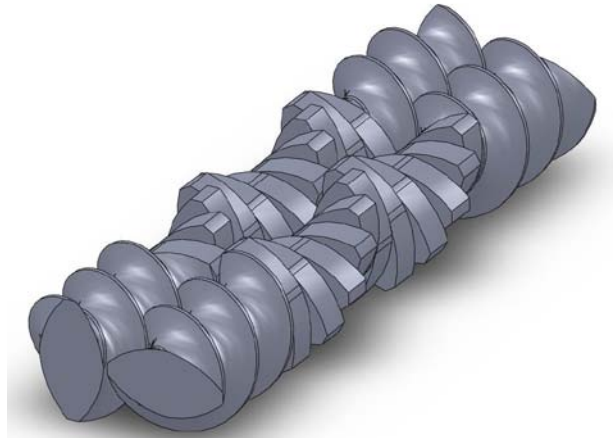

Figure 2: Screw elements for Geometry 1. The outer casing of the mixing is not shown.

The rotation speed of each screw element is $\omega = 1$ rad/s. Using the gap between the elements as the characteristic length, the Reynolds number of the simulation is Re = 37.5.

TWIN SCREW EXTRUDER WITH SCREW AND KNEADING MODULES

This section presents the results from an SPH simulation of the full twin screw mixer geometry, with the combined screw and kneading block modules. In order to analyse the transport and mixing within the device, two Lagrangian volumes of fluid are chosen.
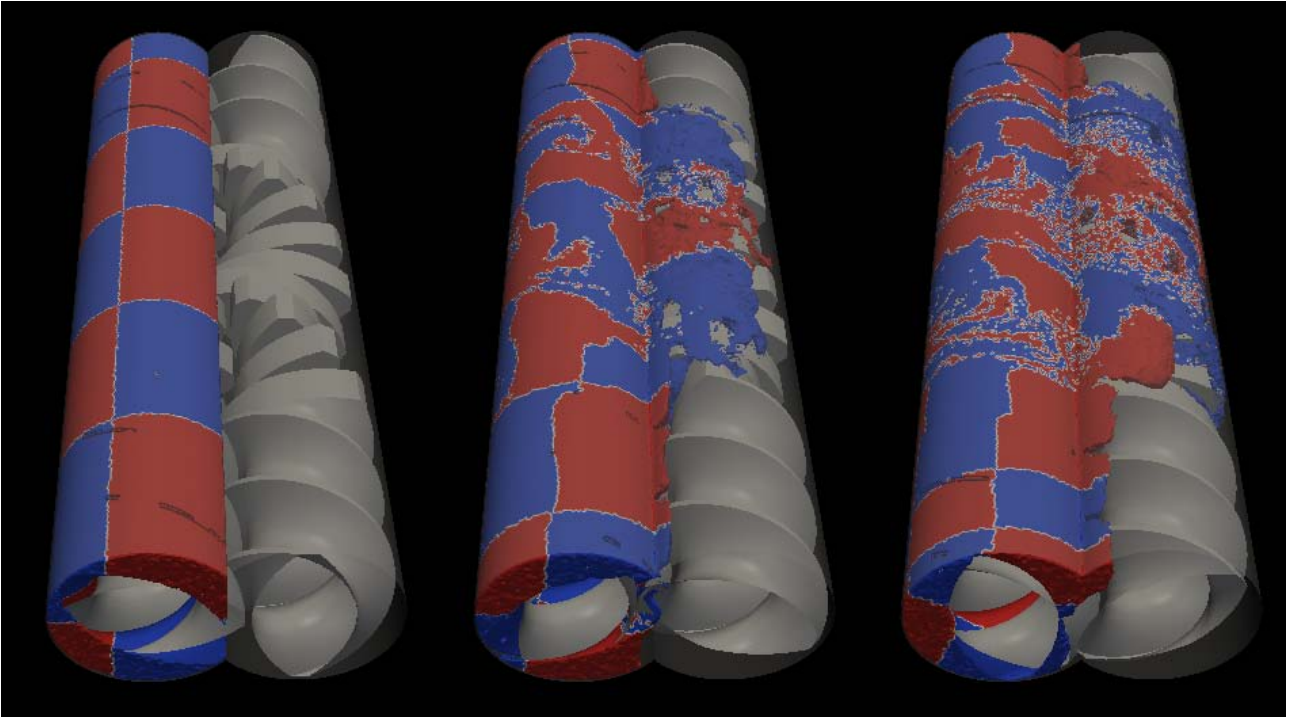
Figure 3: Cross-channel mixing shown by the evolution of Volume One for *t* = 0 s (left), t = 2 s (middle) and *t* = 4 s (right).
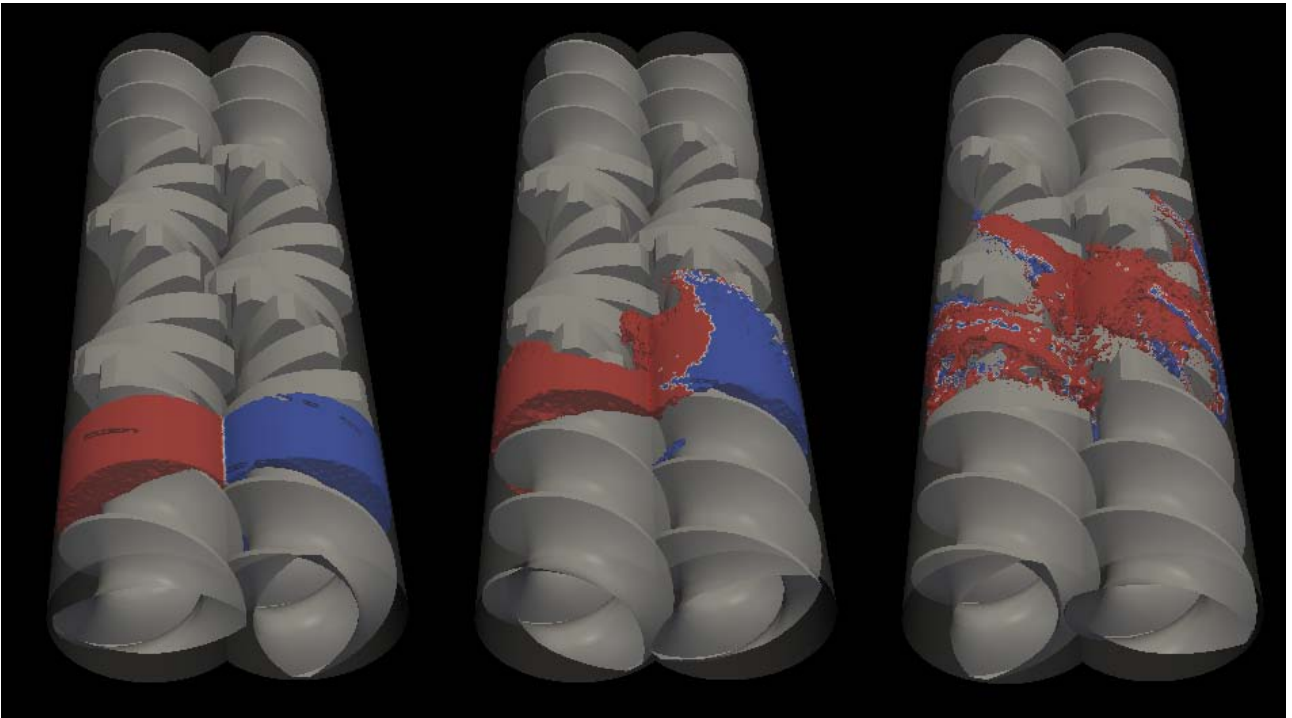
Figure 4: Down-channel mixing shown by the evolution of Volume Two for *t* = 0 s (left), *t* = 2 s (middle) and *t* = 4 s (right).

- Volume One is defined as all the fluid to the left of the *x* = 0 plane at *t* = 0 s. This volume is all the fluid in the left hand barrel of the mixer, and as the simulation proceeds, this volume of fluid will be transported across the centre plane of the mixer. The mixing of this volume is therefore representative of the cross-channel mixing.
- Volume Two is all the fluid within the two planes *z* = 33 mm and *z* = 33+25 mm, where z = 33 mm is a plane in the middle of the first screw module.

This volume will be mixed with the remainder of the fluid in the positive and/or negative axial direction, and is therefore representative of the overall axial or down-channel mixing in the device.

Figure 3 shows the evolution of Volume One over 0 < t < 4 s, which corresponds to approximately 3/4 of revolution of the impellors. The surface of the Lagrangian volume is initially shaded with arbitrary red

and blue checkerboard pattern in order to see the fluid transport within the volume.

The cross-channel mixing shown by the transport of Volume One can be divided into two regions surrounding both the screw and kneading block sections of the mixer. The screw section provides minimal mixing and mainly serves as a bulk transport process in the positive z direction (down the length of the mixer). There is a small amount of cross-channel mixing and this can be seen at the bottom of each plot, as the initially vertical interface between the fluid in the two barrels is stretched out in the direction of fluid flow around the two screws.

However, the mixing in the screw section is small compared to that surrounding the kneading block section. Over the course of the 3/4 revolution shown in Figure 3, Volume One is considerably deformed around the kneading blocks. A large proportion of the volume is transported into the opposite barrel, and the checkerboard pattern is quickly lost due to the mixing processes within the volume. There is also some evidence of axial mixing due to the kneading blocks, as shown by the increasing axial spread of fluid in the right hand barrel over time. However, this is more clearly shown by the transport of Volume Two.

Figure 4 shows the evolution of Volume Two over the same time period ($0 < t < 4$ s). The transport of this volume of fluid shows the axial or down-channel mixing within the twin screw mixer. Once again the surface of the volume is shown and coloured with an arbitrary pattern in order to visualize the mixing. In this case the fluid in each barrel is given a different colour in order to show some of cross channel mixing and to relate this to the transport of Volume One.

As seen previously in the evolution of Volume One, the mixing of Volume Two around the screw modules is minimal and this section only serves to transport the fluid to the main mixing region (i.e. the kneading blocks). There is little deformation of the surface of Volume Two in the axial direction.
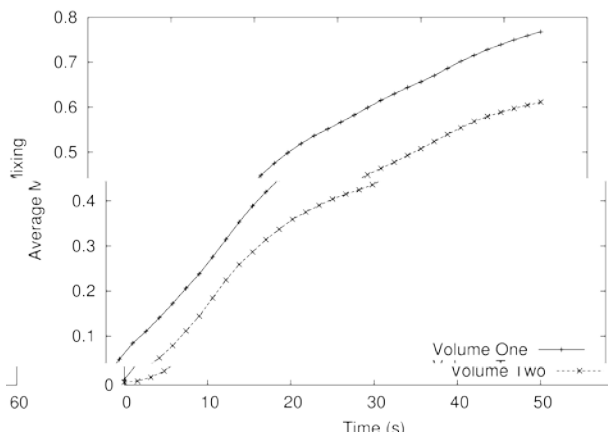
Figure 5: Average mixing <M> versus time for volume one (cross-channel mixing) and volume two (down-channel mixing).

Once the fluid reaches the kneading blocks (see the snapshot at $t = 2$ s) it quickly starts to deform and stretch. The fluid in the right hand barrel is pulled forward in the positive z direction while the fluid in the left hand barrel is held back. At the same time, there is

a fast rotation of fluid clockwise around the mixer, so that the red fluid is transported up and across to the right hand barrel, which the blue is moved down and across to the left hand side (this is obscured in the figure due to the camera angle). At $t = 4$s some reasonable stretching of Volume 2 has occurred, but the amount of mixing is still relatively small.

Figure 5 shows evolution of the average mixing <M> over time for both fluid volumes using a measure that considers the degree of homogeneity of the fluid (see Robinson et al. 2008 for details). This measure is zero for fully unmixed and unity for fully mixed. This allows for a quantitative comparison of the cross-channel and the down-channel mixing rates. In some cases a small non-zero initial value of the measure is observed due to aliasing at the interface between materials. This occurs because there are always some of the averaging cells that are part filled with both materials even in a perfectly unmixed system. The precise value of this initial value depends on the degree of alignment of the averaging cells with the location of the interface. In practice this is small and does not affect the quantification of the mixing.

At small times ($t < 5$ s), the average mixing rate of Volume Two is much lower than Volume One. During much of this time, Volume Two is still in the screw section of the mixer and has not yet reached the kneading blocks. Meanwhile, approximately half of Volume One has moved into the kneading block section, and this strongly increases the average mixing for this fluid volume. While the mixing rate of Volume Two does increase once the fluid reaches the kneading blocks, it is always lower than that of Volume One and it is clear from Figure 5 that the mixing in the cross-channel direction is stronger than along the axis of rotation of the mixer.

INFLUENCE OF SCREW AND KNEADING BLOCK PARAMETERS

Next we consider the effect of variations in the geometric parameters of both impellor types in order to quantify what influence these parameters have on the overall mixing rates. To do this separate screw and kneading block geometries (geometries 2 and 3) are used for these comparisons, instead of the combined impellor geometry (geometry 1). The parameter used to assess the mixing rate is the previously used average mixing measure <M>.

Figure 6 shows the effects of varying the screw pitch length of the screw impellors for geometry 2. A longer pitch means that the length of one rotation of the screw is increased, resulting in an increased distance between subsequent flights (tips) of the screw. The bulk movement of fluid along the mixer is unaffected, as the rotation speed of the screw is constant. The mixing results for both Volume One and Two are consistent, and show that an increase in the pitch length leads to an increase in mixing rate. The effect is slightly stronger for the down-channel mixing. The down-channel mixing is due to changes in the axial velocity near the center-line of the mixer (where the twin screws intermesh). An increased sensitivity of the down-

channel mixing due to a change in pitch length is consistent with this, as a longer pitch will change the angle that the two screws intermesh and is expected to lead to significant changes to the flow field in this region.
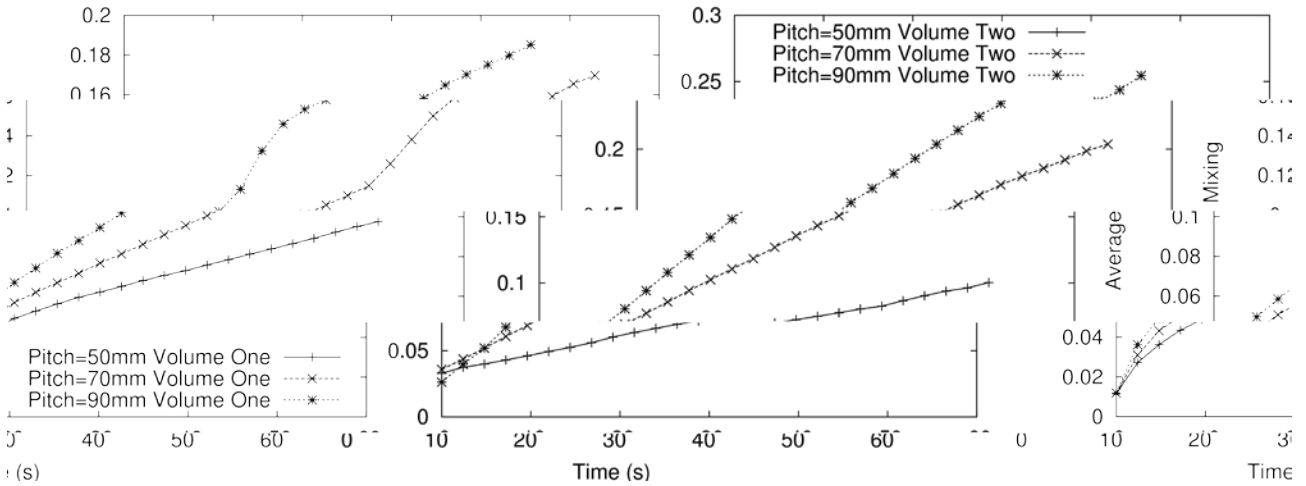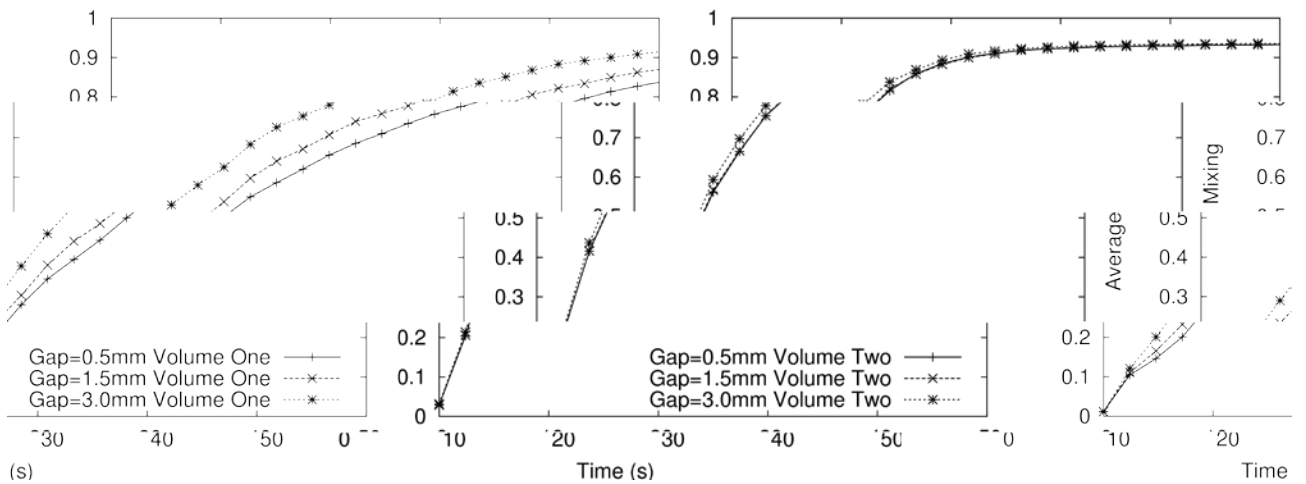

Figure 6: Average mixing versus time for the screw impellors with varying pitch.
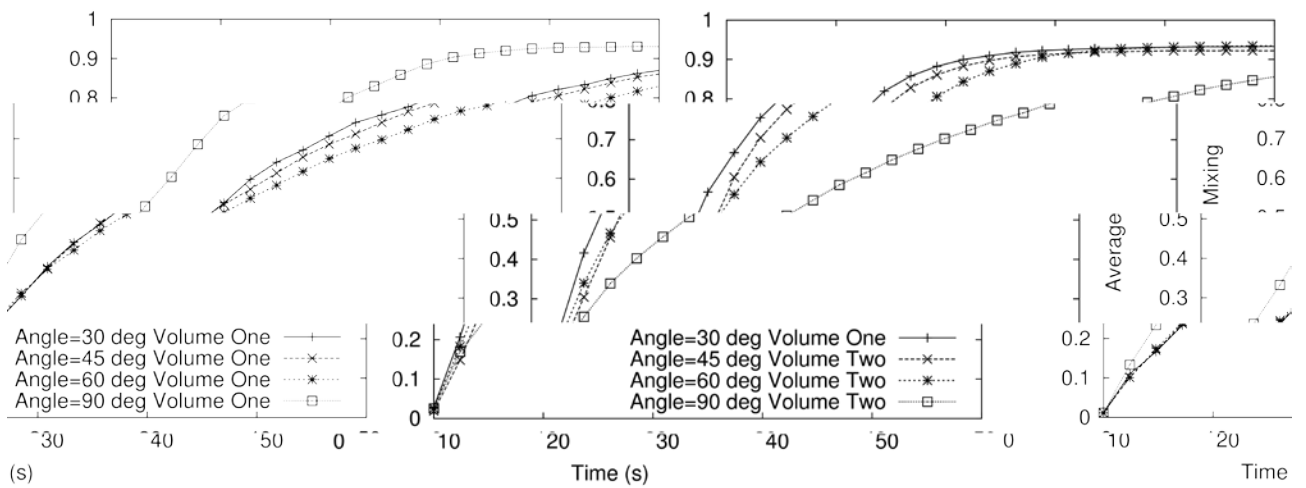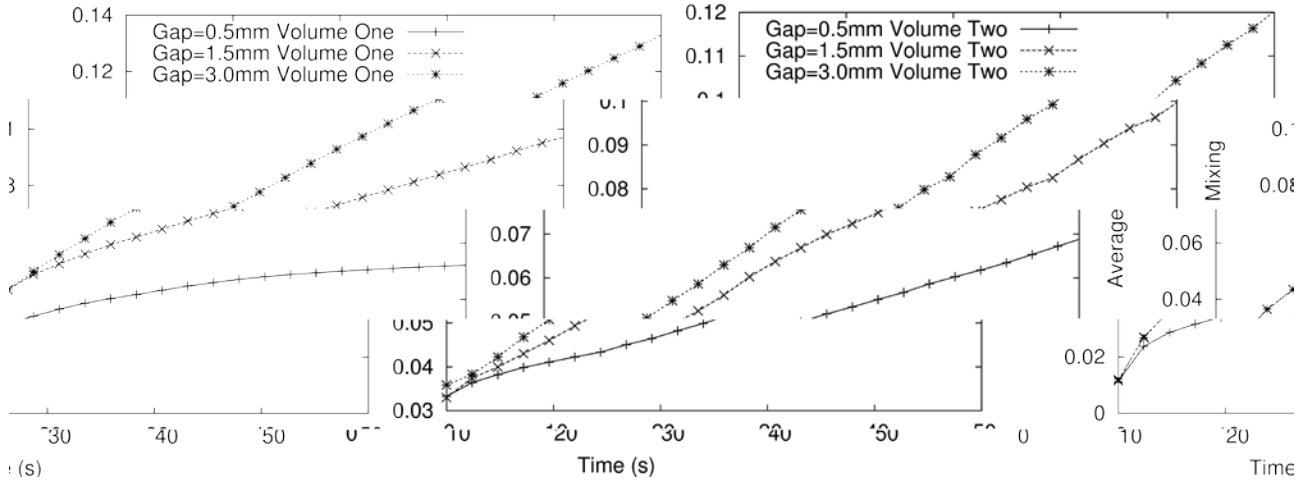

Figure 7: Average mixing versus time for the kneading block impellors with varying block stagger angle.

Figure 8: Average mixing versus time for the kneading block impellors with varying gap width.

Figure 9: Average mixing versus time for the screw impellors with varying gap width.

Figure 7 shows the effect of the stagger angle between subsequent kneading blocks on the average mixing for geometry 3. The range of angles considered here range from 30 degree (the stagger angle used in the original geometry) to 90 degree, where each kneading block is perpendicular to the previous. In general, the original stagger angle of 30 degree leads to the best mixing results. An increase beyond this value leads to a decrease in the rate of both down-channel and cross-channel mixing. However, this trend breaks down at a stagger angle of 90 degree. For this case, the kneading blocks are no longer positioned in a rough "discrete screw" shape but are simply alternating between two different angles. As would be expected, this significantly reduces the down-channel mixing in the device. At the same time, the cross-channel mixing is greatly increased due to the fact that the force exerted on the fluid by the kneading blocks is now primarily acting in the plane perpendicular to the rotational axis of the mixer. These results are consistent with those by Lawal and Kalyon (1995), who visualised the transport of a "blob" of fluid around the kneading block geometry with stagger angles of 30 and 90 degree, and found that the blob experienced minimum spreading in the axial direction for the 90 degree case.

Figure 8 (screw impellors) and Figure 9 (kneading blocks) show the effect of varying the gap size between the two rotating impellors. The general effect of increasing gap size on the mixing is consistent across both geometries and both directions considered. An increase in the gap size leads to an increase in the mixing in both the cross-channel and down-channel direction. The effect is stronger in the cross-channel direction. In the 2D Boundary Element Method simulation of a twin screw mixing by Rios et al (1998), the authors found, using a visualization of a tracer line, that the flux of fluid between the two barrels of the mixer is greater with an increase in the gap size. Their 2D simulations would more closely represent the mixing around the kneading blocks, rather than the screw, and are consistent with the mixing measure data that we have for our 3D kneading block simulations.

This leads to the conclusion that, for the kneading blocks, the effect of varying the gap size on the flow is to increase the transport of fluid solely in the cross-channel direction, with little or no effect of the mixing down the length of the mixer. For the screw module, the angle normal to the surface of the impellor in the intermeshing region is no longer perpendicular to the rotation axis, and therefore a comparison to a 2D simulation is no longer valid. However, the general effect of increased gap size equaling increased mixing is also true here, but this now applies to both the cross-channel and down-channel mixing.

CONCLUSION

We have used numerical simulations of Twin Screw extruders to gain insight into their mixing and transport properties and how these are affected by changes in geometry or fluid fill level. The SPH method was used to simulate the fluid, due to the straight forward incorporation of free-surfaces and complex intermeshing boundary geometry, as well as its suitability to mixing problems due to its Lagrangian nature.

In order to elucidate the mixing processes in the Twin Screw extruder we examined the fluid transport in and around two different impellor geometries comprising of a screw module and a set of kneading blocks staggered by a constant angle. The mixing around the screw module was found to be minimal and its main function was to transport the fluid down the length of the mixer. The kneading blocks functioned as the primary mixing device. Even rotating at the same speed (as the screws), the kneading blocks generate a complex velocity field with maximum velocities an order of magnitude faster than the screw impellors. This field was comprised of strong components both in the cross-sectional plane of the mixer, where it generally served to move the fluid clockwise around the impellors, as well as a strong flow backwards and forward along the axis of rotation. Given that 2D approximations can sometimes be used to model the transport in a Twin Screw extruder, the highly 3D

nature of this flow at a low Reynolds number (Re = 37.5) means that these such approximations should be treated with caution.

The velocity field around the kneading blocks generated strong mixing in all directions. It was found, however, that the mixing rate in the down-channel direction was dominant, contrary to any expectations that the strongest mixing would occur in the same rotational plane as the impellors.

In order to evaluate the effect of different geometric parameters on the mixing, we have calculated measures of mixing in simulations with varying screw pitch length, kneading block stagger angle and gap size between the impellors. Increasing the screw pitch length cause the mixing in both the down-channel and cross-channel directions to be increased. Increasing the kneading block stagger angle in general resulted in a reduction in mixing rate, except at 90% where the fluid transport in the axial direction was restricted. The gap size between the impellors was positively correlated with the cross-channel mixing, but had little or no effect on the down-channel mixing for the kneading blocks.

REFERENCES

AVALOSSE, T. and RUBIN. Y., (1999), "Analysis of mixing in co-rotating twin screw extruders through numerical simulation". *Proc. SPE/ANTEC 1999,* 322+. CRC Press.

BERTRAND, F., THIBAULTA, F., DELAMAREB, L., and. TANGUYA. P. A., (2003), "Adaptive finite element simulations of fluid flow in twin-screw extruders", *Computers & Chemical Engineering,* **27,** 491–500.

BIGIO, D., and WANG, K., (1996), "Scale-up rules for mixing in a non-intermeshing twin-screw extruder", *Polymer Engineering & Science*, **36**, 2832–2839.

CHENG, H., and MANAS-ZLOCZOWER, I., (1998), "Distributive mixing in conveying elements of a zsk-53 co-rotating twin screw extruder", *Polymer Engineering and Science,* **38**, 926–935.

CLEARY, P.W., PRAKASH, M, HA, J., STOKES, N., SCOTT, C., (2007), "Smooth Particle Hydrodynamics: Status and future potential", *Progress in Computational Fluid Dynamics,* **7**, 70-90.

COLE, R. (1948), "Underwater Explosions", Princeton, NJ: Princeton University Press.

CONNELLY, R. and KOKINI, J., (2007), "Examination of the mixing ability of single and twin screw mixers using 2d finite element method simulation with particle tracking". *Journal of Food Engineering,* **79**, 956–969.

DE GRAAF, R. A., WOLDRINGH, D. J., and JANSSEN, L. P. B. M., (1999), "Material distribution in the partially filled zone of a twin-screw extruder", *Advances in Polymer Technology*, **18**, 295–302.

ELLERO, M., AND TANNER, R., (2005), "SPH simulations of transient viscoelastic flows at low reynolds number", *Journal of Non-Newtonian Fluid Mechanics,* **132**, 61–72.

HOSSEINI, S. M., MANZARI, M. T., AND HANNANI, S. K., (2007), "A fully explicit three-step sph algorithm for simulation of non-Newtonian fluid flow", *International Journal of Numerical Methods for Heat and Fluid Flow*, **17,** 715–735.

ISHIKAWA, T., KIHARA, S-I., AND FUNATSU. K., (2001), "3-d non-isothermal flow field analysis and mixing performance evaluation of kneading blocks in a co-rotating twin srew extruder", *Polymer Engineering & Science*, **41**, 840–849.

ISHIKAWA, T., AMANO, T., KIHARA, S-I., and FUNATSU, K., (2002), "Flow patterns and mixing mechanisms in the screw mixing element of a co-rotating twin-screw extruder". *Polymer Engineering & Science*, **42**, 925–939.

KAJIWARA, T., NAGASHIMA, Y., NAKANO, Y., AND FUNATSU. K., (1996), "Numerical study of twin-screw extruders by three-dimensional flow analysis-development of analysis technique and evaluation of mixing performance for full flight screws", *Polymer Engineering & Science,* **36**, 2142–2152.

KAO, S. V., AND ALLISON, G. R., (1984), "Residence time distribution in a twin screw extruder", *Polymer Engineering and Science,* **24**, 645–651.

LAIGLE, D., LACHAMP, P., AND NAAIM, M., (2007), "SPH-based numerical investigation of mudflow and other complex fluid flow interactions with structures", *Computational Geosciences,* **11**, 297–306.

LAWAL, A., and KALYON. D. M., (1995), "Mechanisms of mixing in single and co-rotating twin screw extruders", *Polymer Engineering & Science*, **35**, 1325–1338.

MONAGHAN. J. J., (2005), "Smoothed particle hydrodynamics". *Reports on Progress in Physics,* **68**, 1703–1759.

MONAGHAN, J. J., KOS, A., .and ISSA. N., (2003), "Fluid motion generated by impact", *Journal of Waterway, Port, Coastal, and Ocean Engineering,* **129**, 250–259.

RIOS, A.C., GRAMANN, P.J., and OSSWALD, T.A., (1998), "Comparative study of mixing in corotating twin screw extruders using computer simulation", *Advances in Polymer Technology*, **17**, 107–113.

ROBINSON, M., CLEARY, P.W., MONAGHAN J.J., (2008), "Analysis of mixing in a Twin-Cam mixer", *AIChe Journal*, **54**, 1987-1998.

ROBINSON, M. and CLEARY, P. W., (2011), "The influence of cam geometry and operating conditions on chaotic mixing of viscous fluids in a twin cam mixer", *AIChE Journal*, **57**, 581–598.

RODRIGUEZ-PAZ, M. X. AND BONET, J. A., (2004), "Corrected smooth particle hydrodynamics method for the simulation of debris flows", *Numerical Methods for Partial Differential Equations,* **20**, 140–163.

SHADDEN, S.C., LEKIEN, F., MARSDEN, J.E.. (2005), "Definition and properties of Lagrangian coherent structures from finite-time Lyapunov exponents in two-dimensional aperiodic flows". *Physica D*, **212**, 271–304.

SHAMEKHI, A., SADEGHY, K., BAHRAMI, M. N., AND NAEI, M. H., (2008), "Using mesh free method for numerical simulation of non-Newtonian

fluid flow over a step", *Journal of the Society of Rheology Japan,* **36**, 19–27.

SHAO, S., and LO, E., (2003), "Incompressible sph method for simulating Newtonian and non-Newtonian flows with a free surface", *Advances in Water Resources,* **26**, 787–800.

VALETTE, R., VERGNES, B., and COUPEZ. T., (2008), "Multiscale simulation of mixing processes using 3d-parallel, fluid-structure interaction techniques". *International Journal of Material Forming,* **1**, 1131–1134.

VAN DER GOOT, A. J., POOIWER, O., and JANSSEN, L. P. B. M., (1998), "Determination of the degree of fill in a counter-rotating twin screw extruder". *Polymer Engineering and Science,* **38**, 1193–1198.

8th International Conference on CFD in Oil & Gas, Metallurgical and Process Industries
SINTEF/NTNU, Trondheim NORWAY
21-23 June 2011

CFD11-169

EULER–LAGRANGE MODELING OF MELTING AND SOLIDIFICATION WITH MOVING SOLID PARTICLES

Frank DIERICH[1]*, **Petr A. NIKRITYUK**[†]

[1]CIC VIRTUHCON, Department of Energy Process Engineering and Chemical Engineering,

Technische Universität Bergakademie Freiberg, 09596 Freiberg, GERMANY

* E-mail: frank.dierich@vtc.tu-freiberg.de
[†] E-mail: petr.nikrityuk@vtc.tu-freiberg.de

ABSTRACT

This work is devoted to the development of a mathematical and numerical model for the modeling of particulate flows during the phase change processes including particle melting and solidification. The model used in the simulations is based on the direct numerical simulation (DNS) approach where no additional semi-empirical expressions for the drag force and the heat transfer between particle and fluid are necessary. The hydrodynamic forces acting on the particles are calculated directly through the surface integrals. The particle collisions are modeled directly using the hard sphere approach, taking into account the inelastic collisions. The interface velocity of the melting/solidification (solid-liquid) is calculated by means of the Stefan condition for each particle. As an illustration of the model we consider a two-dimensional system consisting of several circular ice dendrites (40) moving up due to the density difference in a two-dimensional channel filled with hot (first case) and under-cooled (second case) water. The analysis of numerical simulations showed the importance of taking into account the viscous torques in the calculation the melting particle trajectories. This effect is attributed to particles rotation near the walls caused by the Saffman force. However, surprisingly in the case of growing particles this effect does not have significant influence on the particle trajectories.

Keywords: phase change, particles, DNS.

NOMENCLATURE

Greek Symbols
ε Volume fraction, $[-]$
λ Heat conductivity, $[\text{W K}^{-1}\,\text{m}^{-1}]$
ρ Density, $[\text{kg m}^{-3}]$
μ Dynamic viscosity, $[\text{kg m}^{-1}\,\text{s}^{-1}]$
Ω Angular velocity, $[\text{s}^{-1}]$

Latin Symbols
A Area, $[\text{m}^2]$
c_p Heat capacity, $[\text{J kg}^{-1}\,\text{K}^{-1}]$
F Force, $[\text{kg m s}^{-2}]$
Fo Fourier number, $[-]$
Gr Grashof number number, $[-]$
g Gravitational acceleration, $[\text{m s}^{-2}]$
h_f Latent heat, $[\text{J kg}^{-1}]$
I Moment of inertia, $[\text{kg m}^2]$
m Mass, $[\text{kg}]$
p Pressure, $[\text{Pa}]$

Re Reynolds number, $[-]$
u Velocity, $[\text{m s}^{-1}]$
T Temperature, $[\text{K}]$
T_M Torque, $[\text{N m}]$
t Time, $[\text{s}]$
V Volume, $[\text{m}^3]$

Sub/superscripts
0   Initial or reference value
av   Average
i   Particle index

INTRODUCTION

The problem of modeling solid-liquid two-phase flows including physical and chemical transformations is the subject of intense research in many engineering sciences, e.g. in chemistry, metallurgy and geophysics. The basic applications, where solid-liquid flows play the most important role, are fluidized beds, sedimentation columns, slurries and mining. These applications have motivated increasing theoretical and experimental studies of solid-liquid two phase flows. For a detailed review of existing works devoted to the multi-scale modeling of two-phase flow, in particular fluidized beds, we refer the reader to the works published by van der Hoef *et al.* (2008) and Zhu *et al.* (2008).

Applied to the modeling of two-phase flows with solidifying and melting particles the so-called Euler-Euler models are basically used, e.g. see Beckermann and Wang (1996) and Wu and Ludwig (2006). The Euler-Euler models use volume-averaged mass, momentum and energy conservation equations written for each phase in Eulerian space. However, additional source terms in each conservation equation are responsible for the mass, momentum and energy change between the phases (Wu and Ludwig, 2006). It should be noted that, in spite of numerous progress in prediction of dendritic flows, e.g. see Wu and Ludwig (2006), a classical Euler-Euler multiphase model fails to predict adequately the sedimentation of free floating dendrites, for example see the comparison between numerics and experiment published by Beckermann and Wang (1996).

Due to the microscale character of the phase-change process occurring at the interface between solid and fluid phases, the most appropriate model to capture basic physics of moving melting or growing particles is the so-called *direct numerical simulations model* (DNS). It should be noted that originally the term DNS comes from turbulence modeling, e.g. see the

review of Moin and Mahesh (1998), where the "DNS"-term implies that the size of smallest turbulent vortex is larger than the smallest cell in a computational grid. Applied to simulations of moving particles the main idea of DNS models is to embed an irregular solid particle/particles into a larger simple domain and to specify no-slip boundary conditions on the particle boundaries. Thus, the fluid flow is computed only between the solid particles. Basically in DNS models, the hydrodynamic forces acting on the particles are calculated directly through the surface integrals without the use of any semi-empirical correlations. The particle collisions are modeled directly by use of the hard or soft sphere approaches, taking into account the inelastic collisions.

In spite of numerous works devoted to the direct numerical simulation of the isothermal particulate flows, e.g. see the representative works Pan *et al.* (2002) (3D simulation of 1204 spheres sedimentation using the grid with $3.3 \cdot 10^6$ nodes), and Wan and Turek (2007) (sedimentation of 120 particles in a 2D cavity), there are only few works concentrated on modeling the heat and mass transfer process in solid-fluid two-phase flows, e.g. see Gan *et al.* (2003); Yu *et al.* (2006); Feng and Michaelides (2008, 2009), where basically only 2D simulations are presented. In particular, comprehensive DNS modeling of single cylindrical particles settling and melting in a hot fluid with Prandtl number of $Pr = 0.7$ has been carried out by Gan *et al.* (2003). It was shown that the melting rate of each particle has a local character and strongly depends on the sedimentation velocity of the particle. However, these authors considered only two particles. Thus, the influence of particle-particle and particle-wall collisions as well as the hydrodynamic influence of the wall on the particle dynamic has not been investigated.

Recently, Dierich *et al.* (2011) performed 2D DNS of ice particles moving and melting in a closed cavity filled with a hot water. It was shown that near wall regions the effect of particle rotation caused by the viscous torque play significant role in particle trajectories. In this work we perform comparative numerical study of the influence of viscous torques on melting and solidifying particles moving up in hot and undercooled water, respectively. The implicit fictitious boundary method in finite volume formulation is used to solve the problem (Ananiev *et al.* (2009)). The present DNS method directly solves the mass conservation, momentum and energy conservation equations on a fixed Eulerian grid for the whole domain including particles. At the same time the particle dynamics and their collisions are solved on a Lagrangian grid for each particle. The particle-fluid interactions are treated using both grids.

PROBLEM FORMULATION

The setup of the problem under consideration is illustrated in Fig. 1. In particular, the system consists of several circular ice dendrites (40) moving up due to the density difference in a two-dimensional channel filled with hot (first case) and undercooled (second case) water. Initially 20 or 40 cylindrical ice particles are placed in two lines near the bottom of an enclosed cavity. The box has a size of $L_0 = 15\,\text{mm}$ and $H_0 = 25\,\text{mm}$. The particles have an initial diameter of $d_0 = 0.4\,\text{mm}$ and the walls are adiabatic with a no–slip boundary condition. The initial temperature of the water T_0 is 283.15 K in the warm case and 263.15 K in the undercooled case. The temperature of the ice particles is equal to the melting temperature $T_m = 273.15$.

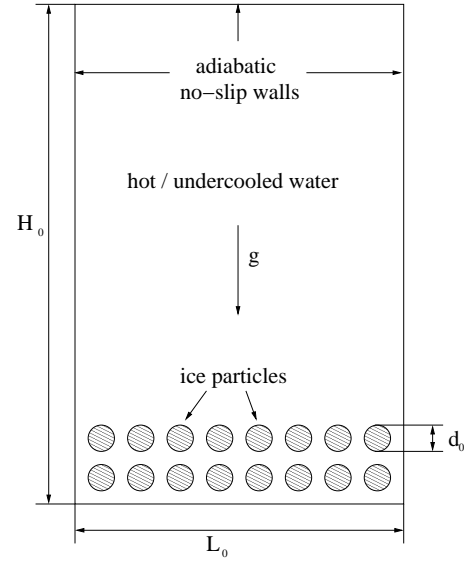To proceed with the governing equations the following basic assumptions have been made:

Figure 1: Setup of ice particles rising up in hot or undercooled water.

- The fluid is incompressible and Newtonian. An Eulerian grid is used to model the entire fluid flow.

- The Boussinesq approximation is used for the fluid field to account for the variation of fluid properties due to the temperature gradients caused by the melting/solidification of the ice particles.

- The local thermodynamic equilibrium is satisfied on the particle interface. Due to the macroscopic size of particles the Gibbs-Thomson effect on the melting temperature is negligible.

- The particle are cylindrical in shape[1].

- The heat transfer inside the particle is not considered. Thus, the heat transfer equation is solved only on the Eulerian grid.

- The rate of particle melting is defined by the surface-averaged heat flux on the particle surface.

- The particle collisions are inelastic and are modeled by use of the hard sphere model.

Taking into account the assumptions made above, the conservation equations describing the behavior of ice in water take the following form:

$$\nabla \cdot \vec{u} = 0 \tag{1}$$

$$\rho \, \frac{\partial \vec{u}}{\partial t} + \rho \, \vec{u} \cdot \nabla \vec{u} = -\nabla p + \nabla \cdot (\mu \nabla \vec{u}) + \vec{F}_B \tag{2}$$

$$\rho \, c_p \frac{\partial T}{\partial t} + \rho \, c_p \nabla \cdot (\vec{u} T) = \lambda \nabla^2 T. \tag{3}$$

where $\vec{F}_B$ is the vector of buoyancy force resulting from the Boussinesq approximation. The conservation equations are only solved in the fluid phase.

The motion of the ice particles is modeled by use of a Lagrangian approach. An impulse conservation equation is

---

[1]To model spherical particles 3D simulations are required

solved for every particle. The collisions are modeled inelastic with a hard sphere model. The equations that govern the particle translation and rotation are the following ones:

$$m_i \frac{d\vec{u}_i}{dt} = \vec{G}_i + \vec{F}_i + \vec{F}_i^{collis} \qquad (4)$$

$$I_i \frac{d\vec{\Omega}_i}{dt} = \vec{T}_{M_i} + \vec{T}_{M_i}^{collis} \qquad (5)$$

where m_i and I_i are the mass and the moment of the particle, $\vec{u}_i$ and $\vec{\Omega}_i$ are its velocity and angular velocity and $\vec{G}_i$, $\vec{F}_i$ and $\vec{T}_i$ are the force of gravity, the hydrodynamic force and moment, respectively. Here $\vec{F}_i^{collis}$ and $\vec{T}_{M_i}^{collis}$ are the force and the torque due to the collision.

The coupling between the bulk flow and the particles is done via the hydrodynamic force $\vec{F}_i$ and the torque $\vec{T}_{M_i}$ calculated directly for each particle by use of following expressions:

$$\vec{F}_i = \oint_{S_i} -p\vec{n} + (\mu \nabla \vec{u}) \cdot \vec{n} \, dA \qquad (6)$$

and

$$\vec{T}_{M_i} = \oint_{S_i} (\vec{r} - \vec{r}_i) \times ((\mu \nabla \vec{u}) \times \vec{n}) \, dA. \qquad (7)$$

where $\vec{r}$ denotes the coordinates of the surface and $\vec{r}_i$ are the coordinates of the mass center. For details on the particle motion and the collisions modeling we refer to Schmidt and Nikrityuk (2011). In this work we consider particle motion with the rotation of the particles caused by the action of the viscous torque and without the rotational effect.

A 1D model is used to track the interface due to the phase change of the ice particles. The shape of the particles is fixed to a cylinder. The change of the volume of the cylinder is modeled using a Stefan boundary condition and the thermodynamic equilibrium at the particle surface in the following form:

$$\rho_s h_f \frac{dV_i}{dt} = -\lambda \oint_{S_i} \frac{\partial T}{\partial n} \, dA, \qquad (8)$$

where V_i is the volume of the particle and the right side is the surface-averaged heat flux.

THERMODYNAMIC PROPERTIES

The thermodynamic properties of water are highly non-linear in the temperature range from 363.15 K to 383.15 K. Especially the density has a maximum at 277.15 K. We use the properties from VDI Gesellschaft (2006) to calculate a cubic form of the Boussinesq approximation

$$\vec{F}_B = \vec{g}\rho_0 \left[\beta_1 (T - T_0) + \beta_2 (T - T_0)^2 + \beta_3 (T - T_0)^3 \right] \quad (9)$$

with the parameters

$$T_0 = 273.15\,\text{K} \qquad \rho_0 = 999.84\,\text{kg m}^{-3}$$
$$\beta_1 = 6.775 \cdot 10^{-5}\,\text{K}^{-1} \qquad \beta_2 = -9.216 \cdot 10^{-6}\,\text{K}^{-2}$$
$$\beta_3 = 1.077 \cdot 10^{-7}\,\text{K}^{-3}$$

valid for 263 K to 283 K. We also derived from VDI Gesellschaft (2006) a polynomial for the viscosity of water in $\text{kg m}^{-1}\,\text{s}^{-1}$ which has the form:

$$\mu = 9.5989 \cdot 10^{-2} - 6.3085 \cdot 10^{-4}\,T + 1.047 \cdot 10^{-6}\,T^2 \quad (10)$$

The other properties were assumed to be a constant with the thermal conductivity of water $\lambda = 0.5723\,\text{W K}^{-1}\,\text{m}^{-1}$ and the thermal capacity $c_p = 4205\,\text{J kg}^{-1}\,\text{K}^{-1}$. The density of the ice $\rho_s = 916.7\,\text{kg m}^{-3}$ and the latent heat $h_f = 333.6\,\text{kJ kg}^{-1}$ are taken from Lide (2007).

NUMERICAL MODEL

The Navier–Stokes equations (1), (2) and the energy equation (3) are discretized using a finite volume technique on a collocated grid. For the diffusive terms a standard second order central difference scheme is used and for the convective terms a blending scheme with deferred correction between first order upwind scheme and second order central difference scheme is used. For the pressure and velocity coupling the SIMPLE algorithm is used with Rhie and Chow stabilization (Rhie and Chow, 1983). The time derivatives are discretized using an implicit three time level scheme. The system of linear equation are solved with the SIP algorithm developed by Stone (1968). For full details of this algorithm we refer to Ferziger and Perić (2002).

The boundary conditions at the particle surface uses an implicit fictitious boundary method (FBM) introduced by Zienkiewicz (1971). The finite volume formulation of this method was developed by Ananiev *et al.* (2009). This method modifies the matrix coefficients of the finite volume cells inside the solid region and at the solid-fluid interface in a simple way to setup the no-slip and Dirichlet boundary conditions. The full details of this method are described in Ananiev *et al.* (2009).

CODE VALIDATION

The interface tracking algorithm was validated with an analytic model for a solidifying cylindrical particle in undercooled melt given by Carslaw and Jaeger (1960) and reported in Dierich *et al.* (2011). In the second test case we validated the FBM with experimental results given by Kuehn and Goldstein (1976, 1978). In this case an annular geometry is considered with natural convection inside. Both validation cases showing good results. For full details of the validation cases and the numerical setup of the validation we refers to Dierich *et al.* (2011).

The validation of the particle motion and the collision modeling can be found in Schmidt and Nikrityuk (2011).

RESULTS AND DISCUSSION

To describe the results of the simulation we introduced the following dimensional parameters:
the initial Reynolds number

$$Re = \frac{\rho_0 \, u_{ref} \, d_0}{\mu_0}, \qquad (11)$$

the Grashof number

$$Gr = \frac{g \, \beta_1 \, d_0^3 \, \rho_0^2 \, (T_0 - T_m)}{\mu_0^2} \qquad (12)$$

the Fourier number

$$Fo = \frac{\lambda \, t}{c_p \, \rho_0 \, d_0^2} \qquad (13)$$

With the reference velocity

$$u_{ref} = \sqrt{g \, d_0 \frac{\rho_0 - \rho_s}{\rho_0}}, \qquad (14)$$

and the water properties at 273.15 K we get $u_{ref} = 0.0181\,\text{m s}^{-1}$, $Re = 4.03$ and $Gr = 0.1325$. The density ratio between ice and water is $\rho_0/\rho_s = 1.091$.
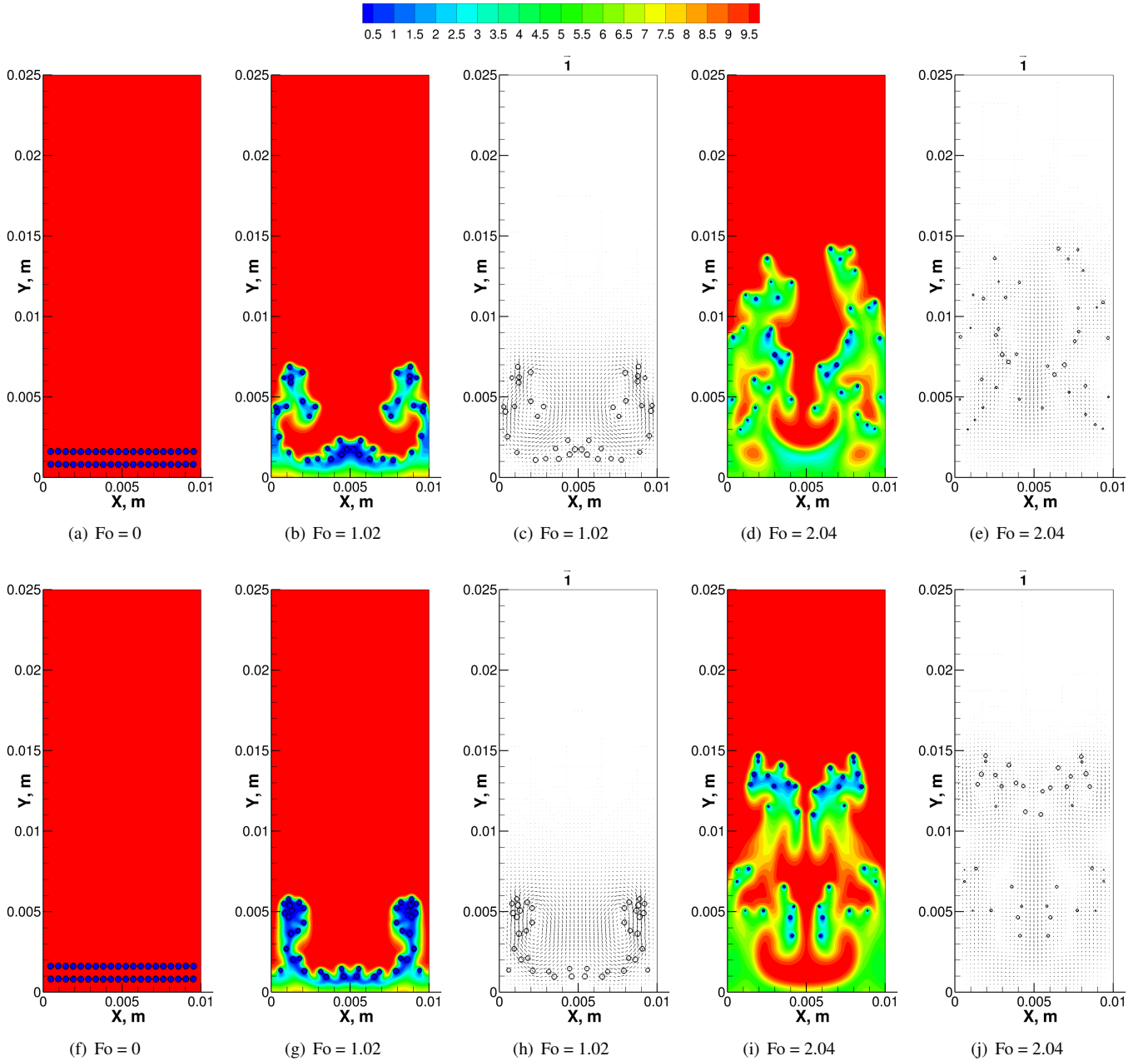
Figure 2: Snapshots of the temperature difference $T - T_m$ and the non-dimensional velocity vectors $\vec{u}/u_{ref}$ for 40 melting ice particles with **rotation in the first line** and without rotation in the second line.

To analyze the temporal development of the global flow field we introduce the volume averaged velocity u_{av}

$$u_{av} = \frac{1}{H_0 L_0} \int_0^{H_0} \int_0^{L_0} \sqrt{u_x^2 + u_y^2} \, dx \, dy \qquad (15)$$

The total volume fraction of liquid ε_{av} is defined similar way with

$$\varepsilon_{av} = \frac{1}{H_0 L_0} \int_0^{H_0} \int_0^{L_0} \varepsilon \, dx \, dy. \qquad (16)$$

to study the dynamics of melting or freezing rate of the particles. *Here ε is the local volume fraction of liquid. It takes unity if a control volume is occupied by the liquid and zero if a control volume is taken by the solid phase.*

Before we proceed with the analysis of results let us briefly recall the problem description under investigation. The principle scheme of this setup is shown in Fig. 1. Initially the

ice particles are placed near the bottom of the enclosed cavity. Due to the gravitational force and the density difference between the ice particles and the surrounding water the ice particles starts rising. While rising the particles starts melting or the surrounding water freezes at the particles surface depending on the initial temperature of the water. In this section we want to study the influence of the particles rotation on the melting and solidification rate and describe the influence of the rotation on the general flow.

For the simulations we use a finite volume grid with 400×1000 cells. The time step was equal to $5 \cdot 10^{-4} s$.

The results of simulations for the melting case are shown in Fig. 2, which depicts snapshots of the contour plots of the temperature difference $T - T_m$ and vector plots of the non-dimensional velocity $\frac{\vec{u}}{u_{ref}}$. The first line shows the particle motion and the temperature field without particle rotation (the viscous torque is neglected) and the second line shows the same setup with particle rotation caused by the action of
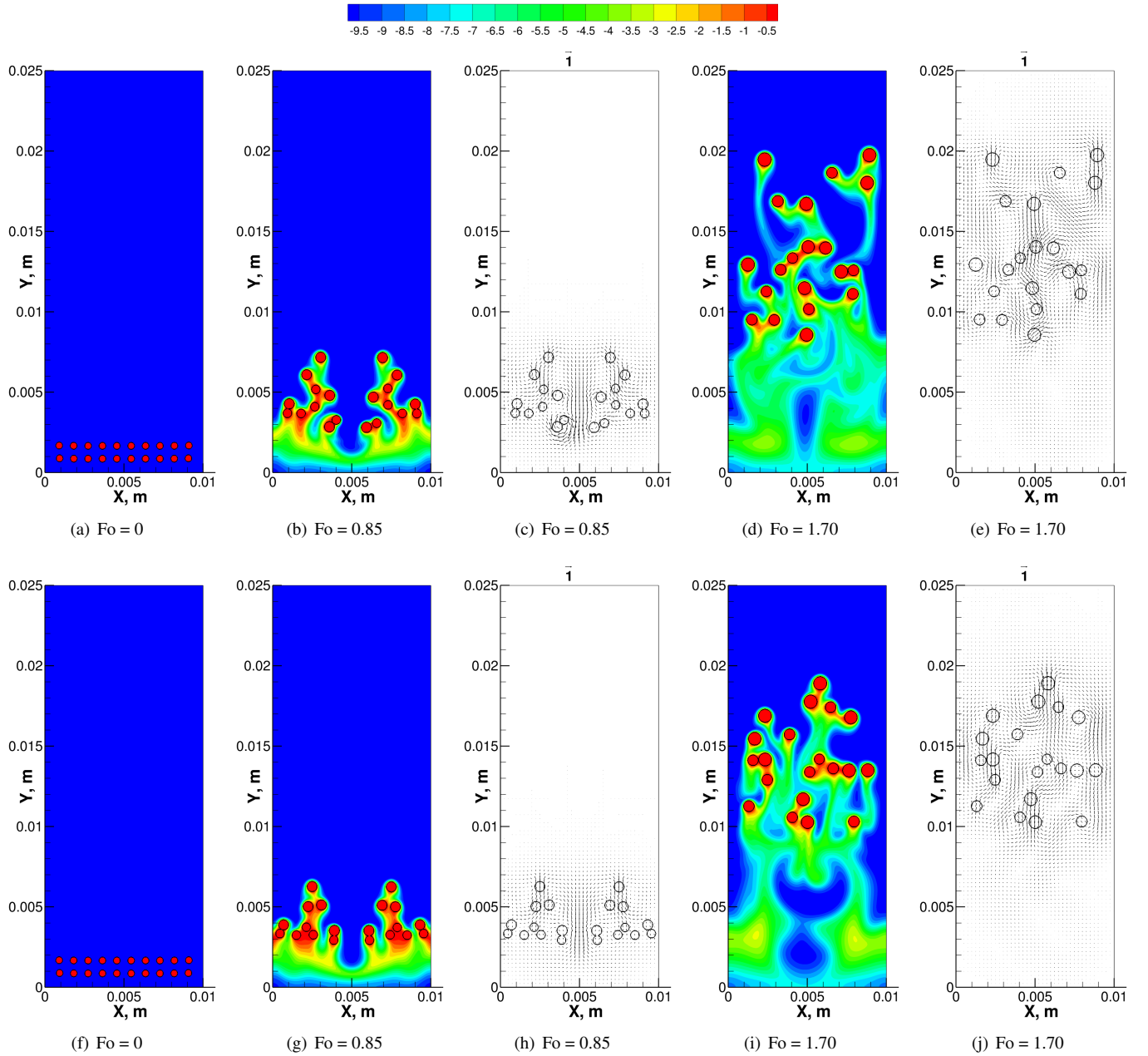
Figure 3: Snapshots of the temperature difference $T - T_m$ and the non-dimensional velocity $\vec{u}/u_{ref}$ for 20 freezing ice particles with **rotation in the first line** and without rotation in the second line.

viscous torque. It can be seen that in the beginning the difference in flow pattern can be detected which is attributed to the particle rotation caused by the viscous torque due to fluid shear near the no-slip wall. As a result of particles rotation and their continuous rise up a lift force appears which shift the particles to the center of the cavity, see Fig. 2. Due to this effect the ice particles with rotational effect form larger clusters in comparison to non-rotating particles. Translating this phenomena into classical theory of particle dynamics, e.g. see Soo (1967), this phenomenon can be classified as Saffman force. In particular, Saffman found out that a lift force acts on a particle moving in a viscous fluid in a simple shear, see Saffman (1965, 1968).

The results for solidifying particles moving in the undercooled water are shown in Fig. 3. Surprisingly, only slight difference between flow pattern for rotating and non-rotating particles can be detected. We explain this effect by the fact, that growth of particles breaks the rotational velocity due to

conservation of rotational impulse. Thus, the Saffman effect plays an insignificant role with progressing solidification of particles.

The buoyancy has a small influence in both cases because of the small-sized geometry. A detailed study of the influence of buoyancy for higher *Gr* can be found in Yu *et al.* (2006) and Feng and Michaelides (2008).

To study the global dynamics if the phase change in the whole cavity we plot the time history of the total volume fraction of liquid in Fig. 4. It can be seen that with particle rotation the melting velocity increases but in both cases (viscous torque is on and off) the time needed for particles to be melted completely is nearly identical. In the case of undercooled water the particle rotation has no influence on the solidification rate. The average solid growth velocity is in both cases $6.7 \cdot 10^{-5}\,\mathrm{m\,s^{-1}}$.

To study the dynamics of flow induced by particles Fig. 5 presents the time history of the volume averaged velocity u_{av}
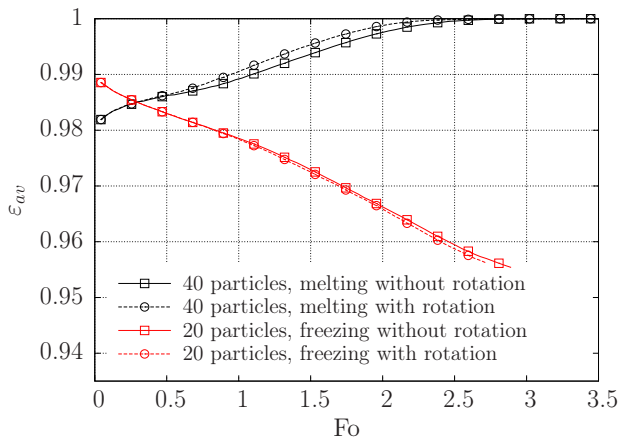
Figure 4: Time history of the total volume fraction ε_{av}.

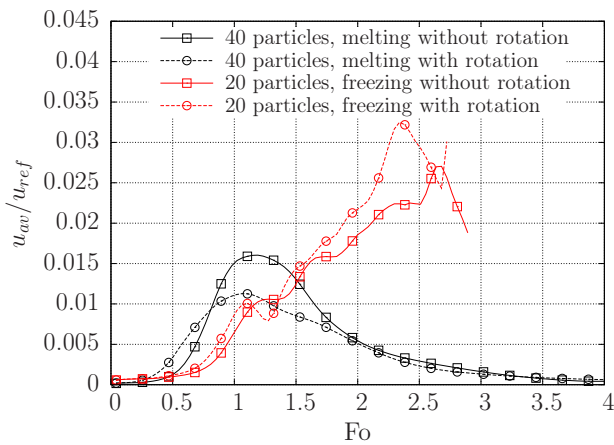which is calculated using Eq. (15). The analysis of Fig. 5

Figure 5: Volume averaged velocity u_{av}.

shows that for the melting case two flow phases can be identified. In particular, the first phase is the acceleration one. The particles accelerate from rest and rising up due to the density difference and the volume averaged velocity u_{av} increases. With particle rotation the acceleration starts earlier but reaches a lower maximum. The general flow structure in both cases is a downstream in the center of the cavity and an upstream with the ice particles at the walls, see Figs. 2(c) and 2(h). The second phase is the breaking phase. Due to the continuous melting of the particles the size of the particle decrease and thus the buoyancy force also decreases. This results in a decrease of u_{av} due to the no-slip boundary conditions at the cavity walls.

In the case of undercooled water only acceleration phase can be recognized, see Fig. 5. Due to the permanent growing particles the buoyancy force increases. As a result the volume averaged velocity increases in time until the particles reach the top of the cavity. In comparison to the melting-case the volume averaged velocity u_{av} of the particulate flow is greater than u_{av} predicted for the not rotating particles-case.

CONCLUSION

In this work the mathematical and numerical models for the modeling of particulate flows during the phase change processes including particle melting and solidification have been developed. The model is based on the direct numerical simulation (DNS) approach where no additional semi-empirical expressions for the drag force and the heat transfer between particle and fluid are necessary. The hydrodynamic forces acting on the particles are calculated directly through the surface integrals. The particle collisions are modeled directly using the hard sphere approach, taking into account the inelastic collisions. The interface velocity of the melting/solidification (solid-liquid) is calculated by means of the Stefan condition for each particle. As an illustration of the model numerical simulations of two-dimensional system consisting of several circular ice dendrites (40) moving up due to the density difference in a two-dimensional channel filled with hot (first case) and undercooled (second case) water have been performed. The analysis of results for the case of melting particles showed significant influence of particle rotation caused by the viscous torque on trajectories of particles in the near wall regions. Due to the so-called Saffman force the particles are shifted from the wall to center of the cavity. However, surprisingly in the case of growing particles this effect does not have significant influence on the particle trajectories. We explain this phenomena by the fact that the growth of particles breaks the rotation of particles due to conservation of rotational impulse. Thus, the Saffman effect plays insignificant role with progressing solidification of particles.

ACKNOWLEDGMENTS

REFERENCES

ANANIEV, S. *et al.* (2009). "Simulation of the heat and flow dynamics in an one-roll mill using fictitious boundary method". K. Hanjalic, Y. Nagano and S. Jakirlic (eds.), *Turbulence, heat and mass transfer 6*, Lecture Notes in Computational Science and Engineering, 1063–1066. Begell House, New York.

BECKERMANN, C. and WANG, C. (1996). "Equiaxed dendritic solidification with convection: Part III. Comparisons with $NH_4Cl - H_2O$ experiments". *Met. Mat. Trans. A*, **27**, 2784–2795.

CARSLAW, H.S. and JAEGER, J.C. (1960). *Conduction of heat in solids*. 2nd ed. Clarendon Press, Oxford.

DIERICH, F. *et al.* (2011). "2D Modeling of Moving Particles with Phase-Change Effect". *Chem. Eng. Sci.* Submitted.

FENG, Z.G. and MICHAELIDES, E.E. (2008). "Inclusion of heat transfer computations for particle laden flows". *Phys. Fluids*, **20(4)**, 040604.

FENG, Z.G. and MICHAELIDES, E.E. (2009). "Heat transfer in particulate flows with direct numerical simulation." *Int. J. Heat Mass Transfer*, **52**, 777–786.

FERZIGER, J.H. and PERIĆ, M. (2002). *Computational methods for fluid dynamics*. 3rd ed. Springer, Berlin.

GAN, H. *et al.* (2003). "Simulation of the sedimentation of melting solid particles." *Int. J. Multiphase Flow*, **29(5)**, 751–769.

KUEHN, T. and GOLDSTEIN, R. (1976). "An experimental and theoretical study of natural convection in the annulus between horizontal concentric cylinders." *J. Fluid Mech.*, **74**, 695–719.

KUEHN, T. and GOLDSTEIN, R. (1978). "An experimental study of natural convection heat transfer in concentric

and eccentric horizontal cylindrical annuli." *Journal of Heat Transfer*, **100**, 635–640.

LIDE, D.R. (ed.) (2007). *CRC Handbook of Chemistry and Physics*, chap. Properties of Ice and Supercooled Water. 87th (CD-ROM Version 2007) ed. Taylor and Francis, Boca Raton, FL.

MOIN, P. and MAHESH, K. (1998). "Direct numerical simulation: A Tool in Turbulence Research". *Annual Review of Fluid Mechanics*, **30(2)**, 539–578.

PAN, T.W. *et al.* (2002). "Fluidization of 1204 spheres: simulation and experiment". *J. Fluid Mech.*, **451**, 169–191.

RHIE, C. and CHOW, W. (1983). "Numerical study of the turbulent flow past an airfoil with trailing edge separation". *AIAA J.*, **21(11)**, 1525–1532.

SAFFMAN, P. (1965). "The lift on a small sphere in a slow shear flow". *J. Fluid Mech.*, **22**, 385–400.

SAFFMAN, P. (1968). "Corrigendum to: The lift on a small sphere in a slow shear flow". *J. Fluid Mech.*, **31**, 624.

SCHMIDT, R. and NIKRITYUK, P. (2011). "DNS of particulate flows with heat transfer in a rotating cylindrical cavity". *Philos. Trans. R. Soc. London, Ser. A*. Accepted.

SOO, S. (1967). *Fluid Dynamics of Multiphase Systems*. Cambridge University Press, Waltham, MA.

STONE, H.L. (1968). "Iterative solution of implicit approximations of multidimensional partial differential equations." *SIAM J. Numer. Anal.*, **5(3)**, 530–558.

VAN DER HOEF, M. *et al.* (2008). "Numerical Simulation of Dense Gas-Solid Fluidized Beds: A Multiscale Modeling Strategy". *Annu. Rev. Fluid Mech.*, **40**, 47–70.

VDI Gesellschaft (ed.) (2006). *VDI Wärmeatlas*. 10th ed. Springer, Berlin.

WAN, D. and TUREK, S. (2007). "Fictitious boundary and moving mesh methods for the numerical simulation of rigid particulate flows". *J. Comp. Phys.*, **222(1)**, 28–56.

WU, M. and LUDWIG, A. (2006). "A three-phase model for mixed columnar-equiaxed solidification." *Met. Mat. Trans. A*, **37A**, 1613–1631.

YU, Z. *et al.* (2006). "A fictitious domain method for particulate flows with heat transfer". *J. Comput. Phys.*, **217**, 424–452.

ZHU, H. *et al.* (2008). "Discrete particle simulation of particulet systems: A review of major applications and findings". *Chem. Eng. Sci.*, **63**, 5728–5770.

ZIENKIEWICZ, O. (1971). *The Finite Element Method in Engineering Science*. MCGraw-Hill, London.

8th International Conference on CFD in Oil & Gas, Metallurgical and Process Industries
SINTEF/NTNU, Trondheim NORWAY
21-23 June 2011

CFD11-170

A NUMERICAL AND EXPERIMENTAL STUDY OF HYDRODYNAMIC BEHAVIOR OF BISOLID CIRCULATING FLUIDIZED BEDS

Nicolas NOUYRIGAT[1,3*], **Eric BOUQUET**[2], **Olivier SIMONIN**[1,3], **Virginie LALAM**[2]

[1]Université de Toulouse ; INPT, UPS

[2]Alstom Power Systems S.A., établissement Boilers, 12 rue Jean Bart, 91345 Massy; FRANCE

[3]Institut de Mécanique des Fluides de Toulouse, Allée Camille Soula, F-31400 Toulouse,

FRANCE,CNRS

* E-mail: nicolas.nouyrigat@imft.fr

ABSTRACT

Chemical-looping combustion is a CO_2 capture technology involving the use of a solid oxygen carrier, typically a metal oxide, which transfers oxygen from combustion air to coal, avoiding thus a direct contact between air and coal. Two inter-connected fluidized beds, a fuel reactor and an air reactor, are used in the process.

This paper is about CFD modeling and simulation of a cold circulating gas-solid fluidized bed with a binary mixture of solid particles with different characteristics. Simulations were carried out using a multi-fluid polydispersed modeling approach (Batrak *et al.* (2005)) implemented in the *NEPTUNE_CFD* code, with separate transport equations for the mean velocity and random kinetic energy for each particle species and accounting for momentum transfer due to collisions between various particle species. 3D unsteady state simulation results are presented and compared to experiments performed at Université Technologique de Compiègne (UTC) by Alstom Power System's team on an experimental cold flow model that is 10 meters high with a cross-section of approximately 0.46 m^2.

This work is focusing on the importance of the mean momentum transfer between classes: the smaller particles transfer momentum to larger ones and trigger their circulation into the larger expanse of the bed. The influence of the particle characteristics and the inventory of each solid phase were studied. This study demonstrated that increasing the proportion of small particles in the bed increases significantly the circulation of large particles.

Keywords: CFD, experimental, hydrodynamics, chemical looping reactors, Euler/Euler approach, polysolid.

NOMENCLATURE

Greek Symbols

α_k Mass fraction of phase k $[-]$
ε Turbulent dissipation $[m^2/s^3]$
μ Dynamic viscosity $[Pa/s]$
ρ_k Mass density of phase k $[kg/m^3]$
$\Sigma_{p,ij}$ Stress tensor in momentum equation of phase p $[N/m^2]$
σ Standard deviation $[-]$
τ^c_{pq} Characteristic time between the collision of a particle of phase p with any particle of phase q $[s]$
τ^t_{gp} Characteristic eddy-particle interaction time $[s]$

Latin Symbols

C_D Drag coefficient $[-]$
d_p d_{50} diameter of solid phase p $[\mu m]$

E Mean value $[-]$
e_c Inelastic restitution coefficient $[-]$
g_{pq} Autocorrelation function $[-]$
$I_{g \rightarrow p,i}$ Drag force on phase p $[N]$
k Turbulent kinetic energy $[m^2/s^2]$
n_p Number of particle of phase p $[-]$
P Gas pressure [mbars]
q_{gp} Gas-particle velocity correlation $[m^2/s^2]$
Q_m Mass flux of gas $[kg/s]$
$q_p{}^2$ Particle random kinetic energy $[m^2/s^2]$
$S_{pq,i}$ Momentum transfer due to collisions between particles of phase p and phase q $[N]$
T Gas temperature $[°C]$
$U_{k,j}$ Mean velocity of phase k $[m/s]$
$V_{r,i}$ Mean relative velocity $[m/s]$
Z_{pq} Parameter representative from collisions between solid phases $[-]$

INTRODUCTION

Chemical-looping combustion involves the use of a metal oxide (MeOx) as an oxygen carrier which transfers oxygen to coal during combustion, thus avoiding a direct contact between air and coal. Usually, the characteristics of MeOx and coal particles are significantly different in terms of mass density or diameter distribution which leads to a special behavior of the fluidized bed hydrodynamic. The experiments of Fabre (1995) allowed to characterize the hydrodynamics of a fluidized bed with a mixture of two particle species with the same density but very different mean diameters. Using the work on Discrete Particle Simulation (DPS) performed by Gourdel *et al.* (1999), a modelling of a binary mixture of particle species has been developed by Batrak *et al.* (2005) and Fede and Simonin (2005) and implemented in *NEPTUNE_CFD*. *NEPTUNE_CFD* is an unstructured finite volume numerical code developed in the framework of the NEPTUNE project which is financially supported by Electricité de France, CEA, AREVA-NP and IRSN.

The recent parallelization of *NEPTUNE_CFD* considerably improved its ability to simulate experimental or pilot set up with a refined grid (Neau *et al.* (2010)). The simulations presented here are performed using the *NEPTUNE_CFD* code with specific adaptations by IMFT. Therefore, the aim of this work is to validate this modeling on experimental set up. Eventually, a characterization of the local mechanisms making small particles trigger the circulation of bigger ones is performed.

N. Nouyrigat[1,3], *E. Bouquet*[2], *O. Simonin*[1,3], *V. Lalam*[2]

EXPERIMENTAL STUDY OF BI-SOLID FLUIDIZED BED

Cold Flow Model description

The Cold Flow Model (CFM) in this study is a Circulating Fluidized Bed (CFB) based in UTC (France) which works with air in cold conditions. The characteristics dimensions were calculated and validated by analogy with the real 125 MWe power plant Emile Huchet (France).

The cold flow model is used for furnace hydrodynamics tests. Picture and schema are given in figure 1 and 3. Solids flow comes from the furnace and goes into the cyclone 1 and returns to the furnace by loop seal 1, the cyclone 2 in series captures the smallest particles (fines) from the exhaust of cyclone 1. Solids from cyclone 2 are reintroduced into the furnace via loop seal 2. The gas coming from the cyclone 2 exhaust goes through the bag filter before being released outside (figure 3).

The furnace in stainless steel has a regular cross-section of 0.456 m^2 and a grate section of 0.155 m^2. The furnace widens with a conical shape. The total height of the furnace is 10 m. In the furnace, three levels of gas injection are available. The first one introduces the gas in the furnace through the fluidization grate. This is the primary air flow. The two other levels, the secondary air flows, introduce the gas directly in the furnace. The lower and upper secondary air are located at the level 400 mm and 800 mm from the grate.

For the bi-solid tests, alumina was mixed with ilmenite with alumina mass ratio between 0 and 7%. According to the data showed in figure 2, the d_{50} is about 62 μm and the d_{90} of about 120 μm. The alumina density is 1500 kg/m^3 (mercury pyctometer).

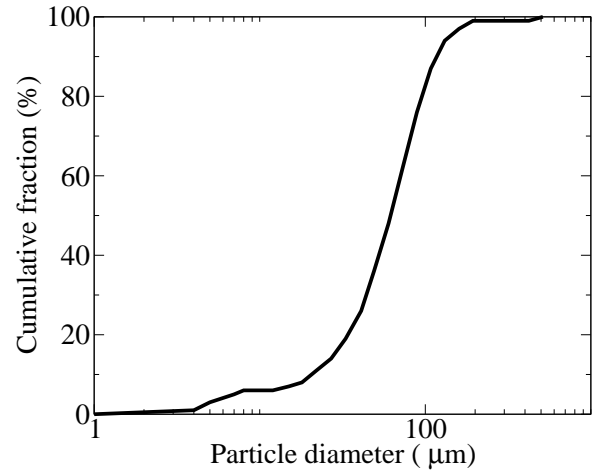Figure 2: Particle Size Distribution of alumina particles

Figure 1: Photo of UTC's Cold Flow Model (CFM)

Two types of solids were used for the tests. The main solid chosen is ilmenite (Titanium-Iron oxide). According to granulometric analysis the d_{50} is about 160 μm. The density of ilmenite, measured by using a helium Pyctometer is 4600 kg/m^3.
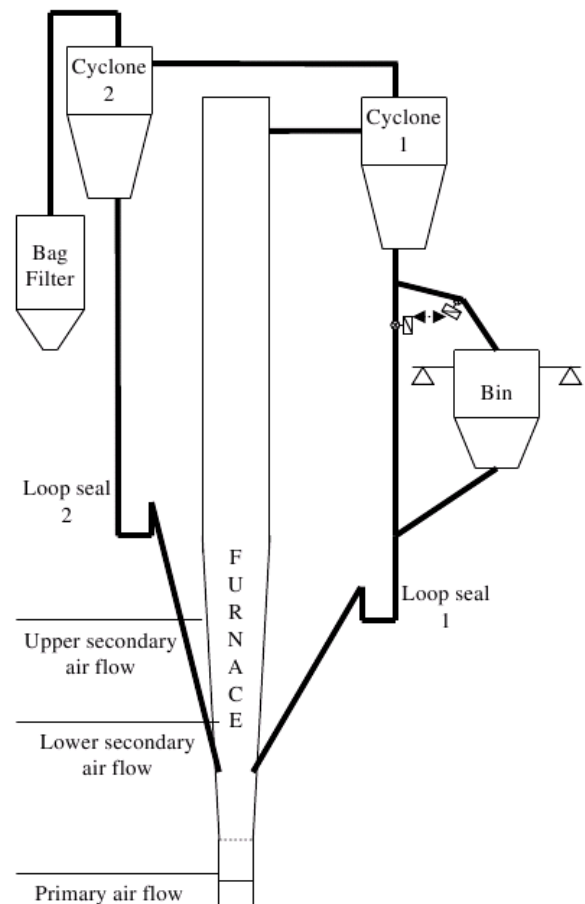

Figure 3: Schematic view of UTC's Cold Flow Model (CFM)

Operating Conditions

The solid mixture, ilmenite with alumina, is introduced in the reactor in start-up phase. When the necessary amount of solids is in the cold flow model the inlet air flow is adjusted to obtain the test conditions. Furnace pressure profile is determined after one hour of stabilization by average value on 5 min. The amount of solids in the reactor is calculated with the pressure profile along the furnace, the circulating flow rate is evaluated by blowing empty method. At the end of a test, when the Cold Flow Model is getting shut-down, the storage bin, which is on a weighing gauge, is getting filled and the evolution of weight versus time is recorded. The circulating flow rate corresponds directly to the curve gradient in the first moment after the loop was stopped.

Experiment uncertainty

In the experiment presented in this paper, the uncertainty on the estimated circulating mass flux is about 7%. It has been estimated according to the following calculation:

$$\frac{\Delta Q_F}{Q_F} = \frac{2\Delta m}{m} + \frac{2\Delta t}{t} \text{ with } t = 30\ s,\ m = 200\ kg,\ \Delta t = 0.25\ s$$

and $\Delta m = 5\ kg$.

It is difficult to estimate the proportion of alumina in the riser. The loading of alumina and ilmenite in the whole installation is known at the beginning of the campaign. The more cycles are performed the less accurate is the estimation of the ratio of alumina in the installation because of solids leaving the cyclone.

Moreover, the link between the ratio of alumina in the global installation and the ratio of alumina in the riser is not easy to determine. The set-up was not made for taking samples inside the riser.

The *EXP*5 experiment was performed at the end of a campaign so it has been assumed that no more than half of the 4% of alumina initially injected has escaped from the circulating system.

The *EXP*6 experiment was performed at the beginning of a campaign so the estimation of 5% of alumina in the installation is fairly accurate.

NUMERICAL MODELING OF THE EXPERIMENTAL SET-UP

Euler/Euler modeling

In the proposed modeling approach, separate mean transport equations (mass, momentum and fluctuating kinetic energy) are solved for each phase and coupled through inter-phase transfer terms (Simonin (2000), Gobin *et al.* (2003)). The transport equations are derived using phase ensemble averaging weighed by the gas density for the continuous phase and by using kinetic theory of granular flows supplemented by fluid drag and turbulence effects for the dispersed phase. The solved equations are presented in Annexe A.

Mesh and geometry

Figure 4 shows a view of the CFB UTC mesh, which is formed by a layer of quadrangles. This mesh is composed of about 850 000 cells with a volume from 1 cm^3 to 10 cm^3. The smallest are placed close to the injection region of the fluidization gas while the largest are in top part of the bed. Secondary injectors are situated at height z= 400 mm (4 injectors) and z= 800 mm (8 injectors).

Boundary conditions and initial conditions

Physical properties

The fluidization gas is air at $T = 50°C$, $P = 1\ bar$. The imposed diameter for particulate phases is chosen to be the d_{50} of each phase.

Gas (Air): $\rho_g = 1.09\ kg \cdot m^{-3}$, $\mu = 1.98.10^{-5}\ Pa \cdot s$

Table 1: Characteristics of modeled particles

Type	Density (kg/m^3)	d_{50} (μm)	Terminal settling velocity
Alumina	1500	60	0.14 m/s
Ilmenite	4600	160	1.7 m/s

Boundary conditions

All simulations have been performed with imposed solid inventory (cf. Table 2) and fluidization velocity so that the solid circulation mass flux is a result of our simulation.

Table 2: Imposed inventory for each case.

Case	Ilmenite	Alumina	Inventory
Alu 0%	259 kg	-	259 kg
Alu 2%	253.9 kg	5.1 kg	259 kg
Alu 4%	253.9 kg	10.6 kg	264.5 kg
Alu 10%	233.1 kg	25.9 kg	259 kg

The gas is injected as follows and corresponds to a gas velocity in the main section of 3.8 m/s.

Fluidization grid : $Q_m = 0.4992\ kg \cdot s^{-1}$.

Secondary inlet flow z=400 mm. For each injector (among 4): $Q_m = 0.2090\ kg \cdot s^{-1}$.

Secondary inlet flow z=800 mm. For each injector (among 8): $Q_m = 0.0699\ kg \cdot s^{-1}$.

The solid mass flux injected at the inlet is equal to the solid

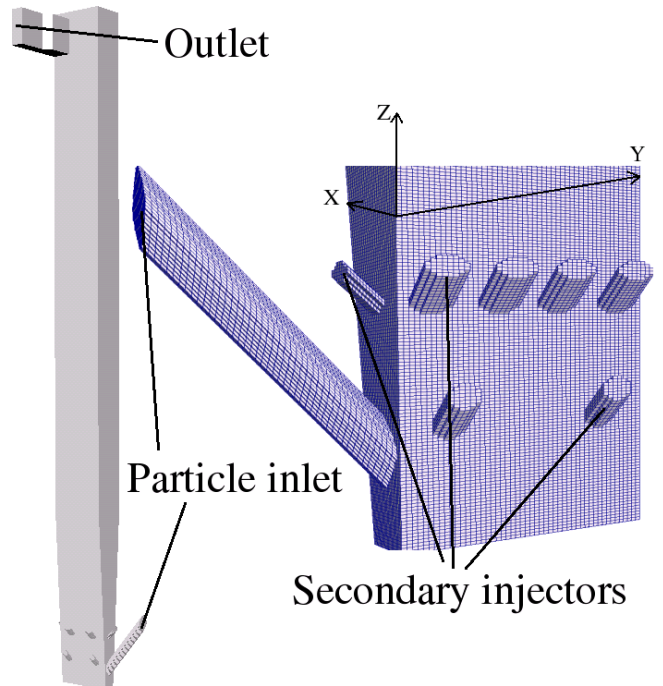Figure 4: Schematic view of the mesh and geometry of UTC's CFM

N. Nouyrigat[1,3], E. Bouquet[2], O. Simonin[1,3], V. Lalam[2]

mass flux at the outlet.

The fluidization grid is considered as a smooth wall for the particle boundary conditions. So, a slip condition for particle velocity and a zero flux for random kinetic energy and flux-particle covariance are imposed. The outlet of the riser is a free inlet-outlet. If the flow is coming back, the volume fraction of particles is imposed equal to 10^{-12}. Standard wall friction functions are used for the velocities and the turbulence properties of the continuous phase. A slip condition for the velocity and zero flux for particle random kinetic energy are imposed on the dispersed phases,corresponding to elastic particle bouncing on smooth wall without friction.

Numerical information

The time of calculation and averaging is sum up in Table 3.

Table 3: Numerical information

Case	Simulation time (s)	Duration of the averaging (s)	CPU time (h) per physical s
Alu 0%	20 s	10 s	10 days, 64 proc.
Alu 2%	42 s	10 s	22 days, 64 proc.
Alu 4%	34 s	10 s	18 days, 64 proc.
Alu 10%	27 s	7 s	15 days, 64 proc.

The processors used for those simulations are referenced below: Intel Xeon Quad-Core E5472 owns 4 cores with a 3 GHz frequency or Nehalem EX owns 4 cores with a 2.8 Ghz frequency.

Whenever possible, the duration of the time averaging is about the duration of the transitory state. The transitory state is considered to be achieved when the circulating mass flux oscillates around a constant value.

RESULTS

Macroscopic results

All presented results of *NEPTUNE_CFD* are time-averaged on the duration of the averaging which can be seen in Table 3. All the plots of a parameter along Y direction are taken in the center of the bed: $x = 0.265\ m$.

Monosolid cases

As expected, in figure 5, the experiments show that increasing the inventory increases the pressure drop inside the bed. Experiment and simulation pressure profiles fit well in figure 5: the simulation predicts the dense part for $z < 1m$ and the dilute zone between $z > 2\ m$. The evolution of the pressure is linear in both zones.

Bisolid cases

Experiment and simulation pressure profiles in figure 6 are taken along the wall and fit well. The influence of alumina makes the pressure profile closer to the case of a perfectly homogeneous bed. This trend is confirmed by the profiles of time and space averaged $\overline{\alpha_s}$ along the bed (figure 7). The space averaging is the mean value of the time averaged quantity at each height. In the monosolid case the volume fraction of solid reaches 21% in the bottom part while the maximum is 17% when there is 4% of alumina in the bed. The ratio of alumina strongly decreases the averaged volume fraction of solid in the dense part of the bed. Figure 7 shows that the hydrodynamics is established for $z > 4\ m$. Figure 8 shows that adding alumina to the inventory decreases the local volume fraction of solid in the dense part of the bed. Moreover, it is
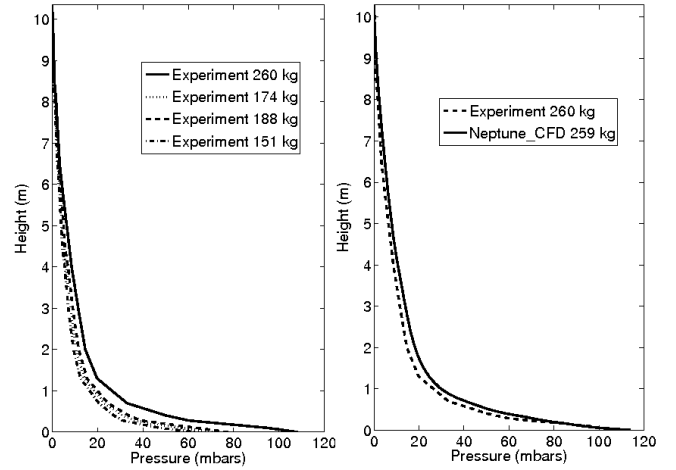

Figure 5: Simulation and experimental pressure vertical profiles of mono-solid comparable cases
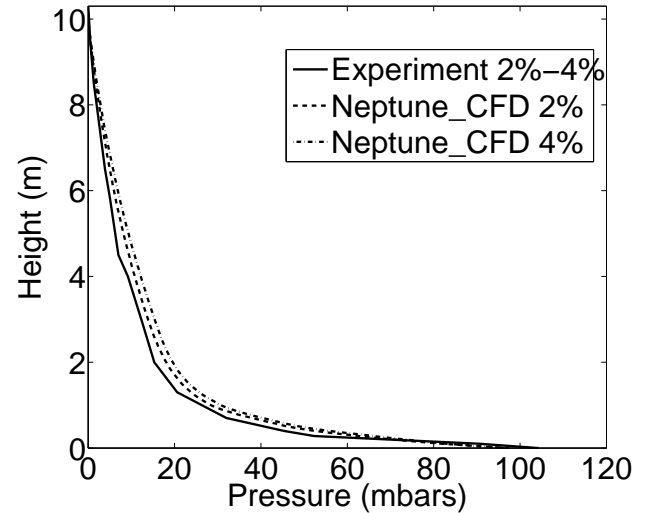

Figure 6: Simulation and experimental pressure profiles of bi-solid comparable cases
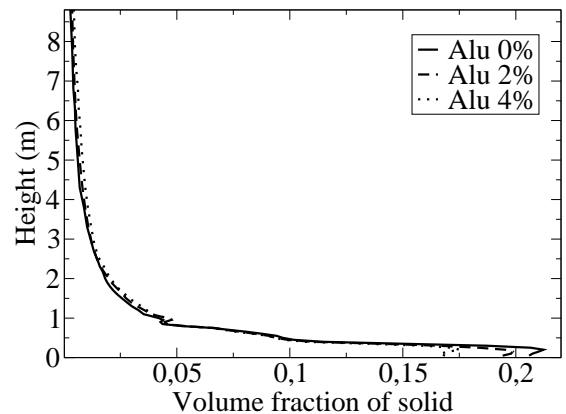

Figure 7: Time and space averaged volume fraction of solid ($\overline{\alpha_s}$) along the bed height

also shown that adding alumina impacts the volume fraction mainly in the dense part of the bed.

Table 4: Monodisperse experiment and simulation

Case	Total inventory	Outlet solid mass flux
EXP 1	260 kg	5.1 kg/s
EXP 2	188 kg	6.2 kg/s
EXP 3	174 kg	5.5 kg/s
EXP 4	151 kg	6.0 kg/s
Neptune_CFD	260 kg	6.5 kg/s

Four similar experiments of a mono-solid circulating fluidized bed have been performed and are presented in Table 4. The difference between those cases remains in the inventory of ilmenite. With an imposed gas flux, the circulation of solids does not seem to be linked to the total mass of solid in the bed. In the range studied the circulating solid mass flux is about 6 kg/s. The monodisperse simulation corresponding to *EXP*1 experiment provides a good estimation of the circulating ilmenite mass flux. Nevertheless, the modeling tends to slightly overestimate the predicted mass flux. This can be due to the modeling of the experiment with a single mean diameter ($d_{50} = 160\ \mu m$). The averaged ilmenite particles residence time goes from 25 s to 50 s for this experiment if it is estimated according to the ratio between the mass of ilmenite in the bed and the circulating flux of ilmenite. It decreases proportionally to the decrease in the inventory of solid.

Table 5: Bi-solid experiment and simulation with Ilmenite and Alumina

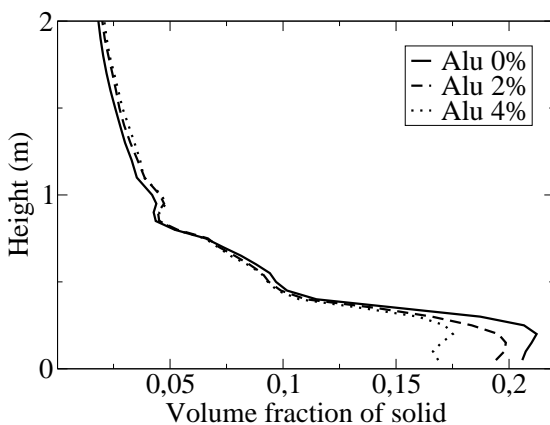| Case	Total inventory	% of Alumina	Ilmenite mass flux	Alumina mass flux	Total mass flux
EXPE 5	259 kg	2%-4%	-	-	9.6 kg/s
EXPE 6	193 kg	$\simeq$ 5%	-	-	9.5 kg/s
Alu 2%	259 kg	2%	7.6 kg/s	0.48 kg/s	8.1 kg/s
Alu 4%	264.5 kg	4%	8.85 kg/s	1.04 kg/s	9.9 kg/s
Alu 10%	259 kg	10%	11.73 kg/s	2.94 kg/s	14.7 kg/s

Figure 8: Time and space averaged volume fraction of solid ($\overline{\alpha_s}$) in the bottom part of the riser for various fraction of alumina in the bed

Considering that the CFB riser is within a loop, it is hard to experimentally estimate the fraction of alumina in the inventory. Both bi-solid experiments give a circulating mass flux between 9 and 10 kg/s. The measurement uncertainty led us to perform 3 bi-solid simulations presented on Table 5. The predicted circulating solid mass flux is similar to the experiment results. Moreover, comparing mono-solid and bi-solid experiment and simulations, there is a significant increase in the circulation of solids due to the alumina particles. Numerical modeling shows that multiplying the ratio of alumina in the bed by a factor 2 increases the circulation of ilmenite of about 16% and multiply the circulation of alumina by a factor 2. Increasing the ratio of alumina in the inventory modifies the average estimated residence time from 33 to 20 s for ilmenite particles and from 11 to 9 s for alumina particles.
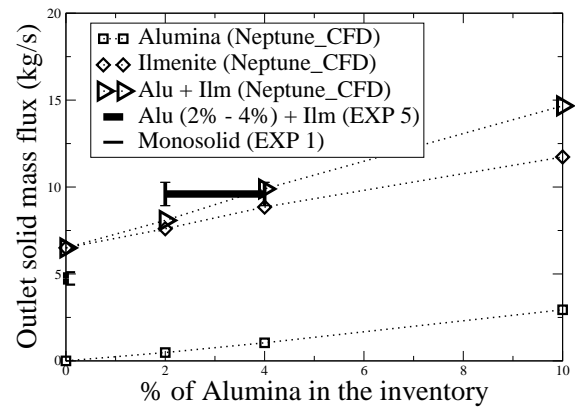

Figure 9: Influence of alumina on the circulating solid mass flux

In the range studied, figure 9 shows that ilmenite and alumina mass fluxes are increasing linearly with the increase in the ratio of alumina. The simulations with *NEPTUNE_CFD* give results within the range of uncertainty of the experiments for bi-solid cases and slightly overestimate the circulation of solids in the monodisperse case.

Local characterization of the hydrodynamic

Flux and velocities

For all phases in Figures 10,11,12 and 13, there is a zone in the center of the riser where the net mass fluxes are positive and constant. This zone tends to widen with the height: for ilmenite particles this zone goes from 5 cm to 60 cm.
In the lower part of the riser, there is a maximum of particles and gas mass fluxes at around 10 cm of the walls. Less than 5 cm from the walls, the particles are falling down.
The shapes of the axial mass fluxes profiles do not depend on the rate of alumina in the bed. Nevertheless, increasing the rate of alumina in the bed tends to make the solid mass flux horizontal profile in the established zone ($z > 4\ m$) more parabolic. For $z < 4\ m$, the influence of alumina particles on the solid mass flux is limited.
Figures 10 and 11 show that the loading of alumina do not impact the gas solid mass, but it can strongly impact the local solid mass flux: its value in the center of the bed goes from $30 kg/m^2/s$ (Alu 0%) to $70 kg/m^2/s$ (Alu 2%).

In the established zone, the maximum local solid mass flux is multiplied by a factor 2.3 while the outlet solid mass flux

N. Nouyrigat[1,3], E. Bouquet[2], O. Simonin[1,3], V. Lalam[2]
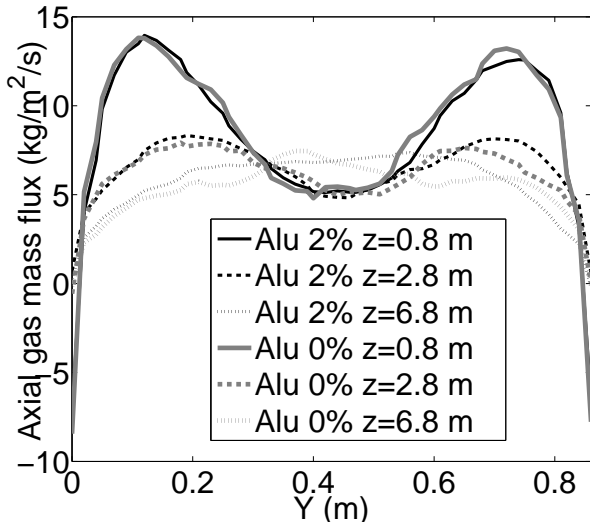
is multiplied by a factor 1.3.

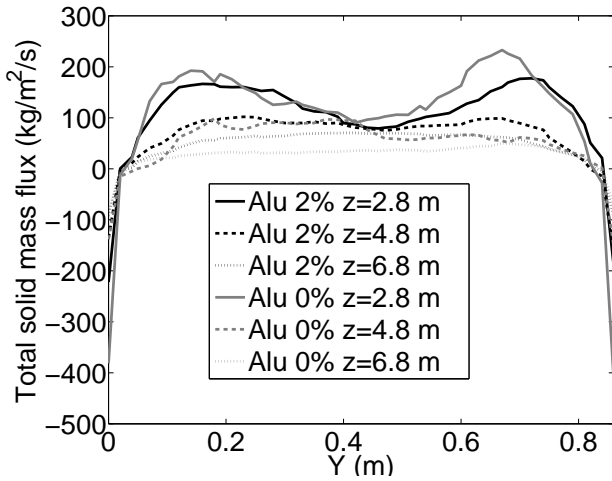Figure 10: Time averaged horizontal gas mass flux for mono-solid and bi-solid cases

Figure 11: Time averaged horizontal solid mass flux for mono-solid and bi-solid cases

Segregation of particles

But in figure 14, it is seen that regardless to the concentration of solid, the mixing between both particle species is quite constant between 0.5 m and 3 m. In both cases, the fraction of ilmenite decreases with the height.

From Alu 2% to Alu 4%, the calculated fraction of alumina in the circulating solid mass flux increased from 5% (corresponding to $\frac{\alpha_{Ilm}}{\alpha_{Ilm}+\alpha_{Alu}} = 84\%$) to 10% corresponding to $\frac{\alpha_{Ilm}}{\alpha_{Ilm}+\alpha_{Alu}} = 73.5\%$). In the outlet region (between z=9.8 m and z=10.3 m), in the center of the bed, the ratio of ilmenite plotted in figure 14 tends to this value.

Figure 14 also shows that from $z = 0$ to $z = z_{outlet}$ the fraction of ilmenite in the solid linearly decreases. Its slope increases while increasing the mass of alumina in the inventory. The fraction of ilmenite in the solid does not change significantly along y axis.

In figure 15, the volume fraction of alumina is fluctuating more than the volume fraction of ilmenite. There is a maxi-

mum of deviation around z=3 m for both phases. In the dense part of the riser (between 0 and 0.6 *m*), $\frac{<\alpha^2>}{<\alpha>^2} \simeq 2$. It corresponds to $\sigma = E$ which means that the local volume fraction of solid fluctuates along time between 7% and 23% in the dense part of the bed. $\frac{<\alpha^2>}{<\alpha>^2} > 1$ is characteristic of cluster formation. It is mainly occurring below 5 meters.

Collisions influence

Fabre (1995) showed experimentally that collisions between two different species can increase the circulating solid mass flux in a CFB.

Gourdel et al. (1999) showed that, if the effect of the correlation induced by fluid turbulence are neglected, the momentum transfer during binary mixture collisions is proportional to the collision frequency and the mean relative velocity. The following equation shows that the frequency of collisions between two different species is linked to the Z_{pq} parameter which represents the ratio between : the mean relative velocity between both particles species and the relative fluctuating velocity variance given in terms of the sum of both particle
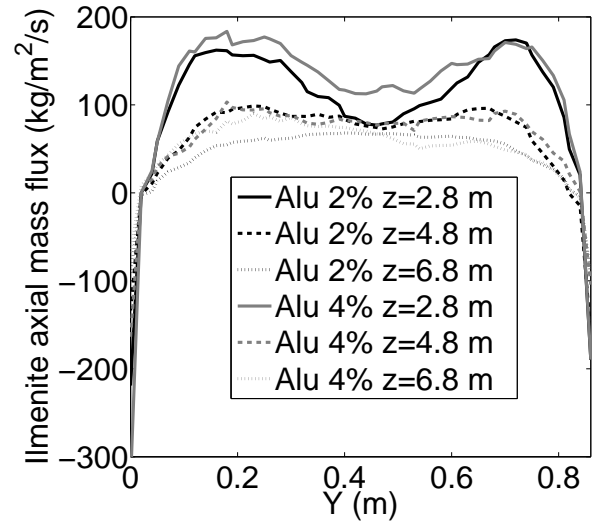

Figure 12: Time averaged horizontal ilmenite mass flux for bi-solid cases
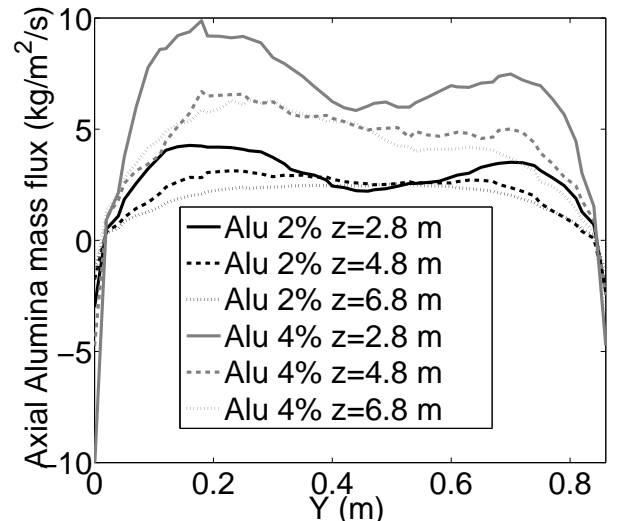

Figure 13: Time averaged horizontal alumina mass flux for bi-solid cases

species agitation.

$$\tau^c_{pq} = \left(g_{pq} n_q \pi d_{pq}{}^2 \sqrt{\frac{16}{3\pi}(q_p^2 + q_q^2)} H(Z_{pq}) \right)^{-1} \quad (1)$$

with $H(Z_{pq}) = \sqrt{1 + \pi Z_{pq}/4}$ and $Z_{pq} = \frac{3}{4}\frac{(U_p - U_q)^2}{(q_q^2 + q_p^2)}$.

Figure 16 shows two regions: in the dense region (cf figure 8), Z_{pq} is nearly equal to unity, so the influence of the mean relative velocity between solid phases is of the same order of magnitude than the averaged granular temperature of the solid species. In the dilute part, $Z_{pq} \ll 1$, so the random kinetic energy is predominant compared to the mean relative velocity between solid phases.

The time averaged equation of momentum for particle phase is written:

$$\overline{\left[U_{p,j} \frac{\partial}{\partial x_j} \right] U_{p,i}} =$$
$$-\overline{\alpha_p \frac{\partial P}{\partial x_i}} + \overline{\alpha_p \rho_p g_i} + \overline{I_{g \to p,i}} - \overline{\frac{\partial}{\partial x_j} \Sigma_{p,ij}} + \sum_{q \neq p} \overline{S_{pq,i}} \quad (2)$$

The first term on the left side of the equation represents the acceleration of particles. On the right side, the first corresponds to the pressure gradient, the second to the gravity contribution, the third to the drag force, the fourth to the stress tensor and the last one to the collisions between solid phases. In figure 17, the contribution of each of those terms in the momentum equation of ilmenite is plotted.
As expected, the stress tensor contribution is negligible.
For both particle species, the contribution of collisions is negligible compared to drag, gravity and pressure gradient. It means that adding alumina particles changes the hydrodynamics of the flow which increases the circulation of solids. In the upper part of the riser, the competition is between drag and gravity only.

Figures 18 shows that there is an acceleration zone at about 10 *cm* from the wall at $z = 1$ *m*. In the middle of the bed there is a deceleration zone. Figure 19 shows that at $z = 6.8$ *m* particles that are falling are accelerating and particles that are going up are slowing.

The results of this study differ from Batrak's simulations of Fabre (1995) experimental work. Batrak showed that in an
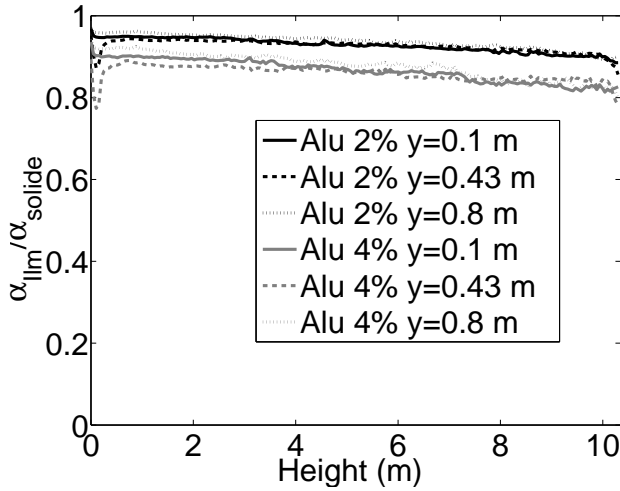

Figure 14: Ratio of the time averaged volume fraction of ilmenite over the total volume fraction of solid along the height for Alu 2% and Alu 4% cases
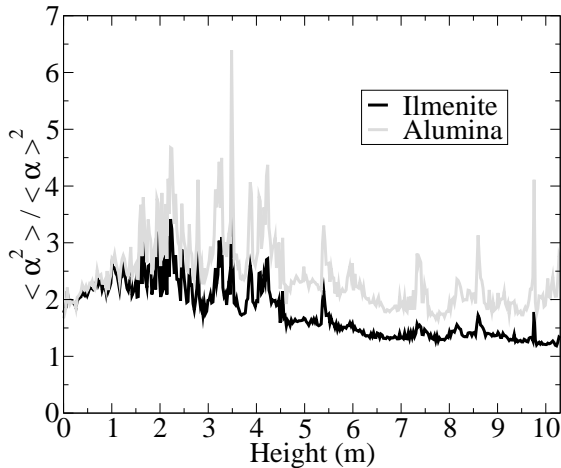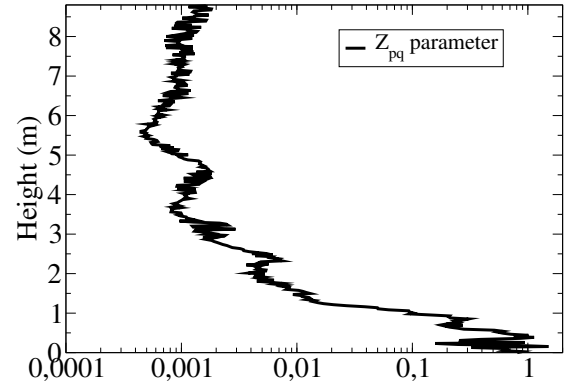

Figure 16: Time averaged value of Z_{pq} parameter in the center of the bed for Alu 2% case
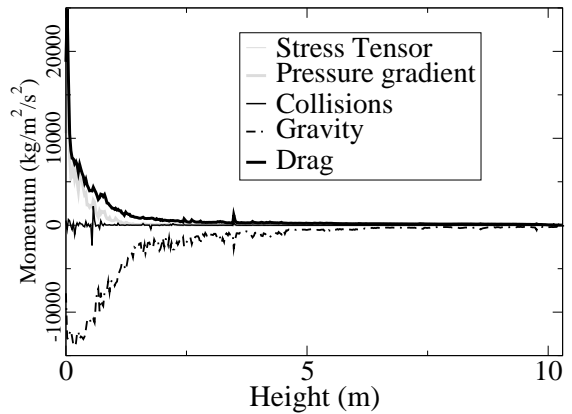

Figure 15: Volume fraction deviation of each solid phase in Alu 2% case

Figure 17: Time averaged terms of the momentum equation of ilmenite phase in the center of the bed in Alu 2% case

N. Nouyrigat[1,3], *E. Bouquet*[2], *O. Simonin*[1,3], *V. Lalam*[2]

extreme case, the contribution of the collisions between solid phases can have a very strong influence on the circulating mass flux of a binary mixture of particles of same density, but very different d_{50} (cf Table 6). The terminal settling velocity of the largest particle phase was larger than the fluidization velocity so that with only drag force modeled, no particle of this solid phase would circulate. In the simulations performed by Batrak, a non negligible amount of large particles were found in the circulating mass flux (depending on the proportion of large sand in the riser).

CONCLUSION

The collaboration between Alstom and IMFT results in the setting of experiments and simulations of mono-solid and bi-solid circulating fluidized bed. This study showed the ability of *NEPTUNE_CFD* to model the hydrodynamics of a laboratory scale CFB cold flow model.

Experimental and simulation pressure profiles fit well for mono-solid and bi-solid experiments. The circulating solid mass flux predicted by *NEPTUNE_CFD* is satisfactory. The influence of the ratio of fine particles (alumina) in the bed on the circulation of solids has been quantified and found in
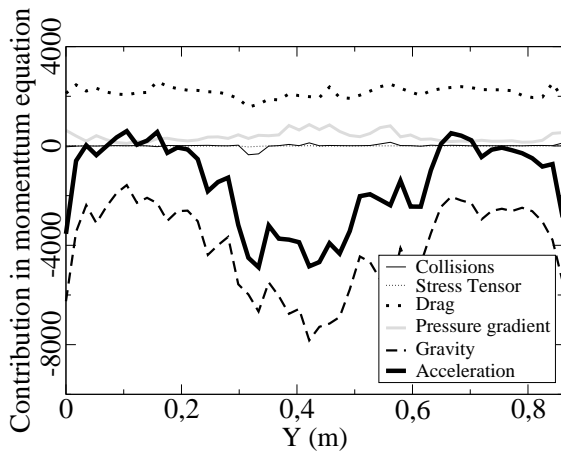

Figure 18: Time averaged radial terms of momentum equation of ilmenite phase at $z = 1$ m in Alu 2% case

Figure 19: Time averaged terms in momentum equation of ilmenite phase at $z = 6.8$ m in Alu 2% case

Table 6: Comparative table between Fabre experiment and results of this study

Current study	Density (kg/m^3)	d_{50} (μm)	Terminal settling velocity
Alumina	1500	60	0.14 m/s
Ilmenite	4600	160	1.7 m/s
Gas velocity in the main section	3.81 m/s		
Fabre (1995)	Density (kg/m^3)	d_{50} (μm)	Terminal settling velocity
Small sand	2650	260	2 m/s
Large sand	2650	1300	9 m/s
Gas velocity in the main section	4 m/s		

the same proportion in both experiment and simulation. The simulation showed that multiplying the ratio of alumina:

- by a factor 2 increases the circulation of ilmenite of 16%.
- by a factor 5 increases the circulation of ilmenite of 54%.

A local characterization of the hydrodynamics of the riser was performed:

- Increasing the ratio of alumina in the bed tends to decrease the maximum volume fraction in the bed.
- The loading of alumina impacts the hydrodynamics that increases the circulating solid mass flux. Momentum transfers during the collisions between solid phases are not important compared to drag force and gravity in the range studied.
- The mixing between both particle species is independent from the local volume fraction of each particle phase.
- The local fraction of ilmenite in the solid slightly decreases when z increases.
- Clustering is observed in the bed between $z = 0$ m and $z = 5$ m.

AKNOWLEDGMENT

REFERENCES

BALZER, G. *et al.* (1996). "Eulerian gas solid flow modelling of dense fluidized bed".

BATRAK, O. *et al.* (2005). "Unlike particles size collision model in 3d unsteady polydispersed simulation of circulating fluidised bed." *Circulating Fluidized Bed Technology VIII, Kefa Cen Ed., International Academic Publishers/Beijing Word Publishing Corporation, 370-378.*

FABRE, A. (1995). *Etude de l'hydrodynamique sur un lit fluidisé circulant d'échelle industrielle.* Ph.D. thesis, Université Technologique de Compiègne.

FEDE, P. and SIMONIN, O. (2005). "Application of a perturbated two-maxwellian approach for the modelling of kinetic stress transfer by collision in non-equilibrium binary mixture of inelastic particles". ASME.

FÉVRIER, P. and SIMONIN, O. (1998). "Constitutive relations for fluid-particle velocity correlations in gas-solid turbulent flows". *Proc. 3rd Int. Conf. Multiphase Flow, Paper*, vol. 538.

GOBIN, A. *et al.* (2003). "Fluid dynamic numerical simulation of a gas phase polymerization reactor." *Int. J. for Num. Methods in Fluids, 43, 1199-1220.*

GOURDEL, C. *et al.* (1999). "Two-maxwellian equilibrium distribution function for the modelling of a binary mixture of particles." *Circulating Fluidized Bed Technology VI, J. Werther Ed., DECHEMA, Frankfurt am Main, Germany, 205-210.*

NEAU, H. *et al.* (2010). "NEPTUNE_CFD high parallel computing performances for particle-laden reactive flows". Proc. 7th Int. Conference on Multiphase Flow, ICMF 2010, Tampa, USA.

SIMONIN, O. (2000). "Statistical and continuum modelling of turbulent reactive particulate flows." *Theoretical and Experimental Modeling of Particulate Flows. Lecture Series 2000-06, von Karman Institute for Fluid Dynamics, Rhode Saint Genèse, Belgium.*

SIMONIN, O. *et al.* (1993). "Eulerian prediction of the fluid/particle correlated motion in turbulent two-phase flows". *Applied Scientific Research*, **51(1)**, 275–283.

VERMOREL, O. *et al.* (2003). "Numerical study and modelling of turbulence modulation in a particle laden slab flow". *Journal of Turbulence*, **4(25)**, 1–39.

APPENDIX A

Transport equations of the two-fluid modeling

The two-fluid modeling is built on a kinetic approach based on a joint fluid-particle Probability Density Function (Simonin (2000)). The set of PDF's moment transport equations is derived from a Boltzmann-like kinetic equation of the PDF. The resulting mass, momentum and particle agitation transport equations needed closure proposed by Gobin *et al.* (2003), Balzer *et al.* (1996), Gourdel *et al.* (1999), Fede and Simonin (2005) and Batrak *et al.* (2005).

The transport equations of the mass and momentum are:

$$\frac{\partial}{\partial t}(\rho_k \alpha_k) + \frac{\partial}{\partial x_i}(\rho_k \alpha_k U_{k,i}) = 0 \qquad (3)$$

$$\alpha_k \rho_k \left(\frac{\partial}{\partial t} + U_{k,j}\frac{\partial}{\partial x_j} \right) U_{k,i} =$$

$$\qquad\qquad (4)$$

$$\alpha_k \rho_k g_i - \alpha_k \frac{\partial P}{\partial x_i} - \frac{\partial}{\partial x_j}\Sigma_{k,ij} + \sum_{q=p,g} I_{(q \to k),i}$$

P is the mean pressure, g_i is the ith composant of acceleration due to gravity imposed to 9.81 $kg \cdot m \cdot s^{-2}$ along z direction, $\Sigma_{k,ij}$ is the viscous stress tensor for the gas phase and the collision stress for a particle phase, $I_{(p \to k)}$ is the average interfacial momentum transfer rate from phase q to phase k. If k=g, that term represents the drag force, if k=p, it represents the mean momentum exchanges by collisions (in case of polydispersion).

Interphase coupling in the momentum equation

Gobin *et al.* (2003) proposed a closure for the drag force.

<u>Drag force</u>

According to the assumption that particles are hard spherical spheres translating in a non-uniform flow, the drag force can be modeled in the momentum equations as a term: $I_{(g \to p)} = -\frac{\alpha_p \rho_p}{\tau_{gp}^F}V_{r,i}$ where $V_{r,i}$ is the mean gas-particle relative velocity .

Definition of the drag force characteristic velocity: the mean gas-particle relative velocity

$$\mathbf{V_r} = \mathbf{U_p} - \mathbf{U_g} - \mathbf{V_d}$$

The drift velocity V_d is due to the transport of particles by gas turbulence. In industrial fluidized beds, particles are breaking the turbulence so its influence is expected to be negligible. Nevertheless, it is modeled according to the work of Simonin *et al.* (1993):

$$V_{d,i} = -D_{gp,ij}\left[\frac{1}{\alpha_p}\frac{\partial \alpha_p}{\partial x_j} - \frac{1}{\alpha_g}\frac{\partial \alpha_g}{\partial x_j} \right] \qquad (5)$$

with $D_{gp,ij} = \frac{1}{3}q_{gp}\tau_{gp}^t \delta_{ij}$. τ_{gp}^t is the characteristic time from gas-particle turbulence (Simonin *et al.* (1993)) and q_{gp} is the fluid-particle velocity correlation.

Definition of the particle relaxation time scale τ_{gp}^F

$$\frac{1}{\tau_{gp}^F} = \frac{3}{4}\frac{\rho_g}{\rho_p}\frac{|<v_r>|}{d_p}<C_D> \qquad (6)$$

Gobin *et al.* (2003) proposed to model $<C_D>$ from the drag law of Wen & Yu limited by the one of Ergun for large solid volume fraction:

$$\begin{aligned}
<C_{D,WY}> &= \overline{C_{D,WY}} & \alpha_p \leq 0.3 \\
<C_{D,WY}> &= min(\overline{C_{D,WY}}, \overline{C_{D,Ergun}}) & \alpha_p > 0.3
\end{aligned}$$
$$\qquad (7)$$

$$\overline{C_{D,WY}} = \frac{24}{\overline{Re_p}}\left[1 + 0.15\overline{Re_p}^{0.687}\right]\alpha_g^{-1.7} \quad (with\,\overline{Re_p} < 1000)$$

$$\overline{C_{D,Ergun}} = 200\frac{\alpha_p}{Re_p} + \frac{7}{3}$$

$$\qquad (8)$$

with $\overline{Re_p} = \rho_g\frac{<v_r>d_p}{\mu_g}$

N. Nouyrigat[1,3], *E. Bouquet*[2], *O. Simonin*[1,3], *V. Lalam*[2]

Collisions between particles

The collisions between particles of different characteristics lead to mean momentum exchange between the two solid phases. According to Gourdel *et al.* (1999), the mean momentum exchange between phase p and phase q writes:

$$I_{q \to p,i} = -\alpha_p \rho_p \frac{m_q}{m_p + m_q} \frac{1 + e_c}{2} \frac{H_1(Z_{pq})}{\tau_{pq}^c} (U_{p,i} - U_{q,i}) \quad (9)$$

m_p and m_q represent the mass of any particle p and q respectively, e_c is the restitution coefficient, τ_{pq}^c the characteristic collision time. $H_1(Z_{pq})$ is a theoretical function due to the adaptation of the kinetic theory of gas that can be approximated by $H_1(Z_{pq}) = \dfrac{8 + 3Z_{pq}}{6 + 3Z_{pq}}$ where Z_{pq} represents the ratio between the square of the mean relative velocity and the relative fluctuating velocity variance given in terms of the sum of both particles specy agitation: $Z_{pq} = \dfrac{(U_p - U_q)^2}{\frac{4}{3}(q_p^2 + q_q^2)}$.

The theoretical expression of the characteristic collision time is: $\dfrac{1}{\tau_{pq}^c} = \left(g_{pq} n_q \pi d_{pq}^2 \sqrt{\frac{16}{3\pi}(q_p^2 + q_q^2)} H(Z_{pq}) \right)$, where $H(Z_{pq})$ is approximated by $H(Z_{pq}) = \sqrt{1 + \frac{\pi Z_{pq}}{4}}$, g_{pq} corresponds to the radial distribution function depending on the maximum random packing of spheres imposed to $\alpha_{max} = 0.64$.

Closure models

Turbulent stress tensor of the gas phase

Due to the multi-physics nature of the studied flow, additional terms to model the mean momentum exchange between the fluctuating motions are needed. Our modeling is based on the work of Balzer *et al.* (1996) and Vermorel *et al.* (2003).

Turbulent stress tensor of the solid phase

Batrak *et al.* (2005) proposed to write the effective stress tensor of a binary mixture of particles as:

$$\Sigma_{p,ij} = \left[P_p - \lambda_p \frac{\partial U_{p,m}}{\partial x_m} \right] \delta_{ij} - \mu_p \left[\frac{\partial U_{p,i}}{\partial x_j} + \frac{\partial U_{p,j}}{\partial x_i} - \frac{2}{3} \frac{\partial U_{p,m}}{\partial x_m} \delta_{ij} \right] \quad (10)$$

where $\mu_p = \alpha_p \rho_p (v_p^{kin} + v_p^{col})$ and the kinetic viscosity v_p^{kin} is modeled as:

$$\left[\frac{1}{3} q_{gp} \tau_{gp} + \frac{1}{2} \tau_{gp}^F \frac{2}{3} q_p^2 (1 + \frac{\tau_{gp}^F}{2} q_p^2 (1 + \widehat{\alpha_p} g_0 \Phi_c)) \right] \times \left[1 + \frac{\tau_{gp}^F}{2} \frac{\sigma_c}{\widehat{\tau_p^c}} \right]^{-1} \quad (11)$$

with $\Phi_c = \frac{2}{5}(1 + e_c)(3e_c - 1)$ and $\sigma_c = \frac{1}{5}(1 + e_c)(3 - e_c)$.

The collisional viscosity, v_p^{col} is modeled as:

$$v_p^{col} = \frac{4}{5} \widehat{\alpha_p} g_0 (1 + e_c) \left[v_p^{kin} + \widehat{d}_p \sqrt{\frac{2}{3} \frac{q_p^2}{\pi}} \right] \quad (12)$$

The only parameter to model the interaction between particles is the restitution coefficient e_c. We imposed $e_c = 0.9$, knowing that the prediction of the bed hydrdynamic is not very sensitive to this parameter.

The granular pressure P_p and λ_p:

$$P_p = \alpha_p \rho_p [1 + 2\widehat{\alpha_p} g_0 (1 + e_c)] \frac{2}{3} q_p^2,$$

$$\lambda_p = \alpha_p \rho_p \frac{4}{3} \widehat{\alpha_p} g_0 (1 + e_c) \widehat{d}_p \sqrt{\frac{2}{3} \frac{q_p^2}{\pi}}$$

The modified volume fraction, collision diameter, collision timescale write: $\widehat{\alpha_p} = \sum_q \alpha_p \frac{2m_q}{m_p + m_q} \left[\frac{d_{pq}}{d_q} \right]^3$,

$$\widehat{d}_p = \frac{1}{\widehat{\alpha_p}} \sum_q \alpha_q \frac{d_{pq}^4}{d_q^3} \frac{2m_q}{m_p + m_q}, \quad \frac{1}{\widehat{\tau_p^c}} = \sum_q \frac{2m_q}{m_p + m_q} \frac{1}{\tau_{pq}^c}$$

The closure of the momentum equation for particles introduced new unknown terms that need closure models too. A transport equation of the particle turbulent kinetic energy (q_p^2) and of the fluid-particle velocity covariance (q_{gp}) is written in the approximate form:

$$\alpha_p \rho_p \frac{\partial q_p^2}{\partial t} + \alpha_p \rho_p U_{p,j} \frac{\partial q_p^2}{\partial x_j} = \quad (13)$$

$$\frac{\partial}{\partial x_j} \left(\alpha_p \rho_p K_p^t \frac{\partial q_p^2}{\partial x_j} \right) - \Sigma_{p,ij} \frac{\partial U_{p,i}}{\partial x_j}$$

$$- \frac{\alpha_p \rho_p}{\tau_{gp}^F} \left[2q_p^2 - q_{gp} \right] + \sum_q \varepsilon_{pq} + \sum_q \chi_{pq}$$

with the kinetic diffusivity coefficient:

$$K_p^t = \left[\frac{v_{gp}^t}{\sigma_q} + \frac{5}{9} \tau_{gp}^F \frac{2}{3} q_p^2 \right] \times \left[1 + \frac{5}{9} \tau_{gp}^F \frac{\xi_c}{\tau_p^c} \right]^{-1}$$

the dissipation rate due to inelastic collisions:

$$\varepsilon_{pq} = -m_p \left(\frac{2m_q}{m_p + m_q} \right)^2 \frac{1 - e_c^2}{4} \frac{n_p}{\tau_{pq}^c} \frac{2}{3} (q_p^2 + q_q^2)$$

and the production and exchange of agitation between classes due to collisions:
$$\chi_{pq} = \frac{m_p m_q}{m_p + m_q} \frac{1 + e_c}{2} \frac{n_p}{\tau_{pq}^c}$$

$$\times \left[\frac{m_q}{m_p + m_q} \frac{1 + e_c}{2} (U_{p,i} - U_{n,i})^2 H_1(Z_{pq}) - \frac{8}{3} \frac{m_p q_p^2 - m_q q_q^2}{m_p + m_q} \right]$$

Finally, the fluid-particle covariance writes:

$$\left[\frac{\partial}{\partial t} + U_{p,j} \frac{\partial}{\partial x_j} \right] q_{gp} = \quad (14)$$

$$\frac{1}{\alpha_p \rho_p} \frac{\partial}{\partial x_j} \left(\alpha_p \rho_p \frac{v_{gp}^t}{\sigma_k} \frac{\partial q_{gp}}{\partial x_j} \right) - R_{gp,ij} \frac{\partial U_{p,i}}{\partial x_j}$$

$$- R_{gp,ji} \frac{\partial U_{g,i}}{\partial x_j} - \frac{q_{gp}}{\tau_{gp}^t}$$

$$- \frac{1}{\tau_{gp}^F} \left[\left(1 + \frac{\alpha_p \rho_p}{\alpha_g \rho_g} \right) q_{gp} - 2k - 2\frac{\alpha_p \rho_p}{\alpha_g \rho_g} q_p^2 \right]$$

Following Février and Simonin (1998), an eddy viscosity assumption is used to predict the fluid-particle velocity correlations tensor components $R_{gp,ij}$.

8th International Conference on CFD in Oil & Gas, Metallurgical and Process Industries
SINTEF/NTNU, Trondheim Norway
21-23 June 2011

CFD11-171

INTERPENETRATING CONTINUA AND MULITIPHASE TURBULENCE

Charles A. PETTY[*] , **Satish MUTHU,**
Karuna S. KOPPULA, and André BENARD

Michigan State University, East Lansing, MICHIGAN 48824, U.S.A

* E-mail: petty@msu.edu

ABSTRACT

The Reynolds averaged mixture model provides a practical means to estimate the low-order statistical properties of multiphase turbulent flows. This approach, however, requires a closure model for the Reynolds stress. In this paper, a recently developed realizable Reynolds stress model for single phase flows is extended to multiphase flows. The closure model is formulated as a non-negative algebraic mapping of the normalized Reynolds (NR-) stress into itself and is, thereby, *realizable* for all flows. The value of the new closure strategy will be illustrated in the presentation with a few selected examples of multiphase flow phenomenon in fluidized beds.

Keywords: multiphase fluids, turbulent flows, Reynolds stress, fluidized beds

NOMENCLATURE

$\underline{\underline{A}}$	defined by Eq.(61); also see Eq.(69)
$\underline{\underline{B}}$	defined by Eq.(62)
B_0, B_1	defined by Eq.(21)
C_i	defined by Eqs.(64) and (65): i = 1, 2
C_I	defined by Eq.(30)
C_I^∞	interfacial drag coefficient for large Re_C
C_{Ri}	defined by Eq.(51) and (53): i = 1, 2, 3, 4
C_{yz}	correlation coefficient, see Figure 1
D_c	defined Eq.(31), m
$\underline{e}_x, \underline{e}_y, \underline{e}_z$	Euclidean base vectors
E^3	Euclidean vector space
$\underline{f}'_{mix}$	defined by Eq.(63) , m/s^2
$\underline{g}$	acceleration due to gravity, m/s^2
$\underline{\underline{I}}$	unit operator
I_S, II_S, III_S	defined by Eq.(18), resp., s^{-1}, s^{-2}, s^{-3}
II_R, III_R	invariants of $\underline{\underline{R}}$, see Eqs.(47) and (48)
$\underline{j}_k$	defined by Eq.(9), kg/(m^2-s)
k_{mix}	defined by Eq.(55), m^2/s^2
$\underline{n}$	defined by Eq.(24)
N_E	defined by Eq.(71)
N_F	defined by Eq.(52)
N_R	defined by Eq.(68)
p_{mix}	instantaneous mixture pressure, kg/(m-s^2)
p'_{mix}	fluctuating mixture pressure, kg/(m-s^2)
R_c	defined by Eq.(30)
Re_c	defined by Eq.(31)
Re_t	defined by Eq.(54)
$\underline{\underline{R}}$	defined by Eq.(59)
$\underline{\underline{R}}_E$	defined by Eq.(70)
$\underline{\underline{S}}_{mix}$	defined by Eq.(16), 1/s
t	time, s
$\underline{\underline{T}}$	Cauchy stress in Eqs.(14a), kg/(m-s^2)
$\underline{\underline{T}}_{mix}$	mixture stress in Eq.(11), kg/(m-s^2)
$\underline{u}$	velocity, m/s
$\underline{u}_k^m$	defined by Eq.(5), m/s
$\underline{u}_{mix}$	defined by Eq.(4), m/s
$\underline{u}'_{mix}$	fluctuating mixture velocity, m/s
$\underline{u}_{2D}$	drift velocity, defined by Eq.(9), m/s
$\underline{u}_{21}$	slip velocity, defined by Eq.(22), m/s
V	volume of flow domain
V_F	finite volume within V ,m^3
V_k	volume of Phase k, m^3
X_k	defined by Eq.(1)
$\underline{x}$	position vector, m
x,y,z	coordinate directions, m

Greek symbols

α , β	defined by Eqs.(64) and (65)
α_k	defined by Eq.(2): k = 1,2
$\alpha_{2\,max}$	defined by Eq.(2)
ε_{mix}	defined by Eq.(56), m^2/s^3
κ_{mix}	defined by Eqs.(15) and (17b), kg/(m-s)
μ_{mix}	defined by Eqs.(15) and (17a), kg/(m-s)
ν_E	defined by Eq.(71)
ρ	instantaneous density, kg/m^3

ρ_k	density of Phase k: k = 1,2, kg/m^3
ρ_{mix}	defined by Eq.(3), kg/m^3
τ_R	defined by Eq.(51), s
$\underset{=}{\tau}_{mix}$	defined by Eq.(14), kg/(m-s^2)
$\underset{=}{\tau}_A, \underset{=}{\tau}_B, \underset{=}{\tau}_C$	defined by Eqs.(14a,b,c), kg/(m-s^2)
τ_E	defined by Eq.(70)
Υ_{wall}	defined by Eq.(53)

MATHEMATICAL OPERATIONS

$\dfrac{\partial \underline{a}}{\partial t}$	time derivative of a vector
$\nabla \underline{a}$	spatial gradient of a vector
$\nabla \cdot \underline{a}$	divergence of a vector
$\dfrac{D_{mix}}{D t}$	defined by Eq.(13)
$\dfrac{D_k}{D t}$	defined by Eq.(28)
$|a|$	magnitude of a scalar
$\|\underline{a}\|$	norm of a vector
$\underline{a} \cdot \underline{b}$	scalar product between two vectors
$\underline{a} \wedge \underline{b}$	cross product between two vectors
$\underset{=}{A}^T$	transpose of a dyadic-valued operator
$\mathrm{tr}(\underset{=}{A})$	trace of a dyadic-valued operator
$\det(\underset{=}{A})$	determinant of a dyadic-valued operator
$\overline{X_k \underline{a}}$	phase average of a vector
$< \underline{a} >$	Reynolds average of a vector

INTRODUCTION

The interpenetrating continua theory for multiphase fluids was developed more than forty years ago. The success of this approach depends on identifying and validating appropriate closure models that connect momentum transport phenomena among discrete immiscible continua with momentum transport phenomena among interpenetrating continua. In this paper, a new closure model for the Reynolds stress is used to close the set of Reynolds averaged balance equations governing the mean mixture momentum and the mean phase concentration. The instantaneous phase averaged balance equations and the Reynolds averaged balance equations are provided in summary form. Specific technical details and arguments related to the general development of the multiphase theory are readily available in the literature (see, esp., Gidaspow,1994; Manninen et al., 1996; Fan and Zhu, 1998; Crow et al., 1998; Drew and Passman, 1999; Jackson, 2000; Kleinstreuer, 2003; Brennen, 2005; Ishii and Hibiki, 2006; and, Prosperetti and Tryggvason, 2009).

The Reynolds average of the instantaneous field equations for the multiphase mixture model yields a set of exact, albeit unclosed, equations for the low-order statistical properties of the mean mixture velocity, the

mean mixture pressure, the mean concentration of each phase, and the mean phase slip velocities among the constituent phases. In this paper, a recently developed Reynolds stress closure for single-phase turbulent flows (see Koppula, 2009) is formally extended to multiphase turbulent flows governed by the mixture model.

INTERPENETRATING CONTINUA

A mixture of two or more immiscible continua is a discrete dynamic system governed by fundamental principles of continuum mechanics. Under many circumstances, the low-order statistical properties of a suspension can be estimated by using ensemble phase averages to replace the space/time discontinuous dynamic problem with a space/time continuous dynamic problem. In general, the theory of interpenetrating continua provides a means to develop a rigorous mathematical description of how momentum, energy, and mass can be exchanged among the constituent phases and, most significantly, how the phases can mix, separate, and react.

In order to illustrate the new approach to multiphase turbulence, this paper begins by defining a multiphase model for two immiscible continua that can exchange momentum, but not internal energy or mass. The dispersed phase is a solid and the continuous phase is a fluid (gas or liquid). The shape and size of individual solid particles do not change in the multiphase flow environment (i.e., no agglomeration or breakage of particles). The intrinsic mass densities of the two constituent phases are constant and unequal ($0 < \rho_1 \neq \rho_2$).

Clearly, the equations presented below can be extended to include non-isothermal flows and other physical phenomena (see the references cited above); however, the main objective of this paper is to illustrate how the instantaneous equations for multiphase fluids can be applied to turbulent flows. Therefore, in the next section, the instantaneous phase averaged equations that govern the behaviour of two immiscible fluids are given. This is followed by a summary of the exact, albeit unclosed, Reynolds averaged equations for the mean mixture velocity and the mean volume fraction of the dispersed phase. Closure models for the transport of mixture momentum and the transport of mixture concentration by turbulent fluctuations are also defined.

Mixture properties for two interpenetrating continua can be derived by using the following discontinuous phase indicator function:

$$X_k(\underline{x}, t) \equiv \begin{cases} 1, & \underline{x} \in V_k \subset V \\ 0, & \underline{x} \notin V_k \subset V \end{cases}. \tag{1}$$

For example, the local volume fraction of the k-th phase is defined as an ensemble average of X_k (see Drew and Passman, 1999; as well as Kleinstreuer, 2003):

$$\begin{aligned} \alpha_k &\equiv \overline{X_k} \quad , \quad k = 1, 2 \\ 0 &\leq \alpha_2 = 1 - \alpha_1 \leq \alpha_{2\max} < 1 \end{aligned}. \tag{2}$$

The parameter $\alpha_{2\,max}$ stems from the physical idea that a discrete, unconnected phase cannot exist as a pure constituent. This packing constraint is an intrinsic property of a specific solid/fluid suspension. It depends on the dispersed phase geometry (sphere, ellipsoid, etc.), the size distribution of the particulate phase, and the physicochemical properties of the solid/fluid interface.

The mixture density of two immiscible, constant density phases is defined as

$$\rho_{mix} \equiv \rho_1 \alpha_1 + \rho_2 \alpha_2 . \tag{3}$$

The mixture velocity is defined as the mass average of the constituent phase averaged velocities:

$$\underline{u}_{mix} \equiv \frac{\alpha_1 \rho_1 \underline{u}_1^m + \alpha_2 \rho_2 \underline{u}_2^m}{\rho_{mix}} . \tag{4}$$

The phase averaged velocity is defined by the following ensemble average:

$$\underline{u}_k^m \equiv \frac{\overline{X_k \rho \underline{u}}}{\overline{X_k \rho}} \quad , \quad k = 1, 2 . \tag{5}$$

The process of phase averaging replaces a non-penetrating mixture of continua with a mixture of interpenetrating continua. The resulting ensemble averages are continuous functions of space and time. The equations-of-change for the low-order moments of the ensemble are exact, but unclosed. There are no *a priori* restrictions on the spatial and temporal behaviour of the phase averaged properties. The primary motivation for phase averaging is to replace a mathematically discontinuous dynamic system with a mathematically continuous dynamic system, not space/time smoothing.

THE MIXTURE MODEL
Mass Balance

An exact equation-of-change for the mixture density is

$$\frac{\partial \rho_{mix}}{\partial t} + \nabla \cdot (\rho_{mix} \underline{u}_{mix}) = 0 \quad . \tag{6}$$

If $\rho_1 \neq \rho_2$, then Eqs.(3) and (6) imply that

$$\nabla \cdot \underline{u}_{mix} = -\frac{(\rho_2 - \rho_1)}{\rho_{mix}} (\frac{\partial \alpha_2}{\partial t} + \underline{u}_{mix} \cdot \nabla \alpha_2) . \tag{7}$$

Equation (7) shows that a mixture of constant density continua has the distinguishing characteristic that the divergence of the phase average mixture velocity is not zero (i.e., $\nabla \cdot \underline{u}_{mix} \neq 0$).

Phase Balance

An exact equation-of-change for the volume fraction of the dispersed phase is

$$\frac{\partial (\rho_2 \alpha_2)}{\partial t} + \nabla \cdot (\rho_2 \alpha_2 \underline{u}_{mix}) = -\nabla \cdot \underline{j}_2 \tag{8}$$

The drift flux of Phase 2 is defined as

$$\underline{j}_2 \equiv \rho_2 \alpha_2 \underline{u}_{2D} \quad , \quad \underline{u}_{2D} \equiv \underline{u}_2^m - \underline{u}_{mix} . \tag{9}$$

It follows from Eqs.(3) and (4) that

$$\underline{j}_1 + \underline{j}_2 = \underline{0} . \tag{10}$$

Momentum Balance

An exact, albeit unclosed, equation-of-change for the mixture momentum per unit volume is

$$\rho_{mix} \frac{D_{mix} \underline{u}_{mix}}{Dt} = + \rho_{mix} \underline{g} + \nabla \cdot \underline{\underline{T}}_{mix}$$
$$\underline{\underline{T}}_{mix} = -p_{mix} \underline{\underline{I}} + \underline{\underline{\tau}}_{mix} \quad , \quad \underline{\underline{\tau}}_{mix} = \underline{\underline{\tau}}_A + \underline{\underline{\tau}}_B + \underline{\underline{\tau}}_C \tag{11a,b,c}$$

The Cauchy mixture stress has an isotopic component and a deviatoric component. For multiphase fluids, the deviatoric component of the stress also has an isotropic component (i.e., $\text{tr}(\underline{\underline{\tau}}_{mix}) \neq 0$). The mixture pressure is determined by solving a Poisson equation, which stems directly from Eq.(3), Eq.(6), and Eq.(11):

$$\nabla^2 p_{mix} = + (\rho_2 - \rho_1)(\nabla \alpha_2) \cdot (\underline{g} - \frac{D_{mix} \underline{u}_{mix}}{Dt})$$
$$+ \nabla \cdot (\nabla \cdot \underline{\underline{\tau}}_{mix}) - \rho_{mix} \nabla \cdot (\frac{D_{mix} \underline{u}_{mix}}{Dt}) \tag{12}$$

The right-hand-side of Eq.(12) is exact. The substantial derivative of the mixture momentum per unit mass is defined as

$$\frac{D_{mix} \underline{u}_{mix}}{Dt} \equiv \frac{\partial \underline{u}_{mix}}{\partial t} + \underline{u}_{mix} \cdot \nabla \underline{u}_{mix} . \tag{13}$$

The deviatoric component of the Cauchy stress is caused by three factors:

    A) interactions at the microhydrodynamic scale;

    B) non-zero drift velocities; and,

    C) non-zero statistical slip between phases.

The deviatoric components of the stress are defined as follows

$$\underset{=A}{\tau} \equiv \sum_{k=1}^{2} \overline{X_k \underset{=}{T}}$$

$$\underset{=B}{\tau} \equiv -\sum_{k=1}^{2} \alpha_k \rho_k (\underline{u}_k^m - \underline{u}_{mix})(\underline{u}_k^m - \underline{u}_{mix}) . \qquad (14\ a,b,c)$$

$$\underset{=C}{\tau} \equiv -\sum_{k=1}^{2} \overline{X_k \rho (\underline{u} - \underline{u}_k^m)(\underline{u} - \underline{u}_k^m)}$$

Equations (14 a,b,c) are exact and stem directly from a phase average over an ensemble of flows of discrete immiscible fluids. Each individual phase is a continuum that satisfies Cauchy's equation-of-motion and the continuity equation. Possible closure models for each of the component stresses in Eq.(14) are briefly discussed below. For a formal development and extended discussion of these equations, the interested reader should refer to Manninen et al. (1996); Drew and Passman (1999); and, Kleinstreuer (2003).

The Mixture Stress Due to Mixture Deformation

A generalized Newtonian model is often employed to account for the stress due to mixture deformation:

$$\underset{=A}{\tau} = +2\,\mu_{mix}\,\underset{=mix}{S} - (\frac{2}{3}\mu_{mix} - \kappa_{mix})\,\text{tr}\,(\underset{=mix}{S})\,\underset{=}{I} . \qquad (15)$$

The mixture strain rate $\underset{=mix}{S}$ is

$$\underset{=mix}{S} \equiv \frac{1}{2}[(\nabla \underline{u}_{mix}) + (\nabla \underline{u}_{mix})^T]\ . \qquad (16)$$

The mixture viscosity coefficients, μ_{mix} and κ_{mix}, depend on the local volume fraction of the "dispersed" phase and the three invariants of the mixture strain rate:

$$\mu_{mix} = \mu_{mix}(\alpha_2, I_S, II_S, III_S)$$
$$\qquad\qquad\qquad\qquad (17a,b)$$
$$\kappa_{mix} = \kappa_{mix}(\alpha_2, I_S, II_S, III_S)$$

The three invariants of $\underset{=mix}{S}$ are defined as follows

$$I_S \equiv \text{tr}[\ \underset{=mix}{S}\ ] = \nabla \cdot \underline{u}_{mix}\ \text{(see Eq.(7) above)}$$

$$II_S \equiv \text{tr}[(\underset{=mix}{S}) \cdot (\underset{=mix}{S})]\qquad\qquad . \qquad (18)$$

$$III_S \equiv \text{tr}[(\underset{=mix}{S}) \cdot (\underset{=mix}{S}) \cdot (\underset{=mix}{S})]$$

For non-isothermal flows, an equation for the mixture temperature can be identified by developing a phase average energy balance for the mixture (see Gidaspow, 1994; and, Kleinstreuer, 2003). In general, the local mixture temperature and the local mixture pressure will also influence the mixture viscosity coefficients. The phenomenological mixture viscosity coefficients connect the physical properties of each discrete phase at the microhydrodynamic scale with the mixture momentum flux in response mixture deformation.

The Mixture Stress Due to Drift Velocities

For a two-phase fluid, the drift velocities (see Eq.(9) above) induce the following exact contribution to the deviatoric component of the mixture stress:

$$\underset{=B}{\tau} = -\sum_{k=1}^{2} \alpha_2\,\rho_k\,\underline{u}_{kD}\,\underline{u}_{kD}\ . \qquad (19)$$

Equation (19) is in closed form. The drift stress dyads can be calculated by using Eqs.(22) and (32) below.

The Mixture Stress Due to Phase Slip

A statistical phase slip between the instantaneous and phase average velocity at the microhydrodynamic scale also induces a stress that contributes to the total mixture stress (see Eq.(14c) above). A plausible, albeit untested, closure hypothesis for $\underset{=C}{\tau}$ is the assumption that (see p. 209, Kleinstreuer, 2003):

$$\underset{=C}{\tau} = \underset{=C}{\tau}(\rho_{mix}\,\underline{u}_{21}\underline{u}_{21})\,, \text{ where} \qquad (20)$$

$\underline{u}_{21}$ is the phase slip velocity, defined by Eq.(22) below. The Cayley-Hamilton (CH-) theorem of linear algebra implies that the most general representation of Eq.(20) is linear in the phase slip dyad:

$$\begin{aligned}\underset{=C}{\tau} = &\ B_0 \text{tr}(\rho_{mix}\,\underline{u}_{21}\,\underline{u}_{21})\underset{=}{I}\\ &+ B_1(\,\rho_{mix}\,\underline{u}_{21}\,\underline{u}_{21} - \frac{1}{3}\text{tr}(\rho_{mix}\,\underline{u}_{21}\,\underline{u}_{21})\,\underset{=}{I}\,)\end{aligned} \qquad (21)$$

The phenomenological dimensionless CH-coefficients B_0 and B_1 may depend on the local volume fraction as well as the local mixture pressure and the local mixture temperature.

Phase Slip Equation

For two immiscible phases, the local drift velocity, the local phase slip velocity, the local volume fraction of the dispersed phase, and the densities of the constituent phases are related by the following equations:

$$\underline{u}_{2D} = \frac{\alpha_1\rho_1}{\rho_{mix}}\,\underline{u}_{21}\quad,\quad \underline{u}_{1D} = \frac{\alpha_2\rho_2}{\rho_{mix}}\,\underline{u}_{12}\,. \qquad (22)$$
$$\Rightarrow\quad \underline{u}_{2D} - \underline{u}_{1D} = \underline{u}_{21} = \underline{u}_2^m - \underline{u}_1^m$$

Note that

$$\underline{u}_{21} + \underline{u}_{12} \equiv \underline{0}\ . \qquad (23)$$

An exact (albeit unclosed) equation-of-change for the phase averaged momentum of Phase k can be written as follows:

$$\alpha_k \rho_k \frac{D_k \underline{u}_k^m}{Dt} = \nabla \cdot (\ \overline{X_k \underline{\underline{T}}} - \overline{X_k \rho \underline{uu}} + \alpha_k \rho_k \underline{u}_k^m \underline{u}_k^m\ )$$
$$+ \alpha_k \rho_k \underline{g} - \overline{\underline{\underline{T}} \cdot \underline{n} |\underline{n} \cdot \nabla X_k|} \tag{24}$$

The vector $\underline{n}$ in Eq.(24) is defined at the microhydrodynamic scale as the outward pointing normal vector at the interface between two phases. For a two-phase fluid, $\underline{n}_2 = -\underline{n}_1$. An exact, but unclosed, equation for the exchange of momentum between Phase k and the mixture follows by taking the difference between Eq.(24) and Eq.(11) multiplied by the volume fraction of Phase k:

$$\{Eq.(24)\} - \alpha_k \{Eq.(11)\} \Rightarrow$$

$$\overline{\underline{\underline{T}} \cdot \underline{n} |\underline{n} \cdot \nabla X_k|} = \tag{25}$$
$$+ \alpha_k (\rho_k - \rho_{mix}) (\underline{g} - \frac{D_{mix} \underline{u}_{mix}}{Dt})$$
$$+ \underline{\underline{T}}_{mix} \cdot \nabla \alpha_k + \underline{N}_k$$

The vector $\underline{N}_k$ in Eq.(25) is defined as follows:

$$\underline{N}_k \equiv \nabla \cdot (\ \overline{X_k \underline{\underline{T}}} - \overline{X_k \rho \underline{uu}} + \alpha_k \rho_k \underline{u}_k^m \underline{u}_k^m - \alpha_k \underline{\underline{T}}_{mix})$$
$$+ \alpha_k \rho_k (\frac{D_{mix} \underline{u}_{mix}}{Dt} - \frac{D_k \underline{u}_k^m}{Dt}) \tag{26}$$

The mixture stress, $\underline{\underline{T}}_{mix}$, is given by

$$\underline{\underline{T}}_{mix} = \sum_{k=1}^{2} \overline{X_k \underline{\underline{T}}} - (\sum_{k=1}^{2} \overline{X_k \rho \underline{uu}} - \rho_{mix} \underline{u}_{mix} \underline{u}_{mix})$$
$$= -p_{mix} \underline{\underline{I}} + \underline{\underline{\tau}}_A + \underline{\underline{\tau}}_B + \underline{\underline{\tau}}_C \quad \text{(see Eq.(14) above)} \tag{27}$$

The acceleration of Phase k is defined as

$$\frac{D_k \underline{u}_k^m}{Dt} \equiv \frac{\partial \underline{u}_k^m}{\partial t} + \underline{u}_k^m \cdot \nabla \underline{u}_k^m . \tag{28}$$

The acceleration of the mixture is defined by Eq.(13) above.

Each term in Eq.(25) sums separately to zero, including the vector $\underline{N}_k$:

$$\sum_{k=1}^{2} \underline{N}_k =$$
$$\nabla \cdot \{\ \sum_{k=1}^{2} (\overline{X_k \underline{\underline{T}}}) - \underline{\underline{T}}_{mix}\ \}$$
$$- \nabla \cdot \{\sum_{k=1}^{2} (\overline{X_k \rho \underline{uu}}) - \sum_{k=1}^{2} (\alpha_k \rho_k \underline{u}_k^m \underline{u}_k^m)\ \} \tag{29}$$
$$+ \sum_{k=1}^{2} (\alpha_k \rho_k) \frac{D_{mix} \underline{u}_{mix}}{Dt} - \sum_{k=1}^{2} (\alpha_k \rho_k \frac{D_k \underline{u}_k^m}{Dt}) \equiv \underline{0}$$

In the absence of mass transfer between phases and interfacial tension, the drag on the left-hand-side of Eq.(25) can be estimated by using the following assumption (see Crow et al.,1998; and, Kleinstreuer, 2003):

$$\overline{\underline{\underline{T}} \cdot \underline{n} |\underline{n} \cdot \nabla X_2|} = C_I(Re_C) \frac{\pi R_C^2}{\frac{4}{3}\pi R_C^3} \frac{1}{2} \rho_{mix} \|\underline{u}_{21}\| \underline{u}_{21} . \tag{30}$$

Equation (30) conforms to the common use of a drag coefficient to account for the quasi-steady transfer of momentum across an interface with a local curvature of $1/R_C$. The characteristic Reynolds number in Eq.(30) is defined as follows:

$$Re_C = \frac{\rho_{mix} \|\underline{u}_{21}\| D_C}{\mu_{mix}} \quad , \quad D_C \equiv 2R_C . \tag{31}$$

An application of Eq.(30) requires a specification of the interfacial drag coefficient $C_I(Re_C)$. For example, if $Re_C \ll 1$, then Stokes' law implies that $C_I = 24/Re_C$; and, if $Re_C \gg 1$, then $C_I \to C_I^\infty > 0$.

The parameter $D_C (= 2R_C)$ in Eq.(31) depends on the local particle size distribution of the underlying suspension and the local magnitude of the volume fraction gradient, $\|\nabla \alpha_2\|$. Phenomenological equations for D_c have been proposed by Ishii and Hibiki (2006).

With $\|\underline{N}_2\| \cong 0$, Eq. (25) reduces to an algebraic equation. This hypothesis (untested) assumes that the local transfer of momentum between the mixture and the underlying dispersed phase involves a quasi-steady balance among three forces: 1) a local drag caused by the transfer of momentum between the two underlying phases; 2) a net buoyant force due to gravity and the acceleration of the mixture; and, 2) a mechano-phoretic force caused by a coupling between the local Cauchy mixture stress and the local spatial gradient of the dispersed phase:

$$\underbrace{\frac{3}{4} C_I(Re_C) \frac{\rho_{mix} \|\underline{u}_{21}\| \underline{u}_{21}}{D_C}}_{\text{drag}} =$$
$$+ \underbrace{\alpha_2 (\rho_2 - \rho_{mix}) (\underline{g} - \frac{D_{mix} \underline{u}_{mix}}{Dt})}_{\text{net buoyancy}} + \underbrace{\underline{\underline{T}}_{mix} \cdot \nabla \alpha_2}_{\substack{\text{stress-induced} \\ \text{phoresis}}} . \tag{32}$$

In summary, the instantaneous mixture model is defined by Eq.(8) for α_2; Eq.(11) for $\underline{u}_{mix}$; Eq.(12) for p_{mix}; and, Eq.(32) for $\underline{u}_{21}$. These equations require an appropriate set of boundary conditions as well as a model for the deviatoric component of the mixture stress (i.e., see Eq.(14) for $\underline{\underline{\tau}}_{mix}$). The flux of Phase 2 in Eq.(8) is algebraically linked to the phase slip velocity determined by Eq.(32) above. Flow simulations based

on the foregoing mixture model requires a specification of initial conditions as well as the following set of physical property parameters: the phase densities ρ_1 and ρ_2; the packing parameter $\alpha_{2\,max}$; and, the transport properties μ_{mix}, κ_{mix}, B_0, B_1, $C_1(Re_C)$, and D_c.

REYNOLDS AVERAGE MIXTURE MODEL

By conjecture, solutions to the instantaneous mixture model defined by Eqs.(8), (11), (12), and (32) are "turbulent" if the following two conditions hold within some finite domain: 1) the local inertial forces are large compared with the local deviatoric forces, i.e.,

$$\left\| \nabla \cdot (\rho_{mix} \underline{u}_{mix} \underline{u}_{mix}) \right\| \Box \left\| (\nabla \cdot \underline{\underline{\tau}}_{mix}) \right\| \, , \, \underline{x} \in V_F \subseteq V \; ; \; (33)$$

and, 2) the instantaneous mixture vorticity is not aligned with the instantaneous mixture velocity, i.e.,

$$\left\| (\nabla \wedge \underline{u}_{mix}) \wedge \underline{u}_{mix} \right\| \neq 0 \quad , \quad \underline{x} \in V_F \subseteq V \; . \quad (34)$$

Under the foregoing two conditions, the instantaneous velocity field is three dimensional, unsteady, and highly sensitive to initial conditions (i.e., the flow is turbulent). These characteristics have been the practical experience with the single-phase Navier-Stokes equation for more than 100 years and have motivated the use of statistical continuum methods as a means to understand the behaviour of ensembles of turbulent flows (bounded, unbounded, rotating, and non-rotating). There is no reason to think that the instantaneous mixture equations behave differently. Fortunately, for some turbulent flows of a Newtonian fluid, low-order statistical properties are well-defined and reproducible. This may also occur for a class of turbulent flows of multiphase mixtures (see Drew and Passman, 1999; Pope, 2000; Prosperetti and Tryggvason, 2009).

Turbulent fluctuating fields are formally defined as the difference between the instantaneous field and the mean field. For example,

$$\begin{aligned}
\alpha_2 &= <\alpha_2>(\underline{x},t) + \alpha'_2(\underline{x},t) \\
\underline{u}_{mix} &= <\underline{u}_{mix}>(\underline{x},t) + \underline{u}'_{mix}(\underline{x},t) \\
p_{mix} &= <p_{mix}>(\underline{x},t) + p'_{mix}(\underline{x},t) \\
\underline{u}_{21} &= <\underline{u}_{21}>(\underline{x},t) + \underline{u}'_{21}(\underline{x},t)
\end{aligned} \quad (35)$$

The drift flux and the deviatoric mixture stress in Eqs.(8) and (11) can also be decomposed into a mean component and a fluctuating component:

$$\begin{aligned}
\underline{j}_2 &= <\underline{j}_2> + \underline{j}'_2 \\
\underline{\underline{\tau}}_{mix} &= <\underline{\underline{\tau}}_{mix}> + \underline{\underline{\tau}}'_{mix}
\end{aligned} \quad (36)$$

The Reynolds average operator is a linear integral operator that commutes with temporal and spatial derivatives. The Reynolds average of any fluctuating field is zero. The Reynolds average of Eq.(3) yields the following relationship among the mean mixture density, the mean volume fractions, and the constituent densities:

$$\begin{aligned}
<\rho_{mix}> &= \rho_1 <\alpha_1> + \rho_2 <\alpha_2> \\
<\alpha_2> + <\alpha_2> &= 1
\end{aligned} \quad (37)$$

For multiphase turbulent flows, the set of instantaneous mixture equations presented above can be averaged over an ensemble of turbulent flows to obtain a set of unclosed mean field equations for the mixture. Closure models are required to account for the turbulent transport of mean mixture momentum and the turbulent transport of constituent phases. The resulting set of coupled equations govern the behaviour of the mean volume fraction $<\alpha_2>$; the mean mixture pressure $<p_{mix}>$, the mean mixture velocity $<\underline{u}_{mix}>$, and, the mean slip velocity $<\underline{u}_{21}>$.

If the above strategy is applied to the Navier-Stokes equation, then the unclosed Reynolds averaged Navier-Stokes (RANS-) equation emerges (see Pope, 2000). If the above strategy is applied to Eq.(11), then the unclosed Reynolds averaged mixture (RAM-) equation emerges (see Eq.(41) below). Like the RANS-equation, the closure for the RAM-equation requires a model for the Reynolds stress, which accounts for the transport of mixture momentum by turbulent fluctuations in the mixture velocity. By definition, the eigenvalues of the Reynolds stress must be non-positive. This realizability condition is one of the most important (and elusive) mathematical properties of any turbulent closure model for the Reynolds stress (see Pope, 2000). This problem is addressed in the approach adopted herein by using a theory developed at Michigan State University by Parks (1997), Weisfennig (1997), and Koppula (2009).

Reynolds Averaged Mass Balance

The ensemble average of Eq.(6) yields an exact, unclosed equation for the mean mixture density:

$$\frac{\partial <\rho_{mix}>}{\partial t} + \nabla \cdot (<\rho_{mix}><\underline{u}_{mix}>) \\
= -(\rho_2 - \rho_1) \nabla \cdot <\alpha'_2 \underline{u}'_{mix}> \quad (38)$$

Equation (38) and the Reynolds average of Eq.(6) place a constraint on the divergence of the mean mixture velocity (i.e., $\nabla \cdot <\underline{u}_{mix}>$) and, thereby, the mean mixture pressure (cf. Eq.(12) above).

Reynolds Average Phase Balance

The Reynolds average of Eq.(8) yields an exact, unclosed equation for the mean volume fraction:

$$\frac{\partial (\rho_2 <\alpha_2>)}{\partial t} + \nabla \cdot (\rho_2 <\alpha_2><\underline{u}_{mix}>) \\
= -\nabla \cdot [<\underline{j}_2> -\rho_2 <\alpha'_2 \underline{u}'_{mix}>] \quad (39)$$

The flux of Phase 2 caused by the fluctuating drift velocity is often neglected compared with the flux caused by the fluctuating mixture velocity. Therefore,

$$< \underline{j}_2 > = \rho_2 < \alpha_2 > < \underline{u}_{2D} > + \underbrace{\rho_2 < \alpha'_2 \underline{u}'_{2D} >}_{\text{neglect}} \ . \qquad (40)$$

The mean drift velocity in Eq.(40) is related to the mean slip velocity by formally averaging Eq.(22) and neglecting turbulent correlations:

$$< \underline{u}_{2D} > \Box \ \frac{< \alpha_1 > \rho_1}{< \rho_{mix} >} < \underline{u}_{21} > . \qquad (41)$$

Reynolds Average Momentum Balance

The Reynolds average of Eq.(11) yields an exact, unclosed equation for the mean mixture velocity:

$$\begin{aligned}
& \frac{\partial}{\partial t} (< \rho_{mix} > < \underline{u}_{mix} >) \\
& + \nabla \cdot (< \rho_{mix} > < \underline{u}_{mix} > < \underline{u}_{mix} >) \\
& = + < \rho_{mix} > \underline{g} - \nabla < p_{mix} > \\
& + \nabla \cdot < \underline{\underline{\tau}}_{mix} > - \nabla \cdot (< \rho_{mix} > \underbrace{< \underline{u}'_{mix} \underline{u}'_{mix} >}_{2}) \\
& - (\rho_2 - \rho_1) \frac{\partial}{\partial t} (\underbrace{< \alpha'_2 \underline{u}'_{mix} >}_{1}) \\
& - (\rho_2 - \rho_1) \nabla \cdot [< \underline{u}_{mix} > < \alpha'_2 \underline{u}'_{mix} > \\
& \qquad\qquad + < \alpha'_2 \underline{u}'_{mix} > < \underline{u}_{mix} >] \\
& - (\rho_2 - \rho_1) \nabla \cdot \underbrace{< \alpha'_2 \underline{u}'_{mix} \underline{u}'_{mix} >}_{3, \text{neglect}}
\end{aligned} \qquad (42)$$

Equation (42), referred to as the RAM-equation, depends on three turbulent correlations: 1) a second-order, vector-valued turbulent flux of the "dispersed" phase, $< \alpha'_2 \underline{u}'_{mix} >$; 2) a second-order, dyadic-valued turbulent flux of mixture momentum per unit mass, $< \underline{u}'_{mix} \underline{u}'_{mix} >$; and, 3) a third-order, dyadic-valued correlation. For a single-phase, constant property Newtonian fluid, Eq.(42) reduces to the RANS-equation.

Reynolds Average Phase Slip Equation

The Reynolds average of Eq.(32) gives an unclosed non-linear, algebraic equation for the Reynolds averaged slip velocity. If all second-order (and higher) turbulent correlations are neglected, then the Reynolds averaged slip velocity can be estimated by the following equation:

$$\frac{3}{4} C_I (< Re_C >) \frac{< \rho_{mix} > \| < \underline{u}_{21} > \| < \underline{u}_{21} >}{< D_C >} =$$

$$+ < \alpha_2 > (\rho_2 - < \rho_{mix} >) \left(\underline{g} - < \frac{D_{mix} \underline{u}_{mix}}{Dt} > \right) . \quad (43)$$

$$- < p_{mix} > \nabla < \alpha_2 > + < \underline{\underline{\tau}}_{mix} > \cdot \nabla < \alpha_2 >$$

The Reynolds average of the mixture acceleration in Eq.(43) can be expressed as

$$\begin{aligned}
< \frac{D_{mix} \underline{u}_{mix}}{Dt} > &= \frac{\partial < \underline{u}_{mix} >}{\partial t} + < \underline{u}_{mix} > \cdot \nabla < \underline{u}_{mix} > \\
& + \underbrace{< \underline{u}'_{mix} \cdot \nabla \underline{u}'_{mix} >}_{\text{neglect}}
\end{aligned} \qquad (44)$$

Reynolds averages of the deviatoric components of the Cauchy stress (see Eqs.(15), (19), and (21) above) also give unclosed, non-linear, algebraic equations for the mean stresses. If all second order (and higher) turbulent correlations are neglected, then the Reynolds averaged equations are formally the same as the instantaneous equations. This approximation is also used to relate the mean viscosity coefficients to the mean volume fraction and mean invariants of the strain rate:

$$\begin{aligned}
< \mu_{mix} > &\Box \ \mu_{mix} (< \alpha_2 >, < I_S >, < II_S >, < III_S >) \\
< \kappa_{mix} > &\Box \ \kappa_{mix} (< \alpha_2 >, < I_S >, < II_S >, < III_S >)
\end{aligned} \qquad (45)$$

The Reynolds averages of the three invariants of the strain rate are approximated by

$$< I_S > = \nabla \cdot < \underline{u}_{mix} > \quad \text{(exact)} \qquad (46)$$

$$< II_S > \cong \text{tr}(< \underline{\underline{S}} > \cdot < \underline{\underline{S}} >) , \qquad (47)$$

$$< II_S > \cong \text{tr}(< \underline{\underline{S}} > \cdot < \underline{\underline{S}} > \cdot < \underline{\underline{S}} >) . \qquad (48)$$

Turbulent Mixing of Phases

A gradient model for the turbulent flux of Phase 2 can be written as (see Monin and Yaglom, 1965; Weispfennig, 1997; Weispfennig et al., 1999; and, Drew and Passman, 1999):

$$< \alpha'_2 \underline{u}'_{mix} > = -\tau_R < \underline{u}'_{mix} \underline{u}'_{mix} > \cdot \nabla < \alpha_2 > \qquad (49)$$

With $\tau_R \geq 0$, Eq.(49) implies that Phase 2 is transported from regions of high concentration to regions of low concentration inasmuch as

$$\begin{aligned}
< \alpha_2 \underline{u}'_{mix} > \cdot \nabla < \alpha_2 > = \\
-\tau_R < \underline{u}'_{mix} \underline{u}'_{mix} > : (\nabla < \alpha_2 > \nabla < \alpha_2 >) \leq 0
\end{aligned} \qquad (50)$$

The above inequality holds for all flows provided the eigenvalues of the dyadic-valued operator $< \underline{u}'_{mix} \underline{u}'_{mix} >$ are non-negative. The phenomenological turbulent transport time in Eq.(49) is defined as follows (see Koppula, 2009)

$$\tau_R = C_{R1} \frac{k_{mix}}{\varepsilon_{mix}} \left(\frac{(1 + C_{R3} N_F^{3/2})}{(1 + C_{R2} N_F^{3/2})} \right) \Upsilon_{wall} \ . \qquad (51)$$

The dimensionless group N_F is defined as

$$N_F \equiv (k_{mix} / \varepsilon_{mix}) \| < \nabla \underline{u}_{mix} > \| \ ; \qquad (52)$$

the dimensionless wall function Υ_{wall} is defined as

$$\Upsilon_{wall} \equiv [\, 1 + C_{R4}(30/\text{Re}_t)^{3/4}\exp(-\text{Re}_t/30)\,]\ ;\ \text{and},\quad (53)$$

the turbulent Reynolds number is defined as

$$\text{Re}_t \equiv \rho_{mix}\, k_{mix}^2 \,/\,(\mu_{mix}\,\varepsilon_{mix})\quad. \qquad (54)$$

The turbulent kinetic energy and the turbulent dissipation are defined as follow:

$$k_{mix} \equiv \frac{1}{2}\text{tr}(<\underline{u}'_{mix}\,\underline{u}'_{mix}>) \ge 0 \qquad (55)$$

$$\varepsilon_{mix} \equiv \nu_{mix} <(\nabla\underline{u}'_{mix}):(\nabla\underline{u}'_{mix})^T > 0\ . \qquad (56)$$

The equations that determine the behaviour of these two statistical properties of the mixture are formally the same as the transport equations used for single phase turbulent flows (see Manninen et al., 1996; Weispfennig, 1997; Koppula, 2009):

$$\frac{\partial k_{mix}}{\partial t} + <\underline{u}_{mix}> \cdot \nabla k_{mix} =$$
$$+ \nabla \cdot [\,(\nu_{mix}\underline{\underline{I}} + \tau_R <\underline{u}'_{mix}\,\underline{u}'_{mix}>)\cdot \nabla k_{mix})\,] \qquad (57)$$
$$- <\underline{u}'_{mix}\,\underline{u}'_{mix}>:<\underline{\underline{S}}_{mix}> - \varepsilon_{mix}$$

$$\frac{\partial \varepsilon_{mix}}{\partial t} + <\underline{u}_{mix}> \cdot \nabla \varepsilon_{mix} =$$
$$+ \nabla \cdot [\,(\nu_{mix}\underline{\underline{I}} + \tau_R <\underline{u}'_{mix}\,\underline{u}'_{mix}>)\cdot \nabla \varepsilon_{mix})\,]. \qquad (58)$$
$$+ C_P\,\frac{- <\underline{u}'_{mix}\,\underline{u}'_{mix}>:<\underline{\underline{S}}_{mix}>}{\tau_R} - C_D\,\frac{\varepsilon_{mix}}{\tau_R}$$

The "production" coefficient C_P and the dissipation coefficient C_D in Eq.(58) may depend on Re_t and N_F. These coefficients are selected to insure that the turbulent dissipation is positive for all turbulent flows. The turbulent transport time τ_R in Eq.(58) is defined by Eq.(51). Near a solid/fluid interface, the turbulent Reynolds number approaches zero and the wall function increases inasmuch as $\Upsilon_{wall} \to \text{Re}_t^{-3/4}$. Consequently, $\tau_R \to \infty$ as $\text{Re}_t \to 0$. Therefore, Eq.(58) can be integrated to the solid/fluid interface.

Turbulent Mixing of Momentum

A recently developed algebraic closure model for the normalized Reynolds (NR-) stress (i.e., $\underline{\underline{R}}$) for single phase fluids (see Koppula, 2009; Koppula et al., 2009) can be used to estimate the NR-stress for multiphase fluids. The new closure, which stems directly from an analysis of the Navier-Stokes equation for the fluctuating velocity, is formulated as a non-negative algebraic mapping of $\underline{\underline{R}}$ into itself and is, thereby, *realizable* for all turbulent flows. The following set of equations defines the universal, realizable, anisotropic prestress (URAPS) closure model for $\underline{\underline{R}}$. Equations

(59)-(61) below define the preclosure equation (Weispfennig, et. al, 1999; Koppula et al., 2009):

$$<\underline{u}'_{mix}\,\underline{u}'_{mix}> = 2\,k_{mix}\,\underline{\underline{R}} \qquad (59)$$

$$\underline{\underline{R}} \equiv \frac{<\underline{u}'_{mix}\,\underline{u}'_{mix}>}{\text{tr}<\underline{u}'_{mix}\,\underline{u}'_{mix}>} = \frac{\underline{\underline{A}}^T\cdot\underline{\underline{B}}\cdot\underline{\underline{A}}}{\text{tr}(\underline{\underline{A}}^T\cdot\underline{\underline{B}}\cdot\underline{\underline{A}})} \qquad (60)$$

$$\underline{\underline{A}} \equiv [\,\underline{\underline{I}} + \tau_R\nabla\langle\underline{u}_{mix}\rangle\,]^{-1} \qquad (61)$$

The NR-stress for the mixture satisfies the same algebraic preclosure equation as the NR-stress for a Newtonian fluid. The algebraic equation for the transport time τ_R, defined by Eq.(51) above, is formally the same as the turbulent transport time for a single-phase Newtonian fluid.

Equation (60) shifts the NR-stress closure problem to the prestress operator $\underline{\underline{B}}$ defined by Eqs.(62)-(67):

$$\underline{\underline{B}} \equiv \frac{<\underline{f}'_{mix}\,\underline{f}'_{mix}>}{\text{tr}(<\underline{f}'_{mix}\,\underline{f}'_{mix}>)} \qquad (62)$$
$$= \underline{\underline{R}} + C_1\,(\underline{\underline{R}} - \underline{\underline{I}}/3) + C_2\,(\underline{\underline{R}}\cdot\underline{\underline{R}} - (\underline{\underline{R}}:\underline{\underline{R}})\,\underline{\underline{R}})$$

$$\underline{f}'_{mix} \equiv \nabla\cdot[\,p'_{mix}\underline{\underline{I}} + \underline{u}'_{mix}\,\underline{u}'_{mix} - <\underline{u}'_{mix}\,\underline{u}'_{mix}>\,] \qquad (63)$$

$$C_1 = +[27\det(\underline{\underline{R}})]\beta(\text{II}_R,\text{III}_R) \qquad (64)$$

$$C_2 = -[\text{II}_R - 1/3]\,\alpha(\text{II}_R,\text{III}_R) \qquad (65)$$

$$-3/2 = \alpha_{min} < \alpha(\text{II}_R,\text{III}_R) < \alpha_{max} = 9 \qquad (66)$$
$$-1 = \beta_{min} < \beta(\text{II}_R,\text{III}_R) < \beta_{max} \equiv \alpha/27 + 4/9\ . \qquad (67)$$

Equations (60) and (62) can be combined to define a mapping of the NR-stress into itself (URAPS-equation). It is noteworthy that all solutions to the URAPS-equation are non-negative operators provided Ineqs.(66) and (67) for the "extra" anisotropic coefficients, α and β, are satisfied (see Koppula, 2009). The "extra" anisotropic coefficients are universal functions of the second and third invariants of $\underline{\underline{R}}$: $\text{II}_R \equiv \text{tr}(\underline{\underline{R}}\cdot\underline{\underline{R}})$ and $\text{III}_R \equiv \text{tr}(\underline{\underline{R}}\cdot\underline{\underline{R}}\cdot\underline{\underline{R}})$.

RESULTS

For simple shear flows, the mean velocity gradient has only one component:

$$\tau_R\nabla<\underline{u}_{mix}> = N_R\,\underline{e}_y\underline{e}_z\ . \qquad (68)$$

For this case, the preclosure operator, defined by Eq.(61) above, is

$$\underline{\underline{A}} = \underline{\underline{I}} - N_R\,\underline{e}_y\underline{e}_z\quad,\quad \underline{\underline{A}}^{-1} = \underline{\underline{I}} + N_R\,\underline{e}_y\underline{e}_z \qquad (69)$$

The URAPS-equation (i.e., a combination of Eqs.(60) and (62) above) was solved by successive substitution with $\alpha = 0.1$ and $\beta = -0.01$. The coefficients α and β were estimated by using experimental results related to

asymptotic homogenous shear for a single phase fluid (see Koppula et a., 2009). Figures 1-4 summarize the results for $0.001 < N_R < 0.1$.
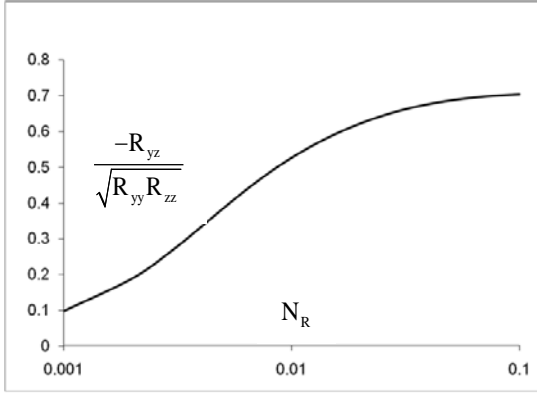

Figure 1. The influence of the local shear group on the correlation coefficient C_{yz} of the NR-Stress for simple shear ($\alpha = 0.1$ and $\beta = -0.01$).

Figure 1 shows that the URAPS correlation coefficient, $C_{yz} (\equiv \sqrt{R_{yz}^2 / R_{yy} R_{zz}})$, increases monotonically with N_R. A necessary condition for the eigenvalues of the NR-stress to be non-negative is $0 \le C_{yz} \le 1$. The URAPS closure predicts that $C_{yz} = 0$ for $N_R = 0$; and, $C_{yz} \to C_{yz}^{\infty} < 0.7$ for $N_R \to \infty$. The specific value of C_{yz}^{∞} depends on the value of α and β. In general, α and β are universal functions of the local invariants of the NR-stress. The results presented herein are encouraging inasmuch as the fundamental coupling between the mean velocity gradient and the underlying fluctuating velocity field has been captured by the URAPS-closure.
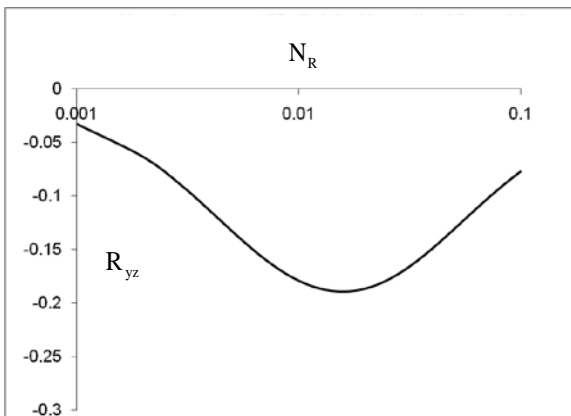

Figure 2. The influence of the local shear group N_R on the shear component of the NR-Stress for simple shear ($\alpha = 0.1$ and $\beta = -0.01$).

Figure 2 shows that the magnitude of the shear component of the NR-stress is consistent with direct numerical simulations of simple shear flows of Newtonian fluids (see Koppula, 2009). The results

presented here assume that the "extra" anisotropy coefficients α and β are constant.

Figure 3 below gives the interesting result that the primary and secondary normal stress differences of the NR-stress are, respectively, positive and negative for all values of N_R. This is consistent with experimental (and simulation) results for simple turbulent shear flows of a single phase fluid (see Koppula, 2009; Pope, 2000). The same behaviour is expected for the NR-stress for a multiphase fluid governed by the mixture model.
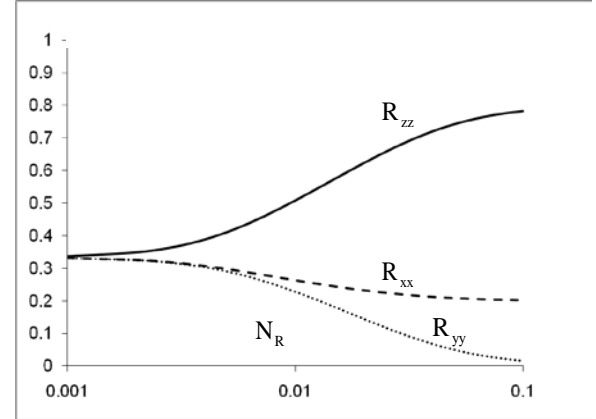

Figure 3. The influence of the local shear group on the distribution of turbulent kinetic energy among the three components of the fluctuating velocity for simple shear ($\alpha = 0.1$ and $\beta = -0.01$).

Finally, Figure 4 illustrates that the URAPS closure for simple turbulent shear flows (either single phase Newtonian fluid or multiphase mixture) acts like a shear thinning fluid.
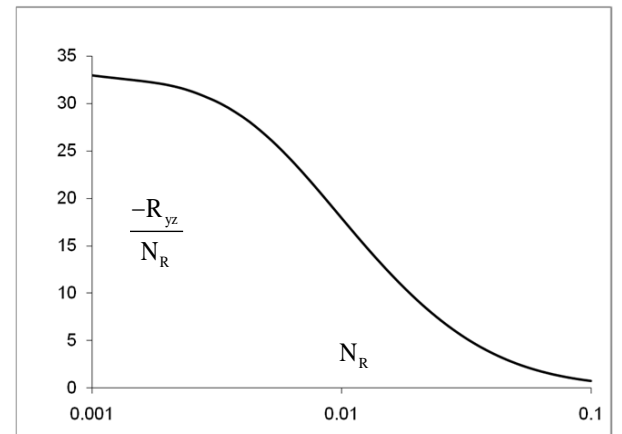

Figure 4. The influence of the local shear group on the viscosity coefficient for simple shear ($\alpha = 0.1$ and $\beta = -0.01$).

CONCLUSION

The foregoing Reynolds averaged equations for the mixture model (see Eqs.(38), (39), (42), and (43) above) are clearly influenced (either explicitly or implicitly) by the following two turbulent correlations: 1) the turbulent mixing of mixture momentum, $< \underline{u}'_{mix} \underline{u}'_{mix} >$; and,

2) the turbulent mixing of the constituent phases, $< \alpha'_2 \underline{u}'_{mix} >$. Other statistical properties will also influence the local behaviour of the mean mixture velocity, the mean mixture pressure, the mean volume fraction of the dispersed phase, and the mean phase slip velocity, but the foregoing two statistical properties are presumably the most significant.

The URAPS-closure for the NR-stress, defined by Eqs.(59)-(67), provides a new paradigm for estimating the low-order statistical properties of turbulent flows for single-phase fluids and for multiphase fluids. The URAPS theory has much potential to replace the ubiquitous, albeit unphysical, "eddy" viscosity (i.e., or Boussinesq-) model for the NR-stress:

$$\underline{\underline{R}}_E = \frac{1}{3}\underline{\underline{I}} - \tau_E (<\underline{\underline{S}}_{mix}> - \frac{1}{3}tr(<\underline{\underline{S}}_{mix}>)\underline{\underline{I}})$$

$$\tau_E \equiv C_E(I_S, II_S, III_S)\frac{k_{mix}}{\varepsilon_{mix}} \qquad . \qquad (70)$$

$$\nu_E \equiv \tau_E k_{mix} \text{ ("eddy" viscosity)}$$

For simple shear flows, Eq.(70) implies that

$$R_{yz} = -N_E \equiv -\tau_E \underline{e}_z \underline{e}_y : \nabla < \underline{u}_{mix} > \quad \Rightarrow$$

   no intrinsic shear thinning phenomenon

$$R_{xx} = R_{xx} = R_{xx} = \frac{1}{3} \quad \forall |N_E| \geq 0 \Rightarrow$$

   (71a,b,c)

   unphysical equipatition of energy

$$C_{yz} = 3N_E \Rightarrow$$

   flow restrictions on realizability

In contrast to the URAPS closure (cf. Figure 3 above), Eq.(71b) shows that the primary and secondary normal stress differences are zero for all values of N_E. This equipartition of turbulent energy among the three components of the mixture fluctuating velocity in simple shear flows is unphysical.

Eq.(71c) shows that the "eddy" viscosity model is realizable provided $|N_E| \leq 1/3$. Thus, unlike the URAPS closure (cf. Figure 1), any realizable "eddy" viscosity model is restricted to the benchmark flow used to calibrate the model parameters. In contrast, the URAPS closure is realizable for all turbulent flows provided the universal Ineqs.(66) and (67) are satisfied.

The "eddy" viscosity closure misrepresents the turbulent flow physics because it assumes that the eigenvectors of the NR-stress are collinear with the eigenvectors of the mean strain rate. By comparison, the URAPS closure assumes that the eigenvectors of the NR-stress and prestress are collinear (see Eq.(62) above). This fundamental phenomenological difference supports the further development of the URAPS closure as a next generation closure for single-phase fluids and for multiphase fluids.

REFERENCES

BRENNEN, C., 2005, *Fundamentals of Multiphase Flow*, Cambridge.

CROW, C., M. SOMMERFELD, AND Y. TSUJI, 1998, *Multiphase Flows with Droplets and Particles*, CRC Press.

DREW, D. A., AND S. L. PASSMAN, 1999, *Theory of Multicomponent Fluids*, Springer.

FAN, L-S, C. ZHU, 1998, *Principles of Gas-Solid Flows,* Cambridge University Press.

GIDASPOW, D., 1994, *Multiphase Flow and Fluidization*, Academic Press.

ISHII, M., AND T. HIBIKI, 2006, *Thermo-Fluid Dynamics of Two-Phase-Phase Flow*, Springer.

JACKSON, R., 2000, *The Dynamics of Fluidized Particles*, Cambridge University Press.

KLEINSTREUER, C., 2003, *Two-Phase Flows: Theory and Applications,* Taylor & Francis.

KOPPULA, K. S., 2009, *Universal Realizable Anisotropic Prestress Closure for the Normalized Reynolds Stress*, Ph.D. Dissertation, Michigan State University.

KOPPULA, K.S., A. BÉNARD, AND C. A.PETTY, 2009, "Realizable Algebraic Reynolds Stress Closure", 2009, *Chemical Engineering Science*, 64, 22, 16 November 2009, 4611-4624.

MANNINEN, M., V.TAIVASSALO, AND S. KALLIO, 1996, "On the Mixture Model for Multiphase Flow", Technical Research Centre of Finland, VTT Publication 288, 67 pages.

MONIN, A. S., and YAGLOM, A. M., 1965, *Statistical Fluid Mechanics of Turbulence*, MIT Press, Boston, MA.

PARKS, S. M., 1997, *Relaxation Model for Homogeneous Turbulent Flows*, Ph.D. Dissertation, Michigan State University.

PARKS, S.M., K. WEISPFENNIG, AND C. A. PETTY, 1998, "An Algebraic Preclosure Theory for the Reynolds Stress", *Physics of Fluids*, **10**(13), 645-653.

POPE, S. B., 2000, *Turbulent Flows*, Cambridge University Press.

PROSPERETTI, A. AND G. TRYGGVASON, 2009, *Computational Methods for Multiphase Flow*, Cambridge University Press.

WEISPFENNIG, K., 1997, *Relaxation/Retardation Model for Fully Developed Turbulent Channel Flow*, Ph.D. Dissertation, Michigan State University.

WEISPFENNIG, K., PARKS, S. M. AND C. A. PETTY, 1999, "Isotropic Prestress for Fully Developed Channel Flows", *Physics of Fluids,* **11**(5), 1262-1271, 1999.

8th International Conference on CFD in Oil & Gas, Metallurgical and Process Industries
SINTEF/NTNU, Trondheim NORWAY
21-23 June 2011

CFD11 - 172

CFD SIMULATION OF HYDROCYCLONE PERFORMANCE UNDER DILUTE OPERATING CONDITIONS

Aurélien DAVAILLES[1,2*], **Eric CLIMENT**[1,2†], **Florent BOURGEOIS**[2,3‡]

[1]Université de Toulouse; INPT, UPS; IMFT (Institut de Mécanique des Fluides de Toulouse); Allée

Camille Soula, F-31400 Toulouse, France

[2]CNRS; Fédération de recherche FERMAT; Toulouse, France

[3]Université de Toulouse; INPT, UPS; LGC (Laboratoire de Génie Chimique); 4 allée Emile Monso - BP

44362, 31432 Toulouse Cedex 4, France

[*] E-mail: aurelien.davailles@imft.fr
[†] E-mail: eric.climent@imft.fr
[‡] E-mail: florent.bourgeois@ensiacet.fr

ABSTRACT

Hydrocyclones have been used since the late 1800's throughout industry for particle size classification. A massive body of experimental work has resulted in a number of empirical models that can predict hydrocyclones' performance under normal operating conditions. Outside such conditions, e.g. at high solids concentration, empirical models are no longer reliable. Numerical simulation is a promising avenue for investigating the behaviour and intrinsic limitations of hydrocyclones outside their normal operating window.

As a necessary first step towards simulating the behaviour of hydrocyclones under any type of conditions, a validation of the numerical methodology has been carried out under dilute condition. Due to the lack of experimental results at high concentration, a pilot test rig has been set up to obtain comparison points with our CFD modelling. These experiments provide usefull informations such as the underflow discharge. This point seems to be the more complicated in numerical modelling due to the disappearance of the air core and the accumulation of particles in the bottom part of the cyclone. After improving the mesh, three phase flows modelling have been set up and are still running.

Keywords: Hydrocyclone, Air core, Turbulence model .

NOMENCLATURE

Greek Symbols

α_k Volume fraction of phase k $[-]$
ε Turbulent dissipation $[m^2/s^3]$
μ Dynamic viscosity $[Pa/s]$
ρ_k Mass density of phase k $[kg/m^3]$
$\tau^F{}_{lp}$ Characteristic relaxation time between liquid and particles $[s]$

Latin Symbols

C_D Drag coefficient $[-]$
d_p d_{50} diameter of solid phase p $[\mu m]$
E Mean value $[-]$
g Gravity $[m/s^{-2}]$
$I_{p,i}$ Drag force on phase p $[N]$
k Turbulent kinetic energy $[m^2/s^2]$
n_i Number of particle of phase i $[-]$
P Pressure $[Pa]$
r Radius from the centre of the hydrocyclone $[Pa]$
Re_p Particulate Reynolds number $[-]$
$U_{k,j}$ Mean velocity of phase k $[m/s]$
$U_{\theta,p}$ Tangential velocity of phase p $[m/s]$
$V_{r,i}$ Fluid velocity seen by the particles $[m/s]$

INTRODUCTION

Context

The growing need for energy leads petroleum companies to seek out new oil and gas resources and more particularly to liquify non-conventional oils. In particular, beneficiation of tar sands, which represent nearly 66% of global oil reserves, has become a major challenge for oil companies. Oil extraction from tar sands can be done ex-situ by conventional mining techniques followed by separation of oil from water and sand through a series of unit operations. One driver behind technological developments is the recognition that beneficiation of tar sands has many severe environmental impacts. One such problem, which has become particularly acute, is water consumption. Indeed, very large amounts of water are needed regardless of whether beneficiation is carried out ex- or in-situ. With the ex-situ option, unit operations must operate at the highest possible solids content so as to consume as little water as possible. The hydrocycloning stage being a key unit operation with ex-situ beneficiation, successful operation of hydrocyclones at high solids concentration is a cornerstone for optimizing the ex-situ process. This is the context of this research work.

Several parameters can be adjusted to control the operation and performance of hydrocyclones:

- Geometrical features: diameter and length of the cylindrical section, angle and length of the conical section, diameter of both the spigot and the vortex finder, or the geometry of the inlet.

- Feed conditions: solids concentration and flow rate (inlet pressure).

- Pressure control. The split between upward and downward flow is achieved by controlling the pressure drop across the hydrocyclone.

Separation performance is based on many such parameters and has led to numerous experimental studies, mainly in the field of mineral processing. This large body of experimental data has led to a number of robust empirical correlations ((Plitt, 1976), (Nageswararao *et al.*, 2004), Krebs Engineering (Arterbum, 1978)) that permit hydrocyclone selection and prediction of separation performance. These correlations are embedded into the main commercial steady-state process simulators used in the minerals industry. As long as the operating conditions remain inside the domain of validity of these

A. Davailles[1,2], E. Climent[1,2], F. Bourgeois[2,3]

correlations, the predictions made with these experimentally-based models are reliable. One issue with these models lies with the fact that we seek to operate at solids concentrations that are on the high side of their domain of validity, and possibly beyond. Citing Plitt himself (Plitt, 1976) about high feed solids content, "it is impossible to represent all slurries accurately with a single simple relationship. At best, the solids content term only represents an average trend.". This statement implies that these models do not capture the physics of particle transport inside a hydrocyclone, which becomes a significant issue as solids concentration increases. Investigation of hydrocyclone operation by numerical simulation, coupled with supporting experiments, has the potential to overcome the limitations of empirical models and yield a phenomenological understanding of the internal workings of a hydrocyclone, and including the relationships between solids concentration and hydrocyclone performance.

Computational Fluid Dynamics: a literature overview

Computation Fluid Dynamics (CFD) simulations of hydrocyclones did start in the 1990s. A reference paper in this field is that published by Hsieh and Rajamani (Hsieh and Rajamani, 1991), which resulted from Hsieh's 1988 PhD thesis (Hsieh and Rajamani, 1988). Initially, the axisymmetric assumption was imposed to reduce the simulation domain to two dimensions. The simulated water flow matched closely the fluid motion measured by Laser Doppler velocimetry inside the hydrocyclone. Qualitatively, the predictions were correct: fluid motion in rotation downward along the wall and the presence of a strong upward central vortex. Close inspection of the measurements revealed the presence of asymmetrical fluid flow patterns inside the device (resulting from single injection or multiple tangential injections). Consequently, the simplified symmetrical geometry was eventually surpassed by truly three-dimensional simulations. Ever since this pioneer work, three-dimensional simulations of hydrocyclones have been improving steadily due to the continuous improvement of CFD simulation, such as computer technology, physical modelling and numerical algorithm.

It goes without saying that all aspects of the flow cannot realistically be captured by numerical simulations due to strong turbulence, anisotropy and the three-phase nature of the flow (particles, liquid and an air core). Nevertheless, the question of selecting a suitable turbulence model is an important issue. Keeping in mind that Hsieh and Rajamani applied a simple first order turbulence model throughout their work, a number of significant turbulence models have been proposed over time: Renormalization Group (RNG), Reynolds Stress Model (RSM) and more recently the Large Eddy Simulation (LES). Because of the strong anisotropy of the flow, the RSM model must be preferred over models that assume local isotropy of the Reynolds stress tensor. However, the precession of the air core is problematic because it contributes to the global unsteadiness of the flow. Thus, fluctuating velocity (or turbulence level) profiles are generally not predicted in the central part of the flow. As shown by Slack et al. (Slack et al., 2000), LES is probably the more accurate turbulence modelling approach. It simulates the motion of high-energy vortices at large scale and applies a turbulence model at small scale. Unfortunately, this technique is very costly in computing time and requires algorithms with low numerical diffusion that pose numerical stability problems. Also, from a physics point of view, the validity of LES models for two-phase dense flow is still a much debated issue.
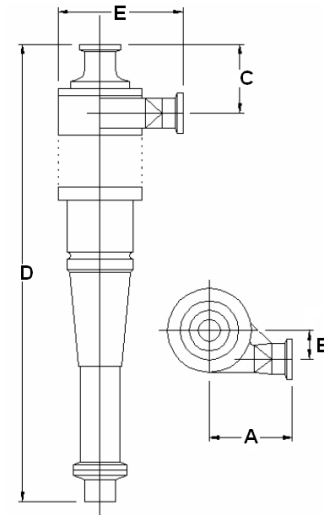
Cyclone dimensions (mm)	A	B	C	D	E
	140	56	109	760 (+100)*	236

*: for each additional extension section

Figure 1: Geometric features of Neyrtec's HC100 hydrocyclone.

Over the past decade, numerous publications on hydrocyclones have highlighted the importance of the presence of the air core ((Sripriya *et al.*, 2007), (Neesse and Dueck, 2007), (Dyakowski and Williams, 1995), (Doby *et al.*, 2008), (Gupta *et al.*, 2008), (Evans *et al.*, 2008)). Indeed, it is sometimes simply mentioned ((Bhaskar *et al.*, 2007), (Narasimha *et al.*, 2006)) without actually being studied. A suitable method for deformable interface simulations (VOF - Volume Of Fluid) can be coupled to a RANS turbulence model or to large eddy simulation ((Wang and Yu, 2006), (Delgadillo and Rajamani, 2007), (Chu *et al.*, 2009), (Brennan, 2006)). However, there was no validation of the simultaneous use of all these simulation approaches for multiphase flow. Many questions remain open regarding the reliability of coupled simulations LES-VOF with solid particles.

EXPERIMENTAL SET-UP

We will apply our CFD model to data of our own using a pilot test rig whose dimensions are reported in Figure 1. Only operating parameters and global balance (water split and partition function) are accessible with this set-up.

The Neyrtec's HC100 hydrocyclone is made of interchangeable polyurethane parts, allowing various geometrical configurations to be tested (see technical specifications in Table 1). The length of the cylindrical body can be adjusted by three $100mm$ extensions, and several diameter spigots ($6mm$ to $18mm$) are available. Only one $100mm$ cylindrical extension has been installed for the experiments reported here, and the $18mm$ diameter spigot was used. The hydrocyclone is fed using a centrifugal pump that is connected to a $1m^3$ agitated sump.

The accurate modelling of the slurry injection is essential to obtain the right flow simulation inside the hydrocyclone. The data provided by Neyrtec Mineral are not enough described to reproduce accurately the inlet pipe. As it can be seen in Figure 2, the pipe is connected to the cylindrical part through a rectangular and tangential channel. This area reduction

Model	HC 100
Feed rate (m^3/h)	7 - 13.5
Feed pressure (bar)	0.6 - 2.5
Cut size (μm)	7 - 18
Material	Polyurethane
Overflow (mm)	33
Underflow (mm)	18

Table 1: General features of Neyrtec's HC100 hydrocyclone.

leads to a significant increase of inlet velocity compared to a cylindrical pipe. The rectangular section is about 10mm over 30mm.

Figure 2: HC100 injection.

MODEL DESCRIPTION

Simulations were performed with NEPTUNE_CFD (see (Ozel *et al.*, 2010), (Galassi *et al.*, 2009), (Laviéville and Simonin, 1999), (Laviéville *et al.*, 2006) for details).

NEPTUNE_CFD presentation

The behaviour of multiphase flows can be modelled using the general Eulerian multi-field balance equations. It may correspond to distinct physical materials (e.g. gas, liquid and solid particles) which can be split into different groups (e.g. water and several groups of different diameter particles); different thermodynamic phases of the same component (e.g. liquid and its vapour) or physical components, where some of which may be split into different groups. The following multi-fluid balance equations are obtained from the fundamental conservation laws of Physics, restricted to Newtonian mechanics:

- mass conservation

- momentum balance

These two conservation laws are written under differential form which is valid for arbitrary time and location within the continuum, except across the interfaces between two physical phases. At the interfaces, jump conditions derived from the continuous equations are written and integrated through source and sink terms in the equations.

Equations for m fields that can be a physical phase or a model field of a physical phase, are written in a symbolic coordinate-free notation. The particular Cartesian coordinate system is used only when it makes things clearer. The algorithm, based on the elliptic fractional step method, enforces mass conservation with original pressure step actualization.

Transport equations

The multi-field mass balance equation for field k is written:

$$\frac{\partial}{\partial t}\left(\alpha_k \rho_k\right) + \frac{\partial}{\partial x_i}\left(\alpha_k \rho_k U_{k,i}\right) = 0 \tag{1}$$

with α_k, ρ_k, U_k, the volumetric fraction, the density and the mean velocity of phase k.

The multi-fluid momentum balance equation for phase k is defined as follows:

$$\frac{\partial}{\partial t}\left(\alpha_k \rho_k U_{k,i}\right) + \frac{\partial}{\partial x_j}\left(\alpha_k \rho_k U_{k,j} U_{k,i}\right) =$$
$$\tag{2}$$
$$-\alpha_k \frac{\partial P}{\partial x_i} + I_{k,i} + \alpha_k \rho_k g_i + \frac{\partial}{\partial x_j} T_{k,ij}$$

with P the mean pressure, $I_{k,i}$ the average interfacial momentum transfer, g_i acceleration due to gravity and $T_{k,ij}$ the effective stress tensor.

$I_{k,i}$, which accounts for momentum transfer rate from liquid to solid phase, can be modelled using an estimate of the drag force between phases (when $k = l$, we refer to the liquid and $k = p$ to the class p of particles).

$$I_{l,i} = -I_{p,i} = \frac{\alpha_p \rho_p}{\tau_{lp}^F} V_{r,i} \text{ with } \frac{1}{\tau_{lp}^F} = \frac{3}{4}\frac{\rho_l \langle C_D \rangle_p}{\rho_p d_p}\langle |V_r| \rangle$$

τ_{lp}^F is the particle relaxation time scale, $<>_p$ the ensemble average operator over the particulate phase (Simonin, 1996). $V_{r,i}$ is the average of the local relative velocity and can be expressed in terms of the averaged velocity between phases and drift velocity (which is modelled). The mean drag coefficient of a single particle, $\langle C_D \rangle_p$ can be written as a function of particulate Reynolds number. It is defined by Wen and Yu and Ergun's correlations. The combination of these two correlations was proposed by Gobin et al. in (Gobin *et al.*, 2003):

$$\langle C_D \rangle_p = \begin{cases} Min\left[\left\langle C_D^{Wen\&Yu}\right\rangle_p ; \left\langle C_D^{Ergun}\right\rangle_p\right] & \text{if } \alpha_p > 0.3 \\ \left\langle C_D^{Wen\&Yu}\right\rangle_p & \text{if } \alpha_p \le 0.3 \end{cases} \tag{3}$$

with

$$\left\langle C_D^{Ergun}\right\rangle_p = 200\frac{\alpha_p}{Re_p} + \frac{7}{3} \tag{4}$$

$$\left\langle C_D^{Wen\&Yu}\right\rangle_p = \begin{cases} \alpha_l^{-1.7}\frac{24}{Re_p}\left(1 + 0.15Re_p^{0.687}\right) & \text{if } Re_p < 1000 \\ 0.44\alpha_l^{-1.7} & \text{if } Re_p \ge 1000 \end{cases} \tag{5}$$

$$Re_p = \frac{\alpha_l \rho_l d_p \langle |V_r| \rangle}{\mu_l} \tag{6}$$

Turbulence modelling

Ensemble averaging is usually applied to instantaneous Navier-Stokes equations in order to study industrial flows. It is convenient to analyse the flow into two parts: the mean (or average) flow field and fluctuations ($\tilde{u}_i = U_i + u_i$). These new equations are called Reynolds Averaged Navier-Stokes (RANS) equations. The effective stress tensor, $T_{k,ij}$, in Eq. 2 contains two contributions: a collisional or molecular viscosity term $\theta_{k,ij}$ respectively for solid or liquid phase, and the Reynolds stress tensor $\langle \rho_k u_{k,i} u_{k,j} \rangle_k$ due to turbulence or fluctuations in phase k.
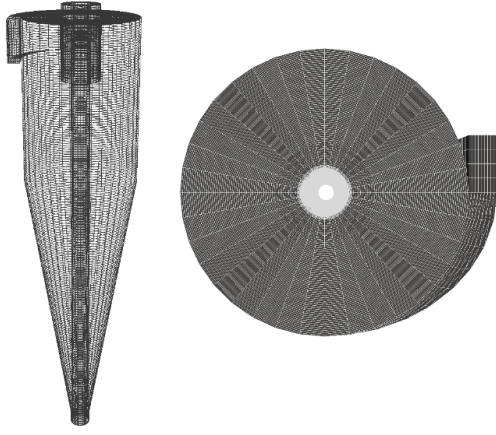
A. Davailles[1,2], E. Climent[1,2], F. Bourgeois[2,3]

Figure 3: Mesh with air-core modelling by a vertical tube

For the solid phase, the kinetic stress tensor, $\langle \rho_p u_{p,i} u_{p,j} \rangle_p$, represents the transport of momentum by particle velocity fluctuations. The collisional stress tensor, $\theta_{p,ij}$, accounts for transport and sink of the momentum. The constitutive relations for viscosity and diffusivity are derived in the framework of the kinetic theory of dry granular flows.

The Reynold's stress model (RSM) is a second order turbulence model. With RSM, the turbulent viscosity approach has been complemented and the Reynolds stresses are computed directly. The exact Reynolds stress transport equation accounts for the directional effects of the Reynolds stress fields. The Reynolds stress model involves calculation of the individual Reynolds stresses, $\langle \rho_k u_{k,i} u_{k,j} \rangle_k$, using differential transport equations and leads to higher computational costs. The individual Reynolds stresses are then used to obtain closure of the Reynolds-averaged momentum equation.

Computational domain

Most hydrocyclones operate with a central air core resulting from air aspiration through the spigot ; this forces the fluid and lighter particles to exit through the vortex finder. The origin of the air core comes from air being sucked through the spigot that is open to the atmosphere. The air accumulates in the area of low pressure, which forms the air core. One consequence of the presence of the air core is that it reduces the effective area available for the fluid to exit through the spigot. This reduction in section contributes to increasing the pressure drop across the hydrocyclone, which has a major effect on water split.

The introduction of a metal rod at the centre of the cyclone ((Sripriya *et al.*, 2007), (Gupta *et al.*, 2008), (Evans *et al.*, 2008)) has been reproduced but with gas-liquid interface boundary conditions (shear free condition allowing slip). By this way, the air core is fixed at the centre of the hydrocyclone. The incentive for using this air-core modelling approach is that it is clearly less computer intensive than a fully resolved solution, which requires solving a three-phase (gas-liquid-solid) flow modelling over an even greater number of cells. The air core diameter is not fitted with any optical means in the experiments and is estimated through several computations with different tube diameter and has been fixed to 90% of the spigot diameter (16.2*mm*). The sensibility to this parameter has been carried out and the choice of tube diameter does not appear to be critical for prediction of hydrocyclone separation performance from CFD simulation.

Details on simulation

The inlet flow assumes uniform solid concentration. In the inlet section, the Reynolds number reaches $700,000$ and fully turbulent conditions are used for the boundary conditions. With a tube approach for modelling the air core, shear free boundary conditions are imposed as per a gas-liquid interface. Outlet boundary conditions are similar for all cases and are adapted for water and particles simulations. A fixed pressure (atmospheric pressure) is applied at both outlets, which allows species to enter through the outlets (underflow and overflow sections) if the pressure inside the device becomes lower than atmospheric pressure. With liquid-solid simulation, the vertical tube replaces the air core and no species should flow in when the tube diameter is given its correct value.

The flow in the narrow section of the conical part is a critical point with meshing of the domain. Indeed, meshing the region between the air core and the spigot wall requires care (diameter 18*mm* where 90% is filled by the air core). The size of the cells is almost uniform within the grid while the smallest dimension is about $1.5 \, 10^{-4} m$. The mesh is composed of roughly $450,000$ hexahedral and pentahedral structured cells. At the beginning of a simulation, the hydrocyclone is full of water. During the transient part of the simulation, particles are fed into the domain. Eventually, a steady-state is reached, and time averages are formed for all system variables to analyze their statistics. For instance, the total CPU time on 40 processors took about $3.5 \, 10^6 s$ (1 day) for the calculation with the tube approach and $1wt\%$ of silica with solid-solid interactions.

RESULTS

Description of particle separation

A hydrocyclone is a size classifier used to process slurries. The separation mechanism is based on enhanced gravity and takes advantage of particle size and density. Although the hydrocyclone may be used to different ends, this study deals only with solid-liquid separation. The slurry is tangentially injected into the cylindrical zone, which provides a very high rotation rate to the slurry. Solid particles, associated to higher density than the liquid, are efficiently dragged towards the outer wall by centrifugal forces induced by the curvature of streamlines (see Figure 4).

The centrifugal acceleration can be several thousand times the acceleration of Earth's gravity, typically between 1000g and 5000g depending on dimensions and operating conditions of the hydrocyclone. The particulate bed that forms on the wall of the cylindrical body flows down the conical section, which ends through a narrow section tube (spigot).

The overflow (which carries fine and light particles) exits through a tube (vortex finder) that dips into the cylindrical body. The progressive downward reduction in section of the cone and the continuous increase of the solid fraction yield a significant pressure drop increase, which dictates the flow through this tube.

Consequently, the water split (recovery of water to overflow) is generally high (around 90%). However, in multiphase flow, a small amount of water exits through the underflow and bypasses the separation process, recovering fine particles to the underflow by entrainment.

Numerical validation under dilute conditions

The first part of our numerical work was the validation of our simulations on a reference test case (Davailles *et al.*, 2011).
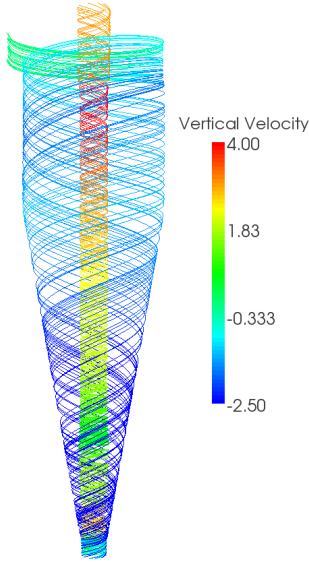
Figure 4: Water streamlines

This reference presents single phase flow results, with velocity profiles and mass balance information. For multiphase flows, under dilute conditions, partition curves are presented. The selection of both turbulence and air-core models was carried out simultaneously, as both air-core modelling techniques were tested with two turbulence models, $k - \varepsilon$ and $R_{ij} - \varepsilon$ (RSM, second order model). The air core has been modelled by a vertical tube as explained previously and by a real air core.

For the real air-core with $k - \varepsilon$ turbulence model, the predicted behaviour of the hydrocyclone is not relevant because there is no air sucked by the underflow due to a poor prediction of the pressure distribution in the central part of the device.

The $R_{ij} - \varepsilon$ model reproduces accurately axial and tangential velocity profiles, but the $k - \varepsilon$ model underestimates axial velocity in the centre of the cyclone and yields a poor prediction of tangential velocity. From these results, we can conclude that velocity profiles are the right parameters for the selection of a suitable turbulence model, here $R_{ij} - \varepsilon$. In addition, since predictions with the real air-core or with the vertical tube are very close, we can also conclude that an appropriate turbulence model together with the air core modelled as a constant diameter tube is suited for simulating the physics of the hydrocyclone.

Overall, we find that our CFD predictions are in good agreement with the behaviour of the hydrocyclone measured by Hsieh (Hsieh and Rajamani, 1988), from the velocity profiles measured locally inside the separator to the macroscopic performance of the hydrocyclone, as the water split and the partition function. These encouraging results confirm that the hypotheses and boundary conditions used for our CFD simulation of the hydrocyclone capture the key features of the physics of the separation that takes place inside a hydrocyclone under dilute conditions.

Computation of LGC experiments

Water split

For a hydrocyclone operating under continuous processing conditions with fixed inlet parameters, we first compared ex-

perimentally measured water split values with simulation results.

The pressure drop across the hydrocyclone is caused by the section restriction in the conical region and spigot, and by the presence of the air core. Most of the feed water flows through the vortex finder and is recovered to the overflow (see Table 2).

Experimental water-split	94%
Numerical water-split	98%

Table 2: Comparison of experimental and numerical water-split.

The numerical value of water split is close to the experiments. It has been shown (Davailles *et al.*, 2011) that a correct water-split is necessary but not sufficient to validate a simulation method.

Tangential Velocity

Centrifugal force is the origin of particles separation. Induced by the high tangential inlet velocity, it depends on density and particles diameter (see Equation 7). In our case, particles differ only by their size.

$$F_c = (\rho_p - \rho_l) \frac{\pi d_p^3}{6} \frac{U_{\theta p}^2}{r} \qquad (7)$$

In the central part of the cyclone, where tangential velocity is higher (see a hydrocyclone slice coloured by tangential velocity in Figure 5 and profiles in Figure 6), centrifugal force is large. This also depends strongly on the size of particles (see Figure 7 for a solid volume fraction repartition).
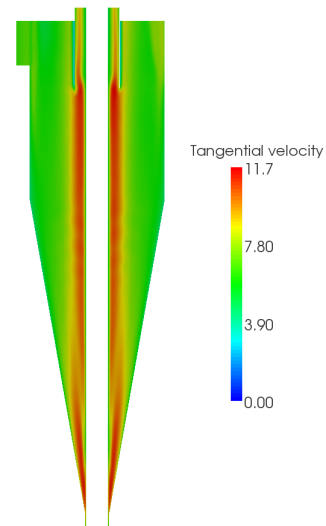

Figure 5: Tangential velocity within the hydrocyclone.

Velocity profiles are similar to those previously computed (Davailles *et al.*, 2011) and experimentally measured (Hsieh and Rajamani, 1988). Due to the high velocity and the low radius of streamline curvature in the central part, centrifugal force is very high and larger particles can not flow through the overflow. Figure 7 shows separation differences between particles. Smallest particles are insensitive to centrifugal force and are homogeneously dispersed within the hydrocyclone whereas largest particles are concentrated along the walls.
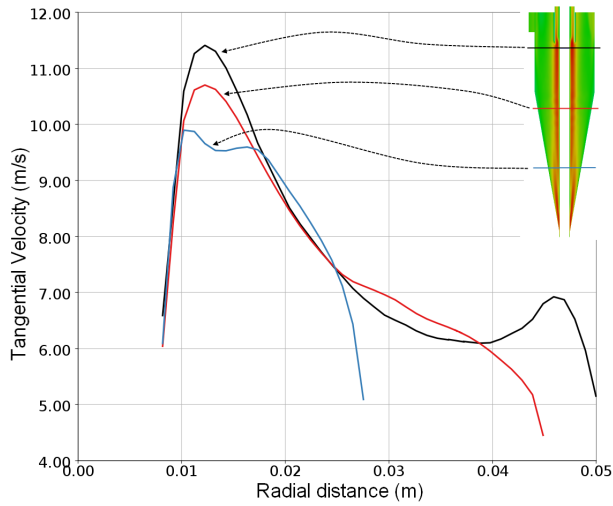
A. Davailles[1,2], E. Climent[1,2], F. Bourgeois[2,3]

Figure 6: Tangential velocity profiles at three hydrocyclone heights.
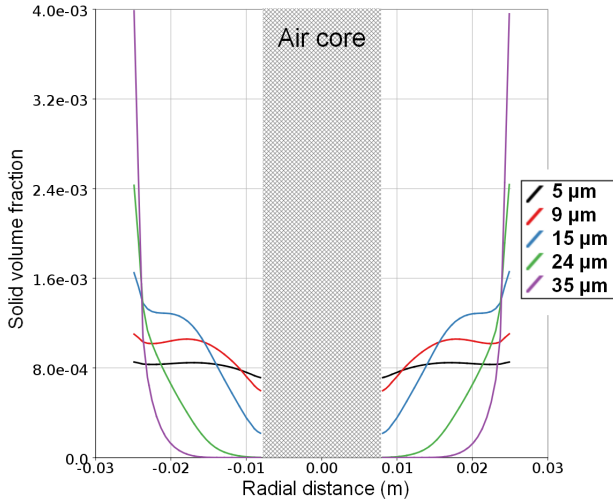

Figure 7: Solid volume fraction $0.1m$ above the underflow outlet.

Partition curve

A computation of $1wt\%$ silica feed case has been done. This level of dilution falls also well inside the domain of applicability of empirical models, so that measured, CFD-predicted and Plitt's model predictions can be compared. Measured and predicted partition functions are plotted in Figure 8 for one particular set of operating conditions.
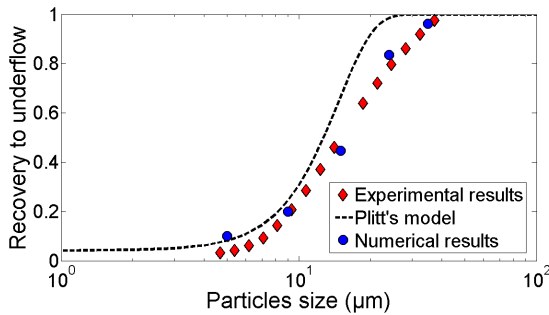

Figure 8: Partition function for 1wt% silica feed.

CONCLUSION AND PERSPECTIVES

Conclusion

A CFD model, previously derived and validated against experimental data, has been applied to a new hydrocyclone without any adjustments. Separation performances have been well described in dilute regime.

All things considered, the agreement between the partition functions plotted in Figure 8 is quite remarkable. Adding to the thorough validation we made against Hsieh's data (Davailles *et al.*, 2011), this confirms that the numerical approach we have presented here for simulating hydrocyclones, which does not require any empirical parameter adjustment, yields accurate prediction of the behaviour of hydrocyclones under dilute conditions.

Perspectives

The increase of feed solids content highlights some important points. In dilute regime, the underflow discharges in spray and an air core exists in the middle of the hydrocyclone. At higher concentration and higher inlet pressure, too much particles are centrifuged in the bottom part of the cyclone and block the air suction. Numerically, with the air core modelling as a tube and with high feed solids content, after the transient regime where particles are injected into the cyclone, the computation stops when an accumulation of particles blocks the flow in the conical part.

A full mesh option with a real computation of the air core must be considered. The accumulation of particles in the conical part stops air's aspiration and make the underflow discharges in rope. The air core cannot totally disappear and it terminates in the solids stored in the conical part of the cyclone.

REFERENCES

ARTERBUM, R. (1978). "The Sizing and Selection of Hydrocyclones". *Krebs Engineers, Literature Publication.*

BHASKAR, K. *et al.* (2007). "CFD simulation and experimental validation studies on hydrocyclone". *Minerals Engineering*, **20(1)**, 60–71.

BRENNAN, M. (2006). "CFD Simulations of Hydrocyclones with an Air Core Comparison Between Large Eddy Simulations and a Second Moment Closure". *Chemical Engineering Research and Design*, **84(6)**, 495–505.

CHU, K. *et al.* (2009). "CFD-DEM modelling of multiphase flow in dense medium cyclones". *Powder Technology*, **193**, 235–247.

DAVAILLES, A. *et al.* (2011). "Simulation of the centrifugal separation of particles within hydrocyclones". *submitted to Separation and Purification Technology.*

DELGADILLO, J. and RAJAMANI, R. (2007). "Exploration of hydrocyclone designs using computational fluid dynamics". *International Journal of Mineral Processing*, **84(1-4)**, 252–261.

DOBY, M. *et al.* (2008). "Understanding air core formation in hydrocyclones by studying pressure distribution as a function of viscosity". *International Journal of Mineral Processing*, **86(1-4)**, 18–25.

DYAKOWSKI, T. and WILLIAMS, R. (1995). "Prediction of air-core size and shape in a hydrocyclone". *International journal of mineral processing*, **43(1-2)**, 1–14.

EVANS, W. *et al.* (2008). "The simulation of the flow within a hydrocyclone operating with an air core and with an inserted metal rod". *Chemical Engineering Journal*, **143(1-3)**, 51–61.

GALASSI, M. *et al.* (2009). "Two-Phase Flow Simulations for PTS Investigation by Means of Neptune CFD Code". *Sci. Technol. Nucl. Install.*, **2009**, 12.

GOBIN, A. *et al.* (2003). "Fluid dynamic numerical simulation of a gas phase polymerization reactor". *International Journal for Numerical Methods in Fluids*, **43(10-11)**, 1199–1220.

GUPTA, R. *et al.* (2008). "Studies on the understanding mechanism of air core and vortex formation in a hydrocyclone". *Chemical Engineering Journal*, **144(2)**, 153–166.

HSIEH, K. and RAJAMANI, K. (1988). "Phenomenological model of the hydrocyclone". *PhD Thesis, University of Utah, Department of Mettalurgy and Mettalurgical Engineering.*

HSIEH, K. and RAJAMANI, R. (1991). "Mathematical model of the hydrocyclone based on physics of fluid flow". *AIChE Journal*, **37(5)**.

LAVIÉVILLE, J. and SIMONIN, O. (1999). "Equations et modèles diphasiques du code Astrid 3.4 et du code saturne polyphasique". *Technical report HE-44/99/041/A, EDF R&D.*

LAVIÉVILLE, J. *et al.* (2006). "NEPTUNE_CFD V1.0 - Theory Manual". *NEPTUNE report H-I81-2006-04377-EN - Nept_2004_L1.2/3, EDF R&D.*

NAGESWARARAO, K. *et al.* (2004). "Two empirical hydrocyclone models revisited". *Minerals engineering*, **17(5)**, 671–687.

NARASIMHA, M. *et al.* (2006). "Large eddy simulation of hydrocyclone–prediction of air-core diameter and shape". *International Journal of Mineral Processing*, **80(1)**, 1–14.

NEESSE, T. and DUECK, J. (2007). "Air core formation in the hydrocyclone". *Minerals Engineering*, **20(4)**, 349–354.

OZEL, A. *et al.* (2010). "3D Numerical Prediction of Gas-Solid Flow Behavior in CFB Risers for Geldart A and B Particles". *Proceedings of the 20th International Conference on Fluidized Bed Combustion.*

PLITT, L. (1976). "A mathematical model of the hydrocyclone classifier". *CIM bulletin*, **69(776)**, 114–123.

SIMONIN, O. (1996). "Continuum modelling of dispersed two-phase flows Combustion and Turbulence in Two-phase Flows (Lecture Series 1996–02)". *Rhode Saint Genese: Von Karman Institute for Fluid Dynamics.*

SLACK, M. *et al.* (2000). "Advances in cyclone modelling using unstructured grids". *Trans. IChemE*, **78**, 1098–1104.

SRIPRIYA, R. *et al.* (2007). "Studies on the performance of a hydrocyclone and modeling for flow characterization in presence and absence of air core". *Chemical Engineering Science*, **62(22)**, 6391–6402.

WANG, B. and YU, A. (2006). "Numerical study of particle–fluid flow in hydrocyclones with different body dimensions". *Minerals Engineering*, **19(10)**, 1022–1033.

8th International Conference on CFD in Oil & Gas, Metallurgical and Process Industries
SINTEF/NTNU, Trondheim Norway
21-23 June 2011

CFD11-173

DESIGN OF A CHEMICAL LOOPING COMBUSTION SYSTEM USING PROCESS SIMULATION AND COMPUTATIONAL FLUID DYNAMICS

Schalk CLOETE[1] & Shahriar AMINI[2*]

[1] NTNU Department of Energy and Process technology, Richard Birkelands Vei 3, 7034 Trondheim, NORWAY

[2] SINTEF Materials and Chemistry, Richard Birkelands Vei 3, 7034 Trondheim, NORWAY

* E-mail: Shahriar.Amini@sintef.no

ABSTRACT

A strategy for design and optimisation of chemical processes involving multiple fluidized bed reactors is presented through a combination of standard design calculations, process simulation and computational fluid dynamics (CFD). This strategy aims to give a superior level of confidence in the process design of interconnected fluidized beds. The strategy is demonstrated in designing a chemical looping combustion (CLC) process that generates 12.5 kW of heat in the air reactor. The air reactor was operated as a fluidized bed riser and the fuel reactor as a bubbling fluidized bed. Operation in a suitable flow regime for each reactor was the starting point for the design. Flow rates and reactor diameters were subsequently calculated based on the limitations imposed by the fluidization regime selected. Process simulation was used to design the heat extraction strategy and complete the energy balance. Finally, CFD was used to find the required height of the riser and bed mass of the bubbling bed. CFD was selected among other simpler and faster modelling alternatives because of the generality it offers. The complexity of a reactive gas-solid flow system combined with the wide range of flow regimes achievable in a fluidized bed demands the use of a fundamental flow modelling tool such as CFD. The resulting design strategy will allow for very economical investigations into various design and optimization considerations related to interconnected fluidized bed reactor systems. It also offers a platform from which to conduct virtual prototyping investigations for new process concepts which will lead to significant economic benefits when compared to a traditional experimental process development strategy.

Keywords: Computational Fluid Dynamics; Design; Process Simulation; Chemical Looping Combustion; Multiphase Reactors; Fluidization.

NOMENCLATURE
Main Symbol definitions:
Greek symbols:
α Volume fraction
Δt Time step size (s)
Δx Cell width (m)
Δy Cell height (m)
ϕ Specularity coefficient
ϕ_{gs} Interphase energy transfer
φ Angle of contact
γ Dissipation rate
γ Stoichiometric coefficient
H_{sg} Interphase energy exchange coefficient
μ Viscosity (kg/m.s)

Θ_s Granular temperature (m^2/s^2)
ρ Density (kg/m^2)
τ_s Particle relaxation time (s)
$\vec{\tau}_s$ Shear stress at the wall (N/m^2)
$\bar{\bar{\tau}}$ Stress tensor
υ Superficial velocity (m/s)
υ_r Terminal velocity (m/s)
$\vec{\upsilon}$ Velocity vector (m/s)
Regular symbols:
A   Cross sectional area (m^2)
C_D Drag coefficient
C Molar concentration (mol/m^3)
d Diameter (m)
e Restitution coefficient
f Drag function
g Gravitational acceleration (m/s^2)
$\vec{g}$ Gravity vector (m/s^2)
$g_{0,ss}$ Radial distribution function
h Enthalpy (J)
$\bar{\bar{I}}$ Identity tensor
$\vec{J}$ Diffusive flux (kg/m^{2}s)
K_{sg} Interphase momentum exchange coefficient (kg/m^{3}s)
k Reaction rate constant (m/s)
k Diffusion coefficient (kg/m.s)
M Molar weight (kg/kmol)
m Mass (kg)
N Number of moles (mol)
Nu   Nusselt number
Pr   Prantl number
p Pressure (Pa)
q_s Granular temperature at the wall
$\vec{q}$ Energy diffusion
Re$_s$ Slip Reynolds Number
R^H Heterogeneous reaction rate (kmol/m^{3}s)
S Source term
T Temperature (K)
t Time (s)
$\vec{U}_{s,\parallel}$ Solids velocity parallel to the wall (m/s)
u x-velocity (m/s)
v y-velocity (m/s)
V Volume (m^3)
x Species mass fraction
Y Species mass fraction

Sub- and superscript definitions:
Greek symbols:
Θ_s Granular temperature
$\vec{\upsilon}$ Momentum
Regular symbols:
g Gas
f Formation
h Gas
i Species i
max   Maximum or maximum packing
net   Average property of a mixture of phases
O_2 Oxygen
ox   Oxidation
p Product
r Reactant
red   Reduction
s Solid
ss   Solid-solid
sw   Solid-wall
T Transposed
tot   Total

INTRODUCTION

In recent years, extensive research effort has been directed at methods for reducing CO_2 emissions. Fossil fuel combustion is the major source of these emissions and will be for many years to come. Power production is responsible for roughly one third of CO_2 emissions (Hertzog, *et al.*,2000), making it a suitable field in which to implement CO_2 reduction strategies. CO_2 capture and storage has emerged as the most promising of these strategies. Many options exist for CO_2 storage and methods for achieving this are reasonably well developed (Lyngfelt, *et al.*,2001). The separation and capture of CO_2 can be very costly, however. Separation processes either require large amounts of energy or involve highly toxic compounds.

The process of chemical looping combustion (CLC) operates in such a way that a relatively pure stream of CO_2 and water vapour is delivered as one of the outlet streams. This inherent CO_2 separation eliminates the need for additional costly or dangerous separation processes. A good review of the CLC process can be found in a published review paper (Hossain and de Lasa,2008), but a short summary will be given here: The CLC process operates by recirculating an oxygen carrier between two reactors where it is contacted separately with air and fuel. In the so called 'air reactor', the oxygen carrier is oxidized by air, producing a flue gas stream of oxygen depleted air. The oxidized carrier then transports the oxygen to a 'fuel reactor' where it is again reduced by the fuel gas. Flue gas from this reactor contains only CO_2 and water vapour and therefore requires only cooling for complete CO_2 separation.

Fluidized bed reactors are used in the CLC process, with the oxygen carrier serving as the bed medium. Reactivity studies have led to a consensus about the use of a bubbling fluidized bed for the fuel reactor and a circulating fluidized bed for the air reactor (Kronberger, *et al.*,2005), although a circulating fluidized bed has also recently been used for the fuel reactor (Kolbitsch, *et al.*,2009).

The design of fluidized bed reactors is very challenging though. Complex gas-solid hydrodynamics inherent to these reactors is closely coupled to heat transfer and reaction kinetics. Due to this intimate coupling leading to a highly non-linear system, the development of a sufficiently general empirical model is not possible. Such an empirical model has been proposed (Kolbitsch, *et al.*,2009), based on results from a functional CLC test rig, but such a tool will not have the generality required to investigate the wide range of conditions for which the present design methodology is intended.

This paper explores the possibility of using computational fluid dynamics (CFD) and process simulation where the intimate coupling between hydrodynamics, reaction kinetics and energy transport is inherently accounted for. A reliable CFD-based simulation tool, integrated into a mass and energy balance design strategy, would allow the designer to explore many different process setups at minimal costs. This would not only be beneficial in terms of process design, but also in terms of optimization and process scale up.

GENERAL DESIGN METHODOLOGY

A flow diagram of the design process proposed in this work is given in Figure 1. The design is begun by some basic decisions involving process operating temperature and pressure as well as the type of oxygen carrier used. This is followed by standard design calculations to select the appropriate flow regime for each reactor and then performing mass balance calculations to calculate the stream flow rates and cross sectional area of each reactor. Subsequently, process simulation is used for the energy balance and for determining the points at which heat will be extracted from the system. Finally, CFD simulations are employed to find the height of the reactor that will be required to deliver the performance of the process unit used in the process simulation.
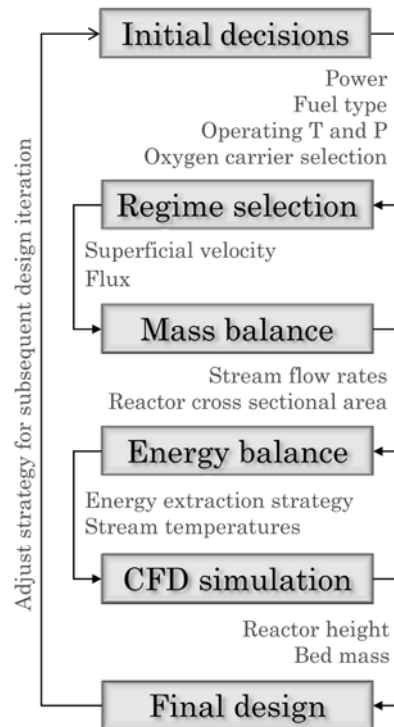
Figure 1: Summary of the design procedure.

Coupling standard design calculations, process simulation and CFD in this way offers a virtual prototyping platform to analyse the response of overall system performance to changes in any design or operating variable. When considering the large number of variables that are involved in the design and operation of a CLC system, such a generic design methodology is sorely needed to ensure a reasonably optimized design at an acceptable cost.

DESIGN OUTLINE

The following sections will complete a typical first iteration in the design process of an interconnected fluidized bed system in order to demonstrate the proposed design methodology. A CLC system generating 12.5 kW of heat in the air reactor will be designed.

Design calculations for the air reactor

The air reactor will be operated as a fluidized bed riser at 1243 K based on the design of a unit at Chalmers University of Technology, Sweden (Lyngfelt, *et al.*,2001). For oxygen carrier materials, Ni/NiO particles with a mean diameter of 80 μm and a density of 1515 kg/m^3 will be used. The particles are supported by Bentonite so that the weight fraction of Ni/NiO is 74% (Ryu, *et al.*,2001). This particle was selected because the associated kinetic data was available within the literature.

The first step is to decide on the superficial gas velocity and solids flux that will be used in the riser. Based on a previous CFD modelling work (Ellis, *et al.*,2011), the riser will be operated in a dilute transport flow regime and a flux of 40 kg/m^{2}s will be selected. This flux is also in the range used by other authors presenting CLC systems (Kolbitsch, *et al.*,2009, Lyngfelt, *et al.*,2001). In order to select the correct superficial gas velocity, the flow regime diagrams of (Bi and Grace,1995) are consulted. The transition velocity to core-annular dilute transport (V_{CA}) is found by the following equation:

$$\frac{V_{CA}}{\sqrt{gd_p}} = 21.6\text{Ar}^{0.105}\left(\frac{G_s}{\rho_g V_{CA}}\right)^{0.542} \qquad (1)$$

Equation (1) can be plotted as a function of superficial velocity and solids mass flux (Figure 2). According to Figure 2, at a solids flux of 40 kg/m^{2}s, the superficial velocity will have to be in excess of 4.1 m/s in order to operate outside the fast fluidization regime. A superficial velocity of 5 m/s will therefore be selected.
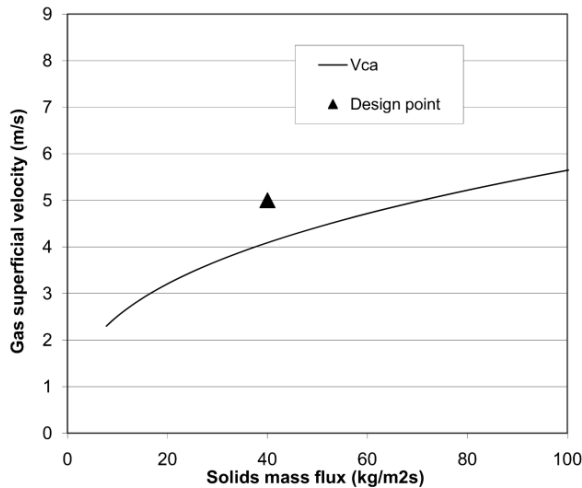
Figure 2: The fast fluidization regime for the specified system design.

The molar conversion rate required to generate 12.5 kW of heat can be calculated from knowledge of the heat of reaction for the specific oxygen carrier employed. The heat of reaction for the oxidation of Ni is 240.3 kJ/mol, resulting in a required conversion rate of

$$\dot{M}_{Ni,con} = \frac{P}{H_{rxn}} = \frac{12.5}{240.3} = 0.052 \text{ mol/s} \qquad (2)$$

The desired level of conversion of the oxygen carrier is the next important consideration to be made. Within the current design methodology this consideration is made iteratively and will be taken as 3.6% (molar) in this case. This value is within the normal range (Lyngfelt, *et al.*,2001). Under this conversion criterion, the molar rate at which Ni/NiO needs to be fed to the system is

$$\dot{M}_{Ni/NiO} = \frac{\dot{M}_{Ni,con}}{x_{con}} = \frac{0.052}{0.036} = 1.445 \text{ mol/s} \qquad (3)$$

The total mass flow rate of oxygen carrier material can now be calculated from the knowledge that each particle contains 74% (mass) of Ni/NiO (Ryu, *et al.*,2001). Here the assumption will

be made that the Ni/NiO has the properties of NiO. This is an acceptable assumption since NiO levels generally do not drop below 95% during the cycling of the oxygen carrier (Lyngfelt, *et al.*,2001).

$$\dot{m}_{OC} = \frac{\dot{M}_{Ni/NiO} \cdot M_{r,Ni/NiO}}{x_{Ni/NiO}} = \frac{1.445 \cdot 0.0747}{0.74} = 0.146 \text{ kg/s} \quad (4)$$

From this mass flow rate and the prescribed flux of 40 kg/m^{2}s, the required area of the riser can be calculated.

$$A = \frac{\dot{m}_{OC}}{G_{OC}} = \frac{0.146}{40} = 0.00365 \text{ m}^2 \qquad (5)$$

This translates to a cylindrical riser with a diameter of 0.068 m. A superficial air flow velocity of 5 m/s in this reactor would introduce the following mass flow of air at 1243 K:

$$\dot{m}_{air} = v_{air}A\rho_{air} = 5 \cdot 0.00365 \cdot 0.284 = 0.00518 \text{ kg/s} \qquad (6)$$

The molar flow rate of oxygen provided by this mass flow rate is

$$\dot{M}_{O_2} = \frac{\dot{m}_{air}x_{O_2}}{M_{r,O_2}} = \frac{0.00518 \cdot 0.233}{0.032} = 0.0378 \text{ mol/s} \qquad (7)$$

Ni reacts with oxygen in a stoichiometric ratio of 2:1, meaning that the prescribed airflow contains sufficient oxygen to oxidize 0.0756 mol/s of Ni. The desired conversion of 0.052 mol/s (Equation (2)) of Ni can thus be attained with only $0.052/0.0756\times100\% = 69\%$ of the available oxygen.

The reactor length required to attain this amount of conversion will depend primarily on the reaction rate and the quality of gas solid contact achieved in the reactor. These gas-solid interactions are highly complex and the required reactor height cannot be determined by simple calculations or correlations. This value therefore needs to be determined from physical or numerical experimentation. CFD simulations will be used for this purpose in the current study.

Design calculations for the fuel reactor

A bubbling bed operated at 1223 K will be used for the fuel reactor following the operating conditions used in (Lyngfelt, *et al.*,2001). Due to the interconnectedness of the system, the 3.6% (molar) oxidation conversion achieved in the air reactor has to be mirrored by reduction in the fuel reactor.

Similarly to the riser calculations, the first step in designing the bubbling fluidized bed is the determination of the correct fluidization velocity. This will be done according to diagrams provided by (Bi and Grace,1995) to ensure that the reactor functions in the bubbling fluidization regime.

Bubbling fluidization occurs between the minimum fluidization velocity (V_{mf}) and the critical velocity (V_C) where the standard deviation of differential pressure fluctuations reaches a maximum and turbulent fluidization ensues. This point occurs somewhat before significant entrainment of particles actually begins to take place. These velocities are non-dimensionalized by means of the Reynolds number $\left(\text{Re} = (\rho_g v d_s)/\mu_g\right)$ and the Archimedes number $\left(\text{Ar} = (\rho_g(\rho_s + \rho_g)gd_s^3)/\mu_g^2\right)$.

$$\text{Re}_{mf} = \sqrt{27.2^2 + 0.0408\text{Ar}} - 27.2 \qquad (8)$$

$$\text{Re}_c = 1.24\text{Ar}^{0.45} \qquad (9)$$

Equations (8) and (9) represent the boundaries of the bubbling fluidization regime and can be plotted in terms of non-dimensional parameters as shown in Figure 3.
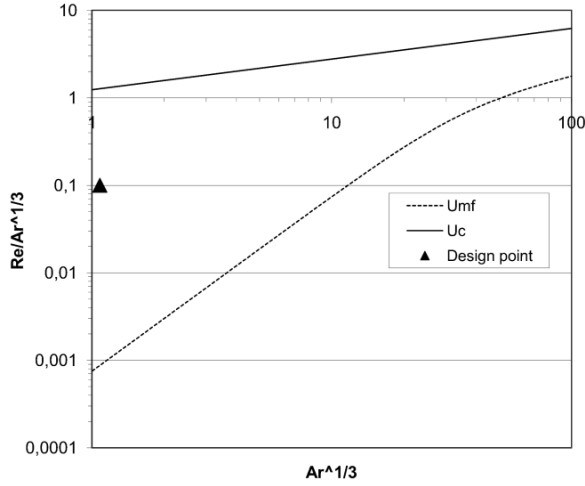
Figure 3: The bubbling fluidization regime for the specified system design.

Since the particles employed in this system are very small, the Archimedes number (1.17) is small as well. At this low Archimedes number, Figure 3 shows a very large region over which bubbling fluidization occurs. A mid-range value of $Re/Ar^{1/3} = 0.1$ will be implemented as a first iteration. This translates to a gas superficial velocity of 0.177 m/s. This velocity was calculated on physical properties that would result from a mixture of 2:1 CO_2 and H_2O since these will be the most abundant species in the actual reactor.

The primary reaction occurring in the fuel reactor converts one mole of CH_4 to one mole of CO_2 and two moles of H_2O. Thus, the volume of gas fed to the system will triple if the reaction goes to completion. The feed rate of the reacting gas will therefore have to be reduced by a factor of 3 in order to ensure that the designed superficial velocity is achieved in the majority of the reactor. The inlet gas will therefore be injected at a velocity of $0.177/3 = 0.059$ m/s.

Reduction in the fuel reactor must occur at the same rate of 0.052 mol/s (Equation (2)) as was the rate of oxidation in the air reactor. NiO reacts with methane in a stoichiometric ratio of 4:1, so a molar flow rate of 0.013 mol/s of methane is required. It is desired that all of the methane be depleted in the reactor, but this might not be practically possible and only a fraction $\left(x_{Me,con}\right)$ will react. Additionally, the fuel gas might not be pure methane, thus containing only a mass fraction of methane $\left(x_{Me}\right)$. With these considerations, the required mass flow rate of fuel gas can be calculated. It will be assumed that 99.9% of the methane is converted and that the feed comprises of 90% methane and 10% argon.

$$\dot{m}_{fuel} = \frac{\dot{M}_{Me} M_{r,Me}}{x_{Me,con} x_{Me}} = \frac{0.013 \cdot 0.016}{0.999 \cdot 0.9} = 0.000231 \text{ kg/s} \quad (10)$$

The required reactor cross sectional area for this mass flow can now be calculated.

$$A_{FR} = \frac{\dot{m}_{fuel}}{\rho_{fuel} v} = \frac{0.000231}{0.17 \cdot 0.059} = 0.0231 \text{ m}^2 \quad (11)$$

This translates to a required reactor diameter of 0.171 m. The bed height required to attain 99.9% conversion of the methane in the feed stream must now be determined by means of physical or numerical experimentation.

ENERGY BALANCE

The oxygen carrier material is also a carrier of a substantial amount of thermal energy. It will be heated up substantially by the exothermic reaction in the air reactor, and subsequently cooled down by the endothermic reaction in the fuel reactor.

Thermal coupling between the reactors is thus of great importance.

Process flow simulation

The commercial software package METSIM (Proware,2009) was chosen to perform the mass and energy balance. Reactions are modelled by specifying an extent of reaction. This value is provided to METSIM to describe the fraction of the component to be reacted provided there are adequate quantities of other reactants taking part in the reaction. Only the primary reactions were simulated. For the air reactor:

$$2Ni + O_2 \rightarrow 2NiO$$
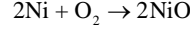
The extent of reaction for this process is 1, implying that all the Ni generated in the fuel reactor will be converted to NiO in the air reactor. The reaction considered for the fuel reactor is:

$$CH_4 + 4NiO \rightarrow 4Ni + 2H_2O + CO_2$$
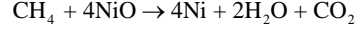
Following the considerations in equation (10), the extent of reaction is defined as 0.999 for this reaction.

In order to ensure a maximum amount of energy extraction in the gas streams, gasses will be fed to both reactors at a temperature of 300 K. The remainder of the heat will be extracted by heat exchanger which extracts the heat directly from the solids stream. A cyclone with a pre-specified separation efficiency of 0.999 was also included. Fines lost in the cyclone are subsequently replaced by fresh solids also entering at 300 K. The resulting process simulation is shown in Figure 4.
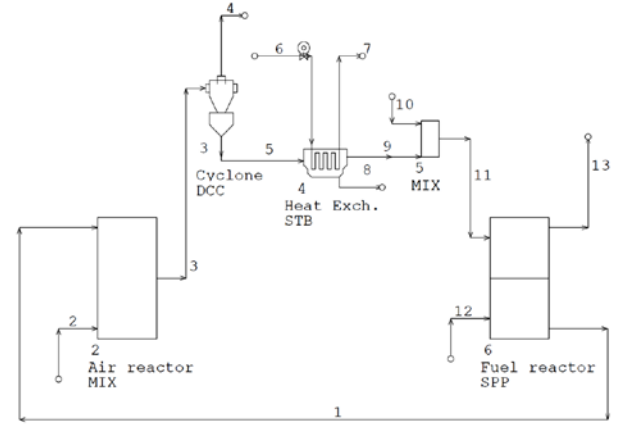
Figure 4: Process simulation of the CLC process.

The heat available for extraction from each of these sources can be calculated from the differences in enthalpies of entering and exiting streams shown in Table 1.

Table 1: Temperature and enthalpy values of all streams in the process simulation.

#	Description	Temp (K)	Enthalpy (kJ/s)
1	Solids recycle from FR to AR	1223.00	139.83
2	Air feed to AR	300.00	0.01
3	Mixed gas/solids from AR	1264.90	152.34
4	Gas and lost fines	1264.90	4.88
5	Solids retrieved by cyclone	1264.90	147.47
9	Cooled solids stream	1239.23	143.39
10	Feed of fresh solids	300.00	0.00
11	Fresh solids stream to FR	1238.40	143.39
12	Fuel gas stream to FR	300.00	0.00
13	Off gas from FR	1223.00	1.51

Table 2: Heat available for extraction from different points in the system.

Unit	Heat rate (kW)	Percentage (%)
Air Reactor outlet gas	4.87	46.56
Fuel Reactor outlet gas	1.51	14.44
Heat Exchanger	4.08	39.00

It is clear from Table 2 that a substantial amount of the heat has to be extracted directly from the solids.

CFD MODELLING OF THE REACTORS

The calculations in the previous sections can now be used to design the reactors by means of CFD. Each reactor has to be designed so that the pre-specified conversion can be achieved. In the air reactor, the conversion will increase with increased reactor length, while the conversion in the fuel reactor will increase with increasing bed height. Computational fluid dynamics was therefore implemented to find the required length of the air reactor and bed height of the fuel reactor.

Equation system

The full set of model equations are given in Table 3. Further description of the equation setup can be found in (Cloete, *et al.*,2011), but a concise version will be given here.

The two phases involved in the simulation was described according to the Eulerian-Eulerian Two Fluid Model (TFM). In this methodology, both the gas and particle phases are treated as fluids with a separate set of conservation equations being solved for each phase. The stresses within the fluid representing the particle phase is modelled according tot the kinetic theory of granular flows (KTGF) in order to approximate the behaviour of the actual particles. The KTGF is derived from the kinetic theory of gasses and likens the uncorrelated particle motions to those of molecules in a gas. In a gas, these motions are expressed as the temperature and an analogous quantity is defined and conserved in the KTGF as the granular temperature. Values for the viscosity and pressure within the fluid are then derived from the granular temperature. The resulting equation set for the KTGF is summarized in Table 3. For the bubbling bed, the conservation equation for the granular temperature was solved in its algebraic form by neglecting the contributions of convection and diffusion. This is an appropriate approximation in a dense, slow moving bed. The fast riser, on the other had, required the solution of the full partial differential equation for granular temperature.

Closure relations are used to model the interaction between phases. The inter-phase momentum exchange is modelled by a drag correlation. Two different drag correlations were employed to model the two reactors in this study based on literature recommendations. The model of (Syamlal, *et al.*,1993) was used for the bubbling bed and the (Wen and Yu,1966) model for the riser.

Heat transfer between the different phases was modelled according to (Gunn,1978).

Heterogeneous reaction kinetics were modelled according to the shrinking core analogy with reaction rate control (Levenspiel,1999). The assumption was also made that the surface area presented by the unreacted shrinking core is constant. This is an appropriate assumption if the conversion that the oxygen carrier undergoes is low (3.6% in this case). Reaction rate constants were taken from experiments performed by (Ryu, *et al.*,2001). The reduction rate was expressed for chemical reaction control and could be used directly, but the oxidation rate was derived for ash layer diffusion control and had to be estimated in chemical reaction control form from data given in the paper. Diffusion through the ash layer will not be controlling for the first 3.6% of conversion since there is practically no ash layer present at this stage. A model using only ash layer control will therefore greatly over-predict the reaction rate in this study where only a small amount of conversion is achieved in the reactor.

Geometry and boundary conditions

The reactor geometry and boundary conditions were determined in the 'design outline' and 'energy balance' sections and can now be used as input to the CFD models.

Riser

The riser was simulated as a simple 2D rectangular geometry, 0.068 m in width and 11 m long. It was meshed with rectangular cells, 20 particle diameters in width and 40 particle diameters in height, following experience from a previous study on dilute risers (Ellis, *et al.*,2011).

The solids entered the reactor from two inlets, 0.0096 m wide, located 0.1 m from the bottom on both sides of the reactor. Solids velocity was specified as 0.312 m/s at a volume fraction of 0.3 and a temperature of 1223K. Air entered at the bottom with a velocity of 1.213 m/s and a temperature of 300K and consisted of 21 mol% O_2 and 79 mol% N_2. The solids stream consisted of 26 weight% bentonite and 74 weight% Ni. No NiO was included even though the vast majority of the particle would consist of NiO in reality. This was done because the reaction would occur on the thin layer of pure Ni that would was deposited on the particle surface in the fuel reactor. The surface reaction would therefore experience the particle to consist of only Ni and no NiO. The heat capacity of the Ni species in the present simulation was set to that of NiO, however, in order to correctly simulate the thermal behaviour of the particle.

A no-slip wall boundary condition was specified for the gas, while a partial slip boundary condition was specified for the solids (Johnson and Jackson,1987). The two tuning constants, the specularity coefficient and particle-wall restitution coefficient, were specified as 0.01 and 0.2 respectively following a previous study (Cloete, *et al.*,2011).

The outlet was specified as a pressure outlet at atmospheric pressure.

Bubbling bed

The bubbling bed was also simulated as a simple 2D rectangular geometry, 0.1715 m in diameter and 0.5 m in height. Separate inlets and outlets were specified for the gas and solids phases. Gas entered from a velocity inlet at the bottom and exited through an atmospheric pressure outlet at the top. Solids entered from the right through a velocity inlet, 0.0096 m wide, located 0.3834 m from the bottom and exited through an atmospheric pressure outlet, 0.05 m wide, located 0.343 m from the bottom. The domain was meshed with square cells, 15 particle diameters in width.

Gas entered the reactor at a velocity of 0.0145 m/s, a temperature of 300K and a composition of 90 weight% CH_4 and 10 weight% Ar. Solids entered the reactor at a velocity of 0.745 m/s, a temperature of 1238.4K and a composition of 0.26 weight% bentonite and 0.76 weight% NiO.

The gas wall boundary condition was specified as no-slip while the (Johnson and Jackson,1987) boundary condition was specified for the solids with a specularity coefficient of 0.5.

Solver settings

The commercial CFD package, FLUENT 12.1 was used as the flow solver to carry out the simulations. The phase-coupled SIMPLE algorithm (Patankar,1980) was selected for pressure-velocity coupling, the QUICK scheme (Leonard and Mokhtari,1990) was employed for volume fraction discretization while a standard second order upwind scheme was used for discretization of all remaining equations. Temporal discretization was carried out using a 1st order implicit scheme in the bubbling bed, but a 2nd order implicit scheme was used for the riser (Cloete, *et al.*,2011).

Table 3: Model equations.

Mass conservation:	
$\dfrac{\partial}{\partial t}\left(\alpha_g \rho_g\right)+\nabla\cdot\left(\alpha_g \rho_g \vec{\upsilon}_g\right)=S_g$	$\dfrac{\partial}{\partial t}\left(\alpha_s \rho_s\right)+\nabla\cdot\left(\alpha_s \rho_s \vec{\upsilon}_s\right)=S_s$

Momentum conservation:	
$\dfrac{\partial}{\partial t}\left(\alpha_g \rho_g \vec{\upsilon}_g\right)+\nabla\cdot\left(\alpha_g \rho_g \vec{\upsilon}_g \vec{\upsilon}_g\right)=-\alpha_g \nabla p + \nabla\cdot\overline{\overline{\tau}}_g +$ $\alpha_g \rho_g \vec{g} + K_{sg}\left(\vec{\upsilon}_s - \vec{\upsilon}_g\right)+S_g^{\vec{\upsilon}}$	$\dfrac{\partial}{\partial t}\left(\alpha_s \rho_s \vec{\upsilon}_s\right)+\nabla\cdot\left(\alpha_s \rho_s \vec{\upsilon}_s \vec{\upsilon}_s\right)=-\alpha_s \nabla p - \nabla p_s + \nabla\cdot\overline{\overline{\tau}}_s +$ $\alpha_s \rho_s \vec{g} + K_{gs}\left(\vec{\upsilon}_g - \vec{\upsilon}_s\right)+S_s^{\vec{\upsilon}}$

Species conservation:	
$\dfrac{\partial}{\partial t}\left(\alpha_g \rho_g Y_{g,i}\right)+\nabla\cdot\left(\alpha_g \rho_g \vec{\upsilon}_g Y_{g,i}\right)=\nabla\cdot\alpha_g \vec{J}_{g,i}+\alpha_g S_{g,i}$	$\dfrac{\partial}{\partial t}\left(\alpha_s \rho_s Y_{s,i}\right)+\nabla\cdot\left(\alpha_s \rho_s \vec{\upsilon}_s Y_{s,i}\right)=\nabla\cdot\alpha_s \vec{J}_{s,i}+\alpha_s S_{s,i}$

Energy conservation:	
$\dfrac{\partial}{\partial t}\left(\alpha_g \rho_g h_g\right)+\nabla\cdot\left(\alpha_g \rho_g \vec{\upsilon}_g h_g\right)=\alpha_g \dfrac{\partial p}{\partial t}+\overline{\overline{\tau}}_g :\nabla\vec{\upsilon}_g -$ $\nabla\cdot\vec{q}_g + \mathrm{H}_{gs}\left(T_g - T_s\right)+S_g^h$	$\dfrac{\partial}{\partial t}\left(\alpha_s \rho_s h_s\right)+\nabla\cdot\left(\alpha_s \rho_s \vec{\upsilon}_s h_s\right)=\alpha_s \dfrac{\partial p}{\partial t}+\overline{\overline{\tau}}_s :\nabla\vec{\upsilon}_s -$ $\nabla\cdot\vec{q}_s + \mathrm{H}_{sg}\left(T_s - T_g\right)+S_s^h$

Kinetic theory of granular flows:	
$\left[\dfrac{\partial}{\partial t}\left(\alpha_s \rho_s \Theta_s\right)+\nabla\cdot\left(\alpha_s \rho_s \vec{\upsilon}_s \Theta_s\right)\right]=\left(-p_s\overline{\overline{I}}+\overline{\overline{\tau}}_s\right):\nabla\vec{\upsilon}_s +$ $\nabla\cdot\left(k_{\Theta_s}\nabla\Theta_s\right)-\gamma_{\Theta_s}+\phi_{gs}$	$k_{\Theta_s}=\dfrac{150\rho_s d_s \sqrt{\Theta_s \pi}}{384\left(1+e_{ss}\right)g_{0,ss}}\left[1+\dfrac{6}{5}\alpha_s g_{0,ss}\left(1+e_{ss}\right)\right]^2+2\rho_s \alpha_s^2 d_s\left(1+e_{ss}\right)g_{0,ss}\sqrt{\dfrac{\Theta_s}{\pi}}$
$\gamma_{\Theta_s}=\dfrac{12\left(1-e_{ss}^2\right)g_{0,ss}}{d_s \sqrt{\pi}}\rho_s \alpha_s^2 \Theta_s^{3/2}$	$\phi_{gs}=-3K_{gs}\Theta_s$
$\lambda_s=\dfrac{4}{3}\alpha_s \rho_s d_s g_{0,ss}\left(1+e_{ss}\right)\left(\dfrac{\Theta_s}{\pi}\right)^{1/2}$	$\mu_{s,col}=\dfrac{4}{5}\alpha_s \rho_s d_s g_{0,ss}\left(1+e_{ss}\right)\left(\dfrac{\Theta_s}{\pi}\right)^{1/2}$
$\mu_{s,kin}=\dfrac{10\rho_s d_s \sqrt{\Theta_s \pi}}{96\alpha_s\left(1+e_{ss}\right)g_{0,ss}}\left[1+\dfrac{4}{5}\alpha_s g_{0,ss}\left(1+e_{ss}\right)\right]^2$	$\mu_{s,fr}=\dfrac{p_s \sin\varphi}{2\sqrt{I_{2D}}}$
$p_s=\alpha_s \rho_s \Theta_s+2\rho_s\left(1-e_{ss}\right)\alpha_s^2 g_{0,ss}\Theta_s$	$g_{0,ss}=\left[1-\left(\dfrac{\alpha_s}{\alpha_{s,max}}\right)^{1/3}\right]^{-1}$

Drag (riser):	
$K_{gs}=K_{sg}=\dfrac{3}{4}C_D \dfrac{\alpha_s \alpha_g \rho_g \left|\vec{\upsilon}_s - \vec{\upsilon}_g\right|}{d_s}\alpha_g^{-2.65}$	$C_D=\dfrac{24}{\alpha_g \,\mathrm{Re}_s}\left[1+0.15\left(\alpha_g \,\mathrm{Re}_s\right)^{0.687}\right]$

Drag (bubbling bed):	
$K_{gs}=K_{sg}=\dfrac{\alpha_s \rho_s f}{\tau_s}$	$f=\dfrac{C_D \,\mathrm{Re}_s \,\alpha_g}{24\upsilon_{r,s}^2}$
$\tau_s=\dfrac{\rho_s d_s^2}{18\mu_g}$	$C_D=\left(0.63+\dfrac{4.8}{\sqrt{\mathrm{Re}_s/\upsilon_{r,s}}}\right)^2$
$\upsilon_{r,s}=0.5\left(A-0.06\,\mathrm{Re}_s+\sqrt{\left(0.06\,\mathrm{Re}_s\right)^2+0.12\,\mathrm{Re}_s\left(2B-A\right)+A^2}\right)$	$A=\alpha_g^{4.14}$
$B=0.8\alpha_g^{1.28} \qquad \alpha_g \le 0.85$ $B=\alpha_g^{2.65} \qquad \alpha_g > 0.85$	$\mathrm{Re}_s=\dfrac{\rho_g d_s \left|\vec{\upsilon}_s - \vec{\upsilon}_g\right|}{\mu_g}$

Heat exchange:	
$\mathrm{H}_{gs}=\mathrm{H}_{sg}=\dfrac{6\kappa_g \alpha_s \alpha_g \,\mathrm{Nu}_s}{d_s^2}$	$\mathrm{Nu}_s=\left(7-10\alpha_g+5\alpha_g^2\right)\left(1+0.7\,\mathrm{Re}_s^{0.2}\,\mathrm{Pr}^{1/3}\right)+$ $\left(1.33-2.4\alpha_g+1.2\alpha_g^2\right)\mathrm{Re}_s^{0.7}\,\mathrm{Pr}^{1/3}$

Heterogeneous reactions:

For reaction $aA+bB\rightarrow cC+dD$ where A and C belongs to the gas phase and B and D to the solids phase

$S_g=R^H\left(cM_c - aM_a\right)$	$S_g^{\vec{\upsilon}}=R^H\left(cM_c\vec{\upsilon}_{net}-aM_a\vec{\upsilon}_g\right)$	$\vec{\upsilon}_{net}=\dfrac{aM_a\vec{\upsilon}_g+bM_b\vec{\upsilon}_s}{aM_a+bM_b}$
$S_s=R^H\left(dM_d - bM_b\right)$	$S_s^{\vec{\upsilon}}=R^H\left(dM_d\vec{\upsilon}_{net}-bM_b\vec{\upsilon}_s\right)$	
$S_{g,i}=R^H\left(\gamma_{g,i}^p M_{g,i}^p - \gamma_{g,i}^r M_{g,i}^r\right)$	$S_g^h=R^H\left(cM_c H_{net}-aM_a H_a - cM_c h_f^c\right)$	
$S_{s,i}=R^H\left(\gamma_{s,i}^p M_{s,i}^p - \gamma_{s,i}^r M_{s,i}^r\right)$	$S_s^h=R^H\left(dM_d H_{net}-bM_b H_b - dM_d h_f^d\right)$	
$H_{net}=\dfrac{aM_a\left(H_a-h_a^f\right)+bM_b\left(H_b-h_b^f\right)}{aM_a+bM_b}$	$R^H=-\dfrac{1}{V}\dfrac{dN_A}{dt}=\dfrac{6}{d_s}\alpha_s k\dfrac{\alpha_g x_{O_2}\rho_g}{M_A}$	
$k_{ox}=1.493e^{\left(-8983.8/T\right)}$ (estimated)	$k_{red}=0.0327e^{\left(-4456.0/T\right)}$	

Wall boundary condition for the solids phase:	
$\vec{\tau}_s=-\dfrac{\pi}{6}\sqrt{3}\phi\dfrac{\alpha_s}{\alpha_{s,max}}\rho_s g_{0,ss}\sqrt{\Theta_s}\vec{U}_{s,\parallel}$	$q_s=\dfrac{\pi}{6}\sqrt{3}\phi\dfrac{\alpha_s}{\alpha_{s,max}}\rho_s g_{0,ss}\sqrt{\Theta_s}\vec{U}_{s,\parallel}\cdot\vec{U}_{s,\parallel}-\dfrac{\pi}{4}\sqrt{3}\dfrac{\alpha_s}{\alpha_{s,max}}\left(1-e_{sw}^2\right)\rho_s g_{0,ss}\Theta_s^{3/2}$

Hydrodynamic CFD validation

Although CFD models have never been thoroughly validated against experimental data collected in a reacting system, hydrodynamic validation has been completed to increase confidence in model predictions. Hydrodynamic validation of CFD models describing riser flows have been carried out in a previous work by the present authors (Ellis, *et al.*,2011). A full length riser was simulated in 2D in a system in which fine particles (78 μm and 1560 kg/m^3) were fluidized with a mixture of helium and air so as to approximate hydrodynamic conditions occurring in reactive flows. These cold flow conditions approximate the system simulated in this paper very closely. The ability of the model to correctly predict radial segregation in riser flows was also validated in (Cloete, *et al.*,2011).

Hydrodynamics occurring in a bubbling bed is generally accepted to be significantly less challenging to model than that occurring in a riser and has been experimentally validated (Taghipour, *et al.*,2005).

Design of air reactor by CFD

Snapshots of instantaneous flow behaviour in the riser are given in Figure 5. The importance of resolving the particulate structures is well emphasised in this figure and is in accordance with a previous work by the authors (Cloete, *et al.*,2011). It is clear that there exists substantial radial segregation in all four variables plotted, even in the very dilute upper regions of the riser (right of Figure 5). The high degree of coupling between the four flow variables can also clearly be

seen, emphasizing the interconnectedness between mass, momentum, energy and species conservation and transport.

It is shown that solids volume fraction is concentrated more towards the walls of the riser in a typical core annular flow pattern with high velocities in the core and low or even negative velocities in the annulus region. These solid structures increase the overall solids holdup in the riser, giving more surface area for reaction. The higher solids concentration at the walls causes a higher reaction rate in this region, consuming O$_2$ at a much higher rate than occurs in the central regions. A situation then arises where the majority of solids are concentrated in areas that are depleted of O$_2$. This will decrease the overall reaction rate. Larger temperatures are observed towards the walls of the riser since the rate of the exothermic reaction is higher in these regions. This, in turn, will cause an increase in the overall reaction rate. In order to capture these effects, it is essential that the cluster formation is adequately resolved. Coarser grid simulations may look alluring due to the decreased computational costs associated, but will be highly inaccurate if clustering is lost.

All of the above-mentioned effects are even more pronounced in the lower regions of the riser (left of Figure 5). It is shown that the reaction can only occur on the surface of the clusters being injected from the solids inlets since the O$_2$ mass fraction is close to zero within the cluster itself. The rapid rate at which the hot solids warm up the cold gas feed is also worth mentioning. Due to the small particles size and the large density difference between the phases, the gas is heated up almost instantly upon contact with the solids.
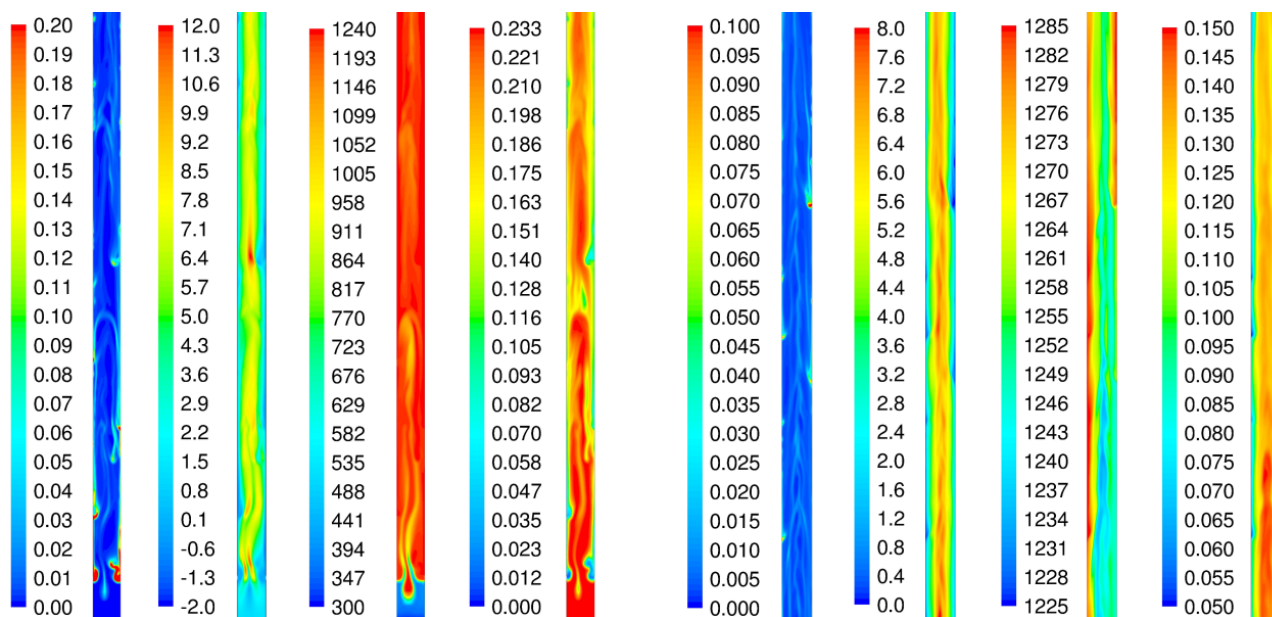
Figure 5: Instantaneous contours of solids volume fraction, gas vertical velocity (m/s), O$_2$ mass fraction and solids temperature (K) in two short sections of the riser. The four figures on the left represent the lower regions where the solids are injected, while the four on the right are in the upper half where the flow is fully developed.

The molar conversion of Ni to NiO along the length of the riser is shown in Figure 6. Recall that the molar conversion of the Ni/NiO in both reactors was assumed to be 3.6% in equation (3). The air reactor will therefore have to be sufficiently long in order to achieve the desired conversion. For this purpose, the Ni conversion along the length of the riser can be plotted as in Figure 6. It is seen that the desired conversion of 3.6 % can be achieved with a reactor height of

10 m. Another interesting feature of Figure 6 is that the conversion curve along the height of the reactor seems to be almost linear. This is somewhat surprising since it was expected that the reaction would slow down more as the oxygen is depleted higher up in the reactor. It is apparent, however, that the decrease in O$_2$ concentration is balanced by the significant increase in temperature which in turn increases the reaction rate constant.

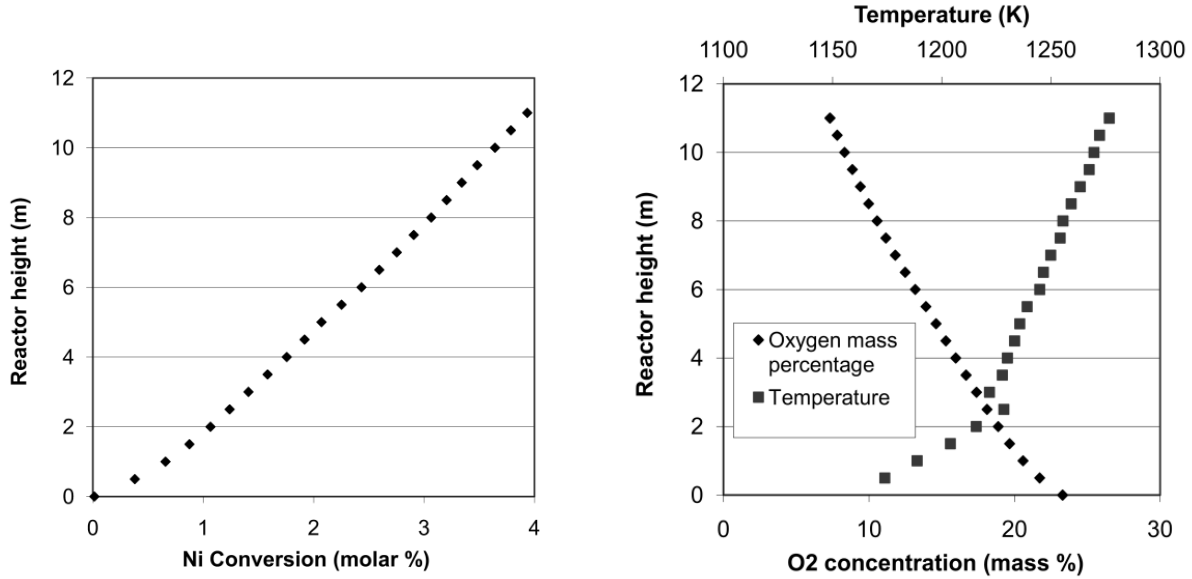**Figure 6: Time averaged Ni conversion, O$_2$ concentration and temperature along the length of the riser.**

Design of the fuel reactor by CFD

Figure 7 shows the instantaneous flow behaviour in the bubbling bed. It is shown that bubbles are not as distinct as is often the case with bubbling bed simulations. This is due to the fine powder used in the present simulation setup. The temperature contours in the bubbling bed indicate a virtually uniform temperature profile. Recall that the gas is injected at temperature of 300K and the solids at a temperature of 1238.4K which could suggest large temperature variations to be present. It is clear, however, that the heat capacity of the dense mass of solids is sufficient to not show any visible impact of the cold gas injection. It can also be seen from Figure 7 that the present solids inlet condition allows the freshly injected solids to slip a significant distance down the wall before being properly mixed into the remainder of the bed. Once the fresh solids are entrained by the rising bubbles, however, mixing is rapid as is characteristic of fluidized beds. There will therefore be no cold-spots in the reactor where the reaction rate is slowed down significantly. Results also indicate that there will be no short-circuiting of the freshly injected solids to the solids outlet on the opposite side of the reactor. The contours of the methane mass fraction indicate the very high reaction rates right at the bottom of the reactor where the dense solids meet the highly concentrated methane feed stream. Some degree of reactant slip can be observed, but this is minimal due to the large reaction rate and the suppressed bubble formation.
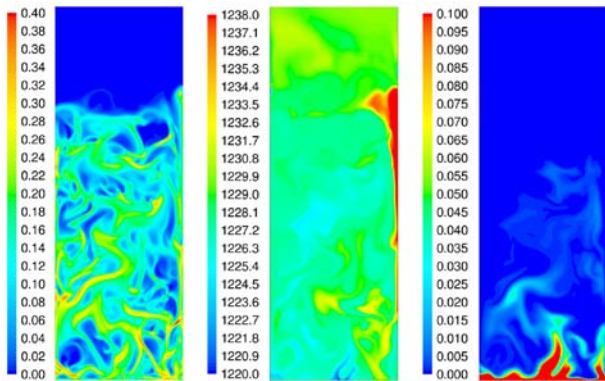
Figure 7: Contours of instantaneous solids volume fraction, solids temperature (K) and CH$_4$ mass fraction for the bubbling bed.

The design specification of the fuel reactor was the conversion of 99.9% (mass) of the incoming methane gas. This conversion factor along the length of the bed is plotted in Figure 8.
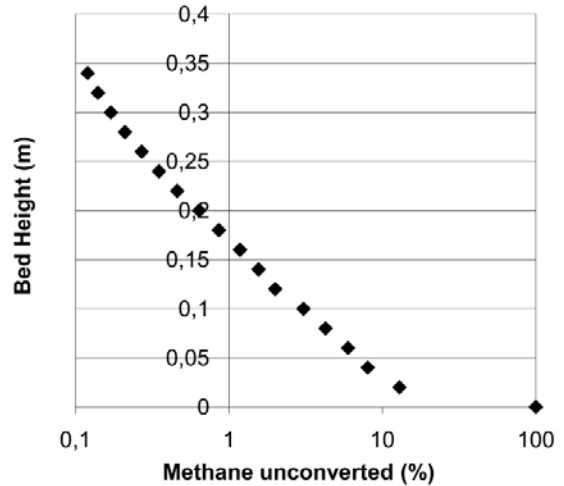
Figure 8: Mass percentage of injected methane remaining.

The bed height required to achieve the designed 99.9% (mass) methane conversion can be taken from Figure 8 as 0.35 m. It is clear that there is an exponential drop in the rate of conversion towards the top of the bubbling bed due to the decrease in the methane available for reaction. The reaction in the fuel reactor is endothermic, so a larger extent of reaction will only slow the reaction down further by lowering the temperature. Figure 8 also shows that about 90% of the bed height is required to achieve the final 10% of conversion. Despite this relatively inefficient use of bed mass, the bed is still quite small due to the high reactivity of methane with the chosen oxygen carrier. A plot of conversion vs. time published previously (Ryu, *et al.*,2001) shows that the oxygen carrier needs less than 2 seconds in an atmosphere of only 5% methane to reach the required conversion of 3.6% at 1023 K. The concentrated form in which the methane was injected also ensured very rapid reaction in the lower parts of the bed.

This high reactivity would support the decision of another work (Kolbitsch, *et al.*,2009) to also operate the fuel reactor as a circulating fluidized bed. If the bed is operated in a more dilute regime, fewer solids will be available for reaction and the gas superficial velocity through the bed will be higher.

Both these factors will require a longer bed height and the required reactor diameter will be reduced.

CONCLUSIONS

A design support tool for interconnected fluidized bed processes has been developed. The strategy is based on a combination of flow regime considerations, mass balance calculations, process simulation and computational fluid dynamics. A typical first iteration in the conceptual design of a small scale CLC system was presented for demonstrative purposes. The air reactor was designed as a riser operating in the dilute core annular transport regime, while the fuel reactor was designed as a bubbling fluidized bed. The design strategy resulted in complete reactor specifications in terms of reactor dimensions as well as feed flow rates and temperatures.

The resulting CLC system clearly indicated the areas in which optimization is required. For example, the air reactor was too tall and the fuel reactor too short, implying that the gas feed velocities to both reactors should be altered accordingly in the next design iteration. It is likely that a substantial number of design iterations will be required before the system is sufficiently optimized.

The design strategy requires the specification of a large number of design variables such as operating temperature and pressure, type of oxygen carrier material, the flow regime in which the reactors will operate and the degree of reactant conversion required. This large number of design variables grants great freedom in the design process, but will require a substantial amount of experimentation to find a suitably optimized combination. The proposed design support tool can complete such design iterations in a timely and cost effective manner.

ACKNOWLEDGEMENT

REFERENCES

BI, H.T. & GRACE, J.R.(1995) Flow regime diagrams for gas-solid fluidization and upward transport. *International Journal of Multiphase Flow* **21**, 1229-1236

CLOETE, S., AMINI, S. & JOHANSEN, S.T.(2011) On the Effect of Cluster Resolution in Riser Flows on Momentum and Reaction Kinetic Interaction. *Powder Technology* **In press**

CLOETE, S., AMINI, S. & JOHANSEN, S.T.(2011) A fine Resolution Parametric Study on the Numerical Simualtion of Riser Flows. *Powder Technology* **In press**

ELLIS, N. *et al.*(2011) Effect of Change in Drag Force in Riser Hydrodynamics - Experimental and Numerical Investigations. *Industrial & Engineering Chemistry Research* **In press**

GUNN, D.J.(1978) Transfer of Heat or Mass to Particles in Fixed and Fluidized Beds. *International Journal of Heat and Mass Transfer* **21**, 467-476

HERTZOG, H., ELIASSON, B. & KAARSTAD, O.(2000) Capturing Greenhouse Gasses. *Scientific American* **282**, 72-79

HOSSAIN, M.M. & DE LASA, H.I.(2008) Chemical-looping combustion (CLC) for inherent CO2 separations--a review. *Chemical Engineering Science* **63**, 4433-4451

JOHNSON, P.C. & JACKSON, R.(1987) Frictional-Collisional Contitutive Relations for Granular Materials, with Application to Plane Shearing. *Journal of Fluid Mechanics* **176**, 67-93

KOLBITSCH, P., PR, LL, T. & HOFBAUER, H.(2009) Modeling of a 120 kW chemical looping combustion reactor system using a Ni-based oxygen carrier. *Chemical Engineering Science* **64**, 99-108

KOLBITSCH, P., PROLL, T., BOLHAR-NORDENKAMPF, J. & HOFBAUER, H.(2009) Design of a chemical looping combustor using a dual circulating fluidized bed reactor system. *Chemical Engineering and Technology* **32**, 398-403

KRONBERGER, B., LYNGFELT, A., LOFFLER, G. & HOFBAUER, H.(2005) Design and fluid dynamic analysis of a bench-scale combustion system with CO2 separation-chemical-looping combustion. *Industrial and Engineering Chemistry Research* **44**, 546-556

LEONARD, B.P. & MOKHTARI, S. (1990) ULTRA-SHARP Nonoscillatory Convection Schemes for High-Speed Steady Multidimensional Flow.in *NASA TM 1-2568 (ICOMP-90-12),* NASA Lewis Research Center.

LEVENSPIEL, O.(1999) *Chemical Reaction Engineering.* 3 edn, John Wiley & Sons.

LYNGFELT, A., LECKNER, B. & MATTISSON, T.(2001) A fluidized-bed combustion process with inherent CO2 separation; Application of chemical-looping combustion. *Chemical Engineering Science* **56**, 3101-3113

PATANKAR, S.(1980) *Numerical Heat Transfer and Fluid Flow*. Hemisphere Publishing Corporation.

PROWARE(2009) METSIM 16.06, Tucson, Arizona, USA.

RYU, H.J. *et al.*(2001) Oxidation and Reduction Characteristics of Oxygen Carrier Particles and Reaction Kinetics by Unreacted Core Model *Korean Journal of Chemical Engineering* **18**, 831-837

SYAMLAL, M., ROGERS, W. & O'BRIEN, T.J.(1993) *MFIX Documentation: Volume 1, Theory Guide.*, National Technical Information Service.

TAGHIPOUR, F., ELLIS, N. & WONG, C.(2005) Experimental and computational study of gas-solid fluidized bed hydrodynamics. *Chemical Engineering Science* **60**, 6857-6867

WEN, C.Y. & YU, Y.H.(1966) Mechanics of Fluidization. *Chemical Engineering Progress Symposium Series* **62**, 100-111

8th International Conference on CFD in Oil & Gas, Metallurgical and Process Industries
SINTEF/NTNU, Trondheim NORWAY
21-23 June 2011

CFD11-174

3D NUMERICAL STUDY OF THE INFLUENCE OF PARTICLE POROSITY ON THE HEAT AND FLUID FLOW

Kay WITTIG[1][*], **Aakash GOLIA**[2], **Petr A. NIKRITYUK**[†]

[1]CIC VIRTUHCON, Department of Energy Process Engineering and Chemical Engineering,

Technische Universität Bergakademie Freiberg, 09599 Freiberg, GERMANY

[2]Department of Mechanical Engineering, Indian Institute of Technology - Guwahati, INDIA

[*] E-mail: kay.wittig@vtc.tu-freiberg.de
[†] E-mail: petr.nikrityuk@vtc.tu-freiberg.de

ABSTRACT

This work is devoted to the three dimensional numerical simulations of the heat and fluid flow past and through a porous spherical particle over a wide range of Reynolds numbers ($20 < \mathrm{Re} < 500$) corresponding to the steady state flow and different values of porosity varied between 0.62 and 0.92. The porosity of a particle is modeled using two approaches corresponding to microscopic and macroscopic representation of pores, respectively. In particular, in the first approach the porous particle is represented by a cluster of small spherical particles distributed inside the diameter of the porous particle. The second approach represents the porosity implicitly utilizing the so-called permeability model adopting Blake-Kozeny relation to treat the fluid and heat flow inside a particle. The comparison of both models showed good agreement for a porosity below 0.7. The analysis of numerical simulations showed, that for a constant Reynolds number ($\mathrm{Re} < 100$) with increase of porosity, the value of the drag coefficient decreases slightly. However with increase of the Reynolds number ($\mathrm{Re} > 100$) a local maximum in the drag force coefficient for the porosity of about 0.76 was observed. Based on the results of simulations expressions for the drag coefficient and the surface averaged Nusselt number are derived and examined.

Keywords: 3D fluid flow, porosity, heat transfer, drag force, Nusselt number, permeability.

NOMENCLATURE

Greek Symbols
β Volumetric expansion coefficient, $[1/K]$.
ε Void fraction (particle porosity).
ζ Volume fraction of fluid in a cell.
ζ_{surf} Volume fraction of fluid in an interface cell.
λ Thermal conductivity, $[W/m \cdot K]$.
μ Dynamic viscosity, $[N \cdot s/m^2]$.
ν Kinematic viscosity, $[m^2/s]$.
ρ Mass density, $[kg/m^3]$.

Latin Symbols
A Surface of non-porous sphere, $[m^2]$.
A_Σ Total solid surface in a porous sphere, $[m^2]$.
A_p Projected frontal surface area, $[m^2]$.
C_D Drag coefficient.
c_p Isobaric heat capacity, $[J/kg \cdot K]$.
d Characteristic inner length, $[m]$.

d_p Diameter of small sphere inside global sphere, $[m]$.
D Diameter of global sphere, $[m]$.
F_D Drag force, $[N]$.
$\vec{g}$ Gravity force, $[kg \cdot m/s^2]$.
Gr   Grashof number.
$\vec{i}_x$ Unit vector in *x*-direction.
$\vec{n}$ Normal vector.
Nu   Nusselt number.
p Pressure, $[Pa]$.
Pr   Prandtl number.
Q Heat, $[J]$.
$\dot{Q}$ Heat flux, $[W]$.
Ra   Rayleigh number.
Re   Reynolds number.
T Temperature, $[K]$.
T_S Surface Temperature, $[K]$.
T_∞ Inflow Temperature, $[K]$.
$\vec{u}$ Velocity vector, $[m/s]$.
u_x Velocity vectors *x*-component, $[m/s]$.
U_0 Inflow velocity, $[m/s]$.
V_Σ Full sphere volume, $[m^3]$.

Sub/superscripts
x With respect to *x*-coordinate.
y With respect to *y*-coordinate.
z With respect to *z*-coordinate.

INTRODUCTION

The understanding of particulate flows has great importance for adequate modeling of fluid-particle flows in many industrial applications, especially in chemical engineering applied to fluidized bed reactors. In spite of the growing use of fluidized bed reactors in many technologies relating to the heat and mass transfer processes, the behavior of fluid-particle flows in this class of reactors is still not completely understood, e.g. see (van der Hoef *et al.*, 2008). Numerical models used in computer simulations of particulate flows, e.g. the most used one is the discrete particle models (DPM) (van der Hoef *et al.*, 2008; Zhu *et al.*, 2008), became important tools in predicting and tuning the performance of industrial facilities. However, closure relations for the particle-fluid interaction and the heat transfer between particle and fluid, which are very often represented in the form of drag coefficient C_D and Nusselt number Nu relations, respectively, are deciding to obtain realistic results using DPM. Basically, most drag

models and heat transfer coefficient closures, e.g. Ranz-Marshall (Ranz and Marshall, 1952), are obtained empirically for ideal spherical particles (Whitaker, 1972; Ranade, 2002). In reality however, particles often are porous initially, or they become porous, e.g. due to drying or pyrolyze. Several authors have studied the influence of sphere-porosity on the drag force, e.g. see (Nandakumar and Masliyah, 1982; Feng and Michaelides, 1998). However the works devoted to the study of the heat flow past a porous sphere are rare. At the same time the heat and fluid flow around spheres for a wide range of Reynolds number have been extensively studied experimentally, analytically and numerically for a long time, e.g see reviews (Whitaker, 1972; Bagchi *et al.*, 2001). On the contrary the heat and fluid flow past porous spherical particles for moderate Reynolds numbers (Re > 10) has attracted relatively less attention in spite of its actuality for many industrial applications, e.g. gasification of coal or biomass. Thereby it should be noted, that a wide variety of analytical and simplified numerical calculations have been performed to study the flow past and within an isolated permeable spheroid for the creeping flow (Re ≈ 0), e.g see works (Joseph and Tao, 1964; Neale *et al.*, 1973), which have rather more theoretical than practical relevance. Almost all of the semi-analytical studies are based on the solution of the Stokes creeping flow equation outside the spheroid and the Darcy equations within the spheroid. The latest study of this art has been done by (Vainshtein *et al.*, 2002). It was found that, at a low Reynolds number, the drag on a permeable sphere is less than that for an impermeable sphere. (Masliyah and Polikar, 1980) confirmed this findings experimentally, but at the same time it was found out, that at Reynolds numbers (7 < Re < 120) the drag for a porous sphere can be higher than the drag of an impermeable sphere. Recently, (Bhattacharyya *et al.*, 2006) and (Yu *et al.*, 2011) studied numerically the steady flow around and through a porous cylinder for the Reynolds numbers 5 < Re < 40, Darcy numbers $10^{-6} \leq \mathrm{Da} \leq 10^0$ and porosity in the range $0.629 \leq \varepsilon \leq 0.999$. In both works the so-called single-domain based models have been utilized, where the porosity has been modeled *implicitly* using Darcy and Forchheimer source terms added to Navier-Stokes equation. It was shown numerically that the drag ratio between porous and non-porous cylinders decreases rapidly by $\mathrm{Da} < 10^{-2}$. However, macroscopic representation of porosity using permeability approach might be fairly inaccurate in respect to prediction of the heat and fluid flow inside a porous particle. Moreover, the prediction of the permeability for various porous media is a problem in itself, e.g. see (Bear, 1988; Kaviany, 1995). From this point of view, the main objective of this work is to investigate numerically the steady flow and heat transfer past and inside a porous sphere using two independent approaches corresponding to microscopic and macroscopic representation of porosity, respectively. The definition of both models is given in the next section. The main aim is to characterize the gas flow and the heat transfer behavior as a function of the Reynolds number and porosity.

PROBLEM AND MODEL DESCRIPTION

Before we proceed with mathematical model formulation let us describe the setup under investigation. The computational domain is presented schematically in Fig. 1 which shows a porous spherical particle of diameter $D = 2R_0 = 788 \cdot 10^{-6}$ m placed in an uniform gas flow with velocity U_0.
The size of the computational domain is $16D$, $4D$ and $4D$ in x, y and z directions, respectively. The center of the particle

is located in the middle of y and z axis having $y = 2D$ and $z = 2D$, respectively, and at $x = 4D$ on the x axis, see Fig. 1. The temperature of the solid surface inside the porous sphere, T_S, is constant and equals to 400 K. The temperature of the inflow gas is $T_\infty = 300$ K. The porosity of the particle is modeled using two approaches defined as follows:

1. *Microscopic approach*: the porosity of the sphere is represented by a cluster of small spherical particles distributed regularly inside the diameter of the porous particle, see Figs. 2 and 3. The porosity of the global sphere is varied with the change of the number of small spheres, n_Σ, in the cluster, see Table 1.

2. *Macroscopic approach*: the porosity is modeled implicitly using the so-called permeability model adopting Blake-Kozeny relation (Bear, 1988) to treat the heat and fluid flow inside a particle, see Fig. 2.

The cluster porosity and Darcy number have the following form:

$$\varepsilon \approx \frac{D^3 - n_\Sigma \, d_p^3}{D^3} \qquad (1)$$

$$\mathrm{Da} = \frac{K}{D^2} \qquad (2)$$

where K is permeability, n_Σ is the number of small spheres inside the global sphere and d_p is the diameter of small sphere, $d_p \approx 100 \cdot 10^{-6}$ m.
The Reynolds number is based on the free stream velocity U_0 and the diameter of the sphere D:

$$\mathrm{Re} = \frac{U_0 D}{\nu}, \qquad (3)$$

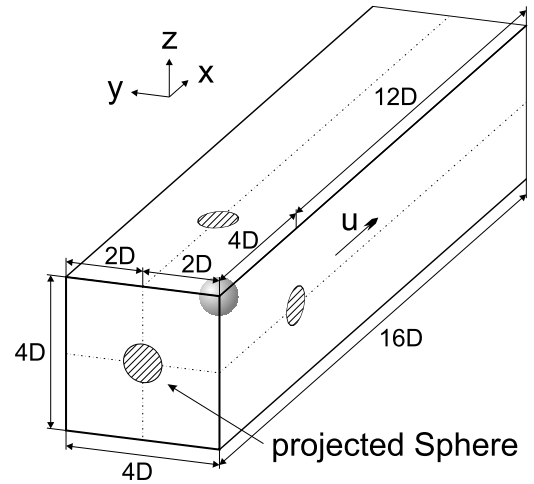where ν is the kinematic viscosity.

Figure 1: Axionometric projection of the computational domain.

To proceed with the governing equations the following basic assumptions have been made:

1. The gas flow is incompressible.

2. The viscous heating effect is neglected.

3. The transport properties are constant resulting in the Prandtl number Pr = 0.71.

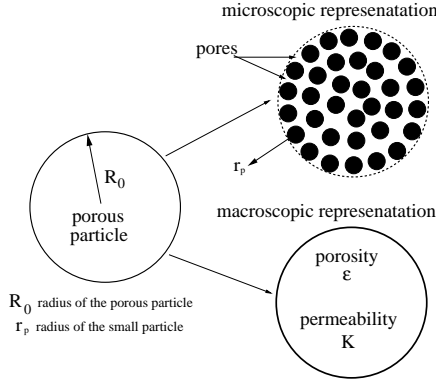4. The buoyancy effect is neglected.

Figure 2: Scheme of a porous sphere representation using explicit (including microscopic features) and implicit definition of porosity.
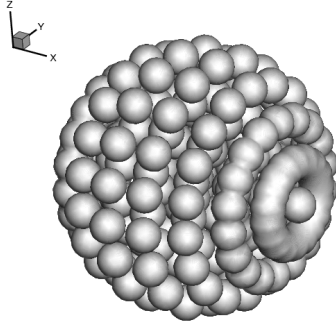

Figure 3: Scheme of a porous sphere represented using cluster of small spheres arranged regularly inside the radius R_0.

Taking into account the assumptions made above, the conservation equations for mass, momentum and energy transport written in Eulerian coordinates have the following form:

$$\nabla \cdot \vec{u} = 0, \tag{4}$$

$$\rho \frac{\partial \vec{u}}{\partial t} + \rho \, \vec{u} \cdot \nabla \vec{u} = -\nabla p + \mu \, \nabla^2 \vec{u} + \vec{F}_{\text{porous}}, \tag{5}$$

$$\rho \, c_p \frac{\partial T}{\partial t} + \rho \, c_p \vec{u} \cdot \nabla T = \lambda \nabla^2 T + Q_{\text{porous}}. \tag{6}$$

It is $\vec{u}$ the velocity vector, ρ the density, p the pressure, μ the dynamic viscosity and c_p the heat capacity.

The last terms on the right hand side in Eqs. (5 and 6) are switched on only for macroscopic model. In particular, the fluid flow in the porous region is modeled by adding the so-called Darcy's term to momentum conservation equations:

$$\vec{F}_{\text{porous}} = \begin{cases} 0, & \text{if} \quad \zeta = 1, \text{ out of porous sphere} \\ -\frac{\mu \vec{u}}{K_u}, & \text{if} \quad 0 \leq \zeta < 1, \text{ in porous sphere} \end{cases} \tag{7}$$

where $\zeta = \zeta(x,y,z)$ is the volume fraction of fluid in a cell. The permeability coefficient K_u is calculated using the Carman-Kozeny relation (Bear, 1988):

$$K_u = \frac{c_u d^2}{180} \cdot \frac{\varepsilon^3}{(1-\varepsilon)^2}, \tag{8}$$

To model the influence of the porosity on the heat transfer through the particle, a Darcy's-like term is introduced (Dierich and Nikrityuk, 2010):

$$Q_{\text{porous}} = \begin{cases} 0, & \zeta = 1 \\ -\frac{1}{K_T}(T - T_S), & 0 \leq \zeta < 1 \end{cases} \tag{9}$$

$$K_T = \frac{c_T d^2}{180} \cdot \frac{\varepsilon^3}{(1-\varepsilon)^2}, \tag{10}$$

where ε is the porosity of the spherical particle and c_u and c_T are constants, which make the dimensions of K_u and K_T consistent with the other terms in the momentum and energy equations, respectively (Dierich and Nikrityuk, 2010). Here, d is a characteristic inner length, which depends on the structure of the porous particle. In this work we use two different models to define d. In the first model, d is calculated as the distance between the centers of two small spheres as follows:

$$d_1 = D \cdot \sin \frac{\pi}{n_\Sigma}, \tag{11}$$

In the second model, d is set in relationship with the full spheres volume V_Σ as well as the given porosity ε as follows:

$$d_2 = \frac{(\varepsilon \cdot V_\Sigma)^{\frac{1}{3}}}{\pi}, \tag{12}$$

The values of d_i, ε and the corresponding number of small spheres n_Σ in the particle cluster are given in Table 1.

Table 1: Characteristic lengths, the surface enlargement A_Σ/A and number of particles in the cluster in dependence of porosity ε

ε	$d_1/10^{-4}$ m	$d_2/10^{-4}$ m	A_Σ/A	n_Σ
0.6212	1.6751	2.6623	2.81	219
0.6728	1.6751	2.8078	2.47	175
0.7614	1.6751	3.0492	1.82	132
0.8703	3.7213	3.3334	0.98	67
0.9175	3.7213	3.4528	0.67	43

The values of Darcy number calculated for different porosities using Eq. (8) are given in Table 2.

Table 2: Darcy-Number calculated for different values of porosity

ε	0.6212	0.6728	0.7614	0.8703	0.9175
$\text{Da}_{d_1}/10^{-4}$	4.194	7.141	19.46	485.5	1406
$\text{Da}_{d_2}/10^{-4}$	10.59	20.06	64.5	389.6	1210

NUMERICS

The numerical simulations of heat and fluid flow past a porous particle represented by cluster of small spheres (*Microscale approach*), see Fig. 3, are performed using commercial CFD solver (ANSYS Inc., 2011). For the solution of the system of linearized algebraic equations an implicit linear equation solver (Gauß-Seidel) is applied in conjunction with an algebraic multigrid method (AMG). The SIMPLE algorithm is used to solve pressure and velocity equations in a coupled way (Patankar, 1980). For spatial discretization of convective terms the QUICK scheme (Leonard, 1979) is applied. The computational grids, which were built using commercial software GAMBIT, have up to $7 \cdot 10^6$ *tetrahedral* elements. The simulations were performed in parallel mode using 8 processors in one run.

The numerical simulations of heat and fluid flow past a porous particle represented by a single sphere with given porosity (*Macroscale approach*) are performed using an open source 3D Cartesian grid-finite-volume code for the isothermal flows (Ferziger and Peric, 2002), which was adopted for the solution of heat transfer problems. The diffusive fluxes are approximated using central difference scheme. The convection terms are discretized using the deferred correction scheme, which converges to the second-order central difference scheme, for details see (Ferziger and Peric, 2002). The SIMPLE algorithm for collocated variables arrangement is used to solve the pressure equation. The linear equation system is solved implicitly by the vectorized incomplete LU decomposition method of Stone (Stone, 1968; Leister and Peric, 1994). The pressure and velocity fields on a non-staggered grid are coupled by the momentum interpolation technique of Rhie and Chow (Rhie and Chow, 1983).

To set the no-slip boundary conditions on the surface of non-permeable sphere we use the so-called *porous medium* approach (Khadra *et al.*, 2000), which can be considered as a variant of *continuous forcing* model within an Immersed Boundary method, for details we refer to the review of (Mittal and Iaccarino, 2005). It should be noted that originally the porous medium approach comes from solidification modeling. In this method, a source term, called the Darcy drag, is added to the Navier-Stokes equations, in order to damp the velocity in the cells occupied by the solid fraction. This solid region is assumed to be a porous medium, characterized by its permeability $K(t, \vec{x})$ which can be variable in time and space (Khadra *et al.*, 2000). Detailed description of this method can be found in (Khadra *et al.*, 2000).

The boundary conditions are set to an inflow at the west side and an outflow at the east side. The remaining boundaries are defined of Neumann type. On the inflow a constant temperature boundary is set and on all other boundaries a symmetry boundary condition is applied.

For the interface reconstruction on fixed Cartesian grid we use the so-called *supersampling* method, see (Watt, 1999). In contrast to the stair-step approximation the supersampling method belongs to the family of SLIC methods (Simple Line Interface Method). Applying SLIC strategy for the interface reconstruction, we assume that the interface thickness has the size of one cell. Figure 4 illustrates the calculation of the volume fraction of fluid ζ_{int} in the interface cell. The porosity in the interface cells, ε_{int}, is defined as follows:

$$\varepsilon_{int} = 1 - \zeta_{int}\,\varepsilon \qquad (13)$$
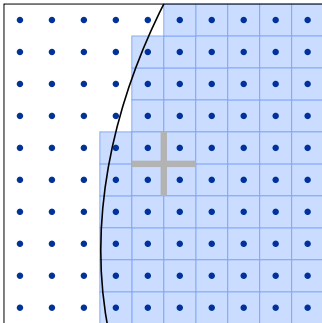
Figure 4: Demonstration of 2D supersampling in a CV with an ordered 10×10 pattern.

The source terms $\vec{F}_{\text{porous}}$ and Q_{porous} in equ. (5) and (6), respectively, are linearized following recommendations given by Patankar (Patankar, 1980) as follows:

$$S = S_C + S_P \Phi_P^{bc}, \qquad (14)$$

where Φ_P^{bc} is the value of the principle variable (T_S or u_S) inside the porous region. Applying the present case to this equation, the S_C and S_P are

$$S_C^u = 0, \quad S_P^u = -\mu\frac{1}{K_u}, \quad S_C^T = \frac{T_S}{K_T}, \quad S_P^T = -\mu\frac{1}{K_T} \quad (15)$$

The grids used are given in Table 3. Local grid refinement inside the particle was used, see Figure 5. The amount of the control volumes inside the particle ranges from the 50th to the 80th part of the particle diameter, see Table 3 for more details.
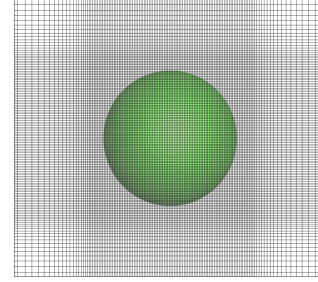

Figure 5: Zoomed frontal view on a used Grid with refinement of the control volume sizes around the particle.

Table 3: Information on the grids used in *macroscale* simulations.

Re	CVs along the diameter D	Grid
21.35	50	$246 \times 96 \times 96$
53.38	50	$246 \times 96 \times 96$
106.78	50	$246 \times 96 \times 96$
213.55	60	$294 \times 114 \times 114$
266.93	60	$294 \times 114 \times 114$
320.32	80	$392 \times 152 \times 152$
389.72	80	$392 \times 152 \times 152$
427.1	80	$392 \times 152 \times 152$
480.48	80	$392 \times 152 \times 152$

CODE VALIDATION

For the purpose of code validation, the results of a 3D simulation are compared with experimental results of Kuehn and Goldstein, see (Kuehn and Goldstein, 1976, 1978). Here, the numerical prediction of temperature profiles along the symmetry lines are compared with experimental data. The experimental set up includes a hot isothermal inner cylinder placed in the center of another cold isothermal outer cylinder, see Figure 6.

Due to the gravity field a buoyancy induced flow occurs. The inner cylinder with the radius of $R_i = 0.0178\,\text{m}$ has the constant surface temperature $T_i = 373\,\text{K}$ and the outer cylinder with the radius of $R_0 = 0.0463\,\text{m}$ has the constant temperature $T_0 = 327\,\text{K}$. The space between the cylinders is filled with the air. The whole set up corresponds to the following non-dimensional numbers:

$$\text{Gr} = \frac{g\beta(T_s - T_\infty)}{v^2}L^3 = 7.963 \cdot 10^4$$

$$\text{Pr} = \frac{v}{a} = \frac{\mu c_p}{\lambda} = 0.707, \qquad (16)$$

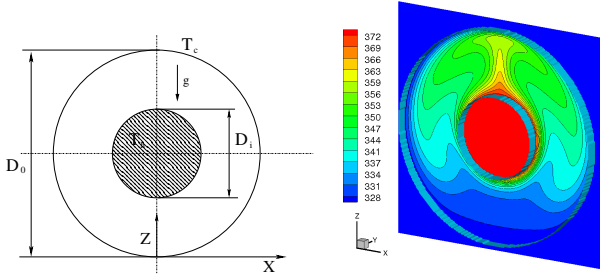$$\text{Ra} = \text{Gr} \cdot \text{Pr} = 5.630 \cdot 10^4.$$

Figure 6: Natural convection between two concentric cylinders *(left)* and 3D contour plot of temperature between the concentric cylinders *(right)*.

The numerical simulations are performed on Grids having $100 \times 100 \times 1$, $100 \times 100 \times 10$, $100 \times 100 \times 50$ and 100×100 CVs, respectively. The boundary conditions in the north and the south direction are set to be symmetric. The fluid is treated as incompressible. Additional simulations which were done by use of a commercial software, where the fluid was taken as a compressible media, showed identical results. The temperature contour plot and flow pattern are shown in Figure 6.
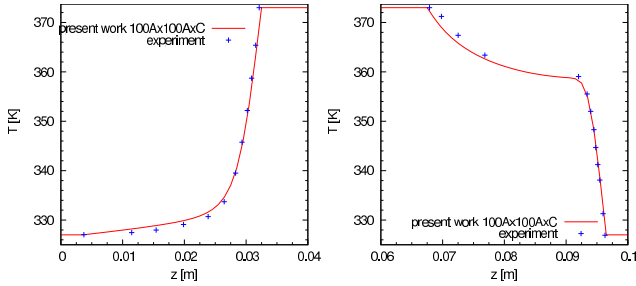
Figure 7: Temperature profiles along the vertical symmetry line against experimental data of Kuehn and Goldstein, see (Kuehn and Goldstein, 1976, 1978).

The comparison of temperature profiles along the symmetry line compared with the data of Kuehn and Goldstein are given in Figure 7. The agreement between the numerical prediction and the experimental results was very good.

In order to check the accuracy of the code in respect to the heat and fluid flow past a single sphere a set of simulations has been performed using the computational domain shown in Fig. 1. The sphere is assumed to be non-porous. We compare the drag coefficient and the surface-averaged Nusselt number calculated using our code against well tabulated values, see (Haider and Levenspiel, 1989; Schlichting and Gersten, 2006) and (Ranz and Marshall, 1952; Bagchi *et al.*, 2001), respectively. The drag coefficient and the surface-averaged Nusselt number are defined as follows:

$$\text{Nu} = \frac{2R_0}{A(T_S - T_\infty)} \int_S \nabla T \cdot \vec{n} \mathrm{d}S \qquad (17)$$

$$C_D = \frac{F_D}{\rho U_0^2 A_p}, \qquad (18)$$

where the drag force F_D is calculated integrating the incompressible stress tensor over the surface of the sphere as follows:

$$F_D = \mu \int_S \nabla u_x \cdot \vec{n} \mathrm{d}S - \int_S p \vec{i}_x \cdot \vec{n} \mathrm{d}S, \qquad (19)$$

Here $\vec{i}_x$ the unit vector in x direction, A is the surface of the sphere, A_p the projected frontal area of the sphere, T_S is the temperature of the isothermal sphere and T_∞ is the inflow temperature of the fluid.

Here we note that by calculation of velocity gradients the linear approximation has been used. This was possible due to good resolved grids providing for the maximum of the dimensionless wall distance lower than $y_{\max}^+ < 0.9$.

The results of the comparison are shown in Fig. 8. A good agreement can be seen.
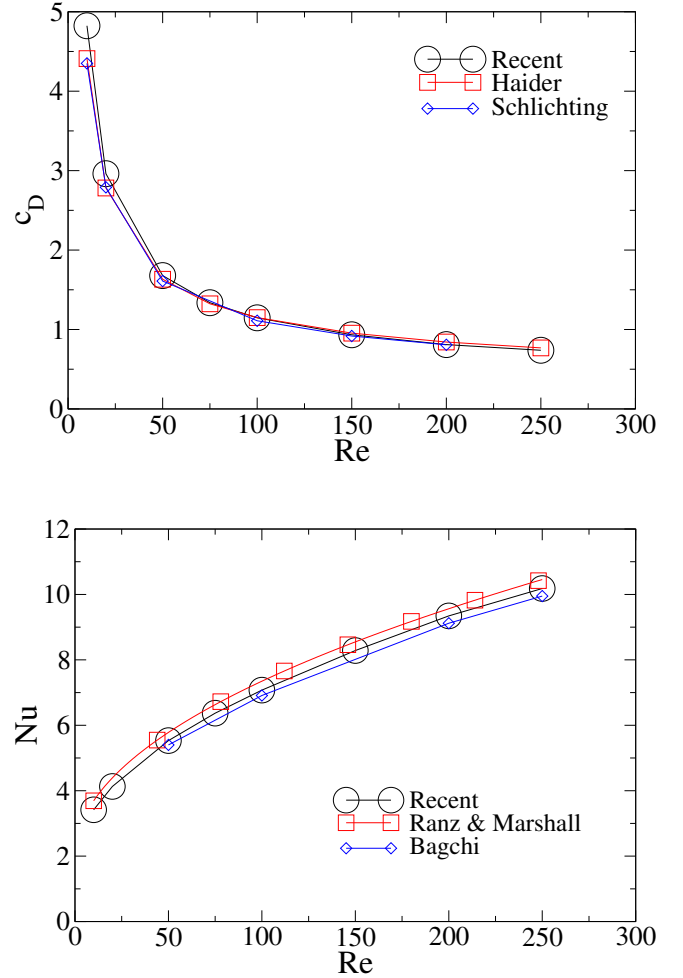
Figure 8: Drag coefficient validation with (Haider and Levenspiel, 1989; Schlichting and Gersten, 2006) *(upper)* and Nusselt number validation with (Ranz and Marshall, 1952; Bagchi *et al.*, 2001) *(lower)*.

RESULTS

Next we present the results of three-dimensional simulations using both *microscale* and *macroscale* models. In the frame of *macroscale* model we use two different expressions for the characteristic size of pores given by Eqs. (11, 12). Next in the text these both equations are referred as 'Model 1' and 'Model 2', respectively. The results of *microscale* model are presented using abbreviation 'Golia et al.' due to the fact that some results are taken from the work (Golia *et al.*, 2011).

It is well known fact, that heat and fluid flow past sphere are governed by Re, Nu and Pr numbers. In the case of a porous sphere the porosity ε or the Darcy number Da and the surface ratio A_Σ/A have to be added into consideration. Here A_Σ/A characterizes the surface difference between porous and non-porous particles.

To proceed, Figs. 9 and 10 present the vector and contour plots of the non-dimensional temperature $\frac{T-T_\infty}{T_S-T_\infty}$ predicted using *microscale* and *macroscale* models for different particle porosities and Reynolds numbers, respectively. It can be seen that when the particle porosity is less than 0.62 corresponding to the Darcy number Da $< 7 \cdot 10^{-4}$, the gas does not penetrate the particle for almost all Re numbers under consideration due to the large flow resistance. In particular, it is evident that for $\varepsilon = 0.62$ and Re $= 213$ the flow pattern are similar to the heat and fluid flow past solid sphere predicted by (Bagchi *et al.*, 2001). The only difference is that both models predict insignificant flow penetration into the porous sphere near the forward stagnation point. The increase of porosity up to $\varepsilon \approx 0.76$ leads to the 'flow trough' effect, when the cold gas flows through the hot porous sphere, see Fig. 9 *(middle)*. As a result, the gas inside the sphere is cooled down and at the same time more gas is heated behind the sphere, see Fig. 11. Next increase of the porosity up to $\varepsilon \approx 0.87$ allows more gas to pass through the porous particle. It should be noted that with increase of porosity the so-called flow re-laminization occurs. This effect increases the value of critical Re when the flow becomes unsteady. This finding is in good agreement with results of (Bhattacharyya *et al.*, 2006; Yu *et al.*, 2011), who discovered similar effect for the porous cylinder using *macroscale* model. Finally, it should be noted that at high Reynolds numbers (Re > 300) and $\varepsilon \geq 0.76$ the flow field predicted using the *macroscale* model completely differs from that obtained by the *microscale* model. This effect continues at higher porosities ε, where the *macroscale* models are only able to predict the correct fluid flow for Reynolds number below Re < 50. To study qualitatively the effect of porosity on the drag coefficient and parallel to compare *microscale* and *macroscale* models we plot in Fig. 12 drag coefficient in dependence on the porosity predicted using both models for different Re. The analysis of results shows that the drag coefficient almost does not change in the range of $\varepsilon \leq 0.7$ and Re ≤ 50. However, the increase of permeability ε leads to the slight decrease of the drag coefficient, which is somehow logically. A highly porous sphere allows the gas to flow through it thus the drag must decrease. Unlikely, the *macroscale* model predicts higher decrease of c_D in comparison to *microscale* model. This fact shows that *macroscale* model overpredicts the change of drag coefficient for high porosity values $\varepsilon > 0.7$. However, at the same time both models produce comparable results for $\varepsilon < 0.7$, see Fig. 12.

Finally, we compare the surface-averaged Nusselt numbers computed using *microscale* and *macroscale* models for different *Re* and ε. Additionally we use well-known Ranz & Marshall (Ranz and Marshall, 1952) and Gunn's (Gunn, 1978) semi-empirical relations, which have the following form:

$$\text{Nu} = 2 + 0.6\,\text{Re}^{1/2}\,\text{Pr}^{1/3}, \tag{20}$$

$$\text{Nu} = \left(7 - 10\varepsilon + 5\varepsilon^2\right) \cdot \left(1 + 0.7\,\text{Re}^{1/5}\,\text{Pr}^{1/3}\right) + \tag{21}$$
$$+ \left(1.33 - 2.4\varepsilon + 1.2\varepsilon^2\right)\,\text{Re}^{0.7}\,\text{Pr}^{1/3},$$

respectively. Here Gunn's correlation, Eq. (21), is based on a stochastic model of the packed bed configuration (Gunn, 1978).
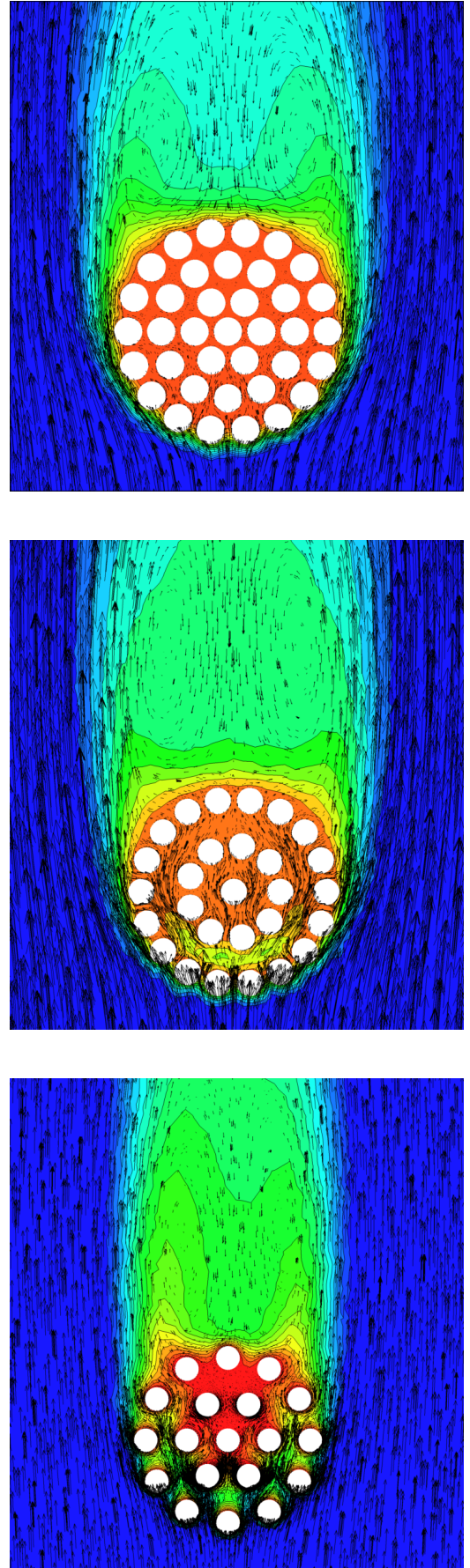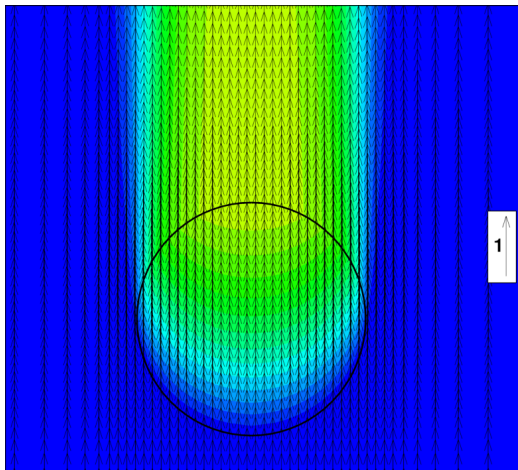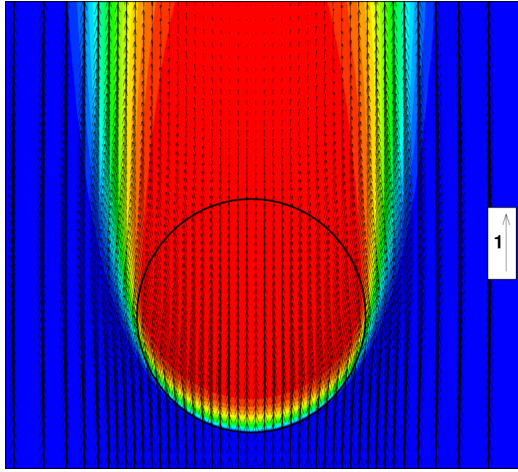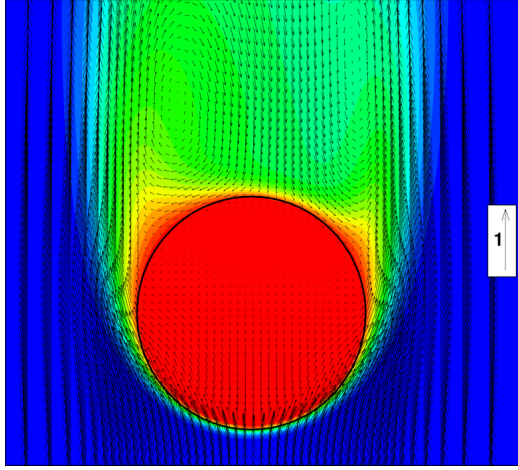

Figure 9: Microscale model: Distribution of the non-dimensional temperature $\frac{T-T_\infty}{T_S-T_\infty}$ predicted for different particle porosity and Re numbers ($x - y$ plane, $z = 0$): $\varepsilon = 0.6212$, Re $= 213.55$ *(upper)*. $\varepsilon = 0.7614$, Re $= 320.32$ *(middle)*. $\varepsilon = 0.8703$, Re $= 480.48$ *(lower)*.
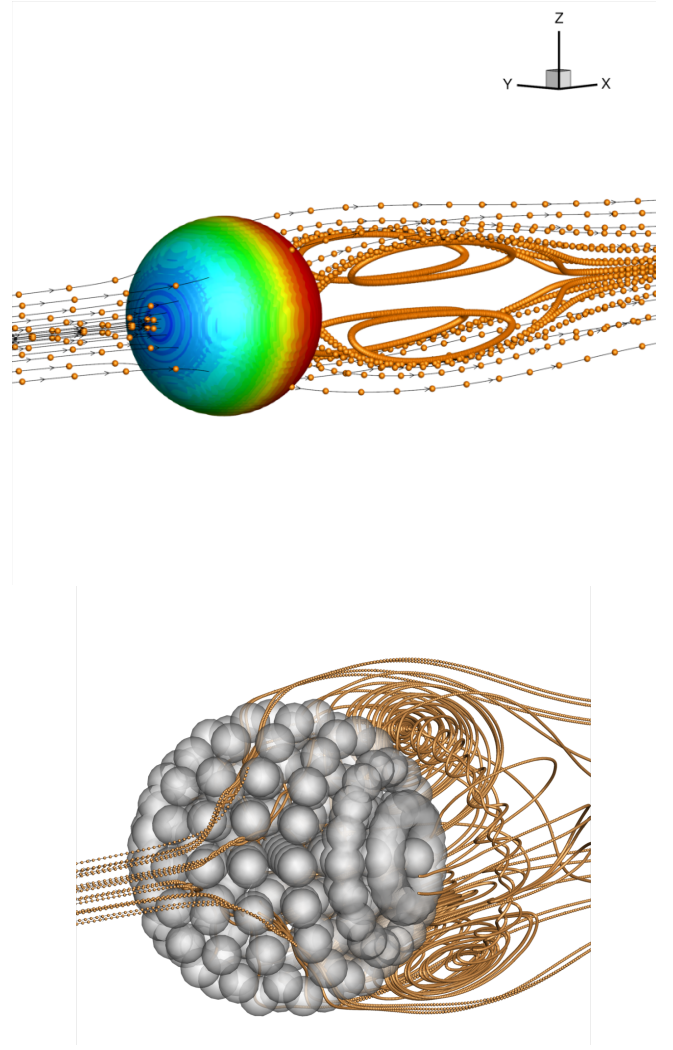
Figure 11: Streamlines and the surface temperature calculated using *macroscale* model for $\varepsilon = 0.7614$, Re = 213.55 *(upper)* and using *microscale* model for $\varepsilon = 0.6212$, Re = 213.55 *(lower)*.

In the case of *macroscopic* model the surface-averaged Nu has been computed using Eq. (17). In the frame of *microscopic* model the surface-averaged Nusselt number was derived as follows:

$$\text{Nu} = \frac{1}{n_\Sigma} \sum_{i=1}^{n_\Sigma} \frac{2r_p}{A(T_S - T_\infty)} \int_{S_p} \nabla T \cdot \vec{n} \text{d}S_p \qquad (22)$$

The Nu calculated using *microscale* model has been approximated as follows (Golia *et al.*, 2011):

$$\text{Nu} = \left(4.31 - 12.71\,\varepsilon + 9.81\,\varepsilon^2\right) \qquad (23)$$
$$\cdot \left(1 + 0.8\,\text{Re}^{0.6}\,\text{Pr}^{1/3}\right)$$

The variations of surface-averaged Nu as a function of Reynolds number evaluated using models described above are depicted in Figs. 13 and 14. In particular, from Fig. 13(upper) it can be seen that the Nusselt number calculated from Ranz & Marshall equation has good agreement with Nu predicted by *macroscale* model. The values of Nu predicted by *microscale* model lie below Ranz & Marshall. Surprisingly we found out, that by dividing the surface averaged Nusselt number with the surface enlargement factor A_Σ/A

Figure 10: Macroscale model: Distribution of the non-dimensional temperature $\frac{T - T_\infty}{T_S - T_\infty}$ predicted for different particle porosity and Re numbers ($x - y$ plane, $z = 0$): $\varepsilon = 0.6212$, Re = 213.55 *(upper)*. $\varepsilon = 0.7614$, Re = 320.32 *(middle)*. $\varepsilon = 0.8703$, Re = 480.48 *(lower)*.

(given in Tab. 1) as follows:

$$\mathrm{Nu}_{por} = \frac{A}{A_\Sigma} \cdot \mathrm{Nu} \qquad (24)$$

the *macroscale* models predict the exact surface averaged Nusselt number of the *microscale* model and Ranz & Marshall relation, see Fig. 13 *(lower)*. However, the increase of the porosity value leads to the deviation between *macroscale* and *microscale* models, see Fig. 14. At the same time the Ranz & Marshall relation corrected using Eq. (24) produced the results close to *microscale* models even for high porosity values for Re < 100. The comparison of Nu behavior predicted for $\varepsilon = 0.87$ using Gunn's relation and *microscale* models showed good agreement. Unlikely the *macroscale* model showed poor performance by high porosities $\varepsilon > 0.8$ and Reynolds numbers Re > 100.
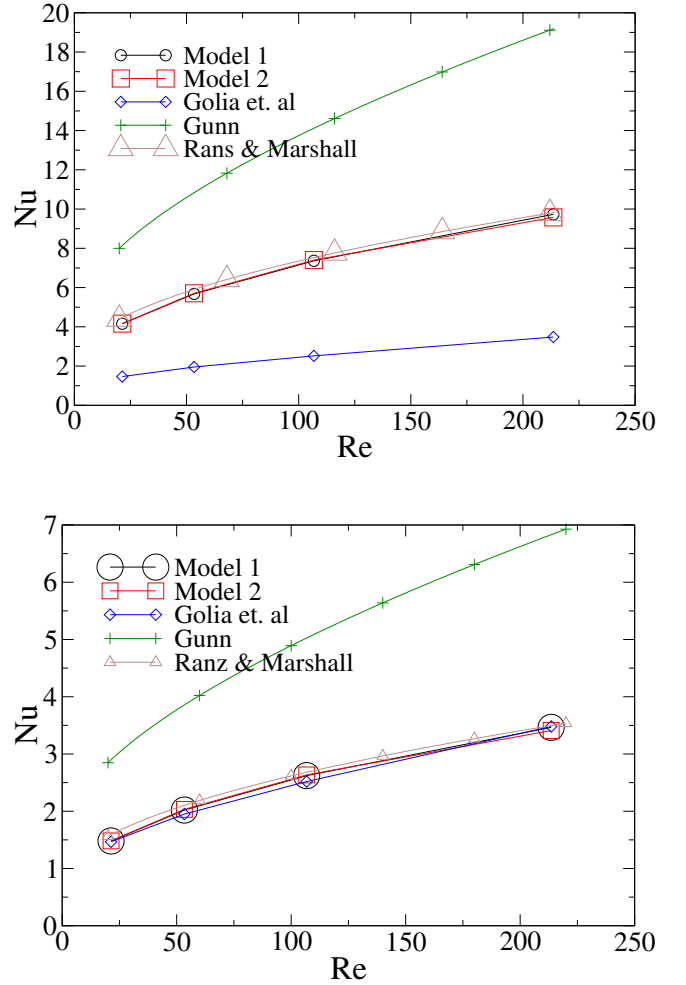
Figure 13: Surface-averaged Nusselt number in dependence on the Reynolds number predicted using microscale (pointed as Golia *et al.*) and macroscale models and compared with semi-empirical Ranz & Marshall (Ranz and Marshall, 1952) and Gunn (Gunn, 1978) relations. Here $\varepsilon = 0.6212$, *(upper)* figure shows the results gained without surface correction and *(lower)* figure depicts results calculated using surface correction, see Eq. (24). Model 1 and Model 2 correspond to Eqs. (11) and (12), respectively.

Figure 12: Drag coefficient in dependence on the porosity predicted for different Re using microscale (pointed as Golia *et al.*) and macroscale models. Here, Re = 20 *(upper)*, Re = 50 *(upper-middle)*, Re = 100 *(lower-middle)*, Re = 200 *(lower)*. Model 1 and Model 2 correspond to Eqs. (11) and (12), respectively.
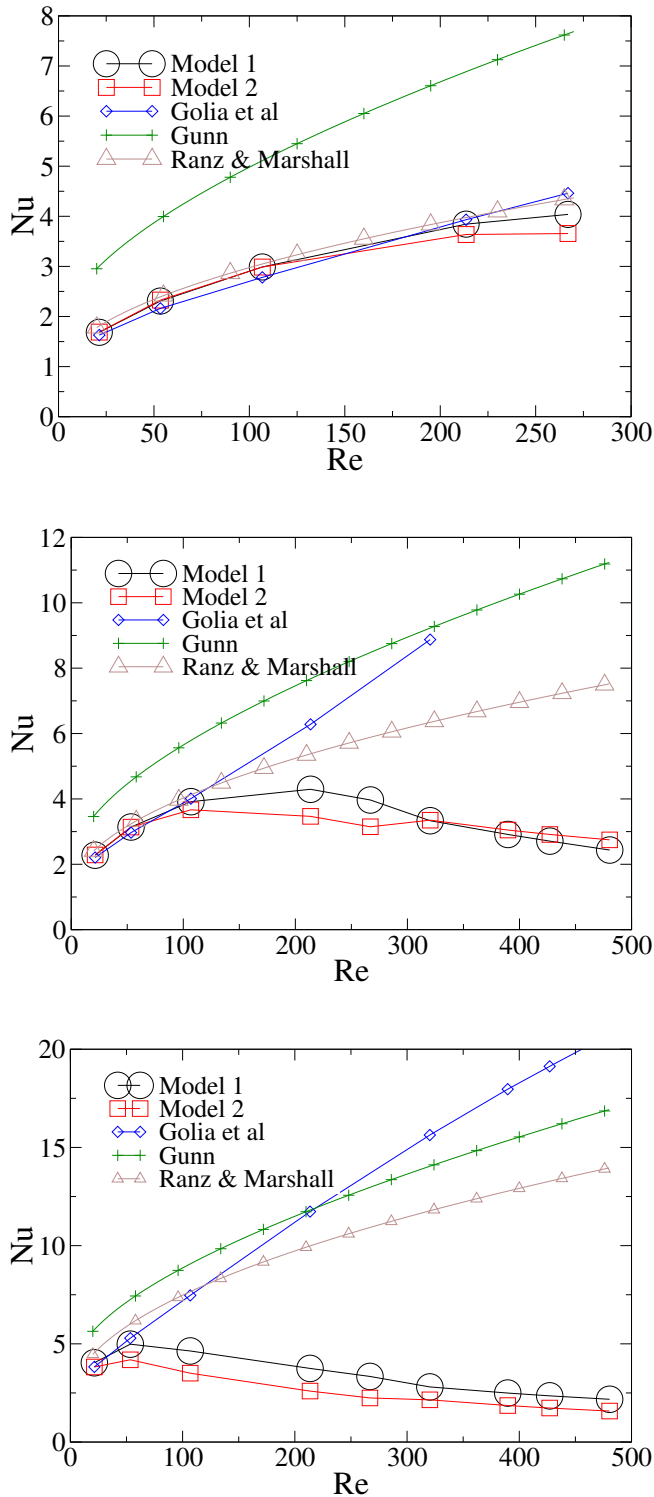
Figure 14: Surface-averaged Nusselt number in dependence on the Reynolds number predicted using microscale (pointed as Golia et al.) and macroscale models and compared with semi-empirical Ranz & Marshall (Ranz and Marshall, 1952) and Gunn (Gunn, 1978) relations. Here $\varepsilon = 0.6728$ *(upper)*, $\varepsilon = 0.7614$ *(middle)*, $\varepsilon = 0.8703$ *(lower)*. Model 1 and Model 2 correspond to Eqs. (11) and (12), respectively.

CONCLUSION

The interphase heat transfer between gas and the porous particle with different porosities has been studied numerically using two independent approaches corresponding to *microscopic* and *macroscopic* representation of pores, respectively. In particular, in first approach the porous particle is represented by a cluster of small spherical particles distributed inside the diameter of the porous particle. Second approach represents the porosity implicitly utilizing the so-called permeability model adopting Blake-Kozeny relation to treat the heat and fluid flow inside a particle. The comparison of both models in the range of parameters $20 < Re < 500$, $0.6 < \varepsilon < 0.92$ showed good agreement for the porosity $\varepsilon > 0.7$ corresponding to the Darcy number $Da > 10^{-3}$. The analysis of microscale numerical simulations showed that for a constant Reynolds number ($Re < 100$) with increase of porosity the value of the drag coefficient decreases slightly. However with increase of the Reynolds number ($Re > 100$) a local increase of the drag coefficient was observed for the porosity of about 0.76. Based on the results of simulations expressions for the drag coefficient and the surface averaged Nusselt number are derived and examined. Syrprisiglu, it was found out that microscale and macroscale simulations agree well for $\varepsilon < 0.7$ if surface enlargement ratio is taken into account by calculation of the Nusselt number. The use of this kind correction in Ranz & Marshall relation produces results close to both numerical models. However, with the increase of Reynolds number and porosity $Da > 10^{-3}$ leads to the deviation in $Nu = f(Re, Pr, \varepsilon)$ calculated using both models due to penetration of gas flow in the porous sphere.

ACKNOWLEDGMENTS

REFERENCES

ANSYS Inc. (2011). "Ansys/fluent^{TM} v 13.0. – Commercially available CFD software package based on the Finite Volume method. Southpointe, 275 Technology Drive, Canonsburg, PA 15317, U.S.A., www.ansys.com".

BAGCHI, P. *et al.* (2001). "Direct numerical simulation of flow and heat transfer from a sphere in a uniform cross-flow". *J. Fluids Engineering*, **123**, 347–358.

BEAR, J. (1988). *Dynamics of Fluids in Porous Media*. Dover Publications. Inc., New York.

BHATTACHARYYA, S. *et al.* (2006). "Fluid motion around and through a porous cylinder". *Chem. Eng. Science*, **61**, 4451–4461.

DIERICH, F. and NIKRITYUK, P. (2010). "A numerical study of the influence of surface roughness on the convective heat transfer in a gas flow". *CMES: Computer Modeling Eng. & Sci.*, **64**, 251–266.

FENG, Z. and MICHAELIDES, E. (1998). "Motion of a permeable sphere at finite but small reynolds numbers". *Phys. Fluids*, **10**, 1375–1383.

FERZIGER, J.H. and PERIC, M. (2002). *Computational Methods for Fluid Dynamics*. 3rd ed. Springer, Berlin.

GOLIA, A. *et al.* (2011). "Three dimensional simulations of the heat and fluid flow inside and past a porous spherical particle". *Computers & Chem. Eng.*, submitted.

GUNN, D. (1978). "Transfer of heat or mass to particles in fixed and fluidised beds". *Int. J. Heat Mass Transfer*, **21**, 467–476.

HAIDER, A. and LEVENSPIEL, O. (1989). "Drag coefficient and terminal velocity of spherical and nonspherical particles". *Powder Technology*, **58**, 63–70.

JOSEPH, D. and TAO, L. (1964). "The effect of permeability on the low motion of a porous sphere in a viscous liquid". *Z. Angew. Math. Mech.*, **44**, 361–364.

KAVIANY, F. (1995). *Principles of Heat Transfer in Porous Media*. Springer-Verlag, Berlin.

KHADRA, K. *et al.* (2000). "Fictitious domain approach for numerical modelling of navier-stokes equations." *Int. J. Numer. Methods Fluids*, **34**, 651–684.

KUEHN, T. and GOLDSTEIN, R. (1976). "An experimental and theoretical study of natural convection in the annulus between horizontal concentric cylinders". *J. Fluid Mech.*, **74**, 695–719.

KUEHN, T. and GOLDSTEIN, R. (1978). "An experimental study of natural convection heat transfer in concentric and eccentric horizontal cylindrical annuli". *J. Heat Transfer*, **100**, 635–640.

LEISTER, H.J. and PERIC, M. (1994). "Vectorized strongly implicit solving procedure for a seven-diagonal coefficient matrix". *Int. J. Num. Meth. Heat and Fluid Flow*, **4**, 159–172.

LEONARD, B. (1979). "A stable and accurate convective modeling procedure based on quadratic upstream interpolation". *Comp. Meth. Appl. Mech. Eng.*, **19**, 59–98.

MASLIYAH, J. and POLIKAR, M. (1980). "Terminal velocities of porous spheres". *Can. J. Chem. Eng.*, **58**, 299–302.

MITTAL, R. and IACCARINO, G. (2005). "Immersed boundary methods." *Annu. Rev. Fluid Mech*, **37**, 239–261.

NANDAKUMAR, K. and MASLIYAH, J. (1982). "Laminar flow past a permeable sphere". *Can. J. Chem. Eng.*, **60**, 202–211.

NEALE, G. *et al.* (1973). "Creeping flow relative to permeable spheres". *Chem. Eng. Sci.*, **28**, 1865–1874.

PATANKAR, S. (1980). *Numerical heat transfer and fluid flow*. Hemisphere Publishing Corporation.

RANADE, V. (2002). *Computational Flow Modeling for Chemical Reactor Engineering*. Academic Press.

RANZ, W. and MARSHALL, W. (1952). "Evaporation from drops, part i & ii". *Chem. Eng. Progress*, **48**, 141–146, 173–180.

RHIE, C. and CHOW, W. (1983). "Numerical study of the turbulent flow past an airfoil with trailing edge separation". *AIAA*, **21**, 1525–1532.

SCHLICHTING, H. and GERSTEN, K. (2006). *Grenzschicht-Theorie*. 10th ed. Springer, Berlin.

STONE, H.L. (1968). "Iterative solution of implicit approximations of multidimensional partial differential equations". *SIAM J. Numer. Anal.*, **5**, 530–558.

VAINSHTEIN, P. *et al.* (2002). "Creeping flow past and within a permeable spheroid". *Int. J. Multiphase Flows*, **28**, 1945–1963.

VAN DER HOEF, M. *et al.* (2008). "Numerical Simulation of Dense Gas-Solid Fluidized Beds: A Multiscale Modeling Strategy". *Annu. Rev. Fluid Mech.*, **40**, 47–70.

WATT, A. (1999). *3D Computer Graphics*. 3rd ed. Addison-Wesley Longman, Amsterdam.

WHITAKER, S. (1972). "Forced convection heat transfer correlations for flow in pipes, past flat plates, single cylinders, single spheres, and for flow in packed beds and tube bundles". *AIChE*, **18**, 361–371.

YU, P. *et al.* (2011). "Steady flow around and through a permeable circular cylinder". *Computers & Fluids*, **42**, 1–12.

ZHU, H. *et al.* (2008). "Discrete particle simulation of particulet systems: A review of major applications and findings". *Chem. Eng. Sci.*, **63**, 5728–577.

CFD SIMULATION OF BATH DYNAMICS IN THE HISMELT SMELT REDUCTION VESSEL FOR IRON PRODUCTION

Darrin STEPHENS[1] , Mandar TABIB[1], Mark DAVIS[2] and M. Philip SCHWARZ[1*]

[1] CSIRO Mathematics Informatics and Statistics Division, Victoria 3169, AUSTRALIA
[2] HIsmelt Corporation Pty Ltd, WA, Australia

* E-mail: Phil.Schwarz@csiro.au; darrin.stephens@csiro.au; mandar.tabib@gmail.com

ABSTRACT

CFD has played a crucial role in enabling the design and scale-up of the HIsmelt® direct smelting technology. The HIsmelt® Process is a potential replacement for blast-furnace technology owing to its efficiency, cost advantage and lower environmental impact. An existing PHOENICS-based CFD model of the molten bath dynamics in the process vessel has been transferred to ANSYS-CFX to improve its accuracy and to enable efficient analysis on an unstructured mesh. The basic model involves Lagrangian particle tracking of iron ore and coal particles through two Eulerian phases representing metal and slag. The model incorporates reactions involving coal devolatilisation, coal dissolution, and ore reduction. A sensitivity study shows that an increase in the number of particles used improves convergence, and the CFD model has been applied to study a 2.7m diameter pilot smelter.

Keywords: CFD, smelt-reduction, multiphase modelling, Lagrangian, iron-making, computational fluid dynamics.

NOMENCLATURE

Greek symbols
- Fractional phase hold-up, [ ]
- Turbulence energy dissipation rate per unit mass, $[m^2/s^3]$
- μ_T Turbulent viscosity, [Pa s]
- ρ Density, $[kg/m^3]$
- σ_k Prandtl number for turbulence kinetic energy, [ ]
- σ_ε Prandtl number for turbulence energy dissipation rate, [ ]
- $\bullet_k$ Shear stress of phase k, [Pa]

Latin symbols
- C_μ Constant in $k\text{-}\varepsilon$ model, [ ]
- g Acceleration due to gravity, $[m/s^2]$
- G Generation term, $[kg/ms^2]$
- k Turbulence kinetic energy per unit mass, $[m^2/s^2]$
- $\mathbf{M_I}$ Total interfacial force between two phases, $[N/m^3]$
- $\mathbf{F_D}$ Drag force, $[N/m^3]$
- P Pressure, $[N/m^2]$
- S Strain rate, $[1/s]$.
- t Time, [s]
- $\mathbf{u}$ Velocity vector, [m/s]

Subscripts
- r Phase
- g Gas phase
- l Liquid bath phase

INTRODUCTION

Computational fluid dynamics (CFD) has played a crucial role in enabling the design and scale-up of the HIsmelt® direct smelting technology (Hardie et al., 1992; Davis et al., 2003; Davis et al., 1998; Schwarz, 1994, 2001). This process, developed by Rio Tinto, has the potential to replace the blast furnace technology for iron-making operations since it offers the advantages of lower operating costs and capital intensity, lower environmental impact, and greater raw material and operational flexibility (Goodman, 2007; Bates and Goldsworthy, 2002; Bates and Coad, 2000). The first commercial HIsmelt plant which is jointly owned by Rio Tinto, Nucor Corporation, Mitsubishi Corporation and Shougang Corporation was hot commissioned in April 2005 at Kwinana, Western Australia.

The process was developed and scaled up over several years with the critical assistance of a substantial amount of CFD and physical modeling (eg Schwarz and Dang, 1995; Schwarz and Taylor, 1998, 2001). The modelling and design studies utilized two linked state-of-the-art CFD models of the smelt reduction vessel (SRV): the "bath model" and the "topspace model" (Davis et al, 2003). The "bath model", described by Schwarz (1994, 2001) covers the bath and the fountain of droplets generated by gas injection and reaction, and the "topspace model" covers the droplet zone and the top gas space including the combustion zone (ie the upper region of the smelter). The driver for developing two models is that different modelling techniques are optimal for the two halves of the SRV, and this enables the flow simulations to be performed in a reasonable time. The information from the bath model is fed to the topspace model, and the topspace model can then be used for fast turn-around design and scale-up analyses, since it takes comparatively much less time to run than the bath model (Davis et al., 2003; Davis et al., 1998). The reason the bath model takes much greater simulation time is because it is a three dimensional transient multiphase multi-component Eulerian-Eulerian reactive CFD model that incorporates both Lagrangian tracking of ore/coal particles and an algebraic slip model to allow for both slag and metal components in the liquid bath, a technique first described by Schwarz and Taylor (1998). It is not surprising that this model

takes substantial computer time, and is challenging in terms of its physics and numerics. Even two-phase simulation of non-reactive gas injection involves substantial challenges, as described by Schwarz (1996) and Schwarz and Dang (1995).

In this work, the focus has been on the transfer of the bath model to the ANSYS-CFX platform to reduce convergence time and to allow the model to easily utilize an unstructured mesh. Several new features have been incorporated in the CFX implementation to improve its convergence speed, accuracy and functionality compared to the earlier PHOENICS-based model. The present paper describes the convergence study performed using the updated CFD bath model as applied to the HIsmelt large-scale pilot SRV. In the following sections, a brief description of the HIsmelt Process is given, followed by a description of the present CFD bath model, and results pertaining to its convergence properties.

THE HISMELT PROCESS

The HIsmelt Process (as illustrated schematically in Figure 1) involves injection of fine iron ores and non-coking coals directly into a molten iron bath, contained within a Smelt Reduction Vessel (SRV) operating at approximately 1450ºC, to produce high quality molten pig iron. Nitrogen gas is used as the conveying medium for lance injection of these particles. The high velocity injection results in significant penetration of these solids into the molten metal and the reactions taking place can be represented in an idealised way by dissolution of coal into the molten iron:

$$C_{coal\ (s)} \longrightarrow [C]_{iron\ (l)} \tag{1}$$

Where, C_{coal} is the fixed (non-volatile) component in the coal particle which gets dissolved into the liquid molten bath to form dissolved carbon $[C]_{iron}$. The reduction of iron ore by the dissolved carbon to form molten iron is represented as:

$$3[C]_{iron} + Fe_2O_3 \longrightarrow 2[Fe]_{iron} + 3CO \tag{2}$$

Gas is generated in the coal devolatilisation process and from moisture associated with the ore/coal, so that the main gases generated in the bath are H_2 and CO:

$$C_{coal\ devolatilisation}\ ,\ H_2O + C \longrightarrow H_2 + CO \tag{3}$$
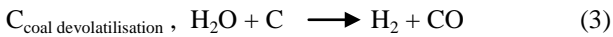
The second reaction being highly endothermic requires a constant external supply of heat to sustain it. This external supply of heat comes from the exothermic post-combustion reaction in the top-space region of smelter. Carbon monoxide and hydrogen released from the bath undergo combustion by reacting with a hot oxygen-enriched air blast. This air blast is injected at 1200ºC into the top-space via a central swirl lance. The Combustion takes place as follows:

$$2CO + O_2 \longrightarrow 2CO_2 \tag{4}$$

$$2H_2 + O_2 \longrightarrow 2H_2O \tag{5}$$

Thus, the key to the process is moving this combustion heat from the top-space combustion region down to the lower smelting region without compromising the oxygen potential in either zone. The reactions (3-5) are modelled in the topspace model, and are described in Davis et al. (2003) and Davis et al. (1998).
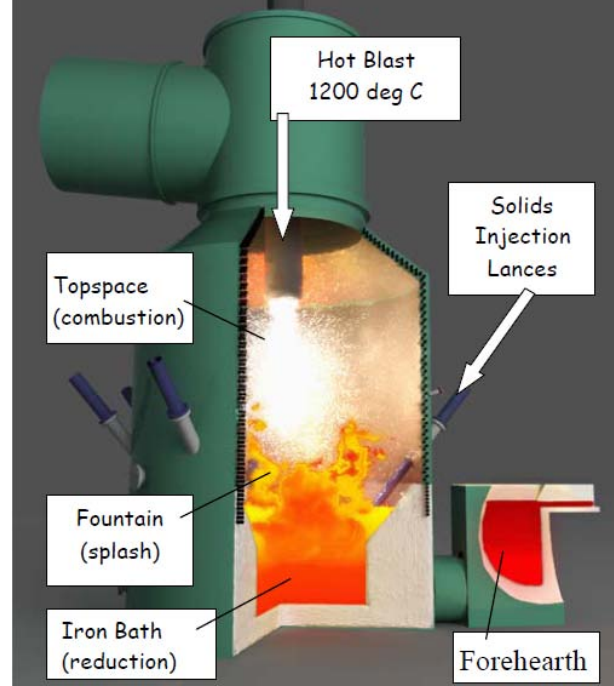
Figure 1: Schematic of the HIsmelt Process

The high rate of production of CO and H_2 in the lower melt regions results in an aggressive eruption of the bath liquid. Metal and slag are thrown upward in a fountain-like manner, forming a gas permeable region with high surface area for heat transfer. Hot combustion gases pass through this region and, in the process, deliver heat to the droplets of slag and metal, which subsequently carry it back to the bath. The high rate of liquid eruption results in only a small increase in temperature for a typical droplet, as it passes through the hot combustion zone. Thus, smelting continues to occur in a region of low oxygen potential in the lower melt regions of smelter, and exothermic combustion continues higher up in the region of the hot blast lance (where oxygen potential is relatively high). This heat loop drives the direct smelting process.

A nearly constant level of molten metal in the hearth is required to avoid submergence of a solids injection lance into it. This is achieved by taking the metal out continuously via an overflow forehearth, while the slag is taken out periodically from the side-wall of the vessel via a water-cooled slag notch.

MODEL DESCRIPTION

As mentioned, HIsmelt design and scale-up has been carried out using two separate but linked models: the bath model and the topspace model. The topspace

model simulates flow of gas (hot blast and bath gases), the fountain of liquid droplets and combustion of char/soot particles including heat transfer effects (radiation and wall heat transfer). The topspace model covers the upper parts of the fountain above the slag surface, where collisions between droplets are rare and a particle tracking approach, first developed by Crowe et al (1977), is best for treating the motion of the liquid phase.

On the other hand in the bath model (which simulates smelting reduction), the volume fractions of both liquid bath phase and gas phase in the system are comparable, and the existence of a large liquid-continuous domain (the bath proper) means that Lagrangian tracking is inappropriate. Both these fluid phases (liquid bath and gas) and the particles are all composed of multiple components (See Table 1 and Figure 2). Hence, a multi-component multi-fluid Eulerian-Eulerian approach is the most appropriate way to model both the liquid bath phase and gas phase, with the iron ore and coal particles in the bath being tracked using the Lagrangian approach. Further, the Eulerian-Eulerian model must simulate both the gas-continuous regions in which the liquid bath phase is assumed to be in dispersed form (splashes of droplets, fingers, sheets, etc in the upper regions of the SRV), as well as the liquid-continuous regions of the bath-proper in which the gas is assumed to be in the form of dispersed bubbles. A continuous interpolation between these two regimes was employed in the PHOENICS HIsmelt bath model to obtain the interfacial area between the phases for enabling computation of interfacial momentum and mass exchange, and this formulation has been coded into CFX using its so-called "mixture model". This basis of the bath model has been described by Schwarz (1992, 2001), Schwarz and Taylor (2000) and Davis et al (2003).

Table 1: Phases and their compositions

Phase	Type	Components
Gas	Eulerian	N_2, CO, H_2
Bath		Fe, Carbon, Slag
Ore (OreG, OreL)	Lagrangian	Fe_2O_3, H_2O
Coal (CoalRawG, CoalRawL)	Lagrangian	Coal fixed component, and Coal volatile component.

The focus of this work is the CFD bath model which is more complex from a multi-phase point of view and consumes more simulation time. Figure 2 shows the possible configurations of the various materials used in the bath model including the material transfer due to the reactions. The bath phase is made up of two components, slag and metal. The slag is treated as a constant composition component, while the metal is considered to be a variable composition mixture of iron and carbon. An Algebraic Slip Model is used to account for the relative motion of slag and metal (Fe/C melt), as first demonstrated in models of gas injection into a slag/metal bath by Schwarz and Taylor (1998). The gas

is a variable composition mixture of nitrogen (the carrier gas for the coal and ore), hydrogen (evolved from coal devolatilisation) and carbon monoxide (a product of coal devolatilisation and ore reduction). The coal is treated as a variable composition mixture of fixed carbon and volatile carbon. The iron ore particles are considered to be composed of hematite and moisture (H_2O). The materials (or mass) are transferred according to the reactions (equations 1-3) describing coal dissolution, ore reduction and coal devolatilisation.
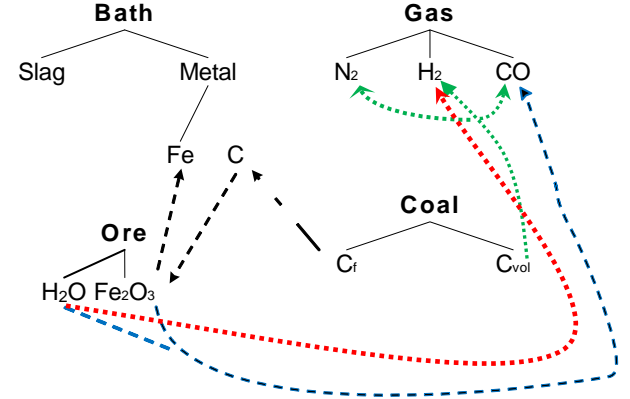
Figure 2: Material descriptions adopted for the multi-phase multi-component model.

Mathematically, the solution of continuity and momentum equations for each Eulerian phase (gas and liquid bath) enables computation of their velocity, volume fraction and turbulence level. These transport equations can be written as:

Continuity equation with mass transfer

$$\frac{\partial}{\partial t}\left(\rho_r \alpha_r\right) + \nabla \cdot \left(\rho_r \alpha_r \mathbf{u}_r\right) = S_r \qquad (6)$$

Here, the phases *r* are liquid bath phase (*r=l*) and gas phase (*r=g*). The term S_r is the net mass transfer to phase *r* from other interacting phases due to various reactions (described in detail in sections below).

Momentum equation

$$\frac{\partial}{\partial t}\left(\rho_r \alpha_r \mathbf{u}_r\right) + \nabla \cdot \left(\rho_r \alpha_r \mathbf{u}_r \mathbf{u}_r\right)$$
$$= -\nabla \cdot \left(\alpha_r \tau_{ij,r}\right) - \alpha_r \nabla P + \alpha_r \rho_r g + M_{F,r} + MS_r^{'} \qquad (7)$$

$$\sum \alpha_r = 1 \qquad (8)$$

The terms on the right hand side of the momentum equation, equation (7), represent respectively the stress, pressure gradient, gravity, momentum exchange between the phases due to interfacial forces (only drag force is considered here) and the net momentum transfer to phase r by other phases due to net mass transfer ($MS_r^{'}$). Pressure is shared by both the phases. The stress term for phase *r* is described as follows:

$$\tau_{ij,r} = -\mu_{eff,r}\left(\nabla \mathbf{u}_r + (\nabla \mathbf{u}_r)^T - \frac{2}{3}I(\nabla \mathbf{u}_r)\right) \tag{9}$$

where, $\mu_{eff,r}$ is the effective viscosity and the strain rate $\mathbf{S}$ is $(\nabla \mathbf{u}_r + (\nabla \mathbf{u}_r)^T)$. The effective viscosity for each phase is composed of two contributions: the molecular viscosity and the turbulent viscosity. The turbulent eddy viscosity is formulated using the k-• turbulence model and turbulence is considered homogeneous for both the phases (so both k and • values are the same for both the phases).

$$\mu_{T,r} = \rho_r C_\mu \frac{k^2}{\varepsilon} \tag{10}$$

The turbulence kinetic energy (k) and its energy dissipation rate (ε) are calculated from their governing transport equations (equations 11-12 respectively). The term τ_m in these equations (as computed by equation 15) takes into account the phasic turbulent viscosity (equation 10) and the molecular viscosity of each phase.

$$\frac{\partial \rho_m k}{\partial t} + \nabla \cdot (\rho_m \mathbf{u}_m k) = -\nabla \cdot (\Gamma_m \nabla k) + (G_m - \rho_m \varepsilon) \tag{11}$$

$$\frac{\partial \rho_m \varepsilon}{\partial t} + \nabla \cdot (\rho_m \mathbf{u}_m \varepsilon) = -\nabla \cdot (\Gamma_m \nabla \varepsilon) + \frac{\varepsilon}{k}(C_{\varepsilon 1} G_m - C_{\varepsilon 2} \rho_m \varepsilon) \tag{12}$$

where,

$$\rho_m = \rho_l \alpha_l + \rho_g \alpha_g \tag{13}$$

$$u_m = u_l \alpha_l + u_g \alpha_g \tag{14}$$

$$\tau_m = \tau_l \alpha_l + \tau_g \alpha_g \tag{15}$$

The model constants used are the standard values, viz. C_μ =0.09; σ_k=1.00; σ_ε=1.00; $C_{\varepsilon 1}$=1.44, $C_{\varepsilon 2}$=1.92. The term G in the above equations is the production of turbulence kinetic energy and is described by:

$$G = \tau_m : \nabla u_m \tag{16}$$

Species Transport

The mass fraction of individual components (CO, H_2) in the multi-component gas phase is computed by solving each component's transport equation with relevant source/sink terms corresponding to the component (equation 17), while the mass fraction of N_2 in the gas phase is determined using constraint equation 18.

$$\frac{\partial \alpha_g \rho_g Y_{gi}}{\partial t} + \nabla \cdot (\alpha_g \rho_g \mathbf{u}_g Y_{gi}) = \nabla \cdot \Gamma_{gi} \alpha_g \nabla Y_{gi} + S_{gi} \tag{17}$$

$$\sum Y_{gi} = 1 \tag{18}$$

where Y is the mass fraction of species i in the r phase. Similarly, the mass fraction of individual components (Fe/C and slag) in the multi-component liquid phase is obtained by applying the algebraic slip model (ASM, equation 19 - 20). This is done in order to enable the

separation of slag from metal. The slag is considered to be continuous in the liquid bath and its fraction is computed using constraint equation 21. The ASM enables computation of the slip velocity between metal (Fe/C) and slag, and the drift velocity of Fe/C. The drift velocity of a component is taken relative to the mixture (ie. the liquid bath) velocity, whereas the slip velocity of a component is taken relative to the velocity of continuous medium in the mixture (ie. slag velocity in this case).

$$\frac{\partial \alpha_l \rho_l Y_{li}}{\partial t} + \nabla \cdot (\alpha_l \rho_l (\mathbf{u}_l + u_{Di}) Y_{li}) = \nabla \cdot (\Gamma_{li} + \frac{\mu_t}{Sc_t}) \alpha_l \nabla Y_{li} + S_{li} \tag{19}$$

where, u_{Di} is the drift velocity of species i, and it is related to the slip velocity u_{Si} by equation 20.

$$u_{Di} = u_{Sig} - \sum_i u_{Sig} Y_{gi} \tag{20}$$

$$\sum Y_{li} = 1 \tag{21}$$

Lagrangian particle tracking of ore and coal

The velocities and trajectories of representative ore and coal particles are computed using the Lagrangian tracking approach, which involves solving the momentum equations based on Newton's second law (equations 22-24). Ore and coal particles are treated as separate phases. The interaction between the carrier fluid and particles has been treated using two-way coupling. The carrier fluid for particles can be the Eulerian gas phase or the Eulerian liquid bath phase, the appropriate phase being decided based on a critical volume fraction of these phases at the location of the particle. Particle drag switches from gas to liquid at this critical voidage. Equations 22-23 compute the particle displacement using forward Euler integration of particle velocity over the Lagrangian time-step. In forward integration, the particle velocity is calculated at the start of the time step and is assumed to prevail over the entire time step. At the end of the time step, the new particle velocity is computed using the particle momentum equation (equation 24). Momentum is transferred between fluid and particles only through the inter-phase forces (equation 24). In general these forces would be drag force, added mass force, pressure force, buoyancy force and Basset force. In this work, drag only has been considered, since it is the dominant force.

$$\frac{dx_i}{dt} = v_i \tag{22}$$

$$x_i^n = x_i^0 + v_{pi}^0 \partial t \tag{23}$$

$$\frac{d(m_p v_i)}{dt} = F_D \tag{24}$$

The effect of turbulent dispersion of particles and the particle-wall interaction has not been considered in the present model. The mass and momentum source transferred by the particles to the phase in contact (gas or bath) is determined by the reactions occurring (ore

4

reduction, coal devolatilisation and coal dissolution). The momentum sources arising from drag are computed as the particle source term for each particle as they are tracked through the flow. These particle sources are applied in the control volume in which the particle is located during the time step. These sources are then applied each time the fluid coefficients are calculated.

Interfacial mass and momentum exchange

The following phases interact during the simulations and exchange mass and momentum (as shown in Figure 2): The Eulerian-Lagrange pairs Gas/Coal (as CoalRawG), Bath/Coal (as CoalRawL), Gas/Ore (as OreG) and Bath/Ore (as OreL)), and the Eulerian-Eulerian phase pair Bath/Gas. A special treatment coded into CFX enables ore and coal particles to be transferred from one Eulerian fluid to another.

Regarding momentum transfer due to interfacial forces between these pairs, only the drag force is considered. The drag coefficient between the gas and liquid bath is computed using a user-defined drag function. For the ore–gas phase and ore-liquid phase interaction, the drag force coefficient is computed using the Schiller-Naumann drag model. For a coal particle that undergoes devolatilisation or dissolution, coal particle porosity is computed and used in a user-defined modified Schiller-Naumann. The mean particle diameter is used for computing drag for ore and coal particles.

Regarding mass transfer, the net mass source term in the continuity equation, equation 6, for a phase (S_r) and the corresponding momentum source term from this net mass transfer in the momentum equation, equation 7 (MS_r) arises from several reactions (ore and water reduction, coal dissolution and coal devolatilisation). Multiphase reactions have been defined for each of these Euler-Lagrange pairs. For the ore reduction reaction the reactants were the Lagrangian component 'Fe$_2$O$_3$' in ore and the Eulerian component 'Carbon' in the liquid bath phase and the products were the Eulerian components 'CO' in the gas phase and 'Fe' in the liquid metal bath phase. For the water reduction reaction, the reactants were the Lagrangian component 'H$_2$O' in ore and the Eulerian component 'Carbon' in liquid bath phase and the products were the Eulerian components 'CO' and 'H$_2$' in gas phase. The coal devolatilisation reaction involves the Lagrangian coal volatile component (C$_{vol}$) devolatilising to form Eulerian 'H$_2$' product in the gas phase. The coal dissolution reaction involves the Lagrangian coal fixed component (C$_f$) dissolving into the metallic bath to form the Eulerian component 'Carbon' in the liquid metal phase. Figure 2 shows these material transformations: the mass source term for the bath phase arises from liquid iron produced from ore reduction reaction, and carbon being dissolved in the bath through the coal dissolution reaction, while the sink term for the bath is the carbon being consumed in the ore reduction reaction. Figure 2 also shows that the source term for the gas phase arises from CO produced from the ore reduction reaction, and the gases (H$_2$, CO and N$_2$) produced from coal de-volatilisation.

The mass transferred is dependent upon the rate of reaction of these reactions as discussed in detail below:

Coal devolatilisation reaction

The volatile carbon component of coal undergoes devolatization while passing through both the bath and gas phase. A simplified coal devolatization reaction is represented as:

$$C_{vol} \rightarrow H_2 + CO + N_2 \tag{27}$$
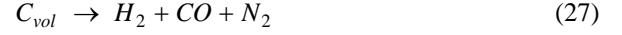
The main aim of including devolatilisation in the bath model is to allow for the generation of large volumes of volatiles gas within the bath (H$_2$, CO and N$_2$) and to approximately simulate the spatial distribution of this generation. Data from the literature have been used to give a simple representation of the way coal particles degas. A simplified linear fit to the Orsten and Oeters (1989) results, as illustrated in Figure 3, was implemented in the previous CFD model in PHOENICS (Schwarz, 1994). According to this approximate fit, no gas is generated during an initial "dead" time interval, t_d, and degassing is completed at time t_f. Values of these parameters interpolated from a diagram of Orsten and Oeters (1989) are given in Table 2 below.
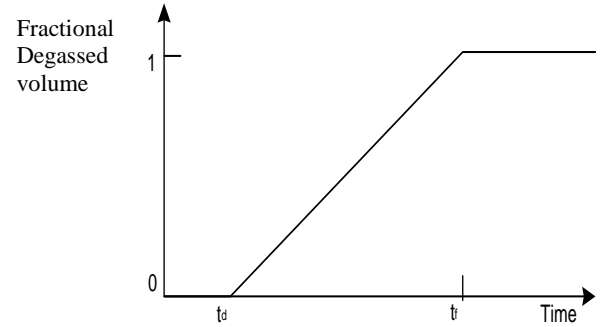
Figure 3: Simplified devolatilisation history used for coal particles in the bath.

While the PHOENICS model used single values for t_d and t_f, the CFX model allows for variable values depending on the particle size. This is achieved using a curve fit to the data in Table 2 allowing calculation of t_d and t_f from intermediate coal particle diameters. The respective equation for t_d and t_f are:

$$t_d = 8.95x10^{11}d^4 - 1.94x10^9 d^3 \\ - 1.75x10^6\ d^2 - 23.8d \tag{28}$$

$$t_d = 5.95x10^{11}d^4 - 1.71x10^9 d^3 \\ - 2.02x10^6\ d^2 - 79.0d \tag{29}$$

Table 2: Coal devolatilisation parameters (derived from Orsten and Oeters, 1989).

Particle diameter (mm)	t_d (s)	t_f (s)
0.1	0.016	0.027
0.2	0.048	0.083
0.4	0.170	0.260
0.6	0.310	0.480

0.8	0.470	0.720

Coal devolatilisation can occur when the particles are in either the gas or liquid phases. The mass fraction of volatile carbon resulting from the devolatilisation step can be used to calculate what the initial particle diameter for each track would have been and hence the values of t_d and t_f. This ensures a mass release from the particles similar to Figure 3. During devolatilisation, the particle diameter stays constant as the particle becomes more porous. While this could be treated using the swelling model already in CFX, such an approach would not allow the particle size to decrease during the dissolution reaction. The solution for this is to calculate the initial particle diameter on each track by using the volatile mass fraction and using this diameter in the drag law. Once devolatilisation is complete the particle diameter can then reduce on a mass basis. The rate of devolatilisation reaction for each track is computed as:

$$Rate = \frac{C_{Vol} V_p \rho_p}{t_f - t_d} \tag{30}$$

where V_p is the initial volume of the particle in the track. The rate of production of each component (CO, H_2 , N_2) is obtained by multiplying the rate with the mass coefficients of component. The mass coefficients are obtained based on the composition of the volatile gas.

Coal Dissolution

$$C_{(s)} \rightarrow C_{(l)} \tag{31}$$

This reaction can only occur between coal and liquid and it is assumed that this process only occurs after devolatilisation is complete. The carbon is allowed to dissolve into the metal. In reality, some of the coal will not contact metal, but will rather react in slag. The metal volume fraction was used in the PHOENICS model to weight the reaction rate. The equation for the mass dissolution rate in metal, R_{coal} , is:

$$\frac{dR_{coal}}{dt} = A_{p,coal}\rho_l h\left(C_{carbon,sat} - C_{carbon}\right)\phi_{metal} \tag{32}$$

where $A_{p,coal}$ is the coal particle interfacial area, ρ_l is the liquid density, h is the mass transfer coefficient for liquid side transport, $C_{carbon,sat}$ is the saturation carbon concentration in the bath, C_{carbon} is the carbon concentration in the vicinity of the particle and ϕ_{metal} is the metal mass fraction in the vicinity of the particle. The particles shrink as they dissolve, so the interfacial area is:

$$A_{p,coal} = \pi d_{p,coal}^2 \tag{33}$$

Incomplete wetting of the surface of the coal particle by the bath at a gas-liquid interface can be taken into account by the bath volume fraction but has been neglected in this work.

Ore Dissolution

$$Fe_2O_{3(s)} + 3C_{(l)} \rightarrow 2Fe_{(l)} + 3CO_{(g)} \tag{34}$$
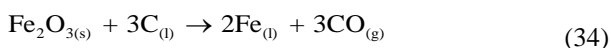
Here, we simplify by assuming that all the iron (Fe) produced reports to the metal phase. In reality, some

ore will melt as FeOx in slag. The equation for the mass reaction rate, R_{ore} is:

$$\frac{dR_{ore}}{dt} = A_{p,ore} \rho_l h S_i C_{carbon} \phi_{metal} \tag{35}$$

where, $A_{p,ore}$ is the ore particle interfacial area. S_i represents the stoichiometric coefficient for component *i*. The stochiometric coefficient of a component in equation 35 enables us to compute the rate of production/disappearance of components.

$$S_{Fe_2O_3} = \frac{160}{196}; S_C = \frac{36}{196}; S_{Fe} = \frac{112}{196}; S_{CO} = \frac{84}{196} \tag{36}$$

The particles shrink as they dissolve, so the interfacial area is:

$$A_{p,ore} = \pi d_{p,ore}^2 \tag{37}$$

The mass transfer coefficient, h, is estimated based on reported reaction rates measured for ore reduction, eg Nagasaka and Banya (1992). Table 3 below summarizes the discussions above.

Table 3: Reaction physics summary

Feed	Physics/ Reaction	Where?	Depends on
Coal	Devolatilisation	Bath and Gas	Time and particle diameter. Particle diameter remains constant.
	Dissolution	Bath (Metal)	Carbon concentration in the Bath. Liquid side mass transfer control. Particle diameter reduces.
Ore	Reduction	Metal	Carbon concentration in the bath. Liquid side mass transfer control. Particle diameter reduces.

SIMULATION PARAMETERS

The 2.7m diameter SRV for the large-scale HIsmelt pilot plant that operated at Kwinana for several years was simulated as a test-base for the upgraded model. The use of a symmetry boundary condition enables the simulation of only half the geometry (see Figure 4). The grid comprises a tetrahedral unstructured mesh with 0.42 million elements (0.08 million nodes), with a high density fine grid near the lance injection to account for high velocity gradients in this region. To account for near wall flow conditions, scalable wall function models have been used. Adaptive time stepping has been used to enable convergence in the least compute time, and a minimum time step of 8 x 10^{-4} s is applied. The highly

transient nature of the simulation involving splashing of liquid into the fountain affects the number of iterations required to ensure convergence at each time-step. Consequently, an adaptive time-step is needed to maintain convergence within 10 coefficient iterations. The convergence criterion has been set at 5×10^{-4} RMS value for momentum and volume-fraction equations. The bath model is simulated for 10 s and this takes around 4 days of computational time on a 4 processor parallel simulation. A high-resolution scheme has been selected as the discretization scheme for computing advection fluxes. The scheme ensures a solution as close to second order accuracy as possible while maintaining boundedness (Barth and Jesperson,1989). The temporal discretization uses a second order backward Euler scheme. The volume fraction equation is solved in a segregated way in the coupled CFX solver. The properties (such as density and dynamic viscosity) of all the components have been computed at the reactor temperature (1437ºC) and pressure (1.65 bar), and the simulation is run at isothermal conditions. For gaseous components, the ideal gas law is used to compute the density at the reactor temperature and pressure. A Rosin-Rammler particle size distribution was used for both coal and ore particles, with Rosin Rammler mean size for coal being 290 µm and for ore being around 1000 µm. These particles are injected uniformly from the lances at a rate proportional to their inlet mass flow rate. A limit of 80,000 particles per phase (ore and coal phase) has been enabled to avoid escalation in computational memory requirements.
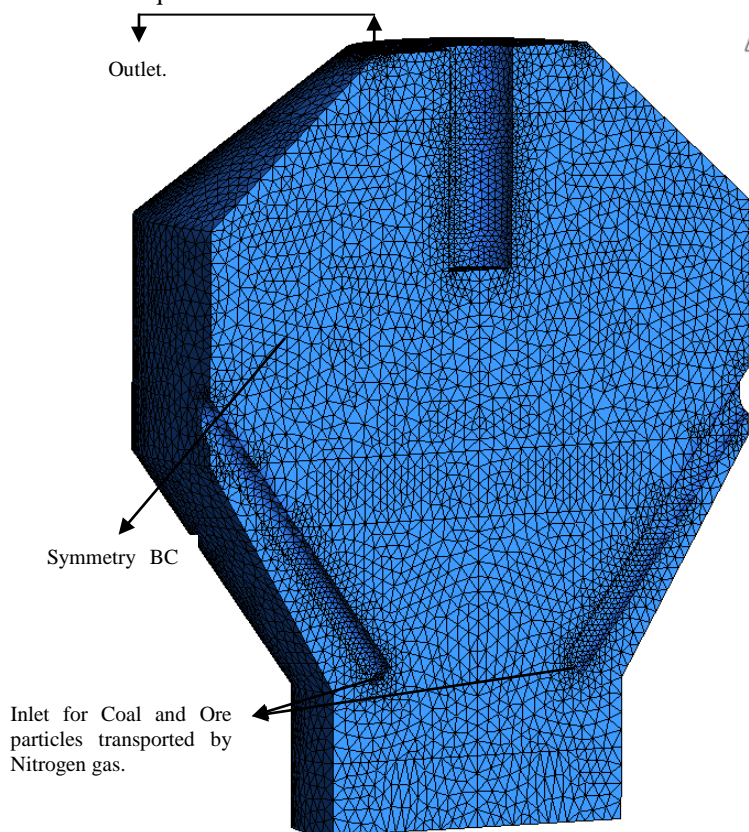
Figure 4 : The grid used in HIsmelt study.

RESULTS – CONVERGENCE STUDY

The purpose of this study was to identify which variables/complexities/coupling-effects were delaying convergence and fixing them so the model could be run with a larger time-step with convergence being achieved within ten coefficient iterations. To accomplish this, we reduced the complexity of the bath model step-by-step and also removed the coupling-effects and source-effects one-by-one to see which made a difference to the convergence. This was done in the following manner:

(a) Model run without particles and without reactions.
(b) Model run without any reactions.
(c) Model run without any particles.
(d) Model run with particles but without any source terms (ie no interphase coupling).
(e) Model run with particles but coupling limited to:
    Gas|Ore phase drag coupling only.
    Gas|Coal phase drag coupling only.
    Bath|Ore phase drag coupling only.
    Bath|Coal phase drag coupling only.
(f) Model run by removing reactions one-by-one:
    Run without the ore reduction reaction.
    Run without Coal devolatilisation reaction.
(g) Model run by increasing the number of particles by factor two, eight, twenty and forty.

It was observed that when the code is run without reactions but with particles turned on, the particle source term from Gas-Coal phase coupling was responsible for the delayed convergence. The increase in number of tracks by a factor of twenty improved the convergence significantly, and the solver was seen to be running with a larger time step. It could be said that the increase in particle tracking time has been outweighed by the improvement in particle source smoothness. However, as the reactions were put back on, the solver convergence slowed down, but this time, the delay in convergence arose from the mass fraction equations (especially, Fe and C). In order to check whether this was because of any specific reaction source term, the reactions were removed one by one. The removal of the ore-reduction reaction ensured that there was no Ore-Fe source terms, and the value of sources for Ore-CO and Ore-Carbon were very low, but this did not lead to a higher time step. Similarly, the removal of other reactions to eliminate the effect of other source-terms (from water-reduction and coal-devolatilisation) did not enable convergence to happen with a larger time step, but at the lower time step of 0.8 msec. It was observed that whenever splashing was occurring and the fountain was being created, the number of coefficient iterations required to reach convergence within a time-step increased. To enable the convergence within 10 coefficient iterations, the solver was lowering the time step. Thus, this exercise helped us to understand that the use of an optimal number of particles in the simulation can play a beneficial role in improving convergence, but the dynamics of the system are such that we will have to run it at a time step of 0.8 msec to achieve convergence within 10 iterations per time step. Nonetheless, the performance of this model was significantly faster than the earlier PHOENICS-based model, and can be used with an unstructured mesh as illustrated below.

MODEL APPLICATION

This model was then applied to study the 2.7m ID HIsmelt reactor. The simulation results from this model (Figures 5-7) highlight its ability to capture the flow dynamics, such as splashing and fountain generation.

(A)

(B)

(C)

(D)
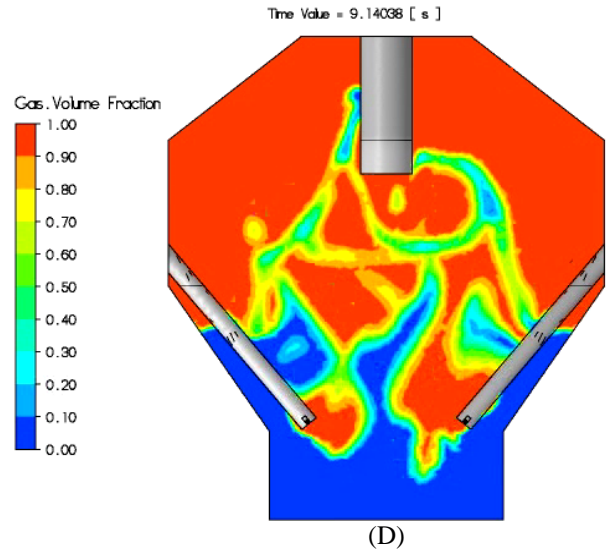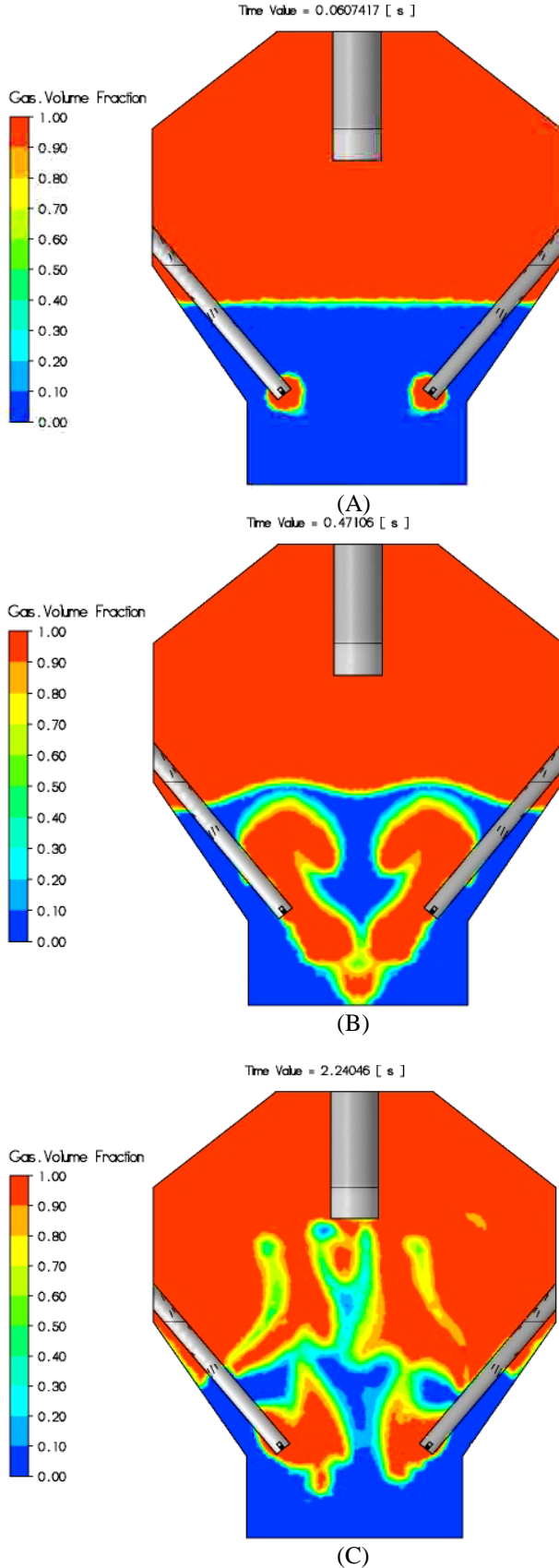
Figure 5 (A-D): Gas volume fraction contours and splashing of liquid at time (A) 0.06 s, (B) 0.47 s, (C) 2.24 s and (D) 9.14 s.

Figure 5 shows the contours of gas volume fraction at four different times. The amount of liquid bath volume fraction can be deduced from these figures by subtracting from unity. The figures show that the model is able to capture the splashing of liquid as a result of reactions and gas entrainment. It should be noted that slopping of the bath can be a major influence on bath dynamics over a longer time frame than simulated here (Schwarz, 1990). Figure 6 shows the typical trajectories of ore particles.
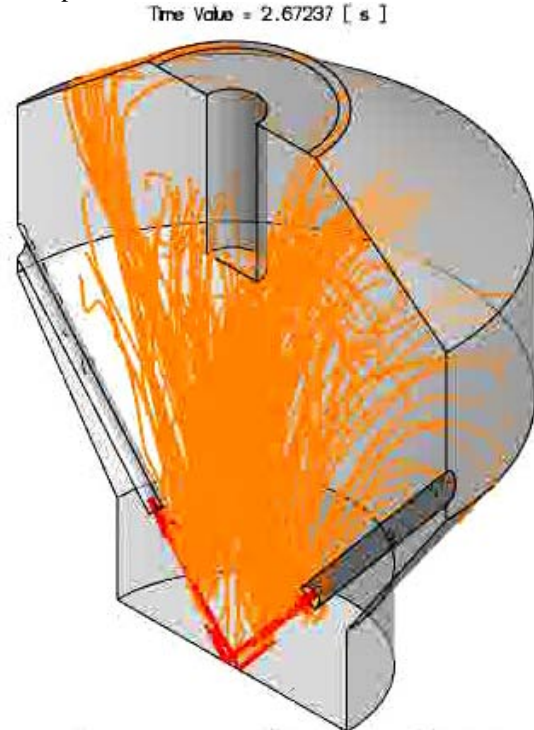
Figure 6: Typical computed trajectories of ore particles.

Figure 7 shows contours of mass-fraction of carbon monoxide produced as a result of ore reduction reaction at four different time steps. The CFX-based model has been able to capture the flow dynamics within the HIsmelt reactor in the same way as the PHOENICS model, but with more flexibility and greater numerical

accuracy. For example: the CFX model has been able to simulate for both unstructured as well as structured grid. Further, the CFX model offers flexibility in terms of enabling volume fraction equations to be solved in a coupled and segregated way. The coupled multigrid CFX solver provides linear scale-up for parallel processing. This model can be improved further by incorporating heat transfer effects.

(A)

(B)

(C)

(D)
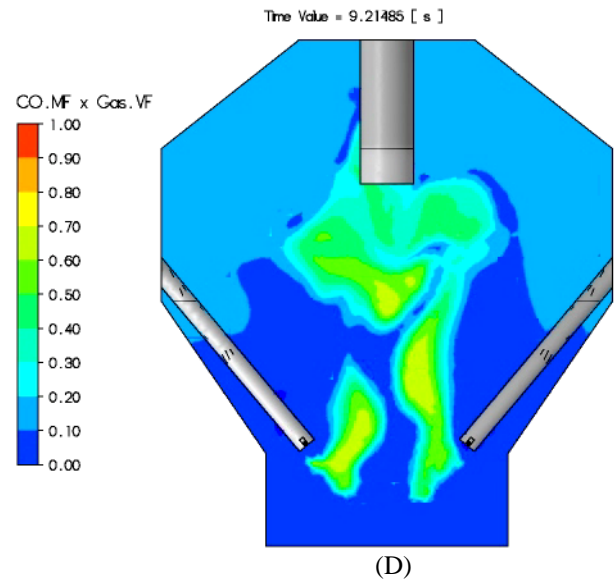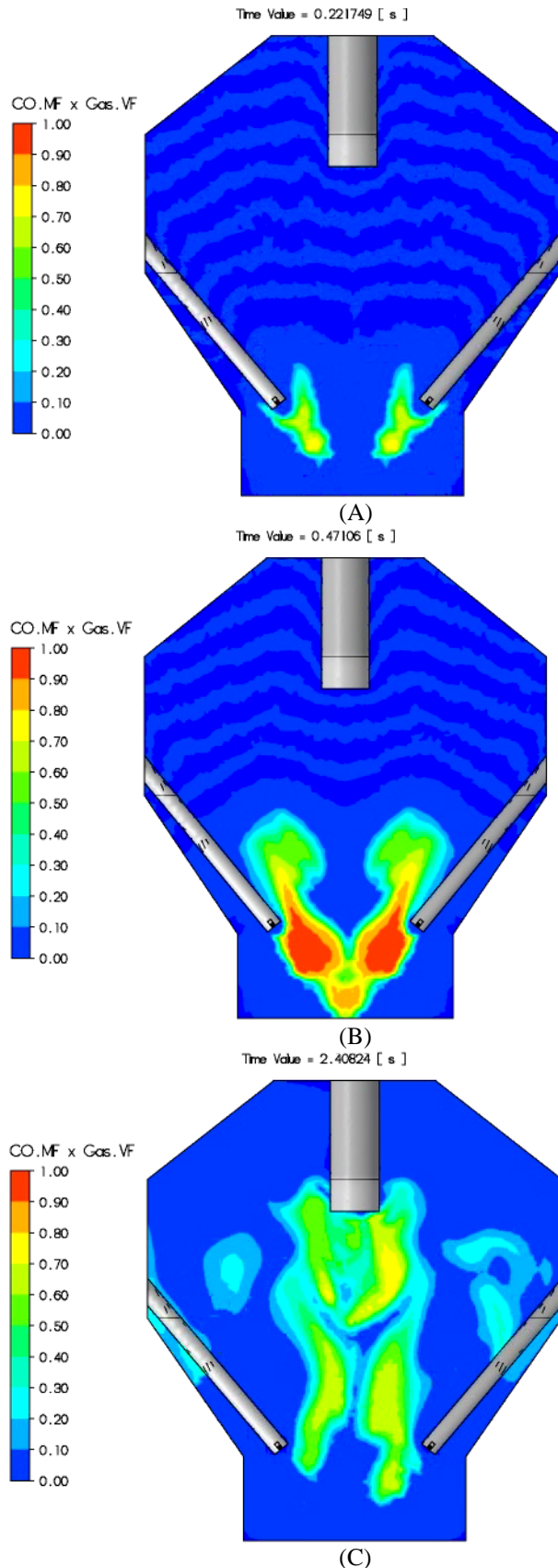
Figure 7 (A-D) shows the contour of Carbon-monoxide mass fraction produced at time (A) 0.22 s, (B) 0.47 s, (C) 2.4 s and (D) 9.2 s.

CONCLUSION

A complex three dimensional transient multiphase multi-component Eulerian-Eulerian reactive CFD model which incorporates Lagrangian tracking of ore/coal particles, the algebraic slip model and multiphase reactions (such as ore reduction, coal dissolution and coal devolatilisation) developed over several years and used to aid design and scale-up of the HIsmelt SRV (Schwarz, 2001) has been transferred from PHOENICS to ANSYS-CFX. The new model implementation is capable of capturing the flow dynamics within the HIsmelt reactor in the same way as the PHOENICS model. A convergence study has elucidated the effect of particle number on convergence, and also suggests how challenging it is to run such a model with a larger time step. The PHOENICS topspace model has been used to assist design of a commercial 6m ID reactor as well, and this model has also been transferred to the CFX platform.

ACKNOWLEDGEMENTS

REFERENCES

BARTH, T., AND JESPERSON, D., (1989), "The design and application of upwind schemes on unstructured Meshes", Technical Report AIAA-89-0366.

BATES, P. and COAD, A., (2000), "HIsmelt, The Future in Ironmaking Technology", *4th European Coke & Ironmaking Conference,* Vol. 2, June 2000, 597-602.

BATES, P. and GOLDSWORTHY, T., (2002), "HIsmelt - Meeting the Global Steel Industry Challenge", *1st Japan-Australia Symposium on Iron & Steelmaking, Fuwa-Ward Symposium, Kyoto.*

CROWE, C. T., SHARMA, M. P. and STOCK, D. E., (1977), "The Particle-Source-in-Cell (PSI-CELL) Model for Gas-Droplet Flows", *J. Fluids Eng.*, **99**, 325-332.

DAVIS, M., DRY, R., SCHWARZ, M. P., (2003), "The Role of CFD modelling in Development of the HIsmelt Process" , *ISS Tech, Proceedings of the Process Technology Conference of the Iron and Steel Society, Indianapolis.*

DAVIS, M., PERICLEOUS, K., CROSS, M., SCHWARZ, MP., (1998), "Mathematical Modelling Tools for the Optimization of Direct Smelting Processes", *Applied Mathematical Modelling,* **22** (11), 921-940.

GOODMAN, N., (2007), "Operations at the HIsmelt Kwinana Plant", *AIST Conference Indianapolis, Indiana.*

HARDIE, G.J., CROSS, M., BATTERHAM, R. J., DAVIS, M. P. and SCHWARZ, M. P., (1992), "The Role of Mathematical Modelling in the Development of the HIsmelt Process", *10th Process Technology Conference Proceedings*, ISS-AIME, 109-121.

NAGASAKA, T. and BANYA, S., (1992), "Rate of Reduction of Liquid Iron Oxide", *Tetsu-to-Hagane*, **78**, 1753-1767.

OETERS F., and ORSTEN S., (1989), "Degassing of coal particles injected into iron melts", *Steel Research*, **60**, 145-150.

SCHWARZ, M.P., (1990), "Sloshing waves formed in gas-agitated baths", *Chemical Engineering Science,* **45**(7) 1765-1777.

SCHWARZ, M.P., (1994), "The role of Computational Fluid Dynamics in process modeling", *Proc. of 6th AusIMM Extractive Metallurgy Conference*, pages 31-36. Aus.IMM, 1994.

SCHWARZ, M.P., (1996), "Simulation of Gas Injection into Liquid Melts", *Applied Mathematical Modelling*, **20**, 1996, 41-51.

SCHWARZ, M.P., (2001), "Computational Modelling of Metals Reduction Processes", *Computational Modelling of Materials, Minerals and Metals Processing*, M. Cross, J.W. Evans, and C. Bailey, eds., San Diego, USA, September 23-26, 2001, TMS (Warrandale), 23-40.

SCHWARZ, M.P. and DANG, P., (1995), "Simulation of blowthrough in smelting baths with bottom injection", *13th Process Technology Conference Proceedings*, Iron and Steel Society, 1995, 415-422.

SCHWARZ, M.P. and TAYLOR, I. F., (1998), "CFD and Physical Modelling of Slag-Metal Contacting in a Smelter", *4th World Conference on Applied Fluid Mechanics*, Freiburg, Germany: WUA-CFD, 4:1-4:15.

SCHWARZ, M.P. and TAYLOR, I. F., (2000), "Mathematical Modelling of Injection Processes", *The Brimacombe Memorial Symposium*, Vancouver, Oct 1-4, 2000, Can Instit Mining, Metallurgy and Petroleum (Montreal).

8th International Conference on CFD in Oil & Gas, Metallurgical and Process Industries
SINTEF/NTNU, Trondheim NORWAY
21-23 June 2011

CFD11-177

EFFECT OF SIO COMBUSTION ON NO$_X$ EMISSION: THEORY AND VALIDATION

Balram PANJWANI[1]*, **Stefan ANDERSSON**[1], **Helge MIDTDAL**[1]

[1]SINTEF Materials and Chemistry, P.O. Box 4760, 7465 Trondheim, NORWAY

* E-mail: balram.panjwani@sintef.no

ABSTRACT

CO and SiO that are emitted from the charge of a silicon furnace burn in contact with air producing CO_2 and SiO_2. The combustion of SiO is very fast and increases local temperature, and the concentrations of radicals and atoms. NO$_x$ emission is one of the major concerns for the metal industry due to strict government regulations because of its impact on the environment. Formation of NO$_x$ strongly depends on the local temperature and the concentrations of atoms and radicals. Little is understood of the role of the SiO combustion mechanism on NO$_x$ formation. In the Present paper the effect of SiO_2 formation on NO$_x$ production is studied. Since there is little available experimental data on reactions of SiO to form SiO_2, a SiO mechanism based on molecular simulations is proposed. In the Present study two SiO mechanisms, one available from literature and another based on molecular simulations, are studied and compared. Performing CFD simulations for a complex 3D industrial furnace is computationally demanding. In the present study microlevel one grid Perfectly Stirred Reactors (PSR) calculations are carried out to establish the effect of SiO combustion on NO$_x$ formation. Furthermore, a validation test is carried out for a 3D combustor where the effect of addition of SiO on NO$_x$ production is established. The study showed that considering only gas phase SiO_2 reduced the local temperature and subsequently the NO$_x$ level, while, more realistically, accounting for the formation of SiO_2 in the solid phase generated exothermic heat thus giving very high local temperatures and subsequently higher NO$_x$ production.

Keywords: CFD, chemical reactors, NOx, PSR, Flamelet.

NOMENCLATURE

Greek Symbols
ρ Mass density, $[kg/m^3]$
ω Source term, $[1/s]$

Latin Symbols
A Arrhenius Reaction Constant, $[cm^3mol/s]$.
E Activation Energy, $[cal/mol]$.
T Temperature, $[K]$.
R Universal Gas Constant, $[J/kg-mol/K]$.
Y Species Mass Fraction, $[-]$.
t Time, $[s]$.
P Pressure, $[Pa]$.
h Enthalpy, $[J/kg]$.

Sub/superscripts
i Species i.

INTRODUCTION

In silicon furnaces CO and SiO gases, emitted from the reaction crater, burn in contact with air that is sucked in through openings in the side doors of the furnace. Combustion of these gases takes place at very high temperatures and produces soot, dioxins, CO_2, NO$_x$ etc. The increase in peak temperature is extreme when blowing of SiO through the charge occurs (Bugge *et al.*, 2008). The flow inside the furnace is very complex involving intense turbulent mechanisms. Formation of NO$_x$ strongly depends on the instantaneous temperature and therefore on turbulence. Solving unsteady turbulent flows is a challenging problem due to the wide range of length and time scales. A fine grid and high order spatial and temporal discretization schemes are desirable for resolving all the length and time scales. Direct numerical simulation (DNS) resolves all the length and time scales. DNS resolves the whole turbulence energy spectrum on the grid scales and does not require modeling. DNS is the most accurate methodology for understanding the physics of unsteady turbulent flows. However, DNS is computationally demanding and limited to simple academic problems. The other approach, called Large Eddy Simulation (LES) resolves the major portion of the turbulence energy spectrum, and is a promising tool for understanding the physics of unsteady turbulent flow at comparatively lower costs. In LES, the large geometrically dependent, energy-carrying eddies are resolved on grid scales, whereas the dynamics of the smaller, more universal scales are modeled using a subgrid scale (SGS) model. However, due to computational constraints DNS and LES are mostly limited to simpler problems. Until now, most of the industrial problems are solved using Reynolds Averaging Technique. In RANS the governing equations are either time averaged or ensemble averaged and turbulence is modeled using a closure model. There are many turbulence closure models and their application depends on the case and the boundary conditions (Wilcox, 1993). Modeling combustion is a challenging task because of its interaction with turbulence. Combustion takes place on dissipative scales (close to Kolmogorov scales) where a reaction between fuel and oxidizer is modeled through the Arrhenius rate law. The Arrhenius rate law depends on the instantaneous temperatures. However, in RANS only mean values are estimated and turbulence is modeled. Therefore closure of the Arrhenius rate law is a challenging task in turbulent flows. In order to solve the turbulence-chemistry interaction problem a closure is required, which is referred to as combustion modeling. Depending on the type of flows, com-

bustion models are divided into three categories: premixed, non-premixed and partially premixed.

Combustion of fuel in the presence of O_2/N_2 leads to the formation of NO_x, especially at high temperatures. NO_x emissions contribute to air pollution, the formation of fine particles and ozone smog, and NO_x also causes acid rain, which reduces the pH of surface water, thereby degrading water quality and harming fish. Thus, a fundamental understanding of the emission of hazardous species such as NO_x during combustion is essential. To develop a low NO_x burner, a better understanding of the interactions between turbulence and chemistry is necessary. NO_x formation in turbulent flames is a complex process that requires accurate modeling of both the chemistry and the turbulence.

Combustion of SiO leads to the formation of SiO_2 particles, which results in substantial heat release. Formation of NO_x depends on the temperature as well as on the concentrations of radicals such as OH and the atoms O, H and N. Therefore, it is very important to estimate the amount of heat and radical generation during the combustion of CO and SiO. The chemical mechanism of CO combustion with and without water is well understood, but the corresponding mechanism of SiO combustion is still unclear. Although SiO combustion has been studied previously (Chagger *et al.*, 1996; Koda and Fujiwara, 1988), these mechanisms were never validated experimentally and furthermore there is no well established theoretical background behind these mechanisms. In the present study a SiO mechanism based on molecular simulations is proposed. In the present paper two steps are assumed for formation of SiO_2. The first step is conversion of gas phase SiO to gas phase SiO_2, which is endothermic, and the second step is conversion of gas phase SiO_2 to condensed phase SiO_2, which is exothermic. In the present study, SiO_2 in the condensed phase is approximated as a gas phase molecule where the heat of formation of the gas-solid phase change is accounted for by adjusting the thermodynamic properties of SiO_2 to those of the condensed phase.

MICRO SCALE MODELING: REACTOR STUDIES

A first step in numerical modeling of any reactive flow is grid generation for the complex domain. Then Navier-Stokes (N-S) equations along with transport equations are solved on each grid cells as shown in Figure 1. In reactive flows, combustion-turbulence interaction is performed through a model such as flamelet, Eddy Dissipation Concept (EDC) etc. The EDC model is quite popular for industrial furnace modeling. In EDC, transport equations for species are solved and reaction kinetics is accounted for with Perfectly Stirred Reactors (PSR) (Magnussen, 1981). Performing PSR calculation at each cell throughout the flow domain (millions of cells) is quite computationally demanding. Since in the EDC model, all the information about kinetics is modeled through PSR, it is possible to study the effect of the SiO mechanism with a stand alone PSR. In the present study a PSR calculation of a single cell as shown in Figure 2 is carried out. Figure 2 shows the homogeneous Perfectly Stirred Reactors (PSR), which is interacting with a control volume (CV). A perfectly stirred reactor is an ideal reactor where perfect mixing occurs. While implementing EDC model for turbulent flows, the product mass fraction Y_i^* is estimated at each computational cell from the reactant mass fractions and reactor residence time, τ^*. The τ^* is calculated from the turbulence models and it is a parameter for the problem. Initially small values of residence time is chosen to allow combustion for a

given equivalence ratio. On further decreasing the residence time, the system of equations has no solution. This gives the blowout limit, which indicates that there is not enough time for the reaction to occur within the reactor. Since blowout was not the major concern for the present study a complete mixing between fuel and oxidizer is assumed and the reactor is considered as a closed PSR as shown in Figure 3. The following system of equations, one for each species, are solved to estimate the final species mass fractions.
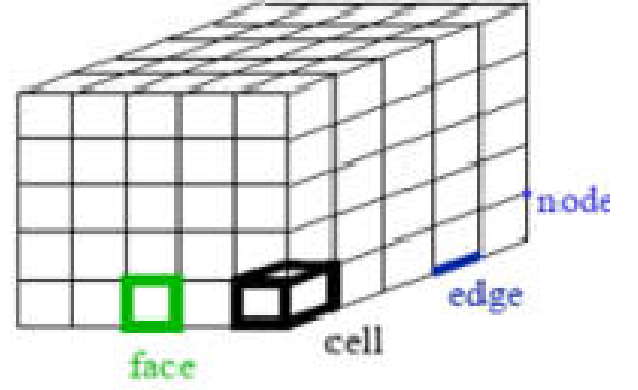

Figure 1: A Typical Grid Used for the CFD study

$$\frac{dh}{dt} = 0 \tag{1}$$

$$\frac{dp}{dt} = 0 \tag{2}$$

$$\frac{dY_i}{dt} = \omega_i \tag{3}$$

where ω_i is evaluated from a chemical mechanism. Accordingly, in PSR a set of ODEs needs to be integrated to the steady state or the reactor residence time. The mechanisms used in the stand alone PSR study consists of a CO-H_2 mechanism of M. C. Drake and R. J. Blint (Drake and Blint, 1989) either combined with the SiO mechanism given in table 1, hereafter referred to as 'SiO-1' or the SiO mechanism given in table 2, hereafter referred to as 'SiO-2'. The SiO-1 mechanism (Andersson, 2011) is based on the molecular simulation studies and SiO-2 was taken from the available literature data (Chagger *et al.*, 1996; Koda and Fujiwara, 1988). Furthermore, the mechanisms also consist of three routes of NO_x formation (1) thermal, (2) prompt and (3) N_2O. In order to perform a comparison between these mechanisms, the PSR calculations were performed with a well tested numerical reactor code (Lilleberg *et al.*, 2009). The ODE-integrator RADAU5 (Hairer and Wanner, 1996) was used to integrate Equations (1), (2) and (3).

Table 1: SiO combustion mechanism SiO-1:Proposed

reaction	A	β	E_a
$SiO + O_2 \rightarrow SiO_2(g) + O$	$2 \cdot 31 \times 10^{13}$	0	$26 \cdot 0 \times 10^3$
$SiO + OH \rightarrow SiO_2(g) + H$	$1 \cdot 8 \times 10^{10}$	0.78	$1 \cdot 218 \times 10^3$

REACTION RATE CALCULATIONS

Two reactions for forming SiO_2 were considered for creating the data in Table 1 (mechanism SiO-1): $SiO + O_2 \rightarrow SiO_2 +$
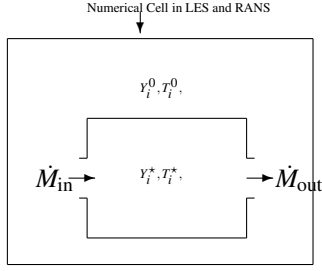
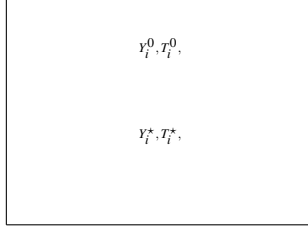Figure 2: Fine-structure interaction with surroundings

Figure 3: Close Reactor Modeling

Table 2: SiO combustion Mechanism SiO-2 (Chagger *et al.*, 1996)

reaction	A	β	E_a
SiO + O$_2$ → SiO$_2$(g) + O	1·0x10^{13}	0	6·5x10^3
SiO + OH → SiO$_2$(g) + H	4·0x10^{12}	0	5·7x10^3
SiO + O +M → SiO$_2$(g) + M	2·5x10^{18}	0	4·3x10^3

Table 3: SiO$_2$ gas to SiO$_2$solid phase: Assumed

reaction	A	β	E_a
SiO$_2$(g) → SiO$_2$(s)	2·0x10^{13}	0	1·0x10^3

concentration of the O radical, decreasing the formation of thermal NO and N$_2$O, while the larger concentration of OH decreases the amount of NO formed through the Fenimore mechanism. PSR calculations with an initial temperature of 1600 K with fuel composition of CO/SiO/H$_2$O were carried out. As an oxidizer O$_2$ was used. Figure 4 shows the effect of H$_2$O on temperature and NO$_x$ at different equivalence ratio for 5% 10% and 15% of water. The equivalence ratio of a system is defined as the ratio of the fuel-to-oxidizer ratio to the stoichiometric fuel-to-oxidizer ratio: $\phi = \frac{\text{fuel-to-oxidizer ratio}}{\text{(fuel-to-oxidizer ratio)}_{st}}$. It is observed that by increasing the water content temperature is decreasing. It is also observed that NO$_x$ increases up to an equivalence ratio of 5 and thereafter it decreases. We also studied the effect of solid phase SiO$_2$ and gas phase SiO$_2$ combustion. However, we did not study the mechanism behind the SiO$_2$ particle formation. We only accounted for the heat formation effect from gas phase SiO$_2$ to SiO$_2$ particle formation. Figure 5 shows the effect of increasing the amount of SiO which is converted into gas phase SiO$_2$. The conversion from SiO to SiO$_2$ gas is an endothermic reaction. It is observed that increasing the amount of SiO decreases the temperature and NO$_x$ concentration. Figure 6 shows the H atoms and OH radicals for different SiO mass fraction. It is observed that the H atoms and OH radicals are decreasing with increase in SiO mass fraction. Since in the present study the SiO mechanism is studied with the detailed CO mechanism the effect of independent SiO mechanism is difficult to identify except the heat of formation.

The SiO species is a relatively stable entity that reacts with O, OH or O$_2$ to form SiO$_2$ in the gas phase. The formed SiO$_2$ then condenses to produce liquid droplets, and it has been proposed that the molten oxide droplets grow by Brownian collision (Chagger *et al.*, 1996). Effect of SiO$_2$ particle formation have been studied experimentally and numerically. Chagger et al. (Chagger *et al.*, 1996) studied the CH$_4$-N$_2$ air diffusion flame with and without SiO$_2$ where they use the HMDS precursor. The color of the flame was blue with a pale-yellow zone on the rich side without HMDS, the color was changed to the whitish pink and became more luminous with addition of HMDS. On increasing the HMDS the flame was orange in color in fuel side and a stronger blue emission was observed on the lean side. This process is accompanied by the release of large amounts of heat. For example, the reaction SiO$_2$(g) → SiO$_2$(s) liberates about 180 kcal/mol at 2000 K (Schick, 1960). At the same time, large amounts of heat may be lost via radiative heat transfer from the particle surface. If so, the surrounding gas might not be heated up to the values estimated by the above adiabatic temperature calculation. However, these effects are not accounted for in the present study. In the present study the effect of SiO$_2$ particle

O and SiO + OH → SiO$_2$ + H. The rates of these reactions have not been studied experimentally and we therefore decided to use calculated data from molecular simulations. The rate coefficients for the SiO + OH reaction were taken from a previous theoretical study (Zachariah and Tsang, 1995). Due to the lack of reliable data on the SiO + O$_2$ reaction we calculated the rate coefficients using molecular simulation techniques (Andersson, 2011) in the temperature range 300 - 3000 K. These rate coefficients were then fitted to an Arrhenius expression for ease of inclusion in the CFD modeling. The methods used for calculating the rate coefficients were a combination of quantum chemical electronic structure calculations with molecular geometry optimization using the Gaussian 09 program package (Frisch *et al.*, 2009) and Transition State Theory (Steinfeld *et al.*, 1989) rate calculations where the rate coefficients are calculated using data on reaction barrier height and molecular vibrational and rotational energy levels. All the needed data can be calculated using quantum chemistry methods and the only concern is to choose a method that gives sufficient accuracy for the application in question. We chose to use Density Functional Theory with the M06-2X density functional (Zhao and Truhlar, 2008) since this has been shown to give very good to excellent results for calculating reaction barrier heights and at the same time be computationally affordable.

RESULTS AND DISCUSSION ON PSR CALCULATION

Oxidation of CO in the presence of water occurs faster than oxidation in dry conditions. Therefore addition of small amounts of water can produce better combustion efficiency in a furnace. In silicon furnaces, water is also emitted from the crater of the furnace along with CO and SiO. On the other hand, the presence of water can reduce the final temperatures, leading to lower thermodynamic efficiencies and can, also, affect ignition conditions, blowout characteristics and the mechanisms of pollutant formation (Costa *et al.*, 2003). Bhargava et al. (Bhargava *et al.*, 2000) compared experimental results (obtained by injecting humid air in aeronautical turbines) with a series of perfectly stirred reactors calculations. They concluded that water vapor presence reduces the

formation is taken into account through the heat of formation of the gas-solid phase change. The reaction kinetics (phase change:$SiO_2(g) \rightarrow SiO_2(s)$) is assumed very fast as given in table 3. Figure 7 shows the effect of increasing SiO, which was converted into solid phase SiO_2. It is observed from the Figure 7 that the temperature and NO_x is increasing with increasing SiO mass fraction. However, in gas phase SiO_2 this trend was opposite as shown in Figure 5. A comparison between the mechanism SiO-1 and SiO-2 is shown in Figure 8 for temperature and NO_x at 15% of SiO. The difference between these two mechanisms can hardly be seen. The reason for this behavior is that in this study the mechanism is a combined mechanism of CO and SiO, where CO combustion is the dominating mechanism. Furthermore, SiO combustion is faster than CO combustion, which means that all the SiO is converted into SiO_2 immediately. Therefore, the heat of formation is the same for both reactions. Moreover, the combustion kinetics of SiO also depends on the reaction time but in the present study the PSR equations were integrated to the steady state. Due to lack of time dependent data of SiO combustion (ignition delay etc) it is difficult to compare the SiO-1 and SiO-2 mechanism, further experimental and numerical tests are required to validate the SiO mechanism.

VALIDATION

The previous section discussed the two SiO mechanisms and it seems that both mechanisms give similar results. We prefer the proposed SiO mechanism 1 for further studies. To further established the effect of SiO_2 formation in practical geometries, a CFD simulation of a 3D model was carried out, for which experimental data were available. The experiment was
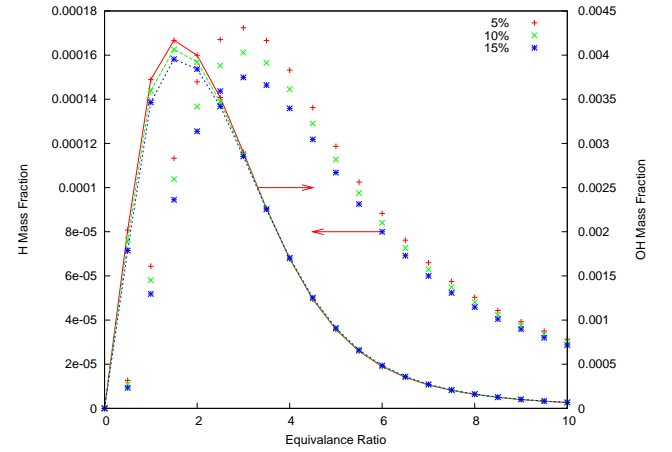

Figure 6: Effect of $SiO_2(g)$ on the H and OH(5% of H_2O and CO=(0.95-SiO))
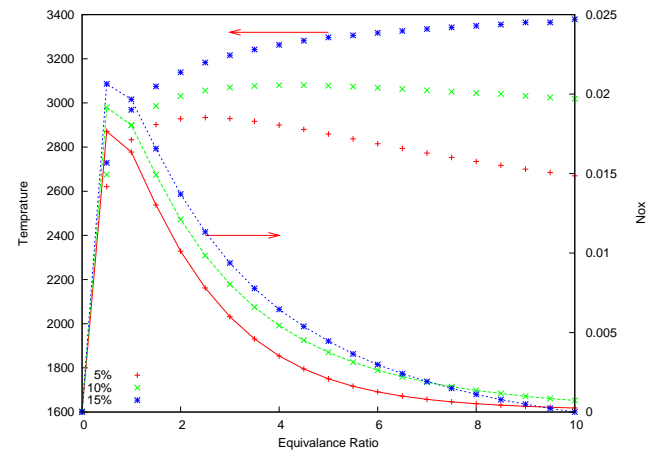

Figure 4: Effect of H_2O on Temperature and NO_x (5% of SiO and CO=(0.95-H_2O))

Figure 7: Effect of $SiO_2(s)$ on the Temperature and NO_x, the solid phase is exothermic(5% of H_2O and CO=(0.95-SiO))

Figure 5: Effect of $SiO_2(g)$ on the Temperature and NO_x, the gas phase is endothermic(5% of H_2O and CO=(0.95-SiO))

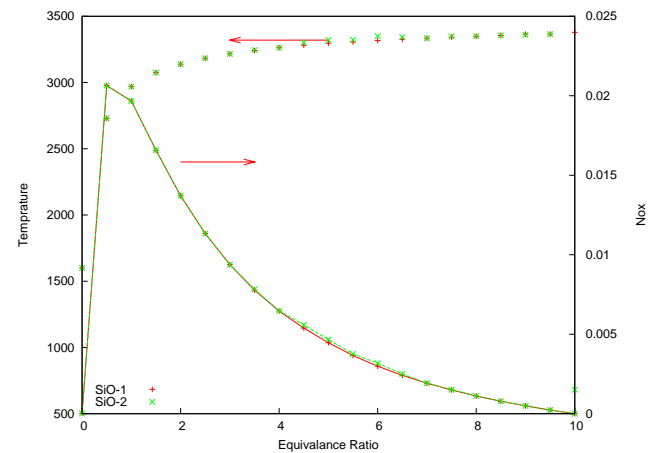

Figure 8: Comparison of SiO-1 and SiO-2 mechanism(5% of H_2O and CO=(0.95-SiO))

performed by Jurgen et al.(LOUIS *et al.*, 2001) in a 16kW cooled combustor facility. In this experiment, special emphasis was placed on the NO$_x$ estimation. Figure 9 shows the schematic of the combustor. The fuel comes from the central core(diameter 24 mm), and the air through an annular pipe. The flow is mixed and stabilized by a bluff body right after the fuel and air enter the reactor. The gas used was a syngas mixture with CO 40%, H$_2$ 40%, N$_2$ 20%. The calorific value of the fuel was 11.9 MJ/kg when burnt together with air. The gas is comparable to a pyrolysis gas, and is therefore relevant for our study. Measurements of CO, CO$_2$, O$_2$, and NO were taken with a suction probe at several locations in the combustion chamber. Although accuracy is somewhat degraded by uncertainty in positioning, quenching by the probe, and the cooling procedure, the measurements are considered to give a good representation of the actual values. The model has been studied numerically by Jurgen et al.(LOUIS *et al.*, 2001). However, they used a quite sophisticated combustion model based on the progress variable approach. Since the main purpose of this study is to establish the effects of SiO addition on NO$_x$, a simple combustion model ❝Flamelet❞ was used in the study.
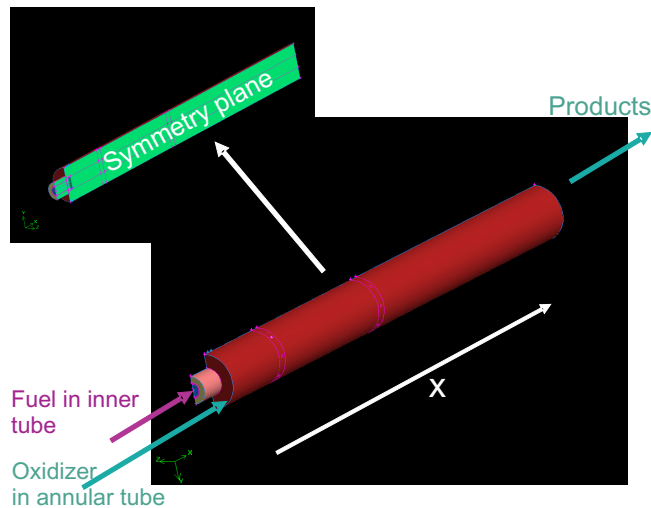

Figure 9: Schematic diagram of geometry.

CFD MODEL

The model was split at a vertical symmetry plane. Axis symmetric conditions were prohibited by gravity generated buoyancy effects. Velocity inflow boundary condition was used at fuel and air inlet. The fuel velocity was 4.13 m/s at temperature 303 K and the air velocity was 2.88 m/s at temperature 303 K. A mesh as shown in Figure 10 and 11 consisting of 240000 cells was generated taking into consideration the effect of boundary layers by decreasing the cell size toward the walls. The grid in the central core of the reactor was refined in order to capture the main gradients in the strong mixing/combustion region. Once the simulation was converged for the coarse mesh, then mesh was refined based on the gradient of mixture fraction. The CFD study was carried out using the Commercial CFD code Fluent V 12.1. (Fluent, 2009). Fluent has RANS and LES module for turbulent flows. In present study RANS was used. Flow inside the combustor involves very complex phenomena mostly dominated by the unsteadiness, which cannot be estimated with the steady RANS. However the main purpose of the study is to understand the effect of SiO mechanism on NO$_x$, therefore RANS was chosen for present study. It

is well known that the RANS turbulence modeling is flow and geometry dependent, which means that understating the effect of different turbulence models is very important. The effect of different turbulence models for this geometry has been studied by Simonsen (Simonsen, 2001). He concluded that with respect to NO$_x$ prediction the realizable $k - \varepsilon$ performed better than other turbulence closure models. In this study the realizable $k - \varepsilon$ turbulence model was used.
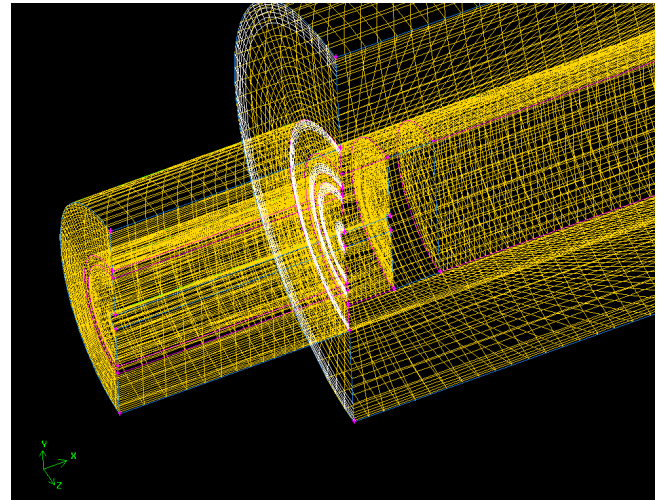

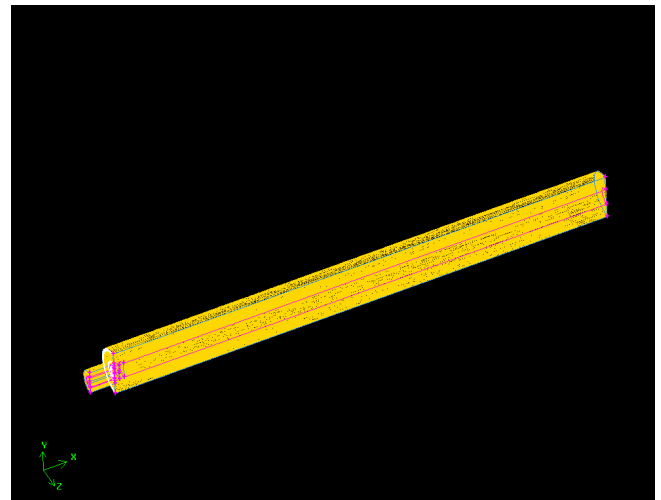Figure 10: Grid used for the study:Enlarged View

Figure 11: Grid used for the study.

The flamelet approach is an attractive method for modeling turbulent flames due to the low computational cost. In the flamelet approach, the chemistry is decoupled from the mean flow. Although the flamelet approach is widely accepted for the prediction of major species and global temperatures, the applicability of the flamelet approach for pollutants such as NO$_x$ prediction is questionable (Bilger, 1989). A detailed investigation was carried out by Vranos et al. (Vranos *et al.*, 1992), who studied the formation of NO$_x$ and differential diffusion in a turbulent CH$_4$/H$_2$ diffusion flame and obtained large discrepancies between the predicted results and the actual NO$_x$ levels. Thus, the authors concluded that transient behavior and flamelet interactions had a significant effect on the formation of NO$_x$. Moreover, they speculated that deviations from the experimental data were attributed to premixing and homogeneous reaction effects, transients phenomena, and flamelet interactions. In the aforementioned

study, the effects of radiation heat loss were insignificant due to the relatively low flame height. However, under other circumstances, the effects of radiative heat losses during NO_x formation are important. For instance, Chen and Chang (Chen and Chang, 1996) applied a joint scalar probability density function (PDF) approach and performed tradi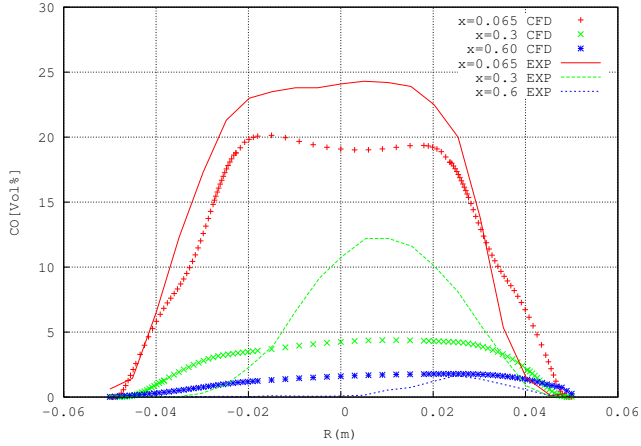tional flamelet modeling of NO_x formation in a turbulent, non-premixed jet flame. The importance of various effects such as transient phenomena, flame interactions, differential diffusion and radiative heat loss during NO_x formation were evaluated. The results suggested that radiative heat loss had a significant effect on NO_x levels in the far field. When radiative heat losses were considered, the predicted values were reduced by a factor of 3, and the fit of the model to the experimental data was improved. Alternatively, differential diffusion had a minor effect on the overestimation of NO_x levels, which is similar to the results of Vranos et al. (Vranos *et al.*, 1992). Lee and Choi (Lee and Choi, 2009) showed that the inclusion of radiation caused a reduction in the temperature, which improved the NO_x prediction to the experimental data. In this study also radiation was included using the Discrete Ordinates Method. As mentioned the flamelet model is inappropriate for NO_x, because it tends to overpredict the NO_x level. Simonsen (Simonsen, 2001) performed NO_x studies using Post-Processing Mixture fraction approach and unsteady non-equilibrium flamelets. In the present study the unsteady non-equilibrium flamelets approach is used for the NO_x modeling.

RESULTS AND DISCUSSION

In total three simulations were carried out. The case-1 refers to the standard simulation where Syngas ($CO/H_2/N_2$) was

Figure 12: Predicated CO volume fraction compared with experiments at different axial locations
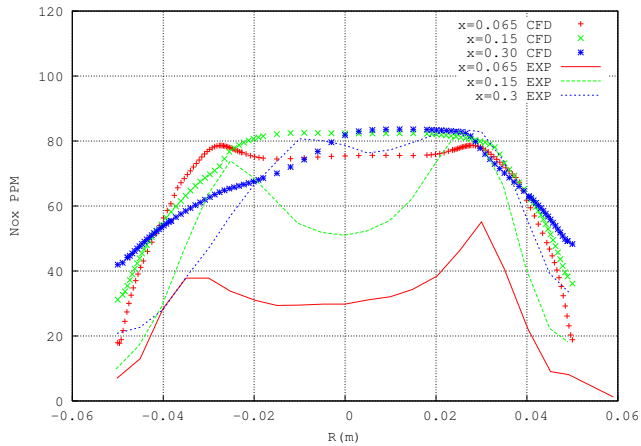
Figure 13: Predicated NO_x PPM compared with experiments at different axial locations

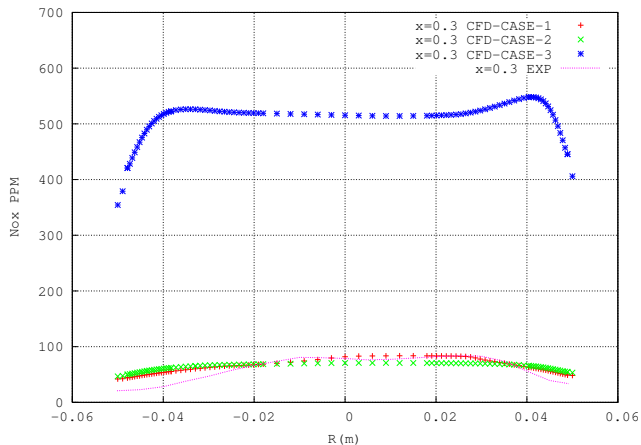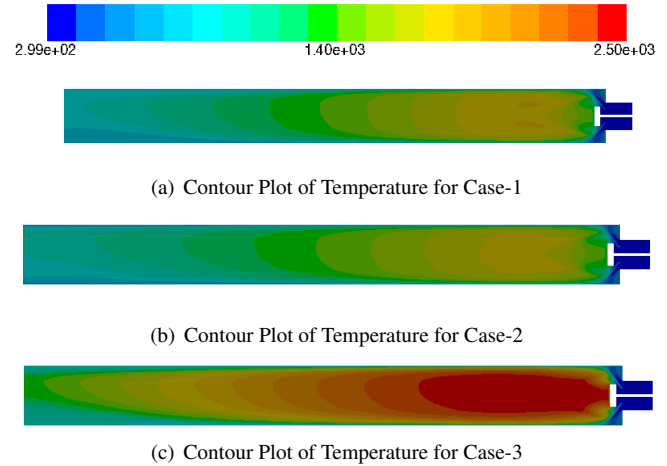Figure 14: Predicated NO_x PPM for three cases compared with experiments

(a) Contour Plot of Temperature for Case-1

(b) Contour Plot of Temperature for Case-2

(c) Contour Plot of Temperature for Case-3

Figure 15: Contour Plot of Temperature in Kelvin

(a) Contour Plot of NO_x in PPM for Case-1

(b) Contour Plot of NO_x in PPM for Case-2
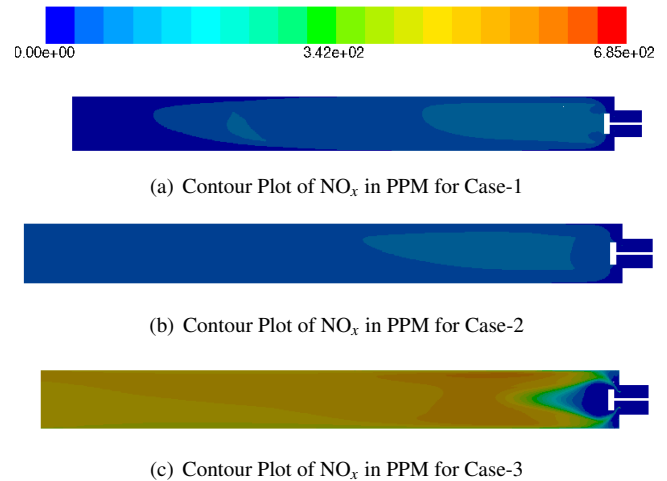

(c) Contour Plot of NO_x in PPM for Case-3

Figure 16: Contour Plot of NO_x in PPM

used at the fuel inlet. Two more simulation with modified fuel composition at the fuel inlet were carried out. A fuel composition of CO 40%, H$_2$ 20%, N$_2$ 20% and SiO 20% was used. Case-2 refers to the condition where SiO gas was converted into the gas phase SiO$_2$. Case-3 is similar to the case-2, except in this case gas phase SiO$_2$ was converted into the solid phase. The results for the case-1 is compared with the experimental data. Figure 12 shows the volume fraction of computed CO compared with the experiments. At x=0.065m CO is slightly under predicted, at x=0.3m CFD does not predict the peak. This is because the present calculations are based on standard flamelet model. A combustion model based on the progress variable approach might improve the results. Figure 13 shows the computed NO$_x$ PPM compared with the experiments. CFD overpredicts the NO$_x$ levels at x=0.065m and x=0.15m, but the NO$_x$ predictions are satisfactory at x=0.3m. Figure 14 shows the comparison of the NO$_x$ levels at x=0.3m for the case-1, case-2 and case-3. The NO$_x$ levels for case-3 are one order of magnitude higher than the case-1. This is because of a large increase in temperature for case-3. Figures 15(a) and 16(a) show the temperature and NO$_x$ PPM contour plot at the symmetry plane for case-1. The maximum temperature around 1900 K occurs close to the flame holder, where fuel and oxidizer are mixed. Figures 15(b) and 16(b) show the temperature and NO$_x$ PPM contour plot at the symmetry plane for case-2. Figures 15(c) and 16(c) show the temperature and NO$_x$ PPM contour plot at the symmetry plane for case-3. The maximum temperature for case-2 was 1780 K and for case-3 was 2650 K.

CONCLUSION

CFD studies were carried out with special emphasis on the NO$_x$ formation. In large industrial furnaces performing detailed CFD simulation is a time consuming process. Then parametric studies is not possible due to computational constraints. Therefore, stand alone one grid PSR calculation were carried out to understand the effect of two SiO mechanisms. A new SiO mechanism based on molecular simulations is proposed. The present study showed that considering SiO gas phase reaction is endothermic, which reduces local temperature and subsequently NO$_x$. However, considering subsequent SiO$_2$ conversion into the solid phase releases large amount of heat, which results in large increase in local temperature and subsequently NO$_x$. The PSR results were applied to the 3D combustor with complex flows, which showed a clear effect of SiO$_2$ on NO$_x$ and local temperature. The NO$_x$ levels were increased with inclusion of the solid phase SiO$_2$.

REFERENCES

ANDERSSON, S. (2011). *to be published.*

BHARGAVA, A. *et al.* (2000). "An experimental and modeling study of humid air premixed flames". *Journal of Engineering for Gas Turbines and Power*, **122(3)**, 405–411.

BILGER, R. (1989). "The structure of turbulent nonpremixed flames". *Proceedings of The Combustion Institute*, **22(1)**, 475 – 488.

BUGGE, M. *et al.* (2008). "A status on NOx related to waste combustion and pyro-metallurgical processes". Fortrolig SINTEF F7129, SINTEF Materialteknologi.

CHAGGER, H. *et al.* (1996). "The formation of SiO2 from hexamethyldisiloxane combustion in counterflow methane-air flames". *Symposium (International) on Combustion*, **26(2)**, 1859 – 1865.

CHEN, J.Y. and CHANG, W.C. (1996). "Flamelet and PDF modeling of CO and NOx emissions from a turbulent, methane hydrogen jet nonpremixed flame". *Proceedings of The Combustion Institute*, **26(2)**, 2207 – 2214.

COSTA, F.D.S. *et al.* (2003). "Effects of wet CO oxidation on the operation of engines and power generators". *Journal of the Brazilian Society of Mechanical Sciences and Engineering*, **25**, 341 – 346.

DRAKE, M.C. and BLINT, R.J. (1989). "Thermal NOx in stretched laminar opposed-flow diffusion flames with CO/H$_2$/N$_2$ fuel". *Combustion and Flame*, **76(2)**, 151 – 167.

FLUENT, . (2009). *Fluent Users Guide*. Fluent Incorporated, Holmworth House, Corthworth Road, Sheffield, S11 9LP, UK.

FRISCH, M.J. *et al.* (2009). *Gaussian 09, Revision A.02*. Gaussian, Inc., Wallingford CT.

HAIRER, E. and WANNER, G. (1996). *Solving Ordinary Differential Equations II: Stiff and Differential-Algebraic Problems*. 2nd ed. Springer-Verlag, Springer Series in Computational Mathematics.

KODA, S. and FUJIWARA, O. (1988). "Silane combustion in an opposed jet diffusion flame". *Symposium (International) on Combustion*, **21(1)**, 1861 – 1867. Twenty-First Symposuim (International on Combustion).

LEE, K. and CHOI, D. (2009). "Analysis of NO formation in high temperature diluted air combustion in a coaxial jet flame using an unsteady flamelet model". *International Journal of Heat and Mass Transfer*, **52(5-6)**, 1412 – 1420.

LILLEBERG, B. *et al.* (2009). "Modeling instabilities in lean premixed turbulent combustors using detailed chemical kinetics". *Combustion Science and Technology*, **181(9)**.

LOUIS, J.J. *et al.* (2001). "Modeling and Measurement of a 16-kW Turbulent Nonadiabatic Syngas Diffusion Flame in a Cooled Cylindrical Combustion Chamber." *Combustion and Flame*, **125**, 1012–1031.

MAGNUSSEN, B.F. (1981). "On the structure of turbulence and a generalized eddy dissipation concept for chemical reaction in turbulent flow". *19 AIAA Aerospace Science Meeting*.

SCHICK, H.L. (1960). "A thermodynamic analysis of the high-temperature vaporization properties of silica." *Chemical Reviews*, **60(4)**, 331–362.

SIMONSEN, A.J. (2001). "3D CFD modeling of NOx combustion". Fortrolig SINTEF TR F5553, SINTEF Materialteknologi.

STEINFELD, J.I. *et al.* (1989). *Chemical Kinetics and Dynamics*. Prentice-Hall, Englewood Cliffs, NJ.

VRANOS, A. *et al.* (1992). "Nitric oxide formation and differential diffusion in a turbulent methane-hydrogen diffusion flame". *Proceedings of The Combustion Institute*, **24(1)**, 377–384. Cited By (since 1996) 7.

WILCOX, D.C. (1993). *Turbulence Modeling for CFD*. DCW Industries Inc., La Cañada, CA.

ZACHARIAH, M.T. and TSANG, W. (1995). "Theoretical Calculations of Thermochemistry, Energetics and Kinetics of High-Temperature Si$_x$H$_y$O$_z$ Reactions". *Journal of Physical Chemistry*, **99**, 5308 – 5318.

ZHAO, Y. and TRUHLAR, D.G. (2008). "The M06 suite of density functionals for main group thermochemistry, thermochemical kinetics, noncovalent interactions, excited states, and transition elements: two new fucntionals and systematic testing of four M06-class functionals and 12 other functionals". *Theoretical Chemistry Accounts*, **120**, 215 – 241.

8th International Conference on CFD in Oil & Gas, Metallurgical and Process Industries
SINTEF/NTNU, Trondheim NORWAY
21-23 June 2011

CFD11-178

FLUID MOTION FOR MICRO-GRAVITY SIMULATION IN A RANDOM POSITIONING MACHINE

Carole A.D. LEGUY[1]*, **René DELFOS**[1], **Mathieu J.B.M. POURQUIE**[1], **Christian POELMA**[1], **J KROONEMAN**[2], **Jerry WESTERWEEL**[1], **Jack J.W.A. VAN LOON**[3]

[1]Laboratory for Aero and Hydrodynamics, Delft University of Technology, THE NETHERLANDS

[2]Bioclear, Groningen, THE NETHERLANDS

[3]DESC OCB-ACTA, VU-University Amsterdam, THE NETHERLANDS

* E-mail: c.a.d.leguy@tudelft.nl

ABSTRACT

The Random Positioning Machine (RPM) is widely used to reproduce a micro-gravity environment for biological systems in Eearth-based experiments. The gravitational effects cancel out over time by the generation of a 3 dimensional random motion. Even if some agreements have been found between simulated microgravity and space studies, some differences remain and their causes are unclear. These differences may be explained by undesirable stresses acting on the culture cells that may originate from the instationary motion of the fluid inside culture container during random motion. The aim of this study is to predict fluid flow behavior, wall shear stresses and suspended cell motion in an RPM container experimentally using Particle Image Velocimetry (PIV) and numerically using 3-D Direct Numerical Simulation (DNS) of the flow.

A dual-axis rotating frame facility is used to reproduce the motion of a RPM. A flask, of dimension $6.5 \times 4.0 \times 2.0$ cm^3, filled with water and fluorescent tracer particles, is positioned at the center. A PIV system composed of a double-frame camera and a green light continuous wave dye-laser allows to record the particles inside the flask while the system is moving with a maximum angular speed of 30 degrees per second. To be able to reproduce the same experiment numerically, a DNS model is used. Rotation is simulated by adding extra forces (angular acceleration, centrifugal, Coriolis) to the momentum equation.

For rotation with a periodic angular velocity pattern, fluid motion induced by inertia is observed parallel to the wall. An average difference of 6% of the maximum velocity has been obtained between simulated and measured velocity field which is considered as a validation of the numerical model. Furthermore, the time evolution of the boundary layers can be observed near the flask wall. In the near future, we aim to extend this study to 2-axis motion as used in real RPM and develop a user protocol for the RPM users.

Keywords: Microgravity, Random Positioning Machine, Particle Image Velocimetry, DNS .

NOMENCLATURE

DNS parameters
μ Dynamic viscosity, $[kg/ms]$
a_i Additional body forces, $[N]$.
V Fluid Velocity, $[m/s]$.
r Distance from the axis of rotation, $[m]$.
Ω Angular velcoity, $[rad/s]$.
τ Wall shear stress, $[Pa]$.

PIV parameters

ε Velocity estimate error, $[m/s]$.
Δz Distance of the light sheet from the flask wall, $[m]$.
θ_x Deflection angle of the light sheet for the X axis, $[rad]$.
θ_y Deflection angle of the light sheet for the Y axis, $[rad]$.
n_t Number of measured time steps.
n_v Number of estimated velocity vector per frame.

INTRODUCTION

Many space missions have shown that extended exposure to weightlessness may seriously affect the health of astronauts (White and Averner, 2001; Buckey, 2006). Considering a long space flight like a mission to Mars, a better understanding of the effects of microgravity on the cellular level will be crucial to improve countermeasure programs.
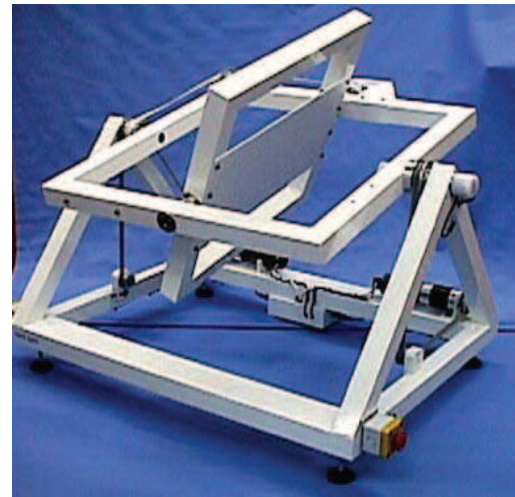

Figure 1: Random Positioning Machine (Dutch Space, the Netherlands).

To understand the role of gravity in biological systems, one may decrease gravity by going into free-fall conditions such as available on various platforms like sounding rockets, manned or unmanned spacecraft (Cogoli, 1993; Crawford-Young, 2006). Unfortunately, performing space experiments is cumbersome, expensive and can only be done infrequently. Thus, alternative techniques like fast rotating 2-D-clinostat and Random Positioning Machines (RPM) are now widely used to simulate the micro-gravity environment (Briegleb, 1967; Borst and van Loon, 2009;

Pardo *et al.*, 2005; Schwarzenberg, 1999). These instruments generate continuous movements so that gravitational effects cancel out over time. The classic 2-D-clinostat provides a rotation around one horizontal axis so that the object experience gravity changes over one vertical plane. The Random Positioning Machine generate a 3 dimensional random motion from a 2-axis rotating frames controlled independently (Borst and van Loon, 2009). It has been shown that the RPM provides a better simulation of microgravity environment compared to the classic 2-D clinoration (Kraft *et al.*, 2000). However, unexplained differences remain between studies performed with the RPM and space flight experiments. These differences may be explained by undesirable stresses acting on the culture cells. They may be caused by internal fluid motion, originating from the instationary motion of the fluid filled culture flask during random rotation. The aim of this study is to predict fluid flow behavior, wall shear stresses and suspended cell motion in an RPM container experimentally using Particle Image Velocimetry (PIV) and numerically using 3-D Direct Numerical Simulation (DNS) of the flow.

METHOD
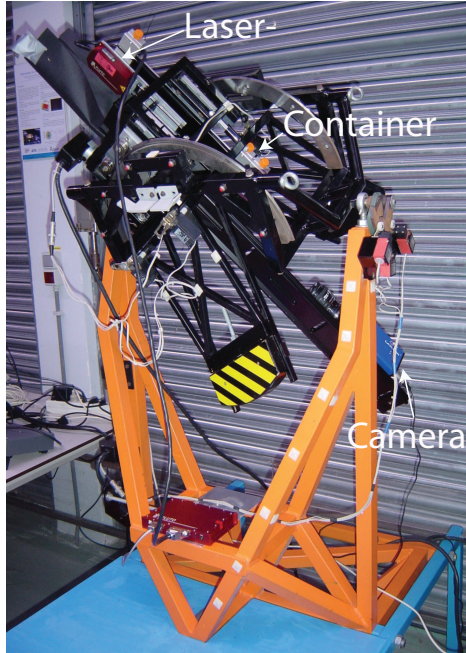
Experimental set-up

Figure 2: Particle Image Velocimetry system mounted on a two-axis rotating frame

A dual-axis rotating frame machine is used to reproduce the motion of a RPM in a controllable way. A flask filled with water and fluorescent tracer particle of 13 µm (Fluostar, Kanomax, USA) is positioned at the center. A PIV system allows to record the particles inside the flask while the system is rotating (Adrian and Westerweel, 2011), see Figure 2. The rectangular container dimension is $6.5 \times 4.0 \times 2.0$ cm^3 that corresponds to the dimension of the most commonly used culture flask $T25$. A green light continuous wave dye-laser of 532 nanometer wavelength is used to create a light sheet inside the flask at a distance Δz of 3.0 mm from the container's wall, see Figure 3. A transverse system is used to adjust the position of the light sheet by sliding the reflecting mirror. The deflecting angles θ_x and θ_y of the light sheet, with respect to the x and y axis, is minimized by correcting
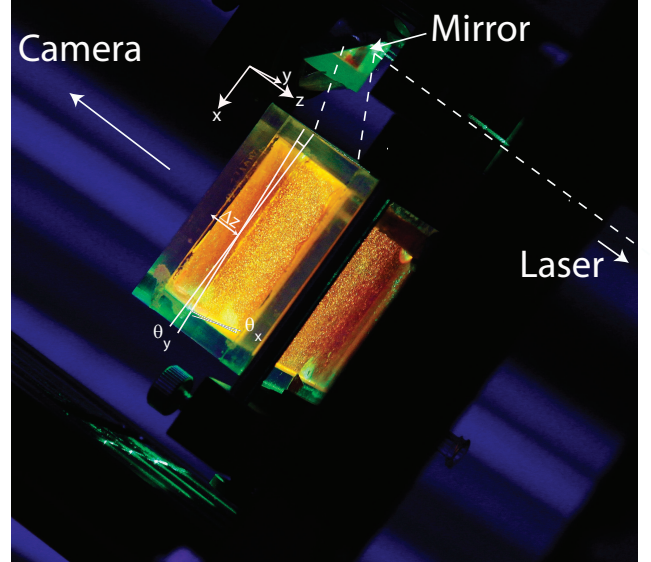
the mirror angular position.

Figure 3: Detailed view of the PIV system mounted on the 2-axis rotating frame. A light sheet is created in the XY plane at a distance Δz from the flask wall with deflection angle θ_x and θ_y.

A double-frame camera (Sensicam QE, 1 megapixel) is used to record the particles inside the flask. The time interval between each image pair is 400 *ms*, corresponding to a frequency of 2.5 *Hz*, whereas the image pair are recorded with a delay of 50 *ms* (20 *Hz*). The illumination of the laser is controlled for each exposure and equals 18 *ms*.

The PIV system described above is co-rotating with the flask according to a sinusoidal motion with a frequency of 0.2 *Hz* and a maximum angular speed Ω_x of $\pi/6$ rad/s. The motor motion is generated with a servo-control system driven by the dedicated software Galil (Galil Motion Control, Rocklin, USA). Images have been recorded for a duration of 30 s corresponding to 6 motion cycles.

Consequently, the fluid velocity vector field are obtained from the recorded image-sets. First, the image background noise is removed by subtracting the calculated image average. The images are further post-processed using a multipass cross correlation algorithm. Finally, outlier vectors are detected using the normalized median test proposed by Westerveel and Scarano in 2005 (Westerweel and Scarano, 2005) and replaced by interpolation.

DNS simulations

To be able to reproduce the same experiment numerically, a Direct Numerical Simulation (DNS) model is used. In the DNS code, rotation is simulated by adding extra body forces a_i (angular acceleration, Coriolis, centripedal) to the momentum equation.

$$a_i = \frac{d\Omega}{dt} \times r + 2\Omega \times V + \Omega \times (\Omega \times r) \qquad (1)$$

with Ω the angular velocity, V the fluid velocity (relative to the container) and r the distance from the axis of rotation.

A sinusoidal motion with a frequency of 0.2 *Hz* and a maximum angular speed Ω_x of $\frac{\pi}{6}$ rad/s was applied in accordance with the experimental study. The flask geometry equals the one used for the experiment ($6.5 \times 4.0 \times 2.0$ cm^3).

Validation

To validate the numerical model, the simulated velocities have been compared to the measured vector field. To quantitatively evaluate the quality of the fit, the average mean error ε is calculated. It is defined as follows

$$\varepsilon = \frac{1}{n_t n_v} \sum_{i,j}^{n_t,n_v} |V_{m_{i,j}} - V_{s_{i,j}}| \qquad (2)$$

with n_v the number of measured velocities in one recording, n_t the number of recording, and V_m and V_s the measured and simulated velocities, respectively.

The simulated velocity field has been interpolated at the PIV 2-D measurement plane. The uncertainties in the measurement light sheet distance from the flask wall Δz and its deflection angles θ_x and θ_y (see Figure 3) have been taken into account for the fitting by interpolating the simulated velocity field considering these positioning errors.

The cumulative error was evaluated to an uncertainty of ± 0.3 mm for Δz and ± 3 degrees for the deflection angles. Consequently, the values of Δz, θ_x and θ_y that provide the minimum difference between the simulated and measured velocity field have been obtained.

Wall shear stress

The wall shear stress at the X-Y plane, where the cultured cells are generally attached, is calculated both from the simulation and the measurement results. It is defined as

$$\tau = \mu \frac{dV}{dz} \qquad (3)$$

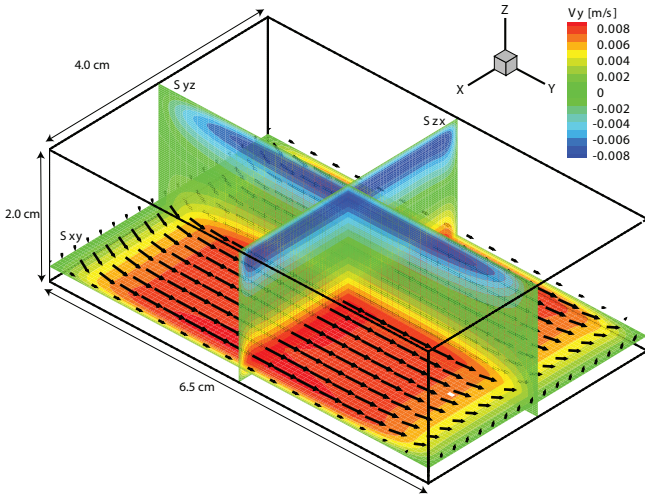with μ, the dynamic viscosity ($\mu = 1.005 \times 10^{-3}$ kg/ms).

RESULTS

Figure 4: Simulated velocity field in the y direction at time $t = 6.3$ s with slice view of the X-Y, Y-Z and Z-X plane.

For rotation around a single axis with a periodic angular velocity pattern, fluid motion induced by inertia is observed parallel to the wall, see Figure 4. The minimum cumulative difference between the simulated and measured velocity field is equal to 0.5 mm/s, 6% of the maximum velocity, at a distance of 3.30 mm from the wall. This distance is taken as the corrected position of the light sheet. No further improvement of the fit was obtained by changing the angles θ_x and θ_y, thus

they have been set to 0. The quantitative result demonstrates the good agreement between the simulated and the measured velocity profiles.
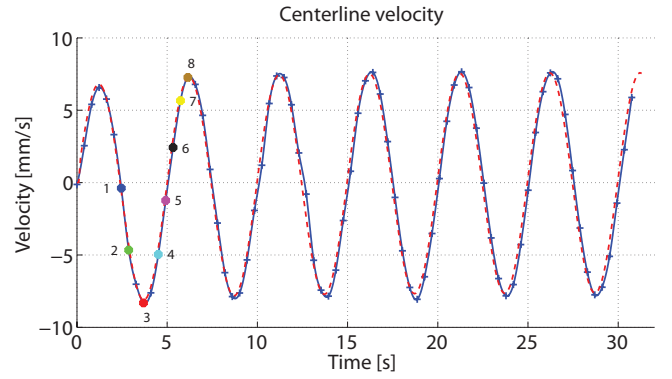

Figure 5: Velocity in the Y direction at the center of the measured plane (the intersection of S_{xy}, S_{yz} and S_{xz} planes) obtained from the measurements (in blue) and from the simulated data (in red).
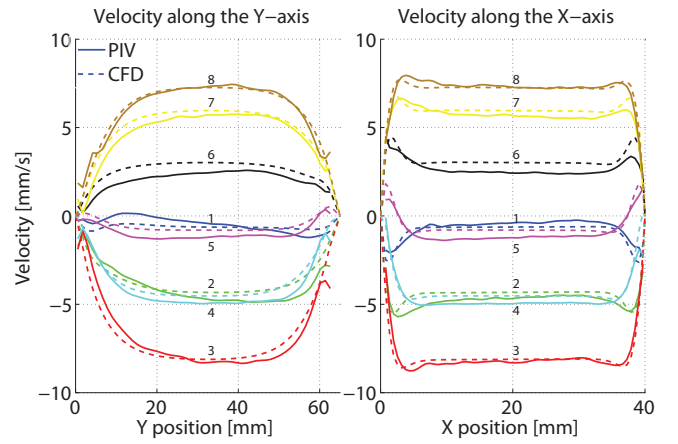

Figure 6: Comparison between the simulated and measured velocity profiles at several time steps as a function of the Y position, at the intersection of the S_{xy} and S_{yz} plane (left), and as a function of the X position at the intersection between the S_{xy} and S_{zx} planes (Right).

In Figure 5, measured and simulated velocities at the center of the measurement plane are depicted as a function of time. It can be seen that a periodic state is reached after only one period with a maximum velocity of 8.1 mm/s. The time evolution of the velocity profiles are shown on Figure 6 for the velocity in the y direction. The increasing and decreasing pattern of V_y can be seen along the y direction, whereas along the axis of rotation x, flattened profile are observed with end-effects near the flask wall.

Since the PIV measurements provided the velocity field only over the 2-D XY plane at a distance of 3.3 mm from the wall, the 3-D simulated results are used to study the velocity profile along the z axis. The evolution of the boundary layer can be seen near the flask wall. The wall shear stress obtained from the simulated data are represented on Figure 7. A maximum wall shear stress of 6.2 mPa is obtained with an angular phase shift of 54 degree with respect to the angular velocity of the rotating axis. An estimate of the wall shear stress was obtained from the measured data by linear approximation from the measured plane (at 3.3 mm from the

flask wall). It shows a large underestimation of the wall shear stress compared to the one determined from the DNS data.
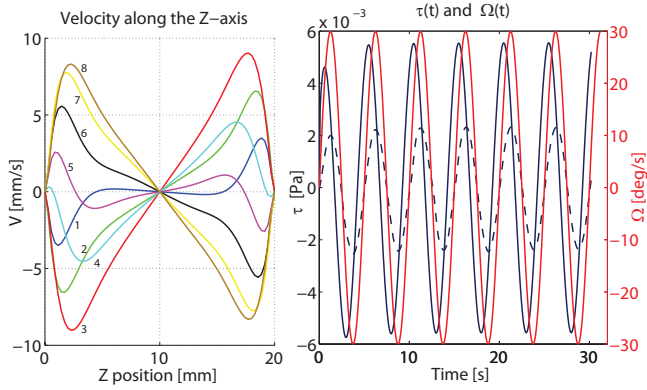

Figure 7: Left: Simulated velocity profile as a function of Z direction, at the intersection of the S_{yz} and S_{zx} plane. Right: In black, the Wall shear stress obtained from the simulated data and derived from the measurements (dashed) at the flask wall. In red, the axis angular velocity $\Omega(t)$.

DISCUSION

In this study, fluid flow behavior and wall shear stresses, as induced in a Random Positioning Machine, has been investigated experimentally using Particle Image Velocimetry and numerically with using Direct Numerical Simulations. Good agreement has been obtained between the simulated and measured velocity field for a sinusoidal motion with a frequency of 0.2 Hz and a maximum angular speed of $\frac{\pi}{6}$ rad/s. A average difference between the measured and simulated vector field of 0.5 mm/s has been obtained. This is considered to be a validation of the DNS code.

The obtained wall shear stress suggested that the stresses induced by the fluid flow for cells cultured at the flask wall is relatively low. A large underestimation of the wall shear stress is obtained when using a linear interpolation of the velocity profile to the flask wall. This is due to the fact that the fluid boundary layer at the wall is much smaller than the distance of the measurement plane. A better estimation could be obtained if the velocity profiles can be estimated at several positions.

FUTURE WORK

In a real RPM, higher angular velocities are used (up to π rad/s), thus higher stresses can be expected. Further investigations are required to estimate the fluid motion and induced stresses for higher angular velocities. Furthermore, simultaneous motion of the 2-axis, as used in a real RPM, will be studied both experimentally and numerically.

From the obtained velocity profiles, it is shown that a periodic state is reached after only one oscillation period. It would be interesting to perform a parameter study in order to determine which dimensionless number could be used for scaling. In this way, the general behavior of such flow could be described.

CONCLUSION

For a sinusoidal motion with a maximum angular speed of $\frac{\pi}{6}$ rad/s, a good agreement between simulated and measured velocity field has been found which is considered as a validation of the numerical model. A steady oscillatory state is obtained after only one period. In the near future, we aim

to study fluid motion behavior for higher angular velocities and dual axis motion. Furthermore, we are developing a user protocol for the RPM users.

REFERENCES

ADRIAN, R.J. and WESTERWEEL, J. (2011). *Particle image velocimetry*. Cambridge University Press.

BORST, A. and VAN LOON, J. (2009). "Technology and Developments for the Random Positioning Machine, RPM". *Microgravity Science and Technology*, **21(4)**, 287–292.

BRIEGLEB, W. (1967). *Ein Modell fuer Schwerlosichkeits-Simulation an Mikroorganismen*.

BUCKEY, J.C. (2006). *Space Physiology*. NewYork, USA.

COGOLI, A. (1993). "The effect of hypogravity and hypergravity on cells of the immune system". *Journal of Leukocyte Biology*, **54(3)**, 259–268.

CRAWFORD-YOUNG, S.J. (2006). "Effects of microgravity on cell cytoskeleton and embryogenesis." *The International journal of developmental biology*, **50(2-3)**, 183–191.

KRAFT, T.F.B. *et al.* (2000). "Plastid position in *Arabidopsis* columella cells is similar in microgravity and on a random-positioning machine". *Planta*, **211(3)**, 415–422.

PARDO, S.J. *et al.* (2005). "Simulated microgravity using the Random Positioning Machine inhibits differentiation and alters gene expression profiles of 2T3 preosteoblasts." *American journal of physiology. Cell physiology*, **288(6)**, C1211–C1221.

SCHWARZENBERG, M. (1999). "Signal transduction in T lymphocytes: A comparison of the data from space, the free fall machine and the random positioning machine". *Advances in Space Research*, **24(6)**, 793–800.

WESTERWEEL, J. and SCARANO, F. (2005). "Universal outlier detection for PIV data". *Experiments in Fluids*, **39(6)**, 1096–1100.

WHITE, R.J. and AVERNER, M. (2001). "Humans in space". *Nature*, **409(6823)**, 1115–1118.

8th International Conference on CFD in Oil & Gas, Metallurgical and Process Industries
SINTEF/NTNU, Trondheim NORWAY
21-23 June 2011

CFD11-184

THREE DIMENSIONAL NUMERICAL SIMULATION OF BUBBLE AND DROPLET DYNAMICS WITH A PARALLEL PARTICLE LEVEL SET SOLVER

Hans BIHS

SINTEF Coast and Harbor Research Center, 7491 Trondheim, NORWAY

E-mail: hans.bihs@sintef.no

ABSTRACT

A three dimensional numerical model is used to predict the movement of a rising gas bubble in a fluid and the splash of a drop on a liquid film. For the bubble, the combination of the surface tension and the hydrostatic pressure leads to a large deformation of the gas-liquid interface. In the other case, the impact of the falling drop leads to the rise of a thin liquid film, followed by the formation of a vertical liquid jet.

The numerical model uses the level set method (Osher and Sethian, 1988) for the calculation of the interface between gas and liquid. With this front-capturing method the free surface is modeled as the zero level set of a scalar signed distance function. In order to maintain this property and to ensure mass conservation, the level set function is reinitialized after each time step. Surface tension is taken into account with the continuum surface force method (Brackbill *et al.*, 1992). For improved mass conservation the level set method is supplemented with a particle correction scheme (Wang *et al.*, 2009). All convective terms including the level set function are discretized with the fifth-order finite difference WENO scheme (Jiang and Chu, 1996). It ensures a smooth and oscillation free solution for large gradients and even shocks while maintaining a high order discretization at the same time. The pressure is discretized with the projection method. The Poisson equation for the pressure is solved with the preconditioned BiCGStab algorithm. The staggered grid configuration leads to a tight velocity-pressure coupling. For time discretization a second order Adams-Bashforth scheme is used. Parallelization of the numerical scheme is achieved by using the domain decomposition framework together with the MPI library.

Keywords: CFD, level set method, multiphase flow, parallel solver .

INTRODUCTION

Fluid Flow Problems with more than one phase are quite common in many engineering disciplines. Predicting the correct location of the interface between different fluids or gases is important for many applications, such as melt dynamics, reacting flows, breaking surface waves and air-water dynamics. The numerical computation of such flow cases is challenging in many ways. The numerical procedure is required to be stable, fast and accurate. Qualities which are harder to obtain for multiphase flow systems, as discontinuities in the material properties i.e. the density and the viscosity occur.

In addition, numerical discretization schemes need to be of high-order of accuracy in order to preserve the sharp division between the phases.

Different approaches to the numerical solution of the interface capturing exist. One of the earliest is the Marker-and-Cell (MAC) scheme (Harlow and Welch, 1965). Here massless marker particles are used to represent the phases. The distribution of the particles determines the location of the interface, which must be reconstructed explicitly. The computing effort is rather large because the grid needs to be refined along interface in order to avoid smeared solutions. In the Volume of Fluid method (VOF) (Hirt and Nichols, 1981) the marker particles are replaced by a scalar field, which describes the volume fraction of one fluid for each discretization cell. A convection equation is solved in order to move the scalar field along with the external velocity field. For the extraction of the geometrical interface from the fraction function, a reconstruction algorithm needs to be used. In the accurate reconstruction of the interface lies the main difficulty of this method, and it negatively affects mass conservation. In addition, an effect known as foaming, the smearing of the interface can be a problem, due to the numerical diffusion resulting from the discretization of the fraction function.

In the present paper the level set method is used (Osher and Sethian, 1988). The main idea behind this method is that the location of interface is represented implicitly by the zero level set of the smooth signed distance function. In contrast to the VOF method the level set function varies continuously across the interface. The location of the interface is readily available and does not require any reconstruction procedure. Since mass conservation is not enforced directly by the level set method, it is supplemented with a particle correction algorithm. The numerical model is used to calculate the deformation of a rising gas bubble in a liquid column and the the splash of a water drop on a liquid film.

NUMERICAL MODEL

Equations of Motion

For the investigations in the present paper a three-dimensional numerical model is used. The governing equations for the mass and momentum conservation are the continuity and the incompressible Reynolds-averaged Navier-Stokes (RANS) equations:

$$\frac{\partial U_i}{\partial x_i} = 0 \tag{1}$$

$$\frac{\partial U_i}{\partial t} + U_j \frac{\partial U_i}{\partial x_j} = -\frac{1}{\rho}\frac{\partial P}{\partial x_i}$$
$$+ \frac{\partial}{\partial x_j}\left[\nu \left(\frac{\partial U_i}{\partial x_j} + \frac{\partial U_j}{\partial x_i} \right) - \overline{u_i u_j} \right] + g_i \qquad (2)$$

U is the velocity averaged over the time t, x is the spatial geometrical scale, ρ is the water density, ν is the kinematic viscosity, P is the pressure, g is the gravity, u is the velocity fluctuation over time with $\overline{u_i u_j}$ representing the Reynolds stresses. At solid boundaries the surface roughness is accounted for by using wall laws (Schlichting, 1979).

Level Set Method

The level set method was first presented by Osher and Sethian (Osher and Sethian, 1988). It was devised for computing and analyzing the motion of an interface Γ between two phases in two or three dimensions. The location of interface is represented implicitly by the zero level set of the smooth signed distance function $\phi(\vec{x}, t)$. In every point of the modeling domain the level set function gives the closest distance to the interface and the phases are distinguished by the change of the sign. This results in the following properties:

$$\phi(\vec{x}, t) \begin{cases} > 0 \; if \; \vec{x} \in phase \; 1 \\ = 0 \; if \; \vec{x} \in \Gamma \\ < 0 \; if \; \vec{x} \in phase \; 2 \end{cases} \qquad (3)$$

Also the Eikonal equation $|\nabla \phi| = 1$ is valid. When the interface Γ is moved under an externally generated velocity field $\vec{v}$, a convection equation for the level set function is obtained:

$$\frac{\partial \phi}{\partial t} + U_j \frac{\partial \phi}{\partial x_j} = 0 \qquad (4)$$

When the interface evolves, the level set function looses its signed distance property. In order to maintain this property and to ensure mass conservation the level set function is initialized after each time tep. In the present paper a PDE based reinitialization equation is solved (Sussman *et al.*, 1994):

$$\frac{\partial \phi}{\partial t} + S(\phi)\left(\left| \frac{\partial \phi}{\partial x_j} \right| - 1 \right) = 0 \qquad (5)$$

$S(\phi)$ is the smoothed sign function by Peng et al. (Peng *et al.*, 1999).

$$S(\phi) = \frac{\phi}{\sqrt{\phi^2 + \left| \frac{\partial \phi}{\partial x_j} \right|^2 (\Delta x)^2}} \qquad (6)$$

With the level set function in place, the material properties of the two phases can be defined for the whole domain. Without special treatment there is a jump in the density ρ and the viscosity ν across the interface which can lead to substantial numerical stability problems. The solution is to define the interface with the constant thickness 2ε. In that region smoothing is carried out with a regularized Heavyside function $H(\phi)$. The thickness ε is proportional to the grid spacing, in the present paper it was chosen to be $\varepsilon = 1.6\Delta x$. The density and the viscosity can then be written as:

$$\rho(\phi) = \rho_1 H(\phi) + \rho_2 (1 - H(\phi)),$$
$$\nu(\phi) = \nu_1 H(\phi) + \nu_2 (1 - H(\phi)) \qquad (7)$$

and

$$H(\phi) = \begin{cases} 0 & if \; \phi < -\varepsilon \\ \frac{1}{2}\left(1 + \frac{\phi}{\varepsilon} + \frac{1}{\Pi}sin\left(\frac{\Pi\phi}{\varepsilon} \right) \right) & if \; |\phi| < \varepsilon \\ 1 & if \; \phi > \varepsilon \end{cases} \qquad (8)$$

Lagrangian Particle Correction

Using the level set method for the interface capturing has many advantages for the numerical behavior of the solver and the quality of the results. But it is important to remember, that the level set equation does not explicitly enforce mass conservation. In certain cases, due to numerical dissipation, interface areas of high curvature and sharp edges can be smoothed out to some extend. This may lead to an unwanted loss of mass as a result.

A fine grid will preserve details of the topological change of the interface much better than a coarse grid. One option then is to refine the grid locally around the interface (Bürger, 2008). Because this has a negative effect on the CFL-criterion and the implementation requires changes in the grid architecture, a different path is followed in the present study. Massless particles are used to correct the level set function in underresolved regions. This idea was first presented in (Enright *et al.*, 2002). Here a hybrid particle level set method was tested successfully on several cases and showed a positive effect on the mass conservation. Later several improvements were added to the original method (Wang *et al.*, 2009). This method is implemented into the current numerical model.

Negative particles are seeded on the negative side of the level set function in a narrow band of $1.6\Delta x$ near the interface. The positive particles are respectively placed on the positive side of the interface. Each cell in the narrow band contains 64 particles and for each particle its position $\vec{x}_p$ and radius r_p are stored. The radius of each particle is determined by:

$$r_p = \begin{cases} r_{max}, & if \; s_p \phi(\vec{x}_p) > r_{max}, \\ s_p \phi(\vec{x}_p) & if \; r_{min} \le s_p \phi(\vec{x}_p) \le r_{max}, \\ r_{min}, & if \; s_p \phi(\vec{x}_p) < r_{min}. \end{cases} \qquad (9)$$

Here s_p is the sign of the particle. The minimum radius is defined as $r_{min} = 0.1\Delta x$ and the maximum radius as $r_{max} = 0.5\Delta x$ (Δx is the uniform mesh width). The particles are advected with the third-order accurate TVD Runge-Kutta scheme (Shu and Osher, 1988) in each time step of the computation. In underresolved areas, particles may move across the interface. When a particle passes the interface by more then its radius, it is used to correct the level set function. The level set value ϕ_p of an escaped positive particle is given by:

$$\phi_p(\vec{x}) = \begin{cases} s_p\left(r_p - |\vec{x} - \vec{x}_p| \right), & if \phi(\vec{x}) \le 0, \\ s_p\left(r_p + |\vec{x} - \vec{x}_p| \right), & if \phi(\vec{x}) > 0. \end{cases} \qquad (10)$$

For an escaped negative particle, the level set value of this particle is:

$$\phi_p(\vec{x}) = \begin{cases} s_p\left(r_p - |\vec{x} - \vec{x}_p| \right), & if \phi(\vec{x}) > 0, \\ s_p\left(r_p + |\vec{x} - \vec{x}_p| \right), & if \phi(\vec{x}) \le 0. \end{cases} \qquad (11)$$

After the level set value of the escaped particle is determined, the correction procedure begins. When a cell holds an escaped particle, the level set values in its corners are ϕ^+ in an area of positive level set values and ϕ^- in areas of negative level set values.

$$\phi^+ = max\left(\phi_p, \phi^+ \right) \qquad (12)$$

$$\phi^- = min\left(\phi_p, \phi^-\right) \qquad (13)$$

The level set function is then rebuild by choosing the value of ϕ^+ and ϕ^-, which has the smallest absolute value:

$$\phi = \begin{cases} \phi^+, & if\ |\phi^+| \leq |\phi^-|, \\ \phi^-, & if\ |\phi^+| > |\phi^-|. \end{cases} \qquad (14)$$

The original particle level set method used only negative particle to correct the negative level set values and only positive particles to correct the positive level set values. In contrast, the improved version uses positive and negative particles to correct level set values of both signs. This makes the method more efficient, requiring the narrow band with the particle to be only half as thick. In addition, the particle correction step needs to be performed only once, after the convection of the level set function. A problem can occur, when the corrected level set value is larger in magnitude, than the distance of the escaped particle to the interface. This may result in a damaged interface. In order to prevent this, the particle is projected through through the cell corner along the normal direction of the level set function.

$$\vec{x'} = \vec{x}\,\gamma\,proj_n\left(\vec{x_p} - \vec{x}\right) \qquad (15)$$

with

$$\gamma = 1 - \frac{r_p}{|\vec{x_p} - \vec{x}|} \qquad (16)$$

When this projection falls inside the cell with the escaped particle, the level set value in the corner of the cell will be corrected, otherwise no correction is performed.

In the current implementation, the particle correction scheme is fully parallelized following the domain decomposition approach of the rest of the numerical model. A special routine is coded in a way, that particles are exchanged between neighboring processes.

Surface Tension

Cohesive forces act between the molecules of a liquid. At the interface liquid-gas the molecules of the liquid phase do not have neighbors of their own phase. Since the cohesive forces of the liquid molecules are larger than that of the gas, they are attached stronger to each other on the interface than inside the fluid. In order to consider the surface forces in the momentum equations, they need to be transformed into volume forces. This is done with the continuum surface force (CSF) model by Brackbill et al. (Brackbill *et al.*, 1992). The following source term $S_{CSF,i}$ needs to be added to the momentum equations:

$$S_{CSF,i} = \sigma\kappa(\phi)\,\delta(\phi)\,\frac{\partial\phi}{\partial x_i} \qquad (17)$$

The surface tension coefficient σ is a material property. For the water-air interface at 20 $\degree C$ it is 0.07275 N/m. The calculation of the interface curvature is straightforward with the level set method, no reconstruction is of the free surface is necessary:

$$\kappa = \nabla \cdot \left(\frac{\nabla\phi}{|\nabla\phi|}\right) \qquad (18)$$

In order to activate the surface tension near the interface only, the source term is multiplied with a regularized Dirac delta function.

$$\delta(\phi) = \begin{cases} \frac{1}{2\varepsilon}\left(1 + cos\left(\frac{\Pi\phi}{\varepsilon}\right)\right) & if\ |\phi| < \varepsilon \\ 0 & else \end{cases} \qquad (19)$$

Discretization of the Convective Terms

For complex flow situations such as free surface flows, it is essential to employ a high order discretization method while at the same time maintain a high level of numerical stability. With that in mind the fifth-order WENO (weighted essentially non-oscillatory) scheme by Jiang and Shu (Jiang and Chu, 1996) in the finite-difference framework is chosen. The great advantage of the WENO scheme is that it can handle large gradients right up to the shock very accurately by taking local smoothness into account. The overall WENO discretization stencil consists of three local ENO-stencils. These stencils are weighted depending on their smoothness, with the smoothest stencil contributing the most significantly. In comparison to popular high resolution schemes such as MUSCL (van Leer B., 1979) or TVD (Harten, 1983) schemes, the WENO scheme does not smear out the solution. Instead it maintains the sharpness of the extrema. The WENO scheme is used to treat the convective terms for the velocities U_i and the level set function ϕ (W., 1997). In the following, the scheme is presented exemplary for the discretization of the level set function in the x-direction.

Simple upwinding is used to choose between ϕ_x^- or ϕ_x^+, the convection velocities at the cell centers are obtained by interpolation:

$$\phi_x^{\pm} = \omega_1^{\pm}\phi_x^{1\pm} + \omega_2^{\pm}\phi_x^{2\pm} + \omega_3^{\pm}\phi_x^{3\pm} \qquad (20)$$

The three ENO stencils are defined as:

$$\begin{aligned} \phi_x^{1\pm} &= \frac{q_1^{\pm}}{3} - \frac{7q_2^{\pm}}{6} + \frac{11q_3^{\pm}}{6}, \\ \phi_x^{2\pm} &= -\frac{q_2^{\pm}}{6} + \frac{5q_3^{\pm}}{6} + \frac{q_4^{\pm}}{3}, \\ \phi_x^{3\pm} &= \frac{q_3^{\pm}}{3} + \frac{5q_4^{\pm}}{6} - \frac{q_5^{\pm}}{6} \end{aligned} \qquad (21)$$

with

$$\begin{aligned} q_1^- &= \frac{\phi_{i-2} - \phi_{i-3}}{\Delta x},\ q_2^- = \frac{\phi_{i-1} - \phi_{i-2}}{\Delta x},\ q_3^- = \frac{\phi_i - \phi_{i-1}}{\Delta x}, \\ q_4^- &= \frac{\phi_{i+1} - \phi_i}{\Delta x},\ q_5^- = \frac{\phi_{i+2} - \phi_{i+1}}{\Delta x} \end{aligned} \qquad (22)$$

and

$$\begin{aligned} q_1^+ &= \frac{\phi_{i+3} - \phi_{i+2}}{\Delta x},\ q_2^+ = \frac{\phi_{i+2} - \phi_{i+1}}{\Delta x},\ q_3^+ = \frac{\phi_{i+1} - \phi_i}{\Delta x}, \\ q_4^+ &= \frac{\phi_i - \phi_{i-1}}{\Delta x},\ q_5^+ = \frac{\phi_{i-1} - \phi_{i-2}}{\Delta x} \end{aligned} \qquad (23)$$

the weights are written as:

$$\omega_1^{\pm} = \frac{\alpha_1^{\pm}}{\alpha_1^{\pm} + \alpha_2^{\pm} + \alpha_3^{\pm}} \qquad (24)$$

$$\omega_2^{\pm} = \frac{\alpha_2^{\pm}}{\alpha_1^{\pm} + \alpha_2^{\pm} + \alpha_3^{\pm}} \qquad (25)$$

$$\omega_3^{\pm} = \frac{\alpha_3^{\pm}}{\alpha_1^{\pm} + \alpha_2^{\pm} + \alpha_3^{\pm}} \qquad (26)$$

and

$$\alpha_1^{\pm} = \frac{1}{10} \frac{1}{\left(\widetilde{\varepsilon} + IS_1^{\pm}\right)^2} \qquad (27)$$

$$\alpha_2^{\pm} = \frac{6}{10} \frac{1}{\left(\widetilde{\varepsilon} + IS_2^{\pm}\right)^2} \qquad (28)$$

$$\alpha_3^{\pm} = \frac{3}{10} \frac{1}{\left(\widetilde{\varepsilon} + IS_3^{\pm}\right)^2} \qquad (29)$$

with the regularization parameter $\widetilde{\varepsilon} = 10^{-6}$ and the following smoothness indicators:

$$IS_1^{\pm} = \frac{13}{12}(q_1 - 2q_2 + q_3)^2 + \frac{1}{4}(q_1 - 4q_2 + 3q_3)^2,$$

$$IS_2^{\pm} = \frac{13}{12}(q_2 - 2q_3 + q_4)^2 + \frac{1}{4}(q_2 - q_4)^2, \qquad (30)$$

$$IS_3^{\pm} = \frac{13}{12}(q_3 - 2q_4 + q_5)^2 + \frac{1}{4}(3q_3 - 4q_4 + q_5)^2$$

Projection Method for the Pressure

The pressure is included in the modeling procedure by employing Chorin's projection method (Chorin, 1968) for incompressible flow. Here the actual pressure gradient is neglected in the momentum equations. Instead for each time step an intermediate velocity U_i^* is computed using the transient RANS-equation:

$$\frac{\partial(U_i^* - U_i^n)}{\partial t} + U_j^n \frac{\partial U_i^n}{\partial x_j} =$$
$$\frac{\partial}{\partial x_j}\left[\nu(\phi^n)\left(\frac{\partial U_i^n}{\partial x_j} + \frac{\partial U_j^n}{\partial x_i}\right) - \overline{u_i u_j}\right] + g_i + S_{CSF,i}^n \qquad (31)$$

The Poisson equation for pressures is formed by calculating the divergence of the intermediate velocity field.

$$\frac{\partial}{\partial x_i}\left(\frac{1}{\rho(\phi^n)}\frac{\partial P}{\partial x_i}\right) = -\frac{1}{\Delta t}\frac{\partial U_i^*}{\partial x_i} \qquad (32)$$

The Poisson equation is solved using the Jacobi-preconditioned BiCGStab algorithm (van der Vorst H., 1992). The pressure is then used to correct the velocity field, making it divergence free.

Time Advancement Scheme

For the time discretization a second-order accurate Adams-Bashforth scheme is used. The time step size is determined through adaptive time stepping. This ensures a stable and efficient choice of the time step. The spacial discretization is represented by the operator L. The formulation is given for the level set equation and a non-equidistant time steps.

$$\phi^{n+1} = \phi^n$$
$$+ \frac{\Delta t_n}{2}\left(\frac{\Delta t_n + 2\Delta t_{n-1}}{\Delta t_{n-1}}L(\phi^n) - \frac{\Delta t_n}{\Delta t_{n-1}}L(\phi^n)\right) \qquad (33)$$

The Numerical Grid

All model equations are discretized on a Cartesian grid with a staggered arrangement of the variables. The velocity variables are defined on the center of the cell faces, while all others such as the level set function, the pressure or the variables of the turbulence model on the cell centers. This way oscillations due to velocity-pressure decoupling are avoided.

At the solid boundaries of the fluid domain a ghost cell immersed boundary method is employed. In this method the solution is analytically continued through the solid boundary by updating the fictitious ghost cell in the solid region by extrapolation. That way the numerical discretization does not need to account for the boundary conditions explicitly, instead they are enforced implicitly. The algorithm is based upon the local directional approach by Berthelsen and Faltinsen (Berthelsen and Faltinsen, 2008) which was implemented in 2D. In the current implementation the extrapolation scheme is decomposed into the components of the three-dimensional coordinate system. Because the computational domain in the present paper consists of rectangular cuboids, no cut cells are present.

The ghost cell approach has several advantages: Grid generation becomes trivial, the numerical stability and order of the overall scheme is not affected. In addition the method integrates well into the domain decomposition strategy for the parallelization of the model. Here ghost cells are used to update the values from the neighboring processors via MPI.

RESULTS

Rising Bubble

The first case is a rising gas bubble in a tank filled with a fluid. The extend of the tank is $0.15m$ x $0.15m$ x $0.2m$. In the beginning of the simulation, the bubble has a radius of $r = 0.03m$ and its center is located at a height of $h = 0.06m$ (Figure 1). The density of the fluid is 100 times the density of the gas. The computations are performed with the mesh size of $\Delta x = 0.0025m$, once with the regular level set method and once with the particle level set method. Figures 1-5 show the process of the rising bubble, as it is calculated with the particle level set method. Due to the higher hydrostatic pressure on the bottom of the bubble, the lower interface is moving towards the center. The beginning of this process can be seen after $0.05sec$ in Figure 2. Here in addition to the interface also the magnitude of the velocity is shown, which is considerably higher on the bottom side of the bubble. After $0.10sec$, the bottom interface has moved very close to lid of the bubble (Figure 3). In Figure 4 it can be seen, that after $0.15sec$ the bubble has now the geometrical form of a torus. Figure 5 depicts the positive and negative particles around the zero level set contour from that time step. When using the regular level set method, 91% of the initial mass is conserved until $t = 0.15sec$, with the particle level set method this values increases to 95%. For the current case, the particle level set method takes about 20% more time to compute than the original level set method. But it only adds about 2% to the total computation time, as the numerical model spends most of the time in the pressure solver. These performance and mass conservation numbers are varying from case to case, because they depend on the grid size and on the ratio of the interface area to the total number of cells.

Droplet

Another application of the particle level set method is the calculation of the impact of a falling droplet on a fluid surface. The rectangular computational domain is $0.15m$ x $0.15m$ x $0.1m$ with a droplet radius of of $r = 0.015m$ and its center is located at a height of $h = 0.07m$ (Figure 6). The vertical velocity around the droplet is initialized with $w = -2.0m/s$. The density of the water is 1000 times higher than the surrounding air. For this case only the particle level set results are presented. After the droplet has plunged into the body of water, the free surface moves downward in the center of

the impact, while on an outer ring it moves upwards due to the increased pressure and the incompressibility of the water (Figure 7). When the water in the center moves back upwards, a vertical water jet is formed (Figure 7).

CONCLUSION

In the paper computations of bubble and droplet dynamics are performed using an interface capturing scheme. The results obtained with particle level set method show improved mass conservation properties. The Lagrangian particle scheme also proved its numerical stability. Because the method is fully parallelized, the extra computational effort is not too large.

The presented numerical model has a huge potential also for practical multiphase applications. Future research will be focused on making the model more versatile for engineering purposes.

REFERENCES

BERTHELSEN, P.A. and FALTINSEN, O.M. (2008). "A local directional ghost cell approach for incompressible viscous flow problems with irregular boundaries". *Journal of Computational Physics*, **227**, 4354–4397.

BRACKBILL, J. *et al.* (1992). "A continuum method for modeling surface tension". *Journal of Computational Physics*, **100**, 335–354.

BÜRGER, M. (2008). "Eine adaptive hamilton-jacobi level-set reinitialisierung für zweiphasenströmungen".

CHORIN, A. (1968). "Numerical solution of the navier-stokes equations". *Math. Comput.*, **22**, 745–762.

ENRIGHT, D. *et al.* (2002). "A hybrid particle level set method for improved interface capturing". *Journal of Computational Physics*, **183**, 83–116.

HARLOW, F. and WELCH, J. (1965). "Numerical calculation of time dependent viscous incompressible flow of fluid with a free surface". *Physics of Fluids*, **8**, 2182–2189.

HARTEN, A. (1983). "High resolution schemes for hyperbolic conservation laws". *Journal of Computational Physics*, **49**, 357–393.

HIRT, C. and NICHOLS, B. (1981). "Volume of fluid vof method for the dynamics of free boundaries". *Journal of Computational Physics*, **39**, 201–225.

JIANG, G.S. and CHU, C.W. (1996). "Efficient implementation of weighted eno schemes". *Journal of Computational Physics*, **126**, 202–228.

OSHER, S. and SETHIAN, J.A. (1988). "Fronts propagating with curvature- dependent speed: Algorithms based on hamilton-jacobi formulations". *Journal of Computational Physics*, **79**, 12–49.

PENG, D. *et al.* (1999). "A PDE-based fast local level set method". *Journal of Computational Physics*, **155**, 410–438.

SCHLICHTING, H. (1979). *Boundary layer theory*. McGraw-Hill Book Company.

SHU, C.W. and OSHER, S. (1988). "Efficient implementation of essentially non-oscillatory shock capturing schemes". *Journal of Computational Physics*, **77**, 439–471.

SUSSMAN, M. *et al.* (1994). "A level set approach for computing solutions to incompressible two-phase flow". *Journal of Computational Physics*, **114**, 146–159.

VAN DER VORST H. (1992). "BI-GStab: A fast and smoothly converging variant of BI-CG for the solution of nonsymmetric linear systems". *SIAM J. Sci. Stat. Comput.*, **13**, 631–644.

VAN LEER B. (1979). "Towards the ultimate conservative difference scheme V. A second order sequel to Godunovs method". *Journal of Computational Physics*, **32**, 101–136.

W., S.C. (1997). *Essentially Non-Oscillatory and Weighted Essentially Non-Oscillatory Schemes for Hyperbolic Conservation Laws*. ICASE Report.

WANG, Z. *et al.* (2009). "An improved particle correction procedure for the particle level set method". *Journal of Computational Physics*, **228**, 5819–5837.
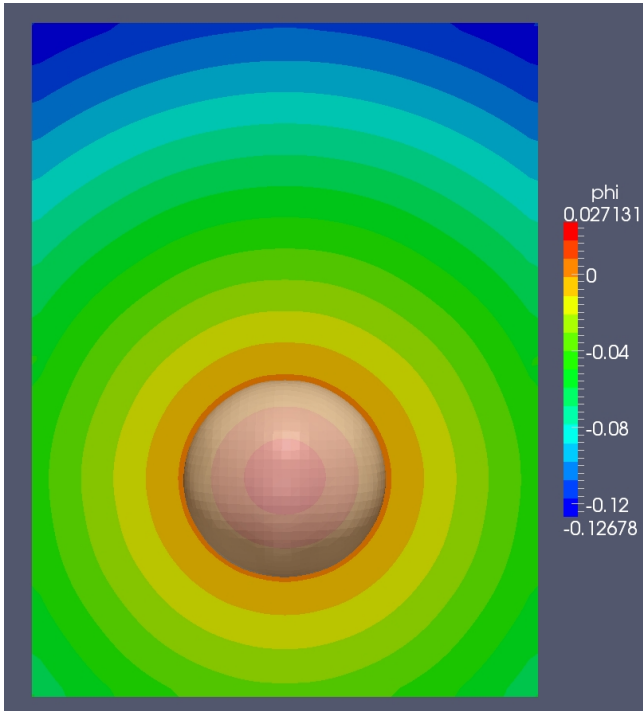
APPENDIX A

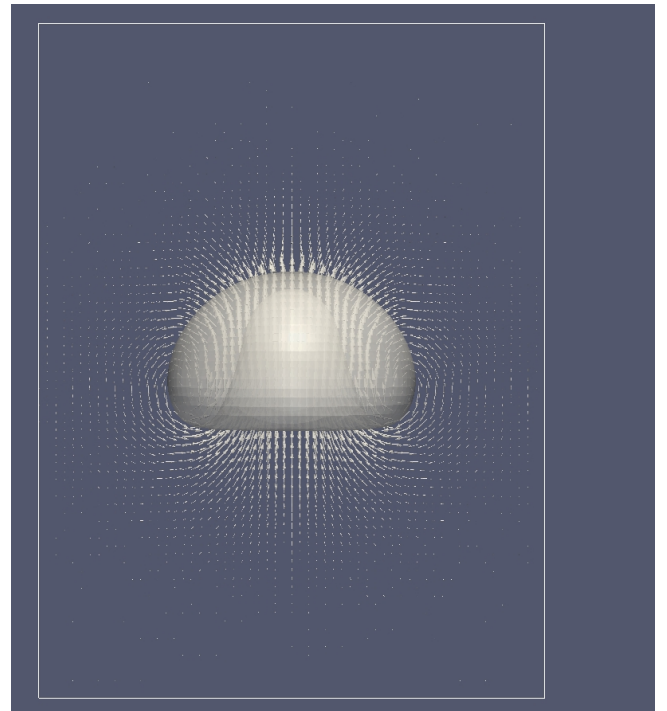Figure 1: Rising Bubble at $t = 0.00sec$, level set function contour
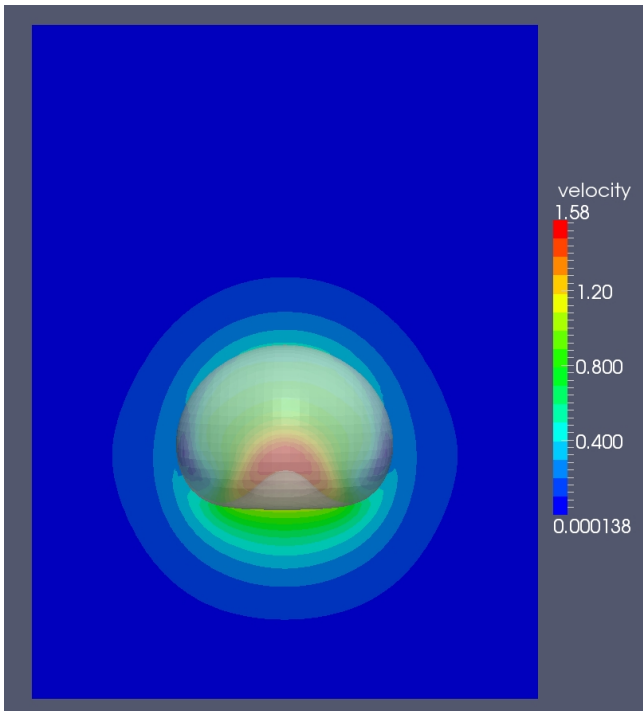

Figure 2: Rising Bubble at $t = 0.05sec$, velocity magnitude contour

Figure 3: Rising Bubble at $t = 0.10sec$, velocity vectors
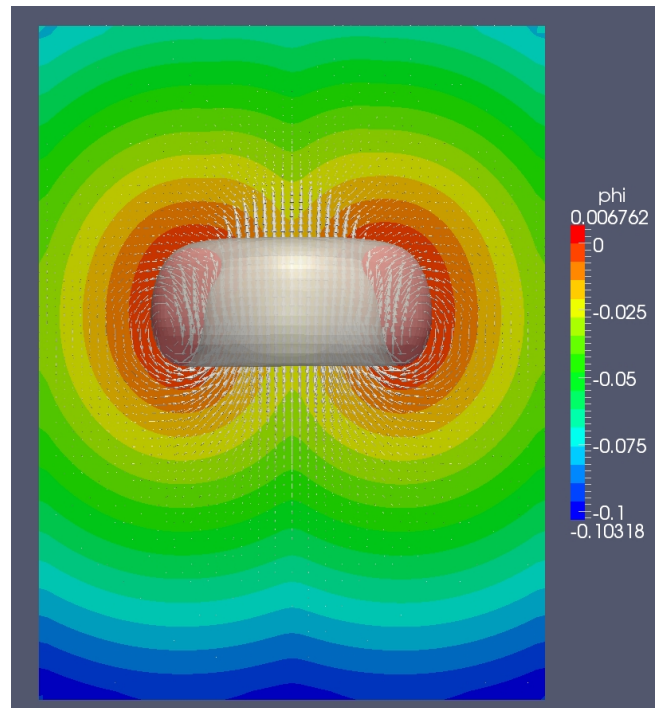

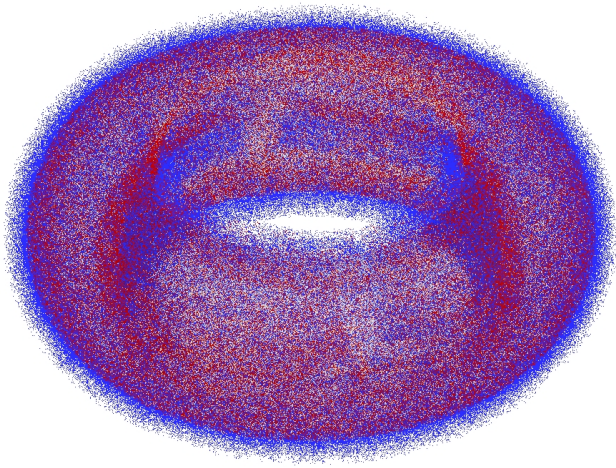Figure 4: Rising Bubble at $t = 0.15sec$, level set function contour and velocity vectors

6

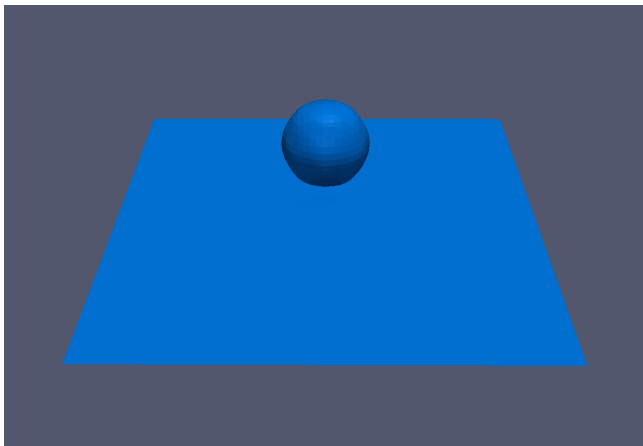Figure 5: Rising Bubble at $t = 0.15sec$, positive (red) and negative (blue) particles
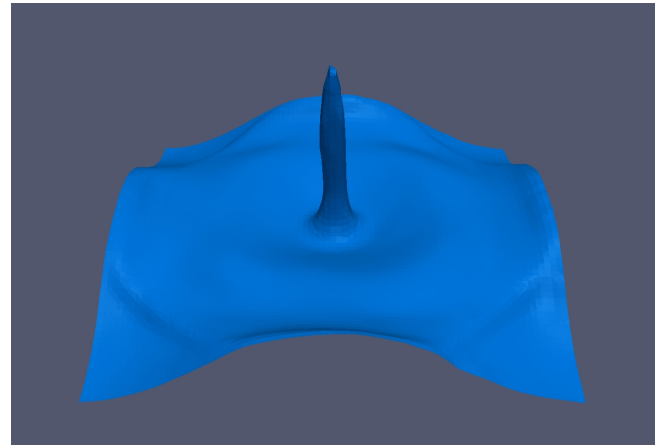

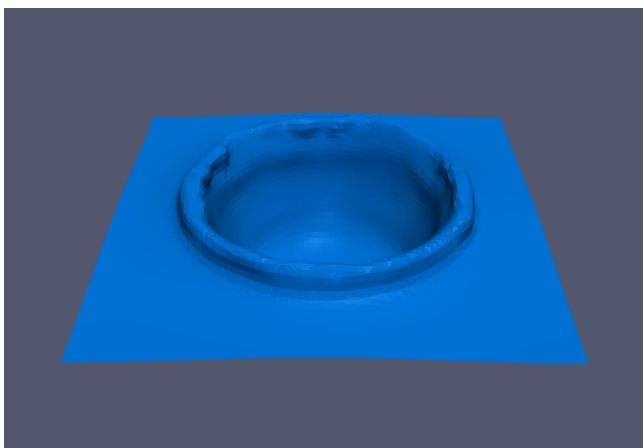
Figure 6: Droplet at $t = 0.00sec$

Figure 8: Droplet at $t = 0.34sec$

Figure 7: Droplet at $t = 0.06sec$

8th International Conference on CFD in Oil & Gas, Metallurgical and Process Industries
SINTEF/NTNU, Trondheim Norway
21-23 June 2011

CFD11-195

ANALYSIS OF SUB-SEA GAS RELEASE BY AN EULERIAN-LAGRANGIAN MODELLING CONCEPT

Paal SKJETNE , Jan Erik OLSEN

SINTEF Materials and Chemistry, 7465 Trondheim, NORWAY

* E-mail: Paal.Skjetne@sintef.no

ABSTRACT

A modelling concept for analysing the fate of a sub-sea gas release is presented. The concept is based on a coupled Eulerian-Lagrangian method. The gas bubbles are modelled and tracked as particles in a Lagrangian discrete phase model. The continuous water and atmospheric gas are covered by an Eulerian VOF model. The model accounts for compressible gas effects, bubble size, gas dissolution and is fully transient. It compares well with experiments performed in a in a 6x9x8m basin from a release depth of 7m. The concept is applied to a set of release scenarios and the results are presented.

Keywords: CFD, sub-sea gas release, bubble plume, oil & gas, Lagrangian.

NOMENCLATURE

Greek Symbols
ρ Mass density, [kg/m^3].
μ Dynamic viscosity, [kg/m.s].

Latin Symbols
A surface area [m^2]
d bubble diameter [m]
F force [N]
g gravity [m/s^2]
J mass flux [kg/m^{2}s]
k mass transfer coefficient
M molar mass [g/mol]
m mass transfer rate [kg/s]
n solubility []
t time [s]
u velocity, [m/s]
Y mass fraction []

Sub/superscripts
b bubbles
D drag
L lift
TD turbulent dispersion

Acronyms
VOF volume of fluid
DPM discrete phase model
CFD computational fluid dynamics
HSE health safety and environment
PRESTO pressure staggering option
PISO pressure-implicit with splitting of operators

INTRODUCTION

Several incidents of sub-sea gas release in the past years have underlined the need for improved knowledge about sub-sea release of hydrocarbons. Sub-sea release of gas poses a threat to the safety of operations, integrity of assets and safety of third parties operating offshore. As the number of sub-sea installations and pipelines increase, the risk of potential faults will also increase. In order to perform risk assessments it is important to understand the qualitative behaviour and to make reliable quantitative estimates of how the gas will surface. Since quantitative descriptions of sub-sea gas releases do not exist and performing realistic experiments offshore would be prohibitively expensive, quantitative models have been identified as interesting research tools.

Traditional integral methods (Fanneløp and Sjøen 1980, Yapa and Zheng 1999 and Johansen 2000) provide a good representation of the rising bubble plume if the model coefficients are tuned properly. However, the method does not yield any results on the surface behaviour, which is a major limitation since this is where the plume will interact with offshore structures, floating installations and ships. Multiphase computational fluid dynamics (CFD) provides greater generality since it is more fundamental and can, in principle, provide information on both the bubble plume and the surface behaviour. The authors have demonstrated that a 3D transient multiphase CFD model can be applied to the study of the ocean plume and the free surface behaviour (Cloete, Olsen & Skjetne, 2009). Here we employ the model to investigate the dynamic behaviour of bubble plumes with different release rates released from different depths. Where possible we compare the results with anectodial data from offshore incidents. These results are applicable as boundary conditions for companies performing HSE analysis of fire and explosion hazards related to the atmospheric dispersion of the surfacing gas.
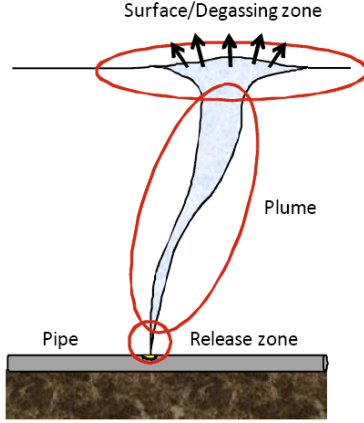
Figure 1: Schematic of sub-sea gas release

MODEL DESCRIPTION

By coupling the discrete phase model (DPM) which describes moving particles, bubbles or droplets with the volume of fluid model (VOF) which governs the behaviour of continuous fluids and the interface between them, it is possible to quantitatively describe a sub-sea gas release. The coupled DPM and VOF model was originally developed to study mixing in gas stirred ladles (Cloete, Eksteen & Bradshaw, 2009). It was subsequently extended to study the bubble plumes originating from a sub-sea gas pipe rupture (Cloete, Olsen & Skjetne, 2009). The model is designed to study systems of bubble plumes which potentially carry enough momentum to influence the shape of the free surface. The atmospheric air and sea water are treated as Eulerian phases who interact with each other at the surface, while the gas bubbles in the plume (see Figure 1) are described as Lagrangian particles interacting with the Eulerian phases through momentum source terms.

The continuous phases, i.e. air above the surface and water below the surface, is mathematically described by the VOF model which is a modified single fluid Eulerian-Eulerian mixture model where a single set of governing equations is shared between different phases. The VOF model solves for conservation of mass and momentum with a momentum contribution from the gas bubbles. Turbulence is modelled by the standard k-ε turbulence model with default model constants (Launder & Spalding, 1972). Solving the continuity, momentum and turbulence equations is standard for the mixture model. The distinction of the VOF model, however, is that it places strong emphasis on accurate tracking of the interfaces between various phases that might be present in the domain.

Since the VOF model does not track bubbles at an "affordable" grid resolution, the DPM is used for the bubble plume. The DPM model is a highly efficient method of tracking the bubble plume of dilute and moderately dense plumes. The DPM model tracks discrete particles through the domain in the Lagrangian sense by implementing a force balance over each particle:

$$\frac{d\mathbf{u}_b}{dt} = \frac{\mathbf{g}(\rho_b - \rho)}{\rho_b} + \mathbf{F}_D\left(u - u_b\right) + \mathbf{F}_{VM} + \mathbf{F}_L + \mathbf{F}_{TD} \qquad (1)$$

Equation 1 equates the particle acceleration to the influences of buoyancy, drag, virtual (or added) mass, lift and turbulent dispersion. The influence of lift and virtual mass is normally insignificant for the phenomena of interest. Drag is calculated based on the universal drag law of Kolev(1994) which account for the size and shape of the bubbles and the swarm effect from the neighbouring bubbles. The particle motion is influenced by the velocity of the continuous phases since the velocity, *u*, of these phases are present in the drag term. Thus we have a two-way coupling between the Lagrangian bubbles and the continuous phases.

The bubble density is based on the ideal gas law and is thus updated as the bubbles moves upwards due to changes in the hydrostatic pressure seen in the surrounding VOF phases. This is picked up by the bubble size model which is mainly governed by the local turbulence dissipation. For the gas rates studied, bubble break up is dominating. A more thorough model description, including the bubble size model, is provided in the aforementioned articles (Cloete, Eksteen & Bradshaw, 2009) (Cloete, Olsen & Skjetne, 2009). The model was validated against experiments conducted in a 7 meter deep water basin, and the model compared well with the experiments. This is seen in Figure 2.

At larger depths the effect of gas dissolution becomes more important. This mass transfer effect is accounted for by the following expression (Olsen,Cloete & Skjetne, In press):
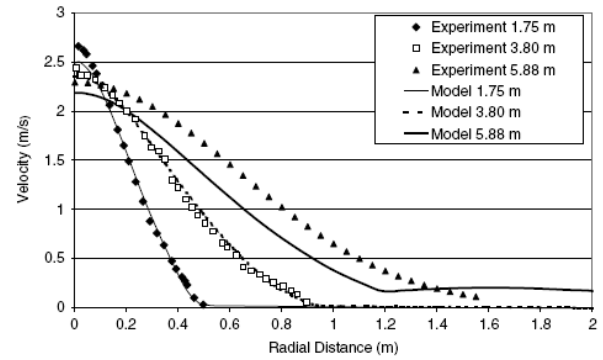

Figure 2: Theoretical and experimental plume velocities at three different basin heights at a flow rate of 170 Nl/s.
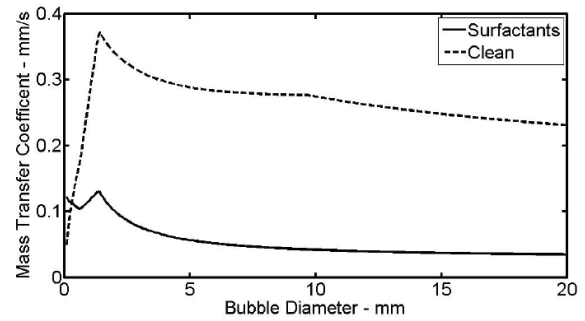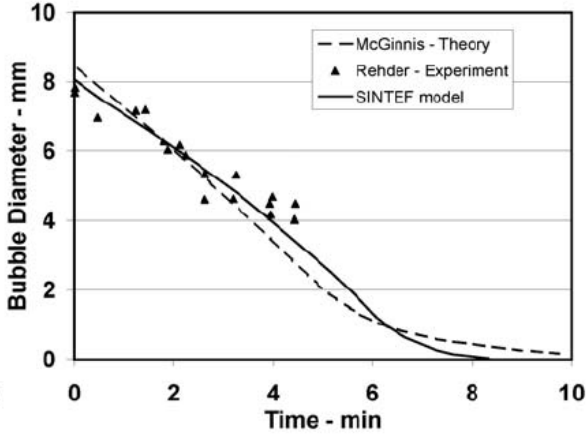

Figure 3: Mass transfer coefficient for methane bubbles with clean and contaminated surface.

$$(1)$$

Figure 4: Evolution of bubble size from methane bubbles released at 479 m with sea conditions as in Monterey Bay during experiments of Rehder *et.al.*

$$\dot{m} = A_b J = \pi d^2 k_{CH_4} \rho_{H_2O} \left(n_{CH_4}^{sol} \frac{M_{CH_4}}{M_{H_2O}} - Y_{CH_4}^w \right) \qquad (2)$$

Here we assume that the gas of interest is methane (CH4) which is the dominating component in natural gas. Expressions for the mass transfer coefficient and solubility of methane are available in the literature and discussed by Olsen et.al. (in Press). An unresolved issue is whether surfactants are influencing the mass transfer coefficient or not. Surfactants will contaminate the bubble surface and make the bubbles act more like rigid bubbles with a slower mass transfer. This is seen in Figure 3 where the mass transfer coefficient is plotted for different bubble sizes rising with the corresponding terminal velocity. Due to this unresolved issue, expressions for both clean and contaminated bubbles are implemented in the model. Results from experiments conducted on single bubbles of methane released at great depths in the Monterey Bay are available for validation (Rehder et.al, 2002). The implemented model for mass transfer from clean bubbles compares well against these measurements on single bubbles released in deep waters as seen in Figure 4. McGinnis et.al.(2006) where also able to match these results by theory, but this was not a transient 3D model. This does not confirm that the clean bubble assumption is valid for a real case scenario where an intense bubble plume may stir up bottom sediments or be co released with produced oil. However, it serves as verification that the model is implemented correctly. In this work we have chosen to apply the mass transfer model of a contaminated bubble since this will result in a lower mass transfer rate and give a higher mass flux at the sea surface. With respect to the resulting hydrodynamic loads, fire and explosion hazards close to the bubble plume this will serve as a conservative assumption.

In a realistic bubble plume there will be trillions of bubbles present. It is not practical to track all of these bubbles. To remedy this, the method tracks groups of bubbles in an item known as a parcel. All bubbles in a parcel have the same density, size and velocity. By doing so, the method becomes computationally affordable.

The model is implemented in Fluent 6.3 with a set of user defined functions. Unsteady particle tracking is applied to the Lagrangian bubbles (DPM) which has a two way coupling with the Eulerian continuous phases. The interface tracking of the VOF model is carried out by the Geo-Reconstruct scheme and the implicit body force formulation is activated to improve model stability under the gravity field imposed. Simulations of sub-sea gas release are carried out with a first order transient solver at higher order discretization in the spatial dimensions. For pressure discretization we use the PRESTO! scheme, and for continuity, momentum and turbulence equations we used the second order upwind scheme. For pressure-velocity coupling, the PISO scheme was used.

Table 1: Overview of cases investigated.

Depth ↓	Release rates [kg/s]				
	10	30	100	300	1000
30m	x		x		x[1]
65m		x		x	
100m	x		x		x
300m		x		x	
400m	x[2]		x		x

[1]Spouting plume. [2]All gas is dissolved into ocean, plume does not surface.

RESULTS

In this study we have investigated the dynamics resulting from releases from five depths and six constant release rates. The cases are summarized in Table 1. In most real applications the mass rate of gas will be highly transient, starting with a high initial peak and dropping off quickly towards an almost constant rate. However, the aim of this study is not to investigate a specific release scenario but rather the general dynamics of sub-sea gas releases. In categorizing the dynamics of large scale bubble plumes we distinguish between transient and steady state plume dynamics. We refer to the dynamics from the initialization of the sub-sea gas release until (quasi) steady state conditions are reached in the surface region as transient and after this period for steady state.

An impulsively started release of gas will form a jet close to its source, and in this region the flow is dominated by inertia. The detailed dynamics of this region is poorly understood due to limited amounts of experimental data at relevant release rates. The thrust of this gas jet will interact strongly with its source and could influence the integrity of the source. At the interface between the liquid and gas jet, liquid fragments and droplets will be entrained into the jet and gradually the jet changes character until all the gas is dispersed as bubbles in a liquid continuous phase. Once this transition has taken place buoyancy will dominate the flow. This is the buoyant jet that is commonly known as a bubble plume (see schematic in Figure 1). For a starting plume, gas will feed into a cap region at

the advancing upper edge of the plume. The motion of this gas cap is retarded due to drag between the cap and stagnant ocean waters. The acceleration of the water through interfacial drag tends to slow the rising plume and spread the cap laterally. Once the rising cap gets close to the ocean surface, the entrained water cannot follow the gas into the atmosphere and will be diverted radially outwards in the horizontal surface plane. This "stagnation flow" towards the free surface will influence the area over which the gas surfaces since the liquid flow will drag the dispersed gas bubbles radially outwards from the plume axis. Furthermore, the buoyancy of the gas and the momentum of the entrained liquid will determine the "stagnation pressure" on the plume axis at the position of the undisturbed free surface. This stagnation pressure will be larger than the atmospheric pressure and result in an elevation of the ocean surface. The hydrostatic head of this elevation will be equal to the difference between the "stagnation pressure" and the atmospheric pressure. Thus, there is

no danger of loss of buoyancy for any vessel or installation being affected by a subsea release. Had there been a loss of hydrostatic pressure in the region of the plume this would have been compensated by sea water instantly flowing along the pressure gradient towards the plume axis. This argument discredits the famous "Bermuda Triangle" hypothesis that giant bubble plumes have sunk ships due to loss of buoyancy. However, several incidents have shown that the surface dynamics of bubble plumes are indeed able or have the potential to sink both vessels and installations. A number of factors influence the area over which the gas surfaces. However we find that rate and depth are the most important parameters. A well developed steady state release is shown in Figure 5.
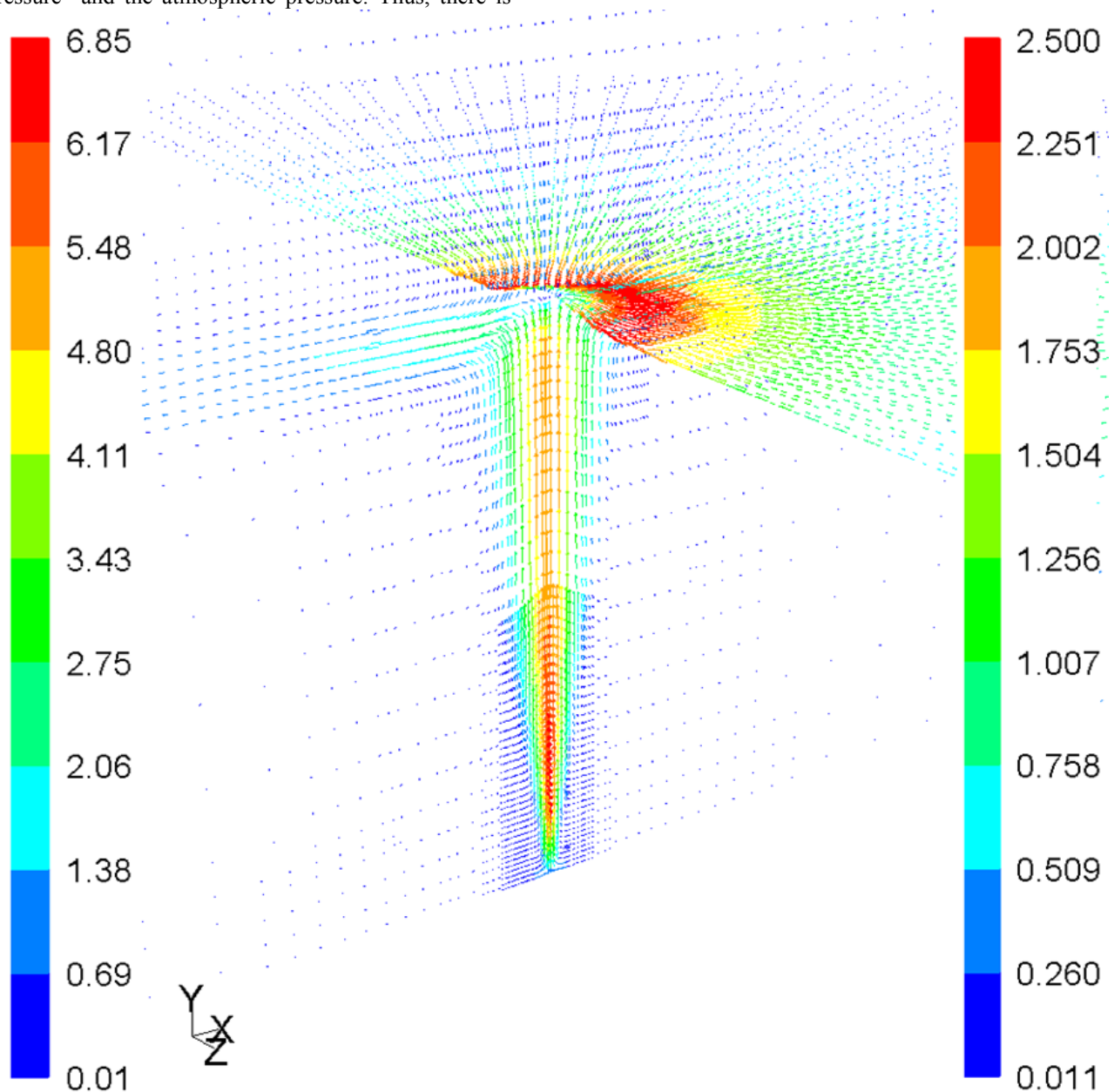

Figure 5: A cut plane through the plume axis showing the liquid velocity vectors, and the velocity vectors of the liquid at the sea surface. Legends show velocity magnitude; Left legend is valid for the vertical cut plane and the right legend is valid for the sea surface.

Transient plume characteristics:

We investigate the following characteristics of the transient surface plume; surface flux, surface flux profile, radius of surface flux profile, rise time, rise velocity and finally mass transfer from plume to ocean by the time it breaks the surfaces.

In Figure 6 (top and middle charts) the plume rise time and rise velocity is plotted against the "average release rate", i.e. the release rate when correcting for total mass transfer to the ocean before the plume surfaces. We use this quantity since it gives a more correct measure of how much buoyancy is in the plume as it surfaces. This is especially true for releases from large depths where mass transfer starts to dominate. The fraction of the released gas that has been dissolved into the sea water at the time when the plume breaks the sea surface is shown in the bottom chart of Figure 6. In the top chart of Figure 6 the rise time of starting plumes are plotted as a function of release rate. The different curves correspond to different release depths. As expected the rise time depends on the release depth (the distance the gas needs to ascend through the water column) and the release rate (the momentum available to accelerate the entrained water).

Deep plumes will loose some of their buoyancy due to dissolution of gas into the sea water. Thus we also plot the average rise velocity as a function of the "average release rate" in the middle chart of Figure 6. Although the data does not fall onto a well defined master curve, a clear trend can be seen. The deep releases exhibit a much lower low rise velocity than the shallow releases. This can be attributed to the fact that these plumes loose a large percentage of their buoyant momentum source due to mass transfer (bottom chart Figure 6). Furthermore, they need to accelerate a much larger body of sea water before reaching the surface. An additional factor contributing to this is gas expansion. Gas expansion is insignificant for most of the ascending distance for deep plumes, whereas it is very prominent for the full rise length for shallow plumes, e.g. if one considers a release from 70m depth the gas will see a volume increases by 14%, 17%, 20%, 25%, 33%, 50% and 100% for every 10m until it reaches the surface. So by the time the gas reaches the surface it has increased its volume eight times. For a release from 400m the gas will have expanded to forty times its original volume by the time it reaches the sea surface. However, from 400m to 70m depth it will only expand five times, although this distance makes up just over 80% of the rise distance.

Next we turn our attention to the characteristics of the surface flux. Running averages of the total surface flux (averaged over periods of one second) are shown in Figure 7. As can be seen no peak in surface flux is observed for the release from 65m depth, whereas for the same release rates from 300m depth a clear peak is seen. Table 2 shows what cases exhibit a peak in surface flux and which do not. As can be seen from the table releases from 100m depth define a transition between the two regimes. A further investigation into the characteristics of the plumes at the time they surface show that the plumes that exhibit a peak in the surface flux profile have lost more than 20% of their mass due to gas dissolving into the sea water. Where

the dividing line should be drawn is not clear from the data but we hypothesise based on the data in Table 3 that the transition takes place when between 15 and 20% of the total plume mass has been dissolved. Also, note that the surface flux, either it peaks or not, never exceeds the actual release rate.
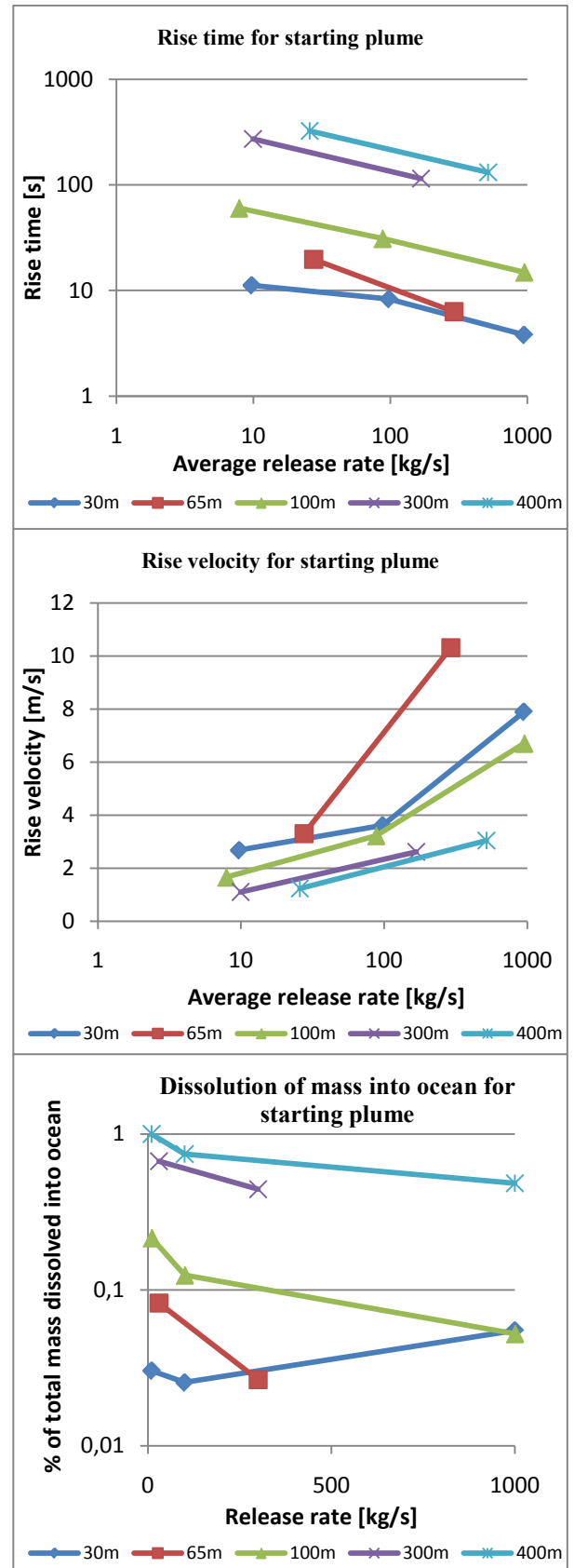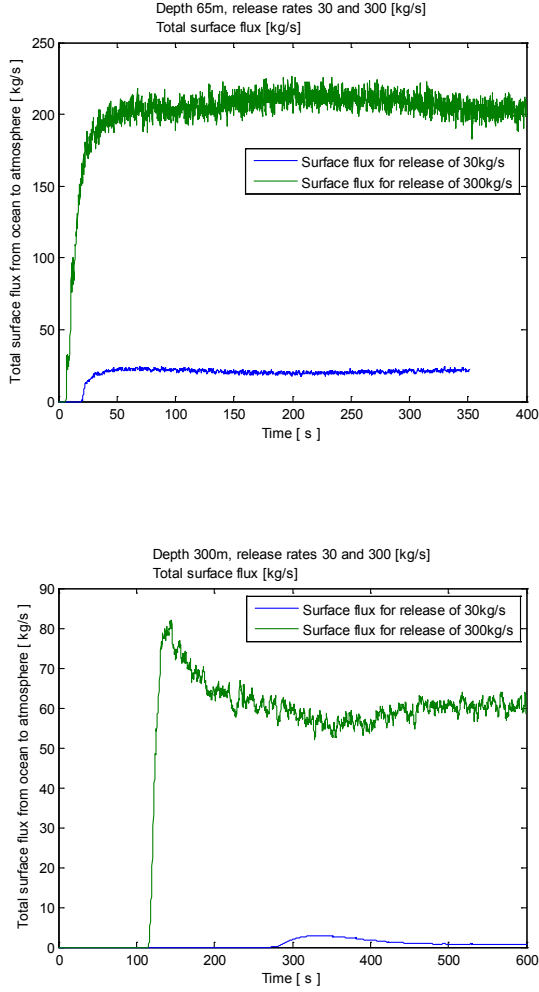

Figure 6: Rise time (top) and rise velocity (bottom) for a starting plume.

Figure 7: The surface flux as a function of time from release. Top: release from 65m. Bottom: release from 300m.

**Table 2:** Does surface flux exhibit a peak?

Depth ↓	Release rates [kg/s]				
	10	30	100	300	1000
30m	NO		NO		?
65m		NO		NO	
100m	YES		NO		NO
300m		YES		YES	
400m	N/A		YES		YES

Table 3: Fraction of released gas that has been dissolved into sea water when the plume surfaces. Steady state values are shown in parentheses. Fractions given in %.

Depth ↓	Release rates [kg/s]				
	10	30	100	300	1000
30m	3 (11)		3 (23)		5.5
65m		8 (31)		3 (33)	
100m	22 (49)		12 (35)		5 (36)
300m		67 (98)		44 (80)	
400m	100		74 (99)		48 (80)

We now proceed to investigate the evolution of the zone of "visible gas" at the surface. Since even small amounts of dispersed gas bubbles will easily be identified at the surface we define this zone as the area

with a non-zero surface flux of gas in our simulations. Figure 8 shows the evolution of the surface radius of the plume. It is very difficult to measure the surface flux in an experiment due to interactions between the surface and the atmosphere. However it is easy to see and characterize the zone of "visible gas" which is the region where gas bubbles can be seen near the surface.
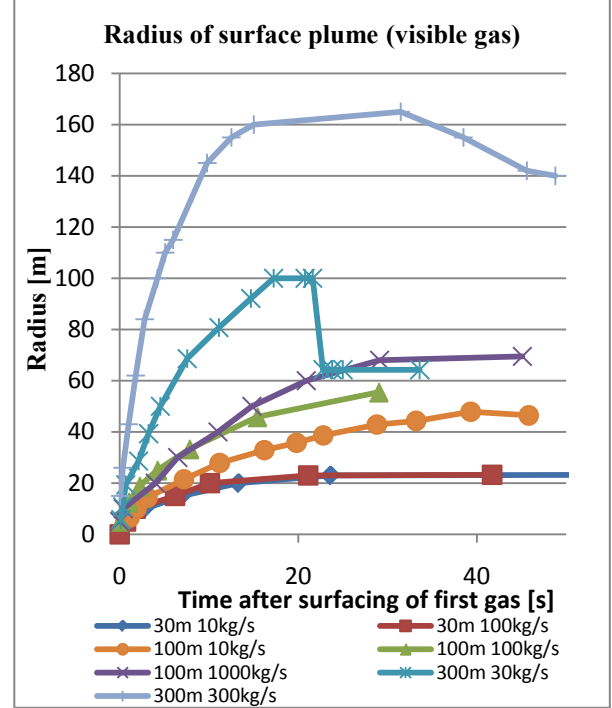
Figure 8: Evolution of the radius of the surface plume where dispersed bubbles would be seen (the radius of the degassing zone). The time scale for the 300m 30kg/s and 300kg/s releases has been divided by 10.

As can be seen the plume radius seems to increase asymptotically towards a steady state value. The time scale for reaching this asymptotic value will depend on depth, as will the radius itself. By normalizing the time with the actual rise time for a given release rate it becomes clear that some of our simulations had not fully reached a steady state. Notice that if the surface flux exhibits a peak, so too will the surface radius.

The data presented in this paper can be used as boundary conditions for studying atmospheric dispersion resulting from sub-sea gas releases. For steady state conditions one would typically be interested in the amount of gas being released into the atmosphere, over how large an area gas is released and how the surface flux is distributed over this area. Figures 7 and 8 show examples of the evolution of the total flux and the area over which the gas is being released. Figure 9 shows how the surface flux profile over the release area changes with time from first gas towards steady state. Figure 9 shows this development for a 30kg/s release from 300m. Notice the transition from a top hat profile at 300s, through a profile with a Gaussian core with heavy tails at 400s and 450s towards a pure Gaussian profile at steady state around 600s. The points represent the surface flux projected onto a vertical plane going through the centre of the plume.
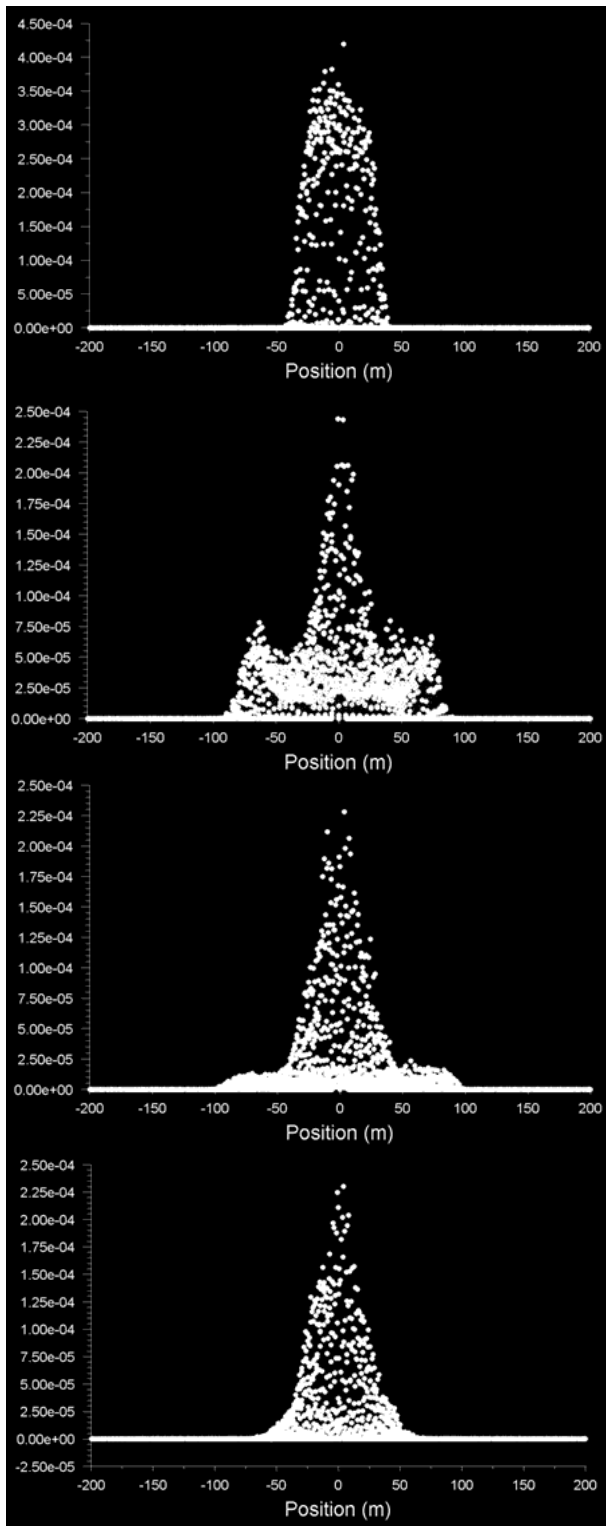
Figure 9: Development of the surface flux profile. Time from top to bottom; 300, 400, 450 and 600 seconds, respectively.

As mentioned previously the dynamic head of the plume will have the capability to lift the free surface of the ocean. In a time averaged sense this will form a fountain around the plume axis and the fountain height will go through a maximum just after the first gas surfaces. This maximum is due to the formation of the rising plume cap (lead bubble cloud). The top and middle chart of Figure 10 shows the trace of the maximum fountain height for depths of 30 and 400m. The maximum fountain height for all cases is show in the bottom chart of Figure 10.
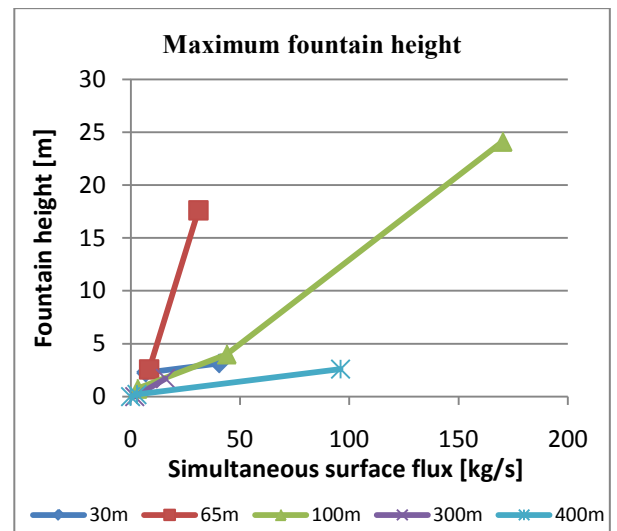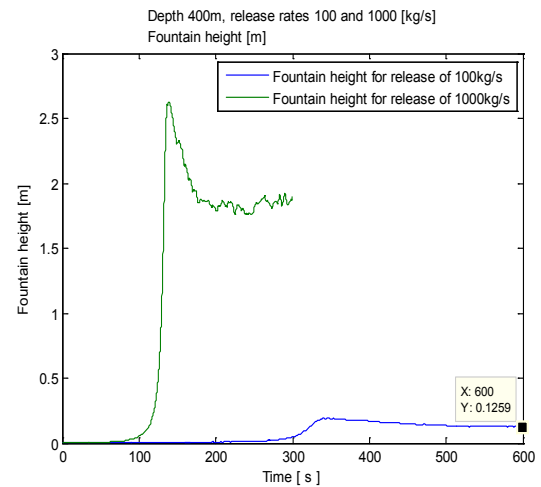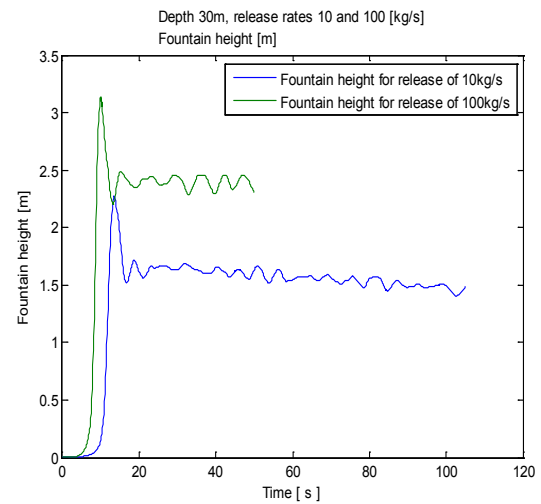

Figure 10: Top and middle: Maximum fountain height of plume versus time. Bottom maximum fountain height versus simultaneous surface flux.

Notice how the fountain heights are almost identical for 10 and 100kg/s from 30m depth compared to the 1000kg/s release from 400m depth. We will return to this observation when we discuss the steady state results.

Steady state plume characteristics:

We now turn our attention to some steady state characteristics of these bubble plumes. We investigate; radial velocity profiles in and near the surface, maximum velocity at the surface, steady state mass transfer into the ocean, steady state surface flux, radius of surface plume and fountain height.

The transient characteristics of the plumes only lasts a short period before the dynamics settle into a steady state. As can be seen from Figures 7 and 10 (top and middle charts), the transient is roughly twice the rise time of the plume. Thus as can be seen from the top chart in Figure 6, shallow releases have a transient period consisting of a few tens of seconds, whereas deep releases are in the order of several minutes. This can be understood quite simply by considering that the transient is equal to the time it takes for the first gas to reach the surface plus the time needed for the radial surface flow to propagate far enough in the radial direction so that its velocity is e.g. small or comparable to the rise velocity of bubbles.

For an idealized surface flow the surface velocity magnitude will be inversely proportional to the distance from the plume axis this is illustrated in. Figure 11. In the same figure the radial velocity profile 10 and 20 m below the surface is also plotted. It is this surface shear flow that poses a hazard for vessels, equipment and installation at the surface through the generation of forces and torques on these objects. This is especially true if the objects are physically moored to the sea bottom since this will constrain the response/motion of the objects at the sea surface.

The maximum surface velocity (always found close to the plume axis) at steady state for all cases investigated are plotted in Figure 12. The results are plotted as a function of the steady state surface flux, since this is a good measure of how much buoyant momentum is carried by gas in the surface layer. It should be noted that the horizontal axis is given on a logarithmic scale. In order to conclude weather the surface velocity is approaching a limiting value or not more data would be needed, preferably also at higher rates, e.g. 10000kg/s.

The total mass transfer to the ocean per second is reported as a percentage of the release rate in Figure 13, and listed in parentheses in Table 3. This plot clearly illustrates that deep plumes indeed loose most of their gas to the ocean through dissolution. The reason for this is simply that sea water in most cases is under saturated with gas, and thus has a large capacity to dissolve gas. The long contact time between the gas and the sea water thus facilitate mass transfer for deep plumes. It should be noted that mass transfer not only takes place in the vertical plume region, but also to a substantial degree in the surface region beneath the surface plume. For shallow releases it seems the mass transfer might increase with the release rate. For deep releases it seems the mass transfer goes down with increasing release rate. This can be understood from a saturation point of view. At some point the plume core will not see the background ocean, and thus the entrained water in this core will be saturated with gas. For intermediate releases the transfer rate seems to be roughly constant over the range of rates investigated.
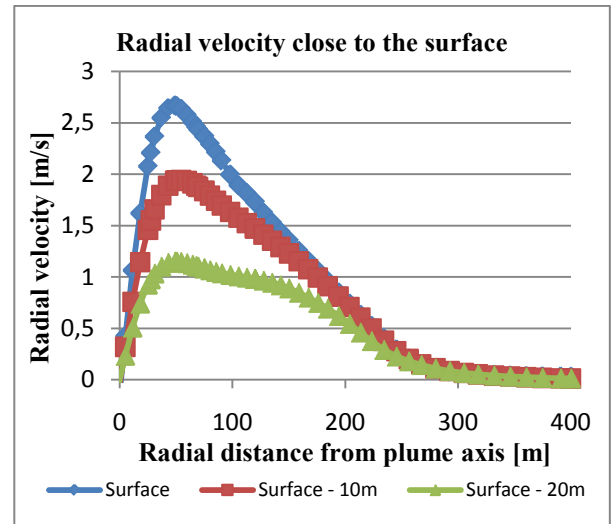

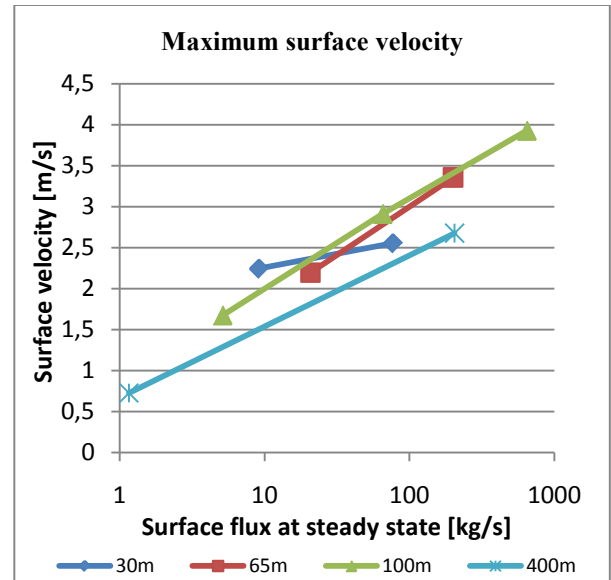**Figure 11: Surface velocity profile for 100m 1000kg/s.**

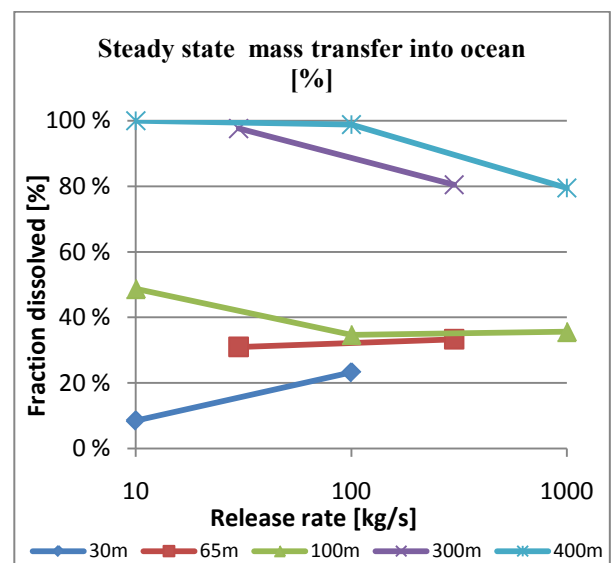**Figure 12: Maximum liquid velocity at ocean surface.**

Figure 13: Relative mass transfer of gas (methane) into ocean, assuming a sea temperature of 5C at steady state conditions.

As mentioned earlier the results in this paper can be used as boundary conditions for investigations of atmospheric dispersion of methane for estimation of fire and explosion hazards in the area surrounding the surface plume. The resulting steady state surface flux is shown in Figure 14. The surface profiles have a Gaussian shape.

Figure 15 shows the variation of the surface plume radius. This is an interesting figure. It shows that although the deep plumes transfer most of their gas to the sea water, and give the lowest surface fluxes (Figure 14) they nevertheless give rise to the widest surface plumes. Although most of the gas has dissolved into the sea water, the gas has managed to impart a substantial amount of its buoyancy to the liquid before being dissolved. Thus, this liquid will continue to rise with the plume and must be diverted at the surface giving rise to a wide surface plume although most of the gas has been dissolved and the resulting surface flux is low.

This observation could have important practical applications. Based on visual observations of a surface plume one make a qualitative estimate what depth a leak on e.g. a riser originates if the following parameters are known: surface radius and release rate.

The last quantity we investigate is the steady state fountain height plotted in Figure 16. The fountain height will be a time varying quantity. Here it is reported as the maximum vertical position of the ocean surface as described by the VOF model at the time the simulation was terminated. It is again plotted as a function of the steady state surface flux. As can be seen it is a strong function of the surface flux as would be expected. Recall that the surface radius was not a strong function of the surface flux. Furthermore, it is observe that the ratio between the steady state and maximum fountain height is on average approx 1.8±0.4.

CONCLUSION

The proposed CFD model has previously been compared against known experimental data (Cloete, Olsen, Skjetne 2009), and has in this work been used to investigate plume dynamics from five different depths and release rates of interest to the oil and gas industry. Simulations were robust but time consuming for some of the deep cases (taking several days to complete on an 8 core workstation). Substantial effort was also needed to post process data.

The CFD model has shown that the resulting plume dynamics is rich and not always intuitive when mass transfer is important. In fact the selected rates and depths span such a wide range of dynamics that it is difficult to draw any general conclusions without performing a substantially larger number of simulations. However, in general terms we can outline three dynamic regimes based on the simulation matrix outlined in Table 1:

1. Shallow depth releases dominated by volume expansion of the gas
2. Intermediate depth releases where volume expansion competes with mass transfer
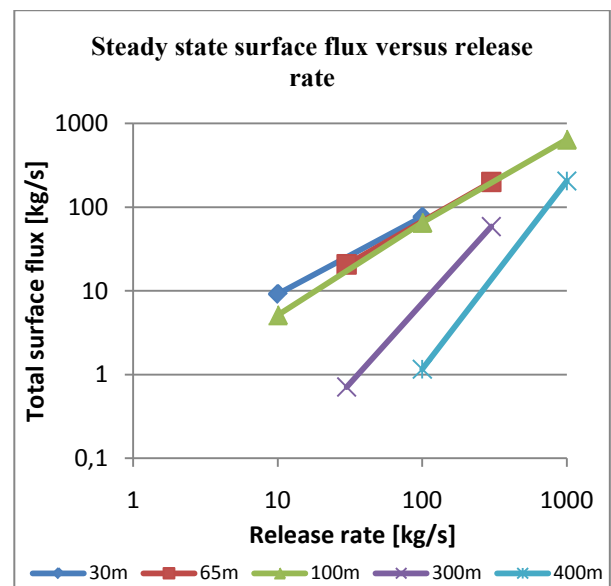3. Deep/large depth releases where mass transfer dominates

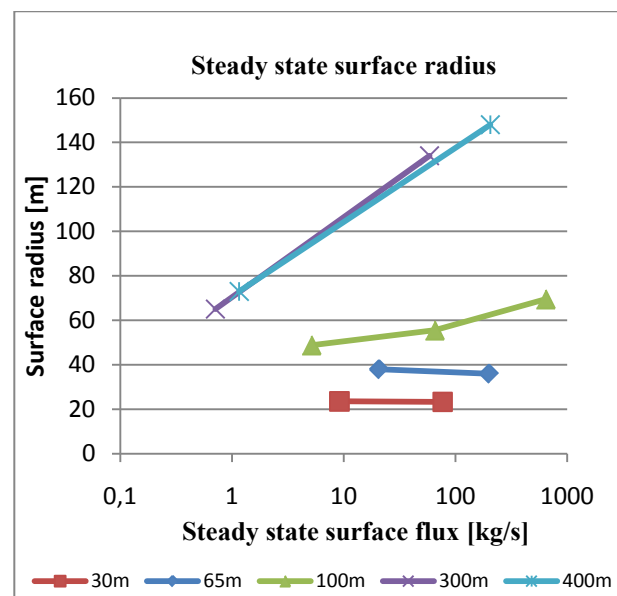**Figure 14: Steady state surface flux versus release rate.**

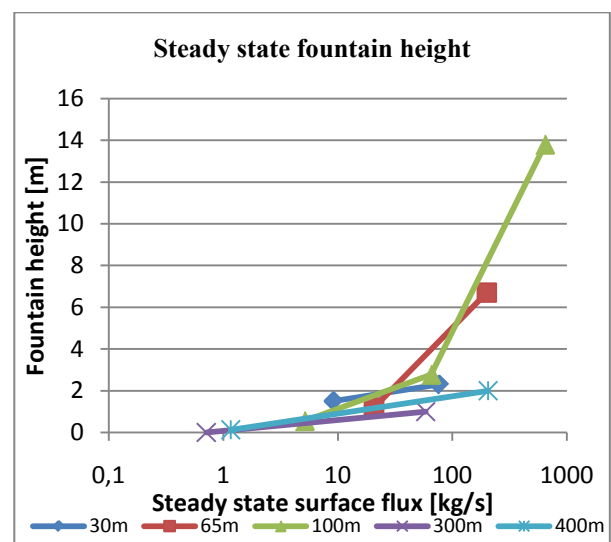**Figure 15: Steady state surface radius versus surface flux.**

Figure 16: Steady state fountain versus surface flux.

In this work we have mainly focused on the resulting surface dynamics. Among the transient features of plume dynamics the model has revealed that;

- The rise velocity decreases with increasing release depth.
- The surface flux never exceeds the source mass flux.
- Weather a peak is observed in the surface flux seems to depend on how much of the plume mass has been dissolved into the liquid phase. Only starting plumes that have lost more than 20% of their total mass as the plume surfaced exhibited a peak in the surface flux.
- Cases that exhibit a peak in surface flux also exhibit a peak in surface radius.
- The surface flux profile starts out as a top hat profile which progresses to a Gaussian profile at steady state.

Among the steady state features the model predicts;

- Deep plumes experience substantial mass transfer to the liquid, but the resulting plume radius seems not to be strongly affected by this.
- The surface flux and fountain height are strong functions of the surface flux.
- Strong shear flows are formed in the surface region.

The surface flux rates and surface radii found in this work can be used as boundary conditions for calculations of atmospheric dispersion of flammable methane.

The model has clearly shown how different the dynamics are for flows that are dominated by gas expansion are from those that are dominated by mass transfer. This means that small to meso scale (~1-10m) laboratory experiments cannot be used to develop general scaling rules for large scale releases (~100m). Thus in order to validate models there is a need for large scale validation data.

CFD seems to be a promising tool to explore the varied dynamics of such large scale bubble plumes. CFD is able to capture characteristics that are outside the reach of classical integral models for bubble plumes. They also offer attractive features for coupling with oceanographic data/models.

REFERENCES

CLOETE,S., EKSTEEN,J.J, and BRADSHAW ,S.M.(2009) "A Mathematical Modelling Study of Fluid Flow and Mixing in Full Scale Gas Stirred Ladles", *Progress in Computational Fluid Dynamics*

CLOETE,S., OLSEN,J.E. and SKJETNE,P.(2009)."CFD modeling of plume and free surface behavior resulting from a sub-sea gas release." *Applied Ocean Research*, **31**, 220-225

FANNELØP, T. K. and K. SJØEN (1980) "Hydrodynamics of Underwater Blowouts." AIAA(Paper No. 80-0219).

JOHANSEN,Ø. (2000) "DeepBlow – a Lagrangian plume model for deep water blowouts", *Spill Science & Technology Bulletin*, **6**, 103-111.

KOLEV,N.I.(1994) Multiphase Flow Dynamics 2: Thermal and Mechanical Interactions. Springer, Berlin, Germany, 2nd edition edition 2005

LAUNDER,B.E. and D.B. SPALDING (1972) *Lectures in Mathematical Models of Turbulence*. London: Academic Press

McGINNIS,D.F., GREINERT,J., ARTEMOV,Y., BEAUBIEN,S.E. & WÜEST,A.(2006); Fate of rising methane in stratified waters: How much methane reaches the atmosphere, *Journal of Geophysical Research*, **111**

OLSEN,J.E., CLOETE,S. & SKJETNE,P (In press) CFD modeling of sub-sea gas release and the dissolution of gas, submitted to *Applied Ocean Research*

REHDER,G., BREWER,P.W., PELTZER,E.T. & FRIEDRICH, G. (2002)."Enhanced lifetime of methane bubble streams within the deep ocean", *Geophys.Res.Lett.*, **29**(15),1731, 2002

YAPA,P.D. & ZHENG,L. (1999) "Modelling underwater oil/gas jets and plumes", Journal of Hydraulic Engineeering, ASCE **125**(5), 481-491

ACCNOWLEDGEMENTS

Technology for a better society
www.sintef.no